Fatigue & Fracture Mechanics:

33rd Volume

EDITORS:
Robert S. Piascik
and Walter G. Reuter

ASTM INTERNATIONAL
Standards Worldwide

STP 1417

STP 1417

Fatigue and Fracture Mechanics: 33^{rd} Volume

Walter G. Reuter and Robert S. Piascik, Editors

ASTM Stock Number: STP1417

ASTM International
100 Barr Harbor Drive
PO Box C700
West Conshohocken, PA 19428-2959

Printed in the U.S.A.

ISBN: 0-8031-2899-1
ISSN: 1040-3094

Library of Congress Cataloging-in-Publication Data

Peer Review Policy

Each paper published in this volume was evaluated by two peer reviewers and at least one editor. The authors addressed all of the reviewers' comments to the satisfaction of both the technical editor(s) and the ASTM International Committee on Publications.

To make technical information available as quickly as possible, the peer-reviewed papers in this publication were prepared "camera-ready" as submitted by the authors.

The quality of the papers in this publication reflects not only the obvious efforts of the authors and the technical editor(s), but also the work of the peer reviewers. In keeping with long-standing publication practices, ASTM International maintains the anonymity of the peer reviewers. The ASTM International Committee on Publications acknowledges with appreciation their dedication and contribution of time and effort on behalf of ASTM International.

Printed in Bridgeport, NJ
December 2002

Foreword

The Thirty-Third National Symposium on Fatigue and Fracture Mechanics was held June 25–29, 2001, at Jackson Lake Lodge in Moran, Wyoming. ASTM Committee E08 on Fatigue and Fracture was the sponsor. The symposium co-chairman and co-editors of this publication are W. G. Reuter, Idaho National Engineering and Environmental Laboratory and R. S. Piascik, NASA Langley Research Center.

Contents

Constraint and/or Welds

Fatigue

Overview

The ASTM National Symposium on Fatigue and Fracture Mechanics is sponsored by ASTM Committee E08 on Fatigue and Fracture Testing. The objective of the symposium is to promote a technical forum where researchers from the United States and worldwide can discuss recent research findings related to the fields of fatigue and fracture. The photograph above documents a portion of those who attended the symposium.

The volume opens with the paper authored by Massachusetts Institute of Technology Professor Emeritus Frank McClintock who delivered the Twelfth Annual Jerry L. Swedlow Memorial Lecture. Professor McClintock's presentation provided a description of slip-line fracture mechanics (SLFM) and its application to fracture problems. SLFM is expected to fill some of the gap for materials/conditions where J-integral no longer applies (too much ductility and/or too much crack growth) and plastic collapse.

The thirty-seven papers that follow Professor McClintock's paper are broadly grouped into four categories. These categories include Practical Applications, Constraint and/or Welds, Fatigue, and Assorted Topics.

Practical Applications

The section contains ten papers and starts with a description and discussion of the damage that occurred during the Northridge earthquake. The section includes papers that describe the use of fracture mechanics based techniques developed in Europe to predict structural integrity and papers describing the effects of hydrogen or fatigue on sub-critical crack growth. Three papers provide specific examples of structural problems and the final paper provides a discussion for selecting materials based on structural performance.

Constraint and/or Welds

The section contains nine papers and starts with four papers discussing the effects of constraint. Two papers are concerned with crack-front stress fields. The third paper provides a basis for using plane-strain fracture toughness/constraint to predict the applied stress-intensity factor/constraint and the location around the perimeter where crack growth initiation will occur within a surface crack. The fourth paper uses the T-stress in analyses of fracture toughness data. The following five papers are based on welds. The first paper examines the role of localized plasticity and crack-tip constraint in under matched welds. The second paper examines cleavage fracture in welds, while the third discusses the importance of fabrication history relative to weld fracture and durability. The final papers describe studies of creep-crack growth and the effects of a compressive load when applied to homogenize the residual stresses through the specimen thickness.

Fatigue

The section contains nine papers and starts with the uncertainty of fatigue crack growth rates and the applied stress-intensity factor ranges. The second paper looks at load interactions on the growth of small cracks. The following papers are concerned with mean stress effects on fatigue crack growth rates, the fatigue crack growth mechanisms in alumina at high temperatures, frequency effects, non-planar crack growth, and corrosion fatigue.

Assorted Topics

The section contains nine papers with the first two discussing aspects of crack closure. The next three papers discuss problems related to the ductile-brittle transition zone. The following papers discuss decohesion and crack initiation, crack arrest toughness in ferritic steels, cracks with multiple kinks and an innovative method for measuring fracture toughness.

The technical quality of the papers contained in this STP is due to the authors and to the excellent work provided by the peer reviews. The Symposium organizers would like to express our appreciation to all reviewers for a job well done. Because of the large number of papers, camera-ready manuscripts were used to develop the STP. The organizers of the symposium hope that it meets with your approval.

The National Symposium on Fracture Mechanics is often used to present ASTM awards to recognize the achievement of current researchers. At the Thirty-Third Symposium, the award for the Jerry L. Swedlow Memorial Lecture was presented to Professor Emeritus Frank A. McClintock, Massachusetts Institute of Technology, and the award of Merit was presented to Professor Robert Dodds, University of Illinois, Urbana. The organizing committee would like to congratulate the above award winners as considerable time, effort and hard work were put forth to win these awards.

We would like to end this overview by highlighting the fact that the symposium venue (The Teton National Park) is a special place for Prof. McClintock. Not only has Prof. McClintock climbed these mountains, but also, a mountain peak within the Teton mountain range is named after his father.

Dr. Walter G. Reuter
INEEL
Idaho Falls, Idaho

Dr. Robert S. Piascik
NASA Langley Research Center
Hampton, Virginia

Twelfth Annual Jerry L. Swedlow Memorial Lecture

Frank A. McClintock[1]

Slip Line Fracture Mechanics: A New Regime of Fracture Mechanics

---

Reference: McClintock, F. A., "**Slip Line Fracture Mechanics: A New Regime of Fracture Mechanics,**" ***Fatigue and Fracture Mechanics: 33rd Volume, ASTM STP 1417***, W. G. Reuter and R. S. Piascik, Eds., ASTM International, West Conshohocken, PA, 2002.

Abstract: In accidents some structures should be fully plastic, even during extensive crack growth, to help share the load. *K* and *J* fracture mechanics apply to initial but not extensive growth. Plane strain, rigid-plastic, non-hardening plasticity often gives just two symmetrical slip lines at the crack tip for Mode I; one for mixed mode. These lines are the basis for the new slip line fracture mechanics, SLFM2,1. In SLFM2, the crack tip driving parameters CTDP are the angle of, and the normal stress and slip displacement across, the two slip lines. The response functions of the CTDPs can be taken as the crack tip opening displacement for initiation, $CTOD_i$, and the angle CTOA for growth. SLFM1 has different response functions of only the stress and slip as driving parameters.

Slip line analyses for exact and approximate stress and deformation fields are given for typical specimens that provide data for structures. For structural steels the CTOA is typically 8 to 25°. The relations to *K*, *J*, and FEA are discussed, as are instability and cleavage.

Keywords: Fracture mechanics, fully plastic, slip line, crack tip opening displacement, crack tip opening angle, mixed mode, finite element, linear elastic, elastic-plastic, non-linear elastic, power law, initial crack growth, continuing crack growth, crack path, hole, void, cleavage.

It is an inspiration to be asked to write and present this Professor Jerry L. Swedlow Memorial Lecture. I knew Jerry from his extensive work in fracture and the ASTM. In the late 1960's it was my privilege to collaborate with him on numerical methods for elastic-plastic problems, including work toward the representation of principal stress and strain by oriented vector rosettes. In those days we had trouble finding a common tape format to exchange programs and results. We finally resorted to shipping boxes of punched cards! Slow as that communication was, it was reliable and rewarding.

---

[1]Professor Emeritus, Department of Mechanical Engineering, Room 1-304, Massachusetts Institute of Technology, Cambridge, MA 02139.

Nomenclature

Location of first use is given as being before (b.), after (a.), or within an equation.

Acronyms

CTD_i	b. Eq. 23a	Crack tip displacement for initial crack growth in SLFM1
CTDP	a. Eq. 9	Crack tip driving parameter
$CTOD_i$	b. Eq. 6	Crack tip opening displacement for initial crack growth in SLFM2
CTRF	a. Eq. 9	Crack tip response function
DFCT	a. Eq. 42	Doubly face-cracked plate in tension
EPFM	b. Eq. 1	Elastic-plastic fracture mechanics
FEA	b. Eq. 37	Finite element analysis
LEFM	b. Eq. 1	Linear elastic fracture mechanics
LUB	b. Eq. 34	Least upper bound
SFCB	a. Eq. 42	Singly face-cracked plate in bending (plane strain)
SFCT	a. Eq. 9	Singly face-cracked plate in tension (plane strain)
SENT	a. Eq. 9	Singly edge-notched plate in tension (plane stress)
SLFM1,2	a. Eq. 9	Slip line fracture mechanics with one or two slip planes

Symbols

a	a. Eq. 1	Crack depth
A_2	a. Eq. 41b	Higher order parameter for a J field
a_n	b. Eq. 24	Net ligament dimension
b	Fig. 8	Central constant-state half-thickness (plane strain)
B	b. Eq. 28	Bulk modulus
$c_{,u}$	Eq. 18	Micro-cracking per unit slip in SLFM1,2
d	b. Eq. 9	Differential operator; b. Eq. 33, leg length in a fillet weld
D	b. Eq. 26	Diameter of a pressure vessel
D_{nh}	Eq. 6	Dimensionless $CTOD_i$ function of n_h in power-law stress-strain
E	b. Eq. 3	Modulus of elasticity
F_θ	b. Eq. 24	Circumferential force on a longitudinal section of a pressure vessel
I_{nh}	Eq. 5	Dimensionless function of n_h in power-law stress-strain
J	b. Eq. 4	Scalar coefficient of power-law stress, strain, and displacement fields
L	b. Eq. 24	Length of longitudinal weld in pressure vessel
k	b. Eq. 2	Plane strain shear flow strength
K	b. Eq. 1	Stress intensity factor
M	b. Eq. 33	Bending moment on a web welded to a base plate
n	b. Eq. 9	Unit normal along a path
n_h	b. Eq. 3	Strain hardening exponent in power-law stress-strain; $0 < n_h < 1$
n_ε	b. Eq. 3	Plastic straining exponent in power-law stress-strain; $1 < n_\varepsilon < \infty$
p	b. Eq. 26	Pressure
P	Table 2	Load
Q	a. Eq. 41b	Parameter for normal stress in addition to that from J-distribution
r	Eq. 4	Radius

R	b. Eq. 33	Radius
t	a. Eq. 9	Thickness
T	b. Eq. 2	Stress parallel to the crack in LEFM
TS	a. Eq. 1	Tensile strength
u	b. Eq. 15	Displacement increment or velocities with respect to pseudo-time
$\tilde{u}$	Eq. 4	Normalized displacement function of angle for power-law stress-strain relations
u_s	b. Eq. 17	Shear displacement discontinuity across a slip line
V	b. Eq. 26	Volume of pressure vessel
W	b. Eq. 37	Plastic work per unit volume
x, y	b. Eq. 9	Cartesian coordinate axes
Y	Eq. 32	Flow strength; a function of $\varepsilon_{eq}{}^{p}$
α, β	b. Eq. 10	Curvilinear slip lines of maximum shear stress, and also
	Fig. 8	Their angular coordinates relative to those at point O.
γ	b. Eq. 42	Shear strain $2\varepsilon_{\alpha\beta}$ behind moving slip line
Γ	b. Eq. 9	Path for J-integral
δ	b. Eq. 15	Incremental operator over time
Δ	b. Eq. 33	Difference operator
ε_y	b. Eq. 3	Elastic strain at yield strength, σ_y
$\tilde{\varepsilon}$	Eq. 4	Normalized strain function of angle for power-law stress-strain
ϕ	b. Eq. 10	Counter-clockwise angle from x to α axis in slip line mechanics
ν	Eq. 27	Poisson's ratio
σ_1	b. Eq. 3	Flow strength at unit strain
σ_{ij}	Eq. 4	ij component of stress
σ_n	b. Eq. 17	Normal stress on a slip line at the crack tip
$\tilde{\sigma}$	Eq. 4	Normalized stress function of angle for power-law stress-strain
σ_y	b. Eq. 3	Yield strength (equivalent uniaxial)
τ	b. Eq. 42	k; shear stress on slip line
θ_c	b. Eq. 19	Micro-cracking angle from the crack path in SLFM1
θ_s	b. Eq. 17	Angle of crack tip slip line from the crack path in SLFM1
θ_{sc}	b. Eq. 19	$\theta_s - \theta_c$, angle of micro-cracking from slip line in SLFM1

Subscripts

1, 2	b. Eq. 9	Cartesian coordinate axes
I	b. Eq. 1	Opening mode on a crack
II	b. Eq. 1	Shear mode normal to the leading edge of a crack
c	b. Eq. 1	Critical value of a variable
eq	Eq. 32	Mises equivalent stress or strain
i	b. Eq. 17	Critical value for initiation of crack growth
i, j	b. Eq. 9	Dummy subscripts over range 1, 2 for coordinate axes
lub	Eq. 33	Least upper bound
L	b. Eq. 32	Limit load
n	Eq. 41a	Normal component of stress across a slip line
P	b. Eq. 32	Component in direction of load

r, θ	b. Eq. 26	Polar coordinate axes
ub	b. Eq. 32	Upper bound (to limit load)
x, y	b. Eq. 10	Cartesian coordinate axes
α, β	b. Eq. 15	Curvilinear coordinate axes of maximum shear stress

Superscripts

p	Eq. 32	Plastic part of strain or work

Introduction

The Need for Predicting Extensive Plastic Crack Growth

The Practical Needs – Many large welded structures in accidents, such as buildings and refinery piping in earthquakes, and ships in collisions and groundings, should require fully plastic flow during the growth of any pre-existing cracks. This is helpful in sharing the load with other parts of the structure. Neither linear elastic fracture mechanics (LEFM, or K-controlled) nor elastic-plastic fracture mechanics ("EPFM", or J-controlled) deals with large-scale, fully plastic growth beyond the zone of dominance of the original K- or J-controlled fields. This is because in both linear and non-linear elasticity or "EPFM" (the so-called deformation theory of plasticity), the current stress sets the ratios of the *total* components of strain, not the ratios of the strain *increments* as in plasticity. For growth beyond the initial zone of J-dominance, a power-law relation "EPFM" more nearly characterizes rubber elasticity.

Valid as the above cautionary arguments are, Ponte Casteñeda [1] has shown that for flow theory plasticity with sufficient linear strain hardening, the stress fields around a growing crack are similar to those for a stationary crack. Further work is needed on displacements and to link these fields to the far-field geometry and loading. The J concept has also been adapted to large scale crack growth by Ernst [2], differently in different cases.

In the meantime, a further need for an available non-hardening approximation is that even if for some heavy-section structures fully plastic flow is not attained during crack growth, the critical plastic zones may be so large that small, centimeter-sized specimens cut from the structures are fully plastic before crack growth. Then the local fields may be so distorted from K and J fields that the specimens do not give valid predictions of critical values of K or J in the structure.

Simplifying Assumptions – Here consider only the effects of short duration, quasistatic overloads. Ignore the effects of fatigue, dynamics, strain rate, diffusion, strain-aging, and corrosion. Conceptually, think of cracking as occurring by one or a mixture of a few idealized micro-mechanisms: (a) cleavage at a critical normal stress over a nanometer in glass, or after a nominal plastic strain at a critical normal stress over one or a few grains (tens or hundreds of micrometers) in steel [3], (b) the formation and growth of micron scale holes as result of stress-modified straining and rotation [4,5], or (c) the linkage of holes either as a result of hole growth on a finer scale (e.g. [6,7]), or flow localization, perhaps into fine cracks (e.g. [8–10]).

Note that the micromechanisms of fracture do not uniquely determine the ductility of structures. For example, aluminum alloys never cleave, but cracked structures of hard aluminum alloys can fracture before appreciable plastic deformation of the structure as a whole: there can be *brittle structures that fracture by a ductile micro-mechanism*. Likewise for cracked structures of steel at some temperatures, when there is tearing be-tween facets or crack meandering and undercutting. On the other hand, cracked steel structures can be ductile enough to require large plastic deformation before much crack growth, and yet can finally fracture by cleavage: there can be *ductile structures that frac-ture by a cleavage micro-mechanism.*.

An Example: A Longitudinally Cracked Pressure Vessel – As a practical example, consider a ferritic steel pressure vessel with an austenitic steel weld along the entire length of the vessel, given to the INEEL for destructive testing. A stress-corrosion crack was reported to be half-way through from the inside, starting from the heat-affected zone between the wide cap and the base metal, and progressing into the base metal. What is its susceptibility to an accidental over-pressure, an earthquake, or an explosion, first by radial crack growth to penetration of the wall, and then by longitudinal growth of the through-crack? In a chemical or nuclear plant one may need to be very, very sure.

The State of the Art in Fracture Nano and Micro Mechanics

Fracture mechanics is essentially using the equations of equilibrium and the strain-displacement relations, along with appropriate flow and evolutionary equations for the deformation of the material, to predict the growth of cracks in loaded or deforming structures using boundary conditions at the tip of a crack that represent its initial and continuing growth. The crack tip boundary conditions can be posed at scales from roughly a nanometer (the atomic) through a micrometer (grains, phases, and hole-nucleating inclusions) to the macroscopic scale of millimeters to meters, or to kilometers in geophysics.

Analytical Predictions of Cracking in Structures from Nano and Micro Mechanics – For glass, which is homogeneous from the nano to the macro scales except for strength-impairing surface micro cracks, Griffith in 1920 predicted the low strength in terms of the balance between rates of strain energy release and of increase of surface energy as the crack grew [11]. For compression and combined stress he predicted the strength in terms of the local strain energy density (or stress) around the most stressed micro crack [12]. Orowan [13,14} and Irwin [15] showed that the energy analysis applied to steels but the plastic work per unit area far exceeded the surface energy. Orowan [14] also showed that the energy point of view was equivalent to attaining the theoretical strength at the most strained point. Both Irwin [16] and Williams [17] found that the local stress in the neighborhood of a sharp crack was governed by a single parameter depending on the far-field geometry and loading. This parameter is now called the stress intensity factor K. It determines the stress in the elastic region surrounding the crack tip and its associated plastic zone, so that fracture occurs at a critical value K_C. An excellent history by Rossmanith [18] refers to a very similar development and application of fracture mechanics in 1907 by Wieghardt [19,20].

With plasticity, plane stress Mode I is similar to antiplane shear (Mode III) in the sense of having a plastic zone predominantly ahead of the crack. In the analytical solution for Mode III, the majority of the elastic strain energy release rate comes from within the plastic zone (in only one quarter of the plastic zone does the plastic strain exceed the elastic). Thus the K-concept only becomes valid when there exists an annular region around the crack tip that is large compared to the plastic zone but small compared to the crack length or the distance to any other free surface [21]. Also plastic flow will not occur outside a sufficiently long decohering zone, as postulated almost simultaneously by Barenblatt, Panasyuk, and Dugdale [22–24]. Such planar, normal, decohering zones do not occur in plane strain of typical steels with cracks growing by a hole growth micromechanism (e.g. [25]).

The decohering zone model applies to necking in plane stress (thin sheets) where the active plastic zone occurs in a zone with a width of the order of the sheet thickness. This model correlates crack initiation, but not the usually observed stable growth. The model also applies to plane strain with a decohering zone of cleavage facets with ligaments between cleavage facets that only give local plastic flow. The more remote surroundings are elastic. Here there is rarely stable growth. Energy concepts are useful because, if long enough, the decohering zone is a boundary condition on purely elastic surroundings. For shorter decohering zones, the plastic flow in the surroundings must be taken into account. Some insight can be obtained by analogy with the diffuse plastic zone that exists ahead of a crack in both plane stress and Mode III shear. McClintock [26] derived the initiation, the stable growth under an approximate doubling of the load, and the final instability with the elastic-plastic field embedded in elastic surroundings. The instability seems to arise from the gradual flattening of the strain gradient in front of the crack by plastic straining due to crack growth, until the strain due to growth is itself sufficient to supply the critical displacement across the crack tip for further growth (see also [27], pp. 67-70). The idea that this is due to a crack resistance curve of the material can be shown to be not always valid as follows. A possible interrupting of monotonic loading by fatigue or stress corrosion cracking would give a very different gradient in front of the crack. That is, the gradient is a function of loading history, not a material characteristic such as a crack resistance. (Final instability may be almost path-independent in the limiting cases of either pre-loading the foil and then cutting the crack, or growing a precrack under increasing loads. Then the crack advances through a number of zones of large plastic strain at nearly constant load before instability.)

Numerical Predictions of Cracking in Structures from Nano and Micro Mechanics – In principle, fracture could be predicted from nano mechanics, roughly the scale of atoms. Shortening the calculations by incorporating the finer scale results into coarser scale models every factor of ten in distance from a point on the crack front would require about nine layers of models. Likewise doubling finite element size every four elements radially from a point on a crack front out to 10^9 atomic diameters would still require so many elements that a practical solution time of a few days could only be achieved in decades, even with the current rate of increase of computer power. It would also require perhaps a half-dozen models of material behavior at intermediate scales, along with the material parameters required for the models. Work on the smallest of such intermediate scales is reviewed in [28,29]. The feasibility for other scales is not yet established.

An alternative is to start at the micro mechanics scale of grains, phases, and inclusions, as has been done for structural steels [30] based on the elastic-nonhardening spherical hole, dilating potential model of Gurson [31] extended to nucleation and linkage of holes by Tvergaard and Needleman [6,7,32]. In principle this requires auxiliary tests to evaluate some nine parameters. In practice many of the nine can be assumed rather arbitrarily. Further, the growth and rotation of holes in shear bands should be included, perhaps using [5].

There has been real progress at these nano (nm) and micro (μm) scales, and they give valuable insights. But quantitative predictions are also needed for the complex thermally and mechanically processed alloys, perhaps after years of service. Intentional and accidental effects on the microstructure include a half dozen alloying elements, many more impurity elements, aging, possibly radiation, segregation of trace elements to dislocations and to phase and inclusion boundaries, and evolution of and interaction between dislocation and metallurgical structures. With all these effects and changes, describing the nano and micro structures in sufficient detail to predict fracture in structures will usually be impractical, even if the subsequent computations could be carried out in a reasonable time. Fracture macro (mm to m scale) mechanics is needed to use the results of tests on centimeter-sized specimens to predict the initial and continuing growth of cracks in parts and structures with sections as much as ten times larger or smaller.

The State of the Art in Fracture Macro Mechanics

Fracture macro mechanics is based on an annular zone around a crack tip that is described by only one to three parameters. These are found from the geometry and loading using homogeneous continuum mechanics. The crack response is an empirically determined function of these parameters. First consider idealized modes of deformation.

Contrasting Power-Law (Non-Linear) Elastic with Plastic Deformation – The elastic strain depends only on the current stress. It disappears on release of stress, and has a potential (releasable mechanical) energy. It may be linear or non-linear. Il'yushin proved in 1946 that if elasticity follows a power law relation, then as in linear elasticity the stress is proportional to the applied load and strains are proportional to applied displacements [33]. The inverse also holds; proportionality implies a power law relation [34].

Once a yield strength is reached, plasticity is an added straining caused primarily by the motion of dislocations. These tend to interlock and remain in place on release of stress; in mechanics, plastic strain is defined as the strain that remains on release of stress. Plastic strain has no potential energy; in an isothermal process, almost all the work is converted into heat, with only a small fraction left in the material, mostly due to the increase of dislocation density.

The scalar yield strength usually rises with plastic strain, but the slope may be only a few percent of the elastic modulus, so that to a first approximation it can be neglected. Other times the increasing yield or flow strength can be approximated by a power law function of the accumulated scalar magnitude of the plastic strain increments. Either way, the current stress apportions the *increments* of plastic strain, not their accumulated values. That is, the effects of plastic strain are history-dependent. When the strain increments stay in a constant ratio to each other during loading ("radial" straining), power-law plasticity is, except for incompressibility, indistinguishable from power law elasticity. During loading before crack growth but away from shape changes at the crack tip, power-law elasticity can be used for plasticity. Once the crack grows a significant distance through the section, however, important regions may be affected by the plastic strains left around the prior crack tip positions, and the incremental, or "flow" form should be used. Non-linear elasticity can no longer be relied on, even though it is historically called "deformation theory plasticity".

Linear Elastic Fracture Mechanics – It was gradually recognized (see e.g. [21]) that the elastic stress fields for brittle materials are also valid with local plasticity if an annular zone around a crack tip exists that is large enough to be unaffected by the plastic zone, and small enough to be unaffected by the distance to the next nearest boundary of the part or structure. In this region the stress and strain components are uniquely determined by a single scalar, the stress intensity factor K. Thus K determines everything within the zone, including the initiation of growth from the pre-crack at a critical value K_c. For various mixtures of the modes of loading K_I (for pure opening) and K_{II} (for pure shear normal to the crack front), the condition for initial growth of a pre-crack is that a value of K determined by the loading equal a critical value depending on the material and loading mode. This is the essence of linear elastic fracture mechanics (LEFM):

$$\text{Growth initiates when } K(\text{geometry, loading, mode}) = K_c(\text{material, mode}) \qquad (1)$$

(For quick estimates, a more visual descriptor of crack toughness is the critical surface crack length, $2a_c$, at a working stress of, say, half the tensile strength TS: $2a_c = (8/\pi)(K_{Ic}/TS)^2$.)

For Mode I, tables of K_I(geometry, loading) [35–37] and K_{Ic}(material) [38,39] are available. For Mode II and for mixed modes, analyses and data are more widely scattered, (but see e.g. [40]).

At higher loads, the growing plastic zone squeezes out the annulus of validity from the inside. The valid annular zone can be expanded by adding to the Mode I K-field the next term in the expansion of stress around a purely elastic crack tip, which is the T-stress parallel to the crack, here normalized with respect to the plane strain yield strength $2k$. Then LEFM expands to

$$\text{Growth initiates when } K \text{ geometry, loading, mode}) = K_c(\text{material, mode}, T/2k) \qquad (2)$$

Mechanical and material data involving T are even more scattered than for Mode II.

Power-Law Stress, Strain, and Displacements around Crack Tips – The presentation here will be in terms of a single strength parameter σ_1 (a hypothetical flow strength at unit strain) and the plastic strain *hardening* exponent n_h, instead of the elastic strain at yield $\varepsilon_y = \sigma_y/E$ and the non-linear elastic reciprocal *straining* exponent n_ε:

$$\sigma = \sigma_1 \varepsilon^{n_h} \text{ rather than } \varepsilon = \alpha\varepsilon_y\left(\frac{\sigma}{\sigma_y}\right)^{n_\varepsilon}, \text{ where } \alpha = \frac{1}{\varepsilon_y}\left(\frac{\sigma_y}{\sigma_1}\right)^{n_\varepsilon} \text{ and } n_\varepsilon = \frac{1}{n_h} \qquad (3)$$

As in the linear elastic singularity governed by K, the distribution of stress and strain around a crack tip opening in Mode I, for the power-law model of Eq. 3, can be characterized in terms of a single scalar, the J-parameter, as well as the strain-hardening exponent n_h [41,42]:

$$\frac{\sigma_{ij}}{\sigma_1}=\left(\frac{J}{\sigma_1 I_{n_h} r}\right)^{\frac{n_h}{n_h+1}}\tilde{\sigma}_{ij}(\theta,n_h),\ \varepsilon_{ij}=\left(\frac{J}{\sigma_1 I_{n_h} r}\right)^{\frac{1}{n_h+1}}\tilde{\varepsilon}_{ij}(\theta,n_h),\ \frac{u_i}{r}=\left(\frac{J}{\sigma_1 I_{n_h} r}\right)^{\frac{1}{n_h+1}}\tilde{u}_i(\theta,n_h) \tag{4}$$

The dimensionless functions $\tilde{\sigma}_{ij}(\theta,\ n_\varepsilon = 1/n_h)$, $\tilde{\varepsilon}_{ij}(\theta,\ n_\varepsilon = 1/n_h)$, $\tilde{u}_i(\theta,\ n_\varepsilon = 1/n_h)$, and $I_{n_\varepsilon=1/n_h}$ are plotted or tabulated functions [41–43,44 p.309,45]. The parameter I is also given within 1% by a form modified from [46]:

$$I_{nh} = 10.4\sqrt{0.13+n_h} - 4.8n_h = 4.51 \text{ and } 5.01 \text{ for } n_h = 0.1 \text{ and } 0.2, \text{ respectively} \tag{5}$$

For physical insight, one may think of J in terms of the crack tip opening displacement CTOD, approximated as that subtended by a pair of 45° lines behind the crack tip:

$$CTOD = D_{n_h} J / \sigma_1 \tag{6}$$

where $D_{n_h} = 1 \mp 8\%$ for the typical range $0.1 < n_h < 0.2$ and is 0.79 at $n_h = 0$.

Power Law Fracture Mechanics – As discussed above, the power law stress strain relation is a good approximation to plasticity as long there is no crack growth beyond the originally valid zone of Eqs. 4, often rather arbitrarily taken as 1.5 mm [45]. This approximation is often called elastic-plastic fracture mechanics, "EPFM", with the quotes retained here as a warning about the misnomer for crack growth. In analogy with Eq. 1,

$$\begin{gathered}\text{Growth initiates when } J(n_h, \text{ geometry, loading, mode}) = \\ J_c(\text{material, mode})\end{gathered} \tag{7}$$

As in LEFM, the annular zone of validity of Eq. 7 can be expanded by considering further terms, here set by the coefficient A_2 [47,48]. Thus in principle,

$$\begin{gathered}\text{Growth initiates when } Jn_h, \text{ geometry, loading, mode}) = \\ J_c(\text{material, mode}, A_2(n_h, \text{ geometry, loading, mode}))\end{gathered} \tag{8}$$

In practice, these ideas are too new for the functions to be available, except for the few crack depths, loading modes, geometries, and exponents $n_\varepsilon = 1/n_h$ treated in [47,48]. Even the older Q-parameter [49,50] has limited data.

Evaluating the J-parameter – For the left side of the "EPFM" Eq. 8, J can be evaluated in terms of the geometry and loading in several ways.

First, although Rice initially found J from work arguments applied to crack growth in a power-law elastic material, the form he found that is useful for incremental plasticity is that J is a path-independent integral [51]. In terms of a plane strain Cartesian coordinate system with a crack normal to the x_2 direction growing in the x_1 direction, for any path Γ around the crack tip from flank to flank, with local normal n_i and differential length ds,

$$J \equiv \int_{\Gamma}\left[\left(\int \sigma_{ij}d\varepsilon_{ij}\right)dx_2 - \left(\sigma_{ij}n_i\right)\frac{\partial u_j}{\partial x_1}ds\right] \equiv \int_{\Gamma}\left[\left(\int \sum_{i,j=1}^{2}\sigma_{ij}d\varepsilon_{ij}\right)dx_2 - \sum_{j=1}^{2}\left(\sum_{i=1}^{2}\sigma_{ij}n_i\right)\frac{\partial u_j}{\partial x_1}ds\right] \quad (9)$$

where $\int\sigma_{ij}d\varepsilon_{ij}$ is the work per unit volume, $\sigma_{ij}n_i$ is the j-component of the force per unit area (traction) on the element of the path ds, and u_j is the j-component of the displacement. The path may be taken either near the crack tip, or around the boundary of the part if that is more convenient. Either way, the calculations must be accurate enough to satisfy the consistency conditions mentioned below in Paragraph (b).

Second, J can be found from the literature. Caution is needed, however, as discussed in detail in [52] and summarized here. Consider singly face-cracked plane strain tension SFCT (the term is more accurate than the carry-over from the elastically equivalent but plastically very different "singly edge notched tension" SENT, which suggests plane stress).

(a) For a plate of thickness t with crack depth a, Shih and Needleman pointed out that extrapolation to short cracks is out of the question [53]. For example at typical exponents n_h of 0.1 and 0.2, the tabulated coefficients increase by factors of 7.2 and 2.8 from a/t = 0.25 to 0.125. Further calculations or better normalization are needed. Anticipated solutions for $a/t = 0.05$ [53] are in abeyance.[2]

(b) Furthermore most of the tabulated solutions (e.g. [54], reported also in [44,45]) were worked out before it was reported by Parks, Kumar, and Shih [55] that the coefficients of the functions giving J and load point displacement in terms of load had to satisfy consistency equations following from J being a strain energy release rate (see Appendix). Recalculations for SFCT [56] showed the old J-coefficients were low by a factor of two or more for $n_h < 0.06$ with any a/t, and for $n_h \leq 0.1$ with a/t around 0.625–0.75. *Thus the consistency checks can be essential.*

Calculations that have been shown to be consistent do not seem to be available beyond single-face-cracked tension [53], very deep cracks under combined loading [57], and internal plane and penny-shaped cracks in an infinite medium [58]. The extensive finite element calculations for the many other cases of practical interest must be checked and possibly redone to verify that they satisfy consistency.

At least one reason for the sensitivity of the calculations to a/t seems to be that in the non-hardening limit, the equations become hyperbolic and the far-field differences between bending and tension penetrate all the way to the tips of sharp cracks. St. Venant's principle breaks down. At the distances of fracture mechanics, small compared to the size of the part but large compared to a fracture process zone or the initial crack tip blunting, the local plastic stress and strain fields then differ strongly between bending and tension and between plane stress and plane strain, rather than being very similar as in elasticity. Thus as $n_h \to 0$ there is thus no single asymptotic J-field for both bending and tension. (Differences in the blunted regions at the original crack tip are discussed in **Further Topics**, *Blunting and Crack Tip Fans.*) For the crack growth that is of primary interest here, and that is observed in low strength and in tough structural alloys, both the

---

[2] Needleman, A., Brown University, Providence RI, personal communication with Frank A. McClintock, M. I. T. Cambridge MA, June 2000.

micromechanisms of fracture and slip line mechanics continually resharpen the tip, giving a finite crack tip opening angle.

Third, J can be found experimentally from bend tests by comparing the compliance of specimens with different crack lengths, or by partial unloading to determine the compliances at different crack lengths (see [44 pp.323–334] and [45]). The writer is still concerned about the difference between non-linear elasticity and plasticity in comparing the state with a crack grown by plastic deformation with that first cut (or fatigued or corrosion cracked) nearly to length and then loaded to the same value. These states would be identical in non-linear elasticity. As Rice [59] wrote,

> "We are thus forced to employ a deformation plasticity formulation [non-linear elasticity] rather than the physically appropriate incremental formulation. This is a regrettable situation, but no success has been met in attempts to formulate similar general results for incremental plasticity. Also, energy variation methods permit the treatment of several nonlinear problems presently well beyond the reach of more conventional analytical methods, either of the deformation or incremental type."

Those nonlinear elasticity methods have turned out to be very useful for *initiation*, but the object here is to treat fully plastic continuing crack *growth* with realistic incremental plasticity, even restricted to the limiting case of no strain hardening.

The Structure of the Paper – After a review of plane strain slip line mechanics, the crack tip driving parameters (CTDPs) and response functions (CTRF) are introduced for exact or approximate fields with one or two active slip lines emanating from the crack tip, comprising slip line fracture mechanics (SLFM1 and 2). Examples and approximate methods are given. Further topics include the relation of SLFM1 and 2 to K and J, embedding SLFM2 in finite element analysis, crack tip blunting and the problems of crack flank deformation and tip fans, and contraindications for SLFM. Applications include sections on finding the CTDPs from geometry and loading, general methods for experiments to find CTRFs, and some data from the literature for CTRFs. A number of recommended studies are mentioned, followed by conclusions.

An Introduction to Slip Line Fracture Mechanics

Rigid-Plastic, Non-Hardening, Plane Strain Plasticity – Readers primarily interested in known slip line fields may wish to skim this section and later return to any parts they need. For derivations of equations see [27 pp.67–70, 60, 61 pp.407–412, 62 pp.375–378], but beware of errata such as ambiguous or mis-directed arrowheads. Here detailed methods are presented for applying the equations to find stresses and displacements within a given or postulated slip line field.

Stress Distributions in Plane Strain Slip Line Fields – In non-hardening plane strain, the three in-plane components of stress must satisfy the yield condition and the two partial differential equations of equilibrium. Incompressibility, plane strain, and the stress-strain increment relations make the out-of-plane normal component of stress σ_{zz} equal to the average of the two in-plane normal components. The Mises yield criterion then makes the radius of the in-plane Mohr's circle a constant equal to the yield strength in shear k. This suggests expressing the stress state in terms of three parameters of Mohr's circle: (a) the center $\sigma = (\sigma_{xx} + \sigma_{yy})/2$, (b) the radius k, and (c) the angular orientation ϕ, which is the counter-clockwise (CCW) angle from the x-axis to the α slip line (Figure 1). The α- and β-lines are mutually perpendicular curved lines locally parallel to the directions of the maximum shear stress, so $|\sigma_{\alpha\beta}| = k$. They are chosen so that the local direction of maximum principal stress lies 45° CCW from the α-line toward the β-line.

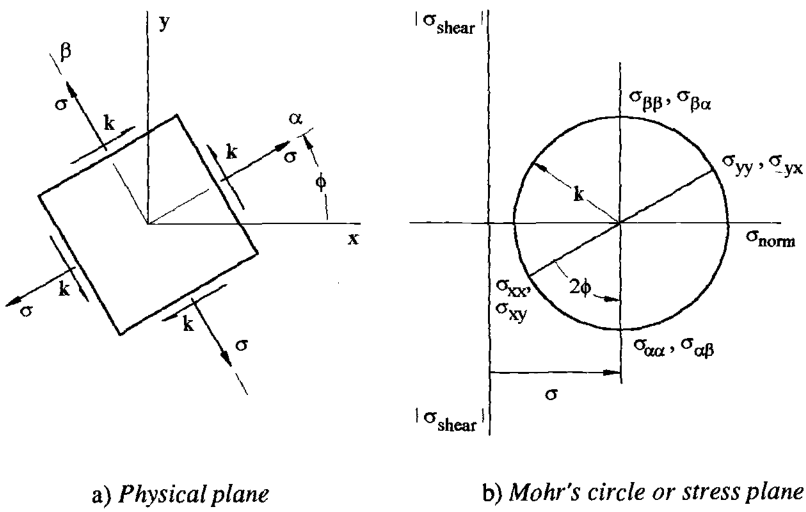

Figure 1 – *Definition of local α, β coordinates of maximum shear*

In terms of σ, k, and ϕ, the Cartesian components of stress are

$$\begin{aligned} \sigma_{xx} &= \sigma - k \sin 2\phi \\ \sigma_{yy} &= \sigma + k \sin 2\phi \\ \sigma_{xy} &= \quad\; k \cos 2\phi \end{aligned} \tag{10}$$

The beauty of the change of variables to σ, k, and ϕ is that the constancy of k reduces the number of variables from three to two: σ and ϕ. Further, along the α and β slip-lines, the in-plane partial differential equations of equilibrium turn out to become ordinary ones:

$$\text{along an } \alpha\text{-line, } d\sigma = 2k\, d\phi, \quad \text{and} \quad \text{along a } \beta\text{-line, } d\sigma = -2k\, d\phi \tag{11}$$

Frequently there are enough stress boundary conditions to solve Eqs. 11 for the plastic stress field without simultaneously considering the displacements.

Such a solution of Eqs. 11 can be done as follows for the region between the crack in Figure 2 and the traction-free face opposite it. This is a special case of a region subtended by a boundary subject to known stress components ("tractions") neither of which is equal in magnitude to the shear stress k.

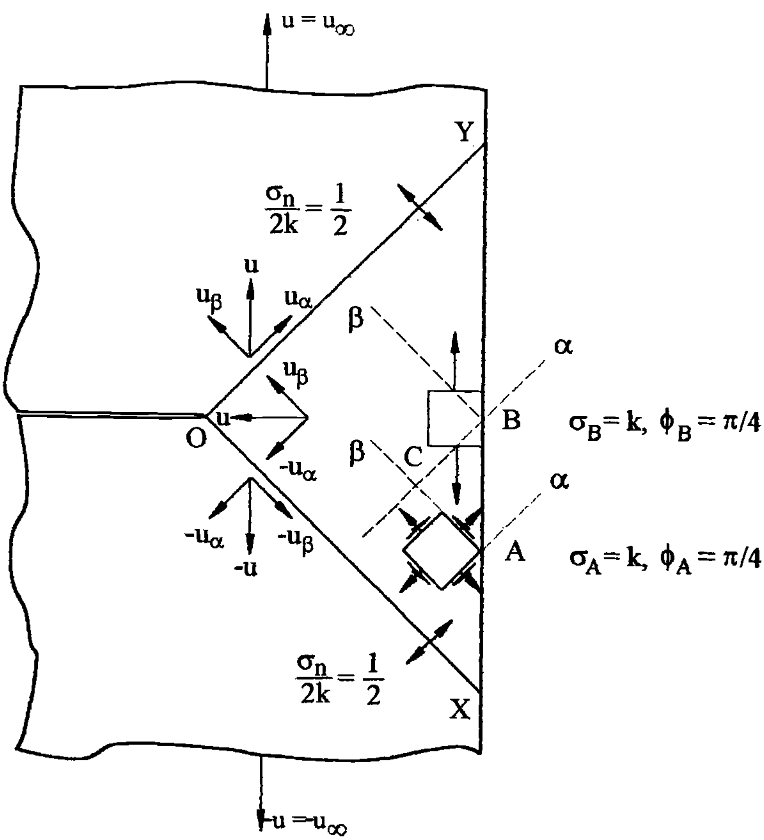

Figure 2 – *Elements A and B in the net section segment of a singly-face-cracked plate under tension (SFCT), showing components of stress referred to the free surface and to the* α, β *axes of maximum shear stress. Note that the term "face-cracked" rather than "edge-notched" or "panel" is used to suggest plane strain rather than plane stress*

1) Start with two neighboring elements on a free surface at *A* and *B* in a presumably (plastically) deforming region of the boundary. Guess (and verify later) that the stress along the boundary is tensile or compressive. For insight, sketch one element with x, y coordinates and one with α, β coordinates, here with α at 45° counterclockwise from x so $\phi = 45° = \pi/4$ radians (Figure 2). Write the mean stress $\sigma/2k$ and the orientation ϕ for each point. Here the back face is more likely to be in tension than in compression:

$$\sigma_A = k,\, \phi_A = \frac{\pi}{4}, \quad \sigma_B = k,\, \phi_B = \frac{\pi}{4} \tag{12}$$

2) Sketch the (possibly curved) α- and β-lines through the points A and B which meet at an interior point C. Note from Eq. 10 that for a unique stress at point C, the lines must give the same ϕ_C.

3) Write the equilibrium Eqs. 11 from A to C (here along a β-line) and from B to C (here along an α-line):

$$\sigma_C - \sigma_A = -2k(\phi_C - \phi_A),\ \ \sigma_C - \sigma_B = 2k(\phi_C - \phi_B) \tag{13}$$

4) Solve Eqs. 13 for σ_C, ϕ_C. Eliminate the states at A and B with Eqs. 12:

$$\begin{aligned} \sigma_C &= \frac{1}{2}\left[\sigma_A + \sigma_B + 2k(\phi_A - \phi_B)\right] = k, \\ \phi_C &= \frac{1}{2}\left[\phi_A + \phi_B + \frac{1}{2k}(\sigma_A - \sigma_B)\right] = \frac{\pi}{4} \end{aligned} \tag{14}$$

Thus here the state of stress at the interior point C is the same as that on the surface.

5) Repeat for all points along the first interior layer inward from equally spaced points along the free surface. Then use those results for the second, incrementally shorter layer, and so on.

For a segment of a straight, traction-free boundary at the plane strain yield strength, as in Figure 2, the result is that for all points within the region subtended by 45° lines from the ends of that segment, the stress is constant and the slip lines are straight. The stresses integrate to a tensile force, as required by equilibrium in tension. If the boundary segment had been circular, the field would have been a logarithmic spiral, derived in most plasticity texts. Sometimes there is a fan at a re-entrant corner at the end of the segment. In the example of Figure 2 the extent of the segment is limited by the slip lines from each end encountering the crack face behind the tip, where $\sigma_{yy} = 0$, in contrast to the field OXY. In between, the field is likely to have dropped below yield and become rigid.

Displacement Increments in Plane Strain Slip Line Fields – To quantify ductile crack growth, one must also consider the incremental displacement fields $\delta u_x(x,y)$, $\delta u_y(x,y)$. In the slip line fracture mechanics discussed here, the fields near the crack tip are either exactly, or sometimes approximately, sliding on one or two slip lines between rigid regions. How this sliding depends on the far-field geometry and displacements follows from an understanding of the displacement fields. Here these fields will be discussed in some detail, because they are less commonly treated than the stresses in slip line fields. Readers for-tunate enough to find a field of displacement increments for the problem at hand need only skim this sub-section and the next, and continue with the sub-section *Appreciating the Simplifications from the SLFM Assumptions.*

The field of displacement increments must be consistent with the stress field, be incompressible, and satisfy any displacement boundary conditions.

First, consistency with the stress field requires inextensibility of slip lines; if only one of the lines is active, the deformation is like shearing of a possibly bent deck of cards. Inextensibility is proved as follows. The α- and β-lines are in the local directions of maximum shear stress. From Mohr's circle, they then have equal normal stress across them, so that $\sigma_{\alpha\alpha} = \sigma_{\beta\beta}$.. Isotropy of the relations between stress and plastic strain increments then requires that $\delta\varepsilon_{\alpha\alpha} = \delta\varepsilon_{\beta\beta}$. In rigid-plastic plane strain, the out-of- plane *stress* is the average of the two in-plane normal components, so all three are equal. From the relations between stress and strain increment, all three normal *strain* increments are equal. From incompressibility, they must all be zero. Thus there is no normal strain increment along a slip line and the slip lines are inextensible. Similarly, there can be no discontinuity in normal displacement increments across slip lines; such would require strain increments that are infinite, rather than zero.

Second, incompressibility is expressed in terms of the strain increments derived from the displacement increments, $\delta\varepsilon_{xx} = \partial\delta u_x/\partial x$, $\delta\varepsilon_{yy} = \partial\delta u_y/\partial y$, so that $\delta\varepsilon_{xx} + \delta\varepsilon_{yy} = 0$. For generality it is common to normalize the displacement increments with respect to some particular boundary displacement increment δu_{norm}. Then for typographical convenience at the expense of clarity, the normalized variable is replaced by the variable itself, $\delta u_x/\delta u_{norm} \rightarrow u_x$. For brevity, again at the expense of clarity, u_x is now called a "velocity", as if the normalizing increment δu_{norm} were an increment of time δt. The resulting incompressibility equation is called a vanishing of the sum of the normal strain "rates", really normal strain increments, written: $\varepsilon_{xx} + \varepsilon_{yy} = 0$. (Henceforth the quotation marks will be dropped from "velocities" and "rates".)

In the example of the pressure vessel given in the **Introduction**, with the cracked net section shown in Figure 2, the velocities u are supplied by the rest of the circumference as it contracts elastically under the rate of load drop due to the crack growth rate in the net section. Locally, near the cracked net section, the strain rates are negligible compared to the infinite strain rates in some of the (infinitesimally thin) slip lines.

The conditions of incompressibility for the velocities in a possibly curved slip line field are known as the Geiringer equations. In terms of the velocities u_α and u_β along the curvilinear α- and β-lines, a change of variable in the partial differentials from the two-dimensional equation for incompressibility in rectilinear Cartesian coordinates turns out to give ordinary differential equations along the two slip lines:

$$\text{along an } \alpha\text{-line, } du_\alpha = u_\beta d\phi \text{ and along a } \beta\text{-line, } du_\beta = -u_\alpha d\phi \tag{15}$$

Note that *across* an α-line (along a β-line) there is no limit to the change in u_α; shear velocities can be discontinuous but υ_β is continuous. Similarly across β-lines.

Third, with given rigid-body boundary conditions around an active slip line region, consider the general method of solving Eqs. 15, although for Figure 2 the result could be obtained more simply. The method is most easily understood by writing the details for one point at a time on an enlarged sketch of Figure 2; when you become bored writing the details, you no longer need them:

1) If there are any bands of slip-lines with no velocity boundary conditions at either end, remove the resulting non-uniqueness by assigning velocities at one end, often keeping the strain rates relatively uniform by assuming uniform velocity gradients across such bands.

To make normal components vanish across the rigid-plastic boundary, it may be convenient to fix local coordinates in the rigid region, and later add in the velocities of these local coordinates relative to the global ones.

2) Look for a corner between α- and β-lines where outside the corner both u_α and u_β are known, either from rigid body displacements outside the corner or from the assumptions of Step 1. Inside the corner they are known by continuity along α- and β-lines respectively from Eqs. 15 with $d\phi = 0$.

3) Find u_α at a new point incremental distance inside the corner by integrating the first of Eqs. 15, subject to the initial condition on u_α.and a value of u_β set by Step 2. Similarly, find u_β along the β-line at the new point inside the corner. There are now new corners to work from.

For increased precision one can find the velocities at a new point incrementally along the α-and β-lines from the old corner by solving Eqs. 15 simultaneously for u_α and u_β at the new corner, using their averages along each line segment in Eqs. 15.

4) Repeat Steps 2 and 3 from the new corners.

For Figure 2, Step 1 is not needed since there are no bands of slip-lines that are free at both ends. For Step 2, the boundary conditions on *OXY* imposed by the rigid region are the normal conditions along the β-line *OX*, $u_\alpha = -u_\infty/\sqrt{2}$, and along the α-line *OY*, $u_\beta = u_\infty/\sqrt{2}$. Just inside *OX and OY* at O the u_α- and u_β-velocities are the same. The integrations of Step 3 are simple, since $d\phi = 0$ along an α-line, so regardless of u_β, $du_\alpha = 0$ and u_α is still $-u_\infty/\sqrt{2}$. Similarly just inside *OX*, $u_\beta = u_\infty/\sqrt{2}$. In Step 4, repeatedly integrating from new corners shows that the velocities are constant throughout *OXY*:

$$u_\alpha = -u_\infty/\sqrt{2}, \quad u_\beta = u_\infty/\sqrt{2}; \quad \text{or} \quad u_x = -u_\infty, \; u_y = 0 \tag{16}$$

Discussion of the Displacement Field of Figure 2 – Consider the assumption of rigidity outside of *OXY*. First, since a velocity field has been found, the load is an upper bound to the limit load [27 pp.64–67, 61 pp.96–98, 62 pp.364–368]. To obtain a lower bound, one must show a stress field satisfying equilibrium and the yield condition not only in the deforming region, but throughout the body. This has been done by extending the constant plane strain stress field of Figure 2 out to the uniformly translating ends of the part, with zero stress in the shoulders [62 pp.368–371]. (This solution does not give a compatible strain field, but that is not required for a lower bound.) In this case the lower and upper bounds to the limit load are the same, giving a complete solution. A theorem [63, 62 p.379] states that any region necessarily rigid in any complete solution is rigid in all. But there is no deformation in the stress-free shoulders, and by boundary condition arguments similar to the above, there can be no deformation in the region extended from *OXY*. Thus all regions beyond *OXY* are rigid, and further the deformation is unique.

Under load boundary conditions, however, the displacements are not unique. Discontinuous sliding could occur across either *OX* or *OY* alone, in which case it would be the single-plane SLFM1. With equal slip on the two planes under symmetrical displacement boundary conditions, as in Figure 2, SLFM2 applies. An intermediate mixture can sometimes be observed around the rim of a cup and cone fracture in a round tensile test specimen. If one slip dominates, the fracture can be treated with SLFM1, but there are as yet no data on the crack tip response in plane strain with the mixtures that would occur with various oblique displacements of the ends

The absence of fully plastic strain outside the active plastic field does not mean that there cannot be plastic strains of the order of the yield strain in a "rigid" region. These may arise not only on initial loading but also during crack growth. In fact as discussed in more detail below, for opening bending of a fillet weld the maximum principal stress can be higher there, so cleavage can occur even if unexpected in the fully plastic region.

A decohering zone trailing the very crack tip due to roughness or ligaments behind the main front adds to the limit load, but does not affect the stress and velocity fields based on the leading edge of the decohering zone unless possibly there would have been deformation along the traction-free crack flank [64].

Appreciating the Simplifications from the SLFM Assumptions – Consider the problems that would arise without the assumptions:

a) With elasticity as well as plasticity, residual stresses would help drive the crack. Their distribution would depend on the prior history, including crack growth. There would be a changing strain gradient ahead of the crack tip which would affect growth, as found for Mode III crack growth [26].

b) Strain-hardening would expand a slip line into a lobe or zone of strain analogous to those of LEFM and "EPFM". Crack advance would involve the damage gradient as a crack resistance parameter and would require its integration as the crack grows, as was done in a very approximate model for Mode II cracking with strain-hardening [65]. This damage gradient is part of what limits the applicability of LEFM and "EPFM" to crack growth no further than the outer boundary of the valid annular zone of the original crack. In SLFM, the rigid-plastic and non-hardening approximations make each step in crack growth the same as into original material.

c) Anisotropy would affect the direction and magnitude of cracking.

d) Plane stress requires not only no stress components acting on the plane, but also no gradients into the plane, to simplify the partial differential equations of equilibrium. In elasticity, the in-plane components of plane stress are the same as those in plane strain, but in plasticity they are often very different, and governed by equations that can be elliptic or parabolic as well as hyperbolic. Stress gradients into the plate preclude using plane stress within a few sheet thicknesses of the crack tip. The varying thickness $t(x, y)$, and its change as the crack advances, affects the equilibrium equations and does not appear in most formulations of plane stress. It would introduce an entire new function into the changing state of the system, in contrast to the few crack tip driving parameters and response functions of SLFM.

Here the above complications are neglected, leading to the limiting cases of plane strain, rigid-plastic, non-hardening, isotropic material with two intense slip lines for symmetrical growth of the crack (SLFM2), or a single intense slip line for asymmetrical growth (SLFM1). SLFM treats the first-order mechanics of the problem, allowing other effects to show through more clearly.

Available Solutions from Slip Line Plasticity – The SLFM assumptions allow using many of the available solutions of slip line plasticity. These solutions give stress fields, but seldom the displacement fields and even more rarely the fields for deformed geometries. Approximate methods based on straight and circular arc slip lines are discussed below. Later, tables are given for the necessary crack tip variables and experimental results.

Slip Line Fracture Mechanics

Cracking Criteria for Slip Line Fracture Mechanics, SLFM – In many cases of plane strain, the crack tip field can be approximated by just two symmetrical intense slip-lines (planes) with an angle $2\theta_s$ between them (SLFM2) or, for asymmetry, by one line (SLFM1), as shown in Figure 3. In either case, there is a normal stress σ_n across a line and (reverting to the displacement rather than the velocity meaning of u for the rest of the paper) an increment δu_s in the shear displacement discontinuity across the line due to an increment in far-field displacement δu_g. The quantities θ_s, σ_n, and δu_s are found from the slip-line solution for the given geometry and loading and are called the *crack tip dri-ving parameters* CTDP. (As in [66], the term driving *force* is avoided because of its connotation as a derivative of energy, inapplicable to plasticity.) In a way, SLFM2 is a generalization of the single Barenblatt-Panasyuk-Dugdale line of plastic displacement discontinuity in plane stress, or of a linear decohering zone in elastic plane strain, extended to plasticity off the crack path by splitting the single line into two that fork from the current crack tip in order to accommodate plastic incompressibility. The concept of SLFM is that within an annular region described by a given set of CTDPs, the crack responds in a material-determined way by initial or continuing crack growth.

In the idealized model of Figure 3a for SLFM2 the pre-crack first blunts by alternating sliding off on the slip planes at $\pm\theta_s$, upward to the right and then downward to the right by the critical displacement u_{si}. This leaves the profile shown by the heavy lines. (*Simultaneous* slip, as with a rate-dependent plastic continuum, would leave an unrealistic tip shape.) Then for the steady state crack growth of Figure 3b, an increment of slip δu_s upward to the right would take A to A'. Slip downward to the right would take B to B'. Together, these would trigger an increment of micro-cracking by δc to C, leaving an average crack tip opening angle CTOA between $A'C$ and $B'C$. Now characterize this process in terms of criteria for initial and continuing crack growth.

From Eq. 11 for equilibrium and Eq. 15 for incompressibility, a straight slip line between two adjacent rigid regions would have a constant stress and a constant slip displacement discontinuity across it. A cracking criterion satisfied at one point would lead to simultaneous cracking along the entire length. This abrupt behavior is avoided by considering first the displacement across the slip-line to initiate crack growth, u_{si}, and then the micro-crack growth δc per unit slip displacement across the line, δu_s. These are *crack tip response functions* CTRFs of the material and the CTDPs. (They incorporate the amount of discontinuous slip into the CTRFs, reducing the number of CTDPs by one.)

The crack tip response functions CTRF for modes of Figure 3 can be stated in forms similar to Eqs. 2 and 8 for linear and non-linear elasticity:

For the symmetrical Mode I SLFM2 of Figures 3a and 3b [64,67]:

Given θ_s(geometry, loading), σ_n(geometry, loading), and u_s(geometry, loading),

growth initiates when $u_s = u_{si}$(material, θ_s, $\sigma_n/2k$, and (17)

progresses at $c_{,u}$(material, θ_s, $\sigma_n/2k$), where $c_{,u} + \delta c/\delta u_s$ (18)

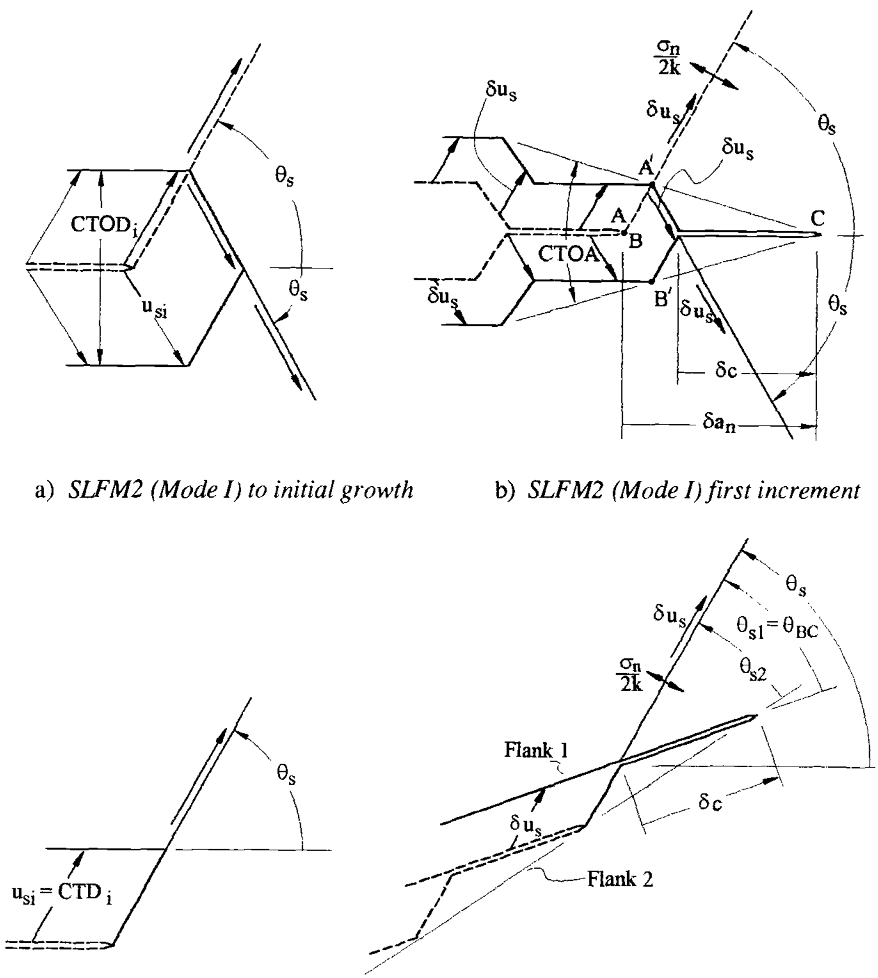

a) *SLFM2 (Mode I) to initial growth* b) *SLFM2 (Mode I) first increment*

c) *SLFM1 (mixed mode) to initial growth* d) *SLFM1 (mixed mode) first increment*

Figure 3 – *Idealized crack tip deformation for the slip u_{si} to initial crack growth, and for δu_s on the first increment of growth. Both are relative to the ligament ahead of the crack*

For the mixed-mode SLFM1 of Figures 3c and 3d, with the cracking relative to the slip line, there is only one CTDP, $\sigma_n/2k$, but there are two CTRFs, $c_{,u}$ and $\theta_{sc} \equiv \theta_s - \theta_c$, if the crack growth direction depends only on the current slip-line, not on the prior crack direction [68,69 p.289]:

Given σ_n(geometry, loading) and u_s(geometry, loading):

growth initiates when $u_s = u_{si}$(material, $\sigma_n/2k$), and (19) progresses at $c_{,u}$(material, $\sigma_n/2k$), where $c_{,u} \equiv \delta c/\delta u_s$, (20)

in the direction $\theta_s - \theta_c \equiv \theta_{sc}$(material, $\sigma_n/2k$) toward the more tensile crack flank (21)

(Note that in non-hardening, plane strain plasticity, slip lines are lines of maximum shear stress. By Mohr's circle, the normal stress across them, σ_n, is the mean normal stress σ of the equilibrium Eqs. 11. Although the subscript ($_n$) could thus be dropped, it will retained to imply connection with the slip line as a CTDP.)

After incremental deformation and crack growth, the slip line field is recalculated and the process is repeated.

The CTOD$_i$ and the CTOA as CTRFs – For SLFM2, the trigonometries of Figure 3a and 3b, along with θ_s, convert the u_{si} to the CTOD$_i$ and the $c_{,u}$ to the CTOA:

$$CTOD_i \approx 2u_{si}\sin\theta_s, \quad CTOA = 2\tan^{-1}\left(\frac{\sin\theta_s}{\cos\theta_s + c_{,u}}\right), \text{ where } c_{,u} \equiv \frac{\delta c}{\delta u_s} \tag{22a}$$

Since the slip line field that determines θ_s and $\sigma_n/2k$ may change slightly during CTOD$_i$, the first of Eqs. 22a may be somewhat approximate. More important, *since u_{si} and $c_{,u}$ are both functions of θ_s and $\sigma_n/2k$, so are CTOD$_i$ and CTOA*. They are material *functions* or CTRFs, not just parameters. Conversely, the CTRFs u_{si} and $c_{,u}$ (at the particular values of θ_s and $\sigma_n/2k$) can be found by solving Eqs. 22a for them in terms of the slip plane angle and the macroscopic variables CTOD$_i$ or CTOA:

$$u_{si} \approx \frac{CTOD_i/2}{\sin\theta_s}, \quad c_{,u} = \frac{\sin\theta_s}{\tan(CTOA/2)} - \cos\theta_s \tag{22b}$$

In SLFM1, the displacement to initiation is purely along the slip line: u_{si} = CTD$_i$, and is in the slip direction. For growth, shown in Figure 3d, denote the less and the more stretched of the flanks by (1) and (2), respectively. (The notation here differs from that of [69 p.289].) Then the angle from Flank 1 to the slip line is just $\theta_{s1} = \theta_{sc} \equiv \theta_s - \theta_1$ and Flank 1 is unstretched. For an increment of micro crack growth dc, Flank 2 has the angle found from the tangent of the opening angle in terms of the normal from the prior crack tip to Flank 1. Altogether, for initiation and growth in SLFM1, in terms of the micromechanism parameters u_{si}, θ_{sc}, and $c_{,u}$,

$$CTD_i = u_{si}, \quad \theta_{s1} = \theta_{sc}, \quad \theta_{s2} = \tan^{-1}\left(\frac{\sin\theta_{s1}}{\cos\theta_{s1} + 1/c_{,u}}\right) \tag{23a}$$

Note that from broken specimens, measurements can be made of the two macroscopic flank angles, θ_{s2} and θ_{s1}. Solving the third of Eqs. 23a then gives $c_{,u}$. Measurements can also be made of the ratio of flank lengths (relative stretch), da_1/da_2. From Figure 3d this ratio can be found analytically by dropping the normal from the new tip to the slip line. The ratio gives a check on the accuracy of the experiments and the SLFM1 approximation. Together, these results are

$$u_{si} = CTD_i, \ c_{,u} = \frac{1}{\cos\theta_{s1}\left(\frac{\tan\theta_{s1}}{\tan\theta_{s2}} - 1\right)}, \ \frac{da_1}{da_2} = \frac{\sin\theta_{s2}}{\sin\theta_{s1}} \tag{23b}$$

An example of SLFM1 is given in [69 pp.288-290] for the tension of a web attached to a plate by two non-penetrating fillet welds. The slip line and deformation fields are exactly those of Figures 3c and d. Data will be discussed in **Further Topics**, *Applications*.

Example of the Longitudinally Cracked Pressure Vessel – Apply the ideas of the above two sections to the over-pressure test of the long, closed-end pressure vessel mentioned first in **Introduction**, *The Need for Predicting Extensive Crack Growth*, and later before Eq. 15. Ultrasonic inspection had indicated that a crack was half-way through along almost the entire length L. First assume radial crack growth along the entire length and use SLFM2; later assume slant growth and SLFM1. Consider the pressure vessel to be divided circumfer-entially into two segments: the short segment of the cross section shown in Figure 2 both sides of the radial crack, and the remainder of the circumference. To determine stability, consider a small extension $2\delta u$ in the short cracked segment and an equal contraction in the remainder. For this thin walled shell ($D = 1000$ mm, $t = 25$ mm), assume that the bending due to off-center forces in the cracked segment has negligible effects on the force and plastic extension in the cracked section and on the circumferential compliance of the remainder. Further, assume elastic extension in the cracked segment to be negligible. From Figure 3b, the extension in the cracked segment, $2\delta u$, causes a reduction in ligament of

$$\delta a_n = -(2\cos\theta_s + c_{,u})\delta u_s = -(2\cos\theta_s + c_{,u})\delta u / \sin\theta_s \tag{24}$$

The resulting drop in circumferential force in the cracked segment, with elastic deflections neglected, is

$$\delta F_{\theta c} = 2kL\delta a_n = -\frac{2kL(2\cos\theta_s + c_{,u})}{\sin\theta_s}\delta u \tag{25}$$

where $2k$ is the strength in plane strain extension, $2TS/\text{v}3$.

The drop in circumferential force in the remainder can be found by first considering a differential arc of the cylinder, which gives $F_{\theta r} = \sigma_{\theta\theta} tL = pDL$. Differentiating, introducing the pressure change in terms of the bulk modulus, $\delta p = -B\delta V/V = -B(2\delta D/D + \delta L/L)$, and neglecting p/B compared to unity for liquids at normal pressures, together give

$$\delta F_{\theta r} = pDL\left(\frac{\delta p}{p} + \frac{\delta D}{D} + \frac{\delta L}{L}\right) = -DL\left[B\left(2\frac{\delta D}{D} + \frac{\delta L}{L}\right) + \frac{p}{B}\left(\frac{\delta D}{D} + \frac{\delta L}{L}\right)\right],$$

$$\delta F_{\theta r} \approx -BLD\left(\frac{2\delta D}{D} + \frac{\delta L}{L}\right) \tag{26}$$

The differential diameter and length changes follow from the stress-strain relations for a closed-end cylinder. Substituting these into Eq. 26 and solving for $\delta F_{\theta r}$ as a function of δu gives

$$\frac{\delta D}{D} = \delta\varepsilon_{\theta\theta} = \frac{\delta F_{\theta r}}{tLE}\left(1-\frac{\nu}{2}\right)+\frac{2\delta u}{\pi D}, \quad \frac{\delta L}{L} = \delta\varepsilon_{zz} = \frac{1}{2}\frac{\delta F_{\theta r}}{tLE}(1-2\nu).$$

$$\delta F_{\theta r} = -BLD\left(\frac{\delta F_{\theta r}}{tLE}(2-\nu)+\frac{4\delta u}{\pi D}+\frac{\delta F_{\theta r}}{tLE}\left(\frac{1}{2}-\nu\right)\right);$$

$$\delta F_{\theta r}\left(1+\frac{BD}{tLE}\left(\frac{5}{2}-2\nu\right)\right) = -BL\frac{4\delta u}{\pi} \tag{27}$$

Instability occurs by the above displacement mode if the force drop in the cracked segment is more than that in the remainder of the circumference. The difference between the two drops would leave a net circumferential force on the cracked segment to produce an acceleration within it:

Instability if $$-\delta F_{\theta c} > -\delta F_{\theta r} \tag{28}$$

Substituting Eq. 25 for the load drop in the cracked segment and Eq. 27 for the load drop in the remainder into Eq. 28, eliminating $c_{,u}/\sin\theta_s$ with Eq. 22b, and simplifying, all together give:

Instability if $$\frac{2kL(2\cos\theta_s + c_{,u})}{\sin\theta_s}\delta u > \frac{\frac{4}{\pi}BL}{1+\frac{BD}{Et}\left(\frac{5}{2}-2\nu\right)}\delta u, \text{ or}$$

$$\frac{2}{\sqrt{3}}\frac{TS}{E}\frac{\pi}{4}\left[\frac{1}{\tan\theta_s}+\frac{1}{\tan(CTOA/2)}\right]\left[\frac{E}{B}+\frac{D}{t}\left(\frac{5}{2}-2\nu\right)\right] > 1 \tag{29a}$$

Note that as expected, instability is more likely with a higher elastic strain TS/E, a lower CTOA, a lower bulk modulus of the liquid, B/E, and a lower wall thickness t/D.

For the pressure vessel in question, introducing dimensions in mm and $TS = 0.55$ GPa, $E = 207$ GPa, $\nu = 0.3$, $B_{water} = 2.25$ GPa, $\theta_s = 45°$ from Figure 2, and CTOA = 26° from the fracture profile data of Table 3 of [70] for the medium strength C-Ni-Mn-Si steel HY-80 (0.648 GPa YS, 0.745 GPa TS), also at $\sigma_n/2k = 0.5$, all together give:

Instability if

$$\frac{2}{\sqrt{3}}\left(\frac{0.55}{207}\right)\frac{\pi}{4}\left[\frac{1}{\tan 45^\circ}+\frac{1}{\tan\left(26^\circ/2\right)}\right]\left[\frac{207}{2.25}+\frac{1000}{25}\left(\frac{5}{2}-2(0.3)\right)\right] > 1,$$

$$0.002410[1+4.33][92.0+76.0]=2.16 > 1,$$

or for stability $\quad \text{CTOA} > 68^\circ$, or from Eq. 22b, $c_{,u} < 0.341 \qquad$ (29b)

The micro cracking ratio $c_{,u}$ from Eq. 22b would be 4.7 for the assumed CTOA. That is, for stability $c_{,u}$ would have to be 13.8 times lower than expected. Even an austenitic stainless steel pressure vessel would be likely to be unstable.

Next assume slip only on the line OY of Figure 2, and use SLFM1 for the resulting slant growth, as in Figure 3d. The radial component of motion across the cracked segment would be accommodated by a negligible bending of the remainder of the circumference of the pressure vessel. From Figure 3d the total circumferential displacement δu across the cracked segment and the change in ligament are given in terms of the slip δu_s by

$$\delta u = \delta u_s \sin\theta_s,$$

$$\delta a_n = -\delta u_s \cos\theta_s - \delta c\cos\left(\theta_s-\theta_{s1}\right) = -\left[\cos\theta_s + c_{,u}\cos\left(\theta_s-\theta_{s1}\right)\right]\frac{\delta u}{\sin\theta_s} \qquad (30)$$

The stability condition is again given by Eq. 28, with $\delta F_{\theta c} = 2kL\delta a_n$ and $\delta F_{\theta r}$ as in Eq. 27 except dropped by a factor of two due to the relative displacement across the cracked segment being only δu instead of $2\delta u$. Thus $\delta F_{\theta r} = -BL(2/\pi)\delta u$. Introducing the second of Eqs. 30 for δa_n and Eq. 23b for $c_{,u}$ then gives:

$$\text{Instability if}\quad 2kL\left[\cos\theta_s + c_{,u}\cos\left(\theta_s-\theta_{s1}\right)\right]\frac{\delta u}{\sin\theta_s} > \frac{\frac{2}{\pi}BL}{1+\frac{BD}{Et}\left(\frac{5}{2}-2\nu\right)}\delta u, \quad \text{or}$$

$$\frac{2}{\sqrt{3}}\frac{TS}{E}\frac{\pi}{2}\left[\frac{1}{\tan\theta_s}+\frac{\cos\left(\theta_s-\theta_{s1}\right)}{\sin\theta_s\cos\theta_{s1}\left(\frac{\tan\theta_{s1}}{\tan\theta_{s2}}-1\right)}\right]\left[\frac{E}{B}+\frac{D}{t}\left(\frac{5}{2}-2\nu\right)\right] > 1 \qquad (31a)$$

As a numerical example, in the notation of Figure 3d and again for the HY-80 steel from [70], take θ_s to be its far-field slip direction of 55° and the angles from Flanks 1 and 2 to θ_s to be $\theta_{s1} = \theta_{sc} = 16^\circ$ and $\theta_{s2} = 14^\circ$:

$$\text{Instability if } 0.004819\left[\frac{1}{\tan 55^\circ}+\frac{\cos(55^\circ-16^\circ)}{\sin 55^\circ \cos 16^\circ(\tan 16^\circ/\tan 14^\circ-1)}\right][92.0+76.0]>1$$

$$\text{or } 0.004819[0.700+6.58][92.0+76.0]=5.89>1 \tag{31b}$$

Alternatively, for stability at the same cracking direction θ_{s1}, from the first of Eqs. 31a,

$$c_{,u}<\left[\frac{\sin\theta_s}{\frac{2}{\sqrt{3}}\frac{TS}{E}\frac{\pi}{2}\left[\frac{E}{B}+\frac{D}{t}\left(\frac{5}{2}-2\nu\right)\right]}-\cos\theta_s\right]/\cos(\theta_s-\theta_{s1})=0.564 \tag{31c}$$

The micro cracking ratio for slant cracking, $c_{,u}$ from Eq. 23b, would be 6.93 for the assumed flank angles and less than 0.564 for stability. That is, for stability $c_{,u}$ would have to be 12.2 times lower than the data indicate. This ratio is near the 13.8 for normal cracking. Again, stability would be doubtful even with an austenitic stainless steel pressure vessel.

It is tempting to convert the $c_{,u}=4.7$ for SLFM2, based on micro cracking on the symmetry plane, to the $c_{,uz}$ based on micro cracking along the symmetry plane by zigzagging on the slip planes [64]. Then it could be compared with the $c_{,u}=6.93$ for slant cracking. From the geometry of the two modes of alternating sliding and micro cracking, such $c_{,uz}=c_{,u}/(2\cos\theta_s)=4.7/\sqrt{2}=3.3$. From this it would appear that dimple micro cracking was twice as rapid when the crack is advancing into or near pre-strained material along a slip line. This is consistent with the interpretation of tests on slant and normal cracks as showing reduced structural ductility for slant cracks [70], but it should not be taken seriously since the comparison is applying fracture macro mechanics to the fracture process zone inside the annular zone of validity of SLFM.

Although zigzagging on a macroscopically normal plane is sometimes observed, the micrograph of Bluhm and Morrissey (see labeled cross section in [4,27 p.51]) shows that in a tensile test on copper a normal macro crack does not grow in that way. Rather, the cup-cone transition is in an abrupt change between competing modes, with occasional precursor slant growth regions being bypassed by the growing normal crack. FEM micro-mechanics work [32], on the other hand, indicates that a normal-to-slant transition may be predicted qualitatively even without the rotations observed in the precursor shear bands. More study is needed, including statistical, roughness, and three-dimensional effects. For this pressure vessel, however, the question of normal or slant crack through-cracking is moot: both modes appear to be unstable. With a symmetrical net section and negligible constraint against lateral motion as here, the choice appears to be made by the material and fracture micro mechanics.

Meanwhile, further ultrasonic testing after retirement of the pressure vessel had shown that in two regions along the weld, the crack was 75% of the way through over lengths of few cm. In the actual test, the crack growth was stable, and the test was terminated when a major leak developed in one of the deeply cracked regions. In retrospect, the above stability analysis is no more appropriate than classical stability analysis applied to a slightly pre-bent plastic column. In 1946 Shanley [71] showed that one must follow the growth of the pre-bending as the load increases. The initial perturbation lowered the maximum load to that of the tangent plastic modulus, rather than that of an elastic-plastic modulus found for perturbations from a plastic state. This is another example of history effects being important in plasticity. For predicting maximum pressure in the vessel, one must follow the actual path of pressure versus crack growth, not apply a pressure and then a perturbation to the original crack. Elasticity is path-independent: the two histories would give identical results. Perhaps the pressure for leaking of this vessel by progressive localization could be predicted with a line spring model of the shell [72] and slip line fracture mechanics. Otherwise, a three-dimensional, locally fully plastic analysis appears necessary.

Approximate Fields for SLFM from Least Upper Bounds to Limit Loads

Limit Loads – In the rigid-nonhardening idealization, the limit load is that at which deformation is first possible. As the shape changes, the limit load changes. In the elastic-nonhardening idealization, plastic deformation spreads under increasing load until finally the non-hardening limit load for the current geometry is reached. At this point no further elastic strains are required and the stress distribution becomes constant, except for changes in geometry. The limit loads for the rigid- and elastic-nonhardening models are then the same except for differences in geometry, which are small for low yield strain materials. Important exceptions are buckling or elastic-plastic crack growth.

Limit loads can be approximated by using the bound theorems [27 pp.64–67, 61 pp.95–99, 62 pp.363–368]:

A lower bound to the limit load is given by any stress distribution which

a) satisfies any stress boundary conditions,
b) *everywhere* (even in the rigid region) satisfies equilibrium of stress gradients, and
c) *nowhere* (not even in the rigid region) violates the yield criterion.

An upper bound P_{ub} to the limit load P_L is a load for which a complete field of displacement *increments* $\delta u_i(x_j)$ can be found such that it

a) satisfies any displacement boundary conditions,
b) gives no change in volume *anywhere*, and
c) gives an integral of the plastic work increment throughout the body that is the upper bound P_{ub} times the corresponding increment in the displacement component in the direction of the load, δu_P:

$$P_L\, \delta u_P \le P_{ub}\, \delta u_P = \delta W^p = \int_V \left(Y_0\, \delta \varepsilon_{eq}{}^p\right) dV \tag{32}$$

Analogous bound theorems exist for the stiffness of an elastic body (e.g. [62 pp.360–362]) and for the loads for a given deformation in power-law hardening plasticity or a given deformation rate in power law creep.

Lower bounds to the limit load are seldom found because it is difficult to satisfy the equilibrium and yield conditions throughout the *rigid* regions. For this reason a slip line field does not provide a lower bound. Finite elements can be used for individual cases.

Upper bounds are easier to find and often accurate to within 10–20%. They are often used without realizing it to design riveted or bolted joints against tearing, shearing, or crushing. Here, as an example, consider the bending of a web on the base plate of a ship as in Figure 4. This bending might occur in the grounding of a ship. In commercial ships the typical stresses are so low that the web is attached by two fillet welds leaving a gap between. For simplicity, consider only the opening bending of the left-hand fillet weld. This will illustrate what can be learned from bounds to the limit load and how finite element analysis can lead to the exact slip line field, giving a check on both the bound analysis and the finite element mesh. For details see[69 pp.292–297,299–305].

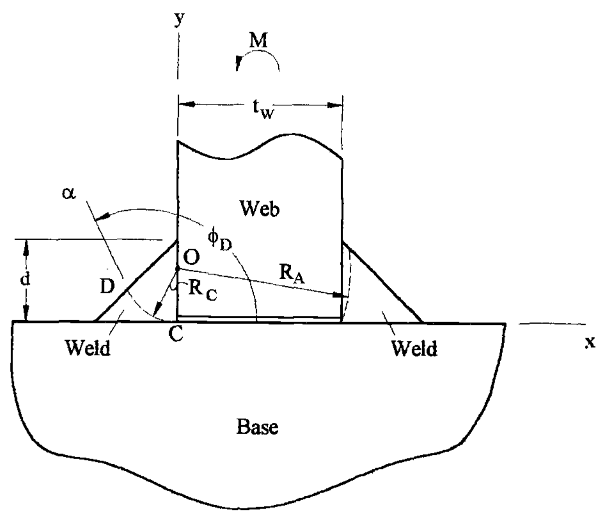

Figure 4 –*T-joint with two non-penetrating fillet welds under bending, with sliding along dashed arcs for an upper bound to the limit moment (after [69 p.292])*

Microhardness tests by Middaugh [69 p.283] have shown that the hard, heat-affected zones of the weld are in the base and the web, and that the lower hardness in the weld metal is constant within 10%, so homogeneity can be assumed. The hard zones in the base and web confine the deformation to the fillet itself.

For a deformation field for an upper bound, assume the web rotates about O, with the welded corner of the web sliding tangent to the face of the base plate. Upper bounds to the limit moment, M_{ub}, are found by equating the work done by the moment, as it rotates through the angle $\delta\theta$, to the work done by sliding with shear stress k and slip $R_C\delta\theta$ across the slip line of length $R_C(\phi_C - \phi_D) \equiv R_C\Delta\phi$. (The definition of ϕ as the counter-clockwise angle from the x-axis to an α-line is consistent with Eq. 10 for slip line analysis, and will be used below.) Because of the hard zone outside the fillet, $\phi_C \leq 180°$. Initially take $\phi_C = 180°$ and verify later that it gives a least upper bound. Then relate the arc radius R_C to $\Delta\phi$ so as to take the arc to the surface of the fillet, $y - x = d$. For a weld of length L this gives an upper bound to the limit moment in terms of $\Delta\phi$. Finally choose $\Delta\phi$ to minimize M_{ub} and normalize with the plane strain limit moment of a plate of the same thickness (net ligament length across the fillet, $a_n = d/\sqrt{2}$). Together these steps give the least upper bound for deformation fields consisting of sliding on an arc:

$$\frac{M_{\text{lub}}}{2kL\left(d/\sqrt{2}\right)^2/4} = \frac{M_{\text{lub}}}{2kLa_n^{\,2}/4} = 1.475 \text{ at } \Delta\phi = 1.923 \text{ radians} = 110.2°;$$
$$\phi_D = 1.219 \text{ radians} = 69.8°; \quad R_C/a_n = 0.619 \tag{33}$$

One can verify graphically that choosing $\phi_C < 180°$, in effect rotating the arc clockwise about C at constant radius, would increase the subtended angle needed to reach the face of the weld. Hence it would increase the upper bound. Thus $\phi_C = 180°$ and the angle to the slip line from the ligament is $\theta_s = 45°$.

Using the LUB Slip Line Arc for the SLFM Crack Tip Driving Parameters – With the asymmetry of this example, the response parameters are measured from the slip-line, here at $\theta_s = 45°$ from the net ligament. The slip increment δu_s per unit far-field bend angle $\delta\theta$ is given by the radius ratio R_C/a_n: $\delta u_s = a_n(R/a_n)\delta\theta$.

Although the upper bound theorem deals with limit loads, insight into the normal stress across the slip line at the crack tip, $\sigma_n/2k$, can sometimes be obtained from the slip line by using a theorem that LUB arcs in homogeneous material at least satisfy global equilibrium [73 pp.24–27,52–59, 69 pp.302–304]. This, along with the Hencky equations, gives an estimate of the normal stress along the arc and in particular at the crack tip. Here, however, the inhomogeneities consisting of the hard, heat-affected zones prevent applying the theorem.

An alternative estimate of $\sigma_n/2k$ at the crack tip is made with the plausible assumption that the mean normal stress where the arc meets a free face, here the face of the fillet, is of a form that (a) goes to the right limits if the arcs intersect the weld face at ±45° and (b) is zero if the arc is normal to it, under pure transverse shear of the ligament (consistent with [74]):

$$\frac{\sigma_D}{2k} = \left(\phi_D - \frac{3\pi}{4}\right) / \left(\frac{\pi}{2}\right) = \frac{\phi_D}{\pi/2} - \frac{3}{2} \tag{34}$$

Thus for $\phi_D = 90°, 135°$, or $180°$, $\sigma_D/(2k) = -0.5, 0$, or 0.5. Along an α–line, as here, the first Hencky equation of equilibrium (from Eqs. 11) is $d\sigma = 2kd\phi$. Then, with angles in radians, from Eqs. 33 and 34,

$$\frac{\sigma_n}{2k} = \frac{\sigma_C}{2k} = \frac{\sigma_D}{2k} + \Delta\phi = \left(\frac{\phi_D}{\pi/2} - \frac{3}{2}\right) + \Delta\phi = \left(\frac{1.219}{\pi/2} - \frac{3}{2}\right) + 1.923 = 1.099 \tag{35}$$

The slip line displacement du_s per unit far-field rotation $d\theta$ is given by the appropriate radius: $\delta u_s = R_C\delta\theta$. With θ_s, $\sigma_n/2k$, and δu_s known, single slip line fracture mechanics (SLFM1) can be applied. Rigorously, the slip line fields should be found repeatedly for each incrementally new geometry as the crack grows, but a one-step approximation might be tried first.

Using Finite Element Analysis to Find Slip Line Fields

One would like to check the accuracy of the limit load approximations by finding an exact field. Originally this was done by Hundy by annealing a specimen of high nitrogen steel, deforming it slightly, aging it again, and etching to reveal a slip line pattern. Then Green would idealize the pattern and in effect say "Let us consider the following slip line field". Many of the results were summarized in [75]. The method is used here with finite elements, for bending of the T-weld of Figure 4. For simplicity, the slip line field was studied for only the left-hand fillet of Figure 4 in opening [76,69 pp.292–297]. The boundary representing the face of the weld was free. The base and web flanks were rigid due to their hard, heat-affected zones. The web flank was rotated about O of Figure 4, with OC chosen by iteration to give zero net x-force on that side. The mesh was terminated short of the corner to avoid singularities, although by hindsight the corner could have been better modeled with elements having one side squeezed into the corner, and the corner nodes independently numbered but with the same initial coordinates. The program ADINA [77] was used with hybrid elements, each having nine displacement points and three pressure points.

The original mesh and one deformed to a displacement several times that to reach the limit load were both plotted, but were not revealing. Better was a plot of rosettes of principal strains. The first impression was of a single slip line of varying radius, for which sliding would violate incompressibility. To show more detail in the low-strain region, the truncated plot of Figure 5 was made. This reveals a region along the face of the weld with constant slip line angle $\phi = \pi/2$ and constant mean normal stress $\sigma_n/2k = -1/2$ ("constant state" as in Figure 2) and discontinuous slip on an arc $R < R_C$ of Figure 4 that runs into the corner at $\phi_C = \pi$, as closely as expected from finite elements.

The corresponding slip line field has the radius $R = OC$ chosen for no net x-force by the web on the fillet of Figure 4 using an idea from Hill (referred to in [78]) that for equilibrium the resultant force on an arc is the same as that on the radii which bound the sector de-fined by the arc [69]. Along with the Hencky equilibrium Eqs 11, this turns out to give

$$\frac{\sigma_A}{2k} = \frac{\pi}{2} - \frac{1}{2} = 1.071 \quad \text{and} \quad R = \frac{d}{\pi} \ ; \ \frac{R}{a_n} = \frac{\sqrt{2}}{\pi} = 0.450 \tag{36}$$

The value $\sigma_n/2k = 1.071$ at the crack tip in the corner of the weld is to be compared with $\sigma_n/2k = 0.5$ for tension (Figure 2), 1.543 for a singly, deeply face-cracked, homogeneous plate in bending [79,27 p.145], and 2.571 for the symmetrical, doubly face-cracked plate in tension. This last case is the negative of the punch indentation problem first worked out by Prandtl in 1920 (see [61 p.620]).

With the higher $\sigma_n/2k$ in opening bending than in the tension of Figure 2, both u_{si} or $CTOD_i$ and CTOA should be less ($c_{,u}$ greater) than in the SLFM tension of [70].

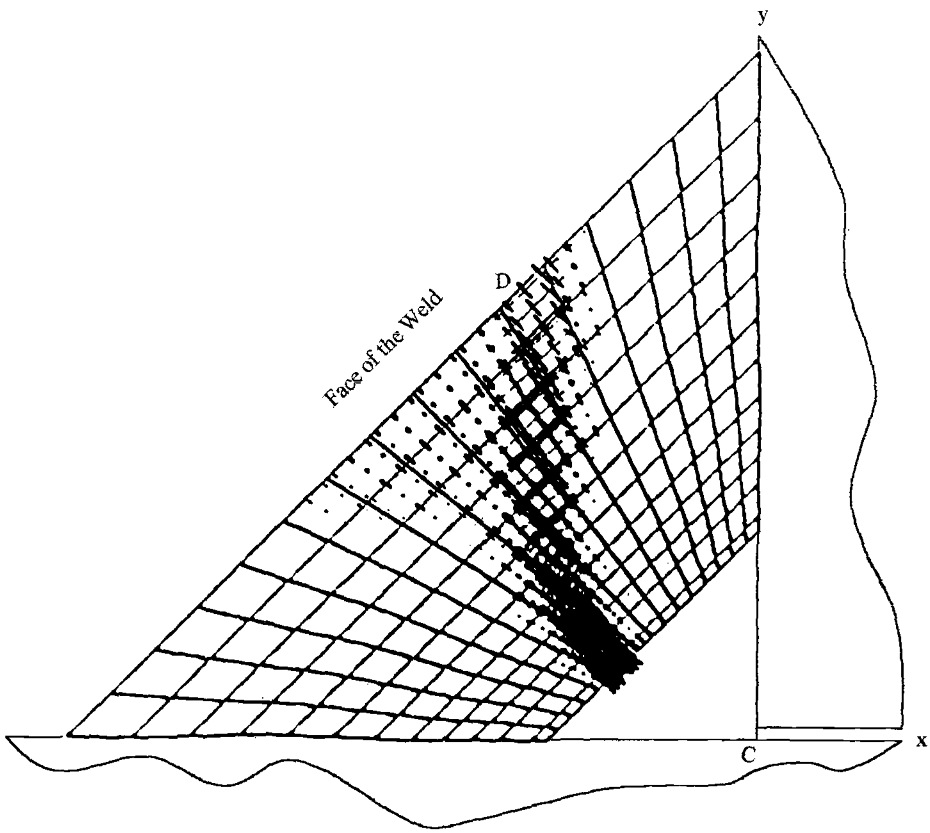

Figure 5 – *Principal plastic strains in the low–strain region (1/3 ≤ y/d ≤ 1) for opening bending of the left-hand fillet weld of Figure 4 [76 Figure 4.7b]*

As a check on the finite element analysis, contours of $\sigma_n/2k$ from the finite element analysis were plotted along with the analytical values along the active slip line. Note that if the flanks of the fillet weld were deformed symmetrically, the resulting $\sigma_n/2k$ would be symmetrical. But it was not! The answer seems to lie in the fact that away from the active slip lines, in the "rigid" region of slip line plasticity, the stresses are the ones left over from the original elastic-plastic loading of the finite element model, modified *but not wiped out* by the fully plastic deformation. This is further evidence of the fact, pointed out by others, that the maximum mean stress in the lens-shaped region between the slip lines is greater than the normal stress across them. (Furthermore, from Mohr's circle, the maximum normal stress exceeds the mean normal stress by k.) *Thus cleavage frac-*

ture cannot be predicted from SLFM alone; it may be affected by residual stress in the "rigid" zones, along with plastic strains of the order of the yield strain.

As the crack grows by a micro-ductile mechanism, the tip will deviate inward but not as far as in the direction of the current throat. Soon the classical slip line field [79] could fit inside the right flank, if not the left. Even before that point, the right-hand slip line arc would become active because it would have the lower limit load. The crack should then turn sharply to the right, until it reached the line of the original throat, after which the two arcs would become equally active. The crack should then follow symmetrically along the original throat. At the same time, $\sigma_n/2k$ will *rise* from the original value of 1.071 to the classical value of 1.543, while the half-angle between the slip lines increases from 45° to 72.0°. The effect of higher $\sigma_n/2k$ would probably outweigh the blunter slip line angles, and the crack growth per unit bend angle should increase. Certainly the likelihood of cleavage would increase. It will be interesting to see how well these predictions are confirmed by experiments on fillet welds.

Table 1 for opening bending gives a comparison of the finite element and least upper bound results with the slip line solutions for the crack tip driving parameters. Those for asymmetrical opening bending (SLFM1) of the single, left-hand fillet weld of Figure 4 are shown in the first three columns. The limit moments, slip line directions, and normal stresses at the crack tip are all within about 10%. The radius of curvature, giving the displacement across the slip line at the crack tip, is high by about 40% for the LUB arcs.

Table 1 – *Limit load and crack tip driving parameters for initial bending of single fillets and for deeply single-face-cracked plates (SFCB)*

Definitions:

a_n = net ligament (throat) = $d/\sqrt{2}$ for a 45° fillet of leg length d

k = yield strength in shear = $Y_0/\sqrt{3}$ for isotropic material

$M_L/(2ka_n^2/4)$ = limit moment normalized by that of a corresponding flat plate

θ_s = angle of slip line from the ligament direction at the crack tip

σ_n = mean normal stress across slip line at the crack tip

R = radius of curved slip line = slip displacement per far-field rotation, $\delta u_s/\delta\theta$

	Single Fillets			Deeply Face-cracked Plates	
Method:	FEA	LUB arc	Slip line	LUB arc	Slip line
Result:					
$M_L/(2ka_n^2/4)$	1.30	1.475	1.363	1.380	1.26
θ_s, °	45	45	45	66.8	72.0
$\sigma_n/2k$	1.2	1.099 Eq. 34	1.071	1.590 As Eq. 34	1.543
from [73]		Inapplicable		1.166	
R/a_n = $\delta u_s/(a_n\delta\theta)$	0.465	0.619	0.450	0.544	0.389

For comparison, the last two columns of Table 1 give the LUB and slip-line results for symmetrical opening bending (SLFM2) of a deep face crack in a homogeneous plate. Here the Kim theorem [73] does apply. The value of σ_n calculated from it and the LUB is 25% low, whereas that calculated using the back face estimate as in Eq. 34 is 3% high. For the deeply face-cracked plate, as expected from the loss of constraint of the hard heat-affected zone adjacent to the fillet, the limit moment is lower than for the fillet. The mean normal stress at the crack tip is less for the deeply face-cracked plate than for the fillet, apparently due to the larger rotation of the slip lines in the plate.

In summary, with due regard to mesh refinement along active slip lines, and with deformations large compared to the elastic or with incremental deformations at the limit load so the elastic strain increments are negligible, FEA gives good crack tip driving parameters from far-field loading. Of the LUB methods in some cases, including singly face-cracked plates under pure shear and under opening bending combined with small tension, a circular arc provides good approximations to the limit load and to the three crack tip driving parameters θ_s, σ_n, and $\delta u_s/\delta\theta$. In other cases, including symmetrical externally face-cracked tension and the singly face-cracked plate under pure bending, the estimates of local stress may be low and of the crack tip displacement per unit far field displacement may be high by 30–50% [73]. Even worse would be the singly grooved plate under a small opening bending with a compressive load, where the exact solution gives a larger constant state region and a small region of high curvature. Insight into other cases should be obtained by FEA.

Further Topics in Slip Line Fracture Mechanics

Comparison of the SLFM with the J and K Regimes of Fracture Macro-mechanics

The J-Integral – The path-independent J-integral of Eq. 9 is the scalar coefficient of the singular fields of Eqs. 4 around a crack tip in a power-law material. While these equations and their dimensionless functions are valid for non-hardening material, with a strain hardening exponent $n_h = 0$, they are not unique. As we have seen, tension and bending fields have different values of θ_s and $\sigma_n/2k$. (For a finite crack opening angle and for deformation along the flank of the crack, as in doubly face-grooved tension and in singly face-groove bending with a groove angle greater than 3.2°, the work along the flanks of the crack affects the contour integral on which J is based, but we neglect the effect here.). Consider J in terms of the crack tip field and driving parameters of SLFM2, with sliding by u_s across the two dashed slip lines emanating from the crack tip of Figure 6. Let the upper crack flank ($_b$) move vertically up by $u_{2b} = u_s \sin\theta_s$ and the lower flank move down similarly. Region ($_a$), ahead of the crack and between the slip lines, moves to the left by $u_{1b} = u_s \cos\theta_s$ to maintain continuity of normal displacement across the slip lines. It is convenient to evaluate J along the rectilinear path of Figure 6, within the annular zone of validity of SLFM2. Denote the plastic work per unit volume by W, the outward normal along the path by n_i, and a scalar element of the counterclockwise contour by ds. Then Eq. 9 becomes [51,59]

$$J \equiv \int_{\Gamma}\left[Wdx_2 - \sigma_{ij}n_i\frac{\partial u_j}{\partial x_1}ds\right] \tag{37}$$

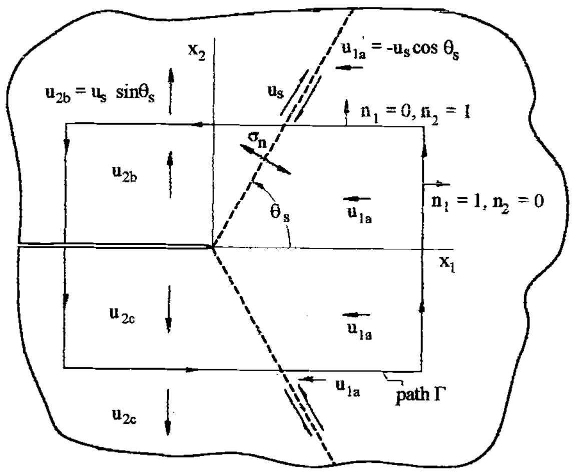

Figure 6 – *Path for finding the J-integral for SLFM2*

The only non-zero W is where the path crosses the slip-lines. Here $dx_2 = 0$, so the first term vanishes for even an infinitesimal width of shear band. Near the crack tip the slip-lines can be regarded as straight, so the rigid regions undergo pure translation and the gradients $\partial u_j/\partial x_1$ vanish. Thus the second term of Eq. 37 need be evaluated only where the path crosses the slip-lines. Consider the upper crossing and take the slip line to be of infinitesimal width δs in the x_1-direction, with a linear change in u_s across it. Then using Mohr's circle or Eqs. 10 for the stress components in terms of the normal and shear stress on the α–line gives the contribution of the upper slip-line to J. For SLFM2, the contribution of the lower slip-line to J turns out to be the same, so

$$J = -2\left[\sigma_{21}\frac{u_{1a} - u_{1b}}{\delta s} + \sigma_{22}\frac{u_{2a} - u_{2b}}{\delta s}\right]\delta s = -2\left[\sigma_{21}\frac{-u_s\cos\theta_s - 0}{\delta s} + \sigma_{22}\frac{0 - u_s\sin\theta_s}{\delta s}\right]\delta s$$

$$J = 2ku_s\left[\cos 2\theta_s\cos\theta_s + \left(\frac{\sigma_n}{k} + \sin 2\theta_s\right)\sin\theta_s\right] = 2ku_s\left[2\frac{\sigma_n}{2k}\sin\theta_s + \cos\theta_s\right] \tag{38}$$

In terms of the crack tip opening displacement CTOD = $2u_s\sin\theta_s$ with $u2a = u1b = 0$,

$$J = 2kCTOD\left[\frac{\sigma_n}{2k} + \frac{1}{2\tan\theta_s}\right] \tag{39}$$

Fitting J- and K-Mechanics to SLFM – If a problem is understood in terms of SLFM, the corresponding J behavior can be found from Eq. 39. Unfortunately the inverse procedure is incomplete: knowing J, for example by a contour integral in FEA, and having test data on J_c for the material in a particular configuration will not suffice to define the behavior if the CTDPs θ_s and $\sigma_n/2k$ are important and different from those fitting the J-singularity. For example for $n_h = 0$, the CTDPs might be approximated from the displacement functions along the crack flank and the normal stress at the resulting angle θ_s using Eqs. 4 and the tables in [43] for the $\tilde{u}_i$- and $\tilde{\sigma}_{ij}$-functions of θ extrapolated to $n_h = 0$:

$$\theta_s = \tan^{-1}\left(\frac{\tilde{u}_2(\pi,0)}{\tilde{u}_1(\pi,0)-\tilde{u}_1(0,0)}\right), \quad u_s = \frac{J}{\sigma_1 I_0}\sqrt{[\tilde{u}_1(\pi,0)-\tilde{u}_1(0,0)]^2+[\tilde{u}_2(\pi,0)]^2},$$

$$\frac{\sigma_n}{2k} = \frac{\sigma_1}{2k}\frac{\tilde{\sigma}_{11}(\theta_s,0)+\tilde{\sigma}_{22}(\theta_s,0)}{2} = \frac{\sqrt{3}}{2}\frac{\tilde{\sigma}_{11}(\theta_s,0)+\tilde{\sigma}_{22}(\theta_s,0)}{2} \tag{40}$$

To enable a reciprocal relation in general would require extending J-mechanics to include not only a normal stress effect, such as the Q of [49,50] or the A_2 of [47,48], but also a θ_s effect, if that is important. (In turn, of course, SLFM is incomplete, for example in not incorporating strain hardening effects and the resulting CTDP describing the current strain and damage gradient in front of a growing crack. These effects should be explored with FEA, even though the effect of strain-hardening would be less for a growing crack that tends to leave the strain-hardened material behind.)

For structures large enough for initiation under contained yielding with an annular K-defined field, $K_{Ic} = \sqrt{[J_cE/(1-\nu^2)]}$.

Relating the Contained Crack Growth of dJ/da to SLFM – For limited Mode I crack growth within the originally J-valid zone, the crack growth is often characterized by dJ/da, where da is the increment of crack length relative to the flank behind it. Combining the derivative of Eq. 38 for SLFM2 with the relation of da to the slip du_s from Figure 3b, solving for $c_{,u}$, and in turn introducing Eq. 22a for the CTOA in terms of $c_{,u}$, give

$$\frac{dJ}{da} = \frac{dJ/du_s}{da/du_s} = \frac{2k[2(\sigma_n/2k)\sin\theta_s+\cos\theta_s]}{\cos\theta_s + c_{,u}}$$

$$c_{,u} = \frac{2k[2(\sigma_n/2k)\sin\theta_s+\cos\theta_s]}{dJ/da} - \cos\theta_s \tag{41a}$$

$$CTOA = 2\tan^{-1}\frac{(dJ/da)\sin\theta_s}{2k[2(\sigma_n/2k)\sin\theta_s+\cos\theta_s]} \tag{41b}$$

It is probably preferable to derive the CTDPs θ_s and $\sigma_n/2k$ from SLFM2 for the specimen tested rather than from J-Q or J-A_2 analysis, although tests should be run.

Similar relations could be developed for asymmetric crack growth (SLFM1), but they depend on the crack growing in a straight path, rather than in the curved path which is often the case. It appears to be more important to apply SLFM1 directly to the data.

Embedding SLFM2 in Finite Element Analysis

The Need – The connection between far-field geometry and loading and the CTDPs can be carried out with analytical or approximate solutions in many cases; in many others it is worth using finite element methods for improved accuracy and the effects of more realistic stress-strain relations, including especially strain hardening during crack growth. FEA can also suggest either exact or simple upper bound slip line fields. At the same time, non-hardening analytical solutions give test cases for the adequacy of finite element mesh refinement.

The Mesh – In some FEA, quadrilateral elements are preferred over triangular ones for incompressible behavior and where slip discontinuities occur. The quadrilaterals can be simple, or grouped in triangles as in Figure 7. The triangular grouping has been suggested to facilitate mesh generation from arbitrary arrays of points, especially in later three-dimensional calculations with tetrahedral elements [80].

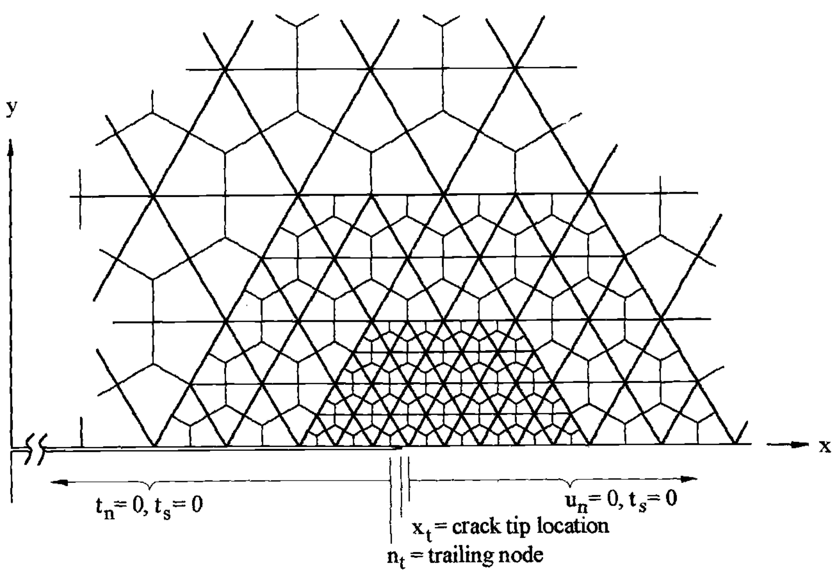

Figure 7 – *Triangular FEM mesh progressively refined where the crack tip approaches points in the mesh, and later coarsened where the crack tip leaves points behind. All triangular groups consist of four quadrilateral elements to facilitate computation*

Either triangular or quadrilateral meshes should be refined by factors of two for points being approached by the crack tip and later coarsened by factors of two for those being left behind. If the finite element code does not support constraining the node of a half-size element to the midpoint of the adjoining full-scale element, a transition involving triangles may be used, at the cost of increased complexity of interpolation of element states on refinement and coarsening.

The refinement need only be carried down to the scale of the coarsest source of inhomogeneity. For growth it us usually the crack roughness rather than the hole nucleus spacing or the grain size. Unfortunately the roughness may grow by a factor of ten during fracture of a Charpy-type specimen, and become a fraction of a millimeter.

Increased roughness is expected to decrease $c_{,u}$. The spacing of refinements must also be limited according to a rough form of St. Venant's principle: the stiffness of an element affects the strain distribution perhaps one or two elements away. Thus there should be at least one standard element between each successive refinement or coarsening by a factor of two.

Determining the CTDPs – From the finite element results for any given increment of loading or crack growth, the CTDPs θ_s, u_s, and $\sigma_n/2k$ can be found by a procedure similar to that of Eqs. 40, except that the radius used should be that at a few node spacings from the crack tip, corresponding to that for physical homogeneity. From Mohr's circle, σ_n is $(\sigma_{xx} + \sigma_{yy})/2$ at θ_s. $2k$ should be that at the local flow strength of the material.

Crack advance – The conceptually simplest criterion for crack advance is abrupt release of the crack tip node when the crack growth, accumulated as a fraction of the current distance to the next node, reaches unity. From Figures 3a or 3b, the advance before node release is given by Eq. 25, where $c_{,u}(\theta_s, \sigma_n/2k)du_s$ is zero before CTOD$_i$, but sliding off during blunting still advances the crack.

To simplify the boundary conditions on the nodes, one finite element program [77] can advance ("shift") the crack tip node according to the crack growth of Eq. 25. Eventually, at some preassigned fraction of the mean node spacing either side of the crack tip, the original tip node is released and the next node becomes the tip node.

The details of these node relaxation and release rules can be chosen to minimize the computation time to reach some reasonable error relative to an SLFM solution.

Blunting and Crack Tip Fans

Introduction – During the blunting before micro cracking, if the CTOD$_i$ is significantly larger than the microstructural fracture process zone, slip line analysis can help give insight into the processes determining CTOD$_i$. During quasi-steady crack growth, successive steps of crack tip blunting are accumulated into crack flank deformation and the CTOA. Crack flank deformation itself also causes a fan at the crack tip which contributes further to the CTOA. Both blunting and crack flank deformation will be discussed briefly, even though they are beyond the scope of this review since they involve sub-CTOD$_i$ sizes and more than two active slip lines.

Crack Tip Blunting – For insight into blunting in SLFM2 and SLFM1, consider first some results for general fields. As found by Joyce (see [27 pp.155–162]), the details of the blunted shape are very dependent on initial irregularities in the crack tip. In a sense, the logarithmic spiral fields assumed by many, e.g. [81,82,83], are kinematically unstable. For example, a small groove in the circular root will cause rigid shoulders on both sides of the groove. These focus deformation into the tip of the groove, deepening it. but also blunting it. An example of a nearly self-generating shape is shown in Figure 8 for the far-field displacements in the upper left quadrant of a doubly face-cracked plate in tension (DFCT), with a total downward displacement of $2u$ relative to the top [52]. At the three tip vertices, shear across each of the pair of fans generates fresh surface that adds to the flank across that vertex, while approximately maintaining the flank angles.

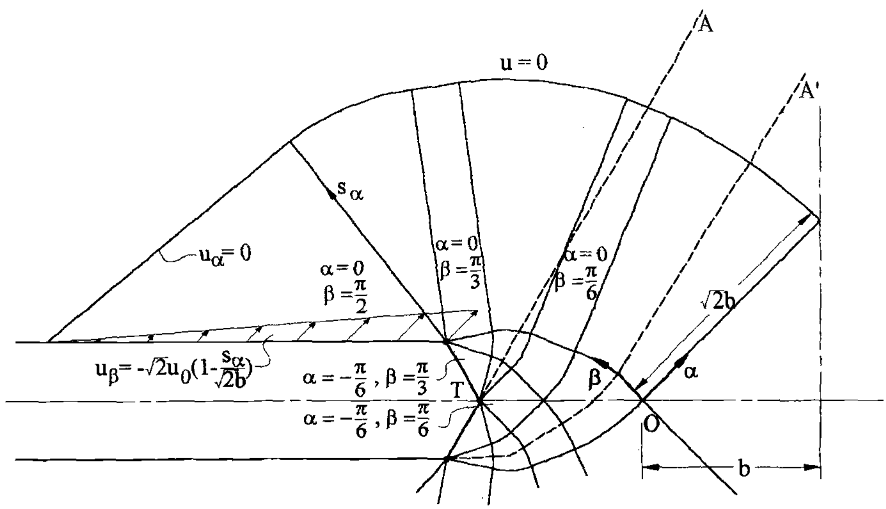

Figure 8 – *Quadrant of a self-similar blunting field for a doubly face-cracked plate in tension, with alternative slip lines A and A' for SLFM2 or SLFM1 superimposed*

As an alternative tip shape, consider the near-tip field with a single slip line *TA* at θ_s = 60°. With symmetry, SLFM2, this is one of a pair that remains straight all the way to the tip *T*. They generate a macroscopically blunted tip like that of Figure 3a. The nor-mal stress on the slip line *TA* is limited by the possibility of yielding in the fan between *TA* and the new free surface at the tip just above *T*. The angle of the fan between *TA* and the constant state region just above *T* is $\pi/12$ radians, so from the Hencky equilibrium Eq. 11, the fan will remain rigid if the normal stress on *TA* is less than $\sigma_n/2k = 1/2 + \pi/12 = 0.762$.

For larger σ_n, the corner at *T* between the slip line and the flanks could not remain rigid [84,61 pp.425–9]. The far-field slip lines must come in farther ahead of the tip, as along the dashed slip line *A'*, so that their normal stress will be lowered in the blunted region. For instance for *A'* and the blunted field of Figure 8, from Eq. 11 $\sigma_n/2k = 1/2 + \pi/3 = 1.547$. The accompanying deformation at the tip to prevent a gap from opening up along the now-curved slip line will mean that a different quasi-steady tip shape will develop. This will also happen with other values of θ_s and $\sigma_n/2k$, complicating the relation $CTOD_i(\theta_s, \sigma_n/2k)$, and making empirical determination of it more advisable.

With a line of discrete slip, as on A', and its symmetrical twin crossing in front of the tip, an important further phenomenon occurs. Since the slip lines cross at 90°, if the slip increments on one are equal to those on the other the increments on each will be offset by the amount of slip. This leaves an average shear strain of $\gamma = 1$ behind each, and $\gamma = 2$ where both have swept over. The corresponding equivalent strain can be found directly from the work per unit volume: $\varepsilon_{eq}\sigma_{eq} = \gamma\tau$ or $\varepsilon_{eq} = \gamma(\tau/\sigma_{eq}) = 2/\sqrt{3}$. This large strain at the large normal stress will cause subsurface crack formation early in yielding, even with the requirement that critical conditions be attained over a critical volume. Therefore there will be subsurface initiation near the tip of a logarithmic spiral region, as often reported. This will further complicate the relation $CTOD_i(\theta_s, \sigma_n/2k)$.

In mixed mode with a single slip line (SLFM1), the deformed shape will be that of the first step of Figure 3a. At first for TA to interact with the flank, the fan angle would be $\pi/4 + \pi/6$ radians. From Eq. 11 the normal stress on TA need only be less than $\sigma_n/2k = 1/2 + 5\pi/12 = 1.809$. However, once the sliding off on TA at the tip develops, that surface could only remain rigid if the normal stress were less than given by the fan between its rigid region and the normal to TA (not shown), or $\sigma_n/2k \leq 1/2 + \pi/4 = 1.285$. Higher normal stresses than this would again shift the slip line from A to A'. It remains to be seen how the quasi-steady tip shape would evolve. Note that finite elements have difficulties in treating these problems because they normally do not allow the sliding off of near neighbor nodes, although that has been observed experimentally [27 pp.155–162].

In conclusion for blunting in SLFM2 initiation, θ_s and $\sigma_n/2k$ should be regarded as setting boundary conditions at a scale large compared to the $CTOD_i$. For surface initiation mechanisms, blunting reduces the effect of normal stress on near-surface nucleation, but induces sub-surface initiation at high $\sigma_n/2k$. Blunting also induces transients and requires that any FEA treatment of it utilize mesh sizes that are only a fraction of the $CTOD_i$, and account for sliding off at multiple vertices at a crack tip.

In SLFM1 fields (Figure 3c), similar effects exist but are less of a problem because the crack flanks are usually more nearly parallel to the slip direction, and there is no crossing of slip lines to promote high strains for sub-surface initiation.

Crack Flank Deformation and Fans – Most of the characteristics of deforming flanks and fans have been introduced in the discussion of the blunting of Figure 8. Another can be summarized from an examination of the slip line field of that figure:

$$\text{Flank yielding when } \frac{\sigma_n}{2k} \geq \frac{1}{2} + \frac{3\pi}{4} - \theta_s \tag{42}$$

Two other characteristics of flank yielding should be pointed out. First, there may be significant shape changes due to flank rotation, which must be accounted for in finding the fields for later strain increments. More important is the contrast in fracture tendency between a slip line that is the limit of a narrow fan where the displacement is *normal* to the slip line, as in the left-most fan of Figure 8, and a slip line between rigid regions, where the displacements are along the slip line, as in SLFM. Shear due to displacements along a slip line tends to form elliptical holes that are drawn out *along* the slip line, making it more prone to transverse fracture. Shear due to displacements across the slip line limit of a fan tend to draw out elliptical holes perpendicular to the slip line, making it less prone to transverse fracture. Thus *a complete fracture criterion should include rotation, as well as strain and stress.*

Contraindications for SLFM

Several aspects of fracture that limit the applicability of SLFM have already been mentioned. Some as well as others deserve emphasis here. The classical Prandtl field foı doubly face-cracked tension (DFCT) has multiple slip lines and counter-rotation in a fan It requires a deep groove leaving a 10% ligament to prevent shoulder yielding, so it is seldom encountered in specimens or in service, but its analytical elegance has perhaps blinded others as well as the author to the simplicity and the manifold presence of situations where SLFM1 and 2 are applicable.

The non-hardening assumption is good for stresses and limit loads but poor for strain and less so for displacements. A reasonable rule of thumb might be that for SLFM to be a good approximation, the ratio of the limit load for any plausible, markedly different, displacement field should be greater than that of the proposed field by the ratio of the tensile strength to the yield strength [68]. The same applies to the choice between the symmetrical SLFM2 and the unsymmetrical SLFM1 that occurs more often in practice.

Applications

Sources of CTDPs – Collections of solutions for slip line fields around cracks, e.g. [27,61] provide the CDTPs θ_s, $\sigma_n/2k$, and du_s as functions of the far-field geometry and loading. Often the results in the literature must be adapted or supplemented by applying the fundamentals, as in Eqs. 10–16, or the bound ideas as in Eqs. 32–35. This is especially true for du_s and for the deformed geometries encountered with ductile alloys. An application of the fundamentals for asymmetric SLFM1 fields, from the initiation of crack growth to final separation, is given in [69 pp. 282–291] for cracking in non-penetrating fillet welds that attach a web to a base plate. Finite element analyses for general geometries and, more rarely, adapting J-Q or J-A_2 results can also provide insight that can be sharpened with the fundamental equations.

General Methods for Finding CTRFs – Pending a very detailed micro mechanical analysis based on the dislocation, grain, phase, and impurity microstructure, the crack tiı response functions must be found experimentally. The two most common are the load-deformation and fracture topographic or profile methods. The following example includes data, with further data in the next two sub-sections.

Tensile experiments [70] provided the initiation displacements and the crack growth rate for both symmetrically and asymmetrically single grooved 12.7 mm round bars fror both load-deformation curves and post-fracture profile data. The profiles were recorded from the focal height and a traveling microscope stage. From the load data, the initiatioı displacement was taken along the horizontal line through the maximum load as the difference between the intercepts of the lines of initial loading and the steepest load drop. A crack growth ductility D_g was defined in terms convenient for predicting the required structural stiffness of the surroundings for stability in tension, but inconvenient for

SLFM. There were, however, sufficient other data to determine the CTRF data of Table 2 for both SLFM2 and 1.

Table 2 – *Crack tip response function data. Six structural alloys at* $\theta_s = 45^\circ$, $\sigma_n/2k = 1/2$. *From Table 2 of [70] with Eqs. 22b and 23b*

Alloy	1018 CF		HY-80		HY-100		5086-H111		1018 Norm		A36HR	
YS, TS, MPa	411	500	648	745	772	869	225	333	305	457	337	469
ε_u	0.04–0.09		0.13		0.07		0.15		0.17		0.24	
σ_f, MPa, ε_f	660	0.72	1200	1.25	1350	1.24	480	0.58	830	1.19	880	1.14
n_h,	0.04–0.13		0.10–0.17		0.06–0.18		0.15–0.18		0.14–0.27		0.20–0.26	
(calculated over strain ranges of from 0 to ε_u through 0.25 to ε_f)												
In terms of CTOD$_i$ and angles												
Method	P–u[1]	Prof.	P–u	Prof.	P–u	Prof.	P–u	Prof.	P–u	Prof.	P–u	Prof.
Symmetric, SLFM2												
CTOD$_i$, mm	0.18	0.05	0.27	0.13	0.21	0.13	0.46	0.20	0.85	0.54	0.44	0.20
CTOA, °	13	18	18	26	20	28	9.5	18	15	24	11	20
Asymmetric, SLFM1												
CTD$_i$, mm	0.13	0.04	0.19	0.09	0.15	0.09	0.32	0.14	0.60	0.38	0.31	0.14
θ_{s1}, °	9.6	9.5	14.4	14	14.2	14	15.2	15	22.6	22	21.2	20.5
$\theta_{s2} = \theta_{sc}$, °	10.4	10.5	15.6	16	15.8	16	16.8	17	27.4	28	24.8	25.5
In terms of SLFM crack tip response function values u_{si}, $c_{,u}$, and θ_{sc}												
Method	P–u	Prof.	P–u	Prof.	P–u	Prof.	P–u	Prof.	P–u	Prof.	P–u	Prof.
Symmetric, SLFM2												
u_{si}, mm	0.13	0.04	0.19	0.09	0.15	0.09	0.32	0.14	0.60	0.38	0.31	0.14
$c_{,u}$	5.5	3.8	3.8	2.4	3.9	2.1	7.8	3.8	4.7	2.6	6.6	3.3
Asymmetric, SLFM1												
u_{si}, mm	0.24	0.11	0.34	0.22	0.31	0.16	0.49	0.22	0.72	0.43	0.60	0.32
$c_{,u}$	13.7	9.5	10.9	6.9	9.4	6.9	9.4	7.4	4.7	3.6	5.6	4.0
$\theta_{sc} = \theta_{s2}$, °	10.4	10.5	15.6	16	15.8	16	16.8	17	27.4	28	24.8	25.5

[1]"P–u" denotes from load-displacement data; "Prof." denotes from fracture profiles.

Several aspects of Table 2 should be discussed briefly. The strain hardening exponents n_h evaluated at large strains tend to be high by a factor of about two, so the lower value, nearly the uniform strain ε_u, should be used. Note that while strains of unity can be reached in crack tip blunting, those in the wake of a 45° slip line are about CTOA/2. CTOD$_i$s from the P-u data are too high by a factor of roughly two, compared to the more accurate profile data. They are 0.05–0.1 mm for low n_h and 0.2 for high n_h both with and without symmetry, although this implies twice as much total slip in the symmetric case. With symmetry, the profile CTOAs are 1 1/2 times higher than the P-u values; for the related $c_{,u}$ the inverse ratio holds. Neither is strongly affected by n_h. With asymmetric single slip, the micro cracking direction relative to the slip line, θ_{sc}, increases roughly from 10° to 20° with n_h. The CTOA is very small, but the more distinctive $c_{,u}$ decreases from a very high 12 to 5. In summary, the HY steels are good performers except for asymmetric crack growth, and strain hardening has an effect of a factor of two in initiation and asymmetric growth. The inverse effect of measurement method on symmetric crack growth is unexplained. Table 2 provides a good basis of comparison with other alloys in other tests.

For bending, interpretation is more difficult. Approximate slip line field calculations for deformed singly face-cracked bend tests (SFCB) are in process. Preliminary results show that the fields are simpler for three-point than four-point bending because the slip lines do not cross under the central tup, thickening the back side [78]. During wrapping the specimen around the tup, $\sigma_n/2k$ first rises. It then drops abruptly when the ligament shrinks to the point where pivoting around the outer contact points, loading the ligament more nearly in tension, requires a lower limit load. The converse of this analysis should provide a more accurate method of reconstruction of the CTOA as a function of crack growth than currently available to use with topographic data collected from the curved specimen surface, e.g. [85,86].

A wedge opening loading jig has been used to measure anisotropic behavior in 22 mm cubes cut from plates [87]. Tests on 1018 HR steel (HB 108 kg/mm^2 ≈ 360–410 MPa) were only run on the double face-grooved tension configuration with fans and flank deformation, so their very low CTOAs cannot be compared with SLFM2. The proposed back-to-back single face-grooved and double unequally face-grooved specimens could provide data for SLFM2 with varying $\sigma_n/2k$.

Crack Tip Response Function Data for SLFM2 – No complete set of data is available for the dependence of the response functions CTOD$_i$ and CTOA or u_{si} and $c_{,u}$. on θ_s and $\sigma_n/2k$. Some results beyond the data of Table 2 will be given here. Bend tests quoted from the literature [70] gave CTOAs of 12° for A533B, 9° for A471 rotor steel, 17° for annealed free-cutting mild steel, and 14° for BS 4360 Grade 50.

Preliminary tests on cold finished 1018 steel bars of hardness-estimated tensile strengths of 560–570 MPa were intended to give data for unequally double face-grooved specimens in tension and bending [67]. The tests were limited by cleavage to θ_s = 45°–67° and $\sigma_n/2k.$ = 0.76–1.18. Overall, CTOAs ranged from 5° to 28°, with replications varying by factors of typically 1.5. CTOAs from *P-u* curves tended to be half those from profiles, whereas in Table 2 the ratio was typically 2/3. There was perhaps more effect of θ_s than expected and less of $\sigma_n/2k$, but the data are too sparse and scattered to draw firm conclusions.

A back-bend test on a very deeply face-cracked specimen puts the remaining ligament in low-constraint tension [88] and requires less testing machine stiffness for stability during crack growth. Back-bend and conventional open-bend tests were carried out on A572 Gr50 (HRB 83, *TS* = 560 MPa) to study the back-bend test and find the effect of $\sigma_n/2k$ on CTOD$_i$ and CTOA, with the results shown in Table 3. The CTOD$_i$ tends to be more when determined from the loads, as before, and to be markedly less for higher normal stress, though not as much as expected from the exponential relation for hole growth. The CTOA is comparable from *P–u* and profile data, and is only halved by tripling the normal stress while increasing θ_s from 45° to 75°.

Table 3 – *Crack tip response function data for open- and back-bending A572 Gr50, HRB 83, TS = 560 MPa [88]*

	Back bend		Open bend	
	$\theta_s = 45°$, $\sigma_n/2k = 1/2$		$\theta_s = 72°$, $\sigma_n/2k = 1.543$	
Method	P–u[1]	Profile	P–u	Profile
$CTOD_i$, mm	1 –3	0.4	0.1–0.4	0.1–0.2
CTOA, °	30→23[2]	35→20	17–19	13→17

[1]"P–u" denotes from load-displacement data; "Profile" denotes from fracture profiles.
[2]Arrows denote changes with crack growth.

Crack Tip Response Function Data for SLFM1 – Limited experimental data for a variety of steels [70,74,82,89] indicate that the slip line spreads out somewhat due to strain hardening and the crack grows to the tensile side of the slip line. Specifically, for $\sigma_n/2k$ = 0 to 0.8, θ_{sc} = 0 to 30° and $c_{,u}$ = 4 to 10. In non-penetrating fillet welds, profiles showed considerable variation along the welds; and similarly, $\sigma_n/2k = 0.5$, θ_{sc} = 18° to 45° and $c_{,u}$ = 1.6 to 9 [69]. It would be interesting to work out the CTDPs and CTRFs for the mixed-mode data on ductile metals in [90].

Recommended Studies

A wide variety of experiments and analyses are needed to determine the ranges of validity of the new slip line fracture mechanics, to find values and means of determining the crack tip driving parameters (CTDPs) in terms of the shapes and loadings for both specimens and structural parts, and to find the crack tip response functions (CTRFs) of those CTDPs for typical alloys.

Three-Point Bend (Slow Charpy-Type) Tests

Experimental – Interpret load-deflection and fracture profile data, especially for temperatures around the upper shelf of the cleavage transition temperature, for representative alloys. Use available twin arc approximate slip line fields to get the history of the crack tip normal stresses and slip directions, which comprise the CTDPs. Find the resulting crack tip response parameters, consisting of the crack tip opening displacements for initial growth, $CTOD_i$, and the crack tip opening angles for extensive crack growth. Load-deflection data give a first approximation to $CTOD_i$ and CTOA, although they are confounded by shear lips. Fracture profile data over the region between the shear lips are preferred. Visual examination of broken Charpy specimens suggests that the tests may involve considerable scatter.

Offset the pre-cracks from the striker to introduce shear.

Analytical – Use the twin arc approximation for the inverse problem of finding the local CTOAs from fracture profiles.

Embed SLFM2 into FEA. Use FEA to check the twin arc approximation for the CT-DPs and for the resulting crack growth in terms of the CTOA and the far-field displacement increments.

Patch SLFM2 for extended growth into (J, A_2) fields for initiation and early growth.

Analyze the offset shear test with SLFM1.

General Analytical

Specimens for Studying, Interpreting, and Applying to Practice the Effects of the Following Variables –

Slip line angle and normal stress for finding the functions CTRFs(CTDPs).

Strain hardening, including FEA.

Finite flank angles and fans adjacent to discrete slip lines.

Growth-retarding counter-rotation in slip line fans, as in the Prandtl field for double face cracked plates.

Single-plane slip line fracture mechanics (SLFM1).

Normal Stress for Cleavage – Estimate and validate maximum principal stress concept for initiation in rigid regions of SLFM2 and SLFM1. Quasi-static arrest model based on a single reduction in cleavage strength for any running crack.

Specimens for Bending Combined with Shear, Tension, or Both – See also *Three-Point Bend* with offset.

$CTOD_i$ from Micro Mechanics of Blunting – From sliding off at crack tips and machine-grooved surfaces, find criteria for both surface and sub-surface nucleation. Blunting may reduce the effect of mean normal stress if surface initiation of crack growth, but increase that if subsurface initiation. Incorporate sliding off into FEA.

Quasi-Steady Growth of Through-Cracks in Plates – Apply two-plane, mixed mode slip models around the peripheries of tunneling cracks ranging from slant through shear lip to flat. (For example, the tips of tunneled slant cracks are under combined Modes I and III, while the trailing edges of deeply tunneled cracks approach Mode I loading but Mode II deformation and mixed Mode I and II cracking.)

Generalized Plastic "Plane Stress" – This is much more difficult than plane strain. Base a fracture mechanics on elements large enough to include thinning as well as tunneling and necking mechanisms. Otherwise use elements small enough so they involve strain gradients or varying thicknesses around their peripheries as boundary conditions or internal variables, and increments in those variables as response functions. If these are too complex, use FEA from the far field either down to local, generalized, mixed mode SLFM planes around a slanted, tunneling crack front, or all the way down to three-dimensional fracture micro mechanics.

An special imtermediate case is crack growth along a neck under locally rigid-body displacements, as observed in foil [26].

In Plates, Transition from Through-Growth of Face Cracks to Quasi-Steady Lateral Growth of Through-Cracks –

Progressive Localization of Through-Growth of Longitudinal Cracks in Pressure Vessels – Try a line spring model [72], with the net-section growth ranging from elastic K-controlled to fully plastic SLFM2-controlled.

Local Displacements and Transitions to Far-Field Macro Mechanics for the Extended Bilinear Elasticity of [1] – A bilinear elastic field, approximately corrected for crack growth with linear unloading and plastic re-loading, should have the displacement fields evaluated and be linked to the far-field geometry and loading. See the power-law analysis in [91]. Compare with dJ/da and SLFM2.

General Experimental

Test and Validate the Above Analyses – Slip line angle and normal stress, strain hardening, finite CTOAs leading to flank deformation in bending, counter rotation of deformed holes relative to the material in shear bands, cleavage, mixed mode, micro mechanics of blunting, growth of through-cracks with shear lips, as well as the transition to it from through-growth of face-cracks, and progressive localization of long face cracks.

Explore Other Variables – Inhomogeneities from welds or graded alloys, anisotropy, roughness (especially for growth).

Asymmetrical Cracking or Slip in SLFM2 Stress Fields – With symmetrical slip, when is the cracking asymmetrical in plane strain? —in plane stress? What happens with different asymmetries applied by displacement boundary conditions in these cases? Normal, zigzag, or asymmetric growth in the neck of a round bar? —in a bar in bending? For growth of a through-crack in a sheet, is the choice between slant, double-vee, and flat fracture determined by out-of-plane boundary conditions?

Growth of Shear Lips – For how much of the width of a member is the plane strain assumption of SLFM valid in bending and in tension? Transition regions between plane stress and plane strain for bars or plates with various cross-sections.

Problems from Practice – Structural joints. Plate specimens to model conditions at the tip of a long crack in a pipeline, essentially with a plastic circumferential and axial displacement field that extends a significant fraction of the pipe diameter, with possible out-of-plane bending due to gas forces on the split part of the pipe [92]. A similar problem arises in the bending of radial petals in a plate perforated by an explosion.

Conclusions

The need for predicting extensive plastic crack growth arises in buildings, ships, and refineries subject to earthquakes, accidents, or explosions. The complexities and uncertainties of metallurgical structure make computation from a nano or micron scale impractical in most cases. A new plane strain fracture mechanics at the millimeter scale is based on the result that for non-hardening plasticity, the local displacement field is often characterized exactly or primarily in terms of either two symmetric planes or a single asymmetric plane at the crack tip (Mode I SLFM2 and mixed mode SLFM1, respectively). For SLFM2 the crack tip driving parameters (CTDPs) consist of the normal stress across the slip plane and its angle from the plane of symmetry. The crack tip response functions (CTRFs) of the CTDPs are the empirically determined crack tip opening displacement for initial growth, $CTOD_i$, and the crack tip opening angle CTOA, which gives the continuing crack growth per unit far-field displacement. The loads, CTDPs, and crack growth per unit far-field displacement in terms of the CTOA are found from the geometry of the crack and the far-field deformation by using slip line plasticity or a twin arc approximation to it, by finite element analysis, or from linear or non-linear (K or J) solutions.

SLFM2, and the SLFM1 treated elsewhere, provide force-deformation curves for cracked structures. The integral of these curves is the plastic work, the extension of the energy of elasticity. For geometrically similar structures, the deformation to initiation scales inversely with size; the deformation during crack growth is scale invariant. While the total work cannot be simply scaled, the force-deformation curves and SLFM help in predicting the behavior of structures.

Together, SLFM2 and 1 provide a third leg to fracture macromechanics, complementing $K(T)$ and $J(A_2)$ for crack initiation and early growth.

The paper includes a number of other topics:

Descriptions of fracture mechanics at the nano, micro, and macro scales.

An introduction to plane strain, rigid-plastic, slip-line plasticity and limit loads, illustrated with an application to face-cracked plates in tension.

References to plasticity solutions for a number of cracked parts.

For typical sizes of test specimens of a number of alloys that are ductile during crack growth, summaries of $CTOD_i$s running from 0.1 to 0.5 mm and CTOAs from 1° to 30°.

A method of finding approximate crack tip slip angles, stresses, and displacements from least upper bounds to the limit loads.

Relations for embedding SLFM in FEA and in the K and J regimes of fracture macro mechanics.

An application to proof testing of a pressure vessel with a long part-through crack. This illustrates that in plasticity, progressive localization in the crack depth (sometimes fortunately) precludes reaching the load for classical instability, as found by a perturbation from a uniform crack. That gives a form of leak before break, although at a lower pressure than uniform growth. This is analogous to the growth of eccentricity in plastic buckling. In elasticity, by contrast and aside from finite changes in geometry, path independence gives instability at the same load by either a progressive loading or a perturbation path.

An introduction to using slip line mechanics to find $CTOD_i$ from micro mechanics and the sliding-off ("blunting") process with either surface or subsurface crack formation. These would show markedly different sensitivities to the normal stress on the macroscopic crack tip slip line.

A description of a number of recommended studies. One of these, SLFM2 for three-point bend (static Charpy) tests predicts transitions to and from cleavage. It does not require finite elements and has been programmed in a common numerical computing code [93]. A second recommended study is the use of slip line plasticity to validate meshes in finite element analyses, and in turn to use FEA to suggest slip line fields for cracked and possibly deformed specimens and structures, such as the partial fillet weld in bending that was reviewed here. A third is the fracture mechanics of cracking in fans at crack tips, where the growing holes counter-rotate with respect to the material in the shear band.

Acknowledgments

Among many, especially to Prof. David M. Parks for insights, stimulating discussions, and for including me in the research supported by the Engineering Research Program, Office of Basic Energy Sciences, Department of Energy through Grant DE-FG02-85ER13331 to M. I. T. under the good offices of the late Dr. Oscar Manley and then Dr. Robert Price. Acknowledgments also to many students and colleagues, especially to Dr. Walter G. Reuter of the Idaho National Engineering and Environmental Laboratory, a co-contractor with the Department of Energy in this field, and to Prof. Xiaodong Wang for stimulating and rewarding discussions on embedding SLFM into FEA. Sincere thanks to the reviewers who coped with and ill-prepared manuscript and thoughtfully suggested many improvements.

My deep thanks too, to the myriad of others who have found with Aristotle that "the search for truth is in one way hard and another easy, for no one can grasp it fully nor miss it wholly, but each [has added] to the store of knowledge and from it a certain grandeur arises."

Finally, as engineers we should follow the New England teacher Alcott, who said that "Knowledge is chaff until you have taken it into yourself and used it."

References

[1] Ponte Castañeda, P., "Asymptotic Analysis of a Mode I Crack Propagating Stead-ily in a Deformation Theory Material," *Transactions of the American Society of Mechanical Engineers,* Vol. 109, *Journal of Applied Mechanics*, Vol. 54, 1987, pp. 79–86.

[2] Ernst, H. A., "Material Resistance and Instability Beyond J-controlled Crack Growth," *Elastic-Plastic Fracture: Second Symposium, Volume I—Inelastic Crack Analysis, ASTM STP 803*, American Society for Testing and Materials, Philadelphia PA, 1983, pp. I-191–I-213.

[3] Ritchie, R. O., Knott, J. F., and Rice, J. R., "On the Relationship Between Critical Tensile Stress and Fracture Toughness in Mild Steel," *Journal of the Mechanics and Physics of Solids*, Vol. 21, 1973, pp. 395–410.

[4] McClintock, F. A., "A Criterion for Ductile Fracture by the Growth of Holes," *Transactions of the American Society of Mechanical Engineers,* Vol. 90, *Journal of Applied Mechanics*, Vol 35, 1968, pp. 363–371.

[5] McClintock, F. A., Kaplan, S. M., and Berg, C. A., "Ductile Fracture by Hole Growth in Shear Bands," *International Journal of Fracture Mechanics*, Vol. 2, 1966, pp. 614–627.

[6] Tvergaard, V., "Material Failure by Cavity Nucleation Between Larger Voids," *Journal of the Mechanics and Physics of Solids*, Vol. 30, 1982, pp. 265–286.

[7] Tvergaard, V., "Material Failure by Void Growth to Coalescence," *Advances in Applied Mechanics Vol. 27*, J. W. Hutchinson and T. Y. Wu, Eds., Academic Press, New York NY, 1990, pp. 83–151.

[8] Neimark, J. E., "The Fully Plastic Plane Strain Tension of a Notched Bar," *Transactions of the American Society of Mechanical Engineers,* Vol. 90, *Journal of Applied Mechanics*, Vol. 35, 1968, pp. 111–116.

[9] Cockroft, A. D., "Ductile Fracture in Cold Working Operations," *Ductility*, H. W. Paxton, Ed., American Society for Metals, Metals Park OH, 1968, pp. 199–225.

[10] Becker, R., "An Analysis of Shear Localization During Bending of a Polycrystalline Sheet," *Transactions of the American Society of Mechanical Engineers*, Vol. 114, *Journal of Applied Mechanics*, Vol. 59, 1992, pp. 491–496.

[11] Griffith, A. A., "The Phenomena of Rupture and Flow in Solids," *Philosophical Transactions of the Royal Society (London)*, Vol. A221, 1920, pp. 163–198.

[12] Griffith, A. A., "The Theory of Rupture," *Proceedings of the First International. Congress of Applied Mechanics*, Delft, 1924, pp. 55–63.

[13] Orowan, E., "Notch Brittleness and the Strength of Metals," *Transactions, Institution of Engineers and Shipbuilders in Scotland*, Vol. 89, 1945, pp.165–215.

[14] Orowan, E., "Fracture and Strength of Solids," *Reports on Progress in Physics*, Vol. 12, 1949, pp. 185–232.

[15] Irwin, G. R. "Fracture Dynamics," *Fracturing of Metal*, F. Jonassen, W. P. Roop, R. T. Bayless, Eds., American Society for Metals, Cleveland OH, 1948, pp. 147–166.

[16] Irwin, G. R., "Analysis of Stresses and Strains Near the End of a Crack," *Transactions of the American Society of Mechanical Engineers*, Vol. 79, *Journal of Applied Mechanics*, Vol. 24, 1957, pp. 361–364.

[17] Williams, M. L , "On the Stress Distribution at the Base of a Stationary Crack," *Transactions of the American Society of Mechanical Engineers*, Vol. 79, *Journal of Applied Mechanics*, Vol. 24, 1957, pp. 109–114.

[18] Rossmanith, H. P., "George Rankin Irwin - The Father of Fracture Mechanics," *Cleavage Fracture, George R Irwin Symposium*, K. S. Chan, Ed., The Minerals, Metals & Materials Society (TMS), Warrendale PA, 1997, pp. 3–38.

[19] Wieghardt, K. (1907), "Über das Spalten und Zerreissen elastischer Körper," *Zeit-schrift Mathematik und Physik*, Vol. 55(1–2), pp. 60–103.

[20] Wieghardt, K. "On Splitting and Cracking of Elastic Bodies," H. P. Rossmanith translation of Wieghardt (1907), *Fatigue and Fracture of Engineering Materials and Structures*, Vol. 12, 1995, pp. 1371–1405.

[21] McClintock, F. A., and Irwin, G. R. "Plasticity Aspects of Fracture Mechanics," *Fracture Toughness Testing and its Applications, ASTM STP 381*, W.F. Brown Jr., Ed., American Society for Testing and Materials, Philadelphia PA, 1965, pp. 84–113.

[22] Barenblatt, G. I., "On the Equilibrium Cracks Due to Brittle Fracture," *Doklady Akademii Nauk SSSR*, Vol. 127, 1959, 47–50.

[23] Leonov, M. Ya., and Panasyuk, V. V., "The Development of the Smallest Cracks in Solids," *Prikladnaia Mekhanika*, Vol. 5, No. 4, 1959, pp. 391–401.

[24] Dugdale, D. S., "Yielding of Steel Sheets Containing Slits," *Journal of the Mechanics and Physics of Solids*, Vol. 8, 1960, pp. 100–104.

[25] McClintock, F. A., "Crack Growth in Fully Plastic Grooved Tensile Specimens," *Physics of Strength and Plasticity*, A. S. Argon, Ed., MIT Press, Cambridge MA, 1969, pp. 307–326.

[26] McClintock , F. A., "Ductile Fracture Instability in Shear," *Transactions of the American Society of Mechanical Engineers*, Vol. 80, *Journal of Applied Mechanics*, Vol. 25, 1958, pp. 581–588.

[27] McClintock, F. A., "Plasticity Aspects of Fracture," *Fracture Vol. 3*, H. Liebowitz, Ed., Academic Press, New York NY, 1971, pp. 47–225, esp. pp. 51, 64–70, 145, 155–162.

[28] Farkas, D. "Atomistic Studies of Intrinsic Crack-Tip Plasticity," *MRS Bulletin*, Vol. 25, No. 5, 2000, pp. 35–38.

[29] Gumpsch, P., "Modelling Brittle and Semi-Brittle Fracture Processes," *Materials Science and Engineering*, Vol. A319–321, 2001, pp. 1–7.

[30] Ishikawa, N., Parks, D. M., Kurihara, M., "Micromechanism of Ductile Crack Initiation in Structural Steels," *Iron and Steel Institute of Japan International*, Vol. 40, No. 5, 2000, pp. 519–527.

[31] Gurson, A. L., "Continuum Theory of Ductile Rupture by Void Nucleation and Growth. Part I Yield Criterion and Flow Rules for Porous Ductile Materials," *Journal of Engineering Materials and Technology*, Vol. 99, 1977, pp. 2–15.

[32] Tvergaard, V., and Needleman, A., "Analysis of the Cup–Cone Fracture in a Round Tensile Bar," *Acta Metallurgica*, Vol. 32, 1984, pp. 157–169.

[33] Il'yushin, A. A., "The Theory of Small Elastic–Plastic Deformation," *Prikladnaia Matematika i Mekhanika, PMM*, Vol. 10, 1946, pp. 347–356.

[34] Chang, S. J., and Witt, F. J., "Application of the J–Integral to Obtain Some Similarity Relations," *Fracture Analysis, ASTM STP 560*, American Society for Testing and Materials, Philadelphia PA, 1974, pp. 226–239, esp. pp. 232–3.

[35] Tada, H., Paris, P. C., and Irwin, G.R., *The Stress Analysis Handbook*, 3rd Ed., ASME Press, New York, NY and ASM International, Materials Park OH, 2000.

[36] Rooke, D. R. and Cartwright, D. J., *Compendium of Stress Intensity Factors*, Hillingdon, Uxbridge, England, 1987.

[37] Murakami, Y., et al., Eds. *Stress Intensity Factors Handbook*, 3rd Ed., Pergamon Press, Oxford, 2001.

[38] Hudson, C. M., and Seward, S. K., "Compendium of Sources of Fracture Toughness and Fatigue Crack Growth Data for Metallic Alloys, "*International Journal of Fracture*, Vol. 14, 1978, R151–R184.

[39] Hudson, C. M., and Seward, S. K., "Compendium of Sources of Fracture Toughness and Fatigue Crack Growth Data for Metallic Materials, Part II," *International Journal of Fracture*, Vol. 20, 1982, R59–R117.

[40] Laukanen, A., Wallin, K., and Rintamaa, R., "Evaluation of the Effects of Mixed-Mode I–II Loading on Elastic-Plastic Ductile Fracture of Metallic Materials," *Mixed-Mode Crack Behavior, ASTM STP 1359*, K. J. Miller and D. L. McDowell, Eds., American Society for Testing and Materials, West Conshohocken PA, 1999, pp. 3–20.

[41] Hutchinson, J. W., "Singular Behavior at the End of a Tensile Crack in a Hardening Material," *Journal of the Mechanics and Physics of Solids*, Vol. 16, 1968, pp. 13–31.

[42] Rice, J. R. and Rosengren, G. F., "Plane Strain Deformation near a Crack Tip in a Power-Law Hardening Material," *Journal of the Mechanics and Physics of Solids*, Vol. 16, 1968, pp. 1–12.

[43] Shih, C. F., "Tables of Hutchinson-Rice-Rosengren Singular Field Quantities," Report from Division of Engineering, Brown University, Providence RI 02912, June 1983.

[44] Kanninen, M. F. and Popelar, C. H., *Advanced Fracture Mechanics*, Oxford University Press, New York, NY, 1985, esp. p. 309.

[45] Anderson, T. L., *Fracture Mechanics, Fundamentals and Applications*, CRC Press, Boca Raton FL, 1991, esp. pp. 440–449.

[46] Joyce, J.A., and McClintock, F.A., "Predicting Ductile Fracture Initiation in Large Parts", *Strength and Structure of Solid Materials*, H. Miyamoto, T. Kunio, H. Okamura, V. Weiss, M. Williams, and H. Liu, Eds. Noordhoff, Leyden, 1976, pp. 157–181.

[47] Chao, Y. J., and Zhu, X. K., "J-A_2 Characterization of Crack-tip Fields: Extent of J-A_2 Dominance and Size Requirements," *International Journal of Fracture*, Vol. 89, 1998, pp. 285–307.

[48] Chao, Y. J., and Zhu, X. K., "Constraint-Modified J-R Curves and its [their] Application to Ductile Crack Growth," *International Journal of Fracture*, Vol. 106, 2000, pp. 135–160.

[49] O'Dowd, N. P., and Shih, C. F., "Family of Crack-Tip Fields Characterized by a Triaxiality Parameter: Part I—Structure of Fields," *Journal of the Mechanics and Physics of Solids*, Vol. 39, 1991, pp. 989–1015.

[50] O'Dowd, N. P., and Shih, C. F., "Family of Crack-Tip Fields Characterized by a Triaxiality Parameter: Part II—Fracture Applications," *Journal of the Mechanics and Physics of Solids*, Vol. 40, 1992, pp. 939–963.

[51] Rice, J. R., "A Path Independent Integral and the Approximate Analysis of Strain Concentrations by Notches and Cracks," *Transactions of the American Society of Mechanical Engineers*, Vol. 90, *Journal of Applied Mechanics*, Vol. 35, 1968, pp. 379–386.

[52] McClintock, F. A., "The Paris Law for Fatigue Crack Growth in Terms of the Crack Tip Opening Displacement," *High Cycle Fatigue of Structural Materials, Symposium Proceedings in Honor of: Professor Paul C. Paris*, W. O. Soboyejo and T. S. Srivatsan, Eds., The Minerals, Metals and Materials Society (TMS), Warrendale PA, 1997, pp. 3–24. Note missing "n" in numerator of exponent of first of Eqs. 19.

[53] Shih, C. F., and Needleman, A., "Fully Plastic Crack Problems Part 1: Solutions by a Penalty Method," *Transactions of the American Society of Mechanical Engineers*, Vol. 106, *Journal of Applied Mechanics*, Vol. 51, 1984, pp. 48–56.

[54] Kumar, B, German, M. D. and Shih, C. F., "An Engineering Approach for Elastic-Plastic Fracture Analysis," Report EPRI NP-1931, Electric Power Research Institute, Palo Alto CA, 1981.

[55] Parks, D. M., Kumar, B., and Shih, C. F., "Consistency Checks for Power-Law Calibration Functions," *Elastic-Plastic Fracture: Second Symposium Vol. I—Inelastic Crack Analysis, ASTM STP 803*, C. F. Shih and.J. P. Gudas, Eds., American Society for Testing and Materials, Philadelphia PA, 1984, pp. I-370 – I-383.

[56] Shih, C. F., and Needleman, A., "Fully Plastic Crack Problems Part 2: Application of Consistency Checks," *Transactions of the American Society of Mechanical Engineers*, Vol. 106, *Journal of Applied Mechanics*, Vol. 51, 1984, pp. 57–64.

[57] Shih, C. F., and Hutchinson, J. W., "Combined Loading of a Fully Plastic Ligament Ahead of an Edge-Crack," *Transactions of the American Society of Mechanical Engineers,* Vol. 108, *Journal of Applied Mechanics*, Vol. 53, 1986, pp. 271–277.

[58] Hê, M. Y., and Hutchinson, J. W., "The Penny-Shaped Crack and the Plane Strain Crack in an Infinite Body of Power Law Material," *Transactions of the American Society of Mechanical Engineers,* Vol. 103, *Journal of Applied Mechanics*, Vol. 48, 1981, pp. 830–840.

[59] Rice, J. R., "Mathematical Analysis in the Mechanics of Fracture," *Fracture, Vol. 2*, H. Liebowitz, Ed., Academic Press, New York, 1968, pp. 191–311, esp. pp. 210, 213.

[60] Hill, R., *The Mathematical Theory of Plasticity*, Clarendon Press, Oxford, 1950, esp. pp. 128–136. Reprinted.

[61] Chakrabarty, J., *Theory of Plasticity*, McGraw-Hill, New York, NY, 1987, esp. pp. 95–99, 407–412, 425–429, 620. Note that in Figure 6.1 the complement of 2ϕ is labeled as 2ϕ and the upper right stress point should be σ_{yy}.

[62] McClintock, F. A. and Argon, A. S., Eds., *Mechanical Behavior of Materials*, 1999, esp. pp. 360–379. Reprinted with Errata List, Ceramic Book and Literature Service (CBLS), Tel. 740-374-9458, e-ml: cbls@cbls.com, www.cbls.com, from Addison Wesley, Reading, MA, 1966.

[63] Bishop, J. F. W., Green, A. P., and Hill, R., "A Note on the Deformable Region in a Rigid Plastic Body," *Journal of the Mechanics and Physics of Solids*, Vol. 4, 1956, 256–258.

[64] McClintock, F. A., Kim, Y. J., and Parks, D. M., "A Criterion for Plane Strain, Fully Plastic, Quasi-Steady Crack Growth," *International Journal of Fracture*, Vol. 72, 1995, pp. 197–221.

[65] McClintock, F. A. and Slocum, A. H., "Predicting Fully Plastic Mode II Crack Growth from an Asymmetric Defect," *International Journal of Fracture*, Vol. 27, 1985, pp. 49–62.

[66] Donne, C. D., "The Crack Tip Displacement Vector Approach to Mixed-Mode Fracture," *Mixed Mode Crack Behavior, ASTM STP 1359*, K. J. Miller and D. L. McDowell, Eds., American Society for Testing and Materials, West Conshohocken PA, 1999, pp. 21–40.

[67] McClintock, F. A., Kim, Y. J., and Parks, D. M., "Tests and Analyses for Fully Plastic Fracture Mechanics of Plane Strain Mode I Crack Growth," *Fracture Mechanics: 26th Volume, ASTM STP 1256*, W. G. Reuter, J. H. Underwood, and J. C. Newman Jr., Eds., American Society for Testing and Materials, Philadelphia PA, 1995, pp. 199–222.

[68] McClintock, F. A., Kenney, K. L., Jung, S., Reuter, W. G., and Parks, D. M., "Asymmetric, Fully Plastic Crack Growth Mechanics and Tests for Structures and Piping," *Proceedings of Symposium on Development, Validation, and Application of Inelastic Methods for Structural Analysis and Design, PVP-343*, R. F. Sammataro and D. J. Ammerman, Eds., American Society of Mechanical Engineers, New York NY, 1996, pp. 153–167.

[69] McClintock, F. A., "Slip Line Fracture Mechanics Applied to Fillet-Welded T-Joints under Tension or Folding," *Koichi Masubuchi: A Welding Research and*

Engineering Festschrift, rev. ed., R. G. Morris, Ed., M. I. T. Sea Grant Program, Cambridge MA, 2000, pp. 275–313, esp. pp. 283, 288–305.

[70] Kardomateas, G. K., and McClintock, F. A., "Tests and Interpretation of Mixed Mode I and II, Fully Plastic Crack Growth from Simulated Weld Defects," *International Journal of Fracture*, Vol. 35, 1987, pp. 103–124.

[71] Shanley, F. R., "The Column Paradox," *Journal of Aeronautical Sciences*, Vol. 13, 1946, p. 678. See also "Inelastic Column Theory," *Journal of Aeronautical Sciences*, Vol. 14, 1946, pp. 261–268.

[72] Lee, H., and Parks, D. M., "Line-Spring Finite Element for Fully Plastic Crack Growth—II. Surface-Cracked Plates and Pipes," *International Journal of Solids and Structures*, Vol. 35, 1998, pp. 5139–5158.

[73] Kim, Y. J., "Modeling Fully Plastic, Plane Strain Crack Growth," Ph.D. Thesis, M. I. T. Department of Mechanical Engineering, May 1993, esp. pp. 24–27, pp. 46–47, pp. 52–59.

[74] McClintock, F. A. and Clerico, M., "The Transverse Shearing of Single–Grooved Specimens," *Journal of the Mechanics and Physics of Solids*, Vol. 28, 1980, pp. 1–16.

[75] Hundy, B. B., "Plane Plasticity," *Metallurgia*, Vol. 49, 1954, pp. 109–118.

[76] Atmadja, J., "Weld Failures in Oil Tankers Due to Groundings—A Finite Element Approach," Ocean Engineer and M.S. Thesis, M. I. T. Dept. of Ocean Engineering, August 1995.

[77] ADINA R&D Inc.,"ADINA-In for ADINA, User's Manual," Report ARD 92-4, "ADINA-Plot User's Manual", Report ARD 92-7, "ADINA Theory and Modeling Guide," Report ARD 92-8, 1992, Watertown MA.

[78] Ewing, D. J. F., "Calculations on the Bending of Rigid/Plastic Notched Bars," *Journal of the Mechanics and Physics of Solids*, Vol. 16, 1968, pp. 81–98.

[79] Green, A. P., and Hundy, B. B., "Initial Plastic Yielding in Notched Bend Tests," *Journal of the Mechanics and Physics of Solids*, Vol. 4, 1956, pp. 128–144.

[80] Naagtegaal, J. C., "Computer Process for Prescribing Second-Order Tetrahedral Elements During Deformation Simulation in the Design Analysis of Structures," U. S. Patent 6 044 210, 2000.

[81] Rice, J. R., and Johnson, M. A., "The Role of Large Crack Tip Geometry Changes in Plane Strain Fracture," *Inelastic Behavior of Solids*, M. F. Kanninen, W. F. Adler, A. R. Rosenfield, and R. I. Jaffee, Eds., McGraw-Hill, New York NY, 1970, pp. 641–672.

[82] Shum, D. K. M., and Merkle, J. G., "Crack Initiation under Generalized Plane-Strain Conditions," *Fracture Mechanics: 23rd Symposium, ASTM STP 1189*, R. Chona, Ed., American Society for Testing and Materials, Philadelphia PA, 1993, pp. 37–54.

[83] Merkle, J. G., "Near-Crack-Tip Transverse Strain Effects Estimated with a Large Strain Hollow Cylinder Analogy," *Fracture Mechanics: 23rd Symposium, ASTM STP 1189*, R. Chona, Ed., American Society for Testing and Materials, Philadelphia PA, 1993, pp. 95–114.

[84] Hill, R., "On the Limits Set by Plastic Yielding to the Intensity of Singularities of Stress," *Journal of the Mechanics and Physics of Solids*, Vol. 2, 1954, pp. 278–285.

[85] Lloyd, W. R., and Reuter, W. G., "Evaluation of Elastic-Plastic Surface Flaw Behavior and Related Parameters Using Surface Displacement Measurements," *Fracture Mechanics: Twenty-First Symposium, ASTM STP 1074*, J. P. Gudas, J. A. Joyce, and E. M. Hackett, Eds., American Society for Testing and Materials, Phil-adelphia PA, 1990, pp. 322–336.
[86] Lloyd, W. R., and Piascik, R. S., "Three-Dimensional Crack Growth Assessment by Microtopographic Examination," *Fracture Mechanics: 26th Volume, ASTM STP 1256*, W. G. Reuter, J. H. Underwood, and J. C. Newman Jr., Eds., American Society for Testing and Materials, Philadelphia PA, 1995, pp. 303–308.
[87] McClintock, F. A. and Wineman, S. J., "A Wedge Test for Quantifying Fully Plastic Fracture," *International Journal of Fracture*, Vol. 3, 1987, pp. 285–295.
[88] Haq, F., McClintock, F. A., Parks, D. M., and Bass, M. K., "Fully-Plastic Back-Bend Tests for Low-Triaxiality Plane Strain Crack Growth," submitted to *Engineering Fracture Mechanics*, 2002.
[89] McClintock, F. A., "Reduced Crack Growth Ductility due to Asymmetric Configurations," *International Journal of Fracture*, Vol. 42, 1990, pp. 357–370.
[90] Miller, K. J., and McDowell, D. L., Eds., *Mixed Mode Crack Behavior, ASTM STP 1359*, American Society for Testing and Materials, West Conshohocken PA, 1999.
[91] Zhu, X. K. and Chao, Y.J., "Constraint Effects on Crack Tip Fields in Elastic-Perfectly Plastic Materials," *Journal of the Mechanics and Physics of Solids*, Vol. 49, 2001, pp. 363–399.
[92] Rothwell, A. B., "Fracture Propagation Control For Gas Pipelines—Past, Present, and Future," *Pipeline Technology, Proceedings of the 3rd International Pipeline Technology Conference, Brugge*, Vol. I, R. Denys, Ed., Elsevier Science B. V., 2000, pp. 387–405.
[93] McClintock, F. A., and Speth, R. L., "Dimple-Cleavage Transitions in Crack Growth: Deterministic in Charpy Tests from Slip Line Fracture Mechanics, and Statistical in Structures," *Mechanisms and Mechanics of Fracture: Symposium in the Honor of Prof. J. F. Knott*, W.O. Soboyejo, L. L. Lewandowski, and R. O. Ritchie, Eds., The Minerals, Metals & Materials Society, TMS, Warrendale, PA 2002.

Appendix: Consistency Condition for Coefficients for J and Load Point Deflection in Power-Law Material, after [55].

For a structure of power-law elastic material under a load P giving a work-conjugate deflection Δ and a strain energy W, J is the strain energy release rate per unit growth of a crack of length a:

$$J \equiv \frac{\partial W}{\partial a} \tag{A1}$$

In appropriately normalized form, J and Δ can be expressed in terms of two coefficients that are dependent on a and other geometry: $h(a, \text{geom})$ and $f(a, \text{geom})$. They are found by finite element analysis of the geometry of the structure such that:

$$J = P^{n_\varepsilon+1} h(a,\ \text{geom}) \ ,\ \Delta = P^{n_\varepsilon} f(a,\ \text{geom}) \tag{A2}$$

The differential of the second of Eqs. A2 can be integrated to give the elastic strain energy:

$$W = \int P d\Delta = \int P n_\varepsilon P^{n_\varepsilon - 1} f(a,\ \text{geom}) dP = \frac{n_\varepsilon}{n_\varepsilon + 1} P^{n_\varepsilon+1} f(a,\ \text{geom}) \tag{A3}$$

Substituting the first of Eqs. A2 and the derivative of the strain energy of Eq. A4 with respect to a into Eq. A1 then gives the consistency condition between the coefficients h and f that must be satisfied by a finite analysis of the geometry involved.

$$P^{n_\varepsilon+1} h(a,\ \text{geom}) = \frac{n_\varepsilon}{n_\varepsilon + 1} P^{n_\varepsilon+1} \frac{\partial f(a,\ \text{geom})}{\partial a} \ ;\ h = \frac{n_\varepsilon}{n_\varepsilon + 1} \frac{\partial f}{\partial a} \tag{A4}$$

Practical Applications

John M. Barsom[1]

Fatigue and Fracture Behavior of Moment Frame Connections Under Seismic Loading (Northridge Earthquake)

Reference: Barsom, J. M., **"Fatigue and Fracture Behavior of Moment Frame Connections Under Seismic Loading (Northridge Earthquake),"** *Fatigue and Fracture Mechanics: 33rd Volume, ASTM STP 1417*, W. G. Reuter and R. S. Piascik, Eds., ASTM International, West Conshohocken, PA 2002.

Abstract: The Northridge earthquake of January 17, 1994, caused structural damage to a number of welded steel moment-frame (WSMF) buildings of different heights and ages. The structural damage indicated that WSMF connections were susceptible to fracture when subjected to strong ground shaking. This paper describes the geometry and fracture behavior of pre-Northridge and of unreinforced post-Northridge WSMF connections. The origin, size, and geometry of the fracture initiating defects are discussed, as are the stresses and strains, and the materials at the fracture initiation sites. The factors needed for an accurate fracture mechanics analysis of pre-Northridge WSMF connections are discussed. Analysis of the crack propagation paths and the different types of fractures in the pre-Northridge and in the post-Northridge WSMF connections are included.

Keywords: Northridge earthquake, seismic loading, moment-frame connections, crack initiation, crack propagations, fracture path, stress, materials, defects, fracture mechanics.

The Northridge earthquake was the first incident in which a large number of welded steel moment-resisting frame (WSMF) buildings were subjected to strong ground shaking. The ground motion induced high-strain, low-cycle displacements on the structural connections. The earthquake caused structural damage to a number of structures ranging in age from buildings under construction to 30 years old, and in height from one to twenty-six stories [*1*]. The structural damage indicated that the WSMF connections were susceptible to fracture. The fractures were contrary to the expectations of engineers who believed that WSMF buildings would undergo large plastic deformation when subjected to intense ground shaking. The WSMF buildings damaged by the Northridge earthquake did not behave in this manner.

Figure 1 shows a typical pre-Northridge WSMF connection. The connection had

---

[1]President, Barsom Consulting, Ltd., 1316 Murray Avenue, Suite 300, Pittsburgh, PA 15217.

complete-joint-penetration (CJP) groove welds joining the beam flanges to the column flange and a shear tab either fillet welded or groove welded to the column and bolted to the beam web. Steel backing bars were placed at the weld root and were left in place becoming an integral part of the connection. Run-on and run-off tabs were left in place.

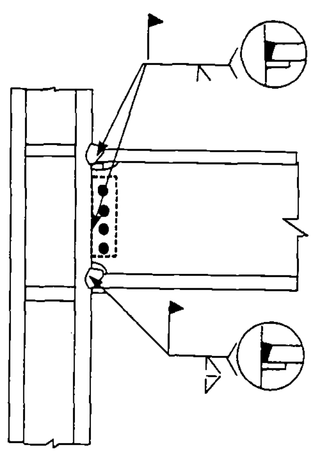

Figure 1 – *Pre-Northridge WSMF connection*

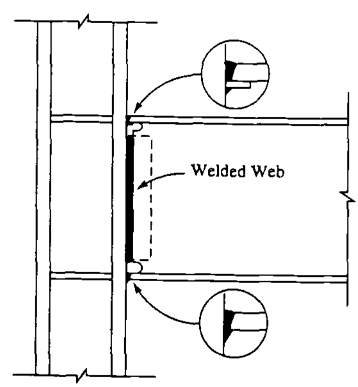

Figure 2 – *Post-Northridge connection*

Based on extensive post-Northridge research, the SAC Joint Venture described several factors that contributed to fracture of pre-Northridge WSMF connections [*1*]. These factors related to design, material, fabrication, inspection, and erection. For example, engineers minimized the number of connections in buildings resulting in large members and in increased loads on connections. The design configuration and geometry of the beam-to-column joints produced high triaxial stresses at mid-length of the CJP welds. The welding procedure resulted in lack of fusion along the weld root and in large weld defects at mid-length of the CJP weld between the bottom beam flange and the column flanges where the stresses and strains are most severe. The deposited weld metal did not have a specified minimum notch toughness.

One method investigated to improve the inelastic performance of WSMF connections involved the removal of the backing bar of the beam bottom flange, back gouging the root weld and depositing a reinforcing fillet weld, Figure 2. Also, the filler metal was changed from one that had no minimum Charpy V-notch (CVN) requirements to a "notch tough" filler metal having a minimum CVN requirement. These changes improved the inelastic performance of WSMF connections but not to a level sufficient to prevent fracture under seismic loads [*2,3*].

The connection shown in Figure 2 had been designated an unreinforced post-Northridge connection. The CJP groove welded joints of reinforced post-Northridge WSMF connections were strengthened by welding attachments between the beam and the column including haunches between the beam flanges and the column flange and cover plates on the beam flanges.

This paper describes the location of stress concentrations and crack initiation in pre-Northridge and in unreinforced post-Northridge WSMF connections. The results of a failure analysis investigation on several connections demonstrated that fracture behavior was governed by the joint design configuration and geometry [*4,5*]. This paper discusses the factors involved in conducting a fracture mechanics analysis of connection failures and the potential for erroneous conclusions when the analysis is based on simplified assumptions that do not model the joints accurately.

Stress and Strain Concentration in Beam-to-Column WSMF Connections

Figures 3 and 4 are schematics of pre-Northridge and unreinforced post-Northridge joints, respectively [*4,5*]. These figures indicate the locations in each joints where the magnitude of the stresses and strains magnify and where cracks may initiate and propagate.

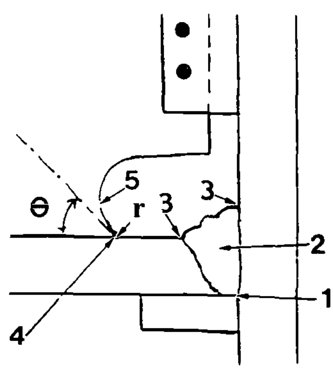

Figure 3 – *Pre-Northridge WSMF welded joint*

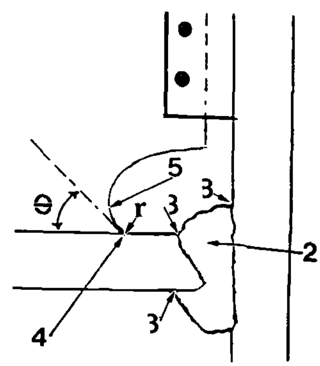

Figure 4 – *Post-Northridge WSMF welded joint*

The root of the weld, No. 1 in Figure 3, is subjected to a very severe state of stress. The unwelded surfaces between the column face and the backing bar and the presence of lack-of-fusion discontinuities at the weld root act as pre-existing cracks. The effective length of this crack would depend on the dimension of the lack-of-fusion discontinuity and whether the backing bar edge away from the column flange was welded to the surface of the beam bottom flange. Assuming that the presence of the backing bar does not generate an effective crack, the 90-degree angle between the bottom surface of the bottom flange and the column face results in a severe stress concentration. Lack-of-fusion defects that occurred frequently at the weld root, produced a sharp pre-existing crack-like discontinuity at the tip of the backing bar notch. These discontinuities were common at mid-length of the CJP weld where analyses have shown the principal stresses to be maximum and triaxiality to be more severe [*1*]. Most fractures initiated at this location.

The results of a finite-element analysis [*6*] indicated that the size of the backing-bar notch had a negligible effect on the ratio of the stress-intensity factor and the nominal applied stress, K_I/σ_n, at the tip of the lack-of-fusion discontinuity. The analysis indicat also, that conservative estimates of the K_I/σ_n ratio at the tip of the lack-of-fusion discontinuity may be computed by assuming the presence of a pre-existing crack havir length equal to the length of the backing-bar notch plus the lack-of-fusion discontinuit

Removing the backing bar, back gouging the root pass and placing a reinforcing fil weld in place of the backing-bar significantly reduces the severity of the stress state at this location. Fracture initiation then shifts to the next most severe point of stress, the intersection of the beam web and the beam flange at the weld access hole [4]. Improvi the weld access hole geometry transferred crack initiation to weld discontinuities withi the deposited weld metal or to the toe of the reinforcing fillet weld [4].

Fracture Initiation in Pre-Northridge WSMF Connections

Most fractures of pre-Northridge WSMF connections initiated at the root of the CJI weld between the beam bottom flange and the column flange. The fracture initiation location was at the tip of the crack-like notch formed by the edge of the backing bar ar the surface of the column flange. In many cases, the root pass did not fuse to the colur flange, the beam flange, or the backing bar. The lack-of-fusion defect between the roc pass and the column flange and between the root pass and the slanted edge of the bean flange sharpened the tip of the backing bar notch and extended its effective length. Th size and shape of the lack-of-fusion defects varied along the length of the CJP weld, Figure 5. In all connections examined, the lack-of-fusion front was irregular, sometim resulting in multiple initiation locations. Results of failure analyses demonstrated that fracture of pre-Northridge WSMF connections initiated from lack-of-fusion defects on the column flange surface [5].

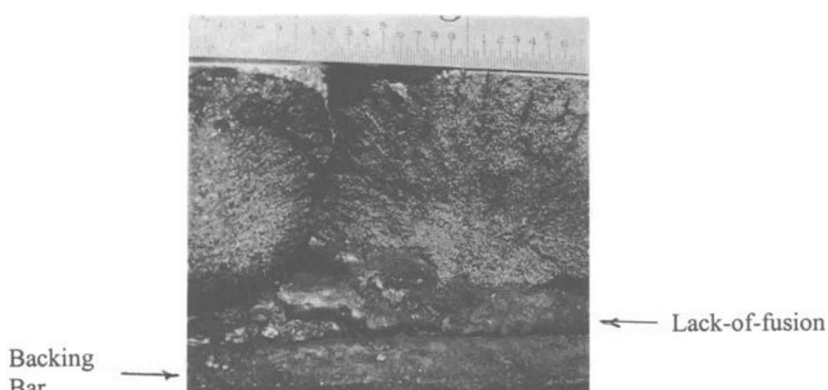

Figure 5 – *Variable lack-of-fusion depth*

The welded joint between the beam bottom flange and the column flange was made a downhand field weld, often by a welder sitting on top of the beam top flange. To ma the weld from this position, each pass must be interrupted at the beam web with either start or stop of the weld at this location. This welding technique often resulted in poor quality weld with lack-of-fusion and slag inclusions, Figure 6. The stress magnitude was highest at the location of these weld defects and they were subjected to the maximum triaxial state of stress in the connection. The large size of some of these defects decreased the load-carrying capacity of the connections. Their size, shape, and location decreased the fracture resistance of the connections. Fractures of some connections initiated from these defects.

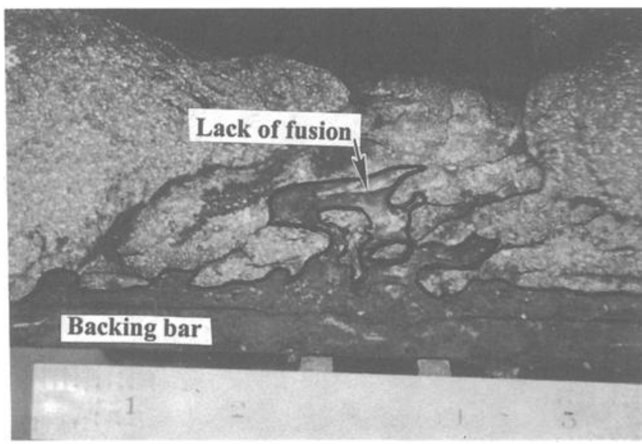

Figure 6 – *Irregularly shaped lack-of-fusion defect through the thickness of the complete-joint-penetration groove weld*

Fracture Propagation Path In Pre-Northridge WSMF Connections

Fracture of pre-Northridge WSMF connections propagated along a number of different paths. In some cases, the fracture pulled free a piece of the column face adjacent to the CJP weld. This fracture pattern has been termed a "divot" fracture, Figure 7 [*1*]. In other cases, the propagating crack partially or completely severed the column, Figure 8 [*1*].

Failure analysis of unreinforced post-Northridge WSMF connections tested at the University of Michigan demonstrated that during bending of the beam, the beam web at the weld access hole pulls the beam flange out-of-plane and in the plane of the web [*4*]. This mode of deformation caused the beam flange to bend about the centerline. The flange outside surface formed less than a 180-degree angle with its apex at the beam-to-web intersection, Figure 9 [*4*]. This deformation produced a tensile stress component at the tip of the crack-like notch formed by the backing bar on the beam bottom flange. This stress component was inclined to the column-flange surface. The superposition of this stress component and the tensile stress in the beam flange formed a stress field at the tip of the backing-bar notch, which deviated from the plane of the notch into the column flange [*7*]. This stress field was the driving force for the initial extension of a crack from the backing-bar notch tip. Therefore, the initial crack extension from the crack-like backing-bar notch was toward the column flange.

Figure 7 – *Divot type fracture*

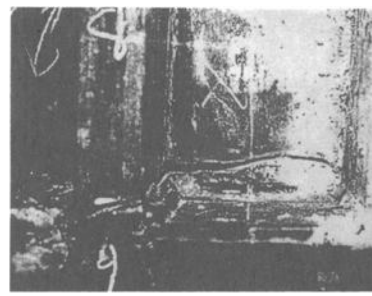

Figure 8 – *Column fracture*

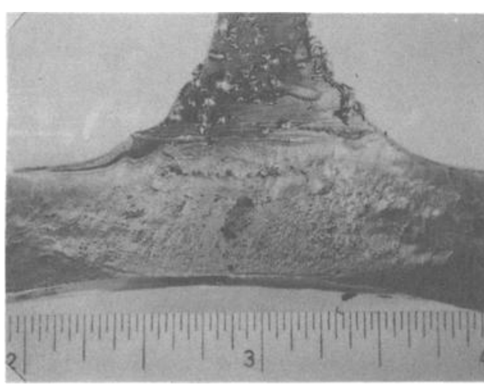

Figure 9 – *Out-of-plane bending of the beam bottom flange*

The propagation path of the crack that extended from the backing-bar notch was governed by the relative strength of the beam-flange tensile stress component and the out-of-plane tensile stress component. The effect of the out-of-plane stress component was maximum at the tip of the backing-bar notch and decreased as the crack extended deeper into the column flange. The stress field developed in the column flange by the bottom beam-flange decayed rapidly above and below the CJP groove weld. Thus, as t crack extended into the column flange, the influence of the out-of-plane stresses on the propagating crack decreased, whereas the influence of the beam-flange stresses increas The crack that initially extended from the tip of the backing-bar notch into the column flange turned back toward the column-flange surface. This crack-propagation path produced a divot-type fracture.

The preceding discussion shows that, in the absence of longitudinal tensile stresses in the column flange, cracks in a pre-Northridge connection initiate at the tip of the crack-like backing-bar notch and then propagate into a divot fracture. Longitudinal tensile stresses in the column flange, in the vicinity of the CJP groove weld, facilitate the propagation of the inclined crack further into the column flange. As the magnitude of these stresses increases, the crack propagates across the column. Longitudinal tensile stresses in the column may be caused by different loads and deformations including inelastic deformation of a weak panel zone and uplift during the seismic event.

Fracture Mechanics Analysis of Pre-Northridge WSMF Connections

Fracture mechanics analysis of pre-Northridge WSMF connections should model the unique characteristics of the connections under consideration. These characteristics include the material, the stresses and strains, and the crack-like discontinuities.

Fractures in pre-Northridge WSMF connections, initiated from lack-of-fusion defects between the deposited weld model and the column flange. The tip of this defect is surrounded by the heat-affected zone in the column flange, the fusion line and the fusion zone of the deposited weld metal. These materials usually have different strengths, ductilities, and fracture properties. The principal stresses at this location are inclined to the plane of the defect forcing the fracture to extend from the tip of the lack-of-fusion defect into the column flange. The shape of the plastic zone at the tip of the defect would, therefore, be asymmetric. A lack-of-fusion defect at this location is similar to a crack at the fusion plane of a laminate composite of dissimilar metals, whose properties change as the distance from the plane of the defect increases. These and other factors require an understanding of the properties of the different materials at the tip of the crack-like defect, their relative contribution to the fracture and the characteristics of the fractures. These characteristics should be derived from properly conducted metallographic and fractographic failure analyses.

The magnitude and distribution of stresses in a pre-Northridge WSMF connection depend on several factors, including the strength of the steels in the beam and column and the deposited weld metal, the size of the beam and of the column, the strength of the column panel zone, the size and shape of the weld access hole, the size of the shear plate, and whether the shear plate is welded or bolted to the beam web. Weld metal over-match, as would be the case for WSMF connections made of A36 steel, "increase the stress level in the heat affected zone due to material constraint and thereby reduces the fracture resistance" [*8*]. The design configuration and geometry of a pre-Northridge WSMF connection produce a maximum stress at mid-length of the backing-bar notch. The magnitude of this stress decreases along, transverse and through the thickness of the CJP weld. The cyclic deformations of a pre-Northridge WSMF connection under seismic loads accumulate strains at mid-length of the CJP weld. The level of strain accumulation (ratcheting) is higher for connections designed without continuity plates. Therefore, the demands on the material at mid-length of the CJP weld are higher than they would be under monotoric loading. Also, the high-strain cyclic properties of the materials surrounding the lack-of-fusion defect may play a significant role in the fracture of a connection.

Fracture surfaces of pre-Northridge WSMF connections showed that the lack-of-fusion defects had different shapes and sizes in different connections. In most instances, lack-of-fusion defects extended from the tip of the backing-bar notch and along its length. In many cases, the depth of the defect changed abruptly, Figure 5, or was interrupted by an irregularly shaped part-through lack-of-fusion defect at mid-length of the CJP weld, Figure 6.

The maximum stress-intensity factor in tension occurs at the maximum depth, a, of the part-through crack. The maximum stress-intensity factor for a part-through crack in bending shifts along the perimeter of the crack towards the surface [*9*]. The location of the maximum stress-intensity factor under tensile and bending stresses depends on the size and shape of the part-through crack and on the relative magnitudes of the tensile and bending stresses. The superposition of a part-through crack onto a single edge notch type defect would complicate the analysis further. The irregular depth of the lack-of-fusion defects along the root of the CJP weld produced peninsulae of metals along the defect front. The metal at the tip of the peninsulae, triggered the fracture once it reached its ultimate tensile strength, Figure 10. Therefore, the use of a single edge-notch crack model to analyze the fracture behavior of actual pre-Northridge WSMF connections is an oversimplification of a very complex fracture problem that can lead to erroneous conclusions.

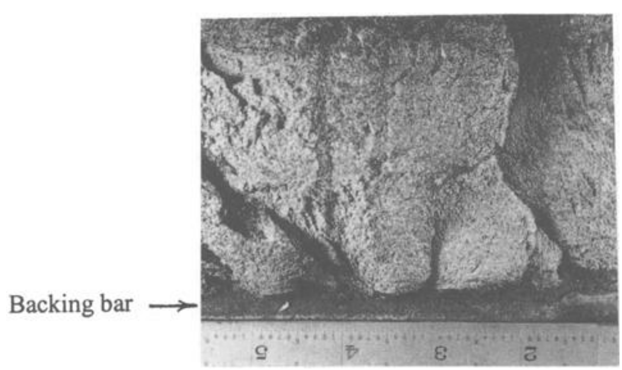

Figure 10 – *Crack initiation from tips of weld peninsulas*

Post-Northridge WSMF Connection Tests

Several unreinforced post-Northridge WSMF connections were tested at the University of Michigan [*2*] and at Lehigh University [*3*] to determine if newly detailed fully-restrained connections can behave satisfactorily in future earthquakes. The base metal for the beams and columns of all tested connections were produced to ASTM A572 steel specification. The CJP groove weld between the beams and columns were made using notch-tough E70TG-K2 electrode. The backing bar was removed using the air-arc process, the weld root was back-gouged and a reinforcing fillet weld was deposited using notch-tough E71T-8 electrode

There were significant differences between the connections tested at the University of Michigan and at Lehigh University. These differences had a direct effect on the test results. There were differences among the tests conducted at each institution. Some of the differences include: (1) bolted versus welded shear tabs; (2) AISC/AWS-type weld access hole versus a newly developed weld access hole geometry and surface finish; (3) panel zone strength; and (4) weld toe grinding for some of the Lehigh University specimens, as well as other differences. The specific differences among the test specimens can be derived from the reports by Goel et al. [*2*] and Ricles et al. [*3*].

Fatigue Crack Initiation Sites in Unreinforced Post-Northridge Connections

The unreinforced post-Northridge WSMF connections tested at the University of Michigan and at Lehigh University were studied to identify all the sites within a connection where fatigue cracks initiated [*4*]. The results of the study demonstrated that fatigue cracks initiated from the web-to-beam intersection at the weld access hole, the valleys in the flame-cut surface of the weld access hole, the weld toe and from weld imperfections. The data showed that fatigue cracks initiated at the web-to-beam intersection at the weld access hole in 89 percent of the connections and at the weld toe in about 50 percent of the connections. In about 20 percent of the connections, fatigue cracks initiated from the flame-cut surface as well as from weld imperfections.

Similar analyses of fatigue crack initiation sites were performed on five connections tested at Lehigh University. The results of four exterior frame tests and one interior frame test showed that fatigue crack initiation was limited to the weld toe region, weld imperfections within the complete joint penetration groove weld joining the beams to columns and at the end of the shear tabs. Also, the data showed that 80 percent of the beam flanges had fatigue cracks that initiated from weld imperfections and 80 percent had fatigue cracks that initiated at weld toes. The complete absence of fatigue crack initiation from the web-to-flange intersection at the weld access hole and the flame-cut surface is significantly different from the results of the University of Michigan tests. The reason for this difference is explained in the following discussion.

The weld access hole geometry was one of the most detrimental factors in reducing the fatigue strength of the connections tested at the University of Michigan. In several connections, the web-to-beam intersection at the weld access hole was very close to a 90-degree angle with very small radius, Figure 11(a). In other specimens, Figure 11(b), the transition between the web and the beam-flange surface at the weld access hole had a gentle slope and a shallow angle. Unfortunately, the intersection was coincident with the toe of the CJP weld that had appreciable weld reinforcement. This condition resulted in a region of severe strain concentration and a maximum fatigue damage location.

The other contribution of the weld access hole to the degradation of the fatigue strength of the beam-to-column connection was the roughness of the flame-cut surface. Although an attempt may have been made to decrease the surface roughness on the flame-cut surfaces by grinding, the grooves made by the cutting operation were visually evident on all the connections. These grooves are shallow notches that cause strain localization and intensification and may become sites of fatigue crack initiation. In fact, many fatigue cracks initiated from these grooves. These fatigue cracks did not cause failure of any specimens only because other imperfections were more damaging. However, the fatigue cracks that initiated from the flame-cut surface grooves would have led to fracture of the specimens had the more damaging imperfection been eliminated.

The preceding discussion demonstrates that (to ensure improved fatigue performance of the rigid beam-to-column connection) the weld access hole geometry and the surface

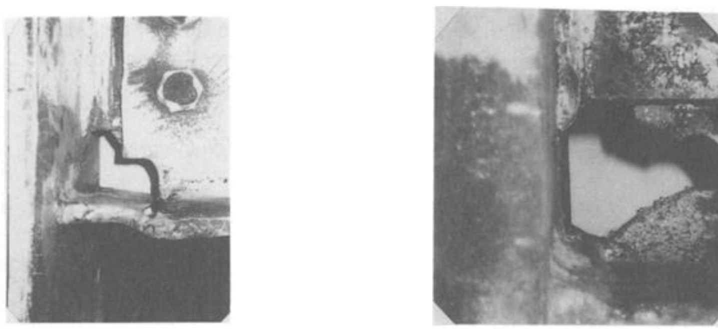

(a) (b)

Figure 11 – *Two significantly different geometries of weld access holes*

roughness of its flame-cut surface must be controlled. Control measures were implemented by Lehigh University, which eliminated the weld access hole geometry and surface as crack initiation sites.

Figure 12 – *Improved weld access hole*

Based in part on the results from the University of Michigan tests, the researchers at Lehigh University performed finite element analyses on different weld access hole geometries to evaluate the magnitude and distribution of the stress and strain fields in that region. The results indicated that the weld access hole geometry in Figure 12 exhibited the most promising behavior [3]. Consequently, this geometry was used in the fabrication of all the Lehigh University specimens. The flame-cut surface of the weld access hole was ground smooth to bright metal with no visible surface roughness. Finally, the web-to-beam flange intersection at the weld access hole was fared in to form a smooth transition. These measures eliminated the initiation of fatigue cracks from the web-to-beam intersection at the hole and from the flame-cut surface.

Fractures Caused by Weld Discontinuities

University of Michigan Connection Tests – Weld geometry had a significant detrimental effect on the fatigue strength of the connections tested at the University of Michigan [*2*]. Geometric discontinuities at the toe of the fillet welds caused the formation of fatigue cracks in all the connections tested at the University of Michigan. These cracks initiated within the mid-length of the flange-to-column CJP weld in the vicinity of the column web centerline. These cracks either caused the failure of the connection or would have caused the fracture had the weld access hole geometry been less severe.

Lack-of-fusion and slag inclusions caused the initiation and propagation of fatigue cracks in a few connections tested at the University of Michigan. The severity of these imperfections depended on their size and geometry. The larger the size perpendicular to the tensile stress component and the more planar the geometry, the more severe was their stress and strain field and the more detrimental was their effect on the fatigue strength of the connection.

Lehigh University Connection Tests – Fracture of a component subjected to fluctuating loads and deformations is caused by the initiation and propagation of fatigue cracks at the location where the stress and strain fluctuations are a maximum. The use of the modified weld access hole geometry with its smoothly ground surface shifted the fatigue crack initiation site in the Lehigh University connections to weld imperfections and weld geometric discontinuities. Geometric discontinuities at weld toes caused the formation of fatigue cracks in 80 percent of the beam flanges analyzed [*4*]. These fatigue cracks did not reach a critical size to cause fracture. Fractures of the beam flanges and shear tabs in the 5 connections investigated were caused by large weld imperfections including lack-of-fusion, hydrogen damage evident from the presence of fish eyes on the fracture surface, and from slag inclusions. Some of the weld imperfections were 3-inches long. Figure 13 presents an example of these imperfections.

Figure 13 – *A 3-inch long weld defect at the edge of a beam flange*

Comparison of Test Results

As stated earlier, there were significant design differences among unreinforced post-Northridge moment-frame connection tests conducted at the University of Michigan and at Lehigh University. It is not the purpose of this section to determine the contribution c the design changes to the performance of the connections. Rather, the purpose is to compare the fatigue crack initiation locations, and the fracture-causing imperfections among the tests as identified by failure analysis of the components.

In the University of Michigan connections, fatigue cracks initiated at the intersection of the weld access hole and the beam flanges, the weld access hole flame-cut surface, at the toe of welds and from weld imperfections. Fractures were caused primarily by crack that initiated and propagated to critical size at the intersection of the weld access hole with the beam flange or at the weld toes.

In the Lehigh University connections, fatigue cracks initiated at weld toes, weld imperfections and at the fusion line of the beveled edge of the groove weld exposed on the bottom surface of the bottom flange. Fractures were caused exclusively by large wel imperfections in the complete joint penetration groove weld between the beam flange an the column. These weld imperfections were 1.5 to 3 inches long and, in several instances, were as wide as the flange thickness.

The geometric discontinuities of the weld access hole that caused fatigue and subsequent fracture of the beam flanges in the University of Michigan connections were avoided in the Lehigh University connections by using a modified geometry and ground smooth surface. Although cracks did initiate at geometric discontinuities at toes of weld in the Lehigh University connections, unlike the University of Michigan test, they did nc cause fracture of the connections.

The quality of the complete joint penetration groove welds joining the beam flanges and the columns in the University of Michigan connections were superior to those in the Lehigh University connections. Had the modified weld access hole geometry been used in the University of Michigan connections, fatigue and subsequent fracture would have occurred from the toe of the welds. Similarly, had the groove weld quality of the Lehigh University connections been equal to that of the University of Michigan connections, fatigue and subsequent fracture would have occurred from the geometric discontinuities at the weld toes or from imperfections in the fusion line of the groove weld exposed to the bottom surface of the bottom flange.

The preceding observations demonstrate that fatigue and subsequent fracture occur at the location of the most severe stress and strain concentration. Eliminating the most severe location shifts the fatigue crack initiation site and fracture to the most severe location remaining. Progressive elimination of the most severe stress and strain concentrators should improve the performance of connections. This would not be the case when severe stress and strain concentrations are re-introduced into the connection a happened with the presence of the very large weld imperfections in the Lehigh Universit connections.

Effects of Applied Load

As discussed earlier, during bending of the beam, the beam web at the weld access hole pulls the flange out of plane of the beam flange and in plane of the web. The stress and strain field generated by this out-of-plane deformation would produce a parabolic crack with its apex ahead of the web-to-flange intersection at the weld access hole, Figure 14. Such cracks have been observed at the end of transverse stiffeners welded to the web of bridge girders that are subjected to out-of-plane bending. The driving force generated by these stresses and strains decays in both directions away from the beam web across the flange width. The tensile stress and strain components in the beam flange away from the web-to-flange intersection would propagate a straight transverse crack across the beam width, Figure 14. Superimposing these components of stresses and strains would result in a crack propagation path as shown in Figure 14.

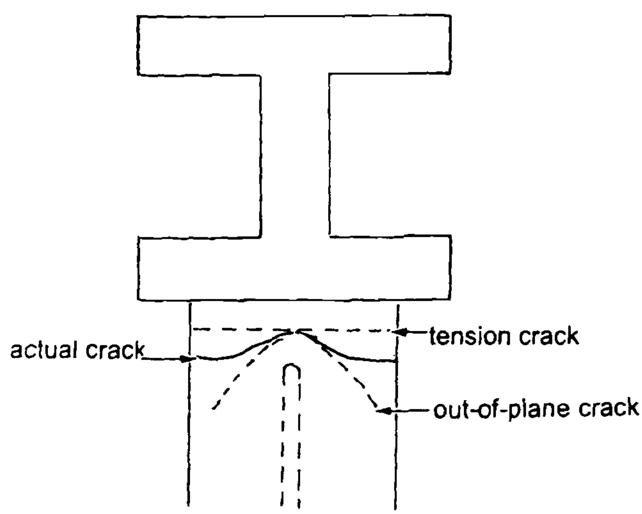

Figure 14 – *Schematic of cracks in a beam flange*

A comparison between the crack front predicted in Figure 14 and an actual specimen fracture, Figure 15, shows that the crack front at the mid-width of the beam in the test specimen was straight rather than curved. This difference is caused by the overriding effect of the stress concentration at the toe of the weld. This crack propagation geometry was observed in all the connections tested at the University of Michigan. Except for one specimen, this crack propagation geometry was not observed in the Lehigh University connections because fracture extended from the edges of the flanges where the large weld imperfections resided rather than from mid-width of the beam flanges where the stresses, strains and constraint are highest.

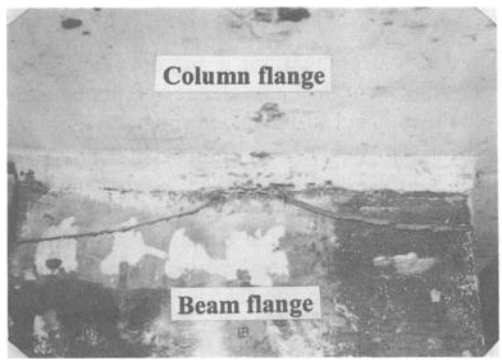

Figure 15 – *Crack in a beam flange*

Comparison of Fractures in Pre- and Post-Northridge WSMF Connections

One of the most significant differences between pre-Northridge and post-Northridge WSMF connections is the change in the fracture behavior of the connections. Fracture of pre-Northridge connections propagated along a number of different paths. The majority of these fractures, however, were either divots or column fractures. The removal of the backing bar from the beam bottom flange, back gouging the root weld and depositing a reinforcing fillet weld, eliminated the severe crack-like defect on the face of the column flange in pre-Northridge WSMF connections and changed the stress field that forced the defect to propagate into the column. This modified connection geometry known as the unreinforced post-Northridge WSMF connection contains three primary locations where cracks can initiate and propagate. These locations are the intersection between the weld access hole and the bottom beam flange, the toe of the reinforcing fillet weld and the weld defects. Crack initiation and propagation from these locations would fracture the beam flange or the CJP groove weld but not the column. All the connection tests conducted at the University of Michigan and at Lehigh University confirm this observation. Consequently, for unreinforced post-Northridge connections, the beam flange and the CJP groove weld properties become important considerations in analyzing and in preventing connection failures. The required material properties depend on the design loads, the design configuration and geometry of the connection and of the welded joint, and on the fabrication and the inspection requirements.

Summary

This paper describes crack initiation and propagation in pre-Northridge and in unreinforced post-Northridge WSMF connections. Fractures of pre-Northridge connections initiated from lack-of-fusion defects at the tip of the backing-bar notch.

Crack instability was caused by the design configuration and geometry of the connection. The location of crack initiation was dictated by the applied tensile and bending stresses and strains, and by the size, shape, and location of the lack-of-fusion defects. The stress field acting on the defect forced the crack to propagate into the column flange. The material at the tip of the defects included the fusion line, the heat-affected zone of the column flange and the fusion zone of the deposited weld metal. Accurate modeling of the stresses and strains, the geometry of the crack-like defects and the properties of the different materials at the tip of the defect are needed to predict the fracture behavior of a particular connection.

The elimination of the backing bar from the unreinforced post-Northridge WSMF connections shifted crack initiation and subsequent propagation from the tip of the backing bar notch to the remaining stress raisers. These stress raisers are located at the intersection of the beam web and the beam flange at the weld access hole, the toe of the reinforcing filet weld and the weld defects. The use of an improved weld access hole geometry prevented the initiation of cracks at this location. Fatigue crack initiation and propagation from the two remaining stress raisers make the properties of the beam flange and of the CJP groove weld important considerations in analyzing and in reducing the propensity for failures of unreinforced post-Northridge connections.

References

[1] Federal Emergency Management Agency, Recommended Seismic Evaluation and Upgrade Criteria for Existing Welded Steel Moment-Frame Buildings, FEMA 351, Washington, D.C., July 2000.

[2] Goel, S. C., et al., "Parametric Tests on Unreinforced Connections," SAC Steel Project – Task 7.02, SAC Joint Venture, Richmond, CA, 1999.

[3] Ricles, J. M. et al., "Supplemental Testing of Unreinforced Connections with Integration of T-Stub Weld Tests and Analysis," SAC Steel Project – Task 7.05, SAC Joint Venture, Richmond, CA, 2000.

[4] Barsom, J. M. and Pellegrino, J. V., Jr., "Failure Analysis of Welded Steel Moment-Resisting Frame Connections – Part I: Unreinforced Post-Northridge Welded Steel Moment Frame Connections," SAC Steel Project Task 7.1.3, SAC Joint Venture, Richmond, CA, April 11, 2000 (a).

[5] Barsom, J. M. and Pellegrino, J. V., Jr., "Failure Analysis of Welded Steel Moment-Resisting Frame Connections – Part II: Unreinforced Pre-Northridge Welded Steel Moment Connections," SAC Steel Project Task 7.1.3, SAC Joint Venture, Richmond, CA, May 7, 2000 (b).

[6] Chi, Wei-Ming, Deierlein, C. G. and Ingraffea, A. R., "Finite Element Fracture Mechanics of Welded Beam-Column Connections," Report No. SAC/BD-97/05, SAC Joint Venture, Sacramento, December 15, 1997.

[7] Schafer, B. W., Ojdrovic, R. P. and Zarghamee, M. S., "Triaxiality and Fracture of Steel Moment Connections," Journal of Structural Engineering, Vol. 126, No. 10, October, 2000.

[8] Moltubakk, T. and Thaulow, C., "Influence of Crack Position and Strength Mismatch on the Fracture Toughness of Steel Welds", *Engineering Fracture Mechanics*, Vol. 62, No. 4, 1999.

[9] Newman, J. C., Jr., and Raju, I. S., "Stress-Intensity Factor Equations for Cracks in Three-Dimensional Finite Bodies Subjected to Tension and Bending Loads", Computational Methods in the Mechanics of Fracture, Volume 2 in Computational Methods in Mechanics, Satya N. Atluri, ed., Elsevier Science Publishers, New York, 1986.

Stephen Webster[1] and Adam Bannister[2]

A Structural Integrity Procedure Arising from the SINTAP Project

Reference: Webster, S. E. and Bannister, A. C., "**A Structural Integrity Procedure Arising from the SINTAP Project**," *Fatigue and Fracture Mechanics: 33rd Volume, ASTM STP 1417,* W.G. Reuter and R. S. Piascik, Eds., ASTM International, West Conshohocken, PA, 2002.

Abstract: SINTAP (Structural INTegrity Assessment Procedure) was a multidisciplinary collaborative project, part-funded by the European Union, with the aim of devising a unified procedure for such assessments, offering a range of assessment routes giving it maximum applicability, from the smallest organisation to major industrial users. The project commenced in April 1996 and was completed in April 1999.

Although many such methods did and do exist, most have conflicting approaches, unspecified levels of empiricism or do not fully reflect the performance of modem materials or the current state of knowledge. SINTAP covered both modelling and experimental work and a large element of the project was concerned with the transfer of knowledge and data between industries and scientific organisations together with its compilation and interpretation to provide the required solutions. The culmination of this work is a procedure which is applicable to a wide cross section of users because of its ability to offer routes of varying complexity, reflecting data quality and the scope for a final interpretation reflecting the preference of the user.

Keywords: fracture, structural integrity, plastic collapse, strength, toughness, welded joints

Introduction

Structural Integrity Assessment procedures are the techniques used to assess the fitness-for-purpose of critical components and welded structures. Such approaches can be used at the design stage to provide assurance for new structures, at the fabrication phase to ensure the integrity in the construction and at the operational phase to provide assurance throughout the life of the structure. Used correctly, they can prevent over design and unnecessary inspection and provide the tools to enable a balance between safety and economy to be achieved.

[1] Department Manager, Transport Applications, Corus Research, Development & Technology, Swinden Technology Centre, Moorgate, Rotherham, South Yorkshire, United Kingdom, S60 3AR
[2] Knowledge Group Leader, Structural Integrity, Transport Applications, Corus Research, Development & Technology, Swinden Technology Centre, Moorgate, Rotherham, South Yorkshire, United Kingdom, S60 3AR

Over the years, a number of fracture mechanics-based assessment procedures hε been developed [1–10] within Europe, the USA, and Japan, and their use has spread b in terms of the industries that use them and their analysis capability. However, no c technique was capable of providing all of the answers, and the accuracy of some were the best, unquantified. In addition, recent years have seen the adoption of a new range higher strength steels presenting different analysis problems, such as high yield to tens strength ratio, which has demonstrated a lack of knowledge of the behavior of joi which have a mismatch in strength. Substantial amounts of work have been undertak on this subject [11,12], but it remained an area for which practical guidance and analy methods were not available.

Philosophy and Approach of the Project

In view of the comprehensive nature of the project and the necessity to consi carefully the requirements of the end user, a wide-ranging consortium was establish This was comprised of a material supplier (British Steel, now part of the Corus Grou An electricity generator (British Energy, formerly Nuclear Electric Ltd., with AEA), oil and gas supplier (Shell), a chemical processor (EXXON), safety assessors (Health Safety Executive and SAQ Inspection Ltd., the latter now part of DNV), Resea Institutes (GKSS, Fraunhoffer IWM, Institut de Soudure, TWI, VTT, JRC (IAM), t universities (Cantabria and Gent), a software developer (Marine Computation Servic and a consultancy (Integrity Management Services).

The project was co-ordinated by Swinden Technology Centre, Corus (UK) with the f principal tasks and Task Leaders being:

Task 1: Mismatch—Leader: GKSS

To quantify the behavior of strength mismatched welded joints and to prov recommendations for their treatment in a procedure.

Task 2: Failure of Cracked Components—Leader: British Energy

To extend the understanding of the behavior of cracked components in the speci areas of constraint, yield/tensile ratio, prior overload, leak-before-break, stress intens factors and limit load solutions.

Task 3: Optimized Treatment of Data—Leader: VTT

To provide an industrially applicable method for a reliability-based defect assessm procedure.

Task 4: Secondary Stress—Leader: IdS

The determination and validation of the most appropriate method of accounting residual stress, including a compendium of residual stress profiles.

Task 5: Procedure Development—Leader: Corus

Development and validation of the procedure.

Each task comprised a number of subtasks (see Table 1), the first step being comprehensive collation of existing data, procedures, and codes. This was then follow by experimental work to cover omissions and to validate the approaches a assumptions relevant to the particular study area.

TABLE 1— *Subtasks in project.*

Task 1. Mismatch	Task 2. Cracked Components	Task 3. Optimized Data Treatment	Task 4. Secondary Stress	Task 5. Procedure Development
1.1 Review	2.1 Review	3.1 Review	4.1 Review	5.1 Review
1.2 Bi-Materials	2.2 Constraint	3.2 Toughness	4.2 Collate Profiles	5.2 Procedure
1.3 Multipass Weld	2.3 YS/UTS Ratio	3.3 Charpy Correlations	4.3 Experiment & Modelling	5.3 Software
1.4 Modelling	2.4 Prior Overload	3.4 NDE Guidance	4.4 Profiles Library	5.4 Validation
1.5 Procedure	2.5 Leak-before-break	3.5 Probabilistic Assessment	4.5 Procedure	5.5 Documentation
	2.6 SIF & LL Solutions	3.6 Procedure		
	2.7 Procedure			

Procedure Scope and Novel Features

A key aspect of the finished procedure is that a range of assessment routes can be followed which reflect the quality of the input data. The most sophisticated and accurate levels require high quality input data, whilst assessments can still be carried out with knowledge of only basic parameters, but this is penalized by a higher degree of conservatism; The underlying principles of the method are:

- a hierarchical structure based on the quality of available data inputs;
- decreasing conservatism with increasing data quality;
- detailed guidance on determination of characteristic input values such as fracture toughness;
- the choice of representation of results in terms of a Failure Assessment Diagram (FAD) or Crack Driving Force (CDF);
- specific methods incorporating the effect of weld strength mismatch;
- guidance on dealing with situations of low constraint and, for components containing fluids, leak before break analysis;
- compendia of solutions for stress intensity factors, limit load solutions and weld residual stress profiles.

The procedure provides advice on the basic inputs and calculations needed to follow the approach. The aspects covered are: tensile properties, fracture toughness data, flaw characterization, and the treatment of primary and secondary stresses. While some of this information is standard, there is novel information arising from the work performed, which may be summarized as follows:

- Assessments have been made of tensile data so that, in the absence of detailed data, estimates of strain hardening properties, Lüders strain, and yield to tensile strength ratios can be made from limited information.

- Statistical treatments of fracture toughness data have been given taking account of the number of specimens regardless of failure mode. In the cleavage regime for ferritic steels, the Master Curve [*13*] approach has been further developed to provide improved estimates of lower bound fracture toughness. Improved correlations are given to enable fracture toughness data to be estimated from Charpy impact energy.
- The flaw characterization rules in the SINTAP procedure are essentially those in the British Standards document BS7910 [*10*]. SINTAP, however, goes beyond this in providing guidance on the reliability of nondestructive examination techniques.
- The basic approach for treating combined primary and secondary stresses is that in R6 [*1*]. However, an alternative approach has been developed, in which the effect of secondary stresses is described by the Factor V. Values of $V>1$ correspond to cases where plasticity leads to values of J arising from secondary stresses, which are increased from those assessed elastically. Conversely, $V<1$ corresponds to plastic relaxation of secondary stresses, and $V = 0$ indicates that the secondary stresses could be neglected.

The third chapter of the procedure provides guidance on selection of the level of analysis and includes compendia of stress intensity factor and limit load solutions and residual stress profiles. These compendia have built on those available at the start of the project but have added a number of new features. For example:

- New stress intensity factor solutions have been developed for defects in cylinders for complex primary or secondary stress fields.
- A large number of mismatch limit load solutions have been provided for plates and cylinders. These provide reduced conservatism compared to classical methods, which treat the weld as if it is composed entirely of the lowest strength material.
- The compendium of weld residual stress profiles covers a range of geometries with surface and through-thickness residual stresses being given for longitudinal and transverse orientations. Residual stresses can be determined from knowledge of the material and weld heat input or more conservatively from bounding stress fields. Advice on the effects of post-weld-heat-treatment is also included.

The final chapter of the procedure covers alternatives and additions to standard methods and basic methodology:

- Ductile tearing analysis methods are given that allow for the increase in fracture toughness beyond initiation. These methods can be applied regardless of the level of knowledge of tensile data but do, of course, require additional information about the ductile tearing toughness.
- Reliability methods are presented along with associated software, PROSINTAP, developed during the course of the project. This approach uses Monte Carlo simulation and approximate First Order Reliability routines. Associated partial safety factors are given for a range of target reliabilities, in a similar manner to BS7910 [*10*].
- Fracture toughness data are generally collected from deeply cracked bend specimens, whereas shallow defects under membrane loading are often assessed in

components. The former is often referred to as high constraint, whereas the latter is low constraint. Use of high constraint data in structural assessments can be over-conservative, and the SINTAP procedure describes a method for calculating the actual level in terms of the elastic T-stress or the hydrostatic Q stress ahead of a crack tip, and then modifies the FAD or CDF methods to allow for the effects. A range of solutions for Q for surface defects[*14*] has been developed to enable the constraint approach to be applied.

- A procedure for making a leak-before-break case is outlined. This is based on an approach within R6 [*1*], but includes new guidance on the shape development of part-penetrating flaws.
- Guidance is given on the effects of prior overload on the mechanical relaxation of residual stress and the effects of warm prestressing on fracture toughness.

Compatibility of FAD and CDF Approaches

Initially, the current situation concerning existing procedures and their pending development was assessed [*15*]. The two principal methods for analysis that are used are the Failure Assessment Diagram (FAD) and the Crack Driving Force (CDF), Fig. 1. The former method is used in approaches such as R6 [*1*], BS 7910 [*10*], SAQ [*3*], EXXON [*4*], INSTA [*5*], MPC [*6*], and API 579 [*7*]; whilst the CDF approach is favored in ETM [*8*] and GE-EPRI [*9*] procedures.

The basis of both approaches is that failure is avoided so long as the structure is not loaded beyond its maximum load bearing capacity defined using fracture mechanics criteria and plastic limit load analysis. The CDF approach involves comparison of the loading on the crack tip (often called the crack tip driving force) with the ability of the material to resist fracture (defined by the material's fracture toughness or fracture resistance). Crack tip loading must, in most cases, be evaluated using elastic-plastic concepts and is dependent on the structure, the crack size and shape, the material's tensile properties, and the loading. In the FAD approach, both the comparison of the crack tip driving force with the material's fracture toughness and the plastic load limit analysis is performed at the same time. Whilst both approaches are based on elastic-plastic concepts, their application is simplified by the use of only elastic parameters.

A critical review of these procedures was carried out for fifteen key areas, which demonstrated that there is relatively little difference between results obtained. The major discrepancies arise primarily because of the limit load or stress intensity factor solutions rather than any fundamental differences in concepts. Furthermore, although FAD and CDF routes represent two different calculation methodologies, the underlying principles remain the same, comparison between the applied stress and the material's resistance. It is only in their development, through different simplifications, that they diverge.

In the following description, the term 'yield stress' is used to infer either the yield stress in the case of discontinuous yielding, or 0.2% proof stress for continuous yielding. Differentiation between these two parameters is only made where necessary. In the CDF method, calculations are made of an applied parameter such as the J-integral or crack opening displacement that characterizes the state of stress and strain ahead of the tip of a crack in a component.

J is estimated as

$$J = J_e\,[f(L_r)]^{-2} \qquad (1)$$

where J_e is the elastic value of the J integral, which can be deduced from the stress intensity factor K_I as

$$J_e = K_I^2 / E' \qquad (2)$$

where E' is Young's modulus E in plane stress and $E/(1-\nu^2)$ in plane strain, where ν is Poisson's ratio. The function $f(L_r)$ is defined in terms of the load ratio

$$L_r = F/F_Y \qquad (3)$$

where F is the applied load and F_Y is the limit load defined from the yield strength, as

$$f(L_r) = (1 + 0.5L_r^2)^{-\frac{1}{2}}[0.3 + 0.7\exp(-0.6L_r^6)] \qquad (4)$$

For $L_r > 1$, Eq 4 can be refined for materials described by power-law plasticity. For higher levels, the function can be refined in terms of strength mismatch and/or the shape of the stress-strain curve.

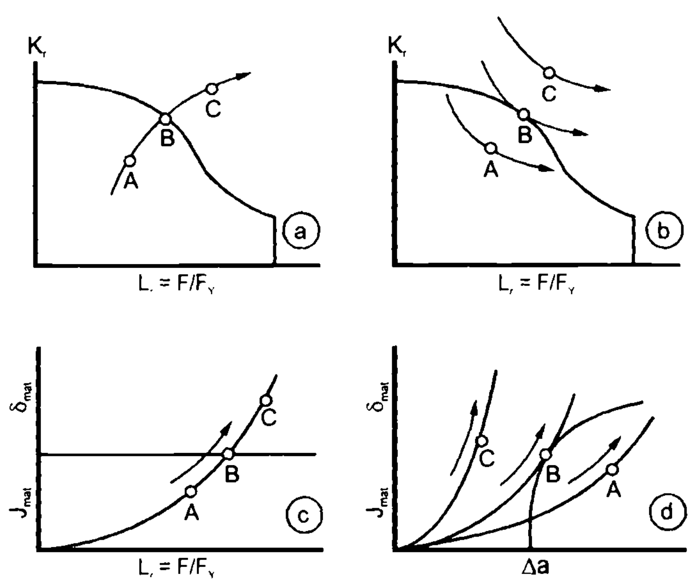

A = Safe Case
B = Critical Case
C = Unsafe Case

a FAD with fracture initiation
b FAD with tearing analysis
c CDF with fracture initiation
d CDF with tearing analysis

FIG. 1—*Failure Assessment Diagram (FAD) and Crack Driving Force (CDF) approaches for fracture initiation and ductile tearing analyses.*

It can be seen that J can be estimated from Eqs 1–4 provided the applied load F is known, a stress intensity factor solution is available (note K_I is proportional to F and depends on geometry and flaw size) and a limit load solution is available (note F_Y is proportional to yield stress (YS) and depends on geometry and flaw size). In the CDF method, fracture is conceded when J exceeds a material property value, J_{mat}, which is related to fracture toughness, K_{mat} by

$$J_{mat} = K_{mat}^2 / E' \qquad (5)$$

in a similar manner to Eq 2.

The CDF method described above is based on approaches within the ETM [8] method developed at GKSS in Germany. In particular, the functions f (L_r) within the SINTAP approach for power-law materials are based directly on the equations in ETM.

In the FAD method, two parameters are calculated. One is the load ratio L_r already defined by Eq 3. The second is a ratio K_r defined by

$$K_r = K_I / K_{mat} \qquad (6)$$

Once these two parameters have been calculated, fracture is avoided if the point (L_r,K_r) is within a region defined on a failure assessment diagram as depicted in Fig. 1. The failure avoidance region is given by the failure assessment curve

$$K_r = f(L_r) \qquad (7)$$

and a cut-off

$$L_r = L_r^{max} \qquad (8)$$

Manipulation of Eqs 1–7 shows that the condition $K_r \leq f(L_r)$ is equivalent to $J \leq J_{mat}$, so that the CDF and FAD representations within the SINTAP procedure are fully compatible. The criterion (8) is imposed to provide a plastic collapse limit with L_r^{max} dependent on the strain hardening characteristics of the material. This limit is imposed in both the CDF and FAD methods.

Analysis Levels in the SINTAP Procedure

A range of analysis options is offered that enables advantage to be taken from increasing data quality and reflects the variation in user knowledge and experience. Each level is less conservative than the one before, such that 'penalties' and 'rewards' accrue from the use of poor and high quality data, respectively. This structure means that an unacceptable result at any level can become acceptable at a higher level. Consequently, the user needs only perform the work necessary to reach an acceptable result and need not invest in unnecessarily complicated tests or analysis.

There are three standardized levels and three advanced levels, including the special case of a leak before break analysis for pressurized systems. The different standardized levels produce different expressions for $f(L_r)$, which define the FAD or CDF to be used in the analysis. The level of analysis is characterized mainly by the detail of the material's tensile data used. The levels available and the options provided within each level are summarized in Table 2. The equations used to generate $f(L_r)$ for Levels 1 and 2 are based upon conservative estimates of the materials' tensile properties for situations when complete stress strain curves are not known. More accurate and less conservative results can be obtained by using the complete stress strain curve, and this option is given in Level 3 as the *SS* (stress-strain) level.

TABLE 2—*Selection of analysis levels from tensile data.*

LEVEL	DATA NEEDED	WHEN TO USE
Default Level		
Default	Yield or proof strength.	When no other tensile data available.
Standard Levels		
I. Basic	Yield or proof strength: ultimate tensile strength.	For quickest result. Mismatch in properties less than 10%.
2. Mismatch	Yield or proof strength: ultimate tensile strength. Mismatch limit loads.	Allows for mismatch in strength of weld and base material. Use when mismatch greater than 10%.
3. SS (Stress-strain defined)	Full stress-strain curves.	More accurate than Levels 1 and 2. Mismatch option included.
Advanced Levels		
4. Constraint Allowance	Estimates of fracture toughness for crack tip constraint conditions relevant to structure.	Allows for loss of constraint in thin sections
5. J-Integral Analysis	Needs numerical cracked body analysis.	
6. Special Case: Leak before Break Analysis		Piping and pressure vessel components.

Treatment of Toughness Data in the SINTAP Procedure

Toughness Options

A subdivision of a level arises from the details of fracture toughness data that are used. There are two options for this, one characterizing the initiation of cracking (whether by ductile or brittle mechanisms), the other characterizing crack growth by ductile tearing. The value of fracture toughness to be used in the SINTAP procedure is termed the characteristic value. Table 3 gives guidance on the selection of the options available.

The basic level of analysis, Level 1, is the minimum recommended level. This requires measures of the material's yield or proof strength and tensile strength and a value of fracture toughness, K_{mat}, obtained from at least three fracture toughness test results, which characterize the initiation of brittle fracture or the initiation of ductile tearing. For situations where data of this quality cannot be obtained, there is a default level of analysis, which is based only on the material's yield or proof strength and Charpy impact energy.

TABLE 3—*Selection and treatment of toughness data.*

PARAMETERS REQUIRED	FRACTURE MODE CHARACTERIZED	INPUT OBTAINED
Initiation Option Fracture toughness at initiation of cracking From 3 or more specimens	Onset of brittle fracture: or Onset of ductile fracture	Single characteristic value of toughness either initiation or maximum load.
Tearing Option Fracture toughness as a function of ductile tearing From 3 or more specimens	Resistance curve	Characteristic values as function of ductile crack growth
Default Level Charpy energy	All modes	Correlated characteristic values

It is currently common for the treatment of the fracture toughness data to be used in analyses to vary depending on the type of data (K_{IC}, J or CTOD (δ)) that are available. This complicates structural integrity assessment and makes it difficult to apply any single, unified procedure. In reality, fracture toughness data may not exist at all due to lack of material or the impracticability of removing material from the actual structure. In these cases, Charpy data may be all that are available, and it is necessary to use a reliable correlation between Charpy impact energy and fracture toughness.

Thus, a methodology capable of incorporating all these factors on a unified basis, could serve as a key to a procedure tailored towards the practical user. In the 'SINTAP' framework, a fracture toughness estimation methodology [*16,17*] has been developed for such a purpose. The methodology is written in the form of a procedure, in which one material-specific toughness parameter, K_{mat}, together with its probability density distribution $P(K_{mat}\}$ is defined, irrespective of the type of original data. For assessment against brittle fracture, the SINTAP evaluation procedure is based upon the maximum likelihood concept (MML) [*18*] that uses a 'Master Curve' method [*13,19*] to describe the temperature dependence of fracture toughness. As a final result, a conservative estimate of the mean fracture toughness (and the distribution) is obtained.

The present methodology can be as easily applied to indirect (i.e., Charpy) data, as to actual fracture toughness data, and is suitable for the treatment of data at both single and different temperatures. The procedure enables a reliable fracture toughness estimate to be obtained for various forms of data sets containing results from both homogeneous and inhomogeneous material. Thus, it works, not only for base materials, but for weld metals and heat-affected zones. It is initially structured in a way that the more sufficient or accurate the original data, the more the user will be rewarded in the probabilistic fracture mechanics assessment.

Estimation of Fracture Toughness from Charpy Impact Energy

For indirect determination from Charpy impact energy, no single correlation can be applied to all parts of the toughness transition curve, hence it is necessary to use various correlations; the following options are available, as described in [*17*]:

- A lower bound correlation for brittle (lower shelf) behavior;
- A statistical method for the transition regime (The 'Master Curve');
- A lower bound correlation for the ductile (upper shelf) behavior.

The 'Master Curve' concept is based on the correlation between the Charpy 28 J temperature and the temperature for K_{mat} = 100 MPa$\sqrt{m}$. The relationship is then modified to account for the required failure probability, thickness effect, and the shape of the fracture toughness transition curve. The transition curve for fracture toughness in the transition regime, using a 95% confidence limit, can be defined as:

$$K_{mat} = 20\{11+77 \exp (0.019 [T-T_{28J} - 3°C])\} (25/B)^{1/4} \cdot \{\ln (1/[1-P_f])\}^{1/4} \qquad (9)$$

T = design temperature (°C)
T_{28J} = 28/27 J Charpy transition temperature (°C)
B = specimen thickness or flaw length (2 · c) (mm)
P_f = probability of failure
Std. dev. = 13°C

At a Charpy impact energy of 28 J, the use of Eq 9 with the lower 5th percentile of fracture toughness and a 90 % confidence level leads to a simple equation which represents a conservative lower bound estimate of fracture toughness:

$$K_{mat25} = 12 \sqrt{Cv} \qquad (10)$$

where K_{mat25} is the estimated K-based fracture toughness of the material in MPa$\sqrt{m}$ for a thickness or flaw width (2c) of 25 mm, and Cv the Charpy impact energy (V-notch) in J.

For the cases where Charpy data corresponding to an energy level different to 28/27 J are available, the use of limited extrapolation is permitted. Where a material is potentially operating in a high loading rate regime, corrections can be made based on the Zener-Holloman strain rate dependence of yield strength. Consequently, the method provides a powerful tool for fracture toughness estimation in materials selection, design and structural integrity analyses and is fully coherent with the approach used in the fracture avoidance clauses of Eurocode 3[*20*].

There is, at present, no equivalent of the 'Master Curve' for upper shelf behavior, consequently a deterministic approach is used for the ductile regime. Within the SINTAP procedure, a ductile regime correlation is presented that enables estimation of the R-curve behavior from knowledge of the upper shelf Charpy impact energy. The decision tree for these methodologies is given in Fig. 2.

Treatment of Actual Fracture Toughness Data

For reasons of cost and/or restrictions on the amount of material available, fracture toughness is often measured using a limited number of specimens. The determination of an appropriate statistical distribution from limited data can be arbitrary and unreliable.

Consequently, the selection of a characteristic value from such a distribution for use in a flaw assessment procedure may be unconservative, or at least give inconsistent assessments. However, some of the inconsistency can be removed by assuming the fracture process is governed by a weak link process that follows a three parameter Weibull distribution. For ferritic steels this is given by:

$$P(K_c) = 1 - \exp - \left[\frac{K_c - 20}{K_o - 20}\right]^{-4} \tag{11}$$

where

$P(K_c)$ is the cumulative probability of fracture toughness, K_c(MPa√m)

K_0 is the scale parameter (the 63rd percentile of the distribution)

20 is the shift parameter in the Weibull distribution (MPa√m)

4 is the value of the shape parameter in the Weibull distribution for small scale yielding

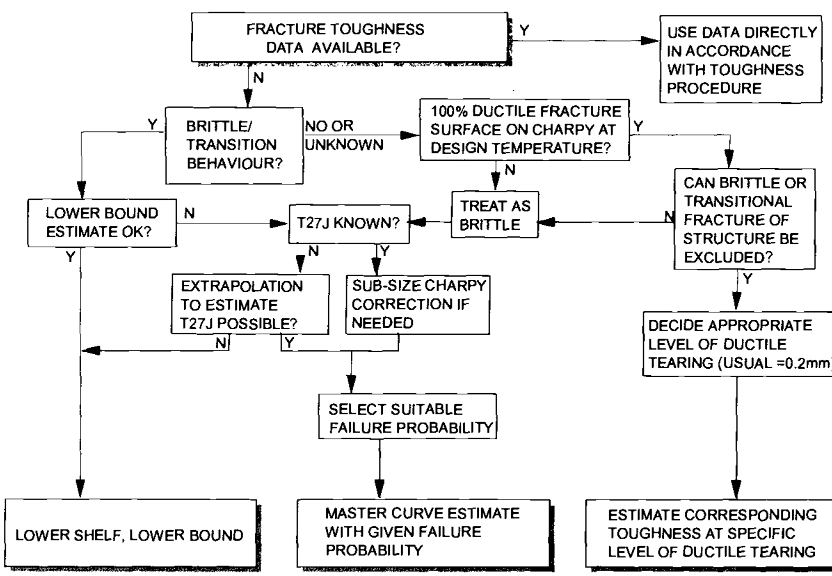

FIG. 2—*Flowchart for the treatment of charpy data.*

Equation 11 may be rewritten as follows to provide an estimate of K_c with a given probability level once K_0 is known:

$$K_c = 20 + (K_o - 20)\left\{-\ln\left(1 - P\left(Kc\right)\right)\right\}^{0.25} \tag{12}$$

The distribution fitting procedure involves finding the optimum value of the K_0 for a particular set of data. Unfortunately, test results may be biased when specimens are extracted from inhomogeneous materials, such as weld metals and heat affected zones

(HAZs). Since every specimen in a series of tests is unlikely to sample local b zones (LBZs) that may be present, the fracture toughness distribution will be bias the higher toughness regions resulting in nonconservative assessments being made avoid this potential problem, the maximum likelihood estimation (MML) procedure is used to provide conservative, but realistic, estimates of fracture toughness.

The MML procedure involves a series of stages. The first stage is to check that al data meet the acceptance criteria of the relevant testing standard. Where CTOD dat available, these may be converted into equivalent K_c values.

Next, the specimen capacity limit (K_{climit}) is determined from:

$$K_{c\,limit} = \left(Eb_o YS / 30\right)^{0.5} \tag{13}$$

where YS is the yield or proof stress, b_o (m) is the initial ligament below the notch (in the test specimen.

Equation 13 ensures that fracture occurs under small-scale yielding and results specimens that exceed this limit or do not fracture are censored. The cens parameter, δ, is set at 0 and the fracture toughness set at K_{climit}. Results from specimens are not censored and δ is set at 1.

Then the toughness values are corrected to a reference thickness of 25 mm, K_{c25}. values of K_{c25} and their associated censoring parameters are then used to make the estimate K_o. This is STEP 1 in the MML procedure (referred to as 'normal estimation') and K_o is obtained from:

$$K_o = 20 + \left[\frac{\sum_{i=1}^{N} (K_{c25i} - 20)^4}{\sum_{i=1}^{N} \delta_i}\right] \tag{14}$$

where:
N = number of results, i = i_{th} result

Note that the MML procedure uses all the test results and that K_o is biased tow the uncensored data (δ=1). For homogeneous materials, the estimate of K_o from E could be inserted into Eq 12 to provide a K_c value for a specified probability l although for the value to be used in a defect assessment procedure, it is necessa correct it to the appropriate thickness. However, when the data are from inhomogen materials, further censoring is required. STEP 2 in the MML procedure, (referred 'lower tail MML estimation') involves censoring all data above the 50th percentile, setting δ = 0 for all values above the 50th percentile. This ensures that the estimate is biased towards the lower tail of the toughness distribution, so as to include re from specimens containing LBZs. Results from specimens that do not contain LBZs that are likely to give high fracture toughness values tend to be excluded by STE The censored values are assigned the median value of toughness.

$$\overline{K}_{c25} = 20 + (K_o - 20)0.91 \tag{15}$$

After censoring, K_o is re-estimated using Eq 14. However, since both Eqs 14 an contain K_o, the procedure is iterative with K_o and $\overline{K}_{c25}$ being continually adjusted u consistent minimum K_0 is obtained.

The final step, STEP 3 (referred to as 'minimum value estimation'), requires an estimate of K_0 using the minimum fracture toughness value in the data set. The values of K_0 from each of the three steps are now compared and the lowest value taken, except when K_0 from STEP 3 is not less than 90% of the lower of K_0 from STEPS 1 or 2. If the value from STEP 3 is less than 90%, it would be conservative to use this value. However, if not, the procedure is highlighting an outlier and a judgement has to be made as to its significance. If the data set is large and the fit to the assumed distribution is good, then the result from STEP 3 can be treated as representing an anomaly and can be ignored. However, if the data set is small, it would be unreasonable and unconservative to ignore STEP 3. If the result from STEP 3 is considered to be unsatisfactory, then further testing should be conducted to define better the lower tail of the fracture toughness distribution.

The procedure described above can also, in principle, be applied to data in the fracture toughness transition regime. A flow chart is given in Fig. 3.

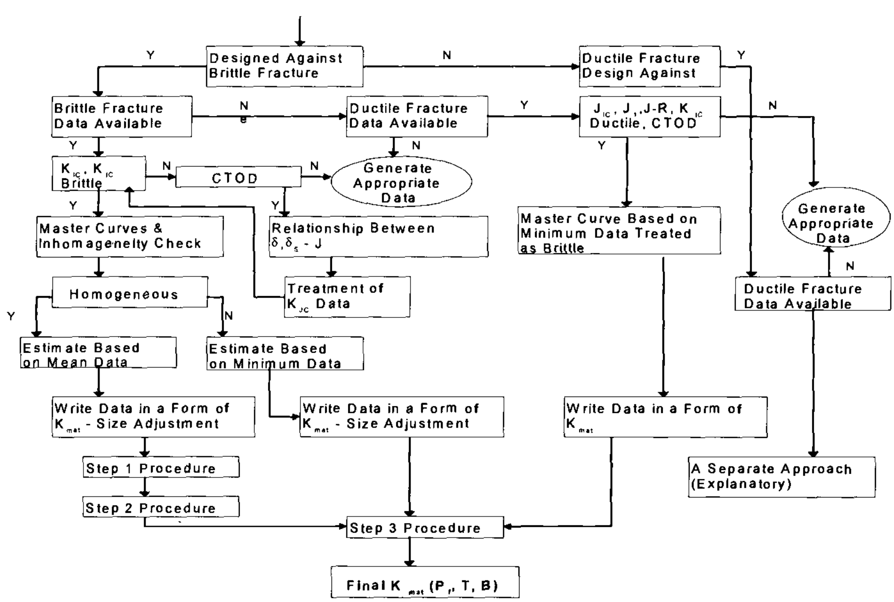

FIG. 3—*Flowchart for treatment of fracture toughness data.*

Derivation of SINTAP Homogeneous Procedure

Development

In order to achieve the hierarchy of Failure Assessment Diagrams, relationships between tensile parameters were derived for a wide range of materials. The following were addressed:

- Estimation of Yield Stress/ UTS (Ultimate Tensile Stress) ratio (*Y/T*) from a knowledge of yield strength.
- Estimation of *N* (the strain hardening exponent) from *Y/T* (for use at Levels 1 and 2).
- Guidance on when to assume the presence of a yield (Lüders) plateau and, in such cases, what expression should be used to estimate its length.
- Implications for structural assessments if only upper yield strength known.
- Methods for ensuing consistency between elastic and plastic components of the FAD.

At Procedure Levels 1 and 2, the yield strength and UTS must be known as the strain hardening exponent, for the material is determined from the *Y/T* ratio. The *N* value is determined from the true stress-strain curve and can be represented as a simple linear function of *Y/T*. At all levels of FAD and CDF, consistency between the elastic and plastic portions is achieved by the introduction of a factor based on yield strength and Young's modulus. This ensures that as the value of strain hardening exponent decreases, the departure of the plastic portion of the FAD from the elastic portion is consistent.

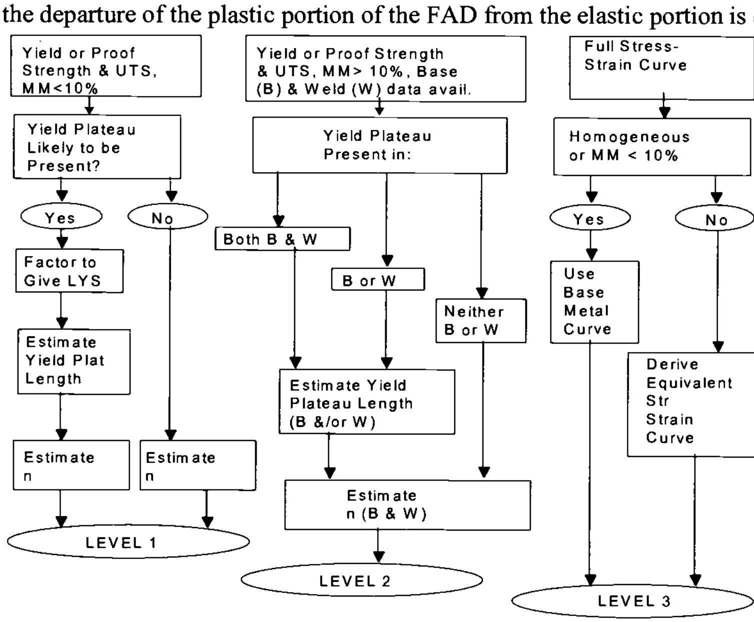

FIG. 4—*Flowchart for the treatment of tensile data — standard levels.*

Validation of Homogeneous Procedure

The ability of the SINTAP method to provide conservative predictions in the correct level of hierarchy was assessed through a number of examples:

1: Planar Geometry - Wide Plates

2: Planar Geometry - Center Cracked Panels
3: Cylindrical Geometry - Pipe Butt Weld

In the first example, seven surface cracked wide plates of different steels were analyzed for an extended range of *Y/T* ratio. These plates were always subjected to single uniform tension, and all of them were 450 mm wide. Particular data, both on the geometry and on the material properties, mechanical behavior and toughness, were assessed. The steels had thickness of 12–40 mm and strength grades 275–1100 MPa.

The objective of the examples was to validate, through the experimental results, the analytically obtained values by varying:

(a) The quality of input data by means of.

- Different hypotheses of knowledge of tensile properties, therefore, changing the Failure Assessment Line and, therefore, the degree of conservatism.
- Different toughness considerations, correlations from Charpy tests or use of Kmat determined from CTOD values.

(b) The crack size

These combinations resulted in 63 calculations of the critical applied stress for a given crack and for each structural situation. These analyses are summarized in Fig. 5. In general, the influence of the toughness option is dictated by L_{rmax}, the toughness data are of minor influence. Conversely, if the failure is toughness dominated then moving from FAD1 to FAD3 will have no effect as they only differ at high values of L_r.

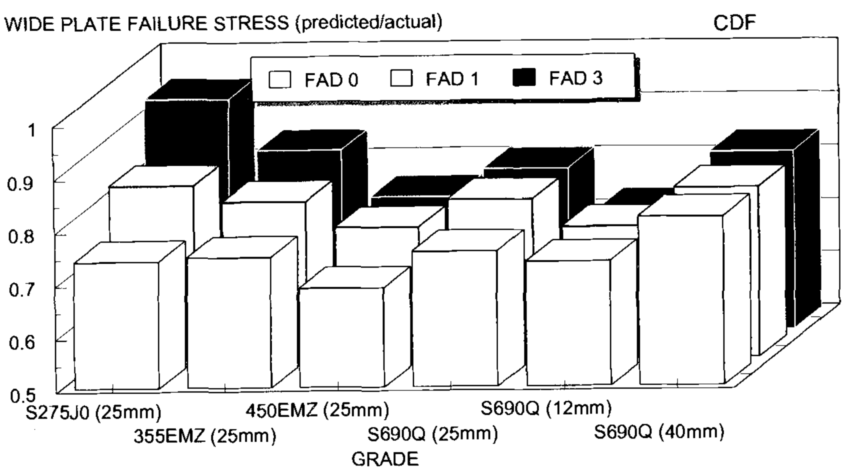

FIG. 5—*Example of the hierarchy of the SINTAP procedure.*

The comparison given in Fig. 5 is based on CTOD data, and it can be seen that the safety factor decreases with increasing assessment level for all of the combinations except one. The exception is the S690Q plate at 12 mm thickness, and this plate has a high *Y/T* ratio that gives an L_r max. cut off of 1.027. The FAD Level 0 cut off is 1.00 as this plate had discontinuous yielding, and plate failure is L_r controlled. Hence, there is little influence of either toughness or FAD type upon the failure stress prediction for this plate.

The second example covered a center-cracked panel subjected to uniform tension. This showed that the values obtained by using both SINTAP and R6 are very close. Also, when using a different solution to SINTAP, considering the finite width of the plate, the figures are, once again, very similar.

The third example dealt with a circumferential butt weld joining two pipe sections subjected to:

- Internal pressure.
- A global bending moment.
- A known residual stress profile.

Two different crack types were assessed:

- Circumferential internal surface crack.
- Circumferential through-thickness.

This structure supports a more complex stress field than the former cases, as well as taking into account the consideration of residual stresses due to the welding process.

Overall, the validation examples on the homogeneous procedure demonstrated that the FAD/CDF methods are conservative, the hierarchy in results is maintained, and that the advantages of moving to a higher level of FAD depends closely on the position of the initial point on the FAD.

Derivation of SINTAP Mismatch Procedure

The method for weld strength mismatched structures has been based on the modified R6 method [*21*] and the ETM-MM [*22*] method. A general structure of the SINTAP method for strength mismatch is shown schematically in Fig 6. It has four levels, depending on the quality of tensile information.

The detailed assessment equations will be illustrated using the failure assessment diagram (FAD) approach only for Level 2 and for two cases within that level: (1) when both base and weld material do not exhibit Lüders strain, and (2) when both materials do.

In the former case the following equation can be used for $0 \leq L_r, < L_{rmax}$,

$$f(L_r)=\left(1+\frac{1}{2}L_r^2\right)^{-1/2}\left[0.3+0.7\exp\left(-0.6.L_r^6\right)\right] \tag{16}$$

The cut-off L_{rmax}, can be determined from

$$L_{rmax}=\frac{1}{2}\left(1+\frac{0.3}{0.3-N_M}\right) \tag{17}$$

In Eq 28, the strain hardening exponent for the mismatched component, N_M, is estimated from

$$N_M=\frac{(M-1)}{\left(F_{YM}/F_{YB}-1\right)/N_W+\left(M-F_{YM}/F_{YB}\right)/N_B} \tag{18}$$

The strength mismatch ratio M is defined at the yield strength:

$$M = \frac{YS_W}{YS_B} \tag{19}$$

where YS denotes the 0.2% proof stress and the subscripts, B and W, denote the properties of the base and weld materials.

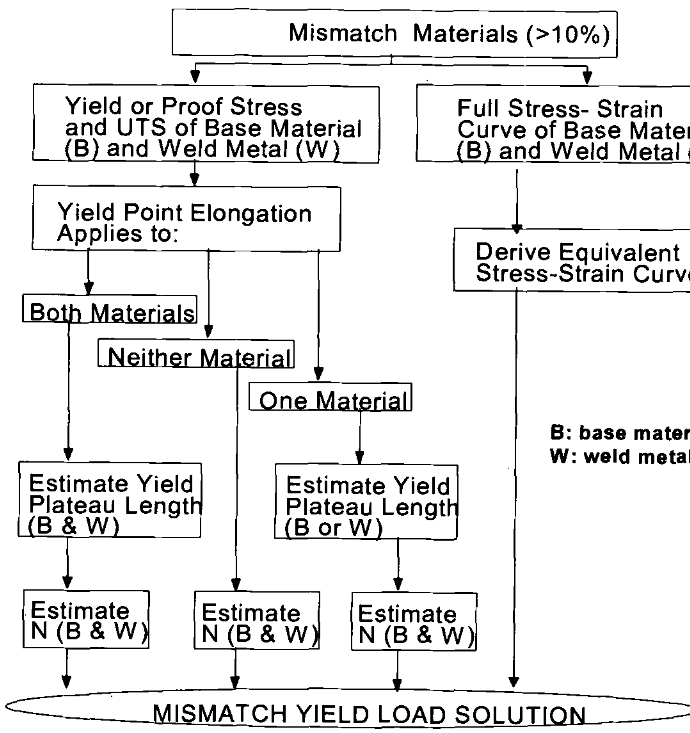

FIG. 6—*Flowchart for mismatch procedure.*

The mismatch yield load, F_{YM}, should be calculated for that value of M, and F_{YB} is the plastic yield load, assuming the component is wholly made of the base material. The hardening exponents for the weld and base material, n_W and n_B, are estimated from

$$\begin{aligned} n_W &= 0.3\left(1 - \frac{YS_W}{UTS_W}\right) \\ n_B &= 0.3\left(1 - \frac{YS_B}{UTS_B}\right) \end{aligned} \tag{20}$$

When both materials exhibit Lüders strain
For $0 \leq L_r > 1$,

$$f(L_r) = \left(1 + \frac{1}{2}L_r^2\right)^{-1/2} \tag{21}$$

At $L_r = 1$, the function $f(L_r)$ is taken as discontinuous and reduces to the value $f(1)$, which is dependent on the extent of the Lüders strain :

$$\begin{aligned}
f(1) &= \left(\lambda_M + \frac{1}{2\lambda_M}\right)^{-1/2} \\
\lambda_M &= \frac{(F_{YM}/F_{YB} - 1)\lambda_W + (M - F_{YM}/F_{YB})\lambda_B}{(M-1)} \\
\lambda_W &= 1 + \frac{E_W \Delta\varepsilon_W}{YS_W}; \Delta\varepsilon_W = 0.0375\left(1 - \frac{YS_W}{1000}\right) \\
\lambda_B &= 1 + \frac{E_B \Delta\varepsilon_B}{YS_B}; \Delta\varepsilon_B = 0.0375\left(1 - \frac{YS_B}{1000}\right)
\end{aligned} \tag{22}$$

where YS denotes the lower yield strength; E is elastic modulus; $\Delta\varepsilon$ represents the estimated extent of Lüders strain; the subscripts, B and W, denote the properties of the base and weld materials. In Eq 22, M and F_{YM}/F_{YB} are also defined at the yield strength (see Eq 20).

For $L_r > 1$, the following equation is used up to $L_r = L_r^{max}$;

$$f(L_r) = f(1).(L_r)^{(N_M - 1)/2N_M} \tag{23}$$

where $f(1)$ is determined from Eq 22; the mismatch hardening exponent, N_M, from Eqs18–20; the cut-off, L_{rmax}, from Eq 17.

Validation of the Mismatch Procedure

Two methods were used, Finite Element Modelling and an experimental program. In the latter, two different materials, having different yield and ultimate strength values, were produced by heat-treating an A533B-1 steel. The yield strength of the higher strength material (designated as M1) is about 50% higher than that of the lower strength material (designated as M3). It should be noted that the M3 material exhibits Lüders strain of a length about 0.8%. In the M1 material, however, a Lüders plateau was not visible, due to its high yield strength and low hardening capacity at low strains.

Strength mismatched specimens with idealized weldments were produced by electron-beam (EB) welding, resulting in two different strength mismatched specimens: highly overmatched ($M \approx 1.48$) and highly undermatched ($M \approx 0.68$) specimens. Single edge notched specimens in three-point bend with a total of 20% side grooving were produced, having the crack in the center of the weldment. Two different crack lengths were chosen, $a/W = 0.45$ and 0.65. All specimens failed by extensive ductile tearing, and the maximum loads were obtained from experimental records.

For both over and undermatched specimens, the predicted maximum loads, F_{max}^{pred}, are shown in Fig. 7, together with the measured maximum loads, F_{max}^{exp}, in the test. The prediction using the level 3 FAD is conservative, but only by 10%. The Level 2 FAD gives slightly more conservative results. Such results are likely to arise from the conservatism embedded in the Level 2 curve for materials with Lüders strain.

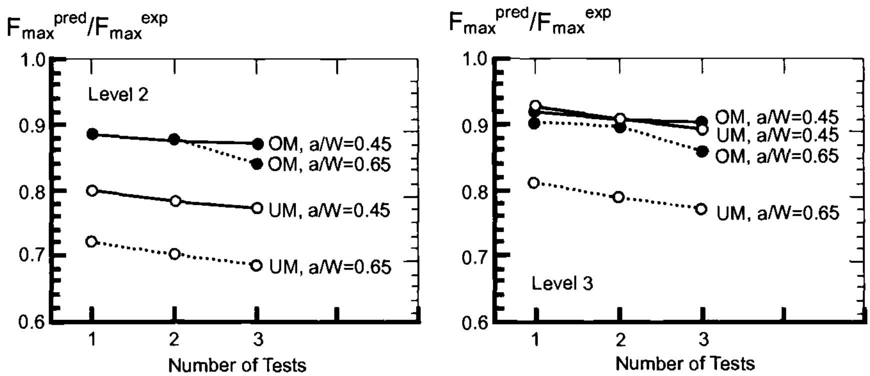

(a) Level 2 (b) Level 3

FIG. 7—*Comparison of predicted maximum loads with experimentally measured loads for the SINTAP mismatch procedure.*

A similar trend has been observed for ductile tearing analyses. As a conclusion, the results from this experimental validation strongly support the methodology of the SINTAP method for weld strength mismatch.

Quantification of Residual Stress Effects

Experimental studies have shown that secondary stresses introduced by welding or temperature gradients can have a significant effect on the load carrying capacity of a component containing a flaw. For this reason, the project included a specific task on residual stresses with the overall aim of determining and validating the most appropriate methods of accounting for residual stresses in as-welded, weld repaired, and post-weld heat treated (PWHT) welded joints [*23*]. This task included a review of existing information on the treatment of residual stresses in fracture prediction, including code-defined secondary stress profiles and a collation of residual stress profiles.

Experimental and numerical investigations of residual stress distributions in welded joints were also carried out. The numerical analysis work addressed the effectiveness of PWHT and the derivation of criteria for PWHT of as-welded and repair-welded structures [*24*] using a Thermo-mechanical Finite Element package [*25*]. Studies of through-wall defects were performed with reference to available experimental data and included further experimental work on thick, welded A533B steel plates. In addition, a study was performed using center-cracked panels into the estimation of J-integral values from dominant residual stresses, thus providing an insight into the influence of residual stresses on fracture behavior.

Standardized residual stress profiles were derived for transverse and longitudinal through thickness distributions in a range of geometries of welded joints manufactured from ferritic and austenitic steels [*23,26,27*]: Residual Stress Intensity Factors were also derived for surface cracks in a range of geometries of welded joints, i.e.,

- plate butt welds
- T-butt and fillet welded joints
- pipe butt welds
- pipe seam welds
- pipe to plate joints
- tubular joints
- repair welds

Treatment of Residual Stresses in SINTAP Defect Assessment Procedure

The principal feature of BS 7910 relating to the assessment of residual stresses involves the relaxation of secondary stresses due to plasticity and is accounted for by:

$$K_r = \left(K_I^P + K_I^s\right) / K_{mat} + \rho = f(L_r) \qquad (24)$$

where ρ is a plasticity correction factor.

An alternative approach for the assessment of plasticity effects on the residual stress distribution has been proposed in SINTAP: a factor, V, is applied to K_s to account for plasticity effects. K_r is then defined thus:

$$K_r = \left(K_p + VK_s\right) / K_{mat} \qquad (25)$$

Equations relating V and ρ have been developed using previously calculated numerical values of ρ to generate values of V/V_o as a function of increasing load for a number of values of secondary stress.

Numerical predictions of V/V_o v. L_r were obtained, and are based on the R6 Option 1 FAD. The results are presented in Fig. 8. They show that V/V_o increases moderately with increasing L_r for L_r values up to approximately 0.9 and decreases at higher L_r values. It has been found [*28*] that V/V_o is very insensitive to the magnitude of the secondary stress, particularly for $L_r > 0.9$, and therefore, a simple approximate approach has been proposed. Two options are included in Fig. 8:

$$L_r \le 0.9, \qquad V/V_o = 1.25 \qquad (26a)$$

$$0.9 < L_r \le 1.4, \qquad V/V_o = 2.78 - 1.7L_r \qquad (26b)$$
$$L_r > 1.4, \qquad V/V_o = 0.4 \qquad (26c)$$
$$L_r \le 0.8, \qquad V/V_o = 1.1 + 0.4L_r \qquad (27a)$$
$$0.8 < L_r \le 1.4, \qquad V/V_o = 2.78 - 1.7L_r \qquad (27b)$$
$$L_r > 1.4, \qquad V/V_o = 0.4 \qquad (27c)$$

Eqs 26 bound the solutions for $[K_p^s / (K_I^P / L_r)] \le 2$ and use a constant value for low L_r, similar to the approximate method in the current version of R6, which uses a constant value of ρ in this region. The plateau value could be made a function of the magnitude of the secondary stress. Equations 27 use a linear fit at low L_r and bound the solutions for $[K_p^s / (K_I^p / L_r)] \leq 5$. At values of $L_r > 0.9$, both equations are identical and correspond to the use of $\rho = 0$ for $L_r = 1.05$ in R6. V/V_o has been set to 0.4 for $L_r > 1.4$ as a bounding value to the numerical data but, in practice, full mechanical stress relief, i.e., $V = 0$, has been observed experimentally [*29*].

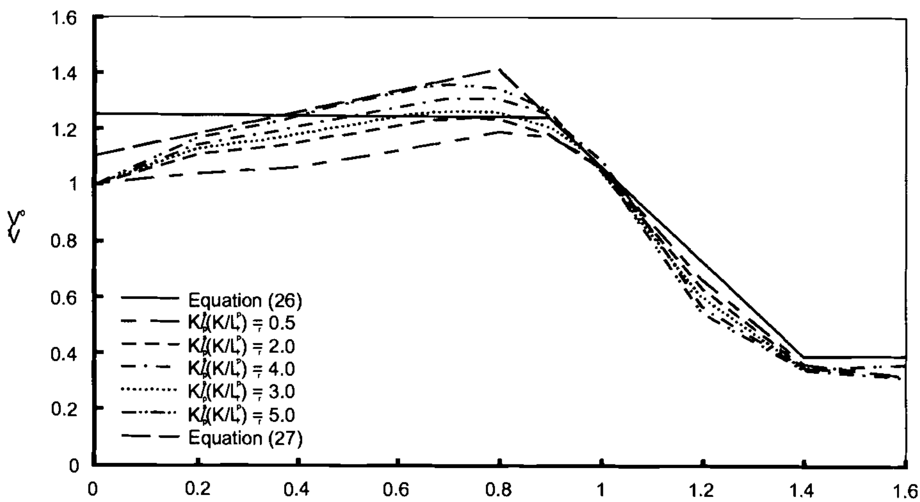

Figure 8 - *Numerical Predictions of V/V_o v L_r*

Reliability of Inspection

Inspection procedures based on Non Destructive Evaluation (NDE) techniques play an important role in structural integrity assessments. Aging of installations and the on-going demand for extending lifetime increase the importance of the inspection techniques used to evaluate the condition of structures. It should be emphasized that inspection procedures are very complex as they involve many specific techniques, decision making, and calibration procedures. Thus, they cannot be regarded simply as a measuring technique and their performance in defect detection, classification, and sizing cannot be fully represented by assigning simple confidence intervals. The analysis of an inspection procedure's effectiveness is a function of the intrinsic capability of the inspection procedure itself and of application features, particularly the inspection performance.

This task within SINTAP concentrated on the provision of guidelines for the statistical treatment of NDE data, as well as on interaction between NDE and fracture mechanics assessment, including probability of detection and sizing errors. The status review highlighted the importance of reliable NDE methods, techniques, and procedures that are capable of providing the required quantitative information on weld fabrication flaws or service-induced flaws in the actual component. Determining a suitable defect density and size distribution is essential for calculating probabilities of failure.

Compilation of NDE Effectiveness Data

Collated NDE data from industry have been used to create a matrix summarizing and grouping the current data in terms of (a) component type, (b) material, (c) thickness, (d) NDE technique, and (e) the type of data on typical flaws found.

The selected data were collected from blind test results or from parametric studies by independent institutions. Specifically, the following NDE programs were taken into account: PISC (three phases including the parametric studies [*30, 31*], DDT exercises in UK [*32*], the PVRC/HSST program results, the IGSCC training program in USA [*33*], Nordtest [*34*], and NIL programs[*35*], TWI projects [*36*], some results of ICON [*37*], and others.

To allow a pragmatic presentation of inspection procedures effectiveness or performance in detection, classification, and sizing of flaws, several categories of components were considered. Also, for any inspection process, different levels of performance can be obtained. Two different classes are:

Q-level: obtained through a Qualification exercise (e.g., European Methodology) that fixes the effectiveness of the inspection procedure at a level considered possible after capability evaluation.

B-level: corresponding to what was shown by 60% of the inspection procedures relevant to the specific situation (Blind trials). In this case, effectiveness can be very good with high performance inspection procedures and very poor with low performance procedures even if applied with care by a good team.

For the presentation of NDE results, particular attention is given to the Flaw Detection Probability (FDP) as a function of the flaw size (depth or length) and to the correct rejection probability (CRP). Estimates of FDP and CRP values based on trials with a limited number of defects will be characterized by an uncertainty that should be taken into consideration when comparing these values. Actually, most of the exercises that generate such data deal with 10 to 40 defects. A possible approach consists of using confidence levels or standard deviations. For instance, for 20 defects the confidence limits at 95% on FDP correspond approximately to $\pm$ 0.2.

With regard to defect sizing, the main parameters used to estimate the inspection performance are the average error of sizing (MES) and the standard deviation (SES). Referring to the depth or the length sizing, the letters (D) or (L) are added to the above symbols, respectively. Unfortunately, it is not always possible to indicate a standard deviation as computed from the measurement set. Often the error band has to be an evaluation based on experience or on very limited trials.

Defect Sizing in Ferritic Steels Components

The PISC program represents the most relevant reference to this category of components. Figures 9a and b illustrate the capability of detection (FDP) and correct sentencing (CRP) for PPD type defects. They were obtained by using UT procedures that were qualified to the best attainable level. In the figures, the FDP and the CRP values were reported as a function of the defect depth size normalized to the component wall thickness. With regard to the detection capability, a very similar behavior was found for heavy pressure vessel components and for large and small diameter piping with thick and thin walls.

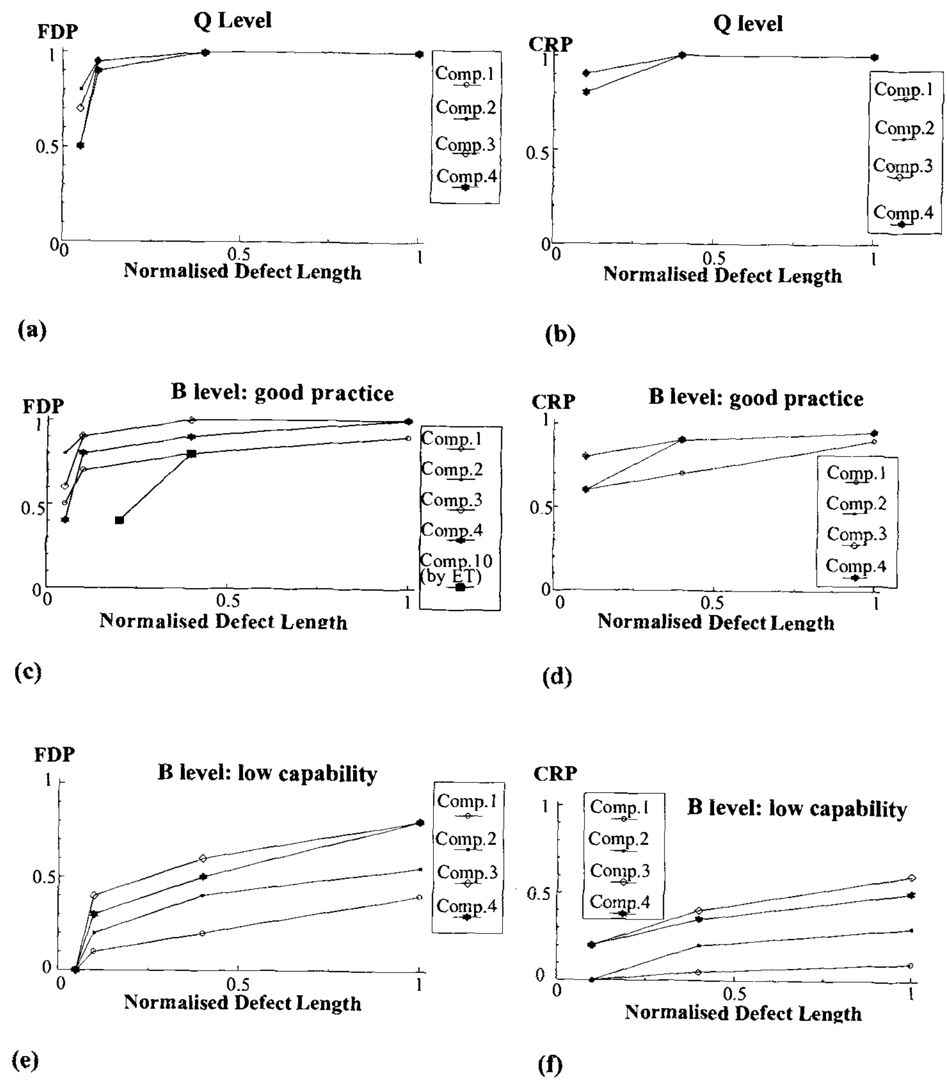

FIG. 9—*Examples of the accuracy of defect sizing.*

However, certain conditions have to be satisfied, like the correct selection of techniques, correct access, and the necessary qualification program. Sizing of multiple defects remains difficult, mainly due to the lack of time or resources often dedicated to defect classification.

Figures 9*c* and *d* report reference effectiveness values when no qualification program is applied. This was obtained using good inspection practices (e.g., 10 or 20% DAC) that, with qualification, would give similar performances to those presented above. Figures 9*e* and *f* refer to B level low capability inspection procedures. These results indicate how poor the performance can be, if poor NDE procedures (e.g., 50 or 100% DAC) are used, or if the application and human factors are not controlled by qualification and the application of a quality assurance program. These values could also correspond to lower bounds for manual inspection conducted in very difficult conditions or environment.

Similar data are also available for Radiography and surface inspection techniques, and for austenitic steel components. Two extensive compilations of NDE capability data were produced within the project [*39,40*].

Specific Analysis Options

Constraint

A particular conservatism implicit in most procedures is that the value of fracture toughness, K_{mat}, is normally derived from deeply cracked bend specimens using recommended testing standards and validity criteria. However, there is considerable evidence that the material resistance to fracture is increased when specimens with shallow cracks, or specimens in tension, are tested. These conditions lead to lower hydrostatic stresses at the crack tip referred to as lower constraint.

Procedures for dealing with this problem are given in the SINTAP procedure; however, it is not intended that these procedures replace those of the conventional SINTAP method; rather that they can be used in conjunction with these to estimate any increase in reserve factors likely to arise under conditions of low constraint.

Leak Before Break Assessment

There are several options by which it may be possible to demonstrate the safety of a structure containing flaws when an initial analysis has failed to show that adequate margins exist. For pressurized components, one of these options is to make a leak-before-break case by demonstrating that a flaw will grow in such a way as to cause, in the first instance, a stable detectable leak of the pressure boundary rather than a sudden, disruptive break. Methods for carrying out such analysis are described and this forms Level 6 of the SINTAP procedure.

Prior Overload

The loading history due to (a) proof or overload tests or (b) warm prestressing of a structure containing flaws may be taken into account when performing an integrity assessment using SINTAP. The effect of loading history is considered with regard to mechanical relaxation of residual stresses and enhancement of lower shelf fracture resistance. The latter is only applicable where the preload constitutes a warm prestress.

Procedures are set out that enable these effects to be quantified, although in practice, the different phenomena may interact, and it may not be possible to separate the different effects simply.

Significance of Results

The procedures discussed to date have been deterministic. In this sense, for any level of analysis chosen, the input data are treated as a set of fixed quantities, and the result obtained is unique. The proximity of this limiting condition to the structural failure condition not only varies from level to level, but it does so even within a given level of analysis. This is because it is dependent on the quality of the data, number of specimens tested, how the value of the input used in the analysis is obtained, how closely these values represent the data in the location of the crack, and on how accurately the loads and stresses on the structure can be determined. The treatments recommended for all these data are conservative, thus when applied alone or in a combined way, an underestimate of the defect tolerance of the structure is obtained. However, the amount of the underestimation is indeterminate because of the uncertainties in the input data.

When assessing the acceptability of a result, confidence is established in two ways: by means of the values chosen for the input data and by assessing the significance of the result. The first of these determines the level of confidence that can be placed in the analysis dependent mainly upon the quality and type of input data. Although this may be high for any one of the data sets concerned, it says little about the overall confidence level of the final result. For this, the whole result must be assessed to establish how all the different confidence levels of the input data interact and combine with each other to provide the final result.

The characteristic value of the fracture toughness takes into account uncertainty inherent in the toughness determination, dependent upon the metallurgical failure mechanism and how they are represented in the analysis. Where the fracture mechanism is brittle, the fracture toughness is often highly scattered, especially where the material is inhomogeneous, as for example in weldments. For this reason, the reliability of the result is dependent on the number of specimens tested, as discussed earlier. The method developed provides a probability distribution of fracture toughness, from which the characteristic value may be derived.

The limiting state, evaluated using values for the input data established following the guidelines in the procedure do define a safe operating condition, although for some engineering purposes, for example in design calculations, additional confidence in determining safe loading conditions is traditionally gained by applying safety or reserve factors. However, the application of previously specified numerical factors in fracture analysis can be misleading because of the inherent and variable interdependence of the parameters contributing to fracture behavior. Confidence in assessments is reinforced by investigating the sensitivity of the result to credible variations in the appropriate input parameters. Software has been produced that allows failure probabilities to be evaluated using both 'Monte Carlo' and 'First Order Reliability Methods (FORM)' techniques, depending upon the relative failure probability and computing power.

Software Developments

Industrial examples of the use of procedures, such as SINTAP, have illustrated the benefits of having software available to automate the calculations. Because the application of the procedure requires large numbers of extensive computation, iterative solutions, and complex interaction between the various parts of the procedure, automation of the SINTAP procedure in the form of software has been an integral part of the project. Further advantages of this are repeatability, accuracy, accountability, and validation, all of which lead to increased effectiveness of the user's time.

The principal factors considered in the development of the SINTAP software have been functionality, consideration of user requirements, modularity, and validation. The software developed in parallel with the technical progress within the individual tasks and now exists as a complete package, although as the overall aim of the software development was to aid verification of the procedure, it is not intended to supply this as a commercial package at the moment.

In addition to the procedure software, as noted above, the probabilistic software, PROSINTAP, uses the procedure to determine failure probabilities for a range of input variables.

This software calculates two different failure possibilities:

- Probability of failure when the defect size is given by NDE.
- Probability of failure when the defect size is not detected by NDE.

Future Development of the Procedure

The dissemination and exploitation of results have been a key aspect of the project. Many of the individual task and subtask areas have been published and the information provided to contribute to the continuing development of procedures, such as R6, BS7910, and ETM. Furthermore, the collaborative nature of the project has enabled technology transfer across industries; specific examples include incorporation of the PISC/NESC data, knowledge from the Nuclear Industry on leak-before-break, data from the offshore industry on tubular joints, and information on steel properties from extensive databases. This collation of existing, but latent, information from across European industry was only possible because of the large consortium. The SINTAP results and procedure have been provided to aid the development of a CEN fitness-for-purpose standard within the remit of the CEN TC 121 Committee.

References

[1] Harrison, R. P., Loosemore, K., and Milne, I., "Assessment of the Integrity of Structures Containing Defects," CEGB Report R/H/R6, 1976.

[2] PD 6493, "Guidance Methods for Assessing the Acceptability of Flaws in Fusion Welded Structures," British Standards Institution, 1991.

[3] Bergman, M., Brickstad, B., Dahlberg, L., Nilsson, F., and Sattari-Far, I., "A Procedure for Safety Assessment of Components with Cracks – Handbook," SA/FoU Report, 91/Ol, AB Svensk Anlaggningsprovning, Swedish Plant Inspection Ltd., December 1991.

[4] "Fitness for Service Guide," EXXON Chemical, 1995.

[5] INSTA Technical Report, "Assessment of the Integrity of Structures Containing Discontinuities," Materials Standards Institution, Stockholm, 1991.

[6] MPC, "Fitness for Service Evaluation Procedures for Operating Pressure Vessels, Tanks and Piping in Refinery and Chemical Service (FS26)." Draft No. 5, Consultant's Report, The Material Properties Council, 1995.

[7] API 579, "Recommended Practice for Fitness-For-Service," Draft Issue 4, 1996, American Petroleum Institute.

[8] Schwalbe, K. H., Zerbst, U., Brocks, W., Comet, A., Heerens, J. and Amstutz, H., "The Engineering Treatment Model for Assessing the Significance of Crack-like Defects in Engineering Structures," (EFAM-ETM 95), GKSS Forschungzentrum, 1996.

[9] Kumar, V., German, M. D., and Shih, C. F., "An Engineering Approach for Elastic-Plastic Fracture Analysis," General Electrical Company, NP- 193 I, Research Project 1237-1, Topical Report, 1981.

[10] British Standard BS7910, "Guidance on Methods for Assessing the Acceptability of Flaws in Metallic Structures," British Standards Institution, 2000.

[11] Schwalbe, K-H and Koçak, M., "Mismatching of Welds," Papers Presented at the International Symposium on Strength Mismatched Welded or Bonded Joints, Reinstorf Luneburg, Germany, 26-28 May 1993, ESIS Publication 17.

[12] Schwalbe, K-H and Koçak, M, "Mismatching of Interfaces and Welds" Papers presented at Second International Symposium on Performance of Strength Mismatched Welded or Bonded Joints, Reinstorf, Luneburg, Germany, 24-26 April 1996.

[13] ASTM, Standard Test Method for Determination of Reference Temperature, T_o, for Ferritic Steels in the Transition Range, ASTM E1921-97, Vol 03.01, 1068-1084, 1998.

[14] Ainsworth, R. A., Sattari-Far, I., Sherry, A. H., Hooton, D. G., and Hadley, I., "Development of Methods for Including Constraint Effects within the SINTAP Procedures," ECF12 Conference, Vol. II, 589-594, 1998.

[15] Ruiz Ocejo, J., Gonzalez-Posada, M. A., Gutiérrez-Solana, F., and Gorrochategui, I., "Review of Existing Procedures," University of Cantabria Report SINTAP/UC/04, 1997.

[16] Wallin, K. and Nevasmaa, P., "Structural Integrity Assessment Procedures for European Industry (SINTAP) - Sub-Task 3.2 Report: Methodology for the Treatment of Fracture Toughness Data - Procedure and Validation," Report VAL A: SINTAP / VTT / 7. VTT Manufacturing Technology, Espoo 1998.

[17] Bannister, A. C., "Structural Integrity Assessment Procedures for European Industry (SINTAP), Sub-Task 3.3 Report: Determination of Fracture Toughness from Charpy Impact Energy: Procedure and Validation," Document No. SINTAP/BS/15. British Steel plc., 1997. 13 p + 7 Appendices.

[18] Moskovic, R., Engineering Fracture Mechanics, 44(1993), p 21.

[19] Wallin, K., International Journal of Pressure Vessels and Pipelines, 55(1993), p. 61.

[20] Langenberg, P., Dahl, W., Sedlacek, G., Stötzel, G., and Stranghörber, N., "Annex C, Material Choice for the Avoidance of Brittle Fracture in Eurocode 3," Proceedings Of Second International Conference on Weld Strength Mismatch, GKSS, April 1996.

[21] R6: Appendix 16: Allowance for Strength Mismatch Effects, Nuclear Electric Procedure R/H/R6, Revision 3 (1998).

[22] K.-H. Schwalbe *et al.*, EFAM ETM-MM 96: "The ETM Method for Assessing the Significance of Crack-like Defect in Joints with Mechanical Heterogeneity (Strength Mismatch)," GKSS 97/E/9, GKSS Research Centre, Germany, 1996.

[23] Barthelemy, J. Y., "Compendium of Residual Stress Profiles," Institut de Soudure, Ennery, France, 1998.
[24] Barthelemy, J. Y., "Post Weld Heat Treatment of a Pipeline Butt Weld," Institut de Soudure, Ennery, France, 1998.
[25] SYSWELD, Instruction Manual, Version 231, Framasoft & CSI, 1991.
[26] Stacey, A. and Barthelemy, J. Y., "Incorporation of Residual Stresses into the SINTAP Defect Assessment Procedures," OMAE '98, Lisbon.
[27] Stacey, A., Barthelemy, J. Y., Ainsworth, R. A., Leggatt, R. H., and Bate, S. K, "Quantification of Residual Stress Effects in the SINTAP Defect Assessment Procedure for Welded Components," OMAE '99 Paper 2044, St. John's, Newfoundland.
[28] Ainsworth, R. A., "The Treatment of Thermal and Residual Stresses in Fracture Assessments," Engineering Fracture Mechanics, Vol. 24, pp. 65–76, 1986.
[29] France, C. C., Sharples, J. K., and Wignall, C., "Experimental Programme to Assess the Influence of Residual Stresses on Fracture Behaviour - Summary Report," Report AEAT-4236, AEA Technology, Risley, 1998.
[30] PISC II: R. W. Nichols, S. Crutzen, "Ultrasonic Inspection of Heavy Section Steel Components," The PISCC II final report, Elsevier Applied Science, Barking, UK, ISBN 1-85116-155-7, 1988.
[31] PISC III: "Evaluation of the Sizing Results of 12 Flaws of the Full Scale Vessel Installation," PISC III Report No. 26 - Action 2 - Phase 1, JRC Report: EUR 15371 EN, 1993.
[32] Watkins, B., Ervine, R. E., Cowburn, K. J., "The UKAEA Defect Detection Trial," UKAEA DDT Symposium, Silver Birch Conf. Centre, Birchwood, Warrington, UK, 7-8 Oct. 1982.
[33] Heasler, P. G., Taylor, T. T., Spanner, J. C., Doctor, S. R., Deffenbough, J. D., "Ultrasonic Inspection Reliability for Intergranular Stress Corrosion Cracks: A Round Robin Study for the Effects of Personal Procedures, Equipment and Crack Characteristics," NUREG/CR-4908, PNL-6196, 1990.
[34] Førli, O., "Development and Optimisation of NDT for Practical Use - Nordtest NDT Programme," 5e Nordiska NDT Symposiet Esbo, Finland, report numbers: IIW-V-967-91, IIW-V-968-91, and IIW-V-969-91, 1990.
[35] NIL, NDT Regulations, NIL Report NDP 95-85, 1995.
[36] TWL Report, "Size Measurements and Characterisation of Weld Defects by Ultrasonic Testing," Part 3, 1982, ISBN 0 85300162.
[37] Rudlin, J. R., Dover, W. D., "Performance Trends for POD As Measured in the ICON Project," Proc. OMAE 96, Vol. II., p. 509, 1996.
[38] Visser, W., Dover, W. D., Rudlin, J. R., "Review of UCL Underwater Inspection Trials," HSE OTN 96, p. 179, 1996.
[39] Crutzen, S. and Franck, F., "SINTAP Sub-task 3.4: Final Report: NDE Effectiveness," JRC Research Report, JRC/IAM, Petten, 30 March 1999.
[40] Visser, W., "Guidance on POD/POS Curves for Non-destructive Examination," Visser Consultancy Ltd., 25 March 1998.

John H. Underwood, Gregory N. Vigilante, and Edward Troiano

Failure Beneath Cannon Thermal Barrier Coatings by Hydrogen Cracking; Mechanisms and Modeling

---

Reference: Underwood, J. H., Vigilante, G. N., and Troiano, E., **"Failure Beneath Cannon Thermal Barrier Coatings by Hydrogen Cracking; Mechanisms and Modeling"**, *Fatigue and Fracture Mechanics: 33rd Volume, ASTM STP 1417,* W. G. Reuter and R. S. Piascik, Eds., ASTM International, West Conshohocken, PA, 2002.

Abstract: Army experience with hydrogen cracking failures of cannons is described, including extensive testing of high strength steel and nickel-iron base alloys to address the failures. Cracking of cannon pressure vessel steels just under bore thermal barrier coatings is now common, and can be explained by the combined action of hydrogen-bearing combustion gases and thermally induced tensile residual stresses. Above-yield transient thermal compression and resultant residual tension stresses beneath the coating are shown to give good predictions of crack arrays observed under the coatings. A similar array of hydrogen cracks in a prototype cannon has recently been explained by contact of combustion gases with uncoated high strength steel that has been yielded by mechanical compressive stresses, leading to residual tension and cracking. The use of nickel-plated hydrogen barrier coatings was shown to eliminate this type of cracking.

Recent cannon experience provides a basis for a summary of mechanisms of hydrogen cracking beneath cannon barrier coatings. The near-bore transient temperature distributions due to cannon firing are calculated by finite difference calculations using temperature-dependent thermal and physical properties and validation by comparison with the known temperatures and the observed depths of microstructural damage. Solid mechanics calculations of transient thermal compressive stresses and resultant residual tensile stresses are made, taking account of temperature dependent coating properties and yielding of the steel substrate near the bore surface. Effects of coating material, coating thickness, and the temperature and duration of firing gases on the depth of thermal damage below the coating are investigated. Direct comparisons between observed and predicted thermal damage and hydrogen cracking are made for coating and firing conditions that correspond to modern cannon firing. This comparison suggests changes in cannon bore coatings to handle the more extreme thermal conditions in modern cannon firing, including thicker or more durable thermal barrier coatings to minimize thermal stresses in the steel substrate and different coating materials that can serve as hydrogen barrier coatings.

Keywords: thermal stress, residual stress, hydrogen cracking, thermal barrier coating, cannon tube, high strength steel, thermo-mechanical model

---

Research Engineers, Army Armament RD&E Center, Watervliet, NY 12189.

Introduction

Damage near the bore surface of a fired cannon can take many forms. Mechanically induced yielding or fatigue cracking due to the gas pressure often start at the bore, but these types of damage are not considered here. Thermally induced expansion or phase transformation of a shallow bore layer will occur if there is sufficient temperature and duration of the pulse of hot firing gases. Environmentally induced cracking or other damage will occur if an aggressive chemical species is present for the required combination of time and temperature. To help cope with these various forms of firing damage, a protective coating is often applied to cannons, typically a 0.1 to 0.2 mm thick electro-plated layer of chromium. As cannon gas pressures and temperatures have increased, the depth and degree of bore damage have likewise increased. One particular type of cannon bore damage is now observed that is closely involved with each of the three forms of damage mentioned above and deserves special attention: thermally induced expansion of a bore layer is observed to cause compressive yielding and associated tensile residual stress, which in turn causes environmental cracking and premature erosion and fatigue failure of the cannon.

The objectives here are (1) to briefly review the recent investigations that support this *thermal expansion – residual stress – environmental cracking* damage scenario, and (2) to use thermo-mechanical modeling to characterize the controlling parameters of this type of thermally-initiated damage, including the thickness and material type of the protective coating and the temperature and time duration of the pulse of hot gases at the cannon bore.

Recent Investigations

Thermally Induced Environmental Cracking

The extreme sensitivity of cannon systems to environmental cracking, particularly hydrogen cracking, has fostered a considerable amount of crack growth testing with the high strength alloys and hydrogen environments typical of cannon applications. Vigilante and coworkers [*1, 2*] have tested a variety of high strength steel and nickel-iron base alloys in electrolytic cell and acid hydrogen environments using automated crack-growth methods with a bolt-load compact specimen incorporating an instrumented-bolt. Their most striking finding in relation to the alloy steels used for cannons was their extreme sensitivity to hydrogen cracking at yield strengths of 1100 MPa and above. A 20% increase in yield strength, from 1145 to 1380 MPa, yielded a *thousand-fold* increase in crack growth rate in carefully controlled laboratory tests. Current work [*3*] has shown a further hundred-fold increase in crack growth rate for 1310 MPa yield alloy steel in a different acid hydrogen environment from that of earlier tests. These results help provide an explanation and background for the upcoming descriptions of hydrogen cracking events in fired cannon.

One particular aspect of cracking that has been observed recently in fired cannons provides a simple yet compelling argument for the importance of hydrogen cracking in cannons. The expected type of mechanical fatigue cracking in a cannon is the C-R orientation shown in Figure 1, with initially a few and then later one dominant crack

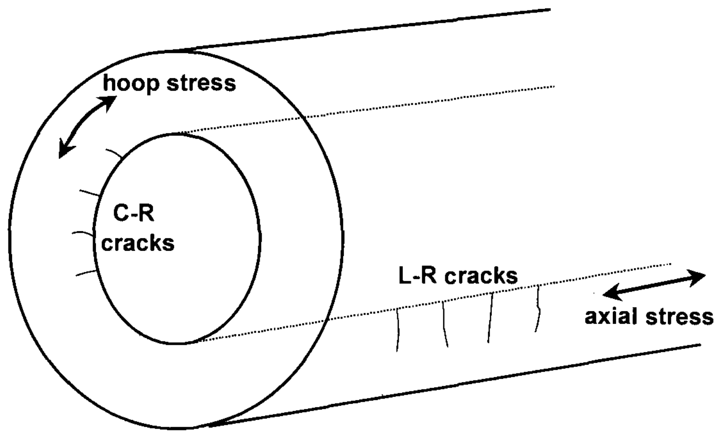

Figure 1 - *Cracking Observed at Bore of Fired Cannon*

growing in the plane normal to the circumferential [i.e., hoop] stress, the dominant applied stress in a pressure vessel. However, an extensive array of nearly constant depth C-R cracks has often been observed in fired tubes, particularly tubes that have experienced a relatively high firing gas temperature. Moreover, the C-R cracks are accompanied by an array of L-R cracks normal to the axial direction with a larger depth than that of the C-R cracks. A deep array of L-R cracks simply can not be explained by a mechanical fatigue process. A cannon, being an open-end pressure vessel, has no significant axial firing stress that could grow L-R fatigue cracks. This and other unanswered questions led Underwood and coworkers [*4, 5*] to investigate other causes and consequences of these arrays of constant depth cracks that are observed in fired cannons.

The typical appearance of an array of L-R cracks and other damage at the bore of a fired cannon is considered next, see Figure 2. A longitudinal metallographic section is shown from a cannon with a 0.12 mm chromium coating, after 40 experimental firings with a relatively high gas temperature. Key features from the top surface of the coating downward into the steel are [*4*]: an extensive array of cracks that grow completely around the cannon bore surface, through the coating and into the steel with an intergranular appearance to an average total depth of 0.46 mm; recrystalization and grain growth (to about 0.01 mm grain diameter) of the chromium coating to an average depth of 0.08 mm, corresponding to a temperature of about 1320 K; transformation of the A723 steel to an average depth of 0.07 mm below the chromium-steel interface for a total depth of 0.19 mm below the surface, corresponding to the 1020 K phase transformation temperature. These damage features, including chromium and steel cracking, chromium recrystalization and steel transformation, have been observed before [*6*], although not nearly to the degree observed here because of the higher gas temperatures in this work. Related damage concerns, such as the volumetric expansion of the steel transformation and the effect of time at temperature on steel transformation, have been discussed in

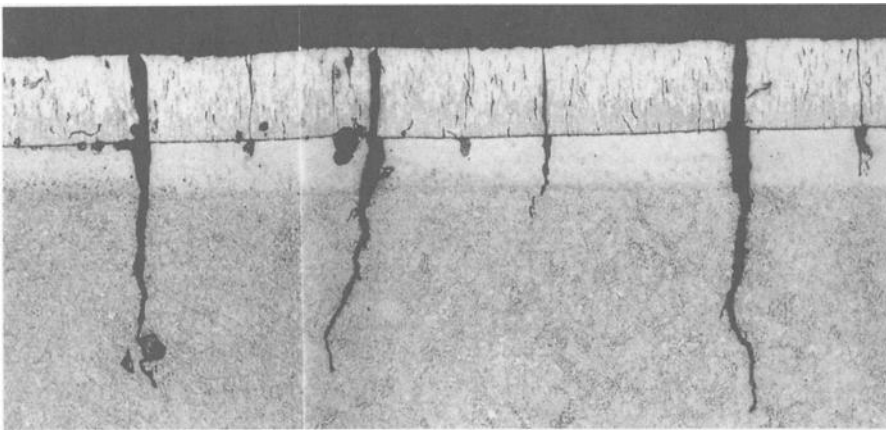

Figure 2 – *Longitudinal Section of Fired Cannon Bore Showing Thermal Damage and L-R Cracking in Chromium Plate and Underlying A723 Steel; 100X*

earlier work [*4*]. The volumetric expansion of transformation is considerably smaller than the thermal expansion, and the few milli-seconds time at temperature of cannon firing was thought to be sufficient for the steel transformation to occur. Recent results using pulsed laser heating of coated steel samples [*7*] have confirmed the time-at-temperature question.

The damage feature most difficult to ignore is the deep cracks through and under the coating, since the cracks critically undermine the coating, as described in reference [*5*]. The observed damage and model calculations from prior work [*4, 5*] can be used to identify the basic cause of the arrayed cracks and also to obtain quantitative descriptions of factors that control the degree of cracking. Regarding the basic cause, environmental cracking is considered much more likely than fatigue cracking, based on the following considerations: the appearance of intergranular cracking in Figure 2; the lack of a significant axial direction fatigue stress; the close proximity of constant-length cracks; the small number of firings experienced; the extreme sensitivity of A723 steel to hydrogen cracking; and the significant concentration of hydrogen in cannon firing gases, believed to be as high as 10 percent. Regarding factors that can control this type of thermal-damage cracking, the observed chromium recrystalization and steel transformation temperatures provide direct verification of the critical information required for describing thermal damage – the near-bore temperature distribution. Knowledge of temperatures directly within the area of thermal damage provides important validation of the thermal damage model used to determine the controlling factors of thermal damage. This is described in upcoming results.

Mechanically Induced Environmental Cracking

One further recent investigation that clearly addresses both the cause and the controlling factors of cannon firing damage is the work of Troiano and coworkers [*8*]. They observed very fast formation of an array of cracks in a maraging steel piston that

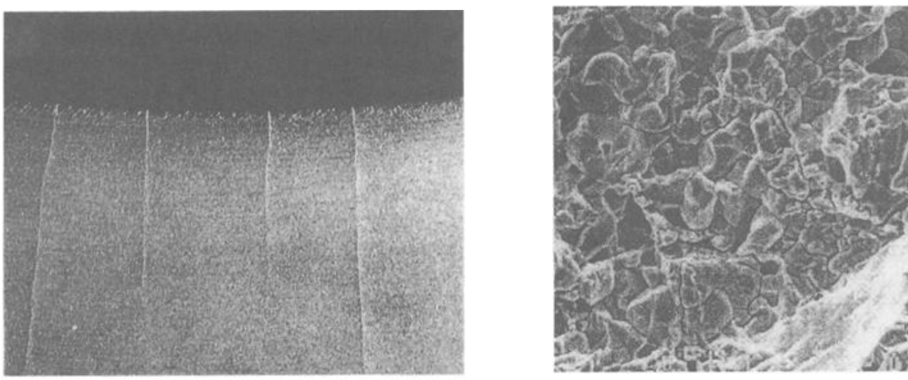

(a) (b)

Figure 3 – *Hydrogen Cracking Observed in Cannon Component; (a) macrograph of surface, 2X; (b) SEM fractograph of opened crack, 400X*

sealed the breech end of a pressure vessel subjected to simulated cannon firing. The piston was subjected to the same hydrogen containing combustion gas and similar gas temperature and pressure as those of gun firing. However, there was very little gas flow over the piston, so the piston surface suffered little thermal damage. The pressure on the piston did result in above-yield-level compression stress at the surface of the piston, as verified by permanent concave 'dishing' of the piston surface that is exposed to firing pressure. The exposed surface developed an array of cracks following a few firings (as few as two), and the cracks could be seen with the unaided eye, Figure 3a. Typically the cracks were up to 20 mm long and spaced about 10 mm apart. A crack was broken open and viewed in a scanning electron microscope to reveal the fracture appearance, see Figure 3b. Evidence of ductile fracture can be seen at the lower right where the specimen was broken open after removal from the cannon. Most of the surface, although partially obscured by what is believed to be reaction product, showed the characteristic intergranular appearance of hydrogen cracking. These classic intergranular cracks observed following cannon firing that involved unambiguous mechanical compressive yielding and hydrogen access provide strong support for the *thermal expansion – residual stress – environmental cracking* damage scenario discussed earlier. Clear evidence of hydrogen cracking due to mechanically induced tensile residual stress supports the contention that thermally induced tensile residual stress is the cause of hydrogen cracking beneath cannon thermal barrier coatings. In the next sections of this work thermo-mechanical modeling will be used to characterize the controlling parameters of this type of cracking in cannons.

Thermo-Mechanical Model

Many of the model concepts were described in prior work [*4, 5, 9*], so only a summary of procedures is given here. The basis of the modeling is the near-bore temperature distribution, obtained by finite difference temperature calculations in [*4*], an approximate expression in [*5*], and most recently, and in this work, by finite difference calculations in a convenient spread-sheet form [*9*]. For the work here finite difference calculations of one-dimensional convective heat flow were used to determine the near-bore temperatures produced by cannon firing conditions. The calculations used increments of about 0.02 mm in depth below the heated bore surface. About fifty increments were required for the temperature to drop from typically 1500 °K at the surface to within 1°K of ambient at about 1 mm below the surface, for the few ms of convective heating typical of cannon firing. Temperature dependent material properties [*10-12*] of chromium, molybdenum and tantulum coatings and the A723 steel substrate were used for the analysis, in the form $fn(T) = C_0 + C_1\,T$, see Table 1. The inputs to the finite difference calculations, in addition to the chromium and steel properties, were: the thickness of the coating, typically 0.1 – 0.2 mm; the initial ambient temperature, T_i = 300 °K; the duration of the convective heating pulse at the tube surface, 0.005 – 0.016 s; the convection coefficient of the heating pulse, h = 193,000 W/m^2 °K; and the mean gas temperature of the pulse, T_{GAS}, with values as discussed in the upcoming results.

Expressions for the near-bore, transient, in-plane, biaxial compressive thermal stress, S_T, and the tensile residual stress, S_R, produced in the steel substrate when the transient stress exceeds the steel yield strength, are as follows,

$$S_T = -E\,\alpha\,[\,T\{x,t\} - T_i\,]\,/\,[1 - \nu] \qquad (1)$$

$$S_R = -S_T - S_Y \qquad \text{for } S_T > S_Y \qquad (2)$$

where ν is Poisson's ratio; the transient temperature, T from the finite difference calculations is for a given depth, x below the bore surface and duration, t of a heating pulse; the term [1 - ν] accounts for the biaxial nature of the temperature and stress distributions. The value of S_R is determined using the linear unloading concept, in which a residual stress is created by a virtual unloading from a calculated elastic applied stress [thermal in this case] that is envisioned to be above the yield level of the material. The residual stress is of opposite sense to the applied stress and of a value equal to the difference between the applied stress and the yield strength, as shown by Equation 2.

Table 1 – *Temperature Dependent Properties of Coatings and Substrate*

	thermal diffusivity; δ, m^2/s		thermal conductivity; k, W/m °K		elastic modulus; E, GPa		thermal expansion; α, 1/°K	
	C_0	C_1	C_0	C_1	C_0	C_1	C_0	C_1
	valid for: (300-2000°K)		(300-2000°K)		(300-1000°K)		(300-1000°K)	
Cr	29.6E-6	-12.6E-9	97.2	-0.0266	--	--	--	--
Mo	56.3E-6	-17.8E-9	144	-0.0291	--	--	--	--
Ta	25.1E-6	-1.20E-9	56.3	-0.0039	--	--	--	--
Steel	11.7E-6	-5.30E-9	43.6	-0.0097	248	-0.097	13.5E-6	0

Modification for Yielding

It is important to account for the change in the steel yield strength with temperature when calculating residual stress using Equation 2. If the room temperature value of strength were used, an underestimate of the tensile residual stress and its depth would result. Yield strength as a function of test temperature is available for AISI 4340 steel [*10*], and this provides a close measure of the temperature dependent strength for cannon steel. Using these results, the following expression was developed for use with Equation 2 to account for the effect of temperature dependent yielding on the tensile residual stress in the steel beneath the coating,

$$S_Y = S_{Y\text{-}RT}\,(1.32 - 0.00105\,T) \qquad (3)$$

where $S_{Y\text{-}RT}$ is the room temperature yield strength of steel, 1100 MPa in this case, and T is temperature in ^{o}K. This approach was used in the model results, considered next.

Model Results

Representative Temperatures and Stresses

Model calculations of near-bore temperatures and transient and residual stresses have been performed for various cannon firing conditions. Some measure of the reliability of these calculations can be obtained by comparison with the results of Perl and Ashkenazi [*13*]. They used a finite element method to calculate temperatures at and below the bore surface of an all steel cannon with T_{GAS} = 3000 ^{o}K , T_i = 294 ^{o}K, h = 145,200 W/m^2 ^{o}K, δ = 12.5E-6 m^2/s, k = 45.2 W/m ^{o}K, and various heating time durations, Δt. Their calculated bore temperature for Δt = 0.008 s is about 1850 ^{o}K, compared with the bore temperature from our finite difference method for the same inputs, 1880 ^{o}K. This close agreement, within 2%, provides independent verification of the methods and results here.

The calculated temperature and stress distributions for the cannon with 40 experimental firings discussed earlier in reference to Figure 2 are shown in Figure 4. The finite difference calculations used the following inputs: the chromium and steel properties from Table 1; a 0.12 mm thick chromium coating; T_i = 300 ^{o}K; h = 193,000 W/m^2 ^{o}K; t = 0.008 s; and mean T_{GAS} = 2160^{o}K. These input values are believed to represent an upper limit of the relatively severe thermal conditions expected in modern cannons, and will serve as a basis of comparison in the results here. The maximum calculated temperature distribution drops from 1480^{o}K at the bore surface, passes near the approximate 1320^{o}K chromium recrystalization temperature [*4*] at the 0.08 mm observed depth, changes slope as expected at the chromium-steel interface at 1240^{o}K, and agrees closely with the most reliable validation point, the 1020 ^{o}K steel transformation temperature at the 0.19 mm observed depth. Considering the good agreement between the calculations and the observed chromium and steel metallographic transformations, these calculated temperatures provide a sound basis for determining the transient and residual stresses in the near-bore region of a fired cannon. These baseline temperatures

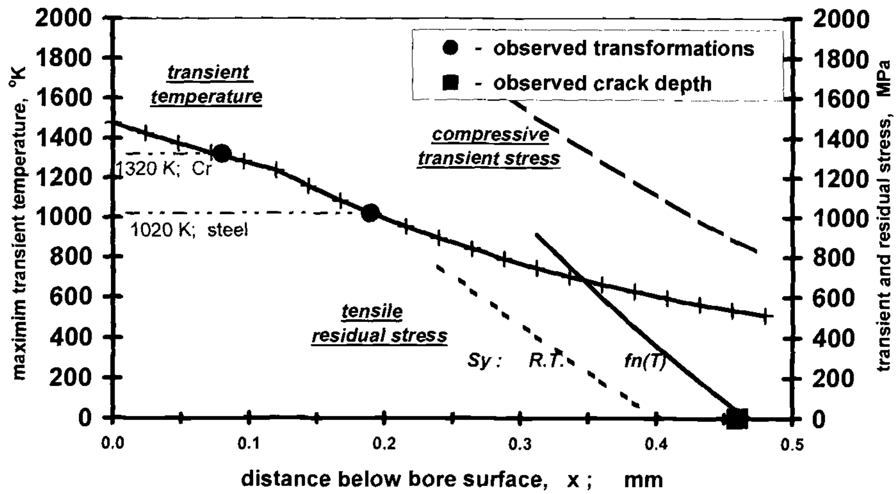

Figure 4 – *Transient Temperatures and Resultant Stresses in a Fired Cannon; 0.12 mm chromium plate;* $\Delta t = 0.008$ *s; mean* $T_{GAS} = 2160°K$

can be compared with those calculated from an erosion model of cannon firing with a new high gas-temperature tank round [*14*]. This gave bore and interface temperatures of about 1560 and 1240°K, which are 6% above and within 1% of the values here, respectively. This is considered to be very good agreement.

Referring again to Figure 4, the transient compressive stress and residual tensile stress distributions based on the calculated temperatures are shown in the plot, along with the temperatures. Note that upon the inclusion of the temperature variation of yielding modification in the residual stress (using Equation 3), the distribution shifts considerably deeper. As would be expected, the reduced yield strength at elevated temperature results in a deeper penetration of residual stresses. It is suggested here that the point at which the tensile residual stress reaches zero may be a useful prediction of the depth of hydrogen cracking. This is consistent with the very low threshold stress for hydrogen cracking observed by Vigilante and coworkers [*1, 2*]. This premise results in good agreement between observed crack depth and the predicted depth (at zero residual stress), and it is consistent with a moderate reduction in the steel yield strength due to its brief exposure to elevated temperature during cannon firing. This approach will be used in all upcoming results.

Parameters Controlling Damage and Cracking

The remaining figures present model results that show effects of key physical parameters on the degree of thermal damage and cracking in the near-bore region of a fired cannon. Figure 5 shows the effect of the type of coating material on the

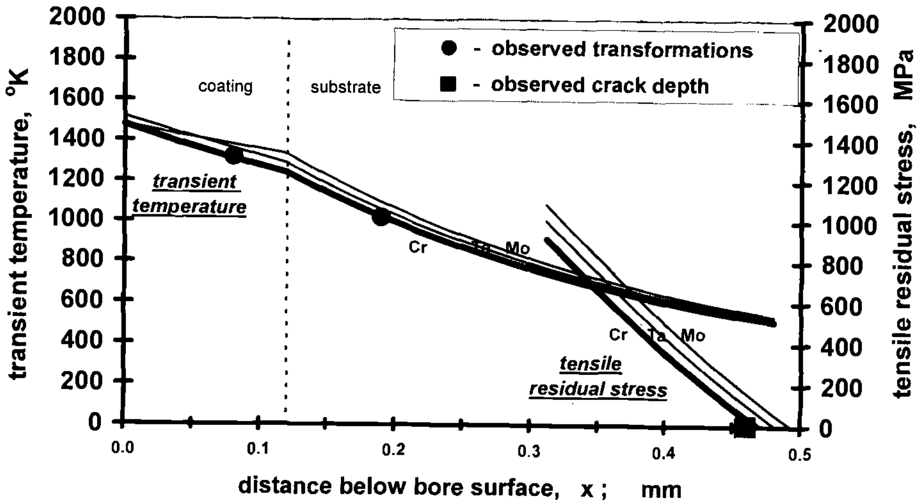

Figure 5 - *Calculated Temperature and Residual Stress for Various Materials: 0.12 mm thick coatings; Δt = 0.008 s; mean T_{GAS} = 2160 K*

temperatures within and below a 0.12 mm thick coating, with the other control parameters unchanged from those discussed in relation to Figure 4. The 4% higher bore temperature for Ta (1540 °K) compared with that for Cr and Mo (1480 °K) and the 5-8% higher interface temperature for Mo (1330 °K) compared with those for Cr and Ta are the result of the different δ and k values for the various materials in this range of temperature. In general, however, the differences in calculated temperature are relatively small for a 0.12 mm thick coating of these three materials. It is clear that thin coatings of good conducting metals can have only small effects on near-bore cannon temperatures. This relative insensitivity to temperature differences is also reflected in the values of residual stress. No significant differences are noted in the residual stress distributions for the three coating materials. Thus, the predicted depth of hydrogen cracks for Mo and Ta coatings (determined for $S_R = 0$) are not much different from that predicted for Cr, or from that observed for Cr, 0.46 mm.

The effect of thickness of a Cr coating on thermal damage and cracking is considered next, see Figure 6. Comparing the bore temperature results for the 0.12 mm thick Cr coating with results for 50 and 100% increases in coating thickness shows little change, only about 1% and 2% decreases in bore temperature, respectively. This can be understood by considering that the thermal properties of Cr and steel in this temperature range are quite similar, so the temperature at any given location in the coating, such as the coating surface in this case, will vary little with coating thickness. Comparing the interface temperatures shows much more effect of coating thickness, with 10% and 18% decreases in interface temperature for 50 and 100% increases in coating thickness, respectively. In this case three different locations below the bore surface are being

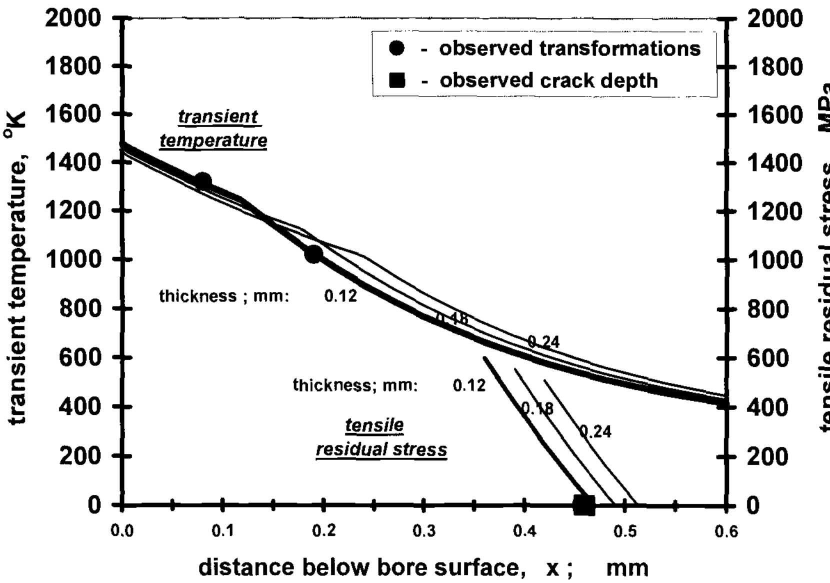

Figure 6 - *Calculated Temperature and Residual Stress for Various Coating Thickness: Cr coatings; $\Delta t = 0.008$ s; mean $T_{GAS} = 2160$ K*

compared, and the steep temperature gradient results in noticeable differences in temperature among the three locations. Finally, comparing a sub-interface temperature, such as at 0.25 mm below the bore surface, shows a moderate *increase* in temperature with an increase in coating thickness. This result may at first seen counter-intuitive, but it can be understood by noting that Cr is somewhat less able to dissipate the heat from the bore surface, as shown by the noticeably shallower Cr temperature gradient compared with that for steel. The lower dissipation of heat for Cr leads to an increase in temperature for thicker Cr coatings. Note that the increased sub-interface temperature for thicker Cr leads to increases in depth of tensile residual stress and thus an increase in the predicted depth of hydrogen cracking. The increases in temperature, residual stress, and crack depth for thicker coatings are moderate, because of the moderate differences in properties noted earlier. Nevertheless, the increased temperature and its effects are clearly expected for a coating that dissipates heat less well than the substrate.

The effect of the duration of the firing heat pulse on thermal damage and cracking is considered next, see Figure 7. Durations of t = 0.005 s and 0.012 s were modeled (with other controls held constant), for comparison with the base value of 0.008 s. A review of Figures 5-7 shows that heating duration has a greater effect on thermal damage and cracking that do the material or thickness of the coating. Considering specific results, the

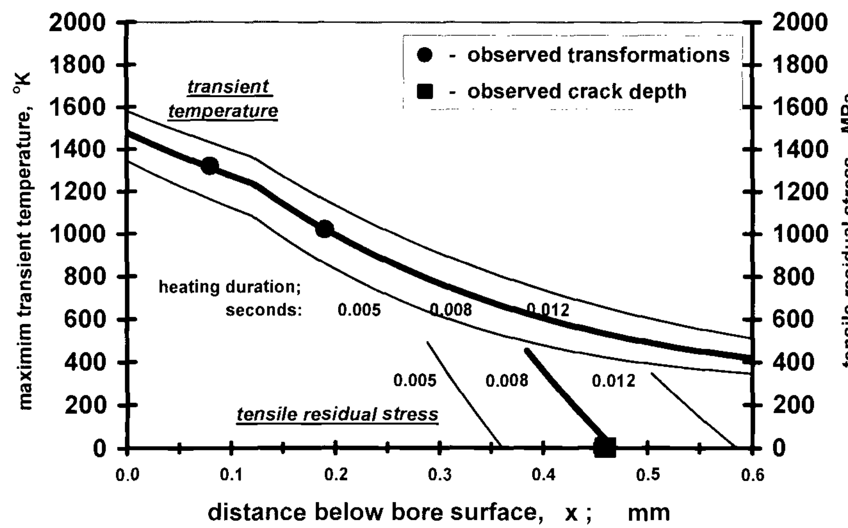

Figure 7 - *Calculated Temperature and Residual Stress for Various Heating Durations: 0.12 mm thick Cr coatings; mean T_{GAS} = 2160 K*

50% increase in heating duration (from 0.008 to 0.012 s) resulted in a 7% increase in bore temperature, a 10% increase in interface temperature, and a 23% increase in expected depth of hydrogen cracking. Figure 8 also shows that the advantages of shorter heating duration are very significant, based on the large decreases in temperature and residual stress predicted for a significant decrease in duration. It is clear that duration of heating pulse during cannon firing exerts significant control over the thermal damage and associated hydrogen cracking.

Finally, the effect of mean gas temperature on thermal damage and cracking is considered, see Figure 8. Gas temperatures of 25 and 50% above the 2160°K base value were considered. The effect of gas temperature was more pronounced near the bore surface, as can be appreciated by comparing Figures 7 and 8. The effect of heating duration, summarized in Figure 7, was seen at all depths, whereas the gas temperature effects diminished somewhat at locations further below the surface in Figure 8. From specific results, the 50% increase in gas temperature resulted in 44% and 34% increases in bore and interface temperatures, respectively and in 13% increase in expected depth of hydrogen cracking. In all cases higher gas temperature resulted in deeper predicted crack depth. This is as expected, because higher temperatures lead to compressive yielding and tensile residual stress at a greater depth, and thus cracks grow deeper. It is clear that mean gas temperature has direct and predictable control over the near-bore thermal damage and associated hydrogen cracking resulting from cannon firing.

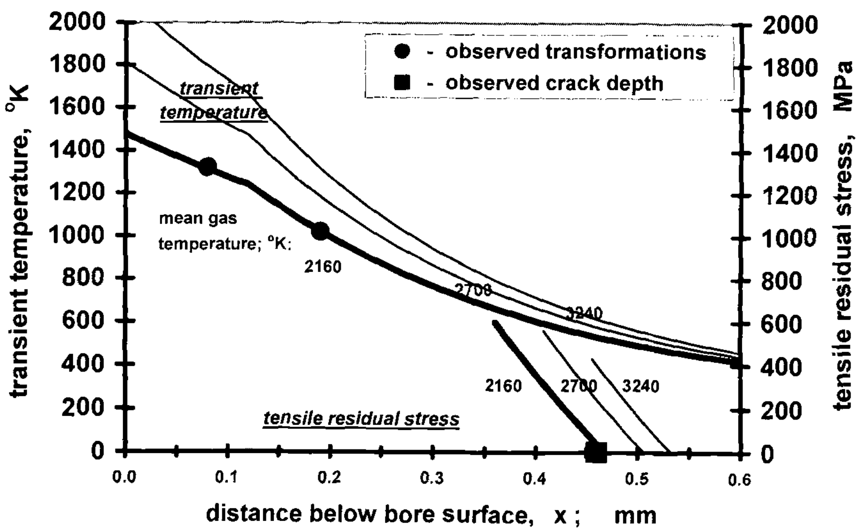

Figure 8 - Calculated Temperature and Residual Stress for Various Gas Temperatures: 0.12 mm thick Cr coatings; Δt =0.008 s

Sensitivity Analysis of Controlling Parameters

A useful summary and comparison of the controlling parameters for thermally initiated cannon bore damage is a sensitivity analysis of the parameters considered. This has been done and is listed in Table 2 as simply the percent change in model temperatures and crack depth predictions for specified changes in the identified control parameters. The parameters and the changes considered are coating material (Cr, Mo, Ta), coating thickness (50% increase), heating pulse duration (50% increase), and mean gas temperature (50% increase). The 50% increase in the various control parameters may not be realistic in some cases, but it does provide a common basis of comparison. The sub-interface temperature results shown are at an arbitrary depth of 0.25 mm below the cannon bore surface, below the coating-steel interface in all cases..

Review of Table 2 shows that gas temperature has far more control over thermal damage and cracking in fired cannons than other parameters, as might have been expected. Second in importance in control of damage is the duration of the pulse of gas temperature, which becomes relatively more important for the deeper sub-interface area and the predicted crack depth that is related to the sub-interface area. Coating thickness and coating material are the least important of the control parameters considered in the modeling, since they typically resulted in 5 to10% predicted change in near-bore temperatures and crack depth, whereas gas temperature and duration typically resulted in 10 to 40% predicted change in near-bore temperatures and crack depth.

Table 2 – *Sensitivity Analysis for Controlling Parameters of Cannon Thermal Damage*

	Bore Temperature % change	Interface Temperature % change	Sub-Interface Temperature %change	Predicted Crack Depth %change
Coating Material				
Mo vs Cr:	0 %	+8 %	+7 %	+5 %
Ta vs Cr:	+4 %	+3 %	+3 %	+3 %
Cr Coating Thickness				
0.18 vs 0.12 mm:	–1 %	–10 %	+11 %	+5 %
Heating Duration				
0.012 vs 0.008 s:	+7 %	+10 %	+16 %	+23 %
Gas Temperature				
3240 vs 2160°K:	+44 %	+34 %	+26 %	+13 %

Conclusions

The key conclusions from this study of cannon bore thermal damage and cracking can be divided into two categories: mechanisms and modeling methods; and characterization of damage control parameters.

Regarding mechanisms and modeling of cannon thermal damage, this study shows:

- The damage mechanism involving *thermal expansion – residual stress – environmental cracking* of the near-bore region of a fired cannon is validated by recent observations of hydrogen cracking in cannon following thermally or mechanically induced compressive yielding.
- A thermo-mechanical model using finite difference calculation of transient temperature with temperature dependent thermal properties and solid mechanics calculations of transient thermal stress and residual stress with account for yielding gives a good representation of near-bore thermal damage in a fired cannon. The model temperatures agree well with observed depths and known temperatures of steel and chromium metallographic transformations.

Regarding characterization of the key control parameters for cannon thermal damage, this study shows:

- In general, the gas temperature and its time duration have significant control over near-bore transient temperatures and sub-interface stresses, whereas the type of coating and its thickness are of secondary importance.
- Increased thickness coatings of metals with poorer heat dissipation than the substrate result in: a slight decrease in bore temperature; a significant decrease in interface temperature; and a significant increase in sub-interface temperature and associated tensile residual stress and hydrogen cracking.

- A 0.12-mm-thick metal coating has limited use as a thermal barrier coating in cannons, because it has little effect on temperatures and associated thermal damage in the near-bore region of a fired cannon.
- A 0.12-mm-thick metal coating has potential use as a hydrogen barrier coating in high temperature cannon firing provided: it limits diffusion of hydrogen; and resists failure by thermal expansion stresses.

Dedication and Acknowledgement

The authors are honored to dedicate this research paper to the memory of the late Joseph F. Cox for his contributions to the work, including the critical concept of validation of thermo-mechanical models using in situ observations of thermal damage.

The authors are pleased to acknowledge Mark Witherell of the Army Armament RD&E Center for his advice and computer programs regarding finite difference temperature calculations.

References

[1] Vigilante, G. N., Underwood, J. H., Crayon, D., Tauscher, S., Sage, T., and Troiano, E., "Hydrogen Induced Cracking Tests of High Strength Steels and Nickel-Iron Base Alloys Using the Bolt-Loaded Specimen," *Fatigue and Fracture Mechanics: 28th Volume, ASTM STP 1321*, 1997, pp. 602-616.

[2] Vigilante, G. N., Underwood, J. H., and Crayon, D., "Use of the Instrumented Bolt and Constant Displacement Bolt-Loaded Specimen to Measure In-situ Hydrogen Crack Growth in High Strength Steels," *Fatigue and Fracture Mechanics: 30th Volume, ASTM STP 1360*, 1999, pp. 377-387.

[3] Troiano, E., Vigilante, G. N., and Underwood, J. H., "Experiences and Modeling of Hydrogen Cracking in a Thick Walled Pressure Vessel," *Fatigue and Fracture Mechanics: 33rd Volume, ASTM STP 1417,* American Society for Testing and Materials, West Conshohocken, PA, 2002, in review.

[4] Underwood, J. H., Parker, A. P., Cote, P. J., and Sopok, S., "Compressive Thermal Yielding Leading to Hydrogen Cracking in a Fired Cannon," *Journal of Pressure Vessel Technology,* Vol. 121, 1999, pp.116-120.

[5] Underwood, J. H. and Parker, A. P., "Thermal Damage and Shear Failure of Chromium Plated Coating on an A723 Steel Cannon Tube,", *Journal of Pressure Vessel Technology,* 2001, to appear.

[6] Turley, D. M., "Erosion of a Chromium-Plated Tank Gun Barrel," *Wear*, Vol. 131, 1989, pp. 135-150.

[7] Cote, P. J., Kendall, G., and Todaro, M., "Laser Pulse Heating of Gun Bore Coatings,"*Surface Coatings and Technology*, 2001, to appear.

[8] Troiano, E., Vigilante, G. N., Underwood, J. H., and Mossey, C., "Analysis of a Piston Experiencing Environmentally Assisted Cracking as a Result of Compressive Overloading," *Progress in Mechanical Behaviour of Materials, ICM8*, Fleming Printing Ltd., Victoria, BC, Canada, 1999, pp. 603-608.

[9] Underwood, J. H., Parker, A. P., Troiano, E., Vigilante, G. N., and Witherell, M. D., "Fatigue and Hydrogen Cracking in Cannons with Mechanical and Thermal Residual Stress," 10th International Conference of Fracture, 2001, to appear.

[10] Incropera, F. P. and DeWitt, D. P., *Introduction to Heat Transfer*, Wiley, 1985, pp. 669-672.

[11] Brown, W. F., Jr., Ed., *Aerospace Structural Metals Handbook, Volume IIA, Non-Ferrous Alloys*, Mechanical Properties Data Center, Traverse City, MI., 1970.

[12] Smithells, C. J., *Metals Reference Book*, Butterworths, Washington, 1962.

[13] Perl, M. and Ashkenazi, A., "A More Realistic Thermal Shock Analysis of a Radially Multicracked Thick-Walled Cylinder," *Engineering Fracture Mechanics*, Vol. 42, 1990, pp. 747-756.

[14] Sopok, S. and Fleszar, M., "Ablative Erosion Model for the M256/M829E3 Gun System," proceedings of 37th JANNAF Combustion Meeting, Monterey, CA, 13-17 November 2000.

Edward Troiano,[1] Gregory N. Vigilante,[1] and John H. Underwood[1]

Experiences and Modeling of Hydrogen Cracking in a Thick-Walled Pressure Vessel

---

Reference: Troiano, E., Vigilante, G. N., and Underwood, J. H., **"Experiences and Modeling of Hydrogen Cracking in a Thick-Walled Pressure Vessel,"** *Fatigue and Fracture Mechanics: 33rd Volume, ASTM STP 1417*, W. G. Reuter and R. S. Piascik, Eds., ASTM International, West Conshohocken, PA, 2002.

Abstract: Hydrogen cracking associated with armament structures has become more prevalent in recent times [1-3]. In this work, a thick-walled, autofrettaged pressure vessel was manufactured from ASTM A723 Grade 2 steel and heat-treated to yield strength of 1170 MPa. An outside diameter keyway was then machined. The keyway was exposed to concentrated sulfuric acid, leading to apparent cracking within 20 hours of exposure.

Investigation of the affected keyway in the pressure vessel indicated that localized hardened areas were present. The base material possessed hardness values of Rc 37-39, while areas near the keyway possessed a local hard zone up to Rc 44. These zones extended to a depth of approximately 4 mm. The different hardness layers suggest that the environmental cracking incubated and propagated in two separate stages. It is speculated that cracking in the hard layer incubated quickly and propagated to approximately the 4 mm depth, then arrested itself once it encountered the more ductile base material. Previously published [2] crack growth (da/dt) test data, and new data verify that this process of incubation and propagation could have occurred in a matter of seconds. The cracking then resumed in the softer base material after approximately 300 hours of incubation time. Additional da/dt testing of this condition has been performed over a range of yield strengths and verifies that incubation times and crack propagation rates are similar to those observed in this pressure vessel.

Keywords: environmental fracture, pressure vessels, crack growth rate

---

[1]Research Engineer, US Army Research and Development Center, Benet Labs, Watervliet, New York, 12189.

Background

Prior history with armament structures has shown a susceptibility to environmental fracture. In 1992, a pressure vessel fractured during manufacturing due to prolonged exposure to a 50% H_2SO_4/50% H_3PO_4 acid solution [3]. The two-meter-long through-thickness crack initiated at an outside diameter keyway. The stress that drove the crack was due to tensile hoop residual stresses near the outside diameter of the pressure vessel. These stresses are the balance of stresses from the autofrettage process, which uses an oversized mandrel to plastically deform the bore of the pressure vessel, resulting in the formation of compressive residual stresses at the bore surface, and tensile residual stresses near the outside diameter. In 1997, a piston being used as a seal component cracked as a result of a compressive overload, which resulted in a tensile residual stress field [1]. This stress field coupled with the aggressive hydrogen-rich gasses within the pressure vessel resulted in cracking in as few as two cycles.

In order to verify previous laboratory hydrogen cracking results on high strength armament steels [4], a hydrogen-cracking test on a full-scale pressure vessel was proposed. A keyway measuring 4.7 mm in width, 12.7 mm in depth, and approximately 450 mm long, with an included radii of 0.4 mm was machined parallel to the axis of the pressure vessel (Figure 1). The pressure vessel was made from A723 Grade2 steel was heat treated to a nominal 1170 MPa yield strength. The tensile residual stress, at the position in the un-notched pressure vessel wall corresponding to the root of the keyway

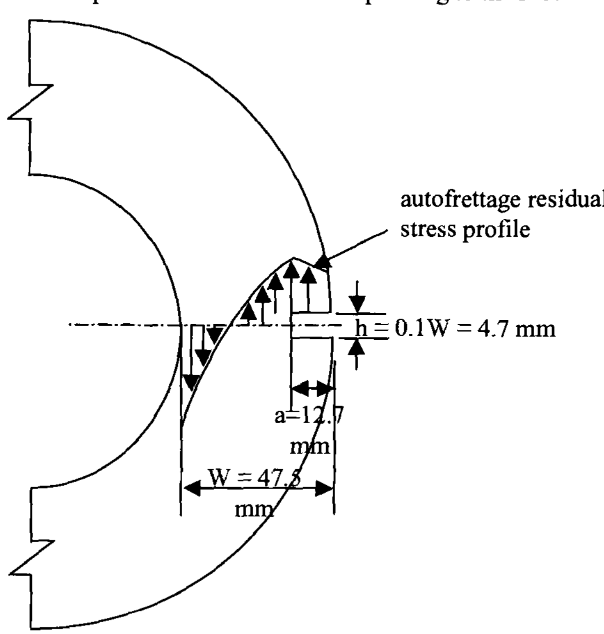

Figure 1 – *Configuration of Pressure Vessel with Residual Superimposed Residual Stress Distribution*

was +500 MPa, well below the yield strength of the material.

Vigilante et al. [2] have conducted environment testing of A723 steel over a wide range of strength levels ranging from 1145 MPa to 1380 MPa, using a 50% H_2SO_4/50% H_3PO_4 acid solution as the source for the hydrogen (Figure 2). An applied stress intensity (K_o) of 55 MPa-m$^{1/2}$ was initially applied for all tests. Their tests were

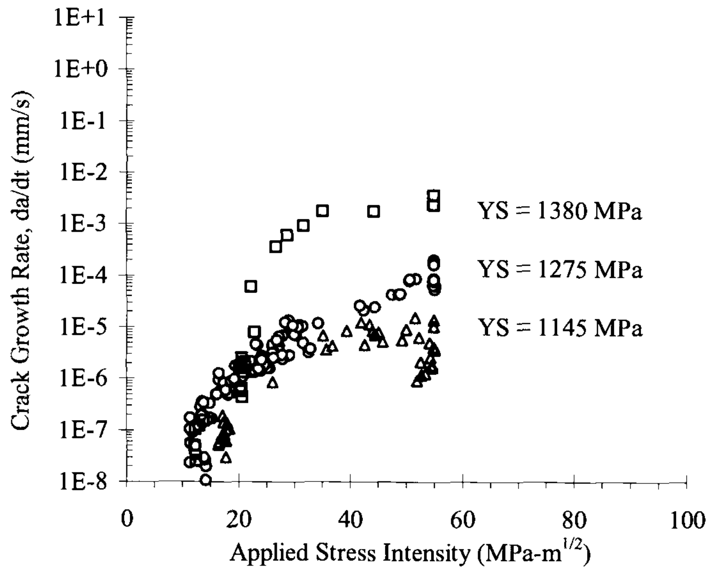

Figure 2 - *da/dt verses K in 50% H2SO4 / 50% H3PO4 acid for ASTM A723 Steel at Three Different Strength Levels [2]*

conducted with a constant displacement bolt loaded compact specimen that had previously been fatigue cracked to induce a sharp crack initiation site. Based on their published da/dt verses K data it was estimated that the pressure vessel would not crack as a result of the sustained +500 MPa residual stress. The following conditions existed that lead to this conclusion: Vigilante's results were conducted with sharp fatigue cracks, whereas the stress concentrator in this pressure vessel was much less severe; Vigilantes results also showed that 3000 hours of incubation time is necessary to initiate cracking at this value of sustained residual stress, whereas the pressure vessel test was completed after 1500 hours.

Analysis/Test Results

Full Scale Keyway Tests

The keyway was inspected using magnetic particle and ultrasonic inspection methods in order to establish a baseline for future inspections. The keyway was then cleaned to remove any oils and dirt, and exposed to 13 ml of concentrated H_2SO_4. It was believed at this time that the H_2SO_4 would behave essentially the same as the 50% H_2SO_4/50% H_3PO_4 solution that Vigilante had used in his prior work. The keyway was inspected visually every hour for the first 24 hours, and daily thereafter, with time being measured with a hand held timer. After less than 20 hours of exposure it was observed that some of the acid had been depleted and an additional 2 ml of acid was added to the keyway to maintain the initial level of acid in the keyway. Since the acid is hydroscopic, it could not have evaporated. It is speculated that the depletion of the acid is the result of cracking, although the exact time when the crack initiated is not known. During the course of the next 300 hours the pressure vessel was monitored both visually and with ultrasonics to detect any cracks; however no cracking was observed.. The inspection process was difficult to accomplish, and the lack of positive identification of cracking in no way suggested that cracking had not occurred. During this time however, the acid had become completely depleted and additional acid was added to restore the initial level of acid in the notch. A white residue (Figure 3) was observed, and is believed to be a by-product of the reaction between the

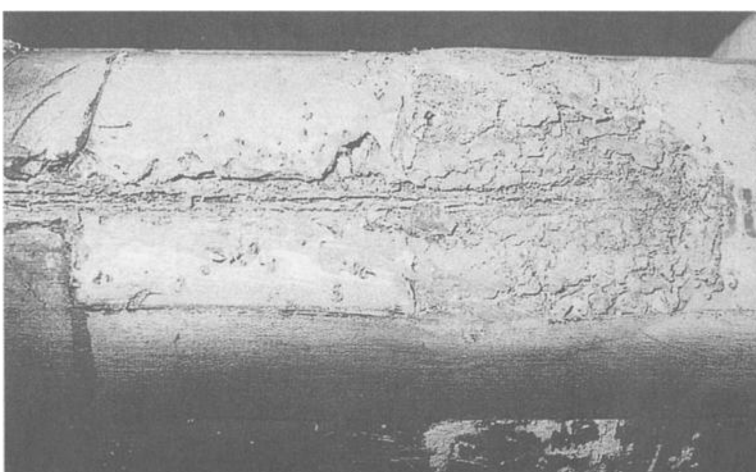

Figure 3 - *Corrosion By-Product on Pressure Vessel Resulting from Acid Environment*

acid and the steel. This residue greatly hindered the inspection process. Over the course of the remaining 1200 hours, the inspections and addition of the acid continued, but no cracking was observed. At this time, the acid was removed and neutralized, and magnetic particle and ultrasonic inspection of the keyway was performed. It was then that a crack-like discontinuity was noticed, however the operator was still unsure as to the extent of the damage. The pressure vessel was then exposed to a single peak pressure cycle of approximately 300 MPa, and the pressure vessel split open exposing the crack surface (Figure 4). The corrosion by-product as well as the exposure to the acid environments suggest that the mechanism of cracking is likely the result of a combination of and hydrogen cracking early during the exposure and stress corrosion cracking (SCC) at later times. Although no further attempt was made to study the impact of the SCC, the hydrogen cracking will be addressed in a later section.

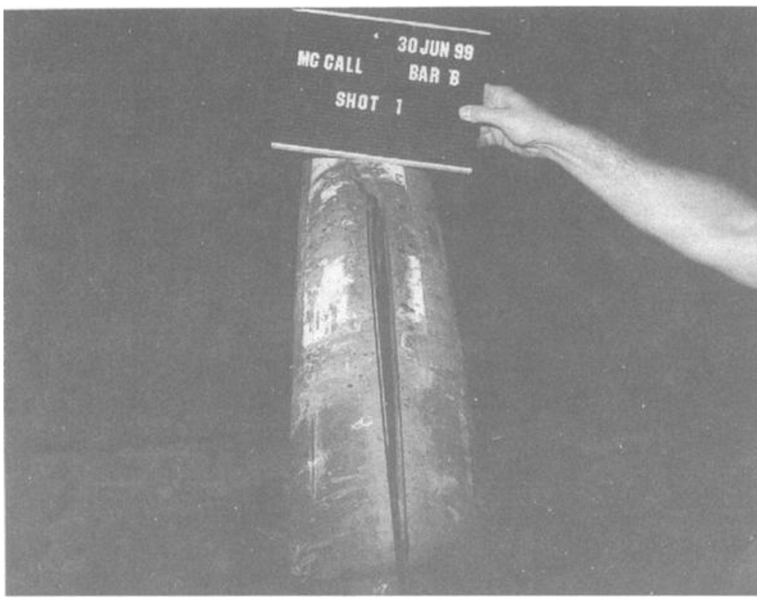

Figure 4 – *Pressure Vessel After Application of Internal Pressure*

Mechanical Property/Microstructure

The material was immediately checked to verify that it was properly heat-treated and that it was free of inclusions or secondary phases, which could have accelerated the failure process. The mechanical properties measured from two areas near the failure are shown in Table 1, and chemical composition is shown in Table 2. In all instances the required mechanical and chemical properties were met.

Table 1 – *As Measured Mechanical Properties*

	0.2% YS (MPa)	UTS (MPa)	RA (%)	El (%)	Charpy (-40C, J)	K_{JIc} (MPa-m$^{1/2}$)
Required	1027 min.	1260 max.	45 min.	13 min.	31 min.	none
Specimen 1	1170	1227	57	15	66	138
Specimen 2	1170	1220	56	14	66	142

Microstructural investigation revealed a fine-grained tempered martensitic structure with very few instances of inclusions or second phases. ASTM grain size measurements were made and found to be 11.5. The mechanical properties closely approximate those from recent work [4], for properly processed A723 steel.

Table 2 – *Chemical Composition – A723 Steel*

	C	Mn	P	S	Mo	Si	Cr	Ni	V
Required min.	0.32	0.55			0.45		0.90	2.5	0.09
max.	0.36	0.65	0.008	0.004	0.55	0.25	0.11	3.2	0.12
Measured	0.32	0.62	0.010	0.004	0.55	0.20	0.10	3.0	0.11

Stress/Fracture/Finite Element Analysis

A logical first step in the analysis was to determine if the pressure vessel would have burst with only the machined keyway present, that is, by mechanical loading only with no acid exposure. A conservative fracture mechanics approach was utilized, where a crack with a very high stress concentrator was used to approximate the keyway, which possesses a lower stress concentration. The stress intensity was the result of both the internal pressure (K_P) and the autofrettage residual stresses (K_R). Rooke and Cartwright [5] have generated a stress intensity profile for the case of a thick walled pressure vessel containing an external crack experiencing internal pressurization. The stress intensity solution is,

$$K_o = 2pR_i^2\sqrt{\pi d} \Big/ \left(R_o^2 - R_i^2\right) \tag{1}$$

where K_0 is the stress intensity (MPa-m$^{1/2}$), p is the internal pressure (MPa), R_i is the internal radius (m), R_o is the outside radius (m) and d is the initial keyway depth (m). K_P, the stress intensity resulting from the applied pressure is calculated from a family of curves in reference 5 (page 241), by knowing K_o, the wall ratio R_o/R_i and the ratio of $d/(R_o^2\text{-}R_i^2)$. Using $R_i = 0.060$m, $R_o = 0.107$m, an initial keyway depth of d = 0.012m and a pressure of 200 MPa (the reduced pressure at this axial location), K_P is calculated to be 45.6 MPa-m$^{1/2}$. The overall stress intensity was also a function of the stress intensity induced from the autofrettage process where,

$$K_R = 1.12 k_t \sigma_{autofrettage} \sqrt{\pi a} \tag{2}$$

where the stress concentration factor, $k_t = 2.55$, is calculated by finite element analysis, $\sigma_{autofrettage}$ = 500MPa, and a = 25 μm, the size of a typical flaw which was observed within the keyway. The calculated K_R = 12.7 MPa-m$^{1/2}$. The resulting $K_{applied} = K_R + K_P$ = 58.3 MPa-m$^{1/2}$, which is well the below the average measured K_{JIc} of 140 MPa-m$^{1/2}$. This simple analysis suggests that the pressure vessel did not burst solely from mechanical loading of the keyway.

A similar approach using actual measurements from the failed vessel is used in the following analysis to determine if hydrogen cracking lead to the final failure of the vessel. At the center of the keyway, where the cracking was deepest, the total notch plus crack depth was measured to be d = 0.045m. K_{Ieac} as previously measured by Vigilante et al. [2] is approximately 15 MPa-m$^{1/2}$. This results in an applied pressure of only 2.9MPa that would be necessary to drive the crack by mechanical means through the small (0.001m) remaining ligament. Since the 2.9 MPa is so much less than the applied 200 MPa internal pressure it is extremely likely that the final remaining ligament was fractured by mechanical means.

The above analyses suggest that the cracking was the result of the hydrogen induced environmental cracking, to the point where final failure by mechanical overload was expected.

Scanning Electron Microscopy/Visual Examination/Metallography

SEM fractography was performed on the fracture surface. The fracture surface was corroded and damaged as a result of the prolonged exposure to the acid environment and the single cycle mechanical overload. The majority of the fracture surface had been so badly damaged, that the details of the event were "etched" away. As a result of this, no conclusive forensic evidence of the fracture morphology was observed. One area of speculative intergranular fracture can be observed in Figure 5.

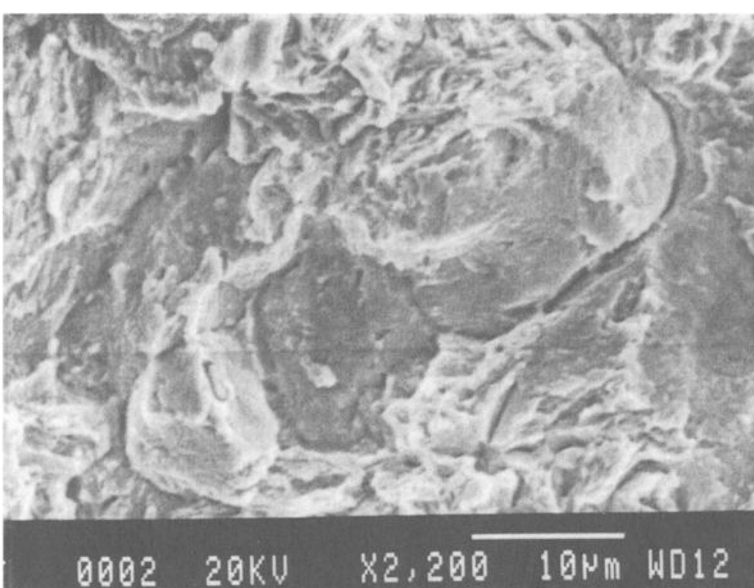

Figure 5 – *Speculative Intergranular Fracture*

Note in this photomicrograph the occurrence of what appears to be secondary cracking in the grain boundaries. ASTM grain size calculation was performed, and a grain size of 10.7 was measured. This measurement is in reasonable agreement with prior results. During the SEM investigation a sharp demarcation line, at a crack depth approximately 4 mm below the base of the notch was clearly observed (Figure 6). It was obvious to the

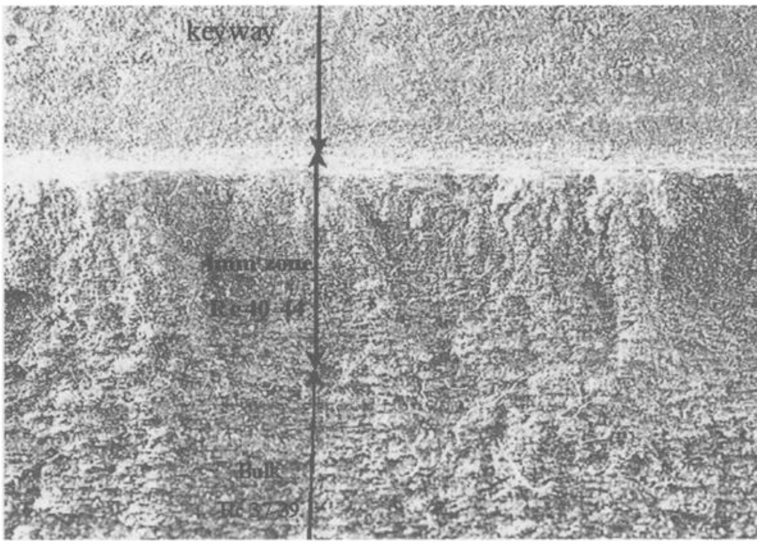

Figure 6 – *4 mm Fracture Zone*

naked eye that there was a different fracture appearance in this 4 mm region than on the remainder of the fracture surface, which extended to within 1 mm of the bore surface. A cross section of the fracture was sectioned and a microhardness profile was taken which emanated from the notch towards the inside diameter of the pressure vessel. The microhardness reading showed a progressive gradient of hardness of R_c 44 at the notch surface and a hardness of R_c 40 at a depth 4 mm below the notch. The bulk of the material beyond the 4 mm region possessed a hardness range of R_c 37 – 39. Although the cause of this local hard region is not known, it may to be the result of local variations in alloy composition that can occur in large forgings

Laboratory Hydrogen Cracking Testing

Hydrogen cracking tests were conducted on modified bolt-loaded compact specimens similar to the one used in reference [1]. In these tests a notch detail similar to the notch in the pressure vessel was utilized (Figure 7). An instrumented bolt, outfitted with strain gages imbedded within the body of the bolt accurately measured the applied

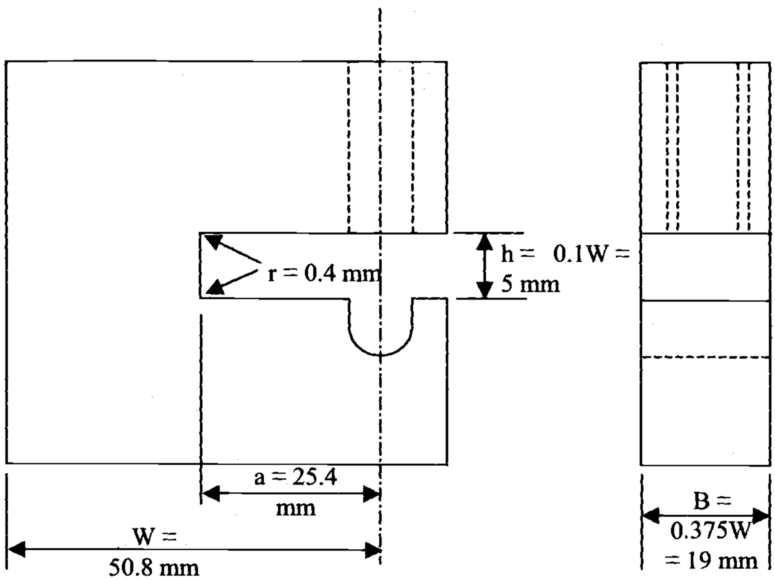

Figure 7 - *Configuration of Modified Bolt Loaded Compact Specimen*

loads, and times were monitored with a digital oscilloscope at rates up to 100,000 points per second. By adjusting the sampling rate and accurately monitoring the voltage output (or load) of the instrumented bolt, the exact point of crack initiation was easily determined. Subsequent crack growth was then monitored as the bolt sheds voltage output as the crack grows. The concept was to model the stress field in the pressure vessel using FE, and simulate the same stress field in the test specimen. Many of the details in the pressure vessel were modeled, including the similar h, W, and r dimensions. Because of load limitations with the instrumented bolt, a deeper notch was necessary to induce the same stress fields.

After over 300 hours of exposure of the specimen to concentrated H_2SO_4 no cracking was observed. It is believed that a different constraint condition present in the pressure vessel when compared to the test specimen is the reason for the differences in cracking behavior. The FEA results matched the stress state of the specimen to that of the pressure vessel in the hoop and radial directions, and disregarded the stresses in the axial direction. However, the free surface of the 19 mm thick test specimen results in a predominately plane stress condition, whereas the much larger pressure vessel is predominately plane strain.

Environmental Testing in Concentrated H_2SO_4

Further testing of bolt-loaded compact specimens was conducted in order to establish a baseline for hydrogen cracking in concentrated H_2SO_4. Although it wasn't known at this time what effect the different acids would have on the crack growth rates, it was speculated that the effects would only be minimally different than those observed with the 50% H_2SO_4/50% H_3PO_4. Further testing of 1310 MPa and 1170 MPa yield strength A723 specimens was performed. The 1310 MPa specimens were loaded to a K_o of 100 MPa-m$^{1/2}$ and 55 MPa-m$^{1/2}$, and the 1170 MPa specimens were loaded to a K_o of 80 MPa-m$^{1/2}$ and 50 MPa-m$^{1/2}$. The result of these tests can be observed in Figure 8. Note however that the crack growth rates are significantly faster in concentrated H_2SO_4 than those tested in the 50% H_2SO_4/50% H_3PO_4.

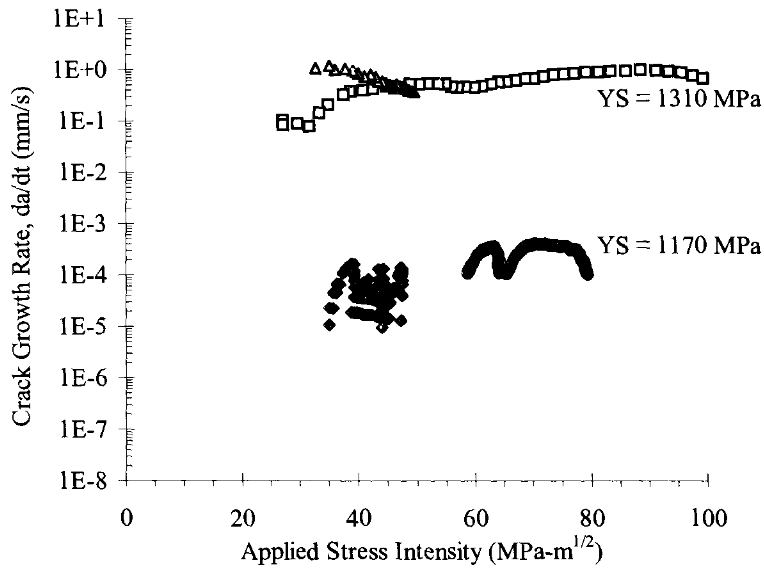

Figure 8 - *da/dt verses K in Concentrated H_2SO_4 for ASTM A723 Steel at Different Strength Levels*

Modeling of Environmental Cracking Events

The following section is provided to help describe the thought process that went into explaining and describing the failure. Several of the scenarios are shown to be incorrect, however their understanding helps to explain the chain of events that lead to the final failure event. The pertinent test results and environmental cracking data in concentrated H_2SO_4 and 50% H_2SO_4/50% H_3PO_4 have been compiled in Figure 9. Several scenarios of environmental cracking will be investigated here. The model used is very simple since we assume that all crack growth that occurs is in the Stage II region. Therefore;

$$\frac{da}{dt} = C \tag{3}$$

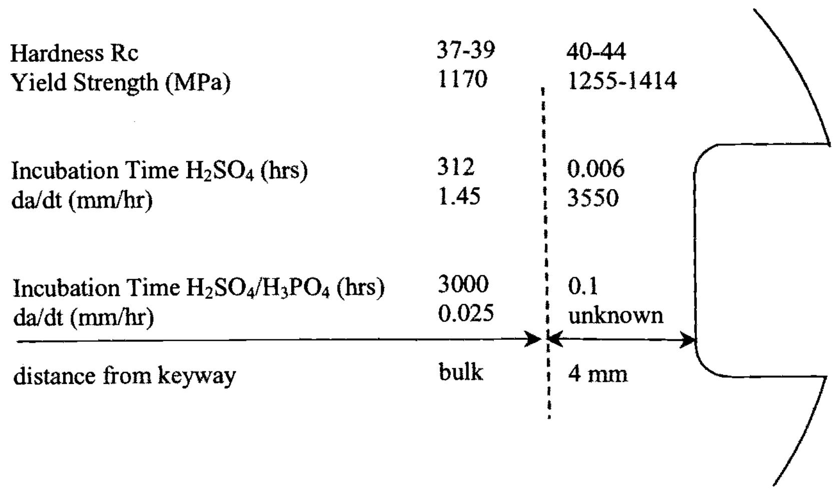

Figure 9 - *Schematic of Keyway Showing Key Parameters for Modeling Hydrogen Cracking Event*

which when integrated, results in

$$a_{final} - a_{initial} = C(t_{final} - t_{initial}) \tag{4}$$

The incubation times are simply added into the model by assuming that a dwell occurs between times of crack advancement. The data presented in Figure 9 is for applied stress intensities of 50 – 55 MPa-m$^{1/2}$. This is approximately the same as the $K_{applied}$ of 58.3 MPa-m$^{1/2}$ for the pressure vessel at the point of cracking, which justifies its use in this model. Three different scenarios of environmental cracking are presented, and plotted in Figure 10. They are:

Scenario #1 - No localized hardened layer in 50% H_2SO_4/50% H_3PO_4
Although this scenario did not exist, it does clearly explain the rationale behind our initial belief that cracking would not have occurred under these test conditions. Under this scenario an incubation time of approximately 3000 hours would have occurred, followed by crack advancement to 47 mm (the width of the pressure vessel wall). This scenario is plotted in Figure 9. Note that the predicted crack advancement is beyond the 1500 hours test duration, which validates our initial belief.
Scenario #2 – No localized hardened layer in concentrated H_2SO_4
Had we simply replaced the 50% H_2SO_4/50% H_3PO_4 with concentrated H_2SO_4, and not had a 4 mm deep hardened layer, it is likely that the cracking would have occurred within the duration of the 1500-hour test. An expected incubation time would be 312 hours followed by crack advancement, nearly through the wall in the next 32 hours of exposure. This scenario however does not explain how cracking was observed (associated with depletion of the acid in the keyway) within the first 20 hours of exposure.

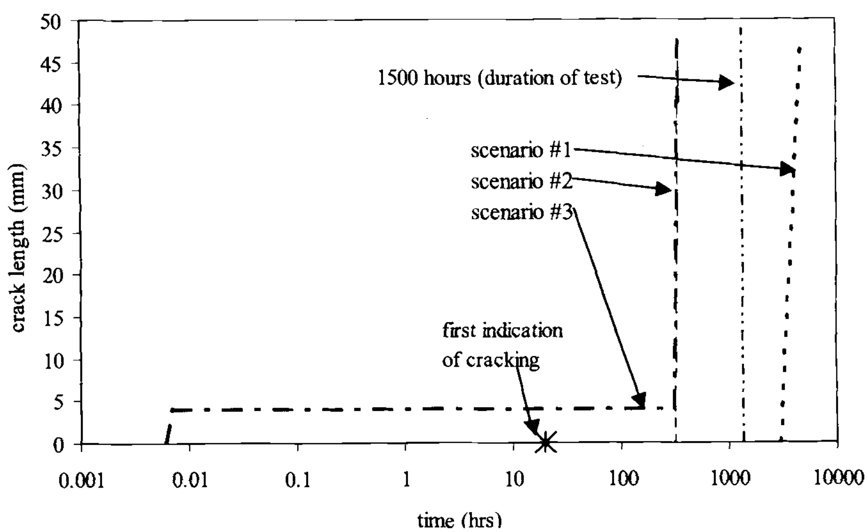

Figure 10 - *Modeling of Several Hydrogen Cracking Scenarios*

Scenario #3 – 4 mm hardened layer in concentrated H_2SO_4
In this scenario cracking incubated in 0.006 hours and propagated to a depth of 4 mm in 0.001 hours, where it arrested. The re-incubation into the softer base material took another 312 hours, after which time it propagated nearly through the wall in approximately 30 hours. This scenario is the most likely scenario because it clearly suggests how cracking started within the first 20 hours, and how the crack extended nearly through the wall within the 1500 hours of exposure.

Summary

An axial keyway was machined in a highly pre-stressed steel pressure vessel and exposed to concentrated sulfuric acid in order to investigate the effects of tensile residual stresses on hydrogen induced cracking. The findings of this and related studies led to the following observations:

1. Speculative intergranular cracking observed during the SEM evaluation, and the presence of an aggressive acid environment, suggests that environmentally assisted cracking comprised hydrogen cracking during the early stages of exposure and SCC during longer exposure times is the likely mechanisms of failure.
2. Because of the rapid cracking seen in the pressure vessel, the most probable scenario for describing the failure event is that the local hard layer resulted in rapid cracking to the interface with the softer base material. A crack formed within 20 hours of acid application and extended to a crack depth of 4 mm. The crack then took time to re-incubate, and after approximately 300 hours of

incubation in concentrated H_2SO_4 the crack continued nearly through the wall of the pressure vessel.

3. Had the test been conducted in 50% H_2SO_4/50% H_3PO_4 it is likely that the crack would have arrested itself after encountering a depth of 4mm. It is not likely that the crack would have re-incubated in the duration of the 1500-hour test.
4. The H_2SO_4 acid environment resulted in several orders of magnitude faster crack growth than the 50% H_2SO_4/50% H_3PO_4.
5. The local hard layer at the root of the notch played a minor role in the premature cracking. The major cause of the premature failure was the substitution of concentrated H_2SO_4 for 50% H_2SO_4/50% H_3PO_4.
6. Slight increases in hardness can result in drastically increased crack growth rates and much shorter incubation times.

Acknowledgments

The authors wish to thank Chris Rickard and Charles Mossey for assisting in various aspects of this study. We would also like to thank Tony Kapusta of Materials Analytical Services for his SEM evaluation.

References

[1] Troiano, E., Vigilante, G. N., Underwood, J. H., and Mossey, C., "Analysis of a Piston Experiencing Environmentally Assisted Cracking as a Result of a Compressive Overload," *Proceeding of the 8th International Conference on the Mechanical Behavior of Materials*, Eds. Ellyin F. and Provan, J. W., Vol. 2, 1999, pp. 603-608.

[2] Vigilante, G. N., Underwood, J. H., and, Crayon, D., "Use of the Instrumented Bolt and Constant Displacement Bolt-Loaded Specimen to Measure In-Situ Hydrogen Crack Growth in High Strength Steels," *ASTM STP 1360*, 1999.

[3] Underwood, J. H., Olmstead, V. J., Askew, J. C., Kapusta, A. A., and Young, G. A., "Environmentally Controlled Fracture of an Overstrained A723 Steel Thick-Wall Cylinder," *ASTM STP 1189*, 1993, pp. 443-460.

[4] Vigilante, G. N., Underwood, J. H., Crayon, D., Tauscher, S., Sage, T., and Troiano, E., "Hydrogen-Induced Cracking Test of High-Strength Steels and Nickel-Iron Base Alloys Using the Bolt-loaded Specimen," *ASTM STP 1321*, 1997, pp. 602-616.

[5] Rooke, D. P., and Cartwright, D. J., *Compendium of Stress Intensity Factors*, London: Her Majesty's Stationery Office, 1976, pp. 240-241.

Monty A. Moshier,[1] Theodore Nicholas[2] and Ben M. Hillberry[3]

High Cycle Fatigue Threshold in the Presence of Naturally Initiated Small Surface Cracks

---

Reference: Moshier, M. A., Nicholas, T. and Hillberry, B. M., "**High Cycle Fatigue Threshold in the Presence of Naturally Initiated Small Surface Cracks**," *Fatigue and Fracture Mechanics: 33rd Volume, ASTM STP 1417*, W. G. Reuter and R. S. Piascik, Eds., ASTM International, West Conshohocken, PA, 2002.

Abstract: The high cycle fatigue (HCF) crack growth threshold of Ti-6Al-4V is investigated when naturally initiated small surface cracks of depths c = 16 μm to 370 μm are present. Small surface cracks are initiated in notched specimens using two different LCF loading histories, R = 0.1 and R = -1.0, at room temperature at a frequency of 10 Hz. Direct current potential difference (DCPD), infrared thermal imaging, and an electrochemical fatigue sensor (EFS) are used to detect crack initiation. Surface crack measurements are made using a scanning electron microscope prior to HCF testing. Heat tinting prior to HCF testing is used to mark the crack front to allow for post fracture crack measurements. HCF thresholds at R = 0.1 are determined for each specimen using step loading at room temperature and 600 Hz. Additionally, the HCF threshold is measured for some specimens that have been stress relief annealed (SRA) to eliminate residual stresses and load history. Long crack thresholds are determined using a similar step loading procedure for specimens which have been precracked using a range of values of K_{max}, including some that have been stress relief annealed prior to threshold testing. Results show that HCF threshold measurements, when naturally initiated small cracks are present, are dependent on the load histories that are used to initiate the cracks. Analysis shows that the measured small crack thresholds, which follow similar trends for load history effects which occur in the long crack threshold data, can be predicted from a simple model developed for long crack thresholds. Specimens precracked at R = -1.0 and SRA specimens precracked at R = 0.1 produce similar threshold values in this material, indicating that R = -1.0 under LCF has no effect on subsequent threshold under HCF.

---

[1] Air Force Research Laboratory, Materials & Manufacturing Directorate (AFRL/MLLMN), Wright-Patterson AFB, OH 45433-7817, currently at Anteon Corporation, 5100 Springfield Pike, Dayton, OH 45431.

[2] Air Force Research Laboratory, Materials & Manufacturing Directorate (AFRL/MLLMN), Wright-Patterson AFB, OH 45433-7817.

[3] Purdue University, School of Mechanical Engineering, West Lafayette, IN 47907.

Keywords: high cycle fatigue, overload, Ti-6Al-4V, load history, threshold, small cracks, fracture mechanics, load history

Introduction

High cycle fatigue (HCF) continues to be a major concern within the U.S. Air Force because of the unacceptable number of HCF-related failures of components, the excessive maintenance costs attributed to HCF, and the effect of HCF on the readiness level of U.S. Air Force assets. No formal definition exists, nor should it, for the condition which is widely referred to as high cycle fatigue, but it is normally associated with vibratory loading, rotating machinery, high frequencies, and large numbers of cycles to failure. While the existence of an endurance limit stress, below which failure will never occur under fatigue, has been questioned in many materials [*1*], an engineering definition of an endurance limit can be developed based on the maximum number of vibratory cycles that can be expected to occur during the lifetime of a component. Whereas the concept of "stable" crack growth is employed in low cycle fatigue, damage tolerant design, retirement for cause, on-condition lifing and other such life management procedures require slow crack growth to allow time for inspection to be performed before a crack has grown to a catastrophic size. Under HCF, on the other hand, once crack growth initiates, the growth rate is generally much too fast to allow an inspection to be performed before the crack becomes too large. For an uncracked body, the nucleation or initiation phase in HCF is usually a large fraction of total life. For these reasons, under HCF, it is critical that stresses be maintained below the engineering endurance limit for uncracked components or below a threshold stress intensity for cracked bodies, even when the cracks are small, or below the the size where LEFM is applicable. The dependence of ΔK_{th}, the threshold stress intensity range, on the load history leading to formation of a crack, and on the size of the crack formed, is a vitally needed piece of information to determine the tolerance of a material to HCF loading.

Many problems attributed to HCF are often the result of other types of damage, such as LCF, which lowers the HCF resistance of a material or component through development of fatigue cracks. Thus, cracks alter the HCF resistance of a material by changing the criterion for crack nucleation and subsequent propagation from one governed by stress (endurance limit) to one governed by fracture mechanics (crack growth threshold). Threshold, as a fracture mechanics concept, can be used to determine a stress level below which a crack of a given size will not propagate. It is valid only for cracks of a certain size and cannot be used indiscriminately for arbitrarily small cracks. Threshold stress intensity is a viable alternative design parameter to the allowable design stress, but it is crack size dependent as cracks get smaller and smaller. The experimental method by which a threshold is determined, and its applicability to real loading conditions, are issues that have not been completely resolved within the technical community. In particular, the influence of the history of loading which produces the crack for which a threshold must be determined, is not well established.

Lenets and Nicholas [*2*] used two different methods for determining the fatigue crack growth threshold in titanium alloy IMI 834 and found a consistent difference between the two thresholds for each test method. Increasing ΔK applied to the initially dormant crack produced the higher fatigue crack growth thresholds as compared to the situation when decreasing ΔK values were applied to a growing crack. They attributed this difference in measured thresholds to the difference in loading histories and raised the question of the validity of a single number for a material threshold.

Loading history effects associated with combined LCF/HCF loading is another crucial element in establishing allowable limits for HCF loading. Most of the work in this area has been associated with combined HCF, generally at high R, accompanied by periodic LCF underloads to zero or near-zero stress. Guedou and Rongvaux [*3*] examined the effect of superimposed HCF on LCF life and found that superimposing HCF cycles at high R on LCF cycles significantly reduced both the initiation and propagation life relative to those measured for LCF-only loading.

Hopkins et al. [*4*], used an increasing load step test to determine an overload modified long crack threshold, ΔK_{th}*, and found that for high values of prior overloads that ΔK_{th}* increased exponentially with the magnitude of the prior applied overload. It was also found that the ΔK_{th}*/overload data could be extrapolated to obtain the basic threshold at low stress ratios where valid precracking is impractical.

Powell, Duggan, and coworkers [*5-8*] examined the crack growth rate of titanium alloys and other materials under combined HCF and LCF loading. Experiments conducted on Ti-6Al-4V [*5, 6*] demonstrated the existence of an onset stress intensity, ΔK_{onset}, below which HCF had no effect on LCF growth rate and above which it dominated the growth rate under combined loading. Linear summation of growth rates obtained from LCF and HCF loadings alone was shown to predict the combined behavior for this material. Thus, ΔK_{onset} was essentially equivalent to ΔK_{th} for HCF alone, provided that the ratio of number of HCF to LCF cycles was large enough so that HCF growth rates per block exceeded those due to LCF alone. These results seemed to indicate that the HCF threshold was insensitive to the superimposed LCF loading. In most of the work, however, the peak stress in LCF was no different than the peak of the superimposed HCF. Recent work in Ti-6Al-4V [*8*] showed the effects of multiple LCF underloads and overloads combined with high stress ratio HCF loading on crack growth. A linear summation model showed that the introduction of overloads caused the fatigue crack growth curves to shift to lower values of ΔK_{HCF}, when compared with multiple underloads. This work was conducted on long cracks where LEFM is applicable.

The issues and background for determining the load history effects due to LCF are discussed more thoroughly in a recent paper [*9*]. It has been noted that little work dealing directly with the determination of load interaction effects on threshold is available and even less with small cracks. Thus, the question of the effect of LCF loading history on subsequent or superimposed HCF cycling and the resultant threshold still remains unanswered. Recent work by the authors studied load history effects on the crack growth threshold in notch specimens with LCF precracks [*9*]. This study dealt mainly with medium size cracks, whereas the current investigation extends this to very small cracks. Further, the authors developed a simple model to predict threshold from LCF load history for long crack data from CT specimens on 2 titanium alloys [*10*]. Stress relief annealing was used to determine an inherent closure free threshold. This paper attempts to extend those modeling and testing concepts to determination of crack growth thresholds for small surface cracks subjected to LCF. An attempt is made to bridge the gap between stress dominated endurance limits for specimens with no cracks to long crack thresholds governed by fracture mechanics.

Experiments

The Ti-6Al-4V alloy used in this study was received as plate in the solution-treated and overaged (STOA) condition. The forging stock material was a double VAR melted Ti-6Al-4V, 6.35 cm diameter bar stock from Teledyne Titanium, produced in accordance with AMS 4928. It was supplied in random lengths of 305 to 427 cm, in mill annealed condition: 704 °C/2 hr/AC. The billet was then sectioned into forging multiples, 40.7 cm in length which were preheated to 938 °C for up to one hour prior to being pressed into their final forging dimensions of 40.7 x 15.3 x 2.0 cm. Forging was done on a National 8000 ton mechanical press with dies initially heated to 149 °C. Glass-lubricant coated bars were preheated to 938 °C ± 11°C for 30 minutes in a continuous furnace and rapidly transferred to the press. After a one stroke forging, the pieces were simply air-cooled. Solution heat treatment was done in a Lindberg air furnace at 932 °C (±14°C) for one hour. The rack of forgings, heat treated on edge, was rolled out of the furnace after heating at temperature and fan air-cooled at a cooling rate from 927 to 538 °C of 200 °C/min. The solution treated forgings were cleaned of glass lubricant; oxide and alpha case using caustic and acid baths as well as grit blasting. The cleaned forgings were vacuum annealed at 704 °C for 2 hours at temperature and fan cooled in argon. This processing resulted in a microstructure consisting of 60 volume percent of equiaxed primary alpha with an average 20 μm grain-size with the remainder transformed beta (Fig. 1) and is identical to the alloy used in several earlier investigations [*9, 10*]. The room temperature mechanical properties of the Ti-6-4 plate as processed and heat treated are σ_y = 930 MPa and σ_{UTS} = 978 MPa.

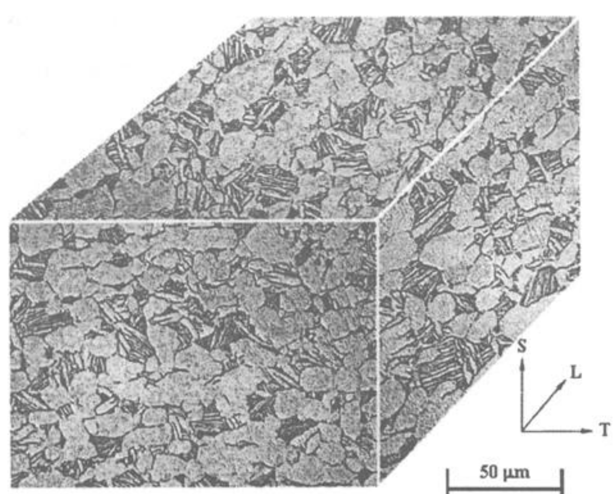

Figure 1 - *Mill-annealed microstructure of Ti-6Al-4V plate forging.*

Double notch tension test specimens were machined from the plate to the dimensions shown in Fig. 2. A low stress grind technique was used to minimize residual stresses due to machining. The specimens were oriented with the loading direction in the L direction and the thickness of the flat specimens in the S direction identified in the micrograph of Fig. 1. After machining, all specimens were subjected to a stress relief by heating them to 704 °C for one hour in vacuum, and then electropolishing the gage section in the vicinity of the notches. Stress concentration factors and notch depths of the two notches were chosen so that failure could be confined to the more severe notch having a elastic stress concentration factor, K_t, based on net section stress of 2.25 (see Fig. 2). Finite element analysis of the specimen geometry confirmed that the use of equal depth for the two notches produced essentially no bending in the specimen whether fixed or pinned grips were used. In the experiments, nominally fixed grips were used.

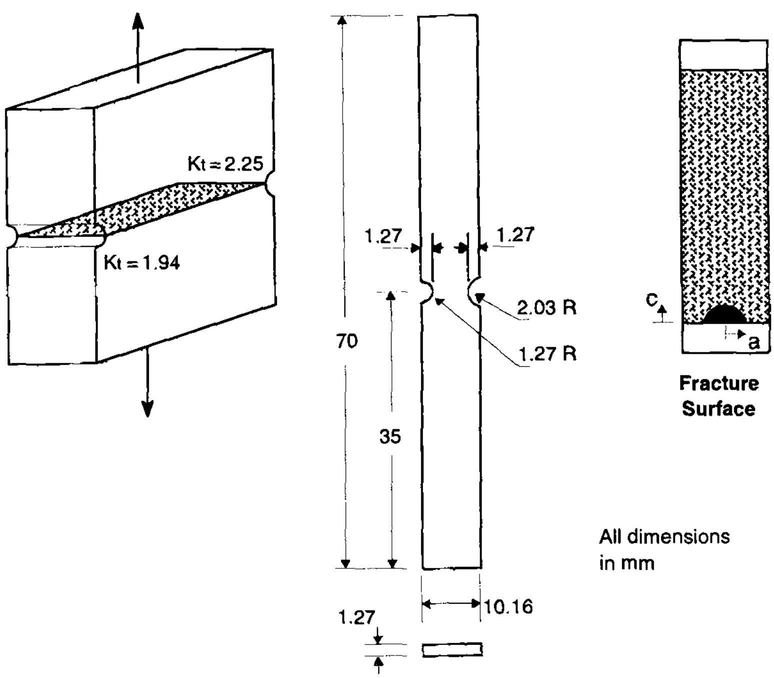

Figure 2 - *Double notch tension specimen geometry and crack shape nomenclature.*

LCF was conducted at stress ratios of −1.0 and 0.1 under load control to initiate a crack using a sinusoidal wave form at a frequency of 10 Hz with a superimposed hold time of 0.5 s on each cycle during which the DCPD measurements could be made. Maximum stress levels were chosen which corresponded to approximately 250 000 cycles to failure. For precracking at R = 0.1 the maximum value of stress was 430 MPa while for R = -1 the maximum stress was 265 MPa. Cracks were typically detected with

DCPD at cycle counts between 20 000 and 100 000 at which point the tests were stopped and the specimens inspected in the SEM to confirm the existence of a crack.

To fully characterize the geometry of these cracks in order to determine ΔK_{th}, the crack shape was determined by heat tinting the LCF cracked specimens at 420 °C for four hours prior to HCF threshold testing. Heat tinting marks the crack profile for post fracture measurement of the crack geometry without affecting any subsequent crack growth properties.

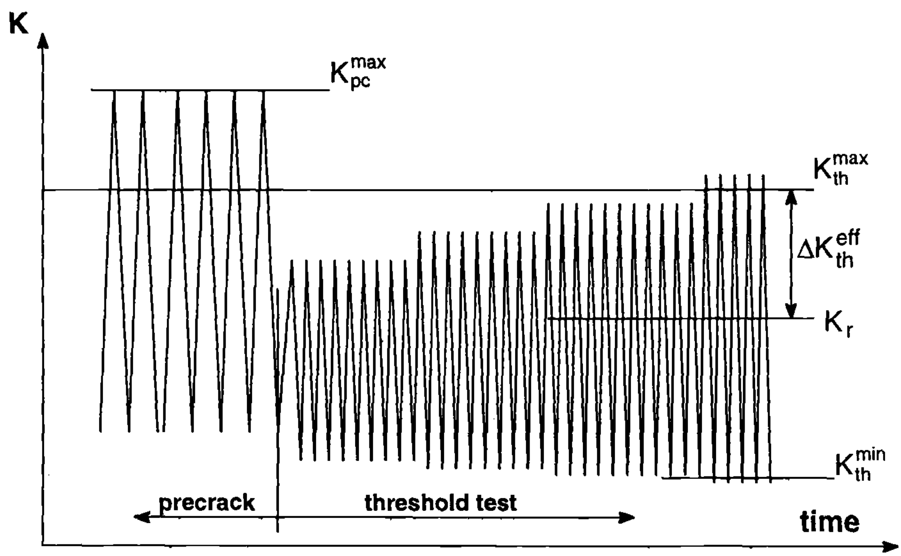

Figure 3 - *Schematic of LCF/HCF loading history and nomenclature.*

The LCF cracked specimens were then tested in HCF to determine the threshold for crack extension using the step-loading procedures described by Maxwell and Nicholas [*11*]. The procedure used is shown schematically in Fig. 3. Each specimen was fatigued to a limit of 10^7 cycles at a stress level lower than the expected threshold stress. After each block of 10^7 cycles, the stress was increased by approximately 5% or less until crack propagation occurred at less than 10^7 cycles. The stress corresponding to the threshold for crack propagation was then determined using the linear interpolation scheme as described in the following equation:

$$\sigma_e = \sigma_o + \Delta\sigma\ (N_{fail}/N_{life}) \tag{1}$$

where σ_e is the maximum fatigue strength corresponding to N_{life} cycles, σ_o is the previous maximum fatigue stress that did not result in failure, $\Delta\sigma$ is the step increase in maximum fatigue stress, N_{fail} are the cycles to failure at the fatigue stress ($\sigma_o + \Delta\sigma$), and N_{life} the defined cyclic fatigue life. Steps of 10^7 cycles were used in this investigation, while $\Delta\sigma$ was taken typically at 5 percent of the initial load block. For the crack sizes encountered here, the increments in stress used in Eq 1 corresponded typically to increments of ΔK ranging from 0.1 to 0.4 MPa$\sqrt{m}$, depending on the particular crack size. While the use of many load steps raises the question of the validity of the step loading techniques, particularly with respect to the history effect referred to as "coaxing," it has been shown that there appears to be no influence of coaxing in this material [*12*]. Further, the step loading technique has been shown to produce data consistent with those obtained from conventional S-N plots for both smooth [*13*] and notched [*14*] configurations.

The tests were conducted in a custom built HCF apparatus at a frequency of 600 Hz. The thresholds in the form of values of ΔK were determined from the interpolated load for crack extension to occur (Eq 1), using the finite element method to modify existing solutions developed for a semi-elliptical surface crack in a single edged notch tension specimen. In this work, ΔK_{th} is defined as the value of ΔK where propagation begins from a no-growth state. ΔK_{th} is then calculated using the crack measurements made from the fracture surfaces, the interpolated threshold stress and the modified stress intensity factor solution. The ΔK_{th} determined here represents the onset of crack propagation and is identical to the terminology ΔK_{onset} used by Powell and coworkers [*5-8*], or ΔK_{th}* used by Hopkins et al. [*4*] as an "overload modified threshold" determined from increasing load step testing on precracked test specimens.

Cracks initiated under LCF were measured under load in a SEM before HCF testing to determine the surface crack length, 2a. The cracks were treated as planar and normal to the loading direction so that all crack lengths refer to the projected length. No attempt was made to account for mixed mode behavior because of the mathematical and physical (measurements into the depth) difficulties that would be encountered. The nomenclature for crack length and depth as shown in Fig. 2 is that used by Newman and Edwards [*15*] whose analysis was applied in this investigation. The depth of the crack, c, was determined from the fracture surface that showed the heat tinted pattern of the crack after LCF but before HCF. Figure 4 shows the experimentally determined "a" and "c" crack data. The values of "a" from the heat tinted surface, covering a range from 15 to 400 µm, were in general agreement with the surface crack measurements in the SEM.

The crack shapes developed under LCF loading were taken into consideration when calculating the values of ΔK for each crack geometry. To represent the trends for all crack sizes, the data shown in Fig. 4 were fit to an equation which best represents the experimental data in the form

$$c = C_1\,[1 - \exp(C_2 a)] + C_3 a \tag{2}$$

where a and c are given in microns and the constants are determined from a least squares fit to be: $C_1 = 5.5054$, $C_2 = 0.06133$ and $C_3 = 0.9155$. Both the actual aspect ratios, as well as the equation, were used in subsequent calculations of threshold values of ΔK for K and modeling analyses as described in the next section.

Because of a desire to study the effects of load history on cracks smaller than those that can normally be detected with DCPD techniques, two additional methods were employed on other specimens. One batch of specimens was precracked under LCF and monitored for crack development using an infrared damage detection system (IDDS) which is based on the concept that heat is released during crack initiation and propagation. Using digital image processing and manipulation allows for the capture of thermal imaging maps of the specimen during testing. These image maps are used to determine the time and location of crack initiation. The system is capable of detecting cracks ranging from depths of 15 μm and above. Illustration of the type of cracks found with IDDS is provided in Fig. 5 which shows cracks with surface lengths 2c = 35 and 80 μm in (a) and (b), respectively. While the IDDS provides the exact location of the crack, placing the specimen in a fixture to apply a bending load to open the crack aids immensely in locating the cracks in the SEM as illustrated in Fig. 5.

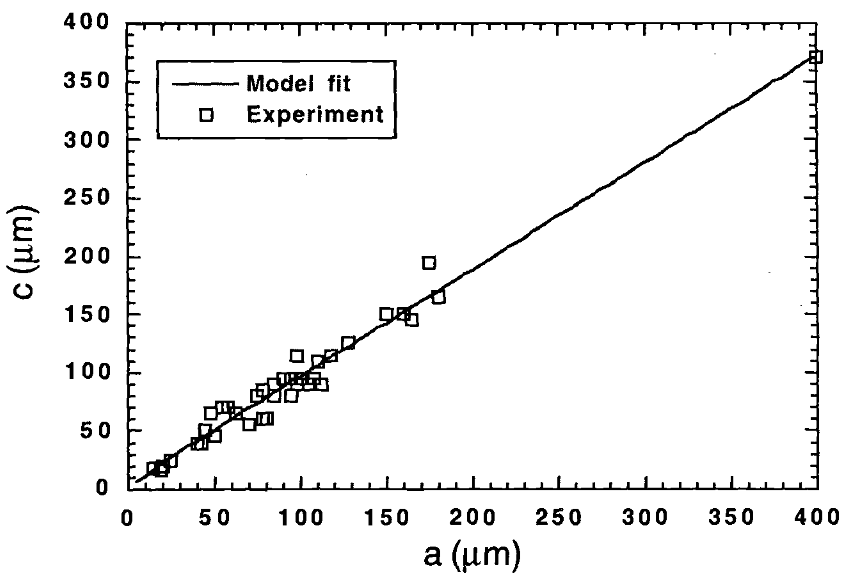

Figure 4 - *Experimental results and model fit for measured crack geometries.*

A second batch of LCF precracked specimens was monitored for crack formation using a newly developed electrochemical fatigue sensor (EFS) [*16*] that can detect cracks in the size range from 40 μm and above in crack depth with reasonable reliability. Changes in the output current were monitored on specimens subjected to a constant voltage potential across the notch section in order to detect crack formation.

In addition to testing the LCF precracked specimens, a number of HCF tests were conducted on uncracked specimens to determine the endurance limit stress for the notched geometry. As in the case of determination of ΔK_{th}, the endurance limit stress is defined as the fatigue strength corresponding to 10^7 cycles and was obtained using the step loading procedure. Nine tests were conducted, producing an average value of the endurance limit maximum stress, σ_e, of 327 MPa at R = 0.1, with test values ranging from a low of 306 MPa to a high of 362 MPa.

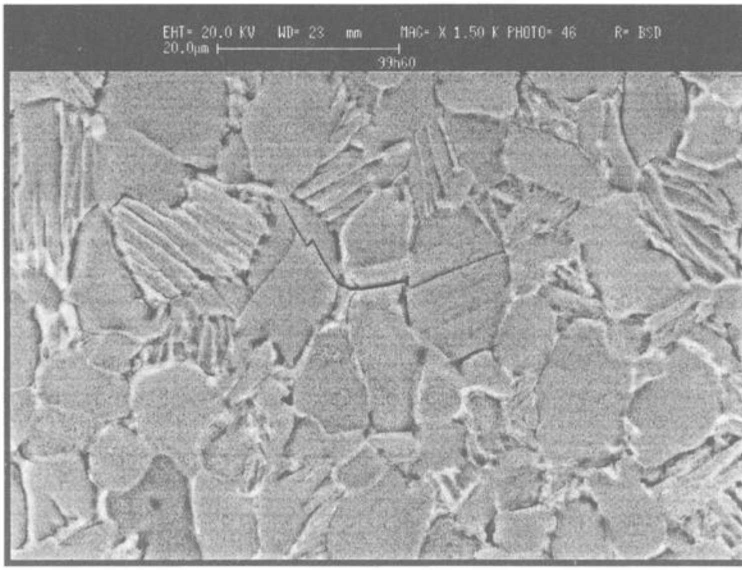

(a) 35 μm crack

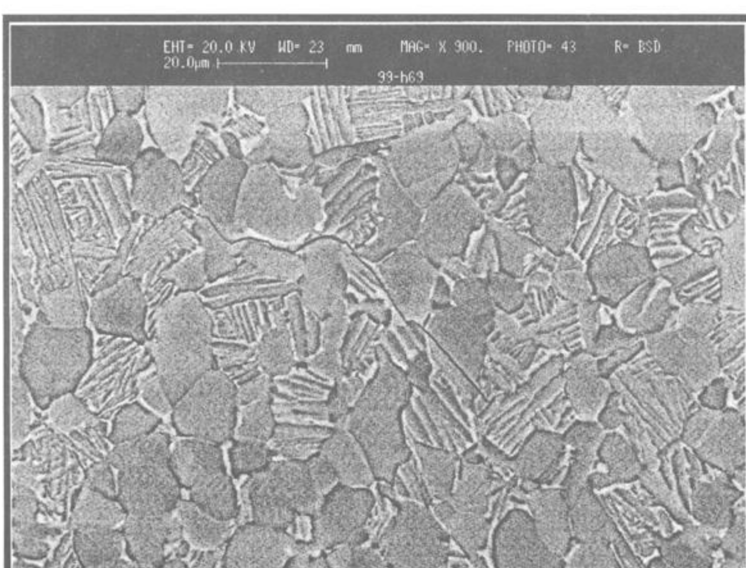

(b) 80 μm crack

Figure 5 - *SEM micrographs showing cracks detected using 1DDS.*

Analysis

The model developed in a prior investigation [*10*] established a linear relation between the HCF threshold and the K_{max} and R values of the LCF precrack for long cracks in C(T) specimens. Figure 6 shows the relationship between ΔK of the precrack and ΔK threshold for precracking and threshold testing at R = 0.1. It should be noted that for stress relief annealing (SRA), the threshold obtained is independent of precrack history. The data agree well with the long crack threshold obtained under conventional load shed techniques, although the data from SRA lie slightly below the long crack threshold. It is speculated that the reason for this is that SRA completely eliminates load history effects and residual stresses whereas the long crack threshold retains whatever residual stresses or closure is present at the end of the conventional load shed procedure. The data for small cracks for which the model is applied are also shown in the figure.

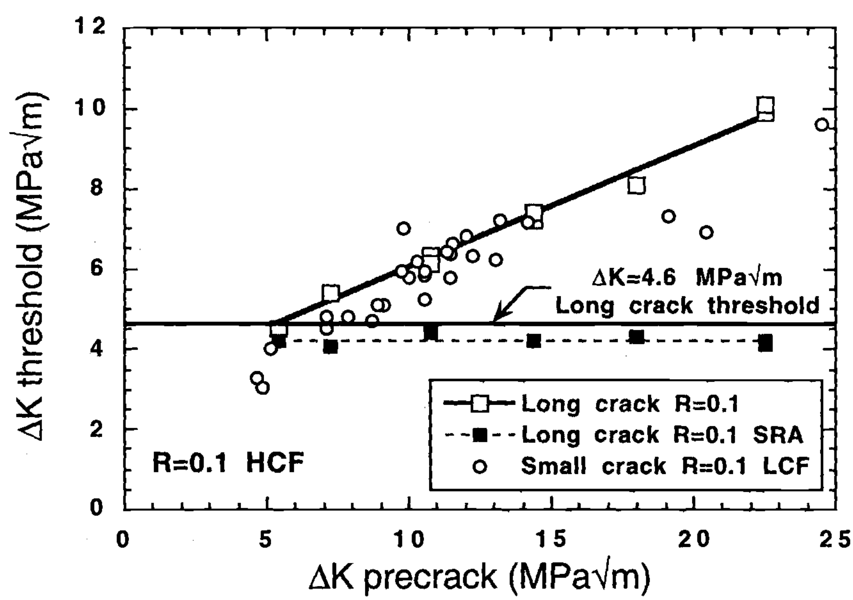

Figure 6 - *Experimental relationship between precrack and threshold stress intensity for R=0.1 threshold tests in long crack C(T) specimens and small surface flaws.*

There is considerably more scatter in the small crack data, partially attributable to the variability in crack shapes. From data of the type shown in Fig. 6 for long cracks in C(T) specimens in both Ti-6-4 and Ti-17, the effective threshold is found to be a material constant given as

$$\Delta K_{th}^{eff} = K_{th}^{max} - K_r \tag{3}$$

$$K_r = \beta\left(K_{pc}^{max} + K_{th}^{min}\right) \tag{4}$$

where the various terms are defined in the loading schematic, Fig. 3, and subscripts "pc" and "th" refer to the LCF precrack and HCF threshold, respectively. K_r serves as a value above which K is effective, and below which it is not, which is analogous to an opening load if discussing closure. The linear relation between ΔK_{th} and ΔK_{pc} is given as

$$\Delta K_{th} = \frac{\left(1 - R_{th}\right)\Delta K_{th}^{eff}}{\left(1 - \beta R_{th}\right)} + \frac{\beta\left(1 - R_{th}\right)}{\left(1 - \beta R_{th}\right)\left(1 - R_{pc}\right)}\Delta K_{pc} \tag{5}$$

where β is a fitting parameter related to the slope of the straight line relation. The ability of this equation to represent threshold data obtained at several values of R after precracking at R = 0.1 is illustrated in Fig. 7 for long cracks in C(T) specimens [*10*]. The empirical fit to the data is made only for the data obtained at R = 0.1. The fit at R = 0.1 provides the constants which, in turn, produce the model predictions shown for other values of R in Fig. 7. It can be seen that the model provides an excellent representation of the entire data set.

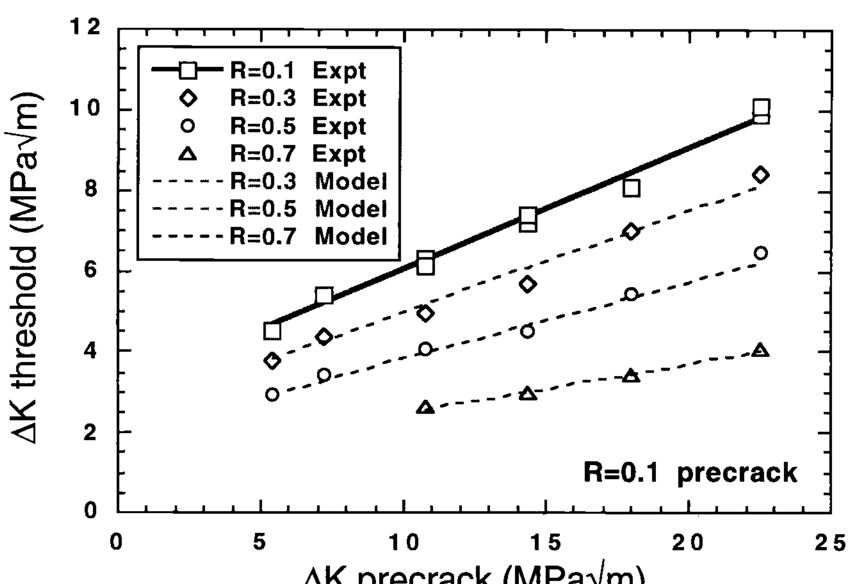

Figure 7 - *Experimental data and model predictions for long crack data.*

The model is extended to the surface flaws in the notched specimens used in this investigation in the following manner, illustrated for the simple case where R is the same for the precrack as for the threshold test. Because the precrack is carried out at a (LCF) stress higher than the (HCF) threshold or endurance limit, the precrack is referred to as an overload. The terminology "overload" is used in a non-conventional sense since it refers to multiple overloads during constant amplitude cycling as opposed to a single peak overload in the conventional usage.

The K solution for the surface flaw in the notch in either the "a" or the "c" direction is written in the form

$$K = \sigma\sqrt{\pi a}\, f(a) \tag{6}$$

where we choose to write the equation for the "a" direction. The K solution [15] along with Eq 2 can be used to determine the appropriate quantities in the "c" direction. The K used to produce an overload condition during precracking, becomes

$$K_{pc} = \sigma_{pc}\sqrt{\pi a}\, f(a) \tag{7}$$

The linear relation between K_{th} and K_{pc}, Eq 5, requires $K_{th} = K_{pc}$ when there is no overload as in the limiting case of steady state crack growth near threshold. In this case, K is the long crack threshold, K_{th}^{lc}, a material constant, and Eq 5 can be rewritten as

$$K_{th} = \alpha\, K_{pc} + K_{th}^{lc}\,(1 - \alpha) \tag{8}$$

where α is an empirical constant. In these equations, K represents the maximum value of K at a given value of R, but could also represent ΔK throughout.

To extend the modeling to small cracks, the concept of ElHaddad et al. [17] is employed to produce the endurance limit stress for arbitrarily small cracks, and the K solution, Eq 6 for long cracks. Following the procedure of modifying the material capability (threshold stress intensity) instead of the crack length [18], the threshold value of K is reduced for small cracks in the following manner:

$$\overline{K}_{th} = K_{th}\left[\frac{a}{a + a_0}\right]^{1/2} \frac{f(a)}{f(a + a_0)} \tag{9}$$

where a_0, as defined by ElHaddad, and modified for the more general K solution of Eq 6, is given by

$$a_0 = \frac{1}{\pi}\left(\frac{K_{th}}{\sigma_e\, f(a_0)}\right)^2 \tag{10}$$

which can be solved for a_0 either graphically or iteratively. The crack length a_0 is not considered in the f(a) term of Eq 6 in [18] when deriving the effective K in Eq 9. For each crack length, the threshold stress is obtained from a combination of Eq 9 and the K solution, Eq 6, in the following equation:

$$\sigma = \frac{\overline{K}_{th}}{\sqrt{\pi a}\, f(a)} \tag{11}$$

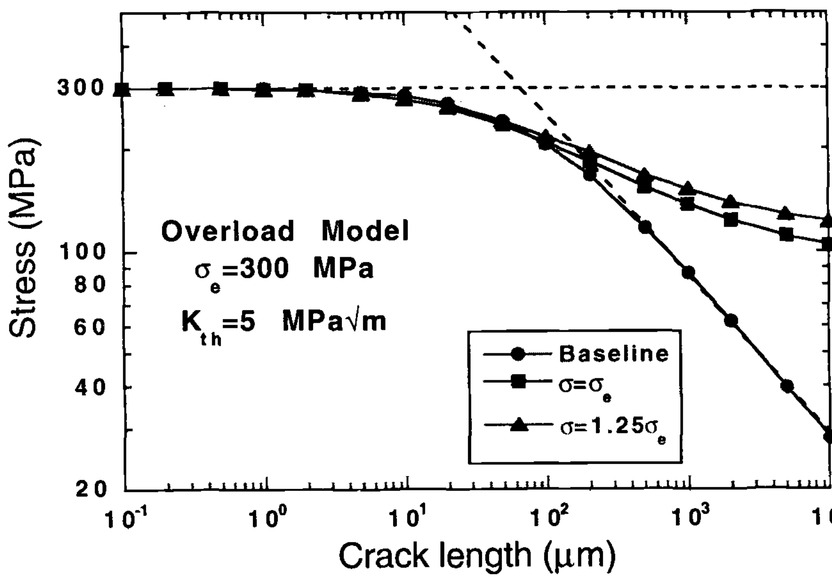

Figure 8 - *Kitagawa diagram for theoretical SEN specimen behavior.*

As an illustrative example, a SEN specimen is cracked at a stress corresponding to the endurance limit, and another one at a stress above the endurance limit, $\sigma = 1.25\sigma_e$ in this case. The K solution is approximated in Eq 6 by setting f(a) = 1. From the K solution, and the small crack correction, Eq 9, the threshold condition for a baseline chosen arbitrarily as K_{th} = 5 MPa√m and σ_e = 300 MPa is represented in the form of a Kitagawa type diagram [*19*] in Fig. 8. The diagram shows the smooth transition from a fracture mechanics dominated long crack threshold, where the slope on a log-log plot is -0.5, Eq 6, to a crack-length independent endurance limit, σ_e = 300 MPa, for arbitrarily short cracks. If, however, the crack is initiated at a stress equal to or above the endurance limit, $\sigma = \sigma_e$ and $\sigma = 1.25\sigma_e$ for the two cases here, then the longer the crack developed under this "LCF" condition, the higher will be the value of K_{OL} as determined from Eq 7. For each case modeled, pairs of values of a and K_{pc} are obtained. Then K_{th} can be calculated from Eq 8 and modified for short cracks using Eq 9 to get an effective value of K_{th}. The relation between σ and a is obtained from Eq 11 to determine points on the Kitagawa diagram as illustrated in Fig. 8. The divergence of the curves for $\sigma = \sigma_e$ and σ

= $1.25\sigma_e$ is due to the increase in K_{pc} due to increase in LCF crack length as well as the model, Eq 8, which shows that the threshold increases with increase in K_{pc}. The one assumption in this analysis, which is applied to the actual geometry used in these experiments, is that the endurance limit is a material constant at a given R and does not depend on any prior load history which does not produce cracks. This assumption has been validated through experiments conducted within our laboratory on both smooth an notched specimens [*9, 20, 21, 22*]. The net result, as shown in Fig. 8, is that the stress required to initiate growth of a crack under HCF which developed under constant load a or above the endurance limit is below the endurance limit stress but above the baseline stress calculated from fracture mechanics with a small crack correction. The difference attributed to the load-history effect.

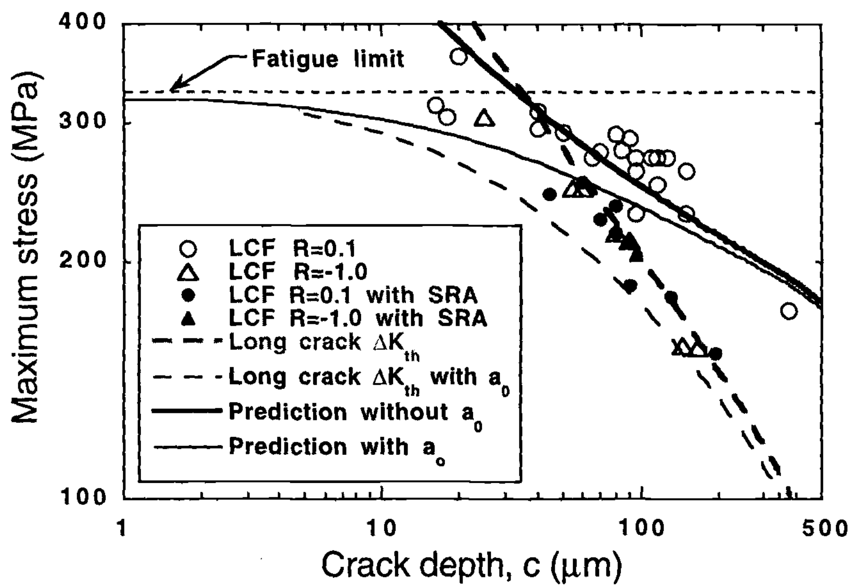

Figure 9 - *Experimental data and model predictions on a Kitagawa diagram.*

The same concept was applied to the actual data. The general K solution, Eq 6 was used to calculate K in both the a and c directions, and the average of the two was used a the actual K at threshold. In all cases, K in the "a" direction (surface) exceeded K in th "c" direction (depth) because of the stress gradient from the notch in the "c" direction. The overload effect on the threshold for K was obtained from the model, Eq 5. To account for a small crack effect, K was then modified in accordance with Eq 9 using th specific value of the a/c ratio in the K solution for each data point in the calculation of a which is where the endurance limit stress and K_{th} equation cross on a Kitagawa diagran [*19*]. The data and the model fit are shown in a Kitagawa diagram in Fig. 9 where the model prediction is based on the long crack model relating HCF threshold as a function of LCF precrack loading parameters, Eq 5. In this investigation, the parameters for the long crack model were $\beta = 0.294$ and $\Delta K_{th}^{eff} = 3.23$ MPa $\sqrt{m}$ [*10*].

Discussion

The data obtained in this investigation are summarized in Fig. 9. They include tests where both R = -1 and R = 0.1 were used for the LCF precracking and both SRA and no stress relief applied prior to HCF testing for both cases. LCF precracking produced cracks with surface half crack lengths ranging from a = 15 μm to 400 μm and depths covering a range from c = 16 μm to 370 μm. For modeling predictions, three curves are shown. In one case, the threshold from long cracks (K_{max} = 5.1 MPa$\sqrt{m}$) is used without any overload or small crack correction. This corresponds to Eq 6 with K being a constant using the aspect ratio in the K solution given by Eq 2. The second analytical curve corresponds to a prediction without any small crack correction. This simply incorporates the overload effect, Eq 5, in the calculation of K_{th}. The third prediction is identical, but the small crack effect is taken into account through the use of Eq 9. Several features of the analytical predictions should be noted. First, the curve for constant K is not a straight line of slope -0.5 as is often noted in a Kitagawa diagram. The reason for this is that the K solution is of a more complex form, Eq 6, than for the simple case where f(a) = 1 corresponding to the simple $\sqrt{a}$ dependence of K on crack length. The second feature for the cases of a constant load to produce an overload effect is that the model predicts behavior quite different than the constant K solution as illustrated for the simple case illustrated in Fig. 8.

The correlation of the data with the analytical models, as shown in Fig. 9, validates the extension of the long crack overload model to small surface flaws in the notch geometry used here. The cracks developed under R = 0.1 loading have thresholds at R = 0.1 which are predicted, somewhat conservatively, by the linear overload model of Eq 5 with the small crack (a_0) correction of El Haddad. It is clear from the data that the threshold is increased when there is an overload history applied during the LCF stage, similar in concept to the retardation effect observed in growing cracks. LCF cracks formed under R = -1 loading, on the other hand, produce thresholds which are predicted by the (constant) long crack threshold value of K_{max} = 5.1 MPa$\sqrt{m}$. The maximum stress or K level in the threshold testing exceeded that of the LCF precracking only for the smallest crack formed in tests at R = -1 where precracking was at a maximum stress of 265 MPa. The remainder at R = -1 and all at R = 0.1 had lower values of K_{max} in threshold tests at R = 0.1 than those in precracking. Thus all tests with the exception of one data point could be expected to demonstrate some type of overload effect. However, unlike precracking at R = 0.1, precracking at R = -1 seems to have no overload effect on the subsequent threshold. The compression portion of the fully reversed loading appears to negate any beneficial effect of the tension portion of the cycle upon the subsequent threshold. For both prior loading at R = 0.1 and R = -1, stress relief annealing produces a condition where the subsequent threshold corresponds to the long crack threshold as shown by the solid symbols in Fig. 9. These data, as well as the data from precracking at R = -1 without SRA, show no history of loading effect on the subsequent threshold determined at R = 0.1. The best representation of these threshold values would be the long crack threshold with a small crack correction for the smallest of cracks in these tests. The small crack correction can be seen in Fig. 9.

Another observation from the experimental data plotted in the Kitagawa diagram of Fig. 9 is that for cracks having depths, c, less than 30-40 μm (the approximate value of a_0 as determined by the intersection of the long crack threshold curve with the constant endurance limit stress) is the value of the stress to produce crack extension. For these small cracks, while calculated values of K might be considerably below the long crack threshold, the values of *stress* at threshold are only slightly below or at the endurance limit stress within a reasonable scatter band. This indicates that very small cracks are not very detrimental in reducing the fatigue threshold stress, even though the location of the failure corresponds to the location of the initial cracks.

Summary

Surface flaws developed under LCF loading at constant values of maximum load at R = 0.1 produce thresholds which depend on the loading history during the crack formation. An overload effect, where the precracking is at higher values of K than the subsequent threshold, is well predicted by a simple overload model which relates maximum K of the threshold to maximum K of the precracking in a linear fashion. This threshold model, developed from long crack data in C(T) specimens in a prior investigation, is applicable to small cracks at a notch. The model predicts a higher value of threshold stress or K than that for a crack without any overload history. Precracking at R = -1, and stress relief annealing to remove residual stresses, both have the effect of eliminating any load history effects on the subsequent threshold. For small cracks, the introduction of a small crack correction as proposed by ElHaddad produces a reasonable, if not somewhat conservative, estimate of the crack growth threshold of surface flaws growing out of a notch. For cracks having a dimension "a" less than a transition length "a_0," the threshold stress corresponding to the onset of crack propagation is not much less, if at all, than the endurance limit stress, even though the calculated stress intensity is below the long crack threshold. This indicates that thresholds for small cracks should be characterized in terms of stress rather than stress intensity in order to show the lack of a detrimental effect of a small crack on the fatigue crack growth threshold.

Acknowledgments

This work was supported by the U.S. Air Force as part of the National Turbine Engine High Cycle Fatigue Program. The authors would like to thank Dr. Joe Gallagher of the University of Dayton Research Institute (UDRI) for presenting this paper at the ASTM 33rd National Symposium on Fatigue and Fracture Mechanics. The assistance of Mr. Rolf Berger, a student at Technical University of Munich, and Mr. Andy Lackey and Mr. Mark Ruddell of UDRI is gratefully acknowledged.

References

[1] Bathias, C., "There is No Infinite Fatigue Life in Metallic Materials," *Fatigue & Fracture of Engineering Materials & Structures*, Vol. 22, 1999, pp. 559-565.

[2] Lenets, Y. N. and Nicholas, T., "Load History Dependence of Fatigue Crack Thresholds for Ti-Alloy," *Engineering Fracture Mechanics*, Vol. 60, 1998, pp. 187-203.

[3] Guedou, J. Y. and Rongvaux, J. M., "Effect of Superimposed Stresses at High Frequency on Low Cycle Fatigue," *Low Cycle Fatigue, ASTM STP 942*, American Society for Testing and Materials, Philadelphia, PA., 1988, pp. 938-960.

[4] Hopkins, S. W., Rau, C. A., Leverant, G. R. and Yuen, A., "Effect of Various Programmed Overloads on the Threshold for High-Frequency Fatigue Crack Growth," *Fatigue Crack Growth Under Spectrum Loads, ASTM STP 595*, American Society for Testing and Materials, Philadelphia, 1976, pp. 125-141.

[5] Powell, B. E., Duggan, T. V. and Jeal, R., "The Influence of Minor Cycles on Low Cycle Fatigue Crack Propagation," *International Journal of Fatigue*, Vol. 4, 1982, pp. 4-14.

[6] Powell, B. E., Henderson, I. and Duggan, T. V., "The Effect of Combined Major and Minor Stress Cycles on Fatigue Crack Growth,". *Second International Congress on Fatigue (Fatigue '84)*, 1984, pp. 893-902.

[7] Hawkyard, M., Powell, B. E., Hussey, I. and Grabowski, L., "Fatigue Crack Growth under Conjoint Action of Major and Minor Stress," *Fatigue & Fracture of Engineering Materials & Structures*, Vol. 19, 1996, pp. 217-227.

[8] Hall, R. F. and Powell, B. E., "The Effects of LCF Loadings on HCF Crack Growth," US AFOSR Annual Report for Phase II, Report Number F567, University of Portsmouth, England, May 1999.

[9] Moshier, M. A., Hillberry, B. M., and Nicholas, T., "The Effect of Low-Cycle Fatigue Cracks and Loading History on the High Cycle Fatigue Threshold," *Fatigue and Fracture Mechanics: 31st Volume, ASTM STP 1389*, G. R. Halford and J. P. Gallagher, Eds., American Society for Testing and Materials, West Conshohocken, PA, 2000, pp. 427-444.

[10] Moshier, M. A., Nicholas, T. and Hillberry, B. M., "Load History Effects on Fatigue Crack Growth Threshold for Ti-6Al-4V and Ti-17 Titanium Alloys," *International Journal of Fatigue*, 2001 (in press)

[11] Maxwell, D. C. and Nicholas, T., "A Rapid Method for Generation of a Haigh Diagram for High Cycle Fatigue," *Fatigue and Fracture Mechanics: 29th Volume, ASTM STP 1321*, T. L. Panontin and S. D. Sheppard, Eds., American Society for Testing and Materials, West Conshohocken, PA, 1999, pp. 626-641.

[12] Nicholas, T. and Maxwell, D. C., "Evolution and Effects of Damage in Ti-6Al-4V under High Cycle Fatigue," *Progress in Mechanical Behaviour of Materials*, Proceedings of the Eighth International Conference on the Mechanical Behaviour

of Materials, ICM-8, F. Ellyin and J. W. Provan, Eds. Vol. III, 1999, pp. 1161-1166.

[13] Bellows, R. S., Muju, S. and Nicholas, T., "Validation of the Step Test Method for Generating Haigh Diagrams for Ti-6Al-4V," *International Journal of Fatigue*, Vol. 21, 1999, pp. 687-697.

[14] Bellows, R. S., Bain, K. R. and Sheldon, J. W., "Effect of Step Testing and Notches on the Endurance Limit of Ti-6Al-4V," *Mechanical Behavior of Advanced Materials*, MD-Vol. 84, D. C. Davis, Ed. ASME, New York, 1998, pp. 27-32.

[15] Newman, J. C., Jr. and Edwards, P. R., "Short Crack Growth Behaviour in an Aluminum Alloy - An AGARD Cooperative Test Programme," Conference Proceedings AGARD R-732, North Atlantic Treaty Organization, 1988.

[16] Li, Y. F., Wang, J., Wang, M. Z., DeLuccia, J. and Laird, C., "Development of the Electrochemical Fatigue Sensor for Evaluating Fatigue Damage," *Proc., Julia Weertman Symposium, TMS Fall Meeting, Cincinnati*, Y.-W. Chung, D. C. Dunand, P. K. Liaw and G. B. Olson, Eds., TMD, Warrendale, PA, 1999, pp. 333-340.

[17] El Haddad, M. H., Smith, K. N. and Topper, T. H., "Fatigue Crack Propagation of Short Cracks," *Journal of Engineering Materials and Technology*, Vol. 101, 1979, pp. 42-46.

[18] Chan, K. S., Davidson, D. L., Lee, Y-D. and Hudak, S. J., Jr., "A Fracture Mechanics Approach to High Cycle Fretting Fatigue Based on The Worst Case Fret Concept: Part I - Model Development," *International Journal of Fracture*, 2001 (in press).

[19] Kitagawa, H. and Takahashi, S., "Applicability of Fracture Mechanics to Very Small Cracks or the Cracks in the Early Stage," *Proc. of Second International Conference on Mechanical Behaviour of Materials*, Boston, MA, 1976, pp. 627-631.

[20] Dr. Tae-Won Park, Air Force Research Laboratory, Visiting Scientist from Republic of Korea, unpublished data.

[21] Lanning, D., Haritos, G. K., Nicholas, T. and Maxwell, D.C., "Low-Cycle Fatigue/High-Cycle Fatigue Interactions in Notched Ti-6Al-4V," *Fatigue & Fracture of Engineering Materials & Structures*, Vol. 24, 2001(in press).

[22] Moshier, M. A., "The Effect of Low Cycle Fatigue Cracks and Loading History on High Cycle Fatigue Threshold," Ph.D. Dissertation, Purdue University, 2000.

Marion Bartsch,[1] Klaus Mull,[2] and Christian Sick[2]

Effects of Thermomechanical Fatigue Loading on Damage Evolution and Lifetime of a Coated Super Alloy

---

Reference: Bartsch, M., Mull, K., and Sick, C., **"Effects of Thermomechanical Fatigue Loading on Damage Evolution and Lifetime of a Coated Super Alloy,"** *Fatigue and Fracture Mechanics: 33rd Volume, ASTM STP 1417*, W. G. Reuter and R. S. Piascik, Eds., ASTM International, West Conshohocken, PA, 2002.

Abstract: Ceramic thermal barrier coatings (TBC) on internally cooled metallic turbine blades give a potential for increasing the turbine gas inlet temperatures in a range of 50-150°C. Since, at higher gas inlet temperatures the remaining lifetime of the blade after failure of the TBC is extremely short, reliable lifetime prognosis for TBCs in service is required. A lifetime assessment concept is presented which is based on realistic thermal and mechanical fatigue (TMF) testing. To achieve short testing times with the TMF test rig kinetic damages, depending on the time at high temperature, are imposed separately so that a TMF cycle lasts about 1% of real service cycles. Substrate materials failed in TMF tests due to fatigue cracks. The fatigue load entailing failure of the substrate at the proposed design life determines the maximal cyclic strain of the ceramic TBC and was therefore chosen for TMF tests on TBC-coated specimens. TBCs in 'as coated' condition survived the required load alternations without any cracks, which implies that the premature failure of TBCs in service is due to interacting kinetic damage mechanisms.

Keywords: thermal barrier coating, gas turbine blade, thermal-mechanical loading, lifetime assessment, fatigue

Introduction

Ceramic thermal barrier coatings (TBC) are used on internally cooled components of hot engines, like gas turbines, to achieve a higher temperature difference between the hot gas and the substrate of the component. Actually, the effect of TBCs is mainly used in aircraft engines and stationary gas turbines to decrease the temperature of metallic parts, for example the airfoils of the first stages of the turbine, resulting in extended life time of the component. Higher benefit towards more economical and ecological gas

[1]Research Scientist, [2]Technical Specialist, Institute for Materials Research, German Aerospace Center (DLR), Linder Hoehe, D-51147 Cologne, Germany

turbines is expected if the thermal gradient provided by a TBC is used for higher gas inlet temperatures. Increasing the turbine inlet temperature implies that the TBC is reliable because otherwise, after failure of the TBC, the remaining lifetime of the component is extremely short. As illustrated in Fig. 1, the lifetime of the component is, for the case of increased turbine inlet temperatures, determined by the lifetime of the TBC. Since, TBCs are known to fail in service, even in conventional engines, reliable and practical methods for TBC lifetime prognosis are essential if more sophisticated service conditions are to be attained.

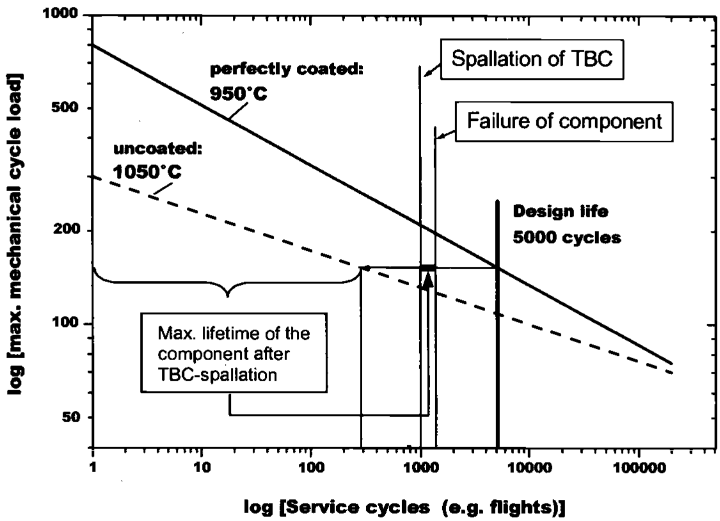

Fig. 1 - *Remaining lifetime of a coated component after failure of the TBC (schematically)*

The TBC coated component under service load

Materials

Aim of this study is to develop a lifetime assessment method for TBCs on rotating blades of an aircraft engine. The commonly used material for the ceramic coating on airfoils in aircraft engines is yttria stabilized zirconia, applied by electron beam physical vapor deposition (EB-PVD). The TBCs are applied on substrates, coated with a metallic, corrosion resistant layer which imparts good adhesion for the TBC on the substrate. This so called bond coat (BC) consists frequently of MCrAlY- or PtAl-alloys. Substrate materials are nickel based super alloys, frequently single crystals or directionally solidified (DS) materials. For our study we used IN 100 DS substrates, coated with a conventional NiCoCrAlY – bond coat (standard-composition wt-%: 20Co, 21Cr, 12Al, 0.15Y, and Ni) and a zirconia TBC, stabilized with 7-8 wt% yttria. Both coatings are processed by EB-PVD. The substrates and the coatings were processed in our institute.

The thermal conductivity of zirconia TBCs is relatively low, about 1.5-1.8$Wm^{-1}K^{-1}$. Due to the low thermal conductivity, zirconia coatings of about 150-300μm thickness maintain a temperature drop of 50° to 150°C from the hot gas to the metallic substrate under stationary conditions, depending on the heat flux in the turbine engine [*1*, *2*]. Since, the thermal diffusivity of the TBC is lower than that of the substrate, the TBC decreases the temperature transients, that means the thermal shock load, in the metallic substrate during start and shut down of the engine.

The thermal mismatch between TBC and nickel-based super-alloy substrates is relatively low due to the similar thermal expansion coefficient which is at maximum service temperature about $9 - 11 \cdot 10^{-6}\ K^{-1}$ for the TBC and $14 - 16 \cdot 10^{-6} K^{-1}$ for the substrate. The elastic properties of the TBC show non-linear behavior with higher stiffness under compression than in tension. However, the values of the load dependent "elastic modulus" are relatively low with about 20 - 60 GPa so that the TBCs show high tolerance against straining and thermal shock. Reason for the low "elastic modulus" is the specific microstructure of the TBC which grows from the vapor phase in a columnar form with single zirconia columns, weakly bonded to their neighbor columns. The TBC system investigated in this study is shown in Fig. 2.

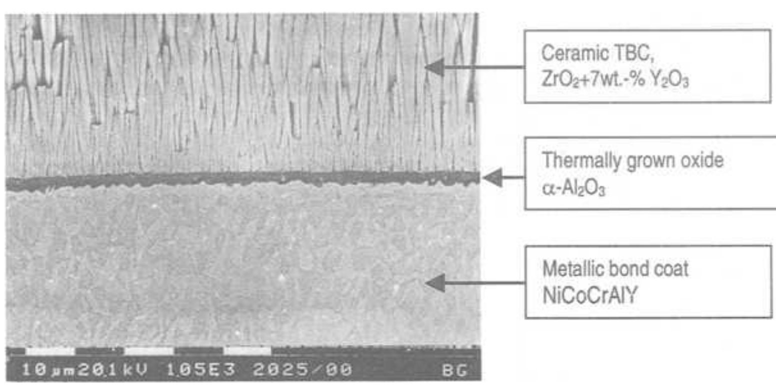

Fig.2 - *Structure of the TBC-system after 150 hours at 920°C in air. Between ceramic topcoat and NiCoCrAlY-bond coat a thermally grown alumina layer of 3μm thickness has formed. The TGO appears in the SEM micrograph dark due to the high aluminum content.*

Damage mechanisms and failure

The failure criterion of the TBC is defined as spallation of the TBC from the substrate because the function of the thermal barrier is impaired most seriously by local loss of the TBC. The damage mechanisms and their interaction, leading to spallation of the TBC, are not well understood. Generally, we can distinguish between fatigue mechanisms which are number-of-cycle dependent and kinetic mechanisms, depending on time-at-high-temperature or exposure time to a corrosive environment. Examples for kinetic damage mechanisms of the TBC-system are

- densification of the ceramic topcoat by sintering, leading to increased "elastic-modulus" and thus decreased strain tolerance,
- phase transformation from partially stabilized tetragonal zirconia to monoclinic phase, resulting in volume changes and hence increase of local stresses. This phenomenon has been observed after annealing above 1200°C [*3*].
- development of residual stresses perpendicular to the coated surface due to the growth of an oxide scale (TGO) on the bond coat,
- development and growth of pores in the TGO due to pore diffusion [*4*],
- diffusion of alloy elements and impurities from the substrate to the interface between bond coat and TGO, reducing the adhesion of the TBC [*5*],
- delayed spallation of heat-treated TBCs at room temperature which is interpreted as moisture-enhanced slow crack growth [*6*].

Fatigue mechanisms in the TBC-system are not yet well investigated, but several models are published:

- growth of delamination cracks [*7*],
- accumulation of plastic deformation of the BC (ratcheting) and subsequent formation of separations between BC and ceramic topcoat or TGO, respectively .

However, the nickel based super alloys are well known to be susceptible to fatigue crack growth under service loading.

TBC-failures due to extraordinary service conditions, like overheating during extreme flight maneuvers, local overheating as a consequence of clogged cooling holes, or foreign object damage are frequently reported, but are not object to damage accumulation rules.

Experimental approach for a lifetime assessment of coated components in service

Separate investigation of fatigue and kinetically induced damages

In service, the several damage mechanisms are impairing the coated component until TBC failure. Thus, lifetime assessment concepts, accumulating the contributions of the single mechanisms from simplified experiments, need a high number of parameters, describing the evolution of the damages. Additionally, damage interaction parameters are needed because the mechanisms are supposed not to act independent from each other. In contrast, lifetime assessment concepts, based on realistic testing, do not need a high number of interaction parameters because in testing the damage mechanisms, including their interactions, are identical to that in service. However, it is impractical to simulate service cycles for turbine blades in real time testing because they are designed for about 20000 h equivalent to 5000 – 10000 flights. If we analyze a flight cycle, we can distinguish several sequences which are dominated by either fatigue or kinetically induced damage mechanisms. Thermal and mechanical load alternations are imposed especially during start, take off, thrust reverse and shut down of the engine. These load alternations are the driving force for the evolution of fatigue damages. On the other hand, quasi-stationary thermal and mechanical loads are imposed during cruising, resulting in time and temperature dependent kinetically induced damages. Also, the time when the engine is out of service, can contribute to damage accumulation if moisture-enhanced slow crack growth at room temperature has to be considered. The attribution of the different damage mechanisms to the sequences of a service cycle is schematically shown in Fig. 3.

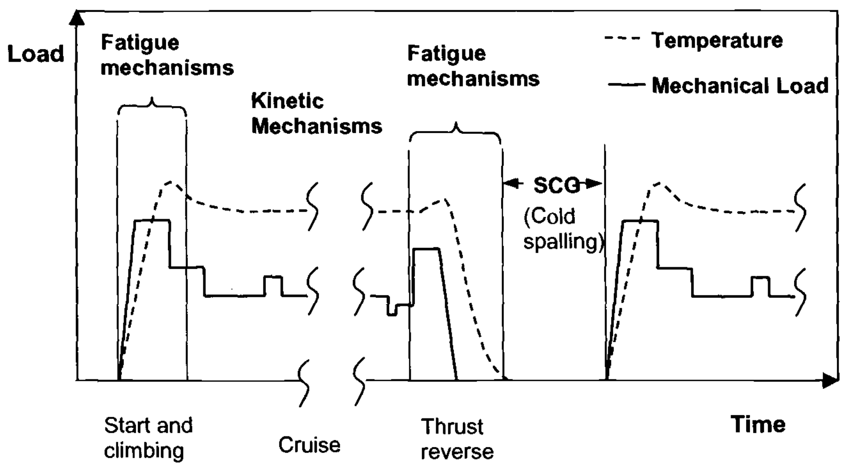

Fig. 3 - *Attribution of different damage mechanisms to the sequences of a service cycle of an aircraft engine (SCG = slow crack growth)*

The fact that fatigue and kinetically induced mechanisms are dominating during different sequences of the service cycle gives us the chance to investigate them separately. In order to estimate the damage accumulation due to fatigue effects, we built a testing facility which can simulate the load alternations of a flight cycle for a turbine blade closely to the service conditions. Since, fatigue damages are induced by the number of load alternations and not by the holding time on a certain load level, we can test the fatigue-susceptibility of the TBC-system within drastically reduced testing times by reducing the holding time. The effect of kinetic damage mechanisms and their interaction with the fatigue mechanisms will be investigated by fatigue-testing of differently heat-treated specimens. Since, several specimens can be heat-treated in a furnace simultaneously, the over-all testing time can be reduced.

Experimental

Facility for realistic fatigue testing - Under service conditions coated turbine blades are loaded simultaneously by thermal and superposed mechanical cycling. Instead of blades we test hollow cylindrical specimens like shown in Fig.4.

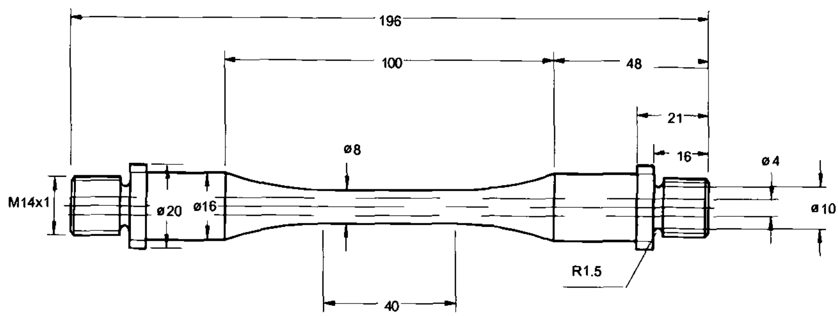

Fig. 4 – *Geometry of the test specimens*

The mechanical loads are imposed by a servo-hydraulic testing machine while the thermal loads are simulated by a radiation furnace. In this furnace, the radiation of four quartz lamps is focused onto the specimen with elliptical mirrors. Since, the combined thermal and mechanical load varies with the blade location, e.g., blade tip or blade fillet, the mechanical and thermal load have to be adjusted independently. Over the cross-section of a coated blade the external heating and internal cooling result in a high thermal gradient which reach about 50°-150°C across the TBC. Since, the strain of the metallic substrate and the TBC-system is identical over the cross section, the thermal gradient induces high stresses in the substrate as well as in the coating. In order to simulate the realistic stress distribution, we generate a thermal gradient by internal air cooling of the hollow specimen. Mass flow and temperature of the cooling air are controlled. Thermal shock during shut down of the gas turbine is simulated by rapid cooling of the outer surface of the specimen with cold air, blown onto the specimens surface from vents which are integrated into two sliders, enclosing the specimen during cooling. Before opening the sliders for the next test cycle, the quartz lamps are switched on, delivering their maximum radiation power to achieve high heating rates, when opening the sliders again. A detailed description of the so-called Thermal Gradient Mechanical Fatigue (TGMF) testing facility is given in [*8*, *9*].

Testing cycle - With the TGMF-testing facility the flight cycle of a turbine blade of an aircraft engine is simulated. Thermal and mechanical loads were imposed simultaneously on the specimens. The mechanical cycle was load controlled with only tensile loads, simulating the centrifugal forces of a rotating turbine blade. Several certain tensile load levels were included with one maximum load level, representing the load during start and climbing of the aircraft and a second maximum load level, representing the thrust reverse after landing. The thermal cycle during testing was rapid heating, until a given stationary temperature was reached, and rapid cooling at the end of the cycle, simulating the shut down of the turbine engine. In contrast to the mechanical loading, no additional temperature changes were imposed because, by reason of the thermal inertia of the system, it would take too much time to reach certain intermediate temperature levels. The stationary cycle temperature was 920°C at the surface of the bond coat for specimens without, as well as for specimens with, ceramic topcoat. Mass flow and inlet temperature of the internal cooling air were kept constant during all experiments. The resulting temperature gradient for the chosen conditions was measured with thermocouples at a specially prepared reference specimen. Between the bond coat surface and the surface of the ceramic topcoat the measured temperature difference was about 35°C and between bond coat surface and the cooled side of the substrate about 85°C.

The cycle time was reduced to a minimum which was essential to reach the maximum stationary temperature. A typical test cycle for a specimen with metallic bond coat but without ceramic topcoat is shown in Fig. 5.

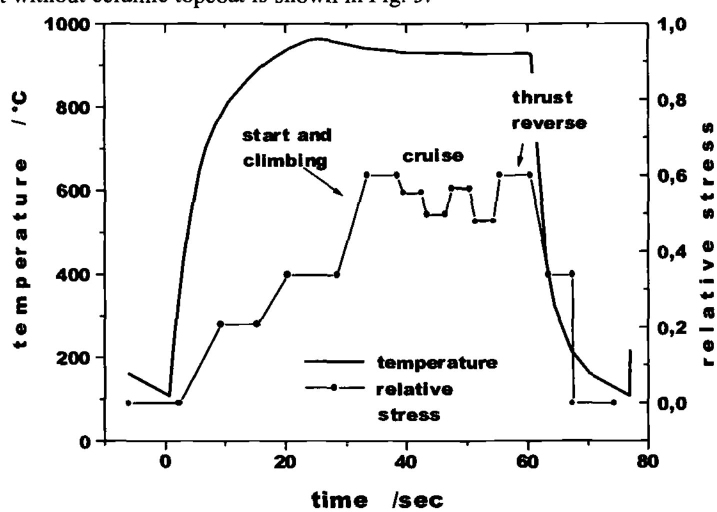

Fig.5 - *Load- and temperature spectrum of a test cycle ('relative stress' is related to the yield stress at stationary cycle temperature)*

The cycle time for specimens without ceramic topcoat was about only 80 second. For specimens with ceramic topcoat the heating and cooling took longer time due to the low thermal diffusivity of the TBC, elongating the cycle time to about 3.5 minutes. The entire time of a test cycle is about only 1% of a service cycle of an aircraft.

Testing program - First experiments were carried out with specimens from directionally solidified nickel-based super-alloy IN100 DS, in order to take into account anisotropy effects like in single crystal blades. All specimens had a 110μm thick NiCoCrAlY- bond coat. Some specimens had an additional 220μm thick ZrO_2 - TBC stabilised with 8wt%Y_2O_3. Both layers were processed by EB-PVD. The substrate material as well as the coatings were processed by the DLR Institute of Materials Research in Cologne.

Experiments with specimens which had only a bond coat were conducted in order to determine a realistic load level for the ceramic TBC. Loading as well as lifetime of the ceramic and the metallic part are strictly interdependent because the strain, the TBC has to withstand, is determined by the cyclic strain capability of the metallic substrate. Since, our substrate material was a model material which is not used in modern gas turbines, we have no data for mechanical straining in service. The mechanical load for the TGMF tests was selected in a way that the substrate with bond coat achieved a life of about 3000 cycles, which is in the range of the flight numbers, the turbine blades are designed for. In order to determine this mechanical load level, we conducted TGMF tests with subsequently decreased load levels, until we achieved the proposed number of test cycles to failure. This mechanical load level was selected for TGMF-testing of TBC-coated specimens.

Results

Specimens without ceramic topcoat – TGMF-tests were conducted on four specimens until fracture. The fracture occurred in all cases at maximum cycle temperature at the first load maximum of the TGMF-cycle which simulates the start and climbing sequence of an aircraft engine. The relation between the number of cycles to failure and the maximum of the mechanical load spectrum of the TGMF-cycle can be described by a power law, which suggests that the dominant damage mechanism was mechanical fatigue. The fracture surfaces were ductile, showing dimple mode at higher magnification. Micrographs of the fracture surface of the specimen which fractured after 3319 cycles are shown in Fig. 6. We found no significant difference to the fracture surface after 324cycles. However, the fracture surfaces did not reveal the fracture origin.

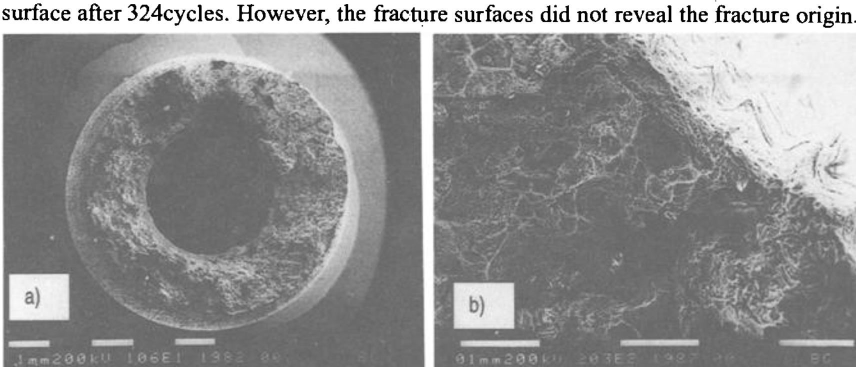

Fig. 6 - *Fracture surface of a TGMF-tested specimen without ceramic topcoat which failed after 3319 cycles at high temperature, a) macroscopic ductile fracture surface, b) dimple mode.*

On the inner surface which was internally cooled during the TGMF-testing we found an oxide scale that showed multiple cracking perpendicular to the tensile load (Fig. 7). The outer surface was protected by the NiCoCrAlY-bond coat, which formed a thin protective oxide scale. In the necking section of the fractured specimens the bond coat was highly plastically deformed so that the thin oxide scale cracked perpendicular to the tensile load (Fig. 8.).

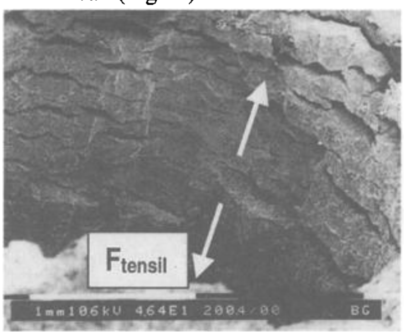

Fig. 7 - *Multiple cracked oxide scale on the internally cooled inner surface of a fractured TGMF-specimen*

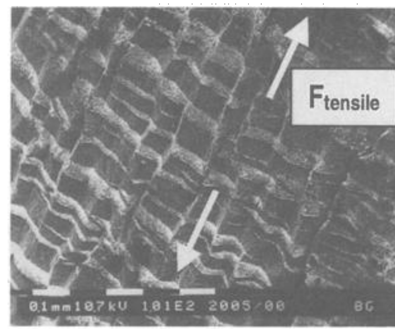

Fig. 8 - *Bond coat surface in the necking region showing cracking of the thin protective oxide scale*

The cross sections of the fractured specimens displayed fatigue cracks, starting at the uncoated internally cooled surface. The cracks were open and in the case of the long term cycled specimen (3319 cycles to failure) the crack surfaces were covered with an oxide scale, revealing that the cracks have been opened during TGMF-testing (Fig. 9).

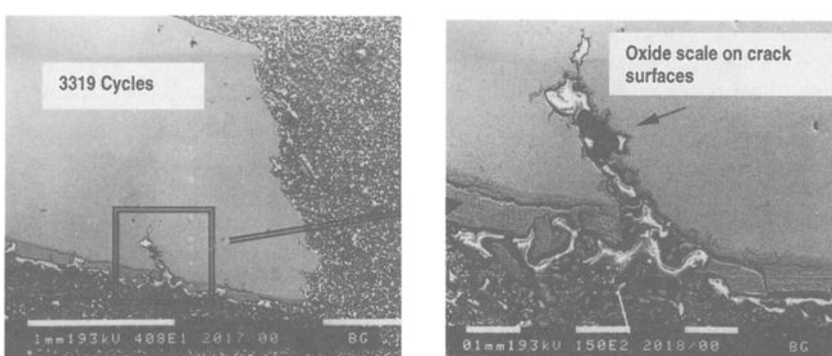

Fig. 9 - *Cross section of a fractured specimen, open fatigue crack starting from the internally cooled inner surface.*

In the vicinity of the lethal crack we also found cracks close to the heated surface. These cracks started at the surface of the substrate but did not go through the bond coat. In all cases the cracks stopped at the bond coat which was plastically deformed but not torn (Fig. 10). No oxide scales were found on the crack surfaces. Thus, these cracks are probably formed due to the high strain, accumulating within the last cycles before failure.

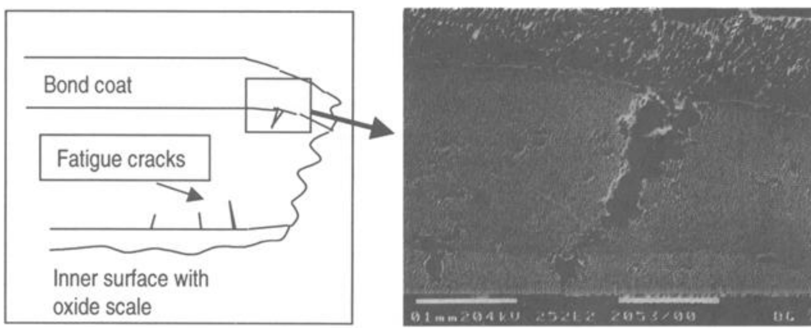

Fig. 10 - *Cross section of a fractured specimen after 3319 cycles. The crack started at the outer surface of the substrate due to high deformation in the tailored section beneath the lethal crack.*

Specimens with ceramic topcoat – Three specimens with ceramic topcoat were TGMF-tested. Considering the measured thermal gradient over the TBC, the stationary maximum surface temperature during testing was adjusted 35°C higher than in the experiments without ceramic topcoat in order to achieve the same bond coat temperature in all TGMF-tests. The first specimen was tested with the mechanical load level which resulted for a specimen without ceramic topcoat in a lifetime of 3319 cycles. After 3527 cycles no spallation or cracks of the TBC were observed. The other two TBC-coated specimens were tested on higher load levels. The tests were also interrupted without failure or obvious damages of the TBC (Fig. 11).

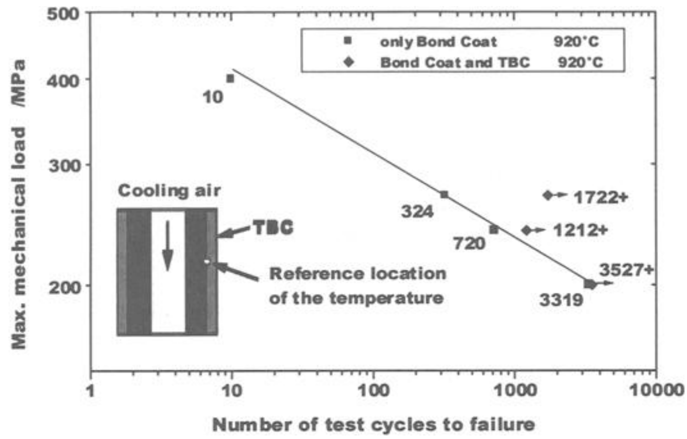

Fig. 11 - *Measured number of test-cycles to failure (specimens with ceramic topcoat did not fail until the termination of the test)*

All experiments were terminated without failure of the specimens. The lifetime of the substrates was significantly higher with TBC than without TBC, even though the bond coat temperature and mechanical load were identical in the thermally highest loaded cross section in the central part of the specimen. Thus, the beneficial effect of the TBC is believed to result from the reduction of thermal shock onto the substrate.

The microstructural investigations of the specimen which survived 3527 TGMF cycles did not reveal any cracks or delaminations in the TBC-system. A thin thermally grown oxide scale of about 2.5 – 3 µm had formed due to the accumulated holding time at high temperature of about 150 hours (Fig. 12). Within the TGO and at the interface between TGO and ceramic topcoat some globular pores had formed.

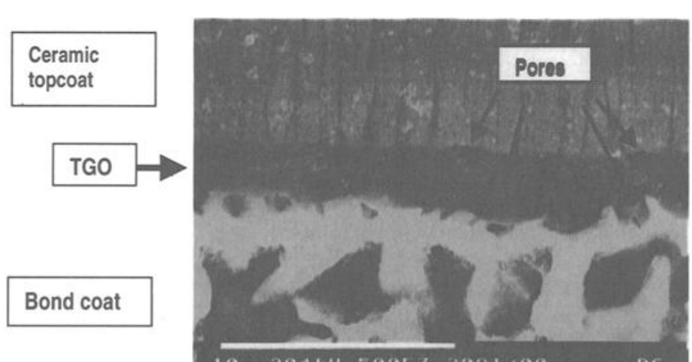

Fig. 12 - *Cross section of the interface between the ceramic topcoat and the bond coat after 3527 TGMF-tests cycles. (Bond coat porosity due to etching)*

Discussion

The actually achieved data suggest some qualitative conclusions. The TGMF-testing of TBC-coated specimens under realistic load alternations but extremely reduced holding times showed that the investigated EB-PVD TBC-system does not fail due to fatigue loading. Thus, the observed premature failure of TBCs in service requires additionally damage accumulation due to kinetic damage mechanisms. Further investigations are intended in order to achieve data for a lifetime assessment of TBCs in service.

It is not practical to conduct TGMF-tests in real time because testing would take several 1000 hours. Our strategy is as follows: Simulating the externally imposed load alternations with the TGMF-tests as realistic as possible – as there are T_{max}, T_{min}, heating and cooling rate (dT/dt), thermal gradient across the TBC cross section and mechanically induced load. In order to investigate the contribution of kinetic and fatigue damage mechanisms to the time to failure, we plan to test separately pre-aged specimens. With information of lifetime behaviour of variable (time and temperature) pre-aged specimens in TGMF-testing we can calculate the lifetime of the TBC for TGMF-cycles or comparable service cycles with extended holding times. Since, the damage mechanisms are supposed to interact, we need additional TGMF-tests with different holding times to calculate the interaction parameters between fatigue and kinetic damage mechanisms. Due to our experience, the TGMF-tests with different holding times have to be conducted with pre-aged specimens in order to achieve TBC failure within acceptable testing time.

TBC failure and consequently, appropriate data for a lifetime assessment under service conditions, are expected by improved testing:

- increasing the heat flux through the specimens wall in order to get higher thermal gradients. In real turbine blades the thermal gradient over the TBC is about 50° – 150°C, depending on the thermal conductivity and the thickness of the TBC-material and the heat flux. In internally cooled turbine blades the stresses resulting from the thermal gradient exceed the stresses due to the centrifugal forces in the rotating blade. Thus, the lifetime of the substrate as well as the strain for the TBC depend on the thermal gradient. In order to achieve a higher thermal gradient, we need to increase the radiation power of the furnace.
- using more oxidation resistant substrate material or protecting the inner surface with an oxidation resistant coating. The substrate material IN 100 DS is extremely susceptible to oxidation. Even though the inner surface was internally cooled to about 830°, a thick oxide scale has formed after only 150 hours. Thus, we believe that for the evolution of the fatigue cracks at the inner surface the formation of flaws due to the oxidation was decisive. For turbine blades in aircraft engines, usually materials are selected which are less susceptible to oxidation, or the internal cooling channels were aluminized to improve the oxidation resistance. Thus, in service the strain amplitudes which have to be tolerated by the substrates are higher than that we imposed to the IN 100 DS – substrates. Consequently, the TBCs had to sustain during the TGMF tests a slightly lower strain amplitude than in service.

Conclusions

Specimens with a ceramic thermal barrier coating were tested in thermal gradient mechanical fatigue with realistic alternating loads but extremely short holding times. The results show that the as-coated properties of EB-PVD TBC-systems are sufficient to survive the required number of load alternations during service life. Thus, the premature failure of TBCs observed in service is due to time-at-high-temperature dependent kinetic mechanisms. Fatigue damages due to cycling are supposed to reduce TBC lifetime simultaneously to damages by kinetic processes. In order to determine the interaction effects between fatigue and kinetic damage mechanisms, TGMF-testing of pre-aged specimen as well as TGMF-testing with extended holding times is supposed to be suitable.

Acknowledgment

The authors thank Ms. Franka Glimm for preparing the specimens for the microstructural investigations.

References

[1] Goward, G. W., "Progress in Coatings for Gas Turbine Airfoils," *Surface and Coatings Technology*, 108-109, 1998, pp. 73-79.

[2] Mariccochi, A., Bartz, A., and Wortmann, D., Proceeding of the "Thermal Barrier Workshop," March 27-29, NASA Conference Publication 3312, 1995, pp. 79-89.

[3] Schulz, U., "Phase Transformation in EB-PVD Yttria Partially Stabilized Zirconia Thermal Barrier Coatings during Annealing," *Journal of the American Ceramic Society*, 83 [4], 2000, pp. 904-910.

[4] Schütze, M., "Protective Oxide Scales and their Break Down," John Wiley & Sons, Cichester, UK, 1997.

[5] Kaden, U., Leyens, C., Peters, M., and Kaysser, W. A., "Thermal Stability of an EB-PVD TBC-System on a Single Crystal Nickel-Base Superalloy," in: *Elevated Temperature Coatings III*, J. M. Hampikian & N. B. Dahotre, Eds., TMS, 1999, pp. 27-38.

[6] Sergo, V. and Clarke, D. R., "Observation of Subcritical Spall Propagation of a Thermal Barrier Coating," *Journal of the American Ceramic Society*, 81 [12], 1998, pp. 3237-3242.

[7] Evans, A. G. and Hutchinson, J. W., "On the Mechanics of Delamination and Spalling in Compressed Films," *International Journal of Solids Structures*, Vol. 20, No. 5, 1984, pp. 455-466.

[8] Marci, G., Mull, K. M., Sick, C., and Bartsch, M., "New Testing Facility and Concept for Life Prediction of TBC Turbine Engine Components," *Thermo-mechanical Fatigue Behavior of Materials: Third Volume*, ASTM STP 1371, H. Sehitoglu and H. J. Maier, Eds., American Society of Testing and Materials, West Conshohocken, PA, 2000, pp. 296-303.

[9] Bartsch, M., Marci, G., Mull, K., and Sick, C., "Fatigue Testing of Ceramic Thermal Barrier Coatings for Gas Turbine Blades," *Advanced Engineering Materials*, 2[11], 1999, pp. 127-129.

M. Guagliano,[1] M. Sangirardi,[1] and L.Vergani[1]

A Hybrid Approach for Subsurface Crack Analyses in Railway Wheels under Rolling Contact Loads

---

Reference: Guagliano, M., Sangirardi, M., and Vergani, L., "**A Hybrid Approach for Subsurface Crack Analyses in Railway Wheels under Rolling Contact Loads,**" *Fatigue and Fracture Mechanics: 33rd Volume, ASTM STP 1417,* W. G. Reuter and R. S. Piascik, Eds., ASTM International, West Conshohocken, PA, 2002.

Abstract: Subsurface internal cracking is one of the most frequent damage mechanisms in railway wheels. In this paper, a hybrid approach is proposed to determine the stress intensity factor of internally cracked bodies, mainly devoted to the analysis of railway wheels but easily adaptable to other practical cases. It is based on the application of the Hertz analytical displacement field to a finite element model of the cracked zone of the wheel. After the description of the method, results are shown referring to cases of practical interest. The comparison with the values experimentally obtained by means of an appropriate photoelastic technique is discussed critically.

Keywords: railway wheel, rolling contact load, penny-shaped crack

Introduction

Due to increasing demand for reliability and performance, contact analysis is becoming a more important phase in the design procedure of many mechanical systems. This is due to the increasingly severe load conditions that components in contact must undergo if lightness is a primary goal of the design process. As an example, dimensions of gears and bearings are continuously reduced and contact pressures are increased. This is possible because of the definition of procedures and methods able to accurately determine

---

[1] Politecnico di Milano, Dipartimento di Meccanica, Via La Masa, 34 20158 Milano (Italy).

actual working conditions without using the empirical coefficients included in international standards, certainly safe but which, at the same time, lead to an oversizing of the element.

The same attention has not been paid to the design of the railway-wheel system, probably due to the fact that only in relatively recent years has the advent of innovative trains led to the demand for components able to resist very high contact pressure and severe dynamic loading.

Consequently, some types of damage, that once were rare, have become more frequent, causing accidents and undesirable noise. For this reason, wheels and rails are periodically subjected to nondestructive tests (NDTs) to check for the existence of internal defects or propagating cracks and to evaluate the criticalness of their dimensions with respect to their position in the component. If the attention is focused on wheels, among the possible damage types, the most typical is "shelling" [*1*] and starts from an internal defect, propagates parallel to the wheel surface until it reaches the free surface, causing the removal of a part of the material and, consequently, putting the wheel out of service.

In fact, the materials and the technological processes used for the construction of railway wheels have led to an increase in the number of these internal defects that NDTs are able to detect: the problem is to judge whether the size and the position of the defect can cause crack propagation or not. Since the defects can be modeled as cracks, the problem can be solved by knowing the stress intensity factor variation of the crack in a contact cycle and by comparing it with the threshold value of the material.

Thus, the first step is to define an approach able to accurately calculate the stress intensity factor (K) of a 3D internal crack due to contact loading. Unfortunately, it is rare to find in literature values of K relating to these cases. Most studies consider two-dimensional cracks in a half-space subjected to the Hertz pressure distribution between two cylinders with parallel axes, also considering the effect of friction between the cylinders in contact, moving with respect to the crack. For example Keer et al. [*2*] find the solution of this case and study the possible direction of propagation of the crack.

More recently, Bastias *et al.* [*3*], by using the finite element method (FEM), solved the same problem and also demonstrated the potential of FEM in achieving accurate solutions in cases not dealt with previously. They considered the contact between crack faces and also a friction coefficient.

Lunden [*4*] developed a 3-D model for crack initiation in a rail wheel and a simplified plane model of crack propagation involving the mode II. In addition, he reported experimental values of the threshold stress intensity factors under mode II loading for a steel commonly used in railway constructions.

Komvopoulos and Cho [*5*] developed a 2-D finite element model able to give the stress intensity factors of subsurface cracks and some indication about the possible direction of propagation of such cracks under contact loading. In these last two cases, the contact between the crack faces was considered as well.

Kaneta et al. [*6,7*] proposed a 3-D approach, based on the Body Force Method, enabling the calculation of the K for subsurface circular cracks in an infinite semi-space subjected to normal and tangential Hertzian pressure distributions, by considering also the effect of the friction between crack faces. They evidenced that the fracture mode mainly involved in this type of damage is the mode II (shear) and they evaluated the variation of K_{II} during the contact cycles. Their attention is, however, focused on roll bearings, whose failure mechanisms are different from those of railway wheels.

The authors of this paper developed 2-D and 3-D finite element models [*8*] in which the wheel is considered as a cylinder and the rail as a rigid plane. Different crack lengths and depths were considered and the results allowed the researchers to draw up an approximate map of the dangerous defect dimensions versus their depth for the contact pressure of interest. In the 2-D plane strain models, subsurface cracks are schematized considering different crack depths. In these models is not possible to simulate the actual crack front shape, while 3-D models were created to simulate internal and circular cracks. To simplify these models, the sub-modeling technique was used. Two different analyses were performed: the first one considers the model of the complete cylinder without the crack in contact with the rigid plane, and the second one considers a model of the surrounding zone, loaded by imposing on the boundaries the displacements calculated in the previous analysis. In this way, we avoid modeling a cracked element of complex geometry and we can use the same submodel to study different crack depths, simply by varying the boundary conditions.

The disadvantage of this procedure is that displacements imposed on the nodes of the sub-model are obtained by the interpolation of the global model displacements: this introduces an error that cannot be ignored if the displacement gradient is high. This error is in addition to the numerical error typical of FE analysis. Due to the different analytical characteristics of contact and fracture mechanics problems, it is better to use first order elements in the global analysis and second order elements in the sub-model analysis: this too introduces numerical errors. Furthermore, if the contact with a deformable rail is considered, the dimensions of the models become larger and larger and the approach becomes time-consuming. These considerations induced the authors to develop another, more accurate, procedure for the calculation of the stress intensity factors of internal cracks under contact loading.

This is the object of the present paper. The approach can be defined as hybrid, since it makes use of the analytical displacements of two bodies in contact, calculated by means of the approach proposed by Bryant and Keer [*9*]. In a second step these displacements are applied as boundary conditions to a finite element model of the zone surrounding the crack, similar to the sub-model of the previously described FE approach. This approach does not have the errors previously described and it can be easily adapted to analyze the case with two elastically deformable contact bodies without increasing the computation time.

However, this approach is not free from approximations either: in fact, we use the displacement field in an uncracked body to analyze a cracked body, and some limitations are necessary to use it successfully. These points are critically discussed in the paper. The model is quite general even though the results reported in the paper refer to a rail wheel. To validate the approach, experimental tests using an appropriate photoelastic technique were performed: the comparison with the numerical values is in satisfactory agreement and is discussed critically.

Description of the Hybrid Approach

The 3-D hybrid approach for the stress intensity factor calculation of an internal crack is based on the analytical determination of the displacement field in the uncracked body and on the development of a FE model of the zone surrounding the crack. In the following, these two distinct parts of the approach are described in detail.

Calculation of the Displacement Field

The analytical evaluation of the displacement field in the wheel due to the contact with the rail is carried out by simplifying the geometry of the two in-contact elements. In fact, in Figure 1 it is possible to note that the pressure distribution due to the contact can be calculated considering the Hertz solution for two cylinders with normal axes. The radii of curvature, for the case considered in the present paper, are R_1 for the wheel and R'_2 for the rail. In particular, $R_1=445$ *mm*, $R'_2=300$ *mm*; R'_1 and R_2 are, of course, infinite. Figure 1 also shows the qualitative trend of the contact pressure as predicted by Hertz and the elliptical shape of the contact area: the length of the semi-axes of the ellipse, c and b, and the maximum pressure, p_o, were calculated according to the Hertz theory.

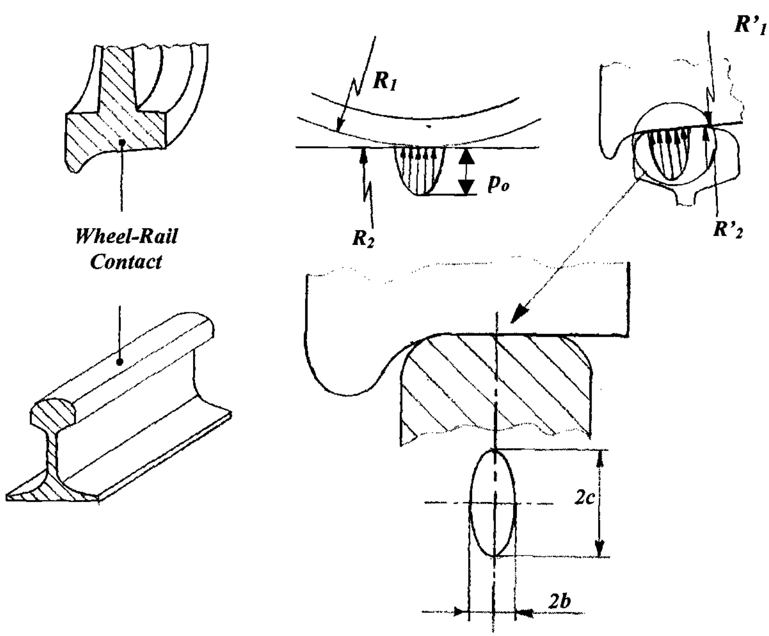

Figure 1- *Schematic view of the wheel-rail contact.*

Once these quantities were known, the displacement field in the wheel due to the contact loading was calculated by applying the Bryant and Keer approach [9] for the calculation of the displacement field in an elastic-linear half-space loaded by the previously described pressure distribution.

This approach is an extension of the work by Hamilton and Goodman [10], and the starting point is the Boussinesq solution. Bryant and Keer consider both the normal pressure and the friction tangential stresses, the latter being calculated in the sliding limit condition, according to the Coulomb theory ($\tau=fp$, where f is the friction coefficient).

Moreover, only the condition of friction stresses acting along the longitudinal axis of the rail was considered, thus simulating the motion of the wheel on a straight rail. Though the solution proposed by Bryant and Keer applies to two geometrically identical curved bodies, the solution can also be applied to bodies with different curvatures by means of finite element and experimental analyses. The solution scheme was implemented in a subroutine and symbolically solved by using the Waterloo Maple V^R programming environment.

Finite Element Models

The second part of the hybrid approach includes finite element calculation of the stress intensity factors concerning mode I, II and III for a subsurface crack of assigned dimensions and geometry, positioned at a given depth with respect to the free surface. As noted in the introduction, by using the proposed approach, the mesh of the zone surrounding the crack is sufficient to solve the case. In fact, the analytically calculated displacements are imposed on the nodes lying on the boundary surface of the model. In this way, it is possible to determine the stress intensity factors for the embedded crack with a limited meshing effort. Moreover, the same model can be used to analyze identical cracks at different depths, simply by changing the boundary conditions. A numerical routine was developed to automatically assign the appropriate boundary conditions as a function of the nodal coordinates.

Figure 2 schematically shows a section of the half-plane containing the larger of the contact ellipse semi-axes, c. The finite element model is introduced in the half-space loaded by the Hertz pressure distribution. By changing e, it is possible to determine the maximum and the minimum value of the stress intensity factor in a load cycle and thus ΔK, which is the quantity governing the fatigue crack propagation rates. By changing d, it is possible to apply the same finite element model for the analysis of cases characterized by different depths.

The construction of the FE model is relatively simple and it is easy to consider different crack front geometries on the basis of an initial model. Thus, a numerical routine was developed to scale and also to reshape the initial model.

In Figure 3, a typical example of the models used in this research is shown: as can be noted, it reproduces an embedded circular crack with a radius equal to a and considers a cylinder around the crack with a radius equal to R and a height equal to H.

The elements used are 20-node brick ones with second order shape functions.

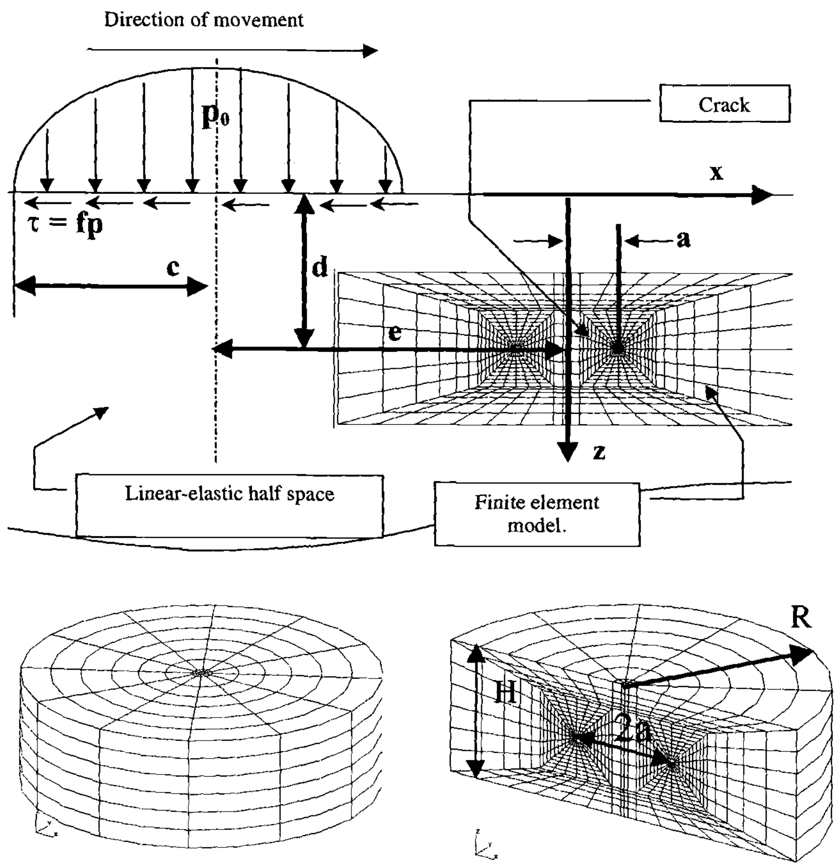

Figure 3 – *Finite element model of the zone surrounding the crack: full view and mid-plane section.*

Due to the nature of the applied loads, in the FE model it is important to avoid overlapping between the crack faces: this was made possible by proper use of the contact elements included in the software utilized, allowing us to consider a Coulomb contact model to simulate sticking/sliding conditions. To correctly simulate the stress singularity in the close neighborhood of the crack front, the elements converging on the crack front were distorted by following the ¼ point technique [*11*].

The main limit of this approach is that the displacement field of the non-cracked body is applied to the cracked one: this is undoubtedly an approximation but its effect on the stress intensity factors calculation can be ignored if an accurate study of the dimensions H and R of the FE model is carried out. In other words, it is necessary to estimate how large the FE model has to be to consider the displacement field unaffected by the presence of the crack. In this case, the dimensions of the model were chosen by bearing in mind the results obtained from 2D analyses concerning similar cases [*8*]: thus, a cylindrical model around the crack was developed with a radius R equal to $5a$ and a height H equal to $3a$. The respect of these conditions limits the applicability of this approach, since large cracks near the surface cannot be dealt with. In fact if the crack is large and close to the free surface the value of $H/2$ could be larger than d. However, from a practical point of view, this latter type of crack is of limited interest, because it prevents the in-service use of the wheel.

The calculation of the stress intensity factors was carried out by considering an elastic linear material (longitudinal elastic modulus $E=206\ GPa$, Poisson Coefficient $\nu=0,3$). Table 1 shows the crack dimension a and depth d considered.

Table 1 – *Crack dimensions and depths considered in the analysis.*

d [mm]	a [mm]				
2	1	2	-	-	-
5	1	2	3	-	-
10	1	2	3	4	5
15	1	2	3	4	5
20	1	2	3	4	5
25	1	2	3	4	5

All the cases of Table 1 were analyzed by varying the following values of contact pressure $p_o=1120MPa$ ($c=6.45mm$, $b=4.96mm$), $p_o=1232MPa$ ($c=7.10mm$, $b=5.46mm$), $p_o=1411MPa$ ($c=8.12mm$, $b=6.25mm$).

In the calculations, the friction coefficient between the crack faces, f_c, was analyzed too, by considering the values $f_c=0$, 0.2, 0.4, 0.6 for all the cases of Table 1.

The effect of the friction coefficient between the wheel and the rail, f, was also studied. Two values ($f=0$, 0.1) were considered. In Figure 2, it is possible to see the direction of τ, which is contrary to the movement one, in order to simulate a trailer wheel.

Numerical Results

The numerical analyses simulate half of the entire contact cycle by varying the crack position e with respect to the Hertzian pressure distribution. During rolling, it is possible to distinguish between the crack tip near the load, called A, and the crack tip far from the load, called B, as shown in Figure 4. In order to simulate all the entire contact cycle, the remaining half cycle is simply obtained (if the friction coefficient $f=0$) by considering in B the results previously obtained in A. In B, the same procedure is applied. The crack tips C and D are also considered in the analysis. The crack propagation is considered along the $\theta=0°$ direction (see Figure 4), according to the results of Kaneta and Murakami [6,7].

The evaluation of the stress intensity factors, K_I, K_{II} and K_{III}, was carried out by means of two different techniques: the first is based on the stress nodal values, the second is based on the virtual crack extension and is directly calculated by the finite element program. In the crack tips A and B, the stress intensity factors K_I and K_{II} were evaluated by using, respectively, the normal, σ_z, and the tangential stress, τ_{zx}, stress patterns along the crack propagation direction:

$$K_I = \lim_{r \to 0} \sigma_z \sqrt{2\pi r} \qquad K_{II} = \lim_{r \to 0} \tau_{zx} \sqrt{2\pi r} \qquad (1)$$

where r is the distance from the crack front.

With the J value, directly calculated by the program, an equivalent stress intensity factor, K_{eq}, is determined:

$$K_{eq} = \sqrt{\frac{JE}{(1-\nu^2)}} \qquad (2)$$

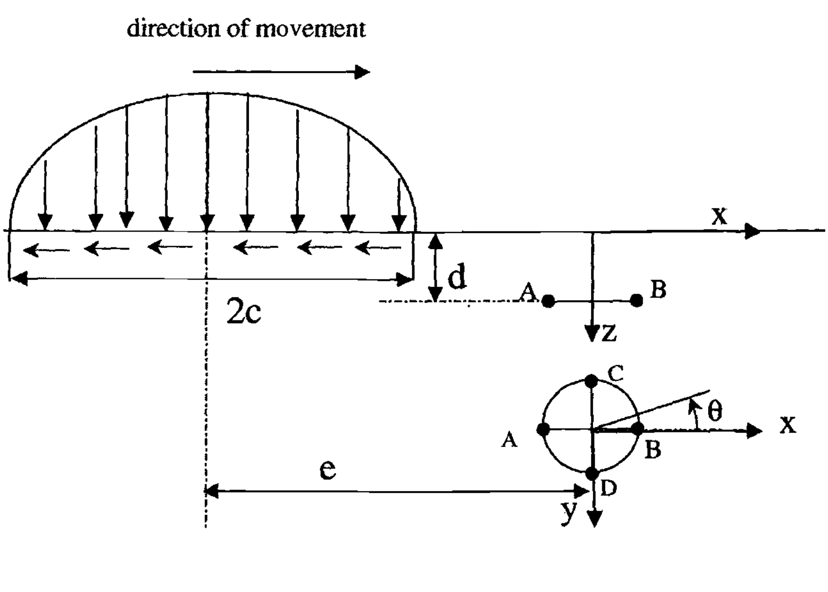

Figure 4 – *Scheme of analysis: simulation of the contact rolling cycle and definition of the leading crack tip A and trailing crack tip B (frontal view, xz) and of the crack tips C and D (top view, xy).*

The K_{eq} value does not distinguish between the I and the II contribution, but the K_{II} and the K_{eq} values are very close; in fact, the mode II is predominant with respect to the other modes in A and B. It is, therefore, possible to evaluate K_{II} directly by means of equation (2).

In the crack tips C and D, on the contrary, the predominant crack propagation is mode III and, by following the same considerations as in the case of tips A and B, the K_{III} values are evaluated using the J values and the equation (2).

It is difficult to find an experimental validation of these crack propagation modes. Some confirmations were found in literature. In fact in [*4, 12*] it is underlined that the profiles of rolling contact cracks are rough and curved and can be related to mode II propagation.

As shown in Table 1, numerous analyses were performed; for each case, the entire rolling cycle was analyzed and the maximum and minimum stress intensity factors, K_{IImax} and K_{IImin}, over the cycle and the corresponding position, e, was determined in all the tips, A, B, C and D.

In order to simulate the entire cycle when the wheel rolls over a crack, in a crack tip it is necessary to consider that the crack is, as an example, near the load for the first half cycle (negative e/c values). For the second half cycle (positive e/c values) the same crack tip is considered far from the load as shown in Figure 4, if the friction coefficient between the wheel and the rail is considered null. On the contrary, when $f=0.1$, the entire cycle was simulated. A dimensionless stress intensity factor was defined as follows:

$$f_{II} = K_{II} / p_o\sqrt{\pi a} \tag{3}$$

Complete contact rolling cycles ($f=0$ and $f_c=0$) are shown in Figure 5, where it is evident the crack depth influence and that the values are approximately symmetrical with respect to the $e/c=0$ position.

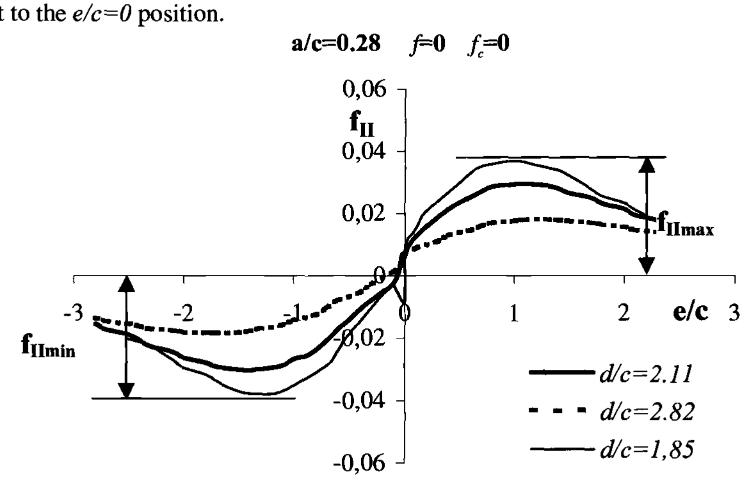

Figure 5– *Effect of the crack depth on* f_{II} *in a complete contact rolling cycle.*

For each rolling cycle, it is possible to define a stress intensity factor range, Δf_{II}, which is evaluated as:

$$\Delta f_{II}=f_{IImax}-f_{IImin} \tag{4}$$

where the f_{IImax} and the f_{IImin} are the maximum absolute values found for the crack tip near and far from the load, as defined in Figure 5. The ΔK_{II} value could be determined by multiplying Δf_{II} for the corresponding values of p_o and a and successively by comparing it with the threshold values, which determine whether a crack is critical or not. If the values reported in literature [13] are used ($\Delta K_{IIth}=1.5MPam^{0.5}$) as threshold ones, it is evident that the crack simulated in the numerical model can be considered critical with respect to the propagation.

For every condition, the rolling cycle was also evaluated in the two crack tips, defined as C and D. All the behaviors found are similar to the ones reported in Figure 5 and the maximum values are always about equal to 80% of the values found in A. The values determined in C and D are similar to each other; in fact, they are at the same distance from the load. Figure 6 shows the values of f_{IImin} obtained by the analyses performed by varying the position, d, of the crack and the friction coefficients between the crack faces, f_c. By these values it is possible to evaluate Δf_{II} which is about the double of f_{IImin}.

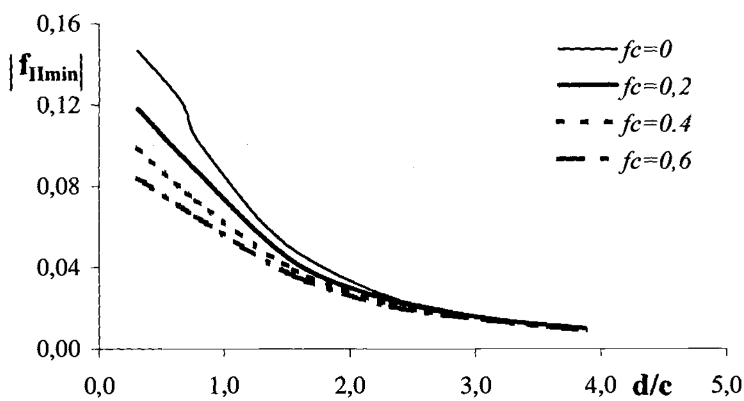

Figure 6 - *Influence of f_c and d on the values of f_{IImin}.*

The influence of the friction coefficient between wheel and rail, f, was considered too. Several analyses by varying the crack dimension and the load were performed. In Figure 7 the comparison between a entire contact cycle with and without the friction coefficient f was shown.

Experimental Measurements

To verify the numerical results and therefore the entire calculation procedure, experimental tests, using the photoelastic technique, were performed. Epoxy resin models were created with internal circular cracks, obtained following a special procedure based on thermal shocks.

The cracks were obtained in small volumes of resin, which were heated in the central zones over the critical temperature ($T_c \approx 125°C$).

Then the resin volumes were cooled in water for some minutes and after in air. This rapid cooling causes the formation of internal cracks. After several attemps the heating and cooling parameters were determined to obtain plane and circular internal cracks.

The cracked small volumes were included in the resin mould, where the resin cylinders were melted. A mechanical device allowed us to put the volumes at a prescribed depth. The cylinders were tempered to remove the eventual residual stresses: a preliminary photoelastic observation was performed to check that these latter were negligible.

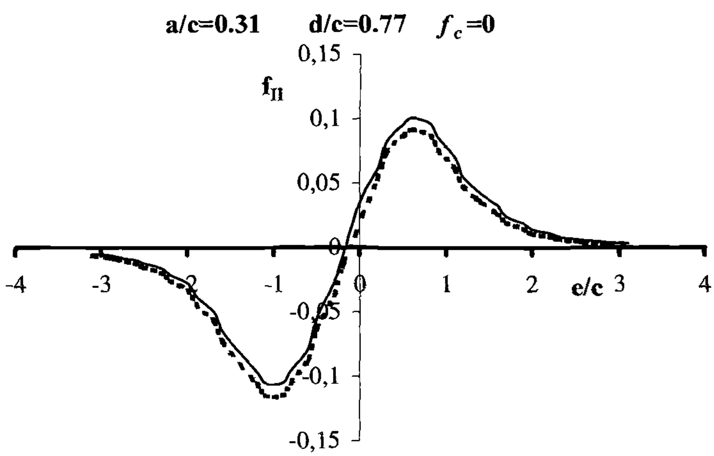

Figure 7 – *Comparison between a complete contact cycle considering different friction coefficients f (continuous line f=0., dashed line f=0.1).*

The complete model is constituted of two cylinders: a cracked one, which simulates the wheel and one, without crack, which simulates the rail. The scale factor, and consequently the cylinder radius, was chosen by considering the contrasting requirements of having small models to reach high values of p_o and large models to suit the dimensions of the cracks that we can insert.

The cylinders were loaded by means of a special loading device that allows modifying the eccentricity of the load with respect of the crack.

The stress freezing method [14] was followed to analyze the stress field near the crack. The model was loaded in an oven, where the temperature was higher than the critical one, and was successively cooled to have a constant birefringence state due to the applied load. After cooling, small slices were cut in correspondence of the two crack diameters: one containing points *A* and *B*, and the other, points *C* and *D*.

The experimental measurements were conducted on two different cracked models. The first one has a cracked cylinder ($a \approx 10mm$ and $d=15mm$) with a radius $R=800mm$ and a cylinder without crack with a radius $R=540mm$. This model was loaded by $P=650N$, which produced a contact ellipse whose axes have dimensions of $c=37mm$ and $b=30mm$, positioned at a distance $e=20mm$ with respect to the crack. The slices cut were analyzed by means of the photoelastic device.

In Figure 8, it is possible to see the picture of the slice, corresponding to the diameter with points *A* and *B* in the rolling direction of the wheel. It is immediately possible to note that the *II* crack opening mode is predominant and the crack tip near the load is more stressed than the tip far from it. Furthermore, it is evident that there are zones where there is localized friction. The comparison with the numerical values is complex; in fact, it is difficult to find an effective value of the stress intensity factor of the cracked photoelastic model, due both to the behavior of the resin, whose mechanical characteristics change when the critical temperature is exceeded, and to the impossibility of knowing the exact friction coefficient of the resin crack faces.

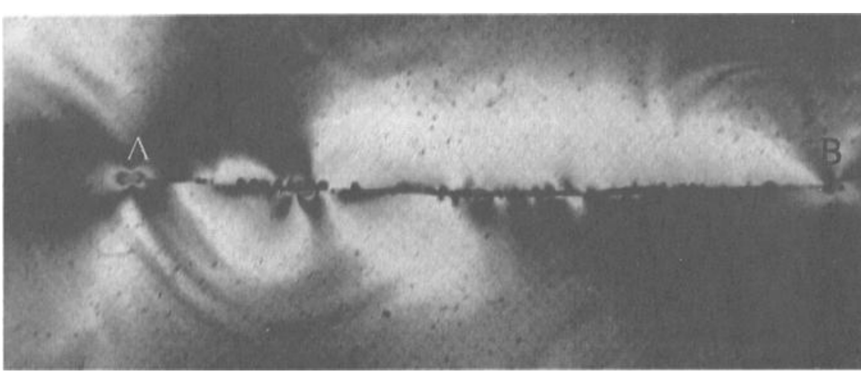

Figure 8 – *Slice corresponding to the crack diameter including the points A and B(model1).*

A numerical model characterized by the geometrical dimensions of the photoelastic model was developed and the K_{II} values in the crack tip A were determined by varying the crack friction, f_c, values. In Figure 9 it is possible to see the K_{II} trend with respect of the f_c values. By imposing $f_c=0.125$, the numerical K_{II} value is close to the experimental one.

Then, crack tip B was considered: by using the same friction coefficient, the K_{II} numerical value is in good agreement with the corresponding experimental value.

The second model has a cracked cylinder (*a≈10mm* and *d=23mm*) with radius *R=930mm* and a cylinder without crack with a radius *R=620mm*.

This model was loaded by *P=450N*, which produced a contact ellipse whose axes have dimensions of *c=33mm* and *b=35mm*, positioned at a distance *e=30mm* with respect to the crack. The slices cut were analyzed by means the same procedure of the first model. The friction coefficient found is f_c*=0.180*, larger than the first model value, in fact the crack obtained is less regular and not perfectly plane.

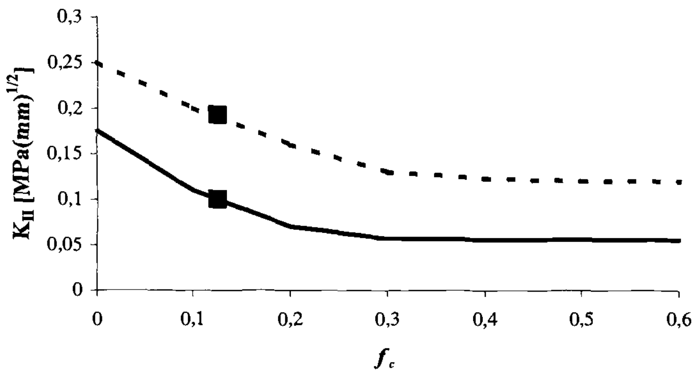

Figure 9– *K_{II} values trend with respect of the friction coefficient, f_c, values numerical obtained by the first model (--- crack tip A, — continuous line crack tip, ■ experimental points).*

From Figure 9 it is evident that the trend of K_{II} is asymptotic for both the crack tips. In the range of f_c considered in this work the behavior of K_{II} is about linear with f_c. In particular if f_c varies from *0.1* to *0.2* the corresponding K_{II} value in crack tip A diminishes of 36% and in crack tip B of 20%.

In Table 2, the results obtained by the two models are shown.

Table 2 *Experimental and numerical values of the stress intensity factors K_{II}*

Model		Experimental K_{II} values [MPa$\sqrt{mm}$]	Calculated K_{II} values [MPa$\sqrt{mm}$]
1	Crack tip A	0.193	0.193
	Crack tip B	0.096	0.100
2	Crack tip A	0.150	0.150
	Crack tip B	0.123	0.125

The comparison can be considered satisfactory, considering the experimental difficulties. The proposed hybrid approach can thus be considered validated.

Conclusions

A hybrid approach enabling the calculation of the stress intensity factors of penny-shaped cracked elements subjected to contact rolling loads was presented. This approach was defined in particular for wheel-rail systems but can be easily applied to other cases.

The approach is defined hybrid because it requires the analytical calculation of the displacement field due to the contact of two nonconforming bodies and the numerical (FE) calculation of the stress intensity factors of 3-D internal cracks (the case of a penny shaped crack was considered).

By this approach it is possible to reduce the calculation error, since the analytical solution of the displacements is adopted and the use of the finite element method is limited to the modeling of the zone surrounding the crack. Another advantage is the flexibility of the approach; in fact, with a little effort (by changing only the boundary conditions of the FE model) it is possible to change the geometrical dimensions, the friction coefficients and the loading parameters. Critical review of the limit of the approach is also included in the paper: the minimal dimensions of the FE mode to use for the stress intensity calculation were also estimated.

The approach was finally validated by experimental measurements of the stress intensity factors by using photoelastic models made of epoxy resin.

References

[1] Polushkin, E.P., "Defects and Failures-Their Origin and Elimination," Elsevier Ltd, 1956, pp. 292-293.

[2] Keer, L.M., Bryant, M.D., and Haritos, G.K., "Subsurface and Surface Cracking Due to Hertzian Contact," *Journal of Lubrication Technology* (Trans. ASME), Vol. 104, 1982, pp. 347-351.

[3] Bastias, P.C., Hahn, G.T., and Rubin, C.A., "Finite Element Modeling of Subsurface Mode II Cracks under Contact Loads," *Engineering Fracture Mechanics,* Vol. 33, 1989, pp. 143-152.

[4] Lunden R., "Cracks in Railway Wheels under Rolling Contact Load," *International Wheelset Congress*, Sydney, Australia, September 1992, pp. 163-167.

[5] Komvopoulos, K., Cho, S.-S., "Finite element analysis of subsurface crack propagation in a half-space due to a moving asperity contact," *Wear*, Vol. 209, 1997, pp. 57-68.

[6] Kaneta M., Murakami Y. and Okazaki T., "Growth Mechanism of Subsurface Crack Due to Hertzian Contact," *Journal of Tribology*, (Trans. ASME), Vol.108, January 1986, pp. 134-139.

[7] Kaneta M., Yatsuzuka H., and Murakami Y., "Mechanism of Crack Growth in Lubricated Rolling/Sliding Contact," *ASLE Transactions*, Vol.28, March 1985, pp. 407-414.

[8] Guagliano, M., La Sana, M., and Vergani, L., "Analysis of cracked elements subjected to contact loading," *Proc. Fracture and Damage Mechanics* (Ed. M.H. Aliabadi), Dept. Engineering – Queen Mary and Westfield College University of London, London (UK), 1999, pp. 191-200.

[9] Bryant, M. D., Keer, L. M., "Rough Contact Between Elastically and Geometrically Identical Curved Bodies," Trans. of ASME, Series E, *Journal of Applied Mechanics*, Vol. 49, 1982, pp. 345-352.

[10] Hamilton, G. M. and Goodman L. E., "The Stress Field Created by a Circular Sliding Contact, *Journal of Applied Mechanics* (Trans. ASME), Vol. 33, 1966, pp. 371-376.

[11] Barsoum, R. S., "On the Use of Isoparametric Finite Elements in Linear Fracture Mechanics," *International Journal of Numerical Methods in Engineering*, Vol. 10, 1976, pp. 25-37.

[12] O'Regan S. D., Hahn G. T. and Rubin A. C., "The Driving Force for Mode II Growth under Rolling Contact", *Wear*, Vol. 101, 1985, pp.333-346.

[13] Otsuka A., Mori K., and Miyata T., "The Condition of Fatigue Crack Growth in Mixed Mode Condition," *Engineering Fracture Mechanics*, Vol.7, 1975, pp. 429-439.

[14] Dally J. W. and Riley W. F., "Experimental Stress Analysis" McGraw-Hill International Editions, New York, 1991.

Claudio Ruggieri[1] *and Eduardo Hippert, Jr.*[2]

Cell Model Predictions of Ductile Fracture in Damaged Pipelines

Reference: Ruggieri, C. and Hippert, E., Jr., "**Cell Model Predictions of Ductile Fracture in Damaged Pipelines,**" *Fatigue and Fracture Mechanics: 33rd Volume, ASTM STP 1417*, W. G. Reuter and R. S. Piascik, Eds., ASTM International, West Conshohocken, PA, 2002.

Abstract: This study explores further extension of the computational cell methodology to model Mode I crack extension in a high strength pipeline steel. Plane-strain analyses of a tubular structure containing longitudinal cracks with varying crack depth to thickness ratios (a/t) are employed to characterize crack-tip constraint for cracked pipes under internal pressure. Laboratory testing of an API 5L X70 steel at room temperature using standard, deep crack C(T) specimens provides the crack growth resistance curve to calibrate the micromechanics cell parameters for the material. The cell model incorporating the calibrated material-specific parameters is then applied to predict the burst pressure of a thin-walled gas pipeline containing longitudinal cracks with varying crack depth to thickness ratios (a/t). The numerical analyses demonstrate the capability of the computational cell approach to simulate ductile crack growth in fracture specimens and to predict the burst pressure of thin-walled tubular structures containing crack-like defects.

Keywords: ductile fracture, crack growth, finite elements, R-curve, pipelines, burst pressure, crack-tip constraint

Introduction

Predictive methodologies aimed at quantifying the impact of defects (e.g., cracks, blunt corrosion, inclusions, weld flaws) in oil and gas pipelines play a key role in fitness-for-service analyses including, for example, repair decisions and life-extension programs of onshore and offshore facilities. Conventional procedures used to assess the integrity of piping systems generally employ simplified failure criteria based upon a plastic collapse failure mechanism incorporating the tensile properties of the pipe material [*1-3*]. These methods establish acceptance criteria for defects based on limited experimental data for low strength

[1] Assistant Professor, Department of Naval Architecture and Ocean Engineering, University of São Paulo, São Paulo, Brazil - E-mail: cruggi@usp.br
[2] Graduate Student, Department of Naval Architecture and Ocean Engineering, University of São Paulo, São Paulo, Brazil.

structural steels which do not necessarily reflect the actual failure mechanism (e.g., stable crack growth of the macroscopic defect prior to pipe collapse) nor do they address specific requirements for the high grade steels currently used.

For high strength pipeline steels, the material failure (leakage or sudden rupture) is most often preceded by large amounts of slow, stable crack growth. Under sustained ductile tearing of the (macroscopic) crack-like defect, large increases in the load-carrying capacity of the structure, as characterized by J-Δa resistance curves (R-curves), are possible beyond the limits given by the crack driving force at the onset of crack growth (J_{Ic}). However, laboratory testing of fracture specimens to measure resistance curves (J-Δa) consistently reveals a marked effect of absolute specimen size, geometry, relative crack size (a/W) and loading mode (tension vs. bending) on R-curves. For the same material, deep-notch bend, SE(B), and compact tension, C(T), specimens yield low R-curves while shallow-notch SE(B), single-edge notch tension, SE(T), and middle-crack tension, M(T), specimens yield larger toughness values at similar amounts of crack growth. These geometry and loading mode effects on R-curves arise from the strong interaction between microstructural features of the material which govern the actual separation process and the loss of *near-tip constraint* in the crack front region due to large-scale yielding. For thin-walled tubular structures with crack-like defects, the strong interaction of crack tip plastic zones with nearby traction-free surfaces very early in the loading significantly lowers the crack-tip stress triaxiality. This behavior further magnifies the constraint-loss phenomenon and introduces additional complexity in the use of R-curves for failure assessments. Consequently, realistic methodologies for structural integrity assessments must include advanced procedures to *transfer* fracture resistance data measured using small laboratory specimens to structural components in engineering applications.

Recent research efforts to address the strong effects of crack-tip constraint on tearing resistance behavior for ferritic steels employ continuum damage plasticity models incorporating material softening due to void growth. In particular, the *computational cell methodology* proposed by Xia and Shih [*4-6*] (hereafter X&S) and extended in a 3-D context by Ruggieri and Dodds [7] and Gullerud et al. [*8*], among others, provides a realistic modeling of ductile crack growth to define the evolution of near-tip stress fields during crack extension. This computational model for ductile growth defines a single layer of void-containing cubical cells having linear dimension D along the crack plane on which mode I growth evolves. Each cell contains a cavity of initial volume fraction, f_0, where void growth and strain softening are modeled by a 3-D form of the Gurson-Tvergaard (GT) dilatant plasticity theory [*9, 10*]. By deleting cells with severe damage when f reaches a critical value (f_E) from the computational model, the pre-existing macroscopic crack grows in length by the amount D. To introduce an explicit length-scale into the model, X&S associate D with the mean spacing between the larger inclusions and treat it as a material parameter in the model calibration process. Once calibrated using a measured R-curve for a standard fracture specimen, the cell parameters D and f_0 must remain fixed in analyses of other configurations for that material. Numerical analyses of fracture specimens using the computational cell model have predicted the effects of geometry on experimental R-curves and measured crack front profiles with surprising accuracy (see [*7,11*] for extensive comparisons).

This study explores further extension of the computational cell methodology to model Mode I crack extension in a high strength pipeline steel. The first section outlines the essential features of the computational cell approach including a very brief description of the element vanish technique to remove highly voided cells; this procedure enables physical growth of the crack in the model. Next, plane-strain analyses of pipes containing longitudinal cracks with varying crack depth to thickness ratios (a/t) are employed to generate numerical solutions for the crack-tip stress fields. These analyses serve to characterize crack-tip constraint for cracked pipes under internal pressure. A key feature of our investigation is the use of a reference field based upon a Modified Boundary Layer (MBL) model to provide a measure of constraint loss when large scale yielding (LSY) effects arise in a tubular structure. The interaction of crack tip plastic zones with nearby traction-free surfaces and with global plastic zones affects strongly the near tip stress fields that develop in cracked pipes. These results indicate that low stress states dominate the fracture behavior of cracked tubular structures and underlie potential difficulties with the simple application of GT-based cell models to predict failure in pipelines. Laboratory testing of an API5LX70 steel at room temperature using standard, deep crack C(T) specimens then provides the crack growth resistance curve to calibrate the micromechanics cell parameters for the material. The paper concludes with an application of the cell model incorporating the calibrated material-specific parameters to predict the burst pressure of a thin-walled gas pipeline containing longitudinal cracks with varying crack depth to thickness ratios (a/t).

Computational Cell Model for Ductile Crack Growth

The *computational cell* methodology proposed by Xia and Shih [*4-6*] (X&S) provides a model for ductile crack extension that includes a realistic void growth mechanism, and a microstructural length-scale physically coupled to the size of the fracture process zone. Void growth remains confined to a layer of material symmetrically located about the crack plane, as illustrated in Fig. 1(a), and having thickness D, where D is associated with the mean spacing of the larger, void initiating inclusions. This layer consists of cubical cell elements with dimension D on each side; each cell contains a cavity of initial volume fraction f_0 (the initial void volume divided by cell volume). As a further simplification, the void nucleates from an inclusion of relative size f_0 immediately upon loading. Progressive void growth and subsequent macroscopic material softening in each cell are described with the Gurson-Tvergaard (GT) constitutive model for dilatant plasticity [*9, 10*] given by

$$g(\sigma_e,\sigma_m,\bar{\sigma},f) = \left(\frac{\sigma_e}{\bar{\sigma}}\right)^2 + 2q_1 f\cosh\left(\frac{3q_2\sigma_m}{2\bar{\sigma}}\right) - \left(1 + q_3 f^2\right) = 0 \qquad (1)$$

where σ_e denotes the Mises equivalent (macroscopic) stress, σ_m is the macroscopic mean stress, $\bar{\sigma}$ denotes the current flow stress for the cell matrix material and f defines the current void fraction. Factors q_1, q_2 and q_3 introduced by Tvergaard [*10*] improve the model predictions for interaction effects present in periodic arrays of cylindrical and spherical voids; here we use $q_1 = 1.5$, $q_2 = 1.0$ and $q_3 = q_1^2$.

Figure 1(b) shows the typical, plane strain finite element representation of the computational cell model where symmetry about the crack plane requires elements of size $D/2$. Material outside the computational cells, the "background" material, follows a conventional J_2 flow theory of plasticity and remains undamaged by void growth in the cells. When f in the cell incident on the current crack tip reaches a critical value, f_E (which typically has a value of 0.15 ~ 0.25), the computational procedure removes the cell thereby advancing the crack tip in discrete increments of the cell size. The final stage of void linkup with the macroscopic crack front occurs by reducing the remaining stresses to zero in a prescribed manner. Tvergaard [*10*] refers to this process as the element extinction or vanish technique. This cell extinction process used in the present work implements a linear-traction separation model which creates new traction-free surfaces in a controlled manner and also eliminates numerical difficulties. Ruggieri and Dodds [*7*] and Gullerud et al. [*8*] provide further details of the computational implementation of the cell extinction scheme used in the present numerical analyses.

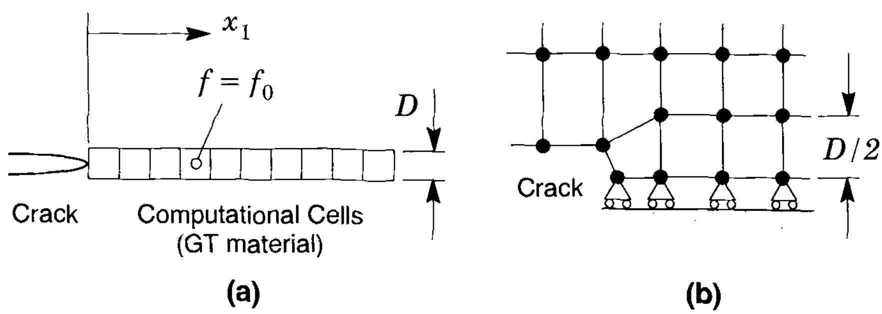

Figure 1 - *Modeling of ductile tearing using computational cells.*

Material properties required for this methodology include: for the background material Young's modulus (E), Poisson's ratio (ν), yield stress (σ_0) and hardening exponent (n) or the actual measured stress-strain curve; and for the computational cells: D and f_0 (and of much less significance f_E). The background material and the matrix material of the cells generally have identical flow properties. Using an experimental J-Δa curve obtained from a conventional SE(B) or C(T) specimen, a series of finite element analyses of the specimen are conducted to calibrate values for the cell parameters D and f_0 which bring the predicted J-Δa curve into agreement with experiment. Once determined in this manner using a specific experimental R-curve, D and f_0 become "material" parameters and remain fixed in analyses of all other specimen geometries for the same material.

Finite Element Models and Numerical Procedures

Small Scale Yielding Model

To generate numerical solutions for stationary cracks under well-defined SSY conditions, we employ the modified boundary layer model [*12*] with the remote-tractions given only by the first term of William's linear elastic solution [*13*], i.e., with the non-singular term $T = 0$. The generated stress fields provide the full *reference* fields used to assess the effects of constraint loss in cracked pipes. Figure 2 shows the plane-strain finite element model for an infinite domain, single-ended crack problem with a initially blunted notch (finite root radius, $\rho = 2.5\mu$m); Mode I loading of the far field permits analysis using one-half of the domain as shown. With the plastic region limited to a small fraction of the domain radius,

$R_p < R/20$, the asymptotic crack-tip stress fields are generated by imposing displacements of the elastic, Mode I singular field on the outer circular boundary ($r = R$) given by

$$u(R,\theta) = K_{\mathrm{I}}\frac{1+\nu}{E}\sqrt{\frac{R}{2\pi}}\cos\left(\frac{\theta}{2}\right)(3 - 4\nu - \cos\theta) \tag{2}$$

$$v(R,\theta) = K_{\mathrm{I}}\frac{1+\nu}{E}\sqrt{\frac{R}{2\pi}}\sin\left(\frac{\theta}{2}\right)(3 - 4\nu - \cos\theta) \tag{3}$$

where K is the stress intensity factor and θ defines the angular variation of in-plane stress components.

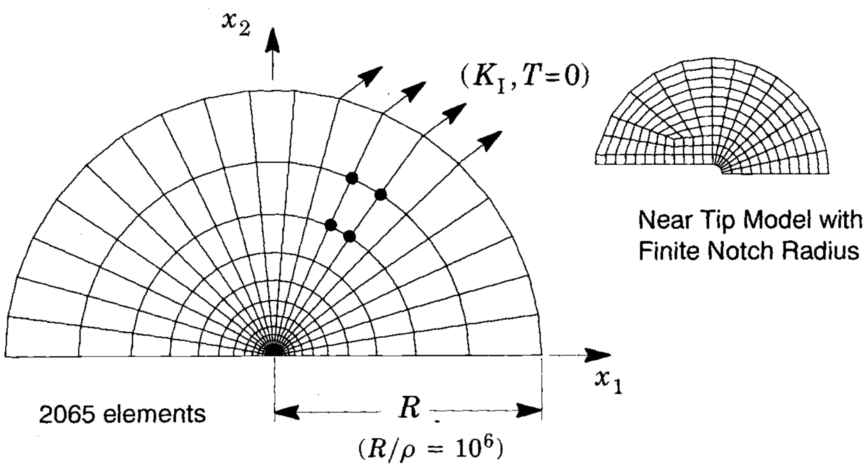

Figure 2 - *SSY model with (K, T) fields imposed on boundary.*

Fracture Specimens

Nonlinear finite element analyses in a plane-strain setting are performed on models for a conventional, side-grooved C(T) specimen and longitudinally pre-cracked pipe specimens. Figure 3(a) shows the finite element model constructed for plane-strain analyses of the 1(T)-C(T) specimen ($B = 25.4$ mm) with $a/W = 0.65$. Here a denotes the crack length and W the specimen width. Symmetry conditions permit modeling of only one-half of the specimen with appropriate constraints imposed on the remaining ligament. The half-symmetric model has one thickness layer of 1622 8-node, 3-D elements; with plane-strain constraints imposed ($w = 0$) on each node. Displacement controlled loading applied at the pin hole indicated in Fig. 3(a) enables continuation of the analyses once the load decreases during crack growth. To simulate ductile crack extension, the finite element mesh contains a row of 117 computational cells along the remaining crack ligament ($W - a$) in a similar arrangement as shown in Fig. 1. The initially blunted crack tip accommodates the intense plastic deformation and initiation of stable crack growth in the early part of ductile tearing.

Plane-strain finite element analyses are also conducted on longitudinally cracked pipes with different crack depth (a) to wall thickness (t) ratios: $a/t = 0.10$, 0.23, 0.54. The pipes have external diameter $D_e = 8\ 5/8$" (219.10 mm) and wall thickness $t = 14.72$ mm. Figure 3(b) shows the finite element model constructed for the longitudinally pre-cracked pipe with $a/t = 0.54$. The half-symmetric model has one thickness layer of 924 8-nodes, 3-D elements with plane-strain constraints ($w = 0$) imposed on each node. Here, the finite element mesh contains a row of 66 computational cells along the remaining crack ligament ($t - a$). Very similar finite element models and mesh configurations are employed for other pre-cracked pipe configurations ($a/t = 0.10$, 0.23).

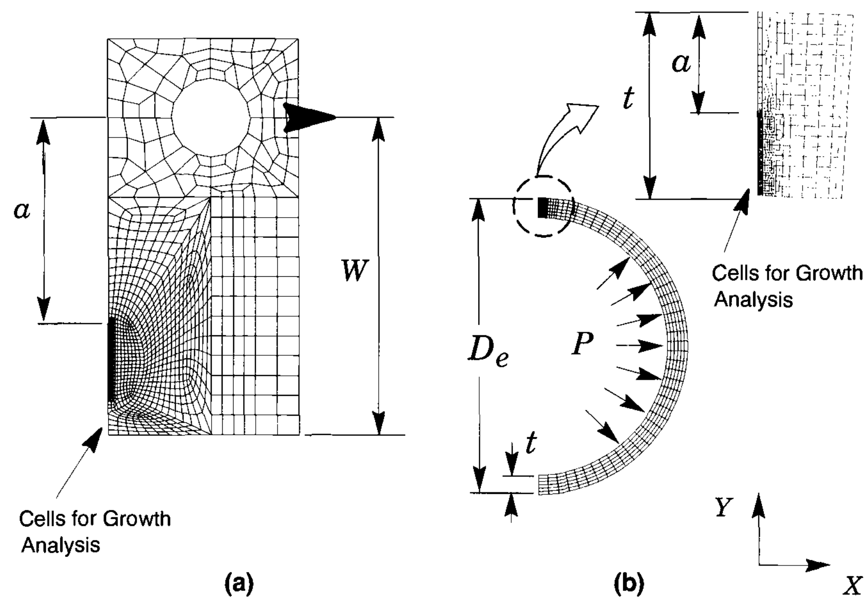

Figure 3 - *Plane-strain finite element models employed in the numerical analyses: (a) C(T) specimen with a/W = 0.65; (b) Pipe with longitudinal crack (a/t = 0.54).*

Numerical analyses to assess effects of constraint loss on crack tip stress fields for longitudinally cracked pipes with different a/t-ratios employ finite element models constructed for pipes with external diameter $D_e = 10$" (254 mm) and wall thickness $t = 9.5$ mm. The a/t-ratios employed in the analyses are $a/t = 0.1$ and 0.5. For these models, a conventional near-tip mesh configuration having a focused ring of elements surrounding the crack front is used with a small key-hole at the crack tip (radius of 2.5μm to maintain similar near-tip refinement with the SSY model). The mesh has 1530 elements with sufficient refinement near the tip to provide adequate resolution of the stress fields. Outside the crack tip region, the mesh details are similar those for the cracked pipes with the computational cells (see Fig. 3(b)).

Constitutive Models and Finite Element Procedures

Flow properties of the matrix elastic-plastic material within the computational cells and of the void-free background material are described by a J_2 flow theory with conventional Mises plasticity. The uniaxial true stress ($\mathcal{S}$) vs. logarithmic strain ($\mathcal{E}$) curve obeys a simple power-hardening model,

$$\frac{\mathcal{E}}{\epsilon_0} = \frac{\mathcal{S}}{\sigma_0} \quad \mathcal{E} \leq \epsilon_0 \; ; \quad \frac{\mathcal{E}}{\epsilon_0} = \left(\frac{\mathcal{S}}{\sigma_0}\right)^n \quad \mathcal{E} > \epsilon_0 \tag{4}$$

where σ_0 and ϵ_0 are the reference (yield) stress and strain, and n is the strain hardening exponent. The constitutive model for porous plastic materials to describe the progressive damage of cells due to the growth of pre-existing voids follows Eq. (1).

The numerical solutions used to assess constraint effects in cracked pipes consider material flow properties represented by $n = 10$ and $E/\sigma_0 = 500$ which is in the range of many moderate strength structural and pipeline steels currently used (e.g., API X60 ~X70). The numerical analyses of the C(T) specimens used in the fracture testing and the cracked pipe specimens used in the burst testing utilize the power law fitting given by Eq. (4) with $n = 11.5$ of the true stress-logarithmic strain curve for the material; this curve is constructed from the measured engineering stress-strain curve for the tested API 5L X70 pipeline steel shown in Fig. 5(a). Other mechanical properties include $E = 206$ GPa and $\nu = 0.3$.

The three-dimensional computations reported here are generated using the nonlinear code WARP3D *[14]* which implements: (1) the GT and Mises constitutive models in a finite-strain setting, (2) cell extinction using the traction-separation model, (3) automatic load step sizing based on the rate of damage accumulation. Evaluation of the J-integral employs a domain integral procedure *[15]* which computes a thickness average value for J over domains defined outside material having the highly non-proportional histories of the near-tip fields. Such domain (path) independent J-values agree with estimation schemes based upon *eta*-factors for deformation plasticity *[16]* and provide a convenient parameter to characterize the average intensity of far field loading on the crack front.

Constraint Effects in Pipes with Longitudinal Cracks

Development of the computational cell methodology incorporating the GT constitutive model relies upon conditions of high stress triaxiality to drive the damage process via void growth. These conditions are typically found along a growing crack front remote from traction-free surfaces. Previous plane-strain cell analyses of thick sections for a nuclear pressure vessel steel conducted by Ruggieri and Dodds *[7]* have provided very good agreement between predicted and measured R-curves. In contrast, their study also shows that the response of the GT model under low stress triaxiality, high plastic strain conditions imposes additional limitations on the ability of the cell methodology to describe crack growth. Thin tubular components may not develop sufficient through-thickness stress triaxiality to provide high levels of crack-tip constraint. This section briefly examines the effects of constraint on the stress fields for the specific problem of a pipe with longitudinal crack that will be discussed later in relation to ductile failure assessments of pipelines.

To quantify the evolving level of stress triaxiality ahead of the macroscopic crack under increased internal pressure, we utilize *reference* fields constructed for small-scale yielding (SSY) conditions using a boundary layer formulation. The modified boundary layer (MBL) model provides a formal (and convenient) framework to assess the degree of near-tip constraint for a cracked pipe based upon the extent of deviation for the stress fields from the high triaxiality, SSY conditions: fields computed for the cracked pipe are compared to SSY fields to define *relative* constraint differences.

Figures 4(a-b) compares the opening mode stresses on the crack plane of the cracked pipe with $D_e = 10$" (254 mm) and wall thickness $t = 9.5$ mm for $a/t = 0.1$ and 0.5, and varying levels of applied loading, as measured by the stress intensity parameter K. The $T = 0$, SSY solution given by the solid line provides the *steady state* reference field obtained upon applying Mode I, elastic displacements given by Eqs. (2) and (3). The numerical solutions were obtained using $E/\sigma_0 = 500$ with $n = 10$. The deformation levels for the cracked pipes corresponding to applied K-fields range from 60 MPa$\sqrt{m}$ to 150 MPa$\sqrt{m}$. In the plots, distances all scale with $(K_I/\sigma_0)^2$ whereas the opening stresses are normalized by σ_0.

The results reveal that constraint over the crack front (as measured by the field differences for the cracked pipe *and* the SSY solution) differs significantly from the levels given by the high triaxiality, SSY model for the entire range of loading and crack configuration. The near-tip stresses for the shallow crack pipe display a strong deviation from the high triaxiality SSY fields, which is fully consistent with several previous studies on constraint effects for shallow crack fracture specimens (see, e.g., Nevalainen and Dodds [*17*] for extensive results). Remarkably, the deeply cracked pipe also shows a severe loss of crack tip constraint upon loading, with the near-tip stresses falling well below the SSY levels for increased K-values. Additional analyses conducted by Ruggieri and Vieira [*19*] for other pipe diameters ($D_e = 20$" (508 mm) with $t = 12.7$ mm, and $D_e = 30$" (762 mm) with $t = 15.9$ mm) with different a/t-ratios and hardening properties reveal essentially similar behavior; to conserve space, these results are not shown here.

The trends displayed in the plots shown in Fig. 4 seem to indicate that low stress states dominate the fracture behavior of cracked tubular structures such as a pipe with longitudinal cracks. Clearly, the interaction of crack tip plastic zones with nearby traction-free surfaces and with global plastic zones affects strongly the near tip stress fields that develop in cracked pipes. Such results underlie potential difficulties with the simple application of GT-based cell models to predict failure in pipelines. This issue is further discussed in latter section which presents an application of the cell model to predict the burst pressure of a thin-walled gas pipeline containing longitudinal cracks with varying crack depth to thickness ratios (a/t).

Experimental Measurements for a Pipeline Steel

Laboratory testing of deep crack ($a/W = 0.65$) 1(T) side-grooved compact tension specimens with thickness $B = 25$ mm provided the tearing resistance curves (J vs. Δa) at room temperature (20°C) to calibrate the cell parameters for a pipeline steel. The material is a HSLA, API 5L X70 steel with yield stress $\sigma_{ys} =$ 484 MPa at test temperature. Table 1 lists the chemical composition for this material. Metallographic examination revealed a well defined microstructure consisting of refined ferrite grains and colonies of perlite, both aligned with the plate rolling direction [22].

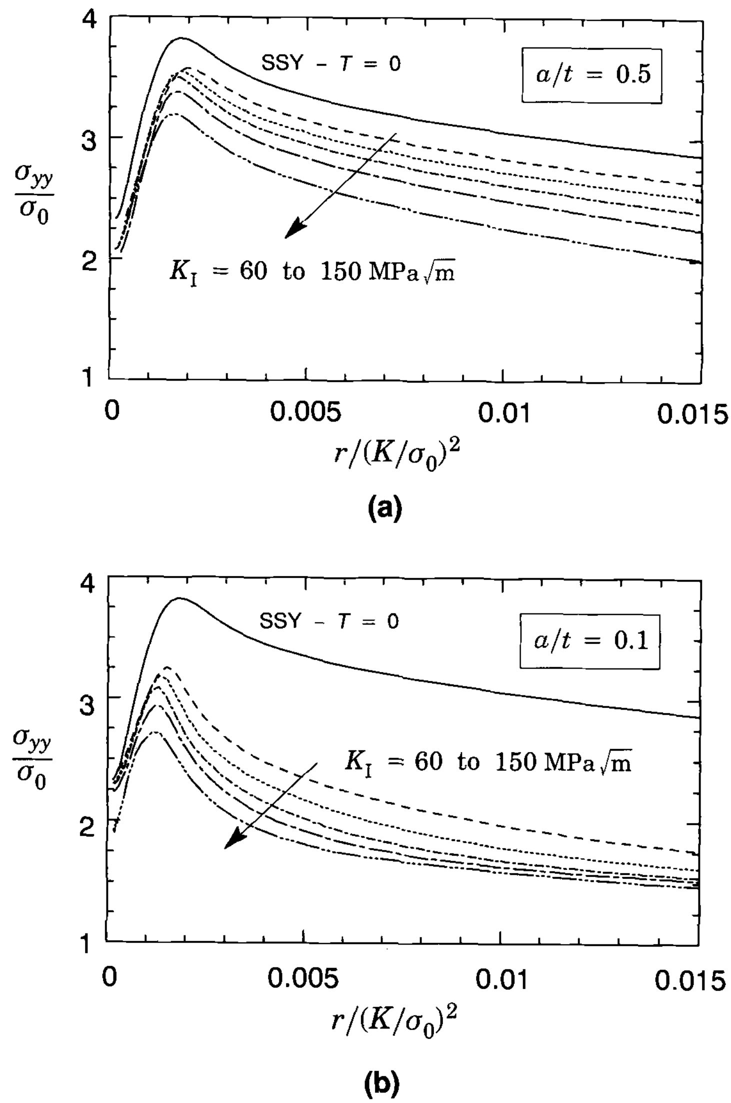

Figure 4 - *Near-tip opening stresses for cracked pipes under internal pressure with $D_e = 10$" (254 mm) and $t = 9.5$ mm for $n = 10$, $E/\sigma_0 = 500$ and different a/t-ratios. Plots are generated for load levels $K_I = 60, 80, 100, 120$ and 150 MPa $\times\ m^{1/2}$.*

Table 1 - *Chemical composition of API 5L-X70 steel (mass %)*

C	Si	Mn	P	Al	Cu	S	Nb	V	Ti	Cr	Ni
0.10	0.17	0.56	0.021	0.021	0.002	0.003	0.052	0.028	0.013	0.12	0.20

Mechanical tensile tests conducted on two different specimen configurations provide the mechanical properties at room temperature. Measured tensile properties for tests performed using rectangular specimens with the same thickness as the steel plate in both longitudinal and transversal directions display only little difference. Tensile tests on standard specimens (ASTM Standard Test Methods for Tension Testing of Metallic Materials - E8M) extracted from the head of the transverse rectangular test specimen also display similar mechanical properties as the plate thickness specimens. Other mechanical properties for the material includes Young's modulus, $E = 207$ GPa and Poisson's ratio, $\nu = 0.3$. Figure 5(a) provides the engineering stress-strain data for this pipeline steel obtained using the standard specimen (average of two tensile tests). Figure 5(b) shows the measured toughness-temperature properties for the material in terms of conventional Charpy-V impact energy (TL orientation). Table 2 summarizes the tensile properties for this material; here σ_{ys} is the 0.2% proof stress, σ_u is the ultimate tensile strength and ϵ_t is the uniform elongation.

Table 2 - *Mechanical properties of API 5L-X70 steel (20°C)*

σ_{ys} (MPa)	σ_u (MPa)	ε_t (%)	σ_u / σ_{ys}
484	590	27	1.22

The 1(T) C(T) specimens were tested at room temperature using an unloading compliance method in the TL orientation to measure the crack growth resistance for the material. After fatigue pre-cracking, the specimens were side-grooved to a depth of $0.1B$ on each side to promote uniform crack growth over the thickness. Figure 6(a) presents the experimentally measured J vs. Δa curves; a simple extrapolation procedure indicates a value of J at initiation of ductile tearing, $J_{Ic} \approx 440$ kJ/m^2. The analysis results represent the center plane J-values vs. crack growth. The fracture tests followed the procedures of ASTM Standard Test Method for Determining J-R Curves (E1152). Experimental J-values are determined using the measured load-load line displacement records.

Micromechanics Calibration of Cell Parameters

The cell model calibration scheme outlined previously has been applied to the pipeline steel employed in this study. The cell size D and initial porosity f_0 define the key parameters coupling the physical and computational models for ductile tearing. The measured resistance curve obtained from testing of the deep crack C(T) specimen is employed to calibrate these parameters.

Consider first the calibration of the cell size D. Competing demands dictate the choice of cell size: (1) D must be representative of the large inclusion spacing to support arguments that it couples the physical and computational model, (2) predicted R-curves scale almost

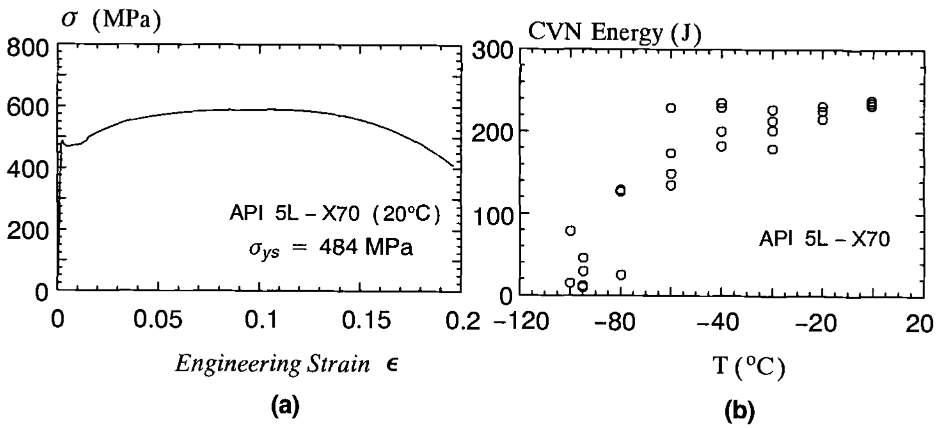

Figure 5 - *(a) Tensile response of API 5L-X70; (b) Measured Charpy-V impact energy for TL orientation.*

proportionally with D for fixed f_0 (a thicker layer requires more total work to reach critical conditions), (3) the mapping of one finite element per cell must provide adequate resolution of the stress-strain fields in the active layer and in the adjacent background material, (4) details of the continuum damage model, and (5) the type of finite element used (linear vs. quadratic). X&S [*4*] suggest the CTOD at initiation of ductile tearing as a good starting value for D, with f_0 then varied to obtain agreement with the experiment. The relationship between CTOD (δ) and J for elastic-plastic materials defined by $\delta = d_n(J/\sigma_{ys})$ [*18*], where d_n denotes a material dependent, dimensionless constant, provides the cell size $D \approx 500$ μm for the material employed in the analyses. However, for the ferritic steels studied thus far with this model, calibrated cell sizes range from 50-200 μm with f_0 in the 0.0001-0.004 range [*4, 7*]. This range of values for D satisfies issue (1) while providing satisfactory resolution of the near-tip fields required in issue (3) after some tearing. Consequently, to avoid potential difficulties associated with too high D-values, the present work adopts $D = 200$ μm as the cell size parameter employed in the numerical analyses.

With parameter D fixed, the calibration process then focuses on determining a suitable value for the initial volume fraction, f_0, that produces the best fit to the measured crack growth data for the deeply cracked C(T) specimen. Figure 6(b) shows the measured and predicted J-Δa curves for this specimen. Predicted R-curves are shown for three values of the initial volume fraction, $f_0 = 0.001$, 0.00075 and 0.000675. For consistency, the location of the growing crack tip in the plane-strain analyses is taken at the cell with $f = 0.1$. This corresponds to a position between the cell currently undergoing extinction and the peak stress location; at this position stresses are decreasing rapidly and the void fraction is increasing sharply. Consequently, the use of slightly different f values, other than 0.1, to define the crack-tip location for plotting purposes does not appreciably alter the R-curves (at a fixed J, the amount of crack extension would vary only by a fraction of the cell size); X&S [*4-6*] discuss this issue in detail. For $f_0 = 0.000675$, the predicted R-curve agrees well with the measured values up to ≈ 4 mm of growth and thereafter lies a little above the measured data. In contrast, the use of $f_0 = 0.001$ produces a much lower resistance curve relative to the measured data. Consequently, the initial volume fraction $f_0 = 0.000675$ is taken as the calibrated (plane-strain) value for the API 5L-X70 steel used in the study.

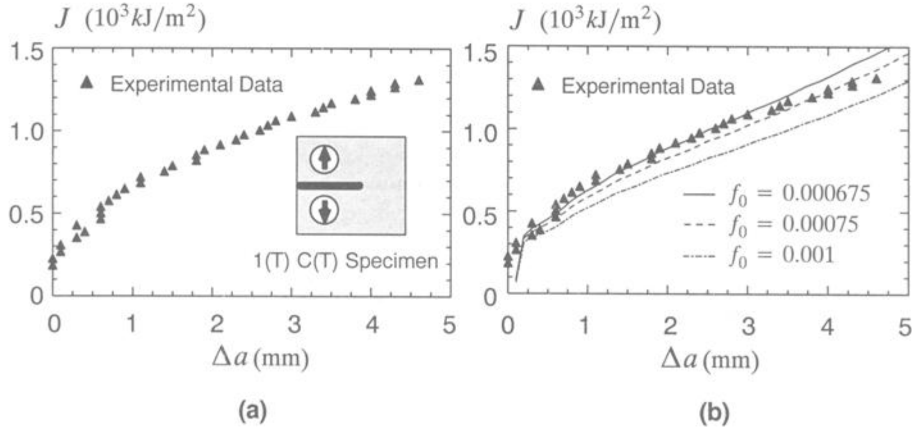

Figure 6 - *(a) Measured R-curve for side-grooved 1(T) C(T) specimen of API 5L-X70 steel; (b) Comparison of measured and predicted R-curve (plane-strain analysis)*

Application to Defect Assessment in Pipelines

Full scale burst tests were performed on longitudinally precracked 8 5/8" O.D. (219 mm) tubular specimens with 14.72 mm wall thickness [*20*]. The experimental program included pipe specimens with different crack depth (a) to wall thickness (t) ratios: $a/t = 0.10$ with $a/c = 0.20$, $a/t = 0.23$ with $a/c = 0.12$ and $a/t = 0.54$ with $a/c = 0.28$. Here, $2c$ is the crack length. The initial semi-elliptical cracks were subjected to a pressure cycle ($\sim$40,000 cycles) to propagate a fatigue crack from the original notch; fatigue crack growth conditions followed ASTM E813. The material is a high strength pipeline API 5L X65 steel with very similar mechanical characteristics to the API 5L X70 steel employed in the fracture testing previously described. The stress-strain response for this material follows closely the tensile response shown in Fig. 5(a) for the API 5L X70 steel with 493 MPa yield stress at room temperature and moderate hardening properties ($\sigma_u / \sigma_{ys} \approx 1.20$); this stress-strain data is used in the numerical analyses.

Predictions of the burst pressure for the pipe specimens using the computational cell methodology require specification of the cell parameters f_0 and D. Ideally, calibration of these parameters based upon R-curves measured using deep-crack specimens extracted from the tested pipe would be used for this procedure. However, these R-curves are not available from the experimental investigation [*20*]. Alternatively, experimental R-curves for conventional laboratory specimens would be suitable to perform the calibration. Because the cell response is governed primarily by the flow and tearing properties of the material, using very similar steel grades with virtually identical flow properties *might* be satisfactory for the calibration process. Here, we adopt the cell parameters previously calibrated ($D = 200\,\mu$m and $f_0 = 0.000675$) for the API 5L X70 as the material-specific parameters to predict the burst pressure for the pipe specimens. The numerical predictions based upon the cell model employ plane-strain finite element analyses of these specimens.

Figure 7 shows the predicted burst pressure for the three pre-cracked pipe configurations. The solid symbols indicate the experimentally measured collapse (burst) pressure for the pipe specimens, denoted p_{burst}, with different a/t-ratios. The comparison between failure predictions and the experimental burst pressure shows an approximate linear dependency of p_{burst} on the a/t-ratio. While the cell model predictions agree relatively well with experimental measures for the shallow cracked pipes ($a/t = 0.10$, 0.23), the failure prediction for the pipe specimen with $a/t = 0.10$ is non-conservative ($\sim 112\%$ of the actual failure pressure). In contrast, the numerical model underpredicts the collapse for the deeply cracked pipe ($a/t = 0.54$) and provides very conservative failure pressure ($\sim 73\%$ of the burst pressure). Moreover, the amount of predicted crack growth, Δa, in all analyses is relatively small ($\Delta a \approx 1$ mm) prior to pipe collapse. This contrasts sharply with the amount of ductile tearing observed in the tested deep-crack C(T) specimens ($\Delta a \approx 5$ mm). Unfortunately, the comparison of ductile tearing predictions with experimental measurements cannot be made here – the amount of crack growth prior to measured burst pressure is not available.

The analyses of constraint effects in pipes with different crack sizes previously presented aid in understanding these trends. As already noted, the behavior of the cell model and void growth response under conditions of varying stress triaxiality influences the amount of crack growth at fixed levels of remote loading (as measured by the internal pressure in the present analyses). For the shallow crack pipe, the lower levels of stress triaxiality that develop ahead of crack tip (see Fig. 4(b)) retards void growth thereby suppressing crack extension for lower load levels. Only with increased internal pressure, when near-tip material becomes sufficiently damaged, can the crack extend and eventually reach a critical size. In contrast, the higher through-thickness stress triaxiality for the deeply-cracked pipe drives void growth for the near-tip cells at higher rates. Consequently, the predicted failure pressure for the deeply cracked pipe is smaller than the failure predictions for the shallow crack pipe at similar amounts of crack growth before pipe collapse. These arguments support the apparent linear dependency of burst pressure on a/t-ratio displayed in Fig. 7.

However, the experimental results also show that the measured burst pressure is relatively insensitive to crack depth which contrasts with the numerical results of Fig. 7. While we have not conducted additional analyses to investigate the sources of such behavior – these studies are currently in progress – we anticipate that 3-D effects are a possible cause for these results. Our 2-D plane-strain analyses of the pre-cracked pipe specimens represent an idealization of the actual pipe geometry; the surface cracks are viewed as infinite longitudinal (planar) cracks which cannot capture the (surface) crack front profile. Since only little crack extension occurs near the free surface of the crack, where plastic constraint remains low over the deformation history, the amount of ductile crack extension at the deepest point of the surface crack is clearly different than the corresponding crack extension for the plane strain crack [*21*]. These effects appear to have a much more important role for the deeply cracked pipe specimens; the plane-strain analyses of shallow crack specimens provide relatively good agreement with experiments. The preliminary results reported here underlie the need of more refined 3-D models to develop the present methodology as an engineering tool for failure assessments of damaged pipelines.

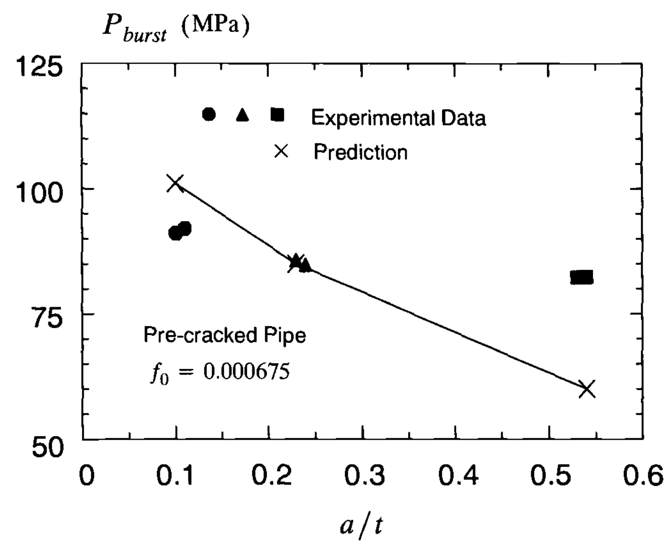

Figure 7 - *Prediction of burst pressure for the pre-cracked pipes with different a/t-ratios using the calibrated cell model.*

Concluding Remarks

This study reports on an exploratory application of the computational cell model to analyze the ductile fracture behavior of a high strength, pipeline steel (API 5L-X70). Plane-strain analyses of tubular structures containing longitudinal cracks with varying crack depth to thickness ratios (a/t) demonstrate a severe loss of crack-tip constraint for cracked pipes under internal pressure. Laboratory testing of a deep crack, compact tension specimen provides the tearing resistance characteristics of the material which is used to calibrate the material-specific parameters, D and f_0. The model accurately reproduces the evolution of crack growth (Δa) with increasing loading, as measured by the J-integral, for this specimen. The cell model incorporating the calibrated cell parameters is then applied to predict the burst pressure of a thin-walled gas pipeline containing longitudinal cracks with varying crack depth to thickness ratios (a/t).

The plane-strain analyses reported here demonstrate the capability of the computational cell approach to simulate ductile crack growth and to predict the burst pressure of thin-walled tubular structures containing crack-like defects. However, our computational studies indicate that fully 3-D models appear to be essential to simulate failure in deeply cracked pipes. Ongoing work with the computational cell framework focuses on 3-D modeling of ductile tearing in cracked pipelines to resolve R-curve transferability issues and to incorporate more realistic failure and crack propagation criteria into the cell methodology.

Acknowledgments

This investigation is supported by the State of São Paulo Research Foundation (FAPESP) through Grant 98/10574-2. This work was also supported by the State of São Paulo Technological Research Institute (IPT-SP) which made available the testing facilities. The authors acknowledge Confab Tubos for providing the API 5L X70 steel plate and the burst pressure data. The authors also acknowledge the many useful discussions and contributions of Prof. Robert H. Dodds (*University of Illinois at Urbana-Champaign*).

References

[1] The American Society of Mechanical Engineers, "Manual for Determining the Remaining Strength of Corroded Pipelines," ASME B31-G, New York, 1984.

[2] Miller, A. G., "Review of Limit Loads of Structures Containing Defects," *International Journal of Pressure Vessels and Piping*, Vol. 32, 1988, pp. 197-327.

[3] Balsara, M. N., "Applications of Advanced Fracture Mechanics to the Assessment of Linepipe Defects," in *Offshore Mechanics and Arctic Engineering Conference (OMAE)*, Vol. V, 1996, pp. 569-585.

[4] Xia, L. and Shih, C. F., "Ductile Crack Growth - I. A Numerical Study Using Computational Cells with Microstructurally-Based Length Scales," *Journal of the Mechanics and Physics of Solids*, Vol. 43, 1995, pp. 233-259.

[5] Xia, L. and Shih, C. F., "Ductile Crack Growth - II. Void Nucleation and Geometry Effects on Macroscopic Fracture Behavior," *Journal of the Mechanics and Physics of Solids*, Vol. 43, 1995, pp. 1953-1981.

[6] Xia, L. and Shih, C. F., "Ductile Crack Growth - III. Statistical Aspects of Cleavage Fracture After Tearing," *Journal of the Mechanics and Physics of Solids*, Vol. 44, 1996, pp. 603-639.

[7] Ruggieri, C., Panontin, T. L., and Dodds, R. H., 'Numerical Modeling of Ductile Crack Growth in 3-D Using Computational Cells," *International Journal of Fracture*, Vol. 82, 1996, pp. 67-95.

[8] Gullerud, A. S., Gao, X., Dodds, R. H., and Haj-Ali, R., "Simulation of Ductile Crack Growth Using Computational Cells: Numerical Aspects," *Engineering Fracture Mechanics*, Vol. 66, 2000, pp. 65-92.

[9] Gurson, A. L., "Continuum Theory of Ductile Rupture by Void Nucleation and Growth: Part I - Yield Criteria and Flow Rules for Porous Ductile Media," *Journal of Engineering Materials and Technology*, Vol. 99, 1977, pp. 2-15.

[10] Tvergaard, V., "Material Failure by Void Growth to Coalescence," *Advances in Applied Mechanics*, Vol. 27, 1990, pp. 83-151.

[11] Xia, L., Shih, C. F., and Hutchinson, J. W., "A Computational Approach to Ductile Crack Growth Under Large Scale Yielding Conditions," *Journal of the Mechanics and Physics of Solids*, Vol. 43, 1995, pp. 398-413.

[12] Larsson, S. G. and Carlsson, A. J., "Influence of Non–Singular Stress Terms and Specimen Geometry on Small Scale Yielding at Crack–Tips in Elastic–Plastic Materials", *Journal of the Mechanics and Physics of Solids*, Vol. 21, 1973, pp. 447-473.

[13] Williams, M. L., "On the Stress Distribution at the Base of a Stationary Crack", *Journal of Applied Mechanics*, Vol. 24, 1957, pp. 109-114.

[14] Koppenhoefer, K., Gullerud, A., Ruggieri, C., Dodds, R., and Healy, B., "WARP3D: Dynamic Nonlinear Analysis of Solids Using a Preconditioned Conjugate Gradient Software Architecture," *Structural Research Series (SRS) 596*, UILU-ENG-94-2017, University of Illinois at Urbana-Champaign, 1994.

[15] Moran, B. and Shih, C.F., "A General Treatment of Crack Tip Contour Integrals", *International Journal of Fracture,* Vol. 35, 1987, pp. 295-310.

[16] Kirk, M.T. and Dodds, R.H., "*J* and *CTOD* Estimation Equations for Shallow Cracks in Single Edge Notch Bend Specimens," *Journal of Testing and Evaluation*, Vol. 24, No. 4, 1993, pp. 228-238.

[17] Nevalainen, M. and Dodds, R. H., "*Numerical Investigation* of 3-D Constraint Effects on Brittle Fracture in SE(B) and C(T) Specimens," *International Journal of Fracture*, Vol. 74, 1995, pp. 131-161.

[18] Shih, C. F., "Relationship Between the *J*-Integral and the Crack Opening Displacement for Stationary and Extending Cracks," *Journal of the Mechanics and Physics of Solids*, Vol. 29, 1981, pp. 305-326.

[19] Vieira, M. H. and Ruggieri, C., "Constraint Effects on Elastic-Plastic Crack Tip Stress Fields for Pipes Under Internal Pressure," *Technical Report BT-PNV-53*, University of São Paulo, 2001.

[20] Confab Tubos S. A., "Defect Evolution During Hydrostatic Testing of an API 5L X65 Grade Linepipe," *Private Report*, 1996.

[21] Gao, X. Falescog, J., Dodds, R. H., and Shih, C. F., "Ductile Tearing in Part-Trough Surface Cracks: Experiments and Cell Model Predictions," *Engineering Fracture Mechanics*, Vol. 59, 1998, pp. 761-770.

[22] Hippert, E. and Ruggieri, C., "Experimental and Numerical Investigation of Ductile Crack Extension in a High Strength Pipeline Steel," in *Pressure Vessels and Piping Conference: Pressure Vessel and Piping Design and Analysis, PVP-Vol. 430* (D. H. Martens, Ed.), 2001, pp.385-392.

Giora Shatil[1] and Alan G. Page[2]

Multiaxial Fatigue Analysis of Interference-Fit Steel Fasteners in Aluminum Al 2024-T3 Specimens

---

Reference: Shatil, G. and Page, A. G., "**Multiaxial Fatigue Analysis of Interference-Fit Steel Fasteners in Aluminum Al 2024-T3 Specimens,**" *Fatigue and Fracture Mechanics: 33rd Volume, ASTM STP 1417*, W. G. Reuter and R. S. Piascik, Eds., ASTM International, West Conshohocken, PA, 2002.

Abstract: Fatigue failure of interference-fit aluminum joints has been investigated by testing several specimens geometries, conducting numerical simulations and using multiaxial fatigue theories. The experiments included center crack, edge crack and uncracked specimens, fitted with a zero load-transfer interference-fit fasteners and tested to failure at different cyclic loads. An elastic-plastic contact finite element (EPFE) analysis was carried out to simulate the local combined interference and cyclic stress distribution in the specimens near the fastener's hole. The simulation and test results were used in a multiaxial fatigue analysis that examined several theories including the critical plane approach (McDiarmid theory) and the octahedral stress parameter (Crossland theory). The experimental lives were correlated by calculating the multiaxial fatigue parameters at different locations along the hole edge. A fairly good correlation was obtained by using the maximum values of the multiaxial stress parameters obtained from the EPFE analysis along the specimens hole edge. The analysis indicated that the fatigue critical location for crack initiation was not always at the location of the maximum nominal principal stress at the hole edge therefore a uniaxial stress analysis may lead to a non-conservative failure prediction for these type of joints.

Keywords: multiaxial fatigue, interference fit joints, aluminum alloy, finite element analysis, generalized Neuber theory, thermal stress analysis

---

[1] Senior Lecturer and [2] Research Assistant, Structural Integrity Group, School of Engineering, CEMS, University of the West of England, Frenchay Campus, Bristol BS16 1QY, UK.

Introduction

Fatigue life of interference-fit joint structures has been the subject of investigation for several decades [1]. The method is widely used in the aerospace industry, usually to join aluminum alloy structures by employing steel or titanium fasteners. For such structures under cyclic loading, the critical location for initiation of fatigue cracks is usually in the plate at the edge of fastener holes due to localised stress concentration. It has been shown previously that radially expanding the fastener hole by using an interference fit (IF) fastener, or other methods, such as cold working, improves the structure life due to the introduction of residual compressive hoop stresses, which act to offset the cyclic (tensile) load [1-4].

In a typical airframe, the cyclic stresses at a fastener joint do not exceed yield stress of the material. However, the residual stress from the IF is often high enough to induce some permanent plastic deformation. This makes the fatigue analysis more complex since: a. the localized stress or strain state is in multiaxial state, b. the stress/strain field is beyond yield and, c. for a typical load sequence each cycle damage is related to the previous material history. The stress state in a typical element of material on the surface of a fastener bore that is subjected to interference fit and cyclic load is shown in Figure 1. It demonstrates the multiaxial stress nature of the problem, where the loads exerted from the fastener interference are usually constant and the applied structural load is cyclic and random. In this work, the load interaction between the fastener and the plate was simplified by assuming that no structural load was applied to the fastener. This is commonly called "a zero load-transfer" situation.

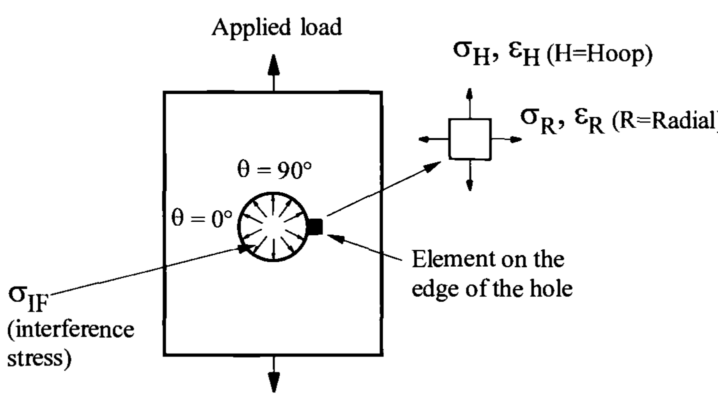

Figure 1 – *Nomenclature of stresses in a typical interference fit component*

For estimation of cycles to crack initiation up to an engineering size (usually 1 mm) it is necessary to know the stress or strain fields during the life cycle in the critical area around the hole edge. Traditionally, a stress concentration factor K_t was used for high cycle fatigue (HCF). It has been suggested that there is a relationship between K_t and a fatigue strength factor K_f via a material notch sensitivity factor, q. However, this approach does not consider the localized inelastic deformation that may occur even at the

HCF regime. Most modern fatigue life techniques include some form of modifications to account for the inelastic deformation. For instance the Neuber's rule [*5*] is widely used for uniaxial application of prismatic bodies stating that for a local yield, the square of the elastic stress concentration is the product of the strain concentration and stress concentration factors. Glinka [*6*] has proposed a similar approach based on energy conservation principals.

However, the above methods are principally limited to uniaxial stress and are not suitable when a multiaxial stress field exists. Therefore, fatigue techniques were developed that usually apply one of the following: a fully nonlinear finite element (FE) analysis or a simplified analysis combining partly numerical and partly analytical approach. The simplified approach uses elastic finite element analysis and an analytical method to take into account the localized inelastic deformation. This numerical-analytical approach has been used previously [*7*] by employing FE results in a deformation plasticity model. A different approach has been developed [*8*] using a generalized Neuber rule to multiaxial stress state, making some simple assumptions regarding the relationship between the principal stresses and using a proportional elastic-plastic theory [*9*].

Numerous theories have been suggested in the past and still being developed every so often to estimate the service lives of components subjected to complex pattern of multiaxial fatigue load and extensive literature reviews exist [*10*]. Traditional methods were usually an extension of the static yield criteria, using for example, a modification of the Mises energy distortion theory to account for the mean or non-cyclic stresses. However, it is now widely accepted to relate the fatigue analysis to the observed damage and crack development. One such method uses the critical plane approach and was developed for high strain [*11*] and for the lower strain regime [*12*].

Previously [*4,13*] it was shown that an improvement in the life prediction of fastener attached joint components could be achieved by using multiaxial fatigue parameters and simple local stress estimation methods. In the following, this approach was further investigated by using results of an extensive experimental program of "zero load transfer" interference fit components. Two methods were used to estimate the experimental cyclic local stress and strain. In the first instance, the local stresses were estimated by using the generalized Neuber's method [*14*] where the principal stresses from an elastic FE analysis were used as input. In the second instance, local stresses were estimated directly in an elastic-plastic finite element (EPFE) analysis.

Correlation of the life of the test components was carried out by comparing three multiaxial parameters: the maximum stress parameter, the Crossland parameter and the McDiarmid parameter.

Experimental Program and Results

All tests were carried out using the same batch of 6 mm-thick aluminum alloy 2024-T3 plate and 1/4" stainless steel fasteners supplied by Airbus UK, Filton (Bristol). The plate material chemical composition per specification by weight (%) is: 4 Cu, 1.5 Mg, 0.6 Mn and remainder Al [*15*].

Fatigue tests were conducted using a 250kN Instron servo-hydraulic fatigue machine at constant amplitude under load control. A positive nominal stress ratio R (R=min/max stress) was used to prevent buckling. The tests were performed at different cyclic maximum, and cyclic mean loads at a range of fatigue life between approximately one thousand and one million cycles to failure. Three basic specimens were investigated, as shown in Figure 2. Testing of the edge crack and center crack specimens consist of specimens having three different crack lengths. These specimens represented a cracked repair section that has been stop-drilled and fitted with an interference plug. The center hole geometry was used to examine the effect of the interference levels on fatigue life, with no artificial cracks in the structure apart from manufacturing defects.

A total of fifty five fatigue tests were carried out as follows: twelve edge crack specimen tests with two different crack lengths (a = 35.8, 16.7mm); twenty four center crack specimens with three different crack lengths (a = 7.94, 33.4, 71.5mm); fourteen tests of center hole, uncracked specimens with three different interference fit levels and finally five tests were conducted using uncracked center hole specimens without a fastener (open hole), Appendix 2. An interference level of approximately 1.4% was used in all the cracked specimen tests. In the uncracked center-hole specimens program the high, medium and low interference fit (IF) levels refer to interference levels of approximately 1.5%, 0.5% and 0.1% respectively.

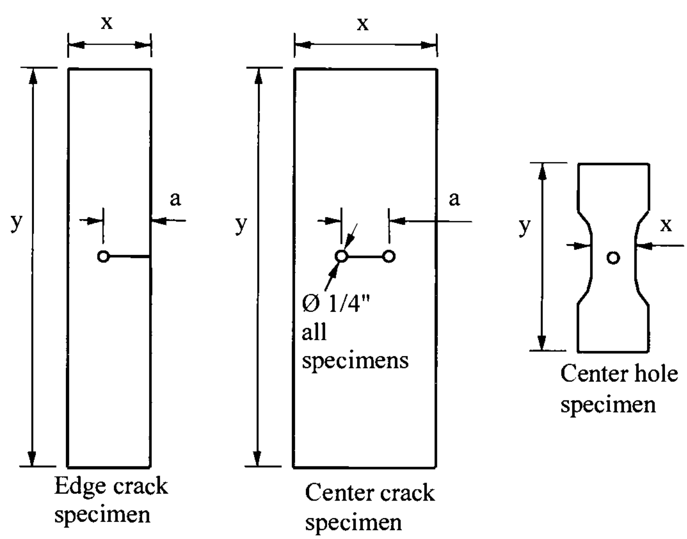

Figure 2 – *Specimens geometry, (detailed dimensions, Appendix 2)*

The detection of crack initiation and propagation was carried out by two different optical methods: a. a video camera recorded the specimen's surface near the interference fastener and a magnified image was recorded on a 21" monitor, with crack length resolution of about 0.1mm, b. surface scanning using thermoelastic stress analysis (TSA) [*16*], with crack resolution of about 0.001mm. An example of the TSA method is given in Appendix 1. In all tests, life to failure was defined as a 1mm crack ahead of the interference hole. However, as to be expected, a different failure mechanism was observed for the two basic types of specimens. During the edge and center crack specimen tests, the initiation stage was about 60 per cent of life, followed by a period of crack propagation. In contrast, the uncracked specimens exhibited 90 to 95% of total life without detection of cracks and in some tests, no crack initiation was detected prior to specimen failure.

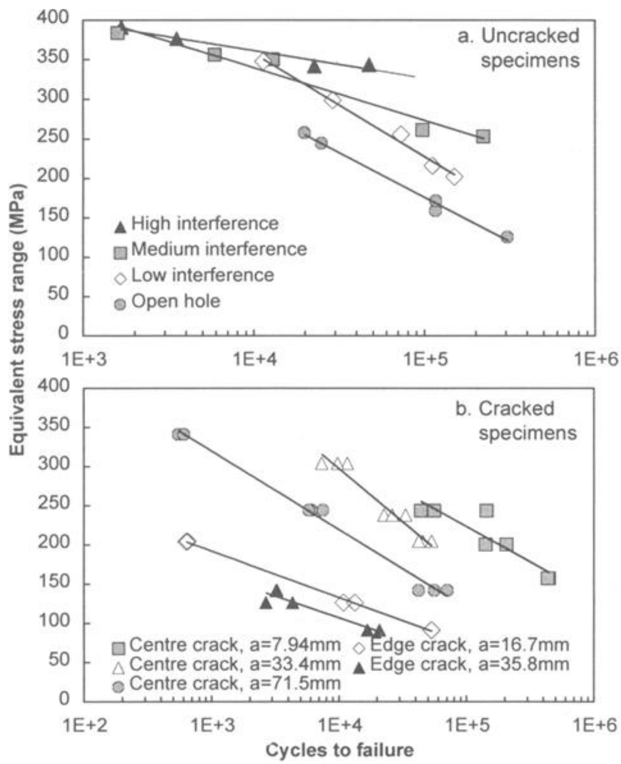

Figure 3 – *Interference fit specimens fatigue life results*

The experimental lives to failure as a function of the net section stress range is shown in Figure 3a (center hole specimens) and Figure 3b (Edge and center cracked specimens). Since different mean stress levels were used in the tests the net section stress shown in Figure 3 was calculated using a Walker type relationship [*13*].

Figure 3a compares the life to failure of different nominal IF specimens tested under range of cyclic loads, with the open hole specimen results. The beneficial effect of higher IF in extending the specimen lives is clearly demonstrated. For example, for an equivalent stress range of 250 MPa, the low IF specimens failed after about 60×10^3 cycles, medium IF specimens failed after about 200×10^3 cycles and by extrapolating the high IF specimen results a failure beyond 10^7 cycles is predicted. However, Figure 3a also shows that for life below $30x10^3$ cycles, or at stress range of above 300 MPa (near material yield) the effect of the IF is greatly reduced, which is due to the increase in high strain deformation.

In Figure 3b the center cracked specimens lives are compared with the edge cracked specimens in term of the applied equivalent stress range. Fatigue lives of the center crack specimens are approximately a factor of ten longer than those of the edge crack specimens. Finally, comparison between the lives of the uncracked and cracked specimens, Figures 3a and 3b, shows that, as expected, the uncracked specimens lives (Figure 3a) are larger than those of the cracked specimens (Figure 3b) for any cyclic stress level.

Finite Element Analysis

A finite element model was constructed for each specimen's geometry using plane-stress eight nodes quadrilateral elements and contact elements between the fastener and the plate employing a commercial code (ABAQUS). A fine mesh was used near the hole edge and the load was applied on the plate boundary. A cyclic stress strain response was used for the elastic-plastic analysis. The stable hysteresis cycle in the tests was estimated by applying a sequence of minimum to maximum load and maximum back to minimum load. Stress range at critical nodes around the fastener hole was obtained by using the difference between the stress at maximum and minimum loads.

Each specimen was modeled by applying the measured interference fit level and the test load range. The finite element elastic-plastic results were used directly in a multiaxial fatigue analysis while the elastic finite element results were used for the generalized Neuber's analysis described below.

Generalized Neuber Analysis

At a stress concentration such as a central hole in a plate with uniaxial applied load, the maximum elastic uniaxial local stress can be determined using the theoretical stress concentration factor K_t [*17*]:

$$K_t = 2 + \left[1 - \left(\frac{a}{w}\right)\right]^3 \qquad (1)$$

where a is the hole diameter and w is the plate width. For the center-hole specimens, where a=6.32mm and w=25.0mm, K_t is 2.42. The theoretical elastic uniaxial local stress σ_{max} can then be determined by using the global stress S. Neuber's rule [*5*] states that the theoretical stress concentration factor K_t is equal to the geometric mean of the actual stress and strain concentration factors.

To employ the Neuber analysis, the stress-strain curve for the material is needed. A material stress-strain curve can be described by a Ramberg-Osgood relationship:

$$\varepsilon = \frac{\sigma}{E} + \left[\frac{\sigma}{k'}\right]^{\frac{1}{n'}} \tag{2}$$

using the material cyclic strength coefficient k' and cyclic strain hardening exponent n'. A generalized Neuber method was proposed [*8*] to estimate an existing multiaxial stress state in a plate, around interference-fit fastener. The uniaxial stress concentration factor K_t is redefined as an equivalent stress concentration factor K_{tq}, using an equivalent theoretical elastic maximum stress $\sigma_{e,q}$:

$$K_{tq} = \frac{\sigma_{e,q}}{S} \tag{3}$$

A von Mises type flow criterion is used to determine the equivalent theoretical elastic maximum stress $\sigma_{e,q}$:

$$\sigma_{e,q} = \sqrt{(\sigma_{e1}^2 - \sigma_{e1}.\sigma_{e2} + \sigma_{e2}^2)} \tag{4}$$

Principal stress values σ_{e1} and σ_{e2}, correspond to hoop and radial stresses at the hole (Figure 1). Stresses in the through-plate direction were neglected, assuming a state of plane-stress. The multiaxial form of the Neuber method also uses equivalent values in the cyclic stress-strain curve:

$$\varepsilon_q = \frac{\sigma_q}{E} + \left[\frac{\sigma_q}{k'}\right]^{\frac{1}{n'}} \tag{5}$$

For the aluminum alloy 2024-T3 tested, k'= 655MPa, n'= 0.065, and E = 69.2GPa. The final form of the generalized Neuber procedure can be described by:

$$\varepsilon_q = \frac{(K_{tq}.S)^2}{E.\sigma_q} \tag{6}$$

The values of the local equivalent stresses, $\sigma_{e,q}$ were obtained from an elastic finite element analysis. K_{tq} was then determined for 7.5° intervals around the specimen hole circumference. The equivalent maximum stress σ_q was calculated in a Newton-Raphson iterative procedure by simultaneously solving equations (5) and (6). To obtain the principal stress or strain components from the Neuber procedure Hencky's flow rule and variable Poisson's ratio [*9*] were used.

A C computer program [*14*] was developed and used to calculate the principal elastic-plastic stress and strain values for the center-hole specimens. An example of the stresses occurring around the hole obtained from this procedure is shown in Figure 4 and compared to elastic and elastic-plastic finite element results for two levels of interference fit, medium (Figure 4a) and low (Figure 4b).

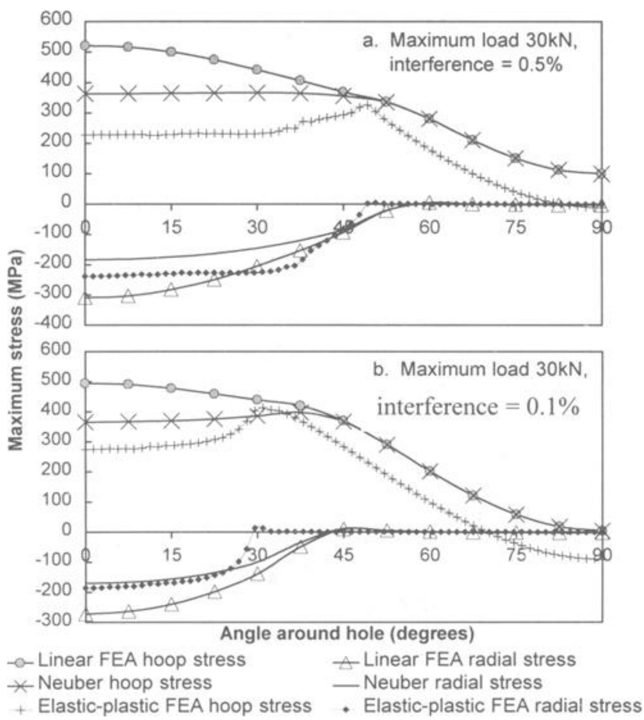

Figure 4 – *Maximum stress distribution near the hole edge of 30kN load range center-hole specimens with medium, 0.5% and low, 0.1% interference fit levels*

Multiaxial Fatigue Analysis

The interference fit specimens' lives were correlated using three multiaxial fatigue stress parameters, namely: the maximum local principal stress range (in this case it was identical to the maximum hoop stress); the Crossland equivalent stress parameter [*4*] and the McDiarmid shear stress parameter [*12*].

Crossland Parameter

The Crossland parameter is based on a combination of the equivalent shear stress amplitude and the maximum hydrostatic stress reached during a load cycle. It has been used previously [*4*] for investigating fatigue life of cold worked fastener holes in a similar aluminium alloy 2024-T3 where the parameter was given as:

$$T_{eqa} + 1.07\, P_{max} \tag{7}$$

where:

T_{eqa} = Equivalent shear stress amplitude
P_{max} = Maximum hydrostatic stress reached during a load cycle

The equivalent shear stress amplitude T_{eqa} is calculated using:

$$T_{eqa} = \sqrt{J_{2a}} = \frac{1}{6}\left[(\sigma_{1a} - \sigma_{2a})^2 + (\sigma_{1a} - \sigma_{3a})^2 + (\sigma_{2a} - \sigma_{3a})^2\right] \tag{8}$$

where:

σ_{1a} = Amplitude of principal stress 1 = (σ_{1max} - σ_{1min})/2
σ_{2a} = Amplitude of principal stress 2 = (σ_{2max} - σ_{2min})/2
σ_{3a} = Amplitude of principal stress 3 = (σ_{3max} - σ_{3min})/2

The maximum hydrostatic stress reached during a load cycle P_{max} is calculated using:

$$P_{max} = \frac{1}{3}(\sigma_{1max} + \sigma_{2max} + \sigma_{3max}) \tag{9}$$

where:

$\sigma_1, \sigma_2, \sigma_3$ = Maximum principal stresses ($\sigma_1 > \sigma_2 > \sigma_3$)

Since the elastic-plastic stress-strain values assumed a state of plane-stress, the terms in the Crossland parameter were modified as follows:

$$\sqrt{J_{2a}} = \frac{1}{3}\left[\sigma_{1a}^{\;2} - \sigma_{1a}\sigma_{2a} + \sigma_{2a}^{\;2}\right] \tag{10}$$

$$P_{max} = \frac{1}{3}(\sigma_{1max} + \sigma_{2max})$$

McDiarmid Parameter

The McDiarmid parameter [*12*] is based on finding a critical plane on which fatigue failure will occur. Fatigue strength is a function of the maximum shear stress and the normal stress occurring on the plane of the maximum shear stress. The critical plane for failure is that subjected to the greatest value of the parameter:

$$\tau_{amp} + C_1\sigma_{n,max} \tag{11}$$

where:

τ_{amp} = maximum shear stress amplitude
$\sigma_{n,max}$ = maximum normal stress occurring on the plane of maximum shear stress amplitude,
C_1 is a material constant, taken as 0.15

For cyclic conditions the McDiarmid parameter is therefore calculated using:

$$\tau_{amp} + 0.15(\sigma_{amp} + \sigma_{mean}) \tag{12}$$

where:

σ_{amp} = Stress amplitude normal to the plane
σ_{mean} = Mean stress normal to the plane

The maximum value of shear stress τ_{max} is always at an angle 45° to the maximum principal stresses, and is calculated using:

$$\tau_{max} = \frac{1}{2}(\sigma_1 - \sigma_3) \quad \text{where:} \quad \sigma_1 \rangle \sigma_2 \rangle \sigma_3 \tag{13}$$

On the plane of the maximum shear stress, the normal maximum stress is given by:

$$\sigma_{n,max} = \frac{1}{2}(\sigma_1 + \sigma_3) \tag{14}$$

Correlation of Results

In Figure 5 the elastic-plastic finite element (EPFE) multiaxial fatigue life correlation (Figures 5e-5h) is compared with results obtained from the generalized Neuber (G-N) analysis (Figures 5a-5d) employing the maximum (hoop) stress parameter (Figures 5a, 5b, 5e, 5f) and the Crossland parameter (Figures 5c, 5d, 5g, 5h). Correlation using the McDiarmid parameter is shown in Figure 6. Interference stresses below material yield were predicted for the low IF specimens (0.1% IF) and therefore the elastic-plastic FE simulations were not carried out for those tests. The generalized Neuber analysis was carried out for the center hole uncracked specimen fatigue results and it was considered

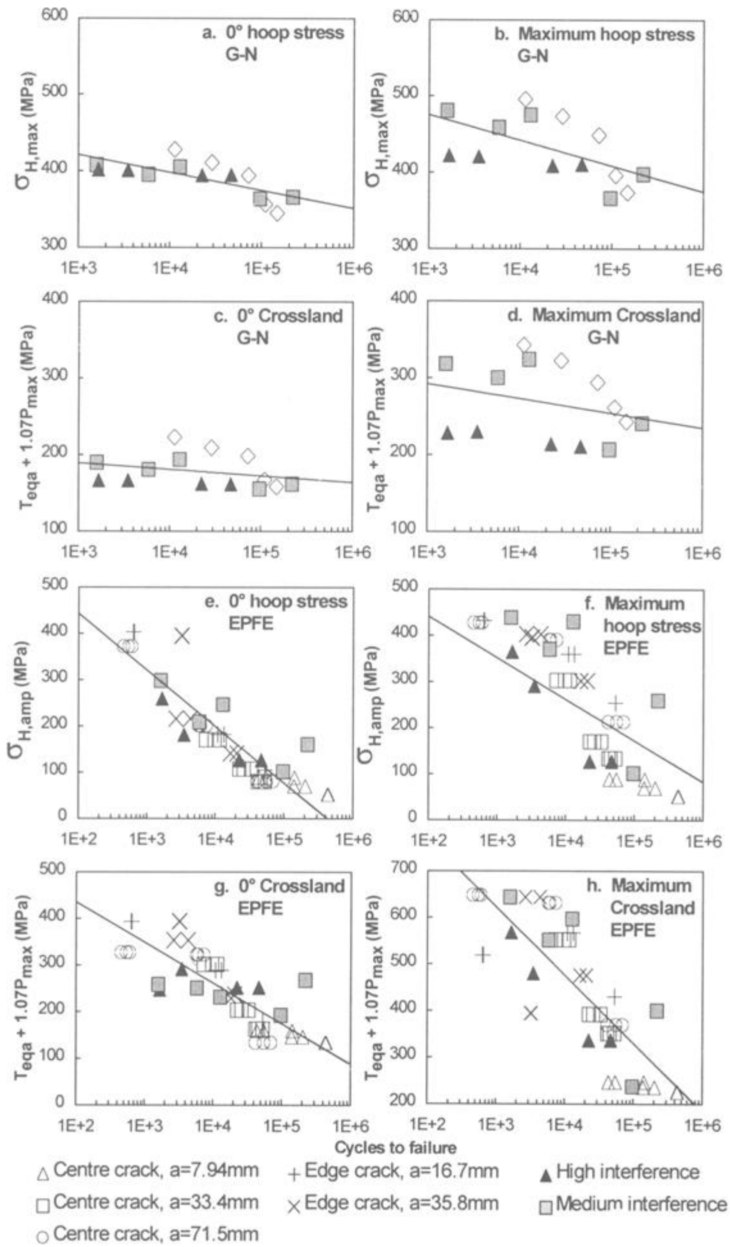

Figure 5 – *Correlation of interference-fit specimen life using local maximum stress and Crossland parameters obtained from elastic-plastic FE and generalized Neuber analyses*

unsuitable for the cracked specimens. All the multiaxial fatigue correlation analyses were carried out twice. First for the stresses at the $\theta = 0^0$ location (notch root) and second, at fixed increments around the fastener hole to obtain the maximum overall value of the multiaxial parameter.

Figures 5a - 5h have shown some similar trends. It appears that a best overall correlation was obtained using the Crossland parameter and stresses at the $\theta = 0^0$ location (Figures 5g and 5c) and most scatter appeared using the maximum hoop stress parameter (Figures 5d and 5h). Comparing the left column ($\theta = 0^0$ location analyses, Figure 5) with the ones on the right (the maximum stress analyses) it appears that a better correlation is obtained in the left column irrespective of the analysis used. However, the stress parameter values in the figures on the right are higher than those values in the left in all the cases, indicating that a safer design should employ the maximum values obtained around the interference fit hole for a particular applied cyclic load.

Finally, the two types of local stress analyses used have not shown a significant difference in terms of the correlation of results. The Neuber analysis (Figures 5a-5d) predicted slightly lower values of stresses in comparison to the EPFE analysis (Figures 5e-5h). This could have been due to the limitations of the Neuber analysis and is discussed later. An improvement of the correlation of the experimental results using a combination of the McDiarmid parameter and elastic-plastic finite element analysis is depicted in Figure 6.

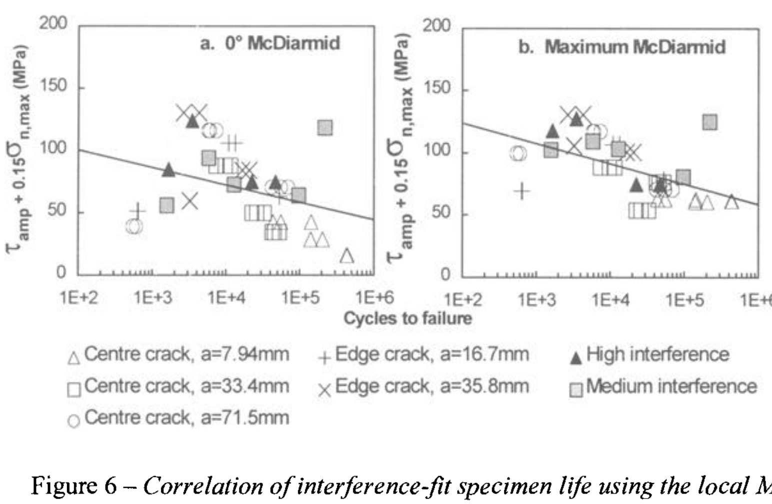

Figure 6 – *Correlation of interference-fit specimen life using the local McDiarmid parameter obtained from elastic-plastic finite element analysis* (EPFE)

Discussion

The main difference between the fully elastic-plastic FE analysis and the generalized Neuber method is the simulation of the interference fit stresses. The EPFE is taking into account the complete stress field developed during the fatigue cycle. This includes both a non-linear geometrical interaction on the interface of the plate/fastener and non-linear elastic-plastic behavior. On the other hand, currently the elastic-plastic Neuber program [*14*] does not consider the elastic-plastic interference interaction and assumes an elastic interaction, using the elastic FE analysis results. This may explain the higher local stresses obtained using the EPFE analysis (Figures 5e-5f) in comparison to the Neuber method, Figures 5a-5d.

The generalized Neuber method applied here was principally developed for proportional loading where two main conditions exist. First, an assumption regarding no rotation of principal stress directions during the loading cycles and second, a fixed ratio of the two principal elastic or elastic-plastic strains at the critical location:

$$\frac{\varepsilon_{e2}}{\varepsilon_{e1}} = \frac{\varepsilon_2}{\varepsilon_1} = \text{constant} \tag{15}$$

For the tested specimens the first condition was satisfied since the hoop and radial stresses were always the principal stresses near the hole surface. The second condition was further investigated for the center-hole specimens. Figure 7 shows the principal strain ratio for a medium interference fit specimen loaded at 5kN steps up to 40kN, for different angles around the hole. Figure 7 demonstrates that the ratio at the $\theta = 0°$ and $90°$ locations are different, but remain reasonably constant during loading. However, there is a significant non-constant transition between the $\theta = 0°$ and $90°$ locations.

The maximum local values of the Crossland parameter, Figure 5d, were found to occur at a location of about $\theta = 30°$ on the low interference specimens edge, between $\theta = 37.5°$ to $52.5°$ on the medium interference specimens edge, and at about $\theta = 90°$ on the high interference specimens using the generalized Neuber method. Similar results were also obtained from the EPFE analysis. This indicates crack initiation at a location away from that predicted by an elastic non-interference analysis of maximum stress concentration at the $\theta = 0^0$ location (notch root). This theoretical prediction requires further experimental work to investigate the crack initiation locations.

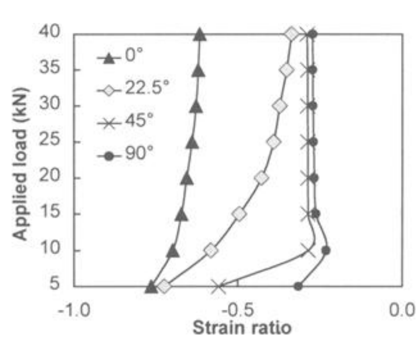

Figure 7 – *Principal strain ratio as a function of the applied load at locations around the edge of a center-hole medium interference fit specimen*

Finally, the Deltatherm TES system [*16*] was used to observe initiation of cracks during the fatigue tests, described in Appendix 1. This has shown promising prospects for an early detection of small surface cracks.

Concluding Comments

1. Fatigue failure of interference-fit aluminum joints has been investigated by testing several specimens geometries, conducting numerical simulations and using multiaxial fatigue theories. The beneficial effect of interference-fit level on fatigue life was demonstrated.
2. Numerical and combined numerical-analytical analyses were used to simulate the material response at the critical location near the fastener hole interface surface and a good agreement has been obtained between the two methods.
3. Multiaxial fatigue parameters improved the correlation of the test results and the use of the parameters is recommended in the structural integrity design of interference-fit components.

References

[1] Hsu, Y. C. and Forman, R. G., "Elastic-Plastic Analysis of Infinite Sheet Having A Circular Hole Under Pressure," *ASME Journal of Applied Mechanics*, Vol. 42, No. 2, 1975, pp 443-473.

[2] Nadai, A., "Theory of expanding of boiler and condenser tube joints through rolling," *ASME Journal of Applied Mechanics*, Vol. 65, 1943, pp 865-880.

[3] McNeill, A. M. and Heston, A. W., "Coldworking Fastener Holes – Theoretical Analysis, Methods of Coldworking, Experimental Results," *Proceeding ASM Conference on Residual stress in design, process and material selection*, Pennsylvania, 1987, pp 193-204.

[4] Duprat, D., Campassens, D., Balzano, M., and Boudet, R., "Fatigue Life Prediction of Interference Fit Fasteners and Cold Worked Holes," *International Journal of Fatigue*, Vol. 18, No. 8, 1996, pp 515-521.

[5] Neuber H., "Theory of Stress Concentration for Shear-Strained Prismatic Bodies with Arbitrary Nonlinear Stress-Strain Low," *Journal of Applied Mechanics*, ASME, 1961, pp 544-550.

[6] Glinka G., "Calculation of Inelastic Notch-Tip Strain-Stress Histories Under Cyclic Loading," *Journal of Engineering Fracture Mechanics*, Vol. 22, No. 3, 1985, pp 839-854.

[7] Heyes P. J., Milsted, M. G. and Dakin, J., "Multiaxial fatigue assessment of automative chasis components on the basis of finite-element models", *Multiaxial fatigue and design*, ESIS 21, 1996, pp. 461-475.

[8] Hoffman M. and Seeger T., "A generalised method for estimating multiaxial elastic-plastic notch stresses and strains", Part 1: Theory; Part 2: Applications, *ASME Journal of Engineering Materials & Technology*, Vol. 107, 1985, pp. 250-260.

[9] Mendelson, A., "*Plasticity: Theory and application*", Kreiger publishing company, 1983 (Reprint).

[10] Yu, B. R. and Lee, S. B., "A critical review on multiaxial fatigue assessments of metals", *International Journal of Fatigue*, Vol. 18, No. 8, 1996, pp. 235-244.

[11] Brown M. and Miller K. J., "A theory for fatigue failure under multiaxial stress-strain conditions", *Proceedings of the Institute of Mechanical Engineering,* Vol. 187, 1973, pp. 745-755.

[12] McDiarmid, D. L., "A shear based critical-plane criterion of multiaxial fatigue failure for design life prediction", *Journal of Fatigue and Fracture of Engineering Materials & Structures*, Vol. 17, No. 12, 1994, pp. 1457-1484.

[13] Shatil, G. and Smith R. M., "Local approach analysis of the fatigue performance of aluminum alloy fastener joints", *Proceedings Fatigue 2000*, Engineering Integrity Society (EIS), Cambridge, 2000, pp. 567-574.

[14] Page, A. G., "Multiaxial fatigue analysis of fastener joints", BEng final project report, University West England, Bristol, UK, 2000.

[15] Irvine, C. A., "*Military handbook MIL-HDBK-5G*", Global Engineering, 1995.

[16] "*Deltatherm user guide*", Stress Photonics Inc., USA, 1998.

[17] Peterson, R. E., "*Stress concentration factors*", John Willey and Sons, 1974.

Acknowledgment

We wish to thank the Fatigue and Damage Tolerance Department, BAE SYSTEMS, Airbus UK Ltd, Bristol, for their contribution of experimental and numerical material presented in this paper and to EPSRC for the TSA facility.

Appendix 1 – Thermoelastic stress analysis (TSA)

The TSA system uses an infrared sensor to measure the change in temperature occurring in a material when a cyclic load is applied. A "focal plane array" is used, which measures the temperature changes for the whole viewing area at one time. The change in temperature is given by:

$$\Delta T = -\frac{\alpha . T}{\rho . C_p}\left(\Delta\sigma_x + \Delta\sigma_y\right) \tag{1a}$$

where:

ΔT = Load-induced temperature change.
α, ρ, C_p = material thermal expansion coefficient, density and absolute temperature, respectively.
$\Delta\sigma_X$, $\Delta\sigma_Y$ = Change in stress in x and y directions.

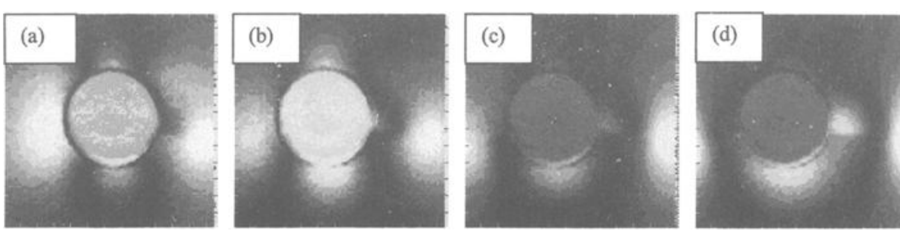

Figure 1a – *Crack initiation observation in a 23.5kN low interference fit (0.1%) fatigue test. The light areas on the plate indicate higher stresses, and dark areas indicate lower stresses. Before crack initiation, the light areas either side of the fastener are symmetrical about the vertical center line. (a) 132780 cycles, crack initiation RHS (b) 141480 cycles, crack growth RHS, (c) 147370 cycles, crack initiation on the LHS and (d) 149120 cycles, just before failure*

Appendix 2 - ***Experimental program and results***

Specimen type	Equivalent net Stress range, MPa	x, mm	y, mm	a, mm	Number of tests	Average cycles to failure[1]
Edge crack	126	60	520	35.8	2	3,514
	91	60	520	35.8	2	18,836
	126	40	520	16.7	2	12,153
	91	40	520	16.7	2	53,307
	141	60	520	35.8	2	3,252
	204	40	520	16.7	2	641
Center crack	244	60	520	7.94	3	81,294
	201	60	520	7.94	2	173,347
	157	60	520	7.94	2	438,342
	304	80	520	33.4	3	9,625
	238	80	520	33.4	3	27,453
	204	80	520	33.4	3	47,120
	341	120	520	71.5	2	580
	244	120	520	71.5	3	6,508
	142	120	520	71.5	3	56,617
Center hole – high IF	343	25	260	-	2	35,112
	384	25	260	-	2	2,597
Center hole – medium IF	257	25	260	-	2	159,318
	353	25	260	-	2	9,415
	384	25	260	-	1	1,588
Center hole – low IF	202	25	260	-	1	150,080
	216	25	260	-	1	111,630
	256	25	260	-	1	72,965
	299	25	260	-	1	29,100
	348	25	260	-	1	11,400
Center hole – open hole	125	25	260	-	1	307,000
	159	25	260	-	1	116,360
	172	25	260	-	1	117,054
	244	25	260	-	1	25,000
	258	25	260	-	1	19,880

[1] 1mm crack at failure

Stephen M. Graham[1] and Jeff Mercier[2]

Applications of Scaling Models and the Weibull Stress to the Determination of Structural Performance-Based Material Screening Criteria

Reference: Graham, S. M. and Mercier, J., "**Applications of Scaling Models and the Weibull Stress to the Determination of Structural Performance-Based Material Screening Criteria,**" *Fatigue and Fracture Mechanics: 33rd Volume, ASTM STP 1417*, W. G. Reuter and R. S. Piascik, Eds., ASTM International, West Conshohocken, PA, 2002.

Abstract: Certification of new welding systems for naval ship construction involves demonstrating that the system will provide adequate structural performance under severe loading conditions. The standard test used by the Navy to demonstrate that a weld can withstand extensive plastic deformation in the presence of a flaw is the Explosion Bulge/Explosion Crack Starter test. This test uses a rather large specimen fabricated from 1 in. or 2 in. (25.4 or 50.8 mm) thick plate that is explosively loaded. Consequently, conducting an explosion bulge test series can be very expensive. The test is also rather extreme in the level of plastic deformation developed in the plate. The loading condition simulates the strain rate that might be caused by direct shock in an underwater explosion, but is not necessarily representative of typical surface ship loading rates.

For certification purposes it would be desirable to develop relevant structural performance requirements and then use a simple, inexpensive test to determine if the welding system will meet the requirement. The objective of this study was to determine what combination of material properties the weld system must have to obtain the required performance. Structural performance was assessed by conducting tests on a structural performance element that was representative of plate thickness and loading conditions. Scaling models are presented that compare the structural performance element with the traditional Explosion Crack Starter specimen. Failure probabilities were calculated using the Weibull stress concept, the transition temperature and the Master Curve. The transition temperature and probability of failure are incorporated into criteria that the weld system must meet to ensure that the structure will have the desired performance.

[1]Senior Engineer, Survivability Engineering Department, Anteon Corporation (work performed under contract to the Naval Surface Warfare Center Carderock Division, 9500 MacArthur Blvd., West Bethesda, MD 20817-5700).

[2]Senior Mechanical Engineer, Concurrent Technologies Corporation, 100 CTC Drive, Johnstown, PA. 15904.

The proposed approach for determining structural performance-based material selection criteria was used to interpret the results from a series of tests on HSLA-65 welds. Fracture toughness, structural elements and the Explosion Crack Starter tests were conducted to characterize the fracture performance of the various welds. The results from these tests are presented and the relationship between the material properties and the resulting structural performance is discussed.

Keywords: constraint, fracture toughness, HSLA-65, transition, toughness scaling, Weibull stress, master curve, reference temperature, explosion bulge

Introduction

The current weld certification process depends heavily on fracture tests that provide more of a qualitative measure of fracture behavior than a material property. Tests such as the Charpy V-Notch, Dynamic Tear Test, Explosion Bulge (EXB) and the Explosion Crack Starter (ECS) are widely used to characterize fracture behavior. The ultimate acceptance or rejection of a weld system is determined by the outcome of the EXB/ECS test series. The Charpy and Dynamic Tear tests are used primarily for quality control.

The Explosion Bulge and the Explosion Crack Starter tests were developed at the Naval Research Lab in the 1950's [*1, 2*]. At the time it was believed that the only way to determine fracture performance was to test full-scale structural details. However, the cost of these tests was prohibitive, and it became clear that fracture usually originated from welds, so simpler tests were developed to evaluate welds fabricated from plates of thicknesses used in ship construction. The original intent of the tests was to evaluate the ability of welds to resist fracture under severe conditions of dynamic loading (explosive) and extensive plastic deformation. The basic test entails placing a welded plate over a die with a circular cutout and the setting off an explosive charge above the weldment. The weldment is exposed to repeated shots until it either reaches a predetermined level of plastic deformation (as measured by a reduction in thickness) or a crack extends into the hold-down region.

The ECS test was intended to investigate the ability of the weld system to arrest a running crack that initiated in the weld. The running crack initiated from a notched brittle weld bead placed on the surface of the weld specifically to start a crack. The first shot in the test series was intended to crack the brittle weld bead, and the second shot evaluated the ability of the weld and baseplate to resist growth of the crack.

The EXB test evaluated the ability of the weld system to resist cracking. For this test there are no intentionally introduced flaws. The weldment is subjected to repeated explosive loadings until a predetermined level of plastic deformation is reached. If a crack extends into the hold-down region before this level is reached, then the weldment fails the test.

The EXB and ECS tests were adopted as part of the weld certification process in MIL-STD-2149(SH), "Standard Procedures for Explosion Testing Ferrous and Non-Ferrous Metallic Materials and Weldments."

Concerns over cleavage fracture

The primary concern is that a welded structure not exhibit a cleavage mode of fracture. Typically, if a weld system is on the upper shelf of its transition behavior for the lowest service temperature, fracture will occur by ductile tearing and will absorb a lot of energy by plastic deformation. Ductile fracture generally occurs in a slow stable manner under the action of increasing crack driving forces for displacement controlled loading. On the other hand, cleavage fracture results in rapid, unstable crack growth with little plastic deformation. This brittle mode of fracture can occur for welds that are in transition or on the lower shelf of their transition behavior. In the transition region fracture behavior is unpredictable, in a deterministic sense, and a transition to cleavage fracture can occur even after extensive plastic deformation and/or ductile crack growth. Consequently, the primary objective of certification testing is to ensure that the weld system is not in transition for the service conditions.

The ECS test has gained considerable importance as the ultimate test to determine a weldment's resistance to fracture. It is important to keep in mind that for welds in transition, the outcome of an ECS test is dependent on the probability of a critical cleavage initiation site being located in the high stress region and oriented perpendicular to the local tensile stresses. A typical certification test series may involve only two ECS specimens, which is not sufficient to obtain a statistical measure of the probability of fracture.

Recent understanding of the cleavage fracture process

It has been understood for some time that cleavage fracture follows a "weakest link" statistical model. The links in this case are cleavage initiation sites within the metal. Fracture will occur when the local stress exceeds the critical stress of an initiation site. Since the distribution of initiation sites and their critical stresses are random, fracture in the transition region can only be addressed using a probabilistic approach. Recent developments in the understanding of cleavage fracture have led to the development of models that allow the probability of failure to be determined based on fundamental material properties that can be measured using simple tests.

The influence of constraint on fracture behavior

These models have shown that the state of stress and the development of plasticity at the tip of a crack can have a significant effect on fracture behavior. When the flow of plasticity is contained, the stresses in the fracture process zone become elevated and the transition to cleavage is more likely to occur. The development of a tri-axial tensile stress state at a crack tip, and the resulting resistance to the development of plasticity, is referred to as constraint. Section thickness, crack depth and type of loading influence the development of plasticity at a crack tip, and consequently these are the factors that determine the level of constraint in a structure.

The EXB/ECS test was developed before the influence of constraint on fracture behavior was fully understood. It was widely believed to be an extreme test that severely tested a material's resistance to fracture. Recent research on the influence of crack depth and loading on constraint has shown that surface cracks have inherently low constraint. Although the deformation and loading rate in an ECS test are severe, the constraint level of the crack that is initiated from the brittle weld bead does not have high constraint.

Too much reliance on the EXB/ECS tests for weld system certification can lead to two possible undesirable consequences; either the ECS test is more severe than the service conditions for the intended application, in which case some acceptable weld systems would be eliminated in the screening process, or, the ECS has lower constraint than the structure, in which case a weld system that may have an unacceptable probability of fracture in the application is determined to be acceptable. To avoid these undesirable outcomes, the constraint of the intended application should be considered in the certification process.

Constraint-based material screening criteria

One example where it is beneficial to consider constraint is in a welded ship hull, where large pieces of relatively thin plate (1/2 in. to 3/4 in. or 12.7 to 19.0 mm) are loaded predominantly in tension. For ductile metals, the thickness of the plate is not sufficient to constrain plastic flow in the thickness direction. However, the in-plane dimensions of the plate tend to contain plasticity for through thickness cracks. The constraint of this structure can be higher than an ECS specimen, even though the level of deformation and the loading rate may be much lower. Consequently, the probability of cleavage fracture before gross section yielding is reached may be higher in the structure than in the ECS test. The relevance of the ECS test to the structure is reduced even further when the lowest service temperature is significantly less than the temperature at which the ECS tests are conducted. As stated previously, temperature can have a dramatic effect on probability of cleavage fracture. This is a case where successful ECS tests could lead to the conclusion that the probability of cleavage is lower than it actually is in the structure. The true risk of fracture would be better represented if the constraint of the structure were taken into account in the weld system certification process.

New approach to certification

It is not practical to test full scale, or even sub-scale structures as part of the weld system certification process. It would be desirable to characterize the probability of fracture of a structure using measurements of material properties from small specimens. Measurements of tensile properties and fracture toughness have been used to predict structural behavior at temperatures that are fully on the lower shelf or the upper shelf of the transition curve. Until recently, the tools were not available to account for the influence of constraint and make predictions of behavior in the transition region. The development of the Weibull stress concept, along with the tools to numerically model cracked structures, has provided a means to make probabilistic assessments of fracture behavior in transition. The challenge is to incorporate these new tools into the weld certification process, and thereby avoid undesirable conservatism or risk.

Prediction Of Cleavage Probability Using The Weibull Stress

The concept of the Weibull stress is based on the "weakest link" theory of cleavage fracture. The theory underlying the Weibull stress has been extensively covered in the literature [*3* - *9*] and consequently will not be presented here. The Weibull stress can be thought of as a driving force for cleavage fracture. The probability of cleavage fracture is related to the Weibull stress (σ_w) by the following equation.

$$P_f(\sigma_w) = 1 - \exp\left[-\left(\frac{\sigma_w - \sigma_{w,\min}}{\sigma_u - \sigma_{w,\min}}\right)^m\right] \qquad (1)$$

The scaling parameter, σ_u, is the Weibull stress under plane strain, small-scale yielding conditions corresponding to 63.2% probability of failure (the mean of the Weibull distribution). The threshold Weibull stress, $\sigma_{w,min}$, represents a minimum value below which cleavage will not occur under plane strain, small-scale yielding conditions. The shape parameter, m, also referred to as the Weibull modulus, determines the shape or spread of the Weibull distribution. This parameter is directly related to the distribution of cleavage initiating particles.

The information required to calculate the Weibull stress are the Weibull modulus and the stress and strain fields in the volume surrounding the tip of the crack. The Weibull modulus is a material property that is determined through a calibration process involving fracture toughness testing of small specimens. The stress and strain fields can be determined using finite element methods. The stress and strain fields must be determined for increments of increasing load or displacement in order to determine the evolution of the Weibull stress and the potential energy release rate, J.

Although it has not been proven, it is reasonable to expect that the Weibull modulus is relatively independent of temperature since temperature does not affect the distribution of initiating particles. Temperature primarily effects σ_u and the flow properties (yield and strain hardening). Since σ_u is related to the mean fracture toughness at a given temperature, the effect of temperature on σ_u should be related to the Master Curve [*10*] since it describes the effect of temperature on fracture toughness in transition. For this study the reference temperature (T_o) and the Master Curve were used to determine the mean fracture toughness (K_o) at any temperature. The scaling parameter, σ_u, was then the Weibull stress in a plane strain SSY model with an applied K of K_o. The connection of the Weibull stress with the Master Curve provides the capability to calculate probability of failure for a structure at any temperature in the transition region based on fracture toughness tests conducted at one temperature near lower shelf. It is still necessary to measure or estimate the flow properties at the temperature of interest; however, tensile tests are simple and inexpensive.

The influence of constraint on cleavage failure probability was investigated by applying the Weibull stress concept to the analysis of three cracked body geometries representing a range of constraint. The high constraint condition was modeled using a deeply cracked single-edge bend [SE(B)] specimen (a/W = 0.55). The combination of the deep crack and the bending stress field in the remaining ligament create a condition of high constraint. An intermediate constraint condition was modeled using a shallow cracked single-edge tension [SE(T)] specimen (a/W = 0.25). The low constraint geometry was the ECS specimen with a shallow surface crack (a/t = 0.20). These three geometries were analyzed using finite element methods to determine stresses in the vicinity of the crack tip. The details of that analysis are presented in the following section. These stresses were then used to calculate Weibull stress and failure probabilities. The comparison of the three geometries provides some insight into the significance of the ECS test and the influence of temperature on cleavage failure.

Numerical Modeling

The SE(B) specimen was 0.39 in. (9.9 mm) thick, 0.78 in. (19.8 mm) wide and had a crack length to width ratio (a/W) of 0.555. The SE(T) specimen was 0.50 in. (12.7 mm) thick, 4.0 in. (101.6 mm) wide and had a crack length to width ratio (a/W) of 0.25. A drawing of the SE(T) specimen is shown in Figure 1. A linearly varying displacement was applied to each end of the SE(T) to simulate the restraint conditions of the wedge grips. The slope of the displacement boundary condition was chosen based on comparison of predicted and measured load-displacement traces from actual tests of this geometry. The ECS specimen was a plate 20.0 in. (508 mm) square and 1.25 in. (31.8 mm) thick. It had a semi-elliptical surface crack 0.25 in. (6.4 mm) deep and 0.60 in. (15.2 mm) long in the center. The length and depth of the crack were chosen to approximate the crack introduced by the brittle weld bead in the first shot of an ECS test. The brittle weld bead was not modeled. The specimen dimensions and flow properties were chosen to model validation tests that will be discussed in the next section.

The material flow properties were modeled using a Mises piece-wise linear, isotropic hardening constitutive model. The true stress-strain curve, shown in Figure 2, was obtained from tests conducted on an HSLA-65 weld. The effect of temperature on the flow properties was not included in this analysis because tensile data was only available at room temperature. Review of tensile data for low-alloy steels in MIL-HDBK-5C, "Metallic Materials and Elements for Aerospace Vehicle Structures," indicated that there is only an 8% increase in yield and a 6% increase in ultimate at 200°F (111°C) below room temperature, which covers the range of temperatures for the tests that will be discussed in the validation section.

The mesh for all three models was refined in the crack tip region to facilitate calculation of J and to accurately capture the stress and strain fields in the fracture process zone (approximated by the volume where $\sigma_1 > \sigma_o$). For all three specimens the crack tip was modeled using a keyhole with a root radius of 0.00015 in. (0.004 mm). For the SE(B) and SE(T) models, the radial dimension of the first ring of elements was 0.0003 in. (0.008 mm) with 15 rings of elements in the radial direction and 18 in the circumferential direction. The SE(B) had 4 elements through the half thickness and the SE(T) had 6. The radial dimension for the first ring of elements in the ECS specimen was 0.0006 in. (0.015 mm) with 9 rings of elements radially, 12 in the circumferential direction and 14 along the crack half-perimeter. All three specimens were modeled using ¼ symmetry and 8-node isoparametric elements.

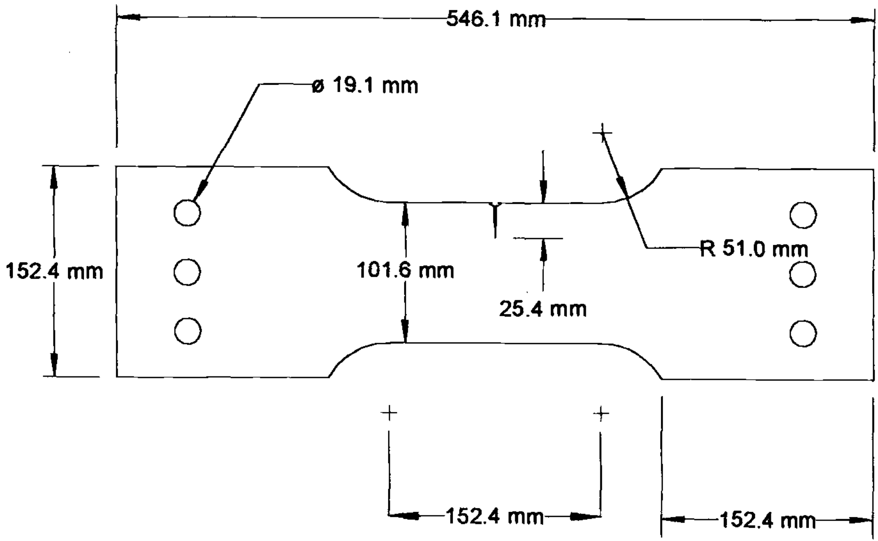

Figure 1— *SE(T) specimen used to model intermediate constraint condition.*

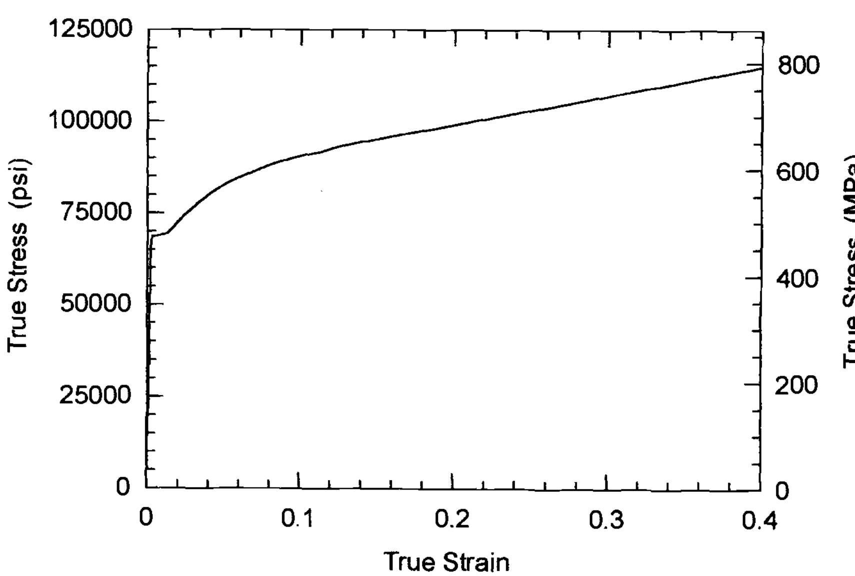

Figure 2—*True stress - true strain curve for typical HSLA-65 70 series weld.*

A plane strain modified boundary layer model was used to generate the Weibull stress under conditions of small scale yielding (SSY) [*5*]. The crack tip mesh refinement and the flow properties were the same as were used in the other analyses. Three separate SSY analyses were conducted with thicknesses equivalent to the crack front length in each of the three specimen geometries. For the SE(B) and the SE(T), the crack front length was the same as the thickness, however, for the ECS the crack front length was the perimeter of the half-ellipse, which yields an effective thickness (B_{eff}) of 0.866 in. (22.0 mm).

The analysis of these models was conducted using the WARP3D finite element code [*11*]. The stress, strain and displacement files generated by WARP3D were read into the code WSTRESS [*12*] to calculate the Weibull stress. A Weibull modulus of 10 was chosen based on recent calibrations for a variety of steels.[3] The Weibull stress predictions for the three geometries are shown in Figure 3. In this plot the Weibull stress has been normalized by the yield strength (σ_o = 67 433 psi or 465 Mpa) and J has been normalized by the product $b\sigma_o$, where b = 1.0 in. or 25.4 mm for all three specimens. Note that for all of the results presented here, b is a non-dimensionalizing parameter, <u>not</u> the remaining ligament.

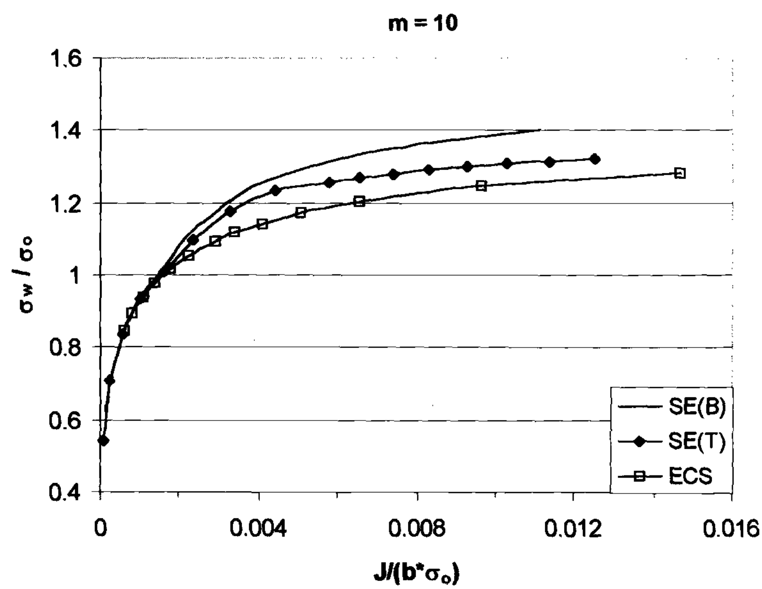

Figure 3—*Weibull stress for SE(B), SE(T) and ECS specimens (m = 10).*

[3] Private communication with R. H. Dodds Jr.

For this analysis the crack was assumed to be stationary. The consequence of this assumption is that the Weibull stress starts to level off for large values of J. This is caused by a decrease in constraint as plasticity spreads away from the crack tip. The effect of ductile crack growth is to increase the volume of metal that could potentially lead to cleavage, and thereby elevate the Weibull stress [*13*]. The increased volume counters the loss of constraint; the net effect being that the slope of the Weibull stress versus J curves at large J would increase for all three geometries.

Constraint Scaling Models

The Weibull stress is a function of thickness (stressed volume), so comparison of Weibull stress versus J curves for geometries with different thickness does not provide a direct indication of how constraint influences the Weibull stress. The influence of constraint can be separated from the thickness effect by comparing the calculated J values with SSY J-values at the same Weibull stress, where the SSY values are calculated using the same crack front length. This removes the thickness effect and reveals the full effect of constraint. The resulting curves provide a constraint scaling model [*6*], as shown in Figure 4 for the same three specimens. The decrease in the slope of the curves is a result of constraint loss. The deeply cracked SE(B) has the highest constraint, and in fact, shows a slight elevation in constraint above the SSY reference. The bending stress in the remaining ligament of the SE(B) tends to contain the plasticity and elevate the constraint relative to the SE(T). The SE(T) specimen maintains plane strain constraint up to a $J/(b\sigma_o)$ of about 0.004, which corresponds to the point at which the approximate plane-stress plastic zone size on the surface extends out to half the specimen thickness. The ECS specimen begins to lose constraint very early in the loading. This is due to the shallow surface crack ($a/t = 0.20$) and the influence of the free surface on the development of plasticity along the crack front. Note that this constraint loss occurs in spite of the fact that the surface pressure loading places the cracked surface in bi-axial tension.

The Influence of Constraint and Thickness on Failure Probability

Probability of failure is dependent on both constraint and thickness. Increasing the thickness results in an increase in the Weibull stress (due to increased volume of stressed metal at the crack tip) and a decrease in $\sigma_u - \sigma_{w\text{-}min}$ (due to decrease in K_o). Since probability of failure increases with the ratio $(\sigma_w - \sigma_{w\text{-}min})/(\sigma_u - \sigma_{w\text{-}min})$, an increase in thickness increases the probability of failure. However, the thickness effect is small relative to the constraint effect, as demonstrated by comparing the probability of failure curves for the three specimens at a constant excess temperature (see Figure 5). The ECS specimen has the lowest probability of failure, even though it has the largest effective thickness. The curves in Figure 4 show that the ECS specimen has the lowest constraint, therefore probability of failure has a strong correlation with constraint.

The Influence of Excess Temperature on Failure Probability

The influence of excess temperature $(T - T_o)$ on failure probability will be demonstrated by examining failure probability for the SE(T) specimen at three values of excess temperature (see Figure 6). The curves show a dramatic decrease in failure probability as excess temperature is increased. There also appears to be a decrease in the maximum failure probability at high J values as excess temperature is increased. Since the effect of temperature on yield strength has not been included in this analysis, the observed effect is entirely due to the variation in K_o with temperature, as described by the Master Curve.

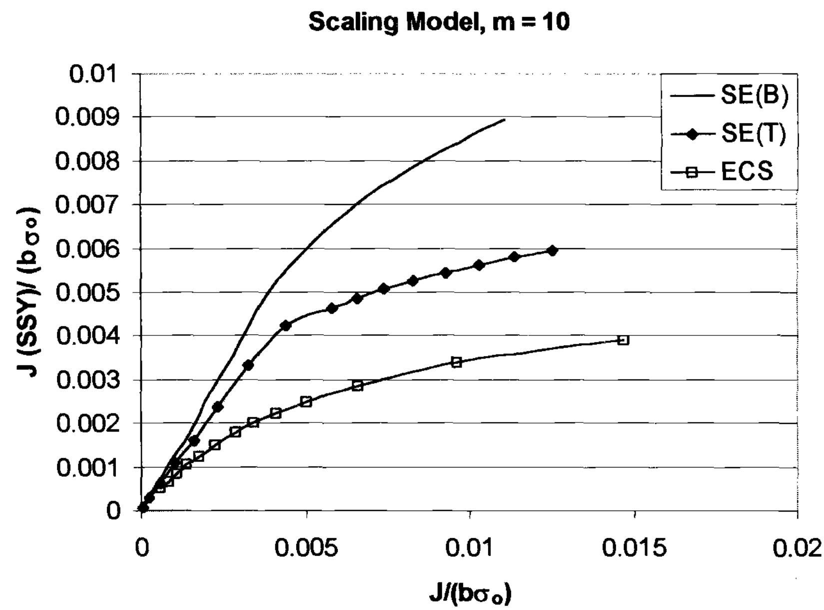

Figure 4—*Constraint Scaling Model based on Weibull Stress*

Interpretation of Test Results for HSLA-65 Welds

The Weibull stress concepts presented previously will be used to interpret test results obtained on a series of welds made using HSLA-65 plate and various 70-series consumables. The welds were created as part of a program to develop optimized welding procedures for fabrication of ship structures from HSLA-65 steel. The welds created for this program are shown in Table 1. Three different thicknesses of plate were used to make the welds, ½ in., 5/8 in. and 1 ¼ in. (12.7 mm, 15.9 mm and 31.8 mm). The ½ in. (12.7 mm) and 5/8 in. (15.9 mm) thick plates were chosen because these are the plate thicknesses that are typically used in fabrication of ship structures. The EXB/ECS specimens could not be made from these plates because there are no established procedures for EXB/ECS testing of plates this thin. Consequently, 1 ¼ in. (31.8 mm) thick plates were used to fabricate welds for EXB and ECS specimens. The welds made from these plates are summarized in Table 2.

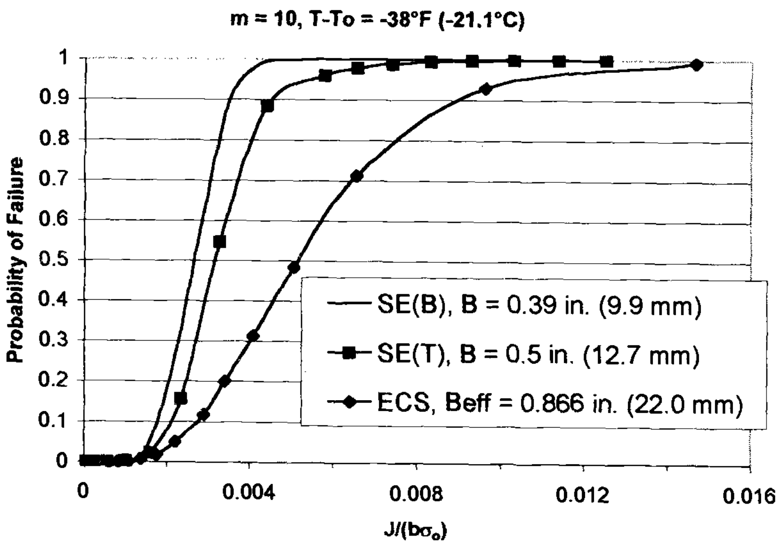

Figure 5—*The influence of constraint and thickness on probability of failure.*

Description of Tests

A variety of tests were run on each weld to characterize the material properties and the fracture behavior. These tests included Charpy, tensile, fracture toughness (conducted according to E1921-97, "Standard Test Method for Determination of Reference Temperature, T_o, for Ferritic Steels in the Transition Range"), EXB/ECS and a structurally relevant test referred to as the Fracture Toughness Structural Performance Element (FTSPE), which is basically a SE(T) loaded up to net section yield. The tensiles, Charpys, fracture toughness and FTSPE specimens for a particular consumable were all made from the same weldment. The tensile tests were all run at room temperature and the yield strengths ranged from 68.1 ksi to 76.5 ksi (470 to 528 Mpa) while the ultimate strengths ranged from 78.8 ksi to 90.9 ksi (543 to 627 Mpa). The results of the Charpy tests are summarized in Figure 7. The reference transition temperatures for the ½ in. (12.7 mm) and 5/8 in. (15.9 mm) welds are also provided in Table 1.

The results from the EXB and ECS tests are summarized in

Table 3. Note that all of the welds passed either the EXB or ECS tests with one exception, and in that specimen the crack propagated through the baseplate, not the weld. If the EXB/ECS test series were used for certification of these welds, all of them would be

considered acceptable. Unfortunately, it is difficult to apply the results from these tests to the evaluation of the welds in the ½ in. (12.7 mm) and 5/8 in. (15.9 mm) thick plates because the cooling rates were different. The thicker plate used for the EXB/ECS specimens resulted in higher cooling rates and slightly higher yield strengths (69.3 to 82.3 ksi, or 478 to 568 Mpa).

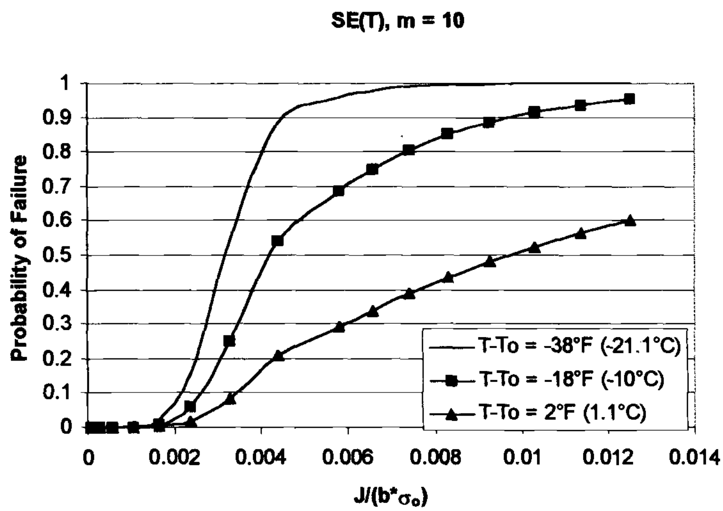

Figure 6—*Effect of excess temperature on probability of failure for a SE(T) specimen (m = 10).*

The FTSPE test was developed in response to concerns about how well the ECS specimen represented the geometry and loading of a ship hull. As mentioned previously, the ECS specimen was made from plate that is thicker than what is used in typical surface ships, and the loading is intended to cause significant plastic deformation at explosive loading rates. The FTSPE specimen was designed to simulate an edge-cracked plate in the hull of a ship subjected to an intermediate strain rate. The dimensions of the FTSPE were chosen to obtain an applied J of about 1,500 lb/in (263 kJ/m^2) at net section yield. The specimen is full plate thickness with a weld running across the center. The test consists of clamping the ends of the specimen and loading it to net section yield in 1 second. If a cleavage instability occurs before net section yield is reached, then the test is considered a FAIL, otherwise it is a PASS. The first test for each weld was conducted at -20°F (-29°C). If the first test was a failure, then the temperature was increased 20°F (11°C) for the next test. If the first test passed, then the temperature was decreased 20°F (11°C) for the next test. Six specimens were available for each weld and two tests were run at each temperature. The results are shown in Figure 8. An open symbol represents a FAIL and a filled symbol represents a PASS. Six of the 10 welds tested failed the FTSPE test at -20°F (-29°C). This is significant because the EXB/ECS tests conducted at 30°F (-1°C) indicated that these welds were acceptable. These welds exhibited a wide variation in reference temperature (-134°F to 18°F, or –92°C to –8°C). The FTSPE test results are plotted in terms of the excess temperature (determined per E1921 using small specimens) in Figure 9. Welds with an excess temperature of less than about 45°F (25°C) did not pass the FTSPE test (with the exception of F17, which had 3 passes at excess temperatures of less than 45°F (25°C)). The reason for the discrepancy between the FTSPE and ECS tests is investigated in the next section.

Table 1—*Welds fabricated for the HSLA-65 weld optimization program*

Weld ID	**Baseplate Type**	**Plate Thickness in. (mm)**	**Welding Process**	**Consumable**	**Heat Input, Preheat-Interpass Temp kJ/in., °F (kJ/mm, °C)**	**Transition Temp., To °F (°C)**
SM8	HSLA-65, CR	½ (12.7)	SMAW	7018-M	55, 250 (2.17, 121)	N/A[1]
G9	HSLA-65, CR	1/2 (12.7)	GMAW	ER70S-3	50, 200 (1.97, 93)	-134 (-92)
SA8	HSLA-65, CR	1/2 (12.7)	SAW	ER70S	66, 200 (2.60, 93)	-24 (-31)
F17	HSLA-65, Q&T	1/2 (12.7)	FCAW	E71T-1	58, 200 (2.28, 93)	-18 (-28)
F18	HSLA-65, CR	1/2 (12.7)	FCAW	E71T-1	58, 200 (2.28, 93)	-18 (-28)
F19	HSLA-65, CR	5/8 (15.9)	FCAW	E71T-1	58, 200 (2.28, 93)	10 (-12)
F20	DH-36, CR	1/2 (12.7)	FCAW	E71T-1	58, 200 (2.28, 93)	N/A[1]
F21	HSLA-65, CR	1/2 (12.7)	FCAW	70T12-H4	58, 200 (2.28, 93)	18 (-8)
F22	HSLA-65, CR	1/2 (12.7)	FCAW	E101T1-G	58, 200 (2.28, 93)	-110 (-79)
F23	HSLA-65, CR	1/2 (12.7)	FCAW	70T12-H4	58, 200 (2.28, 93)	-69 (-56)

[1]Insufficient data to determine T_o.

Analysis of the HSLA-65 Welds

The fracture toughnesses measured from the SE(B) specimens were used to estimate the Weibull modulus. Unfortunately, it was not possible to accurately determine the modulus because of two shortcomings in the data. First, there were only 6 to 10 fracture toughness tests for each weld, while 15 to 20 tests is preferable. Secondly, all of the specimens were deeply cracked and recent research has shown that data at two different constraint levels is required to accurately determine the modulus (m) [*5*]. Even though accurate determinations could not be made, an estimated value of 10 was sufficient to provide a relative comparison of the three different specimen geometries. It was also assumed that the modulus was independent of temperature. For this analysis, all of the welds were assumed to have the same flow properties and the effect of temperature on yield strength was neglected. The assumption that the flow properties were the same is reasonable based on the similar yield and ultimate strengths.

Table 2—*Welds fabricated from 1 1/4 in. (31.8 mm) thick plate for EXB and ECS specimens.*

Welds Made by the National Center for Excellence in Metalworking Technology (NCEMT)				
Weld ID	**Base Metal**	**Welding Process**	**Filler Metal**	**Avg. Heat Input kJ/in. (kJ/mm)**
ECSF01	HSLA-65 TMCP	FCAW	70T12-H4	58 (2.28)
ECSF02	HSLA-65 TMCP	FCAW	70T12-H4	58 (2.28)
ECS-SM01	HSLA-65 TMCP	SMAW	7018-M	58 (2.28)
ECS-SM02	HSLA-65 TMCP	SMAW	7018-M	58 (2.28)
EXBF03	HSLA-65 TMCP	FCAW	70T12-H4	58 (2.28)
EXBF04	HSLA-65 TMCP	FCAW	70T12-H4	58 (2.28)
Welds made by Newport News Shipbuilding				
Weld ID	**Base Metal**	**Welding Process**	**Filler Metal**	**Avg. Heat Input kJ/in. (kJ/mm)**
99-49-01	HSLA-65 QT	SMAW	7018-M	45 (1.77)
99-49-02	HSLA-65 QT	FCAW	71T-1HYM	51 (2.01)
99-49-03	HSLA-65 CR	SMAW	7018-M	45 (1.77)
99-49-06	HSLA-65 CR	FCAW	71T-1HYM	51 (2.01)

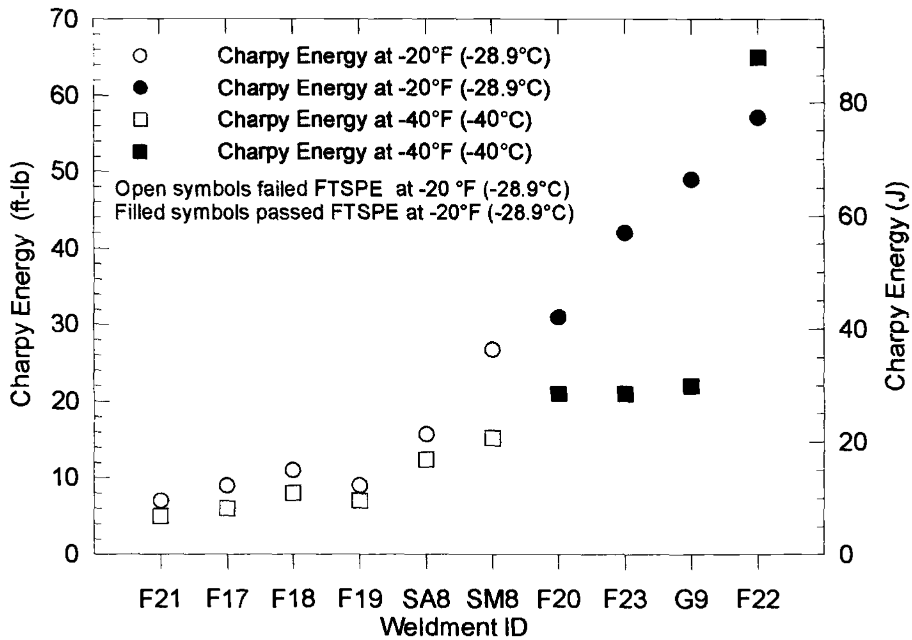

Figure 7—*Correlation of FTSPE test results with Charpy tests at -40 and -20°F (-40 and −29°C).*

Table 3—*Results from Explosion Bulge and Explosion Crack Starter Tests of HSLA-65 Welds.*

Baseplate Type	**Welding Process**	**Consumable**	**Number and Type**	**Results**
TMCP	FCAW	70T12-H4	2 - EXB	Passed
TMCP	FCAW	70T12-H4	2 – ECS	Passed
TMCP	SMAW	7018-M	2 – ECS	One Pass One Failure in Plate
Q & T	FCAW	71T-1HYM	1 – ECS	Passed
CR	FCAW	71T-1HYM	1 – ECS	Passed
Q & T	SMAW	7018-M	1 – ECS	Passed
CR	SMAW	7018-M	1 – ECS	Passed

EXB – Explosion Bulge
ECS – Explosion Crack Starter

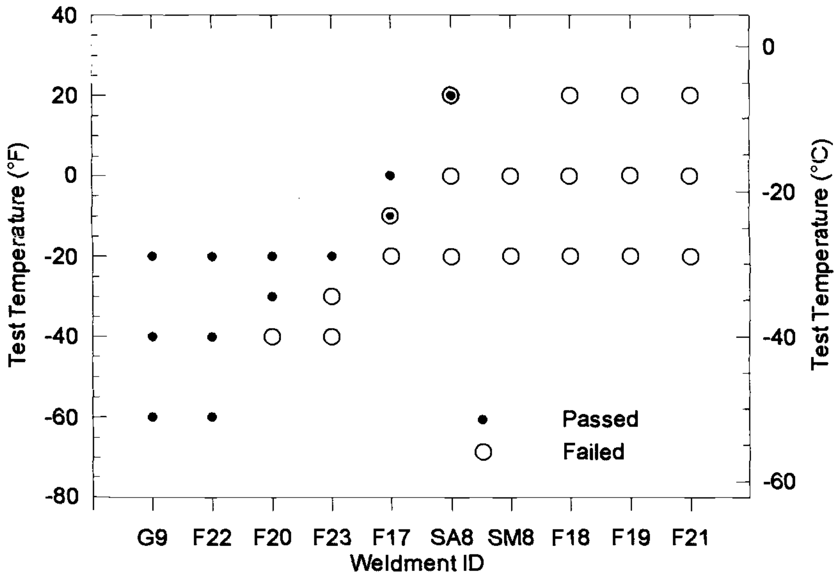

Figure 8—*FTSPE test results for HSLA-65 welds.*

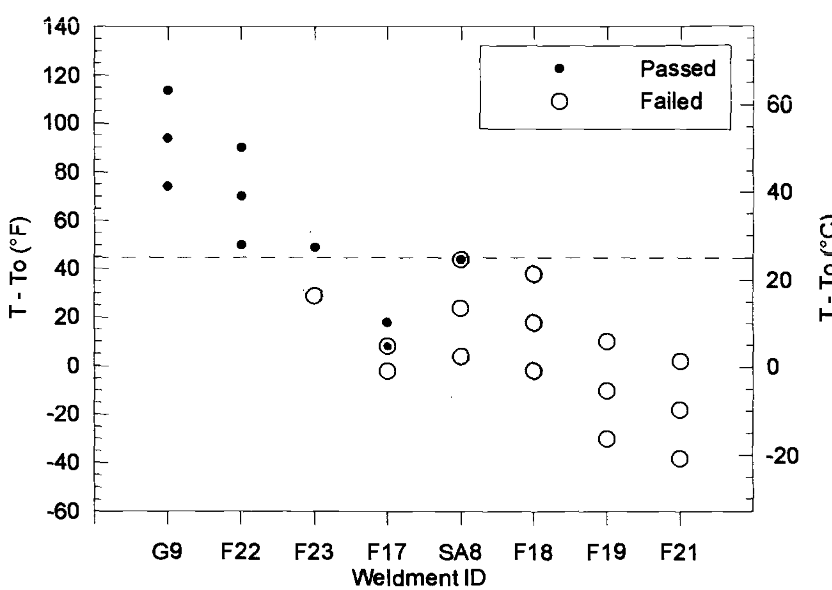

Figure 9—*Results from FTSPE tests plotted in terms of excess temperature (T-To).*

The analysis of the data focused on two welds, F21 and F22. These were chosen because they represented the extremes of behavior. Weld F21 failed the FTSPE tests at -20, 0 and 20°F (-29, -18 and -7°C) and had a T_o of 18°F (-8°C) while F22 passed all tests down to -60°F (-51°C) and had a T_o of -110°F (-79°C). The estimated modulus was used to generate σ_w versus J curves for each specimen. As explained previously, the Master Curve was used together with a SSY analysis to determine σ_u and $\sigma_{w\text{-}min}$ for each specimen at each test temperature. These values were used to generate probability of failure versus J curves for each specimen at the test temperature. The failure probability curve for the ECS specimen of weld F21 is of particular interest because it passed the EXB/ECS tests at 30 °F (-1°C) and failed the FTSPE tests at -20 °F (-29°C). The failure probability curves for weld F21are compared in Figure 10. These results show that the probability of failure for the ECS specimen at 30°F (-1°C) is significantly lower than the FTSPE at -20, 0 and 20°F (-29, -18 and -7°C). This observation at least partially explains why this weld passed the EXB/ECS and failed the FTSPE. The probability of failure for the ECS specimen has not been corrected for the higher loading rate. Dynamic loading may increase the reference temperature, T_o, which would decrease σ_u - $\sigma_{w\text{-}min}$ and increase the probability of failure. However, there was no test data available to estimate the effect of rate on reference temperature for these welds, and data in the literature shows considerable variation from no rate effect to significant rate effect [*14*].

Probability of failure curves for weld F22, which passed the FTSPE down to -60°F (-51°C) and has a T_o = -110°F (-79°C), are shown in Figure 11. The failure probability for the ECS specimen is not shown because it is so low that it is not visible in the graph. The dramatic decrease in failure probability is largely due to the much higher excess temperatures for the tests of F22. The excess temperatures for weld F21 ranged from -38°F to 12°F (-39 to -11°C) while the excess temperatures for weld F22 ranged from 10°F to 90°F (-12 to 32°C). It is apparent that excess temperature has a very strong influence on failure probability.

Concept for Constraint-based Material Screening/Certification

The ability of the Weibull stress and the Master Curve to predict probability of failure for geometries of different constraint level based on material properties obtained from simple tests presents the opportunity to compare weld systems based on probability of failure. The Weibull stress can be used to develop criteria for screening of weld systems to determine suitability for a particular application. These screening criteria could be incorporated into a certification program that explicitly considers the thickness, constraint level and minimum service temperature of the application. Tolerable probability of failure levels could be determined based on performance of current weld systems that have been certified. New systems would then be compared against the certified systems using the following procedure.

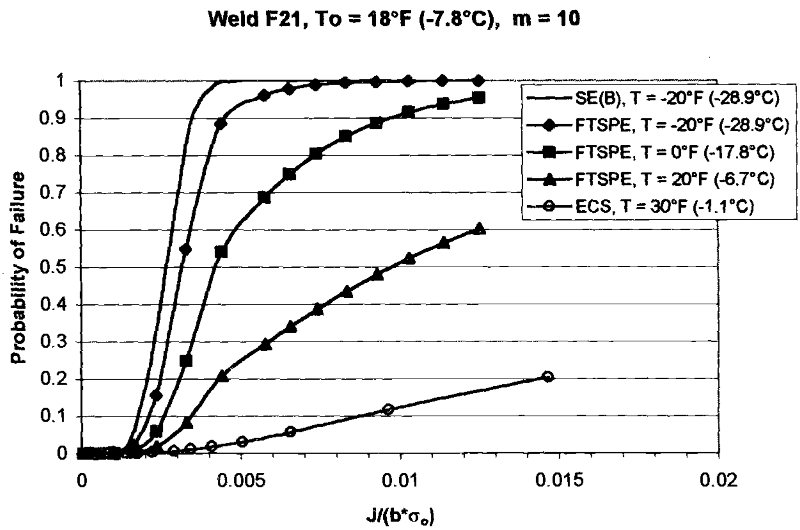

Figure 10—*Probability of failure at test temperature for tests of weld F21.*

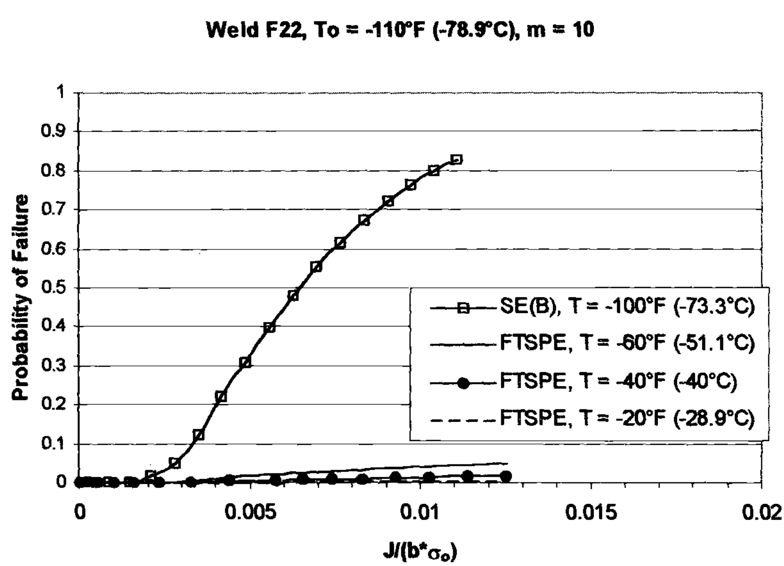

Figure 11—*Probability of failure at test temperature for tests of weld F22.*

It is assumed in the following that the relevant material properties for the certified weld system have been determined.

1. Run a series of fracture toughness tests at low temperature to establish the reference temperature [E1921] and the Weibull modulus.
2. Run tensile tests at the lowest service temperature to get flow properties.
3. Choose a standard specimen geometry (structural element) that represents the constraint level of the intended application and conduct finite element analysis over a range of applied load to determine the stress and strain fields at the lowest service temperature (T_s).
4. Calculate the Weibull stress as a function of applied J for the structural element at T_s.
5. Use the Master Curve and the measured T_o to calculate K_o at T_s.
6. Use a SSY modified boundary layer model to generate the σ_w versus J curve for the same thickness (crack front length) as the structural element and determine σ_u, which is σ_w at K_o, and $\sigma_{w\text{-}min}$, which is σ_w at K_{min}.
7. Calculate probability of failure versus J and T-T_o using the structural element for the candidate weld system and compare it to a certified weld system that is approved for the intended application.

The numerical analysis in steps 3 and 6 could be simplified by creating a library of finite element models for standard geometries. Since the models are being used to compare weld systems, the model does not have to represent the dimensions of an actual structure. It only has to represent the appropriate constraint level. The proposed approach was applied to the HSLA-65 welds using a SE(T) as the structural element. The resulting probability of failure curves are shown in Figure 12. The only aspect of these curves that makes them unique to the HSLA-65 welds is that the true stress – true strain curve shown in Figure 2 was used in the analysis. The curves could be made more general by using the Ramberg-Osgood relation to represent the flow behavior and generating similar plots for various values of strain hardening exponent and yield strength.

The evaluation of a particular weld system would be based on comparison with a certified weld system that is acceptable for use in the same, or a similar, application. The probability of failure for the certified weld system would be determined by generating similar curves for that system at the excess temperature and maximum applied J for the intended application. Once this minimum acceptable failure probability (P_f) is determined, the maximum reference temperature for the system under evaluation could be determined from the excess temperature corresponding to the maximum P_f and J values. For example, if it were determined that a certified weld system has a probability of failure of 10% at an applied J of 443 lb/in. ($J = 77.6$ kJ/m^2, $J/(b\sigma_o) = 0.00657$) and the constraint level of the intended applications can be approximated by a SE(T), then the curves shown in Figure 12 would indicate that a minimum excess temperature of 32°F (18°C) would be required at the lowest service temperature. If the lowest service temperature were 10°F (-12°C), then the maximum T_o would be –22°F (-30°C).

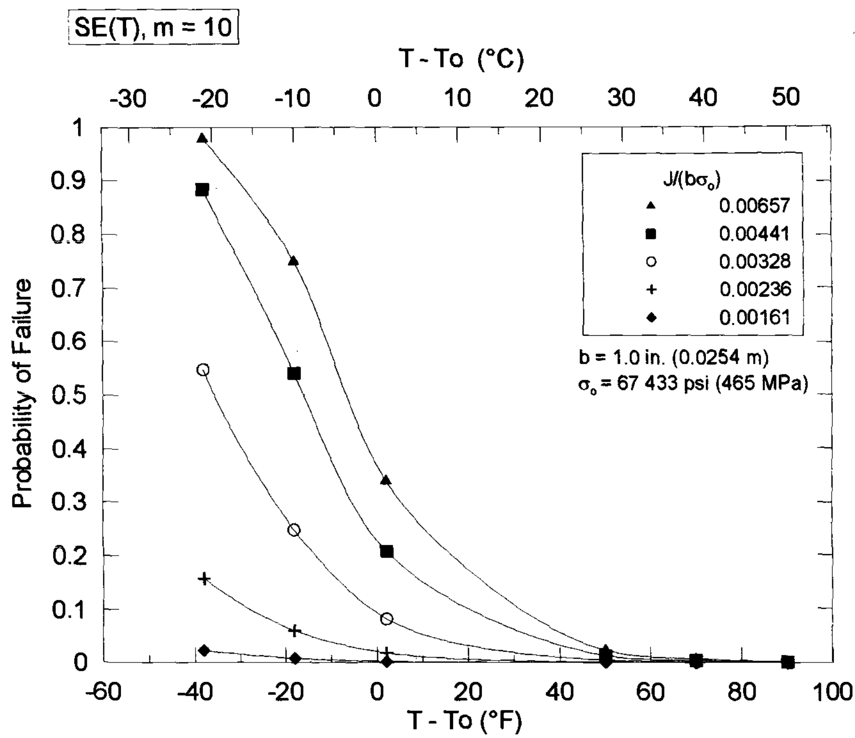

Figure 12—*Example of constraint based material screening criteria applied to the HSLA-65 welds.*

Conclusions

The following conclusions can be made based on the analysis presented:

1. The combination of the Weibull stress and the Master Curve can be used to compare probability of failure for various specimen geometries. The Weibull stress accounts for effects of constraint and thickness, while the Master Curve accounts for effects of temperature.
2. Constraint loss significantly reduces failure probability.
3. An increase in excess temperature causes a decrease in both failure probability at a particular J level, and a decrease in the limiting failure probability at high applied J.
4. The failure probability for an ECS specimen tested at a temperature above the lowest service temperature can be considerably lower than the actual failure probability of a cracked structure of higher constraint at the lowest service temperature. The interpretation of ECS test results should be made with a clear

understanding of how the temperature and constraint level of the test relate a particular structural application.

5. The pass/fail nature of the ECS test provides no means to make relative comparisons of welds that pass the test. There is no way to differentiate between welds that are marginally acceptable, or more than adequate.
6. Too much reliance on the EXB/ECS tests for weld system certification can lead to two possible undesirable consequences. If the ECS test is more severe than the service conditions for the intended application (due perhaps to elevation of reference temperature at high strain rate), some acceptable weld systems could be eliminated in the screening process. Conversely, if the ECS has lower constraint than the structure, a weld system that may have an unacceptable probability of failure in the intended application could be certified as acceptable. To avoid these undesirable outcomes, the constraint of the intended application and the excess temperature for the appropriate loading rate should be considered in the certification process.

References

[1] Pellini, W. S., *Principles of Structural Integrity Technology*, Office of Naval Research, Arlington, VA, 1976.

[2] Pellini, W. S., "Use and Interpretation of the NRL Explosion Bulge Test," Naval Research Lab Report #4034, September 1952.

[3] Beremin, F. M., "A Local Criterion for Cleavage Fracture of a Nuclear Pressure Vessel Steel," *Metallurgical Transactions*, 14A, 1983, pp. 2277-2287.

[4] Busso, E. P., Lei, Y., O'Dowd, N.P. and Webster, G.A., "Mechanistic Prediction of Fracture Processes in Ferritic Steel Welds Within the Transition Temperature Region," Transactions of the ASME, *Journal of Engineering Materials and Technology*, Vol. 120, October 1998, pp. 328-337.

[5] Gao, X., Ruggieri, C. and Dodds, R. H., Jr., "Calibration of Weibull Stress Parameters Using Fracture Toughness Data," *International Journal of Fracture*, 92, 1998, pp. 175-200.

[6] Gao, X. and Dodds, R. H., Jr., "Constraint Effects on the Ductile-to-brittle Transition Temperature of Ferritic Steels, a Weibull Stress Model," *International Journal of Fracture*, 102, 2000, pp. 43-69.

[7] O'Dowd, N. P., Lei, Y. and Busso, E. P., "Prediction of Cleavage Failure Probabilities Using the Weibull Stress," *Engineering Fracture Mechanics*, 67, 2000, pp. 87-100.

[8] Gao, X., Dodds, R. H., Jr., Tregoning, R. L., Joyce, J. A. and Link, R. E., "A Weibull Stress Model to Predict Cleavage Fracture in Plates Containing Surface Cracks," *Fatigue and Fracture in Engineering Materials and Structures*, 22, pp. 481-493.

[9] Ruggieri, C., Gao, X. and Dodds, R. H., Jr., "Transferability of Elastic-plastic Fracture Toughness Using the Weibull Stress Approach: Significance of Parameter Calibration," *Engineering Fracture Mechanics*, 67, 2000, pp. 101-117.

[10] Wallin, K., "Fracture Toughness Transition Curve Shape for Ferritic Structural Steels," Fracture of Engineering Materials and Structures, Edited by S.T. Teoh and K.H. Lee), Elsevier Applied Science, 1991, pp. 83-88.

[11] Koppenhoefer, K., Gullerud, A., Ruggieri, C., Dodds, R. H., Jr. and Healy, B., "WARP3D: Dynamic Nonlinear Analysis of Solids Using a Preconditioned Conjugate Gradient Software Architecture," *Sturctural Research Series (SRS)* 596, UILU-ENG-94-2017, University of Illinois at Urbana-Champaign, 1998.

[12] Ruggieri, C. and Dodds, R. H., Jr., "WSTRESS 2.0: Numerical Computation of Probabilistic Fracture Parameters," *Sturctural Research Series (SRS)* 608, UILU-ENG-95-2013, University of Illinois at Urbana-Champaign, 1998.

[13] Ruggieri, C. and Dodds, R. H., Jr., "A Transferability Model for Brittle Fracture Including Constraint and Ductile Tearing Effects: A Probabilistic Approach," *Sturctural Research Series (SRS)* 611, UILU-ENG-96-2008, University of Illinois at Urbana-Champaign, 1996.

[14] Yoon, K. K., Van Der Sluys, W. A. and Hour, K., "Effect of Loading Rate on Fracture Toughness of Pressure Vessel Steels," *Journal of Pressure Vessel Technology*, Vol. 122, May 2000, PP. 125-129.

Constraint and/or Welds

Ma, F.,[1] Sutton, M. A.,[2] and Deng, X.[2]

Plane Stress Mixed Mode Crack-Tip Stress Fields Characterized by a Triaxial Stress Parameter and a Plastic Deformation Extent Based Characteristic Length

---

Reference: Ma, F., Sutton, M. A., and Deng, X., **"Plane Stress Mixed Mode Crack-Tip Stress Fields Characterized by a Triaxial Stress Parameter and a Plastic Deformation Extent Based Characteristic Length,"** *Fatigue and Fracture Mechanics: 33rd Volume, ASTM STP 1417*, W. G. Reuter and R. S. Piascik, Eds., ASTM International, West Conshohocken, PA, 2002.

Abstract: Residual strength assessment in aircraft fuselage structures requires that a general criterion for mixed-mode fracture of ductile materials be developed. An understanding of mixed-mode crack-tip stress fields is essential to define viable fracture parameters and perform accurate fracture analysis. In the present study, a self-similar family of mixed-mode crack-tip stress fields proposed by the present authors is studied in detail for plane stress problems under conditions ranging from small scale yielding to large scale yielding. Analytical and numerical studies indicate that stress and plastic strain in the crack tip region can be characterized by a plastic strain extent based characteristic length, L^p, and the crack tip region stress triaxiality constraint parameter, A_m, defined as the ratio of mean stress over effective stress (σ_m/σ_e). Results from all cases indicate that the proposed, self-similar family of mixed-mode crack-tip stress fields accurately represents the stress fields for both SSY models and actual fracture specimen geometry. The crack tip stress fields are shown to belong to a family of solutions parameterized by A_m and L^p when the distance from crack tip, r, is measured in terms of its normalized value by the characteristic length scale, r/L^p. Specifically, in the tensile fracture dominated crack growth direction (locally Mode I direction), it is found that stress triaxiality takes its maximum value. This condition will promote the nucleation of micro-voids from large particles, resulting in Mode I dimpled fracture. In the shear dominated crack growth direction fracture (locally Mode II direction), corresponding to the direction of maximum L^p, it is shown that the effective and shear stresses reach their maximum values. This condition promotes the formation of an intense slip-band, resulting in Mode II fracture.
Keywords: Crack tip fields; mixed-mode I/II; plane stress; stress triaxiality; plastic zone length

---

[1] Scientist, Pratt & Whitney, MS 161-05, 400 Main Street, East Hartford, CT 06108.
[2] Professor, Department of Mechanical Engineering, University of South Carolina, Columbia, SC 29208

Introduction

It is well know that the fracture of ductile solids has frequently been observed to be the result of the nucleation, growth and coalescence of voids, both in nominally uniform stress fields and ahead of an extending crack [*1*]. Several studies [*2-7*] have indicated that *stress triaxiality* (defined as the ratio of mean stress to effective stress) and *plastic strain* in the crack tip region play an important role in the process of ductile fracture, with different combinations of plastic strain and stress triaxiality resulting in different fracture process zones. Together, these observations suggest that two independent parameters are needed to characterize stress fields in the near-tip region, one related to stress triaxiality and the other to plastic deformation.

Since cracks in the skin of aircraft fuselages or other shell structures can be subjected to very complex stress states, resulting in mixed-mode crack-tip conditions, residual strength assessment in aerospace structures requires that a general criterion for mixed-mode fracture of ductile materials be developed. Thus, an understanding of mixed-mode crack-tip stress fields is essential to define viable fracture parameters and perform accurate fracture analyses of flawed structures. In an effort to determine whether mixed-mode crack tip fields in ductile materials can be characterized by a small number of parameters, thereby simplifying the process of identifying candidate mixed-mode fracture criteria, the present authors have performed a series of theoretical and detailed elastic-plastic, plane strain finite element analyses [*8*]. Each model was subjected to mixed-mode I/II loading and the crack tip fields were determined. A wide range of length scales (e.g., plastic zone size, specimen dimensions), loading parameters (e.g., J-integral, T-stress, mode mixity, mean stress, see references [*9-15*]) and materials were investigated. Results from these studies demonstrate that a self-similar family of mixed-mode crack-tip stress fields exists. The fields are characterized in terms of (a) a stress triaxiality parameter, A_m, based on the ratio between the mean stress and effective stress, and (b) a characteristic length scale, L^p, based on the spatial extent of crack-tip plastic deformation. Within this framework, L^p and A_m have distinct roles: L^p sets the size scale over which large stresses and strains develop while A_m scales the near-tip constraint level. The parameters A_m and L^p are functions of the angular position, θ. Designated the "A_m-family of mixed-mode crack–tip fields", they are significantly different from previous mixed-mode crack-tip stress fields characterized by the J-integral, mode mixity and a constraint parameter such as T-stress [*9-15*]. Within the crack-tip zone in which L^p scales the fields in the radial direction, the relationship between the angular variations of the crack-tip stresses and $A_m(\theta)$ is found to be independent of the specifics of the problem, such as loading mixity, geometry, and boundary conditions, etc. The direction of maximum A_m corresponds to a local Mode I direction where tensile stress states promote the nucleation of micro-voids from large particles, resulting in conditions promoting locally Mode I dimpled fracture. Similarly, the maximum L^p is in the direction of maximum shear stress and effective stress, leading to conditions that promote the formation of an intense slip-band which promotes shear fracture.

It is noted that the self-similar family of mixed-mode crack-tip stress fields obtained for plane strain conditions are consistent with the findings in recent experimental and analytical work [*16–21*] on mixed-mode crack problems. The work has shown that flaws in ductile materials under local mixed-mode I/II conditions will change direction and undergo stable crack growth along directions that are either predominantly Mode I or Mode II. One model [*18,19,21*] that has been shown to adequately predict the direction and onset of crack extension is crack opening displacement (COD). This model predicts that (a) mode I crack growth will occur in a direction that maximizes the opening component of crack opening displacement (COD_I) and (b) Mode II crack growth will occur in the direction of maximum shear-type crack displacement (COD_{II}). In addition, Bose and Castaneda [*20*] obtained asymptotic crack-tip fields for stable crack growth of a crack along its original direction. They demonstrated that pure Mode I or Mode II stress-state exists directly ahead of a crack tip. In this case, quantities such as maximum in-plane normal stress [*22-24*] for Mode I and either maximum effective stress [*25*], maximum effective plastic strain [*24*] or maximum shear stress [*23*] for Mode II have been used to predict similar trends.

As a companion of the plane strain mixed-mode stress fields [*8*] described above, this study will direct attention at the plane stress A_m-family of mixed-mode crack–tip fields. In the following sections, we first define the problem. Then, detailed analytical and FEM studies are performed for thin sheet material (plane stress problems), including the Arcan mixed-mode I/II fixture-specimen system and small-scale yielding with a modified boundary layer formulation (SSY). The Arcan specimen produces a detailed, full field data base for mixed crack initiation and growth, and the SSY model provides an attractive means to study the effects of mode mixity, specimen geometry and loading on the near-tip fields without geometry specification. Together, the two models are used to demonstrate the accuracy of the A_m-family of mixed-mode crack–tip fields for plane stress crack problems.

Parameters for Plane Stress Mixed Mode I/II Crack Tip Fields

As in the work for plane strain problems, two characteristic parameters, L^P and A_m, are used to characterize the stress variations in the crack-tip region under plane stress conditions and mixed-mode I/II loading. The characteristic plastic zone length, L^p, is defined as follows. For a given angle, θ, the length scale, L^p, based on the extent of crack-tip plastic deformation, is defined to be the radial distance from the crack tip to a point where $\sigma_e = \xi\sigma_0$, where σ_e is the von Mises effective stress, σ_0 is the initial yield stress, and ξ is a constant equal to or larger than 1.0. This situation is shown graphically in Figure 1. The parameter, ξ, is conveniently chosen so that the fracture process zone is well contained within a crack-tip region defined by the length scale, $L^p(\theta)$. Thus, radial variations in the crack tip stress field can be described in terms of the same normalized position within the plastic zone. Using the length scale r/L^p, a typical crack-tip plastic zone under mixed-mode I/II loading (e.g., see Figure 2a) will be circular. As shown in Figure 2b, locations having the same normalized position within the plastic zone are on nested concentric circles within the unit circle in terms of r/L^p. For cases considered in this work, ξ=1.2 was used to determine L^p, which approximately corresponds to a plastic zone size determined by effective plastic strain ε_p=3% for Al 2024-T3 material.

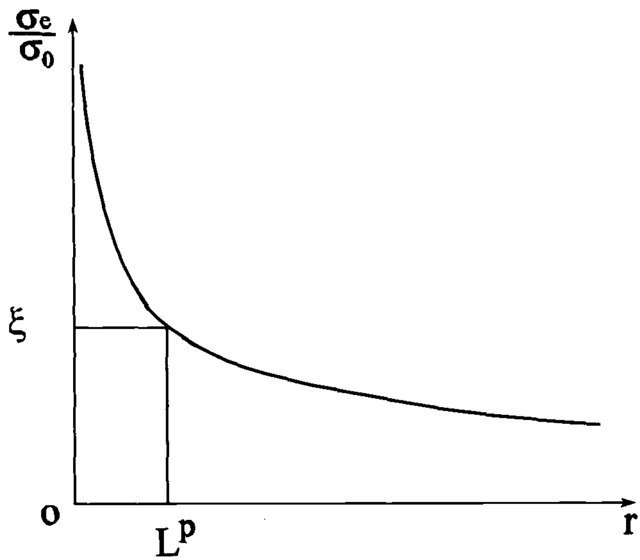

Figure 1. Graphical representation for the definition of characteristic length, L^p.

The second parameter used in the A_m-family of mixed-mode crack–tip is A_m, defined as the magnitude of the quantity σ_m/σ_e in the near-tip region. In this definition, σ_e is the von Mises effective stress defined by

$$\sigma_e^2 = \frac{3}{2} s_{ij} s_{ij} , \tag{1}$$

where s_{ij} represents the deviatoric stress components

$$s_{ij} = \sigma_{ij} - \frac{1}{3} \delta_{ij} \sigma_{kk} , \tag{2}$$

and δ_{ij} is the Kronecker delta. The means stress, σ_m, is defined by the equation

$$\sigma_m = \frac{1}{3} \sigma_{kk} . \tag{3}$$

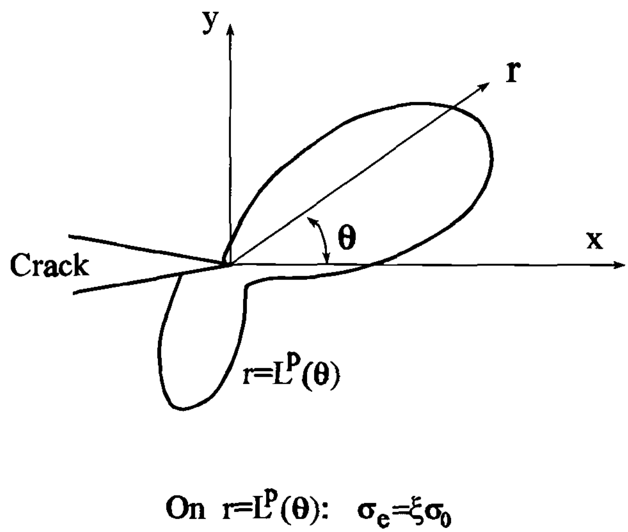

Figure 2(a). A mixed-mode I/II crack tip plastic zone shape defined by $\sigma_e = \xi\sigma_0$.

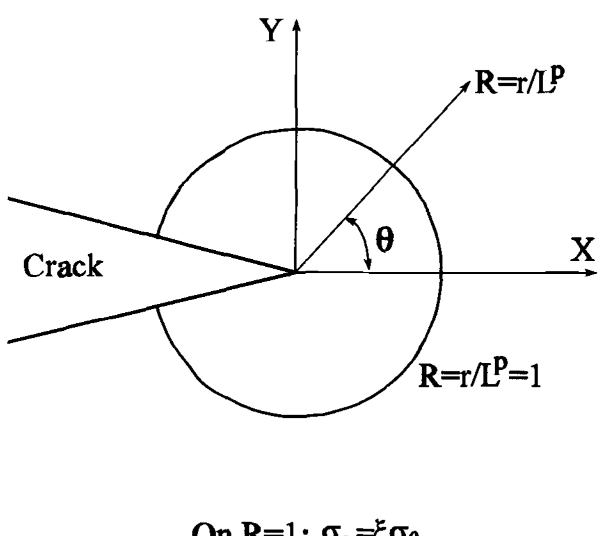

Figure 2(b). A normalized mixed-mode I/II crack tip plastic zone shape in Figure 2(a).

As such, the triaxial stress parameter, A_m, is defined in this paper as the near-tip value of the ratio σ_m/σ_e because numerical results in this paper have shown that this ratio is basically independent of radial distance r within the near-tip region.

With a polar coordinate system located at the crack tip and $\theta=0^\circ$ coinciding with the initial crack direction (see Figure 2), stresses in the crack-tip region are assumed to be self-similar when distance from the crack tip, r, is normalized by the characteristic length, L^p, i.e.

$$\frac{\sigma_{ij}}{\sigma_0} = A_{ij} f(\frac{L^p}{r}) \ , \ L^p = L^p(\theta) \ , \tag{4}$$

and the stress amplitude, A_{ij}, is controlled by the magnitude of stress triaxiality, A_m, as

$$A_{ij} = A_{ij}(A_m, \theta). \tag{5}$$

The A_m-family of mixed-mode crack tip fields is expected to accurately represent crack tip fields for arbitrary specimen geometry under both contained and general yielding conditions. The maximum locations of L^p and A_m can be correlated to crack growth directions in either Mode I or Mode II types. In the following sections, the plane stress A_m-family of mixed-mode crack tip fields for plane stress problems will be demonstrated by describing results obtained using the finite element method for (a) the Arcan-specimen and (b) a small-scale yielding model. Using these results, the underlying basis for the proposed stress triaxiality-based family of crack tips fields for plane stress conditions is explored in more detail.

Numerical Predictions for Plane Stress Crack Tip Fields

The finite element method is used to obtain the stress variation in the crack tip region. A power hardening material that obeys the J_2-deformation theory of plasticity and the uniaxial Ramberg-Osgood relationship

$$\frac{\varepsilon}{\varepsilon_0} = \frac{\sigma}{\sigma_0} + \alpha\left(\frac{\sigma}{\sigma_0}\right)^n , \tag{6}$$

is analyzed in this work. The material constants, n=10 and $\alpha = 1$, $E = 71.2GPa$, Poisson's ratio $\nu = 0.3$ and $\sigma_0 = 344.5MPa$, are taken to approximate Al2024-T3, as shown in Figure 3.

Based on convergence analysis for the crack tip stress fields [*8*], computations for plane stress crack tip stresses were performed with small displacement theory implemented in the finite element code ABAQUS [*26*]. The results reported below are based on a 4-node element with reduced integration, hourglass control and constant pressure capability.

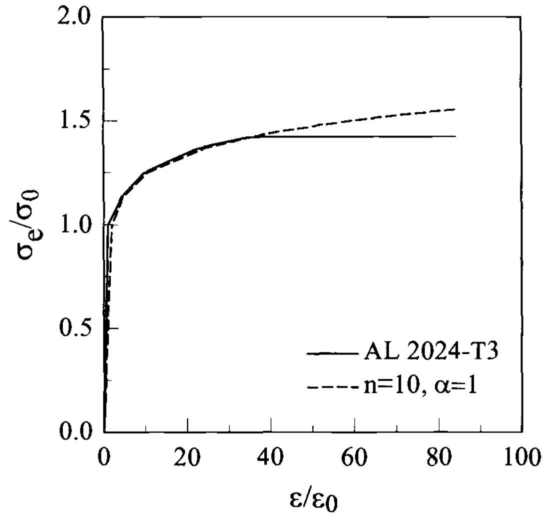

Figure 3. Hardening rules for Al-2024T3 and power-law materials, n=10, respectively.

Arcan Fixture-Specimen System

The modified Arcan fixture-specimen system [*16,17*] was chosen to represent a variety of mode mixity levels through selection of different loading angles, Φ, ranging from 0^0 to 90^0 with increments of 15^0. The Arcan specimen and test fixtures are shown in Figure 4. Increasing the number of bolts and adding hardened drill rod inserts stiffened the specimen-fixture connection. The 15-5PH stainless steel test fixture, as shown in Figure 4a, is nominally 12.7 mm thick and was machined to test 2.3mm thick specimens. The locations of pinholes on the outer edge of the fixture provides a range of loading angles, Φ, which results in a full spectrum of mode mixity. The test specimens are shown in Figure 4b. In this work 2024-T3 aluminum plate was used for all specimens.

The test specimen and fixture are modeled as a single, continuous component in this study. The finite element mesh for the modified Arcan fixture-specimen configuration is illustrated in Figure 5.

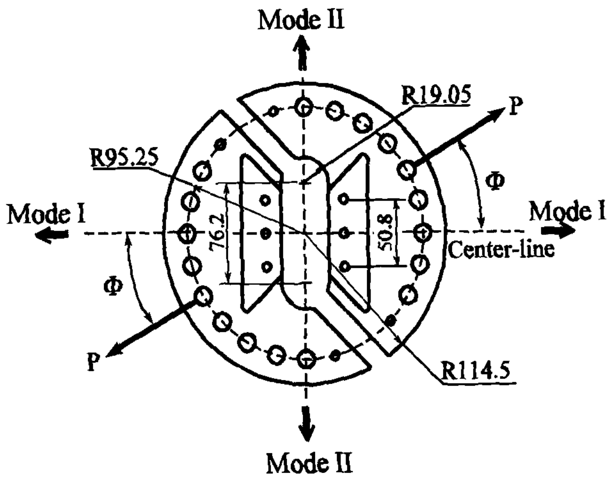

Figure 4(a). A schematic of the Arcan test loading fixture.

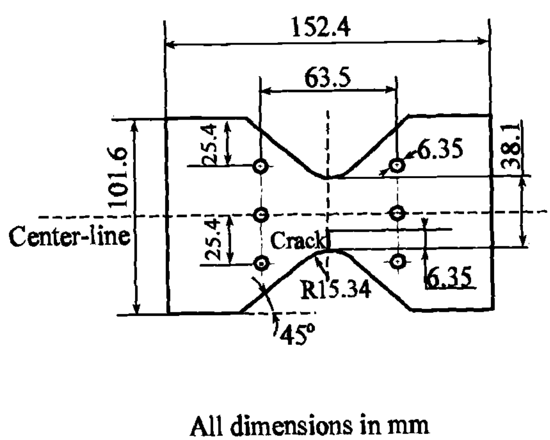

Figure 4(b). A schematic of the Arcan test specimen.

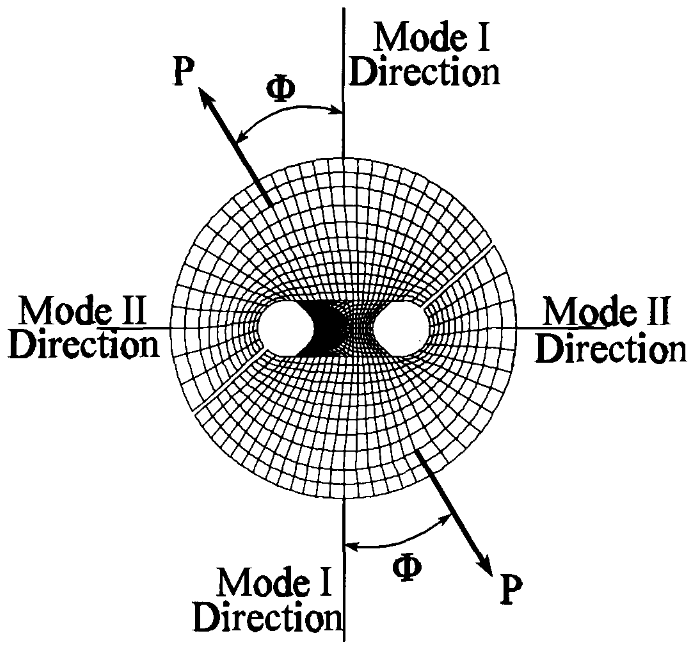

Figure 5. A finite element model of the modified Arcan fixture-specimen system.

Small Scale Yielding Model

The A_m-family of mixed-mode crack tip fields was further verified for the small-scale yielding (SSY) model with modified boundary layer (MBL) formulation [*14,15*]. In the SSY analysis with a MBL formulation, two-term asymptotic elastic crack-tip displacement fields are prescribed at the remote boundary $r = r_a$, corresponding to combined linear Mode I and Mode II stress intensity factors K_I, K_{II}, and T-stress fields,

$$\left.\begin{aligned} u_x &= R_K\left[k_1\cos\frac{\theta}{2}\left(\frac{\kappa-1}{2}+\sin^2\frac{\theta}{2}\right)+k_2\sin\frac{\theta}{2}\left(\frac{\kappa+1}{2}+\cos^2\frac{\theta}{2}\right)\right]+\frac{1+\kappa}{8}\frac{T}{\mu}r_a\cos\theta \\ u_y &= R_K\left[k_1\sin\frac{\theta}{2}\left(\frac{\kappa+1}{2}-\cos^2\frac{\theta}{2}\right)-k_2\cos\frac{\theta}{2}\left(\frac{\kappa-1}{2}-\sin^2\frac{\theta}{2}\right)\right]-\frac{3-\kappa}{8}\frac{T}{\mu}r_a\sin\theta \end{aligned}\right\}. \quad (7)$$

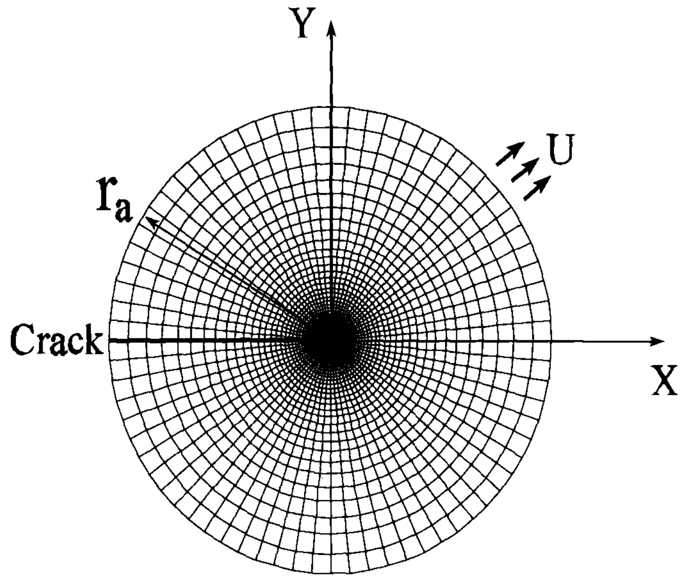

Figure 6. The SSY model and finite element mesh.

with

$$\left.\begin{array}{l} R_K = \sqrt{\dfrac{r_a}{2\pi}}\dfrac{K_{eff}}{\mu}, \quad K_{eff} \equiv \sqrt{K_I^2 + K_{II}^2} \\ k_1 = \dfrac{1}{\sqrt{1+\omega^2}}, \quad k_2 = \dfrac{\omega}{\sqrt{1+\omega^2}} \\ \omega = \dfrac{K_{II}}{K_I} \end{array}\right\}, \tag{8}$$

Here, μ is the elastic shear modulus and $\kappa = (3-\nu)/(1+\nu)$ for plane stress problems and $\chi = \tan^{-1}(\omega)$ is used as a measure of mode mixity for the SSY model. Thus, the crack tip stress fields in the SSY model depend on χ, the length parameter R_K, and T-stress, which is an in-plane measure of constraint level. In this work, increments of K_{eff}, where and T-stress were applied along the circular boundary using Eq. (7), and several combinations of T-stress (T/σ_0=0.5, 0.0, −0.5) and K_{eff} (corresponding to χ=0°, 35°, 72°, 90°) were used to obtain the SSY crack tip stress fields.

As shown in Figure 6, the crack was modeled with a focused mesh, comprising 100 rings of 72 elements concentric with the crack tip, which consisted of 73 independent but initially coincident nodes. Mesh refinement was such that elements adjacent to the crack tip had a radial length that was 1/9239 of the radial length of the outer elements.

Angular Variation of L^p and A_m

Figure 7 highlights the contours of σ_e=1.2σ_0 at a loading level that resulted in observed surface crack growth in the Al-2024 Arcan specimens [*16,17*]. The contours correspond to a plastic zone size determined by an equivalent plastic strain of ε_p_ß%. According to the definition of L^p given previously, a radial distance from the crack tip to the contours is L^p. Thus, the contours shown in Figure 6 represent an angular variation of L^p. In all loading cases corresponding to Φ ranging from 0^0 to 90^0, the maximum value of L^p occurs in the direction of maximum σ_e. As the Mode II loading component increases, the direction of maximum L^p coincides with the local Mode II direction, where the shear stress, effective stress and COD_{II} (shear component of COD) take maximum values, (for details about COD_I and COD $_{II}$, see Ma et al. [*18*]).

Experiments on the Arcan specimen [*16,17*] show that for $\Phi<70^0$, crack growth occurs under local Mode I conditions. For $\Phi > 70^0$, crack growth occurs under local Mode II conditions. Comparing these results with the angular variation of L^p, it is shown that for $\Phi<70^0$ (Figure 7a), L^p is relative small and the intense plastic deformation is confined to a region close to the crack tip region. When angle $\Phi>70^0$ (Figure 7b), the maximum in L^p increases rapidly and intense plastic deformation occurs in a narrow band leading to localization and promoting shear type fracture. Details in the angular variation of L^p for the Arcan specimen are shown in Figure 8 at two loading levels, one corresponding to crack initiation and one to maximum loading, where L^p is normalized by the crack opening displacement at 1mm behind crack tip, i.e. D = COD in Figure 8.

For comparison, the variation of shear stress and effective stress are also shown in the figures. It is found that once the intense plastic deformation occurs in a narrow band leading to localization and shear type fracture, the shear stress, $\sigma_{r\theta}$, effective stress, σ_e, and COD_{II}, reach t heir maximum values, respectively, which corresponds to a local Mode II direction [*18*].

In a direction where the quantities A_m, $\sigma_{\theta\theta}$, and COD_I approach a maximum, L_p is relative small and the intense plastic deformation is confined to a region close to the crack tip region. Along this direction, locally Mode I conditions occurs and the angular variations of A_m can be correlated to tensile type fracture (Mode I type). Figure 9 presents typical results from the Arcan specimen for angular variations in A_m, σ_{rr} and $\sigma_{\theta\theta}$. For all cases considered here, A_m takes its maximum value near the direction where the opening stress reaches its maximum. Along this direction, constraint is maximum, void nucleation under local Mode I conditions is promoted and Mode I crack growth is predicted to occur. Also, along this direction the opening normal stress is maximum, the in-plane shear stress vanishes and the stress-state is locally tensile.

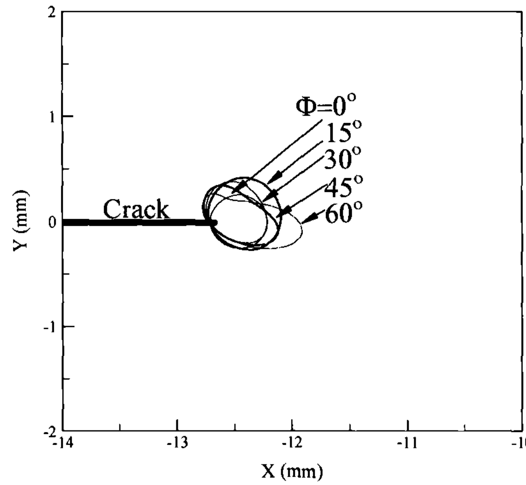

Figure 7(a). Contours of σ_e=1.2σ_0, for Arcan specimen, Φ<70^0.

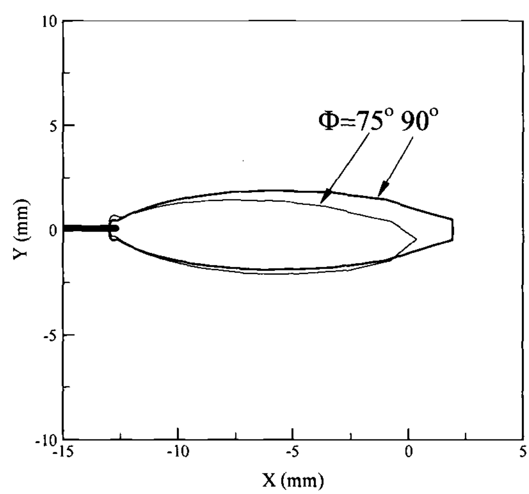

Figure 7(b). Contours of σ_e=1.2σ_0, for Arcan specimen, Φ>70^0.

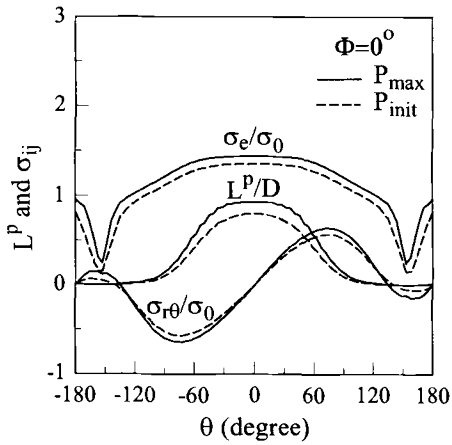

Figure 8(a). Angular variation of L^p, effective stress and shear stress, Arcan specimen, $\Phi=0°$.

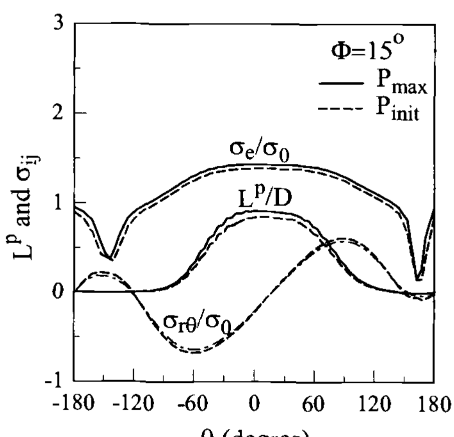

Figure 8(b). Angular variation of L^p, effective stress and shear stress, Arcan specimen, $\Phi=15°$.

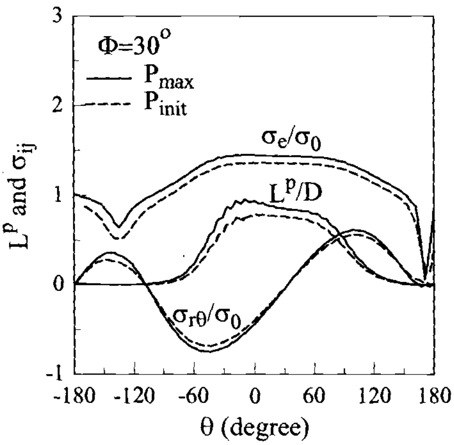

Figure 8(c). Angular variation of L^p, effective stress and shear stress, Arcan specim
Φ=30°.

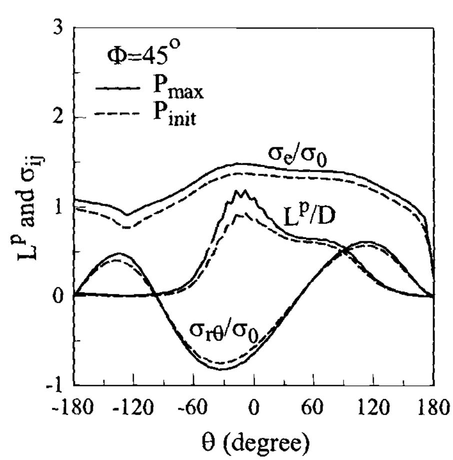

Figure 8(d). Angular variation of L^p, effective stress and shear stress, Arcan specim
Φ=45°.

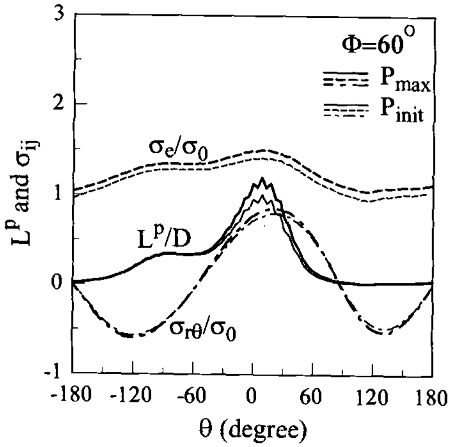

Figure 8(e). Angular variation of L^p, effective stress and shear stress, Arcan specimen, Φ=60°.

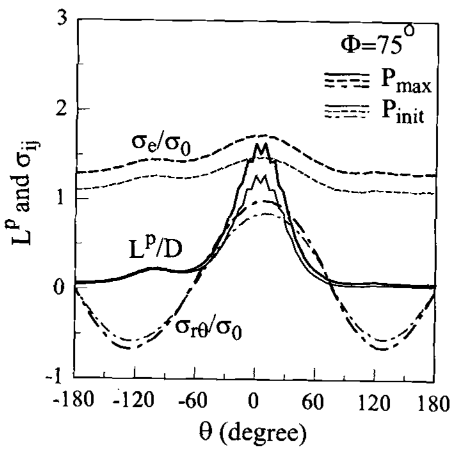

Figure 8(f). Angular variation of L^p, effective stress and shear stress, Arcan specimen, Φ=75°.

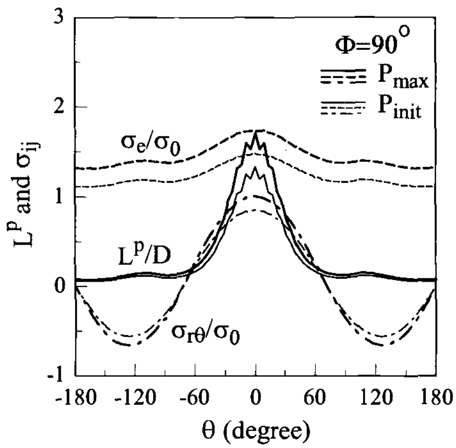

Figure 8(g). Angular variation of L^p, effective stress and shear stress, Arcan specimen, Φ=90°.

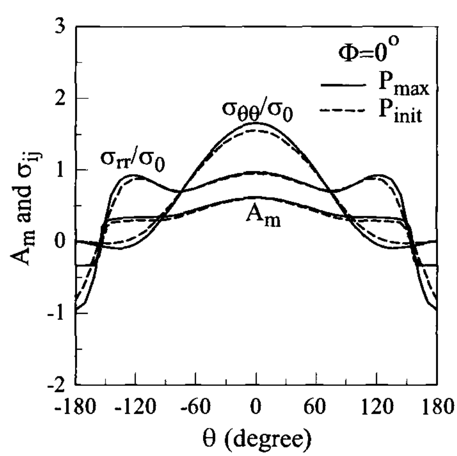

Figure 9(a). Angular variations of A_m, σ_{rr} and $\sigma_{\theta\theta}$, Arcan specimen, Φ=0°.

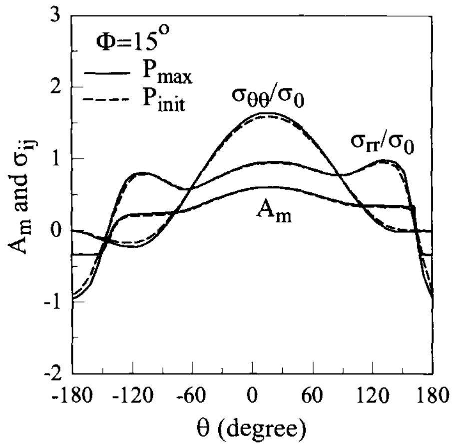

Figure 9(b). Angular variations of A_m, σ_{rr} and $\sigma_{\theta\theta}$, Arcan specimen, $\Phi=15^o$.

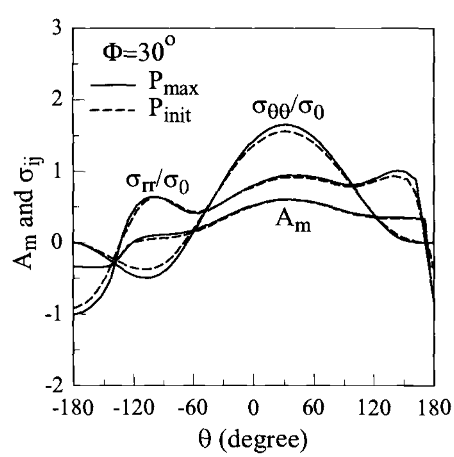

Figure 9(c). Angular variations of A_m, σ_{rr} and $\sigma_{\theta\theta}$, Arcan specimen, $\Phi=30^o$.

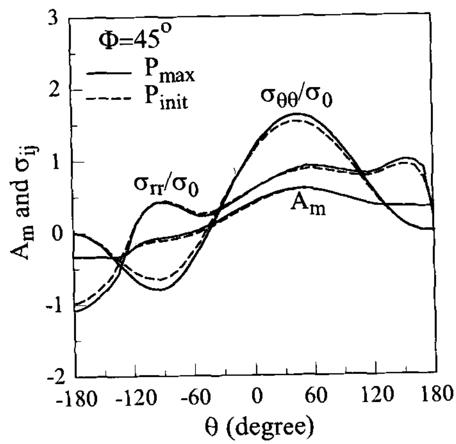

Figure 9(d). Angular variations of A_m, σ_{rr} and $\sigma_{\theta\theta}$, Arcan specimen, Φ=45°.

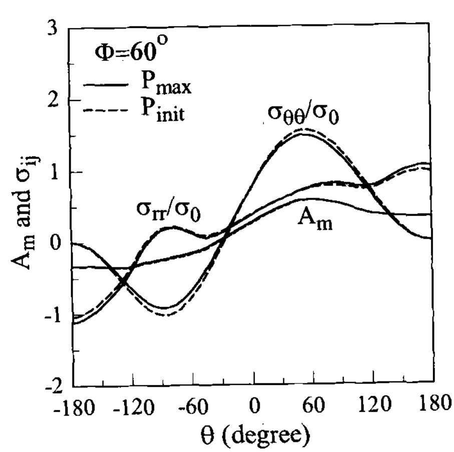

Figure 9(e). Angular variations of A_m, σ_{rr} and $\sigma_{\theta\theta}$, Arcan specimen, Φ=60°.

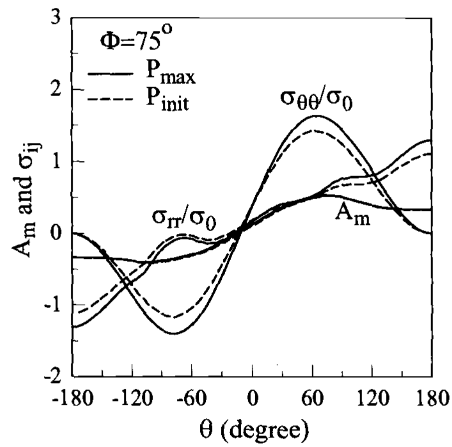

Figure 9(f). Angular variations of A_m, σ_{rr} and $\sigma_{\theta\theta}$, Arcan specimen, Φ=75°.

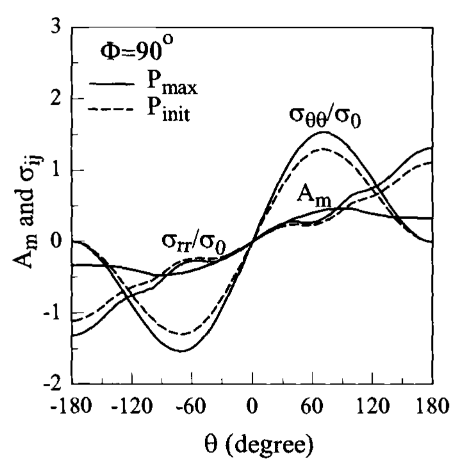

Figure 9(a). Angular variations of A_m, σ_{rr} and $\sigma_{\theta\theta}$, Arcan specimen, Φ=90°.

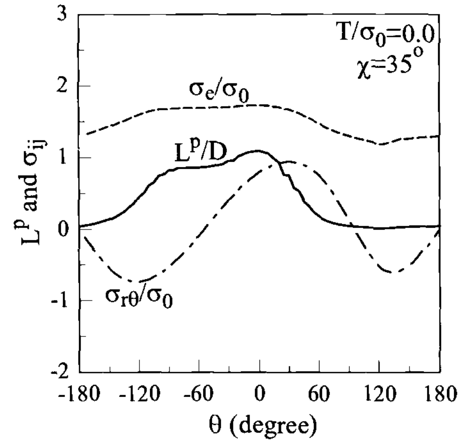

Figure 10(a). Angular variation of L^p, effective stress and shear stress, for SSY model with $T/\sigma_0=0.0$ and $\chi=35°$.

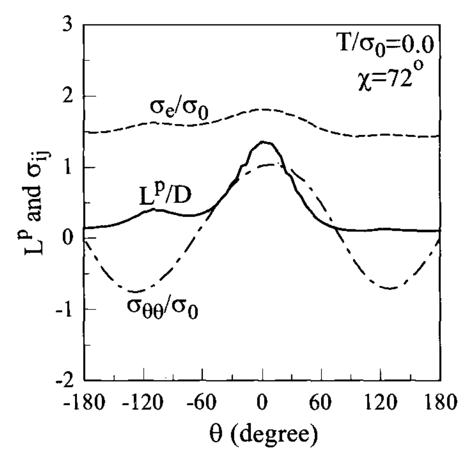

Figure 10(b). Angular variation of L^p, effective stress and shear stress, for SSY model with $T/\sigma_0=0.0$ and $\chi=72°$.

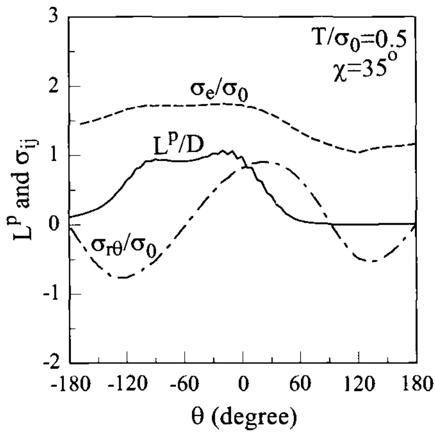

Figure 10(c). Angular variation of L^p, effective stress and shear stress, for SSY model with $T/\sigma_0=0.5$ and $\chi=35°$.

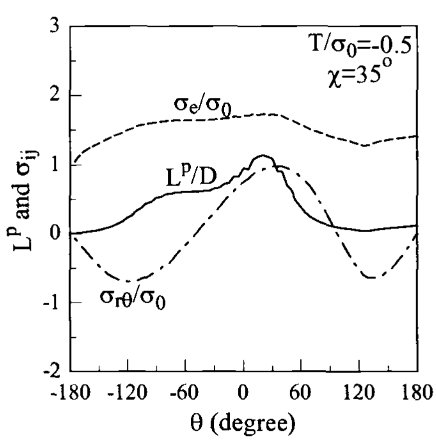

Figure 10(d). Angular variation of L^p, effective stress and shear stress, for SSY model with $T/\sigma_0=-0.5$ and $\chi=35°$.

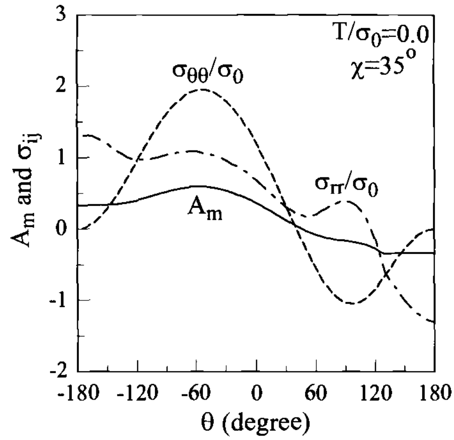

Figure 11(a). Angular variations of A_m, σ_{rr} and $\sigma_{\theta\theta}$, for SSY model with $T/\sigma_0=0.0$ and $\chi=35°$.

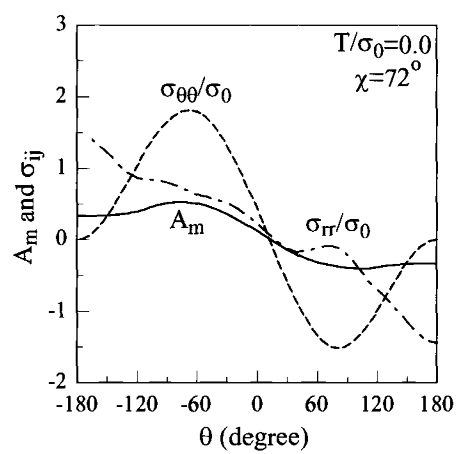

Figure 11(b). Angular variations of A_m, σ_{rr} and $\sigma_{\theta\theta}$, for SSY model with $T/\sigma_0=0.0$ and $\chi=72°$.

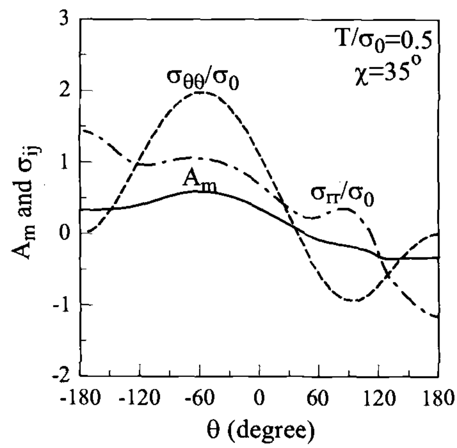

Figure 11(c). Angular variations of A_m, σ_{rr} and $\sigma_{\theta\theta}$, for SSY model with $T/\sigma_0=0.5$ and $\chi=35^o$.

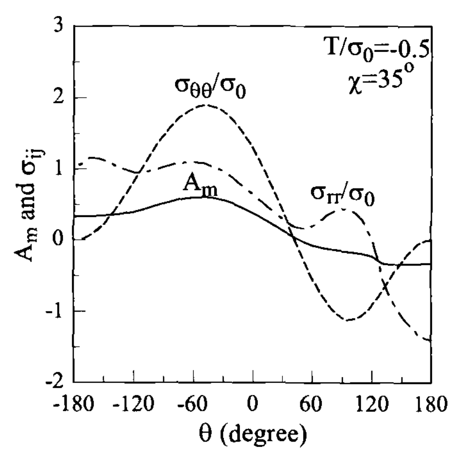

Figure 11(d). Angular variations of A_m, σ_{rr} and $\sigma_{\theta\theta}$, for SSY model with $T/\sigma_0=-0.5$ and $\chi=35^o$.

In order to further understand the effects of crack geometry on L^P and A_m, the angular variations of L^P and A_m in the SSY model are shown in Figures 10 and 11, where L^P is normalized by a characteristic length for this model, R_k, defined in Eq. (8); similar features for L^P and A_m are obtained for the SSY model. Figures 10 and 11 also indicate that, for a given T-stress, increasing the Mode II component of loading will lead to an increase in the maximum value of L^P, while for a given mode mixity, decreasing T-stress increases the maximum value of L^P.

Radial Variations along Local Mode I and Mode II Directions

Since theoretical and experimental studies [*16-21*] have shown that crack initiation and growth occur under either local Mode I or Mode II conditions for a wide range of loading conditions, results in this section are limited to the mixed-mode crack tip fields along the directions that correspond to a maximum in either local Mode I or local Mode II parameters. In all cases, it will be shown that the radial variation of the stress field along these directions is optimally represented as a function of the normalized distance, r/L^P, in that the normalized variations of each of the stress components collapse onto a single curve.

First, the radial distribution of stress is analyzed for Arcan specimen. Along both the Mode I and Mode II directions, Figure12a and Figure 13a show the radial variation of $\Sigma_e=\sigma_e/\sigma_0$ with normalized distance r/L^P, respectively. For all loading angles ($\Phi=0^0$ to 90^0), the data for Σ_e falls on a single curve with amplitude, A_e, (the value of Σ_e at $r/L^P=1$), equivalent to a constant $\xi=1.2$, and independent of loading angle. Clearly, the effective stress can be expressed as

$$\Sigma_e=\frac{\sigma_e}{\sigma_0}=\xi\ f\left(\frac{L^P}{r}\right), \qquad (9)$$

independent of loading and specimen geometry.

For stress components, σ_{rr}, $\sigma_{\theta\theta}$ and $\sigma_{r\theta}$, the radial distribution depends not only on normalized distance, r/L^P, but also on constraint and mode mixity. To observe the radial variation of stress components, we define a normalized stress Σ_{ij} in Eq.(4) as

$$\Sigma_{ij}=\frac{1}{A_{ij}}\frac{\sigma_{ij}}{\sigma_0},\ \text{and}\ \Sigma_m=\frac{1}{A_m}\frac{\sigma_m}{\sigma_0}, \qquad (10)$$

where

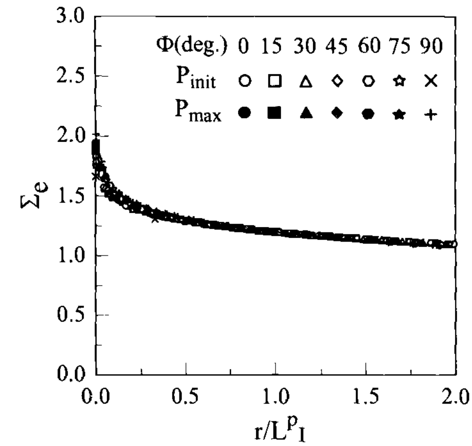

Figure 12(a). Variation of $\Sigma_e=\sigma_e/\sigma_0$ with normalized distance, r/L^P_I ,in the Mode I directions, Arcan specimen.

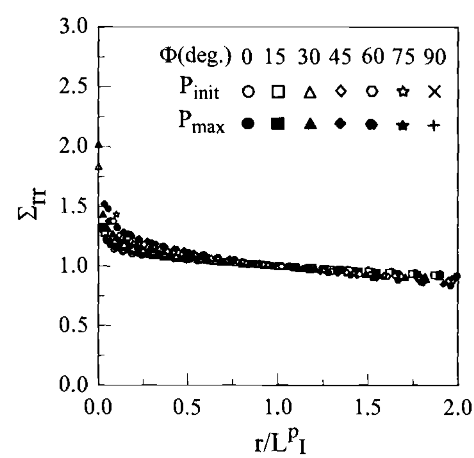

Figure 12(b). Variation of $\Sigma_{rr}=\sigma_{rr}/(A_{rr}\sigma_0)$ with normalized distance, r/L^P_I, in the Mode I direction, Arcan specimen.

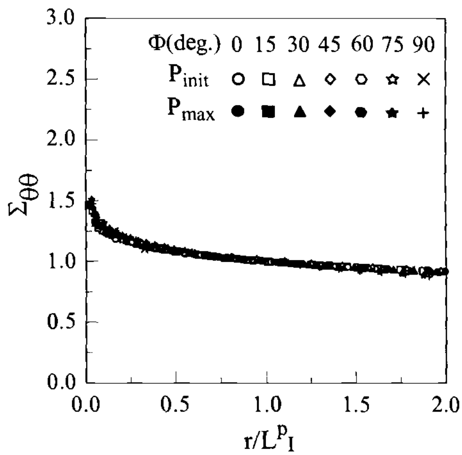

Figure 12(c). Variation of $\Sigma_{\theta\theta}=\sigma_{\theta\theta}/(A_{\theta\theta}\sigma_0)$ with normalized distance, r/L^p_I, in the Mode I direction, Arcan specimen.

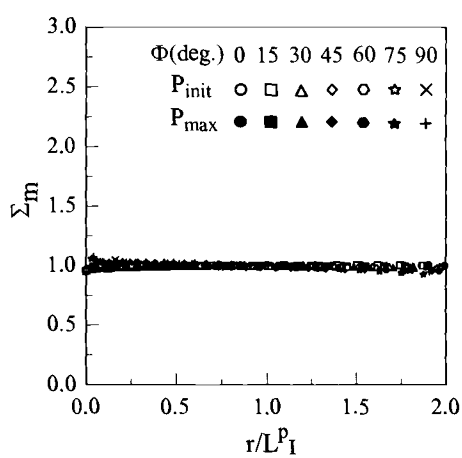

Figure 12(d). Variation of $\Sigma_{mm}=\sigma_{mm}/(A_{mm}\sigma_0)$ with normalized distance, r/L^p_I, in the Mode I direction, Arcan specimen.

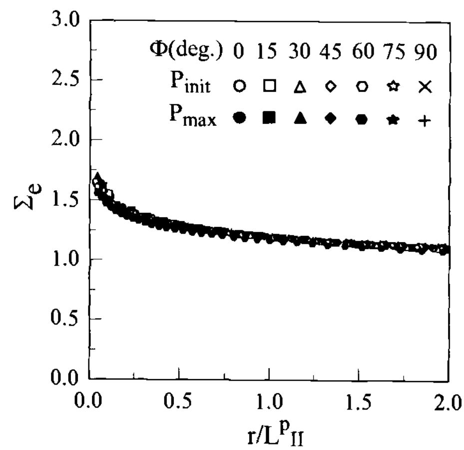

Figure 13(a). Variation of $\Sigma_e = \sigma_e/\sigma_0$ with normalized distance, r/L^P_{II}, in the Mode II directions, Arcan specimen.

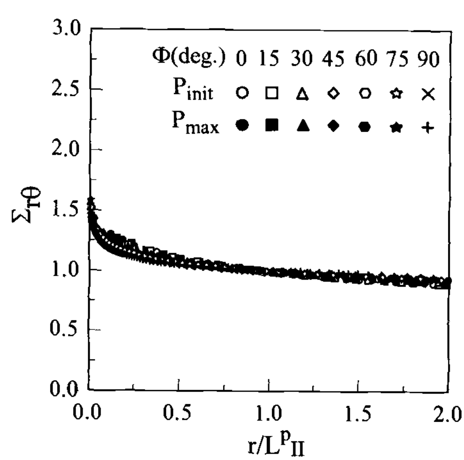

Figure 13(b). Variation of $\Sigma_{r\theta} = \sigma_{r\theta}/(A_{r\theta}\sigma_0)$ with normalized distance, r/L^P_{II}, in the Mode II direction, Arcan specimen.

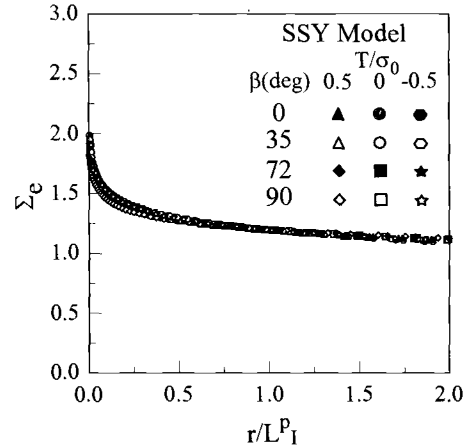

Figure 14(a). Variation of $\Sigma_e=\sigma_e/\sigma_0$ with normalized distance, $r/L^p{}_I$, in the Mode I direction, SSY model.

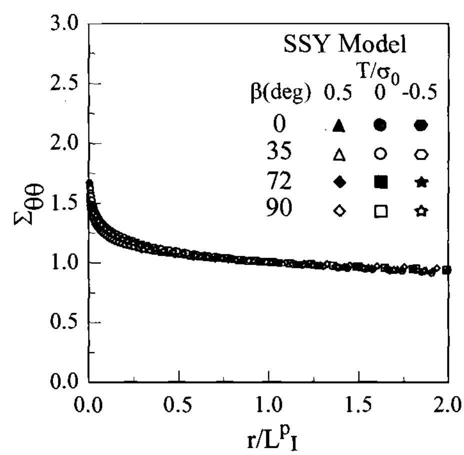

Figure 14(b). Variation of $\Sigma_{\theta\theta}=\sigma_{\theta\theta}/(A_{\theta\theta}\sigma_0)$ with normalized distance, $r/L^p{}_I$, in the Mode I direction, SSY model.

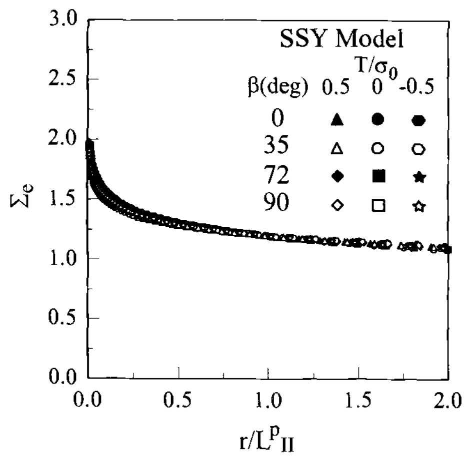

Figure 15(a). Variation of $\Sigma_e=\sigma_e/\sigma_0$ with normalized distance, $r/L^p{}_{II}$, in the Mode II direction, SSY model.

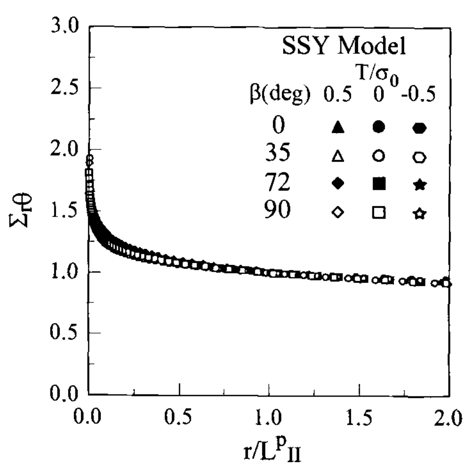

Figure 15(b). Variation of $\Sigma_{r\theta}=\sigma_{r\theta}/(A_{r\theta}\sigma_0)$ with normalized distance, $r/L^p{}_{II}$, in the Mode II direction, SSY model.

$$A_{ij} = \frac{\sigma_{ij}}{\sigma_0}\bigg|_{r/L^p=1}, \text{ and } A_m = \frac{\sigma_m}{\sigma_0}\bigg|_{r/L^p=1} \tag{11}$$

Figures 12b and 12c present the normalized normal stresses and triaxial stress for all cases as a function of normalized distance r/L^p along the local Mode I direction in. As expected, the shear stress is almost zero in this direction for all cases. Figure 13b shows the shear stress variation against the normalized distance r/L^p in the local Mode II direction, with normal stresses along these directions taking small values. Results from all cases (including the Arcan specimen) show that the radial variations of each stress component in the local Mode I and Mode II directions collapse onto a single master curve, provided that the radial distance is normalized by the length scale L^P.

For the SSY model, the radial variation of stresses versus normalized distance r/L^p in both modes I and II directions are shown in Figures 14 and 15, respectively. These results clearly indicate that the stress can be accurately written in the form of Eq. (4).

Relationship between A_{ij} and A_m

The radial distribution results indicate that the mixed-mode crack tip fields are self-similar when L^p is used to normalize radial distance from the crack tip. However, if L^p and A_m are to be used to characterize mixed-mode I/II crack tip fields, the amplitude of the stress fields, A_{ij},, defined as value of σ_{ij}/σ_0 at $r=L^p$, must be a well-defined function of the stress triaxiality parameter A_m. Furthermore, at least along the directions corresponding to either local Mode I or local Mode II, the relationship $A_{ij}(A_m)$ must be independent of mode mixity, specimen geometry and loading (or T-stress for SSY model).

Using finite element results and Eq. (11), A_{ij} can be plotted with A_m for the Arcan specimen and the SSY model. The relationship $A_{ij}(A_m)$ for both Mode I and Mode II directions is presented in Figures 16 and 17, respectively. Results presented in Figs 16 and 17 clearly indicate that the relationship $A_{ij}(A_m)$ is geometry and loading independent, demonstrating that stress amplitudes can be uniquely characterized by A_m. It is noted that the Theory results shown in Figs. 16 and 17 use Eqs 24 and 27, respectively, which are derived in the following section.

Theoretical Consideration of Am-Family of Crack Tip Field

The results strongly suggest that plane stress, mixed-mode I/II crack tip stress fields have the form of Eqs. (4) and (5). In this section, the underlying basis for the A_m-family of crack tip fields is further analyzed.

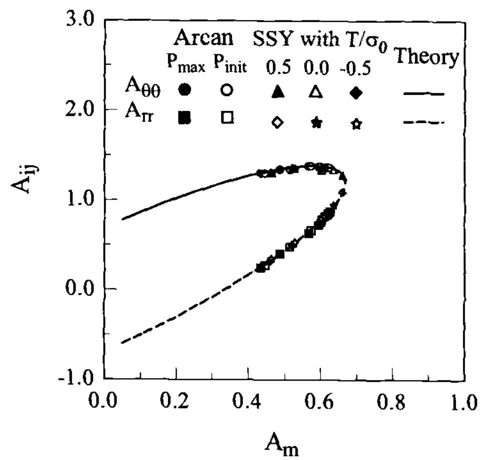

Figure 16. A_{ij} as a function of A_m in Mode I direction.

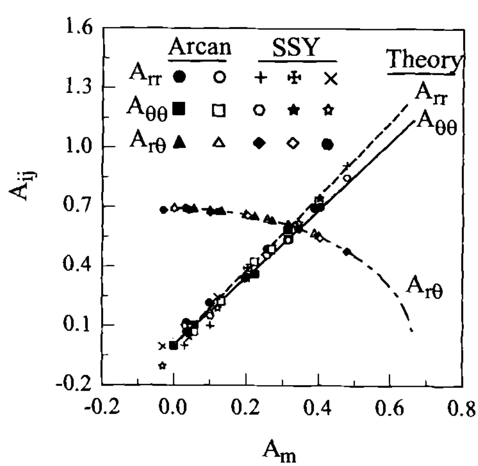

Figure 17. A_{ij} as a function of A_m in Mode II direction.

Basic Equations and General Results

First, we utilize the stress-based equilibrium equations to identify key features of the stress field given in Eqs (4) and (5). Without loss of generality, the radial distribution function $f(r/L^p)$ in Eq.(4) is assumed to be dependent on material properties, reducing to a constant for a perfectly plastic material.

The equilibrium equations for a planar state of stress in polar coordinates are written;

$$\left.\begin{aligned} &\frac{\partial \sigma_{rr}}{\partial r} + \frac{1}{r}\frac{\partial \sigma_{r\theta}}{\partial \theta} + \frac{\sigma_{rr} - \sigma_{\theta\theta}}{r} = 0 \\ &\frac{\partial \sigma_{r\theta}}{\partial r} + \frac{1}{r}\frac{\partial \sigma_{\theta\theta}}{\partial \theta} + \frac{2\sigma_{r\theta}}{r} = 0 \end{aligned}\right\}. \tag{12}$$

Substitution of Eqs (4) and (5) into (12) gives

$$\left.\begin{aligned} &A_{rr}\frac{\partial}{\partial r} f + \frac{1}{r}\frac{\partial}{\partial \theta}(A_{r\theta} f) + (A_{rr} - A_{\theta\theta})\frac{f}{r} = 0 \\ &A_{r\theta}\frac{\partial}{\partial r} f + \frac{1}{r}\frac{\partial}{\partial \theta}(A_{\theta\theta} f) + 2A_{r\theta}\frac{f}{r} = 0 \end{aligned}\right\}. \tag{13}$$

Introducing the variable, $r^* = L^p/r$, Eq. (13) can be rewritten in variables-separable form in an $r^* - \theta$ polar coordinate system as

$$\left.\begin{aligned} &\frac{\dfrac{dA_{r\theta}}{d\theta} + A_{rr} - A_{\theta\theta}}{A_{rr} - \dfrac{A_{r\theta}}{L^p}\dfrac{dL^p}{d\theta}} = -\frac{r^*}{f}\frac{df}{dr^*} = s \\ &\frac{\dfrac{dA_{r\theta}}{d\theta} + A_{rr} - A_{\theta\theta}}{A_{rr} - \dfrac{A_{r\theta}}{L^p}\dfrac{dL^p}{d\theta}} = -\frac{r^*}{f}\frac{df}{dr^*} = s \end{aligned}\right\}. \tag{14}$$

It is noted that the constant, s, is a function of material properties and is independent of (θ, r^*). Using Eq. (14), it is easily shown that

$$f\left(\frac{L^p}{r}\right) = \left(\frac{L^p}{r}\right)^s, \tag{15}$$

and

$$\left.\begin{aligned} & -sA_{rr} + \frac{dA_{r\theta}}{d\theta} + sA_{r\theta}\frac{1}{L^p}\frac{dL^p}{d\theta} + \left(A_{rr} - A_{\theta\theta}\right) = 0 \\ & \left(2-s\right)A_{r\theta} + \frac{dA_{\theta\theta}}{d\theta} + sA_{\theta\theta}\frac{1}{L^p}\frac{dL^p}{d\theta} = 0 \end{aligned}\right\}. \tag{16}$$

When the plastic strain is assumed to be much greater than the elastic strain in the near crack tip, i.e., the elastic strain is negligible compared to the plastic strain, it has been shown for a power-law material (Hutchinson, [*2*]; Rice and Rosengren, [*3*]; and Shih [*4*]) that s is a function of the hardening exponent n,

$$s = \frac{1}{n+1}, \tag{17}$$

Thus, the normalized form given in Eq.s (4) and (5) is consistent with existing solutions for power-law hardening materials where the elastic response is neglected.

The equilibrium equations given in (16) can be further reduced to

$$\left(1-s\right)A_{rr}A_{\theta\theta} - A_{\theta\theta}^2 + A_{\theta\theta}\frac{dA_{r\theta}}{d\theta} = \left(2-s\right)A_{r\theta}^2 + A_{r\theta}\frac{dA_{\theta\theta}}{d\theta}. \tag{18}$$

For plane stress problems, the out-of-plane normal stress vanishes, σ_{zz}=0, and one can write the von-Mises effective stress in the form of

$$\frac{\sigma_e}{\sigma_0} = A_e\left(\frac{L^p}{r}\right)^s, \tag{19}$$

where

$$A_e = \left(A_{rr}^2 + A_{\theta\theta}^2 - A_{rr}A_{\theta\theta} + 3A_{r\theta}^2\right)^{\frac{1}{2}} \tag{20}$$

is the amplitude of σ_e the in the crack-tip region. According to the definition for L^p, $\sigma_e = \xi\sigma_0$ at r/L^p=1, so that

$$A_e = \xi. \tag{21}$$

Thus, the stress triaxiality parameter can be expressed as

$$A_m = \frac{\sigma_m}{\sigma_e} = \frac{A_{rr} + A_{\theta\theta}}{3A_e}. \tag{22}$$

Thus, there are 5 unknown functions: A_{rr}; $A_{\theta\theta}$; $A_{r\theta}$; A_e; and A_m within the stress fields. Four equations; (18), (20), (21) and (22) relate these five functions. Therefore, the first four functions can be written in terms of the fifth function, A_m, in the form of Eq. (5).

In summary, direct application of the stress equilibrium equations to the form given in Equs (4) and (5) indicates that (a) the radial variation of all stress components, $f(r/L^P)$, is generally a power relationship $(r/L^P)^s$, where s is 1/n+1 when elastic deformations are neglected and (b) the amplitude of all stress components is determined by A_m in the crack tip region. Taken together these results indicate that, under quite general conditions, the crack tip stress fields are controlled by two parameters, L^P and A_m. Since specimen geometry and mixed-mode loading conditions result in variations in crack tip constraint conditions, the proposed model indicates that these effects will result in changes in the parameters L^P and A_m.

Specific Form of $A_{ij}(A_m)$ along Local Mode I and Mode II Directions

Explicit forms for the relationship $A_{ij}(A_m)$ can be obtained along radial lines corresponding to local Mode I conditions (i.e., approximately maximum in the parameters A_m, tensile stress or COD_I) or local Mode II conditions (i.e., maximum in parameters σ_e, in-plane shear stress or COD_{II}). As noted earlier, these directions have physical significance since crack growth has been shown to occur along local Mode I or Mode II directions [*16-21*].

Along the local Mode I direction, one can use the presence of a maximum in the opening stress ($d\sigma_{\theta\theta}/d\theta = 0$) to write

$$dA_{\theta\theta}/d\theta + sA_{\theta\theta}\, dL^p/L^p d\theta = 0\,. \tag{23}$$

Substitution of Eq. (21) into the second equation of Eq. (15) leads to $A_{r\theta} = 0$, so that, the shear stress vanishes ($\sigma_{r\theta}$=0) in that direction. Using Eqs. (20), (21) and (22), we arrive at

$$\left.\begin{aligned} A_{rr} &= \xi\left(\frac{3}{2}A_m - \frac{\sqrt{12-27A_m^2}}{6}\right) \\ A_{\theta\theta} &= \xi\left(\frac{3}{2}A_m + \frac{\sqrt{12-27A_m^2}}{6}\right) \\ A_{r\theta} &= 0 \end{aligned}\right\}. \tag{24}$$

In Mode II direction, one can use the fact that the in-plane shear stress reaches its maximum, i.e.,

$$\partial\sigma_{r\theta}/\partial\theta = \partial A_{r\theta}/\partial\theta + sA_{r\theta}\, \partial L^p/L^p\partial\theta = 0\,, \tag{25}$$

in Eqs. (16), leading to

$$(1-s)A_{rr} - A_{\theta\theta} = 0 . \tag{26}$$

Using Eqs. (20), (21), (22) and (26), one can obtain

$$\left.\begin{aligned} A_{rr} &= \frac{2}{2-s}\ \xi\ A_m \\ A_{\theta\theta} &= \frac{2(1-s)}{2-s}\ \xi\ A_m \\ A_{r\theta} &= \xi\sqrt{\frac{1}{3} - \left(\frac{s}{2-s}\right)^2 A_m^2} \end{aligned}\right\} \tag{27}$$

Conclusions

Results from a detailed finite element and theoretical analysis for the Arcan specimen and SSY models are in excellent agreement with FE stress distributions for models ranging from small scale yielding to large scale yielding. Specifically, the results indicate that (a) the mixed-mode I/II stress fields are *self similar* when the distance from the crack tip is normalized by L^P, (b) the stress amplitude is a function of A_m; the magnitude of the stress distribution depending solely on A_m, (c) the characteristic length scale, L^P, sets the size scale over which large stresses and strains develop, and (d) L^P is the normalizing factor in a unique set of radial variations for the crack-tip stress fields.

Since the A_m-family of mixed-mode crack-tip fields provides a simple yet accurate framework for describing mixed-mode crack-tip fields, a wide range of fracture criteria can be more readily evaluated to determine which ones have the potential to be viable predictors of fracture process.

Acknowledgements

The authors wish to thank Major Scott Fawaz, Dr. James C. Newman, Jr., Mr. Daniel Shrage and Dr. David Stargel for their technical advice and support for this project.

References

[1] Thomason, P.F., Ductile Fracture of Metals, Pergamon Press, 1990.
[2] McClincock, F. A., "A Criterion for Ductile Fracture by the Growth of Holes," *ASME J. Appl. Mech.*, 1968, 35, pp.363-371.
[3] Argon, A.S. and Im, J. and Safoglu, R., "Cavity Formation from Inclusions in Ductile Fracture," *Metall. Trans.* 1975, 6A, pp.825-837.

[4] Goods, S. H. and Brown, L.M., "The Nucleation of Cavities by Plastic Deformation", *Acta Metallurgica*, 1979, 27, pp.1-15.
[5] Cox, T. B. and Low, J.R., "An Investigation of the Plastic Fracture of AISI 4340 and Nickel-200 Grade Maraging Steel", *Metallurgical Transactions*, 1974, 5A, pp.1457-1470.
[6] Rice, J. R. and Tracey, D. M., "On the Ductile Enlargement of Voids in Triaxial Stress Fields," *J. Mech. Phys. Solids, 1969, 17, pp.210-217.*
[7] Gurson, A. L., " Continuum Theory of Ductile Rupture by Void Nucleation and Growth" *J. Engng. Mater. Tech., 1977, 99, pp.3-15.*
[8] Ma, F., Sutton, M. A. and Deng, X., "Plane Strain Mixed Mode Crack-Tip Stress Fields Characterized by a Triaxial Stress Parameter and a Plastic Deformation Extent Based Characteristic Length," *J. Mech. Phys. Solids,* 2001, 49, pp2921-2953.
[9] Rice, J. R., "A Path Independent Integral and the Approximate Analysis of Strain Concentration by Notches and Cracks," *J. Appl. Mech.*, 1968, 35, pp379-386.
[10] Hutchinson, J. W., "Singular Behavior at the end of a Tensile Crack in a Hardening Material," *J. Mech. Phys. Solids,* 1968, 16, pp13-31.
[11] Rice, J. R. and Rosengren, G. F., "Plane Strain Deformation Near a Crack Tip in a Power Law Hardening Material", *J. Mech. Phys. Solids*, 1968, 16, pp13-31.
[12] Shih, C. F., "Small-Scale Yielding Analysis of Mixed Mode Plane Strain Crack Problems," *Fract. Anal., ASTM STP* 560, American Society for Testing and Materials, West Conshphocken, PA , 1974, pp187-210.
[13] Pan, J. and Shih, C. F., "Elastic Plastic Analysis of Combined Mode I, II and III Crack-Tip Fields Under Small-Scale Yielding Conditions," *Int. J. Solids & Struct*s., 1992, 29, pp.2795-2814.
[14] Larsson, S. G., Carlsson, A. J., "Influence of Non-singular Stress Terms and Specimen Geometry on Small-Scale Yielding at Crack Tip in Elastic-Plastic Materials", *J. Mech. Phys. Solids*, 1973, 21, pp.263-278.
[15] Rice, J. R, "Limitations to the Small Scale Yielding Approximation for Crack Tip Plasticity", *Journal of the Mechanics and Physics of Solids*, Vol.22, 1974, pp.17-26.
[16] Amstutz, B. E., Sutton, M. A., Dawicke, D. S. and Newman, J. C., Jr., "An Experimental Study of CTOD for Mode I/ II Stable Crack Growth in Thin 2024-T3 Aluminum Specimens," *Fracture Mechanics, ASTM STP 1256,* American Society for Testing and Materials, West Conshphocken, PA, 1995, pp.256-271.
[17] Amstutz, B. E., Sutton, M. A., Dawicke, D. S. and Newman, J. C., Jr., "Effects of Mixed Mode I/II Loading and Grain Orientation on Crack Initiation and Stable Tearing in 2024-T3 Aluminum Specimens," *Fatigue and Fracture, ASTM STP* 1296, American Society for Testing and Materials, West Conshphocken, PA , 1995, pp.105-125.
[18] Ma, F., Deng, X., Sutton, M. A. and Newman, J.C., Jr., "A CTOD Based Mixed Mode Fracture Criterion," *Mixed Mode Crack Behavior, ASTM STP 1359,* K. J. Miller and D. L. McDowell, Eds., American Society for Testing and Materials, West Conshphocken, PA , 1999, pp.86-110.
[19] Sutton, M. A., Deng, X., Ma, F., Newman, J C. Jr, and James, M., "Development and Application of a Crack Tip Opening Displacement-Based Mixed Mode Fracture Criterion," *Int. J. Solids & Struct*s, 2000, 37, 3pp.591-3618.

[20] Bose, K. and Ponte Castaneda, P., "Stable Crack growth under Mixed Mode Conditions ," *J. Mech. Phys. Solids*, 1992, 40, pp.1053-1103.

[21] M. A. Sutton, M. L. Boone, *F. Ma*, and J. D. Helm, "A Combined Modeling-Experimental Study of the Crack Opening Displacement Fracture Criterion for Characterization of Stable Crack Growth under Mixed Mode I/II Loading in Thin Sheet materials", *Engineering Fracture Mechanics*, 2000, 66, pp. 171-186.

[22] Erdogan, F. and Sih, G. C., "On the Crack Extension in Plates under Plane Loading and Transverse Shear", *Transactions of the ASME, Journal of Basic Engineering,* 1963, 85, pp.519-527.

[23] Maccagno, T. M., Knott, J. F., "The Mixed Mode I/II Fracture Behavior of Lightly Tempered HY130 Steel at Room Temperature," *Engineering Fracture Mechanics*, 1992, 41, pp.805-820.

[24] Hallback, N., Nilson, F., "Mixed Mode I/II Fracture Behavior of an Aluminum Alloy," *J. Mech. Phys. Solids*,, 1994, 42, pp.1345-1374.

[25] Sutton, M. A., Zhao, W., Boone, M. L., Reynolds, A. P. and Dawicke, D. S., " Prediction of Crack Growth for Mode I/II Loading Using Small-Scale Yielding and Void Initiation/Growth Concepts," *International Journal of Fracture*, 1997, 83, pp. 275-290.

[26] ABAQUS Users Manual 5.8, Hibbitt, Karlsson and Sorensen Inc, Providence, Rhode Island, 1998.

Xian-Kui Zhu,[1] Yil Kim,[1] Yuh-Jin Chao,[1] and P. S. Lam[2]

Constraint Effect on 3-D Crack-Front Stress Fields in Elastic-Plastic Thin Plates

---

Reference: Zhu, X.-K., Kim, Y., Chao, Y.-J. and Lam, P. S., "**Constraint Effect on 3 Crack-Front Stress Fields in Elastic-Plastic Thin Plates,**" *Fatigue and Fracture Mechanics: 33rd Volume, ASTM STP 1417*, W. G. Reuter and R. S. Piascik, Eds., ASTM International, West Conshohocken, PA, 2002.

Abstract: Using the J_2 deformation theory of plasticity, three-dimensional (3-D) elasti plastic finite element analyses are performed to study the crack-front constraint in finit sized thin plates under large-scale yielding. Two fracture specimens, center-cracked plate (CCP) and single edge-notched bend specimen (SENB), are modeled, which represent a low and a high constraint geometry, respectively. Numerically determined stress fields near the crack front are compared with those from the HRR field and the J A_2 three-term solution. Results show that the in-plane stress fields near the crack front for various applied loads possess the plane strain nature throughout the thickness exce in the region near the free surfaces, and can be characterized by the three-term solution within the region of interest, $1 < r/(J/\sigma_0) < 5$. In the area near the free surfaces, the crack-front field approaches the plane stress state if the plastic zone size is close to or greater than the plate thickness. The transition of the stress field from the far field, in t plane stress state, to the near crack-front field, dominated by the plane strain state, is demonstrated by the iso-contours of the effective stress. Variations of the J-integral an the constraint parameter A_2 along the crack front are also investigated for the two specimens.

Keywords: finite element analysis, constraint effect, J-integral, crack-front field, asymptotic solution, three dimension, elastic-plastic material

Introduction

The constraint effect in fracture is generally attributed to the effect of the geometr and loading configuration of a respective specimen or structural component. It has a

---

[1] Research scientist, graduate student and professor, respectively, Department of Mechanical Engineering, University of South Carolina, Columbia, SC 29208.
[2] Fellow engineer, Savannah River Technology Center, Materials Technology Section, Westinghouse Savannah River Company, Aiken, SC 29808.

significant effect on the crack-tip fields, and therefore the fracture resistance of the flawed components.

Studies on the constraint effect have been carried out extensively for the two-dimensional (2-D) plane-strain and plane-stress crack problems, but not for three-dimensional (3-D) cracks. The difficulty for 3-D crack problems lies in the 3-D characteristics of the stress and strain fields at the crack front. Furthermore, the mechanism of fracture for 3-D cracks is more complex than for 2-D cracks. Normally, the plane-strain state exhibits the highest constraint level and generates the highest triaxiality of stresses, whereas the plane-stress state yields the lowest limit. A real cracked structure is generally 3-D, and has both in-plane and out-of-plane constraints at the crack front. Therefore, the fracture constraint in 3-D may be different from 2-D cases typically assumed as plane strain or plane stress conditions.

It is generally agreed among researchers in fracture mechanics on the necessity of introducing a second parameter to quantify the crack-tip constraint. Various approaches along this direction have been taken for both brittle (elastic) fracture and elastic-plastic fracture. Chao and Zhang [*1*] introduced the elastic T-stress concept and used it to study the constraint effect as the specimen fails in brittle manner and the crack tip fields are governed predominantly by the linear elastic fracture mechanics. Extension of their work can be found in Chao and Reuter [*2*] and Chao *et al.* [*3*]. The elastic T-stress is also used for the interpretation of constraint for elastic-plastic crack tip fields. Larsson and Carlsson [*4*] first employed the K_I-T description in the boundary layer analysis to investigate the effect of finite size of specimens on the plastic zone at the crack tip. They found that the shape and size of plastic zones for some plane-strain specimens are substantially different under different T-stress for the same applied K_I. Betegon and Hancock [*5*], Al-Ani and Hancock [*6*] extended and mixed the K_I-T description for elastic materials to the two-parameter J-T description for elastic-plastic materials through the finite element analysis (FEA). Their results showed that loss of J dominance is attributed to negative T-stress, while zero or positive T-stress retains J dominance. Since 1991, numerous 2-D FEA analyses have been performed to investigate the constraint effect on the elastic-plastic crack-front fields, [*5-14*].

Using the asymptotic mathematical method and the deformation theory of plasticity, Sharma and Aravas [*15*] theoretically obtained a two-term expansion of stress fields for a plane strain mode-I crack in power-law hardening materials. The first term is the well-known HRR solution [*16-17*], the second is an additional term relating to the constraint. Based on the FEA results, O'Dowd and Shih [*7-8*] proposed a simple two-term solution with a constant second term, that is the so-called J-Q theory. However, the hydrostatic-stress parameter Q is an engineering definition, which depends on the location within the region of interest [*13*]. To remove the distance dependence, O'Dowd and Shih [*11*] suggested to use the standard small-scale yielding solution with $T = 0$ as the reference field in the J-Q theory.

Through complete asymptotic analysis, Yang *et al.* [*18*, *19*] and Chao *et al.* [*20*] presented higher-order crack-tip fields in power-law hardening materials. They have shown that a two-term expansion is not sufficient to describe the near-tip fields, while more than three terms are redundant for plane-strain mode-I cracks. Thus, a three-term solution controlled only by two parameters, J and A_2, is developed. The constraint parameter A_2 is independent of distance from the crack tip within the region of interest.

Based on the three-term solution, Chao and Zhu [*21*] determined the size requirements of specimens for a two-parameter fracture testing. Zhu and Chao [*22*] have further explored the application of the three-term solution to non-hardening materials. Recently, the J-A_2 concept has been extended to quantify the constraint effect on the J-resistance curves in ductile crack growth [*23-24*], and on the crack-tip fields in creeping materials [*25-26*].

To explore the constraint effect on 3-D crack-front fields, Brocks and Olschewski [*27*] carried out the FEA for various 3-D cracked structures. Nakamura and Parks [*28*] performed 3-D FEA calculations using the boundary layer method, and concluded that the crack-front field is dominated by the plane-strain HRR solution only for very small applied loads. Parks [*29*] pointed out that the 3-D crack-front fields significantly deviate from the plane-strain SSY solution. Henry and Luxmoore [30] indicated that the Q-stress and the stress-triaxiality factor are equivalent at the mid-plane of 3-D fracture specimens. In the context of the J-Q approach, Nevalainen and Dodds [*31*] investigated the 3-D constraint effect on brittle fracture in SE(B) and C(T) specimens numerically. Pardoen et al. [*32*] reported the thickness dependence of fracture resistance in thin aluminum plates. Yuan and Brocks [*33*] conducted 3-D FEA, and showed that the crack-front stress field is dominated by the plane-strain solution only for extremely small plastic zone sizes. They concluded that the 3-D crack-front field could not be correctly described by the J-Q theory for higher loads. Most recently, Kim *et al.* [*34*] performed the 3-D modified boundary layer analysis for thin plates, and found that the J-A_2 solution can characterize the 3-D crack-front field throughout the thickness except for the region near the free surface. Since it is a boundary layer analysis, the results are only valid under the small-scale conditions (SSY). In addition, there are numerous elastic-plastic 3-D FEA investigations for surface-cracked plates in open literature, such as Wang et al. [*35*] and Wang [*36*].

The objective of the present work is to extend our previous analysis [*34*] to the large-scale yielding (LSY) case. The constraint effect on the crack-front stress field for finite-sized cracked thin plates is investigated and quantified using the J-A_2 three-term solution. FEA stress fields are calculated for 3-D CCP and SENB specimens based on a power-law material and the J_2 deformation theory of plasticity. Detailed comparisons between the numerical results, the HRR field and the three-term solution for the stress components along the crack front are presented. Variations of the J-integral and the constraint parameter A_2 along the crack front are also reported for the two specimens.

Theoretical Background

For 3-D elastic crack problems, Kassir and Sih [*37*] and Zhu et al [*38*] have theoretically proved that the 3-D crack-front field at a plane normal to the crack front under arbitrary loads is the linear sum of the plane strain mode-I, mode-II and mode-III crack-tip fields. Nakamura and Parks [*28*] pointed out that a pointwise plane-strain state will prevail within a 3-D elastic body, if the out-of-plane strain components are bounded or have lower order singularity than the in-plane strain components at the crack front. In analogy with the linear elastic results, it is assumed that asymptotic plane strain fields will also prevail for 3-D elastic-plastic crack problems. As such, in the present paper the elastic-plastic crack-front field will be analyzed and characterized using the HRR field and the J-A_2 solution on planes normal to the crack front.

HRR Singularity Field

Based on the power-law description and deformation theory of material constitutive behavior, the HRR field [*16,17*] gives the asymptotic stress and strain fields near the tip of a 2-D crack as

$$\begin{aligned} \sigma_{ij} &= \sigma_0 \left(\frac{J}{\alpha \varepsilon_0 \sigma_0 I_n r} \right)^{1/(n+1)} \tilde{\sigma}_{ij}(\theta; n) \\ \varepsilon_{ij} &= \alpha \varepsilon_0 \left(\frac{J}{\alpha \varepsilon_0 \sigma_0 I_n r} \right)^{n/(n+1)} \tilde{\varepsilon}_{ij}(\theta; n) \end{aligned} \tag{1}$$

where σ_0 is a reference (or yield) stress, $\varepsilon_0 = \sigma_0 / E$ is a reference (or yield) strain with E as Young's modulus, and α is a material constant. The integration constant I_n and the dimensionless angular functions of stresses, $\tilde{\sigma}_{ij}$, and strains, $\tilde{\varepsilon}_{ij}$, depend on the strain hardening exponent n and the stress state at the crack tip, either plane stress or plane strain. Numerical values of these angular functions are given in Shih [*39*].

J-A₂ Three-Term Solution

Using the J_2 deformation theory of plasticity and the asymptotic series expansion, Yang *et al.* [*18, 19*] and Chao *et al.* [*20*] carried out a complete asymptotic analysis for the higher-order crack-tip fields in power-law hardening materials. A three-term expansion is thus developed, and controlled only by two parameters, J and A_2. The three-term asymptotic stress and strain fields can be written as

$$\begin{aligned} \sigma_{ij} &= A_1 \sigma_0 \left[\left(\frac{r}{L} \right)^{s_1} \tilde{\sigma}_{ij}^{(1)}(\theta) + A_2 \left(\frac{r}{L} \right)^{s_2} \tilde{\sigma}_{ij}^{(2)}(\theta) + A_2{}^2 \left(\frac{r}{L} \right)^{s_3} \tilde{\sigma}_{ij}^{(3)}(\theta) \right] \\ \varepsilon_{ij} &= A_1^n \alpha \varepsilon_0 \left[\left(\frac{r}{L} \right)^{n s_1} \tilde{\varepsilon}_{ij}^{(1)}(\theta) + A_2 \left(\frac{r}{L} \right)^{(n-1)s_1 + s_2} \tilde{\varepsilon}_{ij}^{(2)}(\theta) + A_2{}^2 \left(\frac{r}{L} \right)^{(n-1)s_1 + s_3} \tilde{\varepsilon}_{ij}^{(3)}(\theta) \right] \end{aligned} \tag{2}$$

where the angular functions $\tilde{\sigma}_{ij}^{(k)}$ and $\tilde{\varepsilon}_{ij}^{(k)}$ (here $k = 1, 2, 3$), the stress-singularity exponents s_k ($s_1 < s_2 < s_3$), and the integration constant I_n are only dependent on the hardening exponent n, and independent of the other material constants (i.e. α, ε_0, σ_0) and the applied loads. L is a characteristic length parameter which can be chosen as the crack length a, the specimen width W, the thickness B, or unity.

The first term in equation (2) is the HRR filed as shown in equation (1). From the HRR field, therefore, the parameters A_1 and s_1 in (2) are given by

$$A_1 = \left(\frac{J}{\alpha \varepsilon_0 \sigma_0 I_n L} \right)^{-s_1}, \quad s_1 = -\frac{1}{n+1} \tag{3}$$

The power exponent s_3 is given by $s_3 = 2s_2 - s_1$ for $n \geq 3$. A_2 in (2) is an undetermined parameter and may be related to the geometry and loading configuration of the specimens. Numerical values of the non-dimensional angular functions and s_2 in (2) are given in Chao and Zhang [*40*] which is available upon request.

For 3-D elastic-plastic cracks, the J-integral varies along the crack front [*28*], and also varies along the radial direction at a plane normal to the crack front [*34*]. As such, local values of the J-integral near the 3-D crack front will be used in (1) and (2) to present the following results. To investigate the constraint effect and the dominancy of the plane strain state by the 3-D local field, the stress fields at different planes normal to the 3-D crack front are calculated from the HRR field, (1), and the J-A_2 solution, (2), and then compared with FEA results in the region of interest: $1 \leq r/(J/\sigma_o) \leq 5$.

Computational Model

Material Constitutive Model

The elastic-plastic constitutive behavior of materials is modeled using the isotropic J_2-deformation theory of plasticity under the small strain condition. The uniaxial tensile stress-strain relation follows the Ramberg-Osgood relationship, which can be generalized to the multi-axial states as follows

$$\frac{\varepsilon_{ij}}{\varepsilon_o} = (1+\nu)\frac{\sigma_{ij}}{\sigma_o} - \nu\frac{\sigma_{kk}}{\sigma_0}\delta_{ij} + \frac{3}{2}\alpha\left(\frac{\sigma_e}{\sigma_o}\right)^{n-1}\frac{s_{ij}}{\sigma_0} \tag{4}$$

where ν is Poisson's ratio, δ_{ij} is the Kronecker delta. σ_0 and $\varepsilon_0 = \sigma_0/E$ are the yield stress and the yield strain, respectively. s_{ij} are the deviatoric stress components, and σ_e is the von Mises effective stress defined as $\sigma_e = \sqrt{3s_{ij}s_{ij}/2}$. α is a material constant, and n is the strain-hardening exponent.

Notice that the rectangular coordinate system is employed in this work so that the x-axis lies in the crack plane, and normal to the straight crack front; the y-axis is vertical to the crack plane, the z-axis is tangential to the crack front. In all calculations, the material properties are chosen as E = 222.5 GPa, σ_0 = 445 MPa, ν = 0.3, α = 1, and n = 3. These values are typical for the nuclear reactor vessel steel A533B at the room temperature.

Specimen Geometry and FEA Model

Two typical fracture specimen geometries are considered, i.e. the center-cracked plate (CCP) and the single edge-notched bend (SENB) specimen as shown in Figure 1. These two geometries are chosen because they represent a very low and a very high constraint, respectively. For the CCP, the specimen length is $2H$, the specimen width is

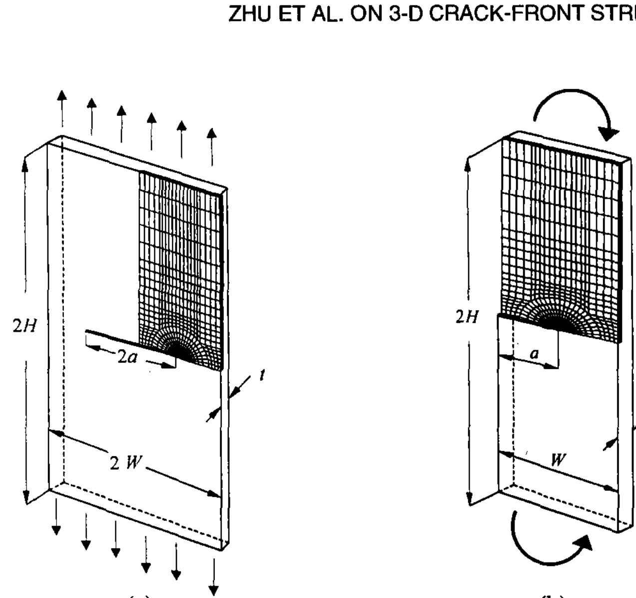

Figure 1 – *Geometry and FE Model for the Analysis:* (a) *Center-Cracked Plate (CCP) Specimen, and* (b) *Single Edge-Notched Bend (SENB) Specimen*

$2W$, the specimen thickness is t, and the crack length is $2a$. For the SENB, the specimen width is W, the specimen span is $2H$, the specimen thickness is t, and the crack length is a. In this calculation, $a/W = 0.5$, $t/W = 0.1$ and $H/W = 2$. This ratio of the specimen length to the specimen width can eliminate the influence of the crack length on the crack-tip fields [*41*]. Due to symmetry, only 1/8 of the CCP specimen and 1/4 of the SENB specimen were modeled, as shown in Figure 1. Appropriate symmetry boundary conditions were applied on the symmetric planes. These specimens were computed and analyzed under a variety of loading.

All FEA calculations were conducted in this work using the commercial code: ABAQUS (2000, version 6.1). Only one finite element mesh was used for the two specimens as shown in Figure 1. This typical finite element model has 41921 nodes and 9016 elements, and the 3-D elements are 20-noded quadratic brick elements with reduced integration. In the finite element mesh shown in Figure 1, twenty-four wedge-shaped degenerated 20-noded elements comprise the upper half of the crack tip. In order to obtain the drastic change of the stress field at the free surface, seven-layers of elements in the thickness direction are used. The size of these elements is exponentially decreased from the mid-plane toward the free surface. On the plane perpendicular to the crack front, the element size is gradually increased with radial distance from the crack front, while the angular increment of each element is kept constant throughout the mesh. In the direction of thickness, the identical planar mesh is repeated from the mid-plane, (i.e. $z = 0$) to the free surface (i.e. $z/t = 0.5$). All radial elements are biased, and the element size is increased as the radial distance is increased from the crack front. The

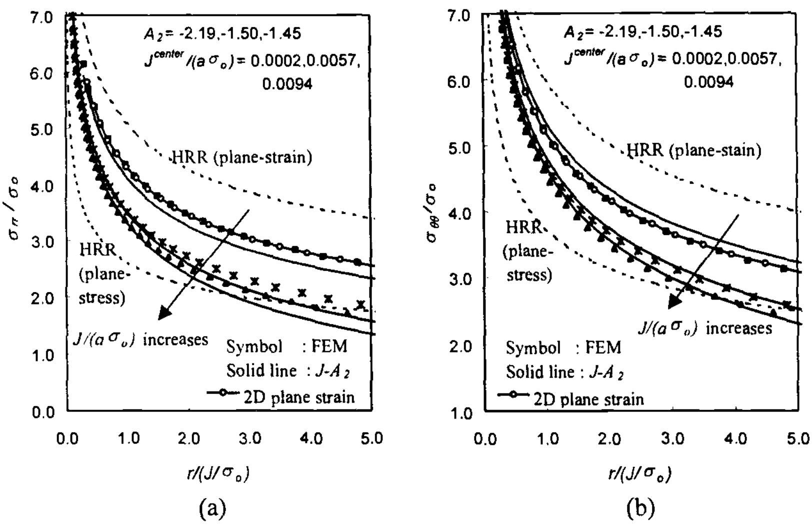

Figure 2 – *Variation of Stresses with Normalized Radial Distance at $\theta = 0^o$ at the Mid-Plane (z/t = 0) for ~~the CCP Specimen under Various Loading:~~*
(a) σ_{rr}, *and* (b) $\sigma_{\theta\theta}$

innermost ring of elements has one side collapsed onto the crack tip. All the nodes in the collapsed side are kept separate. The radial extent of the smallest element is $1.16\times10^{-5}a$ for both specimens.

Numerical Results and Analysis

Since the similar trends were found for the two specimens, the results reported in this paper are primarily for the CCP specimen. Three loading levels, 15%, 53% and 62% of the yield stress, are considered as the remote applied stresses for the CCP in calculations to represent the low-to-high loading conditions. Under these loadings, $J/(a\sigma_o) \approx$ 0.0002, 0.0057 and 0.0094 at the mid-plane, which create the plastic zone size $r_p = 0.0032t$, $1.3t$ and $3t$, or 0.064%, 26% and 60% of the uncracked ligament, respectively. The LSY is therefore achieved in the higher load case. The J (= J^{local}) integral is determined by the ABAQUS, and hereafter denotes the local J-integral throughout the text.

Stress Field at the Mid-Plane

Figure 2 shows the radial distributions of stress components σ_{rr} and $\sigma_{\theta\theta}$ obtained from FEA and the J-A_2 solution at $\theta = 0^\circ$ at the mid-plane (z/t=0) of the CCP specimen under the three loading conditions. Figure 3 depicts the angular distributions of σ_{rr}, $\sigma_{\theta\theta}$ and $\sigma_{r\theta}$ at $r\sigma_o/J = 2$ at the mid-plane of the CCP specimen subject to the three loadings. For comparison, the stress components from the plane-strain HRR field and plane-stress HRR field are also plotted in all figures. Moreover, the values of the parameter A_2 corresponding to the three loading conditions are also shown in the figures. The values

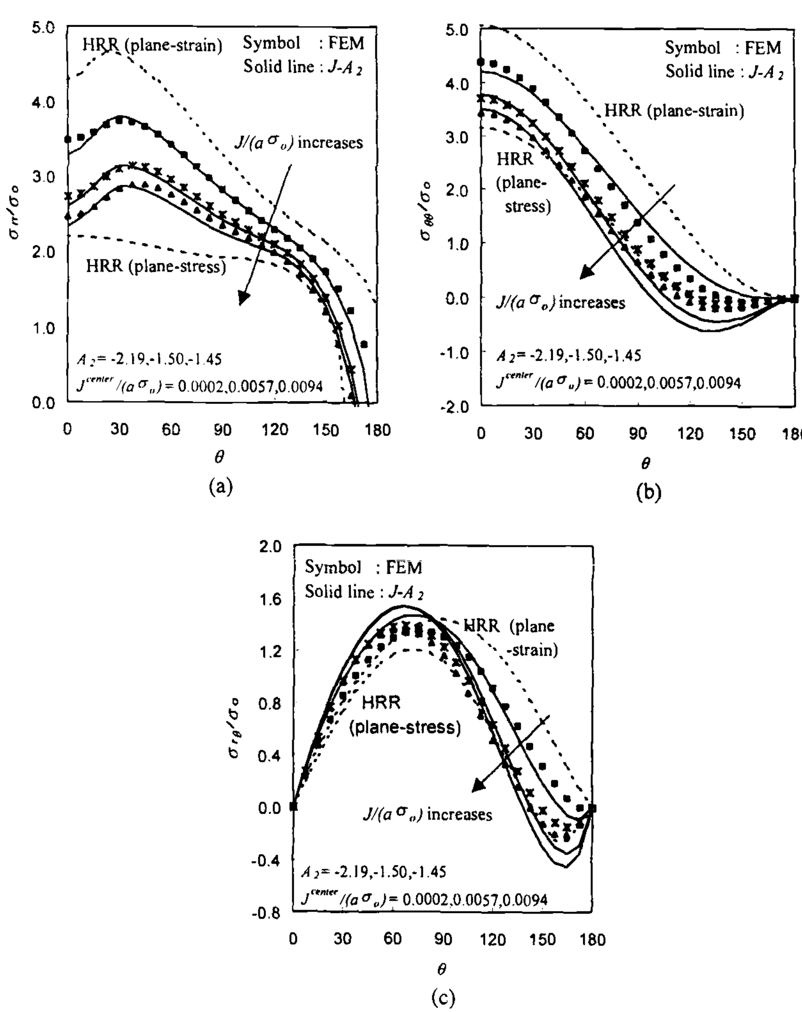

Figure 3 – *Angular Distribution of Stresses at $r\sigma_o/J = 2$ at the Mid-Plane ($z/t = 0$) for the CCP Specimen under Various Loading:* (a) σ_{rr}, (b) $\sigma_{\theta\theta}$, *and* (c) $\sigma_{r\theta}$

of A_2 in the present paper are determined by a point matching technique. The length parameter, L, is chosen as a. At a specific plane normal to the crack front, an average value of A_2 is obtained by matching the stresses σ_{rr} and $\sigma_{\theta\theta}$ obtained by FEA results to those by the J-A_2 solution (2) at $1 < r/(J/\sigma_0) < 2$ and $\theta = 0^\circ$. Noted that both J and A_2 vary along the 3-D crack front for a specific loading condition (see Section 4.5).

As noted in the figures, when loading $J^{center}/(a\sigma_0) = 0.0002$, 0.0057, and 0.0094, the parameter $A_2 = -2.19$, -1.50, and -1.45, respectively. This trend is consistent with the theoretical result [*23*] that under fully plastic conditions (or LSY) A_2 reaches a constant value. Therefore, the three loading studied indeed represent the low-to-high loading conditions.

Figures 2 and 3 show that at the mid-plane, the J-A_2 solutions indeed match very well with the FEA results in both angular and radial directions for the three loading conditions within the region of interest: $1 \le r/(J/\sigma_o) \le 5$, but not the HRR field. It is also found that all FEA results for stress components, σ_{rr}, $\sigma_{\theta\theta}$ and $\sigma_{r\theta}$, fall between those bordered by the plane-strain HRR solution and the plane-stress HRR solution. In addition, as noted in Figure 2, the 3-D FEA results for both stresses σ_{rr} and $\sigma_{\theta\theta}$ at the mid-plane are identical to the 2-D plane-strain FEA results under the lowest loading. This indicates that the stress state at the mid-plane at the 3-D crack front can be predicted with the plane strain solution as long as the three-term solution is used.

Stress Field near the Free Surface

The radial distributions of stresses σ_{rr} and $\sigma_{\theta\theta}$ obtained from FEA, the HRR field and the J-A_2 solution along $\theta = 0^\circ$ at the plane near the free surface (z/t=0.49) are plotted in Figure 4 for the CCP specimen under the three loading conditions, while the angular distributions of σ_{rr}, $\sigma_{\theta\theta}$ and $\sigma_{r\theta}$ at $r\sigma_0/J = 2$ are depicted in Figure 5. The plane strain FEA results for the lowest loading are also shown in Figure 4, which already deviate from the 3-D FEA results. This indicates that, in contrast to the stress state at the mid-plane, the stress state at the plane near the free surface cannot be reasonably described by the plane strain solution even at very small loading. It is also observed that only the numerical results for the lowest loading fall between the HRR-field solutions under plane strain and plane stress conditions. The FEA results for the other two loading cases are below the plane-stress HRR-field solution.

As shown in Figures 4 and 5, the J-A_2 solutions at the plane near the free surface can approximately match with the FEA results for the smallest loading at both the angular and radial directions. For the two higher loading cases, however, the J-A_2 solutions remain a good approximation for the FEA results only when $r/(J/\sigma_o) < 2.0$ and $0^\circ \le \theta < 45^\circ$.

The conclusion from the numerical results for the SENB specimen is similar to the CCP specimen, and hence detailed figures for the stress distribution, as shown in figures 2-5 for the CCP specimen, are not reproduced here.

Evaluation of Plastic Zones

Figure 6 shows evolution of the normalized plastic zones for the SENB specimen as the load is increased. In the figure, the solid and dashed curves represent the contours of

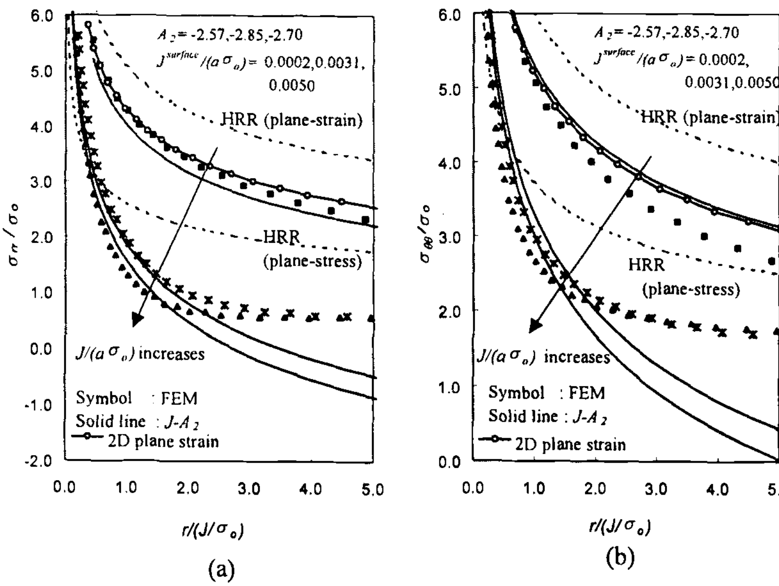

Figure 4 – *Variation of Stresses with Normalized Radial Distance at $\theta = 0^o$ at the Plane near the Free Surface (z/t = 0.49) for the CCP Specimen under Various Loading:* (a) σ_{rr}, *and* (b) $\sigma_{\theta\theta}$

plastic zones at the mid-plane and at the plane near the free surface, respectively. It is observed that (1) the plastic zone size and shape are nearly identical at the mid-plane and near the free surface, (2) as the load increases the plastic zone shape evolves from those from the plane strain case to those from the plane stress case. Specifically, the plastic zone shape at the mid-plane resembles the plane strain state when loading $J/(a\sigma_0) \le 0.0011$, and that for the plane stress case when loading $J/(a\sigma_0) > 0.0011$ or under LSY.

The iso-contour of effective stress is studied in this work as an indication of the dominance of plane stain state at the crack tip. Figure 7 displays the iso-contours of effective stress at the mid-plane for the SENB specimen under the loading $J/(a\sigma_0) = 0.0056$. In this case, the plastic zone size is larger than the plate thickness and is in LSY. The largest contour for $\sigma_{eff}/\sigma_0 = 1$ in Figure 7 represents the plastic zone which resembles the plane stress shape. However as the crack front is approached the shape of the iso-contour of effective stress gradually changes to that for the plane strain states. Figure 7(b) clearly indicates that the plane-strain state dominates over the region of interest, $1 \le r/(J/\sigma_o) \le 5$, although the outside plastic zone shape looks like that under the plane stress state. Accordingly, it is verified that near the crack front the plane strain state dominates at the mid-plane of a thin plate, while the plane stress condition exist near the free surface. This conclusion is identical to our earlier findings [34] in the SSY boundary layer studies.

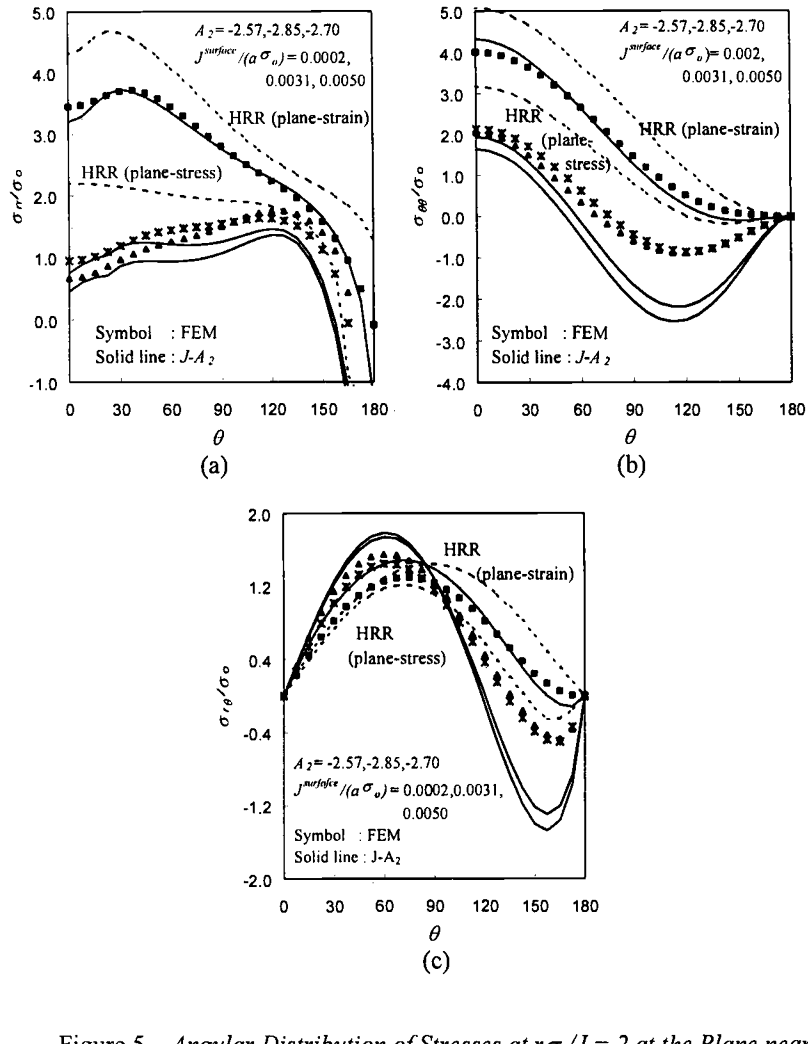

Figure 5 – *Angular Distribution of Stresses at $r\sigma_o/J = 2$ at the Plane near the Free Surface ($z/t = 0.49$) for the CCP Specimen under Various Loading:* (a) σ_{rr}, (b) $\sigma_{\theta\theta}$, *and* (c) $\sigma_{r\theta}$

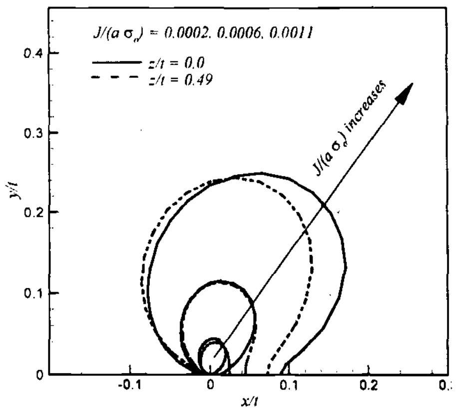

(a)

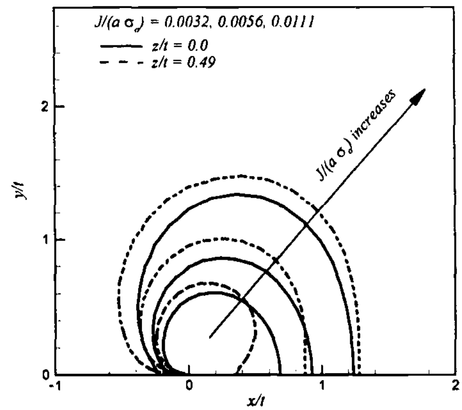

(b)

Figure 6 – *Contours of Plastic Zones at the Mid-Plane and at the Plane near the Free Surface for the SENB Specimen under Different Loads:* (a) *for Loading Level $J/(a\sigma_o)$ = 0.0002, 0.0006, 0.0011, and* (b) *for Loading Level $J/(a\sigma_o)$ = 0.0032, 0.0056, 0.0111.*

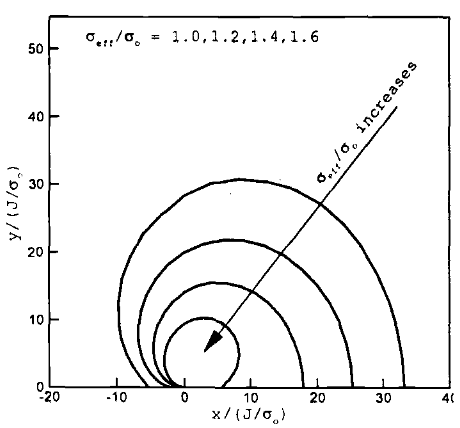

(a)

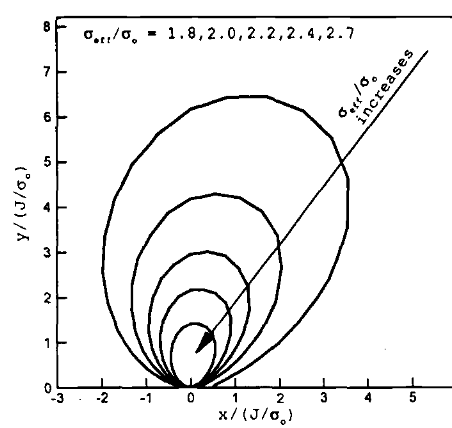

(b)

Figure 7 – *Iso-Contours of Effective Stress at the Mid-Plane (z/t = 0) for the SENB Specimen under the Loading $J/(a\sigma_o)$ = 0.0056:* (a) σ_{eff}/σ_o = *1.0, 1.2, 1.4, 1.6, and* (b) σ_{eff}/σ_o = *1.8, 2.0, 2.2, 2.4, 2.7.*

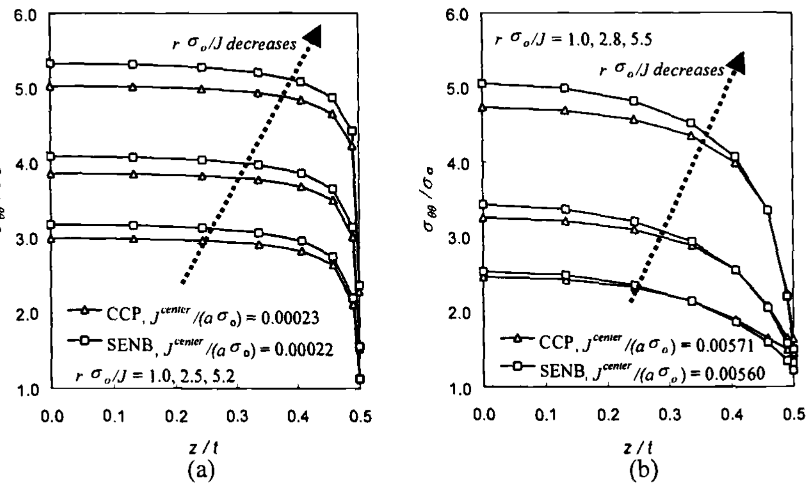

Figure 8 – *Variation of $\sigma_{\theta\theta}$ through the Thickness at radial Distance at $\theta = 0^o$ for the CCP and SENB Specimens:* (a) *under Low Load, and* (b) *under High Load*

Constraint Effect on Opening Stress

The through-thickness variations of the opening stress, $\sigma_{\theta\theta}$, at various distances from the crack front for the CCP and SENB specimens are shown in Figures 8(a) and 8(b) for low loading and high loading conditions, respectively. For both loading cases, the opening stress (1) has higher values in the SENB than in the CCP, (2) has a maximum at the mid-plane and a minimum at the near the free surface for both of the two specimens, and (3) is approximately a constant through the thickness except near the free surface where a sharp drop is seen. The drop appears to be more severe as the crack front is approached. Accordingly, the geometry constraint has a more pronounced effect on the opening stress in the CCP than in the SENB, and the 3-D thickness effect is primarily in the region near the free surface of thin plates.

J and the Constraint Parameter A_2

Figures 9(a) and 9(b) show the variation of the local *J*-integral through the thickness for the low loading and the high loading, respectively. It is observed that (1) maximum *J* occurs at the mid-plane and (2) the variation of the *J*-integral vs. thickness is slightly affected by the specimen geometry.

The through-thickness variations of A_2 for the two specimens under the low and high loadings are shown in Figures 10 (a) and (b). For these two loading cases, the values of A_2 remain relatively constant throughout the thickness, and decrease remarkably at the region near the free surface. In addition, the magnitude of A_2 for the CCP is less than that for the SENB. This coincides with the previous findings that, under the same applied *J*, the low constraint specimen has low A_2 value relative to the high constraint specimen, the A_2 value for a less constrained specimen is lower than that for a highly constrained specimen.

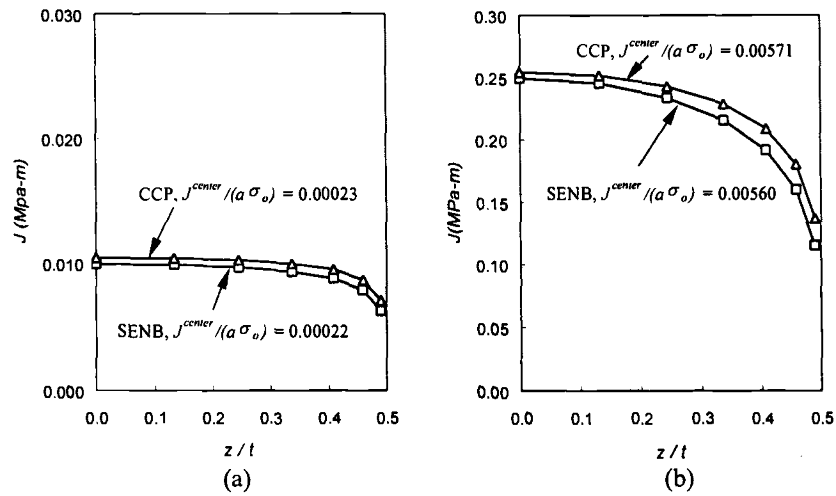

Figure 9 – *Variation of J^{local} through the Thickness for the CCP and SENB Specimens:* (a) *under Low Load, and* (b) *under High Load*

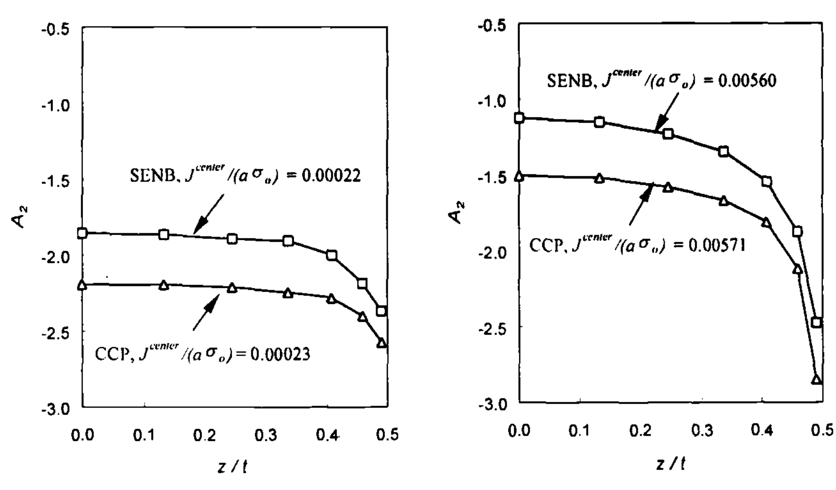

Figure 10 – *Variation of the Constraint Parameter A_2 through the Thickness for the CCP and SENB Specimens:* (a) *under Low Load, and* (b) *under High Load*

Conclusions

The present paper investigates the constraint effects on 3-D crack-front fields for two thin-plate fracture specimens, CCP and SENB, based on detailed elastic-plastic FEA calculations. The applied loads range from low to high, corresponding to the conditions from SSY to LSY. Numerical results are compared with the J-A_2 three-term solutions to demonstrate the validity of the parameter A_2 for characterizing the constraint of 3-D cracks.

The results show that, under both SSY and LSY conditions, the J-A_2 solutions can indeed match well with the FEA stress results within the range of interest, $1 \leq r/(J/\sigma_0) \leq 5$, at the mid-plane, but not near the free surfaces. The dominance of the plane strain state at the mid-plane is demonstrated by both the plastic zone shape and the iso-contour of effective stress, even when the far field is controlled by the plane stress conditions. The crack opening stress $\sigma_{\theta\theta}$, the constraint parameter A_2 and the J-integral reach the maximum values at the mid-plane, and remain constant along the crack front except in the region near the free surfaces of the two specimens. This is consistent with the experimental observation that crack growth always initiates at the mid-plane of a plate where the highest loading and highest constraint level occur.

The J-A_2 solution can effectively characterize the 3-D crack-front stress fields except for the region near the free surfaces of thin plates under different loading conditions. The parameter A_2 thus can be used as a parameter for quantifying the constraint effect in the interpretation of fracture of 3-D specimens or structural components.

In general, the findings in the current paper indicate that the crack-tip behavior under LSY condition is similar to that as previously reported by the authors [*34*] for the case under SSY condition.

Acknowledgement

The authors appreciate the support of this work by the National Science Foundation through Grant CMS0116238, Program director Dr. K. P. Chong, and NASA through the NASA/EPSCoR Program Consortium Agreement No.NCC5-174.

REFERENCES

[1] Chao, Y. J. and Zhang, X., "Constraint Effect in Brittle Fracture," *Fatigue and Fracture Mechanics: 27th Volume, ASTM STP 1296*, R. Piascik, Ed., American Society for Testing and Materials, Philadelphia, 1997, pp. 41-60.

[2] Chao, Y. J. and Reuter, W. G., "Fracture of Surface Cracks under Bending Loads," *Fatigue and Fracture Mechanics: 28th Volume, ASTM STP 1321*, J. H. Underwood, B. MacDonald, and M. Mitchell, Eds., American Society for Testing and Materials, Philadelphia, 1997, pp. 214-242.

[3] Chao, Y. J., Liu, S., and Broviak, B., "Brittle Fracture: Constraint Effect and Crack Curving under Mode-I Conditions," to appear in *Experimental Mechanics*, 2001.

[4] Larsson, S. G. and Carlsson, A. J., "Influence Of Non-Singular Stress Terms and Specimen Geometry on Small-Scale Yielding at Crack Tips in Elastic-Plastic Materials," *Journal of the Mechanics and Physics of Solids*, Vol. 21, 1973, pp. 263-277.

[5] Betegon, C. and Hancock, J. W., "Two-Parameter Characterization of Elastic-Plastic Crack-Tip Fields," *Journal of Applied Mechanics*, Vol. 58, 1991, pp. 104-110.

[6] Al-Ani, A. M. and Hancock, J. W., "*J*-Dominance of Short Cracks in Tension and Bending," *Journal of the Mechanics and Physics of Solids*, Vol. 39, 1991, pp. 23-43.

[7] O'Dowd, N. P. and Shih, C. F., "Family of Crack-tip Fields Characterized by a Triaxiality Parameter – I. Structure of Fields," *Journal of the Mechanics and Physics of Solids*, Vol. 39, 1991, pp. 989-1015.

[8] O'Dowd, N. P. and Shih, C. F., "Family of Crack-tip Fields Characterized by a Triaxiality Parameter – II. Fracture Applications," *Journal of the Mechanics and Physics of Solids*, Vol. 40, 1992, pp. 939-963.

[9] Dodds, R. H., Anderson, T. L., and Kirk, M. T., "A Framework to Correlate *a/W* Ratio Effects on Elastic-Plastic Fracture Toughness (J_C)," *International Journal of Fracture*, Vol. 48, 1991, pp. 1-22.

[10] Shih, C. F., O'Dowd, N. P., and Kirk, M.T., "A Frame Work for Quantifying Crack Tip Constraint," *Constraint Effects in Fracture, ASTM STP 1171*, E. M. Hackett, K.-H. Schwalbe, and R. H. Dodds, Eds., American Society for Testing and Materials, Philadelphia, 1993, pp. 2-20.

[11] O'Dowd, N. P. and Shih, C. F., "Two-Parameter Fracture Mechanics: Theory and Applications," *Fracture Mechanics, ASTM STP 1207*, J. D. Lands, D. E. McCabe, and J. A. M. Boulet, Eds., American Society for Testing and Materials, Philadelphia, 1994, pp. 21-47.

[12] Kirk, M. T., Dodds, R. H., and Anderson, T. L., "An Approximate Technique for Predicting Size Effects on Cleavage Fracture Toughness Using Elastic *T* Stress," *Fracture Mechanics, ASTM STP 1207*, J. D. Lands, D. E. McCabe, and J. A. M. Boulet, Eds., American Society for Testing and Materials, Philadelphia, 1994, pp. 62-86.

[13] Nikishikov, G. P., Bruckner-Foit, A., and Munz, D., "Calculation of the Second Fracture Parameter for Finite Cracked Bodies Using A Three-Term Elastic-Plastic Asymptotic Expansion," *Engineering Fracture Mechanics*, Vol. 52, 1995, pp. 685-701.

[14] Yuan, H., Lin, G., and Cornec, A., "Quantification of Crack Constraint Effects in an Austenitic Steels," *International Journal of Fracture*, Vol. 71, 1995, pp. 273-291.

[15] Sharma, S. M. and Aravas, N., "Determination of Higher–Order Terms in Asymptotic Elastoplastic Crack Tip Solutions," *Journal of the Mechanics and Physics of Solids*, Vol. 39, 1991, pp. 1043-1072.

[16] Hutchinson, J. W., "Singular Behavior at the End of a Tensile Crack Tip in a Hardening Material," *Journal of the Mechanics and Physics of Solids*, Vol. 16, 1968, pp. 13-31.

[17] Rice, J. R. and Rosengren, G. F., "Plane Strain Deformation near a Crack Tip in a Power-Law Hardening Material," *Journal of the Mechanics and Physics of Solids*, Vol. 16, 1968, pp. 1-12.

[18] Yang, S., Chao, Y. J., and Sutton, M. A., "Higher Order Asymptotic Fields in a Power Law Hardening Material," *Engineering Fracture Mechanics*, Vol. 45, 1993, pp. 1-20.

[19] Yang, S., Chao, Y. J., and Sutton, M. A., "Complete Theoretical Analysis for Higher Order Asymptotic Terms and the HRR Zone at a Crack Tip for Mode I and Mode II Loading of a Hardening Materials," *Acta Mechanica*, Vol. 98, 1993, pp. 99-106.

[20] Chao, Y. J., Yang, S. and Sutton, M. A., "On the Fracture of Solids Characterized by One or Two Parameters: Theory and Practice," *Journal of the Mechanics and Physics of Solids*, Vol. 42, 1994, pp. 629-647.

[21] Chao, Y. J. and Zhu, X. K., "J-A_2 Characterization of Crack-Tip Fields: Extent of J-A_2 Dominance and Size Requirements," *International Journal of Fracture*, Vol. 89, 1998, pp. 285-307.

[22] Zhu, X. K. and Chao, Y. J. "Characterization of Constraint of Fully Plastic Crack-Tip Fields in Non-Hardening Materials by the Three-Term Solution," *International Journal of Solids and Structures*, Vol. 36, 1999, pp. 4497-4517.

[23] Chao, Y. J. and Zhu, X. K., "Constraint-Modified *J-R* Curves and its Application to Ductile Crack Growth," *International Journal of Fracture*, Vol. 105, 2000, pp. 187-207.

[24] Chao, Y. J., Zhu, X. K., Lam, P. S., Louthan, M. R., and Iyer, N. C., "Application of the Two-Parameter J-A_2 Description to Ductile Crack Growth," *Fatigue and Fracture Mechanics, ASTM STP 1389*, G. R. Halford and J. P. Gallagher, Eds., American Society of Testing and Materials, West Conshohocken, PA, 2000, pp. 165-182.

[25] Nguyen, B. N., Onck, P., and Giessen, E. van der, "Crack-Tip Constraint Effects on Creep Fracture," *Engineering Fracture Mechanics*, Vol. 65, 2000, pp. 467-490.

[26] Chao, Y. J., Zhu, X. K., and Zhang, L., "Higher-Order Asymptotic Crack-Tip Fields in a Power-Law Creeping Material," *International Journal of Solids and Structures*, Vol. 38, 2001, pp. 3853-3875.

[27] Brocks, W. and Olschewski, J., "On *J*-Dominance of Crack-Tip Fields in Largely 3-D Structures," *International Journal of Solids and Structures*, Vol. 22, 1986, pp. 693-708.

[28] Nakamura, T. and Parks, D. M., "Three-Dimensional Crack Front Fields in a Thin Ductile Plate," *Journal of the Mechanics and Physics of Solids*, Vol. 38, 1990, pp. 787-812.

[29] Parks, D. M., "Advances in Characterization of Elastic-Plastic Crack Tip Fields," *Topics of Fracture and Fatigue*, ed. By A.S. Argon, Springer Verlag: New York, 1992, pp. 59-98.

[30] Henry, B. S. and Luxmoore, A. R., "The Stress Triaxiality Constraint and the Q-Value as a Ductile Fracture Parameter," *Engineering Fracture Mechanics*, Vol. 57, 1997, pp. 575-390.

[31] Nevalainen, M. and Dodds, R. H., "Numerical Investigation of 3-D Constraint Effects on Brittle Fracture in SE(B) and C(T) Specimens," *International Journal of Fracture*, Vol. 74, 1995, pp. 131-161.

[32] Pardoen, T., Marchal, Y., and Delannay, F., "Thickness Dependence of Cracking Resistance in Thin Aluminium Plates," *Journal of the Mechanics and Physics of Solids*, Vol. 47, 1999, pp. 2093-2123.

[33] Yuan, H. and Brocks, W., "Quantification of Constraint Effects in Elastic-Plastic Crack Front Fields," *Journal of the Mechanics and Physics of Solids*, Vol. 46, No.2, 1998, pp. 219-241.

[34] Kim, Y., Zhu, X. K., and Chao, Y. J., "Quantification of Constraint on Elastic-Plastic 3D Crack Front by the J-A_2 Three-Term Solution," *Engineering Fracture Mechanics*, Vol. 68, 2001, pp. 895-914.

[35] Wang, Y. Y., Parks, D. M., Lloyd, W. R., Reuter, W. G., and Epstein, J., "Elastic-Plastic Deformation in Surface-Cracked Plates - Experiment and Numerical-Analysis," *Journal Of Applied Mechanics*, Vol. 58, 1991, pp. 895-903.

[36] Wang, Y. Y., "On the Two-Parameter Characterization Elastic-Plastic Crack-Front Fields in Surface-Cracked Plates," *Constraint Effects in Fracture, ASTM STP 1171*, E. M. Hackett, K.-H. Schwalbe, and R. H. Dodds, Eds., American Society for Testing and Materials, Philadelphia, 1991, pp. 120-138.

[37] Kassir, M. K. and Sih, G. C., "Three-Dimensional Stress Distribution around an Elliptical Crack under Arbitrary Loadings," *Journal of Applied Mechanics*, Vol. 33, 1966, pp.601-611.

[38] Zhu, X. K., Liu, G. T. and Chao, Y. J., "Three Dimensional Stress and Displacement Fields near an Elliptical Crack Front," *International Journal of Fracture*, Vol. 19, 2001, pp. 383-401.

[39] Shih, C. F., "*Tables of Hutchinson-Rice-Rosengren Singular Field Quantities*," Brown University Report, MRL E-147, 1983.

[40] Chao, Y. J. and Zhang, L., "*Tables of Plane Strain Crack Tip Fields: HRR and Higher Order Terms*," ME-Report 97-1, Department of Mechanical Engineering, University of South Carolina, 1997.

[41] Zhu, X. K. and Chao, Y. J., "Fully Plastic Crack-Tip Fields for CCP and DECP Specimens under Tension in Non-Hardening Materials," *International Journal of Solids and Structures*, Vol. 37, 2000, pp. 577-598.

Yong-Yi Wang,[1] Walt Reuter,[2] and James Newman[3]

Analysis of Brittle Fracture in Surface-Cracked Plates Using Constraint-Corrected Stress Fields

Reference: Wang, Y.-Y., Reuter, W. G., and Newman, J. C., **"Analysis of Brittle Fracture in Surface-Cracked Plates Using Constraint-Corrected Stress Fields,"** *Fatigue and Fracture Mechanics: 33rd Volume, ASTM STP 1417*, W. G. Reuter and R. S. Piascik, Eds., ASTM International, West Conshohocken, PA, 2002.

Abstract: Recent work in constraint-based fracture mechanics has shown that the crack-tip fields of surface-cracked plates (SCPs) can be accurately represented by J and T dominated two-parameter fields for remote loads up to general yield. When the parametric expressions of J and T are known, it is possible to have the full crack-tip fields of SCPs from the J-T dominated modified boundary layer (MBL) solutions.

The validity of fracture toughness tests can be assessed by examining the deviation of the crack-tip fields of the test specimens from the single parameter (K_I or J) dominated singular fields. The deviation of the crack-tip stress fields of SCPs from the K_I dominated singular fields is estimated using the constraint parameter T-stress. For tension-loaded SCPs, the specimen size requirement is estimated at $L_{nom} \geq (0.5$ to $2.5)(K_I/\sigma_0)^2$, where L_{nom} is the characteristic specimen size, i.e., the maximum crack depth in shallow-cracked SCPs and the minimum remaining ligament in deeply-cracked SCPs. The size requirement for SCPs under bending is estimated at $L_{nom} \geq (K_I/\sigma_0)^2$. However, this requirement may be overly stringent for some crack configurations.

The distribution of crack-opening stress at a fixed physical distance from the crack tip along the entire crack front was obtained from a parameterized MBL solution. Attempts were made to correlate the critical fracture locations observed in the experimental tests with the locations of peak stresses along the crack front. Some reasonable agreements were observed. However, more work is needed to fully validate this method.

[1]Vice President, Engineering Mechanics Corporation of Columbus, 3518 Riverside Dr., Suite 202, Columbus, OH 43221.

[2]Engineer/Scientific Fellow, Idaho National Engineering & Environmental Laboratories, Lockheed Martin Idaho Technologies Company, P. O. Box 1625, Idaho Falls, ID 83415.

[3]NASA Langley Research Center, Hampton, VA 23665-5225. Currently at Mississippi State University, 330 Walker Engineering Lab, Mississippi State, MS 39762.

Keywords: surface crack, fracture, *K*-dominance, two-parameter characterization, constraint, toughness testing

Introduction

The application of fracture mechanics is based on the premise that the crack-tip fields of specimens and structures of different types can be characterized by the fracture parameters such as the stress intensity factor *K*, *J*-Integral, or Crack Tip Opening Displacement (CTOD). These fracture parameters are uniquely related to the asymptotic crack-tip stress and strain fields at the crack tip. When the crack-tip fields of a specimen or structure are accurately represented by the asymptotic fields, the fields are referred to as "dominated" or "characterized" by the fracture parameters. The "loss of dominance" refers to the condition that the crack-tip fields of a specimen or structure deviate appreciably from the asymptotic fields.

To apply the fracture toughness measured from a laboratory specimen to the fracture assessment of a structure, it is necessary to ensure that the fracture parameter dominates the crack-tip fields at the event of the fracture. The conditions that lead to the loss of dominance of a fracture parameter received great attention in the later 1970s and early 1980s. McMeeking and Parks conducted plane strain finite element analysis of single-edge-notched bend bar (SENB) and center cracked panel (CCP) for materials with low to moderate strain hardening (n=10 and ∞) [*1*]. They compared the crack-tip fields of the SENB and CCP specimens with the finite strain small-scale yielding (SSY) solutions of McMeeking [*2*]. For the SENB specimen, the crack-tip fields agreed with the SSY solutions well into the large-scale yield range. In contrast, the crack-tip fields of the CCP specimen deviated from the SSY solution for loads beyond contained plasticity at the crack tip. They concluded that the length of the ligament in the CCP specimen had to be 5 to 10 times larger than that in the SENB specimens. Shih and German reached a similar conclusion in their study of the crack-tip fields of single-edge-notched tension bar (SENT), SENB, and CCP specimens for materials with a wide range of strain hardening rate (n=3 to ∞) [*3*]. They used small strain formulation and the HRR fields [*4, 5*] as the baseline solution. The work of MeMeeking and Parks and Shih and German became the basis of specimen size requirements in the ASTM Standard Test Method for Measurement of Fracture Toughness (E 1820).

Defects found in engineering structures are often surface cracks from either fabrication processes (e.g., welding) or exposure to aggressive environment, such as stress corrosion cracking. Fitness-for-service assessment of such defects can be made using relevant fracture toughness parameters. For instance, plane strain fracture toughness, K_{Ic}, can be measured per ASTM Standard Test Method for Plane-Strain Fracture Toughness of Metallic Materials (E 399) if the material and test conditions satisfy the linear fracture mechanics (LEFM) requirements. With appropriate expressions of the crack driving forces, such as the Newman-Raju K_I solutions [*6*], a fracture event can be predicted by assuming $K_{max} = K_{Ic}$, where K_{max} is the maximum stress intensity factor along the crack front. Indeed, the Newman-Raju solutions were used to predict the failure of surface-cracked specimens of high-strength β-titanium alloy and a monolithic ceramic [*7, 8, 9*]. The tests showed that the catastrophic failures occurred soon after crack initiation. It was observed that the K_{max} at the failures generally exceeded K_{Ic}. The ratio of K_{max}/K_{Ic} was 1.0-1.4 for tension-loaded specimens, and 1.0-2.0 for bending loaded specimens. One of the contributing factors to this discrepancy could be, at the onset of the failures, the stress intensity factor, K_I, lost the dominance of the crack-tip fields. In other words, the crack-tip fields were perhaps not as strong as the asymptotic fields that are characterized by K_I. To ensure that a specimen geometry independent stress intensity factor is obtained from the tests of surface-cracked specimens, it is necessary to examine the specimen size requirements as specified in ASTM Fracture Testing with Surface-Crack Tension Specimens (E 740).

This paper describes an effort in establishing the size requirements for the fracture toughness testing of surface-cracked plates (SCPs). In contrast to the work of McMeeking and Parks and Shih and German, in which detailed plane strain finite element analysis of specimens were carried out, we utilize the constraint-based fracture mechanics that has been developed since the late 1980s. This methodology provides an accurate description of crack-tip fields of SCPs through the modified boundary layer (MBL) solutions. Since the MBL solutions are fully represented by the J and T parameters, the crack-tip fields of the SCPs are effectively characterized by those two parameters. It is therefore unnecessary to conduct detailed finite element analysis of the SCPs.

J-T Characterization of the Crack-Front Fields of Surface-Cracked Plates

The loss of single parameter dominance at large plasticity is not unique to CCP specimens. In has been shown that specimens with lower constraint, which is generally related to the low crack-tip triaxiality, lose single parameter dominance when the loads are beyond well-contained plasticity. Recent work in constraint-based fracture mechanics has demonstrated that the crack-tip fields of the low constraint specimens can be characterized by two fracture parameters. The first parameter, such as J or crack tip opening displacement (CTOD), measures the degree of crack-tip deformation. The second parameter, which is often referred to as the constraint parameter, is related to a member of a family of crack-tip fields. Hancock and co-workers [*10, 11, 12*] showed that the T-stress, the second Williams [*13*] coefficient in the expansion of isotropic linear elastic crack-tip field, is an effective constraint parameter for loads up to general yielding. O'Dowd and Shih [*14, 15*] proposed the Q-stress as the constraint parameter. The dominance of J-T family of crack-tip fields extends far beyond that of the single parameter singular fields for specimen with low constraint [*16*].

In the following sub-sections, we review the elements of the J-T characterization of the crack-tip fields of SCPs. These elements form the basis from which the specimen size requirements and other results are derived.

Modified Boundary Layer Solutions

The linear elastic stress fields outside the crack-tip plastic zone under contained plasticity may be approximated by the first two terms of the Williams eigen-expansion [*13*],

$$\sigma_{ij}(r,\theta)=\frac{K_I}{\sqrt{2\pi r}}f_{ij}(\theta)+T\delta_{1i}\delta_{1j}, \tag{1}$$

where the Cartesian subscripts i and j range from one to two. The cylindrical coordinate system (r,θ) is centered at the crack tip, and θ=0 lies along the un-cracked ligament. The function f_{ij} provides the angular variation of the in-plane stress fields, and δ_{ij} is the Kronecker delta. The T-stress is parallel to the cracked plane. The corresponding in-plane displacement fields are given as,

$$u_i=\frac{K_I}{E}\sqrt{\frac{r}{2\pi}}g_i(\theta,\nu)+\frac{T}{E}rh_i(\theta,\nu), \tag{2}$$

where E and ν are Young's modulus and Poisson's ratio, respectively. The functions g_i and h_i provide the angular variations of the in-plane displacement fields due to K_I and T, respectively.

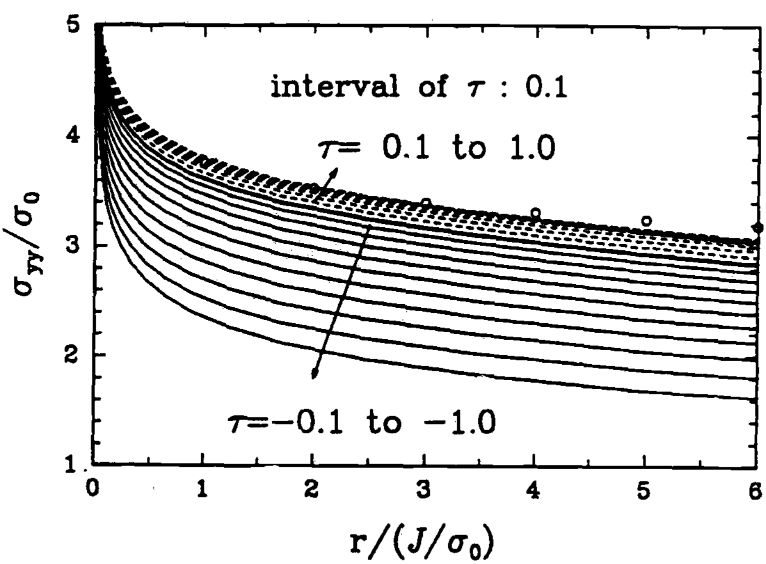

Figure 1 - *Normalized crack-opening stresses at various values of τ. The open circles are HRR singularity fields.*

A family of plane strain elastic-plastic crack-tip fields can be obtained by applying the displacement of Eq. (2) at a remote boundary condition far from the crack tip. Since the fields are effectively scaled by K_I, it is a customary practice that the value of the applied K_I is fixed while the magnitude of the T-stress is varied.

Consider a linear/power law stress strain relation under uniaxial tension condition,

$$\frac{\varepsilon}{\varepsilon_0}=\frac{\sigma}{\sigma_0} \qquad \text{for} \quad \sigma\le\sigma_0, \quad \text{and} \tag{3a}$$

$$\frac{\varepsilon}{\varepsilon_0}=\left(\frac{\sigma}{\sigma_0}\right)^n \quad \text{for} \quad \sigma>\sigma_0, \tag{3b}$$

where σ_0 is the yield stress, $\varepsilon_0 \equiv \sigma_0/E$ is the yield strain, and n is the strain hardening exponent. Wang obtained a family of crack-tip fields using the linear/power law stress strain relations with n=10 and σ_0/E=0.0025 [*17*]. The normalized crack-tip opening stress, σ_{yy} ($\sigma_{\theta\theta}$ at θ=0), is plotted with respect to the normalized radial distance from the crack tip in Figure 1 for various value of $\tau \equiv T/\sigma_0$. The SSY solution (τ=0) and the asymptotic HRR field for the same material is also shown in Figure 1. The significant features of the family of the crack-tip fields are that the negative T-stress leads to significant reduction in the crack-opening stress while only moderate elevation of stress is seen for the positive T-stress. Within the region that the small strain formulation provides accurate solution ($1 < r/(J/\sigma_0) < 6$), the change of the crack-opening stresses with respect to the SSY solution is insensitive to the radial distance from the crack tip, as observed earlier by Betegón and Hancock [*10*]. This change can be fitted to a 3rd order polynomial as a function of τ at $r_n \equiv r/(J/\sigma_0)$=2 [*17*],

$$\frac{\sigma_{yy}^{MBL}-\sigma_{yy}^{SSY}}{\sigma_0}=0.6168\tau-0.5646\tau^2+0.1231\tau^3. \tag{4}$$

Equation (4) can be applied in the range of $1 < r/(J/\sigma_0) < 6$ due to its insensitivity to the radial distance. The SSY solution may be expressed as a function of r_n,

$$\frac{\sigma_{yy}^{SSY}}{\sigma_0}=m_0+m_1r_n^1+m_2r_n^2+m_3r_n^3+m_4r_n^4+m_5r_n^5 \qquad \text{for} \quad 0.5<r_n\le 5.0 \tag{5a}$$

$$\frac{\sigma_{yy}^{SSY}}{\sigma_0}=n_0+n_1r_n^1+n_2r_n^2+n_3r_n^3. \qquad \text{for} \quad 5.0<r_n\le 20 \tag{5b}$$

The values of m_k (k=0, 1, 2, 3, 4, and 5) and n_l (l=0, 1, 2, and 3) are given in Table 1.

Table 1 - *Fitted coefficients of Eq. (5)*

m_0	m_1	m_2	m_3	m_4	m_5
4.432E+00	1.522E+00	9.937E-01	-3.647E-01	6.529E-02	-4.470E-03
n_0	n_1	n_2	n_3		
3.527E+00	-1.505E-01	6.910E-03	-1.429E-04		

Equations (4) and (5) provide the full description of the crack-opening stresses at a given set of r, σ_0, J and T for n=10 and σ_0/E=0.0025 in the range of $1 < r/(J/\sigma_0) < 6$.

T-Stress Solutions of Surface-Cracked Plates

The application of the MBL solutions requires the solutions of K_I and T of the structure of interest. The K_I solutions are generally well documented. Several computational methods have been developed to derive T-stress solutions in planar geometries [*18, 19, 20*]. Wang and Parks [*21*] applied the line-spring method to the computation of T-stress in surface-cracked plates. Nakamura and Parks [22] developed a general T-stress computational procedure for 3-D cracks. A good review of T-stress solutions is given by Sherry [23].

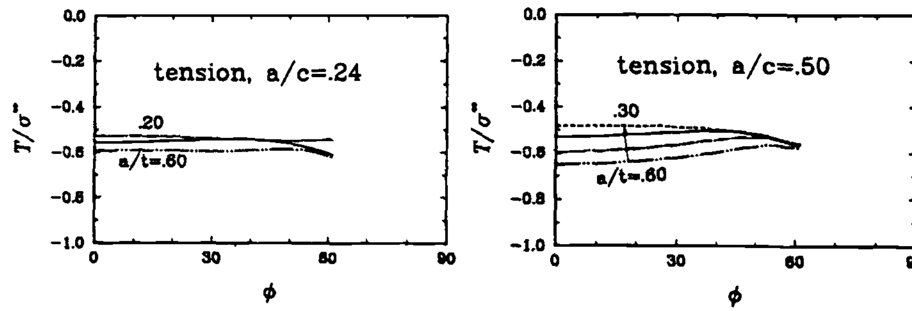

Figure 2 - *The* T-*stress along the crack front under remote tension. The interval of* a/t *is constant from the minimum to the maximum numbers [21].*

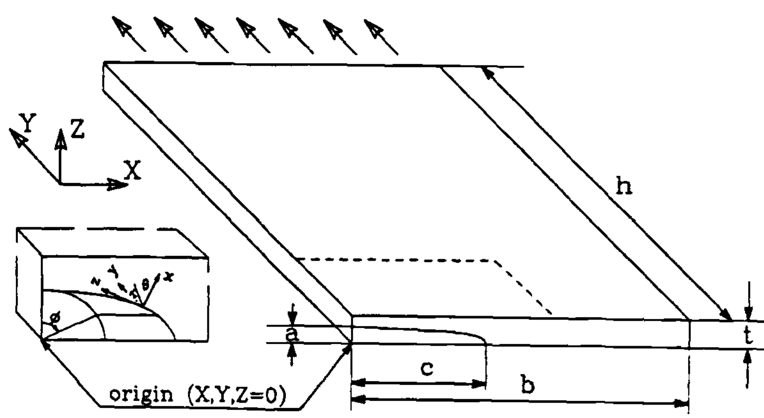

Figure 3 - *Schematic of one-quarter of a SCP. The local Cartesian coordinate system and the crack location parameter are shown in the left inlet.*

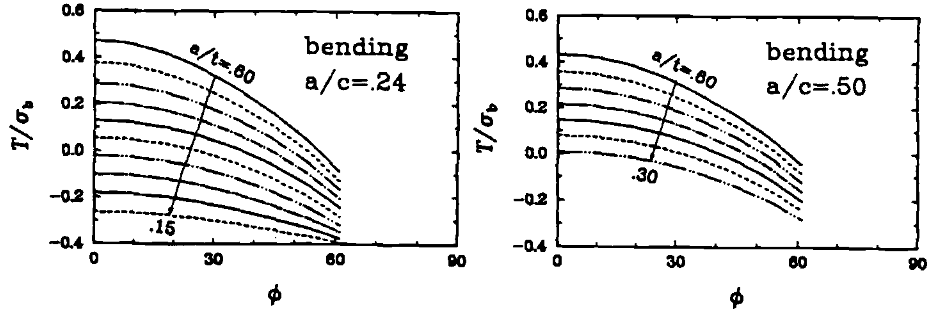

Figure 4 -*The* T-*stress along the crack front under remote bending. The interval of* a/t *is constant from the minimum to the maximum numbers [21].*

The T-stress of SCPs under remote tension is relatively uniform along the crack front, see Figure 2. The remote stress, σ^{∞}, is the applied stress over the gross section of the plate. Deeper cracks have higher negative values of the T-stress. The notations of the crack size parameters, a and c, and crack front location parameter, ϕ, are given in Figure 3. The T-stress of the SCPs under remote bending generally varies from positive values at the deepest point to negative values towards the free surface, see Figure 4. The bending stress σ_b is the remote tensile stress on the outer fiber of the plate (Z=0 in Figure 3).

The T-stress distribution of Figure 4 was fitted to a set of parametric equations [*24*].

$$\frac{T}{\sigma_b} = \left(\frac{T}{\sigma_b}\right)_{\phi=0} + A\phi^p \tag{6a}$$

$$\left(\frac{T}{\sigma_b}\right)_{\phi=0} = L_1 + L_2\beta \tag{6b}$$

$$A = M_1\beta + M_2 \sin[\pi M_3(\beta - M_4)] \tag{6c}$$

$$p = N_1\beta + N_2 \sin[\pi N_3(\beta - N_4)] \tag{6d}$$

where $\beta \equiv a/t$ is the normalized the defect depth. The L_i, M_j, and N_k, are linear functions of aspect ratio α ($\alpha \equiv a/c$),

$$L_i; M_j; N_k = G\alpha + H\,. \tag{6e}$$

The constants G and H are given in Table 2.

Table 2 Fitted coefficients of Eq. (6) for SCPs under bending [24]

	L_1	L_2	M_1	M_2	M_3	M_4	N_1	N_2	N_3	N_4
G	3.48E-01	-7.62E-01	1.97E-01	9.00E-02	-8.51E+00	-3.23E-03	2.51E-01	9.97E-02	2.79E-01	-3.09E-02
H	-5.88E-01	1.81E+00	-8.65E-01	-6.53E-03	6.73E+00	3.82E-01	1.90E+00	-1.62E-01	3.34E+00	-5.39E-02

Validation of J-T Characterized Crack-Tip Fields

Wang performed extensive 3-D finite element analysis of SCPs under remote tension and bending conditions [*25*]. In the topological planes perpendicular to the crack front, the crack-opening stresses were compared with the MBL solutions using the local J and T-stress. Figure 5 summarizes the comparison between the crack-opening stress from the 3-D finite element analysis and the MBL solution for load levels from SSY to general yielding. The agreement is better than 94% for levels up to general yielding for the entire crack front. The data marked by the diamonds indicate the impingement of global bending stress to the stress field at r_n=2 under remote bending [*25*].

The remarkable agreement shown in Figure 5 proves that the MBL solution accurately represents the crack-opening stresses of SCPs under both remote tension and bending loads for load levels up to general yielding. The MBL solutions are used exclusively to represent the crack-opening stress of the SCPs in the subsequent sections.

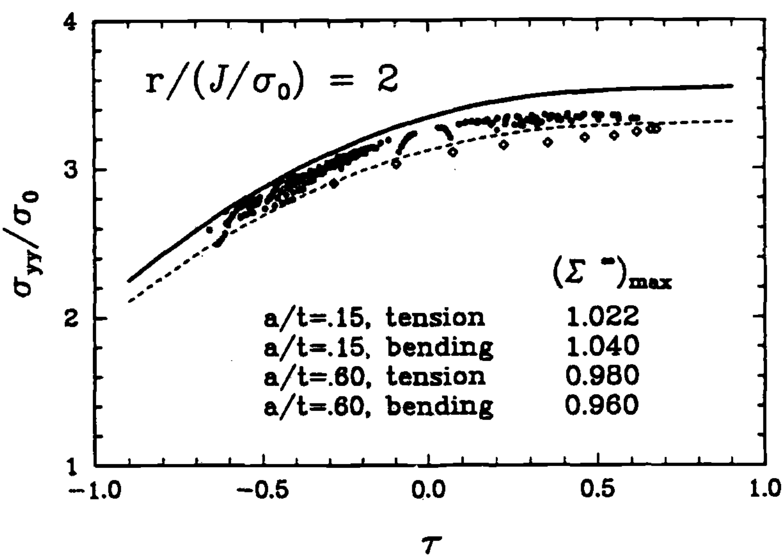

Figure 5 - *Comparison of the crack tip stresses from the 3-D finite element analysis and those of MBL solutions at* r_n=2. *The thick solid line is the MBL solution. The broken line represents the 5% deviation line. The parameter* $(\Sigma^\infty)_{max}$ *indicate the maximum load level for each geometry. The only data points that are outside the 5% deviation line (marked diamond) are from deeply-cracked plate* (a/t=0.6) *at the remote load* $(\Sigma^\infty)_{max}$=0.96.

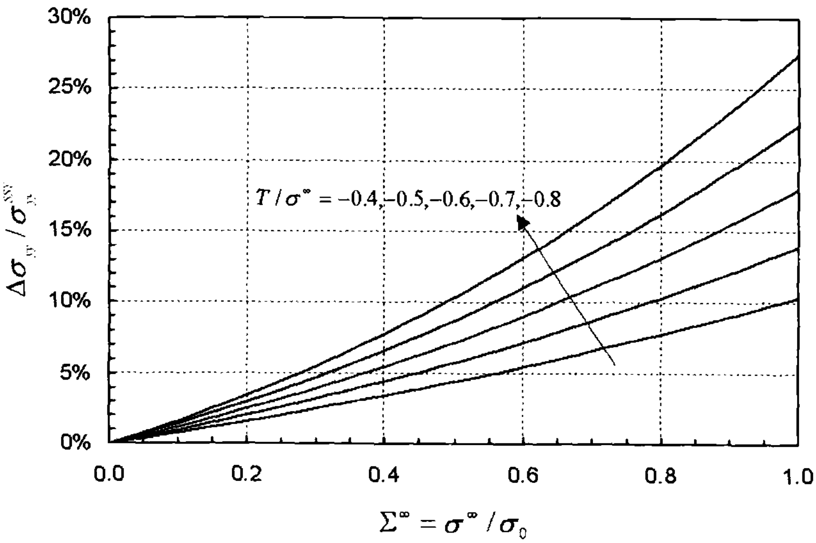

Figure 6 - *The deviation of the crack-opening stress at* r_n*=2 with respect to remote load magnitude at various levels of the crack-tip constraint*

Size Limits of K_C Testing of Surface-Cracked Plates

Tension-Loaded Specimens

Since the crack-opening stresses of SCPs can be accurately represented by the MBL solutions, the deviation of the stresses from the SSY solution is given in Eq. (4) for the material with n=10 and σ_0/E=0.0025. The normalized T-stress is related to the magnitude of the applied load, $\Sigma^{\infty}\equiv\sigma^{\infty}/\sigma_0$,

$$\tau \equiv \frac{T}{\sigma_0} = \frac{T}{\sigma^{\infty}} \cdot \frac{\sigma^{\infty}}{\sigma_0} = \frac{T}{\sigma^{\infty}} \Sigma^{\infty}, \tag{7}$$

where T/σ^{∞} is related to the crack geometry and the loading type, see Figures 2 and 4. Figure 6 shows the deviation of the crack-opening stress, $\Delta\sigma_{yy}\equiv(\sigma_{yy}^{MBL}-\sigma_{yy}^{SSY})$ as a function of the remote load magnitude and the constraint level. For tension-loaded SCPs, the values of T/σ^{∞} are typically in the range of –0.5 to –0.7. Using a 5% deviation criterion, the remote load magnitude is limited to 32-45% of the general yield load. A 7.5% deviation criterion limits the load to 45-62% of the general yield load. With a typical value of T/σ^{∞}=-0.6 and a 7.5% deviation criterion, the load is limited to approximately 50% of the general yield load.

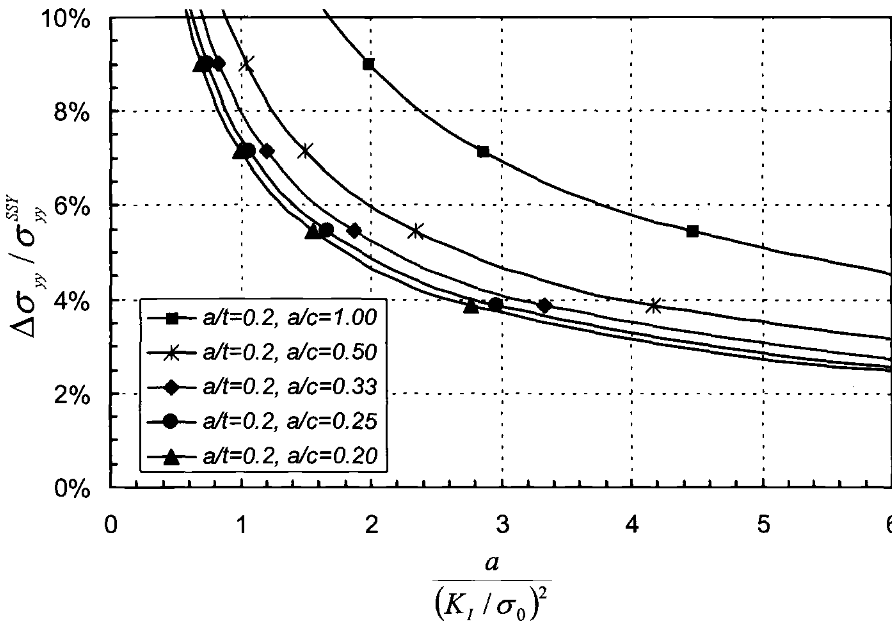

Figure 7 - *Deviation of the crack-opening stress as a function of applied* K_I *for SCPs with shallow cracks of various aspect ratios*

In fracture toughness (K_I) testing of SCPs, it is sometimes necessary to estimate the required specimen size for an anticipated toughness value. Alternatively, a set of specimen size requirements is needed to determine if the toughness value from a test is "valid." Figure 7 shows the expected deviation of crack-opening stress from SSY solution as a function of the applied stress intensity factor K_I. For a SCP at an assumed remote load level Σ^{∞}, the parameter τ is computed from Eq. (7), where T/σ^{∞} is taken from either Figure 2 or Eq. (6). The corresponding deviation of crack-opening stress is computed using Eq. (4) with the appropriate SSY value of Eq. (5). The stress intensity factor K_I at the deepest point at the same load level is computed from the Newman and Raju solution [*6*]. The same process is repeated for other assumed load levels. The curves in Figure 7 illustrate the increased deviation of crack-opening stress from the SSY values as the load level (and K_I) increases (from right to left in the figure).

Relations shown in Figure 7 become the basis of specimen size requirements. For a given material's toughness, a minimum crack depth (therefore the specimen thickness) is required to achieve an accepted level of deviation. For instance, $a \geq 0.95(K_I/\sigma_0)^2$ is required for a/t=0.2 and a/c=0.2 with a 7.5% deviation criterion. A larger specimen would be required if a more stringent deviation criterion is selected.

Relations similar to those shown in Figure 7 were generated for SCPs with a wide range of defect depth and aspect ratio. The specimen size requirements were obtained by setting a specified deviation criterion. Figure 8 shows the normalized specimen size for a range of defect sizes using 7.5% and 5.0% deviation criteria. Here L_{nom} is the nominal crack size dimension. It is set to the crack depth for shallow cracks (a/t<0.5) and the remaining ligament (t-a) for deep cracks. The required specimen size increases with the increase of the aspect ratio (a/c) for a given crack depth. The upper bound size requirement is estimated at $L_{nom} \geq (0.5 \text{ to } 2.5)\ (K_I/\sigma_0)^2$ with the 7.5% deviation criterion. The size requirement of $L_{nom} \geq (1.0 \text{ to } 5.0)\ (K_I/\sigma_0)^2$ is estimated with the 5.0% deviation criterion.

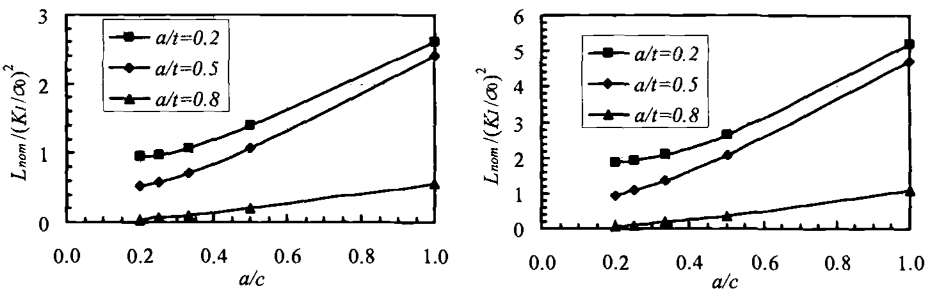

Figure 8 - *Size requirements for defects of various sizes using 7.5% (left) and 5.0% deviation criteria, respectively*

Bending Loaded Specimens

For SCPs under remote tension, the maximum K_I is always at the deepest crack point. In SCPs under remote bending, however, the point of maximum K_I depends on the crack depth and aspect ratio. An example is given in Figure 9 for a SCP with t=6.25 mm, $2W$=50 mm, σ_0=1700MPa, Σ^{∞}=0.9, and a/t=0.5 from the K_I solution of Newman and Raju [6]. The point of maximum K_I moves from the surface to the deepest point when the crack length is increased (decreasing a/c ratio for the fixed a/t ratio).

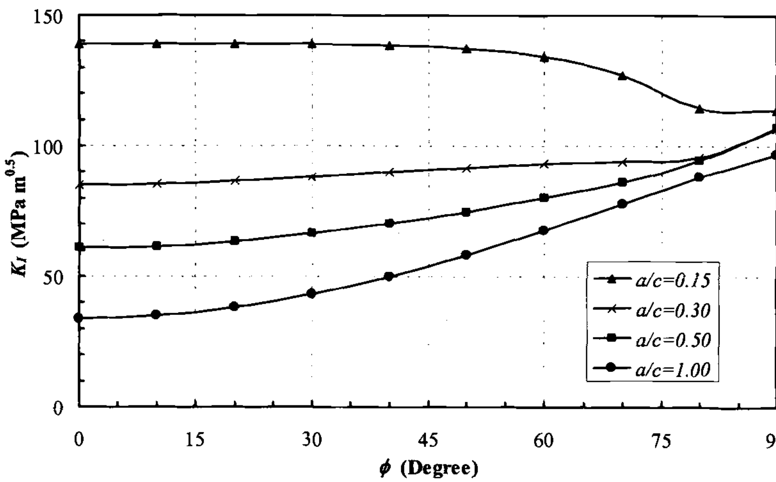

Figure 9 - *The variation of* K_I *along the crack fronts of SCPs with various aspect ratios using the* K_I *solution of Newman and Raju [6].*

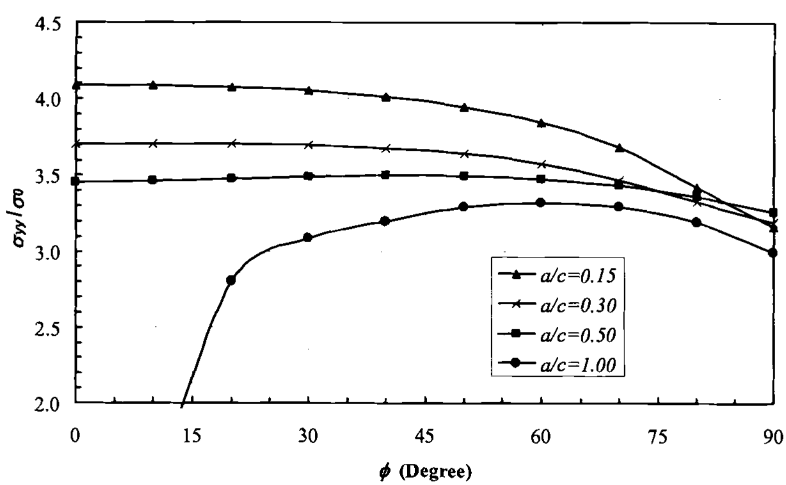

Figure 10 - *The variation of the crack-opening stress of SCPs with a range of aspect ratios at a fixed physical distance* r=*0.02 mm from the crack tip*

Referring to Figure 4, the *T*-stress generally varies from positive at the deepest point (ϕ=0^0) to negative at the free surface. The negative *T*-stress at the free surface lowers the crack-opening stress with respect to the SSY solution. Applying the *T*-stress solution of Eq. (6) and the K_I solution of Newman and Raju to Eqs. (4) and (5), the crack-opening stress along the crack front may be obtained. The variations of crack-opening stresses of SCPs with the same dimensions and material property as those of Figure 9 are shown in Figure 10. The location of the maximum stress moves from approximately

ϕ=60^0 at the crack front to the deepest point (ϕ=0^0) when the aspect ratio varies from 1.0 to 0.15.

The changing locations of the maximum stress intensity factor and the crack-opening present practical challenges as to which location should be selected to set specimen size requirements. A rigorous treatment implies that the size requirements be established for the particular crack geometry on a case-by-case basis. Such a procedure would be cumbersome to apply. We tentatively selected both ϕ=0^0 and ϕ=60^0 locations for our investigation.

Figure 11 shows the deviation of crack-opening stress for SCPs with four different crack sizes at ϕ=60^0. The magnitude of the deviation is relatively insensitive to the a/c ratio. At a/t=0.5, the deviation is very small even at large values of K_I. Figure 12 is similar to Figure 11, except the crack-opening stresses were at ϕ=0^0. Interestingly, the positive T-stress at ϕ=0^0 of a/t=0.5 leads to *negative* deviation. This implies that the predicted crack-opening stress from the MBL solution is *higher* than the SSY solution. At a/t=0.2, the magnitude of the deviation is quite small. It may be concluded from Figures 11 and 12 that $L_{nom} \geq (K_I/\sigma_0)^2$ is sufficient to ensure that the deviation is less than 7.5%.

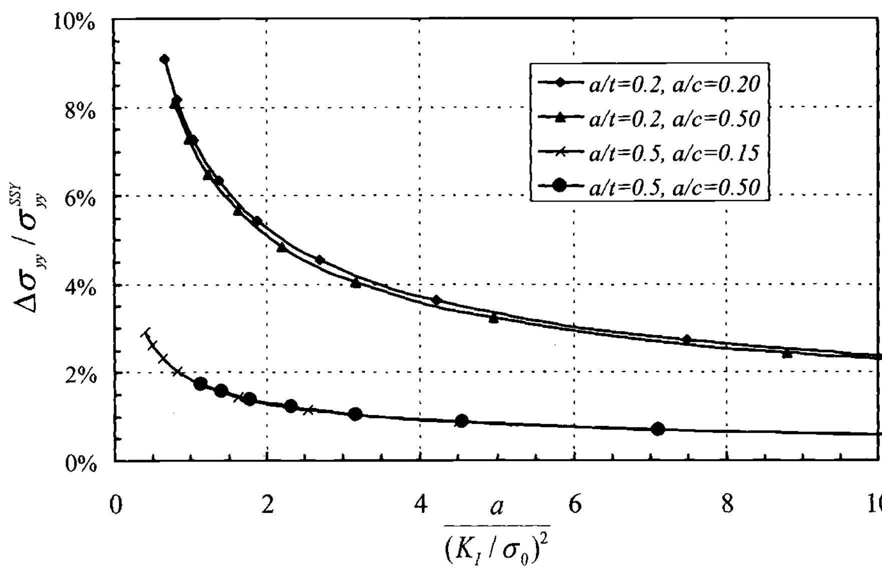

Figure 11 - *Deviation of crack-opening stress as a function of applied* K_I *for SCPs under remote bending at* ϕ=60^0.

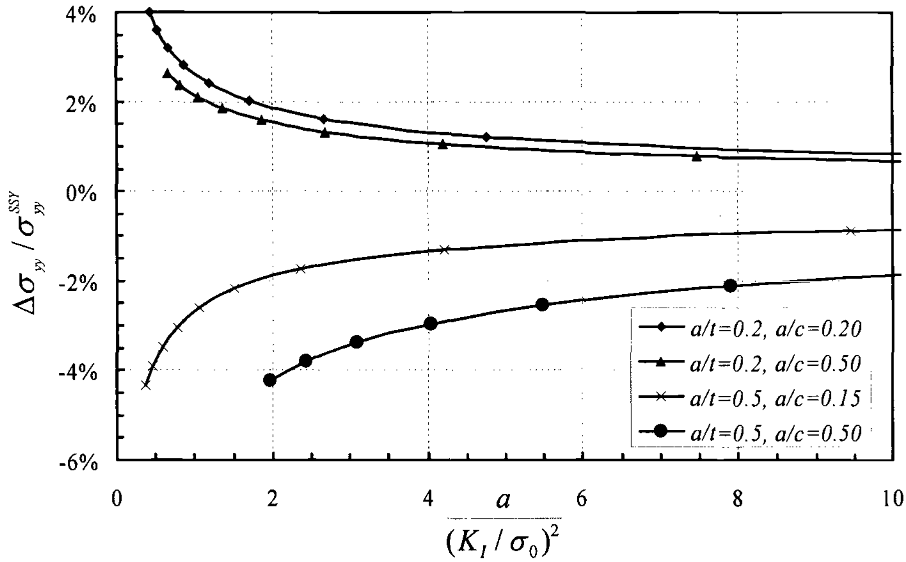

Figure 12 - *Deviation of crack-opening stress as a function of applied* K_I *for SCPs under remote bending at* $\phi=0^0$.

Correlation of Crack-Front Stress Distribution with Critical Fracture Location

Newman, et al, conducted elastic and elastic-plastic finite element analysis of SCPs under both remote tension and bending loads [*26*]. They developed stress intensity factor solutions that cover a wider range of crack-length-to-width ratios than those by Newman and Raju [*6*]. The crack-tip constraint and the critical fracture locations were studied using a hyper-local constraint parameter α_h. This constraint parameter is based on the averaged normal stresses acting over the plastic zone on a line in the crack plane perpendicular to the crack front. The critical fracture location, identified as the location of the maximum product of K_I and α_h, agreed with the experimental data within ±20%. The experimental data were from fracture tests of high-strength D6Ac motor case with surface cracks under both tension and bending loads [*27*].

With the K_I solution of Newman and Raju [*6*] and the *T*-stress solution of Eq. (6), it is possible to obtain the crack-opening stress profile along the entire crack front from Eqs. (4) and (5) assuming the equivalence of $J=K_I(1-\nu^2)/E$. This distribution may be correlated with the location of the fracture initiation assuming the fracture events are primarily controlled by the crack-opening stress. Such attempt is made for two specimens tested under remote bending [*27*]. The specimen No. 14 tested at INEL had a thickness (*t*) of 3.18 mm, crack depth (*a*) of 2.29 mm and crack length (2*c*) of 5.31 mm, and yield stress of 1546 MPa. The maximum bending stress at the fracture was 1689 MPa. The specimen No. B1 tested at NASA Ames had a thickness (*t*) of 6.32 mm, crack depth (a) of 1.38 mm, crack length ($2c$) of 3.48 mm, and yield stress=1700 MPa. The maximum bending stress at fracture was 1378 MPa.

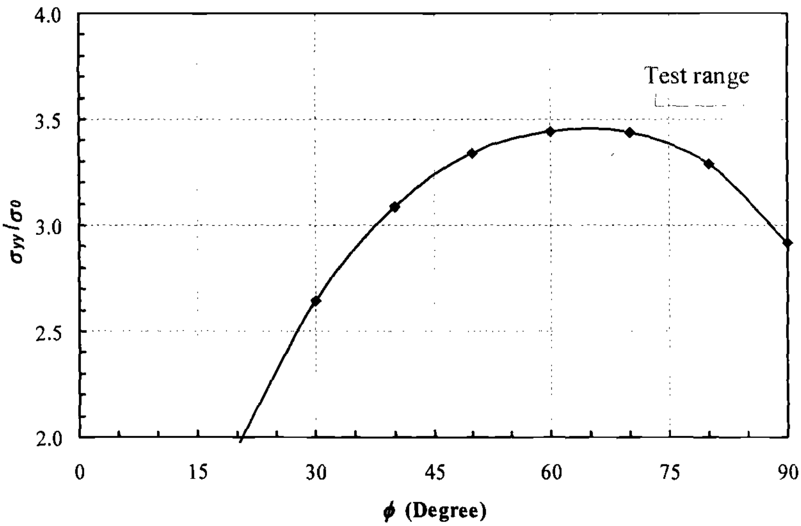

Figure 13 - *The distribution of crack-opening stress along the crack front at* r=*0.01 mm for Specimen No. 14 tested at INEL. The crack initiation region observed in the test specimens is denoted by the "Test range."*

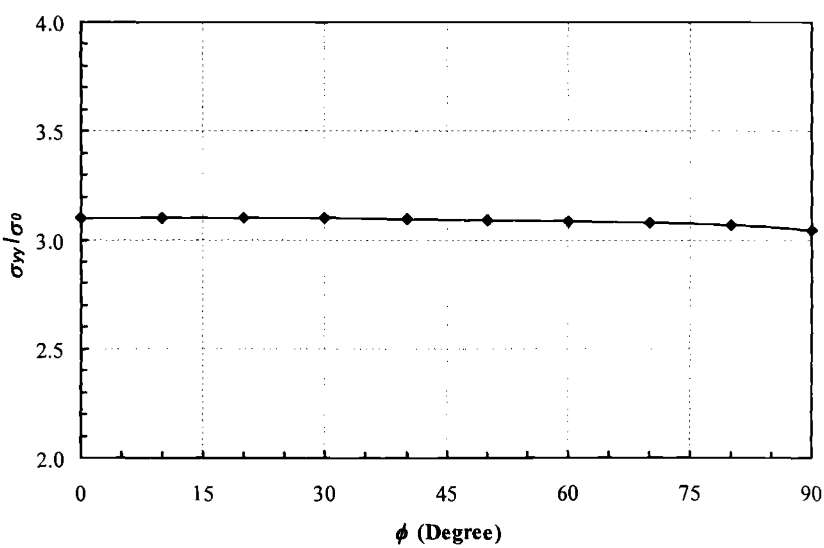

Figure 14 - *The distribution of crack-opening stress along the crack front at* r=*0.02 mm for Specimen B1 tested at NASA Ames.*

Figure 13 provides the distribution of crack-opening stress along the crack front at r=0.010 mm for the Specimen No. 14 tested at INEL. The peak stress is located approximately at 68°. The location does not change within the radial distance (r) range of 0.01-0.02 mm. The critical fracture location is 73-84° [*27, 28*]. Figure 14 shows that the crack-opening stress is almost constant along the crack front of the Specimen No 1B tested at NASA Ames. This constant stress profile may indicate that the critical fracture location can be wide spread.

Concluding Remarks

The MBL solution characterized by the J and T parameters can effectively represent the crack-tip fields of SCPs. With known K_I and T-stress solutions, the crack-tip fields of SCPs can be parameterized using the MBL solutions. We have made use of this feature to derive the specimen size requirements of the linear elastic fracture testing of SCPs. Attempts were also made to correlate the stress distribution along the crack front with the critical fracture locations.

In comparison to the plane strain specimens, establishing the specimen size requirement of SCPs is more complex. For a given stress deviation criterion, the size requirement is a function of both crack depth and aspect ratio. For tension-loaded SCPs, the requirement is estimated at $L_{nom} \geq (0.5 \text{ to } 2.5)\ (K_I/\sigma_0)^2$, where L_{nom} is the characteristic specimen size, i.e., maximum crack depth for shallow-cracked specimens and minimum remaining ligament for deeply-cracked specimens. McMeeking and Parks proposed a size requirement of $L_{nom} \geq 200\ J/\sigma_0$ for center-cracked panels under remote tension [*1*]. Assuming σ_0/E=0.0025 and using the equivalence of $J=K_I(1-\nu^2)/E$ with ν=0.3, the size requirement is converted to $L_{nom} \geq 0.455\ (K_I/\sigma_0)^2$, which is close to the lower bound value of the current recommendation. The upper bound value is the same as that in ASTM E399.

The crack-tip stresses of SCPs under remote bending are generally closer to SSY solution than those under remote tension. The size requirement for SCPs under bending may be set at $L_{nom} \geq (K_I/\sigma_0)^2$. However, this requirement may be overly stringent for some crack configurations.

Predicting the critical fracture locations using the profiles of crack-opening stresses showed some promise. However, more work is needed to fully validate the method.

The MBL solution used the analysis here had a strain-hardening exponent of 10. MBL solutions with materials of other strain hardening exponents can be easily obtained. The effects of strain hardening on the size requirements are worth further investigation.

Acknowledgment

The assistance of Mr. David Rudland at Emc^2 in proof reading the manuscript is greatly appreciated.

References

[1] McMeeking, R. M. and Parks, D. M., "On Criteria for *J*-Dominance of Crack-Tip Fields in Large Scale Yielding," *Elastic-Plastic Fracture, ASTM STP 668*, American Society for Testing and Materials, Philadelphia, 1979, PA, pp. 175-194.

[2] McMeeking, R. M., "Finite Deformation Analysis of Crack-Tip Opening in Elastic-Plastic Materials and Implications for Fracture," *Journal of the Mechanics and Physics of Solids*, Vol. 25, 1977, pp. 357-381.

[3] Shih, C. F. and German, M. D., "Requirements for One Parameter Characterization of Crack Tip Fields by HRR Singularity," *International Journal of Fracture*, Vol. 17, No. 1, 1981, pp. 27-43.

[4] Hutchinson, J. W., "Singular Behavior at the End of a Tensile Crack in a Hardening Material," *Journal of the Mechanics and Physics of Solids*, Vol. 16, 1968, pp. 13-31.

[5] Rice, J. R. and Rosengren, G. F., "Plane Strain Deformation near a Crack Tip in a Power Law Hardening Material," *Journal of the Mechanics and Physics of Solids*, Vol. 16, 1968, pp. 1-12.

[6] Newman, J. C., Jr. and Raju, I. S., "Analysis of Surface Cracks in Finite Plates Under Tension and Bending Loads," *NASA Technical Paper 1578*, NASA, Washington, D. C., December 1978.

[7] Reuter, W. G. and Epstein, J. S. "Experimental Evaluation of an Equation Applicable for Surface Cracks Under Tensile and Bending Loads," *Fracture Mechanics: Nineteenth Symposium, ASTM STP 969*, T. A. Cruse, Ed., American Society for Testing and Materials, Philadelphia, 1987, pp. 597-619.

[8] Reuter, W. G., Epstein, J. S., and Haggag, F. M., "Comparison between 'Standard' Fracture Toughness Results and Surface Flaw Data for Silicon Carbide," *International Journal of Fracture*, Vol. 47, 1991, pp. 181-200.

[9] Reuter, W. G., Newman, J. C., Jr., Macdonald, B. D., and Powell, S. R., "Fracture Criteria for Surface Cracks in Brittle Materials," *Fracture Mechanics: Twenty-Fourth Volume, ASTM STP 1207*, John D. Landes, Donald E. McCabe, and J. A. M., Boulet, Eds., American Society for Testing and Materials, Philadelphia, 1994, pp. 617-635.

[10] Betegón, C. and Hancock, J. W., "Two-Parameter Characterization of Elastic-Plastic Crack-Tip Fields," *Journal of Applied Mechanics*, Vol. 58, 1991, pp. 104-110.

[11] Al-Ani, A. M. and Hancock, J. W., "*J*-Dominance of Short Cracks in Tension and Bending," *Journal of the Mechanics and Physics of Solids*, Vol. 39, No. 1, 1991, pp. 23-43.

[12] Du, Z.-Z. and Hancock, J. W., "The Effect of Non-Singular Stress on Crack-Tip Constraint," *Journal of the Mechanics and Physics of Solids*," Vol. 39, 1991, pp. 555-567.

[13] Williams, M. L., "On the Stress Distribution at the Base of a Stationary Crack," *Journal of Applied Mechanics*, Vol. 24, 1957, pp. 111-114.

[14] O'Dowd, N. P. and Shih, S. F., "Family of Crack-Tip Fields Characterized by a Triaxiality Parameter: Part I – Structure of Fields," *Journal of the Mechanics and Physics of Solids*, Vol. 39, 1991, pp. 989-1015.

[15] O'Dowd, N. P. and Shih, S. F., "Family of Crack-Tip Fields Characterized by a Triaxiality Parameter: Part II – Fracture Applications," *Journal of the Mechanics and Physics of Solids*, Vol. 40, 1992, pp. 939-963.

[16] Wang, Y.-Y, and Parks, D. M., "Limits of *J-T* Characterization of Elastic-Plastic Crack-Tip Fields," *Constraint Effects in Fracture, Theory and Applications, Second Volume, ASTM STP 1244*, Mark Kirk and Ad Bakker Eds., American Society for Testing and Materials, Philadelphia, 1995.

[17] Wang, Y.-Y., "A Two-Parameter Characterization of Elastic-Plastic Crack Tip Fields and Applications to Cleavage Fracture," Ph.D. dissertation, Department of Mechanical Engineering, MIT, 1991.

[18] Larsson, S. G. and Carlsson, A. J., "Influence of Non-singular Stress Terms and Specimen Geometry on Small-Scale Yielding at Crack Tips in Elastic-Plastic Material," *Journal of the Mechanics and Physics of Solids*, Vol. 21, 1973, pp. 263-278.

[19] Kfouri, A. P., "Some Evaluation of the Elastic *T*-term Using Eshelby's Method," *International Journal of Fracture*, Vol. 30, 1986, pp. 301-315.

[20] Sham, T.-L., "The Determination of the Elastic *T*-term Using Higher Order Weight Functions," *International Journal of Fracture*, Vol. 48, 1991, pp. 81-102.

[21] Wang, Y.-Y. and Parks, D. M., "Evaluation of the Elastic *T*-Stress in Surface-Cracked Plates Using the Line-Spring Method," *International Journal of Fracture*, Vol. 56, 1992, pp. 25-40.

[22] Nakamura, T. and Parks, D. M., "Determination of Elastic *T*-stress along 3-D Crack Fronts Using an Interaction Integral," *International Journal of Solids and Structures*, Vol. 29, 1992, pp. 1597-1611.

[23] Sherry, A. H., France, C. C., Goldthorpe, M. R., "Compendium of *T*-stress Solutions for Two and Three Dimensional Cracked Geometries," *Fatigue and Fracture in Engineering Materials and Structure*, Vol. 18, 1995, pp. 141-155.

[24] Wang, Y.-Y. and Parks, D. M., "Evaluation of the Elastic T-stress in Surface-Cracked Plates Using the Line-Spring Method," Reports of Research in Mechanics of Materials, Department of Mechanical Engineering, MIT, Cambridge, MA, 1990.

[25] Wang, Y.-Y., "On the Two-Parameter Characterization of Elastic-Plastic Crack-Front Fields in Surface-Cracked Plates," *Constraint Effects in Fracture, ASTM STP 1171*, E. M. Hackett, K.-H. Schwalbe, and R. H. Dodds, Eds., American Society for Testing and Materials, Philadelphia, 1993, pp. 120-138.

[26] Newman, J. C., Jr., Reuter, W. G., and Aveline, C. R., Jr., "Stress and Fracture Analyses of Semi-Elliptical Surface Cracks," *Fracture and Fatigue, ASTM STP 1360*, P. C. Paris and K. L. Jerina, Eds., American Society for Testing and Materials, Philadelphia, 1999, pp. 403-423.

[27] Reuter, W. G., Elfer, N. C., Hull, A., Newman, J. C, Jr., Munz, D., and Panontin, T. L., "Fracture Toughness Results and Preliminary Analysis for International Cooperative Test Program on Specimens Containing Surface Cracks," *Fatigue and Fracture Mechanics: 28th Volume, ASTM STP 1321*, J. H. Underwood, B. D. MacDonald, and M. R. Mitchell, Eds., American Society for Testing and Materials, 1997, pp. 146-166.

[28] Chao, Y. J. and Reuter, W. G., "Fracture of Surface Cracks Loaded in Bending," *Fatigue and Fracture Mechanics: 28th Volume, ASTM STP 1321*, J. H. Underwood, B. D. MacDonald, and M. R. Mitchell, Eds., American Society for Testing and Materials, 1997, pp. 214-242.

Robert L. Tregoning[1] *and James A. Joyce*[2]

Application of a T-Stress Based Constraint Correction to A533B Steel Fracture Toughness Data

Reference: Tregoning, R.L., and Joyce, J.A., "**Application of a T-Stress Based Constraint Correction to A533B Steel Fracture Toughness Data,**" *Fatigue and Fracture Mechanics: 33rd Volume, ASTM STP 1417*, W.G. Reuter and R.S. Piascik, Eds., ASTM International, West Conshohocken, PA 2002.

Abstract: Over the past 18 months, a large data set has been developed on an A533B plate material removed from the decommissioned Shoreham nuclear power pressure vessel. The specimens in this data set were tested in the ductile-to-brittle transition regime using the procedures of the new ASTM Standard, *Standard Test Method for Determination of Reference Temperature, T_o, for Ferritic Steels in the Transition Range* (E 1921). Results presented earlier [*1*] showed that crack length ratio has a clear effect on the reference transition temperature, and also that SE(B) and C(T) specimens define clearly different reference temperatures for this material. The observation that the extent of plasticity had little effect on the observed specimen geometry shift led to an investigation of the elastic T-stress as a potential measure of constraint for these results. It was found that T_0 did correlate well with the median T-stress [*2*] obtained from standard equations [*3*] for the sample geometries used.

The effect of T-stress on specimen crack-tip constraint on T_0 has been investigated recently by Gao and Dodds [*4*], who noticed the strong effect that the T-stress had on plane strain finite element models under small-scale yielding conditions. Using finite element analysis and a Weibull stress-based failure model, Gao and Dodds calculated and developed polynomial fitting relationships for their T-stress scaling function [4]. Application of this method of constraint adjustment seemed promising [*5*] to predict the shift of the T_0 reference temperature between different specimen geometries.

This work applies the T-stress based constraint correction functions of Gao and Dodds to the new A533B data set. The analysis shows that a Weibull modulus can be chosen that resolves the observed constraint differences between the shallow and deep crack SE(B) data sets, while a slightly different Weibull modulus is required when deep crack C(T) data sets are substituted for the deep crack SE(B) data sets. However, the constraint correction procedure does not account for the difference observed in this data set between the deep crack SE(B) and C(T) data sets.

Keywords: fracture, fracture toughness, ductile-to-brittle transition, ductile fracture, T_0 reference temperature, master curve, constraint, cleavage

[1] Mechanical Engineer, Naval Surface Weapons Center, West Bethesda, MD 20817
[2] Professor, U.S. Naval Academy, Annapolis, MD 21402

Background

The scope of ASTM E 1921 defines the reference temperature (T_o) as a crack front length dependent material property if evaluated using C(T) or SE(B) specimens that meet the various size, testing, and sampling requirements. The inference is that one can obtain T_o using a deep crack specimen geometry and transfer the result to an application of grossly different size and crack geometry. Recent work by Joyce and Tregoning [*1*], Wallin [*6*], and Gao et al [*5*] has clearly demonstrated, however, that T_o is dependent on the constraint of the test geometry, and different T_o results can be expected even when one uses different "valid" specimen geometries, i.e. SE(B) or C(T) geometries. Joyce and Tregoning [*1*] and Wallin [*6*] both correlate the differences in T_o with the crack tip stress field elastic T-stress. Joyce and Tregoning evaluated a T-stress for each test specimen using the elastic J integral component to estimate an elastic K_{Jc} that was then multiplied by the "biaxiality coefficient," β, to obtain the T-stress at the cleavage initiation load for each sample. A median T-stress was then obtained for each unique specimen geometry and test temperature data set. Their results showed a difference in T_o of approximately 25°C between the shallow and deep crack SE(B) geometries, and a further 14°C difference between the deep crack SE(B) and the C(T) geometries. The T_o differences between standard (deep notch) specimen geometries call into question the transferability of the E 1921 Master Curve from fracture specimen geometries to structural applications without the application of geometry and/or constraint corrections.

Wallin [*6*] proposes a shift of the measured T_o based on the median T-stress of the specimens on which it is based. Since the experimental data were often not available, the T-stress was estimated in [*6*] using the procedure proposed by Sumpter [*7*] that estimates K_{Jc} based on the material yield stress. Wallin estimates the magnitude of the shift to be approximately 1°C for each 10 MPa change in T-stress, which translates to +35°C for shallow crack SE(B) data sets and -10°C for C(T) specimens, in comparison to specimens of deep crack SE(B) geometry.

Gao et al [*5*] predict a T_o shift between specimens of different T-stress and provide a constraint correction (toughness scaling) procedure to account for the differences. This approach involves utilizing a Weibull stress model proposed by Beremin [*8*], Mudry [*9*], and Minami [*10*] to define a critical failure parameter over the local crack tip fracture process zone. Gao and Dodds [*4*] utilize a 2D, plane strain formulation for the Weibull stress to naturally account for variations in K_J along the crack front in a weighed manner. The toughness scaling model requires the attainment of the same Weibull stress (based on equal probabilities of fracture) in different specimens, even though the K_J values differ widely. A generalized procedure was developed to construct a family of transfer functions ($\mathfrak{I}$-function) which convert toughness results between applications characterized by different T-stress magnitudes and stressed volumes. This function acts to scale toughness values and the corresponding T_o values between crack configurations exhibiting different constraint levels and replaces the need for more detailed finite element analysis once the material calibration parameters are known. The mechanics of this procedure are presented more completely in a later section of this paper. In this work, this toughness scaling procedure is evaluated using cleavage fracture toughness data sets obtained from C(T) and SE(B) specimens having dramatically different crack tip constraint.

Experimental Details

Material Characterization

The A533B test material was extracted from a portion of the 150 mm thick shell plate from the decommissioned Shoreham nuclear plant boiling water reactor pressure vessel. The test piece was originally located in the upper section of the vessel just below the nozzle inserts. The chemical composition for the test steel is provided in [*1*], and the tensile-mechanical properties at four temperatures are presented in Table 1. Results presented in [*1*] illustrate that this plate material has uniform tensile properties throughout the central 100mm of the plate. All specimens were machined from a block that measured 30 cm along the rolling direction by 214 cm in the transverse direction. The Table 1 properties represent the averages of specimens taken throughout the central 100 mm of the plate thickness.

TABLE 1—*A533B tensile mechanical properties.*

Temp. (°C)	σ_{ys} *(MPa)*	σ_{ult} *(MPa)*	*% Elong. (25 mm)*	*% R.A.*
-120	*603*	*760*	*28*	*63*
-80	*569*	*733*	*32*	*67*
-40	*520*	*694*	*24*	*66*
24	*488*	*644*	*28*	*70*
115	*445*	*589*	*23*	*70*

Fracture Toughness Tests

The test matrix containing the specimen geometries evaluated and the chosen test temperatures is summarized in Table 2. This table summarizes the parameters for the current database of 212 standard fracture toughness values for this material. Of these results, 180 results are uncensored as per ASTM E 1921 requirements. The test matrix is comprehensive in that all the allowable specimen were evaluated at more than one test temperature with respect to the best estimate of T_o. All C(T) and 1/2T SE(B) specimens (Table 2) were side-grooved with a depth corresponding to 20% reduction of the nominal thickness. However, the 1T 1x1 Bend groove depth was 10% of B_{max}, while the

1T SE(B) specimens were not side-grooved. The side-groove radius in all cases is 0.25 mm. As with the tensile specimens, fracture toughness specimens were cut from the center 100 mm of plate material using a cutting scheme presented in [*3*]. All specimens were oriented with the crack in the L-S direction as defined by ASTM E399.

In Table 2, the specimen size description follows the standard ASTM E399 convention of xT, where x is the nominal specimen thickness, B_{max}. Three distinct specimen geometries were studied: a square cross-section single-edged notch bend {1x1 Bend} geometry, a standard rectangular cross-section single-edged notch bend {SE(B)}

TABLE 2—*Matrix of test data for A533B steel.*

Specimen Geometry	Size (B_{max})	a/W	Test Temp.(°C)	N	r	T_o (°C)
Deep Crack Testing						
SE(B)	1T	0.50	-118	10	10	-95.9
		0.53	-42	12	12	-86.9
		0.53	-27	7	7	-84.2
		0.53	-12	7	4	-80.2[1]
	1/2T	0.52	-116	8	8	-87.7
		0.52	-79	8	7	-101.7
		0.53	-60	6	6	-82.3
		0.54	-50	6	3	-94.0[3]
		0.53	-40	8	2	-97.5[3]
		0.76	-115	7	7	-99.2
		0.75	-79	8	6	-94.9
1x1 Bend	1T	0.51	-118	8	8	-94.5
		0.51	-76	8	8	-94.2
		0.51	-50	12	7	-90.5
C(T)	1T	0.55	-40	14	14	-74.9
		0.57	-85	8	8	-82.0
		0.51	-110	8	8	-69.9
		0.52	-60	6	6	-74.5
		0.53	-25	8	8	-67.8
		0.52	-11	4	1	-93.2[3]
0.8T Plan C(T)	1T	0.50	-60	7	7	-85.0
		0.50	-80	7	7	-76.0

C(T)	*1/2T*	*0.56*	*-39*	*13*	*5*	*-82.3*[3]
		0.57	*-40*	*8*	*7*	*-57.8*
		0.57	*-86*	*8*	*8*	*-79.5*
		0.55	*-118*	*6*	*6*	*-84.6*
Shallow Crack Testing[3]						
SE(B)	*1T*	*0.15*	*-120*	*5*	*NA*	*-97.5*
		0.15	*-120*	*6*	*NA*	*-128.5*
		0.15	*-120*	*6*	*NA*	*-114.1*
		0.12	*-40*	*12*	*NA*	*-112.8*
	1/2T	*0.12*	*-115*	*7*	*NA*	*-130.0*
		0.12	*-115*	*8*	*NA*	*-126.5*
		0.12	*-96*	*8*	*NA*	*-108.5*
1x1 Bend	*1T*	*0.12*	*-120*	*8*	*NA*	*-110.0*
		0.12	*-92*	*8*	*NA*	*-126.6*

[3] These data sets do not meet all the requirements of E 1921.

geometry, and the compact tension {C(T)} geometry. The planar dimensions for each specimen type scale self-similarly with respect to B_{max} so that the specimen width (W) to B_{max} ratio is constant for each geometry regardless of absolute specimen size. The W/B ratio is 2 for the C(T) and SE(B) specimens, and W/B is 1 for the 1x1 bend geometries.

There was also testing conducted using a 0.8T-plan C(T) geometry. This notation denotes that the planar dimensions of this C(T) specimen were scaled with respect to a 0.8T specimen thickness. However, the specimen thickness was 1T, and W/B =1.6 for this specimen. This geometry was used to extract C(T)-type specimens directly from the ends of several 1T SE(B) specimens, and this provides a direct assessment of any significant material variability between the different plate locations of the C(T) and SE(B) specimens.

Additionally, several SE(B) and 1x1 Bend specimens were tested with a/W $\leq$ 0.15. These short crack specimens were utilized to determine material-dependent calibration factors within the Weibull stress-based model of cleavage fracture, and also to evaluate the effect of significant in-plane constraint loss on measured T_o properties. A total of 54 tests were conducted for these low constraint geometries. The T_{oq} values representative of these geometries obviously are not expected to be equivalent to the "material" T_o and are therefore not valid tests within the context of E 1921.

T_o Evaluation

The T_o value was determined for each unique data set (temperature and specimen type) as per E 1921 methodology. T_o is valid according to E 1921 for nearly all of the individual deeply cracked specimen data sets reported here. Specimen constraint can be quantified by the following expression:

$$M = \frac{b\sigma_{ys}}{J_c} = \frac{Eb\sigma_{ys}}{K_{Jc}^2} \tag{1}$$

where b is the remaining ligament, σ_{ys} is the material yield strength, J_c is the value of the J integral at cleavage (defined as K_{Jc}^2/E), and M is defined as the constraint limit. E 1921 requires data censoring for specimens with M < 30 in an effort to assure that K_{Jcmed} for the data set is not affected by constraint loss.

In most cases, the median M values of the data sets (M_{med}) presented in Table 2 are quite large (M_{med} > 80). As prescribed, the censoring limit ($K_{Jc(limit)}$) was based on the material's yield strength (σ_{ys}) at the test temperature. Linear interpolation between the tensile properties was used for censoring when the measured σ_{ys} (Table 1) and fracture toughness testing temperatures did not coincide.

The shallow crack specimen data sets were also analyzed as per E 1921 except that no censoring was applied. The values calculated are designated as T_q to reflect this deviation, and the fact that E 1921 does not apply for a/W < 0.45.

Analysis

$\mathfrak{J}$ Constraint Correction

The toughness scaling model used here has been developed by Gao and Dodds [*4*] using a two-parameter Weibull distribution developed originally by Beremin [*8*], Mudry [*9*] and Minami et al [*10*] in the form:

$$P_f(\sigma_w) = 1 - \exp\left[-\frac{1}{V_o}\int_V \left(\frac{\sigma_1}{\sigma_u}\right)^m dV\right] = 1 - \exp\left[-\left(\frac{\sigma_w}{\sigma_u}\right)^m\right] \tag{2}$$

where V denotes the volume of the cleavage fracture process zone, V_o defines a reference volume, and σ_1 is the maximum principal stress acting on the material points inside the fracture process zone. Parameters *m* and σ_u in Eq. 1 denote the Weibull distribution modulus and scale parameter respectively. Defining the Weibull stress (σ_w) as the stress integral over the fracture process zone yields:

$$\sigma_w = \left[\frac{1}{V_o}\int_V \sigma_1^m dV\right]^{1/m} \tag{3}$$

The Weibull stress thus defines a micromechanical model which couples the remote loading to the probability of microcrack initiation based on weakest link fracture. This is the essence of the "local approach" proposed initially by Beremin [*8*]. Under increased remote load, defined by J or K_J, differences in the Weibull stress can develop, reflecting strong variations in the crack-front stress fields due to differences in constraint loss and sampling volume. Three dimensional variations in J along the crack front can be accommodated in the Weibull stress approach, and the method shows great promise as a tool to aid in the transfer of fracture toughness measurements from laboratory data to structural applications [*5*].

Under conditions of plane strain, small scale yielding (SSY), Gao and Dodds [*4*] demonstrated that the crack-tip fields are governed by J and the non-singular T-stress parallel to the direction of crack extension. This allows expressing the Weibull stress explicitly in terms of J as:

$$\sigma_w^m = J^2\left(\frac{B\sigma_o^{m-2}}{V_o}\right)\int_0^{2\pi}\int_0^{\bar{\rho}} f^m \rho\, d\rho\, d\theta \tag{4}$$

where f denotes a non-dimensional function and $\bar{\rho}$ represents the non-dimensional radius of the fracture process zone.

Additionally,

$$f = f(n,\nu;E/\sigma_o,T/\sigma_o,m) \tag{5}$$

where n = material strain hardening, ν = Poisson's ratio, E = material elastic modulus, T = T-stress, and m = Weibull modulus. For simplicity, the integral in Eq. 4 can be redefined as:

$$\sigma_w^m = J^2\left(\frac{B\sigma_o^{m-2}}{V_o}\right)\Omega(n,\nu,E/\sigma_o;T/\sigma_o;m) \tag{6}$$

showing the separation accomplished between the applied load level J and the non-dimensional parameter, Ω, which is only a function of material and geometric parameters. Equation 6 enables construction of a toughness scaling model relating J_c values (J at the onset of cleavage) at two different SSY configurations having $T \neq 0$ and $T = 0$ by requiring:

$$\sigma_w^m(T \neq 0) \equiv \sigma_w^m(T = 0) \tag{7}$$

Substituting from Eq. 6 and computing a ratio of critical fracture toughness values gives:

$$\frac{J_c^{T\neq 0}}{J_c^{T=0}} = \sqrt{\frac{\Omega_{T=0}}{\Omega_{T\neq 0}}}\left(\frac{B_{T=0}}{B_{T\neq 0}}\right)^{1/2} \tag{8}$$

Or in terms of K_J as:

$$\frac{K_{Jc}^{T\neq 0}}{K_{Jc}^{T=0}} = \left[\frac{\Omega_{T=0}}{\Omega_{T\neq 0}}\right]^{1/4} \left(\frac{B_{T=0}}{B_{T\neq 0}}\right)^{1/4} \tag{9}$$

Gao and Dodds then define $\Im$ as follows:

$$\left[\frac{\Omega_{T=0}}{\Omega_{T\neq 0}}\right]^{1/4} = \Im(n, \nu, E/\sigma_o; T/\sigma_o; m) \tag{10}$$

As with f previously, $\Im$ as defined by Eq. 10, is simply a function of material properties, (n, ν, E, σ_o, and m), specimen geometry, and constraint as defined by the T-stress. One issue related to the use of the Weibull stress-based model is whether the Weibull modulus m is effectively independent of the constraint conditions. It is assumed in this work that this is the case.

Gao and Dodds [4] explicitly determined the $\Im$ function using plane strain finite element analyses and the SSY boundary layer model over the expected range of material flow properties and constraint levels (T/σ_o). They then empirically fit these results using polynomial relationships of the form:

$$\Im(n, \nu, E/\sigma_o; T/\sigma_o; m) = 1 + \sum_{i=1}^{N_1}\left[\sum_{j=0}^{N_2} b_{ij}(n, \nu, E/\sigma_o) m^j\right]\left(\frac{T}{\sigma_o}\right)^i \tag{11}$$

The b_{ij} coefficients were developed for strain hardening and E/σ_0 ratios typical of ferritic structural steels. This formulation allows a user to determine $\Im$ without numerical analysis. Three sets of b_{ij} coefficients applicable here are presented in Table 3 and a comparison of the numerical results and the polynomial fits are shown in Figure 1.

In the following sections, the $\Im$ formulation is used to constraint adjust the experimental data presented in Table 2 by requiring that different specimen types and crack lengths yield consistent "adjusted" T_0 values. Therefore, it is sometimes necessary to extrapolate beyond the range of $10<m<20$ which was utilized in [4] to develop the b_{ij} coefficients. For the case with $n = 10$ and $E/\sigma_0 = 500$, Figure 2 shows an extended plot of Figure 1c for $6<m<40$. While the accuracy of the extrapolated curves cannot be assured without additional numerical confirmation, this figure at least shows that the polynomial fitting function remains well behaved over the expanded region of m.

T-stress Evaluation

The T stress relationships used here were obtained from the work of Sherry et al [3] who fit polynomial relationships to the computational results of several authors [11-15]. The T stress is written in the standard form as:

$$\frac{T}{\sigma_o} = \frac{\beta K}{\sigma_o \sqrt{\pi a}} \tag{12}$$

Polynomial relationships for the biaxiality parameter β were then obtained as functions of a/W as [*3*]:

$$\beta = B_0 + B_1\left(a/W\right) + B_2\left(a/W\right)^2 + B_3\left(a/W\right)^3 + B_4\left(a/W\right)^4 \tag{13}$$

where the B_i coefficients for each geometry are tabulated in Table 4. These relationships are plotted in Figures 3 and 4 for the SE(B) and C(T) cases respectively. These estimates of the T-stress were obtained using different methods and it is a cause for concern that such large differences exist between the various T-stress estimates. The effect of these variations on the present analysis will be investigated further in a later section of this paper.

TABLE 3(a)—*b_{ij}(j = 0→ 4) values for n = 7.5, E/σ_o=650.*

b_{1j}	0.47794	-0.16895	0.84314E-2	-0.18826E-3	0.15453E-5
b_{2j}	-0.31509	0.83814E-1	0.39382E-2	-0.42616E-3	0.86299E-5
b_{3j}	0.61345	-0.18869	0.11455E-1	-0.22479E-3	0.19398E-6
b_{4j}	-2.2230	0.76577	-0.80695E-1	0.33585E-2	-0.48744E-4

TABLE 3(b)—*b_{ij}(j = 0→ 4) values for n = 10., E/σ_o=500.*

b_{1j}	0.43210	-0.15705	0.76406E-2	-0.22737E-3	0.42764E-5
b_{2j}	-0.29155	0.10117	-0.21217E-2	0.15307E-3	-0.35846E-5
b_{3j}	0.22016	-0.29644E-1	-0.86138E-2	0.48119E-3	-0.83446E-5
b_{4j}	-1.6930	0.46576	-0.28522E-1	0.54138E-3	0.55008E-7

TABLE 3(c)—*b_{ij}(j = 0→ 5) values for n = 20, E/σ_o=300.*

b_{1j}	0.43908	-0.16092	0.77264E-2	-0.29123E-3	0.42764E-5
b_{2j}	-0.56272	0.22326	0.14097E-1	0.69782E-3	-0.12765E-4
b_{3j}	0.16609	-0.29455E-1	-0.44368E-2	0.55463E-3	-0.12577E-4
b_{4j}	-0.92400	0.18058	-0.74768E-2	0.52981E-3	0.29898E-5
b_{5j}	0.79230E-1	0.41083E-1	-0.18202E-1	-0.35299E-3	-0.35051E-5

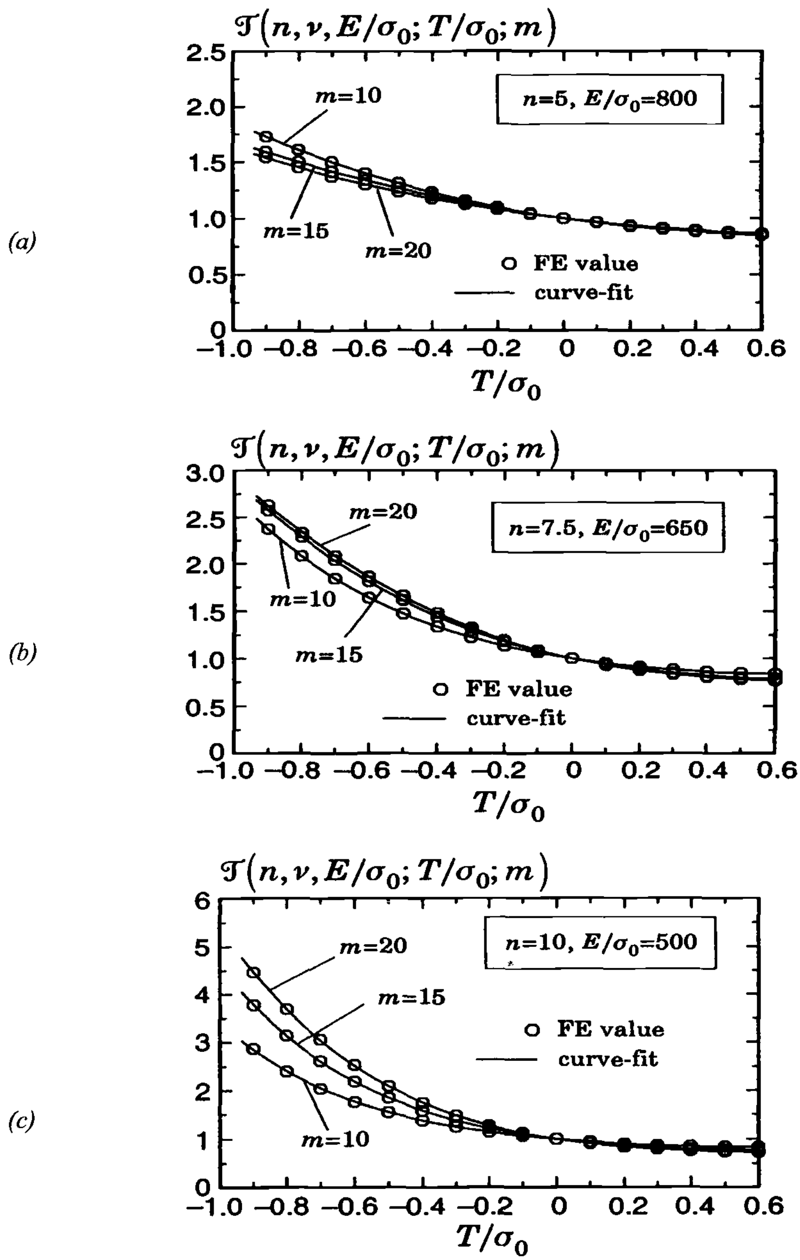

FIG. 1—*Comparison of the computed $\mathfrak{J}$ vs. T/σ_o with the polynomial fit for three Weibull m values for three typical sets of material flow properties.*

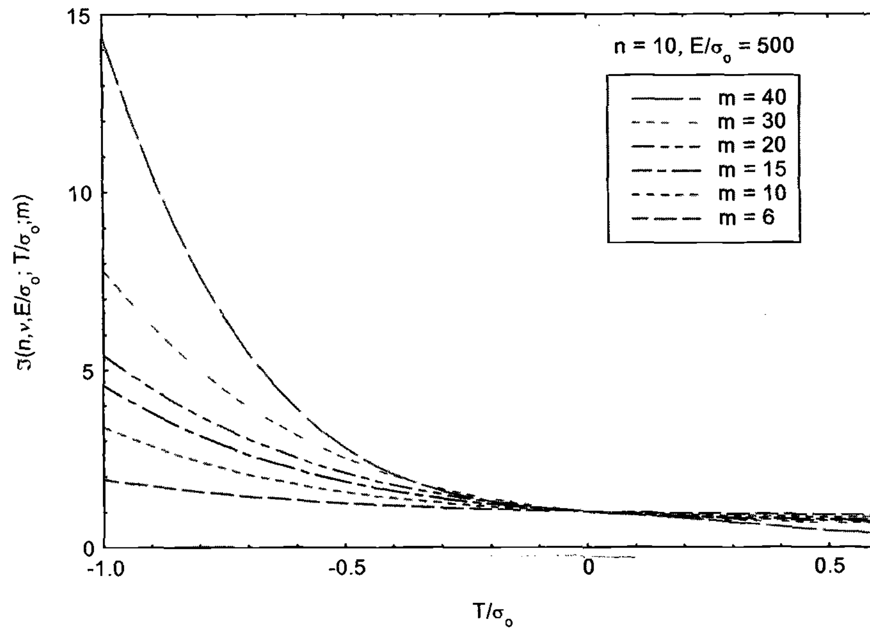

FIG. 2—*ℑ vs. T/σ_o with the polynomial fit using an extended m range.*

TABLE 4a—*Polynomial fitting coefficients for T-stress geometry (β) coefficient – SE(B) geometry, Sherry et al [3].*

Reference	B_0	B_1	B_2	B_3	B_4
Leevers and Radon [*13*]	-0.693	2.464	-2.475	0.970	2.131
Kfouri [*11*]	-0.429	0.699	1.683	-2.745	1.875
Cardew et al [*15*]	-0.472	0.995	0.250	--	--
T.-L. Sham [*12*]	-0.439	0.445	4.056	-6.777	4.253

TABLE 4b—*Polynomial fitting coefficients for T-stress geometry (β) coefficient – C(T) geometry, Sherry et al [3].*

Reference	B_0	B_1	B_2	B_3	B_4
Leevers and Radon [*13*]	-0.513	1.708	13.404	-39.750	29.583
Cotterell [*14*]	-0.058	-0.276	12.790	-27.875	17.292
Kfouri [*11*]	-0.353	-1.702	23.667	-47.33	28.333

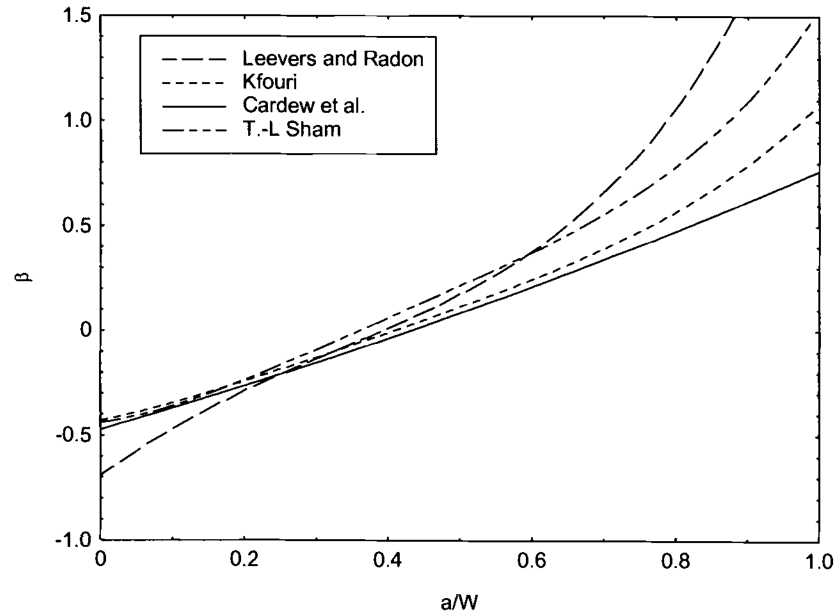

FIG. 3—*T-stress geometry coefficient β versus a/W for the SE(B) geometry.*

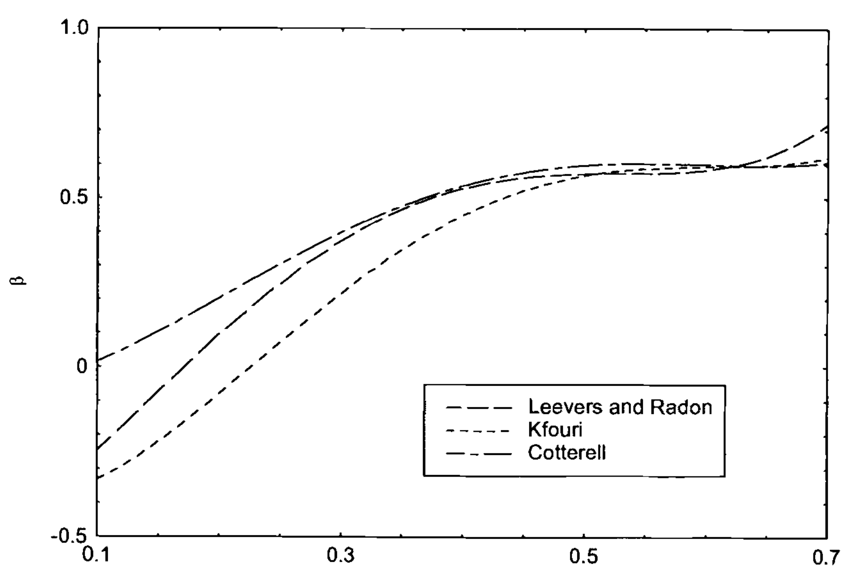

FIG. 4—*T-stress geometry coefficient β versus a/W for the C(T) geometry.*

Application to the A533B Steel Data

The data presented in Table 2 includes 35 sets of data that can be used to calculate the reference temperature T_o. Included in these data sets are 14 deep crack 1/2T and 1T SE(B) specimens with both square and rectangular cross-sections, 12 deep crack 1/2T, 0.8T, and 1T C(T) data sets, and 9 shallow crack 1/2T and 1T SE(B) specimens with both rectangular and square cross-sections. Each specimen type and size was tested at multiple test temperatures. The T_o results obtained using the E 1921 procedure are presented in Table 2 and plotted in Figure 5 versus specimen type. A clear dependence on specimen type is demonstrated in Figure 5. The highest average T_o value (T_{oAvg}) = -77.5 ^{o} C and corresponds to the C(T) geometry. The deep crack SE(B) follows in magnitude with T_{oAvg} = -91.7^o C, while the shallow crack SE(B) has the lowest T_{oAvg} = -117.7^{o}C.

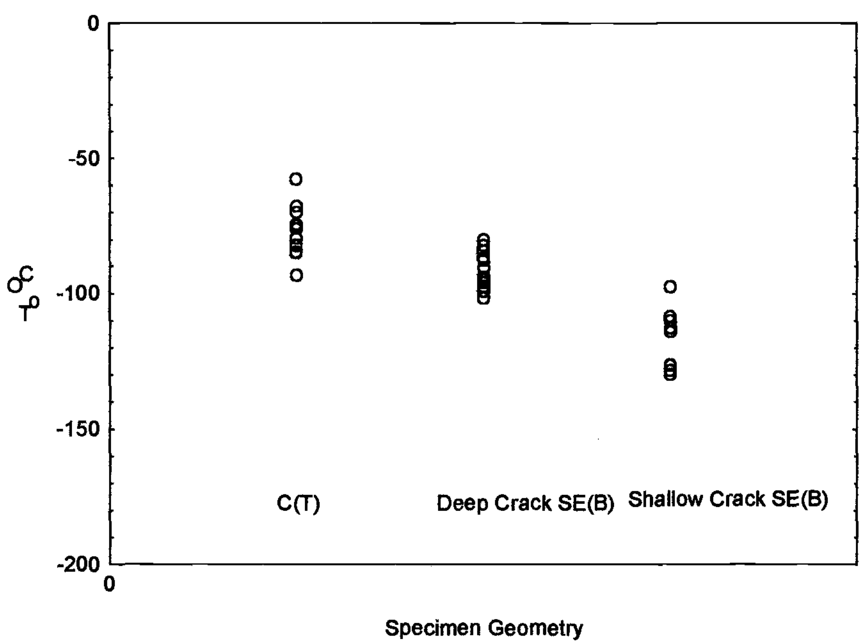

FIG. 5—*Test results showing T_o calculated according to E 1921 for the three specimen geometries. (No constraint corrections.)*

Application of the Gao-Dodds constraint correction procedure results in an adjustment of the K_{Jc} measured at cleavage initiation according to Eqs. 8-10. The magnitude of this adjustment is a function of the specimen geometry, the a/W ratio, the uncorrected K_{Jc}, material tensile properties (E, n, ν, and σ_0), and the Weibull modulus m. The Weibull modulus m is taken to be a material property obtainable from the fracture toughness tests. It is implicitly assumed in this analysis that *m* and the scale parameter (σ_u in Equation 2) is not a function of test temperature. Gao and Dodds [*4*] suggest using two sets of fracture toughness data to obtain the Weibull modulus for a ferritic material of interest. The two sets should demonstrate very different levels of constraint, but be tested under predominantly small scale yielding conditions. The two data sets are then constraint corrected with the procedure presented above using different *m* values until the median K_{Jc} values ($K_{Jc(med)}$) are consistent. Gao et al [*16*] determined that a Weibull modulus of $m = 11.2$ was required to obtain similar adjusted results in shallow and deep crack SE(B) data forA515-70 structural steel. A similar analysis in reference [*5*] yielded $m = 15$ for A533B steel.

A much more extensive data set is available here for the A533B material then in previous studies. Applying the Gao-Dodds constraint procedure to this full data set, with $m = 10$, $n = 10$, and $E/\sigma_o = 500$, yields the result shown in Figure 6. For these calculations, the T-stress was evaluated using the Kfouri [*11*] analysis polynomial of Eq. 11. This study was chosen because it is represents a "median" result over the range of tested crack sizes. The T_{oAvg} values for the three data sets are now: –84.4°C for the C(T), -97.2°C for the deep crack SE(B), and –89.9°C for the shallow crack SE(B). This correction has clearly reduced the average deviation with the shallow crack SE(B) result now falling between the C(T) and deep crack SE(B) averages, but the difference between the C(T) and deep SE(B) specimens has changed very little. The choice of Weibull modulus *m* has a strong effect on these results.

To evaluate the effect of the choice of the Weibull *m*, the Gao et al $\Im$ procedure was applied using linked Excel worksheets. Each worksheet contains a unique data set as presented in Table 2. The sheets develop the constraint adjusted K_{Jc} values as per the $\Im$ procedure outlined previously for the selected *m* value. The constraint corrected K_{Jc} values were in turn linked to a summary sheet where the best estimate "multi-temperature" (and multi-geometry) procedure of E 1921 was used to evaluate an overall "average" T_o, T_{oAvg}. This procedure was repeated for the deep SE(B), shallow SE(B), and C(T) data sets in turn.

Applying the Gao et al $\Im$ procedure to the deep and shallow SE(B) data sets, and calculating the T_{oAvg} over a range of Weibull modulus *m* values from 2 to 20 gives the results shown in Figure 7. The adjusted deep and shallow values of T_{oAvg} for the SE(B) specimens are in agreement for these two geometries when $m \approx 8.5$. This is consistent with earlier results for A515 and A533B steel [*5, 16*]. The sensitivity of the shallow crack SE(B) correction to changes in *m* is evident in Figure 7. This feature allows *m* to be uniquely determined with relatively little error.

Repeating the analysis for the C(T) and shallow SE(B) data leads to somewhat different results (Figure 8). The Kfouri study [*11*] was again utilized here to calculate the T-stress in the C(T) specimen data sets since it represents the median result. Now a Weibull modulus of approximately 12 is required for agreement between the constraint adjusted, SSY, T_{oAvg} estimates obtained by comparing the C(T) and shallow SE(B) geometries. The choice of using the deep crack SE(B) specimen data set or the C(T) data set as the high constraint reference data set leads to the different estimate of the Weibull modulus, *m*. This difference in Weibull slope (8.5 versus 12) corresponds to a shift in the T_{oAvg} of approximately 10°C, a considerable difference in many applications.

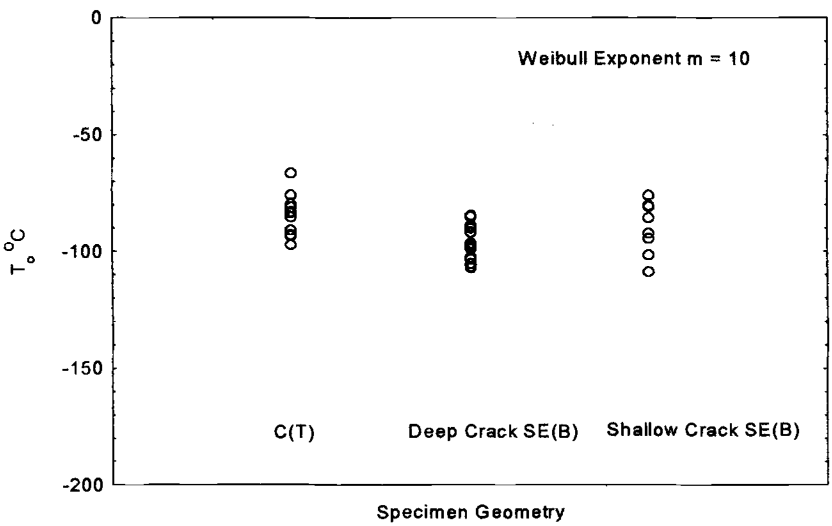

FIG. 6—T_o *values calculated according to E 1921 using constraint corrected* K_{Jc} *values for the three specimen geometries.*

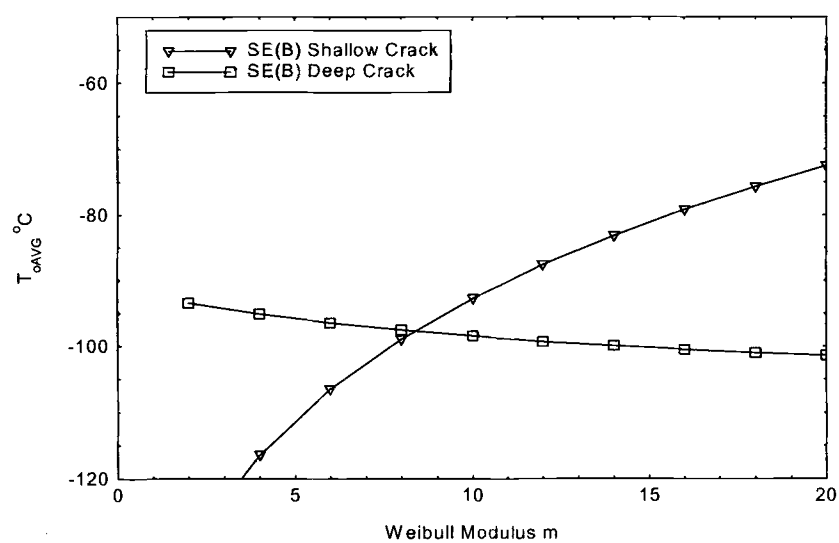

FIG. 7—T_{oAvg} *versus the Weibull modulus m comparing the deep SE(B) and shallow SE(B) specimen geometries.*

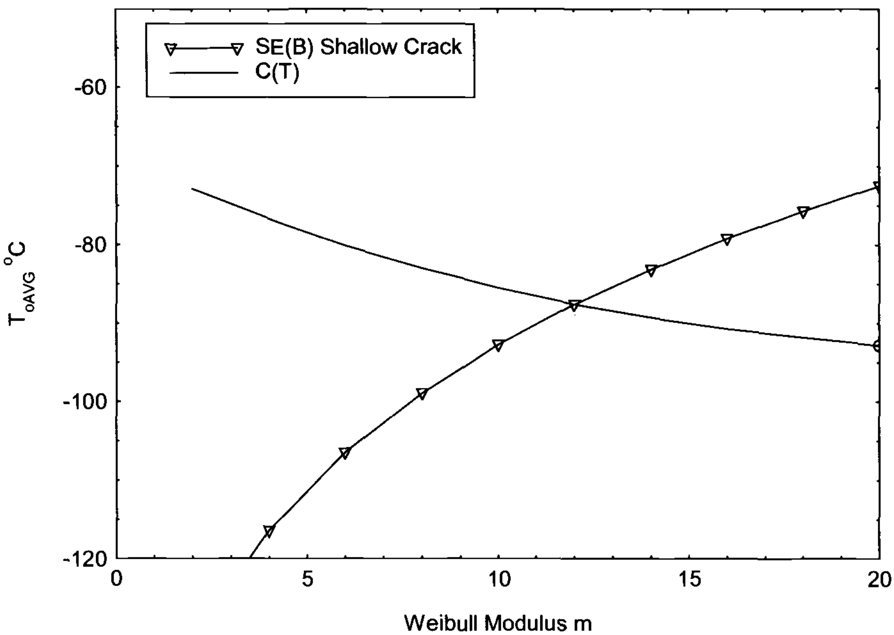

FIG. 8—*Comparison of constraint corrected T_{oAvg} results obtained by applying the Gao et al procedure to the C(T) and shallow crack SE(B) data sets.*

Figure 9 shows the comparison of these calculations for all three data sets. Figure 9 illustrates a potential deficiency in the Gao $\Im$ correction procedure. The negative T-stress, shallow crack SE(B) geometry data set is strongly dependent on *m*, while the deep SE(B) and C(T) data sets are only weakly dependent on *m*. These deep SE(B) and C(T) specimens possess similar, positive T-stresses, and while constraint adjustment does rectify differences between the two specimen types, the magnitude of the change is small, except at high Weibull modulus values. This is attributed to the insensitivity of $\Im$ to constraint differences between $T/\sigma_0>0$ geometries (Figure 2). The end result is that the 14°C difference measured on this material is diminished only if a large Weibull modulus of approximately 36 is used in the analysis. This is much larger than the *m* values needed to resolve the differences observed between the deep and shallow crack specimen types (Figure 9). Therefore agreement among the three specimen types does not result from any unique value of the Weibull modulus *m*.

The variability among T-stress solutions (Figures 3 and 4) obviously contributes some uncertainty to the Weibull modulus determination. This uncertainty is estimated by performing the constraint adjustment with different T-stress solutions. The

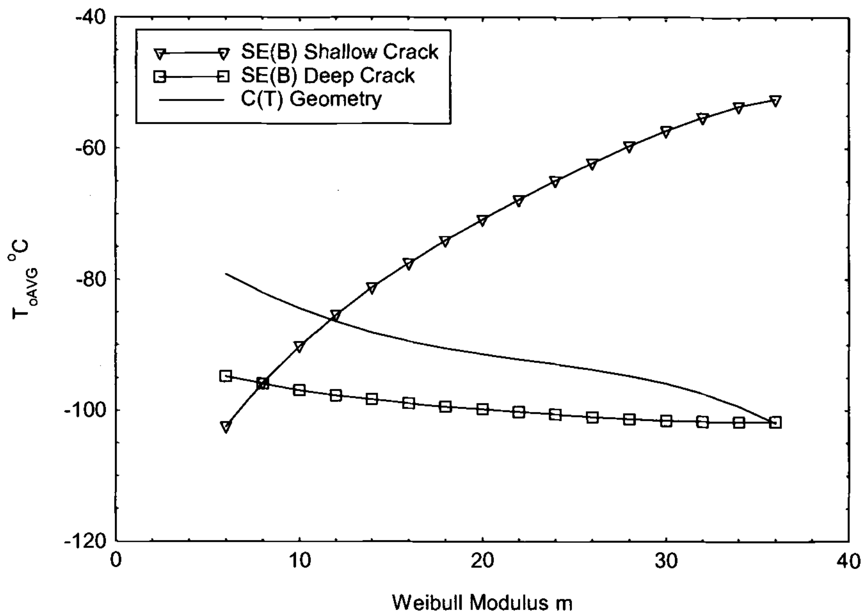

FIG. 9—*Comparison of constraint corrected T_{oAvg} results.*

variability in the T-stress solutions is minimal for the C(T) specimens over the crack length range of the tested specimens, 0.50 < a/W < 0.57 (Table 2). The Leevers and Radon [13] SE(B) solution exhibits the largest difference from the Kfouri solution [*11*] (Figure 3), especially for shallow crack (a/W < 0.25) and deeply-cracked (a/W > 0.6) geometries.

However, constraint adjustment using the $\Im$ formulation is relatively insensitive to positive T-stress variability since $\Im \approx 1.0$. Therefore, the use of an extrapolated Leevers and Radon solution results in very little difference from the Kfouri solution even for the a/W = 0.75 SE(B) specimens.

The largest constraint adjustment variability due to T-stress uncertainty occurs in the shallow crack specimens. The Leevers and Radon T-stress solution for these specimens leads to the constraint adjustment plot shown in Figure 10. While discrete calculations are still being utilized with distinct values of *m*, smooth curves have been substituted for clarity of the following comparison. This T-stress formulation does shift the intersection point of the shallow crack SE(B) specimens toward smaller *m* values. The intersection with the deep crack SE(B) specimens occurs at $m = 6.5$ instead of $m = 8.5$ for the Kfouri solution, while the intersection with the C(T) specimens now occurs at $m = 9$ instead of $m = 12$. While the differences between the C(T) and SE(B) intersection points are not alleviated, they are diminished with respect to m through use of the Leevers and Radon solution. This results from the greater sensitivity (higher slope) of the shallow crack SE(B) adjustment to *m* due to lower predicted T-stress in these specimens. However,

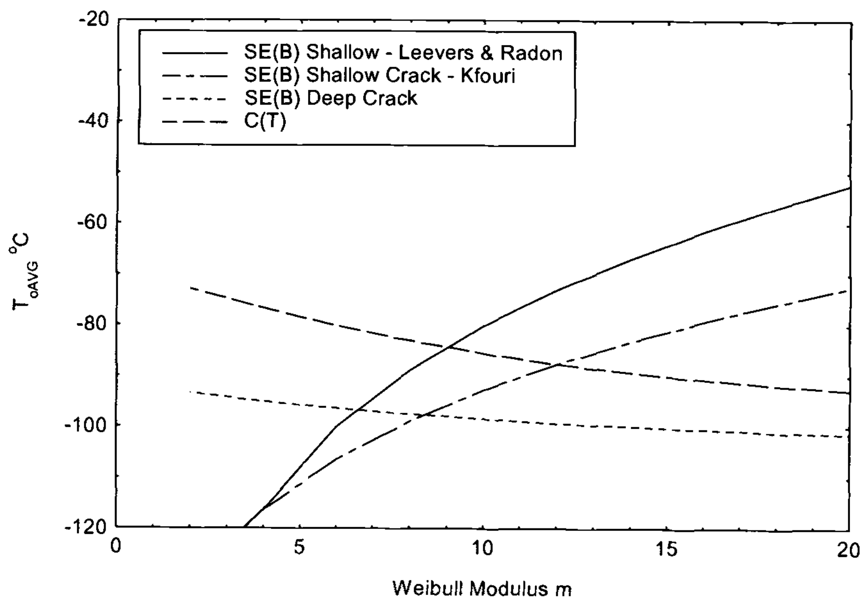

FIG. 10—*Comparison of constraint corrected T_{oAvg} results obtained from the Leevers and Radon T-stress analysis with that of the Kfouri analysis.*

closer agreement in *m* still results in a T_{oAvg} of approximately 10°C due to the relative insensitivity of the deep crack T_{oAvg} curves to *m*. Also, the specific T-stress analysis utilized ultimately only results in an additional uncertainty in the nominal constraint adjusted T_{oAvg} value of 2° to 3°C.

Conclusions

A constraint adjustment scheme was applied to deeply cracked SE(B), C(T), and shallow cracked SE(B) fracture toughness data in an attempt to rectify measured T_o differences among the various specimen types. The scheme relies on the basic assumptions that small scale yielding applies, and that cleavage fracture initiation is governed by the development of equal values of Weibull stress between different geometries. A Weibull modulus, *m*, can be chosen that removes the observed T_o differences among various specimens types to ideally determine a geometry independent T_o value. A Weibull modulus of 8 was required to obtained identical adjusted T_{oAvg} values between the shallow and deep crack SE(B) data sets. A Weibull modulus of 12 was necessary to resolve differences between C(T) and shallow crack SE(B) data. The variability in the calibrated *m* values as a function of the deep crack specimen type leads to a difference in the adjusted T_{oAvg} of approximately 10°C. Therefore the constraint correction procedure effectively reduces the variation in T_0 measured from sets of shallow and deep SE(B) specimens, and deep crack C(T) specimens from approximately 40°-45°C to 10°C.

The remaining 10°C gap stems from the insensitivity of the constraint correction scheme to measured toughness differences between deep crack SE(B) and C(T) data sets. Both of these specimen geometries have a positive T-stress. The initial measured 14°C is reduced to 10°C upon calibration with the shallow crack SE(B) specimens. However, an unreasonably large Weibull modulus of 36 is required to eliminate the entire difference and to achieve consistent adjusted T_{0Avg} values in these deep crack data sets. Additionally, this *m* value results in a final T_{0Avg} value well below what is expected to resolve differences between these specimen types. This conundrum illustrates that the $\mathfrak{I}$ correction scheme should not be applied between geometry types with positive T-stress values, and that any application has an inherent uncertainty on the order of 10°C. This result is consistent with the requirement of Dodds and Gao that their constraint correction method should be calibrated using specimen geometries of distinctly different T-stress values.

The constraint adjustment scheme has also been shown to be somewhat sensitive to the specific T-stress analysis utilized. While *m* can vary by as much as 30% for widely varying T-stress solutions, the corresponding adjusted T_0 differences only varies by 2° to 3 °C. This uncertainty could be reduced by more accurately determining the T-stress values within these specimens through more refined numerical analysis.

References:

[1] Joyce, J.A., Tregoning, R.L., "Quantification of Specimen Geometry Effects on the Master Curve and T_0 Reference Temperature", ECF13, San Sebastian, Spain, 2000.

[2] Williams, M.L., *J. Appl. Mech.* **Vol. 24**, p.109, 1957.

[3] Sherry, A.H., France, C.C., Goldthorpe, M.R., *Fatigue Fract. Engng Mater. Struct.* **Vol. 18**, pp.141-155, 1995.

[4] Gao, X., and Dodds, R.H., "An Engineering Approach to Access Constraint Effects on Cleavage Fracture Toughness," *Engineering Fracture Mechanics*, Vol. 67, No. 2, pp. 101-117, 2000.

[5] Gao, X, Dodds, R.H., Tregoning, R.L., and Joyce, J.A., "Prediction of T_0 Shift Between Specimens of Different Constraints Using the T-Stress Based $\mathscr{T}$-Functions," *The International Journal of Fracture*, **Vol. 104**, pp. L3-L8, 2000.

[6] Wallin, K., "The Effect of T-Stress on the Master Curve Transition Temperature T_0," ECF13, San Sebastian, Spain, 2000.

[7] Sumpter, J.D.G., "An Experimental Investigation of the T Stress Approach," ASTM STP 1171, E.M. Hackett, K.-H. Schwalbe, and R.H. Dodds, Eds., American Society for Testing and Materials, pp. 492-502, 1993.

[8] Beremin, F.M., "A Local Criterion for Cleavage Fracture of a Nuclear Pressure Vessel Steel," *Metallurgical Transactions*, Vol. 14A, pp 2277-2287, 1983.

[9] Mudry, F., "A Local Approach to Cleavage Fracture," *Nuclear Engineering and Design*, Vol. 105, pp 65-76, 1987.

[10] Minami, F., Bruckner-Foit, A., Munz, D., and Trolldenier, B., "Estimation

Procedure for the Weibull Parameters used in the Local Approach," *International Journal of Fracture*, Vol. 89, pp 245-268, 1998.

[11] Kfouri, A.P., "Some Evaluations of the Elastic T-term Using Eshelby's Method," *Int. J. Fract.*, **Vol. 30**, 301-315, 1986.

[12] Sham, T.-L., "The Determination of the Elastic T-term Using Higher Order Weight Functions," *Int. J. Fract.*, **Vol. 84**, pp. 81-102, 1989.

[13] Leevers, P.S., and Radon, J.C., "Inherent Stress Biaxiality in Various Fracture Specimen Geometries," *Int. J. Fract.*, **Vol. 9**, pp. 311-325, 1982.

[14] Cotterell, B., "On Fracture Path Stability in the Compact Tension Test," *Int. J. Fract.*, **Vol. 6**, pp.189-192, 1970.

[15] Cardew, G.E., et al, "On the Elastic T-term," *Fundamentals of Deformation and Fracture*, Bilby, B.A., Miller, K.J., and Willis J.R., (eds), Cambridge University Press, pp. 456-476, 1984.

[16] Gao, X., Dodds, R.H., Tregoning, R.L., Joyce, J.A., and Link, R.E., "A Weibull Stress Model to Predict Cleavage Fracture in Plates Containing Surface Cracks," *Fatigue and Fracture of Engineering Materials and Structures*, **Vol. 22**, pp.481-493, 1999.

Gerard P. Mercier[1]

The Effect of Localized Plasticity and Crack Tip Constraint in Undermatched Welds

---

Reference: Mercier, G. P., **"The Effect of Localized Plasticity and Crack Tip Constraint in Undermatched Welds,"** *Fatigue and Fracture Mechanics: 33rd Volume, ASTM STP 1417*, W. G. Reuter and R. S. Piascik, Eds., ASTM International, West Conshohocken, PA, 2002.

ABSTRACT: Four weldments of varying levels of weld joint to baseplate strength (mismatch) were examined to determine the effects of this ratio on fracture performance. Cracks were placed within the weld metal at several ratios of weld fusion margin. This margin is defined as the ratio of crack tip proximity to the weld fusion line and crack length (L_{crk}/a). Finite element studies were then performed on each variation of weld fusion margin and mismatch level to determine the crack driving force not accounted for in a typical fracture analysis, which assumes monolithic, homogenous weld metal specimens and ignores the weld/baseplate interaction. Assuming homogenous weld metal specimens results in crack growth resistance behavior that depends on crack tip proximity to the weld fusion line. Once local plasticity and the additional constraint caused by the weld/baseplate interface are included in the analysis, fracture behavior is independent of crack tip proximity to the fusion line up to and slightly beyond initiation. Errors in fracture toughness at weld fusion margins greater than or equal to 1.5 are less than 10% and can reasonably be ignored. Errors at smaller values of L_{crk}/a are considerable, and effects of local plastic deformation and constraint must be accounted for in the fracture analysis. Furthermore, uncorrected estimates of initiation toughness (J_{IC}) in specimens where the weld fusion margin are less than 1.5 result in overly conservative estimates. The percentage of weld mismatch was found not to be a major factor in determining either crack growth resistance or crack initiation behavior. An increased propensity toward unstable fracture was observed in specimens with smaller L_{crk}/a ratios. This effect may be attributed to a local microstructural defect and requires further study.

---

[1] Senior Mechanical Engineer, Product Analysis Department, Concurrent Technologies Corporation, 100 *CTC* Drive, Johnstown, PA 15904.

KEYWORDS: fracture testing, SE(B), constraint, plastic eta factor, local plasticity, short cracks, welds, undermatch welds, J-R curves, weld joint geometry, gamma factor

Introduction

Established standards typically require welded structures be composed of a weld metal of higher strength than the joined baseplate [*1, 2*]. Traditional U.S. Navy requirements specify weld consumables must have a higher yield strength than the base metal [*3*]. The assumption in this policy is that the weld metal is more apt to have defects such as porosity, slag entrapment, lack of fusion or other planar and/or volumetric discontinuities. Overmatching (using higher strength weld metal) shields these defects from plastic strain by shunting plasticity into the lower strength baseplate. The baseplate material is generally more ductile and has more consistent properties and fewer defects, lessening the likelihood of fracture. However, as the strength of the baseplate steel increases, overmatching becomes problematic. Developing weld consumables of even higher strength while retaining good weldability and toughness is difficult and expensive. Extensive preheat and interpass requirements to prevent hydrogen embrittlement in the higher strength consumable expend time and energy. Furthermore, the level of overmatch within a weld system is not assured [*4, 5*]. Undermatch welding (using lower strength weld consumable) allows lower preheat and interpass requirements and higher heat inputs. These changes increase productivity by increasing the weld metal deposition rate [*6*]. However, undermatch welds, unlike overmatching, do not protect the weld from strain. While the fracture toughness of the undermatched consumable may be better than the baseplate, undermatch welds focus strain within the weld, potentially increasing the risk of fracture.

In an overmatched system the lower yield baseplate generally shields a crack from excessive strain thus lowering the local stress/strain fields and crack driving force (J). Conversely, an undermatched system will concentrate the strain within the weld metal and raise the local stress/strain fields and J [7 - 9]. While there are special cases where the weld joint geometry can be ignored and J can be calculated using just weld metal or base metal properties [10], in most cases the proximity of the weld/base metal interface has a large influence on crack driving force [7 - 9]. This is expected since J is defined as a path independent contour integral [11]. Path independence of J is lost as soon as the contours are calculated across the weld/baseplate interface. Treatment of welded specimens as monolithic, single materials certainly invalidates the path independence of J and brings into question the validity of the measurement.

However, treatment of welded structures and specimens using just weld metal material properties and ignoring the weld geometry has been shown to be of value [12, 13]. Still, these global estimates do not account for the changes in stress states or variation in constraint at the crack tip in a mis-matched weld. Various authors have noted this effect and determined that undermatch welds increases the level of stress triaxiality or constraint at the crack while overmatching decreases it [14, 15]. Furthermore, the geometry of the welded joint and proximity of the crack to the weld fusion line also contribute to the level of crack tip constraint [15 - 17]. With these studies in mind an investigation of the fracture behavior of undermatched weld systems was conducted using short crack single edge notched bend specimens. An effort was made to characterize the crack driving force at the crack tip by including constraint effects of the weld/baseplate interface and any local plasticity not usually account for in typical analysis of short crack single edge notched bend specimens [18, 19].

Finite element models of the test weldments in this study were constructed to examine the crack driving force and the effects of crack proximity to the fusion line. The weld fusion margin characterizes the proximity of the crack to the weld/baseplate fusion line and is defined as the ratio of crack tip distance to the weld fusion line (L_{crk}) to the crack length (a), L_{crk}/a. Prior studies have indicated that crack growth resistance behavior is sensitive to this ratio (L_{crk}/a) [20]. Tregoning's study [20] indicated that as the weld fusion margin decreased, constraint increased, driving the crack growth resistance curve (J-R curve) down. He suggested that the global treatment of the specimens as monolithic weld metal altered the resistance curves of specimens with small weld fusion margins by not including the effects of constraint and local crack tip deformation. Results from Burstow et al. [16] seem to agree with Tregoning's assessment and show that self similar stress fields forward of the crack tip are obtained by normalizing the load parameter by the weld height. Other authors [12, 13] have shown that homogenous equations work up to J levels of 350 kJ/m^2. However, above this level error in the fracture toughness calculation occurred. This study examines the effects of both constraint caused by weld geometry and mis-match level and determines the error associated with using global measurements while assuming homogenous weld metal properties.

New coefficients (η-factors) are developed to relate the crack driving force at the crack tip within the undermatched weld to the globally measured plastic work done to the specimen during testing. Comparisons of specimen analyses using these η-factors and analyses assuming all weld metal properties in a homogenous specimen are shown.

Weld Production and Material Characterization

Joint Design

Two standard military welding consumables, MIL-70s and MIL-100s, were used to fabricate four two-inch thick weldments. The consumables have nominal yield strengths of 480 MPa (70 ksi) and 690 MPa (100 ksi). One weldment used the MIL-70s and the remaining three used MIL-100s. All four plates used HY-100,a typical naval steel, with a yield strength of 725 MPa, creating three approximately 10% undermatched and one 38% undermatched weld systems. Specified chemical compositions for these three materials are summarized in Table 1 and are given in more detail in references 21 and 22.

Three different weld joint geometries were selected for study, a single 45° vee with no root gap, a single 45° vee with a 1.25-cm root gap and a symmetric double 60° vee with no root gap. The double vee joint had two permutations, one 38% undermatched with MIL-70s and the second 11% undermatched with MIL-100s. The four different weld systems were chosen to isolate effects of weld joint undermatch welds and study the concentration of deformation within the weld material. Each weldment is summarized in Table 2 with the weld joint geometry shown in Figure 1.

Table 1 – *Specified Chemical Composition*

Material	C	Mn	P	S	Si	Ni	Cr	Mo	Va	Ti	Cu	Ar	Sn	An	Zr	Al
HY-100	0.10-0.22	0.10-0.45	0.02	.002-0.02	0.12-0.38	2.67-3.57	1.29-1.86	0.27-0.63	0.03	0.02	0.25	0.025	0.03	0.025	–	–
MIL-70s	0.07-0.19	0.90-1.40	0.025	0.035	0.40-0.70	–	–	–	–	–	–	–	–	–	–	–
MIL-100s	0.08	1.25-1.80	0.012	0.008	0.20-0.55	1.40-2.10	0.30	–	0.10	0.10	–	–	–	–	0.10	0.10

Table 2 – *Weldment Parameters*

Weld Metal	ID	Geometry	Root Gap	L_{crk}/a	% Mismatch
MIL-70s	HBA	Double Vee	None	1.35	-38
MIL-100s	HBB	Double Vee	None	1.5	-11
MIL-100s	HBC	Single Vee	1.25 cm	0.75 / 3.3	-6
MIL-100s	HBD	Single Vee	None	0.20 / 2.9	-13

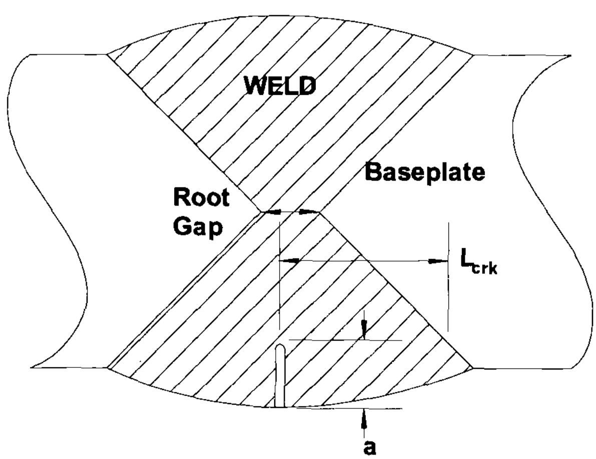

Figure 1 – *Weld Joint Geometry*

Gas metal arc welding was used for all weldments with preheats and interpass temperatures of 175 °C. Heat inputs for the MIL-70s weld ranged from 2.5-2.75 kJ/mm and heat input for the MIL-100s welds was 3.15 kJ/mm. The parameters were chosen to create consistent weld metal properties and do not fall within the allowable ranges for production welds. The welds were flipped regularly during production to alleviate residual stresses and weldment deformation. Radiographs were taken after completion.

Specimens were removed from areas where radiographs showed no or inconsequential indications.

Specimen Removal and Weld Characterization

Charpy V-notch specimens were taken transversely (T-S orientation) from both the top and bottom of each weld with the notch centered within the weld metal. Testing was conducted in accordance with ASTM E23 [23] to compare variability among weldments and determine upper and lower transition regions. Within the transition region a minimum of five specimens were tested at each temperature. Upper and lower shelf energies were measured with three specimens at each temperature.

A minimum of four 0.505 inch all weld tensile specimens were removed from each weldment (L orientation), two from the weld top and two from the bottom. Specimens from the root gap of single vee weldments were removed far enough away from the weld surface to ensure an all weld specimen. The specimens were tested in accordance with ASTM E-8 [24] at –2 °C to provide tensile data at our subsequent fracture test temperature.

Six short crack (a/W=0.15) single edge bend SE(B) specimens were removed from each double vee weldment in the T-S orientation with the notch tip centered in the weld metal. The notches on the six specimens were located so that the crack sampled material from the top side of the weld in three specimens and the bottom on the remaining three. Ten short crack SE(B) specimens were removed from each single vee weldment in the T-S orientation with the notch tip centered in the weld metal. The notches on the ten specimens were located so that the crack sampled material from the top side of the weld in five specimens and the bottom on the remaining five.

Charpy Testing – Figure 2 contains all the Charpy V-notch energies (CVE) from each weld specimen. Plotted are the means for each temperature and bars indicating 95% confidence intervals. The plot shows limited variability of the MIL-100s consumable within transition and lower shelf and none of significant statistical importance. Surprisingly, the largest inconsistency occurs at upper shelf energy values. An analysis of the variance using a 95% confidence criterion shows that significant statistical differences do not occur between HBC and HBB MIL-100s welds at upper shelf CVEs. The MIL-70s weld metals shows considerably lower CVE at all temperatures except upper shelf where it is equivalent to the MIL-100s. While CVE values from these four weldments satisfy requirements set in reference [21], past testing of production welds indicates that upper shelf behavior should occur prior to 0 °C [25].

Tensile Testing - Weld tensile testing was conducted at –2 °C to provide yield and ultimate tensile strength at the same temperature used during fracture testing. Table 3 summarizes the reduction in area, strain to failure and percent undermatch for each weldment. Strain was recorded past maximum load for all specimens. This data was then used to generate true stress/strain curves, shown in Figure 3, for finite element analysis. Portions of the curves beyond 12% true strain were extrapolated linearly to avoid convergence problem in the numerical analysis. The HY-100 data was developed from compression tests conducted on an Office of Naval Research platform structural materials program. No further analysis on weld joint tensile performance was conducted since previous report [20] dealt extensively with weld joint strength and structural performance.

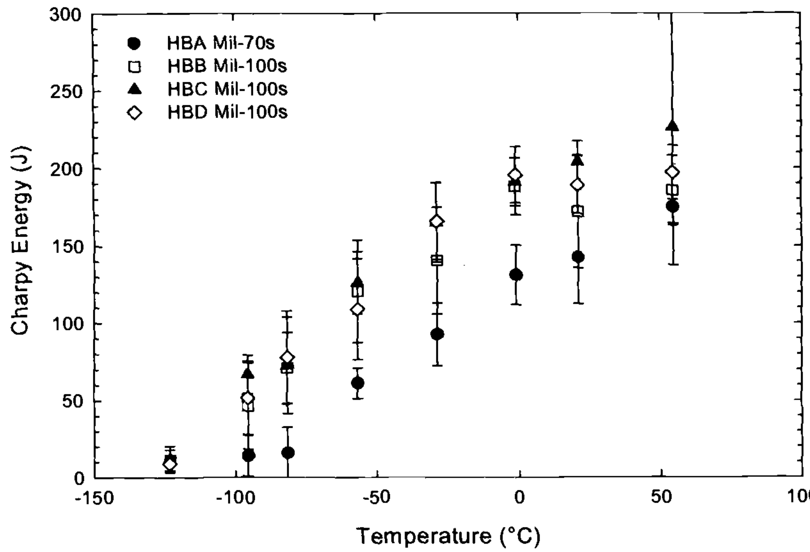

Figure 2 – *Charpy Data.*

Table 3 – *Basic Tensile Properties of Weldments*

ID	e_f *(%)*	*Reduction in Area (%)*	σ_{ys} *(MPa)*	σ_{uts} *(MPa)*	σ_{FL} *(MPa)*	*% Mismatch*
HBA	29	70	450	600	525	-38
HBB	26	70	645	730	687.5	-11
HBC	25	71	680	740	710	-6
HBD	27	71	630	700	665	-13

Short Crack Single Edge Notched Bend Test Procedures

All SE(B) specimens underwent one cycle of reverse precompression in 4 point bending to 50% of limit load based on flow properties of the weld metal. Reverse precompression homogenizes crack tip residual stress fields thereby allowing straight crack fronts to grow under cyclic fatigue loading. This technique has proven effective for the T-S orientation in previous tests [20] and resulted in consistently straight precracks in this test series. ASTM 1820-96 requires that deviation from the average of nine physical precrack length measurements be less than 5%. For short crack specimens, a/W=0.15, this requirement is overly stringent and disqualifies precracks with a deviation greater than 0.4 mm from the average. Several precracks did not meet this strict requirement. The precrack in Figure 4 varied by 6.5% from the average physical measurement and is technically invalid. However, analysis of thumbnailed or circular arced crack fronts with radii equal to three times the specimen thickness show almost constant stress intensity

(K_I) values along the crack front [26]. These K_I values are consistent with standard calculations of stress intensity using straight cracks [27]. Therefore, specimens with precracks exhibiting shapes consistent with the above statements are included in this study.

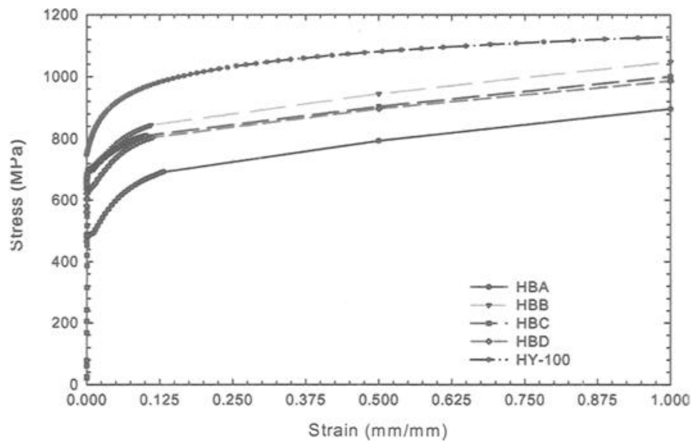

Figure 3 – *True Stress/Strain Data Used in Finite Element Analysis.*

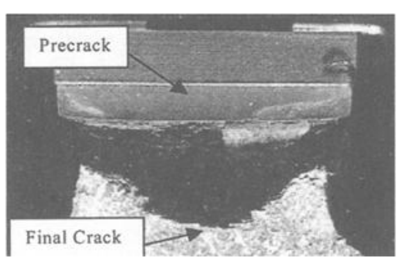

Figure 4 – *Precrack with Length Deviations Greater than ASTM Specifications.*

While precompression effects on toughness have been shown to decrease plane strain fracture toughness (K_{IC}) [28, 29] other studies indicate that this method [30] as well as a high R ratio method [31] have little effect on toughness if ductile tearing is the mode of failure. All specimens in this study exhibited substantial ductile crack growth negating any effect induced by the reverse precompression. Further, since all specimens were deformed at a consistent level during precompression, any residual stress effects would also be consistent making comparisons appropriate.

After homogenization of residual stresses was complete, fracture toughness testing was performed in accordance with reference [32] where appropriate. Single specimen unloading compliance tests were conducted on a computerized data acquisition system in a 250 kN screw driven test frame. A compliance equation for short crack SE(B) specimens was found in [19] and is valid for 0.05 □a/W □0.45. Joyce has shown that as a/W decreases, limit load increases, allowing for deeper unloads during testing and only slightly reducing the resolution of the compliance measurement [33]. Loadline displacement (Δ_{LL}) was measured directly on the specimen via a flex bar. This method avoids errors due to brinnelling and load train compliance estimates.

J Estimation

Several authors [18, 19, 34] have developed equations for applied J in a short crack SE(B) specimen with the general format:

$$J = J_{el} + J_{pl} = \frac{K^2}{E'} + \left[J_{pl(i-1)} + \frac{\eta_{(i-1)}}{b_{(i-1)}} \left(\frac{A_{pl(i)} - A_{pl(i-1)}}{B_N} \right) \right] * \left[1 - \lambda_{(i-1)} * \frac{a_{(i)} - a_{(i-1)}}{b_{(i-1)}} \right] \quad (1)$$

Where:

K = the elastic stress intensity factor,
E' = the plane strain elastic modulus,
$A_{pl(i)}$ = the area under the load versus plastic load line displacement curve at increment i,
B_N = the net specimen thickness,
a_i = the crack length at increment i,
b_i = the remaining specimen ligament at increment i,
W = the specimen width,
η_{pli} = the plastic eta factor at increment i,
γ_i = the gamma function at increment i.

$$\gamma_i = \left[\eta_{pli} - 1 - \frac{b_i \eta_{pli}}{W \eta_{pli}} \right] \quad (2)$$

However, their analysis assumed a monolithic, homogeneous material. A cracked specimen composed of more than one material is not defined solely by the geometry of the specimen or depth of the crack. Crack tip stress fields are also controlled by both weld geometry and degree of mismatch [13 - 15]. Furthermore, it has been shown that the distance from the crack tip to the weld/baseplate interface has a pronounced effect on crack tip stresses [15-17]. Typical test procedures and analysis do not account for the increased driving force created at the crack tip as the baseplate metal constrains the deformation within the weld. Prior work has shown that homogenous J equations are accurate for J = 350 kJ/m^2 [12, 13]. However, above this level dramatically different tearing resistance behaviors have been observed due to the inability of the homogenous analysis technique to account for the crack tip local plasticity [20].

Gordon and Wang [13] developed η_{pl} factors for straight butt weld deep crack SE(B) specimens (a/W=0.5) with weld height to width ratios, shown in Figure 5, ranging from 0.05 to 2.

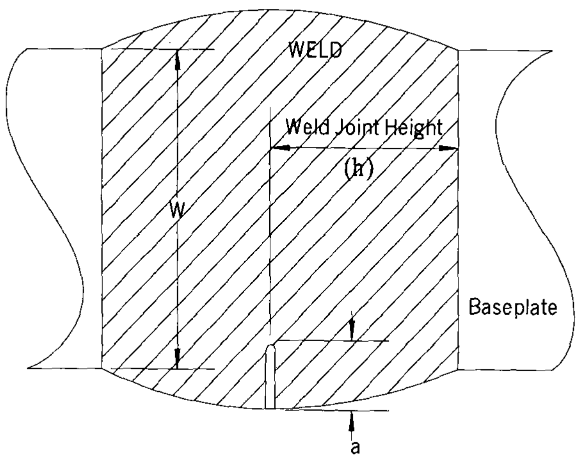

Figure 5 – *Weld Joint Defined by Gordon and Wang [13].*

They determined that at h/W values greater than one and also at very low values of weld joint height (h/W<0.25) the specimen behaved independent of h/W. And that η_{pl} approached values similar to homogenous all weld specimen or all baseplate specimens at these values of h/W. Between these limiting values η_{pl} increased for undermatched welds and decreased for overmatched. However, Gordon and Wang concluded that for deeply cracked welded specimens the variation in η_{pl} between weld joint heights of 0.25<h/W<1 still provided reasonable estimations of J to within 10%.

Several authors [33 - 36] have studied crack length and work hardening effects on homogenous SE(B) specimens. They determined that for short cracks, work hardening played a major role in the calculation of J using η_{pl} factors. It is apparent that for short crack bend specimens, each combination of mismatch level, L_{crk}/a, and hardening characteristics must be taken into account for a correct estimation of crack driving force. To accomplish this, finite element models were constructed to correct for the local plasticity or crack tip deformation not accounted for with standard analysis techniques. New plastic η factors were calculated for Equation 1, accounting for weld mis-match, crack length and weld fusion margin effects.

Finite Element Model Verification - The commercial finite element package, ABAQUS, was used to calculate plastic J-Integral solutions for lengths ranging from a/W of 0.10 to 0.30. A typical model has 1000 to 1500 eight noded plane strain reduced integration elements with 15 to 20 elements along the two-inch width of the specimen. Mesh studies indicated that a minimum of 10 elements is required to capture variation in strain along the width of the specimen. Half symmetry was used to reduce modeling and computing times. As shown in Figure 6, loading was accomplished by applying displacement to two nodes at the specimen top surface along the symmetry plane and by simply supporting one node at the half span of the specimen. A symmetry boundary condition was applied to the elements along the remaining ligament in the same plane that contained the crack. A keyhole with a 0.0127-mm radius, shown in Figure 7 is used to model the crack. Typically, forty to sixty radial rings of elements surround the crack tip, gradually increasing in size from 0.00635-mm at the keyhole to 1.27-mm at the last ring. Each ring contained 24 elements dispersed equally around the keyhole. All nodes along the keyhole radius, with the exception of the one node that was on the symmetry plane, were unconstrained to simulate blunting behavior. J values were calculated at between 15 to 30 contours to ensure path independence was maintained.

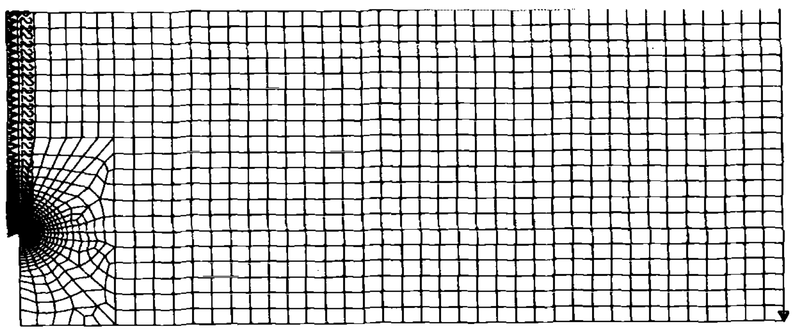

Figure 6 – *Loading and Mesh Design.*

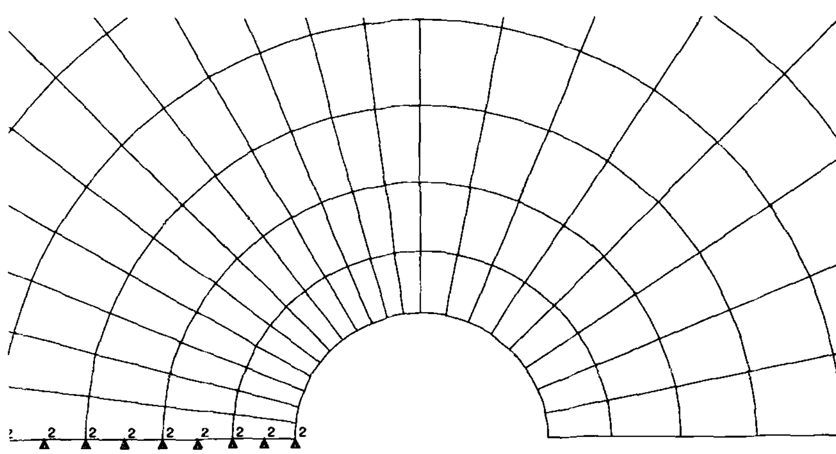

Figure 7 – *Crack Tip Mesh.*

Mesh Verification - The accuracy of the finite element model and data reduction techniques were verified by reproducing accepted solutions for homogenous SE(B)s. Three linear elastic finite element models (a/W= 0.15, 0.20, 0.30) were displaced to a loadline displacement of 1.27 mm. Load (P) and elastic J-Integral (J_{el}) values were computed at the end of each loading. The normalized compliances (BE'C) predicted from this analysis display little deviation from the predicted handbook values [37]. This result confirms that the model boundary conditions correspond to three point bending boundary conditions.

To ensure that the mesh was suitable for fracture analysis, J_{el} values were compared with values calculated by Tada [37]. J_{el} is defined as:

$$J_{el} = \frac{K^2}{E'} \qquad \text{Where } K = \sigma\sqrt{\pi a}F(a/W) \tag{3}$$

In Equation 3, F(a/W) is a geometry dependent function of normalized crack length, σ is the remote stress and a is the crack length. While J_{el} can be determined with a relatively coarse mesh, gross variation in values from the reference values would indicate a problem with crack definition or boundary conditions. Variations with handbook values were less than 1% for all three crack lengths.

Mesh refinement and crack tip geometry were verified by comparison of η_{pl} with published results from references 18 and 33. Loading and boundary conditions for all three models were maintained the same as in the previous elastic analysis. However, the plastic response of the models was defined by a Ramberg-Osgood stress/strain relationship (σ_{ys}=700 MPa, n=10, α=0.5). Elements at the support and point of load application were defined as elastic to distribute displacements evenly and save computational time. Each loading was separated into 20 steps. At each step, load, load-line displacement and J-Integral values were determined and the plastic area (A_{pl}) and J_{pl} calculated. A_{pl} is defined by:

$$A_{pli} = \frac{(P_{i-1} + P_i)}{2}(\Delta_{i-1}^{LLpl} - \Delta_i^{LLpl}) \qquad \text{and} \tag{4}$$

$$J_{pl} = J_{total} - J_{el} \tag{5}$$

Where J_{el} was found using Equation 3

The plastic eta factor, η_{pl}, is defined as:

$$\eta_{pl} = \frac{J_{pl}B_N b}{A_{pl}} \tag{6}$$

If J_{pl} is normalized by the flow stress (σ_o) and remaining ligament (b) and A_{pl} normalized by the net thickness (B_N), b and σ_o, then η_{pl} can be determined by the slope of the normalized J_{pl} vs. A_{pl} curve.

$$\eta_{pl}\frac{A_{pl}}{B_N b^2 \sigma_o} = \frac{J_{pl}}{b\sigma_o} \tag{7}$$

The normalized values of J_{pl} and A_{pl} are plotted for a/W=0.3 in Figure 8. Table 4 shows a comparison of the analyses with Sumpter [18] who used the same Ramberg-Osgood stress/strain coefficients and Joyce [33] who used piecewise linear data from actual HY-100 tensile tests, which confirms that the crack tip geometry, mesh refinement and data reduction techniques used are suitable and consistent.

J Analysis of Weldment Specimens

Once the finite element mesh was verified as accurate, the models where redefined to include joint geometry and both weld and baseplate material properties. Table 5 shows the weld geometry, weld fusion margin and percent mismatch for the four weldments in this study. Plastic η-factors were developed for each unique weldment and joint design. These new plastic η-factors were then incorporated into an in-house analysis code using linear curve fits to generate crack growth resistance data. The new curve fits are shown in Figure 9. All η_{pl} values of models with a weld fusion margin less than 1.5 were elevated above the homogenous (Sumpter) weld metal η_{pl}. Models with larger fusion margins will show little deviation from the homogenous weld metal results. Models at a/W=0.30 converged at η_{pl}=2.0 where they agreed with homogenous results. However, the severity of the weld fusion margin in weldment HBD (0.2) immediately placed η_{pl} above 2.0 and increased until a/W=0.3. Further, results for weldment HBB and the wide sides of welds HBC and HBD were nearly identical to the homogenous weld metal results of Sumpter and are plotted as HBB/Sumpter in Figure 9. Therefore, for these geometries ($L_{crk}/\Delta a$=1.5), Sumpter's third degree polynomial expression is used in the subsequent analysis.

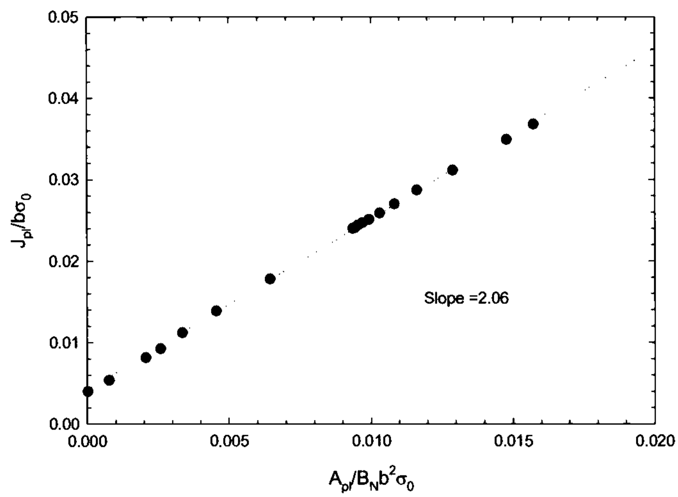

Figure 8 – *η_{pl} Analysis in SE(B) at a/W=0.30.*

Table 4 – *η_{pl} Factors for Monolithic, Homogenous Specimen*

a/W=	0.15	0.2	0.3
Sumpter	1.34	1.54	2
Joyce	1.6	1.82	1.89
Mercier	1.36	1.62	2.06

Table 5 – *Weldment Geometry and Mismatch Level*

ID	*Geometry*	*L_{crk}/a*	*% Mismatch*
HBA	Double V	1.35	-38
HBB	Double V	1.5	-11
HBC	Single V	3.3 / 0.75	-6
HBD	Single V	2.9 / 0.2	-13

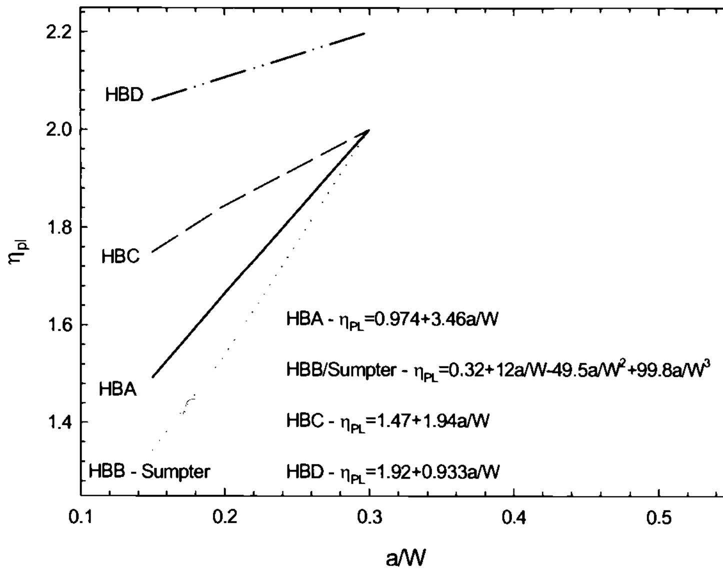

Figure 9 – *Curve Fits of η_{pl}-Factors for Undermatched Welds.*

Results and Discussion

J values were calculated for each specimen where the weld fusion margin was less than 1.5 using both the η-factors from reference 18 and the η-values from Figure 9. Comparisons of crack growth resistance and initiation were then made between the two separate analyses. Finally, initiation toughness and crack growth resistance comparisons were made on various levels of weld/baseplate mis-match and L_{crk}/a to study the effects of undermatch welds and joint geometry respectively.

Due to the steep slope of the initial portion of the J-R curves in these specimens, slight changes in initial estimated crack lengths (a_{oq}) result in relatively large changes in the calculated value of J_{IC}. These changes can be well within limits defined by reference 32 and still provide unacceptable changes in initiation toughness estimates. For example, a change in initial crack length of 1% in specimen HBA-5 from 7.75 to 7.67 mm results in a 25% change in J_{IC}. To avoid large inaccuracies in comparisons between analysis techniques, care was taken to set the initial crack length as close as possible to the physically measured length. This length was then maintained for each subsequent analysis.

Effect of L_{crk}/a on Initiation Toughness and the J-R Curve

The first weldment analyzed by both homogenous and local plasticity methods was HBA, MIL-70s, double vee with a weld fusion margin of 1.35. Six specimens, three from each side of the double vee, were first analyzed using homogenous weld metal properties, then reanalyzed accounting for driving force missed by the global homogenous analysis. Since the mis-match level is high (-38%), extra strain will be funneled into the weld metal and not be accounted for by the homogenous analysis. Figure 10 shows results from the two analyses and 95% confidence limits based on a power law fit through all specimen data points from each analysis. Clearly at this level of mis-match and weld fusion margin the amount of driving force missed by the homogenous weld metal analysis is minimal. A slight increase in crack growth resistance can be noted. However, the additional effort required to determine this increase is not trivial and may only be of interest to an experimentalist.

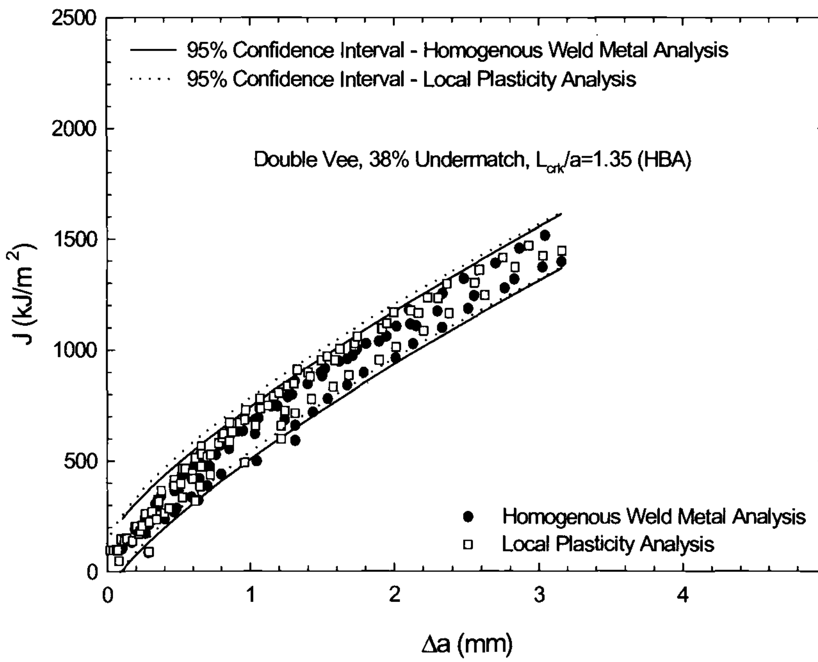

Figure 10 – *Crack Growth Resistance Curve for Weldment HBA.*

Initiation values, shown in Table 6, vary depending on specimen location (top or bottom of weld). However, the significance of this difference is difficult to quantify with so little data. J_{IC} is elevated approximately 10% if local plasticity is accounted for in the calculation of J. As with the crack growth resistance behavior, the extra effort required to include local plasticity in the J_{IC} calculation may not be of value.

Four of the six tests in this series experienced crack growth instabilities ending the test. While three of these specimens had considerable ductile growth prior to failure, specimen HBA-4 experienced unstable growth after only 0.03 mm of crack extension and was excluded from calculations of average J_{IC} values. Zhang et al. [38] has shown that cleavage failure in multi-pass MIL-70s welds is governed by a brittle fusion line band that forms between each welding pass. Zhang et al. used stereo section fractography to determine the cleavage initiation site and show the underlying microstructure related to that site. They defined microstructural zones present in multi-pass weldments and illustrated the inherent inhomogeneity associated with a single weld bead. These zones range from a coarse columnar region that resembles a casting to several different heat affected zones whose properties depend on maximum temperature and cooling rates. One or more of these zones may act as a brittle region or weak link within the surrounding microstructure. As the crack samples this brittle area, cleavage initiation is triggered. The distance between the end of the fatigue crack and this brittle band determines the amount of ductile crack growth.

Table 6 – *Initiation Toughness Values for Weldment HBA*

ID	***Location***	***Analysis***	J_{IC} ***(lbs/in)***	J_{IC} (kJ/m^2)	Valid	***Comments***
HBA-1	TOP	Homogenous	2502	438	YES	
HBA-1	TOP	Local Plasticity	2775	486	YES	
HBA-2	TOP	Homogenous	3252	569	YES	
HBA-2	TOP	Local Plasticity	3645	638	NO	Invalid Thickness
HBA-3	TOP	Homogenous	3013	527	YES	
HBA-3	TOP	Local Plasticity	3337	584	NO	Invalid Thickness
HBA-4	BOTTOM	Homogenous	250	44	NO	Valid J_c
HBA-4	BOTTOM	Local Plasticity	250	44	NO	Valid J_c
HBA-5	BOTTOM	Homogenous	1675	293	YES	
HBA-5	BOTTOM	Local Plasticity	1848	323	YES	
HBA-6	BOTTOM	Homogenous	2623	459	YES	
HBA-6	BOTTOM	Local Plasticity	2810	492	YES	Excluding HBA-4
Average	TOP	Homogenous	2922	511	S.Dev.	67
Average	TOP	Local Plasticity	3252	569	S.Dev.	77
Average	BOTTOM	Homogenous	2149	376	S.Dev.	117
Average	BOTTOM	Local Plasticity	2329	408	S.Dev.	119

The second weldment studied was HBC, MIL-100s, single vee with weld fusion margins of 0.75 and 3.3. Ten specimens, 5 from the wide side of the single vee (L_{crk}/a=3.3) and 5 from the narrow side (L_{crk}/a=0.75) were analyzed as previously explained. Figure 11 shows the results from both homogenous analysis and the local plasticity analysis of the narrow side of the weld. Again 95% confidence intervals are shown for each data set.

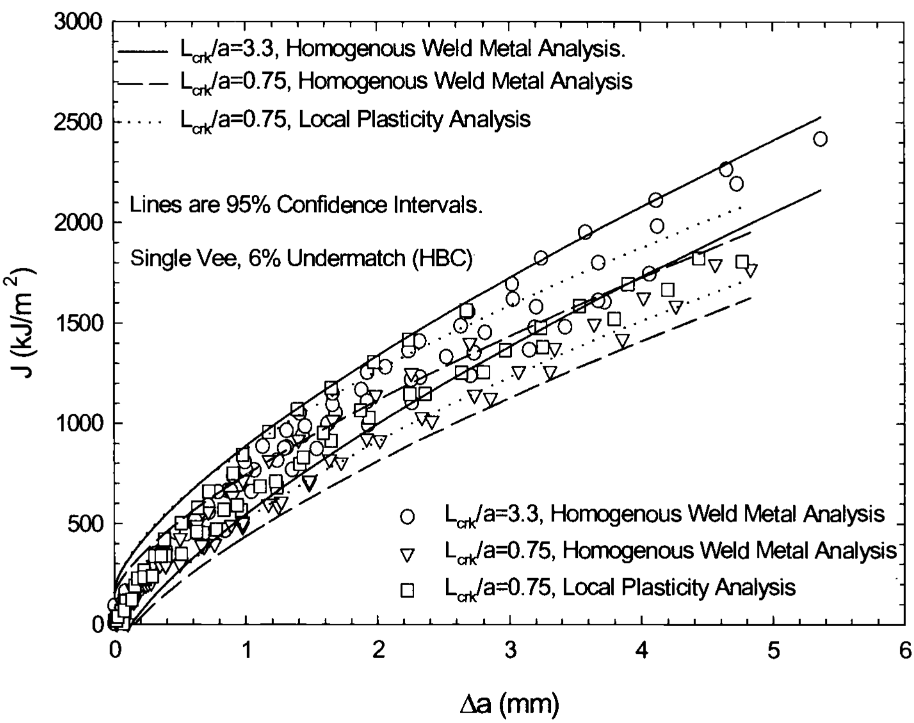

Figure 11 – *Crack Growth Resistance Curves for Weldment HBC.*

Clearly, the local plasticity analysis shifts the low weld fusion margin data onto the larger weld fusion margin curve. In fact, the confidence limits for both sets are virtually identical until J>1000 kJ/m^2. However, the homogenous weld metal analysis confidence limits deviates immediately and would indicate two separate material behaviors based on specimen location or a large increase in crack tip constraint resulting in a depressed resistance curve prior to initiation. The local plasticity confidence limits generously overlaps the large weld fusion margin data well beyond initiation. This would indicate one material behavior for this weldment and little or no effect from additional crack tip constraint.

Table 7 contains initiation values for weldment HBC using both the homogenous weld metal and local plasticity for the small weld fusion margin and homogenous only for the larger fusion margin. Comparisons of the two homogenous analyses would indicate two separate material behaviors based on specimen location in the weld. The difference in initiation behavior between the two homogenous analyses is significant at the 95% confidence level. While comparisons of the smaller weld fusion margin analysis accounting for localized plasticity and the large weld fusion margin homogenous analysis show variations, these variations are not statistically significant at the same level. Accounting for local plasticity elevates the average initiation toughness value by slightly more than 25%. This could have a significant influence on structural design since the uncorrected value is unduly conservative.

Table 7 – *Initiation Toughness Values for Weldment HBC*

ID	*Location*	*Analysis*	J_{IC} *(lbs/in)*	J_{IC} *(kJ/m²)*	*Valid*	*Comments*
HBC-1	Wide	Homogenous	2697	472	YES	
HBC-2	Wide	Homogenous	2880	504	YES	
HBC-3	Wide	Homogenous	2785	487	YES	
HBC-4	Wide	Homogenous	2516	440	YES	
HBC-5	Wide	Homogenous	2570	450	YES	
HBC-6	Narrow	Local Plasticity	1712	300	YES	
HBC-6	Narrow	Homogenous	1392	244	YES	
HBC-7	Narrow	Local Plasticity	1902	333	YES	
HBC-7	Narrow	Homogenous	1589	278	YES	
HBC-8	Narrow	Local Plasticity	1913	335	YES	
HBC-8	Narrow	Homogenous	1683	295	YES	
HBC-9	Narrow	Local Plasticity	2024	354	YES	
HBC-9	Narrow	Homogenous	1432	251	YES	
HBC-10	Narrow	Local Plasticity	3279	574	YES	
HBC-10	Narrow	Homogenous	2443	428	YES	
Average	Wide	Homogenous	2690	471	S.Dev.	26
Average	Narrow	Local Plasticity	2166	379	S.Dev.	111
Average	Narrow	Homogenous	1708	299	S.Dev.	75

All of the HBC specimens in this study failed unstably after significant ductile growth. This is not unexpected given the results from Zhang et al. discussed previously. Typically more than 3.5-mm of crack extension occurs prior to failure. The data appears to suggest that for smaller weld fusion margins the propensity for unstable failure increases. However, an analysis of the variance between the amount of ductile growth prior to cleavage failure shows no statistical significance at the 95% confidence level.

Weldment HBD, MIL-100s, single vee with weld fusion margins of 2.9 and 0.2, was investigated next. Figure 12 show the two analyses with confidence intervals for this weldment. After accounting for the local plasticity, the tearing modulus for the narrow side is still lower. While variation in tearing resistance between weld sides is not unlikely given the differences in cooling rates during welding, residual stress variation across the plate thickness and local microstructural variation between weld beads is a more probable explanation than the increased crack tip constraint. In a typical short crack bend specimen, global tensile stress/strain fields near the front face allow the local crack tip fields to relax and interact with the free surface. A schematic of the plastic zone shapes in both deep and short crack SE(B) specimens is shown in Figure 13.

This quickly lowers constraint at higher deformation levels resulting is strains and stresses no longer defined by a single parameter such as J [39]. Short crack or low constraint specimens have more plasticity and lower stresses at equivalent deformation (J) levels than higher constraint specimens. This additional plastic strain influences the measured applied J and raises the crack growth resistance curve. This increase in tearing resistance has been shown in many experimental and numerical studies [19, 20, 40, 41] and is expected in homogenous specimens. However, as the higher strength baseplate impinges on the crack tip stress/strain fields and forces the plasticity away from the front face, plasticity within a short crack SE(B) approaches the fields exhibited by deeply cracked specimens. Figure 14 shows the influence of the high strength baseplate containing the weld metal plasticity and funneling it though the specimen ligament. The magnitudes of the strains in Figure 14 are not important, as it is the geometry of the strain field that influence behavior. The plastic fields in this short crack specimen are now clearly highly constrained and more closely resembles the deep crack plastic zone shape illustrated in Figure 13. Therefore, using the short crack homogenous equation to calculate J plainly is in error and the new η_{PL} formulation will provide a more accurate representation of the actually J-R behavior in this specimen.

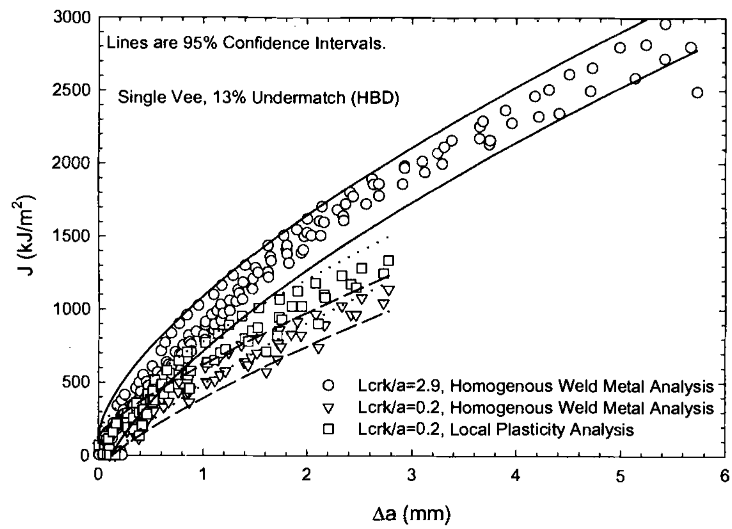

Figure 12 – *Crack Growth Resistance Curves for Weldment HBD.*

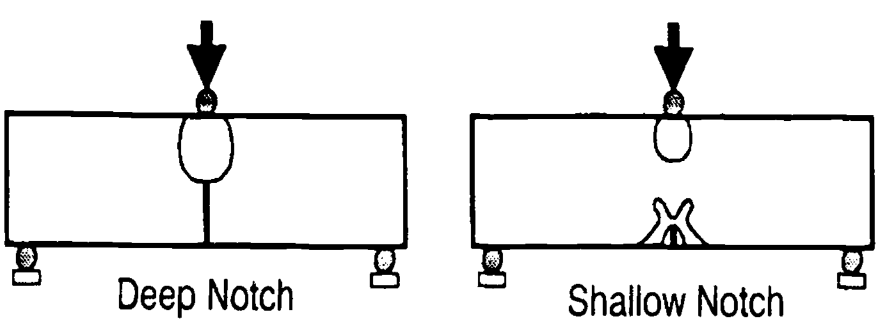

Figure 13 – *Schematic of Plasticity in Deep and Short Cracked SE(B) Specimens (from [40]).*

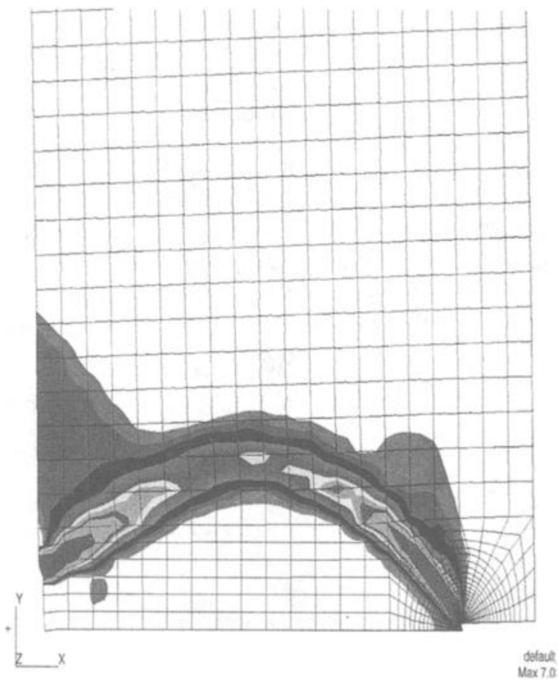

Figure 14 – *Finite Element Equivalent Plastic Strain Results for a/W=0.15 SE(B) Specimen with 13% Undermatched Single Vee Weld (HBD), Notch is in Narrow Side of Weld.*

Another discrepancy that occurs using the standard homogenous equations is in the formulation of γ in Equation 2 (repeated below). The third degree polynomial used to create Sumpter's η-factor fit may cause some of the deviation between the lower constrained (higher J-R curve) and the localized plasticity curves shown in Figure 12. Sumpter's polynomial fit for η_{PL}, shown in Figure 9, results in strongly negative γ factors thereby raising J values calculated in Equation 1 and the resistance curve. Figure 15 shows the results of Equation 2 using the η_{pl}-factors defined in Figure 9.

The curve for Sumpter's fit begins at –4, quickly rises to –2, then begins to decreases again before jumping to positive 1 at a/W=0.282. While nothing in the mathematics in Equation 9 specifies that the γ-function should be continuous, physically the jump in the Sumpter formulation is inconsistent. The sudden jump and sign change in Sumpter's γ would mean that at a crack length of a/W=0.282, the change in J_{pl} for an increment of crack growth would also change dramatically. The γ-factors for the weldments gradually increase linearly as a/W increases with no sudden discontinuities. While the discontinuity in Sumpter's γ is troubling, none of the welded specimens reach a/W=0.282

prior to test conclusion. Regardless, the disparity between γ-functions in the two analyses may cause some of the divergence in J-R curves at higher J levels.

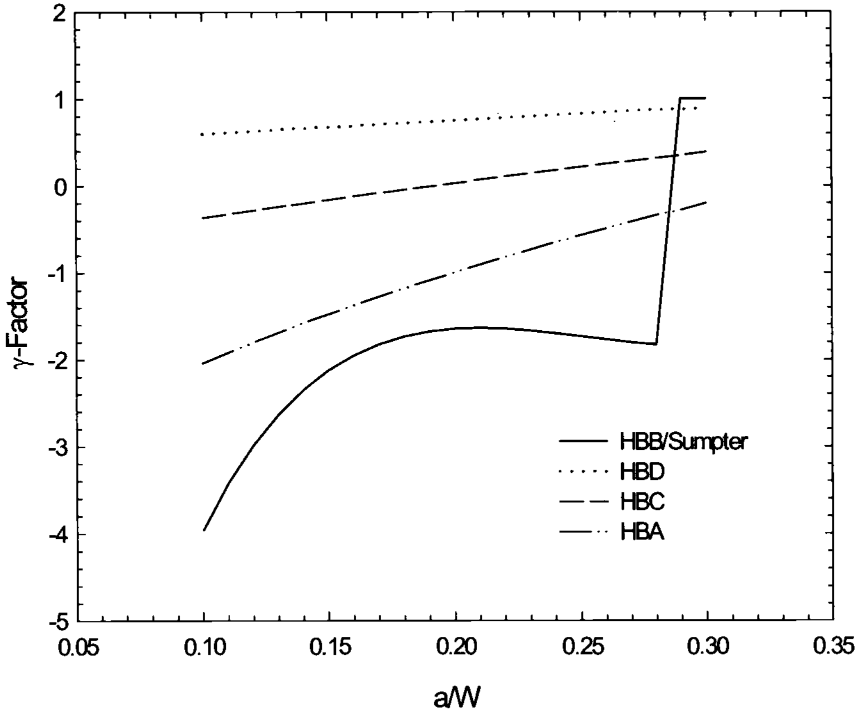

Figure 15 – *γ-Factors from η_{pl}-Factors in Figure 9.*

The homogenous analysis uses Sumpter's η and γ-factors, while the local plasticity analysis uses the results from the finite element analysis. It is clear from Equation 1 that negative γ values will increase J for an increment of crack growth and positive values will lower J. This will either raise or lower the tearing resistance results, respectively. Sumpter's γ-factor is highly negative throughout the range of a/W exhibited in the specimens tested, while the local plasticity γ-factor is positive. Therefore, for each increment of crack extension, J is adjusted up by Sumpter's γ-factor in the homogenous analysis and adjusted down slightly by the local plasticity analysis γ-factor. While these slight adjustments are not the root cause of the differences in tearing resistance they are a contributing factor.

Figure 16 shows that up to initiation (J=500 kJ/m^2) the local plasticity values are close to the values from the wide side of the weldment, resulting in consistent initiation values. Initiation values, shown in Table 8, generated from the homogenous approach deviate quickly and erroneously produce lowered values. As in weldment HBC, if only homogenous weld metal properties are used in the analysis, the results would indicate two separate behaviors near initiation. However, once the local deformation near the crack tip is included, no statistical significance can be associated with the differences at and around initiation. These results are consistent with other published reports that J_{IC} values are relatively insensitive to constraint conditions at the crack tip [42].

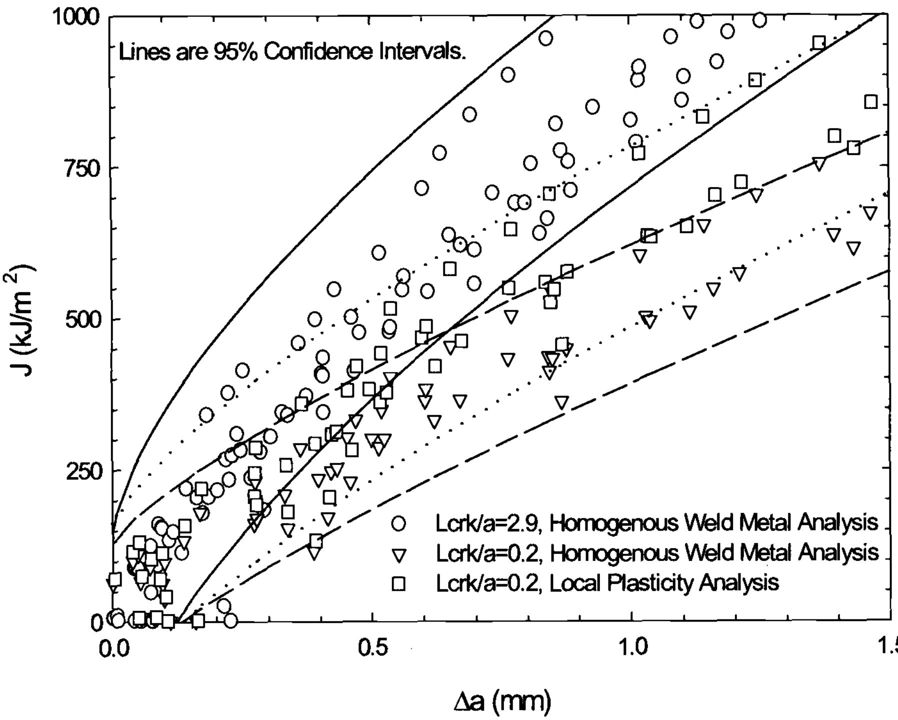

Figure 16 – *Crack Growth Resistance Curves Near Initiation for Weldment HBD.*

All of the low weld fusion margin HBD specimens in this study failed due to unstable growth after significant ductile crack growth. Typically more than 2 mm of crack extension occurs prior to failure. Only one specimen with a larger weld fusion margin failed prior to test conclusion. The remaining four tests exhibited an average crack growth of more than 5.0-mm. The results, shown in Table 9, suggest that for smaller L_{crk}/a the propensity for unstable failure increases. Further, an analysis of the variance between the amount of ductile growth prior to cleavage failure or test conclusion shows statistical significance at the 95% confidence limits. Some of the variation can easily be attributed to the increased stress triaxiality in the small weld fusion margin. Unstable fracture is a stress driven event and as crack tip plasticity is constrained, stresses, including opening mode or principal stresses, increase. Obviously, factors other than fusion line proximity and constraint level influence this tendency toward unstable failure [38]. Local weld bead microstructure at the crack tip could cause local brittle zones that only specimens from the narrow side of the weld would sample resulting in the data shown in Table 9. Further investigation would be required to determine what factors determine the amount of ductile crack growth prior to instability. Moreover, as mentioned in the discussion of Charpy results, as seen in Figure 2, these welds are not typical production welds and have a significantly higher transition temperature. Production welds would be on upper shelf at the test temperature and fully ductile behavior would be expected.

Table 8 – *Initiation Toughness Values for Weldment HBD*

ID	Location	Analysis	J_{IC} (lbs/in)	J_{IC} (kJ/m^2)	Valid	Comments
HBD-1	Wide	Homogenous	5853	1024	NO	Invalid Thickness
HBD-2	Wide	Homogenous	3832	671	YES	
HBD-3	Wide	Homogenous	3797	664	YES	
HBD-4	Wide	Homogenous	2772	485	YES	
HBD-5	Wide	Homogenous	3141	550	YES	
HBD-6	Narrow	Local Plasticity	2478	434	YES	
HBD-6	Narrow	Homogenous	1470	257	YES	
HBD-7	Narrow	Local Plasticity	2100	368	YES	
HBD-7	Narrow	Homogenous	1159	203	YES	
HBD-8	Narrow	Local Plasticity	3609	632	YES	
HBD-8	Narrow	Homogenous	1904	333	YES	
HBD-9	Narrow	Local Plasticity	2778	486	YES	
HBD-9	Narrow	Homogenous	1841	322	YES	
HBD-10	Narrow	Local Plasticity	1809	317	YES	
HBD-10	Narrow	Homogenous	1266	222	YES	HBD-1 Excluded
Average	Wide	Homogenous	3386	592	S.Dev.	91
Average	Narrow	Local Plasticity	2555	447	S.Dev.	122
Average	Narrow	Homogenous	1528	267	S.Dev.	59

The final weldment analyzed was HBB (MIL-100s, double vee, 11% undermatch, $L_{crk}/a=1.5$). Figure 17 is a plot of the six resistance curves from weldment HBB, three specimens from each side of the double vee weld. Only the homogenous weld metal analysis was performed on this weldment since L_{crk}/a was relatively large (1.5) and the undermatch welds level low (-11%). Initiation, shown in Table 10, and tearing modulus from both sides of the weldment are consistent.

Error Estimation of Homogenous Analysis

Neglecting the contribution of local plasticity and increased constraint to J_{pl} results in an under estimation of J. Figure 18 depicts the level of error as a ratio of J calculated using homogenous weld metals assumptions over J calculated with local plasticity included. These results are taken from one typical test from each of the three weldments with a L_{crk}/a of less than 1.5 (HBA, HBC and HBD). As expected, initially the error is small, as the contribution of J_{pl} to J total is small. However, as J_{pl} becomes a larger proportion of J total, the error increases until it reaches a peak between $\Delta a/W$ of 0.01-0.02. Franco et. al have shown that variations in crack tip constraint only occur when the plastic zone physically interacts with the weld fusion line [43]. At this point plasticity begins to move away from the crack tip and out into the bulk of the remaining ligament. As the crack grows, the homogenous η_{pl} reflects the increasing crack tip constraint for the deeper crack, and the error is slowly reduced.

Two important points can be taken from Figure 18. First, errors are largest in the initial portion of the curve. This is the area where J_{IC} and tearing modulus is determined; errors in this part of the curve will result in conservative estimations of these values not representative of true material properties. Second, as the crack tip moves closer to the fusion line and the deformation level increases, the error increases dramatically. The smallest weld fusion margin shown is 0.2, which results in 20% error nearly from the outset of the test. The largest weld fusion margin in Figure 18 is 1.35. At this level errors are always less than 10%. Therefore, for L_{crk}/a larger than 1.35 errors can be ignored in all but the most exacting analyses.

Table 9 – *Amount of Ductile Crack Growth Prior to Failure or Test Completion*

ID	*Location*	*Δa (mm)*	**Fracture Mode**
HBD-1	Wide	4.0	Cleavage
HBD-2	Wide	5.1	DNF
HBD-3	Wide	5.4	DNF
HBD-4	Wide	6.1	DNF
HBD-5	Wide	6.4	DNF
HBD-6	Narrow	2.2	Cleavage
HBD-7	Narrow	2.4	Cleavage
HBD-8	Narrow	3.1	Cleavage
HBD-9	Narrow	0.8	Cleavage
HBD-10	Narrow	2.7	Cleavage
Average	Wide	5.4	0.94S. Dev.
Average	Narrow	2.2	0.89S. Dev.
DNF = Did Not Fail			

Comparisons of J-R Curves with Various Level of Mis-Match

Crack resistance curves from three weld systems, two from this study (HBA, HBB) and one from a prior study [20] (GXL), are plotted in Figure 19. Weldment GXL is a 10% overmatched system with a L_{crk}/a of 1.8, and is composed of MIL-100s weld consumable and HY-80 baseplate. Analysis of HBA includes local crack tip plasticity, while the analysis of GXL and HBB does not account for this effect. All three are normalized by σ_{FL}, which is defined as $(\sigma_{ys}+\sigma_{ult})/2$ and the specimen thickness, B. Clearly, once the differences in flow strength are accounted for, no difference can be discerned between any of the three welds. In fact, good agreement is shown between the two MIL-100s weld systems indicating no effect from undermatch welds.

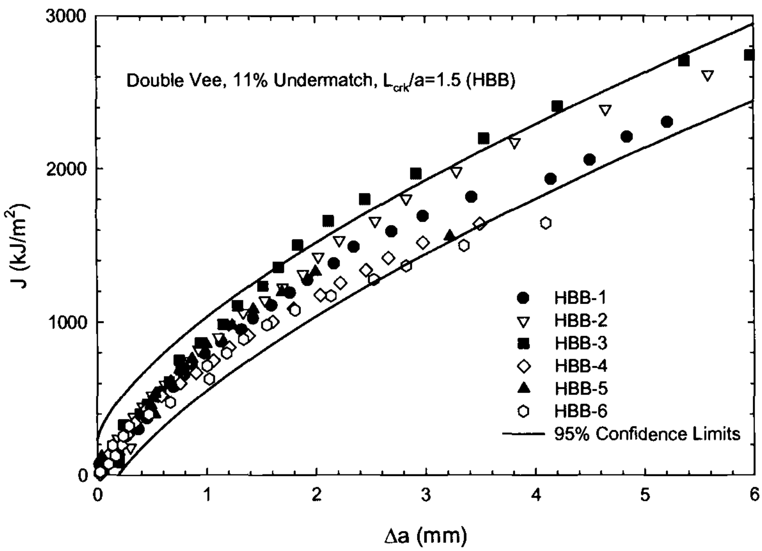

Figure 17 – *Crack Growth Resistance Curves for Weldment HBB.*

Table 10 – *Initiation Toughness Values for Weldment HBB*

ID	*Location*	*Analysis*	J_{IC} *(lbs/in)*	J_{IC} *(kJ/m²)*	*Valid*	*Comments*
HBB-1	TOP	Homogenous	3000	525	YES	
HBB-2	TOP	Homogenous	3436	601	YES	
HBB-3	TOP	Homogenous	3526	617	YES	
HBB-4	BOTTOM	Homogenous	2785	487	YES	
HBB-5	BOTTOM	Homogenous	3517	615	YES	
HBB-6	BOTTOM	Homogenous	2306	404	YES	
Average	TOP	Homogenous	3321	581	S.Dev.	49
Average	BOTTOM	Homogenous	3048	533	S.Dev.	107

Weld Joint Geometry Effects

Figure 20 shows J-R curves for MIL-100s welds with a weld fusion margin greater than or equal to 1.5. These represent the wide side of the two single vee weldments (HBC, HBD) and all the tests from weldment HBB. All three sets of curves do not include local plasticity and are using homogenous weld metal as the basis for the calculation of J. Differences between data sets do not exceed typical scatter associated with toughness testing and no apparent trend in the data is evident. For joint geometries where L_{crk}/a exceeds 1.5, toughness values appear equivalent to all-weld metal toughness, and no penalty in toughness is evident from joint design.

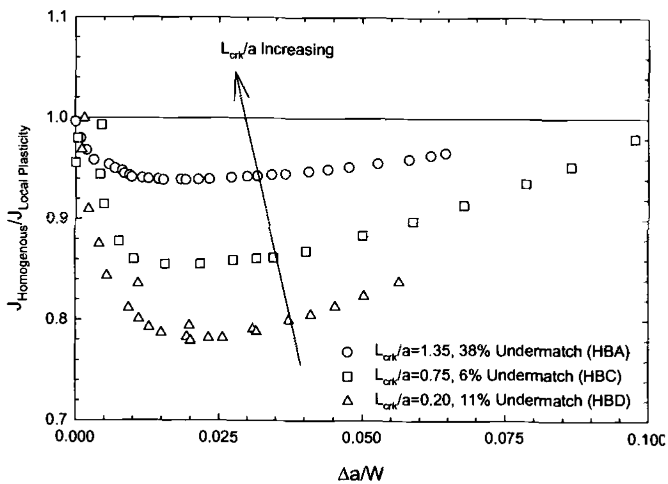

Figure 18 – *Under Estimation of J Using Homogeneous Weld Metal Assumption.*

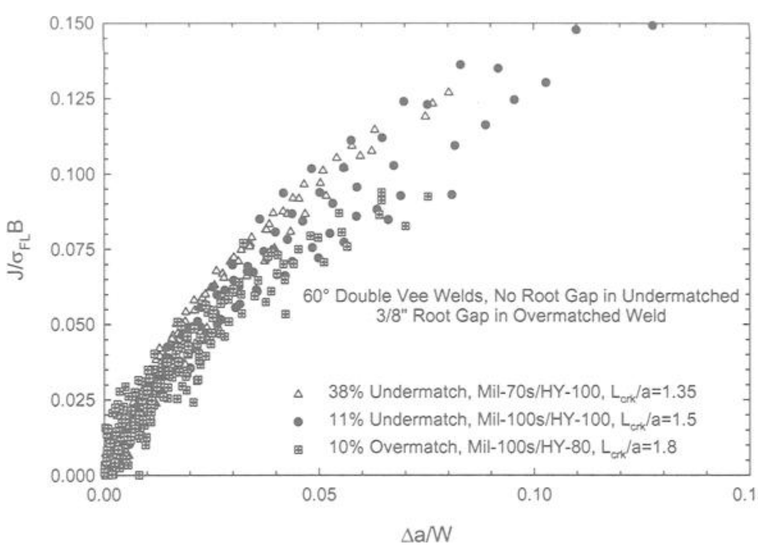

Figure 19 – *Normalized J-R Curves for Various Levels of Mis-Match.*

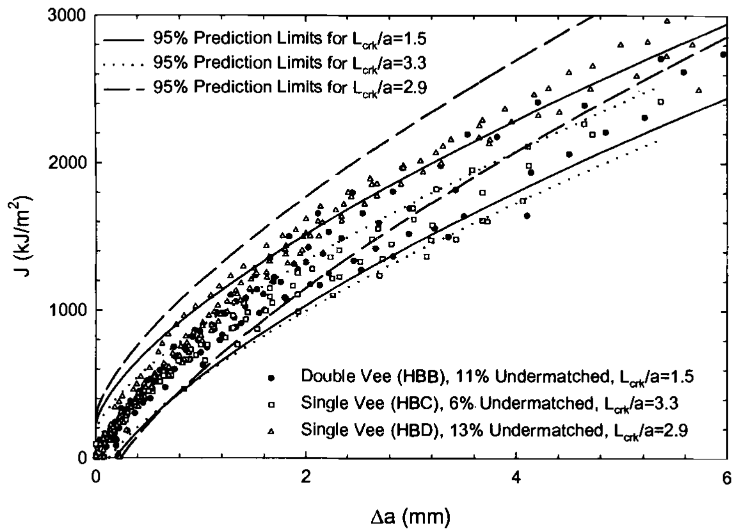

Figure 20 – *J-R Curves for L_{crk}/a □ 1.5.*

Figure 21 shows J-R curves for MIL-100s welds with a weld fusion margin less than or equal to 1.5. These represent the narrow side of the two single vee weldments (HBC, HBD) and all the tests from weldment HBB. Local plasticity and constraint is accounted for in the calculation of J for both HBC and HBD. However, J calculations for HBB assume homogenous weld metal and do not account for local crack tip deformation. Significant differences in material behavior are evident at higher deformation levels. However, a review of initiation values for these three data sets indicates no statistically significant differences in reported values. Scatter in J-R behavior at this level is not unexpected, especially between different weldments. As discussed previously some of the variation in toughness values may be attributed to the loss of constraint in the HBB specimens and the formulation in γ shown in Figure 15.

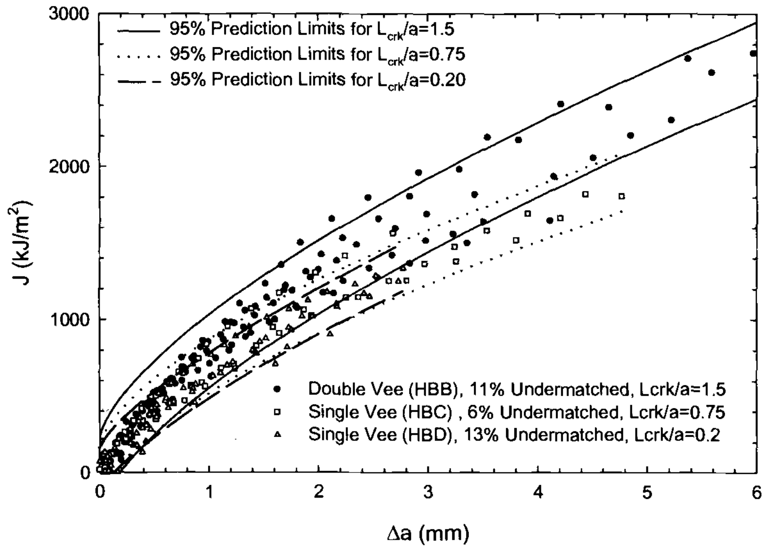

Figure 21 – *J-R Curves for L_{crk}/a □1.5.*

Summary and Conclusions

This report investigates the effects of undermatch welds, joint geometry and weld fusion line margin on fracture performance of weld systems using short crack SE(B) specimens. The contributions of constraint and localized crack tip plasticity to J_{pl} are evaluated for various configurations. Calculating J in short crack SE(B) specimens assuming monolithic, homogenous weld metal properties results in J-R curves that exhibit markedly different crack growth resistance behavior and initiation toughness depending on crack tip proximity to the weld fusion line. Once local plasticity and the additional constraint caused by the weld/baseplate interface is included in the analysis, fracture behavior is independent of crack tip proximity to the fusion line up to and slightly beyond initiation. Variation in behavior beyond this point is attributed to increased constraint caused by the higher strength baseplate funneling the plastic zone through the remaining ligament. This negates the "short crack effects" that would be expected in a homogenous specimen of similar crack length. Additional variation in fracture behavior may result from the formulation of the γ -factor used in the calculation of J_{pl} for homogenous short crack SE(B) specimens and from actual material variation within each weld.

One troubling result from this study is the apparent increased propensity for unstable fracture as the fusion line margin decreased. This result shows that a small (short) flaw in an undermatched weld located in close proximity to a higher strength material or bending field could result in a high constraint condition at the crack tip as the plastic zone was distorted. Normally, such a flaw would have the benefit of a increased tearing resistance as plasticity easily flowed to a free surface. However, in an undermatched weld the loss of constraint is neutralized and stresses increase proportionally to J in front of the crack. In this study all of the specimens with a weld fusion margin less than or equal to 0.75 failed in an unstable manner, albeit after significant prior ductile growth. As discussed previously, factors other than fusion line proximity and constraint level influence this tendency toward unstable failure. Other factors such as local weld bead microstructure at the crack tip could play a significant role. Further investigation will be required to determine what factors are at the root of these failures and determine the amount of ductile crack growth prior to instability.

It is important to note that these weldments were designed to enhance the influence of weld joint undermatch welds and are not production welds. This is clearly evident in the higher than expected transition temperature exhibited in charpy impact testing. Previous testing of production welds clearly indicates that transition to fully ductile behavior occurs prior to –2 °C, which is the test temperature of the weldments in this study. Unstable fracture or cleavage would not be expected from weldments displaying upper shelf behavior.

Other conclusions from this study:

- Error in calculating J using weld metal properties and ignoring the fusion line proximity at L_{crk}/a □ 1.5 can be less than 10% and can reasonably be ignored.
- Errors in calculating J using weld metal properties and ignoring the fusion line proximity at $L_{crk}/a < 1.5$ can be considerable with the error increasing as the fusion line margin decreases. For L_{crk}/a of 0.2 the error can be as high as 25%. Effects of localized plasticity and increased constraint must be accounted for in the fracture analysis.
- Errors in the calculated value of J using monolithic, homogenous weld metal assumptions increase as L_{crk}/a decreases.
- Uncorrected estimates of J_{IC} in specimens where L_{crk}/a is less than 1.5 results in conservative estimations.
- Specimens with unusually steep blunting line behavior make the calculation of J_{IC} problematic. Calculation of this value becomes overly sensitive to the initial estimated crack length. It was observed that small changes in the initial crack length estimate (1%) could result in large changes in J_{IC} (25%).
- ASTM 1820 crack straightness requirements are based on a percentage of average crack length, which is unduly strict for short crack specimens.
- When J values are normalized by the flow strength and thickness, J-R curves for under and over-matched welds are similar. Therefore, the effect of weld-joint mismatch on the J-R curve can be accounted for by adjusting for the difference in flow stress.

References

[1] American Society of Mechanical Engineers, Boiler and Pressure Vessel Code, Section III, Nuclear Plant Components, 1980.

[2] American Welding Society, D1.1-80, Structural Welding Code, 1980.

[3] MIL-STD-1688(SH), Military Standard: Fabrication, Welding and Inspection of HY-80/100 Submarine Applications, Washington, DC, 1981.

[4] Horsley, D. J. and Glover, A. G. "Girth Weld Strength Undermatch in High Pressure Natural Gas Pipelines," presented at the 2nd International Symposium on Mis-matching of Welds, Luneburg, Germany, 1996.

[5] Denys, R., Lefever, T., and Glover, A. G., "Weld Metal Yield Strength Variability in Pipeline Girth Welds," *Pipeline Technology*, Vol. 2, 1995, pp. 591-598.

[6] Howden, et al., "Effective Use of Weld Metal Yield Strength for HY Steels," National Advisory Board Report, Report No. NMAB-380, Jan. 1983.

[7] Lee, M.M.K., and Luxmoore, A.R., "An Experimental Study of the Elastic-Plastic Deformation of Double 'V' Butt Welds," Journal of Strain Analysis, Vol. 25, No. 4, 1990, pp. 255-265.

[8] Luxmoore, A.R., Lee, M.M.K., and Cray, M.J., "A Finite Element Study of Short Cracks in Mis-matched Double 'V' Welds," Mis-Matching of Welds, ESIS 17, K.H. Schwalbe and M. Koçak Eds., Mechanical Engineering Publications, London, 1994, pp. 614-660.

[9] Cray, M.J., Luxmoore, A.R., and Sumpter, J.D.G., "The Effect of Weld Mismatched on J and CTOD," Proceedings of the Symposium on Elastic-Plastic Fracture Mechanics, Freiburg, Germany 1989.

[10] Joch, J. and Ainsworth, R. A., "Relationship Between the J-Integral and the Crack Tip Opening Displacement for Stationary Cracks in Weldments at Plastic Collapse," Fatigue and Fracture on Engineering Materials and Structures, Vol 17, 1994, pp. 1175-1185.

[11] Rice, J.R., "A Path Independent Integral and the Approximate Analysis of Strain Concentration by Notches and Cracks," Journal of Applied Mechanics , Vol. 35, 1968, pp. 379-386.

[12] Kirk, M. T. and Dodds, R. H., "Experimental J Estimation Formulas for Single Edge Notch Bend Specimens Containing Mismatched Welds," Proceedings of the 11th International Conference on Offshore Mechanics and Arctic Engineering, Vol. 3, part B, American Society of Mechanical Engineers, 1992, pp. 439-448.

[13] Gordon, J. R. and Wang, Y. Y., "The Effect of Weld Metal Mis-Match on Fracture Toughness Testing and Analysis Procedures," Mis-Matching of Welds, ESIS 17, K. H. Swalbe and M. Koçak, Eds., Mechanical Engineering Publications, London, 1994, pp. 351-368.

[14] Burstow, M. C., Howard, I. C. and Ainsworth, R. A., "The Effects of Material Strength Mismatching on Constraint at the Limit Load of Welded Three Point Bend Specimens," International Journal of Fracture, Vol. 89, 1998, pp. 117-142.

[15] Kirk, M. T. and Dodds, R. H., "The Influence of Weld Strength Mismatch on Crack-tip Constraint in Single Edge Notch Specimens," International Journal of Fracture, Vol. 63, 1993, pp. 297-316.

[16] Burstow, M. C., Howard, I. C. and Ainsworth, R. A., "The Influence of Constraint on Crack Tip Stress Fields in Strength Mismatched Welded Joints," Journal of the Mechanics and Physics of Solids, Vol. 46, 1998, pp. 845-872.

[17] Burstow, M. C. and Ainsworth, R. A., "Comparison of Analytical, Numerical and Experimental Solutions to Problems of Deeply Cracked Welded Joints in Bending," Fatigue and Fracture on Engineering Materials and Structures, Vol. 18, 1995, pp. 221-234.

[18] Sumpter, J. D. G., "J_c Determination for Shallow Notch Welded Bend Specimens," Fatigue and Fracture on Engineering Materials and Structures, Vol. 10. No. 6, 1987, pp. 479-493.

[19] Joyce, J. A., Hackett, E. M., and Roe, C., "Effect of Crack Depth and Mode of Loading on the J-R Behavior of a High-Strength Steel." Constraint Effects in Fracture ASTM STP 1171, E. M. Hackett, K. H. Schwalbe, and R. H. Dodds, Eds., ASTM, Philadelphia, 1993, pp. 239-263.

[20] Tregoning, R. L. "Experimental Investigation of Mismatched Weld Joint Performance," Fatigue and Fracture Mechanics: 27th Volume, ASTM STP 1296, R. S. Piascik, J. C. Newman, and N. E. Dowling, Eds., American Society for Testing and Materials, Philadelphia, 1997, pp. 427-450.

[21] MIL-E23765, Military Specifications: Electrodes and Rods – Welding, Bare, Solid or Alloyed Core, Low Alloy Steel, 18 August 1987.

[22] MIL-S-16216J, Military Specification: Steel Plate, Alloy, Structural, High Yield Strength (HY-80 and HY-100), 10 April, 1981.

[23] ASTM E23-96, "Standard Test Methods for Notched Bar Impact Testing of Metallic Materials," 1996 Annual Book of ASTM Standards, American Society of Testing and Materials, Philadelphia, PA, 1996.

[24] ASTM E8-96a, "Standard Test Methods for Tension Testing of Metallic Materials," 1996 Annual Book of ASTM Standards, American Society of Testing and Materials, Philadelphia, PA, 1996.

[25] Montemarano, T. W. et al., "Results of the Evaluation of ASTM A710 Grade A Steel Under the "Certification of HSLA Steels for Surface Ship Construction Program," Navy Technical Memorandum No., DTNSRDC TM-28-84-17, January 1984.

[26] Lee, K.H., "The Effect of Crack Front Curvature on Stress Intensity Factor in Compact Tension Specimens Using the Boundary Integral Equation Methods," The Welding Institute, Abington, England, July, 1979.

[27] Towers, O.L., "Fatigue Crack Front Shape and Its Effect on Fracture Toughness Measurement," Journal of Testing and Evaluation, Vol. 11, No. 1, 1983, pp. 34-45.

[28] Towers, O. L. and Dawes, M. G., "Welding Institute Research on the Fatigue Precracking of Fracture Toughness Specimens," Elastic-Plastic Fracture Test Methods: The User's Experience, ASTM STP 856, E. T. Wessel and F.J. Loss, Eds., American Society for Testing and Materials, Philadelphia, 1985, pp.23-46.

[29] Sakano, K., "Precompression Cracking Method for Fracture Toughness Testing – 2nd Report," Ishikawijima-Harima Heavy Industries (IHI) Engineering Review, Vol. 13, No. 3, July 1980, pp.1-7.

[30] Kirk, M. T., "A Cyclic Reverse Bending Technique for Fatigue Precracking from Shallow Notches in SE(B) Specimens," Fracture Mechanics: 22nd Symposium, Vol. 1, ASTM STP 1131, H. A. Ernst, A. Saxena and D. L. McDowell, Eds., American Society for Testing and Materials, 1992, pp.859-879.

[31] M. Koçak, S. Yao and, K. H. Schwalbe, "Effect of Welding Residual Stresses on Fatigue Precracking of CTOD Specimens," Proceedings of The International Conference of Residual Stresses, Los Angeles, CA, 8-10 August, 1989.

[32] ASTM 1820-96, "Standard Test Methods for Measurement of Fracture Toughness," 1996 Annual Book of ASTM Standards, American Society of Testing and Materials, Philadelphia, PA, 1996.

[33] Joyce, J. A., "J Resistance Curve Testing of Short Crack Bend Specimens Using Unloading Compliance," Fracture Mechanics: 22nd National Symposium, Vol. 1, ASTM STP 1131, H.A. Ernst, A. Saxena, and D.L. McDowell, Eds., American Society for Testing and Materials, Philadelphia, 1992, pp. 904-924.

[34] Shang-Xian Wu, Yiu-Wing Mai and Cotterell, B., "Plastic η Factor of Fracture Specimens with Deep and Shallow Cracks," International Journal of Fracture, Vol. 45, 1990, pp. 1-18.

[35] Kirk, M.T. and Dodds, R.H., "J and CTOD Estimation Equations for Shallow Cracks in Single Edge Notched Bend Specimens," U. S. Nuclear Regulatory Commission Report, NUREG/CR-5969, 1993.

[36] Kumar, V., German, M. D. and Shih, C. F., An Engineering Approach to Elastic-Plastic Fracture, EPRI NP-1931, Electric Power Research Institute, Palo Alto, 1981.

[37] Tada, H., Paris, P. C., and Irwin, G. R., The Stress Analysis Handbook, Paris Productions, Inc., St. Louis, 1985.

[38] Zhang X.J. et al., "SEM Stereo-Section Fractography (SSF) Observations," George R. Irwin Symposium on Cleavage Fracture, Kwai S. Chan, Ed., The Minerals, Metals & Mining Society, 1997, pp. 69-79.

[39] Al-Ani, A. M. and Hancock, J. W., "J-Dominance of Short Cracks in Tension and Bending," Journal of the Mechanics and Physics of Solids, Vol. 39, 1991, pp. 23-43.

[40] Dodds, R. H., Anderson, T L. and Kirk, M. T., "A Framework to Correlate a/W Effects on Elastic-Plastic Fracture Toughness (Jc)," International Journal of Fracture, Vol. 48, 1991, pp. 1-22.

[41] Sun, D.-Z., Kienzler, R., Voss, B. and Schmitt, W., "Application of Micromechanical Models to Prediction of Ductile Fracture," Fracture Mechanics: 22nd National Symposium, Vol. 2, ASTM STP 1131, S. N. Atluri, J. C. Newman, Jr., I.S. Raju and J. S. Epstien, Eds., American Society for Testing and Materials, Philadelphia, 1992, pp. 368-378.

[42] Joyce, J. A. and Link, R. E., "Effects of Constraint on Upper Shelf Fracture Toughness," Fracture Mechanics, Vol. 26, ASTM STP 1256, W. G. Reuter, J. H. Underwood and J. C. Newman, Eds., American Society for Testing and Materials, Philadelphia, 1995.

[43] Franco, C., Gilles, P., Eripret, C. and Nallet, S., "Constraint Effects on the Upper Shelf in Cracked Welded Specimens," Constraint Effects in Fracture Theory and Applications, ASTM STP 1244, Mark Kirk and Ad Baker, Eds., American Society for Testing and Materials, Philadelphia, 1995.

Carlos G. Matos[1] and Robert H. Dodds, Jr.[2]

Modeling of Cleavage Fracture in Connections of Welded Steel Moment Resistant Frames

Reference: Matos, C. G. and Dodds, R. H. Jr., "**Modeling of Cleavage Fracture in Connections of Welded Steel Moment Resistant Frames**," *Fatigue and Fracture Mechanics: 33rd Volume, ASTM STP 1417,* W. G. Reuter and R. S. Piascik, Eds., ASTM International, West Conshohocken, PA, 2002.

Abstract: This study applies an advanced micro-mechanics model of cleavage fracture in ferritic steels to examine the fracture behavior of welded, moment resistant steel frames of the type widely constructed prior to the Northridge earthquake. The Weibull stress model for cleavage, coupled with 3-D analyses of connections containing crack-like defects, provides a quantitative estimate of the cumulative failure probabilities with increasing beam moment. A set of previously conducted, 15 full-scale tests on T-connections of the pre-Northridge design provide fracture moments to calibrate parameters of the Weibull stress model. Once calibrated, the model is used to examine the importance of welding-induced residual stresses in the lower-flange and the effects of seismic loading rates. The model predicts the cumulative failure probability as a function of beam moment for these various configurations.

Keywords: residual stresses, cleavage, Weibull stress, eigenstrain, seismic loading, moment frames

Introduction

Rectangular steel frames with welded connections that resist the full moment capacity of the sections (WSMFs) became popular for building construction in regions of strong seismicity during the 1960s and 1970s. Laboratory tests at the time revealed significant ductility in the connections with a capacity for large, inelastic rotations and energy dissipation. Over the past twenty years, efforts to optimize the design of these structural systems have often led to the use of fewer frames with markedly increased beam and column sizes, including the use of higher strength steels. These changes increased significantly the required levels of inelastic deformation during a strong earthquake. Fractures in the connections during the 1994 Northridge (California) earthquake prompted new research efforts to understand the causes and to develop improved designs [*1*]. WSMFs constructed prior to the Northridge event have large rolled sections of A36 (beams) and A572 (columns) steels with flux-core

[1] Structural Engineer, Jacobs Engineering Group, Inc., 13723 Riverport Dr., Maryland Heights, MO 63043.

[2] M.T. Geoffrey Yeh Chair of Civil Engineering, University of Illinois, Urbana, IL 61801.

field welds (E70T-4) to connect the beam flanges with the column face (see Fig. 1). The geometry of the connection includes an access hole in the beam web, backup bars and runoff tabs left in-place, bolted shear tabs, continuity plates in the columns at the beam flange locations, etc. Post-quake field surveys and laboratory tests of full-scale connections indicated the existence of relatively long, shallow defects in the root pass of the lower-flange weld [*2,3*]. Fractures initiated at this location and propagated in a very rapid, brittle mode possibly preceded by a small amount of stable ductile tearing ($\lesssim$ 1-2 mm) [*4*]. Tests conducted following the Northridge earthquake on these larger, full-scale connections reproduced the fractures observed in the field and exhibited very limited macroscopic plastic deformation prior to the brittle (cleavage) fracture event [*5*].

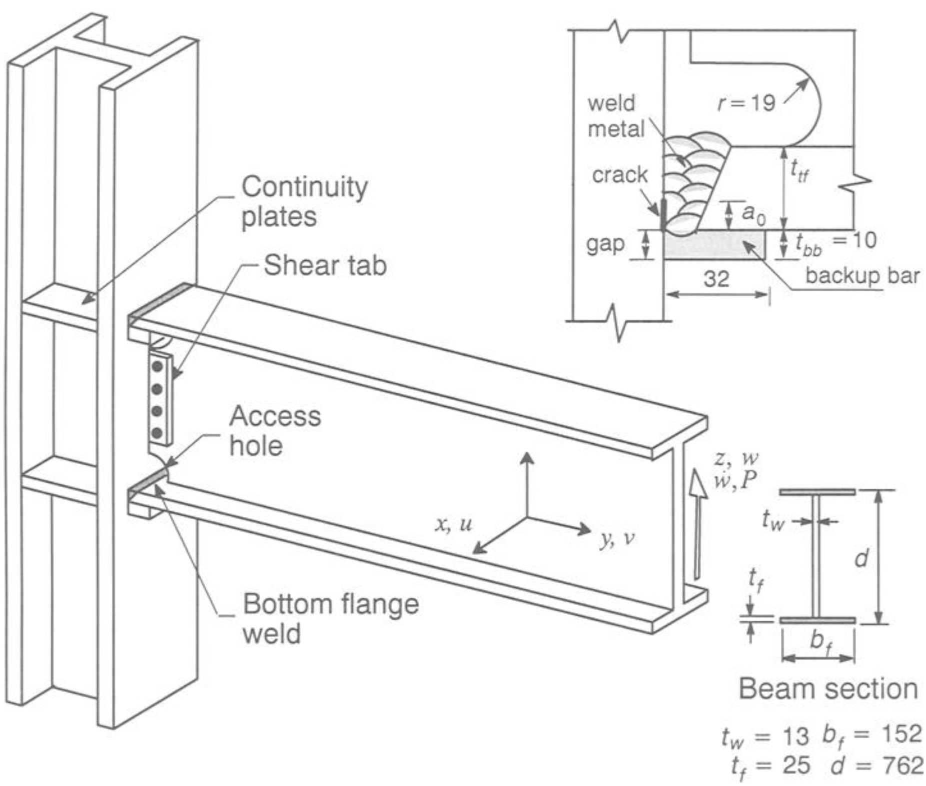

Figure 1. *Schematic of typical pre-Northridge beam-column connection and the beam cross section used in analyses. All dimensions in mm.*

Key factors that enter a fracture mechanics assessment of these connections include: (1) residual stresses induced by the welding process to connect thick flange plates of the beam and the column sections, (2) constraint loss during plastic deformation at the relatively shallow crack fronts located in the weld root pass at the interface between the column flange and weld metal, (3) elevated strain rates from seismic loading acting on strongly rate-sensitive, mild structural steels, and (4) a locally complex, 3-D stress state along the crack front comprised of axial tension in the beam flange and local bending of the beam flange over the length of the access hole caused by a large shear force in the beam flange at the column face.

The relatively low toughness of the E70T-4 electrodes [2] used in the fabrication of these connections, combined with the (locally) elevated strain rates along the crack fronts from the earthquake loading, drive the fracture response into the ductile-to-brittle transition region at room temperature (quasi-static laboratory tests reveal the same brittle fractures). Fracture mechanics tests of similar base plates, weld metals, and heat affected zones (HAZ) along the fusion line all exhibit the considerable scatter expected of ferritic steels operating in the ductile-to-brittle transition region (see [6-8] for examples). This scatter arises from a "weakest link" mechanism of cleavage fracture that develops from inherent inhomogeneities of the material toughness at the metallurgical length-scale [9,10]. Plastic deformation ahead of the shallow cracks causes a loss of local constraint which amplifies this scatter by generating different stress levels at identical J-values, thereby greatly complicating the development of predictive models [11]. Quantitative predictions for cleavage fracture in connections of WSMFs must employ a combination of probabilistic models to describe this material inhomogeneity and continuum plasticity models to describe the complex 3-D stress field and changes in constraint along the crack fronts. Changbin and Chen [12] describe an early probabilistic assessment of these connections based on linear-elastic fracture mechanics but they do not establish a link between the metallurgical cleavage mechanism and the macroscopic fracture of the connections. Chi and Deierlein [13] describe extensive 2-D and some limited 3-D analyses of the connections to examine the elastic-plastic stress fields ahead of weld cracks in WSMF connections but with a focus on more ductile fracture mechanisms (hole growth and subsequent tearing) expected in post-Northridge designs.

This work focuses on understanding and characterizing the brittle fracture behavior for the existing large inventory of WSMFs having the pre-Northridge design constructed over the past twenty years. The present approach combines a probabilistic, micro-mechanical model to describe the cleavage fracture process based on the Weibull stress with large-scale, 3-D finite element analyses of the full connections. These nonlinear analyses provide the local variations of the fracture parameter (J) and constraint changes along the crack front under increased plastic deformation. By coupling the Weibull stress model with 3-D analyses of the full connection, the cumulative probability of cleavage fracture in the connection ($\mathcal{P}_f$) may be expressed simply in terms of the applied beam moment at the column face, i.e., $\mathcal{P}_f$ *vs.* M/M_p where M_p denotes the plastic moment capacity of the beam section. Applications of this analysis capability examine the relative importance of welding induced residual stresses, the plastic deformation that ranges from small-scale yielding (SSY) to full plastic hinge development in the beam and column, and the effects of seismic loading rates on the probability for cleavage fracture initiation at the interface of the beam flange and column face.

The paper is organized as follows. Section 2 describes an assessment of recent full-scale tests conducted on pre-Northridge style connections using Weibull statistics. These tests provide key information to enable calibration of the micro-mechanical model (Weibull stress) for cleavage. Section 3 briefly reviews the Weibull stress model as employed in this study. Section 4 outlines the numerical procedures to analyze the connections under quasi-static and dynamic loading including the effects of residual stresses. Section 5 provides the key results of the numerical study to calibrate the Weibull stress model and its application to assess the relative significance of residual stresses, increased plastic deformation/constraint loss, and elevated crack front strain rates caused by dynamic (seismic) loading. Section 6 lists the key conclusions about the brittle fracture behavior of the pre-Northridge connections derived from the computational studies. Full details of this comprehensive study on pre-Northridge connections may be found in [*14-16*].

Statistical Analysis of Full-Scale Connection Tests

The SAC-Steel research program [*1*] and other programs sponsored full-scale joint tests of pre-Northridge connections (T configuration as shown in Fig. 1). The T-joint specimen with hinges at top/bottom of the column models the conditions at an exterior beam-column connection. Columns are fabricated from A572 steel with $W14 \times 176$ sections; $W30 \times 99$ beams are fabricated from A36 steel. Each of the fifteen tested specimens failed in a brittle fracture mode at widely varying loads, with fracture initiating in the lower-flange beam-to-column weld (Fig. 1 shows details of this region). The fracture moment in the beam at the column face, M_f, is given by $M_f = P\ell$, where P denotes the actuator force at fracture applied to the beam tip a distance ℓ from the column face. Fracture moments are normalized by the plastic moment of the section $M_P = Z\sigma_{ys}$ where σ_{ys} defines the measured yield stress of the beam flange for each test specimen and Z denotes the plastic modulus of each beam cross section,

$$\frac{M_f}{M_P} = \frac{P\ell}{Z\sigma_{ys}}. \tag{1}$$

The fractured surfaces of these specimens all reveal similar patterns of macroscopic, crack-like defects along the root pass of the lower-flange weld with the characteristic markings of cleavage fracture [2]. The strong similarity of geometry and fabrication in these test specimens leads to the key postulate that the large variation in measured fracture moments arises from the expected statistical scatter of toughness values for cleavage fracture in the ductile-to-brittle transition region (combined with observed scatter of flaw sizes).

Median estimates for the rank failure probability of normalized fracture moment are given by $\mathcal{P}_f = (j - 0.3)/(n + 0.4)$, where j denotes the rank (failure) order by increasing M_f/M_P and n denotes the sample size (in this case $n = 15$). Normalized values of fracture moment are expected to follow a Weibull distribution as do toughness values for cleavage fracture [*9,17*]. The two-parameter Weibull distribution for the cumulative failure probability (median rank) has the form

$$\mathcal{P}_f = 1 - \exp\left[-\left(\frac{M_f/M_p}{\beta}\right)^{\alpha}\right] \tag{2}$$

where α denotes the Weibull modulus (characterizes the scatter) and β denotes the normalized fracture moment at 63.2% failure probability. A least squares fit yields values for the Weibull parameters of $\alpha = 7.5$ and $\beta = 1.0$. Figure 2 shows that the Weibull probability distribution fits the experimental data very well with all values inside the 90% confidence bounds on estimates of median rank probabilities.

The total (joint) plastic rotation, denoted Θ_p, defines a non-dimensional measure of plastic deformation in the connection (see Appendix S of the AISC Seismic Provisions [*18*]).

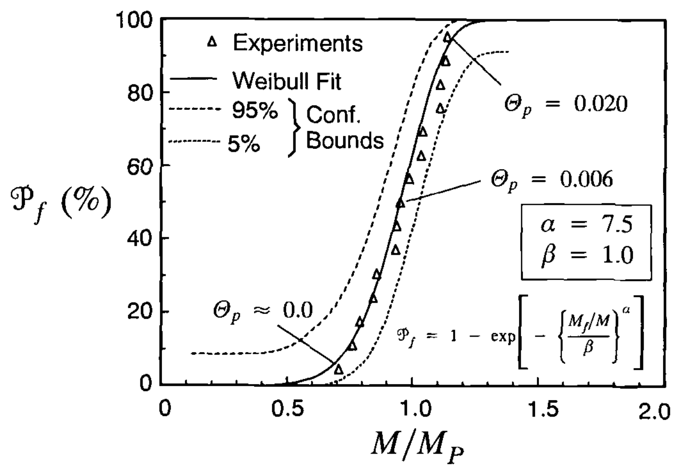

Figure 2. *Weibull fit of measured normalized fracture moments measured during full-scale tests of pre-Northridge connection tests.*

A nonlinear finite element analysis provides the relationship between Θ_p and M/M_P for the connection with dimensions shown in Fig. 1 and with typical flow properties reported for the A36, A572 and E70T-4 materials. Figure 2 includes markers to indicate Θ_p values under increased loading. None of these specimens reach the target rotation capacity of 0.03 radians for special moment frames [*18*, *19*].

The Weibull Stress Model

The Beremin research group [*9*] introduced the local approach to model transgranular cleavage fracture which relates stresses along the crack front to the statistical distribution of micro-cracks (both density and size). This link between the macroscopic loading and the micro-regime of failure is the so-called Weibull stress defined by

$$\sigma_w = \left[\frac{1}{V_0}\int_{\Omega} \sigma_1^m dV\right]^{1/m} \tag{3}$$

where σ_1 denotes the maximum (tensile) stress experienced by a material point to reach the current loading level and Ω denotes the volume of the process zone for cleavage fracture (generally defined by the material within the crack front plastic zone). V_0 defines a normalizing factor for dimensional consistency. The probability of cleavage fracture is expressed in the form

$$\mathcal{P}_f(\sigma_w) = 1 - \exp\left[-\left(\frac{\sigma_w}{\sigma_u}\right)^m\right] \tag{4}$$

where m denotes the shape factor parameter and σ_u denotes the scale factor. In particular, m characterizes the size distribution of micro-cracks and σ_u the material strength at the metallurgical scale [*9*]. The model assumes that m and σ_u represent characteristic material properties at a specific temperature and loading rate, and independent of triaxiality along the crack front. The evolution of Weibull stress under loading of a connection correlates directly with the evolution of normalized beam moment and flange stress (through nonlinear finite element analyses).

To include a threshold toughness in the Weibull stress model, Gao et al. [*39*] introduced the modified, three-parameter probability of cleavage fracture expressed in the form

$$\mathcal{P}_f(\sigma_w) = 1 - \exp\left[- \left(\frac{\sigma_w - \sigma_{w\text{-}\min}}{\sigma_u - \sigma_{w\text{-}\min}} \right)^m \right] \tag{5}$$

where $\sigma_{w\text{-}\min}$ denotes the threshold Weibull stress, i.e., the minimum σ_w-value at which macroscopic cleavage fracture becomes possible. $\sigma_{w\text{-}\min}$ corresponds to the value of σ_w when the entire crack front is loaded to $K_I = K_{\min}$, under (plane strain) SSY conditions, where the crack front length to define the SSY conditions must equal the crack front length in the structural connection for the application of Eq. (3). For ordinary structural steels $K_{\min}$ has an experimentally estimated value of 20 MPa$\sqrt{\text{m}}$ (ASTM E-1921 adopts this value).

Dynamic loading of the connections should increase the probability of cleavage fracture at a specified M/M_p, or alternatively decrease the value of M/M_p at fracture for a specified failure probability. Analyses include the effects of strain rate on the material flow properties which leads to increased values of σ_w compared to those for static loading at the same value of M/M_p. Based on studies [*21, 22, 23*], we assume that the Weibull stress parameters, m and σ_u, remain invariant of loading rate over the range of rates expected during seismic events ($\dot{K}_I <$ 500 MPa$\sqrt{\text{m}}/s$) and $\sigma_{w\text{-}\min}$ has a weak and computable dependence on $\dot{K}_I$.

The computational studies here focus on construction of the failure probability distributions, $\mathcal{P}_f(\sigma_w/\sigma_{ys})$ and $\mathcal{P}_f(M_f/M_p)$, for connections under externally applied, quasi-static and dynamic loads including the potential adverse effects of residual stresses.

Numerical Procedures

Modeling of Residual Stresses

The field welding procedures to complete construction of WSMF connections introduce residual (tensile) stresses in the region of the root pass. Such stresses generate a $K_I > 0$ prior to application of the mechanical loading. Tensile residual stresses acting on shallow cracks at the root pass also increase the local stress triaxiality and thereby partially eliminate the shallow-crack effect that would otherwise be operative (i.e. the increase in apparent fracture toughness due to constraint loss). Two approaches to incorporate residual stresses into finite element models include: (1) non-zero initial stress fields defined by the analyst and (2) the eigenstrain method [*25*]. O'Dowd and colleagues [*24*] recently described an initial stress approach for nonlinear fracture mechanics applications that utilizes an iterative procedure to refine the specified initial stress field to satisfy the equilibrium conditions, and corrections to the J-integral formulation to maintain path independence.

The eigenstrain approach [*25, 26*] used here proves especially convenient to introduce residual stresses in 3-D finite element models of the geometrically complex WSMF connection containing pre-existing cracks in the root pass. Eigenstrains represent analyst specified incompatible elastic strains over the model that are eliminated by the residual stress field generated during the very early steps of an analysis without mechanical loading (only one step when the material remains unyielded). The generated residual stress field thus *automatically* satisfies the equilibrium conditions; no iterative procedure becomes necessary to restore equilibrium and the presence of a pre-existing crack does not complicate the procedure. Hill et al. [*27*] developed a field of eigenstrains to generate residual stresses corresponding to measured values in symmetric welds joining flat plates (double-V groove). Matos and Dodds [*14*] subsequently developed a 3-D field of eigenstrains to generate residual stresses in single-V groove welds used to join the lower beam flange to the column flange in WSMF connections. The residual stress field generated by these eigenstrain functions closely matches the 2-D (plane strain) field computed using thermomechanical simulation of a multi-pass welding process for this configuration [*28*] (Matos and Dodds generalized the 2-D field to 3-D over the width of the lower-flange weld using requirements of the traction free outer edges of the flange).

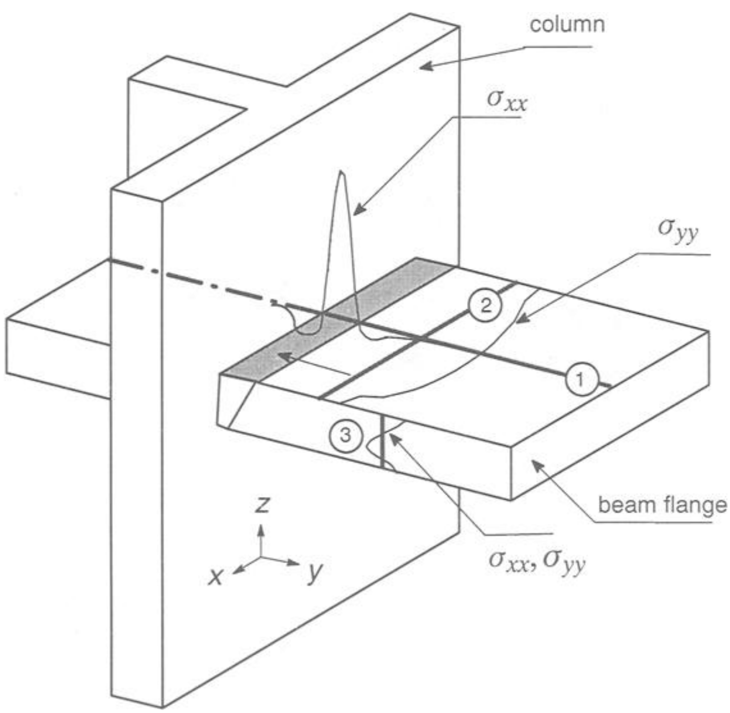

Figure 3. *Key features of residual stress distributions in lower beam flange-to-column weld.*

Figure 3 depicts key features of the residual stress field. The weld longitudinal stresses (σ_{xx}) along line 1 reach values of the weld metal yield stress (σ_{ys}^{wm}) but decay rapidly to zero outside the weld. Weld transverse stresses (σ_{yy}) along line 2 have a smaller magnitude [note that line 2 in the figure and the variation of σ_{yy} are shown outside the weld for clarity; line 2 actually refers to locations in the weld]. Distributions of σ_{xx} and σ_{yy} over the beam flange thickness (along line 3) have tensile stresses at the surfaces and compression at the center. The eigenstrain functions to generate these residual stresses have the form:

$$\epsilon_{ij}^{*} = -\frac{\sigma^{*}}{E} f_{ij}(x, y, z) \tag{6}$$

where $\sigma^{*} = \sigma_{ys}^{wm}$ scales the generated residual stress amplitudes defined by the normalized functions $f_{ij}(x,y,z)$. A unit temperature change coupled with anisotropic thermal expansion coefficients, α_{ij}, equal to the ϵ_{ij}^{*} values sampled at element centers provides a simple mechanism to introduce these eigenstrains into the 3-D finite element model ([*14*] describes this process in more detail).

Specimen Configuration

Finite element analyses of the WSMF connection use a beam section with depth $d = 762$ mm, flange width $b_f = 152$ mm, web thickness $t_w = 13$ mm, and flange thickness $t_f = 25$ mm (see Fig. 1). The column dimensions correspond to a W14 × 176 section. Inspections of welded connections in buildings and in full-scale joints fabricated under laboratory conditions [*2*] reveal lack-of-fusion type defects having variable depth that can extend the full width of the weld. These observations led to the adoption in this study of a uniform depth, sharp crack that extends the full width of the beam flange. The crack "depth" equals the applicable backup bar dimension (10 mm), plus an additional $a_0 = 5.7$ mm to reflect a typical bead size for the weld root pass. The analyses here consider only the pre-Northridge weld configuration at the lower flange shown in Fig. 1. Our detailed studies [*14-16*] examine the effects of suggested improvements in the geometry (e.g. removal of backup bar), changes in material flow properties, access hole geometry, and of the ability of a simple pull-plate specimen [*29, 30*] to reproduce fracture conditions present in connection tests.

Material Properties

Figure 4 shows the true stress-true strain curves for quasi-static loading constructed from the engineering strain-stress curves reported by Kaufmann et al. [*30*]. The finite element models have three different materials (beam A36, column A572 and weld metal E70T-4). The current models neglect changes in material properties across heat-affected zones, i.e., the idealized crack plane lies along a bimaterial interface between the column flange material (A572) and the weld material (E70T-4) as the detail sketch in Fig. 1 indicates.

These three materials (all moderate strength steels) have flow properties that exhibit relatively strong sensitivity to load rates. During a strong near-field earthquake, Deierlein [*31*] estimates the time-to-peak load in the first half-cycle for welded, mid-rise steel buildings lies in the range of 0.25-0.5 seconds. Fracture toughness values in the DBT region at intermediate loading rates in the range of 60-120 MPa$\sqrt{\text{m}}$ (from correlations to CVN data), combined with the estimated times to peak load, lead to expected $\dot{K}_I$ values for welded connections of 100-500 MPa$\sqrt{\text{m}}/s$. Our preliminary dynamic analyses of the connection at imposed beam tip velocities to produce these $\dot{K}_I$-values show that the strain-stress concentration ahead of a sharp fatigue crack in a welded connection amplifies nominal strain rates in the beam flange to levels of 0.05-1 ($1/s$) over localized volumes of material along the crack front where fracture initiates.

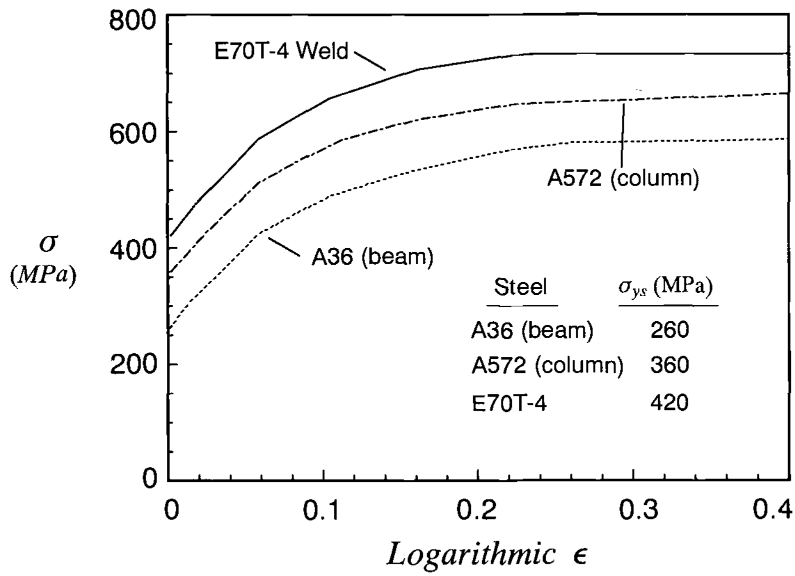

Figure 4. *True stress-logarithmic strain curves for steels used in the quasi-static finite element analyses of the WSMF connection.*

High-rate tensile tests for specimens extracted from actual WSMF connections are not available at this time. To proceed, we estimate values of the ratio $\sigma_{ys}^{dyn}/\sigma_{ys}^{static}$ at different strain rates using the empirical correlation discussed by Barsom and Rolfe [*32*]

$$\frac{\sigma_{ys}^{dyn}}{\sigma_{ys}^{static}} = 1 + \left[\frac{\frac{2}{3} \times 10^6}{\sigma_{ys}^{static} \log\left\{2 + \frac{2}{3} \times 10^6 \frac{\sigma_{ys}^{static}}{\dot{\epsilon}}\right\}(T + 273)} - \frac{190}{\sigma_{ys}^{static}} \right] \tag{7}$$

where σ_{ys}^{static} denotes the static yield stress at room temperature (MPa), and T in (°C) and $\dot{\epsilon}$ refer to the temperature and strain rate of interest, respectively. Figure 5a shows the results of applying this correlation over a wide range of strain rates to the measured σ_{ys}^{static} values ($T = 20$°C, 0.2% strain) reported for A36 (260 MPa), A572 (360 MPa) and E70T-4 (420 MPa) [*29*]. Eq. (7) is evaluated at each decade of strain rate with a smooth curve passed through the resulting values. A36 has a 45% increase of yield stress at a strain rate of 1 ($1/s$) and a 65% increase at a rate of 10 ($1/s$). The less rate sensitive A572 has an increase of 40% in the yield stress at a strain rate of 10 ($1/s$). The higher yield stress E70T-4 shows less sensitivity with a 25% of increase in the yield stress at a strain rate of 10 ($1/s$).

The nonlinear finite element analyses include strain-rate effects on the material flow properties through a viscoplastic overstress model (Perzyna [*33*], Cristescu [*34*]) of the form

$$\dot{\epsilon}^{vp} = \begin{cases} D\left[\left(\dfrac{q}{\sigma_e}\right)^{\gamma} - 1\right] & \dfrac{q}{\sigma_e} > 1 \\ 0 & \dfrac{q}{\sigma_e} \leq 1 \end{cases}, \tag{8}$$

where q represents the rate-dependent (uniaxial) tensile stress and σ_e denotes the static (uniaxial) tensile stress. Here D and γ define material parameters that vary with temperature but not loading rate.

Figure 5b illustrates the fitting process to find D and γ for the A36 steel. The symbols represent the measured (static) yield stress for A36 (260 MPa) scaled for strain-rate effects by Eq. (7), i.e., these points lie along the A36 curve shown in Fig. 5a. The power-law curve reflects the calibrated values of $D = 0.002$ ($1/s$) and $\gamma = 17$ found using a visual fit to the A36 values. A similar calibration for A572 yields $D = 0.075$ ($1/s$) and $\gamma = 17$; for E70T-4 the parameters have calibrated values $D = 0.2$ ($1/s$) and $\gamma = 25$. In each case, the piecewise-linear representation of the measured (static) stress-strain curves from Fig. 4 defines the variation of σ_e with plastic strain.

Figures 6a-b show the complete uniaxial true stress *vs.* logarithmic strain curves used in the finite element analyses for steels A36 and weld metal E70T-4 at different strain rates (results for A572 are very similar and are omitted for brevity). The solid line on each plot describes the measured stress-strain curve for static loading. Stress values are normalized by the static yield stress for each material. In each case, the power-law model evaluated at a low strain rate reproduces the measured, static stress-strain curve. Figure 6 shows clearly the marked effect of strain rate on the flow properties for the A36 steel with diminished effects for E70T-4. The crack front in the root pass of the weld considered in the analyses lies along the interface between the A572 column and E70T-4 weld.

Loading and Boundary Conditions

In all cases the column ends have hinged supports (no translation, rotation unrestrained). The loading protocol for quasi-static analyses follows this sequence: (1) Apply the eigenstrains to introduce residual stresses through a total temperature increase of 1°. The temperature increase acts with specified anisotropic thermal expansion coefficients for each element in the weld region to generate the eigenstrains. Use ten, uniform increments of 0.1° to resolve the small amount of resulting plastic deformation; (2) Increase the beam tip deflection monotonically (quasi-static) through 500 variably sized increments to reach a maximum tip deflection of 254 mm. This loading level develops a full plastic hinge in the connection region. The residual stresses alone generate a $K_I = 15$ MPa$\sqrt{\text{m}}$ at the center of the beam flange.

The dynamic analyses impose eigenstrains in 200 increments of 0.005° (to prevent any rate effects) then increase the displacement imposed at the end of the beam using 500, fixed-size increments of $\Delta w = 0.5$ mm. A range of loading rates, $\dot{K}_I$, then follow in various analyses by fixing the time increment per step. A beam tip velocity of $\dot{w} = 72.6$ mm/s, for example, generates a steady $\dot{K}_I = 200$ MPa$\sqrt{\text{m}}/s$ during yield of the beam flange. At these global loading rates, inertial (stress wave) effects have no influence on the crack front loading. However, the locally elevated strain rates ahead of the initially sharp crack front increase the stresses and reduce the fracture toughness. This permits a simplification in the present

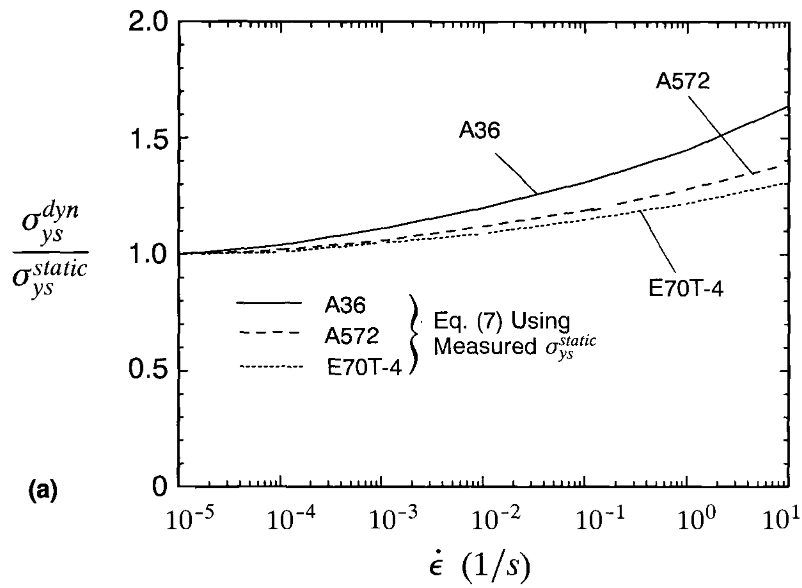

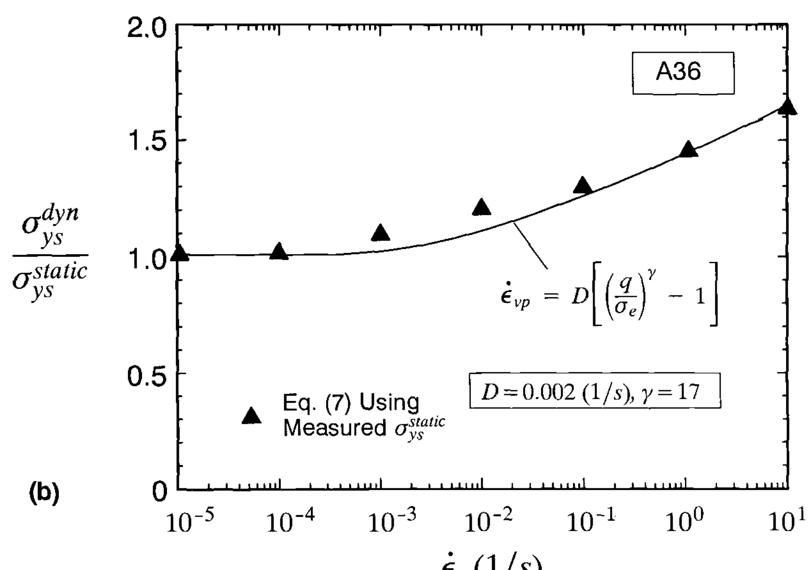

Figure 5. *(a) Estimated effects of strain rate on the yield stress of steels used in welded connections, (b) Fit of power-law viscoplastic model used in finite element analyses to estimated dynamic yield stress for A36 at varying strain rates.*

analyses—the (implicit) computations neglect mass in the model but they have time dependent loading which introduces the applicable strain rate in the stress updating process.

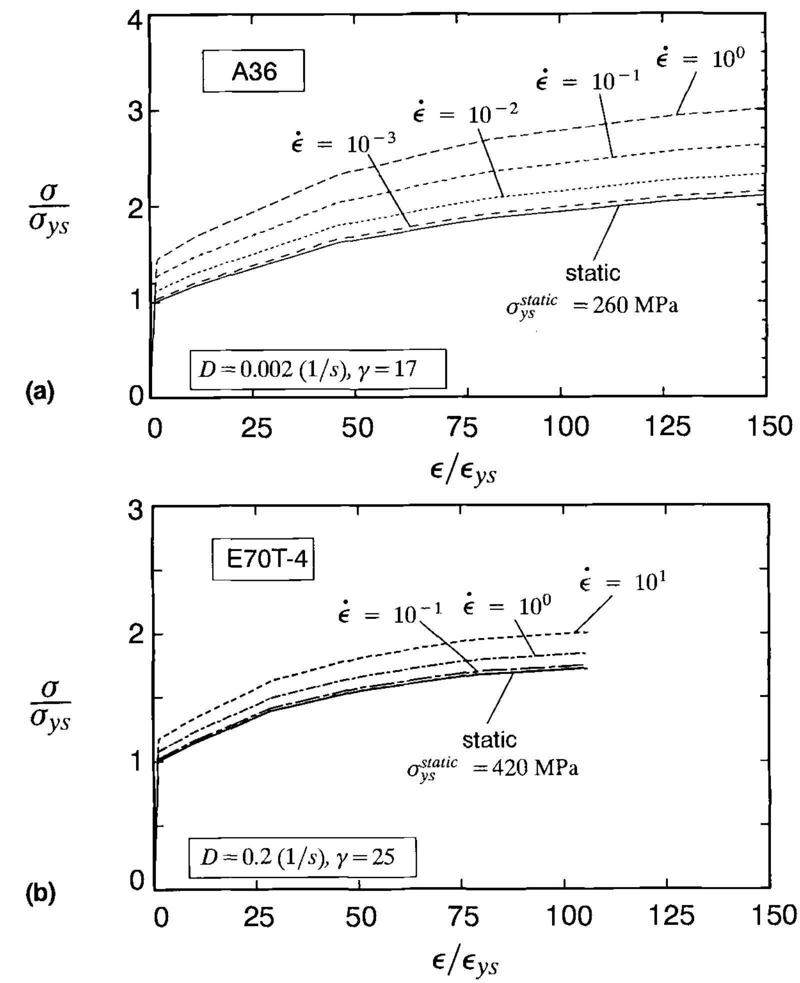

Figure 6. *True stress-logarithmic strain curves at different strain rates for steels used in finite element analyses of the WSMF connection. Rate-dependent curves are obtained from the power-law, viscoplastic model, Eq. (8) with calibrated parameters D and γ shown for each material. Stresses are normalized by the measured static yield stress for each material. Static curves are measured values [29].*

Finite Element Models

Symmetry of the geometry and loading permits modeling of only one-half of the T-connection (see Fig. 7). The mesh has 34 focused rings of elements in the radial direction surrounding the crack front and 20 elements along the crack front length (half of the beam flange width). The smallest element at the crack front has a size of 10 μm. Previous analytical studies [35] have demonstrated the requirement for this level of mesh refinement to resolve accurately the Weibull stress values over the full loading range from SSY to plastic hinge formation. The analysis formulation includes large displacement/rotation effects and finite strain effects along the crack front (the crack tip has an initial radius of 20 μm to enhance convergence of the finite-strain solutions).

To compute the threshold value of Weibull stress, $\sigma_{w-\min}$, needed in Eq. (5) a SSY boundary layer model in plane strain is analyzed for increasing remote boundary velocities corresponding to a mode I field (with zero T-stress). The model has thickness equal to the beam flange width, i.e., the crack front length. The SSY mesh has identical layout to the crack front mesh in the connection. $\sigma_{w-\min}$ then corresponds to the value of σ_w when loading of the SSY model reaches $K_I = 20$ MPa$\sqrt{\text{m}}$ at the $\dot{K}_I$ of interest. Application of standard isoparametric procedures to evaluate Eq. (3) over element volumes yields the numerical value of σ_w at each analysis load step [36] with the reference volume (V_0) set to 1 mm^3 in all calculations. The absence of fracture toughness values for the A572 and E70T-4 materials precludes consideration of two sets of Weibull stress parameters—the calibrated parameters discussed below thus represent an averaged parameter set for cracks on the bimaterial interface.

Models are constructed using three-dimensional, 8-node elements with $\bar{B}$ formulation. J-integral values are evaluated with a domain integral procedure [37] using domains defined outside the material having non-proportional strain histories at the crack front. The computed J-values reflect finite strain effects and thermal strains used to produce the residual stresses. With the inclusion of additional terms that arise from the anisotropic thermal expansion coefficients to model the eigenstrains [14], the J-values maintain a strong path independence. The WARP3D [38] code used for these analyses supports computation of crack front average J-values and pointwise J-values at each node location along the crack front.

Results and Discussion

Calibration of Weibull Stress Parameters

In the absence of fracture toughness values for the materials measured with conventional laboratory tests, e.g., deep-notch C(T) specimens, the distribution of failure moments from the quasi-static, full-scale connection tests provide the only data available to calibrate the values of m, σ_u and $\sigma_{w-\min}$ (see Fig. 2). The following steps comprise the calibration process: (1) conduct a 3-D nonlinear analysis of the full connection containing a crack in the root pass as shown in Fig. 1 under quasi-static loading and including the residual stresses; (2) post-process the finite element stress fields at each load step to construct a σ_w *vs.* M/M_P plot for a range of assumed m values, e.g., $m = 7$–10; (3) for each m value, analyze the SSY boundary layer model to find $\sigma_{w-\min} = \sigma_w$ at $K_I = 20$ MPa$\sqrt{\text{m}}$; (4) using the experimental M/M_P value at 63.2% failure probability (for convenience) in Fig. 2, find the corresponding value of σ_w for each assumed m-value which sets the σ_u-value. This process creates multiple sets of candidate m, σ_u and $\sigma_{w-\min}$ values. Insert these values into Eq. (5) and plot the Weibull stress model predictions of cumulative failure probability with increasing applied beam moment.

Figure 8a shows the results of this calibration procedure. The Weibull stress model of Eq. (5) exhibits a strong sensitivity to variations in the parameters with $m = 8.5$ and corresponding values $\sigma_u = 2.4\sigma_{ys}$, and $\sigma_{w-\min} = 1.25\sigma_{ys}$ giving a good overall, visual fit (the σ_u

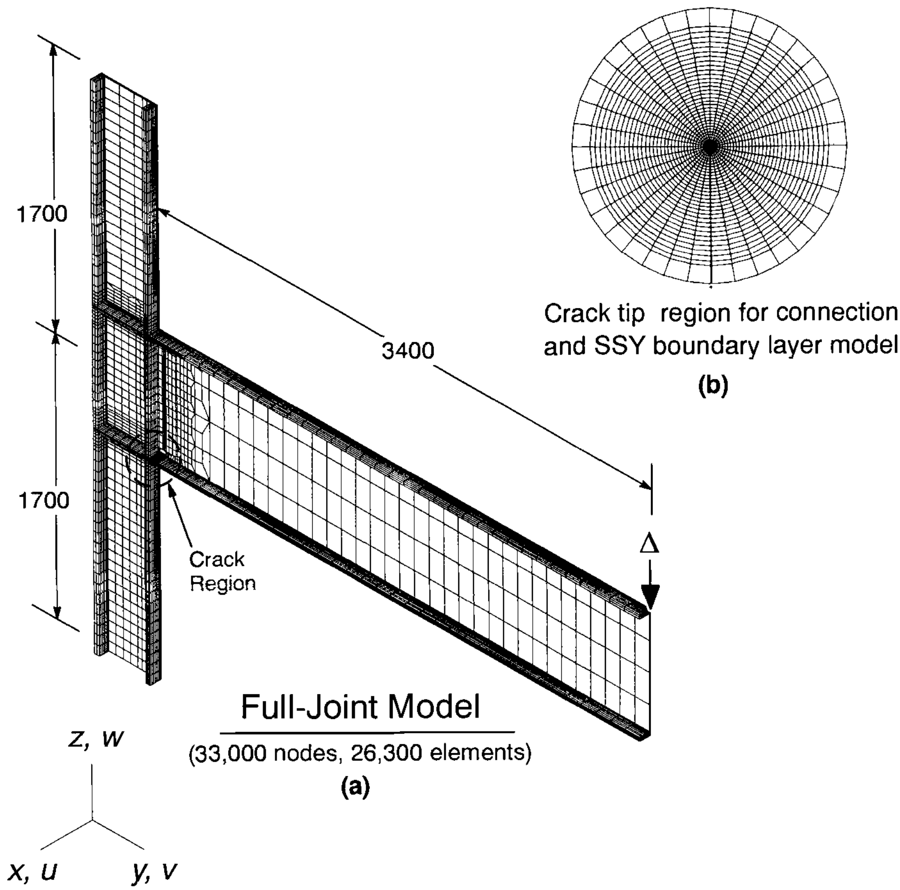

Figure 7. *Finite element mesh for: (a) half-symmetric model for the WSMF connection; (b) mesh at crack tip region in connection model which corresponds to the SSY boundary layer mode . All dimensions in mm.*

must change should the reference volume, V_0, be modified). The assumptions needed to reach this point do not appear to warrant a more elaborate calibration process, e.g., maximum likelihood estimators often used in calibrations with fracture toughness values. Figure 8b shows that the calibrated Weibull distribution from the finite element analyses lies well within the 90% confidence bounds for the median rank estimates of the experimental data. The $m = 8.5$ value calibrated here for the crack located between the A572 column flange and the E70T-4 weld metal compares favorably to values found by Gao et al. [*20,39*] of $m = 7.8$ for A36 steel plate and $m = 10$ for an A515-70 steel plate often found in older pressure vessels.

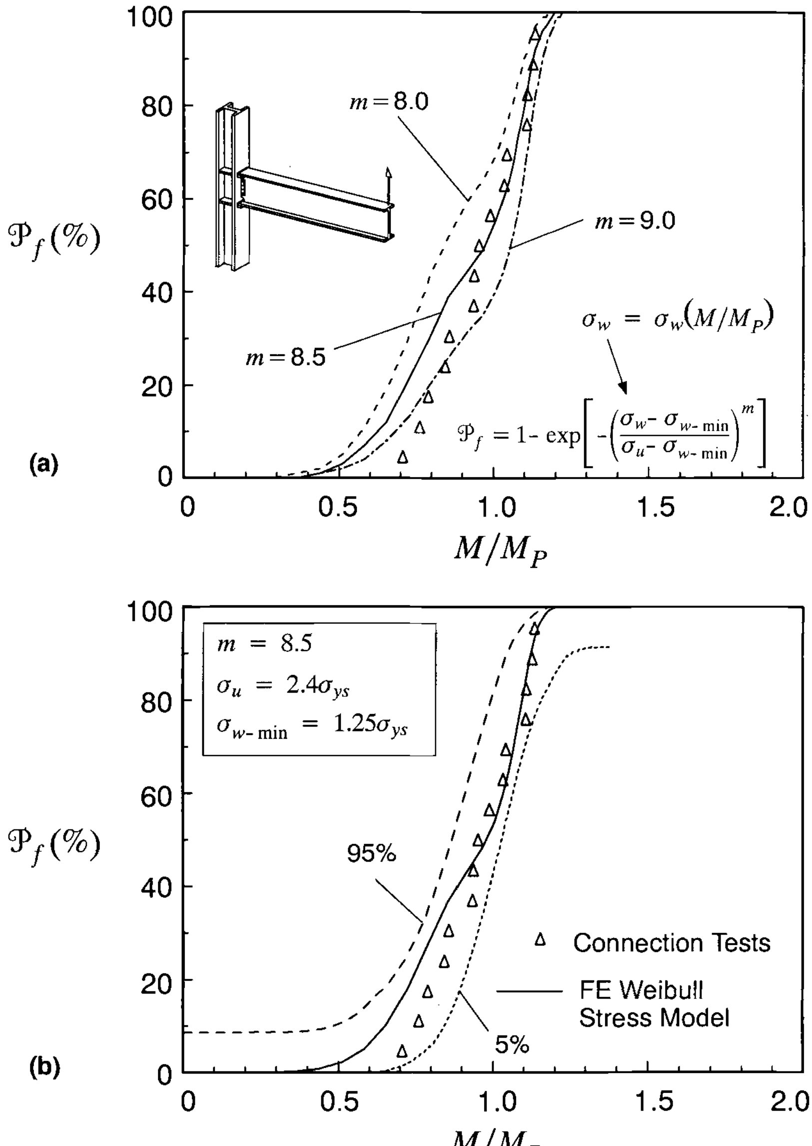

Figure 8. *(a) Sensitivity of cumulative failure probability predicted by the Weibull stress model to the parameters; (b) Fit of calibrated Weibull stress model to median rank estimates of fracture moments measured in full-scale tests on pre-Northridge connections.*

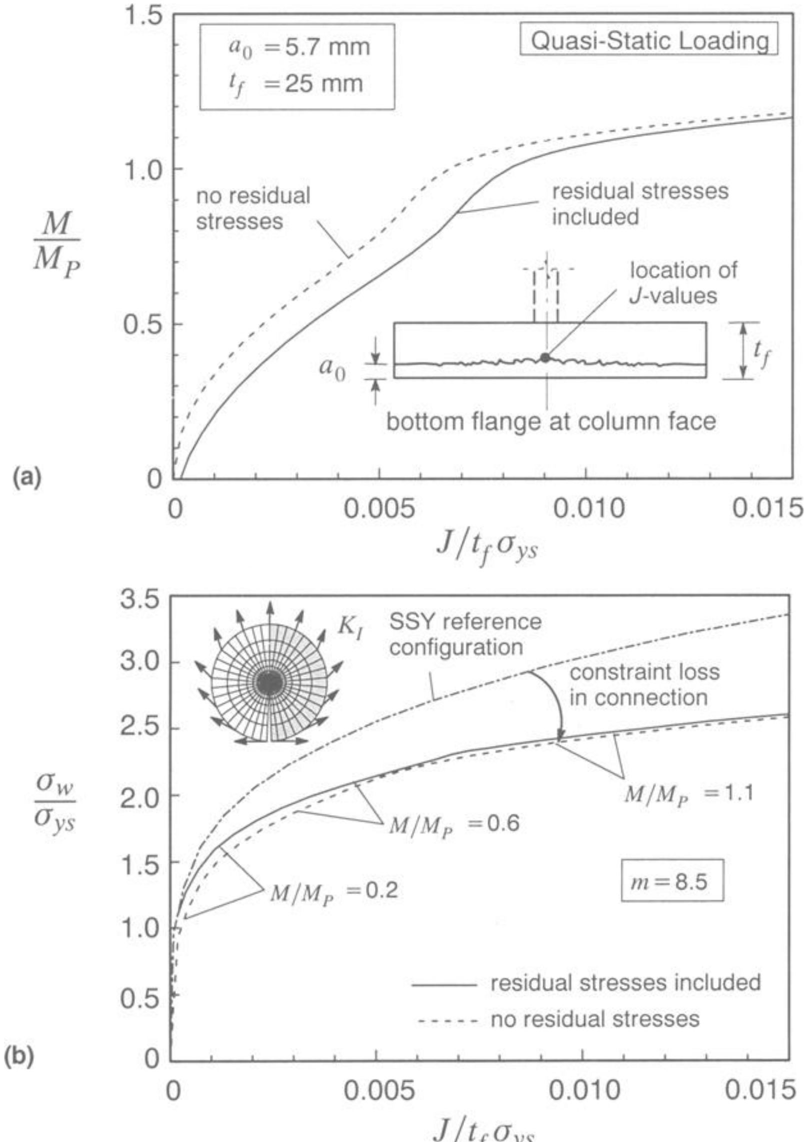

Figure 9. *Effects of welding induced residual stresses on fracture behavior in WSMF connection for a (root pass) weld crack extending full width of the beam flange. (a) Development of J at center of beam flange; (b) Evolution of Weibull stress values with J showing constraint loss relative the SSY reference condition for quasi-static loading.*

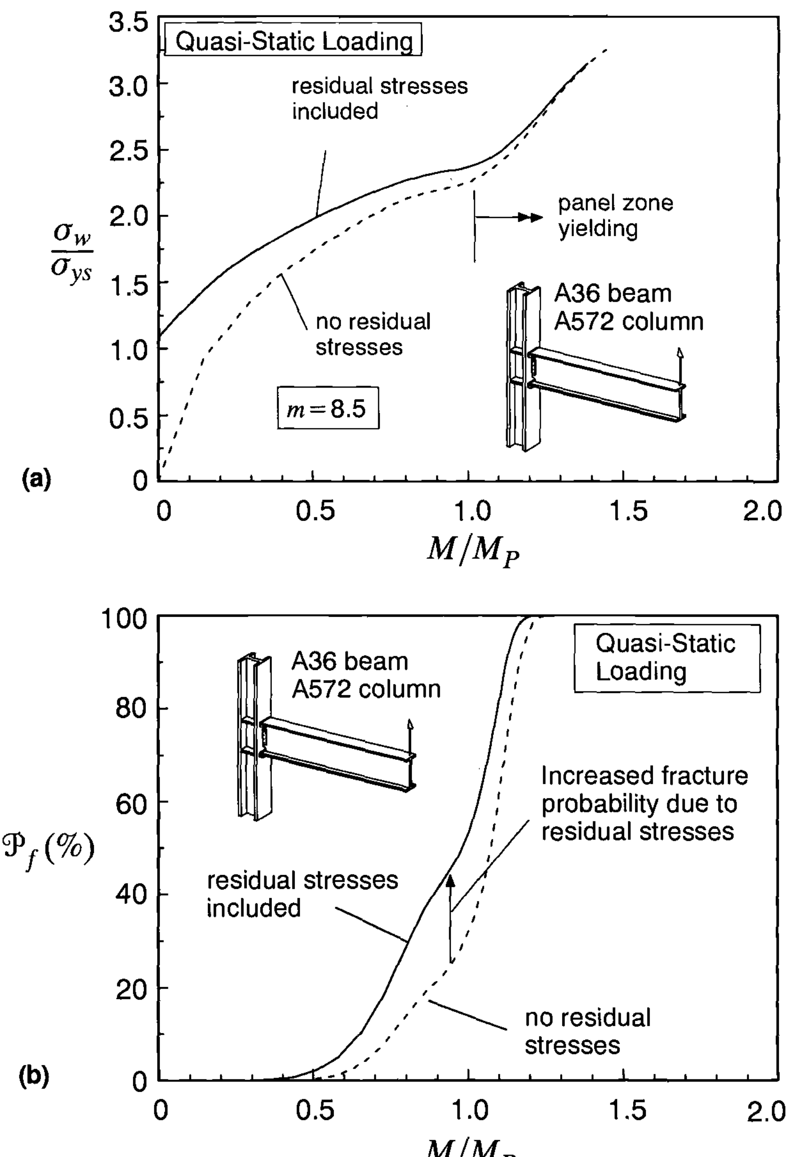

Figure 10. *Effects of welding induced residual stresses on fracture behavior in WSFM connections for a (root pass) weld crack extending full width of the beam flange. (a) Evolution of Weibull stress with moment at the column face. (b) Predicted effects of residual stresses on probability of cleavage fracture.*

Effects of Residual Stresses and Crack Front Constraint

Figure 9a shows the computed relationship between beam moment at the column face and J-values with and without residual stresses. These locally computed J-values refer to the center of the beam flange as indicated on the figure, where the largest values occur across the full-width of the crack. Early in the loading, the residual stresses increase J-values by approximately 20% or equivalently about 15 MPa$\sqrt{m}$ in terms of the stress intensity factor. This approximately fixed increment of crack front loading remains effective throughout but decreases in relative magnitude as the total J-values increase rapidly once the connection progresses toward formation of a plastic hinge.

Figure 9b shows the development of Weibull stress for the crack front with loading described by J-values at the center of the flange. Corresponding M/M_P values are indicated along the connection response curves. In this figure, differences in the σ_w values at fixed J-values develop from variations in the crack front constraint, i.e., the same J-value leads to stress fields having different magnitudes. At relatively low J-values corresponding to $M/M_P \lesssim 0.6$, the residual stresses marginally increase the σ_w values and thus the constraint levels. These two figures make clear that the increased J-values, rather than constraint increases, represent the key effect of residual stresses on fracture.

Figure 9b also shows the Weibull stress computed using the bimaterial, SSY boundary layer solution without residual stresses. This curve represents the high levels of Weibull stress with increased J-values found in deep-notch SE(B) and C(T) specimens tested to measure fracture toughness of materials. Almost immediately upon loading, the Weibull stress values for the connection fall below the SSY levels indicating a significant reduction in crack front stresses compared to the high-constraint, SSY values. From a fracture viewpoint, the relatively shallow crack depth of the lower-flange weld combined with the predominantly tensile (local) loading produces a "low" constraint configuration. Only early in the loading at $M/M_P \lesssim 0.1$ does the small additional constraint generated by the residual stresses restore the connection σ_w values to the SSY levels.

Figure 10a re-plots the development of Weibull stress with loading described by normalized beam moments at the column flange. The strong upswing in σ_w values at $M/M_P \approx 1$ for both curves corresponds to the onset of panel zone yielding in the column (the panel zone is the column web material located between the horizontal continuity plates). When cast in terms of beam moment rather than J, the initial influence of residual stresses prior to mechanical loading becomes far more clear. The relatively large σ_w values early in the loading caused by the residual stresses must substantially increase the probability for cleavage fracture when loading is described by the beam moments. At higher load levels corresponding to a full plastic hinge in the connection, the relative effect of residual stresses diminishes. These observations agree with the conventional tenet that residual stress effects decrease in relative significance under large scale yielding. Figure 9b also shows this result at high J-values where the connection curves with and without residual stresses effectively coincide.

Figure 10b summarizes the computational results for quasi-static loading in the most usable form for engineering assessments. Values of σ_w in Fig. 10a are inserted into Eq. (5) to yield the cumulative probabilities for cleavage fracture with loading described by the normalized beam moments. Residual stresses increase the (absolute) cumulative fracture probabilities by 10% for M/M_P values < 0.75, increasing to 20% at M/M_P values ≈ 0.9. The results in Figs. 9(a,b) confirm that nearly all of the increased failure probability occurs from the increased crack front J-values caused by the residual stresses rather than increased crack front constraint.

Loading Rate Effects on Cleavage Fracture

Figure 11a shows the fracture response of the connection for imposed beam tip velocities of $\dot{w} = 72.6$ mm/s and 127 mm/s. These global loading rates generate nearly constant $\dot{K}_J$ values of ≈ 210 and ≈ 370 MPa$\sqrt{\text{m}}$/s at the center of the beam flange during the time period while plasticity remains confined to the immediate crack front region. These values lie in the "intermediate" range of dynamic loading rates discussed by Barsom and Rolfe [*32*] and characterize the crack front response during well contained plasticity (SSY). The $\dot{K}_J$ value of ≈ 210 MPa$\sqrt{\text{m}}$/s corresponds to the crack front loading rate imposed in the "pull-plate" specimen developed and tested dynamically to simulate the full connection response [*29,30*].

At each time step in the analyses, K_J values are given by the usual plane-strain conversion, $K_J = \sqrt{EJ/(1-\nu^2)}$, with rates then obtained using a central difference method, $\dot{K}_J(t) = [K_J(t+\Delta t) - K_J(t-\Delta t)]/2\Delta t$. The beam lower flange yields gradually starting at 0.2–0.3 sec for the higher loading rate and at 0.4–0.5 sec for the lower rate. Once yielding occurs in the beam at the column face, the localized deformations (curvatures) imposed by the beam continue to load the crack front at sustained $\dot{K}_J$ values.

Figure 11b compares the evolution of Weibull stress with beam moment for the static and the two dynamic loading rates (all three analyses include residual stresses). The local Weibull stress parameter shows an effect of high strain rates (and thus higher stresses) at the crack front immediately upon loading and this increase remains in effect throughout. The non-zero value of σ_w at $M = 0$ both arise from the residual stresses imposed prior to the mechanical load. For each case, σ_w increases more rapidly with the onset of panel zone yielding.

The previously described calibration process to estimate the Weibull stress parameters using experimental data from connection tests performed under quasi-static loading yields values of $m = 8.5$, $\sigma_u = 2.4\sigma_{ys}$, and $\sigma_{w\text{-min}} = 1.25\sigma_{ys}$ ($\sigma_{ys} = 260$ MPa, the yield strength of the beam flange). The dynamic analyses described here include the effects of strain rate on the material flow properties which lead to increased values of σ_w compared to those for static loading at the same value of M/M_p. The effect of loading rate on key Weibull stress parameters m and σ_u remains an active area of research [*21,22,23*]. Based on the experimental/computational studies by Gao et al. [*21*] for an A515-70 low-strength pressure vessel steel and by Minami et al. [*22,23*] for moderate strength structural steels, we assume that the Weibull stress parameters, m and σ_u, remain invariant of loading rate over the range of rates expected during seismic events ($\dot{K}_I < 500$). Loading of the bimaterial, SSY boundary layer model over a range of $\dot{K}_J$ provides the needed $\sigma_{w\text{-min}}$ values as $\sigma_{w\text{-min}} = \sigma_w$ when $K_J = 20$ MPa$\sqrt{\text{m}}$ in each case.

Figure 12 summarizes the dynamic loading results in the most usable form, showing the effects of residual stresses and loading rate on the probability of cleavage fracture with moment at the column face as the loading parameter. For static loading, the residual stresses increase the failure probability approximately 10% (in absolute terms) for $M/M_P < 0.75$, increasing to 20% for $M/M_P \approx 0.9$. At a fixed 5% failure probability, for example, the residual

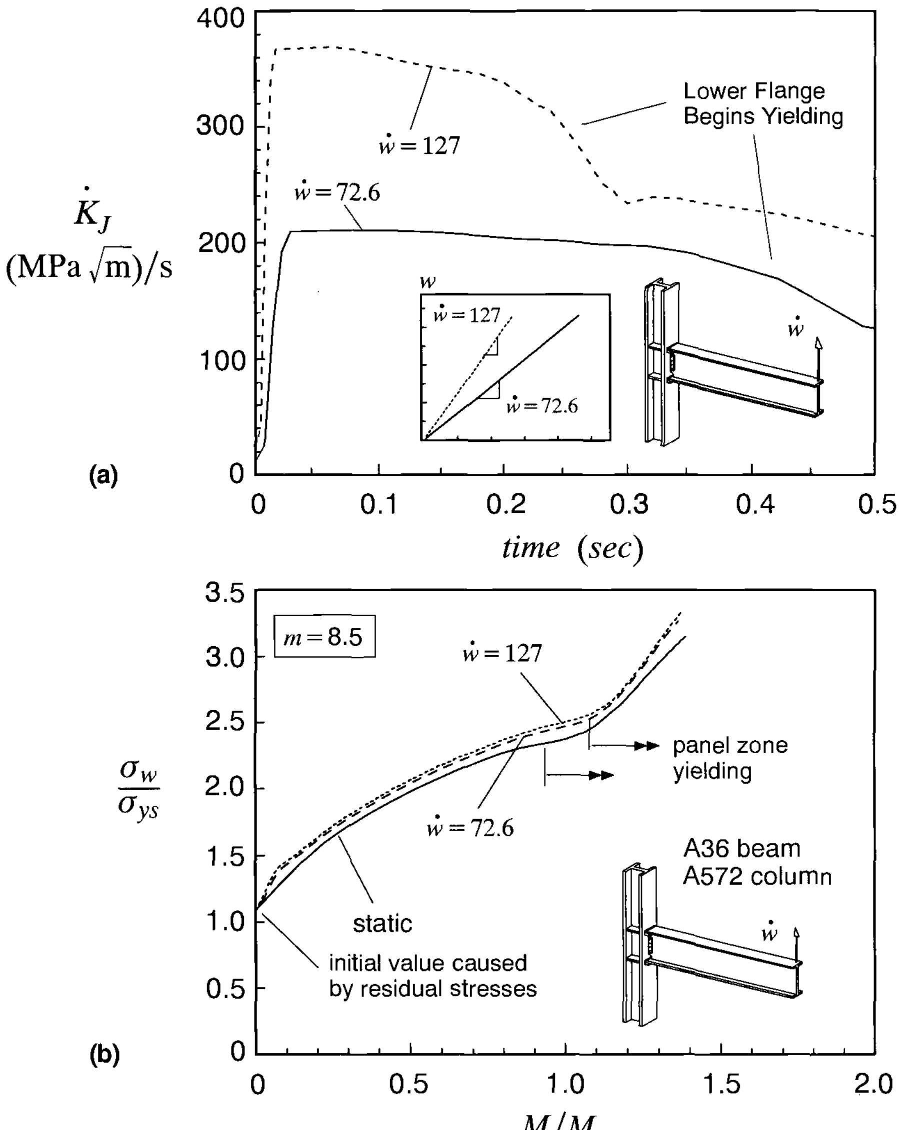

Figure 11. *Loading rate effects in WSMF connection: (a) Stress intensity factor rates. (b) Evolution of the Weibull stress with beam moment. Velocities shown in mm/s.*

stresses reduce the static moment from M/M_P of 0.75 to 0.55; dynamic loading further reduces the moment to 0.5. At such low failure probabilities, these results suggest that dynamic loading has only a small effect on the corresponding beam moment, i.e., the residual stresses continue to play the key role. As the beam flange continues yielding and the panel zone be-

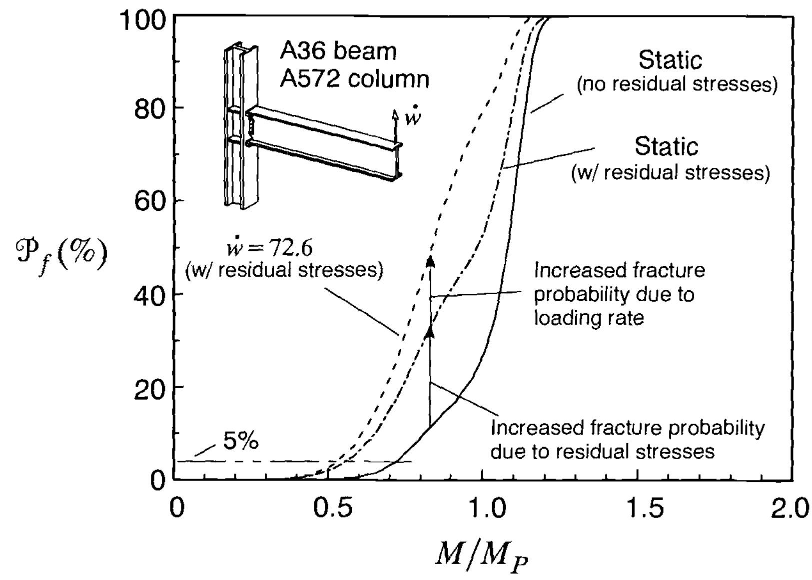

Figure 12. *Cumulative failure probabilities predicted by Weibull stress model. Velocities in mm/s.*

gins to yield, the effects of loading rate increase in relative importance. At $M/M_P = 0.85$ as indicated on the figure, dynamic loading of the connection at the $\dot{w} = 72.6$ mm/s rate increases the failure probability by $\approx 20\%$ (in absolute terms) compared to static loading.

The values of σ_w and thus $\mathcal{P}_f$ in the numerical comparisons here depend directly on the calibrated values of the three parameters m, σ_u, and $\sigma_{w-\min}$ and the rate dependent stress-strain curves for the materials. Changes in these parameters alter the *specific* values of $\mathcal{P}_f$ but not necessarily the relative effects of residual stress and dynamic loading compared to the simpler case of static loading without residual stresses. $\mathcal{P}_f$ varies nonlinearly with changes in the parameters but generally a larger m reduces the scatter, σ_u moves the $\mathcal{P}_f$ curve horizontally and $\sigma_{w-\min}$ affects mainly the tail of the distribution at low probabilities.

Concluding Remarks

This study describes probabilistic modeling of the nonlinear fracture behavior in the beam lower-flange to column welds found in moment resistant frames of the design commonly used prior to the Northridge earthquake. 3-D finite element analyses, coupled with an advanced micro-mechanical fracture model based on the Weibull stress, are used to assess the relative significance of loading rate and residual stresses. The present work considers only the initiation of *brittle fracture* triggered by a *transgranular cleavage* mechanism typical of that exhibited by ferritic steels (and welds) operating in the DBT region.

The finite element models represent the commonly used T-configuration tested in laboratories to simulate exterior connections. Loading takes place through a specified, constant velocity imposed at the end of the beam. Beam tip loading in the connection at 72.6 mm/s provides $\dot{K}_J$ expected in cracked connections. A realistic residual stress field is introduced using an eigenstrain approach. Measured fracture loads from 15 earlier tests conducted as part of the SAC-Steel and other programs on nearly identical, full-scale T-connections of the pre-Northridge design provide a statistically significant data set to enable calibration of the micro-mechanical model. The computational studies present the cumulative failure probabilities predicted by the Weibull stress model with loading expressed in terms of the normalized beam moment at the column flange.

- A two-parameter Weibull distribution describes very well the measured distribution of fracture moments in the 15 nearly identical T-connection tests conducted under quasi-static loading on the pre-Northridge design (A36 beams, A572 columns, E70T-4 welds).
- Post-processing of the 3-D, nonlinear finite element analyses to compute the evolution of Weibull stress values with beam moments at the column face enables calibration of parameters for the modified Weibull stress model: $m=8.5$, $\sigma_u=2.4\sigma_{ys}$, and $\sigma_{w-\min}=1.25\sigma_{ys}$. The calibration shows a strong sensitivity to the $m=8.5$ value. The calibrated Weibull distribution from the finite element analyses lies well within the 90% confidence bounds for the experimental data.
- Welding-induced residual stresses increase the severity of crack front conditions by imposing an initial K_I of ≈ 15 MPa$\sqrt{\text{m}}$. This increment remains present throughout the loading history but decreases, in relative terms, compared to nonlinear J-values generated by the applied loads. Residual stresses increase the (absolute) cumulative fracture probabilities by 10% for M/M_P values < 0.75, and by 20% for M/M_P values > 0.9.
- The Weibull stress model demonstrates that the pre-Northridge weld detail represents a low-constraint, crack configuration for cleavage relative to the crack front conditions experienced in conventional deep notch fracture test specimens (three-point bend and compact tension). The crack front stresses in these connections fall below the (high constraint) reference small-scale yielding values for $M/M_P > 0.2$.
- Under dynamic loading, the crack front loading rate ($\dot{K}_J$) decreases slowly once the beam flange yields in the connection. The crack front in the connection experiences continued loading from localized beam bending at the column face.
- When the beam moment at the column face reaches $M/M_P=0.85$ ($K_J\approx 100$MPa$\sqrt{\text{m}}$), dynamic loading of the connection at intermediate loading rates ($\dot{K}_J\approx 200$ MPa$\sqrt{\text{m}}/s$) increases the failure probability by $\approx 20\%$ (in absolute terms) compared to static loading (both with residual stresses included).

Acknowledgments

The work reported here was supported in part by the NASA-Ames Research Center through grant NAG 2-1126 and by the Nathan and Anne M. Newmark Fund.

References

[1] The SAC Joint Venture is a partnership of the Structural Engineers Association of California, the Applied Technology Council, and the California State Universities for Earthquake Engineering.

[2] Kauffmann, E. J., Fisher, J. "Fracture analysis of failed moment frame weld joints produced in full-scale laboratory tests and buildings damaged in the Northridge earthquake." *SAC* 95-08, part 2, 1996;1-1 - 1-21.

[3] Interim Guidelines: *Evaluation, Repair, Modification and Design of Welded Steel Moment Frame Structures*. FEMA-267, Federal Emergency Management Agency, 1995.

[4] Barsom, J., Pellegrino, J. *Failure analysis of welded steel moment-resisting frame connections.* Part II: *pre-Northridge welded steel moment frame connections*. SAC/ BD-99/23,2000.

[5] Connection Test Summaries. *Program to reduce the earthquake hazards of steel moment frame structures.* FEMA-289, 1997.

[6] Sorem, W., Dodds, R., and Rolfe, S. "Analytical comparison of short crack and deep crack CTOD fracture specimens of an A36 steel," *ASTM STP 1074*, 1988, pp. 3-23.

[7] Joyce, J., and Link, R., "Fracture behavior of surface crack tension specimens in the ductile-brittle transition region," *ASTM STP 1332*, 1999, pp. 55-81.

[8] Ohata, M., Minami, F., Toyoda, M., "Local approach to strength mismatch effect on cleavage fracture of notched material," *Journal de Physique IV*, Vol. 6, 1996 pp. 269-278.

[9] Beremin, FM. "A local criterion for cleavage fracture of a nuclear pressure vessel steel," *Metallurgical Transactions,* Vol. 11, 1983, pp. 2277-2287.

[10] Wallin, K., "The scatter in K_{Ic} results," *Engineering Fracture Mechanics* Vol. 19, 1984, pp. 1085-1093.

[11] Dodds, R., Shih, C., and Anderson, T., "Continuum and micromechanics treatment of constraint in fracture," *International Journal of Fracture*, Vol. 64, 1993, pp. 101-133.

[12] Changbin, J., and Chen, W., "Fracture strength of welded flange-bolted web connections," *Journal of Structural Engineering*, Vol. 125, 1999, pp. 565-571.

[13] Chi, W., Deierlein, G., and Ingraffea, A., "Fracture toughness demands in welded beam-column moment connections," *Journal of Structural Engineering* , Vol. 126, 2000, pp. 88-97.

[14] Matos, C., and Dodds, R., "Modeling the effects of residual stresses on defects in welds of steel frame connections," *Engineering Structures*, 2000, pp. 1103-1120.

[15] Matos, C., and Dodds, R., "Probabilistic fracture modeling of welds in steel frame connections. Part I: Quasi-static loading," *Engineering Structures*, Vol. 23, 2001, pp. 1101-1130 .

[16] Matos, C., and Dodds, R., "Probabilistic fracture modeling of welds in steel frame connections. Part II: Seismic loading," Submitted to *Engineering Structures*.

[17] Mudry, F., "A local approach to cleavage fracture," *Nuclear Engineering. & Design*, Vol. 105, 1987, pp. 65-76.

[18] Seismic Provisions for Steel Buildings. American Institute of Steel Construction, AISC, Chicago, IL, 1997.

[19] Interim Guidelines: Advisory No. 1, Supplement, FEMA-267A, March 1997.

[20] Gao, X., and Dodds, R., "A Weibull stress model to predict cleavage fracture in plates containing surface cracks," *Fatigue & Fracture of Engineering Materials and Structures*, Vol. 22, 1999, pp. 481-493.

[21] Gao, X., Dodds, R., Tregoning, R., and Joyce, J., "Effects of loading rate on the Weibull stress model for simulation of cleavage fracture in ferritic steels," *Fatigue & Fracture of Engineering Materials and Structures*, Vol. 24, 2001, pp. 551-564.

[22] Minami, F., Ochiai, T., Kubo, T., Shimanuki, H., and Arimochi, K., "Evaluation of pre-straining and dynamic loading effects on fracture toughness of structural steels by the local approach," *Structural Integrity of Pressure Vessels, Piping, and Components ASME 2000, Pressure Vessel & Piping Conference.*

[23] Minami, F., Ochiai, T., Hashida, T., Arimochi, K., and Konda, N., "Local approach to dynamics fracture toughness evaluation," to appear in *ASTM STP* 31st National symposium on *Fatigue and Fracture Mechanics*, 2001.

[24] Lei, Y., O'Dowd, N., and Webster, G., "Fracture mechanics analysis of a crack in a residual stress field," *International Journal of Fracture*, Vol. 106, 2000, pp. 195-216.

[25] Mura, T. *Micromechanics of Defects in Solids.* Kluwer Academy Publishers. The Netherlands, 1991.

[26] Ueda, Y., and Fukuda, K., "New measuring method of three dimensional residual stress in long welded joints using inherent strains as parameters-L_z method," *Journal of Engineering Materials and Technology*, Vol. 111, 1987, pp. 1-8.

[27] Hill, M., and Nelson, D., "The inherent strain method for residual stress determination and its application to a long welded joint," *Structural Integrity of Pressure Vessels, Piping, and Components ASME 1995, Pressure Vessels and Piping Conference.*

[28] Zhang, J., and Dong, P., "Residual stresses in welded moment frames and implications on structural performance," *Journal of Structural Engineering*, Vol. 126, 2000, pp. 306-315.

[29] Kauffmann, E., and Fisher, J., "A study of the effects of material and welding factors on moment frame weld joint performance using a small scale tension specimen," Technical Report SAC 95-08, 1995.

[30] Ricles, J., Mao, C., Kaufmann, E., Lu, L., and Fisher, J., "Dynamic tension test of simulated welded beam flange connection," SAC Task 7.05, Preliminary Report, 1999.

[31] Deierlein, G., "The significance of loading rate effects on the fracture resistance of welded connections for seismic design," SAC sub-Task 5.3.3. 1998.

[32] Barsom, J., and Rolfe S., *Fracture & Fatigue control in structures. Applications of Fracture Mechanics.* Prentice-Hall, Inc., New Jersey 1987.

[33] Perzyna, P., *On Thermodynamic Foundations of Viscoplasticity. Mechanical Behavior of Materials Under Dynamic Loads.* (Lindholm Ed.), U. Springer-Verlag New York Inc. 1968.

[34] Cristescu, N., and Suliciu, I. *Viscoplasticity.* Sijthoff & Noordhoff, The Netherlands, 1981.

[35] Gao, X. and Dodds, R., "Constraint effects on the ductile-to-cleavage transition temperature of ferritic steels: a Weibull stress model," *International Journal of Fracture*, Vol. 102, 2000, pp. 42-69.

[36] Ruggieri, C., and Dodds, R., "Numerical evaluation of probabilistic fracture parameters with WSTRESS," *Engineering Computations* Vol. 15, 1998, pp. 49-73.

[37] Moran, B., and Shih, C., "A general treatment of crack tip contour integrals," *International Journal of Fracture* Vol. 35, 1987, pp. 295-310.

[38] Koppenhoefer, K., Gullerud, A., Ruggieri, C., Dodds, R., and Healy B. *WARP3D. Structural Research Series* (SRS) 596, UILU-ENG-94-2017, University of Illinois at Urbana-Champaign, 1998.

[39] Gao, X., Ruggieri, C., Dodds, R., "Calibration of Weibull stress models using fracture toughness data," *International Journal of Fracture* Vol. 92, 1998, pp. 175-200.

Frederick W. Brust[1]

The Importance of Material Fabrication History on Weld Fracture and Durability

Reference: Brust, F. W., "**The Importance of Material Fabrication History on Weld Fracture and Durability,**" *Fracture, ASTM STP 1417*, W. G. Reuter and R. S. Piascik, Eds., ASTM International, West Conshohocken, PA, 2001.

Abstract: Fabricated metallic structures originate as plate stock at the material manufacturer. The residual stresses in the plate stock depend on the steel manufacturing process and the heat treatment and cooling methods applied. The residual history is then carried through and is altered by the cutting, bending, welding, etc. required for the fabrication. This process can create additional residual stresses and/or will alter the residual stress or distortion throughout the parts and components. As will be seen, by the time the material from the steel plant makes its way into the service structure, each component has already seen a history of stresses, nonlinear strains, and corresponding displacements. This history can have an important effect on the service life of the structure. Fatigue, corrosion cracking, fracture, etc. can all be affected by prior history. However, in most cases this prior history is neglected in design or when making a damage assessment of the structure. *Fatigue and fracture assessments are often made by pretending that the service material is pristine, free of prior fabrication history effects.* The fatigue life, corrosion response, and final fracture behavior predicted assuming a pristine structure can be different from that which would be predicted by including prior history.

This paper illustrates the effect of prior history on weld-fabricated structures through the use of several examples. The fatigue behavior, the corrosion response, and the final fracture behavior for several cases where history effects are included are compared with predictions where these effects are neglected. Guidelines for determining when prior fabrication effects must be included in the design and life management process are provided. Finally, simple methods for accounting for these in the design and life management cycle are overviewed.

Keywords: residual stresses, welds, weld fabrication, fracture, weld modeling

Critical components of fabricated structures that are operated in critical applications are often stress-relieved before service life begins, in an effort to eliminate prior history effects. However, the costs associated with stress relief are often not justifiable for many

[1] Research Leader, Battelle Memorial Institute, Columbus, OH 43201(brust@battelle.org)

applications and, in some instances, neglecting the effects of the fabrication history can reduce the accuracy of the life prediction. Such fabrication residual stresses can have an important effect on corrosion life, fatigue life, fracture resistance, creep damage, and local constraint.

This paper attempts to investigate the effects of fabrication history on failures. The paper first illustrates how fabrication residual stresses can be introduced into a structure. Next, a new computational weld model is overviewed. This weld model is used in some examples that are provided later in the text. Finally we provide several case studies that illustrate fabrication effects life.

Material History Dependence

Structures continually degrade during the service performance years. Initial fabrication flaws (especially for welded fabrication) may be present, fatigue and corrosion cracks may initiate and grow, etc. Assuring that these defects do not lead to service failures is an important goal for the product manufacturer and the structural fabricator. Structural integrity can be ensured by assuming the presence of flaws at highly stressed regions of the structure and performing fatigue, corrosion, and fracture analyses of the structure under service conditions. In addition, when flaws are found in service, the repair schedule (timing, type of repair, etc.) can be determined by performing such a fracture assessment.

Usually damage assessments are made by neglecting prior history in the components that make up fabricated structures. Consider the cycle represented by Figure 1 for a fabricated steel structure. Start from the upper left and move clockwise. The different components may be cast, rolled, forged, etc. from the material supplier, and often combinations are used in the service structure. An initial residual stress and distortion pattern develops depending on which process is used. For instance, in rolled plate, tensile stresses usually develop near the plate edges and compressive stresses develop in the interior.

The rough material stock is then transported from the steel mill to the fabrication shop. The transportation, handling, and storage may alter the original stress and deformation history inherent in the rough stock. The material may then be surface treated, depending on the application, further altering the original history in the rough stock. The material is then cut into the desired shape required for the fabrication (for instance, consider a truck frame consisting of a number of components (forged, cast, rolled) and welded together). This cutting process alters the original residual stress history (and thus distortion history). Moreover, the cutting process may induce additional residual stresses near the cut edge (particularly for thermal cutting since the thermo-mechanical flame cutting process induces nonlinear strains near the cut edges).

The component might then be bent and formed into the required shape for the fabrication. Forming again alters the original history, and can add additional significant stresses and strains in the bent regions of the component. Connecting the parts with welds, bolts, adhesives, etc assembles the different components into the desired structure. The connection process further alters the residual history in the component parts.

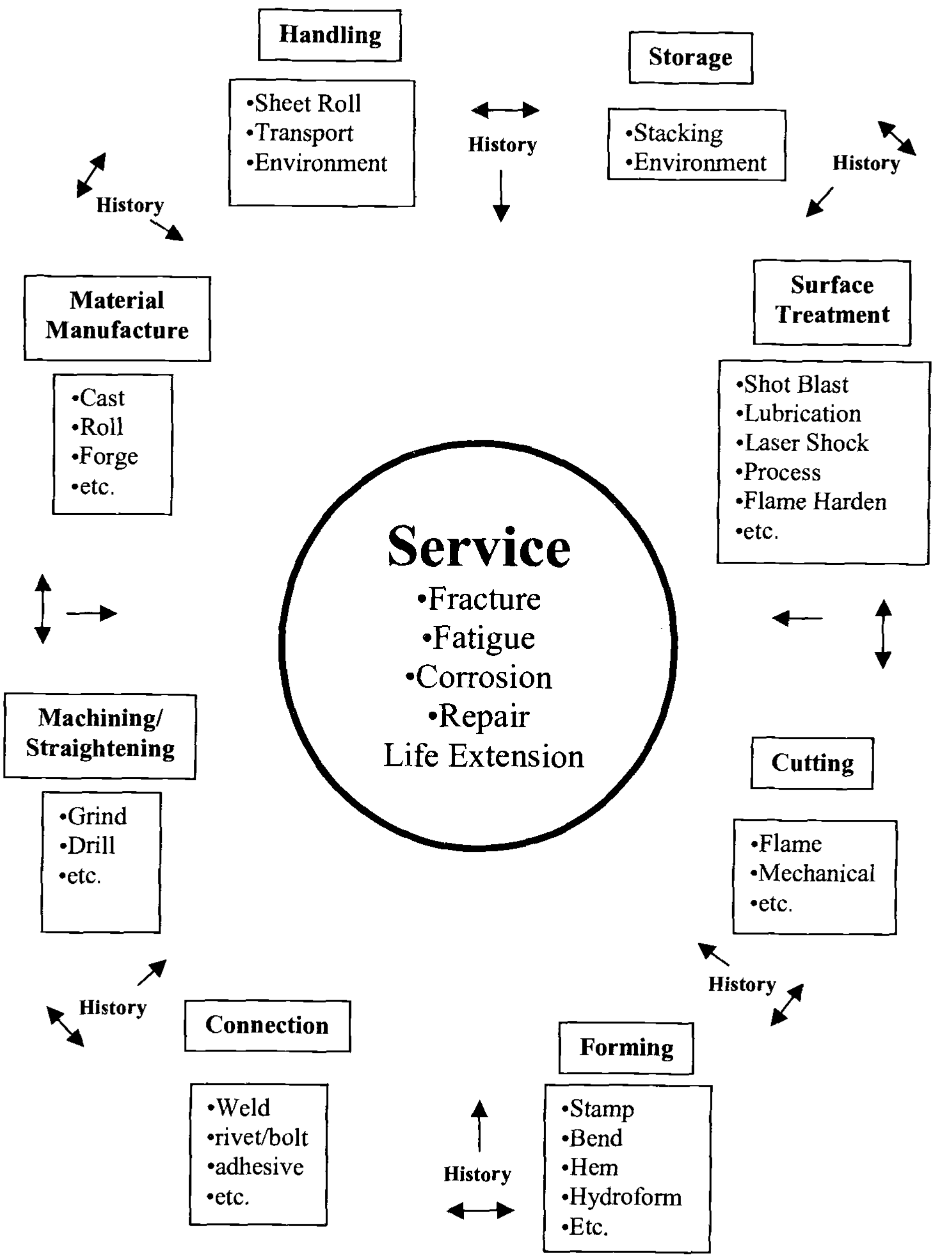

Figure 1 - *Operations History Leading to Structural Fabrication.*

In particular, the welding process induces significant residual stresses and distortions into the assembled structure. Finally, the assembled component or structure might then be straightened to achieve certain desired tolerance requirements. This process further alters the history in the structure.

As seen, by the time the material from the steel plant makes its way into the service structure, each component has already seen a history of stresses, nonlinear strains, and corresponding displacements. As an example, consider Figure 2. This is an example of the effect that bend forming and welding on the service residual stress state for a mild steel. As illustrated on the left of Figure 2, a two-dimensional nonlinear finite element analysis was performed of a plate being bent in a die. Next, a weld bead was deposited on the exterior of the bend curvature. Both the bending and welding processes were modeled via the finite element method (the weld models used are described next). The right side shows black and white contour plots of the "X" component of stress (this component will likely lead to crack growth at the weld toe). The material was a standard structural steel. The stress magnitudes vary between + and – 300 Mpa (the magnitudes are not important for our purposes). It is clearly seen that stresses at the weld toe are markedly different between the two cases.

This history can have an important effect on the service life of the structure. Fatigue, corrosion cracking, fracture, etc. can all be affected by prior history. However, in most cases this prior history is neglected in making a damage assessment of the structure. *Fatigue and fracture assessments are often made by pretending that the service material is pristine, free of history.* The fatigue life predicted assuming a pristine structure is different from that which would be predicted by including the prior history (welding alone (Figure 2 (a) or bending and welding 2(b)). References [*1-5*] further illustrate this point and examples will be shown later that clearly illustrate this effect.

Of course, for some critical structures, stress relief of many of the components is performed before the structure goes into service. However, the costs associated with stress relief are not practical for the vast majority of fabricated structures. In addition, stress relief, annealing, and other processes do not eliminate all residual stresses and strains leading to a pristine structural component.

Because residual stresses caused by the welding process are often dominant compared with other fabrication induced stresses, and because many service failures occur at welds, we spend some time discussing the state-of-the-art of weld process models before providing examples.

Computational Weld Model

Background - Perhaps the first attempt to predict the residual stresses induced by the welding process was carried out by Rodgers and Fletcher [*6*] in 1938 using an analytical approach. A number of other analytical approaches were developed from this time through the early 1970s to predict distortions and residual stresses (see for instance the survey paper by Masubuchi [*7*]). These approaches were quite novel and often provided

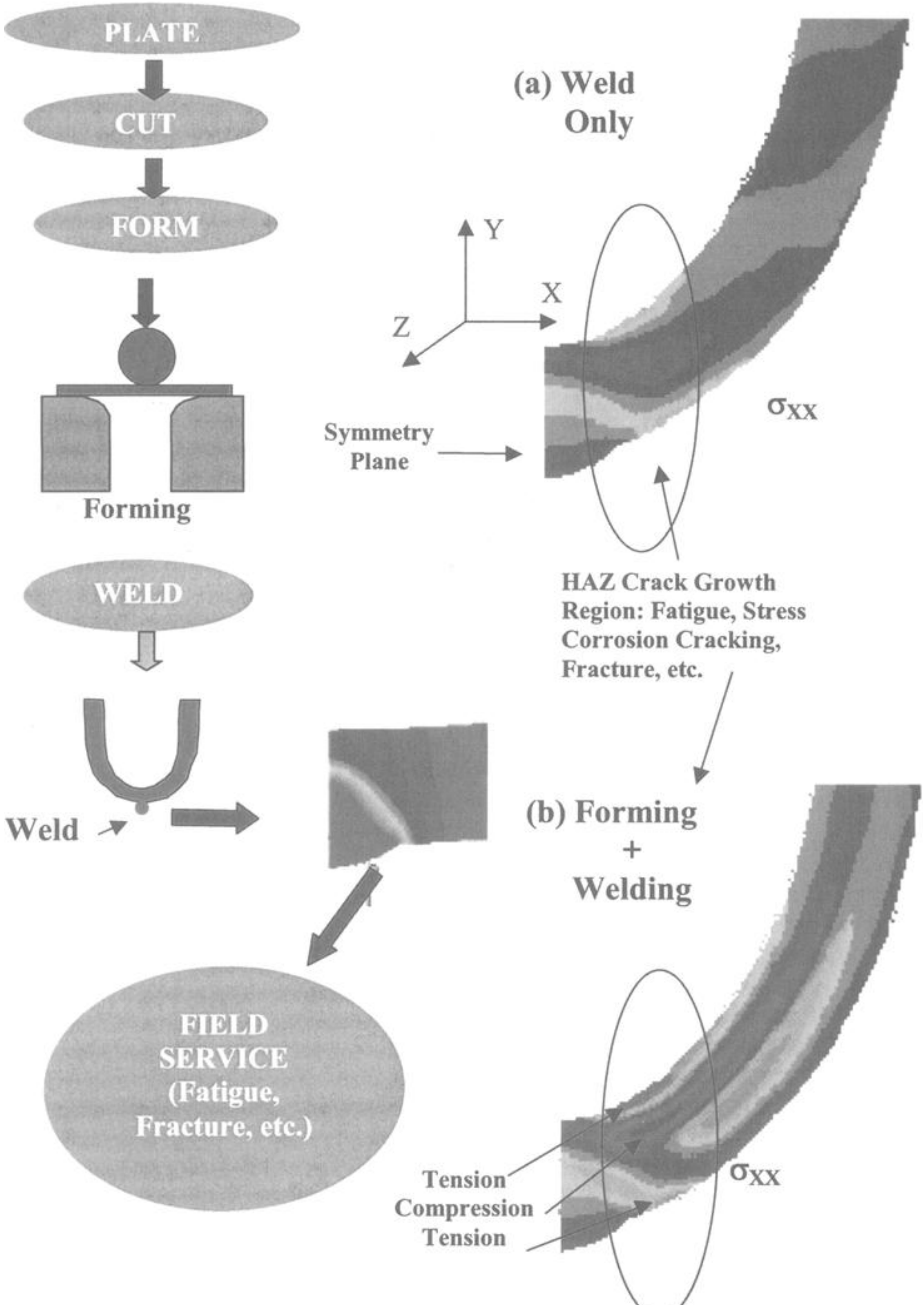

Figure 2 - *Bending and Welding Effects on Residual Stress Development.*

reasonable predictions when compared with experimental measurements, but were often limited to single pass welds.

Such analytical approaches were replaced by numerical approaches in the early 1970s as the power of the finite element method was realized. The earliest published finite element models developed for predicting the residual stresses induced by the weld process were probably developed independently by Kamichika et al in Japan [*8*] and Friedman [*9*] in the USA. Battelle researchers [*10-14*] extended these models in the late 1970s and early 1980s to account for (among other features) multiple pass welds, material re-melting and annealing, phase changes and heat sinks. The Battelle work was also perhaps the first to use closed form analytical solutions to develop accurate high speed weld thermal analysis procedures for finite thickness (including thin) plates. These models were used extensively in studies for the nuclear power industry to develop weld procedures to mitigate inter-granular stress corrosion cracking in piping systems. Methods such as Heat Sink Welding (HSW [*13*]), Induction Heating for Stress Improvement (IHSI [*14*]), and Backlay Welding (BW [*10*]) were developed and optimized using these models and these methods are still used in the nuclear industry. As such, this work probably represented the first industrial application of a weld process model to solve a manufacturing problem.

Since 1990 weld process models have been developed and are being used by several different organizations. References *15-18* summarize methods used by organizations in Germany, Canada, USA (Edison Welding Institute), and Austria, respectively, to model weld induced residual stresses and distortions. No attempt to summarize the methods used by these and other organizations is attempted here; rather the interested reader can consult these references and references cited therein and below for details.

In the early to mid 1990s the present authors in conjunction with Caterpillar, Inc., began to greatly improve all of these weld analysis tools. In particular, the high-speed thermal solution procedures and the structural procedures such as local annealing, melt element detection, etc., References *6-10* were extensively updated and improved for the nuclear industry, the aerospace industry, the Department of Energy, the automotive industry, among others. References *19-20* describe these developments for thick plate nuclear applications, Reference *21* describes this work for thin plate aerospace applications using advanced metals, Reference *22* describes some of the theoretical developments of the model improvements in recent years (developed with by DOE funding), and Reference *23* describes automotive applications.

The Weld Process Model

Model Overview - Since this early work, a number of researchers have developed weld process models or used commercial finite element codes to perform weld analyses. Most commercial codes were not specifically developed to properly account for the many unique features of the welding process. Some of these unique features which must be accounted for include: proper thermal heat flux input, melting/re-melting effects, history annihilation as temperatures are between the phase change temperature and melting, and slow solution speed. The model used here overcomes these deficiencies.

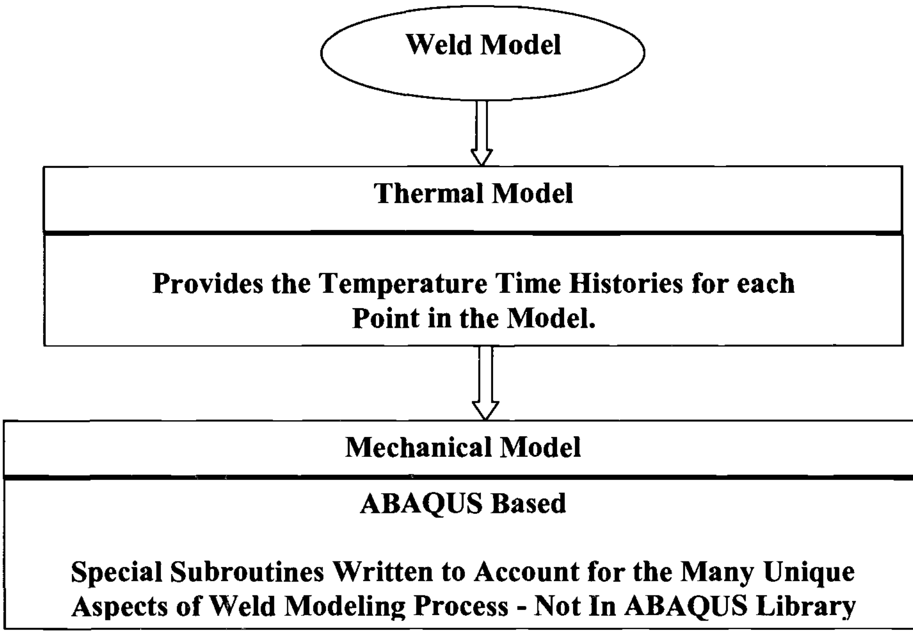

Figure 3 - *Weld Process Model Illustration.*

The model components are illustrated in Figure 3. As seen, there are two parts to the model.

Thermal Model - Analytically based methods and numerical (finite element or finite difference) methods are used to predict the temperature versus time histories in the weld piece. Numerical solutions based on the finite element method, the finite difference methods, control volume techniques, etc., can always be used to obtain the temperature versus time profiles throughout the history of the structure being welded. However, numerical solutions often require extensive manpower and computer resources to analyze complex structures. Analytically based solutions have been developed which are extensions of the Rosenthal type [*24*] methods discussed in references *10-14*. The recently developed advanced versions of analytical solutions can account for radiation and convection losses, weld torch start/stop effects, complex weld geometry's, transient effects, among others. *These are very high-speed solutions, which permit analyses of huge structures to be performed rapidly and quite accurate for many applications.* References *25-28* and references sited therein provide some details of these new solutions.

Thermal Model Verification - The analytically based thermal analysis procedures have been verified through a number of comparisons with numerical solutions and with experimental measurements. A large library of verification solutions on component geometry's such as lap and Tee-fillet joints and on full-scale large structures has been compiled. Here we provide an example validation for a T-fillet weld as seen in Figure 4. Figure 4 shows a T-fillet weld in 12 mm thick plate. The comparisons between thermocouple measurements (designated Exp) and analysis (designated Cal) are shown in these figures. In addition, the ABAQUS thermal solution procedure, in conjunction with a USER DFLUX routine is used where very accurate local temperatures are required. This procedure permits the weld heat input to the piece to be accounted for via a modified Goldak double ellipsoidal approach [*16*, *28*].

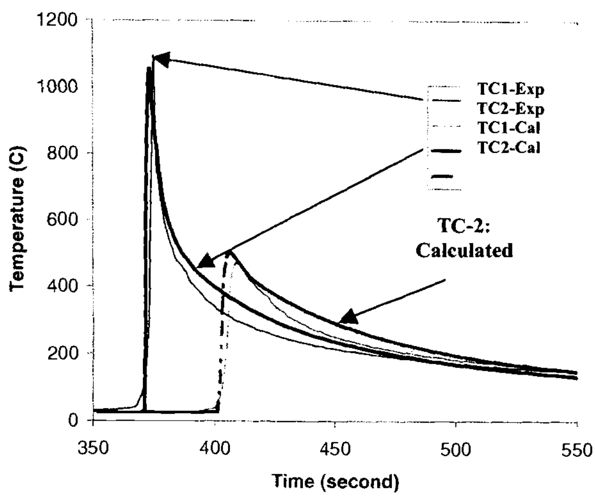

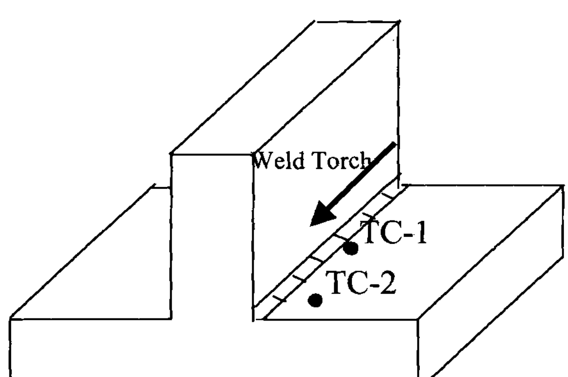

Figure 4 - *Analytical Thermal Model Prediction Compared With Experiment. The weld direction is shown and TC-1 is 0.5 mm and TC-2 is 4.5 mm From the Weld Toe. TC-2 represents a location near the stop point of the weld. This illustrates that the complicated start/stop procedures are working well. TC-1 is a location very close to the weld toe.*

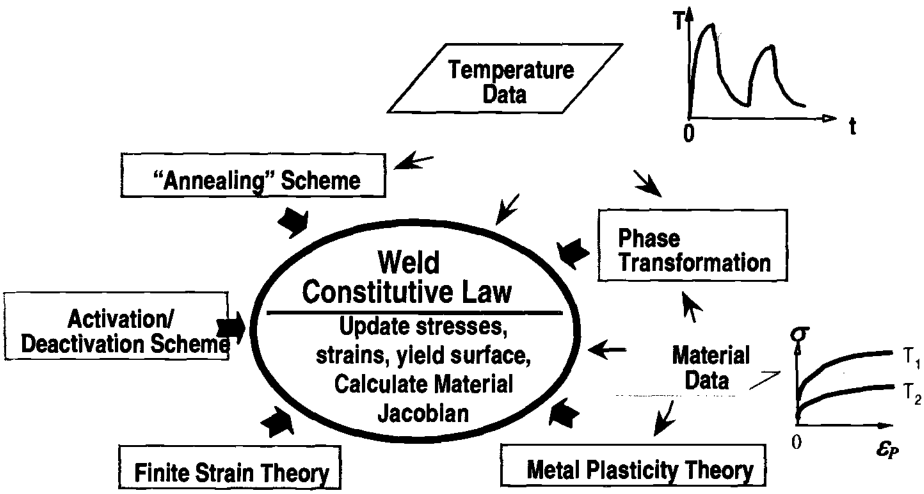

Figure 5. *Mathematical Structure of a Weld Material Routine.*

Structural Model - Unfortunately, there are many unique features associated with the welding process that cannot be correctly nor efficiently modeled using ABAQUS (or other general purpose finite element packages) unless a number of user written features and utilities are added to the weld analysis procedure. In particular, the library of material models (or constitutive laws) available in ABAQUS cannot account for some of the unique features associated with the welding process. This includes history annihilation[2] caused by melting/re-melting as different weld passes are deposited, material phase changes, and thermal cycling, among others. Moreover, the procedures required to model the weld process using ABAQUS are quite awkward. For instance, when modeling the weld process using the finite element method, the weld metal ahead of the current arc position has not been deposited as yet. To correctly account for this effect using ABAQUS one must use a tedious element birth option. This procedure is tedious in terms of manpower requirements and is computer intensive.

To overcome these problems, user interface constitutive subroutines have been written. These interface with ABAQUS to account for the unique features associated in a physically meaningful way. In addition, some the procedural difficulties discussed above as well as solution speed are overcome by using these constitutive routines. Reference 22 provides details of the constitutive law used for weld modeling.

Stress Validation - Figure 6 illustrates an example of the accuracy expected with the weld process model. This shows an example of a lap fillet welded circular plate welded to a larger plate. The residual stresses were measured using X-ray diffraction along the radial line plot illustrated in the Figure 6 inset. This represents location 180 degrees

[2] By "history annihilation" here we refer to the loss of deformation history (such as plastic strains and stresses) that occur when material is heated to temperatures greater than about 70 percent of melting (or near the phase change temperature). One may think of this definition as a sort of "local" stress relief.

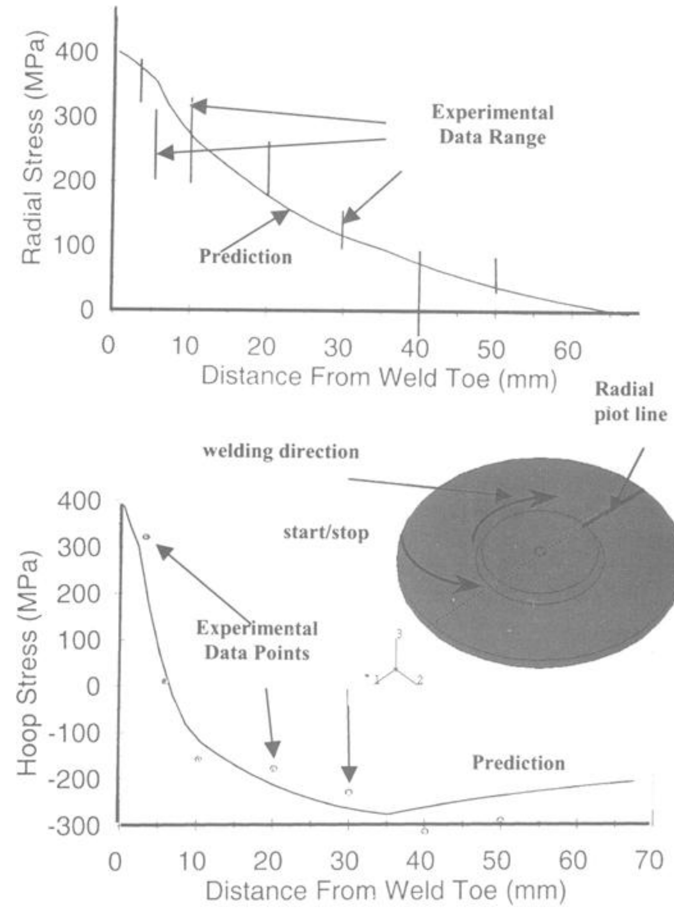

Figure 6 – *One Example of Weld Model Validation for Stresses.*

from the weld torch start/stop position. The range of experimental data for the radial stress plot represents two separate measurements. It is seen that very good predictions are made. *Observe from Figure 6 that tensile radial and hoop residual stresses develop from the welding process in the region adjacent to the weld toe. It is these stresses that can be reduced or made negative that can greatly increase the fatigue life of a structure.* The stress predictive capability of the model has likewise been extensively verified for many different weld geometries, including complex cases as well. As with temperatures, an extensive library of weld model validation examples exists. In addition, extensive library's of distortion prediction validation cases exists.

The weld model has been incorporated into a software package called VFT^{TM} [*29*]. This code has been used extensively over the past several years to develop weld strategies to eliminate distortions and control residual stresses for a variety of large-scale structures. Some examples are provided in References *30-33*. *As with stresses, control of distortions* *can have an important effect on reducing fabrication costs. This weld process model is an important tool used in achieving these objectives.*

Application Example Illustrating History Dependence Effects

Several examples of applications, which illustrate the importance of fabrication history on damage development and fracture, are illustrated in the following sub-sections.

Fracture of Welded Beams - Following the 1994 Northridge earthquake, wide spread damage was discovered in the pre-qualified welded steel moment frames. Detailed inspections indicated that most of the structural damage occurred at the weld connections between the beam and column flanges. In particular, the weld joints between the bottom beam flange and the column face suffered the most severe damage. Cracks mostly initiated at the weld root and propagated with very little indication of plastic deformation. The desired plastic hinges assumed in the structural building codes plastic design were not formed in the weaker beam away from the weld joint. Instead, brittle weld fracture was identified as the dominant failure mechanism.

Welding-induced residual stresses are believed to be one of the factors contributing to the brittle fracture. Indeed, there exist ample evidence that residual stresses can play dominant role in the fracture process of highly restrained welded joints [*34, 35*]. The design of welded moment resistant frame connections presents perhaps the most severe mechanical restraint conditions both during welding and in service. Consequently, the presence of high weld residual stress is expected. In addition, the triaxiality of the residual stress state in these joints can be significant. As such, the anticipated plastic deformation cannot develop before the fracture driving force reaches its critical value, resulting in brittle fracture.

Figure 7 illustrates an analysis of a typical beam-column connection (A36 beam, A572 Gr. 50 column, and E70T-4 weld material). The inserts illustrates the three dimensional cross section of the finite element mesh that was used to model the welds in the beam-column. In addition, a two dimensional model was used as well. The residual stresses (not shown here – see Reference *36*) showed a very high degree of triaxiality and were directly caused by constraints induced by the welding process and the geometry. The two-dimensional mesh illustrated below the beam column (Figure 7) was used to study the fracture response of a typical lower flange in a beam column connection. Nine passes were deposited (see inset mesh of Figure 7). The stress intensity factor is plotted as a function of the ratio of applied tensile stress to weld yield stress in the right of Figure 7. It is seen that including the history of residual stresses in the analysis procedure has a marked effect on the stress intensity factor. Indeed, for fracture in the brittle or transition regime, including prior history in the analysis is critical to obtain correct results.

Car Body Frame - The example illustrated above in the beam-column connection weld joint illustrated that weld induced residual stresses not only increase the stress intensity factor but can also increase the constraint. This can result in lower failure loads than those predicted without including residual stress effects. However, there was no attempt in the above case to develop weld procedures to eliminate or minimize these the deleterious effects caused by the welding itself. There are a number of ways to modify

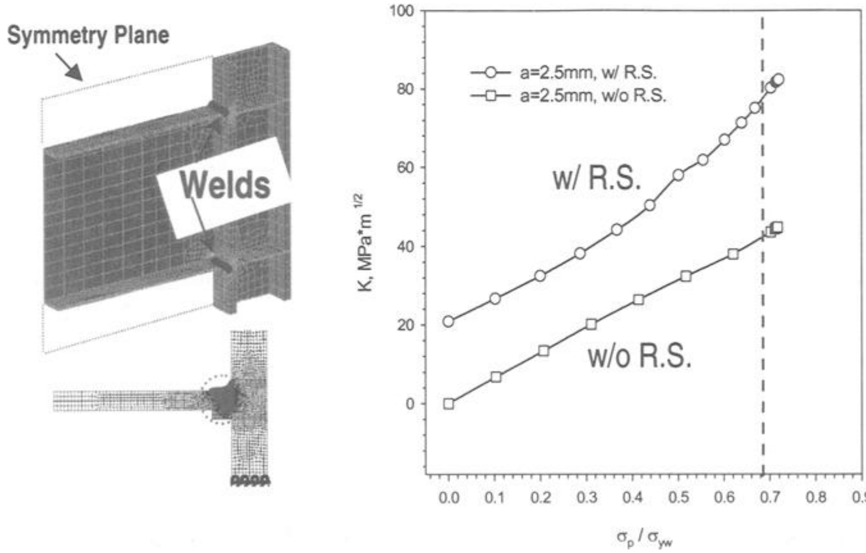

Figure 7 – *Residual Stress Effects on Fracture for a Beam-Column Connection.*

the welding process to either control distortions or to manage residual stresses. These include weld sequence definition, pre-cambering, pre-bending, heat sink welding, thermal stretch welding, heat input control, weld torch travel speed, among many others. The present example illustrates how a service-cracking problem was eliminated by a simple weld sequence change that was determined via VFT analyses.

Consider a swivel frame in a large off road mining vehicle as in Figure 8. The finite element mesh to the left represents an axis-symmetric model of a cylinder welded to a base plate via a Tee-fillet weld. Field cracking was observed in the vehicle, and it sometimes occurred immediately after the weld. The cylinder is quite large with a diameter of 3.5 meters and a thickness of 33 mm while the base plate has a thickness of 100 mm. The original weld sequence is illustrated in the top of Figure 8 and labeled sequential. This led to the type of cracking illustrated in the inset, where the cracks initiated in the cylinder at the inner diameter, near the toe of the weld, through the cylinder.

Since the thickness of the welded parts is large, it was postulated that constraint was a possible cause of the cracking. As such, the VFT code was exercised in an attempt to develop a weld sequence that might eliminate the problem. After several iterations, the sequence illustrated in the bottom portion of Figure 8, labeled alternating was determined to minimize both the constraint and the weld residual stress state. This sequence consists of welding at the inside diameter first, followed by the outer diameter, then inner diameter, outer diameter, etc., until the weld is complete. The residual stress state that develops from the two sequences is illustrated in Figure 9. Here it is seen that the stresses near the toe of the weld are markedly higher with the original sequence compared with the sequential sequence. In addition, though not shown here, the constraint for the alternating weld was also significantly lower than the sequential weld. This new sequence was implemented into the shop floor of the manufacturer and not one failure has been observed since. This is an example that illustrates how clever design and control of fabrication induced residual stresses can eliminate field failures.

Storage Tank Welds - Welded steel storage tanks are used in many industries. The weld sequences of these tanks can have an important effect on how cracks initiate and grow. Consider Figure 10. Large storage tanks are typically fabricated by vertically and horizontally welding sections of curved plate. Here the effect of the weld intersection on

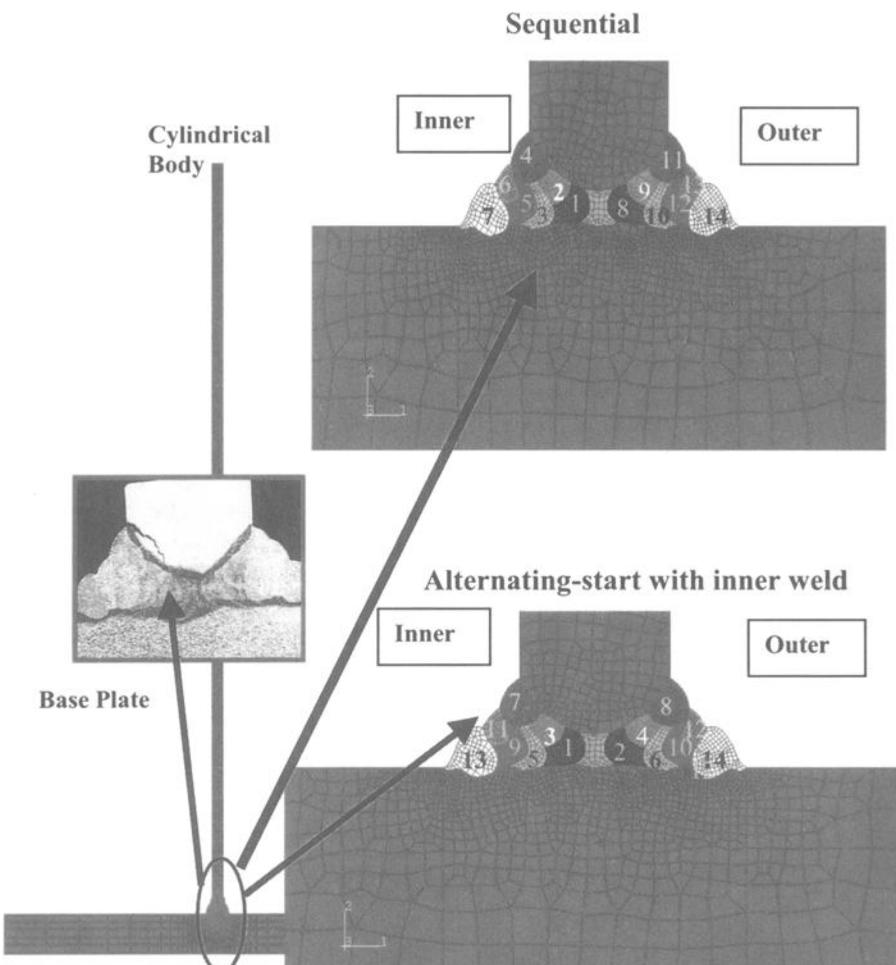

Figure 8 – *Car body Weld Sequence Example.*

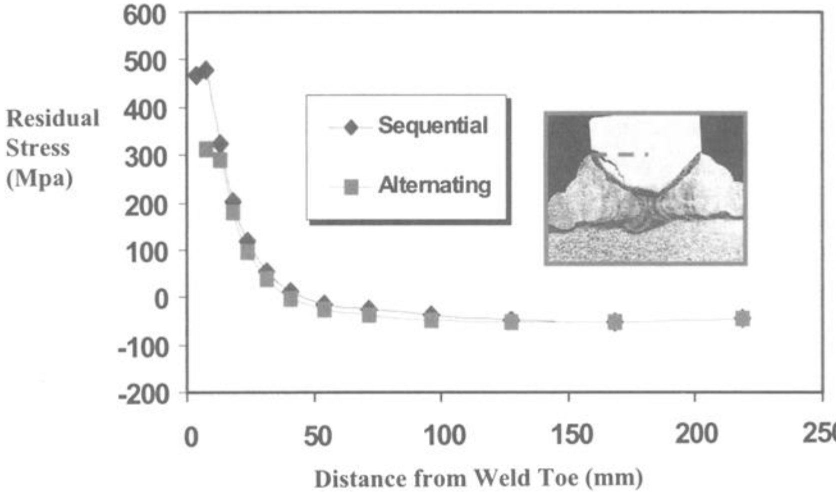

Figure 9 – *Residual Stresses From Sequential and Alternating Welding.*

subsequent corrosion driven crack growth is considered. The tank was considered to have a large radius to thickness ratio so that the finite element model, illustrated in the right half of Figure 10, was made flat. For this example, the horizontal weld (labeled H in Figure 10) was laid first, followed by the vertical weld (labeled V in Figure 10). Both welds were double–V groove welds with 6 passes modeled per weld and the plate thickness was 12.7 mm. VFT was used to predict the initial residual stress state in the tank. A symmetry plane was assumed along the vertical weld line and the dimensions and boundary conditions chosen so as to eliminate edge effects.

Within and near the weld intersection area, the residual stress distributions are rather complex due to the interactions of the two welds. The high longitudinal residual stress of the horizontal weld (in the direction of weld H) is significantly reduced at the weld intersection due to the subsequent introduction of the vertical weld. The heating and

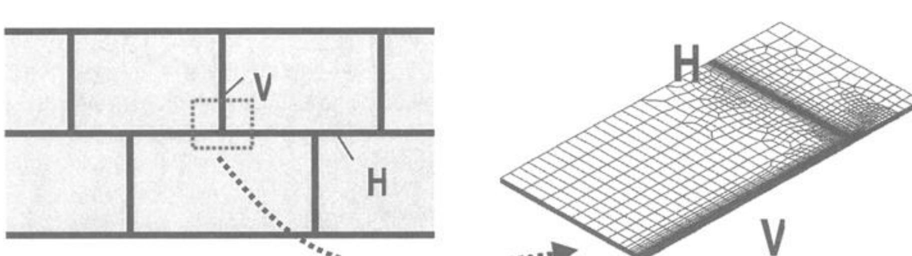

Figure 10 – *Typical Weld Sequence for Large Storage Tank and Analysis.*

cooling process induced by the deposition of the vertical weld passes relieves the longitudinal stresses of the horizontal weld in intersection area. After completion of the vertical weld, the residual stress (in the direction of weld H) distribution at the intersection is dominated by the transverse residual stress component of the vertical weld. The same observation can be made for the distribution of the stress in the vertical weld direction (in the direction of the 'V' weld), where the longitudinal residual stress of the vertical weld dominates the vertical residual stress distribution at the intersection region. In effect, the last weld dominates the residual stress characteristics at the intersection area.

One important consequence of the interaction effects between the horizontal and vertical welds is that the resulting tensile horizontal residual stresses (in the H direction) are increased in both magnitude and area at the intersection region along the side of the vertical weld. (Note that if the weld sequence is reversed, a large tensile vertical residual stress region will occur at the intersection region along the horizontal weld.) The presence of such a tensile residual stress region will certainly impact the stress intensity factor solutions if the horizontal residual stresses become operative for a crack situated along the vertical weld in this region. Such effects on stress intensity factor solutions are discussed next.

Cracks are introduced into the residual stress regions near the intersection of the welds as illustrated in Figure 11. The finite element alternating method (FEAM) (see for instance [37]) was used to calculate the stress intensity factors for the different crack

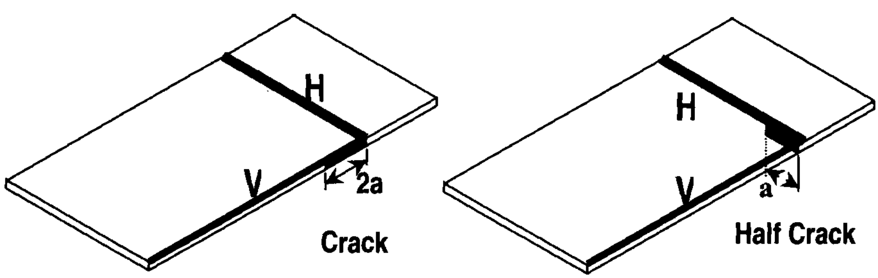

Figure 11 – *Crack Locations for Stress Intensity Factor Calculations.*

sizes considered. FEAM is quite convenient for this application since stress intensity factors are readily evaluated using the mesh of Figure 10 directly, that is no special crack specific finite element mesh is required. Figure 12 shows the stress intensity factors as a function of crack size for cracks located along both the vertical and horizontal welds. For the vertical cracks it is seen that the weld residual stresses in the H direction are the major contributor. K increases as the crack size increases up until about a crack size of about 2.5 inches after which it continually decreases as the crack increases in size. Moreover, the cracks are expected to grow more at both the inner and outer vessel surfaces compared with the mid surface (here we are concerned with K driven stress corrosion crack growth).

For the horizontal cracks, K decreases from an initially large value for small cracks until it appears to reach a steady state value, independent of crack size. The crack at the inner and outer surfaces are expected to grow more so than at the mid plane. These results suggest that the cracks, if driven mainly via the residual stress field, may grow to a rather large size at the inner or outer surface of the vessel before breaking through the vessel wall. It also suggests that the horizontal cracks may grow without bound if the steady state K-value is higher than the threshold for SCC growth.

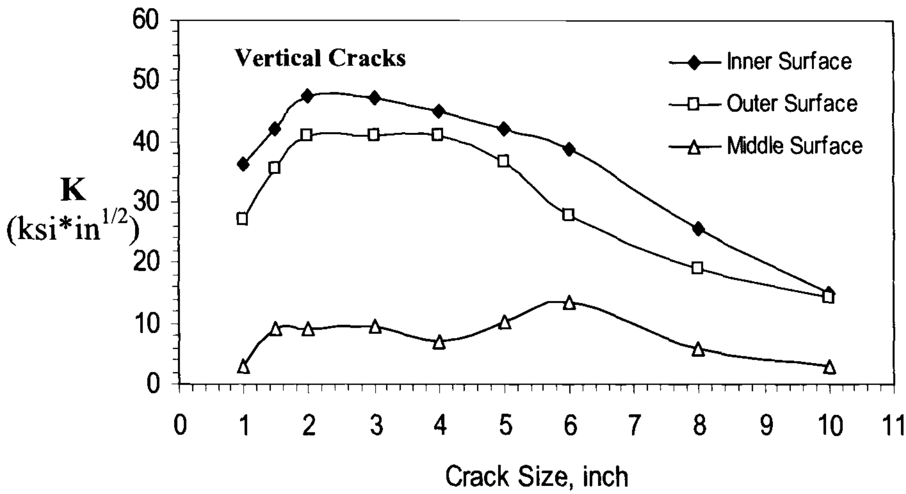

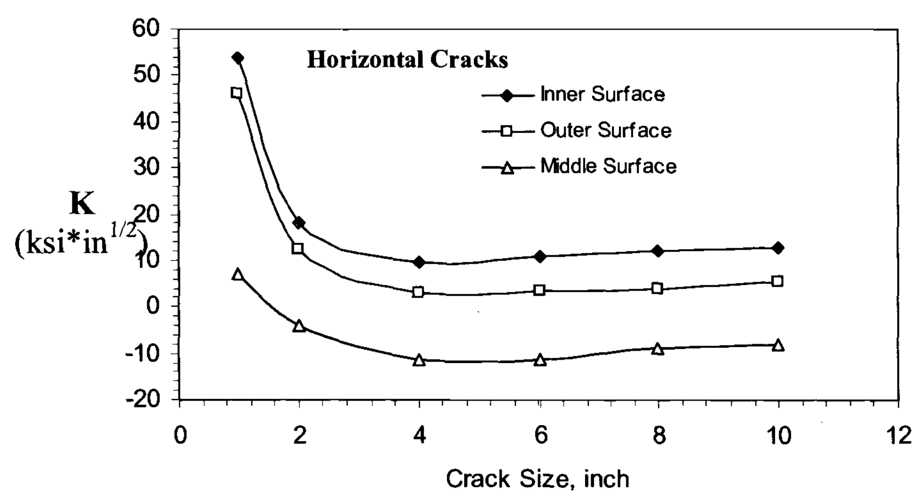

Figure 12 – *Stress Intensity Factors for Vessel Intersection Welds.*

Leak-Before-Break Issues In Piping Systems - An important consideration in leak-before-break (LBB) analysis for nuclear piping system is an accurate prediction of crack-opening area (COA). A comprehensive discussion on this subject can be found in Rahman et al [*38*]. Among some of the important issues, effects of weld residual stresses on crack-opening behavior are not well understood. A comparative study using the special shell element discussed earlier and an elastic superposition method was reported [*38*], where it was demonstrated that a full-field residual stress field can introduce more significant crack closure than predicted using the elastic super-position method.

As the through-wall crack becomes longer, present LBB procedures [*38*] assumes the crack opening area becomes proportionally larger, according to linear elastic analysis results. Consider a 406 mm diameter welded pipe with an R/t ratio of 10 and t = 16 mm (typical of nuclear piping). As shown in Figure 13, the actual circumferential crack opening behavior becomes rather complicated once the full field weld residual stresses are considered. As the crack length increases from 2c = 150 mm to 300 mm and 500 mm, the crack opening profile starts to deviate from the typical elliptical shape, particularly at ID and crack closure effects become more significant. Such non-elliptical opening behavior can be attributed to the increasing effects of the hoop residual stresses along the crack face as the crack increases in length. Accordingly, crack opening area calculations must take such effects into account for LBB assessment.

More importantly, it is seen that the crack opening profiles are negative at the outer diameter (OD) and mid surface (MS). The through wall axial weld residual stress distribution for this pipe (and typically for this thickness pipe) is tension at the ID and compression at the OD. For Of course, this is physically impossible, but it clearly suggests that crack closure (or pinching) of the crack may occur restricting leak flow rates. As such, leak rate detection equipment may not detect leaks as designed for. Since these calculations did not include service loads (only weld induced residual stresses are considered), the cracks in service are expected to be open. For thinner wall pipe, the effect of residual stresses on crack leak rates can be important. This is the subject of an ongoing effort to develop correction factors to account for weld induced crack closure for LBB considerations.

Discussion

This paper provided an overview of some of the issues of concern regarding material fabrication histories. It is now clear that solution to service failures (distortion, corrosion, fatigue, creep, etc.) can be made earlier in the fabrication chain. For instance, if the plate stock material is provided with known (and consistent) residual stress and distortion states, distortion correction issues that may be required at the final stage of fabrication can be eliminated. The use of computational models to address each step of the fabrication process is critical process is critical.

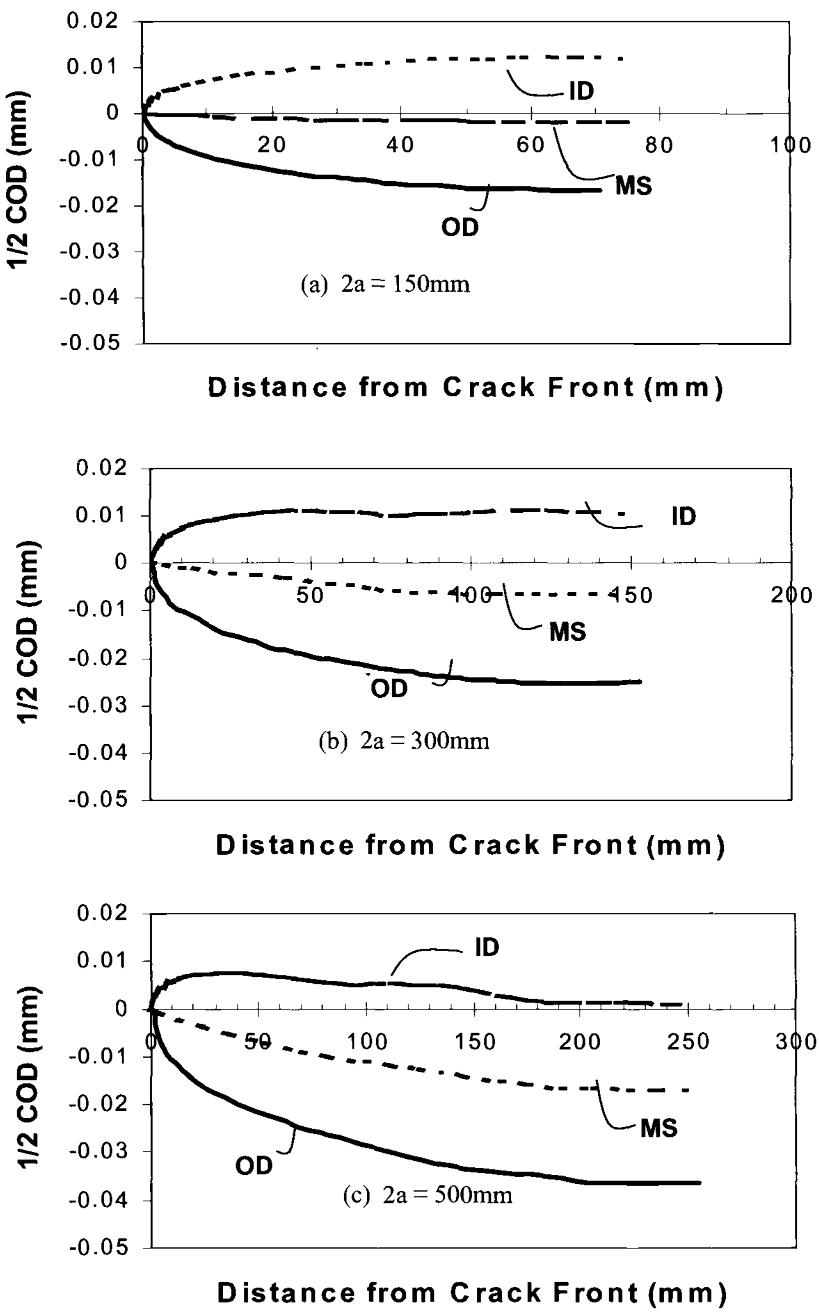

Figure 13 – *Crack Opening Displacements in Pipe with Different Crack Sizes.*

Four examples were provided in this paper that illustrate some of the important features associated with fabrication and residual stresses. Constraint and residual stresses caused by welding can lead to reduced service lives and unexpected failure modes. A number of additional examples can be cited. For instance, creep damage control of weld repairs can be designed via computational models [*39*] and post weld heat treatments. Repair of damaged pipes can be designed using computational models [*40*]. Numerous other examples are cited in the reference list as well.

In our view, the question of fabrication history dependent fracture, including weld fracture where residual stresses and strains are important, is very much open. New fracture parameters that perform and are verified in this regime are needed.

Acknowledgements

This work was supported in part by Department of Energy, Office of Basic Sciences under Grant No. DE-FG02-90ER14135. The author thanks Dr. R. Price and B. Armaly for their support. In addition, the author would like to thank Dr. I. Varol, Dr. T. Jutla, and Mr. P. Crilly of Caterpillar Inc. for the use of an example case and for useful discussions. Finally, many useful discussions with my colleague, Dr. P. Dong, are thankfully acknowledged.

References

[1] Hou, C., Kim, M., Brust, F. W., and Pan, J., "Effects of Residual Stresses on Fracture of Welded Pipes," in Residual Stresses in Design, Fabrication, Assessment and Repair, ASME PVP-Vol. 327, ASME PVP Conference, Montreal, Quebec, Canada, July 21-26, 1996, pp. 67-75.

[2] Abou-Sayed, I. S., Ahmad, J., Brust, F. W., and Kanninen, M. F., "An Elastic-Plastic Fracture Mechanics Prediction of Stress Corrosion Cracking in a Girth Welded Pipe," in Fracture Mechanics: 14th Symposium ASTM-STP 791, (1983).

[3] Kanninen, M. F., Brust, F. W., Ahmad, J., and Papaspyropoulos, V., "An Elastic-Plastic Fracture Mechanics Prediction of Fatigue Crack Growth in the Heat Affected Zone of a Butt Welded Plate," in *Fracture Tolerance Evaluation*, Edited by P. Kanazawa, A. S. Kobya, and K. Iida, published by Poyo Press, Tokyo, 1982, pp. 113-120.

[4] Kanninen, M. F., Brust, F. W., Ahmad, J., and Abou-Sayed, I. S., "The Numerical Simulation of Crack Growth in Weld Induced Residual Stress Fields," *Residual Stress and Stress Relaxation*, E. Kula and V. Weiss, Editors, Proceedings of 28th Army Sagamore Research Conference, Lake Placid, New York, July 13-17, 1981, Plenum Press, 1982.

[5] Zhang, J., Dong, P., and Brust, F. W., "Residual Stress Analysis and Fracture Assessment of Welded Joints in Moment Resistant Frames," in *Modeling and*

Simulation Based Engineering, Ed. S. N. Atluri and P. E. O'Donoghue, Tech Science Press, pp 1894-1902, 1998.

[6] Rodgers, D. E. and Fletcher, P. R., "The Determination of Internal Stresses from the Temperature History of a Butt Welded Pipe," *Welding Journal Research Supplement*, 1938, pp. 4-7.

[7] Masubuchi, K., "Control of Distortion and Shrinkage in Welding," *Welding Research Council Bulletin No. 149*, Apr. 1970.

[8] Kamichika, R., Yada, T., and Okamoto, A., "Internal Stresses in Thick Plates Weld-Overlaid with Austenitic Stainless Steel (Report 2)," *Transactions of the Japan Welding Society*, Vol. 5, No. 1, Apr. 1974.

[9] Friedman, E., "Thermomechanical Analysis of the Welding Process Using the Finite Element Method," *Transactions Journal of Pressure Vessel Technology*, Vol. 97, Aug. 1975, pp. 206-213.

[10] Brust, F. W., and Rybicki, E. F., "Computational Model of Backlay Welding for Controlling Residual Stresses in Welded Pipes," in *Journal of Pressure Vessel Technology*, Trans. ASME, Vol. 103, August, 1981, pp. 294-299.

[11] Brust, F. W., and Kanninen, M. F., "Analysis of Residual Stresses in Girth Welded Type 304-Stainless Pipes," *ASME Journal of Materials in Energy Systems*, Vol. 3, No. 3, 1981.

[12] Brust, F. W., and Stonesifer, R. B., "Effects of Weld Parameters on Residual Stresses in BWR Piping Systems," *EPRI Final Report, NP-1743*, March, 1981.

[13] Barber, T. E., Brust, F. W., Mishler, H. W., and Kanninen, M. F., "Controlling Residual Stresses by Heat Sink Welding," *EPRI Report NP-2159-LD*, December 1981.

[14] McGuire, P. A., and Groom, J. J., "Computational Analysis and Experimental Evaluation for Residual Stresses From Induction Heating," final Report to *EPRI (RP1394-4)*, Battelle Memorial Institute, Dec. 28, 1979.

[15] Fricke, S., Keim, E., and Schmidt, J., "Numeric Determination of Residual Weld Stresses," to be presented at and appear in *Proceedings of ICES'98*, October 7 - 9, Atlanta, 1998.

[16] Goldak, J, et. al., "Progress and Pacing Trends in Computational Weld Mechanics," to be presented at and appear in *Proceedings of ICES'98*, October 7 - 9, Atlanta, 1998.

[17] Yang, Y. Y., and Feng, Z., "Analysis of Welding Processes," *Proceedings of McNU '97*, June 29-July 2, Northwestern University, 1997.

[18] Buchmayr, B., "PC-Based Software in Welding Technology," In: *Mathematical Modeling of Weld Phenomena, Ed. H. Cerjak and K. E. Easterling*, The Institute of Materials, 1993.

[19] Zhang, J., Dong, P., and Brust, F. W., "A 3-D Composite Shell Element Model for Residual Stress Analysis in Multi-Pass Welds," Transactions of the 14th International Conference on Structural Mechanics in Reactor Technology (SMiRT 14), Lyon, France, Vol. 1, pp. 335-344 (1997).

[20] Brust, F. W., Dong, P., and Zhang, J., "Crack Growth Behavior in Residual Stress Fields of a Core Shroud Girth Weld," Fracture and Fatigue, H. S. Mehta, Ed., PVP-Vol. 350, pp. 391-406 (1997).

[21] Dong, P., "Modeling and Analysis of Alloy 2195 Welds in Super Lightweight

Tank," Battelle Project Report to Marshall Space Flight Center, Huntsville, Alabama, July 1995.

[22] Brust, F. W., Dong, P., and Zhang, J., "A Constitutive Model for Welding Process Simulation using Finite Element Methods," Advances in Computational Engineering Science, S. N. Atluri and G. Yagawa, Eds., pp. 51-56 (1997).

[23] Sun, X., Dong, P., and Kimchi, M., "The Coupled Electrical-Thermal-Mechanical Process Associated With Aluminum Welding," Proc. Of the International Body Engineering Conference (IBEC) , Stuttgart, Germany, Sept. 30 – Oct. 2, Vol. 30, pp. 42-48, 1997.

[24] Rosenthal, D., "Mathematical Theory of Heat Distribution During Welding and Cutting," *Welding Journal Research Supplement*, May, pp. 220-234, 1941.

[25] Cao, Z. et al., "A Comprehensive Thermal Solution Procedures for Multiple Pass and Curved welds," 2000 ASME Pressure Vessels and Piping Conference, Seattle, Washington, July 23-27,2000.

[26] Cao, Z. N., "An Efficient Heat-Flow Solution Procedure for Complex Welded Structures," 78th American Welding Society Annual Meeting, Los Angeles, April 13-17, 1997.

[27] Cao, Z. N., Brust, F. W., and Dong, P., "A Heat-Flow Solution With Convective Boundaries," *Modeling and Simulation Based Engineering, Vol. II*, Edited by Atluri and O'Donoghue, Technical Science Press, pp. 1732-1737, 1998.

[28] Cao, Z. Brust, F. W., Nanjundan, A., Dong, Y., and Jutla, T., "A Comprehensive Thermal Solution Procedure for Different Weld Joints," Advances in Computational Engineering and Sciences; ed. S. N. Atluri and F. W. Brust, Tech Science Press, pp 630-636, August, 2000.

[29] VFT™ Weld Modeling Code, Licensed Caterpillar Product distributed by Battelle, 2001.

[30] Brust, F. W., et al., "Weld Process Modeling and Its Importance in a Manufacturing Environment," Society of Automotive Engineers (SAE) Technical Paper Series, Paper No. 981510, Warrendale PA, 1998.

[31] Brust, F. W., "Fabrication Optimization and Cost Savings Using Advanced Weld Modeling Tools," Invited presentation at 2001 American Welding Society (AWS) conference and expedition, Cleveland, OH, May, 2001.

[32] Brust, F. W., et al, "Advantages of Computer Based Weld Modeling In a Manufacturing Environment," Invited Paper, 2000 American Welding Society Conference, April, 2000, Chicago, Ill.

[33] Brust, F. W., Yang, Y., Dong, Y., and T. Jutla, "Weld Process Modeling and its Importance in a Manufacturing Environment," *Advances in Computational Engineering and Sciences; ed. S. N. Atluri and F. W. Brust*, Tech Science Press, pp 630-636, August, 2000.

[34] Gates, W. E.; and Morden M., "Lessons from Inspection, Evaluation, Repair and Construction of Welded Steel Moment Frames Following the Northridge Earthquake," Technical Report: Surveys and Assessment of Damage to Buildings Affected by the Northridge Earthquake of January 17, 1994. Report No. SAC-95-06: 3-1 to 3-79, 1995.

[35] Naeim F.; DiJulio, R. Jr.; Benuska K.; Reinhorm, A. M.; and Li C., "Evaluation of Seismic Performance of an 11-Story Steel Moment Frame Building during the

1994 Northridge Earthquake," *Technical Report: Analytical and Field Investigations of Buildings Affected by the Northridge Earthquake of January 17, 1994*. Report No. SAC-95-04, Part 2: 6-1 to 6-109.

[36] Zhang, J., Dong, P., and Brust, F. W., "Residual Stress Analysis and Fracture Assessment of Welded Joints in Moment Resistant Frames," in Modeling and Simulation Based Engineering, Ed. S. N. Atluri and P. E. O'Donoghue, Tech Science Press, pp 1894-1902, 1998.

[37] Wang, L., Brust, F.W., Atluri, S.N., "The Elastic-Plastic Finite Element Alternating Methods (EPFEAM) and the Prediction of Fracture under WFD Conditions in Aircraft Structure; Part I: EPFEAM Theory," *Computational Mechanics*, 19(5), 1997, pp. 356-369.

[38] Rahman, S., Brust, F. W., Ghadiali, N., Choi, Y. H., Krishnaswamy, P., Moberg, F., Brickstad, B., and Wilkowski, G. M, 1995, "Refinement and Evaluation of Crack-Opening Area Analyses for Circumferential Through-Wall Cracks in Pipes," NUREC/CR-6300, BMI-2184, U.S. Nuclear Regulatory Commission, Washington, D.C.

[39] F. W. Brust, J. Zhang, P. Dong, "Pipe and Pressure Vessel Cracking: The Role of Weld Induced Residual Stresses and Creep Damage during Repair," *Transactions of the 14th International Conference on Structural Mechanics in Reactor* Technology (SMiRT 14), Lyon, France, Vol. 1, pp. 297-306 1997.

[40] F. W. Brust, P. Dong, J. Zhang, "Pipe and Pressure Vessel Cracking: The Role of Weld Induced Residual Stresses during Fabrication and Repair," *Advances in Computational Engineering Science,* Tech. Science Press, S. N. Atluri and G. Yagawa, Eds, pp. 177-182, 1997

Kwang S. Kim,[1] *Nam W. Lee,*[2] *and Yong K. Chung*[3]

Creep Crack Growth in the Base Metal and a Weld Joint of X20CrMoV 12 1 Steel Under Two-Step Loading

Reference: Kim, K. S., Lee, N. W., and Chung, Y. K., **"Creep Crack Growth in the Base Metal and a Weld Joint of X20CrMoV 12 1 Steel Under Two-Step Loading,"** *Fatigue and Fracture Mechanics: 33rd Volume, ASTM STP 1417*, W. G. Reuter and R. S. Piascik, Eds., ASTM International, West Conshohocken, PA, 2002.

Abstract: The creep crack growth behavior in the base metal and a weld joint of X20CrMo 12 1 steel has been investigated under two-step loading at 545°C using 1/2T CT specimens. The crack growth process has been simulated using finite element analyses to examine the transient crack tip field. The results are compared with those under constant loading. In step-up loading, crack growth accelerated greatly after load change due to the effect of prior creep damage and reduced stress relaxation. In step-down loading, further creep-damage at the crack tip nearly ceased after load change due to a sharp drop in crack tip stress, leading to crack arrest for a substantial period of time. Crack growth eventually resumed as the crack tip stress increased by redistribution of the creep strain. Crack growth rates are found to correlate well with C*(t) for both base metal and weld specimens.

Keywords: X20CrMoV 12 1 steel, creep crack growth, heat affected zone, C*(t)

High temperature components in power generation facilities are often subjected to overload due to thermal transients, and minute cracks tend to develop early in life. The assessment of residual lives of these components is normally carried out through fracture mechanics approaches. Time-dependent fracture due to creep crack growth in high temperature materials has been well studied, and established crack growth parameters exist, for example, Refs *1-3*. The high chromium ferritic steel X20CrMoV 12 1 is a material used, especially in Europe, for high temperature components in power plants and chemical industries [4]. The material has high resistance to creep and oxidation. The micromechanism of nucleation and growth of cavities, and creep rupture behavior in this material were investigated by Wu and Sandstrom [5], Eggler et al. [6,7], Tian et al. [8], and Wu et al. [9,10]. The oxidation resistance and high temperature strength were explored by Sandstrom et al. [11], Schneider et al. [12],

[1]Professor, Department of Mechanical Engineering, Pohang University of Science and Technology, Pohang 790-784, Korea.
[2]Engineer, Hyundai Motor Company, Namyang, Kyunggi-do, 445-850, Korea.
[3]Research engineer, Research and Development Center, Korea Heavy Industries & Construction Co., Ltd., Changwon 641-792, Korea.

and Bashu et al. [13]. Creep crack growth behavior has been investigated recently by Park et al. [14] and Kim et al. [15].

A majority of the studies on creep crack growth have been conducted on homogeneous materials under constant loads. In real applications, creep rupture problems are encountered in weld joints as well as in homogeneous materials. The heat-affected zones (HAZ) of weld joints of high temperature components are frequently the sites of crack initiation due to weak creep strength. The service load may be fairly steady in normal operations of power plants; however, in certain applications the adjustment of output power to meet the increased or reduced demand could lead to periodic variation in service load.

This study is aimed at investigating the transient behavior of creep crack growth under two-step loading in the base metal and a weld joint of X20CrMoV 12 1 steel. The type of loading to be investigated includes step-up loading and step-down loading. The purpose is to gain some insight on the transient crack growth behavior associated with sudden load changes. As in Refs 14 and 15, the investigation will be performed in both experimental and computational approaches.

Material and Specimen Preparation

The material used in this study is ferritic-martensite steel X20CrMoV 12 1 that is specified by DIN 17175. The chemical composition of this material is given in Table 1. The test material was provided as a seamless pipe with an outer diameter of 325 mm and a wall thickness of 34 mm. Two pieces of the pipe were butt-welded along a 45° single bevel groove in the circumferential direction. The welding was multi-pass submerged arc welding, the specifications of which can be found in Ref. [14]. Post-weld heat treatment was conducted at 750°C for an hour, followed by cooling in the furnace to 300°C at 75.8°C/hr, then to room temperature in air. The microstructure of the test material was tempered martensite. The weld metal had a finer grain size than the base metal and had a small amount of δ-ferrite. The HAZ was about 3mm wide and had varying grain sizes. The location within the HAZ where cracks are usually found is the intercritical HAZ that has the lowest creep strength [16].

Crack growth specimens used in this study are 1/2T compact tension (CT) specimens with a width (W) of 25.4 mm and a thickness (B) of 12.5mm. Base metal specimens were made such that the crack plane was normal to the axial direction of the pipe and crack growth was in the circumferential direction. Weld specimens were made such that one side of the crack plane was from the weld metal and the other side

TABLE 1—*Chemical compositions of X20CrMoV 12 1 base metal and weld metal (wt. %).*

Element	C	Mn	Cr	Mo	V	Ni	W
Base metal	0.20	0.69	11.32	0.83	0.27	0.42	0.07
Weld metal	0.19	0.58	10.65	0.83	0.39	0.32	0.54

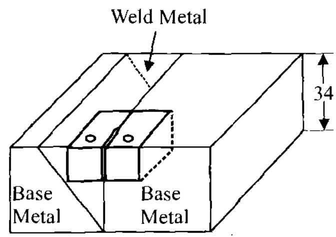

FIG. 1—*Layout of the weld specimen.*

from the base metal, as illustrated in Fig. 1. After machining side faces, the HAZ was identified by chemical etching, and the crack plane was placed along the intercritical HAZ. Then the final machining was done. The specimen was precracked at room temperature under a low-amplitude fatigue loading. A side groove of depth of 1.25 mm was then introduced on each side of the specimen.

Crack Growth Tests

Crack growth tests were conducted using a lever-type creep machine modified for crack growth tests under non-uniform loads. The actual load on the specimen measured by a load cell is fed to a computer in a preset time interval, which turns on or off the motor for load control by comparing the load cell output with the load profile prescribed at the start of the test. The rotational motion of the motor is converted to the vertical motion of a screw jack, which moves the loading pan up or down to reduce or increase the load. The margin of error in the load transferred to the specimen was within ±0.03kN from the prescribed load. The temperature of the test was 545°C, which was produced by a three-zone split furnace and monitored by a temperature controller. The crack length was measured by use of a direct-current potential drop (DCPD) system, and the load point displacement was measured using a bar-and-tube type extensometer with a linear variable differential transformer (LVDT) located outside of the furnace.

Two types of step loading were used in the test. The first type was "step-up loading" in which the load was increased suddenly from an initial load to a higher load at a certain time t*. The second type was "step-down loading" in which the load was reduced suddenly from an initial load to a lower load at time t*. The load levels used in the test were selected from those of constant load tests in Ref. [14]. The load change time t* was selected from the transient part and the steady-state part on the load point displacement versus time curves obtained in constant load tests. The loading conditions are tabulated in Table 2 along with test results except a weld specimen test that went erratic, possibly due to welding defects. In this table the base metal specimens are designated by BUP and BDN, and weld specimens by WUP and WDN. This table also includes the constant load test data obtained in [14] for reference.

TABLE 2—*Summary of test conditions and results.*

Specimen No.	Initial load (kN)	Final load (kN)	Load change time (t^*, hr)	Initial crack length (a_o) (mm)	Final crack length (a_f) (mm)	Δa $(a_f - a_0)$ (mm)	Total test time (hr)
BUP1	7.2	9.1	11.0	13.58	19.53	5.95	30
BUP2	7.2	9.1	50.4	13.65	17.17	3.22	55
BDN1	9.1	7.2	2.0	13.25	19.72	6.47	482
BDN2	9.1	7.2	11.3	13.19	14.44	1.25	376
WUP1	7.6	9.1	25.4	13.65	20.64	6.99	32
WDN1	9.1	7.6	2.7	13.01	18.56	5.55	86
WDN2	9.1	7.6	14.1	13.31	17.55	4.24	184
B7.2	7.2	7.2	.	13.43	16.55	3.12	174
B9.1	9.1	9.1	.	13.23	16.24	3.01	41
W7.6	7.6	7.6	.	13.21	14.76	1.55	394
W9.1	9.1	9.1	.	13.27	15.51	2.24	32

Finite Element Analysis of Crack Growth

The crack growth process was simulated using a commercial finite element code ABAQUS, version 5.8 [17]. For the base metal specimen, only half of the body was modeled in consideration of symmetry. For the weld specimen, the full specimen was modeled. The weld specimen model had three regions of different materials: base metal, weld metal and a HAZ layer in the middle. The actual HAZ consists of four subzones [15]: a fine-grained HAZ, a coarse-grained HAZ, an intercritical HAZ and a softened base metal. The HAZ included in the model was only the intercritical HAZ, which is 1 mm wide. Other subzones were not modeled separately because their constitutive properties were not known. The fine-grained and coarse-grained HAZs were included in the weld metal, and the softened base metal in the base metal. The crack was placed at 0.25mm from the base metal-HAZ interface, following experimental observations that failure usually occurs closer to the softened base metal within the intercritical HAZ.

The finite element mesh consisted of 2755 four-node quadrilateral elements and 2896 nodes for the weld specimen model, and the base metal specimen model was approximately half as big. The state of deformation was assumed to be plane strain. Crack growth was modeled by removing the constraint conditions placed on the crack plane nodes in accordance with the experimentally observed crack length-time history. The "debond" option in ABAQUS was used along with the constraint conditions. Crack path elements had a mesh size of 0.125mm.

Each material in the model was assumed to follow the elastic-plastic-steady state creep constitutive relation given by

$$\varepsilon = \frac{\sigma}{E} + A\sigma^m + B\sigma^n t, \tag{1}$$

where σ is the stress, and E, A, m, B and n are the elastic modulus, plasticity coefficient and exponent, creep coefficient and exponent, respectively. These properties are given in Table 3. It is noted that the properties of the intercritical HAZ were obtained on a simulated material [15]. This material was relatively soft and had a lower elastic modulus and tensile strength than the base metal and the weld metal. For creep in the varying stress field, the time-hardening rule was implemented.

TABLE 3—*Constitutive properties of X20CrMoV12 1 steel at 545°C.*

Material	***Base metal***	Weld metal	Simulated HAZ
Elastic modulus, E (GPa)	132	132	98
Plasticity coefficient, A (MPa^{-m})	6.33×10^{-33}	2.80×10^{-16}	6.25×10^{-28}
Plasticity exponent, m	13.0	5.87	9.7
Creep coefficient, B $(MPa^{-n}hr^{-1})$	6.44×10^{-34}	1.91×10^{-57}	5.85×10^{-40}
Creep exponent, n	12.30	21.6	14.9

Crack Growth Parameter

The parameter C*(t) correlated satisfactorily the crack growth rates obtained in constant load tests. This parameter is used also in this study. It is defined by [18]:

$$C^*(t) = \frac{P\dot{V}_c}{BW}\eta, \tag{2}$$

$$\eta = \frac{n}{n+1}\left(\frac{2}{1-a/W} + 0.522\right), \tag{3}$$

$$\dot{V}_c \approx \dot{V} - \frac{\dot{a}B}{P}\left[\frac{2K^2}{E} - (m+1)J_p\right], \tag{4}$$

where P is the applied load, $\dot{V}$ is the load line velocity, $\dot{V}_c$ is the creep portion of $\dot{V}$, a is the crack length, $\dot{a}$ is the crack velocity, K is the stress intensity factor and J_p is the plastic component of the J-integral.

The values of K and J_p can be obtained using the equations in [19] and [20], respectively. For weld specimens, the values of $\dot{V}$, E, m and n in eq. (3) and eq. (4) were taken to be the average of the base metal and weld metal values. It was reported earlier [14,15] that C*(t) determined in this way correlated creep crack growth rates for the weld specimens under consideration.

It is noted that $\dot{V}$ is the load line velocity while the measured quantity in this study is the load point velocity. It was shown that load point velocities could be greater than load line velocities by over 30% at very small times for constant load tests but the difference decreases quickly as time elapses [15]. This is still valid for the specimens in this study. However, these differences were ignored and the measured load point velocities were used in computation of C*(t).

Results and Discussion

Step-Up Load Tests

The load point displacements of step-up load tests on two base metal specimens (BUP1, BUP2) showed a good agreement with those of the 7.2kN constant load test (B7.2) before the load was raised ($t<t^*$), however a rather steep increase occurred for $t>t^*$; see Fig. 2. Crack growth for $t<t^*$ was faster in these specimens than in specimen B7.2, as illustrated in Fig. 3. This could have a relation to the fact that BUP1 had a slightly larger initial crack length than B7.2, or it could be simply differences in material. Crack growth after load change to 9.1kN progressed faster than in specimen B9.1 at a given time, and even faster for BUP2 with a larger t*.

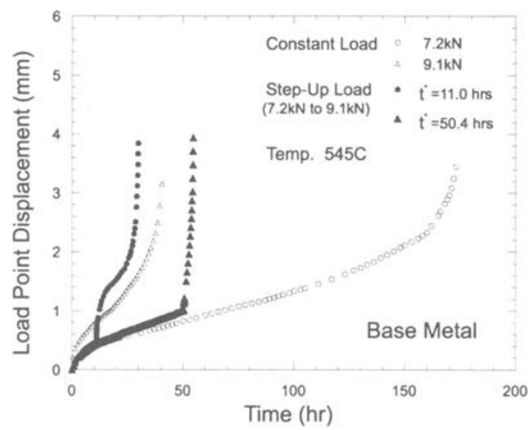

FIG. 2—*Variation of load point displacements in step-up load tests on base metal specimens.*

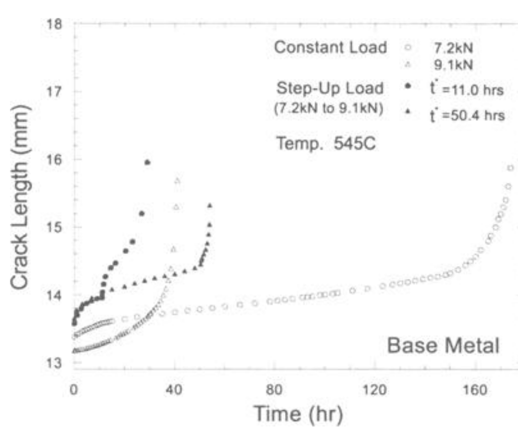

FIG. 3—*Variation of crack length in step-up load tests on base metal specimens.*

As explained in Ref. [15], under constant loads the contours of effective stress shrink because of stress relaxation for much of the transient and steady crack growth stages. They start to expand when the crack accelerates in the final stage of fracture. The initial response in step-up loading had similar characteristics. The normal stress distribution ahead of the crack tip is compared between specimens BUP1 and B 9.1 in Fig. 4. It is observed that the crack tip stresses of B9.1 at t=2.9 hours and at t=25.7 hours are very close to that of BUP1 at t=11 hours (just before load change). It appears for specimen B9.1 that stress relaxation around the crack tip kept abreast with stress elevation due to crack growth for the major part of rupture time. It also reveals that in specimen BUP1, the stress relaxation effect was small and short-lived as the stress elevation effect increased with fast crack growth after load increase. Perhaps the instantaneous stress increase at time t* in the crack tip field with prior damage accelerated the damaging process. These interpretations serve to explain why the rupture time of BUP1 was shorter than that of B9.1 in spite of a shorter duration under 9.1kN. One may also conceive that the differences in initial crack length between B9.1 and BUP1 have contributed to this effect. If the crack length of BUP1 is applied to B9.1, the stress intensity at the crack tip increases by approximately 5%, assuming a purely elastic response. The rupture time will then be shortened. However, the stress relaxation effects make it unclear how significant the change will be. It is also noted that the possibility of material variations cannot be ruled out as a partial source of this seemingly unusual rupture behavior.

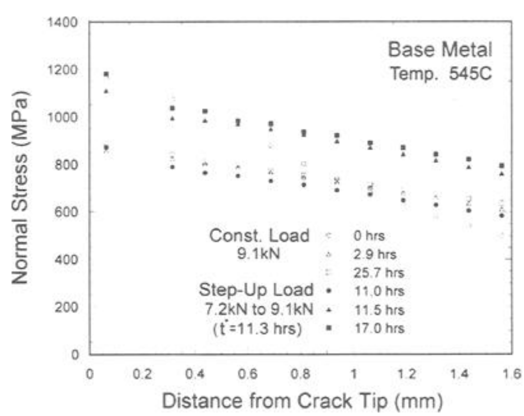

FIG. 4—*Crack tip normal stress distribution in (a) a constant load test, (b) a step-up load test on base metal specimens.*

The load point deformation and crack growth behavior of weld specimen WUP1 was similar to the base metal specimens. Crack growth rates were significantly larger for t<t* than those of the constant load test (W7.6), and these rates shot up after load change. The interpretations for the base metal specimens are also applicable to this weld specimen.

Figure 5 shows the SEM micrograph of the fracture surface of the base metal specimen BUP1. It is apparent that the crack grew in intergranular mode initially, but it was changed to ductile tearing as the crack grew in a faster pace after load change.

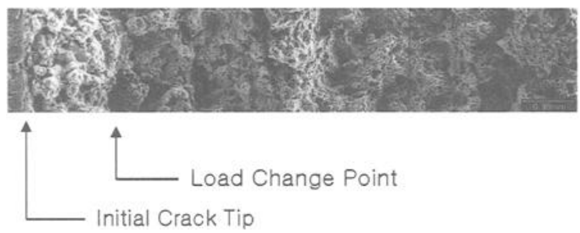

FIG. 5—*SEM fractograph of specimen BUP1.*

Step-Down Load Tests

Load point displacements followed closely the path of a constant load test (B9.1) before load reduction for the base metal specimens (BDN1, BDN2). There were sudden reductions in load point displacements, caused by elastic unloading, as the load was changed to 7.2kN. Then it was followed by a gradual increase at much reduced rates compared with the constant load test (B7.2). For $t^*=2$ hours, a transient response in the load point displacement occurred before the steady state was achieved. However, for $t^*=11.3$ hours, for which the load point was already deflecting at a constant rate under 9.1kN, the steady state deformation was attained immediately after load change to 7.2kN.

An interesting phenomenon in step-down load tests was that crack growth ceased right after the load was reduced. This state of "crack arrest" lasted for a substantial time being (39 hours for BDN1 and 29 hours for BDN2) before the crack resumed to grow. The crack growth rates afterwards were lower than constant load (7.2kN) rates for base metal specimens (BDN1, BDN2). As a result the total test duration was much larger for step-down load tests than the constant load test B7.2, although the specimens were subjected to a more damaging load initially.

The load point displacements of weld specimens under step-down loading, shown in Fig. 6, behaved in a very similar manner to those of base metal specimens. The specimen WDN1 failed earlier than the constant load specimen W7.6, which is believed to be an anomaly caused by material imperfections in the crack path. The crack front of this specimen was highly biased to a side. The crack growth behavior in weld specimens under step-down loading is given in Fig. 7. WDN1 showed an arrest period of 9.5 hours and substantially higher crack growth rates afterwards compared to the constant load test at 7.6kN. Meanwhile, WDN2 had a shorter arrest period (about 3 hours), and the crack resumed to grow at about same rates as the constant load (7.6kN) rates. The weld specimens in general appeared weaker than those used in constant load tests [15] though the same welding specifications were used.

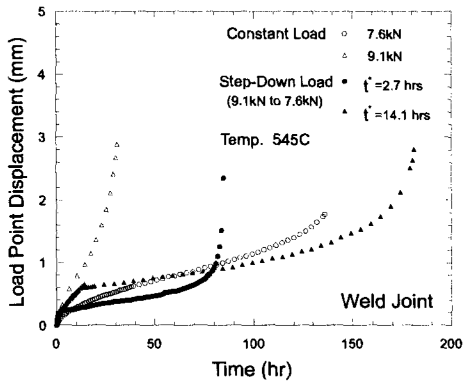

FIG. 6—*Variation of load point displacements in step-down load tests on weld specimens.*

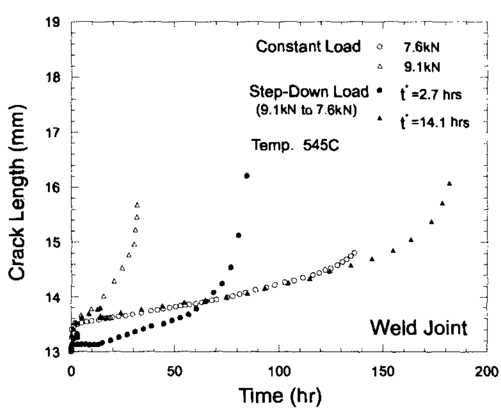

FIG. 7—*Variation of crack length in step-down load tests on weld specimens.*

The crack arrest period was longer for smaller values of t* for both base metal and weld specimens. The reason would be that creep deformation is contained in the very vicinity of the crack tip at small times because of high stress concentration and insufficient time for stress relaxation. Such a distribution of creep strain drives the crack tip stress more in the negative direction upon load reduction. Consequently it will take a longer time for the crack tip stress to rise to the level for resumption of active creep damage and crack growth. Also, the crack tip material is less damaged before load change for a smaller t*, which helps the crack to remain arrested for a longer time. It is also noted that crack arrest after sudden load reduction was also observed in stainless steel 304 under fatigue loading of high load ratio with long hold times at upper and lower peaks [21].

Another point to mention with regard to sudden load reduction is that the crack length determined from DCPD readings decreased by as much as 0.2 mm, as seen in Fig. 7. A possible explanation for this phenomenon would be through crack closure. However, the results of finite element analyses indicate that crack closure did not occur in any of the tests. Consequently, it was construed that closing of microcracks ahead of the crack tip upon elastic unloading would have entailed changes in DCPD. This spurious crack length change was not taken into account in the subsequent steps of crack growth analysis.

Figure 8 illustrates that intergranular crack growth occurred under initial loading and continued after load reduction in WDN2 specimen until transgranular fracture took over at the last stage of the test.

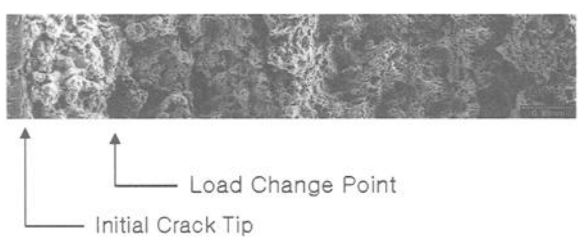

FIG. 8—*SEM fractograph of specimen WDN2.*

The stress and strain fields obtained in finite element analysis reveal interesting transient phenomena after load change. Effective stress contours were examined at various times greater than t* for the base metal specimen BDN2. The 240 MPa contours are shown in Fig. 9. There was a sudden change in the contour size from just before unloading to right after unloading due to elastic unloading. The contour shrank to a much smaller size in an hour, then stayed at about the same size until the crack started to grow again at t = 40.6 hours The effective creep strain contours of ε_c = 0.0148 corresponding to the times in Fig. 9 are given in Fig. 10. It is seen that while the stress contour shrank, the strain contour continued expanding at a slow pace during crack arrest. The additional creep strain caused further shrinking of the stress contour through redistribution of the elastic strain. However, the rate of further creep strain development was insufficient to drive the crack, although it helped increase the load point displacement slowly but steadily.

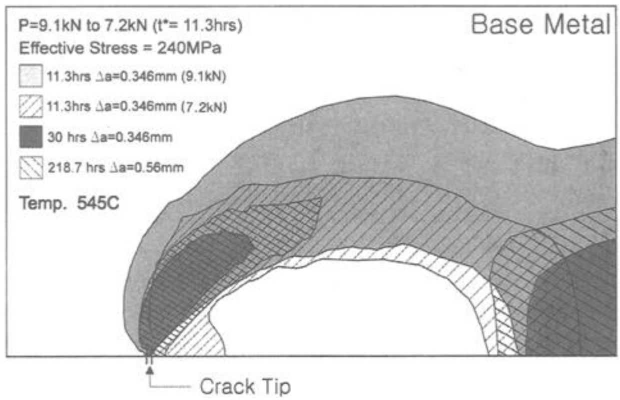

FIG. 9—*Effective stress contours before and after load change in a step-down load test on a base-metal specimen.*

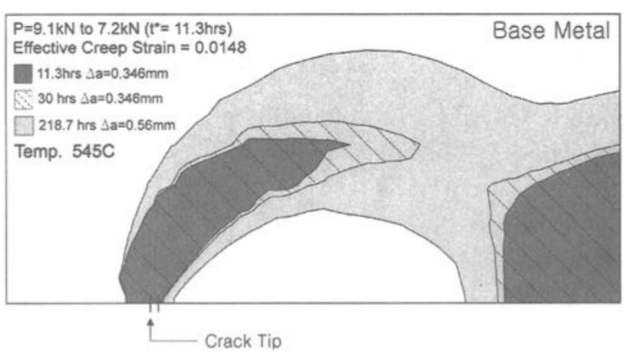

FIG. 10—*Effective creep strain contours before and after load change in a step-down load test on a base metal specimen.*

Figure 11 shows the distribution of the normal stress ahead of the crack tip at several times before and after load change. A large reduction of the normal stress toward the crack tip after load change is caused by suppression of the crack tip material from surroundings because of differences in the degree of creep deformation. The low stress in the very vicinity of the crack tip prevents further development of creep damage, resulting in arrest of the crack. The crack tip stress dips down a little more in a short while. However, as time goes on, more accumulation of creep strain in surroundings redistributes the stress, and the crack tip stress increases. Eventually, the creep damage around the crack tip increases and the crack starts to grow again.

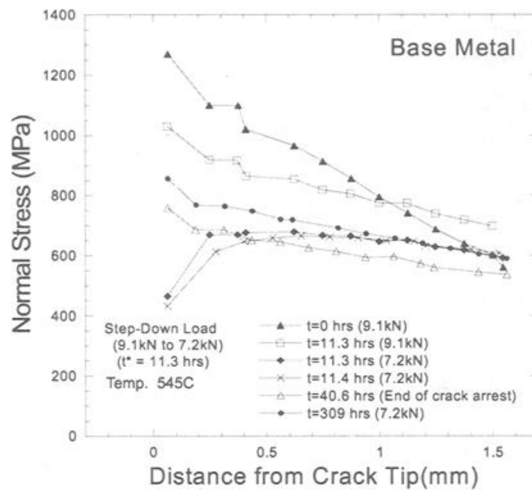

FIG. 11—*Distribution of normal stress ahead of the crack tip.*

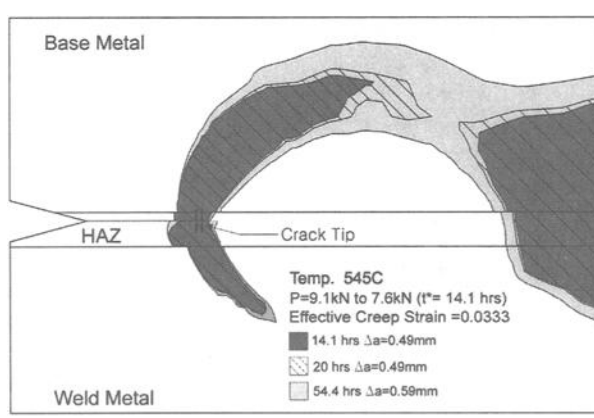

FIG. 12—*Effective creep strain contours before and after load change in a step-down load test on a weld specimen.*

The stress and strain distribution in the weld specimen showed a similar nature of variation with time. The effective stress contours were more or less symmetric except around the crack tip, however the effective creep strain contours showed asymmetry between the weld metal and base metal; see Fig. 12. The base metal had larger creep strain contours as expected.

Correlation of Crack Growth Rates

Crack growth rates under constant loads were found to be correlated well with $C^*(t)$ for both base metal and weld specimens in previous papers [14,15]. Crack growth rates in step-up loading and step-down loading were correlated with $C^*(t)$. The results are shown in Fig. 13(a) for a base metal specimen (BUP1), and in Fig. 13(b) for a weld specimen (WUP1). The overall picture reveals that while there is a little more scatter compared with constant load test data, $C^*(t)$ provides an acceptable correlation in either case. A comparable correlation was also found for specimen BUP2.

The data points in step-up loading moved from right to left at lower loads (solid triangles or diamonds) as time elapsed, then jumped to the right set of data points (solid circles) upon load change, the initial point of jump depending on whether or not there was a transient response. When there was one, the point moved from far right toward left, then back up to right until failure. With no transients, the points moved from left to right within the data set.

Crack growth rates in step-down loading also correlated with $C^*(t)$ reasonably well. Examples are given for a base metal specimen (BDN1) and a weld specimen (WDN2) in Fig. 14(a) and Fig. 14(b), respectively. In these figures the data points moved toward the left at higher loads within the set of solid circles, then jumped to far left of the data set (solid triangles) upon load change and the points moved up to right as the crack grew. The crack arrest part of the data was not included in these figures.

The data presented in this study illustrate that crack growth rates under two-step loading can be correlated, by and large, with $C^*(t)$ with the exception of the crack arrest portion in step-down loading. It is likely that an extension of the loading condition to smoothly increasing loads could lead to the same conclusion. For smoothly decreasing loads, the crack growth behavior would depend on the rate of load change. It may be possible to stop crack growth totally throughout the period of a decreasing load if the rate of load change is maintained greater than a certain level.

Conclusions

The creep crack growth behavior in the base metal and a weld joint of X20CrMoV 12 1 was investigated at 545°C under two-step loading. The transient behavior after sudden load change was examined with particular interest. The major conclusions of this study are as follows:

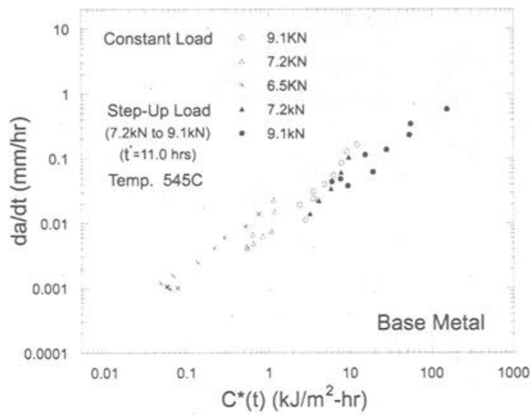

(a)

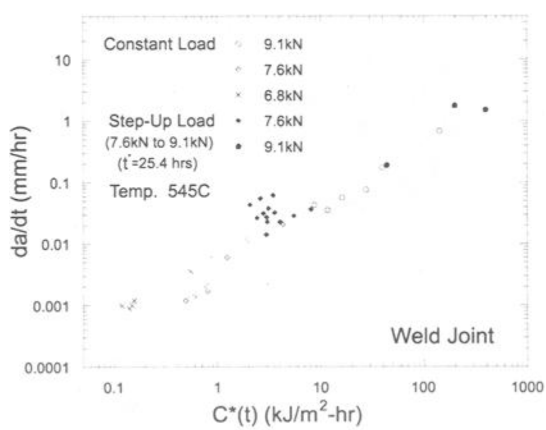

(b)

FIG. 13—*Correlation of crack growth rates with C*(t) for step-up loading; (a) base metal, (b) weld joint.*

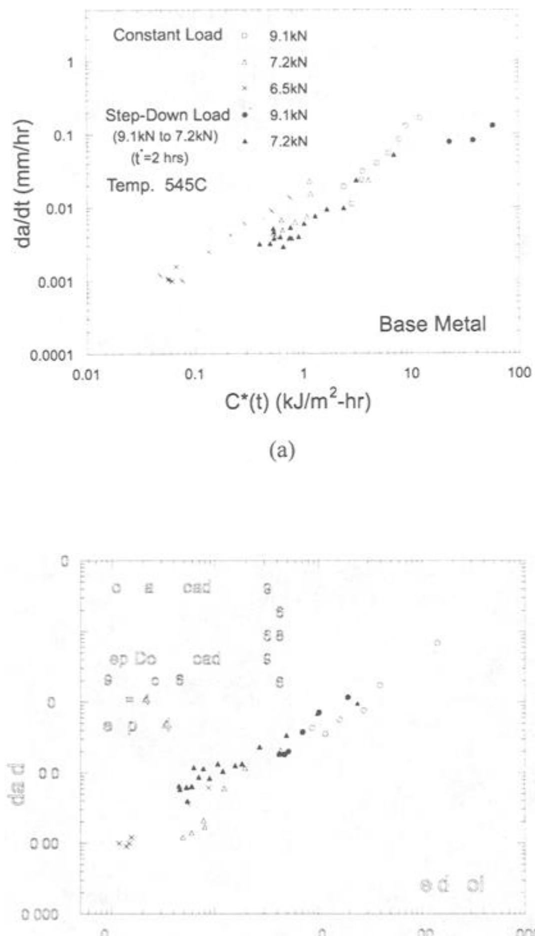

(a)

(b)

FIG. 14—*Correlation of crack growth rates with C*(t) for step-down loading;* (a) *base metal, (b) weld joint.*

1. Crack growth rates can be correlated with C*(t) under step-up or step-down loads as well as under constant loads. A sudden change in load leads to a jump of data points on the da/dt vs. C*(t) curve.
2. A sudden increase to a higher load could shorten the rupture time of a specimen compared to the specimen subjected to the higher load from the beginning. This can be explained in terms of stress relaxation and stress elevation around the crack tip during crack growth.
3. A sudden reduction of load causes crack arrest due to the lowered stresses in the very vicinity of the crack tip. Further development of creep strain in the neighborhood leads to redistribution of the crack tip stress to a higher level, resulting in resumption of crack growth as creep damage accumulates.
4. The period of crack arrest in step-down loading is longer when load change occurs earlier. This phenomenon is related to more localized creep strain and less creep damage at the crack tip for earlier load changes.

References

[1] Landes, J. D., and Begley, J. R., "A Fracture Mechanics Approach to Creep Crack Growth," *ASTM STP 590*, 1976, pp. 128-148.

[2] Saxena A., Creep Crack Growth under Non-Steady-State Conditions, *ASTM STP 905*, 1986, pp. 185-201.

[3] Riedel H., Rice J. R., Tensile Cracks in Creeping Solids, *ASTM STP 700*, 1980, pp. 112-130.

[4] Kalwa, G., "State of the Development and Application Techniques of the Steel X20 CrMoV 12 1," *Nuclear Engineering and Design*, Vol. 84, 1985, pp 87-95.

[5] Wu, R. and Sandstrom, R., "Creep Cavity Nucleation and Growth in 12Cr-Mo-V Steel," *Material Science and Technology*, Vol. 11, 1995, pp 579-588.

[6] Eggler, G., Earthman, J. C., Nilsvang, N., and Ilschner, B., "Microstructural Study of Creep Rupture in a 12% Chromium Ferritic Steel," *Acta Metallurgica.*, Vol. 37, No. 1, 1989, pp. 49-60.

[7] Eggler, G., "The Effect of Long-Term Creep on Particle Coarsening in Tempered Martensitic Ferritic Steels," *Acta Metallurgica*, Vol. 37, No. 12, 1989, pp. 3225-3234.

[8] Tian, Z. L., Coussement, C., De Witte, M., and Steen, N., "Creep Beahvior of 12Cr-Mo-V Steel Weldments," *Int. J. Pres. Ves. & Piping*, Vo. 46, 1991, pp. 339-348.

[9] Wu, R., Sandstrom, R., and Storesund, J., *Materials at High Temperatures*, Vo. 10, 1992, pp. 154-163.

[10]Wu, R., Sandstrom, R., and Storesund, J., *Materials at High Temperatures*, Vo. 12, No. 4, 1994, pp. 277-283.

[11]Sandstrom, R., Karlsson, S., and Modin, S., *High Temperature Technology*, Vol. 3, No. 2, 1985, pp. 71-78.

[12]Schneider, K., Tolksdorf, E., and Grünling, H. W., "Toughness Behavior of the Steel X20CrMoV 12 1 - Results of Optimizing the Base- and Weld Metal," *Nuclear Engineering and Design*, Vol. 84, 1985, pp. 109-122.

[13]Bashu, S. A., Singh, K., and Rawart, M. S., "Effect of Heat Treatment on

Mechanical Properties and Fracture Behavior of a 12CrMoV Steel, *Materials Science and Engineering*, Vol. A127, 1990, pp. 7-15.

[14]Park, Y. K., Kim, K. S., Chung, Y.-K., and Park, J.-J., "Creep Crack Growth in X20CrMoV 12 1 Steel and Its Weld Joint," Transactions of ASME, *Journal of Pressure Vessel Technology*, Vol. 123, 2001, pp. 1-6.

[15]Kim, K. S., Lee, N. W., Chung, Y. K., and Park, J. J., "Creep Crack Growth in X20CrMoV 12 1 Steel Weld Joints," *ASTM STP 1406*, 2001, pp. 179-194.

[16]Joo, C.-H., Chung, Y.-K., Park, J.-J. and Kim, H.-J., "Quantification of Creep Cavitation in Welded Joint and Evaluation of Material Characteristics of Simulated Heat-Affected Zone in X20CrMoV 12 1 Steel," presented in the 2000 Pressure Vessels and Piping Conference, Seattle, Washington, July 23-27, 2000.

[17]*ABAQUS User's Manual*, Version 5.8, Hibbit, Karlsson & Sorensen, Inc., 1998.

[18]ASTM E1457-92, Standard Test Method for Measurement of Creep Crack Growth in Metals, *Annual Book of Standards*, Vol. 03.01, American Society for Testing and Materials, Philadelphia, 1992, pp. 1031-1034.

[19]Murakami, Y., *Stress Intensity Factors Handbook*, Vol. 1, Pergamon Press, 1987.

[20]Kumar, V., German, M., and Shih, C. F., *An Engineering Approach for Elastic-Plastic Fracture Analysis*, EPRI Report NP-1931, EPRI, 1981.

[21]Han, C., and Kim, K. S., "Time-dependent Crack Growth in Stainless Steel 304 in the Plasticity-dominant Field," *Engineering Fracture Mechanics*, Vol. 68, 2001, pp. 39-52.

Wade A. Meith,[1] Michael R. Hill,[1] and Tina L. Panontin[2]

Analytical and Experimental Study of Fracture in Bend Specimens Subjected to Local Compression

---

Reference: Meith, W. A., Hill, M. R., and Panontin, T. L., **"Analytical and Experimental Study of Fracture in Bend Specimens Subjected to Local Compression,"** *Fatigue and Fracture Mechanics: 33rd Volume, ASTM STP 1417*, W. G. Reuter and R. S. Piascik, Eds., ASTM International, West Conshohocken, PA, 2002.

Abstract: This study presents finite element simulations and fracture predictions for experimental conditions in a recent ASTM round-robin program on weld fracture toughness. The simulations include the effects of weld residual stress and residual stress alteration due to local compression of notched SE(B) specimens. Simulations are performed for a variety of material models and local compression details. Fracture is predicted using crack-tip stress and strain as inputs to both a local and a global prediction scheme. The local prediction is based on the RKR micromechanical model. The global prediction is based on obtaining a critical value of the J-integral, computed using a modified domain integral. Results predict that fracture toughness in the round robin was markedly reduced by local compression of the specimens. The amount of the reduction depends on the position of the compression platen relative to the notch-tip, but is largely independent of the amount of local compression applied. Available data from the round robin do not completely confirm the prediction results, but some of these data may have been influenced by warm pre-stressing during fatigue pre-cracking.

Keywords: local compression, weld metal, residual stress, fracture toughness

Introduction

This study presents fracture predictions for welded and locally compressed fracture test coupons used in a recent ASTM round-robin testing program. Residual stresses in fracture test coupons removed from larger welded joints often promote preferential crack growth in some areas (tensile stress) while inhibiting growth in others (compressive stress).

---

[1] Graduate student and Assistant Professor, respectively, Department of Mechanical and Aeronautical Engineering, University of California, One Shields Avenue, Davis, CA 95616.

[2] Chief Engineer, NASA Ames Research Center, MS 213-4, Moffett Field, CA 94035-1000.

This can create a curved crack front following fatigue pre-cracking, which may invalidate subsequent fracture measurement. The process of local compression has been used to alter residual stresses near the machined notch in fracture specimens, enabling a straighter pre-crack to be introduced [*1*]. Although the local compression process provides a straighter crack, it has been argued that it also reduces the fracture load, giving a lower apparent toughness than would be found in the same material free of residual stress [2]. Despite this drawback, the need for fracture measurements in weld metal has caused ASTM to draft a proposed Annex to ASTM Standard Method for Crack-Tip Opening Displacement (CTOD) Fracture Toughness Measurement (E 1290) to allow for local compression when testing weld metals. A recent ASTM round-robin test program was initiated to demonstrate the suitability of the proposed Annex. This paper attempts to quantify the impact of local compression on the results of the test program.

The paper describes residual stress measurement, finite element modeling, and fracture prediction for the experimental conditions in the ASTM round robin. It reports the experimental determination of initial residual stresses in specimen blanks. It further describes simulation of local compression and fracture loading of the residual stress bearing specimens. Fracture is predicted using both a local and a global approach, each based on finite element predictions of crack-tip stress and strain. The local approach uses a critical stress and length scale. The global approach uses the crack driving force, as determined by a modified domain J-integral formulation which properly accounts for prior plastic work and residual stress. Parametric results are provided to investigate the sensitivity of the computations to the position of the locally compressed region, to the amount of local compression, and to the assumed material model. Preliminary round-robin fracture results provided by two participating laboratories are incorporated to calibrate fracture models and assess the modeling results.

Round-Robin Test Program

The ASTM round-robin consisted of fabrication, local compression, fatigue pre-cracking, and fracture testing of SE(B) samples removed from a large-diameter, longitudinally-welded pipe. Local compression (LC) and pre-cracking were performed at room temperature while fracture testing was performed on the lower shelf (-196 C). Notched SE(B) specimens and un-notched specimen blanks were obtained by the authors and used in the present study to investigate the weld geometry, material properties, and to measure residual stresses. The authors did not perform fracture testing, but did obtain fracture test results from two laboratories that responded to a call for data. These laboratories provided detailed information on their laboratory procedures and also submitted fracture toughness results.

The welded pipe from which specimens were removed was fabricated from pressure vessel steel. The SE(B) specimens were removed from the pipe with the span dimension transverse to the weld, the crack growth direction along the weld, and the crack front sampling the entire weld thickness. A typical SE(B) specimen is shown in Figure 1. Material properties for the weld and parent materials were provided in the ASTM round-robin instructions for both ambient and lower-shelf temperatures. These properties are reported in the first four data columns of Table 1, and indicate that the weld and parent materials are low-hardening and closely matched. The last row of this table lists approximate Ramberg-Osgood hardening exponents found from the yield and ultimate strengths as suggested by Kirk and Wang [3]. The last four columns of Table 1 are described below.

The two responding laboratories applied LC differently and reported different fracture toughness. Laboratory A applied LC simultaneously to both sides of the specimen, using 12.7 mm platens centered over the tip of the pre-crack starter notch, as shown in Figure 2(a). The center of the platen was located 0.43W from the front face of the specimen (i.e., d/W = 0.43 where d is the distance from the front face of the SE(B) to the center of the indentation). Laboratory B applied LC in two stages, compressing one side, then the other as shown in Figure 2(b) and (c). Laboratory B used a 12.7 mm platen centered at d/W = 0.65. Laboratory A performed fracture testing for specimens with 0%, 1%, and 2% LC. Laboratory B performed fracture testing for 1% LC. Fracture test results are summarized in Figure 3 and show a disparity in measured toughness at 1% LC.

Residual Stress Determination

In order to assess the influence of pre-existing weld residual stress on the round-robin results, residual stress was measured in an un-notched specimen blank. Relative to the fracture specimen, the opening mode residual stress was measured as a function of the through-thickness position (i.e., relative to the coordinates in Figure 1, the *yy*-component of residual stress was measured as a function of *z*). Since chemical etching revealed no evidence of a weld start-stop cycle in the specimen blank, residual stress was assumed to

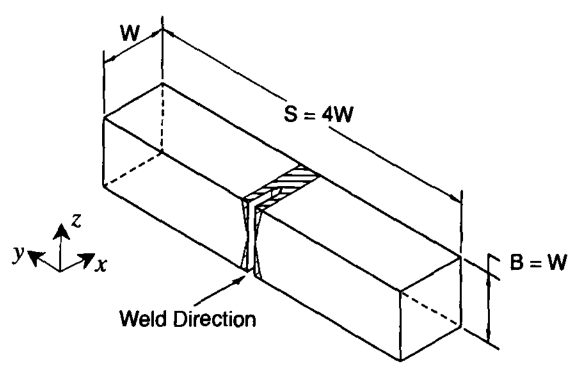

Figure 1 – *Typical SE(B) specimen with coordinate directions assumed*

Table 1 – *Mechanical properties of weld and parent materials*

Source	Round-robin instructions				Hardness-adjusted		Low hardening	
Material	Weld		Parent		Parent		Weld	
Temp (C)	21	-196	21	-196	21	-196	21	-196
S_y (MPa)	548	888	514	848	484	785	548	888
S_u (MPa)	593	989	593	960	524	874	–	–
E (GPa)	206	218	206	218	206	218	206	218
ν	0.3	0.3	0.3	0.3	0.3	0.3	0.3	0.3
n	25.2	20.4	16.8	18.5	25.2	20.4	--	--

be invariant of the position along the weld (x-direction). That is, etching indicated a continuous weld process was used and continuous welding induces residual stress largely invariant of position along the weld [*4*]. The compliance method was used to estimate the residual stress [*5, 6*]. Strain gages were attached on the upper and lower weld surfaces and the specimen blank was sliced incrementally in the z-direction using wire electric discharge machining, as shown in Figure 4. Strain released at the top and bottom gages was gathered as a function of z-direction depth of cut and these data used in a finite-element-based back-calculation scheme to determine residual stress in the specimen

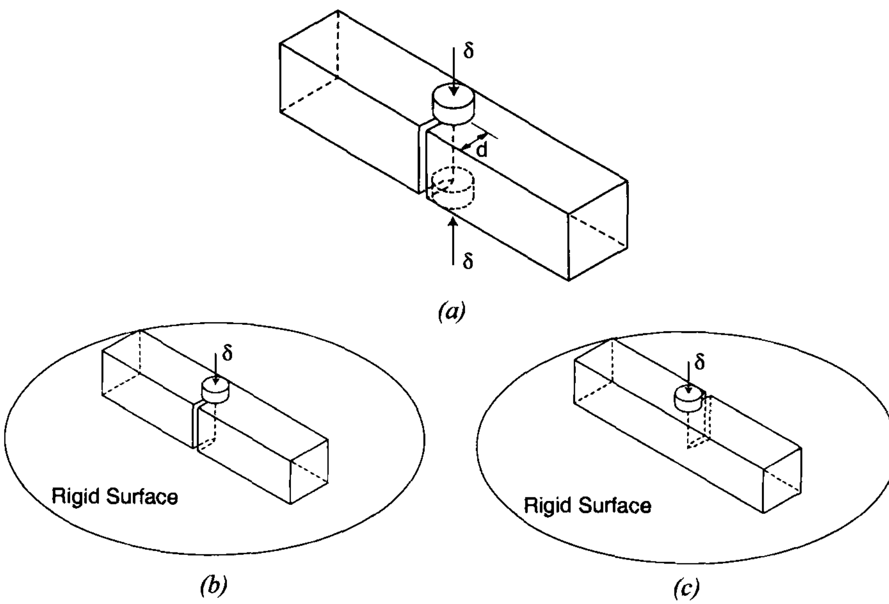

Figure 2 – *Application of local compression: (a) Laboratory A; (b) and (c) Laboratory B*

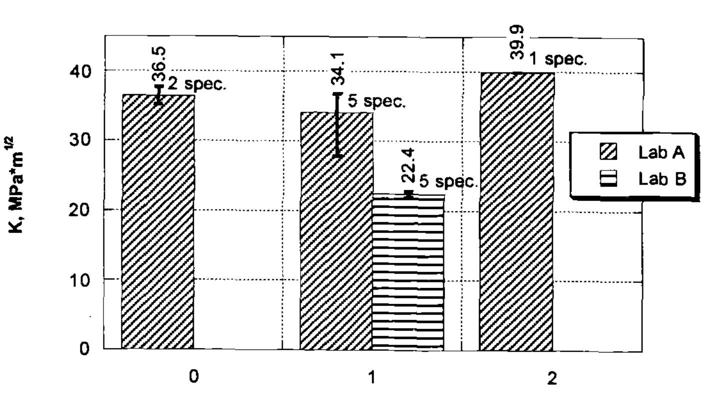

Figure 3 – *Fracture toughness obtained by both laboratories for various amounts of LC*

blank prior to slicing. The resulting residual stress distribution will be used in finite element simulation of the round-robin specimens as described below.

Fracture Prediction

Fracture prediction for specimens in the round robin study requires a significant amount of information and analysis. Fracture in the specimens occurred due to the combined action of applied loading and residual stress. The residual stress in locally compressed specimens is complex, but has been previously predicted by directly simulating the elastic-plastic compression process [*2*]. The material response during LC depends on the pre-existing weld residual stress. So, the crack-tip conditions that initiate fracture depend on weld residual stress, residual stress due to LC, and stresses due to applied three-point bend loading. In the present study, the finite element method is used to account for these three contributions to the crack-tip state. The crack-tip conditions found over a range of applied load are then used to predict the fracture load during three-point bending.

Fracture Models

Fracture is predicted following two distinct approaches. The need for two approaches lies in uncertainty regarding the correct methodology for lower-shelf fracture prediction under varying constraint conditions. Lower-shelf behavior is thought to depend on opening stress and be invariant to the state of strain [*7*]. However, experimental evidence on the lower-shelf suggests that fracture is independent of constraint [*8*]. These two points of view lead to a contradiction since different constraint implies different crack-tip stresses at the same value of driving force. The contradiction is important in the present study because previous finite element modeling of LC indicated that the process markedly increases constraint in three-point bend specimens [*2*]. Therefore, the present study predicts fracture in two ways, one dependent on and another independent of constraint.

The constraint-dependent fracture model is a local approach based on achieving a critical level of opening stress over a fixed length scale. Initiation of cleavage fracture in mild steels can be predicted using the RKR micromechanical model [*7*]. This relatively simple model predicts fracture when the opening stress, σ_{yy}, ahead of the crack-tip

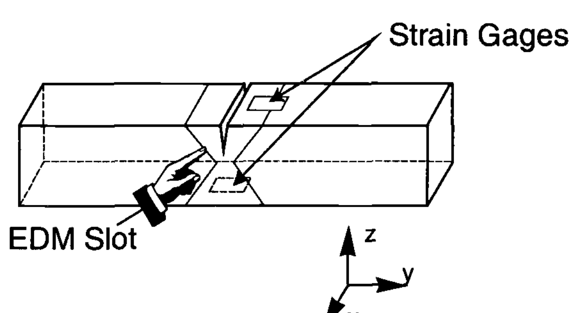

Figure 4 – *Strain gage locations and slot orientation for residual stress determination.*

exceeds a fracture stress, σ^*, over a microstructurally relevant distance, l^*. In applying this model, one monitors the progress of the opening stress ahead of the crack-tip due to residual and applied loading. Once the RKR criterion is satisfied, the associated applied load and deformation can be found from the FEM results and can be used to derive an *apparent* toughness comparable to laboratory results. The parameters in the RKR model are typically found through laboratory testing for a given material and reported ranges for steels are 2 to 5 grain diameters for l^*, and 2 to 4 times the yield strength for σ^* [7].

The constraint independent fracture model is based on achieving a critical level of the J-integral at some point along the crack front. The domain integral technique is used to compute J from finite element predictions of stress, strain, and deformation in domains surrounding the crack tip [9]. The current analysis conditions require special care when computing the domain integral because residual stress and plastic work of LC cause path dependent values of J. Recent research has provided a methodology to obtain contour independent values of J for these conditions [10, 11]. A computer program was written to employ these methods for three dimensional finite element results from the present analyses. Since residual stress due to welding and LC varies along the crack front, the maximum value of J along the front is assumed to control fracture. To highlight the fact that the values of J presented in this study are computed using the domain integral, and therefore include the combined effects of residual stress and applied loading, the results will be referred to as J_{DI}.

The fracture prediction models are calibrated from the test results for non-locally compressed specimens provided by Laboratory A and shown in Figure 3. That is, we impose residual stress and applied three-point bending on a finite element model of the SE(B) specimen (but do not simulate local compression). The three-point bend load for calibration is found from the model geometry, the average toughness found by Lab A ($K_{cal} = 36.5$ MPa$\sqrt{\text{m}}$), and the stress intensity factor solution in ASTM E 1290, and is $P_{cal} = 13.6$ kN. When the model is loaded to this force, the finite element results are used to calibrate the RKR and J_{DI} models. The maximum value of J_{DI} found along the crack front is taken to be the level of J controlling fracture, J_{cal}. Since the RKR model has two fracture parameters and we use only a single calibration condition, we assume two different values of σ^* and identify l^* for each as the largest distance ahead of the crack tip where $\sigma_{yy} = \sigma^*$. The two values assumed for σ^* are 2 S_y and 2.5 S_y, and the corresponding predictors are referred to as RKR_1 and RKR_2. As will be shown, the small range of assumed fracture stress produces length scales that differ by a factor of 2 and therefore predict somewhat different fracture loads in the locally compressed specimens. Given these three calibrated fracture models, we can predict fracture for the specimens with the range of LC shown in Figure 3.

Finite Element Modeling

General - Elastic-plastic finite element computation is used to simulate the response the SE(B) to both applied and residual stresses simultaneously. The finite element solutions employ a non-linear, finite strain formulation. Plasticity is assumed to follow isotropic, incremental J_2 flow theory with a piece-wise linear Cauchy-stress logarithmic-strain curve obtained from power-law fits derived from the material strengths given in the round-robin instructions. The commercial code ABAQUS is used to perform the analyses

[12]. Mesh refinement in the crack-tip region was chosen to assure that stress and strain are accurately captured in the near-tip region. Time stepping in the analysis provides a means to capture the developing crack-tip state with increasing applied load.

The three-dimensional model of the SE(B) is shown in Figure 5. The model is composed of eight-node, hexahedral elements with reduced integration. The model dimensions are as shown in Figure 1 with a crack length of a/W = 0.5. Quarter symmetry was used, with one symmetry plane halving the span of the specimen, and another halving the thickness. To simulate three-point bending, nodal constraints in the x-direction were imposed at the roller location and displacement applied in the negative x-direction on the span symmetry plane. This load was split between two sets of nodes to reduce the tendency for strain localization at the load point. The mesh has an initially blunted crack tip with radius of 4.82 μm to enhance convergence. The mesh has ten layers of elements through the model thickness with a geometric progression of element thickness such that midplane elements are ten times thicker than those at the free surface.

Weld residual stress - Pre-existing weld residual stress (RS) in the SE(B) specimens is included in the finite element computations using eigenstrain. Eigenstrain is a spatially varying, second order tensor that represents the combination of all inelastic, incompatible strains set up during processing of a material [13]. In welding, the eigenstrain is a combination of thermal, plastic, and transformation strains. The eigenstrain field is defined with reference to elastic deformation of the structure, and reproduces the entire RS state when the material behavior is elastic. For a particular process the eigenstrain field is a tensor with spatial dependence, and can be found experimentally [14] or by modeling [15].

The use of an eigenstrain distribution in modeling offers several advantages for further analysis. First, the residual stress present can be determined by imposing the eigenstrain distribution in a linear elastic finite element model of the geometry. (Note that residual stresses, by their nature, do not result in active yielding, and a valid eigenstrain field must impose stresses that satisfy the yield criterion). Although an eigenstrain analysis is complicated by the spatial variation of each component of the eigenstrain tensor, a general-purpose finite element program can be used to produce the RS field. Further, when the eigenstrain field is known, the entire, full-field, triaxial RS state is known at every point within the structure.

When the eigenstrain field is known for the unflawed structure, the analysis of a flawed structure can be performed. The addition of a crack introduces new surfaces, and the RS state in the flawed body depends on these surfaces. If the structure is linear elastic, the state is found simply by modeling the traction-free surfaces. In non-linear materials, crack-tip yielding must be allowed when introducing the flaw. To handle this situation, the eigenstrain distribution is first imposed in the body with crack-face nodes restrained, and the equilibrium RS state found (this step is elastic). Then, the crack-face nodes are released in succession, so that the crack gradually extends from the free surface to simulate fatigue (this step can be elastic-plastic). The rate at which the crack is extended will have a bearing on the crack-tip fields, and one must ensure that the opening is gradual enough (e.g., so subsequent fracture analysis is not adversely affected). When properly executed, this process redistributes the original RS field, allowing for crack-tip yielding, and resulting in a flawed RS bearing structure.

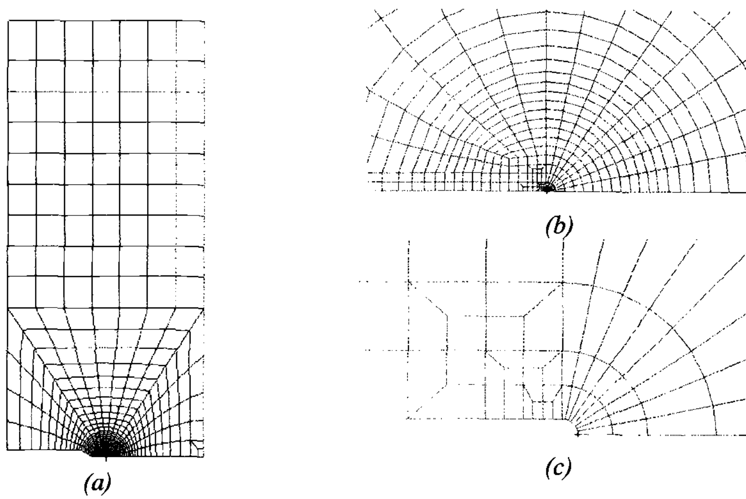

Figure 5 – *Finite element mesh: (a) full mesh, (b) and (c) detail of crack tip*

The specific eigenstrain distribution used in this work was derived from residual stress determined experimentally. As will be shown later, the opening residual stresses were found to closely resemble a sinusoidal variation through the weld joint thickness. The stress measurements were made only on the weld centerline which coincides with the span symmetry plane in the SE(B) specimens. In order to distribute the stresses throughout the SE(B) model it was assumed that the residual stresses are a maximum on the weld centerline and that they decay smoothly with distance from the weld centerline. Previous work on weld residual stresses used a tensor-product representation to distribute eigenstrain spatially in the transverse and through-thickness weld directions [*16*]. We will modify this distribution to match the experimentally determined stress. Since the particular eigenstrain distribution depends on the residual stress results, the eigenstrain distribution is described below.

Local compression - The application of LC is modeled in three distinct steps. The first step drives a mathematically defined rigid surface, which represents the compression platen, into the surface of the SE(B) using contact procedures. The second step removes enough of this displacement so that the third step will be entirely elastic. The third step then completely removes the contact relation between the rigid surface and the SE(B). Because the finite element model employs symmetry about the specimen thickness, the LC simulation most closely reflects the procedures of Laboratory A. Various amounts of local compression are simulated. The rigid surface displaces in the thickness direction of the specimen to compress the surface and leave a final reduction in thickness of 0.5%, 1% or 2% after removal of the rigid surface from the model.

In actual testing, LC is followed by fatigue pre-cracking prior to loading to fracture. To simulate the pre-cracking process, crack-face nodes within 0.07W behind the crack-tip in the SE(B) mesh are restrained during the compression process and are released after compression loads are removed. This strategy leaves a plastic zone due to residual stress remaining after LC, but no attempt is made to account for plasticity or other effects related to fatigue pre-cracking loads. Simulation of a locally compressed specimen, then, consists of seven steps: 1) find residual stress (equilibrium) in the presence of eigenstrain due to welding, 2) apply LC displacements, 3) reduce LC displacements, 4) remove the platen rigid surface from the model, 5) release crack-face tractions to simulate pre-cracking, 6) reduce the ambient temperature to change material properties, and 7) apply three-point bend loads to fracture.

Material Models

Round robin material information and hardness tests preformed on specimen blanks were examined to decide the best method for modeling the welded specimens. Test specimens were fracture tested at low temperature and hence exhibited low toughness and small scale yielding. Since the crack-tip plastic zone was likely small enough to be entirely in the weld metal, a homogeneous material model is a viable option. However, LC causes plastic deformation outside the weld (at room temperature) and this suggests that a bimaterial model may be a better approach, with one flow curve for the weld and one for the base metal. Although the strengths in Table 1 suggest that the weld and parent metal are well matched, a hardness traverse conducted on a specimen blank suggested that the weld metal was considerably stronger than the parent metal, with hardness in the weld bead averaging 94 HRB and in the parent metal averaging 89.5 HRB. Conversion from these hardness values to ultimate strengths (by converting to Brinnell hardness and multiplying the result by 0.5) suggests that the parent metal strength is about 89% of that in the weld metal.

Because the hardness results suggest a contradiction with the strengths shown in the first four data columns of Table 1, three material combinations were investigated in this study. The first material model uses a single, power-law hardening flow curve for each temperature corresponding to the weld metal data shown in Table 1. The second material model uses two flow curves for each temperature, one for the parent and one for the base metal. The parent flow curves were found by multiplying the weld metal power-law flow curves by the ratio of the hardness-indicated strengths (0.89). These flow curves are shown in Figure 6. The weld region of the SE(B) was assumed to be 12.7 mm wide which followed from the hardness traverse and from physical measurements on a polished and chemically etched specimen blank. In order to assess the sensitivity of the modeling to the amount of hardening assumed, an additional material model was considered. The power-law hardening flow curves are an approximation that may not reflect the actual near-yield behavior of the material (e.g., the presence of a sharp yield point would not be accounted for). To assess the sensitivity of the models to initial hardening, a nearly perfectly plastic flow curve was also used. For this model, the SE(B) was assumed to be homogeneous, with yield strength equal to the weld material as reported in Table 1. A small post-yield tangent modulus (0.05% S_y) was added to enhance convergence of the finite element computations.

Again, the objective of the current study is to model the experimental conditions of the round-robin program. Since different experimental approaches were pursued, a parametric study was performed. The parameters related to LC are the location of the compression platen and the amount of compression. The three material models described above were also included as parameters. Table 2 shows the computations performed in the current study. The platen position, amount of compression, and material model were varied as shown.

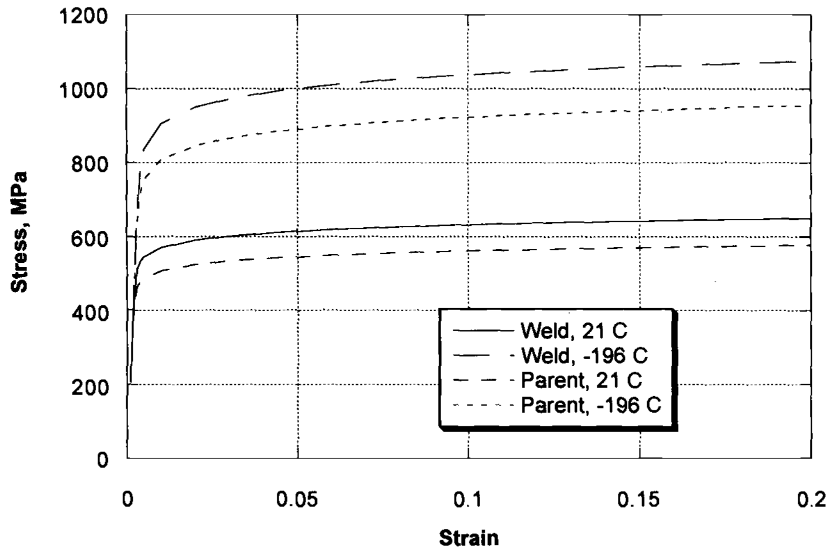

Figure 6 – Ramberg-Osgood material curves for the weld and parent materials at both temperatures

Table 2 – *Seven simulations for various combinations of the platen location, amount of LC, and material model reported in this study*

Platen Center (d/W)	% LC	Material Model		
		All Weld	Bimaterial	Low Hardening
0.43	0.5	X		
	1.0	X	X	X
	2.0	X		
0.5	1.0	X		
0.57	1.0	X		

Results

Residual Stress Distribution

Residual stress found using the compliance method is shown in Figure 7, normalized by the weld metal yield strength. Also shown in the figure are the results of an elastic eigenstrain analysis described below. The experimental results are in contrast to some typical distributions of residual stress that often show yield-level tension on the surfaces and compression in the interior. However, the difference between this distribution and typical results is likely due to residual stress redistribution that occurred when the specimen blank was removed from the larger welded pipe. The magnitude of the residual stress is quite low throughout the specimen in comparison to the yield strength of the material. Although the residual stresses are relatively small, they can still affect the ability to obtain a straight-fronted fatigue pre-crack in the fracture specimens.

Assuming coordinates centered in the SE(B) specimen, and oriented as indicated in Figure 1, the eigenstrain distribution is given by

$$
\begin{aligned}
&\varepsilon^*_{xy} = \varepsilon^*_{yz} = \varepsilon^*_{xz} = \varepsilon^*_{zz} = 0 \\
&\varepsilon^*_{xx} = -\nu\varepsilon^*_{yy}/(1-\nu) \\
&\varepsilon^*_{yy} = -2.8\cdot 10^{-4} f(y)g(z) \\
&f(y) = \begin{cases} 0.5*(1+\cos(2\pi y/t)) & y < t/2 \\ 0 & y \geq t/2 \end{cases} \\
&g(z) = \cos(2\pi z/t)
\end{aligned}
\tag{1}
$$

where, ε^*_{ij} are the components of the eigenstrain tensor, ν is Poisson's ratio, and t is the thickness of the welded joint (25.4 mm). This eigenstrain distribution imposes an opening stress distribution similar to that found experimentally, when imposed in an un-notched specimen geometry. Figure 7 compares the results of an elastic finite element analysis using the eigenstrain given by Equation (1) with the experimentally determined stress. There are four curves for the eigenstrain model, with $y/t = 0$ corresponding to the experimental slotting location. The peak levels of residual stress are in agreement. The eigenstrain results further show how the residual stress magnitude decreases with distance from the center of the weld (i.e., increasing values of y/t).

Fracture Model Calibration

Calibration was performed by simulating a non-locally compressed, weld residual stress bearing SE(B) and using the resulting crack-tip region stresses and strains to satisfy the failure models at a load corresponding to K_{cal}. The material response at the crack tip is slightly different for each of the three material models, so each is calibrated separately. Opening stress for the calibration loading condition and the all weld material model is shown in Figure 8 (the three other curves are described below). The opening stress reaches 2.5 S_y at $x/W = 0.0018$, so the length scale for RKR_2 is 46.9 μm. The length scale for RKR_1 is similarly found to be 111 μm. Simulations and analyses for the other material models provide the calibration parameters reported in Table 3. The J_{Di} model is calibrated by computing J at the calibration loading condition and taking the maximum value of J_{Di} along the crack front. The J_{Di} calibrations are given for each material model in Table 3.

Fracture Prediction

Fracture predictions for the all weld material model with the platen positioned over the notch-tip are shown in Figure 9. Results are presented in terms of the apparent toughness, which is computed from the load and geometry using the stress-intensity factor solution in ASTM E-399. The apparent toughness is normalized by the stress intensity factor used in calibrating the fracture models, $K_{cal} = 36.5\ \text{MPa}\sqrt{\text{m}}$. The fracture models predict that LC should reduce toughness 45 to 65% relative to the un-compressed specimens. The exact predictions depend more strongly on the fracture model assumed than on the amount of LC imposed. The differences among the fracture models result from constraint differences caused by LC. The opening stress distributions for 1% LC

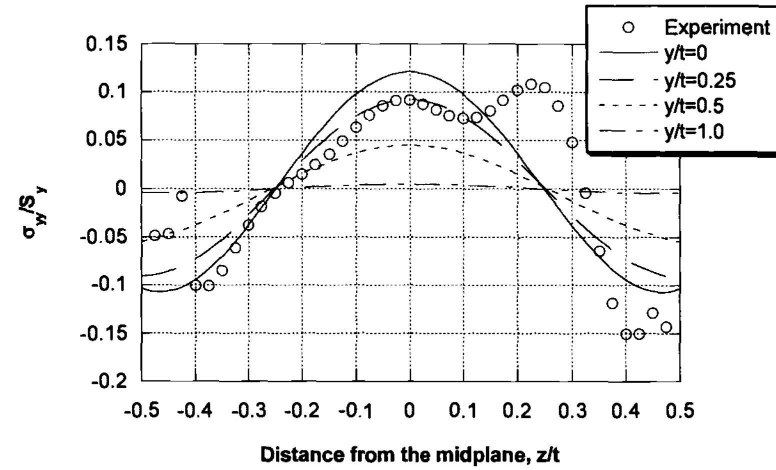

Figure 7 – *Comparison of residual stress from experiment with that created in the specimen blank when loaded by the eigenstrain field given by Equation (1)*

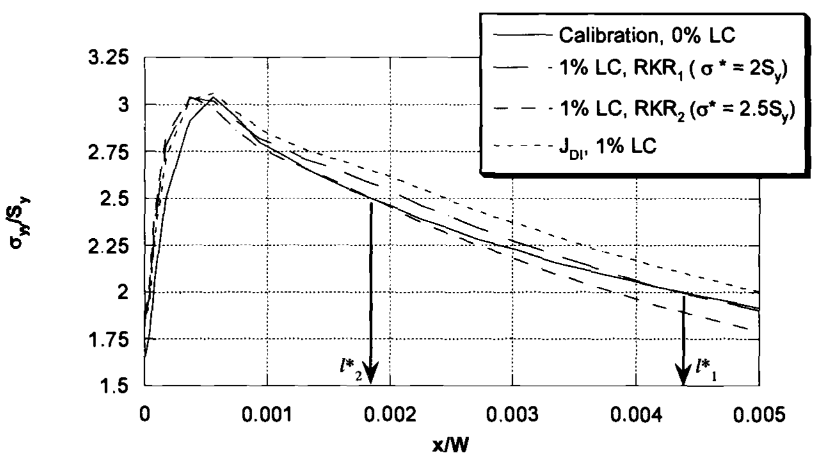

Figure 8 – *Midplane opening stress ahead of the crack-tip for the all weld model at the calibration loading and at failure for 1% LC and d/W = 0.43 as defined by the three fracture models*

Table 3 – *Calibration values*

Material Model	J_{cal}, kJ/m^2	l^* ($\sigma^* = 2S_y$), μm	l^* ($\sigma^* = 2.5S_y$), μm
All Weld Material	7.09	111	46.9
Bimaterial	7.15	111	46.9
No Hardening	7.14	120	48.0

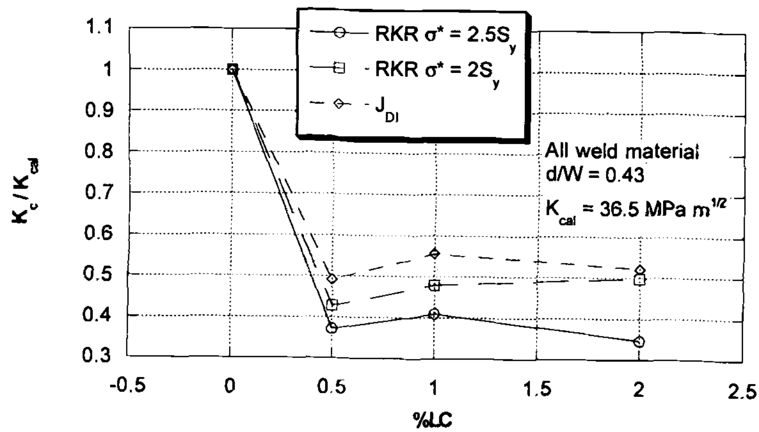

Figure 9 – *Apparent toughness versus % LC for all weld material model, platen centered at d/W = 0.43*

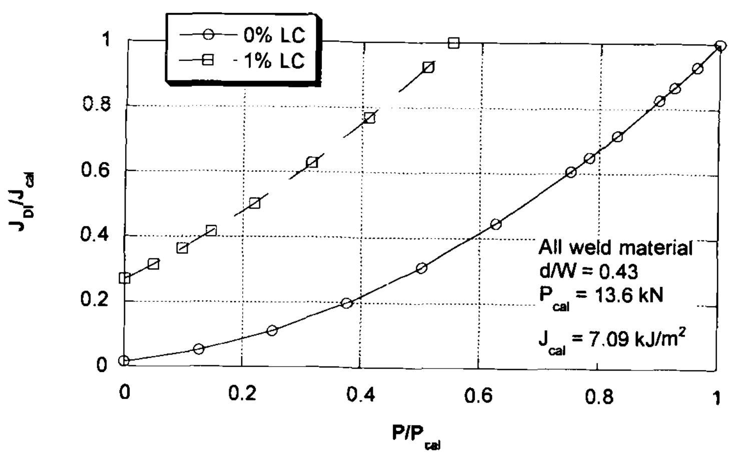

Figure 10 – *Comparison J_{DI} versus applied load for the all weld material model at different amounts of LC*

and the all weld material model are shown with the calibration condition in Figure 8. The three curves show the opening stress at the fracture load predicted by the corresponding model. The J_{DI} curve shows that the same J results in higher opening stresses in the 1% LC model, which indicates higher constraint. The two RKR prediction curves are lower than the J_{DI} curve because they are sensitive to the LC-imposed constraint. The RKR predictors therefore indicate a larger effect of LC.

The impact of LC on crack driving force can be observed by examining the development of J_{DI} with applied load. LC causes a non-zero driving force at zero applied load. This is demonstrated in Figure 10, which plots J_{DI} versus the applied load for un-compressed and 1% compressed models. The large value of J_{DI} at zero applied load in the LC model serves to decrease the predicted fracture load and therefore the apparent toughness. The figure further indicates that the residual stress state in the un-compressed SE(B) produces only a small J_{DI} at zero applied load. The small magnitude is due to the fact that the residual opening stresses are small and nearly equilibrate along the crack front.

Figure 11 illustrates the influence of platen location on apparent toughness. The specific locations of the platen center correspond to the starter notch tip, the pre-crack tip, and a position ahead of the pre-crack tip. The results suggest that moving the platen center toward the back face reduces apparent toughness. Since the RKR and J_{DI} predictions converge when the platen is further over the ligament (d/W = 0.57) the effect at that position is mainly due to the contribution of residual stress imposed by LC to the crack driving force. The smallest effect on apparent toughness occurs when the center of the compression platen is between the pre-crack tip and the front face.

Figure 12 shows the influence of the material model on the apparent toughness for 1% compression with the platen centered on the notch tip. These results indicate a significant sensitivity to the assumed flow curve. The difference between the low hardening and all weld models suggests that strain hardening increases the effect of LC. The bimaterial model predicts a larger influence of LC than either of the two homogeneous material models. The results presented in Figure 12 show that accurate determination of the weld and base metal flow curves is important in predicting the influence of LC on apparent toughness.

To first order, the influence of LC on apparent toughness predicted for the SE(B) depends on the J_{DI} at zero load following compression. Table 4 shows this quantity, normalized by J_{cal}, for each analysis condition, where a larger value suggests a larger LC-induced toughness change. The driving force of residual stress left by LC increases with *d/W* which agrees with the trends in Figure 11. J_{DI} at zero load also suggests the same dependence of the material model on apparent toughness displayed in Figure 12.

Discussion

Comparison of the laboratory toughness measurements shown in Figure 3 with the model predictions suggests the models over-predict the effect of LC. The all weld, J_{DI} prediction trend is shown with the experimental data in Figure 13. While the data from Lab B compare favorably with the prediction at 1% LC, the data from Lab A do not. The test records from Lab A and B indicate that the pre-cracking loads differed significantly, producing final ΔK values of approximately 19 $\mathrm{MPa}\sqrt{\mathrm{m}}$ and 11 $\mathrm{MPa}\sqrt{\mathrm{m}}$, respectively, at $R = 0.1$. It is suspected that the elevated pre-crack levels used by Lab A led to warm pre-stressing and elevated toughness. The simulations suggest that pre-cracking loads in compressed specimens are superimposed on a positive residual driving force left by LC, therefore producing an even greater warm pre-stress effect than indicated by the applied loading. Additional tests are planned by Lab A to provide specimens pre-cracked at lower levels and obtain toughness measurements at 0% and 1% LC.

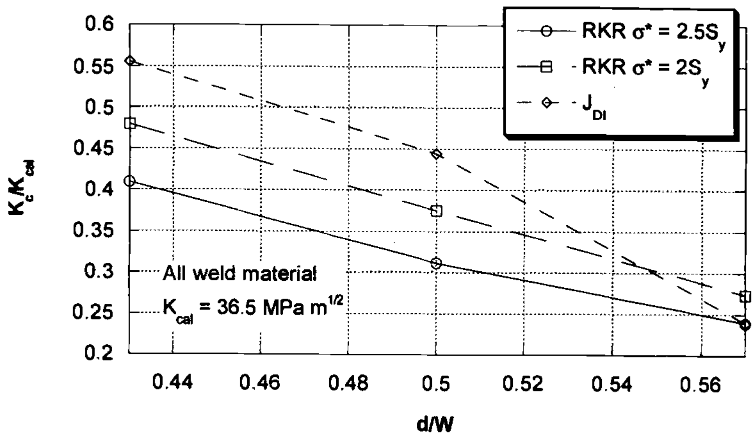

Figure 11 – *Apparent toughness vs. platen location for the all-weld material model*

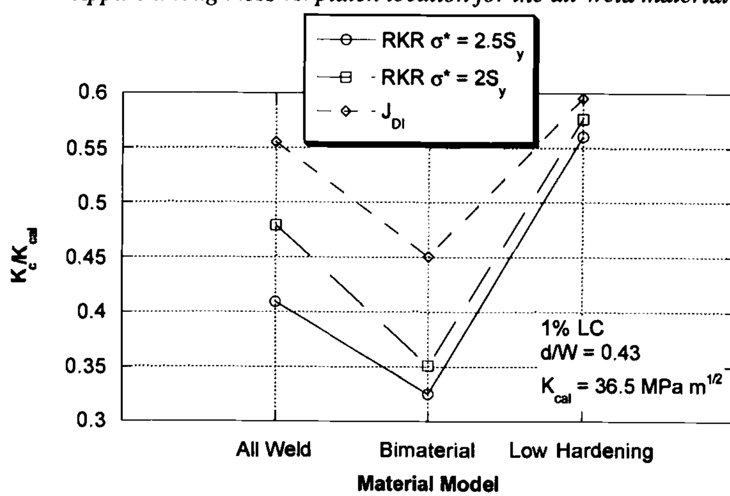

Figure 12 – *Apparent toughness versus material model, 1% compressed and d/W = 0.43*

Table 4 – *J_{DI} at zero load normalized by J_{cal} for all seven cases analyzed (J_{cal} = 7.09kJ/m^2)*

Platen Center (d/W)	% LC	Material Model		
		All Weld	Bimaterial	Low Hardening
0.43	0.5	0.33		
	1.0	0.27	0.38	0.23
	2.0	0.30		
0.5	1.0	0.38		
0.57	1.0	0.62		

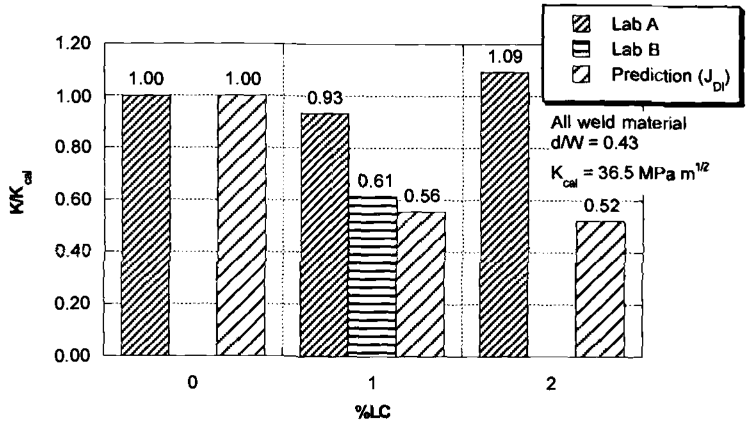

Figure 13 – *Comparison of round robin experimental data with J_{DI} predictions*

Although local compression is predicted to reduce toughness, the necessity of a straight pre-crack may require its use. The simulations provide some sensitivity information for local compression that can allow improved experiment design. The simulations suggest that the amount of local compression is not a significant factor influencing the apparent toughness. They further suggest that positioning the compression platen toward the front face, rather than over the ligament, reduces the effect of LC on apparent toughness. The results also suggest that the material model is an important factor in predicting the impact of LC on apparent toughness. Finally, the results suggest that the mechanisms of failure will have an impact on the effect of LC. In this study, lower-shelf toughness may be best predicted by J_{DI}. If the tests were performed in the transition region, the RKR fracture model may be the better predictor because of it's sensitivity to constraint. The failure mechanism is important, since the RKR predictions suggest a larger effect of LC.

Acknowledgments

The authors are indebted to their colleagues from Laboratories A and B, who submitted their round-robin data and answered many questions.

References

[1] Towers, O. L. and Dawes, M. G., "Welding Institute Research on the Fatigue Precracking of Fracture Toughness Specimens," *Elastic-Plastic Fracture Test Methods: The User's Experience, ASTM STP 856*, American Society for Testing and Materials, Philadelphia, PA, 1985, pp. 23-46.

[2] Hill, M. R. and Panontin, T. L., "Effect of Residual Stress on Brittle Fracture Testing," *Fatigue and Fracture Mechanics: 29th Volume, ASTM STP 1332*, T. L. Panontin and S. D. Sheppard, Eds., American Society for Testing and Materials, West Conshohocken, PA, 1999, pp. 154-175.

[3] Kirk, M. T. and Wang, Y.-Y., "Wide Range CTOD Estimation Formulae for SE(B) Specimens," *Fracture Mechanics: 26th Volume, ASTM STP 1256*, W. G. Reuter, J. H. Underwood and J. C. Newman, Eds., American Society for Testing and Materials, Philadelphia, PA, 1995, pp. 126-141.

[4] Masabuchi, K., *Analysis of Welded Structures: Residual Stresses, Distortion, and Their Consequences*, Pergamon Press, New York, NY, 1980.

[5] Prime, M. B., "Residual Stress Measurement by Successive Extension of a Slot: The Crack Compliance Method," *Applied Mechanics Reviews*, Vol. 52, No. 2, 1999, pp. 75-96.

[6] Cheng, W. and Finnie, I., "Measurement of Residual Stress Distributions near the Toe of an Attachment Welded on a Plate Using the Crack Compliance Method," *Engineering Fracture Mechanics*, Vol. 46, No. 1, 1993, pp. 79-91.

[7] Ritchie, R. O., Server, W. L. and Wullarert, R. A., "Critical Fracture Stress and Fracture Strain Models for the Prediction of Lower and Upper Shelf Toughness in Nuclear Pressure Vessel Steels," *Metallurgical Transactions*, Vol. 10A, 1978, pp. 1557-1570.

[8] Joyce, J. A., "J-Resistance Curve Testing of Short Crack Bend Specimens Using Unloading Compliance," *Fracture Mechanics: Twenty-Second Symposium, ASTM STP 1131*, Vol. 1, American Society for Testing and Materials, Philadelphia, PA, 1992, pp. 904-924.

[9] Carpenter, W. C., Read, D. T. and Dodds, R. H., "Comparison of Several Path Independent Integrals Including Plasticity Effects," *International Journal of Fracture*, Vol. 31, 1986, pp. 303-323.

[10] Lei, Y., O'Dowd, N. P. and Webster, G. A., "Fracture Mechanics Analysis of a Crack in a Residual Stress Field," *International Journal of Fracture*, Vol. 106, No. 3, 2000, pp. 195-216.

[11] Matos, C. G. and Dodds, R. H. J., "Modeling the Effects of Residual Stresses on Defects in Welds of Steel Frame Connections," *Engineering Structures*, Vol. 22, 2000, pp. 1103-1120.

[12] *ABAQUS/Standard, Version 5.8*, Hibbitt, Karlsson, and Sorenson, Inc., Providence, RI, 1999.

[13] Mura, T., *Micromechanics of Defects in Solids*, M. Nijhoff, Dordrecht, Netherlands, 1987.

[14] Hill, M. R., "Determination of Residual Stress Based on the Estimation of Eigenstrain," Doctoral Thesis, Stanford University, 1996.

[15] Goldak, J. A. and Patel, B., "Computational Weld Mechanics," *Advanced Joining of Materials (AGARD CP-398)*, 1985, pp. 1-1 - 1-32.

[16] Hill, M. R. and Nelson, D. V., "Determining Residual Stress through the Thickness of a Welded Plate," *PVP*, Vol. 327, American Society of Mechanical Engineers, New York, NY, 1996, pp. 29-36.

Fatigue

Robert S. Blandford,[1] Steve R. Daniewicz,[2] and W. Glenn Steele[3]

Application of Uncertainty Methodologies to Measured Fatigue Crack Growth Rates and Stress Intensity Factor Ranges

---

Reference: Blandford, R. S., Daniewicz, S. R., and Steele W. G., **"Application of Uncertainty Methodologies to Measured Fatigue Crack Growth Rates and Stress Intensity Factor Ranges,"** *Fatigue and Fracture Mechanics: 33rd Volume, ASTM STP 1417*, W. G. Reuter and R. S. Piascik, Eds., ASTM International, West Conshohocken, PA, 2002.

Abstract:

Methodologies allowing for reliable and informative experimental error or uncertainty calculations are well documented. These methodologies allow researchers to compute the uncertainty associated with experimental results and to determine how specific experimental details contribute to the total uncertainty. While previous statistical studies within the fatigue community have focused on multiple specimen variability, uncertainty analyses will allow single specimen errors to be addressed.

Uncertainty analyses and conventional statistical methodologies were applied to high load ratio fatigue crack growth rate data generated using AA 7075-T651 compact tension [C(T)] specimens. Levels of single specimen uncertainty for the crack growth rates, stress intensity factor ranges, and crack lengths were subsequently determined. Measures of multiple specimen scatter were also statistically quantified.

Multiple specimen uncertainties were found to be greater than single specimen uncertainties. This demonstrates that quantities other than measurement error are dominating the scatter in crack propagation data. Crack mouth opening displacement measurements were observed to exert a dominating influence on the single specimen uncertainty analyses, forcing significant variations in the total uncertainty for crack length, crack growth rate, and the stress intensity factor range.

Uncertainty analyses are not commonly used in the fatigue laboratory. Uncertainty methodologies may gain more acceptance in the testing community because of the valuable measure of error that can be obtained and the numerous improvements that can be made to current procedures as a result.

Keywords: uncertainty analysis, fatigue crack propagation, variability

---

[1]Graduate Research Assistant, Department of Mechanical Engineering, Mississippi State University, Mississippi State, MS 39762.

[2]Associate Professor of Mechanical Engineering, Mississippi State University,

[3]Professor & Head of Mechanical Engineering, Mississippi State University.

Introduction

Since fatigue crack growth rate data are the foundation for successful service life prediction, a quantification of errors and variability is needed. Numerous statistical methods have addressed fatigue crack growth variability but not single specimen error [*1-4*]. In the present study, uncertainty methodologies were applied to fatigue crack propagation data to evaluate single specimen uncertainty while alternate statistical methods were applied to the test groups to evaluate multiple specimen uncertainty.

The premise behind single specimen uncertainty is that the measuring techniques are the only contributing source of uncertainty. In contrast, multiple specimen uncertainty can be affected by geometry, microstructure, environment, and frequency changes in combination with the single specimen uncertainties already present. The majority of experimental work in this area has focused on multiple specimen error [*5-7*]. The uncertainties in crack length a, growth rate da/dN, and stress intensity factor range ΔK were computed and compared with multiple specimen uncertainty measures to evaluate the experimental data using uncertainty analysis principles.

Principles of Uncertainty Analysis

The following overview is taken largely from the work of Coleman and Steele [*8*]. The total uncertainty in a variable is a combination of systematic and random uncertainties. If a large number of measurements of variable x_i are available, the random uncertainty can be estimated as

$$P_{x_i} = 2S \tag{1}$$

where P_{x_i}, and S are the random uncertainty and sample standard deviation. The exception to equation 1 is if variable x_i is a mean value. In this situation the random uncertainty P_{x_i} should be divided by $\sqrt{N}$ where N is the number of values used in the calculation of the mean.

Typically, it is more common to be interested in determining the uncertainty in a calculated value r composed of variables $x_1, x_2, \ldots, x_J$ which results in a random uncertainty

$$P_r = \sqrt{\sum_{i=1}^{J} \theta_i^2 P_i^2} \tag{2}$$

where θ_i and P_i are the sensitivity coefficient and random uncertainty for a variable x_i with $\theta_i = \partial r / \partial x_i$.

Systematic uncertainties are those of a fixed-value nature and are sometimes referred to as bias. The calculation of systematic uncertainty is based on the assumption that the true magnitude of the fixed error lies within a confidence interval. The true error is unknown, but the limits of the confidence interval are taken as the estimate of the systematic uncertainty. The systematic uncertainties $(B_i)_k$ for the elemental fixed error sources in each variable are estimated and are combined by root-sum-square to determine the systematic uncertainty for variable x as

$$B_i = \sqrt{\sum_{k=1}^{M} (B_i)_k^2} \tag{3}$$

When systematic elemental errors for two different variables have the same source, the systematic uncertainties are correlated. Correlated systematic uncertainties are an important part of uncertainty analyzes. The calculation of a correlated systematic uncertainty revolves around determining the covariance estimator of variables x_i and x_k. The covariance estimator B_{ik} can be approximated as

$$B_{ik} = \sum_{\alpha=1}^{L} (B_i)_\alpha (B_k)_\alpha \tag{4}$$

where $(B_i)_\alpha$ and $(B_k)_\alpha$ are the elemental systematic uncertainties that are common for variables i and k. Using the above approximation allows for the determination of a total systematic uncertainty of the result as

$$B_r = \sqrt{\sum_{i=1}^{J} \theta_i^2 B_i^2 + 2\sum_{i=1}^{J-1} \sum_{k=i+1}^{J} \theta_i \theta_k B_{ik}} \tag{5}$$

The proper development of random and systematic uncertainties is important. Using the best possible information and relying on previous experimental work to construct estimates is helpful. Once both random and systematic uncertainties are known, then a total uncertainty can be found as

$$U_r = \sqrt{B_r^2 + P_r^2} \tag{6}$$

A significant aspect of uncertainty analysis is determining which measured variables contribute to the total uncertainty and to what extent. This is important for potentially improving current research and developing more successful future testing. The quantity used to assess the uncertainty for each variable is the uncertainty percent contribution defined as

$$UPC_i = \frac{(\theta_i)^2 (B_i \; or \; P_i)^2}{U_r^2} \tag{7}$$

where the UPC_i is determined for all of the B_i and P_i components. Further details regarding uncertainty analysis may be found in reference [*8*].

Methodologies - Single Specimen Uncertainty

The uncertainty analysis for a single fatigue crack growth specimen is a careful application of uncertainty principles using several data reduction equations. Since da/dN and ΔK use load, displacement, and geometry measurements indirectly, the uncertainty analysis is more difficult. Both da/dN and ΔK are functions of the crack length a, which is a function of the compliance, which finally is a function of the load, specimen thickness, and crack mouth opening displacement CMOD. Extensive use of the chain rule was required to determine the appropriate sensitivity coefficients. From ASTM Test Method for Measurement of Fatigue Crack Growth Rates (E647), the crack mouth opening compliance u is defined as

$$u = \left[\left(\frac{EvB}{P} \right)^{\frac{1}{2}} + 1 \right]^{-1} \tag{8}$$

where E, v, B, and P are the elastic modulus, CMOD, specimen thickness, and applied load respectively. Having the compliance allows the crack length to be calculated as

$$a = w\left(C_o + C_1 u + C_2 u^2 + C_3 u^3 + C_4 u^4 + C_5 u^5\right) \tag{9}$$

where w and C_i are the specimen width and compliance coefficients, respectively. The compliance coefficients were taken from [9]. At this point the calculations for ΔK and da/dN deviate and must be addressed separately.

The calculation of ΔK begins with the determination of the C(T) geometry factor F from E647 expressed as

$$F = \frac{2 + \frac{a}{w}}{\left(1 - \frac{a}{w}\right)^{\frac{3}{2}}} \left[0.886 + 4.64\frac{a}{w} - 13.32\left(\frac{a}{w}\right)^2 + 14.72\left(\frac{a}{w}\right)^3 - 5.6\left(\frac{a}{w}\right)^4 \right] \tag{10}$$

The stress intensity factor range ΔK is then calculated as

$$\Delta K = \frac{P(1-R)}{B\sqrt{w}} F \tag{11}$$

The load ratio R is assumed to be without uncertainty, and for these analyses, $P = P_{max}$.

The calculation of da/dN is less complicated because it involves only the crack length, a, and cycle count, N. However, there are numerous methods used to reduce the a vs. N data, some numerically complex and others elementary in nature. The software used to gather the experimental data employed a 7-point incremental polynomial method.

However, for mathematical simplicity, a modified secant was used to find the uncertainty in da/dN with

$$\frac{da}{dN_i} = \frac{a_i - a_{i-7}}{N_i - N_{i-7}} \tag{12}$$

where i must be greater than 7. The value of seven correlated best with incremental polynomial data. With a suitable method of determining da/dN having been established, a conventional uncertainty analysis was next performed using the appropriate sensitivity coefficients and component uncertainties. The cycle count N was assumed to be without uncertainty.

Methodologies - Multiple Specimen Uncertainty:

The analysis of multiple specimens is much less complex than the preceding single specimen analyses and follows conventional statistical ideas. The multiple test results can be used to calculate the random uncertainty P_r in equation 6 rather than having to estimate it by propagation of the random uncertainties for the individual variables. An ASTM round robin on fatigue crack propagation organized by Clark and Hudak first developed concepts similar to those employed here [*5*]. The round robin test series was a comprehensive examination of various variables possibly contributing to growth rate scatter using a 10Ni-8Co-1Mo steel. A variability factor was defined as

$$VF = \frac{\max \dfrac{da}{dN}}{\min \dfrac{da}{dN}} \tag{13}$$

where the maximum and minimum growth rates were based on a $2S_R$ criterion, where S_R is the residual standard deviation defined for simple linear regression as

$$S_R^2 = \frac{\sum (y_i - y_p)^2}{n-2} \tag{14}$$

where y_i, y_p, and n are the measured values, predicted values, and the number of values, respectively.

A significant modification to the Clark and Hudak variability factor must be made in light of the data generated in the research discussed herein. First, instead of using a residual standard deviation S_R, a sample standard deviation S was employed. Although the degrees of freedom in S and S_R were different an equivalent measure of variability was achieved. Secondly, Clark and Hudak developed their variability factor with large quantities of data and therefore were justified in using a $2S_R$ criterion. For the data presented in this paper a maximum of only five tests were performed and therefore a $2S$ criterion to estimate a 95% confidence interval is invalid. Thus, for the current work, a tS criterion was used, where t is an appropriate student t value. The student t depends on the degrees of freedom present in each sample standard deviation S. It can be shown that using $t = 2$ is valid if the degrees of freedom are greater than 9. For values less than 9, an appropriate student t must be used [*8*].

Once the appropriate student t value is used, variability factors can be calculated. The first factor considers da/dN values at a fixed value of ΔK. Each test will not exhibit identical ΔK values as required, but using the closest possible ΔK is presumed sufficient. The second variability factor is for values of ΔK at a fixed value of da/dN. A similar problem involving a lack of identical da/dN values exists and is addressed in a similar manner. The final variability factor is for the crack lengths at fixed cycle counts. The use of these three variability factors should appropriately measure the multiple specimen uncertainty. Once these variability factors are known they can be compared with equivalent uncertainty values and the results from Clark and Hudak.

Raw Data Acquisition

The fatigue crack growth data was collected using 5 constant maximum load tests and 3 constant K_{max} tests. The constant load tests utilized a P_{max} = 8896 N (2000 lbs.) and R = 0.7, while the constant K_{max} tests used a load shedding procedure and a K_{max} = 13.3 MPa$\sqrt{}$m (12 ksi$\sqrt{}$in) with an initial R = 0.7 and C = 0.16 mm^{-1} (4.06 in^{-1}). All tests were performed at 8 Hz in lab air. The C(T) specimens were cut in an L-T orientation from a 12.7 mm (0.5 in) rolled plate of AA 7075-T651. Figure 1 displays the resulting data generated in conjunction with the data of Hudson [*10*], which was generated using AA 7075-T6 center-crack specimens with R = 0.7.

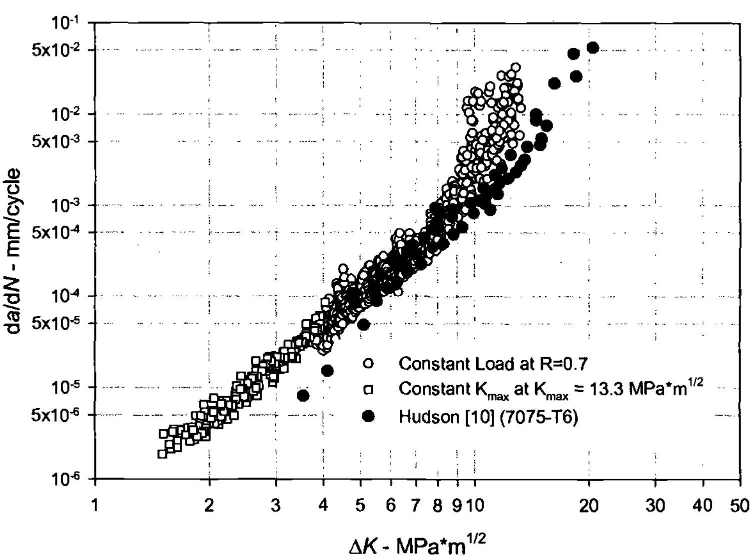

Figure 1 - *Crack Growth Rates*

The transition from the Paris regime to Region III growth can be seen in the figure at a ΔK of 8.5 MPa$\sqrt{}$m. Unfortunately, the transition into the threshold region is not apparent.

Load instabilities forced the constant K_{max} tests to be prematurely ended, thus this data does not extend into the threshold region.

Presenting the data as da/dN vs. ΔK using log-log coordinates may mask some of the variability present in the data. Since variability is important, it is perhaps instructive to plot the data in its original form and observe the amount of variability present. The plot is given as Figure 2.

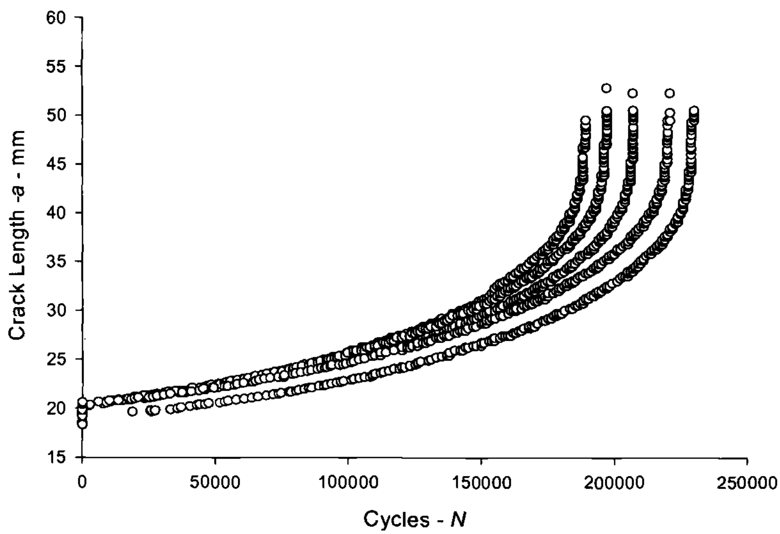

Figure 2 - *Crack Growth*

The major disadvantage to plotting a vs. N is the necessary elimination of the data collected using a constant K_{max}. These tests accumulate large cycle counts and very small changes in crack length, therefore distorting the entire plot. From Figure 2, a clear perspective of specimen variability is presented.

Results - Single Specimen Uncertainty

To correctly perform an uncertainty analysis requires accurate estimates of elemental uncertainties. The load and CMOD random uncertainty estimates were made from previous test data generated using constant load conditions and equation 1. The tests were only run for a short period (~60 cycles) so no crack extension was achieved. The crack extension was verified optically and through compliance techniques. The load systematic uncertainty estimates were a combination of reported values for the test machine (linearity = 1.5% of reading, hysteresis = 2.0% of reading, and threshold = 2.5% of reading) and a previous data estimate for calibration at ± 89 N (20 lb). The CMOD systematic uncertainty estimates included a reported value of 0.25% of reading for linearity and a calibration estimate from previous data at 0.00254 mm (0.0001 in). The specimen thickness was determined using a micrometer. The random uncertainty was calculated using equation 1, and the systematic uncertainty taken from the manufacturers information at 0.0076 mm (0.0003 in) for calibration and 0.018 mm (0.0007 in) for linearity. The width measurements were made using a laboratory ruler. The random uncertainty was found via equation 1 and the systematic uncertainty estimated at 0.254 mm (0.01 in).

Application of uncertainty principles to the fatigue crack propagation data revealed several interesting and relevant conclusions. The uncertainty results for d*a*/d*N* and ΔK are illustrated in Figure 3.

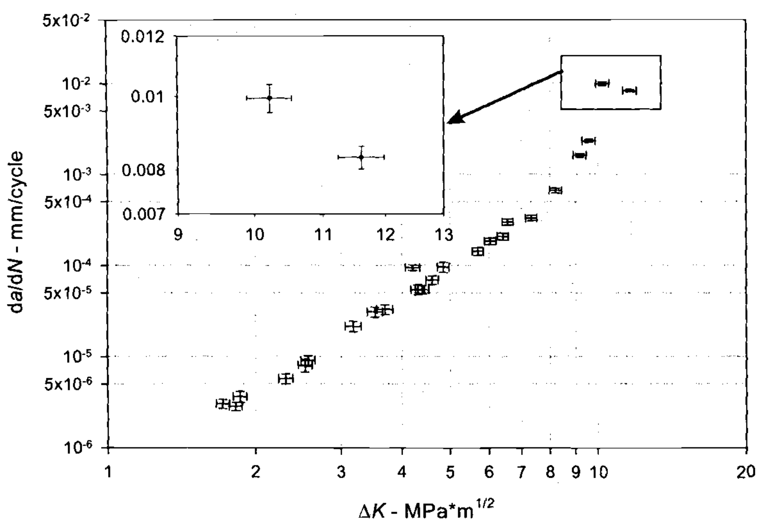

Figure 3 - *Uncertainty in da/dN and ΔK*

The first point to be made concerning Figure 3 is that the log-log scale partially distorts the uncertainty bands, which are symmetrical. The uncertainty values U_x/x for d*a*/d*N* range from 3.5% to 16%, and crack growth rate was determined using a modified secant (equation 12). The systematic uncertainties for the loads and CMODs are correlated and this influences the nature of the d*a*/d*N* uncertainty. Also, the specimen thickness and width were the same for all crack length measurements. Because of the correlated systematic uncertainties and the fact that the modified secant calculation involves a difference, the total systematic uncertainty in d*a*/d*N* ranges from 1% to 20% of the total uncertainty. This forces the total uncertainty in d*a*/d*N* to be predominately random. The ΔK uncertainties range from 2.5% to 4.0%, with a mean of 3.1%. The composition of the ΔK uncertainty at *a/w* of 0.6 was roughly 90% systematic and 10% random with no correlated systematic uncertainties present. The uncertainty percent contribution results are listed in Table 1.

Table 1 - *ΔK Uncertainty Contributions*

a/w	B_B - %	P_B - %	B_P - %	P_P - %	B_w - %	P_w - %	B_v - %	P_v - %
0.6	0.15	1.76	46.9	0.12	0.10	0.45	29.3	21.2
0.35	0.30	3.50	93.4	0.22	0.31	1.37	0.92	0.22

With regard to the notation used in Table 1, B is the systematic uncertainty for variable x and P is the random uncertainty for variable x. The distribution of uncertainties changed significantly with crack length, with the total uncertainty changing by 70%. The systematic uncertainty in load is a large value. As previously discussed, both the test machine documentation and previous experimental work led to the estimates of these uncertainties, which may be too high in light of its dominating influence. However, the reason for the change in B_P is not due to load but rather CMOD. Since this contribution affects all three crack growth variables it will be investigated in a later section.

The results in Figure 3 clearly show that in our laboratory fatigue crack growth rates can be measured to within a 3.5% uncertainty but that the uncertainty may become as high as 16%, while ΔK can be measured consistently to within 3%. Although it may exist, after a thorough literature review reported data of this kind was not found. Such information should prove useful when seeking to improve conventional testing methods.

Fatigue crack growth can also be expressed as a vs. N and this is important since a better characterization of variability is gained. Figure 4 illustrates the a vs. N data for the five constant load tests along with the uncertainties in crack length.

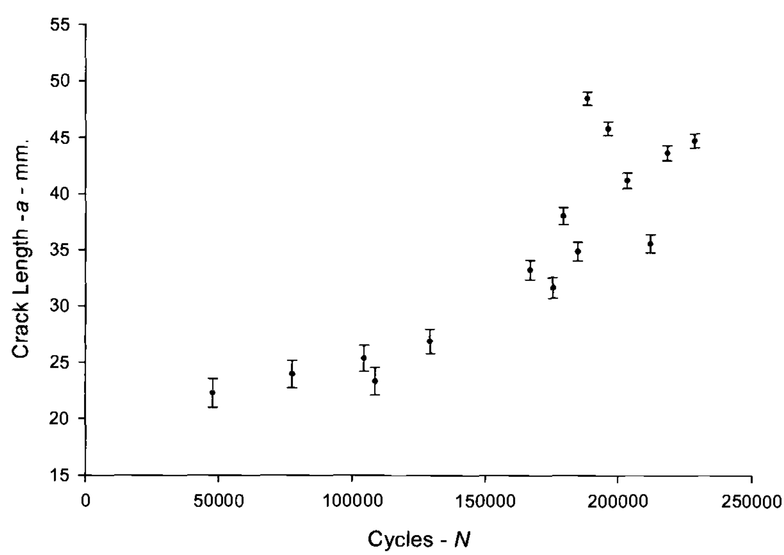

Figure 4 - *Crack Growth Uncertainty*

The uncertainty for the crack length varied from 1.2 to 6.5%. The way in which uncertainty appears to be a function of crack length again revolves around CMOD. A powerful capability of uncertainty methodologies is the analysis of error contributions and acquisition of sensitivity coefficients. The combination of these two tools allows the total uncertainty to be partitioned and the dominating factors revealed. As was already stated, CMOD was the dominating factor controlling all three uncertainty calculations as shown in Figure 5.

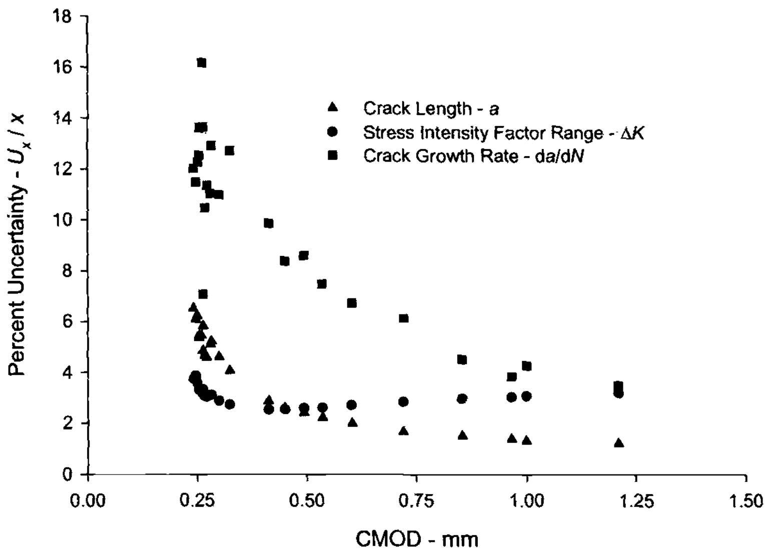

Figure 5 - *Effect of CMOD on Uncertainty*

A CMOD increase causes the total uncertainty in a and da/dN to decrease while causing the total uncertainty in ΔK to increase. The data are clustered at the lower displacements because constant K_{max} testing essentially keeps CMOD low and constant. To further investigate the CMOD effect, changes in uncertainty components and sensitivity coefficients were monitored as CMOD increased. In the case of crack length, the systematic uncertainty increased only marginally, while the sensitivity coefficient $\partial u/\partial v$ increased by 500%. This sensitivity coefficient is, because of extensive chain rule use, present in all three uncertainty calculations. Since $\partial u/\partial v$ is involved with functions containing other sensitivity coefficients, the influence of $\partial u/\partial v$ changes. Only through the use of uncertainty analyses can these types of observations be made, and the quantification of crack propagation uncertainty accomplished.

Results - Multiple Specimen Uncertainty

The determination of variability factors for a, ΔK, and da/dN will provide insight into the behavior of these variables. Table 2 lists the da/dN variability factors for fixed values of ΔK, where the first four entries are for the constant load tests and the remaining three are for the constant K_{max} tests.

Table 2 - *Variability in da/dN at Fixed ΔK Values*

ΔK MPa√m	ΔK Range MPa√m	Mean da/dN 10^{-6} mm/cycle	$S_{da/dN}$ 10^{-6} mm/cycle	*VF*	*V* %
4.40	4.40 – 4.41	60.15	15.42	5.926	71.12
6.59	6.60 – 6.62	257.05	45.85	2.961	49.51
8.79	8.77 – 8.81	1387.86	313.94	4.373	62.78
10.99	11.1 – 11.21	5064.76	1291.59	5.848	70.79
3.30	3.30 – 3.31	26.01	3.69	4.132	61.03
2.47	2.44 – 2.47	8.56	1.01	3.076	50.93
1.92	1.89 – 1.93	3.82	0.47	3.252	52.96

The *V* variable in Table 2 is determined much like a percent random uncertainty and is calculated as

$$V = \frac{tS_{da/dN}}{da/dN} \tag{15}$$

These *V* values are generally much higher than the reported percent uncertainties calculated for a single specimen. The variability factors don't compare as well with the work of Clark and Hudak as expected. This is primarily due to the student *t* value, which is 2.776 for constant load tests and 4.303 for the constant K_{max} tests. Clark and Hudak reported a variability factor for incremental polynomial reduced data of 2.51 and 2.93 for all 0.25-inch thick WOL specimens. If the reported standard deviations remained constant for a total of 10 tests for each loading condition, allowing a $t = 2$ to be used, the variability factors would match almost perfectly. However, it is difficult to determine how representative this sample is with respect to a larger sample relative to the population. It is the opinion of the authors that increasing the number of tests would only marginally effect the scatter, therefore making the variability in current fatigue crack growth rates similar to those reported in 1975 by Clark and Hudak.

Continuing an investigation into multiple specimen uncertainty necessitates an analysis of ΔK at fixed da/dN values. Table 3 lists the variability information computed.

Table 3 - *Variability in ΔK at Fixed da/dN Values*

da/dN 10^{-6} mm/cycle	da/dN Range 10^{-6} mm/cycle	Mean ΔK MPa√m	$S_{\Delta K}$ MPa√m	*VF*	*V* %
7620.00	5740.40 – 8661.4	11.01	0.688	1.420	17.37
1270.00	1206.50 – 1325.88	8.84	0.234	1.158	7.34
177.80	176.53 – 180.59	5.85	0.147	1.150	6.96
50.80	50.29 – 51.82	4.20	0.120	1.171	7.88
20.32	20.07 – 20.83	2.95	0.140	1.514	20.43
10.16	9.91 – 10.41	2.58	0.068	1.258	11.44
5.08	4.83 – 5.33	2.25	0.095	1.444	18.16

Clearly the level of variability in ΔK is much less than that found in da/dN. As with da/dN, the *V* values calculated for ΔK are higher than the single specimen uncertainties.

This may indicate the influence of specimen geometry, microstructure, or environment. Regardless of the source of the multiple specimen uncertainty, it was expected that multiple specimen uncertainties would be larger than single specimen uncertainties, because the multiple specimen uncertainties are composed of single specimen uncertainties and other influential factors.

The variability trends in ΔK are further reinforced by the multiple specimen uncertainty seen in crack length a. Table 4 lists the crack length variability results.

Table 4 - *Variability in a at Fixed N Values*

N 10^3	N Range 10^3	Mean a mm	S_a mm	VF	V %
75	74.1 – 75.5	23.60	0.33	1.094	4.48
100	99.7 - 101	25.30	0.46	1.120	5.66
125	125 - 126	27.31	0.61	1.152	7.05
150	150 - 151	29.97	1.07	1.258	11.44
175	174 - 176	33.96	2.01	1.462	18.77
190	189 - 190	39.62	6.96	3.531	55.86

Only constant load data was used in Table 4 since the constant K_{max} data often exhibits no appreciable change in a for large N values. Concerning the results, the variability in crack length obviously increases with cycle count, which may also be seen in Figure 2. The lower cycle count V values are close to but still higher than calculated single specimen uncertainties. At approximately 150 000 cycles and above multiple specimen uncertainty becomes dominant.

Conclusions

Uncertainty methodologies were applied to fatigue crack growth rates, stress intensity factor ranges, and crack lengths in an effort to understand single specimen error. In addition, a statistical analysis of these same quantities over multiple specimens was also performed to quantify multiple specimen scatter. The single specimen uncertainty analysis revealed uncertainties in da/dN ranging from 3.5 to 16%. With regard to the uncertainty in ΔK, the values were lower at 2 to 4% over the range of crack growth studied. The uncertainties in crack length were also relatively small and ranged from 1 to 6.5%. A clear dependence on crack mouth opening displacement was found in all three uncertainty calculations. As the CMOD increased the total uncertainty in crack length and crack growth rate decreased while the uncertainty in stress intensity factor range increased. The reason for this was found in the sensitivity of these variables to changes in CMOD. A result such as this demonstrates the benefits of uncertainty analysis and can be used to improve future testing recommendations.

The second stage of the analysis, which focused on multiple specimen error, reinforced the single specimen uncertainties. The analysis revolved around the computation of variability factors and percent variability values. Variability factors for da/dN ranged from 2.96 to 5.93 while the percent variability values were consistently higher than the single specimen uncertainties. This is important since multiple specimen uncertainty should contain as a subset the single specimen uncertainty. Comparing the variability factors with previous data generated by Clark and Hudak initially produced poor results. However, when assuming that the variability calculated in this small sample would not increase as specimens tested increased, the variability factors agree very well with the previous work. The variability factors and percent variability values for ΔK and a essentially yielded similar results.

The result of this research is not merely academic in nature. For the design engineer knowledge of fatigue uncertainty can aid in defining safety margins and minimum property curves. A better definition of overall component reliability is also gained from complete disclosure of fatigue uncertainties and the variables behind those uncertainties.

References

[1] Bastenaire, F., Lieurade, H. P., Régnier, L., and Truchon, M., "Statistical Analysis of Fatigue Crack Growth," *Fatigue Crack Growth Measurement and Data Analysis, ASTM STP 738*, 1981, pp. 163-170.

[2] Boganoff, J. L. and Kozin, F., "Probalistic Models of Fatigue Crack Growth – II," *Engineering Fracture Mechanics*, Vol. 20, No. 2, 1984, pp. 255-270.

[3] Ditlevsen, O. and Olesen, R., "Statistical Analysis of the Virkler Data on Fatigue Crack Growth," *Engineering Fracture Mechanics*, Vol. 25, No. 2, 1986, pp. 177-195.

[4] Ostergaard, D. F. and Hillberry, B. M., "Characterization of the Variability in Fatigue Crack Propagation Data," *Probabilistic Fracture Mechanics and Fatigue Methods; Applications for Structural Design and Maintenance, ASTM STP 798*, 1983, pp. 97-115.

[5] Clark, W. G., Jr. and Hudak, S. J., Jr., "Variability in Fatigue Crack Growth Rate Testing," *Journal of Testing and Evaluation*, Vol. 3, No. 6, 1975, pp. 454-476.

[6] Shaw, W. J. D. and Le May, I., "Intrinsic Material Scatter in Fatigue Crack Propagation," *Fatigue and Fracture of Engineering Materials and Structures*, Vol. 4, No. 4, 1981, pp. 367-375.

[7] Virkler, D. A., Hillberry, B. M., and Goel, P. K., "Statistical Nature of Fatigue Crack Propagation," USAF, AFFDL-TR-78-43, 1979.

[8] Coleman, H. W. and Steele W. G., *Experimentation and Uncertainty Analysis for Engineers*, John Wiley & Sons, 2nd Ed., 1999.

[9] Saxena, A. and Hudak, S. J., Jr., "Review and Extension of Compliance Information for Common Crack Growth Specimens," *International Journal of Fracture*, Vol. 14, No. 5, 1978, pp. 453-467.

[10] Hudson C. M., "Effect of Stress Ratios on Fatigue-Crack Growth in 7075-T6 and 2024-T3 Aluminum-Alloy Specimens," National Aeronautics and Space Administration, TN D-5390, 1969.

Ohchang Jin[1] and W. Steven Johnson[2]

Load Interaction Effects on Small Crack Growth Behavior in PH13-8Mo Stainless Steel

---

Reference: Jin, O. and Johnson, W. S., "**Load Interaction Effects on Small Crack Growth Behavior in PH13-8Mo Stainless Steel,**" *Fatigue and Fracture Mechanics: 33rd volume, ASTM STP 1417*, W. G. Reuter and R. S. Piascik, Eds., ASTM International, West Conshohocken, Pa, 2002.

Abstract: Fracture mechanics approaches to life prediction are being considered for applications to highly stressed components operating at high frequencies. One such application is rotor hubs on helicopters. For such applications, it is imperative that the growth behavior of small cracks be well understood. This study intended to examine the effect of material microstructure on the small crack growth behavior of PH13-8Mo stainless steel under both constant and variable amplitude loading. Constant amplitude loading at six different stress amplitudes showed that the crack growth rate did not depend upon the stress amplitude. The small crack growth behavior was greatly affected by the size of the martensite packet. Furthermore, it was observed that the small crack growth rates were a little slower than long crack data. Single overload tests indicated there was inconsistent crack growth behavior (crack growth acceleration and retardation were both observed after overload). It was suggested that this inconsistent crack growth resulted from the crack tip location relative to the microstructural features at the time of overload application. However, the simple block loading showed that there was overall crack growth retardation. As expected, the extent of the crack growth retardation increased with increasing the maximum stress of the overload stress block.

Keywords: microstructure, stainless steel, overloads, crack growth retardation.

Introduction

Recent design approaches for structural components subject to high cycle/high frequency fatigue have been considering using fracture mechanics approaches based on predicting the growth of very small cracks. Small cracks in some materials may grow below the long crack threshold and faster than long cracks at equivalent stress intensity

---

[1]Formerly graduate research assistant, School of Materials Science and Engineering, Georgia Institute of Technology, and currently research associate, Department of Aerospace and Aeronautics, Air Force Institute of Technology, WPAB, OH 45433-7765.

[2]Professor, School of Materials Science and Engineering and G. W. Woodruff School of Mechanical Engineering, Georgia Institute of Technology, Atlanta, GA 30332-0245.

factor range [*1*]. This anomalous crack growth behavior is caused by crack tip interaction with local microstructures and lack of crack closure when it is small. Since a large percentage of the total crack growth life is spent in this small crack region, a good understanding and description of this behavior is necessary if an accurate prediction methodology is to be developed.

Long cracks subject to an overload application have been observed to slow down and, in some cases, completely arrest. However, systematic investigation on the small crack growth under variable amplitude loading is lacking [*2, 3*]. There are experimental difficulties involved in measuring the relevant parameters that characterize the behavior of small fatigue cracks. This paper investigates the effects of overload and block loading on the small crack growth in PH13-8Mo stainless steel.

Background

The crack growth behavior under variable amplitude loading is very dependent upon the size of small crack. Oni [*4*] reported that physically short cracks (0.5 ~1 mm) in high-strength low alloy steels showed a load interaction behavior similar to long crack. The crack growth retardation occurred after a certain number of cycles, not immediately after the overload (a delayed retardation). Changoing et al [*5*] also studied the propagation behavior of physically short fatigue cracks in steel due to a single overload. They found that the physically short cracks were more sensitive to the overload than long cracks. The overload applied when the crack was small resulted in crack growth retardation.

Jono and Sugeta [*6*] observed that the crack growth behavior under block loading also depended on the size scale of the small cracks. Fatigue cracks longer than 0.2 mm were shown to have a plastic deformation in the wake of the crack tip and exhibited retardation after load reduction due to differences in closure levels. However, for cracks smaller than 0.1 mm, closure was not sufficient enough to control the crack growth behavior. They suggested that the growth process of a small crack is a transition process from the incipient, ideal crack to the conventional long crack.

Newman and co-workers [*7-12*] conducted extensive small crack research on various material systems under variable amplitude loading. They found that small crack growth behavior under variable amplitude loading depended upon the material system, specifically its microstructure and yield strength level. In Al alloys, the small cracks grew much faster than long cracks. On the other hand, the small cracks in 4340 steel grew at somewhat slower rates than long crack over the range of available data.

Materials and Specimen

Material

PH13-8Mo stainless steel is a martensitic precipitation-hardened stainless steel used for components requiring corrosion resistance, high strength, high fracture toughness, and oxidation resistance up to 427°C [*13*]. The compositions of major alloying elements are

Table 1-*Chemical composition of the material in percentage by weight*

Major Alloying Elements (wt %)			
Cr	Ni	Mo	Al
12.4~12.9	7.87~8.58	1.73~2.45	0.8~1.18

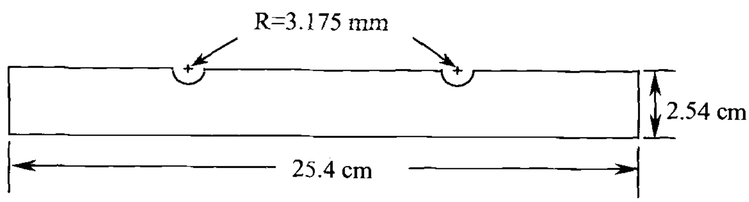

Figure 1-*Double edge notch specimen for constant amplitude loading and variable amplitude loading*

shown in Table 1. The material was heat-treated in order to have desired microstructures: solution treatment at 927°C and aging at 566°C (H1050). Patel et al [*14*] reported that the average 0.2 % offset yield strength and ultimate strength are 1286 MPa and 1325 MPa, respectively, and that the average elastic modulus is 192 GPa.

Specimen

The specimens used in the present study have nominal dimensions of 250 mm x 25.4 mm x 3.81 mm and have two flat notches of radius of 3.175 mm (see Figure 1). The distance between the two notches was 76.2 mm. The specimens were machined in T-L direction using a low stress grind process to minimize the surface residual stresses. The notch roots for all specimens were mechanically polished using 6 μm, 3 μm, and 0.25 μm diamond paste. The polishing was done in circumferential direction so that any polishing scratches would not interfere with fatigue crack observations nor serve as crack initiation sites. Finally, the specimens were electropolished to remove the surface residual stresses due to machining as well as mechanical polishing.

Experimental Procedure

A servohydraulic load frame was used to apply cyclic load on the small crack specimens. Constant amplitude loading was done at six stress amplitudes (186 MPa, 205 MPa, 214 MPa, 217 MPa, 233 MPa, and 248 MPa). The stress ratio was 0.1 except stress amplitude of 186 MPa (S_{max} =621 MPa and R =0.4). Then, overload and simple block loading were conducted based on the stress levels and stress ratios used in the constant amplitude loading. The schematic drawing of the simple blocking loading is shown in

Figure 2. Test matrix is shown Table 2 and 3. The test frequency for both constant and block loading was 10 Hz. The plastic replication method was used to detect crack initiation and to measure the crack increment. For overload tests, the overload was applied when the crack length was of the order of 100 μm.

For tests at the stress ratio of 0.1, the maximum notch root stresses were above the yield strength and the compressive residual stresses were assumed to be present at the notch roots after the first loading. To account for the residual stress, a Neuber analysis was necessary. For this analysis, it was assumed that the current material was elastic-perfectly plastic based on the monotonic tensile test conducted by Patel et al [*14*]. The notch root stress during the loading portion of the first cycle was assumed to be equal to the flow stress (σ_o, the average of the yield and ultimate strength). No yielding was assumed to occur upon unloading because the notch root stress ($K_t \cdot S$) was below the $2\sigma_o$. Therefore, the notch root response was nominally elastic for subsequent loading.

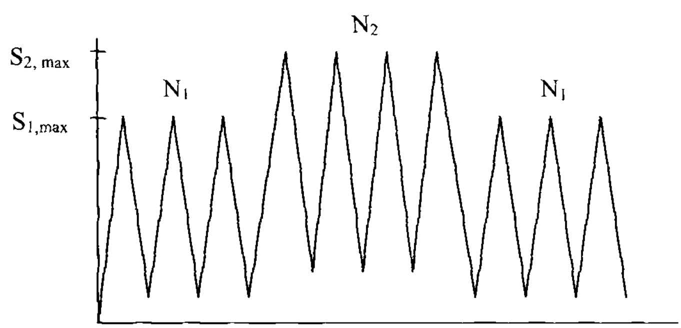

Figure 2-*Schematic drawing of the simple block loading*

Table 2-*Test Matrix for the overload load (OL) tests*

Baseline stress (MPa)	Overload (MPa)	Crack length before OL (μm)
476 (R = 0.1)	517	100
476 (R = 0.1)	621	102
476 (R = 0.1)	621	210

Table 3-*Test Matrix for simple block loading*

$S_{1,max}$ (MPa)	$S_{2,max}$ (MPa)	N_1	N_2
476 (R = 0.1)	517 (R = 0.1)	400	10
476 (R = 0.1)	552 (R = 0.1)	400	10
476 (R = 0.1)	621 (R = 0.4)	400	10

The surface crack inside the notch is so small compared to the notch diameter that we assumed the crack to be a surface flaw in an infinite plate where the remote stress is the local stress caused by the notch stress concentration. This is the same assumption made by Newman et al [7-9]. The current study used the stress intensity factor solution by Dowling [15]. In order to account for the shape of the crack, a shape factor was included in the stress intensity factor [9]. The stress intensity factor range is expressed in the following form:

$$\Delta K = 1.12 \cdot K_t \cdot \Delta S_{nom} \cdot \sqrt{\frac{\pi \cdot a}{Q}} \qquad (1)$$

$$Q = 1 + 1.464\left(\frac{a}{c}\right)^{1.65} \qquad (2)$$

where ΔK is the stress intensity factor range, K_t is elastic stress concentration factor and was found to be 3.46 (using a boundary element code, F.A.D.D.) based on gross section stress, ΔS_{nom} is nominal stress range, Q is the shape factor for an aspect ratio ($a/c \leq 1$), 2a is surface crack length and c is crack depth. It was assumed in the calculation of Q that the a/c is unity. The residual stress at the notch root can be determined by the following equation:

$$\sigma_{res} = \sigma_o - K_t \cdot \Delta S \qquad (3)$$

where σ_o is average of the yield strength and ultimate tensile strength. This residual stress was used in calculating the effective stress ratio.

In order to compute small crack growth rate (da/dN), incremental polynomial method (ASTM E.647) was used. This involved fitting a second-order polynomial to set of three successive data points.

Test Results and Discussion

Microstructure

The microstructure of PH13-8Mo stainless steel was characterized using an optical microscope and a scanning electron microscope (SEM). The overall microstructure is shown in Figure 3a. The microstructure consists of prior austenite grains, lath martensite (light phase) and retained austenite (dark phase). It seems that a significant amount of the retained austenite is present in the microstructure, especially along the boundaries of the lath martensite. The details of the microstructure are shown in Figure 3b and 3c. These micrographs revealed distinct prior austenite grain boundaries and packet boundaries. Prior austenite grain contains several packets of lath martensites and each packet has many lath martensites that have similar lath orientations. Figure 3c show that one prior austenite grain containing three packets of lath martensites.

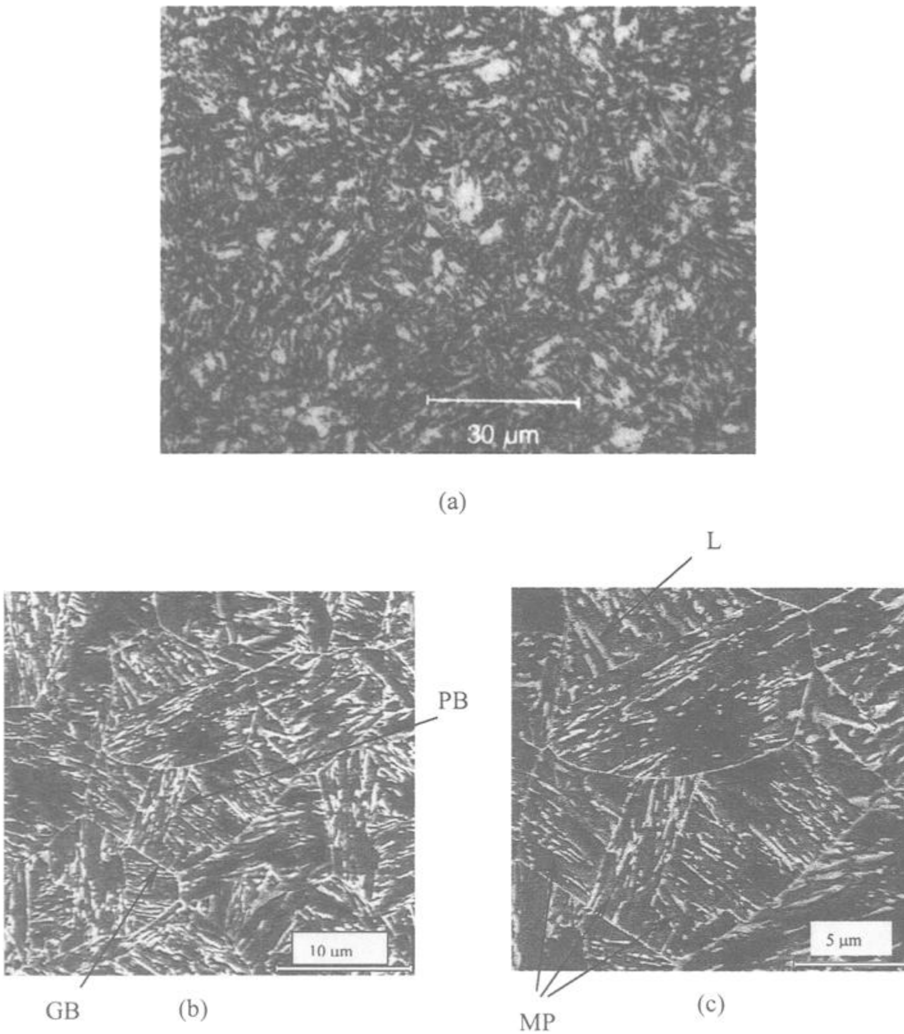

Figure 3-*Microstructure of PH 13-8 Mo stainless steel: a) micrograph by optical microscope, b) micrograph by SEM showing prior austenite grains and packets of lath martensite and c) micrograph by SEM showing a prior austenite grain and lath martensites (GB-prior austenite grain boundary, PB-packet boundary, MP-martensite packet, and LM-lath martensite)*

Grain size measurement was done on 22 grains, and resulted in an average grain size of 14 μm and a standard deviation of 2.72 μm. It should be noted that the packet boundaries are difficult to distinguish from the prior austensite grain boundaries. The average packet size was measured on 24 packets and resulted in the average size of 7 μm and a standard deviation of 2.1 μm. Since the grain size is approximately 10-20 μm wide, one grain may have 2-4 packets depending on the grain size. Based on the microstructural characterization, the martensite packet is a critical dimension and will greatly influence the small crack growth behavior.

Constant Amplitude Loading

Figure 4 shows the test results of constant amplitude loading at six different stress amplitudes. No significant difference in the crack growth rate was observed between different stress amplitudes. At a maximum stress level below 455 MPa, the specimen was cycled 4,000,000 cycles with no observed crack initiation. The range of applied cyclic stress was limited, on the low end stresses take a very large number of cycles to initiate and on the high end, multiple cracks initiate and life is rather short. The ordering of the crack growth rates looks rather random with the applied stress. A potential reason for this will be discussed later. Notice in Figure 4 that the effective stress ratio (R_{eff}) is given that accounts for residual stresses due to notch yielding on the first applied cycle. The R_{eff} varies with the applied stress level. The stress intensity factor range, ΔK in Figure 4 was calculated based on the notch root stress range.

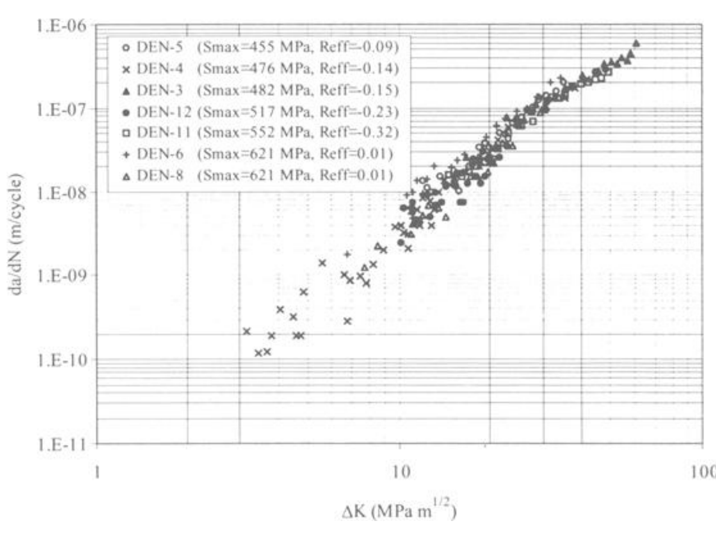

Figure 4-*Plots of the crack growth rate against the stress intensity factor range determined based on the notch root stress range*

At higher stress amplitudes (233 MPa and 248 MPa) multiple cracks were observed (see Figure 5). The crack growth rate of these multiple cracks was plotted in Figure 6. It is noted that the majority of the cracks stopped growing in their early stage and that there was only one dominant crack. The overall crack growth rate at the stress amplitudes 233 MPa and 248 MPa was not different from the tests conducted at the other stress amplitudes (186 MPa, 205 MPa, 214 MPa, and 217 MPa).

Microstructural Effects-In order to examine the effect of microstructure on the crack growth rate, the test result at the stress amplitude of 205 MPa is plotted in Figure 7. The oscillation in the crack growth rate is apparent and continues until the half crack length is approximately 100 μm. Based on Figure 7, the small crack growth stage can be divided into three regions. In region I, the crack growth oscillation was affected by the size of the lath martensite (< 1 μm). The influence of the lath martensite quickly disappeared at the half crack length of 6 μm. Between 6 μm to 50 μm (region II), the average crack extension between two neighboring crack growth rate minimums was 6.92 μm with a standard deviation of 1.88 μm. This crack increment corresponds to the average size of the martensite packets (7 μm±2.1 μm). Up to region II, the average difference in the crack growth rate between the maximum and minimum crack growth rate was 1.83 x 10^{-9} m/cycle with a standard deviation of 1.69 x 10^{-9} m/cycle. The crack growth rate in region III (the half crack length greater than 50 μm) was influenced by the size of the prior austenite grains. Since the grains contain several packets of lath martensites, the net increase in the crack length would be multiple of the size of the martensite packets. This suggests the martensite packet could be the microstructural unit that influences the crack growth behavior. Perhaps this significant oscillation with microstructure has a stronger influence on da/dN for small cracks than does the range of the applied stress level.

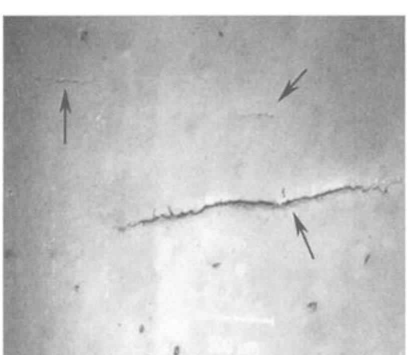

(a)

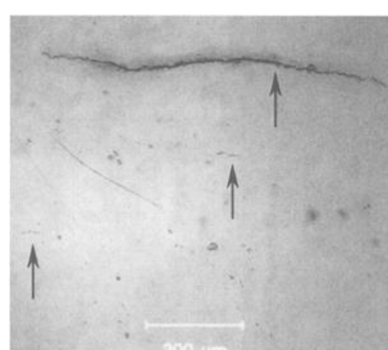

(b)

Figure 5-*Multiple cracks present in the specimen: a) DEN-12 (59,900 cycle at 517 MPa/R_{eff} = -0.23) and b) DEN-11 (36,000 cycles at 552 MPa/R_{eff} = -0.32)*

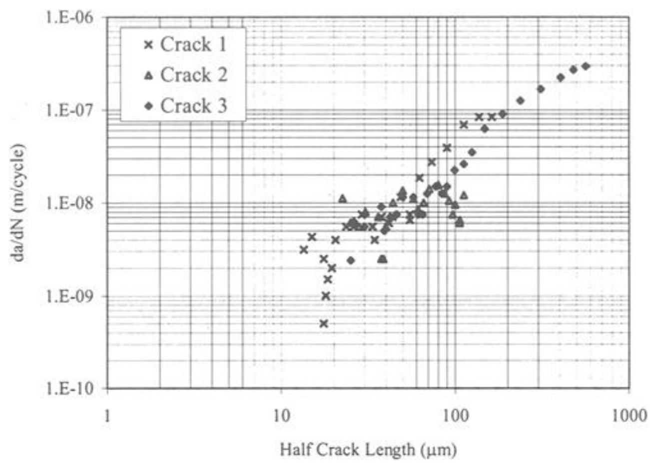

(a)

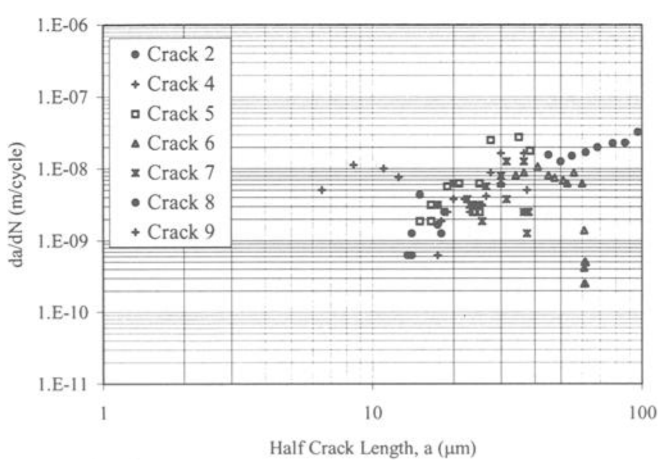

Figure 6-*Growth behavior of multiple cracks in a) DEN-12 at* S_{max} *= 517 MPa/*R_{eff} *= -0.23. Crack 2 eventually stopped growing in the presence of dominant crack 3 and b) DEN-11 subjected to* S_{max} *= 552 MPa/*R_{eff} *= -0.32*

Figure 7-*Regions of small crack growth stage determined based on the microstructural dimensions corresponding to the crack growth oscillation observed in a test conducted at a stress amplitude of 205 MPa (473 MPa/R_{eff} = -0.14): Region I-lath martensite, Region II-packets of martensite, and Region III-prior austensite grain or multiple of martensite packets*

Comparison with Long Crack Data-The results of small crack tests under constant amplitude loading were compared to long crack data obtained from Damage Tolerant Design Handbook [*16*]. The material condition used in the long crack data was similar to the current material. In order to complete the comparison, the constant amplitude loading at a stress ratio of 0.1 was obtained from Patel et al [*14*]. The comparison is shown in Figure 8. Small cracks grew slightly slower than long crack at the stress ratios of 0.1 and 0.4. This phenomenon was also observed by Swain et al [*9*] who conducted small crack tests on 4340 steel.

Variable Amplitude Loading

Since most real world applications, rotorcraft in particular, experience variable amplitude loadings, tests were conducted to assess the response of small cracks. Single overload tests and simple block loading tests were conducted based on the maximum stresses and the stress ratios used in the constant amplitude tests.

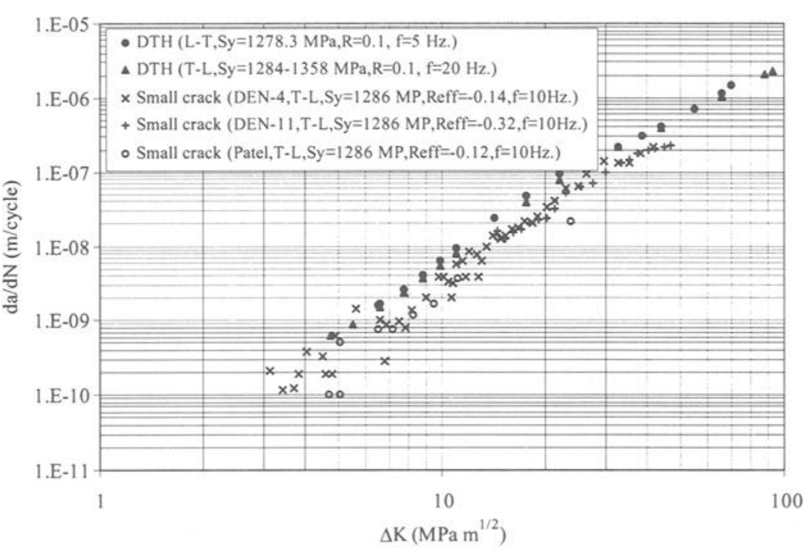

(a)

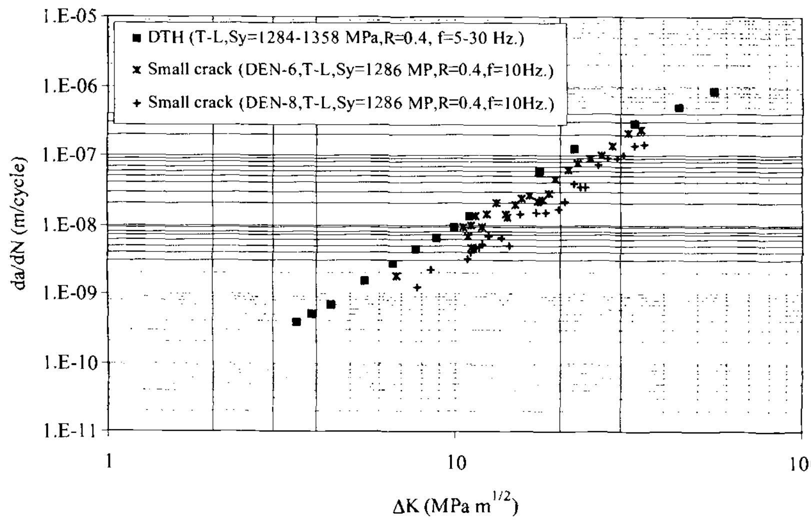

(b)

Figure 8-*Comparison of small crack data with long crack growth at stress ratio of a) R = 0.1 and b) R = 0.4*

Table 4-*Effective stress ratios under simple block loading*

$S_{1,max}$ (MPa)	$S_{2,max}$ (MPa)	Max Stress	Min Stress	R_{eff}
476 (R = 0.1)	517 (R = 0.1)	1163	-319	-0.27
476 (R = 0.1)	552 (R = 0.1)	1043	-439	-0.42
476 (R = 0.1)	621 (R = 0.4)	803	-679	-0.85

The notch root response due to the overload (517 MPa and 621 MPa) and simple block loading (517 MPa/R = 0.1, 552 MPa/R = 0.1, and 621 MPa/R = 0.4) were determined using equation (1) to (3) and listed in Table 4. The overload as well as the block loading resulted in compressive residual stresses upon unloading when the stress ratio was 0.1. This compressive residual stress changed the effective stress ratio and could be responsible for the crack growth retardation since the effective stress ratios are more negative at variable amplitude loading than at constant amplitude loading.

Single Overload-The single overload (see Figure 9) was applied when the crack length was approximately 100 μm. When the crack growth rate returned to the one at constant amplitude loading, the multiple overloads were applied. Figure 9 show the crack growth behavior due to the application of overload(s) superimposed on the constant amplitude at maximum stress of 476 MPa/R = 0.1. In Figure 9a, it is hard to find the crack growth retardation due to the overload(s) of maximum overload stress of 517 MPa. This may result from low overload ratio (1.08). On the other hand, the crack growth rate due to the overload of 621 MPa (overload ratio 1.30) shows some scatter as shown in Figure 9b. Both tests were conducted under identical conditions. The only difference between the two tests was that the overload was applied at different crack length. The overload was applied when the crack was 200 μm long for DEN 2-1 and 100 μm long for DEN 3-1. It is clear in Figure 9 that the crack in DEN 2-1 grew slower than in DEN 3-1. However, the crack growth rate due to the overload shows some inconsistent crack growth: crack growth acceleration and retardation. This may be explained by the role of microstructure in the crack growth. When the crack tip is located at grain boundaries or packet boundaries, the application of the overload could result in insignificant crack increment. On the other hand, if the crack tip is situated within those boundaries, then the overload could induce the measurable crack increment. The crack growth rate due to the overload was compared to the one under constant amplitude loading as shown in Figure 10. It is clear that the crack growth rate after the overload was similar to or slower than the constant amplitude loading.

Under the stress levels and stress ratios used in the current study, the effect of the overload on the crack growth rate was not clear. However, there were two evidences of the effect of the overload. The first evidence was the crack branching at the crack tip after the overload (Figure 11a). No crack branching was found under constant amplitude loading. The second evidence was the plastic deformation at the crack tips (Figure 11b). The overload of 621 MPa resulted in distinct plastic deformation radius of 15 μm which is about the same size as predicted by the following equations:

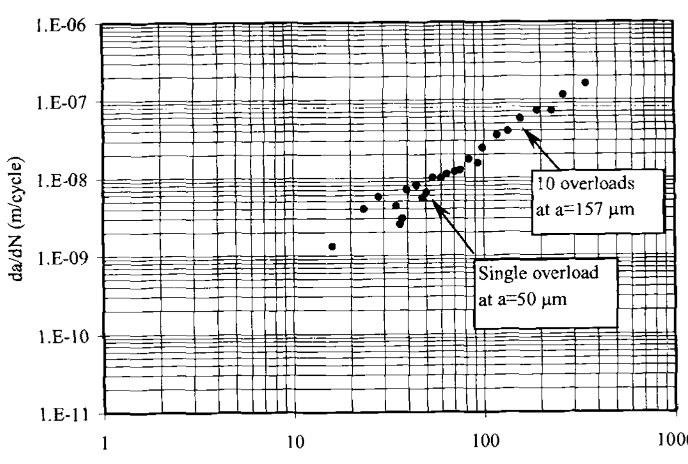

(a)

(a)

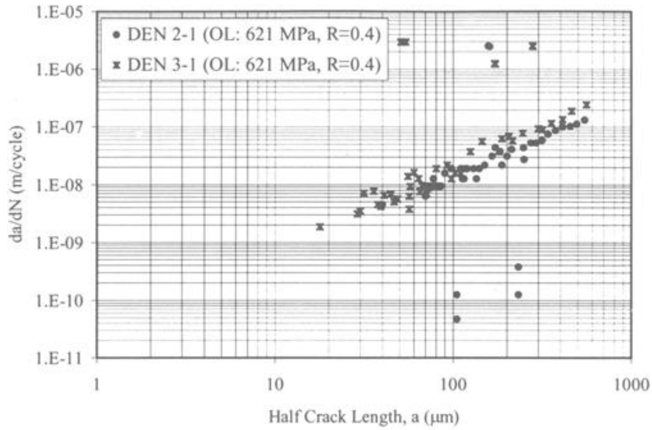

(b)

Figure 9-*Response of crack growth rate due to overload of a) 517 MPa: not much retardation of growth differenced by overload stress cycle and b) 621 MPa: notice different growth behavior of applied overload cycle*

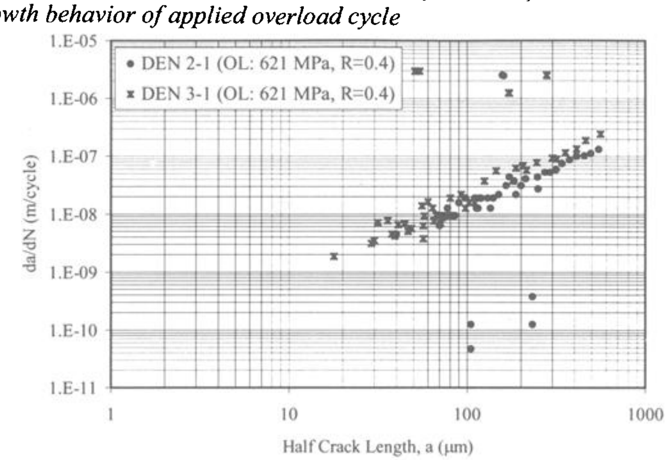

(b)

Figure 10-*Comparison of the results of the overload tests with constant amplitude loading at 476 MPa and R = 0.1*

(a)

Crack tip branching

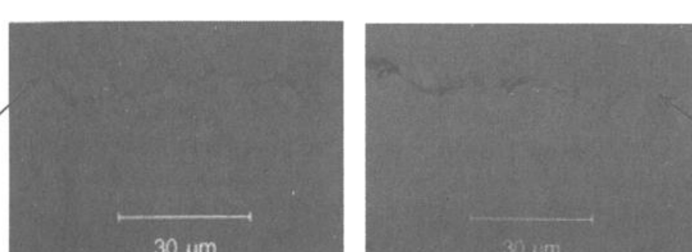

(b)

Plastic deformation

Figure 11-*a) crack branching after 10 overload cycles at 517 MPa and b) crack tip deformation (plastic deformation) after a single overload cycle at 621 MPa.*

$$r_y = \frac{1}{2\pi}\left(\frac{K_{OL}}{\sigma_y}\right)^2 \tag{4}$$

$$K_{OL} = 1.12 \cdot K_t \cdot S_{OL} \cdot \sqrt{\frac{\pi a}{Q}} \tag{5}$$

where r_y is radius of the plastic zone, σ_y is yield stress SOL is nominal overload stress. The expression for Q is shown in Equation (2). The calculated plastic zone size is approximately 17 μm assuming plane stress and the a/c ratio is 1.0. In cases where $(K_t)(S_{OL})$ is greater than the material yield stress, the yield stress value is used. This happens to be the case for the overload of 621 MPa. For the overload of 517 MPa, there was the plastic deformation at both crack tip but was not distinct shape and size.

Simple Block Loading-For the block loading, the crack growth rate was more influenced by the overload stress amplitude than by single overload since there were more than one such cycle. The crack length was measured every four blocks. This means that the crack growth rate was averaged over the growth of the two blocks of different stress amplitudes. In order to compare the extent of load interaction between three different block loadings, the crack growth rate was plotted against half crack length in Figure 12. It seems that the crack growth rate in DEN-10 (overload stress amplitude: S_{max}= 621 MPa/R = 0.4) was slower than the other two loading conditions. It is likely that the crack growth rate will be retarded more at the higher overload stress than at the lower overload stress. Notice that the block containing 100 overloads usually resulted in a higher average da/dN due to more contributions of the additional overload cycles.

The stress intensity factor range under the simple block loading was calculated based on the notch root stress range at the baseline stress amplitude of 214 MPa (S_{max} = 476 MPa/R = 0.1). The ratio of the stress intensity factor range (ΔK_2) based on the overload stress amplitude to the stress intensity factor range (ΔK_1) based on the baseline stress amplitude was reported. Figure 13 show the plots of the crack growth rate against the stress intensity factor range calculated based on the notch root stress range with the results under constant amplitude loading. All of the simple spectrums plotted had the 10 overload cycles. The da/dN was the average growth of the simple spectrum including the overloads. The crack growth rate under simple block loading deviated from that under

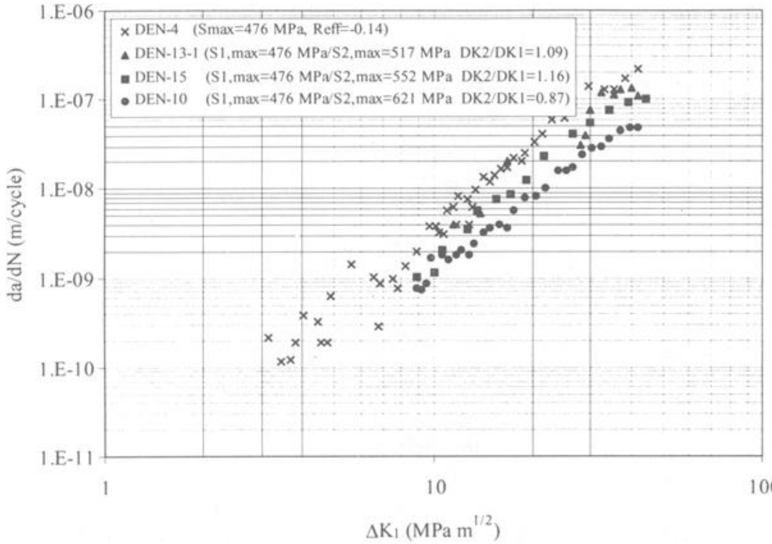

Figure 12-*Comparison of crack growth rate between four different block loading tests*

constant amplitude loading. As the maximum stress in the overload increased, the difference in the crack growth rate between the constant amplitude and simple block loading increased. It is clear that the amount of crack growth retardation increased as the maximum overload stress increased. Therefore small cracks do exhibit crack growth retardation under block loading.

Figure 13-*Comparison of the crack growth behavior between three different block loading*

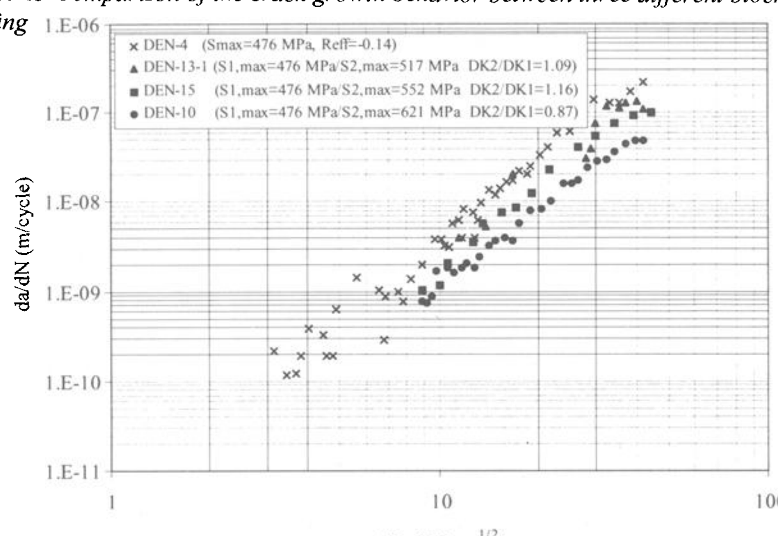

Conclusions

Based upon a rather limited testing the following observation was made regarding the growth of small cracks in PH13-8Mo stainless steels:

1. The crack growth behavior of PH13-8Mo stainless steel was greatly influenced by the microstructure, especially the size of the martensite packet. Therefore, the packet would be a critical microstructural dimension.
2. The randomness of the small crack growth behavior under constant amplitude loading overshadowed the influence of the stress amplitude range used in this study. In addition, small crack growth rate was a little slower than long crack growth rate at the stress levels and stress ratios used in the current study.
3. It was observed that the application of the overload induced plastic deformation and crack branching at the crack tips. The size of plastic zone was similar to the one calculated by a linear elastic fracture mechanics. Single overloads, 8 and 30 percent higher than baseline stress, seemed to have no significant retardation effect. The single overload cycle itself sometimes produced a large growth or hardly none at all. The authors suggest this may be a function of the crack tip location relative to the microstructural features (i.e. grain boundaries) when the overload stress is applied.
4. The crack growth rate under the simple block loading showed the overall crack growth retardation compared to the constant amplitude loading. The amount of crack growth retardation seemed to be affected by the compressive residual stress left on the notch root due to the presence of the overload stress amplitude. The compressive residual stress changed the effective stress ratio at the baseline stress amplitude (S_{max} = 476 MPa/R = 0.1) from -0.14 to –0.27 (S_{max} = 517 MPa/R = 0.1), -0.42 (S_{max} = 552 MPa/R = 0.1) and –0.85 (S_{max} = 621 MPa/R = 0.4). The effective stress ratio of –0.85 for the overload stress cycles at 621 MPa and R=0.4 resulted in the slowest crack growth rate in the three block loading tests.
5. Because of the randomness of the observed crack growth behavior of small cracks in PH13-8Mo stainless steel below 2a = 100 μm due to microstructural influences, a strictly deterministic approach to life prediction should not be used. An approach that recognizes the stochastic nature of the crack growth behavior in this crack size range needs to be developed.

Acknowledgment

This research was supported by the Office of Naval Research (Contract No. N00014-95-1-0539) as part of the M-URI *Center for Integrated Diagnostics*. Experimental help from Mr. Rick Brown of the Material Properties Research Lab at the Georgia Institute of Technology is acknowledged.

References

[1] Suresh, S., *Fatigue of Materials*, Cambridge University Press, 2nd edition, 1998.

[2] Hamm, R. W. and Johnson, W. S., "Survey of the State-of-the Art in Small Crack Research," *Journal of Testing and Evaluation*, Vol. 26, No. 3, March 1998, pp. 168-175.

[3] Skorupa, M., "Load Interaction Effects During Fatigue Crack Growth Under Variable Amplitude Loading-A Literature Review, Part I: Empirical Trends," *Fatigue & Fracture of Engineering. Materials & Structure*, Vol. 21, 1998, pp. 987-1006.

[4] Oni, O., "Effect of Single Peak Overload on the Propagation Behavior of Short Fatigue Crack in Steels," *Scripta Metallurgica*, Vol. 25, 1991, pp. 689-694.

[5] Changoing, Z., Yucheng, J., and Guangli, Y., "Effect of a Single Peak Overload on Physically Short Fatigue Crack Retardation in an Axle-Steel," *Fatigue & Fracture of Engineering. Materials & Structure*, Vol. 19, No. 2/3, 1996, pp. 201-206.

[6] Jono, M. and Sugeta, A., "Crack Closure and Effect of Load Variation on Small Fatigue Crack Growth Behavior," *Fatigue & Fracture of Engineering. Materials & Structure*, Vol. 14, 1991, pp. 165-174.

[7] Newman, J. C, Jr., Swain, M. H. and Phillips, E. P. " An Assessment of The Small Crack Effect for 2024-T3 Aluminum Alloy," *Small Fatigue Cracks*, R. O. Ritchie and J. Lankford, Eds., 1986, pp. 427-452.

[8] Newman, J. C., Jr. and Edwards, P. R., "Short Crack Growth Behavior in An Aluminum Alloy-An AGARD Cooperative Test Program," AGARD Report 732, 1988.

[9] Swain, M. H., Newman, J. C., Jr., Everett, R. A., and Phillips, E. P., "The Growth of Short Cracks in 4340 Steel and Aluminum Lithium 2090," *Short-Crack Growth Behavior in Various Aircraft Materials*, AGARD-767, 1990, pp. 7.1-7.3.

[10] Wu, X. R., Newman, J. C., Jr., Zhao, Swain, M. H., W., Ding, C. F., and Phillips, E. P., "Small Crack Growth and Fatigue Life Predictions for High-Strength Aluminum Alloys: Part I-Experimental and Fracture Mechanics Analysis," *Fatigue & Fracture of Engineering Materials & Structures*, Vol. 21, 1998, pp. 1289-1306.

[11] Newman, J. C., Jr., Phillips, E. P., and Swain, M. H., "Fatigue-life Prediction Methodology using Small Crack Theory," *International Journal of Fatigue*, Vol. 21, 1999, pp. 109-119.

[12] Edwards, P. R. and Newman, J. C., Jr., "An AGARD Supplemental Test Program on the Behavior of Short Cracks under Constant Amplitude and Aircraft Spectrum Loading," AGARD Report No. 767, 1990, pp.1.1-1.43.

[13] Military Handbook 5G, Metallic Materials and Elements for Aerospace Vehicles, 1994, pp. 2-147~2-156.

[14] Patel, A. M., Neu, R. W. and Pape, J. A., "Growth of Small Fatigue Cracks in PH 13-8Mo Stainless Steel," *Metall. & Mater. Trans.* A, Vol. 30, 1999, pp. 1289-1300.

[15] Dowling, N. E., "Fatigue at Notches and the Local Strain and Fracture Mechanics Approaches," *Fracture Mechanics*, ASTM STP 677, C. W. Smith (ed.), American Society for Testing and Materials, Philadelphia, 1979, pp. 247-273.

[16] Damage Tolerant Design Handbook, May 1994.

Theodore Nicholas[1] and David C. Maxwell[2]

Mean Stress Effects on the High Cycle Fatigue Limit Stress in Ti-6Al-4V

Reference: Nicholas, T. and Maxwell, D. C., "**Mean Stress Effects on the High Cycle Fatigue Limit Stress in Ti-6Al-4V,**" *Fatigue and Fracture Mechanics: 33rd Volume, ASTM STP 1417*, W. G. Reuter and R. S. Piascik, Eds., ASTM International, West Conshohocken, PA, 2002.

Abstract: An investigation was undertaken to evaluate the effects of mean stress on the high cycle fatigue (HCF) limit stress under uniaxial loading. Tests were conducted at constant values of stress ratio, R (ratio of minimum to maximum stress), at frequencies from 20 to 70 Hz up to 10^7 cycles using a step-loading technique developed by the authors. Data were presented in the form of a Haigh (Modified Goodman) diagram as alternating stress against mean stress. Tests in the regime $R < -1$ were conducted to determine the effect of negative mean stresses on the material behavior. The lowest mean stress corresponded to $R = -4$, below which the compressive yield stress of the material would be exceeded. While numerous models could provide approximate fits to the data in the constant life Haigh diagram for positive mean stresses, none of them captured the trends of the data over the entire mean stress range including $R < -1$. The Jasper equation, based on a constant range of stored energy density, was found to represent the positive mean stress data quite well. The equation was modified to account for stored energy density at negative mean stresses. The best fit to the data implies that compressive strain energy density contributes less than 30 percent to the fatigue process as compared to energy under tensile stresses. Further, initiation to a fixed crack length beyond which crack propagation occurs does not explain the shape of the Haigh diagram. It is concluded through simple analysis that there is no clear link between HCF crack initiation, which represents a majority of life in some applications, and crack growth threshold, and the two might represent entirely different mechanisms.

Keywords: high cycle fatigue, mean stress, Haigh diagram, Goodman diagram, Ti-6Al-4V, stress ratio

---

[1] Air Force Research Laboratory, Materials & Manufacturing Directorate, (AFRL/MLLMN), Wright-Patterson AFB, OH 45433-7817.

[2] University of Dayton Research Institute, Structural Integrity Division, Dayton, OH 45469.

Introduction

High cycle fatigue is a common occurrence in rotating machinery of all types and can often lead to failure after many cycles. Such failures are of great concern in turbine engines in the U.S. Air Force and have precipitated an extensive study in recent years to alleviate the problem. Among the aspects being studied is the material capability when subjected to large numbers of cycles. Such capability is often called the runout stress, but it is more correct to refer to it as the fatigue limit stress corresponding to a given number of cycles, typically 10^7 or greater. Recent data indicate that fatigue limit stresses continually decrease at cycle counts up to and beyond 10^{10} cycles [*1,2*], thus testing must include large numbers of cycles representative of potential service exposures. This, in turn, requires high frequency testing capability or extremely long testing times. As an engineering compromise, cycle counts of the order of 10^7 using conventional testing machines operating at their maximum frequencies are often used.

In dealing with data on fatigue limit stresses, it is common to plot these stresses as a function of stress ratio (R = ratio of minimum to maximum stress), or, more commonly, of mean stress. The Haigh diagram, incorrectly referred to as a Goodman diagram, is a common method of representing the fatigue limit or endurance limit stress of a material in terms of alternating stress, defined as half of the vibratory stress amplitude. Thus, the maximum dynamic stress is the sum of the mean and alternating stresses. For many rotating components, the mean stress is known fairly accurately, but the alternating stress is less well defined because it depends on the vibratory characteristics of the component. Thus a Haigh diagram represents the allowable vibratory stress as the vertical axis as a function of mean or steady stress as the x axis. While attempts have been made to define the equation which best represents the data on a Haigh diagram, variability from material to material, scatter in the data, and lack of sufficient data in many cases prevent the fitting of an equation to such data.

When mean stress values are negative, or for values of R less than minus one, there are very few data and no general guidelines for extrapolating equations which were meant to represent data on a Haigh diagram for positive values of mean stress. In cases such as contact fatigue, very high compressive stresses can be present, necessitating knowledge of fatigue behavior or fatigue limits for negative mean stresses. One of the most important areas where negative mean stresses can occur is in the case of the introduction of residual stresses into a material or component. Shot peening, for example, is commonly used as a surface treatment to improve the fatigue properties of a material by introducing residual compressive stresses into the material up to depths typically no greater than 0.1 mm. While compressive stresses in the vicinity of the surface reduce the maximum stress from vibratory loading at the surface, they do not reduce the vibratory amplitude. Thus, in effect, they drive the mean stress lower, often into the compressive regime. While such stresses are known to improve the fatigue characteristics in many materials and geometries, these residual compressive stresses are generally not taken into account in design and are used, instead, to improve the margin of safety. If such a condition is to be taken into account in design, a thorough understanding of material behavior and fatigue limits under negative mean stresses is required. It is the purpose of this paper to provide some data on fatigue limit stresses at $R < -1$ and to propose a method of representing such data on an extension of a Haigh diagram into the negative mean stress regime.

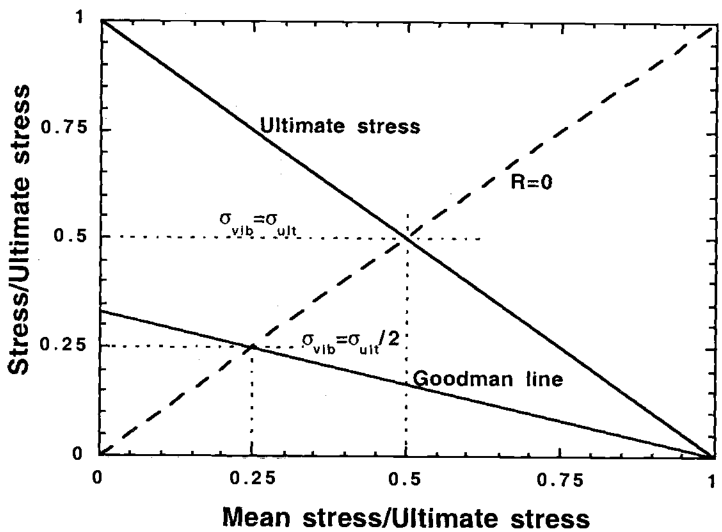

Figure 1 - *Schematic of Goodman diagram showing allowable vibratory stress.*

Background

Equations used to represent fatigue limit stress data in Haigh diagram plots have generally been established from empirical fits to data, yet some of the earliest works tried to establish physical principals for fatigue [*3*]. Goodman [*4*] proposed use of the "dynamic theory" which is explained by Fidler [*5*]. This results in a straight line on a Haigh diagram when the allowable alternating stress is taken equal to half the ultimate stress (see Fig. 1). Of interest is that Goodman proposed such an equation as one that is "very easy of application and is, moreover, simple to remember"[*4*]. He also noted that "whether the assumptions of the theory are justifiable or not is quite an open question." What was originally termed the modified Goodman diagram is to use a straight line fit on a Haigh diagram based on the fully reversed loading data point(s) on the y axis and the ultimate tensile strength on the x axis as described by

$$\sigma_a = \sigma_{-1}\left(1 - \frac{\sigma_m}{\sigma_u}\right) \tag{1}$$

where σ_{-1} represents the alternating stress, σ_a, under fully reversed loading (R = - 1) and σ_m and σ_u represent the mean and ultimate stress, respectively.

Many other modifications of the single straight line, or a bilinear curve, have been used, but the single line between the fully reversed alternating stress and the ultimate strength (or yield strength [6]) appears to be the most common. Whether or not such a line represents actual data very well, it provides a method for determining the alternating stress for all positive values of mean stress, corresponding to values of stress ratio, R, from R = - 1 to R = 1.0. Other formulas are used to fit experimental data, one of the more common ones being the Gerber parabola [7]:

$$\sigma_a = \sigma_{-1}\left[1 - \left(\frac{\sigma_m}{\sigma_u}\right)^2\right] \tag{2}$$

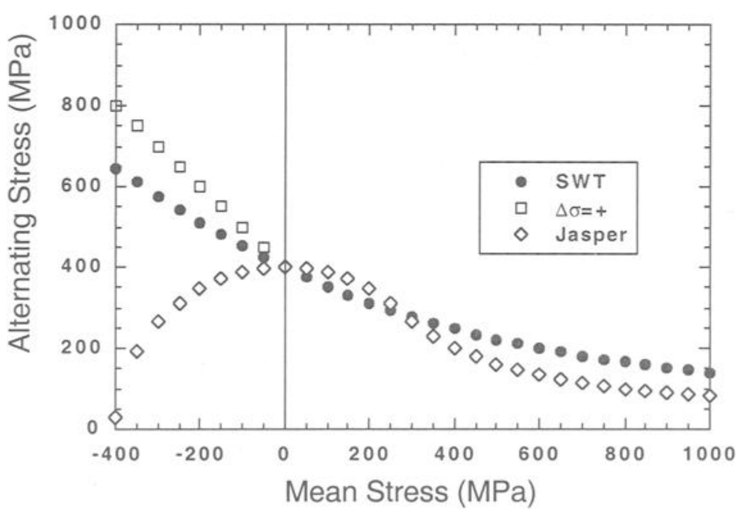

Figure 2 - *Haigh diagram representation of SWT and Jasper equations.*

Other fatigue equations, used mainly to fit data in the low cycle fatigue (LCF) regime, try to account for the effects of mean stress or stress ratio. Two such equations are the one due to Smith, Watson and Topper (SWT) [8] and the commonly used Walker equation. For the SWT equation, an effective stress is given in terms of maximum stress and strain range. In HCF, elastic behavior is assumed, thus strain range and stress range can be used interchangeably when dealing with fatigue limit stress conditions. The SWT equation for elastic behavior is in the form

$$\Delta\sigma_{eff} = \sigma_{-1} = \left(\frac{\sigma_{max}\,\Delta\sigma}{2}\right)^{1/2} = \left(\sigma_{max}\,\sigma_a\right)^{1/2} \tag{3}$$

where $\Delta\sigma_{eff}$ can be treated as a constant, $\Delta\sigma$ is the stress range, $\Delta\sigma = 2\sigma_a$, and σ_{max} is the maximum stress. This equation is plotted in the form of a Haigh diagram in Fig. 2 using a value of $\Delta\sigma_{eff}$ = 200 MPa which is representative of data on a titanium alloy to be presented later. The exponent in eqn (3) is taken as the one used most commonly, namely 0.5. For reference purposes, the Jasper equation, discussed later, is plotted because it is found to describe the shape of the Haigh diagram for positive mean stress quite well. Of greatest interest in Fig. 2 is the shape of the curve for the SWT equation for negative mean stress, which shows an ever increasing alternating stress as mean stress becomes further negative. As an alternative, if we choose to take half the strain range (or half the stress range) as that corresponding to positive stresses only ($\Delta\sigma$ = + in the figure), this changes the curve only slightly in the negative mean stress regime. Note, finally, the symmetric shape of the Jasper equation about zero mean stress. This also will be discussed later.

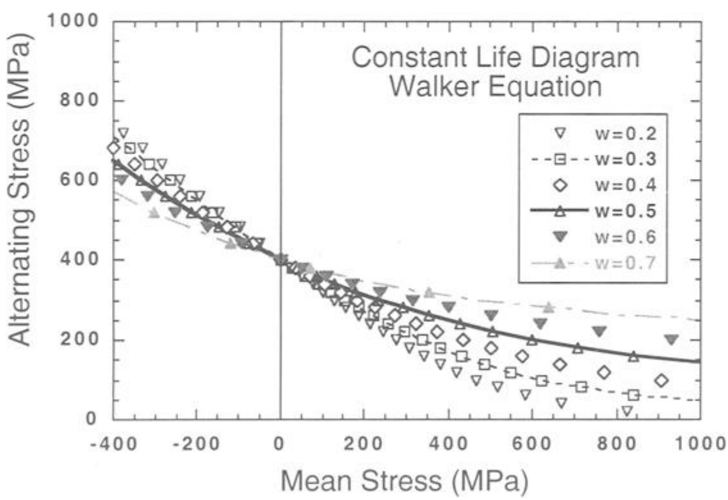

Figure 3 - *Haigh diagram representation of Walker equation.*

A similar treatment can be given to the Walker equation which, as for the SWT equation, is most commonly used to consolidate LCF data obtained at different stress ratios, R. The equation is similar to the SWT equation, but adds a degree of flexibility through the exponent, w. It has the form

$$\sigma_{eq} = 2^{w}\,\sigma_{-1} = \left(\Delta\sigma\right)^{w}\left(\sigma_{max}\right)^{1-w} \tag{4}$$

where w is the Walker exponent. With the exception of the value of the coefficient in eqn (4), it is identical in form to the SWT equation when w = 0.5. Figure 3 is a plot of the Walker equation for various values of the exponent, w, including extension of the equation to account for negative mean stress or values of R < - 1. The curves are all forced to go through the same point at zero mean stress. While some data are handled by changing the value of w for negative values of R, it can be seen that the Walker equation has the same general characteristics as the SWT equation for negative mean stress, namely that alternating stress continues to increase as mean stress goes further negative.

Further, for both equations, the shape of the curves for positive mean stress is concave up over the entire region.

Several attempts were made in the early days of fatigue modeling to account for the observed behavior of the fatigue limit stress when the mean stress was negative. In 1930, Haigh [*9*] pointed out that experimental data indicates that the constant life diagram is not symmetric with respect to σ_m as required by the Gerber and generalized Goodman formulas[3]. He suggested that the data can be represented by the generalized parabolic relation

$$\sigma_a = \sigma_{-1}\left[1 - k_1\left(\frac{\sigma_m}{\sigma_u}\right) - k_2\left(\frac{\sigma_m}{\sigma_u}\right)^2\right] \tag{5}$$

where the constants k_1 and k_2 are selected to give the best fit of the data. A plot of this equation is presented in Fig. 4 for several combinations of k_1 and k_2 with the constraints of the curve going through the ultimate stress point on the x axis and the alternating stress at R = - 1 on the y axis. The case where $k_1 = 0$, $k_2 = 1$ represents the Gerber parabola, eqn (2), symmetric about the y axis. When $k_1 = 1$ and $k_2 = 0$, the modified Goodman line is obtained, extrapolated for negative mean stress.

More complex equations have been proposed, such as that by Heywood [*10*] who used an empirical cubic equation for representing constant life data. His equation has the form

$$\sigma_a = \left[1 - \left(\frac{\sigma_m}{\sigma_u}\right)\right]\left[\sigma_{-1} + \gamma\left(\sigma_u - \sigma_{-1}\right)\right] \tag{6a}$$

$$\gamma = \left(\frac{\sigma_m}{\sigma_u}\right)\left[e + g\left(\frac{\sigma_m}{\sigma_u}\right)\right] \tag{6b}$$

where e and g are either positive or negative constants. Because of the large number of terms, most experimentally determined constant life data may be represented by proper selection of the constants.

---

[3] While the generalized Goodman equation (1) does not indicate symmetry with respect to σ_m, the formulation in the first edition of Goodman's book [*4*] presents equations for the static load capability in terms of the dynamic theory. If it is assumed that the strength is equal in tension and compression,the equations indicate that there is symmetry with respect to mean stress. The lack of data for negative mean stresses prevented any substantial debate on this issue of symmetry. The symmetry of the Goodman equation and its history are discussed in [*3*].

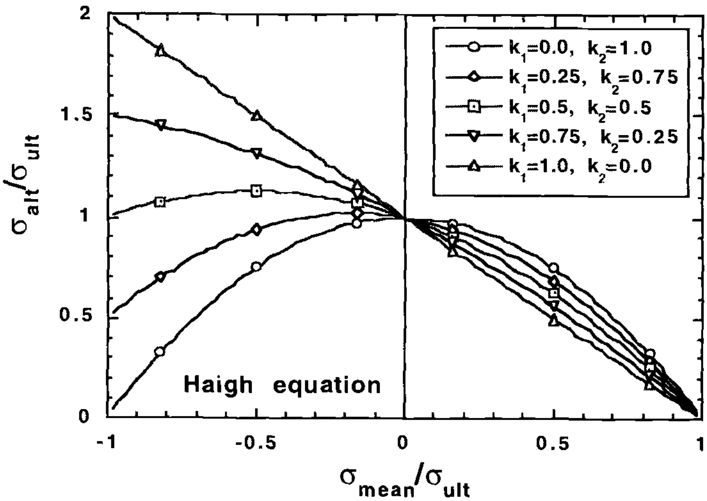

Figure 4 - *Constant life diagram for parabolic equation of Haigh.*

Jasper equation

Jasper [*11*] proposed that fatigue life is related to the stored energy density range per cycle in a material. Applying this concept to HCF conditions, it can be assumed that all stresses and strains are elastic, thus all equations represent purely elastic behavior. For purely uniaxial loading, the shaded area in Fig. 5 illustrates schematically the stored energy for the cases where loading is purely tensile (R > 0). The energy for the case where R < 0, which involves tension and compression in a single cycle, is illustrated in Fig. 6 by the shaded area. The case of purely compressive loading is not treated here for reasons to be explained later. The stored energy density range per cycle is then given for uniaxial loading by

$$U = \int_{\sigma_{min}}^{\sigma_{max}} \sigma \, d\varepsilon = \frac{1}{E}\int_{\sigma_{min}}^{\sigma_{max}} \sigma \, d\sigma \tag{7}$$

since $\sigma = E\varepsilon$, E is Young's modulus. The energy can then be written as

$$U = \frac{1}{2E}\left(\sigma_{max}^2 \pm \sigma_{min}^2\right) \tag{8}$$

where the plus sign is for R < 0 and the minus sign for R > 0 (see Figs. 5 and 6). For purposes of presenting the equation in the form of a Haigh diagram, the stress limits are written in terms of mean and alternating stresses

$$\sigma_{max} = \sigma_m + \sigma_a \tag{9a}$$

$$\sigma_{min} = \sigma_m - \sigma_a \tag{9b}$$

where σ_m and σ_a represent the mean and alternating stresses, respectively.

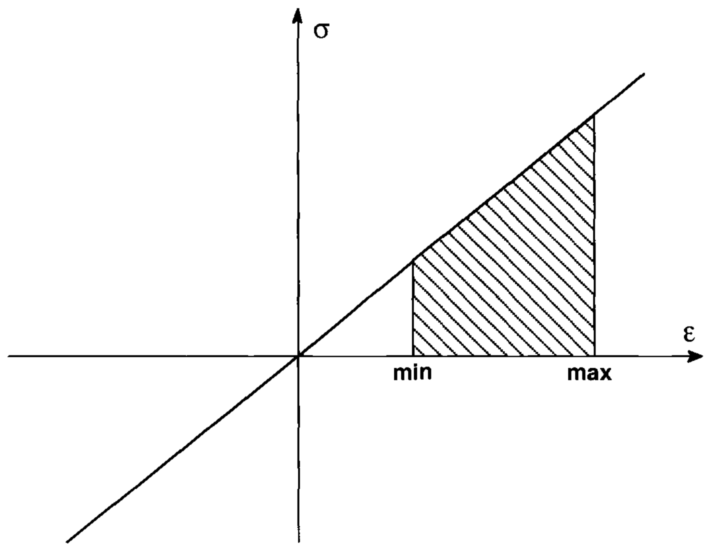

Figure 5 - *Stored energy (shaded) for elastic loading under tension fatigue (R > 0).*

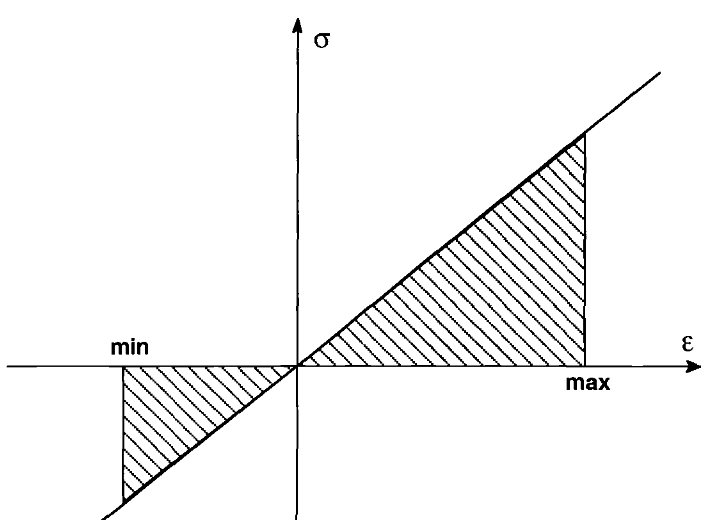

Figure 6 - *Stored energy (shaded) for elastic loading under reversed fatigue (R < 0).*

For the specific case of fully reversed loading, R = - 1, the energy is written as

$$U = \frac{1}{2E}\left(2\,\sigma_{-1}^2\right) \tag{10}$$

where σ_{-1} represents the alternating stress (= maximum stress) at R = - 1. For any other case of uniaxial loading, the following equation is easily derived and can be used to obtain the value of the alternating stress on a Haigh diagram:

$$\sigma_a = \frac{\sigma_{-1}}{\sqrt{2}}\sqrt{\frac{(1-R)^2}{1-R|R|}} \tag{11}$$

It follows that the alternating stress when R = 0, defined as σ_0, is

$$\sigma_0 = \sqrt{\frac{\sigma_{-1}{}^2}{2}} \tag{12}$$

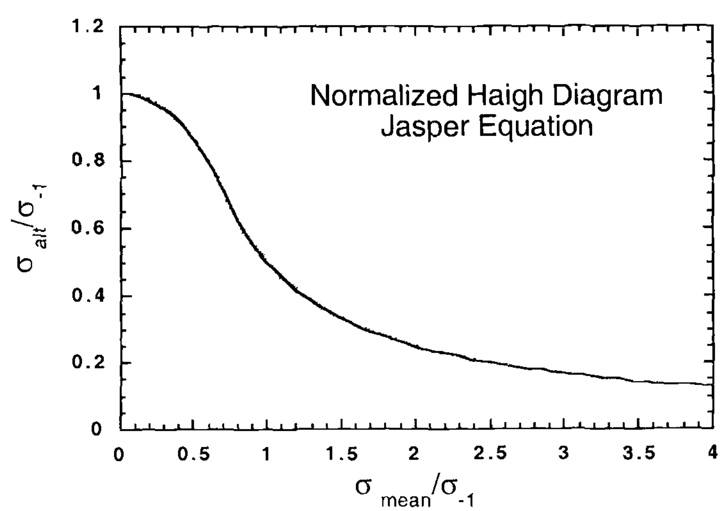

Figure 7 - *Normalized Haigh diagram representing Jasper eqn for positive mean stresses.*

Of interest is the shape of the Haigh diagram corresponding to a constant energy density range for any positive mean stress value. Such a diagram is shown in Fig. 7 which has the same general shape as that for Ti-6Al-4V bar material (Fig. 8) obtained in a previous investigation [*12*]. It should be noted that only a single parameter, σ_{-1}, is required to describe the values on both the x and y axes. This plot (Fig. 7) is the same as shown previously as the Jasper equation in Fig. 2, using typical numbers for titanium plate, where the alternating stresses corresponding to negative mean stresses are also included.

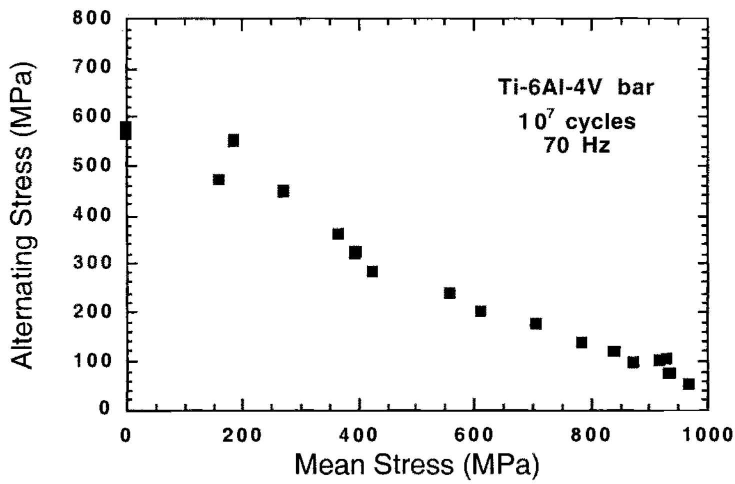

Figure 8 - *Haigh diagram for Ti-6Al-4V bar from prior investigation [12].*

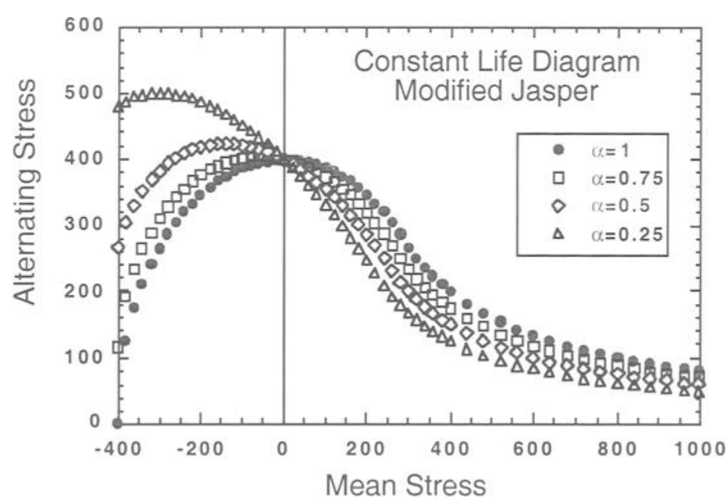

Figure 9 - *Haigh diagram for modified Jasper equation for various values of* α.

Whereas it will be shown later that data for negative mean stress neither follow the Jasper equation nor the SWT or Walker equations (see Fig. 2), a modification to the Jasper equation is proposed. Haigh [9], in 1929, in referring to Bauschinger's results from 1915 and 1917, noted that "this series of tests…was probably the first that ever revealed any difference between the actions of pull and push in relation to fatigue." Referring to data on naval brass, he indicated "In this metal, as in many others, pull tends to reduce the fatigue limit while push increases the resistance to fatigue." Following this idea, it is postulated here that stored energy density per cycle does not contribute towards the fatigue process as much when the stresses are compressive as when they are in tension. Taking the simplest case, where compressive stress energy contributes a fraction, α, compared to comparable energy in tension, then the total effective energy can be formulated in the following manner, where $\alpha < 1$:

$$U_{tot} = U_{tens} + \alpha\, U_{comp} = \text{constant} \tag{13}$$

In the use of this equation, energy terms corresponding to negative stresses have to be modified by the coefficient α. The introduction of the constant α has the effect of modifying the shape of the Jasper equation as shown in Fig. 9 for several values of the constant α. The stresses on both axes are the same as those used in Fig. 2. The constant α can now be used to fit actual experimental data obtained at values of $R < -1$ corresponding to negative mean stresses.

Experiments

The material used in this study was Ti-6Al-4V forged plate approximately 20 mm thick by 152 mm wide in the STOA condition and is identical to that used widely in the U.S. Air Force HCF program [*13*]. The plate was forged from a parent bar, produced in accordance with AMS 4928. The plate was solution treated at 932°C for 75 minutes, fan cooled in air, mill annealed in vacuum at 705°C for two hours, and fan cooled in argon. The result was an alpha-beta titanium alloy microstructure with acicular Widmanstätten structures. Complete details of the processing can be found in [*14*]. The microstructure can be seen in [*14*] or [*15*] for example. The quasi-static mechanical properties of the plate in the longitudinal direction were modulus of 109 GPa, yield strength of 930 MPa, and ultimate tensile strength of 978 MPa.

Test specimens were extracted from the forged plate using wire electro-discharge machining. All specimens were finish machined using standard low stress grind procedures for titanium followed by polishing with 600 grip paper to a 15 μm finish. The specimens were cylindrical with a grip section diameter of 12.7 mm and an hourglass gage section with a minimum diameter of 5.6 mm.

Fatigue tests were conducted under constant amplitude stress conditions using a closed-loop computer controlled servo-hydraulic test machine. All tests were conducted at room temperature in laboratory air. Tests at stress ratios of −1 and above were conducted at a frequency of 70 Hz, but tests below a stress ratio of −1 were conducted at a frequency of 21 Hz. These test frequencies were dictated primarily by test machine capability. The tests covered a range of stress ratios from 0.8 to −4. The minimum stress ratio value at which tests were conducted was limited by the compressive yield strength of the material. For the Ti-6Al-4V plate material used for these tests, a minimum value of $R = -4$ was obtained.

To establish the fatigue strength, samples were fatigue tested using the step-loading procedures described by Maxwell and Nicholas [*12*]. At each stress ratio, a specimen was fatigued to a limit of 10^7 cycles at a stress level lower than the expected fatigue limit. After each runout of 10^7 cycles, the stress was increase by approximately 5% until failure occurred at less than 10^7 cycles. The fatigue limit stress was then determined using the linear interpolation scheme as described in the following equation:

$$\sigma_e = \sigma_o + \Delta\sigma \, (N_{fail}/N_{life}) \tag{14}$$

where σ_e is the maximum fatigue strength corresponding to N_{life} cycles, σ_o is the previous maximum fatigue stress that did not result in failure, $\Delta\sigma$ is the step increase in maximum fatigue stress, N_{fail} are the cycles to failure at the fatigue stress ($\sigma_o + \Delta\sigma$), and N_{life} the defined cyclic fatigue life (i.e., 10^6, 10^7, etc). Steps of 10^7 cycles were used in this investigation, while $\Delta\sigma$ was taken typically at 5 percent of the initial load block. Typically 2 to 5 blocks were necessary to achieve failure. While the use of many load steps raises the question of the validity of the step loading techniques, particularly with respect to the history effect referred to as "coaxing," it has been shown that there appears to be no influence of coaxing in this material [*16*]. Further, the step loading technique has been shown to produce data consistent with those obtained from conventional S-N plots for both smooth [*15*] and notched [*17*] configurations.

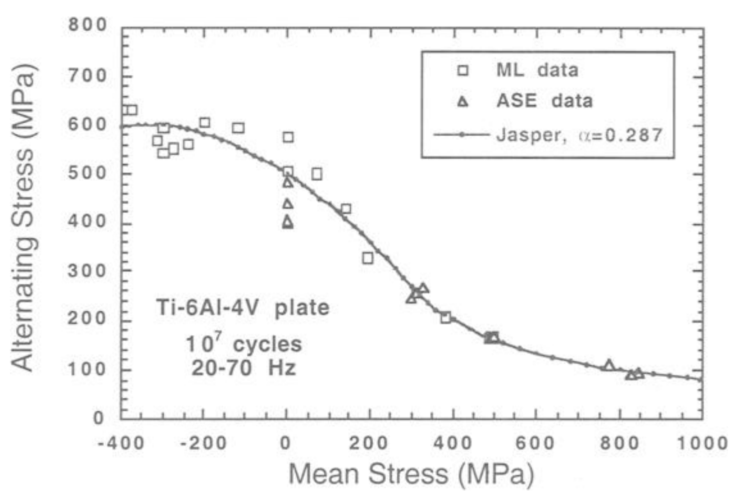

Figure 10 - *Haigh diagram for Ti-6Al-4V plate including modified Jasper equation fit.*

Discussion

Experimental values for the fatigue limit stress were obtained for a broad range of values of R and are plotted in the form of a Haigh diagram in Fig. 10. The data are shown as ML in the figure, and are combined with previously unpublished data from Allied Signal Engines (ASE) on the same material. A best fit of the data using the modified Jasper equation is also shown in the figure. The constant, α, in the modified Jasper equation (13) is obtained as 0.287 by fitting to the experimental data obtained from R = 0.8 to R = - 4.0. The weighted energy is obtained for each data point as a function of the variable α in eqn (13) and the percent least squares error between the average energy of all the data points and the individual energy values is minimized. To plot the resulting modified Jasper equation, the stress corresponding to the average energy at R = - 1 is obtained, this value is 500 MPa.

It is of importance to note that Haigh diagram, especially when extended into the negative mean stress regime, provides useful information on the potential beneficial effects of residual stresses. Notwithstanding the fact that stress gradients play an important role in fatigue, comparing allowable alternating stresses as a function of mean stress can give guidance on the role that residual stress can play in altering the fatigue limit stress. Noting again that compressive residual stresses do not alter the alternating stress applied to a material or structure but, rather, reduce the mean stress, the Haigh diagram provides data on the reduction of the allowable alternating stress as a function of mean stress. Using the Jasper equation as a measure of the allowable alternating stress, eqn (12) shows that if a material is subjected to a vibratory stress field at R = 0, with an alternating stress magnitude denoted by σ_0, then addition of a compressive residual stress of an equal magnitude σ_0 increases the allowable alternating stress by a factor of $\sqrt{2}$. Yet if the original stress state is at R = - 1, then the modified Jasper diagram representing Ti-6Al-4V plate material, Fig. 10 shows that the benefit of compressive residual stress is somewhat limited. Going from a mean stress of zero to a mean stress of -400 MPa, for example, Fig. 10 indicates a benefit in allowable alternating stress of only approximately 20% in going from an alternating stress of approximately 500 MPa to approximately 600 MPa. This can also be seen in a plot of maximum stress against mean stress, see Fig. 11, where the maximum stress corresponding to the fatigue limit is seen to decrease as mean stress decreases in the negative mean stress regime. Thus, it has to be ascertained where the mean stress is without residual stress and where the residual stress will be after a compressive residual stress is developed.

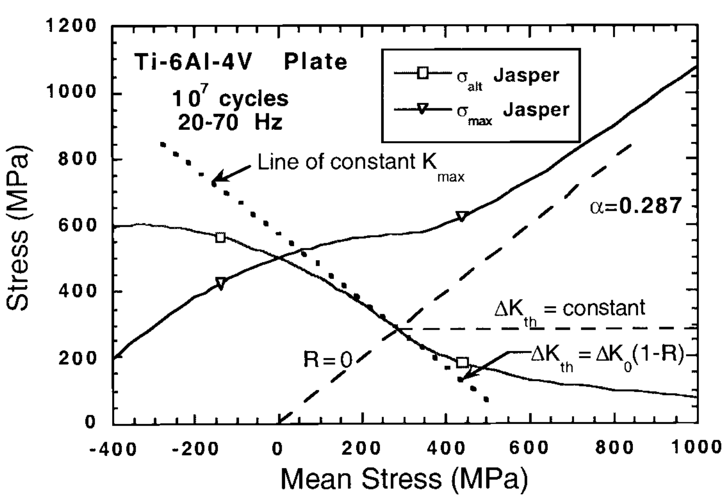

Figure 11 - *Locus of maximum and alternating stresses corresponding to modified Jasper equation fit to experimental data.*

It is of interest to note that under some conditions, the scatter in the experimental data for fatigue limit stress is minimal. In Fig. 10, the data points representing $R = 0.5$ all have a mean stress of approximately 500 MPa. In the figure there are six data points at that location which are very hard to distinguish from one another. Three of the points are from ASE and three are from ML. Of further interest is that two of the data points from ML represent tests on specimens that were stress relieved after machining. This demonstrates that any residual stresses that were present after machining and polishing had no effect on the fatigue behavior of this material.

Lastly, we examine the implications of the shape of the Haigh diagram, as described by the modified Jasper formulation, in terms of the fracture mechanics parameter related to the threshold for crack growth, namely ΔK_{th}. The fatigue limit stress, defined as the maximum stress under which a crack will not initiate and grow, should be related to the threshold for crack propagation using the following logic. At a stress just above the fatigue limit, a crack will both initiate and grow to failure in a smooth bar. If it is assumed that crack initiation can be defined as initiation or nucleation to a defined size, then the driving force in terms of ΔK must be equal to or exceed ΔK_{th} in order for failure to occur. The locus of stresses in terms of the alternating and maximum stresses corresponding to the modified Jasper equation used to fit the data of this investigation are plotted against mean stress in Fig. 11. A line corresponding to $R = 0$ is also shown for references purposes in this modified version of a Haigh diagram. We consider two extreme cases for ΔK_{th} for a fixed crack size for crack initiation. First is the case where crack propagation, and hence the threshold for crack extension, is governed by the total stress range. In this case, ΔK_{th} is proportional to the alternating stress and would be represented by a horizontal line as shown in Fig. 11. A second scenario, one commonly used in fatigue crack growth modeling, is that only the positive stresses contribute to crack extension. Under this hypothesis, the maximum stress is proportional to the threshold, ΔK_{th} , for a fixed crack length. Such a line is shown in Fig. 11 as the line of constant K_{max} and is arbitrarily drawn through the same point at $R = 0$ as the line of constant ΔK_{th}. It can be seen that neither line corresponds to the lines representing the modified Jasper equation which is a best fit to the experimental data. These comparisons do not consider that ΔK_{th} may depend on crack length in the small crack regime (see [*18*], for example), or that is a function of stress ratio, R, as demonstrated in [*18*] and [*19*], for example. These considerations notwithstanding, the simplified analysis of the data presented here indicate that crack initiation to a specific crack length requires either a different crack length for each mean stress, or that the value of ΔK_{th} is different for each value of mean stress. Pursuing the latter postulate, the value of ΔK_{th} is calculated for each value of mean stress using the modified Jasper equation fit to the experimental data. Base on unpublished data for the test material that indicates the value of ΔK_{th} is approximately 5 MPa$\sqrt{m}$ at $R = 0$, the values of ΔK_{th} are plotted in Fig. 12. While the shape of the curve is similar to that seen often in the literature for positive values of R, it is of interest to note that the computed threshold is approximately constant for more negative values of R. For high values of R, however, there is no indication of a constant value of ΔK_{th} above some critical value of R as observed experimentally in some titanium alloys [*19*]. Note again that these numbers are based on a best fit to the experimental data using the modified form of the Jasper equation which accounts for the lesser contribution of compressive stresses to the fatigue process near the endurance limit. For high R, in our case, the data are extrapolated based on the Jasper equation fit which has very little meaning as R approaches unity.

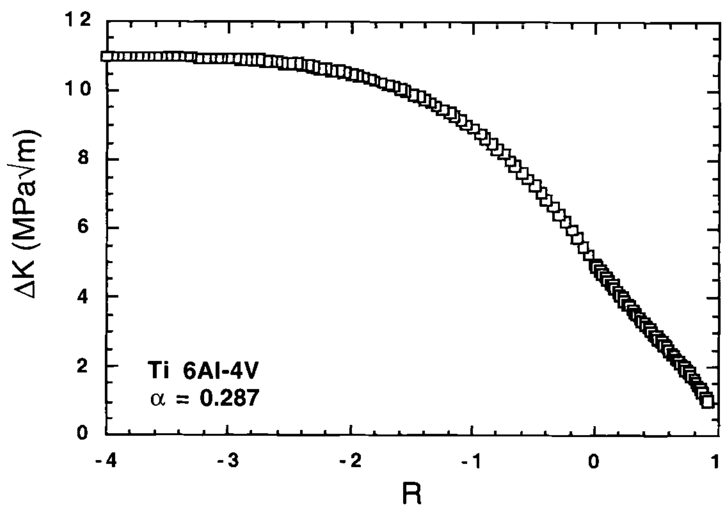

Figure 12 - *Computed ΔKth corresponding to a fixed size to crack initiation and modified Jasper equation fit to experimental data. ΔKth is assumed equal to 5 MPa√m at R = 0.*

Summary

Fatigue limit stress corresponding to 10^7 cycles in Ti-6Al-4V plate, plotted on a Haigh constant life diagram, can be described by an equation representing a constant modified strain energy density. The modification provides that energy under compressive loading contributes less than energy under tensile loading in the fatigue process.

The minimum value of R that can be achieved in a material is limited by the compressive yield stress in compression. The minimum R is also dependent on the allowable alternating stress which depends on mean stress. For the Ti alloy used here, the minimum R achievable was about R = - 4.

A fracture mechanics analysis, combined with the fatigue limit stress, suggests that the threshold for fatigue crack growth, ΔK_{th}, is a function of mean stress or stress ratio, R, if initiation is defined as corresponding to a specified small crack length. From this simple analysis, it is suggested that HCF crack initiation, which accounts for a majority of life, and crack growth threshold are not clearly linked and might represent entirely different mechanisms.

The beneficial effects of a residual compressive stress in Ti-6Al-4V decrease as the mean stress becomes negative. For the case of fully reversed loading, only a 20 percent increase in allowable alternating stress can be achieved by residual compression before the material yields in compression.

References

[1] Bathias, C., Drouillac, L. and Le Francois, P., "How and Why the Fatigue *S-N* Curve Does Not Approach a Horizontal Asymptote," *International Journal of Fatigue*, Vol. 23, Supp. 1, 2001, pp. S143-S151.

[2] Bathias, C., "There is no Infinite Fatigue Life in Metallic Materials," *Fatigue & Fracture of Engineering Materials & Structures*, Vol. 22, 1999, pp. 559-565.

[3] Sendeckyj, G. P., "Constant Life Diagrams – A Historical Review," *International Journal of Fatigue*, Vol. 23, 2001, pp. 347-353.

[4] Goodman, J., *Mechanics Applied to Engineering*, Volume 1, 9th ed., Longmans, Green & Co., Inc., New York, 1930, p.634; see also 1st edition, 1899, p. 455.

[5] Fidler, T. C., *A Practical Treatise on Bridge-Construction*, Charles Griffin and Company, London, 1887.

[6] Soderberg, C. R., "Factor of Safety and Working Stress," *Transactions ASME*, Vol. 52, 1939, pp. 13-28.

[7] Gerber, W. Z., "Bestimmung der zulässigen Spannungen in Eisen-Constructionen" [Calculation of the allowable stresses in iron structures]. *Zeitschrift des Bayerischen Architekten und Ingenieur-Vereins*, Vol. 6, No. 6, 1874, pp.101-110.

[8] Smith, K. N., Watson, R. and Topper, T. H, "A Stress-Strain Function for the Fatigue of Metals," *Journal of Materials*, Vol. 5, 1970, pp. 767-778.

[9] Haigh, B. P., "The Relative Safety of Mild and High-Tensile Alloy Steels Under Alternating and Pulsating Stresses," *Proceedings of the Institution of Automotive Engineers*, Vol. 24, 1930, pp. 320-347.

[10] Heywood, R. B., *Designing Against Fatigue of Metals*, Reinhold Publishing Corp., New York, 1962.

[11] Jasper, T. M., "The Value of the Energy Relation in the Testing of Ferrous Metals at Varying Ranges of Stress and at Intermediate and High Temperatures," *Philosophical Magazine*, Series. 6, Vol. 46, Oct. 1923, pp. 609-627.

[12] Maxwell, D. C. and Nicholas, T., "A Rapid Method for Generation of a Haigh Diagram for High Cycle Fatigue," *Fatigue and Fracture Mechanics: 29th Volume*, ASTM STP 1321, T. L. Panontin and S. D. Sheppard, Eds., American Society for Testing and Materials, West Conshohocken, PA, 1999, pp. 626-641.

[13] Nicholas, T., "Critical Issues in High Cycle Fatigue," *International Journal of Fatigue*, Vol. 21, Supp. 1, 1999, pp. S221-S231.

[14] Moshier, M. A., Nicholas, T. and Hillberry, B. M., "Load History Effects on Fatigue Crack Growth Threshold for Ti-6Al-4V and Ti-17 Titanium Alloys," *International Journal of Fatigue*, Vol. 23, Supp. 1, 2001, pp. S253-S258.

[15] Bellows, R. S., Muju, S. and Nicholas, T., "Validation of the Step Test Method for Generating Haigh Diagrams for Ti-6Al-4V," *International Journal of Fatigue*, Vol. 21, 1999, pp. 687-697.

[16] Nicholas, T. and Maxwell, D. C., "Evolution and Effects of Damage in Ti-6Al-4V under High Cycle Fatigue," *Progress in Mechanical Behaviour of Materials*, Proceedings of the Eighth International Conference on the Mechanical Behaviour of Materials, ICM-8, F. Ellyin and J.W. Provan, Eds. Vol. III, 1999, pp. 1161-1166.

[17] Bellows, R. S., Bain, K. R. and Sheldon, J. W., "Effect of Step Testing and Notches on the Endurance Limit of Ti-6Al-4V," *Mechanical Behavior of Advanced Materials*, MD-Vol. 84, D. C. Davis, et al., Eds. ASME, New York, 1998, pp. 27-32.

[18] Tabernig, B., Powell, P. and Pippan, R., "Resistance Curves for the Threshold of Fatigue Crack Propagation in Particle Reinforced Aluminium Alloys," *Fatigue Crack Growth Thresholds, Endurance Limits, and Design, ASTM STP 1372*, J. C. Newman, Jr. and R. S. Piascik, Eds., American Society for Testing and Materials, West Conshohocken, PA, 2000, pp. 96-108.

[19] Smith, S. W. and Piascik, R. S., "An Indirect Technique for Determining Closure-Free Fatigue Crack Growth Behavior," *Fatigue Crack Growth Thresholds, Endurance Limits, and Design, ASTM STP 1372*, J. C. Newman, Jr. and R. S. Piascik, Eds., American Society for Testing and Materials, West Conshohocken, PA, 2000, pp. 109-122.

C.-C. Chu, R. A. Chernenkoff, and J. J. F. Bonnen[1]

Experiments and Analysis of Mean Stress Effects on Fatigue for SAE1045 Steels

REFERENCE: Chu, C. C., Chernenkoff, R. A., and Bonnen, J. J. F., **"Experiments and Analysis of Mean Stress Effects on Fatigue for SAE1045 Steels,** *Fatigue and Fracture Mechanics: 33rd Volume, ASTM STP 1417,* W. G. Reuter and R. S. Piascik, Eds., ASTM International, West Conshohocken, PA, 2002.

ABSTRACT: Most of the existing fatigue design tools that account for mean stress effects were originally based on limited experimental data with relatively low mean stresses. However, residual stresses resulting from manufacturing processes are frequently at or near the yield stress level of the material. Therefore, to improve the fatigue design of engineering components which have residual stresses, more experimental as well as analytical studies are required in this regime. In this paper data from several constant maximum stress and constant minimum stress fatigue test sets are presented. These tests are designed so that material constants required to implement a closure-based fatigue damage method can be established. It is then shown that mean stress effects on fatigue are more complex than what can be modeled by several of the most commonly used methods. By adopting a more mechanism-oriented crack closure concept in an initiation-based fatigue approach the life prediction capability can be significantly improved.

KEY WORDS: mean stress, fatigue crack closure, crack opening stress, effective strain life curve, cyclic stress strain relationship, constant maximum stress test, constant minimum stress test, initiation fatigue approach

[1]Research Staff, Ford Research Lab, MD 3135, 2101 Village Rd., Dearborn, MI 48124-2053.

Introduction

The generally held concept that a compressive mean stress is beneficial to fatigue performance and a tensile mean stress is detrimental has been a widely used design guideline in the engineering world. However, it has proven difficult to quantitatively predict these mean stress effects on fatigue damage. Part of the reason lies in the fact that experimental data involving mean stresses, and in particular large mean stresses, are scarce. While mean stress correction methods, for example Ref.[*1-3*], abound to help fatigue design under conditions of small and less frequent mean stress presence, the assessment of effects of large mean stresses, such as the residual stresses resulting from manufacturing processes, requires more research.

The common approach to account for mean stress effects on fatigue life is generally based on the dependence on the mean stress value of either the parameter-life curve in crack initiation approaches or the crack growth rate in crack propagation approaches. These common approaches generally fail to explain the small cycle effect wherein small cycles below the fatigue limit become damaging when mixed with yield level loadings [*4*]. A number of recent studies based on periodic overload findings [*5-8*], however, provide a promising closure-based approach. According to these closure-based approaches the "effective" portion of the fatigue cycle, during which the fatigue crack is open, serves as a better parameter to correlate with fatigue damage than the complete range of the cycle. Further, the stress or strain level at which the crack opens was experimentally found to depend on the previously applied maximum and minimum stresses.

In order to use this closure-based method in initiation-based fatigue design, two new fatigue properties need to be determined. They are: (1) the functional dependence of opening stress/strain on previously applied maximum and minimum stresses is needed to estimate the crack opening stress level and hence the effective stress/strain range of a fatigue cycle, and (2) The effective strain versus fatigue life curve is then used to determine the amount of fatigue damage caused by the fatigue cycle. While the effective strain versus fatigue life curve may be readily obtained from periodic overload tests [*9,10*], the dependence of opening stress/strain on applied maximum and minimum stresses requires intricate and tedious fatigue crack growth measurements, see for example [*11*].

In this paper, we will demonstrate that, by utilizing the readily available cyclic stress-strain curve and the effective strain - life curve reported in literature for SAE1045 steels [*12*], the material constants, which describe the functional dependence of the opening stress on previous history, can be derived from results obtained by running several sets of constant-amplitude high mean stress fatigue tests. The fatigue life prediction capability using the closure-based effective strain as damage parameter is then compared with several widely used parameters.

The Crack Closure Concept

The closure-based fatigue damage concept, when integrated into the local strain fatigue life method, maintains that it is the effective, not the total, strain range that

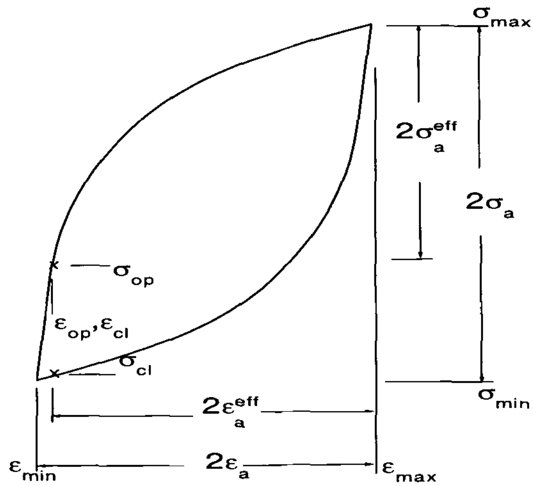

FIG. 1–*A schematic stress-strain plot of a fatigue cycle.*

determines the amount of damage caused by a fatigue cycle. As schematically shown in Figure 1, for a loading cycle between the minimum stress (strain), σ_{min} (ϵ_{min}), and the maximum stress (strain), σ_{max} (ϵ_{max}), the fatigue damage accumulates only while the fatigue crack is open, between the opening stress, σ_{op} and the maximum stress, σ_{max}. Note that the opening stress denotes the stress level at which the crack tip opens during the loading half of the cycle. For the unloading half of the cycle, it has been experimentally observed that the crack tip closes at a strain level ϵ_{cl} which is close to the opening strain level ϵ_{op} (corresponding to σ_{op}) [*13*]. Consequently, the effective range of a cycle can be more conveniently defined by the strain value $\epsilon_{max} - \epsilon_{op}$, rather than by different effective stress range $\sigma_{max} - \sigma_{op}$ for the loading half of the cycle and $\sigma_{max} - \sigma_{cl}$ for the unloading half of the cycle.

For several metals of which opening stress has been studied experimentally [*14,15*], it has been observed that the dependence of σ_{op} on an earlier applied overload assumes the following form:

$$\sigma_{op} = \alpha\sigma^{ol}_{max}\left(1 - (\overline{\sigma}^{ol}_{max})^2\right) + \beta\sigma^{ol}_{min} \tag{1}$$

where σ^{ol}_{max} and σ^{ol}_{min} are respectively the maximum and minimum stress of the overload cycle, α and β are material constants, and notation $\overline{\sigma}$ denotes a stress value normalized against σ_{norm}, $\overline{\sigma} = \sigma/\sigma_{norm}$. While the normalizing stress σ_{norm} is reported in the literature to be approximately the material's yield stress [*15*], it is treated here as an independent constant that needs to be experimentally determined.

A cycle becomes "fully open" or "fully effective" when the opening stress is lowered below the minimum cyclic stress ($\sigma_{op} \leq \sigma_{min}$). The established overload procedure is to periodically apply yield level overload to lower the opening stress of subsequent regular fatigue cycles to be below the minimum stress so that the fatigue cycle becomes fully effective in causing fatigue damage. The resulting strain-life curve then becomes the most conservative strain-life curve and is termed the (intrinsic) effective strain life curve.

The effective strain life curve has been further observed to have a general form:

$$\epsilon_a^{eff} = \epsilon_a^{int} + BN_f^C \tag{2}$$

where the intrinsic strain amplitude, ϵ_a^{int}, is the effective strain amplitude below which a fatigue crack, even when fully open, does not lead to failure, N_f is the observed fatigue life in cycles, and B, and C are fatigue constants.

Closure-Based Analysis

In this paper, we first use a closure-based method to analyze constant-amplitude fatigue test data. As a result of the analysis, special constant-amplitude fatigue tests are then designed to help derive the fatigue constants required for future general purpose application of the closure-based method.

Unlike periodic overload tests where the opening stress, after being lowered by the overload, gradually returns to a "steady state" level, during the constant maximum stress or constant minimum stress, the opening stress is constant throughout the test. That is,

$$\sigma_{op} = \alpha\sigma_{max}\left(1 - \overline{\sigma}_{max}^2\right) + \beta\sigma_{min} \tag{3}$$

The effective strain amplitude can thus be calculated as:

$$\begin{aligned} \epsilon_a^{eff} &= \epsilon\left[\frac{1}{2}(\sigma_{max} - \sigma_{min})\right] - \epsilon\left[\frac{1}{2}(\sigma_{op} - \sigma_{min})\right] \\ &= \epsilon_a - \epsilon\left[\frac{1}{2}(\sigma_{op} - \sigma_{min})\right] \end{aligned} \tag{4}$$

Here $\epsilon[\sigma]$ denotes a cyclic strain value corresponding to the cyclic stress value σ. Similarly, the cyclic stress value corresponding to a cyclic strain value ϵ is later expressed by $\sigma[\epsilon]$. It should be noted that an accurate cyclic stress-strain curve is an important fatigue property and is assumed to have been already established for the material of interest.

The above equation can be rearranged to:

$$\frac{1}{2}(\sigma_{op} - \sigma_{min}) = \sigma[\epsilon_a - \epsilon_a^{eff}]$$

or

$$\sigma_{op} = \sigma_{min} + 2\sigma[\epsilon_a - \epsilon_a^{eff}] \tag{5}$$

If the effective strain versus life curve is known, say, from the periodic overload tests, then, given an observed fatigue life N_f, the effective strain can be interpolated from the effective-strain versus life relationship and expressed as $\epsilon_a^{eff}[N_f]$. The

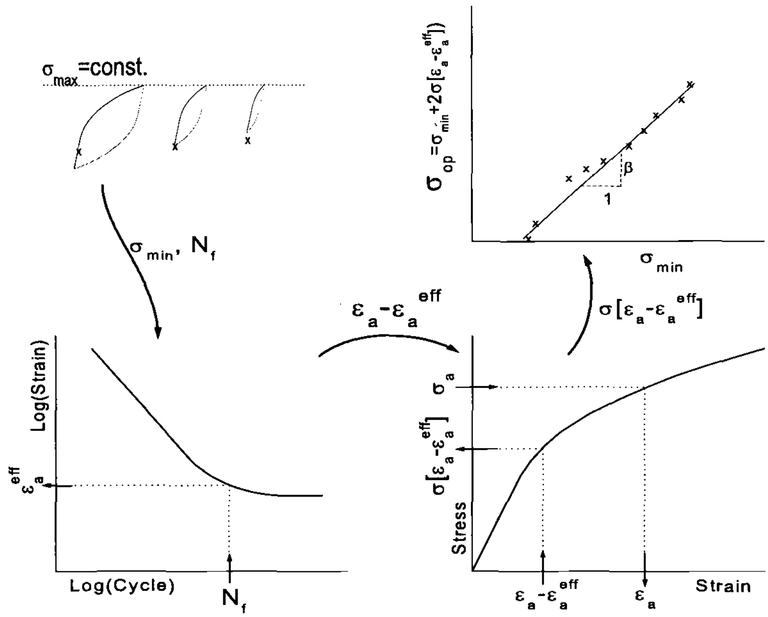

FIG. 2 *Experiment and analysis procedure to determine material constant β.*

opening stress of a constant-amplitude test therefore can be back calculated from the observed life as:

$$\sigma_{op} = \sigma_{min} + 2\ \sigma\ \left[\epsilon_a - \epsilon_a^{eff}[N_f]\right] \tag{6}$$

An integrated and analysis procedure has been proposed earlier [*16*] to utilize the above equation. The flow chart for these procedures are shown in Figures 2 and 3 for the constant maximum stress tests and the constant minimum stress tests, respectively. In part (a) of the figures, a set of constant-amplitude tests are performed with a common maximum/minimum stress level. For each test with measured fatigue life N_f, the effective strain amplitude ϵ_a^{eff} is found from the effective strain – life curve, as shown in part (b). In part (c) of the charts, the cyclic stress-strain curve is used to determine the cyclic strain amplitude ϵ_a corresponding to the applied stress amplitude, and the stress value corresponding to strain $\epsilon_a - \epsilon_a^{eff}$. Part (d) of the procedure involves plotting the opening stress, calculated from Eqn. (6), against the applied minimum stress to reveal their functional relationship.

Material and Testing Procedures

The material used for this work was SAE1045 steel in the normalized condition. Smooth cylindrical specimens, shown in Figure 4, were machined from hot rolled bar

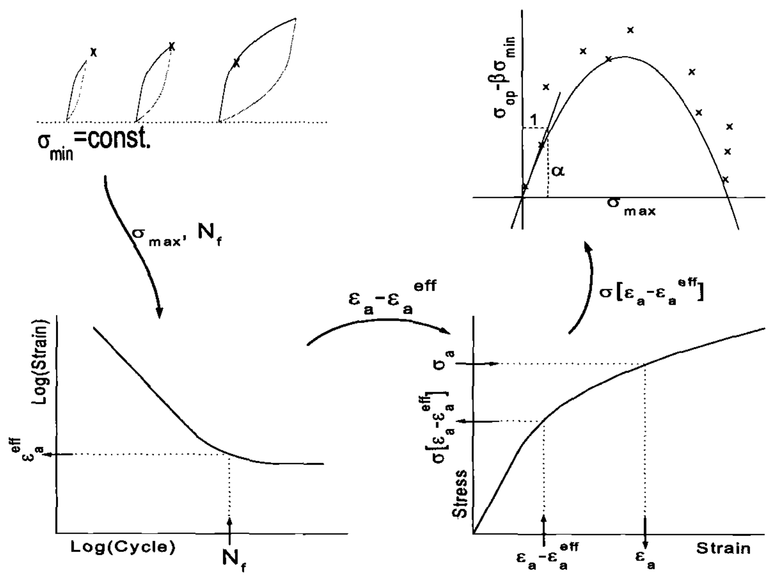

FIG. 3–*Experiment and analysis procedure to determine material constant* α.

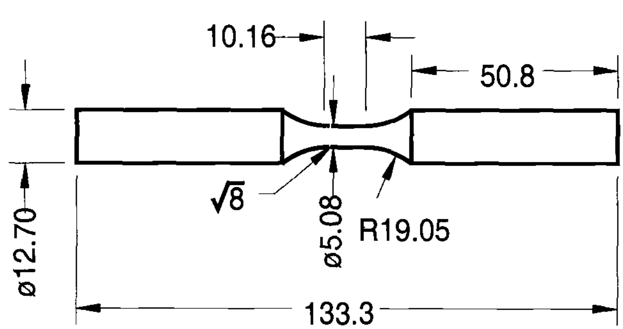

FIG. 4–*Fatigue specimen. All dimensions in mm.*

Table 1–*Normalized SAE 1045 monotonic properties.*

Hardness BHN	Upper Yield Stress MPa	Lower Yield Stress MPa	Ultimate Stress MPa	Modulus GPa	%RA
203	476	397	703	203	48.2

stock and normalized to a hardness of 203 BHN. Monotonic tensile values for this material are shown in Table 1.

Three sets of uniaxial constant-amplitude mean stress fatigue tests were conducted for this study. Each specimen in the first set was tested at a constant maximum stress value of 381 MPa, which is approximately 80% of the material's monotonic upper yield stress, while the minimum stress, being constant during any given test, was varied from -95 MPa to -285 MPa. The second set of tests shared a common constant minimum stress value of -381 MPa while the maximum stress in different tests varied from 105MPa to 333 MPa. The third set of constant-amplitude tests was conducted using a common constant minimum stress value of 0 and a maximum loading which ranged from 90% to 135% of monotonic yield. Several additional tests were run at maximum stress values at or near the upper yield stress and at varied minimum stress values to determine material response.

All tests were conducted in an ambient laboratory environment at room temperature using a 25kN MTS closed-loop servo-hydraulic testing system. The system was operated in load control using a sinusoidal waveform at frequencies of 0.5Hz to 30Hz with a PC-based programmable controller and FLEX software [*9*]. A 7.62 mm extensometer was attached to each specimen to measure strain during testing. An X-Y recorder and an in-house computer-based data collection program were used to monitor the material deformation throughout testing.

All constant maximum test specimens exhibited progressive cyclic creep. The creep behavior initiated at approximately one-half to one percent of the specimen's total number of cycles to failure and continued until specimen fracture. The extent of cyclic creep per loading cycle was heavily dependent on the magnitude of the mean stress, the higher the mean stress the greater the amount of creep per cycle. The constant minimum test specimen also exhibited cyclic creep, although the cycle number when creep starts does not show as much correlation with mean stress value as in constant maximum test set.

The onset of cyclic creep in all of the tests was observed to coincide with a physical change in the stress-strain hysteresis loop. That is, at the onset of cyclic creep, the recorded hysteresis changes from a straight elastic line to a wider loop involving plastic deformation, as shown in Figure 5.

While the aforementioned cyclic creep was continuous but slow, it was observed that cyclic creep during the $\sigma_{min} \equiv 0$ (R=0) tests develops much faster. An example of the recorded stress-strain behavior is shown in Figure 6 for a test in which the maximum stress is higher than the material's yield level. Note here that some small

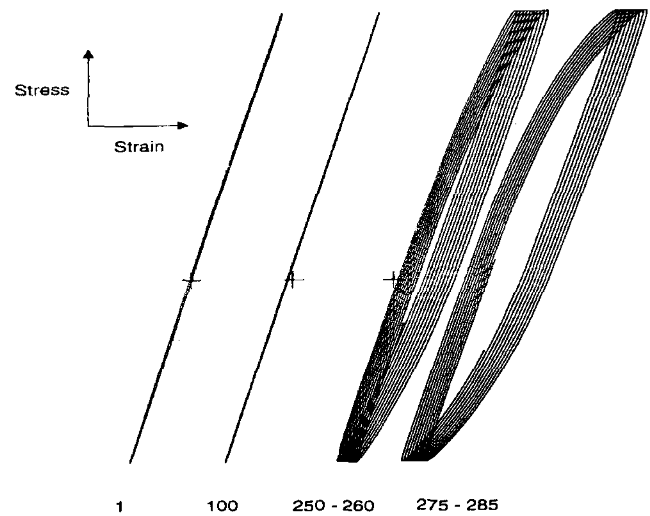

FIG. 5—*Typical cyclic creep behavior of normalized SAE1045 during constant maximum (minimum) tests.*

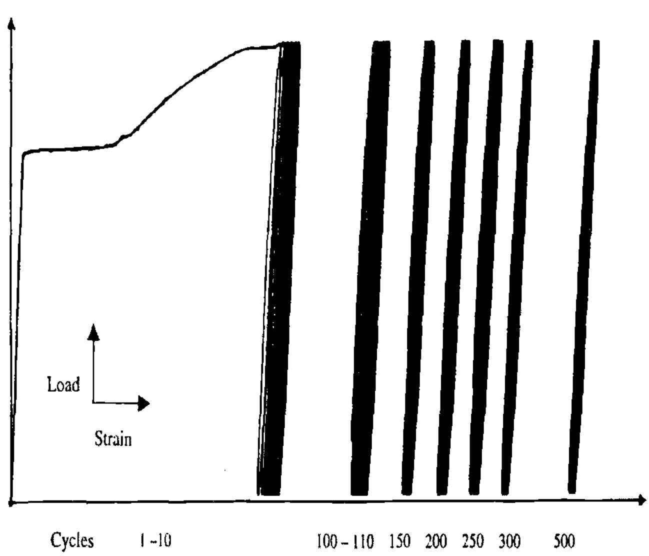

FIG. 6—*Cyclic creep behavior of normalized SAE1045 during a 0-maximum loading.*

Table 2–*The maximum stress, minimum stress and observed life of stress-controlled tests.*

Constant Maximum Tests			Constant Minimum Tests		
σ_{max} (MPa)	σ_{min} (MPa)	N_f (Cycles)	σ_{max} (MPa)	σ_{min} (MPa)	N_f (Cycles)
381	-286	22057	643	0	851
381	-262	26057	619	0	2318
381	-238	42917	619	0	3153
381	-190	83703	595	0	11548
381	-167	123046	571	0	39191
381	-143	180374	547	0	78384
381	-131	278140	524	0	149944
381	-119	589126	524	0	154707
381	-114	559192	469	0	639435
381	-107	4752000+	476	0	1531381
381	-95	4800000+	476	0	2866791
			452	0	12500000+
476	-190	16698			
476	-95	71584	333	-381	43591
476	-24	268686	286	-381	79583
476	0	1531381	238	-381	158328
476	0	2866791	214	-381	1773960
			190	-381	1685400
			179	-381	12500000+
428	-48	320482	143	-381	15741000+
428	0	10225000+	105	-381	9255600+

amount of static creep was introduced in the first half cycle by the momentary pause of the PC controller after the yield stress is reached.

Test and Analysis Results

The maximum stress, minimum stress, and the observed fatigue life of all tests conducted are listed in Table 2. The fatigue properties that are required to perform the $\epsilon \rightleftharpoons \sigma$ and $\epsilon_a^{eff} \rightleftharpoons N_f$ conversions; namely, the cyclic stress-strain relationship and the effective strain-life relationship, are listed in digitized form in Tables 3 and 4.

The constant maximum stress test with $\sigma_{max} \equiv +381$ MPa is analyzed first to determine the simpler functional dependence of σ_{op} on σ_{min}. By plotting calculated σ_{op} against experimental σ_{min} in Figure 7, a linear relationship with slope 0.25, shown by the dashed line, is fitted to the data. That is, $\beta = 0.25$ is chosen here.

Note here that, although a higher value for β can be easily fitted to the data shown in Figure 7, the lower value is chosen here mainly because it was found that a higher β value would make subsequent fitting of constant α difficult. Data recently published in [*17*] also indicate that β for metals of various hardness seems to vary within the small range between 0.15 and 0.25.

Table 3–*Cyclic σ–ϵ relationship for $\sigma \rightleftharpoons \epsilon$ mapping.*

ϵ	σ(MPa)	ϵ	σ(MPa)	ϵ	σ(MPa)	ϵ	σ(MPa)
0.	0.0	.003	332.7	.0075	463.0	.0135	543.2
.00083	172.0	.0035	352.9	.0085	481.1	.0145	552.4
.001	198.0	.004	370.0	.0095	496.8	.0155	561.2
.00125	227.0	.0045	386.1	.01	503.9	.0165	569.6
.0015	249.6	.005	401.4	.011	516.8	.0175	577.6
.002	283.3	.0055	415.9	.012	528.3	.0185	585.2
.0025	310.0	.0065	441.4	.0125	533.5	.02	595.7

Table 4–*Effective strain-life relationship for $\epsilon \rightleftharpoons N_f$ mapping.*

$\log(N_f)$	$\log(\epsilon_a^{eff})$	$\log(N_f)$	$\log(\epsilon_a^{eff})$	$\log(N_f)$	$\log(\epsilon_a^{eff})$
2.31	−1.700	4.96	−2.828	6.05	−3.045
3.2	−2.044	5.08	−2.862	6.22	−3.063
4.46	−2.659	5.21	−2.896	6.4	−3.079
4.54	−2.689	5.36	−2.931	6.55	−3.090
4.63	−2.721	5.54	−2.968	7.45	−3.128
4.76	−2.766	5.74	−3.003		
4.85	−2.795	5.9	−3.026		

The reported dependence of σ_{op} on σ_{max}, Eqn. (1), is non-linear and hence more difficult to fit. Here, the β-dependence of σ_{op} is first extracted so that results from various constant minimum stress tests can be combined to help determine the σ_{op} – σ_{max} dependence for a wider range of σ_{max}. Therefore, as shown in Figure 8, the calculated value $\sigma_{op} - \beta\sigma_{min}$ (instead of σ_{op}) is plotted against σ_{max} to determine the influence of σ_{max} on opening stress. The α-value is selected by noticing the following features of the non-linear term, $\alpha\sigma_{max}(1 - (\sigma_{max}/\sigma_{norm})^2)$: The function (a) rises from 0 at $\sigma_{max} = 0$ with a slope α; (b) reaches its peak value at $\sigma_{max} = \sigma_{norm}/\sqrt{3}$; and (c) changes from positive to negative at $\sigma_{max} = \sigma_{norm}$. We first determined that σ_{norm} = 580 MPa, which satisfies the above features (b) and (c). A value of 0.8 is then chosen for α so that the fitted function, as shown by the solid curve, forms a lower bound of the calculated data. As described in the previous section, most of the constant-amplitude tests involving high mean stresses show continuous cyclic creep throughout the test. This behavior is likely to have caused damage which is not considered by the opening stress model used here. The lower bound fitting is therefore used to ensure a safe or conservative life prediction from the closure-based method.

The closure-based method is now ready to be used to predict fatigue life by using the fitted material constants α = 0.8 and β = 0.25 as follows. For each constant-

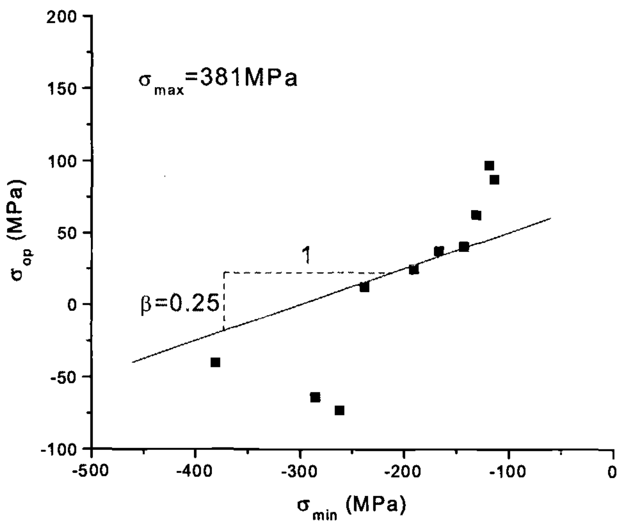

FIG. 7–*The σ_{op} versus σ_{min} plot to determine β.*

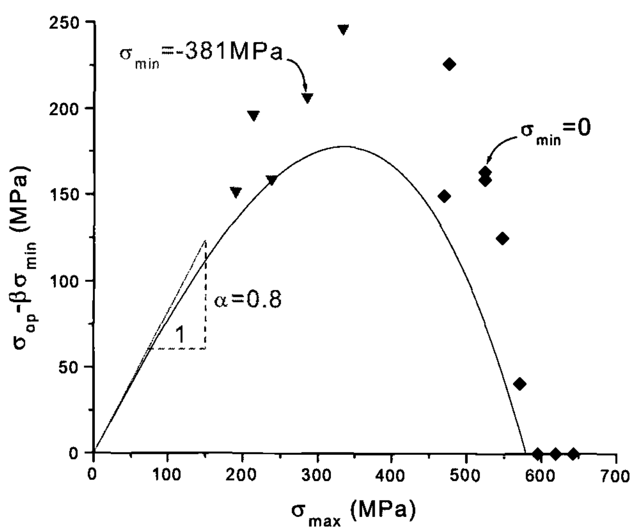

FIG. 8–*The $\sigma_{op} - \beta\sigma_{min}$ versus σ_{min} plot to determine α.*

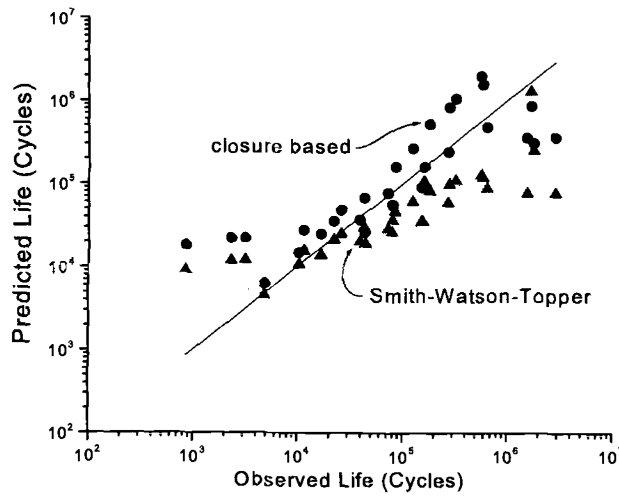

FIG. 9—*Comparison of life prediction capabilities.*

amplitude test where the stress range varies from σ_{min} to σ_{max},

$$\begin{aligned}
\epsilon_a &= \epsilon_{\sigma\to\epsilon}\left[\frac{1}{2}(\sigma_{max}-\sigma_{min})\right] \\
\sigma_{op} &= \alpha\sigma_{max}\left(1-\left(\frac{\sigma_{max}}{\sigma_{norm}}\right)^2\right)+\beta\sigma_{min}
\end{aligned}$$

$$\begin{aligned}
N_f &= N_{\epsilon\to N_f}[\epsilon_a^{eff}] \\
&= N_{\epsilon\to N_f}\left[\epsilon_a-\epsilon_{\sigma\to\epsilon}\left[\frac{1}{2}(\sigma_{op}-\sigma_{min})\right]\right]
\end{aligned}$$

where $\sigma \to \epsilon$ indicates a stress to strain mapping via Table 3, and $\epsilon \to N_f$ indicates a strain to life mapping via Table 3.

The fatigue life prediction for all the tests except runouts are compared with observed life in Figure 9. The solid line here (and also in Figure 10) indicates the ideal case where the predicted fatigue life matches the observed life. The filled circles denote results from closure-based method. For comparison purposes, fatigue life prediction using the Smith-Watson-Topper damage parameter ($\sigma_{max}\epsilon_a$, [3]) was also performed and its results are denoted in Figure 9 by triangular symbols. Note that the fatigue lives of the three largest amplitude $\sigma_{min} \equiv 0$ tests are much shorter than can be predicted. The opening stress calculation of these three tests, shown in Figure 8 by the rightmost points on the x-axis, indicates that the cycles are fully effective, with

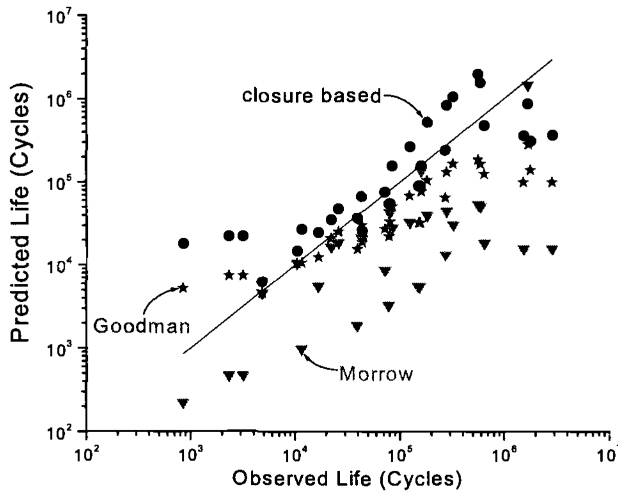

FIG. 10–*Comparison of life prediction capabilities.*

$\sigma_{op} = \sigma_{min} = 0$. This therefore further indicates that additional damage, caused by the substantial amount of cyclic creep and not accounted for by the closure method, may be involved. For all other tests, the Smith-Watson-Topper parameter gives more conservative life predictions than the closure-based method. The difference between the two predictions increases at larger lives. Similar results comparing the current closure-based method with Morrow's [*2*] and Goodman's [*18*] mean stress correction method are shown separately in Figure 10. (Note that σ_{ult} = 703 MPa and σ'_f = 1370 MPa are used for the Goodman and Morrow method, respectively.) It is interesting to note that the Goodman method is conservative enough to account for the three short-lived tests.

A more traditional way to show mean stress effects on fatigue is via its influence on the strain-life relationship. It is this influence observed through constant mean stress tests that commonly used methods, such as Goodman's, are intended to model. Results from the current constant maximum stress and constant minimum stress tests are now presented in strain-life plots.

Summarized in Figure 11 are strain amplitude versus observed life data from all tests. The two sets of tests, $\sigma_{min} \equiv 0$ and $\sigma_{max} \equiv 476$ MPa, for which the observed strain-life curve behavior is most different from the zero-mean (R=-1) constant-amplitude results, are analyzed to compare how well different methods account for mean stress effects. Another popular damage parameter, the Brown and Miller parameter ($\gamma_a + K\epsilon_a$, with $K = 1$, [*19*]), is included here to broaden the number of comparison models. Presented in Figure 12 are comparisons amongst experimental

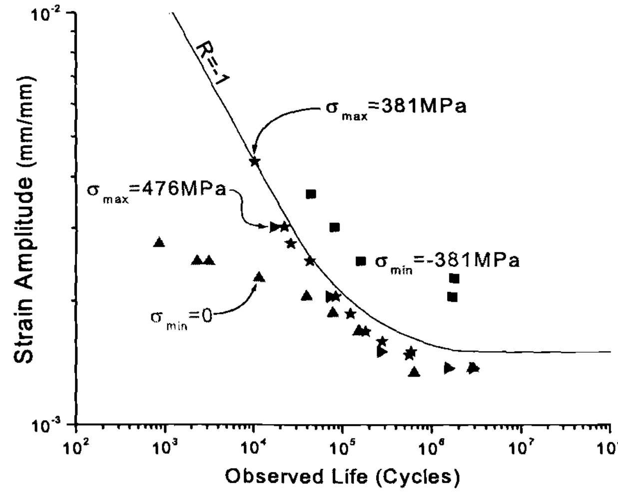

FIG. 11—*Effects of mean stress on the strain-life relationship.*

results, the Goodman method, the Brown and Miller parameter, and the current closure-based method. While all methods seem adequate for predicting strain-life behavior for the test set with $\sigma_{min} \cong -381$ MPa, the $\sigma_{min} \cong 0$ (R=0) test, which has the highest mean stress present among the different test sets, presents a challenge to most prediction methods.

The closure-based method is seen to be superior in its life prediction capabilities. This is not surprising since the material constants used in the model are derived from the same test data. The failure of all common methods, particularly in the long life region where the mean stress is maintained high in the current study, does indicate that past models which were based on the dependence of fatigue curve on mean stress values are generally inadequate in modeling mean stress effects on fatigue.

Conclusions

In this paper, we have tried to show that the material properties that are required for the closure-based fatigue method can be readily established via several sets of stress controlled constant-amplitude fatigue tests with either the maximum stress or the minimum stress maintained constant. These constant-amplitude smooth bar tests are far simpler to run than the traditional crack growth studies previously used to determine σ_{op} behavior. Furthermore, the test data become much easier to analyze than the periodic overload tests because of the constancy of the loading cycles, and hence the opening stress throughout cycling history, according to Eqn. (3). The

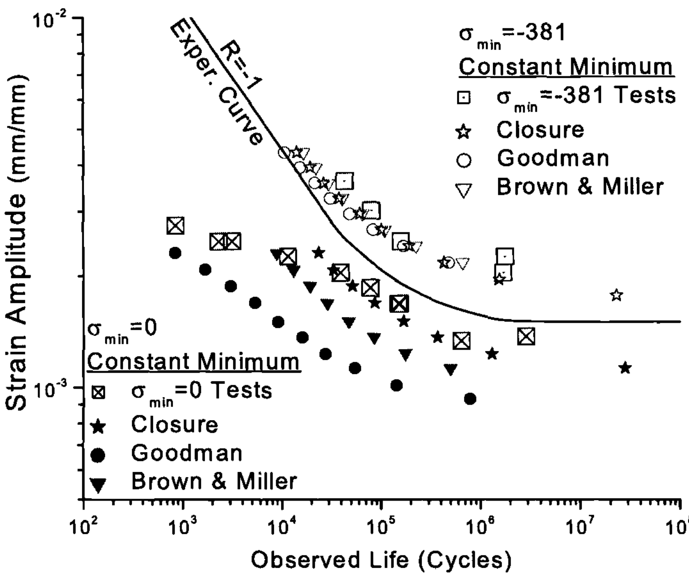

FIG. 12—*Effects of mean stress on the strain-life relationship.*

closure-based method has been shown here to be more accurate than four other widely used methods in predicting mean stress effects on fatigue damage.

Although not elaborated in this paper, the cyclic stress-strain curve and the effective strain versus fatigue life curve are treated here as well-defined material properties. The scatter regularly seen in fatigue test data can make proper fitting of material constants difficult. Results presented with statistical confidence bands and a sensitivity study of a given fatigue method to its material constants are recommended.

References

[*1*] Walker, K. "The effect of stress ratio during crack propagation and fatigue for 2024-T3 and 7075-T6 aluminum," *Effects of Environment and Complex Load History for Fatigue Life, ASTM STP 462*, 1970, pp. 1-14.

[*2*] Morrow, J., "Fatigue Properties of Metals," *Fatigue Design Handbook, SAE AE-6*, SAE Warrendale, PA, 1968, pp. 21-30.

[*3*] Smith, K.N., Watson, P., and Topper, T.H., "A Stress Strain Function for the Fatigue of Metals," *Journal of Materials*, Vol. 5, No. 4, 1970, 767-778.

[*4*] Conle, F.A., and Topper, T.H., "Overstrain Effects During Variable Amplitude Service History Testing," *International Journal of Fatigue*, Vol. 2, No. 3, 1980, pp. 130-136.

[5] Elber, W., "The Significance of Fatigue Crack Closure," *Damage Tolerance in Aircraft Structures, ASTM STP 486*, 1971, pp. 230-242.

[6] Schijve, J., "Fatigue Crack Closure: Observations and Technical Significance," *Mechanics of Fatigue Crack Closure ASTM STP 982*, 1988, pp. 5-34.

[7] Topper, T.H., DuQuesnay, D.L., and Pompetzki, M.A., "Crack Closure, Damage And Short Crack Growth under Variable Amplitude Loading," *Theoretical Concepts and Numerical Analysis of Fatigue*, eds. A.F. Blom and C.J. Beevers, EMAS Warley, UK, 1993, pp. 201-236.

[8] DuQuesnay, D.L., Topper, T.H., Yu, M.T., and Pompetzki, M.A., "The Effect of Compression and Compressive Overloads on the Fatigue Behavior of a 2024-T351 Aluminum Alloy and a SAE1045 Steel," *Low Cycle Fatigue, ASTM STP 942*, 1988, pp. 173-183.

[9] DuQuesnay, D.L., "Fatigue Damage Accumulation in Metals Subjected to High Mean Stress and Overload Cycles," Ph.D. Thesis, University of Waterloo, Waterloo, Ontario, Canada, 1991.

[10] Bonnen, J.J.F., "Multiaxial Fatigue Response of Normalized 1045 Steel Subjected to Periodic Overloads: Experiments and Analysis," Ph.D. Thesis, University of Waterloo, Waterloo, Ontario, Canada, 1998.

[11] Dabayeh, A.A. and Topper, T.H., "Changes in Crack-Opening Stress after Underloads And Overloads in 2024-T351 Aluminium Alloy," *International Journal of Fatigue* Vol 17, 1995, pp.261-269.

[12] Bonnen, J., and Topper, T.H., "The Effect of Periodic Overloads on Biaxial Fatigue of Normalized SAE 1045 Steel," *Multiaxial Fatigue and Deformation: Testing and Prediction*, ASTM STP 1387, 2000, pp.213-231.

[13] Vormwald, M. and Seeger, T., "The Consequences of Short Crack Closure on Fatigue Crack Growth under Variable Amplitude Loading," *Fatigue and Fracture of Engineering Materials and Structures*, Vol. 14, No. 2/3, 1991, pp. 205-225.

[14] MacDougall, C., and Topper, T.H., "The Influence of Variable Amplitude Loading on Crack Closure and Notch Fatigue Behaviour," *International Journal of Fatigue*, Vol. 19, 1997, pp. 389-400.

[15] DuQuesnay, D.L., Topper, T.H., Yu, M.T. and Pompetzki, M.A., "The Effective Stress Range as A Mean Stress Parameter," *International Journal of Fatigue*, Vol. 14, No. 1, 1992, pp.45-50..

[16] Chu and Chernenkoff, "Crack Closure-Based Analysis of Fatigue Tests with Mean Stresses," *International Journal of Fatigue*, Vol. 23, 2001, pp. S187-S194.

[17] Khalil, M, Lam, T., and Topper, T.H., "Estimation of Crack Opening Stresses from Strain-Life Fatigue Data," *Proceedings of Fatigue 2000, Fatigue and Durability Assessment of Materials, Components and Structures*, M.R. Bache et al., Eds., Chameleon Press, Ltd. (London) 2000, pp. 449-456.

[*18*] Goodman, J., *Mechanics Applied to Engineering*, Longmans, Green & Company (London), 1899.

[*19*] Brown, M. and Miller, K., "A Theory for Fatigue Failure under Multiaxial Stress-Strain Conditions," *Proceedings of the Institute of Mechanical Engineering*, 187(65), 1973, pp. 745-755.

Matthew T. Kokaly,[1] Albert S. Kobayashi,[2] and Kenneth W. White[3]

Fatigue Crack Growth Mechanisms in Alumina at High Temperature

---

Reference: M. T. Kokaly, A. S. Kobayashi, and K. W. White, **"Fatigue Crack Growth Mechanisms in Alumina at High Temperature,"** *Fatigue and Fracture Mechanics, 33rd Volume, ASTM STP 1417*, W. G. Reuter and R. S. Piascik. Eds., ASTM International, West Conshohocken, PA, 2002.

Abstract: The wake fracture process zone (FPZ) of an alumina WL-DCB specimen subjected to cyclic loading at room temperature to 800°C was analyzed by a hybrid experimental-numerical procedure involving phase-shifting moiré interferometry and finite element analysis. A residual crack opening profile was found upon unloading and remained during subsequent cyclic loading. This anomaly is attributed to the butting of fully and partially pulled-out grains and provides a mechanistic explanation for the common notion that monolithic ceramics do not fatigue.

Keywords: fatigue, alumina, fracture process zone

Introduction

Crack bridging in the wake fracture process zone (FPZ) during monotonic loading of alumina has been studied extensively in the past. Several theoretical studies of the crack closure stress (CCS), or stress across the crack face, during monotonic loading assumed an a priori "tail dominated" distribution [*1*]. Experimental studies to estimate the CCS have included re-notching of the cracked specimen [*2*], novel procedures for experimentally measuring the stress across a crack face [*3, 4*], and a direct measurement of the stress in individual grain bridges [*5*]. The bridging stress has also been obtained by an inverse analysis using a measured displacement field to drive a finite element (FE) model of an alumina fracture specimen [*6, 7*]. Most recently, the bridging stress determined by Hay et al. [*5*] was replicated using a micro-mechanical model of the grain pullout forces in the FPZ [*8*].

The above studies and others not included showed that the bulk of the fracture energy of brittle materials, such as ceramics and concrete, is dissipated by the work done by the crack bridging forces in the wake FPZ, which can extend several hundred of grain diameters behind the crack tip. Fracture energy is dissipated through frictional resistance

---

[1] Research Engineer, Fatigue Technology Inc., 401 Andover Park East, Seattle, WA 98188.

[2] Professor Emeritus, University of Washington, Department of Mechanical Engineering, Seattle, WA, 98195-2600.

[3] Professor, University of Houston, Department of Mechanical Engineering, Houston. TX, 77204-4792.

to pullout and rotation of wedged grains, breaking of elastic bridges [*9*] and crushing and intra-granular fracture of the bridging grains. The resultant fracture toughness of ceramics is not an intrinsic material property but is dependent on the microstructure as predicted by a two-dimensional numerical modeling of the FPZ [*10*]. The simple grain pullout models of Vekinis et al. [*9*] and Kokaly et al. [*8*] showed that the bulk of the CCS was due to frictional forces between grain bridges induced by the anisotropic thermal contraction during the cool-down process. Both studies postulated a grain pull-out model which was then verified through an inverse analysis by matching the computed and measured crack mouth opening displacement (CMOD) and crack opening profile, respectively. However, a more detailed documentation of these measurements are necessary for assessing the relative contributions of other sources of energy dissipation, such as the breaking of elastic bridges and the crushing and intra-granular fracture of bridged grains. A quantification of the micro-mechanics involved in grain bridging in the FPZ could in theory, lead to a fabrication process in which the grain morphology is optimized for maximum toughness of a given ceramic.

The objective of this paper is to explore the behavior of the grain bridges in the wake FPZ under cyclic tension-tension loading of WL-DCB alumina specimens at room through elevated temperature. Both experimental data on the variation of the crack opening profile and CCS data obtained from a hybrid experimental-numerical analysis will be presented.

Hybrid Analysis

A hybrid experimental-numerical procedure was used to derive the crack closing stress (CCS) versus crack opening displacement (COD) relation of a high density alumina, wedge-loaded double cantilever beam (WL-DCB) fracture specimen (Figure 1).

Experimental Procedure

WL-DCB specimens were machined from AD998 alumina of an average grain size of 15 μm. The 33% side grooving (Figure 1) was necessary to channel the stably growing crack, which would otherwise curve away from its intended straight crack path. A special specimen grating [*11*] developed for high temperature testing was used in both room temperature and elevated temperature testing. In essence, the procedure consisted of fabricating a zero-thickness grating directly on to the highly polished surface of the WL-DCB specimen.

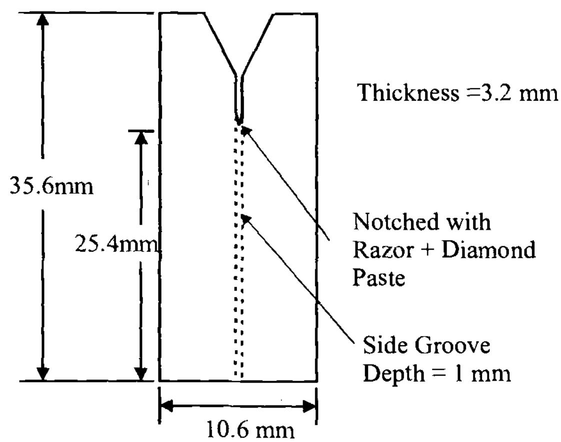

Figure 1 – *WL-DCB specimen.*

The specimen with a grating of 1200 lines/mm was then placed in a two-beam, phase-shifting moiré interferometer with the incident light provided by a HeCd laser. Moiré theory indicates that this optical setup effectively doubles the frequency of the specimen grating to 2400 line/mm while also generating a reference grating of 2400 lines/mm in the space in front of the specimen grating. The CCD camera was focused on the moiré pattern created by the interference of these two gratings. The same optical setup (Figure 2) was used at all temperatures with the exception of the furnace, which was not included in some of the room temperature tests. In this study, only the u-displacement, which is perpendicular to the crack, was recorded.

Phase shifting was used at all temperatures in order to increase the sensitivity and decrease the time and error inherent in fringe interpretation of a traditional moiré analysis. The piezoelectric transducer (PZT) translated one of the oblique beams and effectively shifted the spatial location of the moiré reference grating. Four sequential displacements of the PZT generated phase shifts of 90°, 180°, 270° and 360°. The shifted moiré fringe pattern was recorded as a wrapped phase map. Two-dimensional, spatial unwrapping software was used to generate a map of each pixel to a u-displacement, theoretically ten to one hundred times more accurate than that of digitized fringes. The estimated accuracy of the entire phase shifting moiré interferometry procedure is $\lambda/20$ or 0.03 μm in this case. Details of the phase shifting technique can be found in [*11*].

At elevated temperature, the specimen grating frequency was affected by the uniform thermal expansion of the specimen. The temperature-generated isotropic displacement field was subtracted from the recorded apparent displacements. The thermal coefficient of expansion (CTE) of the specimen was determined from the recorded moiré fringe pattern of the unloaded specimen at elevated temperature. The resultant CTE was experimentally determined to be 7.57×10^{-6} m/°C compared with the manufacturers values of 7.6×10^{-6} m/°C at 800°C.

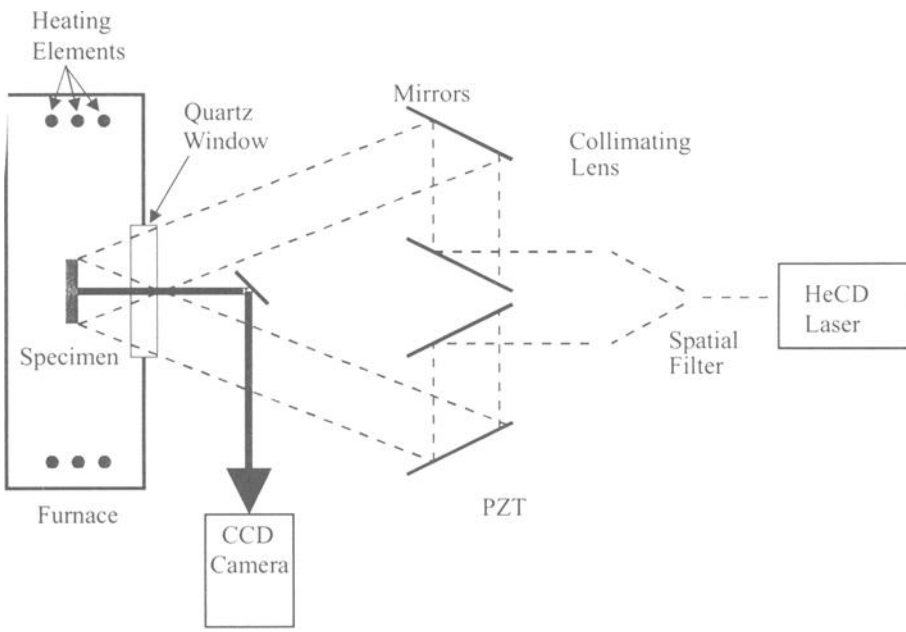

Figure 2 – *High temperature moiré interferometry setup.*

The fracture specimen was loaded in a rigid fixture with cyclic displacement imposed by a PZT controlled by a feedback loop with the load cell. Cyclic loading was limited to 1 Hz. The cyclic loading was stopped for several minutes to capture the moiré fringes at the maximum, minimum as well as intermediate loads at discrete points.

Numerical Procedure

The measured applied load/applied displacement was used to drive a two-dimensional, linearly elastic, finite element model of the WL-DCB specimen. For viewing purposes, a coarser version of the mesh is given in Figure 3. The measured vertical load and the horizontal displacement from the recorded moiré fringe pattern provided the boundary conditions at the loading pin/specimen contact point. The crack tip location was determined to within 0.1 mm from the captured moiré images. Unlike previous studies [*6*, *7*], a smoothed (measured by the phase-shifting moiré analysis) crack opening displacement (COD) was directly prescribed along the FPZ of this boundary value problem. The modulus of elasticity and the Poisson ratio were assumed to be 352 GPa and 0.2, respectively at room temperature and 328 GPa and 0.2, respectively at 800°C.

Results

A total of 5 specimens were tested. The clarity of the moiré fringe pattern of the WL-DCB alumina specimen at 800°C and maximum load (Figure 4) is an indication of the grating efficiency, particularly at elevated temperature.

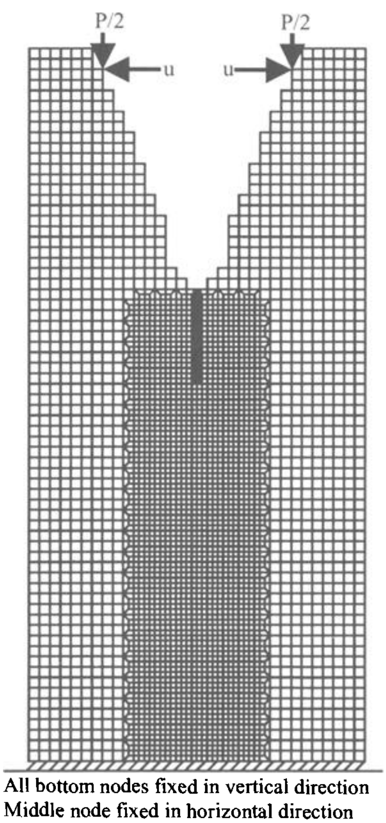

Figure 3. – *Finite element representation.*

Figure 4. - *Moiré fringe pattern, 800°C.*

The large COD at the minimum load of the first cycle of unloading (Figure 5) indicates that frictional bridging grains, which were fully or partially pulled out during the loading process, did not slip back into their original locations upon unloading. This grain butting effect was most prominent where grains just lost contact at the maximum load. This resulted in a larger COD in the crack tip region during the initial stages of unloading (Figure 5) via a cantilever effect. Eventually, as these butted grains were forcefully realigned to their original orientation the cantilever effect diminished and the COD near the crack tip decreased.

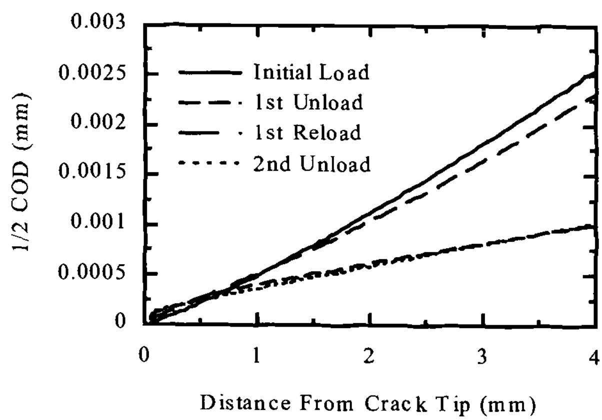

Figure 5 – *Crack profile at maximum load, room temperature.*

Figure 6 shows the CCS versus COD relations at maximum load for the first and 50th cycles obtained via the hybrid analysis. Despite the increasing residual COD at successive minimum loads, the CCS at the maximum load along the FPZ remained relatively unchanged after 50 cycles.

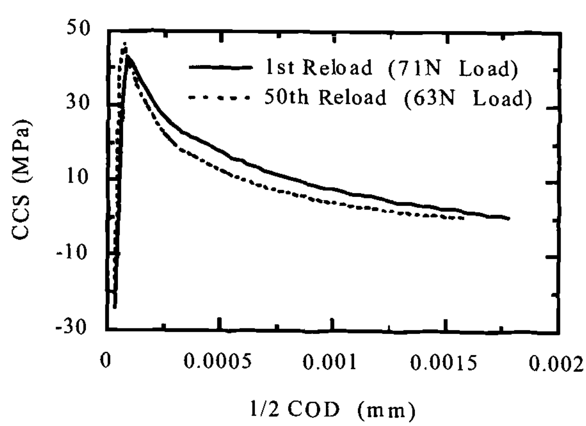

Figure 6 - *CCS versus COD relation, room temperature.*

The residual CCS near zero load (listed as unload on the plot) shows compressive stress throughout much of the crack with a peak tensile stress at the crack tip during the first unload at room temperature (Figure 7). This CCS distribution supports the previous conjecture (Figure 5) that the pulled grains did not return to their original location and were butting up against each other. These butting grains may have fractured (Figure 8) during subsequent cyclic loading.

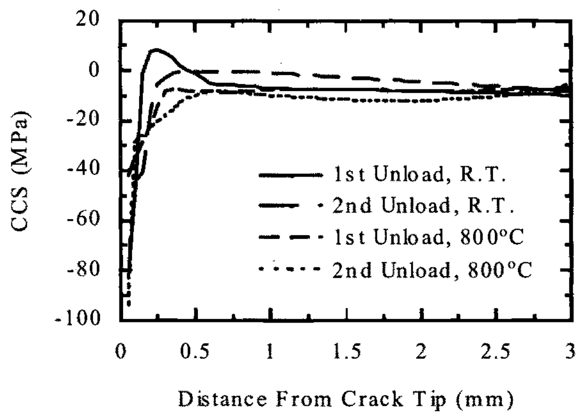

Figure 7 – *CCS distributions in FPZ at unloading.*

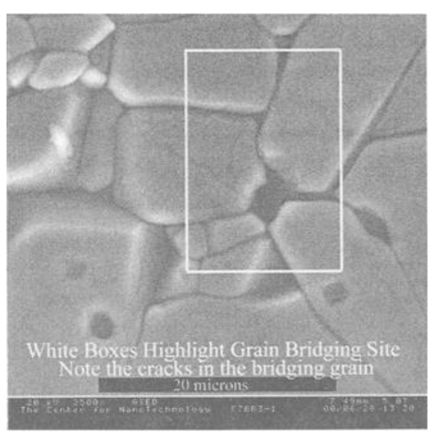

Figure 8 – *Fractured bridging grain.*

The CCS distributions along the FPZ at maximum load (Figure 9) shows that the crack bridging effect diminishes upon reloading. The decrease in CCS is attributed to fracturing of butting grains and intra-granular fracture and fragmentation of the bridged grains during the unloading-reloading process. The CCS at the first maximum load is also lower at 800°C than at room temperature. This decrease in the CCS is due to grain boundary softening at elevated temperature.

Despite the differences between CCS distributions at room temperature and 800°C, the normalized CCS distributions for these two temperatures (Figure 10) are in remarkable agreement.

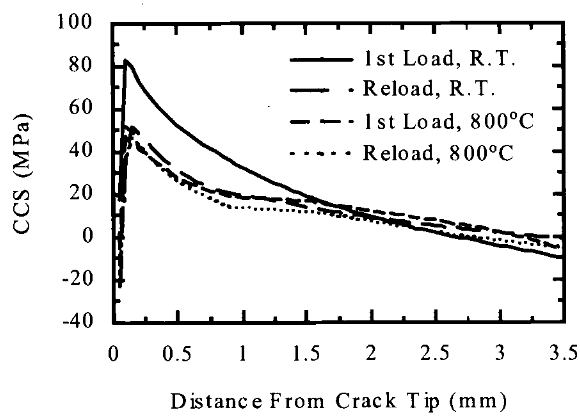

Figure 9 – *CCS distributions in FPZ at maximum load.*

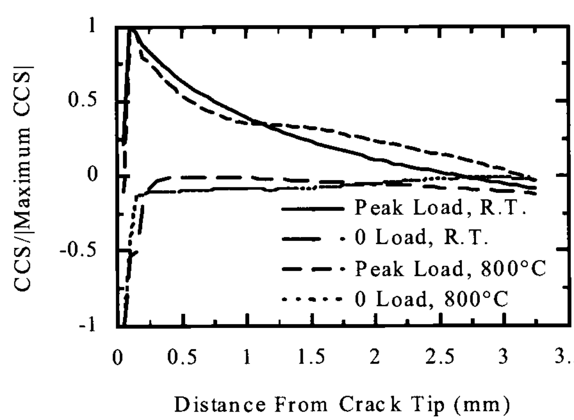

Figure 10 – *Normalized CCS distributions in FPZ.*

Crack Bridging Model

FE Model

Figures 5 - 10 provided the basis for a micromechanical model of crack bridging. The model was cycled between 90% and 5% of the fracture load. The disposable parameters in the model were the relative contributions to the grain bridging force of the elastic grain bridges, the cantilevered grains, and frictional bridges [9]. By necessity, the model was a highly idealized assembly of quadrilateral elements. The elastic grain bridges at the FPZ were modeled by constraining the coincident nodes on the opposite side of the crack surface with the same displacement. Angled cantilevered grains were modeled by adjusting the nodal points of the initial mesh to provide an angled sliding surface. Frictional bridges were modeled, as in previous cases [7, 8], with the frictional properties defined at the crack interface. Examples of implementation of the different grain bridges in the model are shown in Figure 11. Lacking any prior analysis of the behavior of the grain bridges during loading, a time consuming trial-and-error, iterative inverse analysis was used to match the meso-responses of the micro-mechanical model and the experimental data, primarily the applied load, the COD profile and the CCS vs. COD relation.

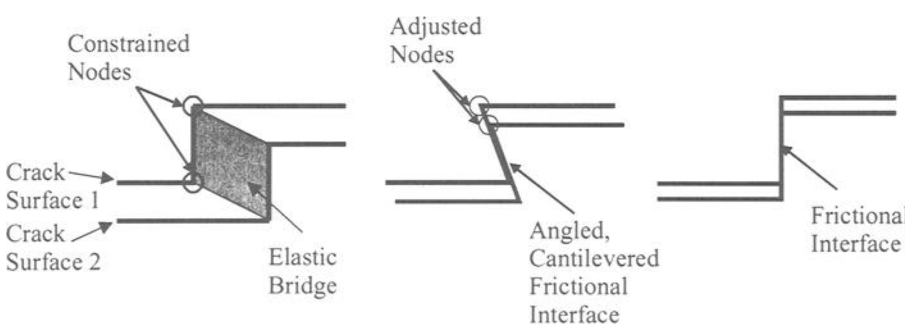

Figure 11 - *Modeling of three types of grain bridges.*

The FE model used in this study accounted for the random grain size distribution and the random orientation of the axes of thermal expansion. Unlike previous studies [8], the current model shown in Figure 12 is a two-dimensional idealization of the complex three-dimensional distribution of grains through the thickness of the WL-DCB specimen of Figure 1. Since the model was a slice through the thickness of the WL-DCB specimen, the width of the FE model was equal to the thickness of the WL-DCB specimen minus the side groove of 2.4 mm. The thickness of the model was equated to the average grain size of 15 μm. A Matlab preprocessor randomly distributed the principal thermal expansion directions from 0 to 165° in 15° increments to ensure a smooth distribution of residual stress while minimizing the complexity of the model. The compressive residual stress, which caused frictional resistance to the grain pullout, was generated by the mismatch in grain shrinkage during the cool down from the processing temperature. The complex distributions of irregular grains of various sizes were replaced by trapezoidal and rectangular grains of varying sizes in the region adjacent to the fracture surface as shown in Figure 12. In order to conserve computing time, three layers of increasingly larger elements with randomly orientated anisotropic thermal coefficients of expansion, were used outside of the fracture region. Grain sizes under 3 μm were considered too small for effective grain bridging in the WL-DCB specimen.

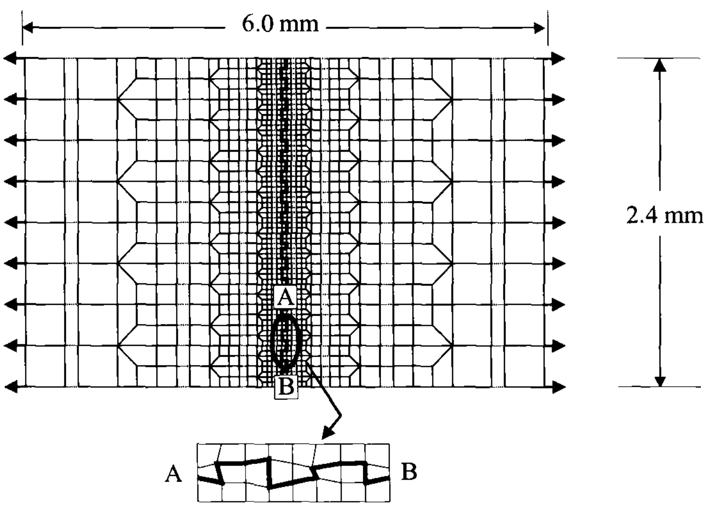

Figure 12 - *FE model of the fracture surface.*

The grain size distribution was incorporated into the model by manipulating the coefficients of thermal expansion. The coefficients were scaled by the ratio of the assigned grain size to the average grain size of 15 μm. This allowed the model to maintain a reasonable residual strain and hence a reasonable compressive stress between grains due to different grain sizes while using a simple mesh. Because of this simplified mesh configuration, the elements pertaining to smaller grains than the average were in essence a cluster of several real grains. Similarly, finite elements pertaining to grains larger than the average grain were in essence fractions of the real grains. Unfortunately, as the size of the grains increased, the strain in the element increased to a point that the strain energy in the grain became too large for the ABAQUS FE code to handle. As a result, only grains as large as 20 μm could be modeled. Fortunately, micrographs of the crack showed that grains directly along the crack were typically less than 20 μm in size. Additionally, small grains tended to cluster near other small grains, supporting the clustering of smaller grains into a larger finite element.

A distribution of the frictional bridging length was obtained from scanning electron micrographs. Bridging lengths smaller than 1 μm and larger than 4 μm were not included due to constraints in element aspect ratio and included angles. The bridging lengths were rounded to the nearest 0.5 μm to minimize the complexity of the model. An iterative inverse process was used to determine the number of elastic and angled cantilever bridges by matching the peak stress and COD in the CCS vs. COD relation. The elastic bridges fractured early in the fracture process (near the crack tip) resulting in the sharp initial drop in CCS followed by failure of the angled cantilever grains. At this point, frictional bridges were the sole contributor to the CCS.

The gradual decrease in the experimental CCS vs. COD relation after this point was due to the pullout of a continuum of frictional grain bridging lengths. The use of discrete bridging lengths in the numerical model resulted in a decreasing "staircase" form of the CCS vs. COD relationship with large drops in the CCS as a given bridging length lost contact. To compensate for this, the frictional coefficient of the bridges was decreased between periods of grain pullout. This was done to simulate a gradual drop in bridging force of a continuous pullout associated with a smooth distribution of grain bridging lengths (as in the "real" material). Following the pullout of a discrete frictional bridge length, the coefficient of friction was increased back to the nominal value.

Material Properties

The linear coefficients of thermal expansion in the two principle directions were assumed to be 8.62×10^{-6} mm/°C in the (0001) plane and 9.38×10^{-6} mm/°C in the [0001] direction. Because of the existence of a symmetry plane, 1/3 of the grains were assigned an isotropic thermal expansion equal to the expansion in the (0001) plane. An isotropic modulus of elasticity of 350 GPa and a Poisson ratio of 0.23 were used. The elastic isotropy assumption was justified on the basis of [13], which showed, by a numerical experiment, that the elastic anisotropy of the alumina grains had negligible effect on the residual thermal stresses, which were generated by thermal anisotropy. In the absence of any micro-mechanical data, the friction coefficient for estimating the resistance to the subsequent intergranular sliding was assumed to be 0.7. The Coulomb friction coefficient was an educated average of the bulk friction coefficients given by Jahanmir and Dong [14] and was adjusted to account for the rougher surfaces due to the presence of the fractured intergranular phase.

Results

Initially, the FE model was subjected to a cool down process from 1500°C to 25°C or 800°C. The model was then subjected to an initial displacement to simulate the initial cracking process. The relative contributions of the various bridging mechanisms to the CCS were adjusted to match the CCS versus COD relation at this initial displacement. The resulting CCS vs. COD relations generated by the FE model are shown in Figures 13 and 14 together with the corresponding experimental data. The applied displacement was gradually decreased to simulate the unloading process. The computed and measured behaviors of the CCS vs. COD during unloading at locations 0.1, 1.0 and 2.0 mm from the crack tip are also shown in Figures 13 and 14. In all cases, the COD did not return to zero. These results show that an additional compressive force is required to return the grains to their original uncracked position. Furthermore, the good agreement of the FE results and the experimental data indicates that the assumptions and modeling techniques used were successful in modeling the micro-mechanics of grain bridging in alumina during loading and unloading.

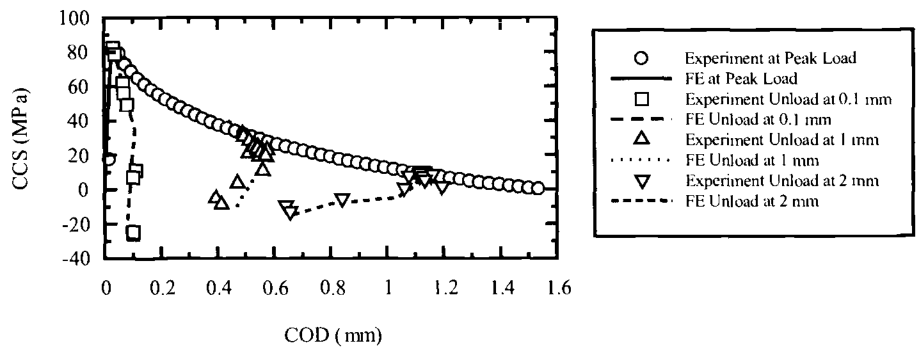

Figure 13 - *CCS vs. COD relations during the first loading and unloading at room temperature.*

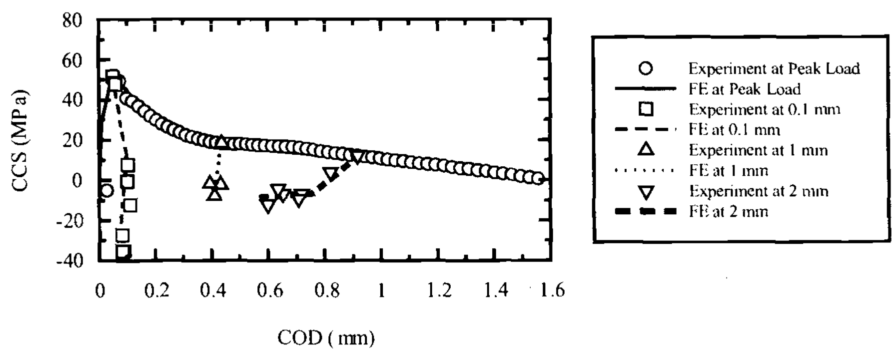

Figure 14 - *CCS vs. COD relations during the first loading and unloading at 800°C.*

Conclusions

1. The crack closing stress versus crack opening displacement relations governing the fracture process zones trailing fatigue crack growth in the high-density alumina, WL-DCB specimens were quantified.
2. A residual COD was found at the initial unloading that remained during subsequent cycling.
3. A mechanistic explanation to the common notion that monolithic ceramics do not fatigue is provided.
4. A micro-mechanical model, which is based on grain pull-out, push-in and butting, intra-granular fracture and crushing, of a WL-DCB alumina specimen was developed through an inverse process. The FE model successfully replicated the measured cyclic load and unload relations of the WL-DCB specimen.

Discussion

The wedging action of the pulled out grains and their inability to return their original location after unloading was predicted by the FE modeling of grain pull out [8]. The results in this study thus provided an experimental justification of the FE modeling.

Acknowledgment

This research was supported by the Air Force Office of Scientific Research Grant no. F49620-93-1-0210. Dr. O. Ochoa was the AFOSR program director..

References

[1] Mai, W. and Lawn, B. R., "Crack Interface Grain Bridging as a Fracture Resistance Mechanism in Ceramics: II, Theoretical Fracture Mechanics Model," *Journal of American Ceramic Society*, Vol. 70, 1987, pp. 289-294.

[2] Reichl, A. and Steinbrech, R. W., "Determination of Crack Bridging Forces in Alumina," *Journal of American Ceramic Society*, Vol. 71, 1988, pp. C299-C301.

[3] Swanson, S. L., Fairbanks, C. J., Lawn, B. R. and Mai, Y. W., "Crack-Interface Grain Bridging as a Fracture Resistance Mechanism in Ceramics: I, Experimental Study of Alumina," *Journal of American Ceramic Society*, Vol. 70, 1987, pp. 279-289.

[4] Roedel, J., Kelly, J. F. and Lawn, B. R., " In Situ Measurements of Bridged Crack Interfaces in Scanning Electron Microscope," *Journal of American Ceramic Society*, Vol. 73, 1990, pp. 3313-3318.

[5] Hay, J. C. and White, K. E., "Grain-Bridging Mechanisms in Monolithic Alumina and Spinel," *Journal of American Ceramic Society*, Vol. 76, 1990, pp. 1025-1032.

[6] Guo, Z. K., Kobayashi, A. S., Hay, J. C. and White, K. W., "Fracture Process Zone of Monolithic Al_2O_3," *Engineering Fracture Mechanics*, Vol. 63, 1999, pp. 115-129.

[7] Tran, D. K., Kobayashi, A. S. and White, K. W., "Process Zone of Polycrystalline Alumina," *Experimental Mechanics*, Vol. 39, 1999, pp. 20-24.

[8] Kokaly, M. T., Tran, D. K., Kobayashi, A. S, Dai, X., Patel, K.. and White, K. W., "Modeling of Grain Pullout forces in Polycrystalline Alumina," *Material Science and Engineering*, A285, 2000, pp. 151-157.

[9] Vekinis, G., Ashby, M. F., and Beaumont, P. W. R., "R-curve Behaviour of Al_2O_3 Ceramics," *Acta Metallurgy and Materials*, Vol. 38, No. 6, 1990,pp. 1151-1162.

[10] Curtin, W. A., "Toughening by Crack Bridging in Heterogeneous Ceramics," *Journal of American Ceramic Society,* vol. 78, 1995, pp. 1313-1323.

[11] Tran, D. K., Kobayashi, A. S. and White, K. W., "Crack Growth in Alumina at High Temperature," to be published in *Engineering Fracture Mechanics.*

[12] Tran, Duc Khanh, "Experimental and Numerical Study of Crack Bridging in Polycrystalline Ceramics at Room and Elevated Temperature", a PhD thesis submitted to the University of Washington, June 1999.

[13] Bower, A. F. and Ortiz, M., "The Influence of Grain Size on the Toughness of Monolithic Ceramics," *ASME Journal on Engineering Material Technology,* Vol. 115, No. 2, 1993, pp. 1349-1355.

[14] Jahanmir, S. and Dong, X., "Mechanism of Mild to Severe Wear Transition in Alpha-Alumina," *Journal of Tribology,* Vol. 114, No. 3, 1992, pp. 403-411.

P. K. Liaw,[1] B. Yang[1], H. Tian,[1] L. Jiang,[1] H. Wang,[2] J. Y. Huang,[3] R. C. Kuo,[3] J. G. Huang,[4] D. Fielden,[1] J. P. Strizak,[2] and L. K. Mansur[2]

Frequency Effects on Fatigue Behavior and Temperature Evolution of Steels

Reference: P. K. Liaw, B. Yang, H. Tian, L. Jiang, H. Wang, J. Y. Huang, R. C. Kuo, J. G. Huang, D. Fielden, J. P. Strizak, and L. K. Mansur, **"Frequency Effects on Fatigue Behavior and Temperature Evolution of Steels,"** *Fatigue and Fracture Mechanics: 33rd Volume, ASTM STP 1417*, W. G. Reuter and R. S. Piascik, Eds., ASTM International, West Conshohocken, PA, 2002.

Abstract: Fatigue experiments on steels were conducted using an advanced electrohydraulic machine, which has a frequency range from approximately 1 Hz to 1000 Hz. Increasing the test frequency from 10 Hz to 1000 Hz will increase the specimen temperature, which, in turn, will decrease the fatigue life in air. However, in mercury, due to the cooling effect by mercury, little change in fatigue life was observed at different frequencies.

A high-speed and high-sensitivity thermographic infrared (IR) imaging system has been used for nondestructive evaluation of temperature evolutions during fatigue testing of steels. The temperature sensitivity of the camera is 0.015°C at 23°C. High-speed data acquisition capabilities are available at 150 Hz with a full frame, and 6100 Hz with a narrow window. Thus, the IR camera can be used to monitor *in situ* temperature evolutions resulting from fatigue.

Five stages of specimen temperature evolutions were observed during fatigue testing: an initial increase of the mean temperature of the test sample, a followed decrease of the temperature, an equilibrium (steady-state) temperature region, an abrupt increase of temperature before final failure, and a temperature after specimen failure. The measurements of temperature oscillations within each fatigue cycle at 20 Hz have been attempted. During each fatigue cycle, the specimen temperature was detected to oscillate within approximately 0.5°C depending on the loading conditions and test materials. When the applied stress reached the minimum, the temperature typically approached the maximum. However, the applied maximum stress did not necessarily correspond to the minimum temperature.

A theoretical framework was attempted to predict temperature evolutions based on thermoelastic and inelastic effects, and heat-conduction models. Temperature oscillation during fatigue resulted from the thermoelastic effects, while the increase in the mean

[1] Professor, students, and staff, respectively, Materials Science and Engineering Department, The University of Tennessee, Knoxville, TN 37996 – 2200, USA.

[2] Research scientists, Oak Ridge National Laboratory, Oak Ridge, TN 37831, USA.

[3] Research scientists, Institute of Nuclear Energy Research (INER), P. O. Box 3-14, 1000 Wenhua Road, Chiaan Village, Lungtan, Taiwan 325, Republic of China.

[4] Research scientist, Taiwan Power Company, Taipei, Taiwan.

temperature derived from the inelastic behavior of the materials. The predicted temperature evolutions during fatigue were found to be in good agreement with the thermographic results measured by the advanced high-speed and high-sensitivity IR camera. Furthermore, the back calculation from the observed temperature was conducted to obtain inelastic deformation and stress-strain curves during fatigue.

Keywords: Thermography, Fatigue, Temperature Evolution, RPV Steel, 316 LN SS

Introduction

Many structural components are subjected to cyclic loading. In these components, fatigue damage is the prime factor in affecting structural integrity and service life. Fatigue behavior is strongly affected by the loading conditions, such as test frequencies and applied loads, environments, and materials [*1-8*]. Moreover, fatigue damage is typically divided into three stages: crack initiation, crack growth, and fast fracture. These three stages are crucial in determining the fatigue life of structural components.

In many cases, the crack-initiation behavior can, however, be the dominant event for life- prediction analyses and design considerations, such as the applications of S (applied stress) versus N (number of cycles to failure) curves. Furthermore, crack initiation is the precursor of fatigue failure. If the early stage of crack initiation can be detected, and the mechanisms of crack initiation can be better understood, fatigue failure may be prevented.

Numerous structural components, such as turbine blades in aerospace jet engines and land-based steam turbines, can experience high-frequency fatigue loading in the range of kilohertz. Conventional fatigue test machines are generally operated in the frequency range of approximately 1 Hz to 200 Hz to develop S-N curves. The S-N curves obtained at lower frequencies may not be suitable for the applications at high frequencies. For accurate life predictions, the influence of test frequency on the S-N curves needs to be examined.

Nondestructive evaluation (NDE) of fatigue damage is of critical importance for life assessments and structural-integrity evaluations. Several NDE methods, including ultrasonics, acoustic emission, and thermography, have been used to monitor fatigue damage [*9-21*]. However, relatively little work has been conducted to assess fatigue characteristics using thermographic infrared (IR) techniques [*12-17*].

In this paper, the fatigue behavior of steels has been investigated in the frequency range of 10 Hz to 1000 Hz using an advanced electrohydraulic machine. Moreover, a high-speed and high-sensitivity IR thermographic technique was employed to examine temperature evolutions during fatigue, which provides an explanation for the frequency effect on S-N curves. Theoretical models, including the thermoelastic, inelastic, and heat-conduction effects, are formulated to explain and predict the observed temperature evolution during fatigue. Furthermore, the back calculation of thermography was conducted to predict the stress-strain behavior during fatigue, which was found to be in good agreement with the experimental results.

Experimental Procedure

Fatigue tests in the frequency range of 10 Hz to 1000 Hz were performed on Type 316 LN (low-carbon, nitrogen-containing) stainless steel (SS) and reactor pressure vessel (RPV) steels (SA533B1I2). All tests were conducted under load control, and several cycles were required for the machine to reach the nominal load level. The chemical compositions of the two steels are shown in Table 1. Type 316 LN SS is an austenitic

Table 1 - *Chemical Compositions of Type 316 LN Stainless Steel and Reactor Pressure Vessel Steel in Weight Percent (wt.*

Material	316 Stainless Steel	Pressure Vessel Steel
C	0.009	0.203
Mn	1.750	1.340
P	0.029	<0.02
S	0.002	0.015
Si	0.390	0.230
Ni	10.20	0.50
Cr	16.31	-
Mo	2.070	0.530
Co	0.160	-
Cu	0.230	0.010
N	0.110	0.005
Fe	Bal.	Bal.

stainless steel, while the microstructure of the RPV steel is a tempered martensite. The 316 LN SS steel is chosen as the prime candidate target-container material for the Spallation Neutron Source (SNS). The target material for the bombardment of a proton beam will be liquid mercury (Hg) contained in the 316 LN SS container. When the protons bombard the mercury to convert into neutrons for SNS, cyclic loading will occur in the 316 LN SS container. Thus, it is important to study fatigue behavior of 316 LN SS steel in the mercury environment. The tensile properties of 316 LN SS steel at 24°C are presented in Table 2.

Table 2 - *Tensile Properties of Type 316 LN Stainless Steel and Reactor Pressure Vessel Steel at 24°C*

Material	Strain Rate (1/s)	0.2% Yield Strength (MPa)	Tensile Strength (MPa)	Elongation (%)	Reduction of Area (%)
316 Stainless Steel	0.01	288.0	587.2	60.0	82.6
Pressure Vessel Steel	0.004	587.0	716.0	29.0	-

Cylindrical bars with a gage length of 19 mm and a diameter of 5.1 mm were used for fatigue testing. The test samples were polished in a sequence of 240, 400, 600, and 800 grit papers, followed by 9.5, 1, and 0.06 μm grit powders. For the higher-frequency (≥ 200 Hz) fatigue experiments in air, a state-of-the-art, high-frequency, electrohydraulic MTS® machine (Model 1000 Hz 810) was used with an R-ratio of 0.1 or 0.2, where $R = \sigma_{min}/\sigma_{max}$, σ_{min} and σ_{max} are the applied minimum and maximum stresses, respectively [*22*]. The servovalves of the machine were activated by voice coils, which provided the necessary frequency of 1000 Hz. The machine has a maximum loading capability of ±25 KN. The cylindrical samples were fastened to the machine using mechanical loading arrangements. To avoid testing noise at 1000 Hz, the machine was situated in a well-designed, soundproof room equipped with a heat pump, which offered the cooling capability to prevent the overheating of servovalves. For the lower-frequency (≤ 20 Hz) fatigue experiments in air, the specimens were loaded in electrohydraulic grips of a MTS machine (Model 810) at R = 0.1 or 0.2. During 20 Hz fatigue tests, an extensometer was mounted on the gage-length section of the specimen to monitor displacements as a function of fatigue cycles.

For Type 316 LN SS, fatigue tests were conducted in air, mercury, and nitrogen-gas environments, while those on RPV steel were performed only in air. In order to conduct fatigue tests in mercury, an attached container of 304 SS was used. The gage section of the specimen was immersed in mercury enclosed in the container. The container was attached to the specimen with a silicone-rubber adhesive sealant, which could be removed from the specimen after the test, and reused. During fatigue tests, the gage section of the specimen remained in contact with the mercury in the container. The nitrogen gas generator was a Dewar containing liquid nitrogen. Two thermocouples were used to monitor the temperature. One was mounted on the surface of the specimen, and the other was fixed near the specimen to read the temperature of the outlet nitrogen gas around the specimen.

A Raytheon Galileo thermographic IR imaging system was used with a 256 x 256 pixel focal-plane-array InSb detector that is sensitive to 3 to 5 μm thermal radiation. The temperature sensitivity of the IR camera is 0.015°C at 23°C. The spatial resolution of the system is equal to 5.4 μm, when a microscope attachment is used. High-speed data acquisition capabilities are available at 150 Hz with a full frame, and 6,100 Hz with a narrow window. During fatigue testing, a thin sub-micron graphite coating was applied on the gage-length section of the fatigue sample to decrease IR reflections. A fully-automated software system was employed to acquire temperature distributions of the test samples during fatigue experiments.

A thermocouple was attached to the sample to calibrate the IR camera at the beginning of each test. During calibration, a heat gun was used to heat up the specimen to a given temperature, and then the specimen was cooled in air. Different temperatures were read from the thermocouple during cooling. The calibrated intensities of the IR camera were used to generate temperature maps. The IR cameras were used in the range of 0.1 Hz to 120 Hz. To capture the detailed thermoelastic effect during 20 Hz fatigue tests, the IR camera was employed at a high speed of 120 Hz.

Results and Discussion

Frequency Effect

Fatigue experiments of Type 316 LN SS were conducted at different stress levels. Test results of the 316 LN SS in air are illustrated in Figure 1. In this test series, efforts were mainly focused on tension-tension fatigue tests with a R ratio of 0.1.

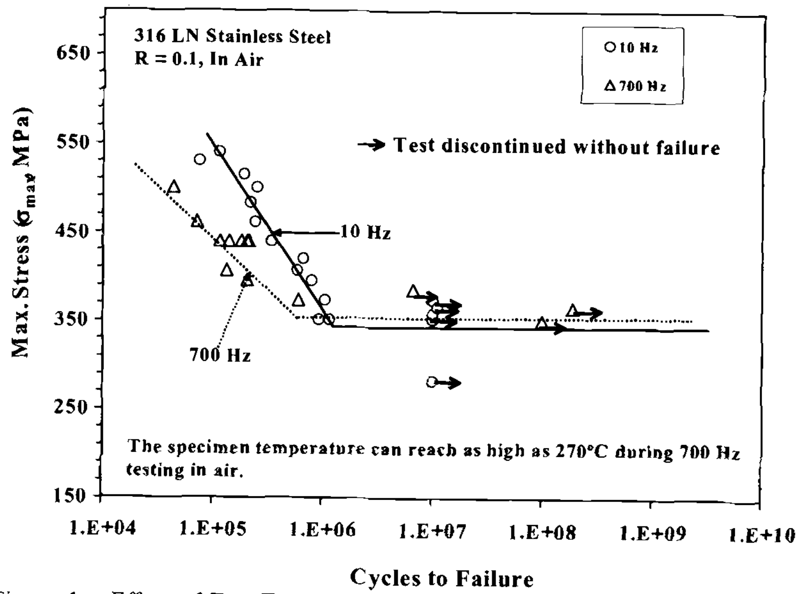

Figure 1 - *Effect of Test Frequency on the Fatigue Life of 316 LN Stainless Steel in Air*

In Figure 1, the 316 LN SS exhibits a fatigue-endurance limit of about 350 MPa at 10 Hz (R = 0.1), and fatigue tests conducted at 700 Hz also showed a similar limit. At a stress level near 350 MPa, the fatigue data exhibit some scatter. This is probably due to an increase in the sensitivity of the crack-initiation behavior to the specimen preparation and microstructure. At a given maximum stress level, the fatigue life in air at the frequency of 700 Hz is shorter than that at 10 Hz, although the fatigue endurance limit tends to be comparable at both frequencies. The difference in the fatigue lives at the two frequencies seems to increase with increasing the maximum stress levels.

To further study the variation of the fatigue life at different frequencies, tests were performed at a specific maximum stress level of 439 MPa with frequencies ranging from 10 Hz to 800 Hz. The fatigue lives at different frequencies are shown in Figure 2. The figure indicates that the fatigue life decreases with increasing frequency. The fatigue life of 316 LN SS at 800 Hz was almost two times shorter than that at 10 Hz. Two factors that may contribute to the differences in the fatigue life as a function of test frequency are self-heating of specimens and strain-rate effects.

The S-N curves of RPV steels at 20 Hz and 1000 Hz are presented in Figure 3. Similar to the results observed for the 316 LN SS, increasing the test frequency from 20 Hz to 1000 Hz generally results in a lower fatigue life at a given stress level.

Specifically, the fatigue endurance limit at 20 Hz seems to be higher than that at 1000 Hz. Thus, in both steels, increasing the test frequency decreases the fatigue life.

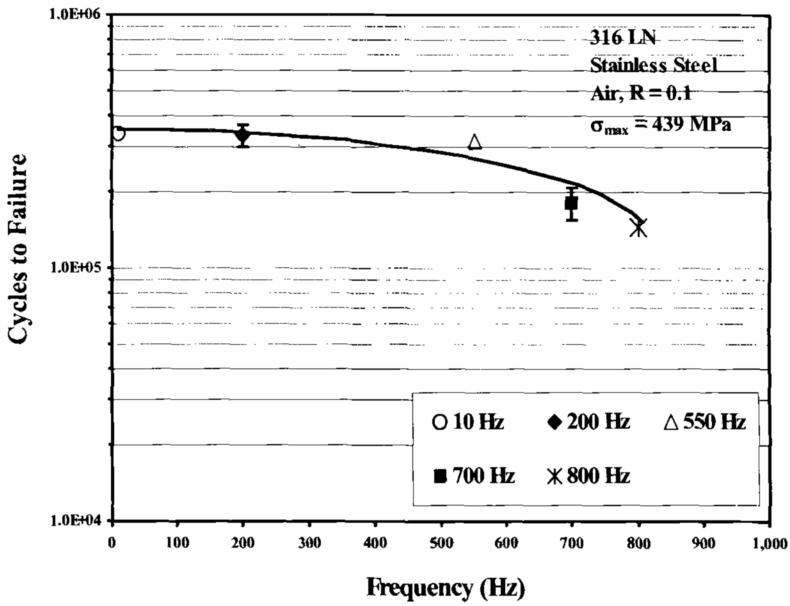

Figure 2 - *Effect of Test Frequency on the Fatigue Life of 316 LN Stainless Steel in Air at σ_{max} = 439 MPa*

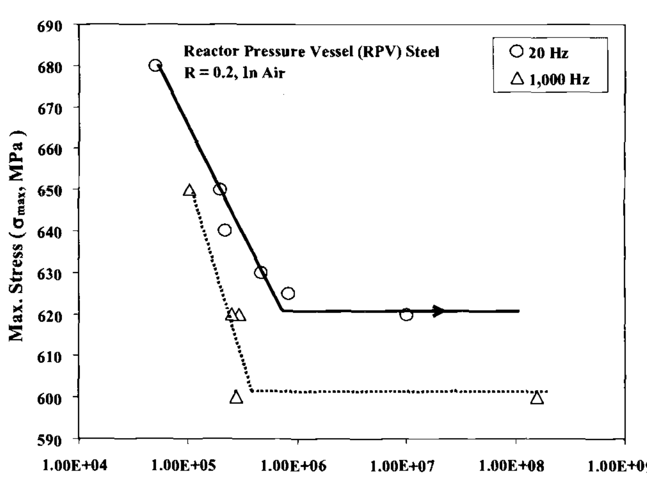

Figure 3: - *Effect of Test Frequency on the Fatigue Life of Reactor Pressure Vessel Steel in Air*

Temperature Evolution

IR Camera at a Low Speed of 0.2 Hz - Figure 4 shows the specimen temperature evolutions at the midpoint of the gage-length section of RPV steels during 1000 Hz fatigue tests at the maximum stresses of 600 MPa and 620 MPa, respectively, and at R = 0.2. Note that the IR camera was taken at a low speed of 0.2 Hz.

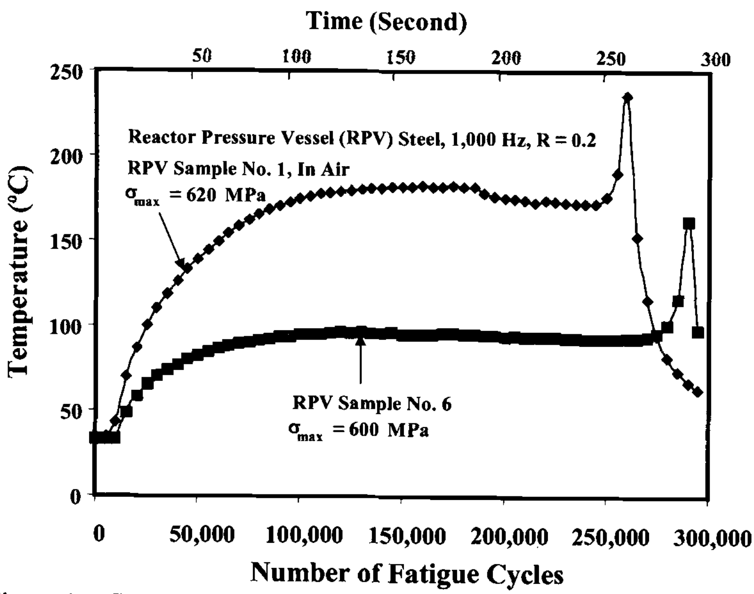

Figure 4: - *Specimen Temperature Evolutions of Reactor Pressure Vessel Steel during 1000 Hz Fatigue Testing, Taken at an IR Camera Speed of 0.2 Hz*

In Figure 4, at 600 MPa, the average specimen temperature at the midpoint of the gage-length section initially increases with increasing fatigue cycles, approaches an equilibrium (steady-state) temperature of about 95°C, and holds steady until the temperature abruptly increases to approximately 160°C at which time the specimen fractures. Following that, the sample fails, and the temperature drops. At 620 MPa, a similar trend was observed. Initially, the average temperature increases until it reaches an equilibrium temperature of approximately 175°C. Later, an abrupt increase in the temperature from about 175°C to 235°C was observed, followed by a drop in the temperature after the specimen fails. Increasing the stress level from 600 MPa to 620 MPa increases the equilibrium temperature from about 95°C to 175°C, and the highest temperature from 160°C to 235°C.

The specimen temperature evolution of a RPV steel sample subjected to a maximum stress level of 680 MPa and a R-ratio of 0.2 during 20 Hz fatigue testing is presented in Figure 5 taken at a low IR camera speed of 0.1 Hz. Similar to the trend found at 1000 Hz, a slight increase in the average specimen temperature (from 22°C to 23°C) was observed, followed by a nearly constant temperature region (23°C to 24°C), extending over many cycles. Then, following an abrupt increase (24°C to 39°C) corresponding to the fast fracture stage, the specimen broke, and the temperature decreased significantly.

Comparing Figures 4 and 5 shows that the temperature rise, the equilibrium temperature, and the highest temperature at 1000 Hz are much greater than those at 20 Hz, which could contribute to the lower fatigue life at 1000 Hz than at 20 Hz (Figure 3).

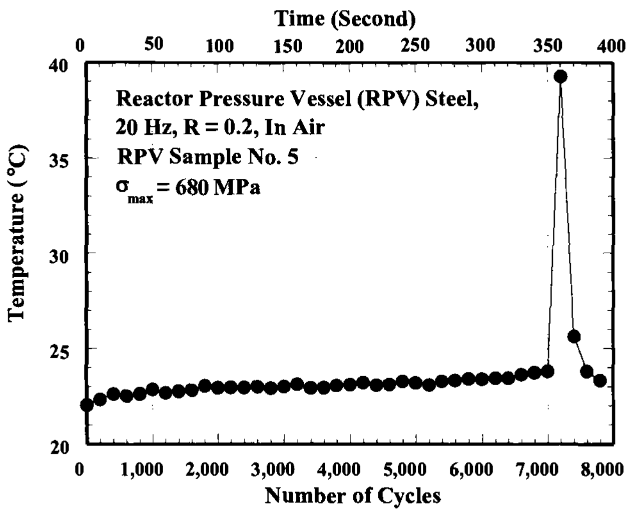

Figure 5: - *Specimen Temperature Evolution of Reactor Pressure Vessel Steel During 20 Hz Fatigue Testing, Taken at an IR Camera Speed of 0.1 Hz*

Further tests were performed concerning the temperature development in the 316 LN SS during fatigue tests. The temperature variations during fatigue tests were determined using the IR camera at a speed of 0.1 Hz, and they are illustrated in Figure 6. Efforts were aimed at confirming the suggestion that an increase in the specimen temperature during a higher frequency test could be responsible for decreasing the fatigue life, as described above.

In Figure 6, the steady-state temperature of 316 LN SS measured by thermography is plotted as a function of the test frequency from 10 Hz to 700 Hz at σ_{max} = 439 MPa. At 10 Hz, the steady-state temperature is approximately 25°C in the air-environment fatigue test, which is much lower than the steady-state temperature of 270°C at 700 Hz. Correspondingly, the fatigue lives of 316 LN SS are longer at 10 Hz than at 700 Hz (Figure 1).

The following experiments were conducted to further prove that the temperature increase during higher-frequency fatigue testing is responsible for the decreased fatigue life with increasing test frequency. During 700 Hz fatigue tests of 316 LN SS at σ_{max} = 439 MPa, the specimen was cooled down by directly blowing the nitrogen gas on the sample. As presented in Figure 7, the specimen temperature was decreased from approximately 270°C to between 58 to 78°C during 700 Hz testing. As a result, the fatigue life at 700 Hz was increased to nearly the same level as that at 10 Hz by cooling of nitrogen gas. Thus, the increased specimen temperature resulting from higher

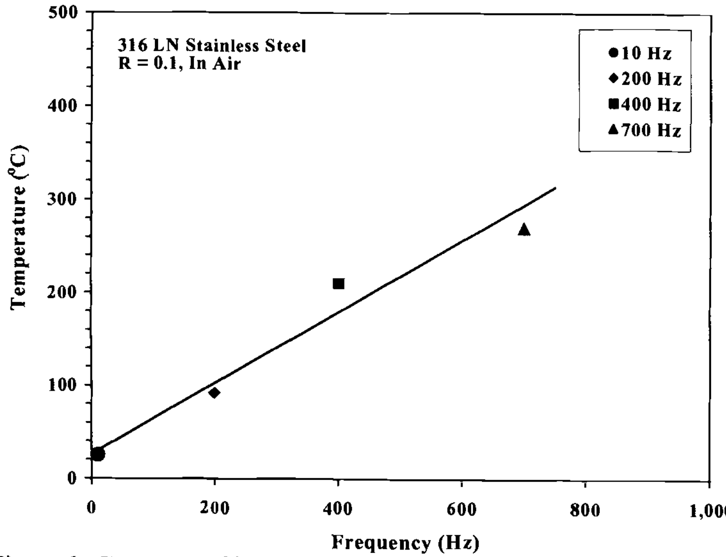

Figure 6 - *Variation of Specimen Temperature with Test Frequency during Fatigue Testing of 316 LN Stainless Steel at σ_{max} = 439 MP*

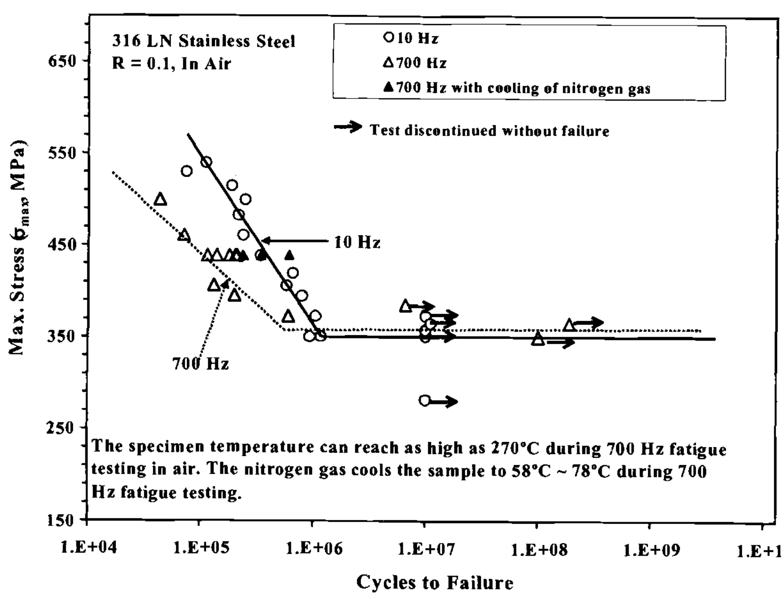

Figure 7 - *Effect of Nitrogen-gas Cooling on the Fatigue Life of 316 LN Stainless Steel*

frequencies offers a possible explanation for the shorter fatigue life with increasing test frequency. The present results suggest that to obtain a consistent S-N curve at different test frequencies, it be essential to cool down the test sample during higher-frequency fatigue tests.

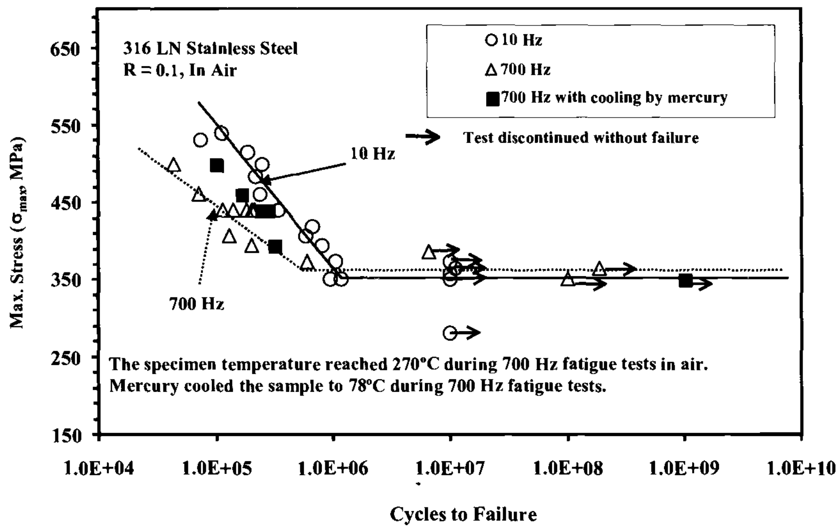

Figure 8 - *Effect of Mercury Cooling on the Fatigue Life of 316 LN Stainless Steel*

Similar results were also observed for fatigue tests performed in mercury at various stresses (Figure 8). The fatigue lives were longer in mercury than in air at 700 Hz. In mercury, the fatigue lives were comparable (though slightly shorter) with those at 10 Hz in air. The mercury around the specimen served as a good heat sink and decreased the specimen temperature. The specimen temperature was about 78°C during 700 Hz fatigue tests in mercury with the maximum stress of 439 MPa. As noted above, a small difference in the fatigue lives at 700 Hz in mercury and those at 10 Hz in air can be detected at stresses above 350 MPa. This variation may result from the liquid-metal embrittlement by mercury [*23*]. However, this effect may not be significant at 700 Hz, since the time for the embrittlement effect to take place during each fatigue cycle may be minimal. Nevertheless, shorter fatigue lives in mercury than in air at stresses above 350 MPa in tests at 10 Hz were attributed to liquid metal embrittlement [*23*]. The somewhat shorter fatigue life at 700 Hz in mercury than that at 10 Hz in air can derive from the higher temperature (e.g. 78°C, σ_{max} = 439 MPa) at 700 Hz in mercury than that (e.g. 25°C, approximately σ_{max} = 439 MPa) at 10 Hz in air.

Figure 9 shows the S-N curve of fatigue tests in mercury at 10 Hz and 700 Hz. The difference in the fatigue life between 10 Hz and 700 Hz is negligible in mercury, which is in contrast with the air-environment results shown in Figure 1. This trend is associated with the fact that the specimen temperature during 700 Hz fatigue tests in mercury was reduced to 78°C, relative to 270°C observed during 700 Hz fatigue tests in air, which minimizes the frequency effect in mercury.

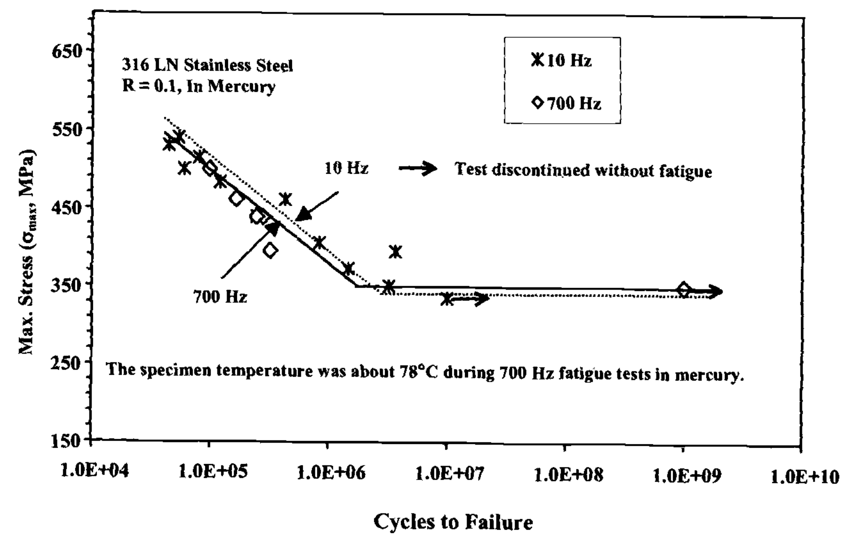

Figure 9 - *Effect of Test Frequency on the Fatigue Life of 316 LN Stainless Steel in Mercury*

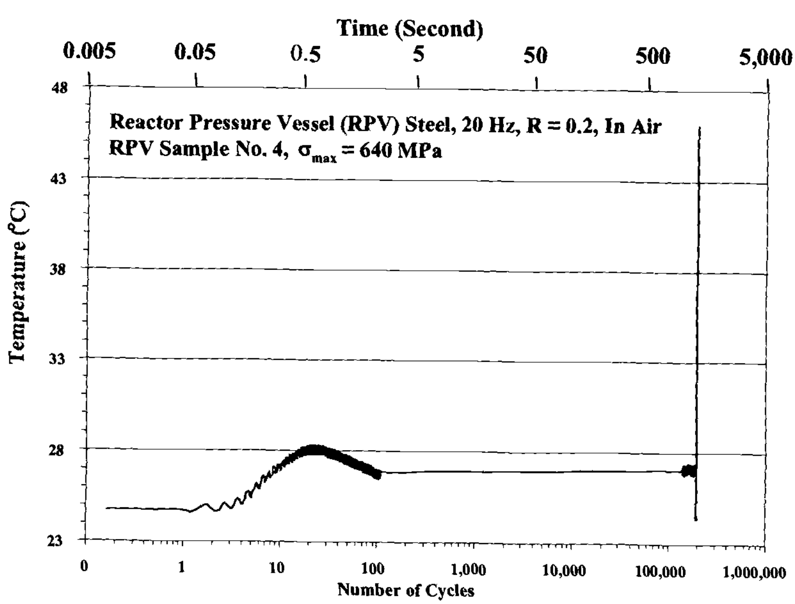

Figure 10 - *Specimen Temperature Evolution of Reactor Pressure Vessel Steel during 20 Hz Fatigue Testing, Taken at an IR Camera Speed of 120 Hz*

IR Camera at a Higher Speed of 120 Hz - As discussed earlier, the specimen temperature evolution at the midpoint of the gage-length section of the RPV steel (Figure 5), subjected to a maximum stress level of 680 MPa and a R-ratio of 0.2 during 20 Hz fatigue testing, was presented. A low IR camera speed of 0.1 Hz was used to record the temperature evolution during the entire fatigue process. The temperature evolution was divided into four stages: (I) the initial temperature increase, (II) the constant temperature region, (III) the abrupt temperature increase before failure, and (VI) the temperature drop after the specimen failed (Figures 4 and 5).

A more detailed investigation on the specimen temperature evolution at the midpoint of the gage-length section of RPV steels, in a 20 Hz fatigue test with σ_{max} = 640 MPa, and R = 0.2, was conducted using a high IR camera speed of 120 Hz (6 data points per fatigue cycle), and the result is shown in Figure 10. Comparing with the previous test results (Figure 5), an initial temperature hump was observed during the first 120 cycles. This was not observed before at a much lower IR camera speed of 0.1 Hz (0.005 data points per fatigue cycle in Figure 5).

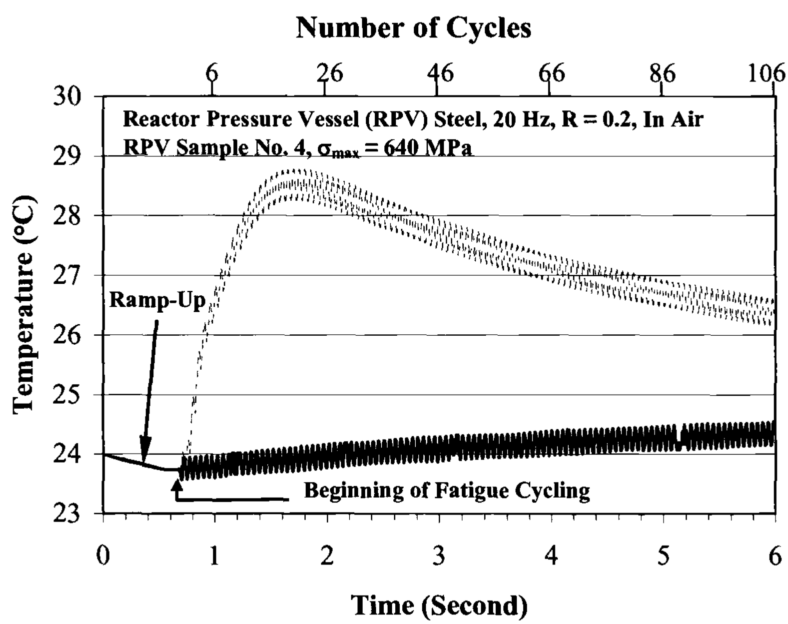

Figure 11 - *Temperature versus Time Evolutions of Reactor Pressure Vessel Steel Tested at 20 Hz, σ_{max} = 640 MPa, Taken at an IR Camera Speed of 120 Hz*

A more detailed observation of the temperature hump is shown as the dashed line in Figure 11. A slight temperature decrease before fatigue cycling at the ramp-up period of the machine was observed, resulting from the thermoelastic effect, as discussed later. Then, there was a rapid temperature increase from the first fatigue cycle at about 0.7 seconds, and the temperature reached a maximum at about 2 seconds (26 cycles). After that, the temperature decreased gradually to a relatively constant value. However, if the test was stopped after the temperature became stable, and then restarted, no temperature hump was observed, and the corresponding results were plotted as the solid line in Figure

11. At the same time, temperature oscillations within the range of approximately less than 0.6°C were found during each fatigue cycle in both tests, indicated by the dashed and solid lines.

The temperature versus time curves for the first 6 seconds (120 cycles) of fatigue tests at different maximum stress levels from 500 MPa to 650 MPa are presented in Figure 12, taken at a high IR camera speed of 120 Hz. For the curves at 630 MPa, 640 MPa, and 650 MPa, a similar trend regarding the presence of the temperature hump was observed, and the maximum temperature hump goes up with the increase of the maximum stress level.

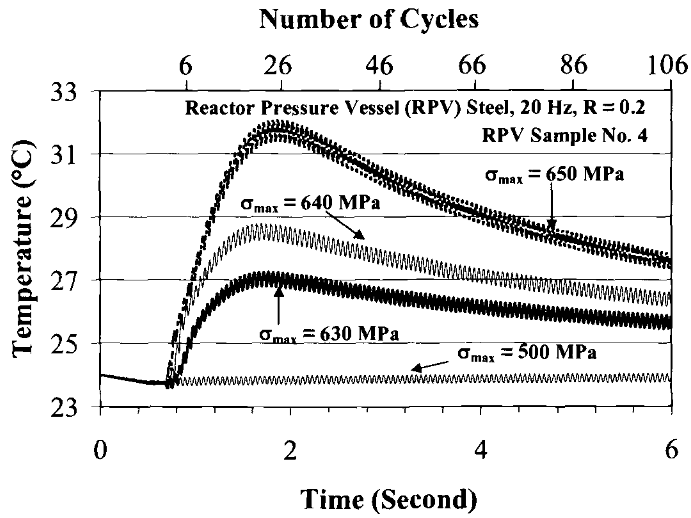

Figure 12 - *Temperature versus Time Evolutions of Reactor Pressure Vessel Steel Tested at 20 Hz, Taken at an IR Camera Speed of 120 Hz*

A reasonable explanation for the presence of the temperature hump can be obtained from the stress-strain curve of RPV steel in Figure 13. This is a typical stress-strain curve for the tension-tension fatigue test. Corresponding to the temperature rise from 0.7 seconds to 2.0 seconds in Figure 11, the stress-strain curve in Figure 13 moves from the first to 26th cycles, and the plastic strain increases from 0 to a nearly saturated value of 4.7%. During this period of time, a great amount of heat is generated from the large plastic deformation, and the temperature of the sample increases quickly. Moreover, the yield-point phenomenon [*24*] of RPV steels was observed in the monotonic tensile test (Figure 14), which contributes to the initial large plastic strain for the first 4 cycles (Figure 13), and, in turn, more heat is generated.

For materials without the yield-point phenomenon, the plastic strain is expected to decrease during each fatigue cycle due to the strain-hardening effect. On the contrary, the areas of the hysteresis loops of RPV steels during fatigue testing were observed to increase during the initial approximately 0% to 2% plastic deformation (Figure 13), which corresponds to the yield-point phenomenon region in Figure 14.

In Figure 12, the maximum temperature in the hump increases with increasing the maximum stress level, as mentioned before. This is because a greater stress level brings

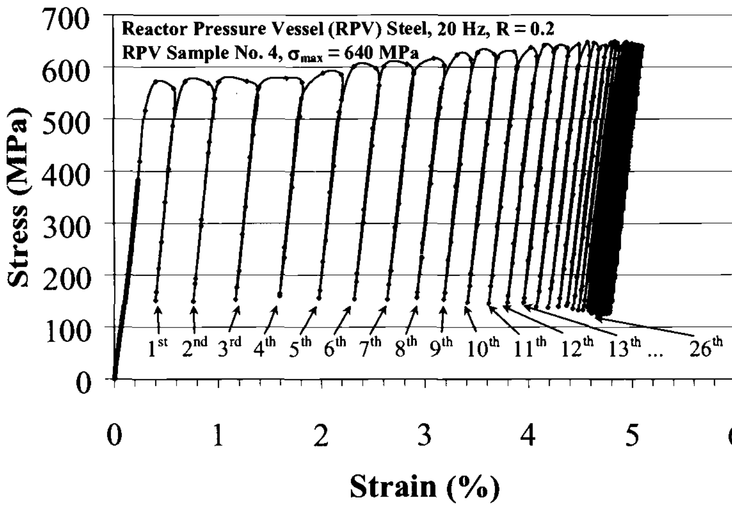

Figure 13 - *Stress versus Strain Result of Reactor Pressure Vessel Steel Tested at 20 Hz,* σ_{max} *= 640 MPa*

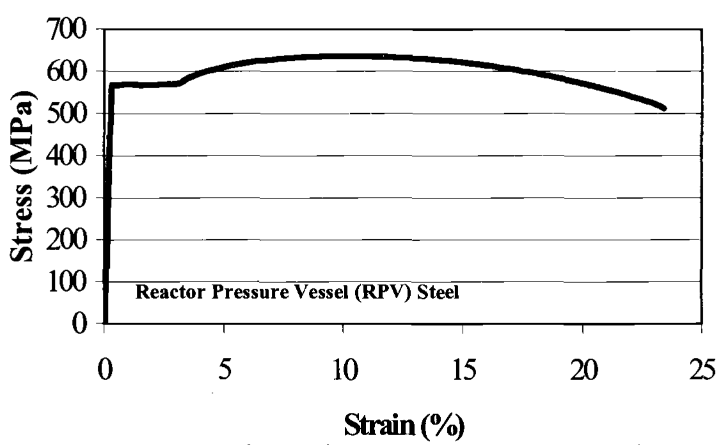

Figure 14 - *Stress versus Strain Curve of Reactor Pressure Vessel Steel during Tensile Testing*

about a larger amount of plastic deformation, which, in turn, generates more heat and raises the temperature. However, at 500 MPa, since the applied stress is much lower than the yielding strength of RPV steels (587 MPa), no plastic deformation and yield-point phenomenon occur during the first 120 cycles, and thus, no temperature hump was found.

Note that a slight increase of the maximum stress with each fatigue cycle at the beginning of the fatigue test was observed in Figure 13. The reason is that the machine has an incubation period to reach the required stress level of 640 MPa in Figure 13.

Actually, the maximum stress approaches the desired value of 640 MPa after about 13 cycles.

Then, if the fatigue test is terminated and restarted, since the plastic strain has already saturated, and the strain-hardening effect is significant, little heat will be generated, resulting from the plastic deformation. Therefore, there will be no rapid temperature rise during the first 100 cycles, shown as the solid line in Figure 11.

I. Initial temperature increase:
- Thermoelastic effect
- Inelastic effects
  - Yield-point phenomenon
  - Plastic deformation
  - etc.

II. Temperature decrease:
- Thermoelastic effect
- Heat-conduction effect
- Strain-hardening effect
- Inelastic effect

III. Equilibrium state:
- Thermal equilibrium with the environment
- Thermoelastic effect
- Inelastic effect
- Heat-conduction effect

IV. Abrupt increase:
- Thermoelastic effect
- Inelastic effects
  - Plastic deformation
  - etc.
- Stress concentration
- Crack propagation

V. Final Drop:
- Specimen failure

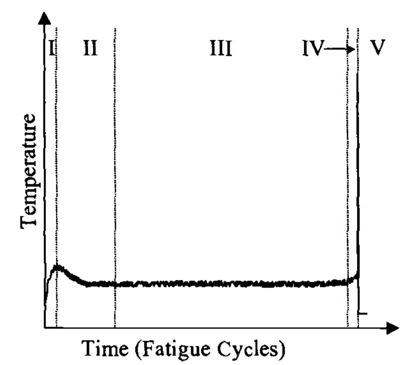

Figure 15 - *Schematic of Specimen Temperature Evolution during a Fatigue Test*

Specimen Temperature Evolution During Fatigue - According to the present results, the specimen temperature evolution of the fatigue test can then be classified into five stages for the materials with the yield-point phenomenon, as schematically summarized in Figure 15, and experimentally observed in Figures 4, 5, and 10. Stage I represents the initial temperature increase due to the large plastic deformation and yield-point phenomenon at the beginning of the test. This stage is dominated by the inelastic effect [*25, 26*]. Stage II corresponds to a gradual temperature decrease after the plastic deformation becomes saturated with strain hardening. This stage is dominated by the heat-transfer effect. In stage III, the temperature reaches a constant value, which presents an equilibrium state between the specimen and environment. Subsequently, the temperature rises up abruptly in stage IV, reflecting the rapid crack propagation before failure and the large plastic deformation in the crack-tip region. The specimen is broken at the highest point of the temperature, and the test stops. Following that, the specimen temperature drops down, as shown in stage V. Throughout the fatigue test except stage

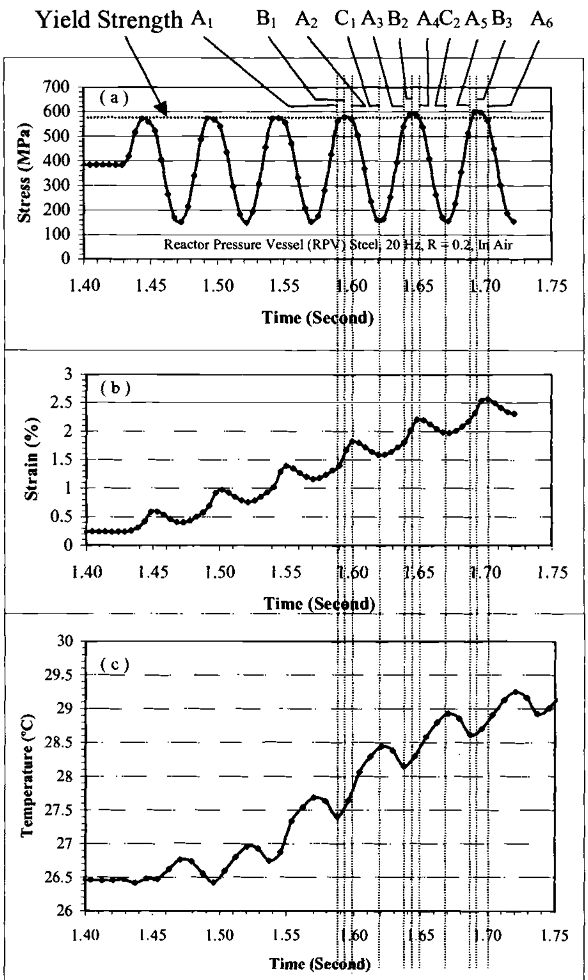

Figure 16 - *Stress-Strain-Temperature versus Time Results of Reactor Pressure Vessel Steel during Initial Fatigue Cycling at 20 Hz, σ_{max} = 640 MPa, Taken at an IR Camera Speed of 120 Hz [(a) Stress versus Time, (b) Strain versus Time, and (c) Temperature versus Time]*

there is a temperature oscillation during each fatigue cycle due to the thermoelastic ect, as further discussed later.

Note that if the material does not have a yield-point phenomenon, the initial ıperature increase followed by a temperature decrease (i.e., a temperature hump) may be observed, as found in the 316 LN SS and a superalloy [*23, 27*]. Instead, a four-ȝe of the temperature profile can be found: Stage I, an initial temperature increase;

Stage II, an equilibrium state (i.e., a constant-temperature region); Stage III, an abrupt temperature increase; and Stage IV, a temperature drop due to the specimen failure.

Figure 16 provides a closer comparison among the stress, strain, and temperature evolutions at the beginning stage of fatigue cycling of the RPV steel. When the stress begins to fluctuate in a sinusoidal wave, the mean strain rises up, while the strain amplitude remains the same. The temperature also fluctuates with the stress, and the mean temperature increases.

Lines, A_1, A_3, and A_5, represent the time when the applied stress increases to the yielding point, while lines, A_2, A_4, and A_6, show the time when the stress decreases to the yielding point. Lines, B_1, B_2, and B_3, correspond to the time when each of the stress cycles reaches the highest point, and lines, C_1 and C_2, to the lowest point. It shows that when the stress reaches the lowest value, the strain also approaches the lowest value (lines, C_1 and C_2), and the temperature rises to the highest point. Since this stress value is much lower than the yielding strength, the observed experimental results match the elastic stress-strain relation and the thermoelastic effect quite well, i.e., decreasing the stress increases the temperature, as reported later.

However, if Figure 16 is examined carefully, there is a phase difference among the stress, strain, and temperature profiles for lines, B_1, B_2, and B_3, which correspond to the highest stresses in the fatigue cycles. The highest value for the strain seems to occur somewhat later than that for the stress, and the lowest point of the temperature appears earlier than the highest stress value. This trend results from the fact that at this time, the stress has already passed the yielding point, and the effect of the plastic deformation should be considered. For the strain, even after the stress passes the highest value, the plastic strain is still increasing due to the yielding phenomenon, which results in large strains. This process continues until the stress drops lower than the yielding point. This is why the highest point for the strain appears later than that for the maximum stress. Lines, A_2, A_4, and A_6, correspond to the unloading period when the stress decreases to the yielding point, and the strain reaches the maximum value of each fatigue cycle, since below the yielding strength, the generation of the plastic strain is insignificant.

On the other hand, the mean temperature will rise up, when the stress reaches the yielding point because of the plastic deformation and yield-point phenomenon. Thus, the lowest value of the temperature appears earlier than the highest value of the stress, which exceeds the yield strength. Lines, A_1, A_3, and A_5, in Figure 16 show that the lowest temperature points appear when the stress approaches the yielding point, which induces the plastic strain, and starts to increase the temperature. Note that a slight increase of the maximum stress with each fatigue cycle was also observed in Figure 16, which has been explained in Figure 13.

Theoretical Modeling

The specimen temperature evolution during fatigue without an outside heat source can be affected by (I) the thermoelastic, (II) the inelastic, and (III) the heat-transfer effects. The thermoelastic effect relates the temperature with the stress and elastic strain [*25, 26*], and it contributes to (1) the initial temperature drop during the ramp-up period of the MTS machine, (i.e., the initial stress-increase region before fatigue cycling) (Figures 11 and 12) and (2) the temperature oscillation during each fatigue cycle (Figures

10, 11, 12, 15, and 16). The inelastic effect uncovers the relationship between the temperature and plastic deformation [*25, 26*]. Along with the heat-transfer effect, the inelastic effect affects the mean-temperature change during fatigue cycling.

In the following, a model combining the thermoelastic, inelastic, and heat-transfer effects will be formulated to predict the temperature profiles observed during fatigue. The relationship among the stress, strain, and temperature will be quantified. Specifically, the temperature evolution during fatigue will be simulated cycle by cycle using this model and compared with the experimental data.

Thermoelastic Effect

The basic relationship among the entropy, temperature, and energy can be derived from the law of thermodynamics in the form [*25, 26*]:

$$ds = \frac{1}{T}\frac{\partial U}{\partial T}dT - \sum^{ij}\frac{\partial \sigma_{ij}}{\partial T}d\varepsilon_{ij}\text{, i, j} = 1, 2, 3 \tag{1}$$

where

s = entropy
U = internal energy
T = absolute temperature
σ_{ij} = stress component, and
ε_{ij} = strain component

Considering $\frac{\partial U}{\partial T} = \frac{\partial Q}{\partial T} = C_\varepsilon \rho$, and using the equations, $\sigma_{ij} = 2G(\varepsilon_{ij} + \frac{v}{1-2v}e\delta_{ij} - \frac{1+v}{1-2v}\alpha\Delta T\delta_{ij})$ and $E = 2G(1+v)$, the following equation can be derived:

$$ds = C_\varepsilon \rho \frac{dT}{T} + \frac{\alpha E}{1-2v}(d\varepsilon_1 + d\varepsilon_2 + d\varepsilon_3) \tag{2}$$

where

Q = outside heat source
ρ = density
ΔT = temperature change
G = shear modulus
v = Poisson's ratio
$e = \varepsilon_1 + \varepsilon_2 + \varepsilon_3$
E = Young's modulus
α = coefficient of linear expansion

$\delta_{ij} = \langle 1(i=j) | 0(i \neq j) \rangle$, and

C_ε = heat capacity at a constant strain

With small changes in temperature, integrating Equation (2):

$$s = \frac{C_\varepsilon \rho \Delta T}{T} + \frac{\alpha E}{1-2\nu}(\varepsilon_1 + \varepsilon_2 + \varepsilon_3) \tag{3}$$

At a constant pressure, using a stress tensor to replace the strain tensor, and considering $C_p - C_\varepsilon = \frac{3E\alpha^2 T}{\rho(1-2\upsilon)}$, Equation (3) becomes:

$$Q = C_p \rho \Delta T + T\alpha(\sigma_1 + \sigma_2 + \sigma_3) \tag{4}$$

where

C_p = heat capacity at a constant pressure

Under adiabatic conditions, Q = 0,

$$\Delta T = -\frac{T\alpha}{C_p \rho}(\sigma_1 + \sigma_2 + \sigma_3) \tag{5}$$

The above equation can be written in the form of

$$\Delta T = -KT(\sigma_1 + \sigma_2 + \sigma_3) \tag{6}$$

where

$$K = \frac{\alpha}{C_p \rho}$$

While the absolute temperature of the material does not change sharply during each fatigue cycle, the temperature will fluctuate proportional to the sum of the principal stresses. While the stress increases, the temperature will decrease and vice versa [Equation (6)]. Experimentally, during fatigue, it was observed that the temperature of the specimen decreases, proportional to the increase of the stress in the ramp-up period of the MTS machine (Figures 11 and 12), and oscillates regularly during each fatigue cycles (Figures 10, 11, 12, 15, and 16). These trends can be attributed to the thermoelastic effect, as described above.

Inelastic Effect

The mean temperature rise region during the first 26 fatigue cycles (Figure 11) can be attributed to the heat from the plastic deformation, which can also be called the inelastic effect. To quantify the inelastic effect in fatigue cycling, the following assumptions need to be made:

a)Consider an isotropic, long, and slender bar, which is subjected to a homogeneously-applied deformation field such that the resulting stress field is everywhere uniaxial in one dimension.

b)Only a fixed system of one-dimensional axis, x, will be considered.

Thus, considering the inelastic effect, the basic thermodynamic equation [*25, 26*] is:

$$\rho C_p \frac{\partial T(x,t)}{\partial t} = Q' \tag{7}$$

where

Q' = heat generated inside the material.

Since $W = \int Q'dt = \int \sigma d\varepsilon$, integrating Equation (7) with time gives:

$$\rho C_p \theta_i = \int_{\varepsilon_1}^{\varepsilon_2} \sigma_u d\varepsilon - \int_{\varepsilon_1}^{\varepsilon_2} \sigma_l d\varepsilon = A_i \tag{8}$$

where

θ = temperature change due to the thermoplastic effect for each fatigue cycle
ε_1 = minimum strain of the hysteresis loop
ε_2 = maximum strain of the hysteresis loop
σ_u = stress in the upper part of the hysteresis loop
σ_l = stress in the lower part of the hysteresis loop
A = area for each hysteresis loop, and
i = number for each fatigue cycle

Heat-Conduction Effect

To provide a better prediction of the thermography results, the heat-transfer effect needs to be considered. For RPV steels tested in air, two heat-transfer processes are involved. One is the heat conduction between the specimen and the main body of the MTS machine through grips, and the other is the heat transfer between the specimen and the air around it. However, comparing with the large heat capacity in steels, neglecting the heat transfer with air will be reasonable.

The equation for heat conduction in solids with a constant thermal conductivity is:

$$\rho C_p \frac{\partial T}{\partial t} = k\left(\frac{\partial^2 T}{\partial x^2} + \frac{\partial^2 T}{\partial y^2} + \frac{\partial^2 T}{\partial z^2}\right) + q \tag{9}$$

where

k = thermal conductivity of the material, and
q = energy conversion rate per unit volume.

For a steady one-dimensional conduction without energy conversion, Equation (9) becomes:

$$\rho C_p \frac{\partial T}{\partial t} = k \frac{\partial^2 T}{\partial x^2} \tag{10}$$

The specimen is held by a pair of grips that are loaded on the machine. For the continuity of the one-dimensional heat-conduction model, the length of the grips and non-gage section of the specimen need to be converted into an effective length of material with the same cross-sectional area as the gage section. The key is that the heat passing through a cross section should be the same before and after conversion. As for the inclusion of the heat-conduction effect, the temperature in the main body of the machine is equal to room temperature, and the length of the grips (20.32 cm) and non-gage length of the specimen (3.83 cm) are converted into an effective length of 14.05 cm with a diameter of 5.1 cm (the same as the gage diameter of the specimen). Combining with the real gage length (1.27 cm), the total effective length will be 15.32 cm. Considering that the specimen is a homogeneous round bar, and assuming that the temperature gradient is constant with the x-axis, a simplification can be made as follow:

$$\frac{\partial T}{\partial x} = \frac{T - T_0}{\Delta x} \tag{11}$$

where

T_0 = room temperature, and
Δx = effective length of 15.32 cm from the center of the specimen to the end of the grip.

Since:

$$k \frac{\partial T^2}{\partial x^2} = k \frac{\partial (\frac{T - T_0}{\Delta x})}{\partial x} = k \frac{1}{\Delta x} \frac{\partial T}{\partial x} \tag{12}$$

Equation (10) can be converted into:

$$\rho C_p \frac{\partial T}{\partial t} = k \frac{1}{\Delta x} \frac{\partial T}{\partial x} \tag{13}$$

The heat-conduction rate can then be determined by the equation below:

$$\frac{\partial T}{\partial t} = k \frac{1}{(\Delta x)^2 \rho C_p}(T - T_0) \tag{14}$$

In the following section, the thermoelastic, thermodynamic, and heat-transfer effects will be combined to predict the temperature evolution versus number of cycles curves. The temperature evolutions will be predicted using the stress and strain results during fatigue, and compared with the experimental data.

Comparisons of Experimental Results and Theoretical Predictions

The relevant material constants of the present RPV steel are:

a) Linear thermal expansion coefficient: $\alpha = 1.1 \times 10^{-5}$ /°C
b) Density: $\rho = 7.8$ g/cm^3
c) Specific heat at a constant pressure: $C_p = 0.48$ J/g°C

In uniaxial fatigue testing, considering the uniaxial-stress condition, there is only one principal stress, σ_1. Thus, Equation (6) can then be simplified to:

$$\Delta T = -KT\sigma_1 \tag{15}$$

The temperature evolution due to the thermoelastic effect can be calculated by Equation (15). Figure 17 shows the predicted temperature oscillation during the first 18 fatigue cycles. The zero point of ΔT corresponds to the initial temperature when the

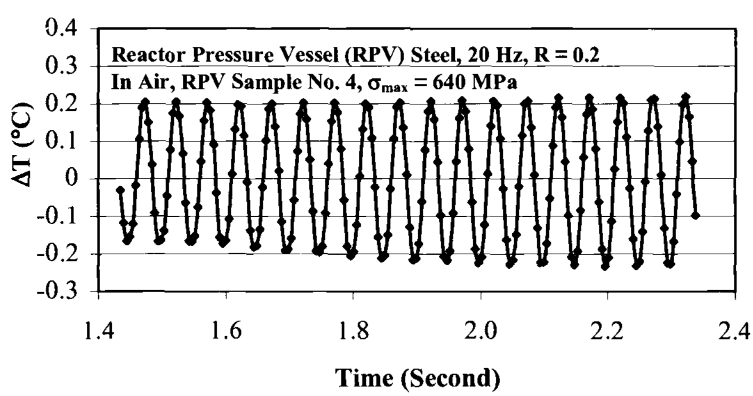

Figure 17 - *Predicted Temperature Oscillation of Reactor Pressure Vessel Steel during the First 18 Cycles of Fatigue Testing at 20 Hz, σ_{max} = 640 MPa*

stress is at the mean stress level. A slight decrease of the minimum temperature during each fatigue cycle was observed due to the increase of the corresponding maximum stress with each fatigue cycle during the initial cycling of the MTS machine (Figures 13 and 16), which has been explained before.

Using the stress-strain data that was recorded during fatigue testing to calculate the area of each hysteresis loop, the mean temperature change due to the inelastic effect can be predicted from Equation (8). Figure 18 represents the predicted change of the mean temperature resulted from the plastic deformation during the first 18 fatigue cycles. Due to the fact that plastic deformation takes place only when the applied stress is greater than the yielding point, which is a small portion of each cycle, the mean temperature will only increase in this portion of each cycle, and thus, a stair shape of the mean temperature versus time curve is expected in Figure 18.

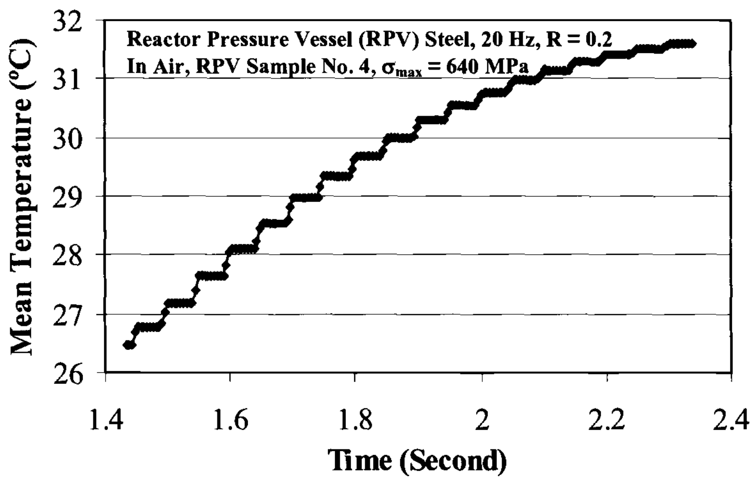

Figure 18 - *Predicted Mean Temperature Change of Reactor Pressure Vessel Steel during the First 18 Cycles of Fatigue Testing at 20 Hz, σ_{max} = 640 MPa*

For each data point recorded in the fatigue test at 20 Hz, the time interval, Δt, is 0.00483 seconds. If considering $dt \approx \Delta t = 0.00483$s, Equation (14) becomes:

$$dT_j = k\frac{1}{(\Delta x)^2 \rho C_p}(T_j - T_0)dt \tag{16}$$

where

j = number of the fatigue data point, and
dT_j = temperature correction due to the heat-conduction effect for each fatigue data point

Using Equation (16) to refine the temperature calculation, the temperature change for each data point becomes:

$$\Delta T_{jc} = \Delta T_j - \sum_{n=1}^{j} dT_n \tag{17}$$

where

ΔT_{jc} = temperature change for each data point after the heat-conduction correction

ΔT_j = temperature change for each data point before the heat-conduction correction, and

$\sum_{n=1}^{i} dT_n$ = accumulation of the heat-conduction effect

Thus, the predicted temperature for each data point after the heat-conduction correction can be written in the equation below:

$$T_{jc} = T_0 + \Delta T_{jc} \tag{18}$$

where

T_{jc} = predicted temperature for each data point after the heat-conduction correction, and

T_0 = room temperature

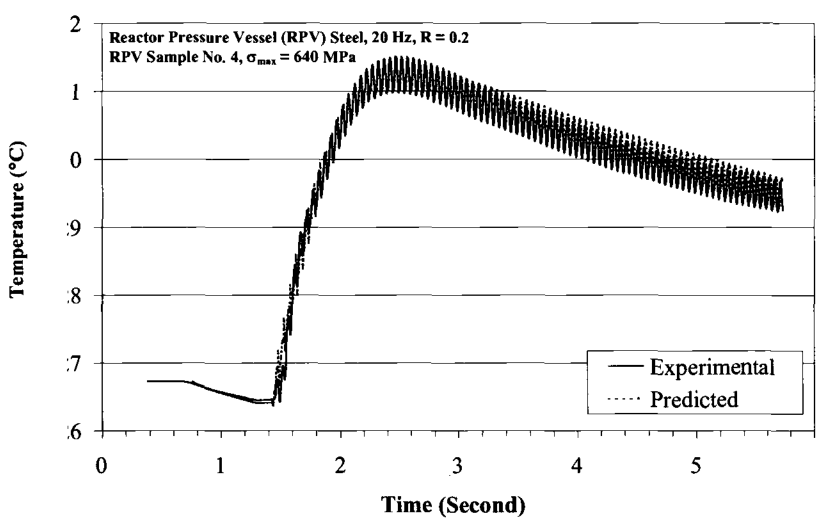

Figure 19 - *Measured and Predicted Temperature Evolutions of Reactor Pressure Vessel Steel during the First 100 Cycles of Fatigue Testing at 20 Hz, σ_{max} = 640 MPa*

Combining the calculation of the thermoelastic, inelastic, and heat-transfer effects, the theoretical temperature profile of the whole temperature hump is predicted in Figures 19 and 20, while Figure 20 is the first 18 fatigue cycles of Figure 19. In Figure 19, the theoretical model predicts the temperature hump, which is in good agreement with the experimental data. However, the predicted and experimental results in the temperature-decrease part do not fit each other exactly in Figure 19. The deviation can be explained by the fact that the present heat-conduction model is a simplified model, while the real heat transfer between the specimen and environment is much more complicated (e.g., the heat transfer between the specimen and the surrounding air, and the temperature gradient not being exactly constant along the loading axis). In Figure 20, for the first two fatigue cycles, the predicted and measured results fail to fit each other closely, which can be explained as follows. The surface and the center of the sample have not reached a uniform thermodynamic state at the very beginning of the test. The surface temperature can be more easily dissipated, relative to the interior of the sample. Thus, the measured surface temperatures of the test specimen by thermography can be lower than the predicted values.

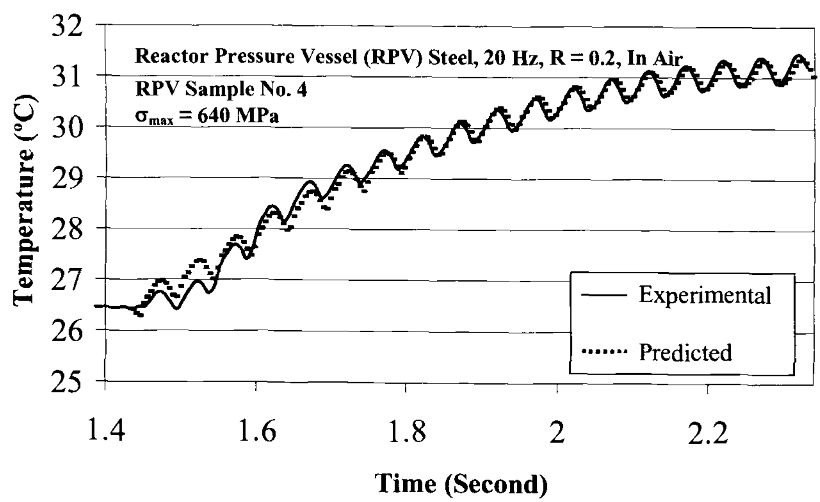

Figure 20 - *Measured and Predicted Temperature Evolutions of Reactor Pressure Vessel Steel during First 18 Cycles of Fatigue Testing at 20 Hz,* σ_{max} = *640 MPa*

Back Calculation

In the previous section, the prediction of the specimen temperature evolutions during fatigue has been conducted using the stress-strain data. At the same time, the mechanical behavior can also be investigated from the original temperature profile. In this section, the back calculation from the measured temperature to predict the stress and strain state during fatigue will be performed.

From the specimen temperature evolution in Figure 11, we can easily calculate the stress state by the thermoelastic effect. At the ramp-up period of fatigue testing, the stress goes from zero to the mean stress. At the same time, the normalized temperature goes down from 24 to 23.665°C. The mean stress can then be calculated by Equation (6) as:

$$\left(\frac{\sigma_{\min}+\sigma_{\max}}{2}\right)=\left(\frac{(23.665-24)}{-KT_0}\right) \tag{19}$$

At the constant temperature region, a temperature oscillation (ΔT_{osci}) of 0.46°C can also be expressed by the equation below:

$$\Delta T_{osci}=-KT(\sigma_{\max}-\sigma_{\min}) \tag{20}$$

Thus,

$$\left(\frac{\sigma_{\max}-\sigma_{\min}}{2}\right)=\frac{\Delta T_{osci}}{-2KT} \tag{21}$$

Using Equations (19) and (21), the minimum and maximum stresses were then calculated as 123 MPa and 638 MPa, respectively, which are very close to the nominal stress levels in the test (σ_{min} = 123 MPa and σ_{max} = 640 MPa). The elastic strain, ε_e, in fatigue testing can then be calculated easily by the equation:

$$\varepsilon_e=\sigma/E \tag{22}$$

However, the inelastic strain of the specimen cannot be directly obtained from the original temperature evolution because the mean temperature change is determined not only by the inelastic effect but also by the heat-conduction effect. Thus, the first step to calculate the inelastic strain will be the back calculation to exclude the heat-conduction effect from the original temperature evolution.

The equation that is used for the back calculation is the same as Equation (14):

$$dT_j=k\frac{1}{\Delta x^2\rho C_p}(T_j-T_0)dt \tag{23}$$

where

j = the j^{th} experimental temperature data point

Using Equation (23) to eliminate the heat-conduction effect from the original temperature evolution, the temperature for each data point becomes:

$$T_{jc}=T_j+\sum_{n=1}^{j}dT_n \tag{24}$$

where

T_{jc} = temperature after the back calculation by excluding the heat-conduction effect.

Since the absolute temperature of the specimen during fatigue testing is nearly a constant, the differences of the thermoelastic effect among each fatigue cycle under a constant load range can be neglected [Equation (6)]. Thus, the changes in the peak temperature for each fatigue cycle can be directly related to the heat generated during each fatigue cycle. Then, Equation (8) can be rewritten as follows:

$$\rho C_p (T_{m+1} - T_m) = \int_{\varepsilon_{min}}^{\varepsilon_{max}} \sigma_u d\varepsilon - \int_{\varepsilon_{min}}^{\varepsilon_{max}} \sigma_l d\varepsilon = A_m \approx \sigma_{max} \times \varepsilon_{in_m} \qquad (25)$$

Where

m = the m^{th} cycle
T_m = peak temperature of the m^{th} cycle
A_m = area of the hysteresis loop of the m^{th} cycle, and
ε_{in_m} = inelastic strain of the m^{th} cycle

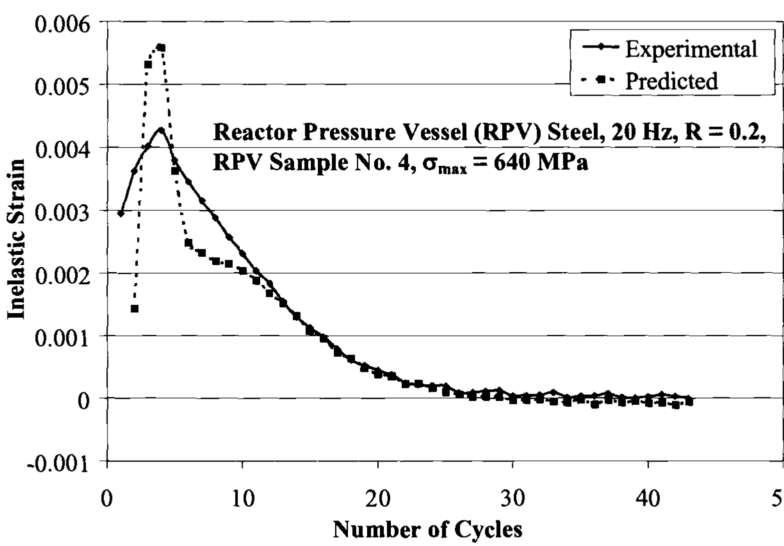

Figure 21 - *Experimental and Predicted Inelastic Strain versus Number of Cycles Results of Reactor Pressure Vessel Steel Tested at 20 Hz,* σ_{max} *= 640 MPa*

Thus, the inelastic strain that is generated in each hysteresis loop can be calculated by:

$$\varepsilon_{in_m} = \frac{\rho C_p (T_{m+1} - T_m)}{\sigma_{\max}} \tag{26}$$

In a stress (load)-controlled fatigue test, since the maximum stress is fixed, the elastic strain of each fatigue cycle is a constant too. Figure 21 represents the experimental and predicted inelastic strains during fatigue testing. The solid line is the experimental data, while the dashed line shows the predicted data. The experimental and predicted results are in reasonably good agreement. However, since the temperature for the first two cycles does not meet the theoretical model well in Figure 20, and the real stress was not very stable for the first 10 cycles, which has been discussed before. Thus, the predicted data do not fit the experimental data quite well for the first several cycles. However, after 10 cycles, both curves match each other well. And the trends of the two curves are similar: i.e., for the first 4 cycles, the inelastic strain increases, due to the yield-point phenomenon; and after 4 cycles, the inelastic strain decreases due to strain hardening.

A more thorough way in calculating the inelastic strain for each fatigue data point can be obtained by excluding the thermoelastic effect from the temperature-evolution through back calculation. The corresponding equation is shown below:

$$T'_{jc} = T_{jc} + KT_{jc}\sigma \tag{27}$$

where

T'_{jc} = temperature after the back calculation by excluding both the heat-conduction effect and the thermoelastic effect.

Figure 22 represents the back-calculated temperature evolutions excluding the heat-conduction and thermoelastic effects. The solid line shows the temperature evolution excluding the heat-conduction and the thermoelastic effects using Equations (24) and (27), the long dash line exhibits the temperature profile excluding the heat-conduction effect using Equation (24) and including the thermoelastic effect. Comparing these two curves shows that the solid line is higher than the short dash line because of the fact that the thermoelastic effect always intends to decrease the temperature in a tension-tension test. A close observation of the solid line shows that temperature fluctuation can not be 100% eliminated during each fatigue cycle, which is due to the simplification in the thermoelastic equation.

After the elimination of the thermoelastic effect, the inelastic strain can be calculated by the equation below:

$$\varepsilon_{in_j} = \frac{\rho C_p (T'_{(j+1)c} - T'_{jc})}{\sigma_{\max}} \tag{28}$$

where

ε_{in_j} = calculated inelastic strain for the j_{th} data point

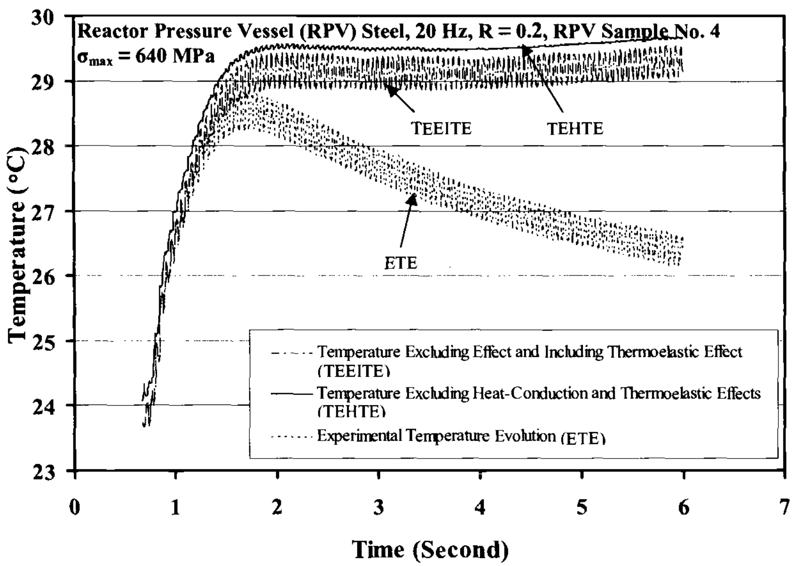

Figure 22 - *Back-Calculated Temperature Evolutions Excluding Heat-conduction and Thermoelastic Effects of Reactor Pressure Vessel Steel Tested at 20 Hz,* σ_{max} *= 640 MPa*

The prediction of the inelastic strain cycle by cycle has been shown to be quite accurate even after inelastic strain saturated. On the other hand, the prediction of the inelastic strain data by data depends on the elimination of the thermoelastic effect, which is difficult to be perfect. Thus, the deviation occurs when the inelastic strain decreases to nearly zero, and the number of cycles is large. However, this method provides a way to predict the evolution of the real hysteresis loops.

Combining the calculated stress, elastic strain, and inelastic strain, the predicted stress versus strain curve is shown in Figure 23. The solid line is the experimental stress versus strain curve, while the dashed line is the predicted one. Comparing the two curves shows that, similar to Figure 21, after 10 cycles, the predicted data fits the experimental result quite well. However, after thousands of cycles, the plastic strain of the predicted curve does not converge to the same upper limit as the experimental one, which is due to the accumulation of the small errors induced by the residual temperature fluctuation, represented by a solid line, during each fatigue cycle (Figure 22). The inelastic strain calculated from the residual temperature fluctuation could not totally cancel out because of the limited number of data points taken during each cycle. These errors can be neglected while the inelastic strain is obvious. However, the errors will cause problems when the inelastic strain is close to zero, and the number of cycles is large.

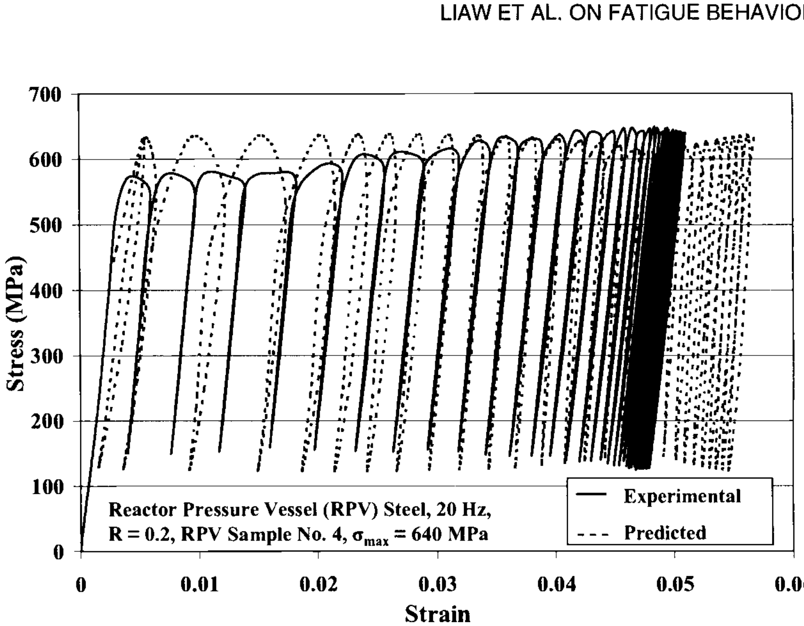

Figure 23 - Experimental and Predicted Stress versus Strain Results of Reactor Pressure Vessel Steel Tested at 20 Hz, σ_{max} = 640 MPa

Conclusion

Increasing the test frequency from approximately 10 Hz to 1000 Hz decreases the fatigue life of steels during load-controlled fatigue tests. The decrease of the fatigue life at higher frequencies results from the temperature increase of the sample subjected to higher-frequency tests. Thus, the effect of test frequency on the S-N curve can be explained by the temperature evolution during fatigue. This explanation is substantiated by the increase of the fatigue life using nitrogen-gas and mercury cooling of a sample during higher-frequency tests. It is suggested that in order to obtain a consistent S-N curve at various frequencies and at a given temperature, it is important to maintain the temperature of the samples, subjected to fatigue tests at different frequencies, at a fixed value.

The temperature evolution during fatigue testing without an outside heat source can be affected by three factors: (I) the thermoelastic effect, (II) the inelastic effect, and (III) the heat-conduction effect. Among them, the thermoelastic effect mainly contributes to the specimen temperature oscillation during each fatigue cycle, while the other two effects dominate the mean temperature change of the specimen. A theoretical model has been formulated to predict the temperature evolutions during fatigue testing.

Typical temperature evolution of the materials with the yield-point phenomenon during fatigue can be illustrated in Figure 15. It can be classified into five stages, as shown in the figure. Stage I represents the initial temperature increase due to the large plastic deformation and the yield-point phenomenon at the beginning of the test. This stage is dominated by the inelastic effect. Stage II corresponds to a gradual temperature decrease after the plastic deformation becomes saturated with strain hardening. This stage is dominated by the heat-transfer and strain-hardening effects. In stage III, the temperature reaches a constant value which presents an equilibrium state between the specimen and environment. Then, the temperature will rise up abruptly in stage IV, reflecting the rapid crack propagation before failure and the large plastic deformation in the crack-tip region. The specimen is broken at the highest point of the temperature, and the test terminated. Then, the specimen temperature drops down, as shown in stage V. Throughout the fatigue test except stage V, there is a temperature oscillation during each fatigue cycle due to the thermoelastic effect.

For the materials without the yield-point phenomenon, a four-stage temperature profile might be found: an initial temperature increase, a constant-temperature region, an abrupt temperature increase, and a final temperature drop [*28, 29*].

With the high-speed IR camera, the temperature oscillation during each fatigue cycle was recorded. For the first several fatigue cycles, when the stress decreases to a minimum, the strain reaches a minimum, the temperature increases to a maximum. When the stress increases to the yielding point, the strain continues to increase, and the temperature decreases to the minimum and will start to increase due to the heat associated with the plastic deformation resulting from the yielding phenomenon. When the stress increases to the maximum, the strain has not reached a maximum, and the temperature has already passed the lowest point. When the stress decreases to the yielding point, the strain increases to the maximum, and the temperature continues to increase. Furthermore, the back calculation based on the measured temperature to predict the stress-strain state can provide a new method to analyze and investigate the fatigue behavior by simply monitoring temperature evolutions.

Acknowledgment

We are very grateful to D. Fielden, J. T. Broome, J. R. Distefano, K. Farrell, D. C. Lousteau, S. J. Pawel, J. G. Yahr, T. T. Yang, and L. F. Lin for their great help and encouragement in the present work. Taiwan Power Company provided the major funding for this research project. It is also gratefully acknowledged regarding the financial support from the National Science Foundation (NSF), the Division of Design, Manufacture, and Industrial Innovation, under Grant No. DMI-9724476, the Combined Research-Curriculum Development (CRCD) Program, under EEC-9527527, and the Integrative Graduate Education and Research Training (IGERT) Program, under DGE-9987548, to the University of Tennessee (UT), Knoxville. This research was also financially supported by the Division of Materials Science and Engineering, Office of Basic Energy Sciences, U. S. Department of Energy, under contact DE-ACO5-00OR22725 with UT-Battelle, LLC, the U.S. Department of Energy Secretary for Energy Efficiency and Renewable Energy, and Office of Transportation Technologies, as part of the High Temperature Materials Laboratory User Program under contract DE-AC05-96OR22464, managed by Lockheed Martin Energy Research Corporation. In addition, appreciation goes to the financial support of the Institute of Nuclear Energy Research, Taiwan, Oak Ridge National Laboratory, and Southeastern Universities Research Association.

References

[1] Suresh, S., "Fatigue of Materials," Cambridge University Press, 1991.

[2] Logsdon, W. A., Liaw, P. K., and Begley, J. A., "Fatigue Crack Growth Rate Properties of SA508 and SA533 Pressure Vessel Steels and Submerged Arc Weldments in a Pressurized Water Environment," *ASTM STP 969*, American Society for Testing and Materials, West Conshohocken, PA, 1988, pp. 830-867.

[3] Liaw, P. K., Logsdon, W. A., and Begley, J. A., "Fatigue Crack-growth Behavior of Pressure-Vessel Steels and Submerged-arc Weldments in a High-temperature Pressurized Water Environment," *Metallurgical and Materials Transaction A*, Vol. 20, 1989, pp. 2069-2085.

[4] Liaw, P. K. and Logsdon, W. A., "The Influence of Load Ratio and Temperature on The Near-Threshold Fatigue Crack-Growth Rate Properties of Pressure-Vessel Steels," *Journal of Engineering Materials and Technology*, ASME, 107, 1985, pp. 26-33.

[5] Liaw, P. K., Yang, C. Y., Palusamy, S. S., and Ren W., "Fatigue crack initiation and propagation behavior of pressure vessel steels," *Engineering Fracture Mechanics*, Vol. 57, 1997, pp. 85-104.

[6] Logsdon, W. A. and Liaw, P. K., "Fatigue Crack-Growth Rate Properties of SA508 and SA533 Pressure-Vessel Steels and Submerged-arc Weldments in Room And Elevated-Temperature Air Environments," *Engineering Fracture Mechanics*, Vol. 22, 1985, pp. 509-526.

[7] Huang, J. Y., Chen, C. Y., Chien, K. F., Kuo, R. C., Liaw, P. K., and Huang, J. G., "Fatigue Behavior of Reactor Pressure Vessel Steels," Julia Weertman Symposium, The Minerals, Metals, and Materials Society (TMS), Chung, Y. W., Dunand, D., Liaw, P. K., and Olson, G., eds., Fall Meeting, October 31-November 4, 1999, pp. 373-384.

[8] Liaw, P. K., "Mechanisms of Near-Threshold Fatigue Crack-Growth in a Low-Alloy Steel," *Acta Metallurgica*, 33, 1985, pp. 1489-1502.

[9] Thomson, W., "On the Dynamical Theory of Heat," Transaction of Royal Society, Edinburgh, 20, 1853, pp. 261-283.

[10] Dillon, O. W., "Coupled Thermoplasticity," *Journal of Mechanics and Physics in Solids*, Vol. 11, 1963, pp. 21-23.

[11] Kratochvil, J. and Dillon, O. W., "Thermodynamics of Elastic-Plastic Materials as a Theory with Internal State Variables," *Journal of Applied Physics*, Vol. 40, No. 8, 1969, pp. 3207-3218.

[12] Henneke, E. G., Reifsnider, K. L., and Strinchcomb, W. W., "Thermography – An NDI Method for Damage Detection," *Journal of Metals*, 31, 1979, pp. 11-15.

[13] Blanc, R. H. and Giacometti, E., "Infrared Radiometry Study of the Thermomechanical Behavior of Materials and Structures," Paper presented at the First International Conference of Stress Analysis by Thermoelastic Technics, Sira Ltd., London, November 1984.

[14] Nayroles, B., Bouc, R., Caumon, H., Chezeaux, J. C., and Giacometti, E., "Telethermographie Infrarouge et Mecanique des Structures," *International Journal of Engineering and Science*, 19, 1981, pp. 929-947.

[15] Lohr, D. T., Enke, N. F., and Sandor, B. I., "Analysis of Fatigue Damage Evolution by Differential Infrared Thermography," Dynamic Failure: Proceedings of the 1987 SEM Fall Conference, October 25-27, 1987, Savannah, Georgia, pp. 169-174.

[16] Liaw, P. K., Wang, H., Jiang, L., Yang, B., Huang, J. Y., Kuo R. C., and Huang, J. G., "Thermographic Detection of Fatigue Damage of Pressure Vessel Steels at 1000 Hz and 20 Hz," *Scripta Materialia*, Vol. 42, 2000, pp. 389-395.

[17] Luong, M. P., "Short-time Measurement of Fatigue Limit of Metals Using Infrared Thermography," *Revue De Metallurgie-Cahiers D Informations Techniques*, Vol. 92, Iss (2), 1995, pp. 203-212.

[18] Jiang, L., Huang, M., Brooks, C. R., and Liaw, P. K., "Nondestructive Evaluation (NDE) and Materials Properties IV," TMS, Liaw, P. K., Arsenault, R. J., Green, R. E., Jr., Murty, K. L., and Thompson, R. B., eds., 1999, pp. 43-60.

[19] Fine, M. E., Connor, Z. M., and Achenbach, J. D., "Nondestructive Evaluation (NDE) and Materials Properties IV," TMS, P. K. Liaw, R. J. Arsenault, R. E. Green, Jr., K. L. Murty, and R. B. Thompson, eds., 1999, pp. 1-9.

[20] Birnbaum G., and Free, G., "Eddy-Current Characterization of Materials and Structures: a Symposium/Sponsored by ASTM Committee E-7 on Nondestructive Testing," American Society for Testing and Materials, Gaithersburg, Md., 5-7 Sept. 1979.

[21] Moss A. A. and Goldberg, H. I., "Computed Tomography, Ultrasound and X-ray: an Integrated Approach," Masson Publication, USA, 1979.

[22] Morgon, J. M. and Millison, W. W., "Symposium Proceedings in Honor of Professor Paul C. Paris," TMS, Soboyejo, W. O., and Srivatsan, T. S., eds., 1999, pp. 305-312.

[23] Tian, H., Broome, J. T., Liaw, P. K., Wang, H., Fielden, D., Jiang, L., Yang, B., Strizak, J. P., Mansur, L. K., DiStefano, J. R., Farrell, K., Lousteau, D. C., Pawel, S. J., and Yahr, G. T., "Influence of Mercury Environment on Fatigue Behavior of Spallation Neutron Source (SNS) Target Vessel Materials," *Materials Science and Engineering*, A314 (1-2), September 15 2001, pp. 140-149.

[24] Dieter, G. E., "Mechanical Metallurgy (3rd Edition)," pp. 197, McGraw-Hill Series in Materials Science and Engineering, McGraw-Hill, Inc.

[25] Biot, M. A., "Thermoelasticity and Irreversible Thermodynamics," *Journal of Applied Physics*, 27(3), March 1956, pp. 240-253.

[26] Rocca, R. and Bever, M. B., "The Thermoelastic Effect in Iron and Nickel as a Function of Temperature," *Transaction of American Institute of Mechanical Engineering*, 188, February 1950, pp. 327-333.

[27] Jiang, L., Wang, H., Liaw, P. K., Brooks, C. R., and Klarstrom, D. L., "Characterization of the temperature evolution during high-cycle fatigue of the ULTIMET superalloy: Experiment and theoretical modeling," *Metallurgical and Materials Transaction A*, 32(9), September 2001, pp. 2279-2296.

[28] Wang, H., Jiang, L., Liaw, P. K., Brooks, C. R., and Klasstrom, D. L., "Infrared temperature mapping of ULTIMET alloy during high-cycle fatigue tests," *Metallurgical and Materials Transaction A*, Vol. 31, 2000, pp. 1307-1310.

[29] Yang, B. Liaw, P. K., Wang, H., Jiang, L., Huang, J. Y., Kuo, R. C., and Huang, J. G., "Thermographic Investigation of the Fatigue Behavior of Reactor Pressure Vessel (RPV) Steels," *Materials Science and Engineering*, A314 (1-2), September 15 2001, pp. 131-139.

Ralph I. Stephens,[1] Robert R. Stephens,[2] and Dwight A. Schoenefeld[3]

Effect of Transient Loads on Fatigue Crack Growth in Mill Annealed Ti-62222 at -54, 25, and 175°C

Reference: Stephens, R. I., Stephens, R. R., and Schoenefeld, D. A., "**Effect of Transient Loads on Fatigue Crack Growth in Mill Annealed Ti-62222 at -54, 25, and 175°C**" *Fatigue and Fracture Mechanics: 33rd Volume, ASTM STP 1417,* W. G. Reuter and R. S. Piascik, Eds., ASTM International, West Conshohocken, PA, 2002.

Abstract: Transient loads consisting of single tensile overloads and single tensile overloads followed by single compressive underloads were applied to Ti-62222 mill annealed titanium alloy at -54, 25, and 175°C. Tensile overload ratios were 2.0 and 2.5 and the compressive underload ratio was -0.5. Four reference steady-state ΔK_{ss} values, using constant ΔK testing at $R = 0.1$, were investigated at each temperature. Cycles of delay, fatigue crack growth during delay, minimum fatigue crack growth rate, and crack extension during a transient load were obtained for all tests. Cycles of delay ranged from zero to crack arrest and mixed results often occurred making it difficult to draw many specific conclusions. Higher tensile overloads caused greater delay cycles and underloads were often detrimental compared to overloads only. Low temperature was mostly beneficial compared to room and high temperature that yielded similar delay. Crack growth delay distance was always greater than reversed plastic zone size. Macro- and microfractography revealed that surface crack closure, mode II displacements, crack tip blunting, branching, and tunneling, local state of stress, and residual compressive stresses contributed to the transient fatigue crack growth behavior.

Keywords: titanium alloy, fatigue crack growth, tensile overloads, compressive underloads, temperature, fractography

Aircraft subjected to subsonic and supersonic speeds experience both low and high outer skin temperatures and spectrum loading. Wing skin temperatures approach -54°C at subsonic flight and 175°C at supersonic flight. Load interaction or sequence effects are important when considering damage-tolerant aspects of fatigue crack growth, (FCG), since they have been shown to significantly affect FCG rates and consequently fatigue lives of engineering components and structures [*1-10*]. In addition, both high and low temperatures affect fatigue crack growth load interaction or sequence effects [*10-13*]. The

[1]Professor, Mechanical Engineering Dept., The University of Iowa, Iowa City, IA 52242.
[2]Associate Professor, Mechanical Engineering Dept., The University of Idaho, Moscow, ID 83843.
[3]Formerly Graduate Research Assistant, Mechanical Engineering Dept., The University of Iowa; currently with General Motors.

objective of this research is to provide fatigue crack growth response and evaluate micro/macro mechanisms for mill annealed Ti-62222 titanium alloy using axial loaded middle tension, M(T), specimens subjected to transient loads at -54, 25, and 175°C. The transient loads consisted of both single tensile overloads and single tensile overloads followed by single compressive underloads. The overload/underload ratios (OLR/ULR) were 2.0/0, 2.0/-0.5, 2.5/0, and 2.5/-0.5. These values are consistent with values found in ground-air-ground flight spectra.

Material

The material used in this research was a 1.61 mm thick sheet of alpha-beta Ti-62222 (Ti-6Al-2Sn-2Zr-2Mo-2Cr) titanium alloy in the mill annealed condition. The equiaxed grain size ranged from 5 to 10 μm and the room temperature (25°C) tensile yield strength, S_y, and ultimate tensile yield strength, S_u, were 1112 and 1162 MPa, respectively. Based upon other Ti-62222 material, tensile yield strengths at -54°C and 175°C were estimated as 1270 and 923 MPa respectively. Figure 1 shows constant-amplitude fatigue crack growth behavior at -54, 25, and 175°C. The figure shows FCG rate versus applied stress intensity factor range, ΔK, for R = 0.1 loading conditions using extended compact tension (EC(T)) specimens. In regions I and III, temperature effects are most notable, while in

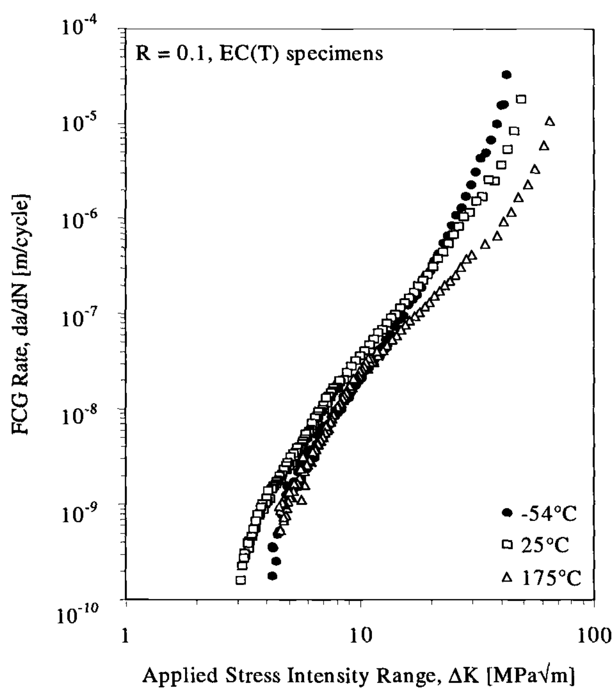

Figure 1 - *Fatigue crack growth behavior of mill annealed Ti-62222 at -54°C, 25°C, and 175°C. Obtained under R = 0.1 loading using EC(T) specimens.*

region II temperature effects are small. Threshold stress intensity factor values, ΔK_{th}, are between about 3 and 4 MPa$\sqrt{m}$, and FCG rates approach instability at approximately 40, 50, and 70 MPa$\sqrt{m}$ at -54, 25, and 175°C, respectively.

Test Procedures

All transient tests were performed with a computer controlled 100 kN electrohydraulic test system using constant ΔK procedures. M(T) specimens were 1.61 mm thick, 50.8 mm wide and 178 mm long and were tested in the L-T grain direction with clamped ends using hydraulic grips. Initial crack lengths were obtained by precracking at test temperature from EDM notches formed on each side of a drilled center hole. Three to seven transient loads were applied to each specimen with precracking involving load shedding between transient loads. Transient loads were applied at 2a/w between 0.25 and 0.66. Specimens were polished in the crack growth region for visual supplementary crack measurements, however, principal crack measurements were made using the compliance method according to ASTM Standard Test Method for Measurement of Fatigue Crack Growth Rates (E 647) with a centered clip gage. Specimens were also etched in the crack growth region for post-test scanning electron microscopy surface observations.

Figures 2 and 3 schematically show the transient loadings and nomenclature used in the test program. Steady-state ΔK_{ss} values of 4.4, 8.8, 13.2, and 17.6 MPa$\sqrt{m}$ with R = 0.1 were used with transient loads. From Fig. 1, this resulted in both region I and II steady-state FCG conditions. Steady-state FCG rates were approximately 10^{-9}, 10^{-8}, 5×10^{-8}, and 10^{-7} m/cycle, respectively, for the four different ΔK_{ss} values and represent typical da/dN rates found in practice. Sinusoidal steady-state fatigue cycling was performed at 20 Hz and transient loads were applied at 0.02 Hz. Between 9 and 15 data points were taken in the pre- and post-transient steady-state regions. Data points were taken every 0.04 mm of crack extension. Crack arrest was defined as 500 000 cycles of delay following a transient load with no measurable crack extension. In general, duplicate tests were performed for each transient condition. A few transient test conditions were not performed when it became evident that crack arrest would occur. Figure 4 shows a schematic transient load response and parameter definitions. b_1 and b_2 represent the pre- and post-steady-state FCG rates which were usually similar for a given test condition, N_d is the cycles of FCG delay caused by the transient load, a_d is the crack extension during delay, and a_s is the crack extension, or stretch that occurred during the transient loading. Note that a_s is not included in the determination of a_d.

All room temperature tests, 25°C, were performed in laboratory air, while low temperature tests, -54°C, were performed by enclosing the test specimen in a temperature chamber cooled by liquid nitrogen. A resistance thermal device was attached to the specimen to provide low temperature measurement and feedback to the coolant controller. All high temperature tests, 175°C, were performed in laboratory air with strip heating elements positioned above and below the crack plane.

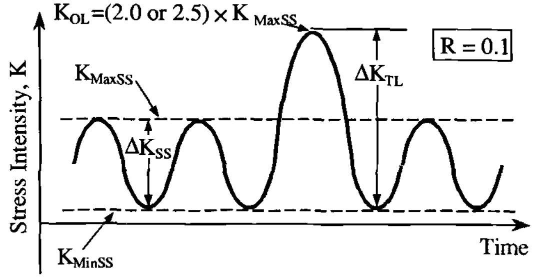

Figure 2 - *Transient load application schematic (without underload).*

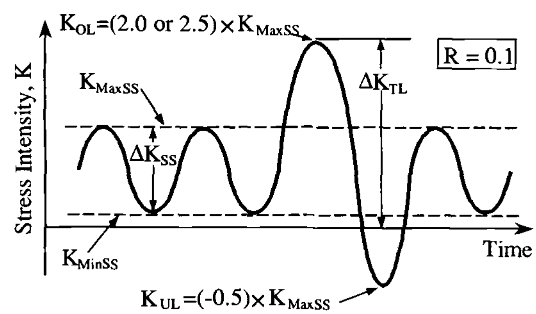

Figure 3 - *Transient load application schematic (with underload).*

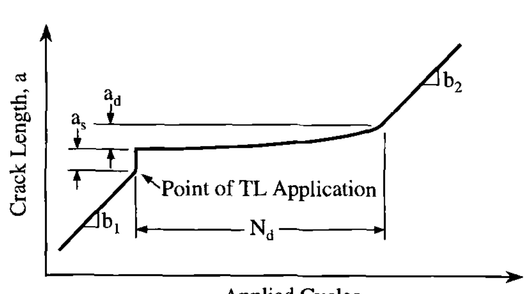

Figure 4 - *a versus N schematic illustrating transient load response parameter definitions.*

Results and Discussion

FCG Delay

The averages of duplicate tests for all transient test results are given in Table 1. This includes a_s, a_d, and N_d for each of the three temperatures based on the given ΔK_{ss} and OLR/ULR conditions. It is seen that a_s, as determined by compliance readings, varied from zero to 0.9 mm, a_d varied from zero to 0.32 mm, and N_d varied from zero to complete crack arrest depending on ΔK_{ss}, the transient event, and the test temperature. In general, duplication of transient tests resulted in variations in a_s, a_d, N_d and pre- or post-steady-state da/dN by less than a factor of about two for a given test condition. This variation was considered to be quite reasonable.

Typical a versus N duplicate test data are shown in Fig. 5 for ΔK_{ss} = 13.2 MPa√m at 175°C for all four transient load types. N = 0 represents the transient load application point. The small scatter in pre- and post-transient a versus N data for a given test condition is evident. The effect of the higher overload ratio of 2.5 as compared to 2.0 is evident in that significant delay cycles or usually crack arrest occurred for the higher overload. This is consistent with data in Table 1 where crack arrest occurred with the 2.5 overload for almost all conditions. The major exception is at ΔK_{ss} = 17.6 MPa√m with an overload of 2.5 at -54°C where fracture occurred during the overload. This fracture is realistic since

Table 1 – *Average Transient Test Results*

		T = -54°C			T = 25°C			T = 175°C		
ΔK_{SS} MPa√m	Transient Event *OLR/ULR*	a_s, mm	a_d, mm	N_d, cycles	a_s, mm	a_d, mm	N_d, cycles	a_s, mm	a_d, mm	N_d, cycles
	2.0/-0.5	0.16	0.00	0	0.00	Arrest	>500 000[a]	0.00	Arrest	>500 000
4.4	2.0/0.0	0.06	0.06	183 500	0.03	Arrest	>500 000	–	–	– b
	2.5/-0.5	0.26	Arrest	>500 000	–	–	– b	–	–	– b
	2.5/0.0	0.12	Arrest	>500 000	–	–	– b	–	–	– b
	2.0/-0.5	0.00	0.05	14 750	0.00	0.07	10 000	0.00	0.09	27 500
8.8	2.0/0.0	0.02	0.07	36 500	0.01	0.10	17 250	0.00	0.10	29 500
	2.5/-0.5	0.18	Arrest	>500 000	0.00	Arrest	>500 000	0.00	Arrest	>500 000
	2.5/0.0	0.20	Arrest	>500 000	0.01	Arrest	>500 000	0.00	Arrest	>500 000
	2.0/-0.5	0.31	0.17	30 250	0.02	0.32	13 700	0.03	0.13	8850
13.2	2.0/0.0	0.33	0.11	68 500	0.11	0.26	29 750	0.00	0.13	13 150
	2.5/-0.5	0.55	Arrest	>500 000	0.20	Arrest	>500 000	0.00	0.24	63 750
	2.5/0.0	0.58	Arrest	>500 000	0.24	Arrest	>500 000	0.00	Arrest	>500 000
	2.0/-0.5	0.90	0.22	40 750	0.47	0.24	16 300	0.00	0.23	8650
17.6	2.0/0.0	0.82	0.21	>210 000	0.34	0.21	42 600	0.07	0.22	11 350
	2.5/-0.5	–	–	– b	0.59	Arrest	>500 000	0.05	0.27	77 500
	2.5/0.0	Fract	Fract	Fractured	0.42	Arrest	>500 000[a]	0.02	0.14	>342 000

[a]Data represents a single test

[b]Removed from test program based on earlier test results

K_{max} = 48.9 MPa√m during the 2.5 overload and fracture instability occurred in the reference -54°C da/dN-ΔK R = 0.1 data in Fig. 1 at about ΔK = 40 MPa√m ($K_{max} \cong$ 44 MPa√m). Also evident in Fig. 5 is that the underload following the overload decreased delay cycles. This occurred with the overload ratio of 2.0 for all ΔK_{ss} values and all temperatures. The underload had little influence on the crack extension, a_s, during a transient event, since this is primarily controlled by the tensile overload.

Figure 6 shows the average da/dN versus a curves associated with Fig. 5. Scatter is increased in the figure due to the secant method used for reduction of data. da/dN following the transient loads is shown to decrease by up to two orders of magnitude. The largest decrease occurred with only the tensile overload and the highest overload ratio. The underload following an overload caused a smaller change in the minimum da/dN. This was typical for all overload and underload transient loads. The minimum da/dN for all tests occurred at less than 0.05 mm of crack extension.

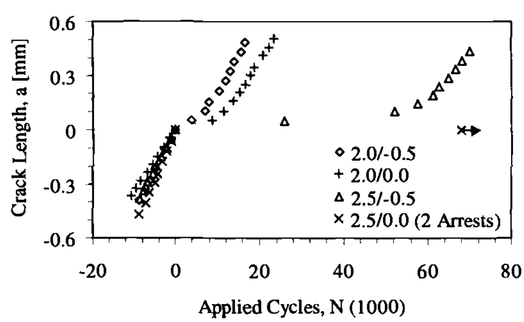

Figure 5 - *Crack length vs. applied cycles:*
ΔK_{SS} = 13.2 MPa√m, T = 175°C, average of two tests.
Zero Reference: Point of transient load application.

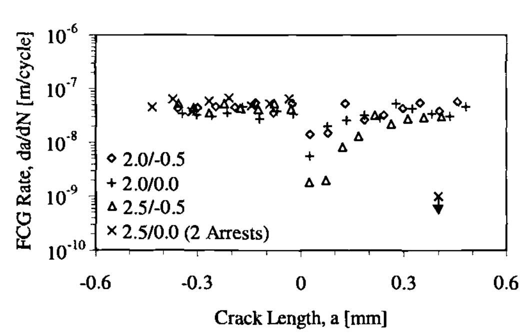

Figure 6 - *Crack growth rate vs. crack length:*
ΔK_{SS} = 13.2 MPa√m, T = 175°C, average of two tests.
Zero Reference: Point of transient load application.

Even though Table 1 includes all the pertinent transient loading results, it does not identify the key trends. Thus, Figs. 7 to 9 have been provided to better evaluate the key parameters a_s, a_d, and N_d as a function of ΔK_{ss} and temperature. These figures are for OLR/ULR = 2.0/0 only; however, OLR/ULR = 2.0/-0.5 resulted in essentially the same trends. The 2.5 tests caused mostly crack arrest or fracture and hence do not provide significant trends.

The stretch distance, a_s, as measured by compliance, increased with higher ΔK_{ss}, higher overload, and lower temperature as shown in Fig. 7 and Table 1. As will be seen in the fractographic section, the stretch zone involved significant crack tunneling that was not brought out in the compliance measured stretch distance values. Only small or no stretch occurred with ΔK_{ss} = 4.4 and 8.8 MPa√m while significant amounts of stretch occurred at the two higher values of ΔK_{ss}. At these higher ΔK_{ss} values the stretch relative to those at room temperature increased significantly at the low temperature and decreased significantly at the high temperature. This is best brought out in Fig. 7. In fact, very little stretch occurred with the high temperature tests. Crack arrest occurred with most 2.5 overload ratios, accompanied by substantial stretch at -54 and 25°C during the overload with values of a_s between 0.01 to 0.59 mm as given in Table 1. Stretch zone size increase with decreasing temperature was consistent with FCG instability dependence on temperature as shown in Fig.1, where as previously mentioned, instability occurred with ΔK for R = 0.1 at approximately 40, 50, and 70 MPa√m for -54, 25, and 175°C respectively.

The fatigue crack growth delay distance, a_d, following a transient load is shown in Fig. 8 and Table 1 to range from zero to 0.32 mm. No a_d measurements occurred for conditions of crack arrest and little differences existed between overload values and overload followed by underload values. These differences are attributed to most of the delay cycles occurring within the first 0.05 mm of crack growth following a transient load. Thus, while underloads caused decreased delay cycles, they had little influence on delay distance. Also, in most cases temperature did not have a significant effect on a_d for a given ΔK_{ss}, however a_d tended to increase with an increase in ΔK_{ss}. Thus, the delay cycles were controlled by crack growth in the first 0.05 mm of crack growth rather than by the crack growth delay distance.

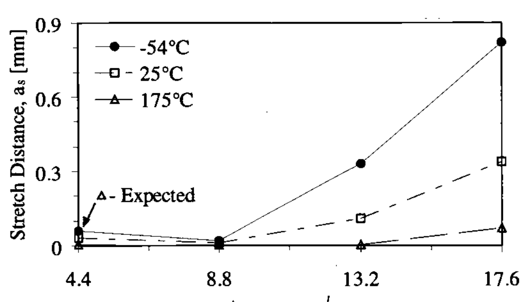

Figure 7 - *Average stretch distance, a_s, vs. ΔK_{SS}, OLR/ULR = 2.0/0.0.*

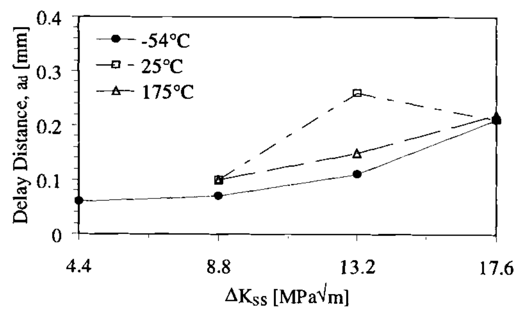

Figure 8 - *Average delay distance, a_d, vs. ΔK_{ss}, OLR/ULR = 2.0/0.0.*

Figure 9 and Table 1 indicate mixed results for delay cycles, N_d, as a function of ΔK_{ss}, transient loading, and temperature. Since transient loads involving the 2.5 overload magnitude in general caused crack arrest or fracture, little can be compared for these conditions except underloads following the overloads showed no discernable difference as crack arrest still occurred and temperature was not significant unless the overload exceeded the pertinent fracture toughness. For the 2.0 tests, the underloads at each temperature decreased delay life by factors of around two with a much larger value in one case at -54°C. Also for 2.0 tests, Fig. 9 shows the low temperature was slightly beneficial in most cases yet detrimental at ΔK_{ss} = 4.4 MPa$\sqrt{m}$. The high temperature and room temperature results were similar in most cases. Delay cycles for 2.0 tests showed some dependency on ΔK_{ss}, with greater delay cycles at the highest and lowest values of ΔK_{ss}.

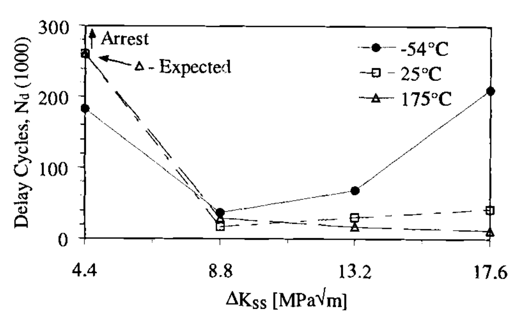

Figure 9 - *Average delay cycles, N_d, vs. ΔK_{SS}, OLR/ULR = 2.0/0.0.*

Plastic Zone Size Correlation with a_d

Plastic zone sizes corresponding to steady-state and transient load levels were calculated using LEFM. However, before such calculations could be made, the stress state related to each of the load levels and specimen geometry had to be determined. Specimen and loading combinations were assumed to be either plane stress or plane strain. No mixed-state assumptions were made. Equation 1 from ASTM standard E647 was used to determine plane strain conditions. If a given set of test conditions violated this criterion, the test was assumed to be associated with plane stress.

$$B, a, (w/2\text{-}a), h \geq 2.5(K/S_y)^2 \tag{1}$$

In Eq.1, B is the specimen thickness, a is the fatigue crack length, (w/2-a) is the uncracked ligament, h is the half-height of the ungripped portion of the specimen, K is the stress intensity factor associated with the applied load, and S_y is the material yield strength for a given temperature. K_{max} values associated with steady-state and transient load levels were used for K in the plane strain criterion calculations. If the plane strain criterion was satisfied, LEFM plastic zone size restrictions were automatically satisfied. Plain strain occurred for all steady-state loading conditions. When the plane strain criterion was not satisfied during transient loadings, Eq. 2 was used to ensure that LEFM assumptions were valid. All loadings satisfied this LEFM criterion.

$$a, (w/2\text{-}a), h \geq (4/\pi)(K/S_y)^2 \tag{2}$$

Monotonic plastic zone size, $2r_y$, and reversed plastic zone size, $2r'_y$, were calculated using Eqs. 3 or 4.

$$\text{for plane stress: } 2r_y = (1/\pi)(K/S_y)^2 \qquad 2r'_y = (1/\pi)(\Delta K/2S_y)^2 \tag{3}$$

$$\text{for plane strain: } 2r_y = (1/3\pi)(K/S_y)^2 \qquad 2r'_y = (1/3\pi)(\Delta K/2S_y)^2 \tag{4}$$

K_{MaxSS} and K_{OL}, defined in Figs. 3 and 4, were used to calculate $2r_y$, while ΔK_{TL} also defined in Figs. 2 and 3, was used to calculate $2r'_{y,TL}$. Steady-state monotonic plastic zone sizes were all under plane strain conditions and ranged from 0.002 to 0.05 mm. Transient reversed plastic zone sizes under plane strain conditions varied from 0.001 to 0.014 mm while those under plane stress conditions varied from 0.05 to 0.22 mm.

Table 2 gives ratios that compare average delay distances with the corresponding calculated transient load reversed plastic zone for tests that resulted in post-transient load FCG. These ratios are denoted $a_d/2r'_{y,TL}$ and are often assumed to be 1 in fatigue crack growth retardation life prediction models. In Table 2, ratios that involve plane strain plastic zone sizes are shown in standard print, and ratios that involve plane stress are shown in bold print.

Table 2 shows $a_d/2r'_{y,TL}$ ratios that involved plane strain plastic zones varied from 0 to 60, but these two extremes are significant outliers that occurred only at low temperature and $\Delta K_{ss} = 4.4$ MPa$\sqrt{m}$. The remaining ratios involving plane strain varied from 7.5 to 13.2. That is, the average delay distance for these conditions were 7.5 to 13.2 times larger than the applicable plane strain reversed plastic zone size. For tests associated with plane stress conditions, the average delay distances were only 1.2 to 5.8 times larger than the applicable plane stress reversed plastic zone size. These results distinctly show a better correlation (closer to the value of 1) with tests associated with plane stress conditions.

Table 2 – *Ratios of the Average Delay Distances to the Transient Load Event Reversed Plastic Zone Sizes ($a_d/2r'_{y,TL}$)*

		ΔK_{SS}, MPa$\sqrt{m}$			
Temp, °C	OLR/ULR	4.4	8.8	13.2	17.6
-54	2.0/-0.5	0.0	8.3	12.1	**2.9***
	2.0/0.0	60.0	11.7	8.5	**3.0**
25	2.0/-0.5	Arrest	8.8	**5.8**	**2.4**
	2.0/0.0	Arrest	14.3	**5.2**	**2.4**
	2.0/-0.5	Arrest	7.5	**1.6**	**1.6**
175	2.0/0.0	Arrest	9.1	**1.8**	**1.7**
	2.5/-0.5	Arrest	Arrest	**1.9**	**1.2**

* standard print represents plane strain transient conditions and bold print represents plane stress transient conditions

For a given state of stress, plastic zone sizes (Eqs. 3 and 4) are proportional to $(1/S_y)^2$. Thus, for a given state of stress, $2r_y'_{TL}$ values at -54°C were about 3/4 that at 25°C, while at 175°C they were about 1.5 times larger than at 25°C. These ratios were valid for all transient test conditions except at ΔK_{ss} = 13.2 MPa$\sqrt{m}$ where plane strain existed at -54°C and plane stress existed at 25 and 175°C. This gives even a smaller value of $2r_y'_{TL}$ at -54°C for these tests. Since delay cycles at 25 and 175°C were reasonably similar or mixed for a given test condition, and delay cycles at -54°C were usually slightly longer than at the other two temperatures, this implies that reversed plastic zone size, $2r_y'_{TL}$, was not a consistent indication of delay in these tests.

Fractography

Fractographic analysis using scanning electron microscopy was made for many of the transient loadings. This analysis included macroscopic study of surface profiles and both macro- and microscopic study of fracture surfaces In all macro- or micrographs that follow, the fatigue crack growth is from left to right and the nominal plane of crack growth is perpendicular to the applied load, which is the plane of the maximum normal tensile stress.

Figure 10 shows fatigue crack profiles for ΔK_{ss} = 13.2 MPa$\sqrt{m}$ with OLR/ULR = 2.0/0.0 at the three test temperatures. Findings in Fig. 10 are typical and were seen with other transient conditions. Under all conditions, fatigue crack growth before and after a transient load was transcrystalline as observed from both surface crack profiles and fracture surface morphology. In Fig. 10, transient load applications are noted with arrows. In all cases, no surface crack closure is evident in the pre-transient fatigue region. However surface mode II displacement can be seen as labeled in Fig. 10(b). Surface crack tip blunting occurred following some transient loads. No surface crack extension (stretch)

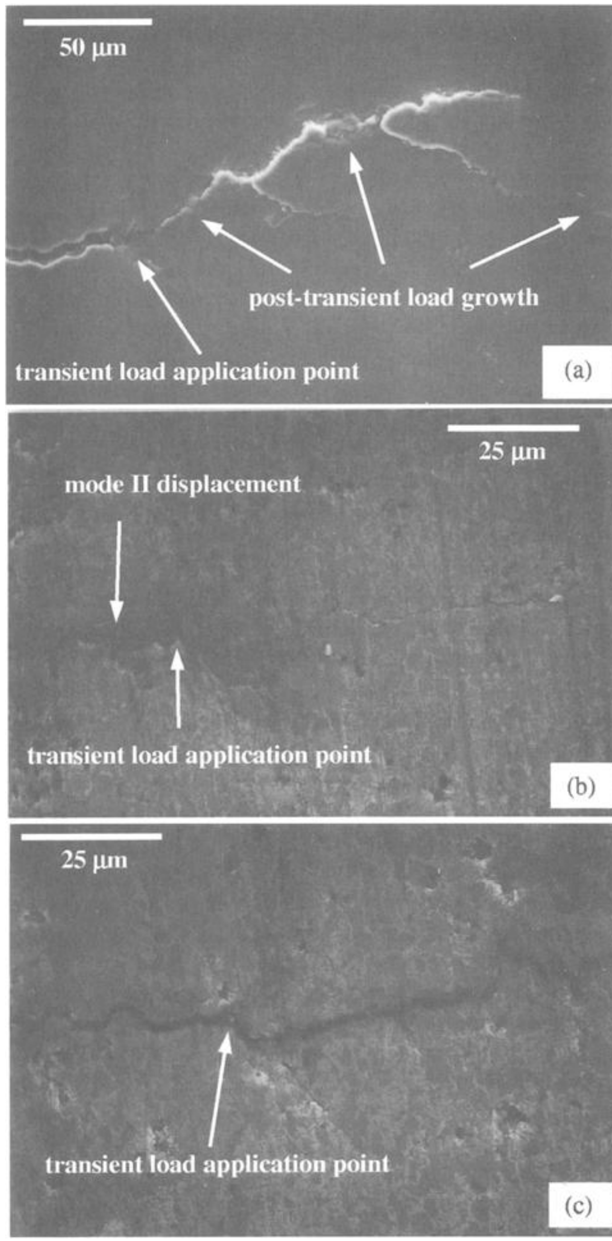

Figure 10 - *ΔK_{ss} = 13.2 MPa$\sqrt{m}$, OLR/ULR = 2.0/0.0, Fatigue crack profile. (a) -54 °C, (b) 25 °C, (c) 175 °C.*

during a transient loading was noted using a 30X traveling microscope for any of the test conditions. Surface crack closure following the transient load is present at all temperatures in Fig. 10 along with initial crack deflections of about 45°. These deflections occurred for about 10 to 50 μm, a few grain sizes, before another significant angle change occurred. This surface deflection behavior was common for all tests. Significant surface crack branching following the transient load is seen in Fig. 10(a) for -54°C. This surface branching was also evident with other -54°C and 25°C tests. No surface branching was evident for the 175°C tests.

Macro fracture surfaces showing typical stretch zones during transient loading are shown in Fig. 11. Stretch zones were usually rough or granular in texture and increased in size with higher ΔK_{ss}, higher overload, and lower temperature. Figure 11 applies to the same transient loads used for surface profiling in Fig. 10, however, Fig. 11(a) contains an additional stretch zone to the right in the macrograph at -54°C for OLR/ULR = 2.0/-0.5. Figure 11(a) indicates similar stretch zone behavior occurred for both overload only and overload followed by underload. Figure 11(a and b) indicates significant crack tip tunneling with zero stretch at the two free surfaces, as indicated in Fig. 10, and maximum stretch at the mid thickness. Also shown in Fig. 11 is the significant increase in stretch at the low temperature and the decrease in stretch at high temperature for a given transient load. The stretch zone in Fig. 11(c) resembles more of a beach mark. It is quite obvious here why the average stretch, a_s, as measured by compliance, does not agree with the maximum stretch. Of interest here is that the cycles of delay, N_d, for Fig. 11 transient loading were about 70 000, 30 000, and 13 000 cycles and crack tunneling during the transient loading was 0.7, 0.2, and 0 mm for the low, room, and high temperature respectively. Thus, an increase in delay cycles corresponded to an increase in crack tunneling and stretch zone size. Also at -54°C the transient loading involved plane strain while at the other two temperatures plane stress existed. These results indicate the importance of both crack tip tunneling and state of stress within the crack tip region on delay cycles.

Figure 12 shows five typical fractographs involving mid thickness fracture surface morphology from the loadings used in Figs. 10 and 11. Figure 12(a) is the -54°C steady-state region before the transient loading, while Figs. 12(b to e) include portions of the stretch zone and crack growth region immediately following the transient load. Under all test conditions, no striations were seen before or after a transient load, and stretch zones were characterized by ductile dimples. Steady-state regions were characterized by elongated flat plateaus, with or without features, separated by ridges primarily parallel to the fatigue crack growth direction along with isolated secondary cracking. Plateaus containing features indicate less rubbing and less crack closure. Figures 12(b and c) indicate a difference in fatigue crack growth morphology following the transient load. Fig. 12(b) is for an overload only and Fig. 12(c) includes an underload following the overload. The underload caused a region of flat featureless plateaus indicating greater rubbing or material compaction occurred due to the underload. In some regions following the transient load, a transition region of more featureless plateaus or cleavage like facets occurred, but as the crack grew approximately 25 μm the crack surface appearance returned to that of the pre transient steady-state condition. In some cases this transition region did not exist. The transition region was always significantly less than the crack

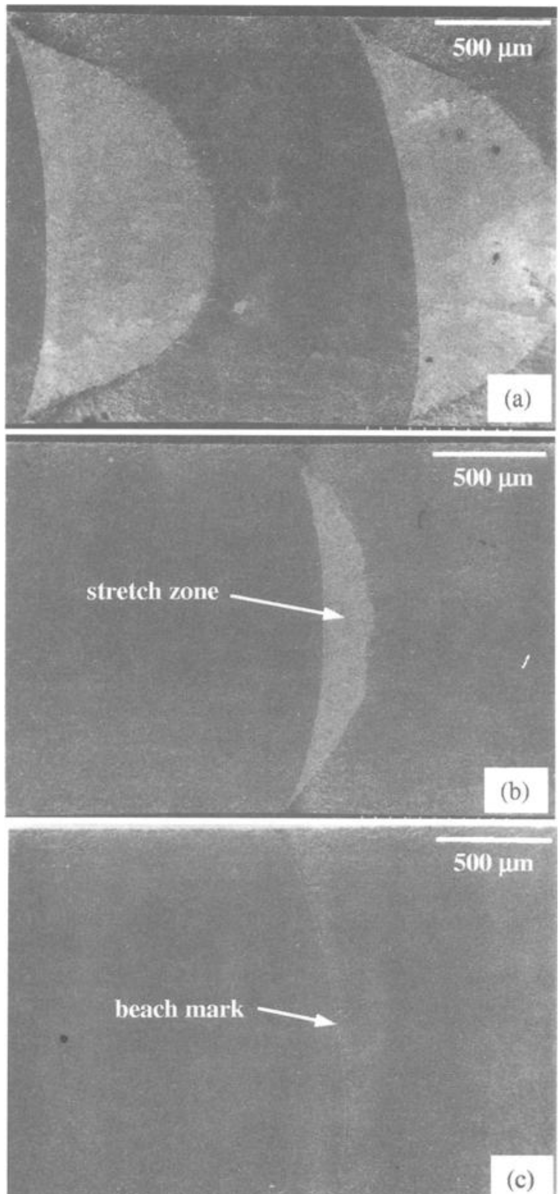

Figure 11 - *ΔK_{ss} = 13.2 MPa$\sqrt{m}$, transient fatigue crack growth region.*
(a) OLR/ULR = 2.0/0.0 and 2.0/-0.5, -54°C, (b) OLR/ULR = 2.0/0.0, 25°C,
(c) OLR/ULR = 2.0/0.0, 175°C

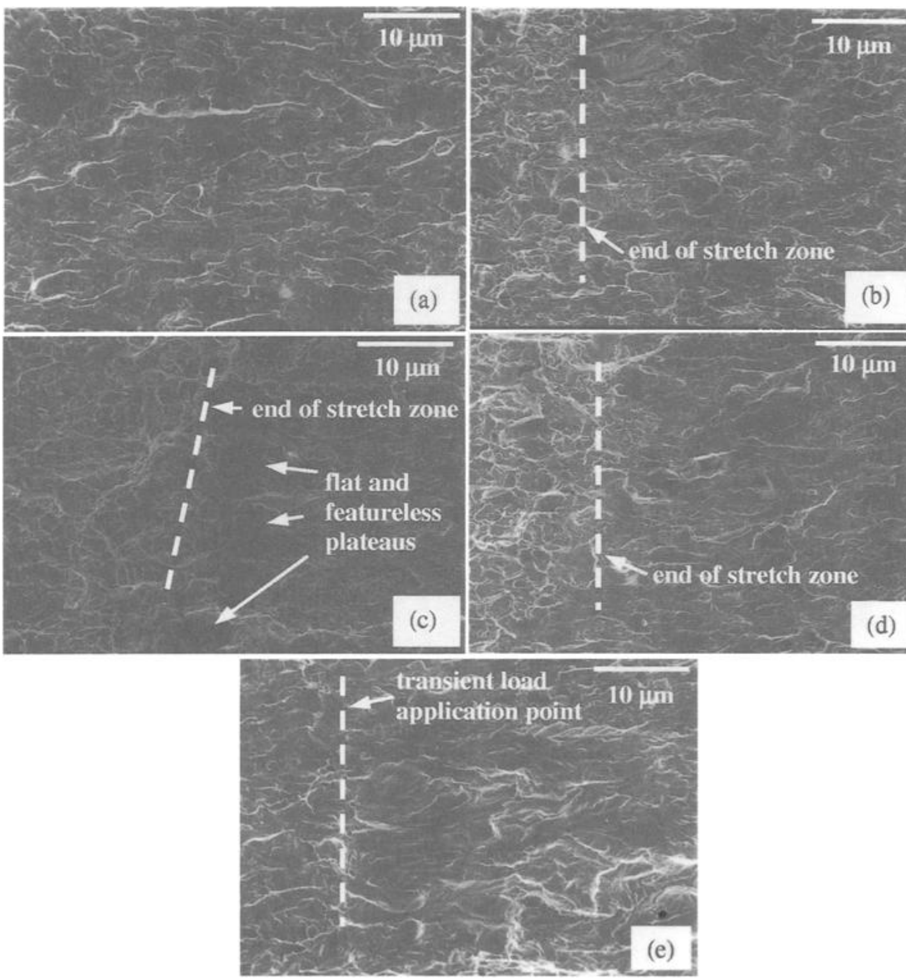

Figure 12 - *ΔK_{ss} = 13.2 MPa$\sqrt{m}$, fracture surface at specimen mid-thickness. (a) T = -54 °C, steady-state fatigue crack growth fracture surface, (b) OLR/ULR= 2.0/0.0, T = -54 °C, transition region, (c) OLRULR = 2.0/-0.5, T = -54 °C, transition region, (d) OLR/ULR = 2.0/0.0, T = 25 °C, transition region, (e) OLR/ULR = 2.0/0.0, T = 175 °C, transition region.*

delay length a_d.

The above morphology suggests multiple mechanisms, that alter the effective stress intensity factor, were involved in the transient behavior observed and these multiple mechanisms were active under different test conditions. These would include crack closure observed on the surface, along with rubbing at the interior, crack tip blunting and branching observed at the surface, crack tip state of stress as altered by crack tip geometry, residual compressive stress at the crack tip, and crack tip tunneling.

Summary and Conclusions

1. Fatigue crack growth response to a transient load was dependent upon ΔK_{ss}, OLR/ULR, and temperature. Specific trends, however, were often mixed making it difficult to draw specific conclusions.
2. Delay cycles, N_d, increased with the overload ratio, but an underload following an overload tended to decrease delay life.
3. Delay cycles, N_d, for a given transient load were usually greater at -54°C and more similar for 25°C and 175°C.
4. Delay cycles, N_d, were greater at the lowest (near threshold) values of ΔK_{ss} and the highest value of ΔK_{ss} where K_{max} approached instability conditions.
5. Stretch zones due to transient loading often experienced significant tunneling that increased with OLR and ΔK_{ss}. Stretch zone size also increased at -54°C but decreased at 175°C. Greater delay cycles accompanied the larger stretch zones.
6. A 1:1 correlation between measured average delay distance, a_d, and reversed plastic zone size, $2r'_{y,TL}$, was not evident, since delay distances were usually much larger than the reversed plastic zone. $2r_y'_{,TL}$ by itself was also not a consistent indication of delay cycles, since most of the delay cycles occurred within about 0.05 mm of crack growth following a transient event.
7. Minimum FCG rates following a transient loading were 1 to 2 orders of magnitude lower than steady-state rates. Underloads following an overload produced smaller changes.
8. Surface crack profiling revealed transcrystalline FCG only, mode II displacements, no crack closure before transient loadings, and crack closure, crack tip deflection, blunting and branching after transient loadings. Fractographic evaluation indicated no striations plus elongated plateaus with or without features separated by ridges primarily parallel to the FCG direction, and isolated secondary cracking. Stretch zones contained ductile dimples. These fractographic findings indicate multiple mechanisms are involved with this transient behavior and include local state of stress, residual compressive stresses, crack closure, crack tip tunneling, blunting and branching.

References

[1] Ward-Close, C. M., Blom, A. F., and Ritchie, R. O., "Mechanisms Associated with Transient Fatigue Crack Growth Under Variable Amplitude Loading: An

Experimental and Numerical Study," *Engineering Fracture Mechanics*, Vol. 32, No. 4, 1989, pp. 613-638.

[2] von Euw, E. F. J., Hertzberg, R. W., and Roberts, R., "Delay Effects in Fatigue Crack Propagation," *Stress Analysis and Growth of Cracks, ASTM STP 513*, American Society for Testing and Materials, West Conshohocken, PA, 1972, pp. 230-259.

[3] Suresh, S., "Micromechanisms of Fatigue Crack Growth Retardation Following Overloads," *Engineering Fracture Mechanics*, Vol. 18, No. 3, 1983, pp. 577-593.

[4] Stephens, R. I., Chen, D. K., and Hom, B. W., "Fatigue Crack Growth with Negative Stress Ratio Following Single Overloads in 2043-T3 and 7075-T6 Aluminum Alloys," *Fatigue Crack Growth Under Spectrum Loads, ASTM STP 595*, American Society for Testing and Materials, West Conshohocken, PA, 1976, pp. 27-40.

[5] Pandey, R. K. and Verma, B. B., "Overload Induced Fatigue Crack Growth and Significance of Retardation Zone," *Advances in Fracture Research: Fatigue of Metallic and Non-Metallic Materials and Structures*, B. L. Karhaloo, M. I. Ripley, and R. O. Ritchie, Eds., Pergamon Press, New York, 1997, pp. 1285-1296.

[6] Jones, R. E., "Fatigue Crack Growth Retardation After Single-Cycle Peak Overload in Ti-6Al-4V Titanium Alloy," *Engineering Fracture Mechanics*, Vol. 5, 1973, pp. 585-604.

[7] Elber, W., "The Significance of Fatigue Crack Closures," *Damage Tolerance in Aircraft Structures, ASTM STP 486*, American Society for Testing and Materials, West Conshohocken, PA, 1971, pp. 230-242.

[8] Carlson, R. L., Kardomateas, G.A., and Bates, P.R., "The Effects of Overloads in Fatigue Crack Growth," *International Journal of Fatigue*, Vol. 13, No. 6, 1991, pp. 453-460.

[9] Bathias, C., and Vancon, M., "Mechanisms of Overload Effect on Fatigue Crack Propagation in Aluminum Alloys," *Engineering Fracture Mechanics*, Vol. 10, 1978, pp. 409-424.

[10] Stephens, R. I., Fatemi, A., Stephens, R. R., and Fuchs, H. O., *Metal Fatigue in Engineering*, 2nd Edition, Wiley Interscience, New York, 2000.

[11] Bray, G. H. and Starke, E. A., Jr., "The Effect of Elevated Temperature Exposure on Fatigue Crack Growth Retardation," *Scripta Metallurgica*, Vol. 27, 1992, pp. 593-598.

[12] Pettit, D. E. and Van Orden, J. M., "Evaluation of Temperature Effects on Crack Growth in Aluminum Sheet Material," *Fracture Mechanics, ASTM STP 677*, C. W. Smith, Ed., American Society for testing and Materials, West Conshohocken, PA, 1979, pp. 106-124.

[13] Stephens, R. R., Stephens, R. I., Lemm, D. E., Berge, S. C., Liknes, H. O., and Cousins, C. J., "Role of Crack Closure Mechanisms on Fatigue Crack Growth of Ti-62222 Under Constant Amplitude and Transient Loading at -54°C, 25°C, 175°C," *Advances in Fatigue Crack Closure Measurement and Analysis, ASTM STP 1343*, R. C. McClung and J. C. Newman, Jr., Eds., American Society for Testing and Materials, West Conshohocken, PA, 1999, pp. 224-245.

William T. Riddell[1], Anthony R. Ingraffea[2] and Paul A. Wawrzynek[3]

Propagation of Non-Planar Fatigue Cracks: Experimental Observations and Numerical Simulations

Reference: Riddell, W. T., Ingraffea, A. R. and Wawrzynek, P. A., "**Propagation of Non-Planar Fatigue Cracks: Experimental Observations and Numerical Simulations,**" *Fatigue and Fracture Mechanics: 33rd Volume, ASTM STP 1417*, W. G. Reuter and R. S. Piascik, Eds., ASTM International, West Conshohocken, PA, 2002.

Abstract: Two types of mixed-mode fatigue crack growth tests are described. Experimental observations of non-planar fatigue crack growth are compared with numerical predictions from the computer code, FRANC3D. In these analyses, the evolution of crack shape is not assumed *a priori*. The code predicts evolving fatigue crack shapes and fatigue crack growth rates based on linear-elastic mixed-mode stress-intensity factor distributions along the evolving crack fronts. The simulations are shown to result in accurate crack front shape predictions, and to predict overall fatigue crack life in a reasonable and/or conservative manner.

Keywords: three-dimensional, non-planar, mixed-mode, fracture mechanics, fatigue life, experimental, numerical, fatigue crack

Many aspects of using fracture mechanics to predict fatigue life are more complicated in practice than in standard laboratory test configurations, textbook examples, or overly-simplified computer programs. The effects of load spectrum [*1*], threshold [*1*], environmental conditions [1, 2], microstructure [*1, 3*], small cracks [*1, 4*], and complex three-dimensional geometry [*5, 6*] all complicate the process of predicting fatigue crack growth in real world applications. This paper focuses on the last of these complications.

Modeling three-dimensional crack growth is inherently more complicated than its two-dimensional counterpart. Three-dimensional crack growth is described by an evolving three-dimensional surface, whereas two-dimensional crack growth is described by elongation of a line. Stress-intensity factors for all three modes [*7*] can vary along a

[1] US DOT/Volpe National Transportation Systems Center, DTS 76, 55 Broadway, Cambridge, MA 02142.
[2] Baum Professor of Civil and Environmental Engineering, Cornell University, 641 Rhodes Hall, Cornell University, Ithaca, NY 14853.
[3] Cornell Fracture Group, 641 Rhodes Hall, Ithaca, NY 14853.

three-dimensional crack front, whereas only two stress-intensity factors are defined at the tip of a crack in a two-dimensional body with in-plane loads. Previous research has evaluated numerical techniques for predicting planar, Mode I fatigue crack growth in a variety of three-dimensional configurations [*8*]. The next step in the complexity of modeling is non-planar, mixed-mode fatigue crack growth. Here, the effects of Modes I, II and III stress-intensity factors must be considered.

Two types of mixed-mode fatigue crack growth test configurations are considered in this paper: type 1 is a penny-shaped surface crack, type 2 is a through crack. In both configurations, initial notches were cut at angles to the direction of maximum far-field principal stress to induce mixed-mode loading. Crack growth for these tests is predicted using FRANC3D [*9*]. In this code, fatigue crack growth can be modeled without assuming the crack shape evolution *a priori*. Both the numerically predicted crack shape and fatigue life are compared to experimental observations, to assess whether non-planar, mixed-mode fatigue crack growth can be predicted accurately using current simulation techniques.

Experiments

A fatigue test on a mixed-mode surface-crack configuration [*10*] manufactured from forged aluminum alloy 2219-T351, denoted type 1, was performed and numerically simulated. The geometry, and boundary conditions for this test are shown in Figure 1. The semi-circular initial notch was cut by electro-spark discharge machining (EDM). The radius of the semi-circle was 6.4 mm, with a width of 0.5 mm. The notch was not pre-cracked. Cyclic constant amplitude loads of $\Delta p = 51.33$ kN, $R = 0.214$ were applied to the specimen. Crack initiation from the notch was observed by 5000 cycles. Initiation was neglected in the analysis and discussion of the test, as it accounts for less than 3% of the duration of the test. Two transitions are defined in this test. The first transition occurs when crack-tip 1 reaches edge A, as defined in Figure 1. The second transition occurs when crack-tip 2 reaches edge B. Cyclic loads were applied until the second transition occurred. Crack lengths a_1, a_2 and a_3 are based on projections onto the center plane of the specimen. Crack lengths a_1 and a_2 are defined as the distances along the free surfaces of the specimen from the center of the initial notch to the respective crack-tips. These definitions result in continuous crack lengths as the specimen transitions from surface-crack to corner-crack to through-crack configurations. Crack lengths a_1 and a_2, and out-of-plane measurements c_1 and c_2 were measured optically along the free surfaces throughout the test using a long-focal-length microscope. As crack lengths a_1 and a_2 are lengths of projections onto a plane, the initial values of a_1 and a_2 are $1/\sqrt{2}$ times the radius of the initial notch. Crack length a_3 is defined within the volume of the specimen. The initial and final values of a_3 were measured when the specimen was broken after the test was completed. Both crack shape evolution and the crack growth rates are compared to FRANC3D predictions.

A series of fatigue tests on mixed-mode, through-crack configurations, performed by Pook [*11*, *12*] on BS 970 En mild steel, and denoted test type 2, were numerically simulated. The geometry and boundary conditions for these tests are shown in Figure 2. An initial notch was cut into each specimen by EDM, at an angle β (defined in Figure 2)

= 90° (pure Mode I), 75°, 60° or 45°. Multiple tests were performed for each angle β. Cyclic loads, with R = 0.1 and Δp ranging from 7 to 18 kN, depending on the test, were applied to each specimen. The direction of the initial crack propagation along the surface of the specimens was reported. Crack growth rates or behavior beyond initiation were not reported. The experimentally observed directions of initial crack growth are compared to the directions predicted using FRANC3D.

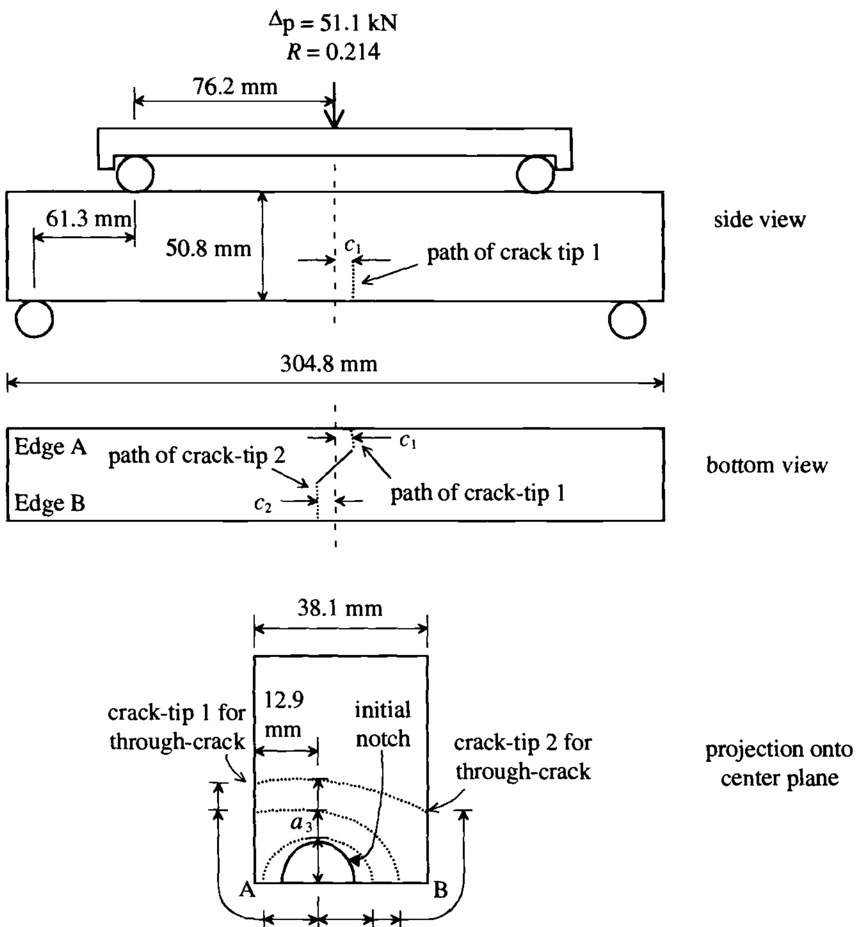

Figure 1 – *Geometry and boundary conditions for non-planar surface crack experiment (test type 1). The projection onto the center plane shows the evolution of the fatigue crack from the initial notch (solid line) to a surface-crack, corner-crack and through-crack (dotted lines), with continuous definitions of a_1, a_2 and a_3 throughout. The lengths c_1 and c_2 represent the out-of-plane coordinate of the two crack-tips.*

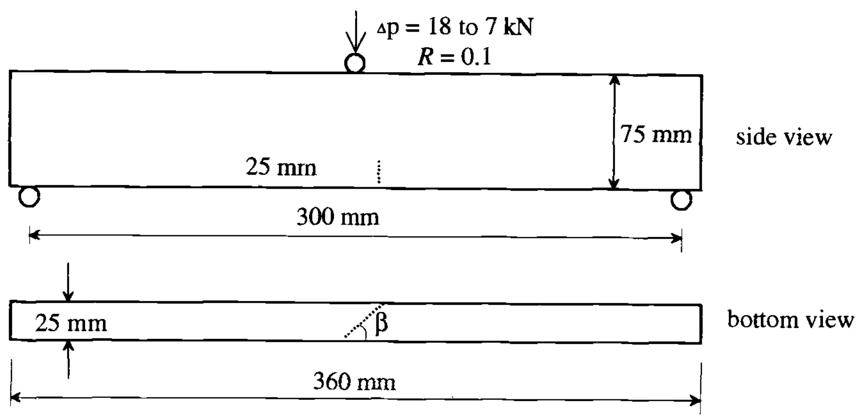

Figure 2 – *Geometry and boundary conditions for non-planar through crack experiments, after Pook [11] (test type 2).*

Numerical Methodology

FRANC3D [*9*] is a pre-and post-processor developed for the simulation of three-dimensional crack growth. It has been used to generate boundary element models for crack growth in three-dimensional solid body problems [*8*, *13*] and finite element meshes for analyses of complex shell structures [*14*]. For the analyses described in this paper, FRANC3D was used with a boundary element code, BES [*15*, *16*]. In FRANC3D, topology is used to manage geometry. This allows great flexibility in the modeling of arbitrary geometries and boundary conditions. The topological database allows the evolution of crack shape to be dictated by the mechanics of a problem, rather than being constrained to a pre-defined crack shape [*17*]. Once displacement and stress fields are obtained, FRANC3D can be used to extract the appropriate fracture mechanics parameters, propagate one or more (not necessarily planar) cracks, and create a new geometry and mesh for further analysis.

Crack propagation in FRANC3D is based on point values of linear-elastic stress-intensity factors calculated along a crack front. The crack front is not constrained to remain a certain shape or to follow a pre-defined path. This approach to modeling crack propagation has been investigated by Manu (and Ingraffea) [*18*]; Gerstle, Martha and Ingraffea [*19*]; Sousa, Martha, Wawrzynek and Ingraffea [*13*]; Wawrzynek, Carter, Potyondy and Ingraffea [*17*]; Sousa and Ingraffea [20]; Martha, Llorca, Ingraffea and Elices [*21*]; Chipalo, Gilchrist, and Smith [*22*, *23*]; Mi and Aliabadi [*24*]; Nykänen [*25*]; Forth and Keat [*26*]; and Dhondt [*27*]. A commercially available code, ZENCRACK [*28*] can also predict three-dimensional crack propagation based on local stress-intensity factors. Also, Sih and Li have investigated three-dimensional crack growth based on local strain energy density values [*29*]. FRANC3D has been shown to result in reasonable and/or conservative fatigue life predictions for three-dimensional cracks subjected to Mode I, constant amplitude loading [*8*]. However, the additional complexity invoked when modeling non-planar, mixed-mode fatigue crack growth merits additional attention.

Prediction of Crack Shape

For a true three-dimensional fatigue crack growth analysis, crack shape as well as crack size must be predicted. The process for numerical simulation of arbitrary fatigue crack propagation in FRANC3D is summarized in Figure 3. Linear-elastic stress-intensity factors for all three modes are extracted at points along a current crack front. The details for the calculation of stress-intensity factors within FRANC3D are given elsewhere [*15, 16*]. Theoretical models for three-dimensional fatigue crack growth suggest Mode III loading, as well as Mode I and II, affects the shape of three-dimensional fatigue cracks [*30, 31*]. However, only Mode I and Mode II stress-intensity factors are used to predict the evolution of crack shape in this paper.

The direction of propagation at each point along a crack front is predicted by treating the crack as a series of plane strain, two-dimensional problems (Figure 3a). For the analyses described in this paper, maximum hoop stress [*32*] is used to predict the direction of crack growth at each point. However, criteria based on assuming the crack will grow in the direction that minimizes a strain energy density function, S, [*33*] or a direction that maximizes the energy release rate, *G*, [*34*] could have been used as well. Analyses by Forth and Keat [*26*] applied various methods to predict crack shape, including a generalized energy release rate approach that included Mode III, to a problem of an inclined penny shaped crack at an angle to a far-field applied stress. Results from these analyses showed little practical difference between the different approaches.

Once the directions of crack propagation along the crack front are found, crack growth increments are predicted using

$$\Delta a_{(i)} = \Delta a_{\max} \frac{\dfrac{\mathrm{d}a_{(i)}}{\mathrm{d}N}}{\left(\dfrac{\mathrm{d}a}{\mathrm{d}N}\right)_{\max}} \tag{1}$$

where $\dfrac{\mathrm{d}a_{(i)}}{\mathrm{d}N}$ is the crack growth rate at the point, *i*, which is calculated by the local ΔK;

$\left(\dfrac{\mathrm{d}a}{\mathrm{d}N}\right)_{\max}$ is the maximum crack growth rate predicted along the crack front; and $\Delta a_{\max}$ is the maximum allowable crack growth increment, input by the user. Substitution of the well-known Paris model [*35*] into Equation (1) yields

$$\Delta a_{(i)} = \Delta a_{\max} \left(\frac{\Delta K_{(i)}}{\Delta K_{\max}}\right)^{n} \tag{2}$$

where $\Delta K_{\max}$ is the maximum stress-intensity factor range along the crack front and *n* is the Paris model exponent.

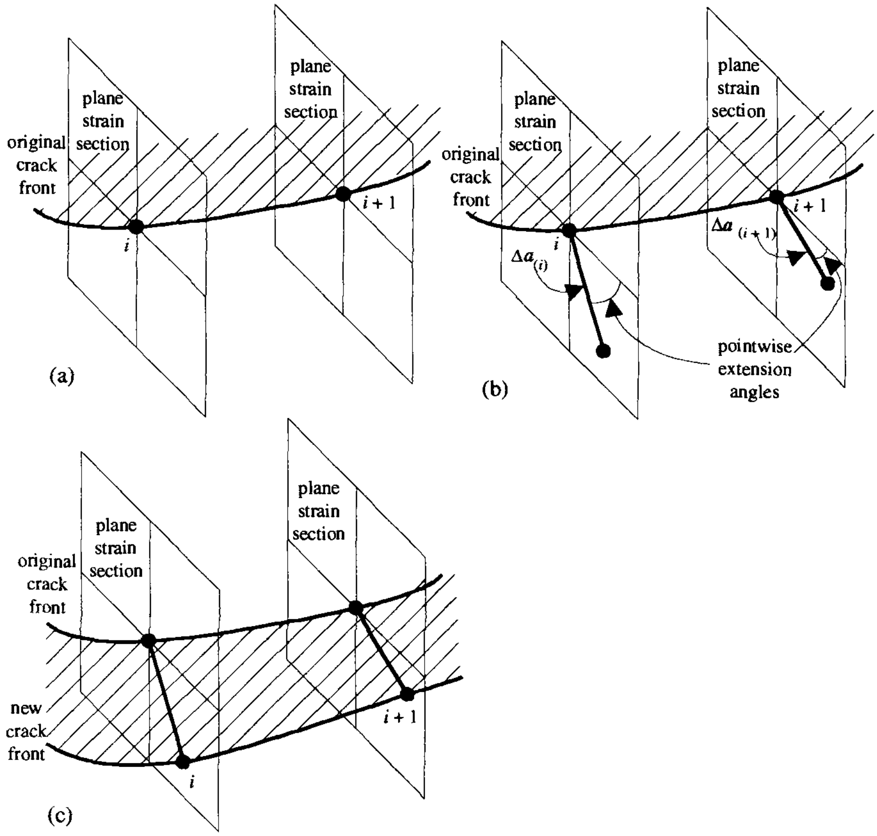

Figure 3 – *FRANC3D-simulated three-dimensional fatigue surface crack propagation.*

The next step is to define the new crack front by connecting the tips of the vectors of length $\Delta a_{(i)}$, defined in the previous step, with splines (Figure 3b). The area between the new crack front and the old crack front is then added to the crack surface (Figure 3c). Only local remeshing is required before a three-dimensional stress analysis is performed on the new geometry, and the process is repeated.

Prediction of Crack Growth Rates

After a series of crack fronts have been predicted, the final step in predicting fatigue life is to calculate the number of cycles between each pair of successively predicted crack fronts. Fatigue life for three-dimensional configurations can be calculated in the same manner as for two-dimensional problems if there exists a global value of ΔK to represent each crack front, and a global value of Δa to represent the difference between each pair of successively predicted crack fronts.

Three methods to define global ΔK and Δa values from local values for each predicted crack front and crack growth increment were considered.

1) ΔK for the entire crack front is taken to be the average of $\Delta K_{I(i)}$ over the entire crack front.
2) ΔK for the entire crack front is taken to be average value of $\left[\left(\Delta K_{I_{(i)}}{}^2 + \Delta K_{II_{(i)}}{}^2\right) + \frac{1}{2\mu E'}\Delta K_{III_{(i)}}{}^2\right]^{1/2}$. This value is the Mode I stress-intensity factor required for the same energy release rate G_{TOTAL} of a mixed mode crack under self-similar propagation [36].
3) ΔK for the entire crack front is taken to be the average value of $(\Delta K_{I(i)}{}^2 + \Delta K_{II(i)}{}^2 + \Delta K_{III(i)}{}^2)^{1/2}$ over the entire crack front. Of the three methods considered, this value provides the upper bound on ΔK for the entire crack front.

In all cases, the global Δa was calculated as the average of local values, $\Delta a_{(i)}$, over the entire crack front. Methods 2 and 3 reduce to method 1 in the event of planar, Mode I fatigue crack growth. It could be argued that the correct value for energy release rate in method 2 should be calculated from G_{TOTAL} at maximum load (p_{max}) minus G_{TOTAL} at minimum load (p_{min}), rather than G_{TOTAL} from the cyclic load amplitude (Δp). However, this approach introduces a stress ratio effect on fatigue crack growth rates that was deemed unrealistic.

Once a global value of ΔK is calculated for each shape, and a global value of Δa is calculated to represent the growth increment between successive fronts, fatigue life can be calculated using the Paris model. Method 1 has been shown to result in conservative and/or reasonable life predictions for planar, Mode I cracks [8]. However, for mixed-mode cracks, method 1, which neglects Mode II and III components, is the least conservative of the three methods considered in this paper. Method 3 is the most conservative with respect to predicting fatigue life of the three methods shown.

Numerically Predicted and Experimentally Observed Crack Shapes

In this section, numerically predicted and experimentally observed crack shapes are compared. The experimentally observed crack face for test type 1 is shown in Figure 4. Two views are shown, to give an indication of the three-dimensional nature of the crack face. The view shown in Figure 4(a) is parallel to the length of the specimen. The initial notch is oriented 45° to the camera. The final fatigue crack front is outlined in white in this figure. The view shown in Figure 4(b) is perpendicular to the plane of the initial notch, and 45° to the direction of the length of the beam. Parts of the fatigue surface show factory-roof, or petal-shaped cracking, which is characteristic of Mode III crack growth [37]. These features are highlighted by the arrows in Figure 4(b).

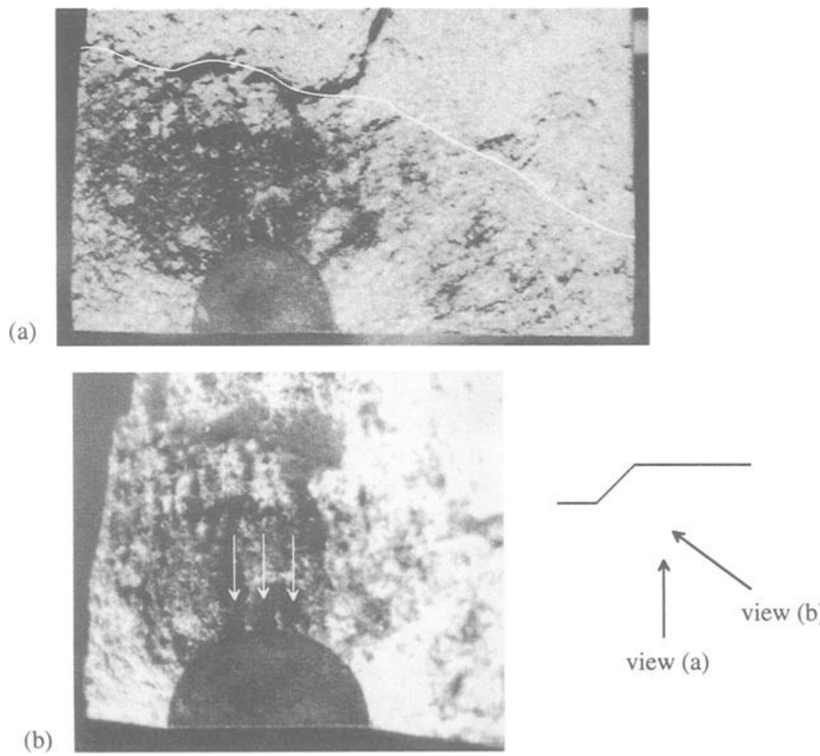

Figure 4 – *Photographs of experimentally observed non-planar surface crack fronts taken from (a) view parallel to the length of the beam and 45° to the initial notch – the final crack front is outlined in white, and (b) view at 45° to the length of the beam, perpendicular to the initial notch - showing the factory-roof cracking facets (at arrows).*

The numerically predicted fatigue crack fronts for test type 1 are shown in Figure 5. The initial notch is labeled "ini" and the predicted crack fronts are numbered 1 through 11, consecutively. The paths of the predicted and experimentally observed crack-tips 1 and 2 are compared in Figure 6. The two side faces and the bottom face are shown on a single plane in this figure. There is excellent agreement between the predicted (open circles) and observed (solid line) paths of the two crack-tips. The predicted crack shape near the top of the initial notch is in general agreement with simulations by Mi [*6*] and Forth and Keat [*28*], including simulations that account for Mode III in crack shape predictions.

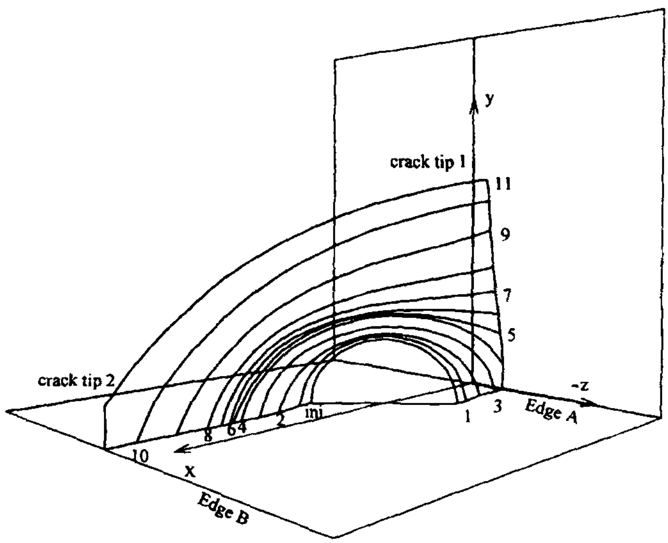

Figure 5 – *Evolution of FRANC3D-predicted crack shapes for non-planar surface crack (test type 1).*

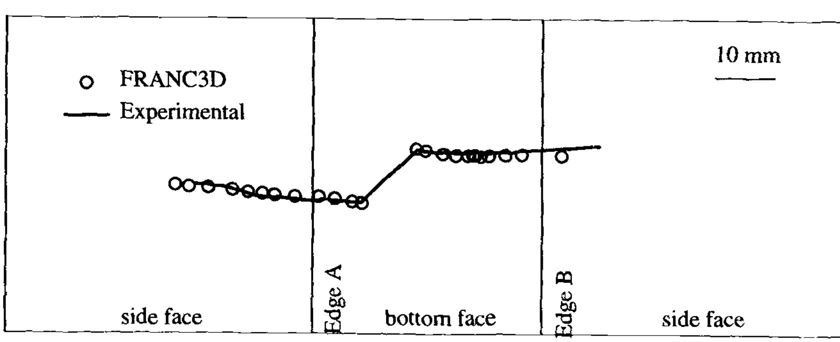

Figure 6 – *Predicted and observed intersection between crack front and free surfaces for surface crack configuration (test type 1).*

The relationship between crack lengths a_1, a_2, and a_3, and out-of-plane measurements c_1 and c_2 can also be used to quantify the surface crack shape for test type 1. Crack lengths a_2 and a_3 and out-of-plane measurements c_1 and c_2 are plotted against the corresponding crack length a_1 for both the experimentally observed and predicted crack shapes in Figure 7. The crack lengths for which crack-tip 1 reaches edge A, and when crack-tip 2 reaches edge B, are denoted on the graphs. Because a_3 is an internal crack length, only initial and final lengths are available for the experimentally observed crack. An equivalent plot for results of planar fatigue crack growth tests [*38*] suggests that crack shape, as quantified by the a_1-a_2 relationship, exhibits less scatter than fatigue crack growth rates do.

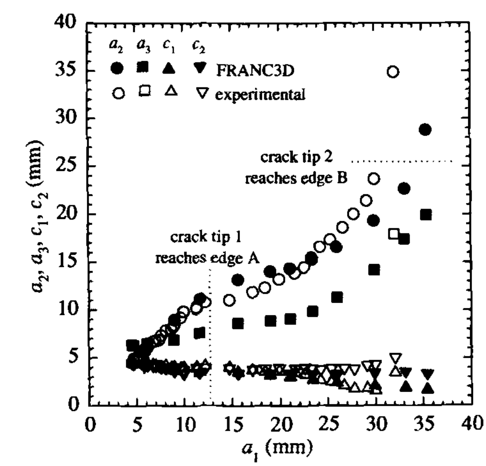

Figure 7 – *Experimentally observed and numerically predicted crack shape evolution for test type 1 in terms of the relation between crack lengths a_2, a_3, c_1 and c_2 against crack length a_1.*

There is excellent agreement between the predicted and the experimentally observed crack shapes for test type 1 when quantified as the a_1, a_2, c_1 and c_2 relationship. Although the a_2 values diverge somewhat after the first transition, the differences between the predicted and observed relationship between a_1 and a_2 remains small compared with test-to-test variation in crack shape seen for the series of planar cracks, and very small compared to the observed scatter in fatigue crack growth rates observed for the planar tests. The experimentally observed pair of a_1 and a_3 from the end of the test falls nearly on the curve of predicted a_1 versus a_3 behavior. There is also reasonable agreement between experimental observations and numerical predictions for the relationship between c_1 and c_2 and a_1.

The stress-intensity factors along the crack fronts change as the simulated crack evolves. FRANC3D calculated cyclic stress-intensity factor distribution for all three modes are shown in Figure 8 for the initial notch and three of the predicted crack fronts for test type 1. These specific crack fronts were chosen for discussion to highlight distinct stages of the predicted fatigue life. In these plots, location along the crack front is normalized such that crack-tip 1 is at 0.0 and crack-tip 2 is at 1.0.

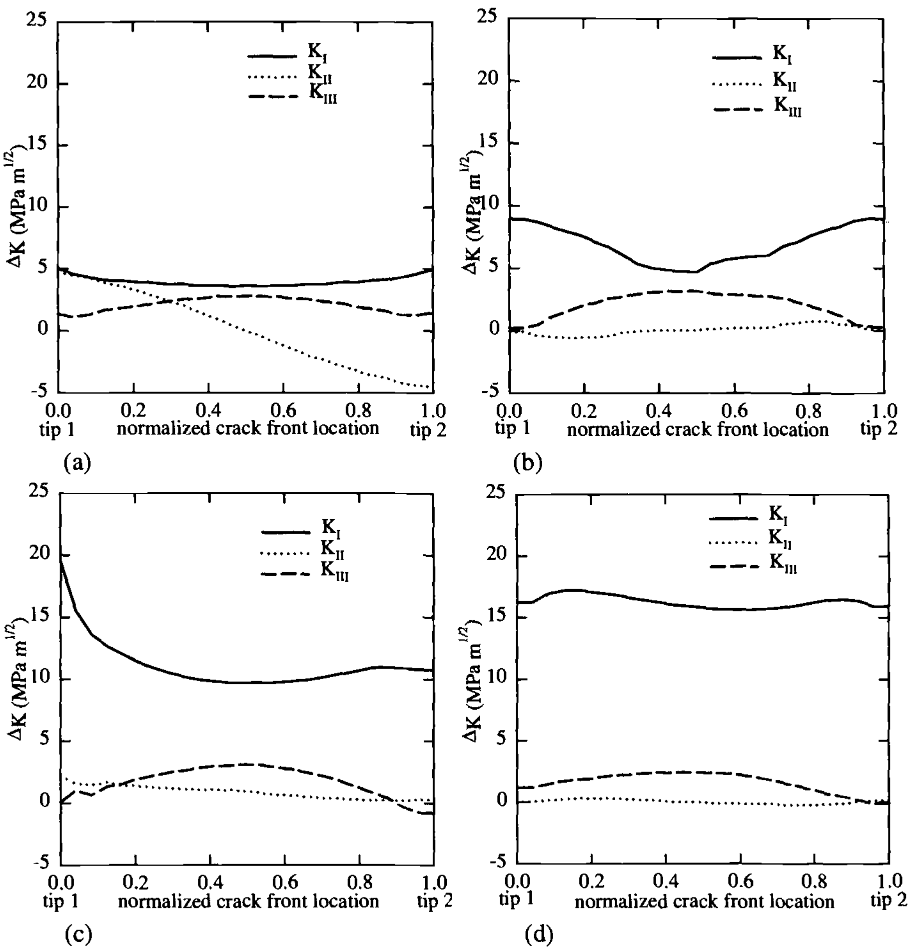

Figure 8 – *Evolution of stress-intensity factors for FRANC3D-predicted surface crack shapes for (a) initial crack front, (b) predicted crack front 1, (c) predicted crack front 4, and (d) predicted crack front 9.*

Calculated stress-intensity factor distributions for the initial notch are shown in Figure 8(a). This front is characterized by the near equality of the absolute value of ΔK_I and ΔK_{II} at the crack-tips. Near the top of the initial notch, the value of ΔK_{III} is approximately equal to the ΔK_I value.

Calculated stress-intensity factor distributions for predicted crack front 1 are shown in Figure 8(b). This predicted crack front resulted from a maximum crack growth increment of 1.9 mm, and an average growth increment of 0.86 mm from the initial notch. Despite the relatively small amount of crack growth, the stress-intensity factor distributions differ greatly from those along the initial crack front. The values of ΔK_I are nearly double the value of ΔK_I for the initial notch near crack-tips 1 and 2. The values of ΔK_{II} is reduced to nearly zero along the entire crack front. The values of ΔK_{III} reduce to near zero at crack-tips 1 and 2, but do not change significantly from the values for the initial notch near the top of the crack. The large change in Mode I and II stress-intensity factors for a relatively small increment of crack growth is attributed to the change in orientation of crack growth with respect to the far-field principle stresses compared to the orientation of the initial notch.

Calculated stress-intensity factor distributions for predicted crack front 4 are shown in Figure 8(c). This is the predicted crack front immediately following the first transition. Here, the effects of the orientation of the initial notch have diminished: both ΔK_{II} and ΔK_{III} are much less than the ΔK_I values. However, the effects of the transition are prominent. Crack-tip 1 is still near edge A, and the crack-front intersects the free surface at an acute angle. The effects of the transition result in an increase in ΔK_I near crack-tip 1 with respect to the value along the rest of the crack front. The slight non-zero component of ΔK_{II} near crack-tip 1 coincides with the evolution of crack-tip 1 towards the same x-y plane (*i.e.*, z component) of crack-tip 2 that is shown in Figure 6 for both numerical predictions and experimental observations.

Calculated stress-intensity factor distributions for the predicted crack front 9 are shown in Figure 8(d). Here, the crack is between the first and second transitions and is approaching pure Mode I conditions. The value of ΔK_{II} is near zero along the entire crack front. The values of ΔK_{III} are less than those for crack front 4 along much of the crack front. The values of K_I along crack front 9 are relatively constant, and greater than the values of ΔK_I along most of crack front 4, with the exception of the high values calculated near crack-tip 1.

There are some theoretical and practical difficulties in calculating the stress-intensity factors at the free surfaces of the specimen [*39*]. The assumption of plane strain conditions are questionable at the free surface. Indeed, at the free surfaces, the normal stress must be zero, and the rate of change of stress parallel to the crack front is not negligible. From a practical standpoint, the algorithm that was used to calculate the stress-intensity factors breaks down near the crack-tip when the crack front intersects the free surface at an acute angle. In these cases, the stress-intensity factor at the free surface is taken as the value a small distance from the free surface. Compared to the variations in crack closure that are likely to occur near the free surface [*40*], these difficulties are likely to have a relatively small effect of predicted crack shape and growth rates.

FRANC3D predictions and experimental observations of crack-tip paths along one side surface for test type 2, $\beta = 90^\circ$, 75°, 60°, and 45° are shown in Figure 9. For each initial notch angle, β, less than 90°, Pook reported the average and extreme directions of initial growth for multiple tests at each angle. The two extreme (dashed line) and average (vertical dark line) direction of initial growth is shown from each initial notch (dark line). FRANC3D-predicted crack paths are shown by open symbols. The predicted directions are nearly identical to the reported average initial directions of growth. Pook mentions that the cracks exhibited factory-roof cracking. As with test type I, this behavior was not captured in the numerical simulations.

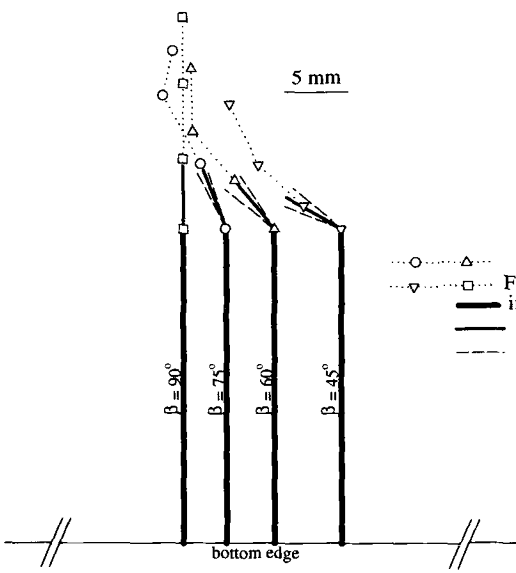

Figure 9 - *Predicted and observed intersection between crack front and free surface for through crack configurations (test type 2). Crack-tip paths for b = 0°, 15°, 30°, and 45° are shown.*

Stress-intensity factors along the initial cracks for test type 2 are shown in Figure 10. As the angle of the initial notch decreases from 90° (pure Mode I) to 45°, the components of Modes II and III stress-intensity factor increase, while the Mode I stress-intensity factor decreases. The Mode III component is comparable in magnitude to Mode II component, and approaches the magnitude of the Mode I component for β = 45°, yet ignoring this component still allows for good prediction of the direction of crack growth at the surface (refer to Figures 6 and 9).

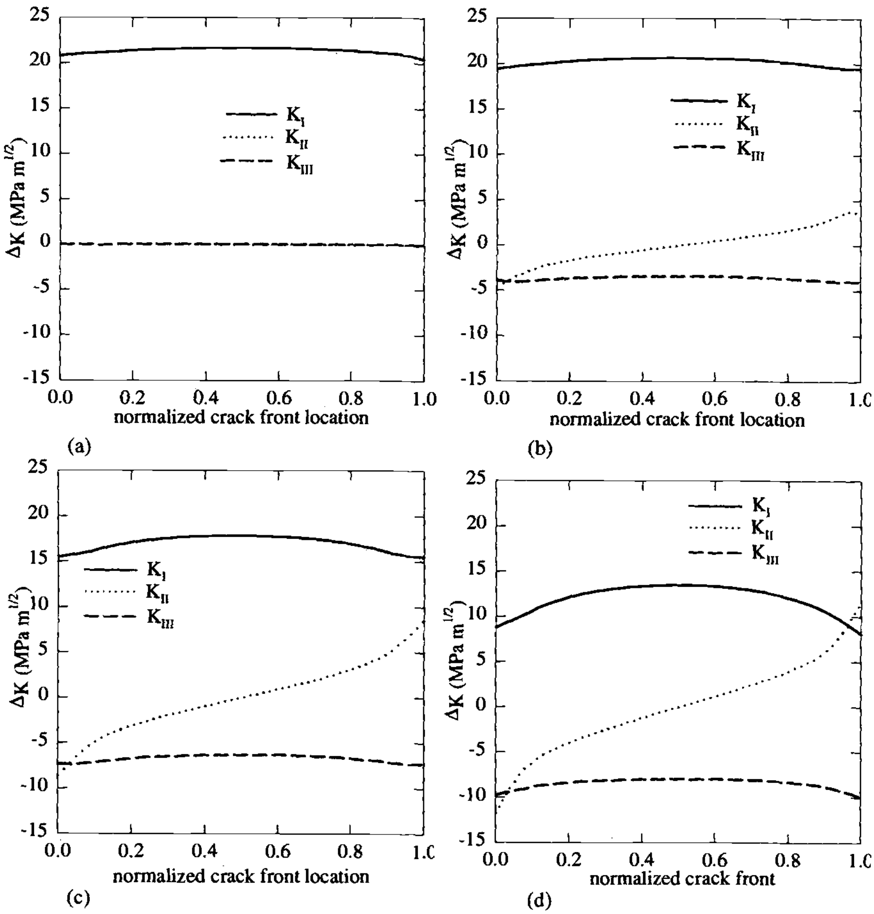

Figure 10 – *Stress-intensity factors along initial notches for test type 2, (a) $\beta = 90^o$, (b) $\beta = 75^o$, (c) $\beta = 60^o$ and (d) $\beta = 45^o$.*

Numerically Predicted and Experimentally Observed Fatigue Crack Growth Rates

In this section, crack growth rates resulting from predictions using the methods described in this paper were compared to each other and to the experimental observations for test type 1. First, the three methods used to calculate global stress-intensity factors are compared. Next, predicted crack growth rates are compared to observed crack growth rates. Finally, the predicted and observed ratios of cycles before transitions are compared.

Calculation of Global Stress-intensity Factors

The global cyclic stress-intensity factors over the range of fatigue crack growth investigated in test type 1 are shown in Figure 11 for all three methods of calculation. In this figure, a for the initial notch is taken to be the initial radius, and all subsequent values of a are calculated by adding the Δa values. As anticipated, the greatest difference in ΔK values calculated using the three methods is for the initial notch. Here, there is a 25% difference between ΔK calculated by method 1 and that calculated by method 3. As the fatigue crack propagates from the initial notch, the contributions of modes II and III diminish, and therefore the three methods yield similar values of global ΔK. After the first crack growth increment, the difference drops to 5.5%. The difference between ΔK values calculated using method 1 and method 3 decreases to less than 0.1% for the final predicted crack shape. In the next section, Fatigue life predictions using both method 1 and method 3 are used to bound the predictions.

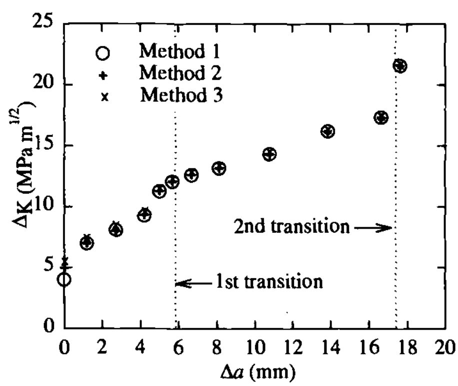

Figure 11 – *Averaged crack length against averaged ΔK for test type 1.*

Fatigue Crack Growth Rates

Numerically predicted and experimentally observed crack growth for test type 1 are plotted against cycles in Figure 12. For these predictions, Paris model [*35*] coefficients c = $1.1\text{x}10^{-9}$ and n = 3.79 for units of MPa m$^{1/2}$ and mm/cycle were used. These values were obtained by fitting a Paris model to rates predicted in the Paris regime for R = 0.2 using properties from the NASA/FLAGRO (now NASGRO) materials database [*41*]. It is noted that there is an implicit assumption of isotropic behavior when a single fatigue crack growth curve for these simulations. Crack length a_1 is plotted against cycles in Figure 12a. Crack length a_2 is plotted against cycles in Figure 12(b). Crack length a_3 is plotted against cycles in Figure 12(c). Experimentally observed crack length a_3 is unavailable except for the initial and final crack length. Methods 1 and 3 predict

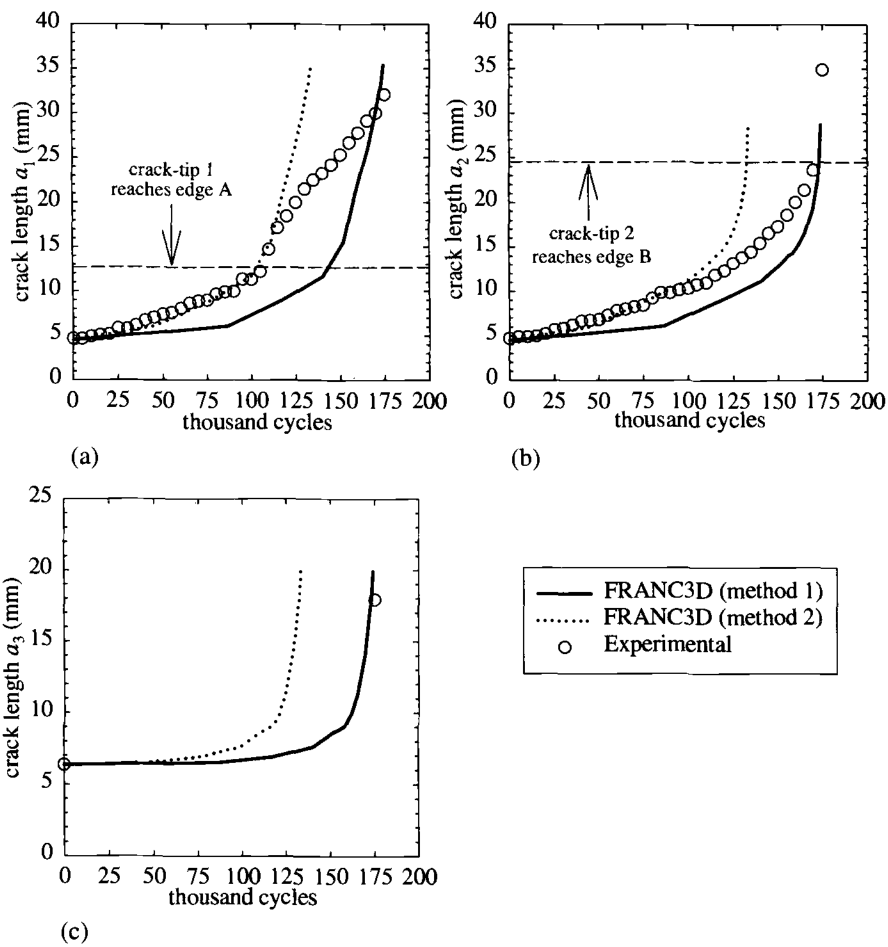

Figure 12 – *FRANC3D predicted and experimentally observed crack length for (a) a_1, (b) a_2, and (c) a_3, against cycles for test type 1.*

different fatigue crack growth rates when the crack is near the initial notch. As the simulated crack grows, the Mode II and III components of the stress-intensity factor along the crack front decrease, and the crack growth rates predicted using the three methods converge. The series of planar crack tests described in [8] exhibited considerable scatter in fatigue crack growth rates, possibly due to seasonal variations in temperature and humidity of "lab air". The difference between the fatigue crack growth rates predicted using Method 1 and Method 3 is within the range of scatter in fatigue crack growth rates observed in the planar crack tests, although it appears that accounting for the Mode II and III components of growth improve the prediction. After the first two or three mm of growth in the a_1 or a_2 direction, the crack growth rates for a given crack front are approximately the same for the two methods of determining ΔK. For a given number of cycles before the first transition (approximately 100 000 cycles) the observed crack length a_1 matches the predicted crack length a_1 when method 3 is used to compute fatigue life. After this transition, the experimentally observed crack growth rates are slower than the predicted fatigue crack growth rates for a given crack size, although the experimentally observed a-N relationship remains bounded by the predictions of method 1 and 3 for nearly the entire fatigue life.

It is interesting that the numerical prediction using method 3 and the experimental observations begin to diverge near the first transition. By the time that the first transition has occurred, there has been a significant amount of crack growth under predominantly Mode I conditions (see Figures 8 and 11). The growth rates for the pre-transition crack growth is predicted accurately. Furthermore, previous efforts have shown that FRANC3D handles similar transitions under pure Mode I conditions well [8]. A potential cause of this discrepancy will be proposed in the discussion section of this paper.

Number of Cycles Before Transitions

Two transitions have been defined for test type 1. These are defined as 1) the transition from surface crack to corner crack (crack-tip 1 reaching Edge A) and 2) the transition from corner crack to through crack (crack-tip 2 reaching Edge B). The number of cycles before the first transition is denoted l_1. The number of cycles before the second transition is denoted l_2. The experimental and numerically predicted values of l_1 and l_2 are summarized in Table 1. For both transitions, the experimentally observed values of l_1 and l_2 are bounded by values of the l_1 and l_2 that were calculated using method 1 and method 2. However, method 1 and method 2 predict 29 200 cycles between the first and second transition, whereas 64 000 cycles were observed in the test. Another way to look at this difference is the ratio of l_2/l_1, which is summarized in Table 2. The predicted l_2/l_1 is 20% to 25% less than the experimentally observed ratio, depending on the method used to predict crack growth rates from stress-intensity factors.

Table 1 – *Predicted and Observed Cycles before Transitions*

Simulation or Experiment	l_1 (cycles)	l_2 (cycles)
Experimental	106 500	170 500
FRANC3D (Method 1)	144 000	173 200
FRANC3D (Method 2)	103 300	132 500

Table 2 – *Predicted and observed number of cycles before transition for non-planar crack*

Simulation or Experiment	l_2/l_1	*Difference from experimental value*
Experimental	1.60	--
FRANC3D (Method 1)	1.20	-25.0%
FRANC3D (Method 2)	1.28	-20.0%

This observation can be compared to the trends in l_2/l_1 that were observed in the previous study on planar fatigue crack growth. These results are summarized in Table 3. All tests had l_2/l_1 values within 7.3% of the average experimentally observed value. The FRANC3D predicted value of l_2/l_1 was 8.8% less than the experimentally observed average. Two conclusions from these planar tests were that (1) the ratio of l_2/l_1 had much less variation from test to test than either l_1 or l_2 had, and (2) the good prediction of l_2/l_1 reflected well on the capability of FRANC3D to capture the mechanics of the crack transitioning. However, the value of l_2/l_1 for the non-planar test type 1 was not predicted as well as the value of l_2/l_1 was for the planar tests described in [*8*]. This observation suggests that there is an aspect of the non-planar fatigue crack growth tests that is not modeled as well as the planar fatigue crack growth tests were modeled.

Table 3 – *Predicted and observed number of cycles before transitions for planar cracks*

Simulation or Experiment [*8*]	l_2/l_1	*Difference from average experimental value*
Experimental (upper bound)	2.07	+ 7.3%
Experimental (average)	1.93	--
Experimental (lower bound)	1.83	-5.2%
FRANC3D (Method 1)	1.76	-8.8%

Discussion

The numerically predicted and experimentally observed behavior for both test types agrees with Pook's concept of "attracting" surfaces [*39*]. Pook states that there can exist a surface to which crack growth is attracted to. Perturbations in crack shape from these surfaces result in crack growth toward the attracting surface. In the cases described in this paper, the initial notches oriented at an angle to the far-field maximum principal stress are perturbations to the attracting surfaces. Subsequent fatigue crack growth from the angled initial notches tends toward the attracting plane, resulting in crack shapes that evolve toward planar crack shapes, and stress-intensity factor distributions that approach pure Mode I. There is good agreement between the numerically predicted and experimentally observed relationship between a_1, a_2, c_1, and c_2 for test type 1. There is also good agreement between the numerically predicted and the experimentally observed direction of crack growth on the surfaces for test type 2. A major difference between the experimentally observed and numerically predicted crack shapes is that factory-roof cracking is experimentally observed in locations where there is a mode III component that is significant compared to the Mode I stress-intensity factor, but this behavior is not predicted in the FRANC3D simulations. This difference is anticipated: the Mode III component of stress-intensity factor is predicted to affect crack shape by Hogden and Sethna [*30*] and Hull [*31*], yet ignored when the crack shape increments are predicted.

It was anticipated that the mixed-mode stress state that characterizes the initial notch for test type 1 might cause errors in the predicted crack growth rates for the early stages of crack growth, but that these errors would be reduced once the crack front evolved to a primarily Mode I loading condition. However, the data plotted in Figure 12 suggests the opposite: relatively good predictions for crack growth rate under mixed mode conditions (when all three modes are used to calculate a global stress-intensity factor), but predicted crack growth rates are faster than experimentally observed when crack growth is under predominantly Mode I.

The errors in predicted fatigue crack growth under Mode I conditions in test type 1 can be explained by the effects of crack closure [*42, 43*]. The predominant mechanism behind closure is typically thought to be a plastic wake, except under near-threshold or especially aggressive environments. Indeed, for test type 1, plasticity induced fatigue crack closure is likely to be especially significant near the free surfaces, *i.e.*, near crack-tips 1 and 2 [*40, 44*]. However, the factory-roof cracking shown in Figure 4 indicates that the Mode III present in the early stages of crack growth had a significant effect on the crack surface morphology. These remnants of mixed mode growth remain on the crack wake, even when the crack front is primarily under Mode I conditions. The dark color of the fatigue fracture surface indicates the presence of oxidized debris, characteristic of fretting [*45*]. This observation strongly suggests that the factory-roof facets near the top of the initial notch lead to roughness induced closure [*46*]. The proposed mechanism is illustrated in Figure 13. Figure 13(a) is a closeup of the crack face near the initial notch, with a schematic diagram of the surface morphology near a factory-roof facet superimposed. Figure 13(b), is a larger version of the surface morphology near a factory-roof facet. Here, the surface at the facet is parallel to the direction of far-field maximum principal stress. On either side of the facet there is a surface that is perpendicular to the direction of far-field maximum principal stress, the right angles between these segments creates a "z" shape. As the crack grows away from the factory-roof facet, the crack front becomes smoother, evolving into a primarily Mode I front. Once it has grown beyond the factory-roof facet, the crack tends to exhibit Mode I opening displacements near the crack front, as shown in Figure 13(c). However, these opening displacements result in effective sliding displacements at the factory-roof facet, which can lead to surface fretting. This behavior is somewhat different from typical roughness induced cracking because it is induced by macro-scale roughness, with the contact relatively far from the crack-tip, and it can be induced without any sliding mode displacements caused by plastic deformation [*47*] or near-tip kinks that induce local mixed-mode displacements [*48*]. Although a model that accounts for crack face geometry, crack-tip and crack face displacements and oxide and/or debris could simulate the contact of the factory-roof facets, it is unclear how to quantify the effect of contact far from the crack front process zone on fatigue crack growth rates.

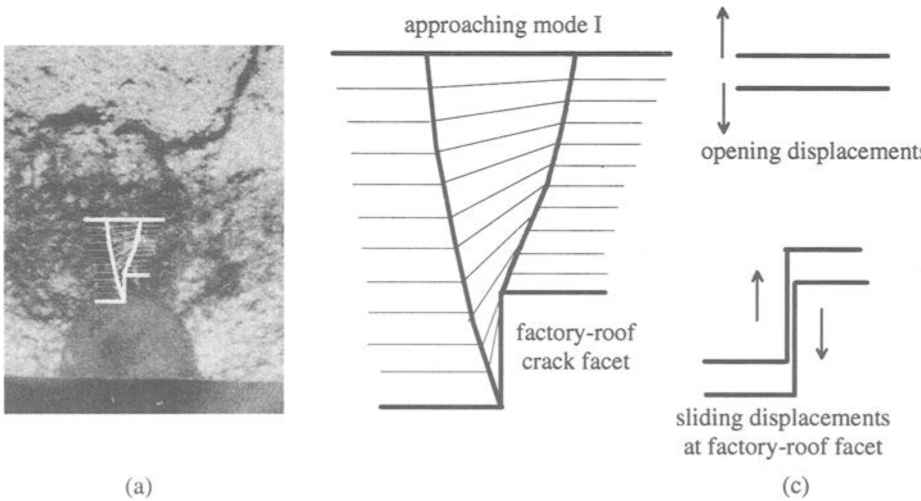

Figure 13 – *(a) Mixed-mode load near top of initial notch results in factory-roof facet that transitions into a primarily Mode I crack, as shown in the superimposed schematic figure in white, (b) close-up of schematic showing the transition from Mode III induced factory-roof facet oriented parallel to principal stress to Mode I crack front oriented perpendicular to principal stress and (c) Mode I opening displacements result in sliding displacements at factory-roof facet.*

Summary and Conclusions

Two distinct aspects of predicting non-planar fatigue crack growth are discussed in this paper: the shape of an evolving crack, and the rate at which the crack front grows. To predict fatigue life for non-planar cracks accurately, both issues must be addressed. FRANC3D predicts the evolving shape of non-planar, mixed-mode fatigue crack growth by calculating stress-intensity factors and predicting growth vectors at points along the crack front. Crack front evolution is not restricted by pre-determined crack shapes. Rather, it is predicted by treating crack growth as a series of two dimensional, plane strain problems, each growing according to two dimensional models for predicting crack path. Mode III components of stress-intensity factor are ignored in this process.

Once the shapes of the crack front throughout the fatigue life are determined, fatigue life for three-dimensional configurations can be calculated in a manner similar to that for two-dimensional configurations if average values of ΔK at the nodes along the crack front, and an average Δa between successive crack fronts are found. Three means to determine an average ΔK along the crack front were considered. The most conservative method proposed accounts for all three modes. This approach gives the best predictions for crack growth rates under mixed-mode stress state. The three methods converge to predict the same crack growth rates as the crack evolves toward a predominantly Mode I crack front.

The most significant discrepancy between predicted and experimentally observed crack shapes is the factory-roof, or petal-shaped cracking that is observed, but not predicted. The Mode III component of stress affects the crack front process zone, causing factory-roof cracking to occur. On one hand, the factory-roof cracking appears to be a local effect, as the global crack shape can be predicted well without accounting for Mode III effects. However, the Mode III component of loading also affects the crack wake. The factory-roof facets on the crack face cause macro-scale roughness induced cracking that affects crack growth rates later in the fatigue life, when the crack is under predominantly Mode I conditions.

FRANC3D is shown to be a useful engineering tool for predicting non-planar, mixed-mode fatigue crack growth. However, mixed-mode fatigue crack growth prediction capability needs further development. Models to predict mixed-mode fatigue crack growth in engineering alloys, particularly the effects of Mode III, need to be developed and rigorously tested. Effects of non-planar crack shape on crack closure, and therefore crack growth rates, must also be better understood to completely model non-planar fatigue crack growth rates.

Acknowledgments

The authors gratefully acknowledge the input of Dr. Bruce Carter, Professor Alan Zehnder, Professor Mircea Grigoriu, Mr. Timmy Clemmons, Mr. Jim Favenesi, and Mr. Jay Lambert. FRANC3D was developed by the Cornell Fracture Group, under the direction of Professor Anthony Ingraffea. This research was sponsored by NASA/Marshal Space Flight Center, under grant NAS8-38103, while WTR was a research assistant in the Civil and Environmental Engineering department at Cornell University.

References

[1] Suresh, S. Fatigue of Materials, Cambridge University Press, Cambridge, 1991.

[2] Gangloff, R. P., "Corrosion Fatigue Crack Propagation in Metals," *Proceedings of the first international conference on the environment induced cracking of metals*, R. P. Gangloff and M. B. Ives, Eds., The National Association of Corrosion Engineers, Houston, TX, 1988, pp. 55-110.

[3] Fine, M. E., Weertman, J. R., Microstructural effects on creep and fatigue. In *Time Dependent Fracture, Proceedings of the Eleventh Canadian Fracture Conference*, ed. A. S. Krausz, Nijhoff Publishers, Dordrecht, 1985, pp. 93-110.

[4] Newman, J. C. Jr., Fracture Mechanics Parameters for Small Cracks," *Small Crack Test Methods, ASTM STP 1149*, J. Larson and J. E. Allison, Eds., American Society for Testing and Materials, Philadelphia, 1992, pp. 6-33.

[5] Parks, D. M., "A Surface Crack Review: Elastic and Elastic-Plastic Behavior," *Surface Crack Growth: Models, Experiments and Structures, ASTM STP 1060,* W. G. Reuter, J. H. Underwood, and J. C. Newman, Jr., Eds., American Society for Testing and Materials, Philadelphia, PA, 1990, pp. 9-33.

[6] Mi, Y. *Three-Dimensional Analysis of Crack Growth,* Topics in Engineering Vol. 28, Computational Mechanics Publications, Southhampton, U.K., 1996.

[7] Kaninnen, M. F. and Poplar, C. H., *Advanced Engineering Fracture Mechanics*, Oxford University Press, New York, NY, 1985.

[8] Riddell, W. T., Ingraffea, A. R., Wawrzynek, P. A., "Experimental Observations and Numerical Predictions of Three-Dimensional Fatigue Crack Propagation, *Engineering Fracture Mech*anics, Vol. 58, No. 4, 1997, pp. 293-310.

[9] Wawrzynek, P. A., Martha, L. F., Ingraffea, A. R., "A Computational Environment for the Simulation of Fracture Processes in Three Dimensions," *Analytical, Numerical, and Experimental Aspects of Three Dimensional Fracture Processes*, Rosakis, A. J., *et al.*, Eds., ASME AMD-Vol. 91., New York, NY, 1988, pp. 321-327.

[10] Riddell, W. T., *Experimental Validation Testing of Three-Dimensional Fatigue and Fracture Mechanics Life Prediction Techniques*, Ph.D. Thesis, Cornell University, 1995.

[11] Pook, L. P., Greenan, A. F., "Fatigue Crack Arrest in Mild Steel Specimens Under Constant Amplitude Loading," *Fatigue of Engineering Materials and Structures*, Vol. 7, No. 1, 1984, pp. 65-73.

[12] Pook, L. P., "The Fatigue Crack Direction and Threshold Behavior of Mild Steel under Mixed Mode I and III Loading," *International Journal of Fatigue*, Vol. 7, No. 1, 1985, pp. 21-30.

[13] Sousa, J. L., Martha, L. F., Wawrzynek, P. A., Ingraffea, A. R., "Simulation of Non-Planar Crack Propagation in Three-Dimensional Structures in Concrete and Rock," *Fracture of Concrete and Rock: Recent Developments*, S. P. Shaw, S. E. Swartz, B. Barr, Eds., Elsevier Applied Science, London, 1989, pp. 254-264.

[14] Potyondy, D. O., Wawrzynek, P. A., Ingraffea, A. R., "Discreet Crack Growth Analysis Methodology for Through Cracks in Pressurized Fuselage Structures," *International Journal for Numerical Methods in. Engineering*, Vol. 38, 1995, pp. 1611-1633.

[15] Lutz, E., Gray, L. Ingraffea, A. R., "Indirect Evaluation of Surface Stress in the Boundary Element Method," *Proceedings of the IABEM-90: Symposium of the International Association for Boundary Element Methods*, 1990.

[16] Lutz, E., *Numerical Methods for Hypersingular and Near-Singular Boundary Integrals in Fracture Mechanics*, Ph.D. Thesis, Cornell University, May, 1991.

[17] Wawrzynek, P. A., Carter, B. J., Potyondy, D. O., Ingraffea, A. R., "A topological approach to modeling arbitrary crack propagation in 3D," *DIANA Computational Mechanics, '94*, G. M. A. Kusters, M. A. N. Hendriks, Eds., Kluwer Academic Publishers, 1994, pp. 69-84.

[18] Manu, C., *Three dimensional Finite Element Analysis of Cyclic Fatigue Crack Growth of Multiple Surface Flaws*, Ph.D. Dissertation, Cornell University, 1980.

[19] Gerstle, W. H., Martha, L. F., Ingraffea, A. R., "Finite and Boundary Element Modeling of Crack Propagation in Two and Three Dimensions," *Engineering Computation*, Vol. 2, 1987, pp. 167-183.

[20] Sousa, J. L., Ingraffea, A. R., "A Numerical Energy-Based Approach for Three-Dimensional Fracture Propagation," *Computer Methods in Geomechanics*, G. Beer, J. R. Booker, J. P. Carter, A. A. Balkema, Eds., Rotterdam, 1991, pp. 1653-1658.

[21] Martha, L. F., Llorca, J., Ingraffea, A. R., Elices, M., "Numerical Simulation of Crack Initiation and Propagation in an Arch Dam," *Dam Engineering*, Vol. 23, 1991, pp. 193-214.

[22] Chipalo, M. I., Gilchrist, M. D., Smith, R. A., "A Finite Element Technique for the Investigation of the Shape Development of Planar Cracks with Initially Irregular Profiles," *International Journal of Fracture*, Vol. 32, 1990, pp. 243-251.

[23] Gilchrist, M. D., Smith, R. A., "Finite Element Modeling of Fatigue Crack Shapes," *Fatigue and Fracture of Engineering Materials and Structures*, Vol. 14, 1991, pp. 617-626.

[24] Mi, Y., Aliabadi, M. H., "Three Dimensional Crack Growth Simulation using BEM," *Computational Structures*, Vol. 52, 1994, pp. 871-878.

[25] Nykänen, T. J., "Fatigue Crack Growth Simulations Based on Free Point Shape Development," *Fatigue and Fracture of Engineering Materials and Structures*, Vol. 19, 1996, pp. 99-109.

[26] Forth, S. C., Keat, W. D., "Nonplanar Crack Growth Using the Surface Integral Method," *Journal of Engineering for Gas Turbines and Power*, Vol. 119, 1997, pp. 964-968.

[27] Dhondt, G., "Automatic 3D Model I Crack Propagation Calculations with Finite Elements," *International Journal for Numerical Methods in Engineering*, Vol. 41, 1998, pp. 739-757.

[28] Timbrell, C., Claydon, P., Cook, G., "Applicaiton of ABAQUS to Analysis of 3D Cracks and Fatigue Crack Growth Prediction," *ABAQUS User's Conference Proceedings*, June 1-3, 1994, Newport, RI, pp. 527-541.

[29] Sih, G. C., Li, C. T., "Initiation and Growth Characterization of Corner Cracks Near Circular Holes," *Journal of Theoretical and Applied Fracture Mechanics*, Vol. 13, 1990, pp. 69-80.

[30] Hogden, J. and Sethna, J. P., "Determination of a General Three-Dimensional Crack Propagation Law: A Generalization of the Principle of Local Symmetry," *Physics Review B*, Vol. 47, No. 9, 1993, pp. 4831-4840.

[31] Hull, D., "Tilting Cracks: The Evolution of Fracture Surface Topology in Brittle Solids," *International Journal of Fracture*, Vol. 62, 1993, pp. 119-138.

[32] Erdogan, F., Sih, G. C., "On the Crack Extension in Plates Under Plane Loading and Transverse Shear," *Journal of Basic Engineering*, 1963, Vol. 85, pp. 519-527.

[33] Sih, G. C., "Strain Energy Density Applied to Mixed Mode Crack Problems," *International Journal of Fracture,* Vol. 10, 1974,pp. 305-321.

[34] Hussain, M. A., Pu, S. L., Underwood, J. H., "Strain Energy Release Rate for a Crack Under Combined Mode I and Mode II," *Fracture Analysis, ASTM STP 560,* American Society for Testing and Materials, Philadelphia, PA, 1974, pp. 2-28.

[35] Paris, P. C., Gomez, M. P., Anderson, W. E., "A Rational Analytic Theory of Fatigue," *The Trend in Engineering*, Vol. 13, 1961, pp. 9-14.

[36] Sih, G. C., Liebowitz, H., "Mathematical Theories of Brittle Fracture," *Fracture, Vol. II.*, H. Liebowitz, Ed., Academic, NY, 1968, pp. 67-190.

[37] Tschegg, E. K., Ritchie, R. O., McClintock, F. A., "On the Influence of Rubbing Fracture Surfaces on Fatigue Crack Propagation in Mode III," *International Journal of Fatigue*, Vol. 7, 1983, pp. 29-35.

[38] Riddell, W. T. "A Model for Probabilistic Growth of Complex Fatigue Crack Shapes," Proceedings of DETC'00, ASME Design Automation Technical Conferences, Baltimore MN, September 10-13, 2000, Paper DETC2000/RSAFP-14474, 2000.

[39] Pook, L.P., "On Fatigue Crack Paths," *International Journal of Fatigue*, Vol. 17, No. 1, 1995, pp. 5-13.

[40] Chermahini, R. G., Shivakumar, K. N., Newman, J. C., Jr., Blom, A. F., "Three-Dimensional Aspects of Plasticity-Induced Fatigue Crack Closure," *Engineering Fracture Mechanics*, Vol. 34, No. 2, 1989, pp. 393-401.

[41] "Fatigue Crack Growth Computer Program NASA/FLAGRO Version 2.0," NASA Johnson Space Center, Houston, TX, 1994.

[42] Elber, W., "Fatigue Crack Closure Under Cyclic Tension," *Engineering Fracture Mechanics*, Vol. 2, 1970, pp. 37-45.

[43] Elber, W., "The Significance of Fatigue Crack Closure," *Damage Tolerance in Aircraft Structures, ASTM 486*, American Society for Testing and Materials, Philadelphia, PA, 1971, pp. 230-242.

[44] Riddell, W. T., Piascik, R. S., Sutton, M. A., Zhao, W., McNeill, S. R., Helm, J. D., "Determining Fatigue Crack Opening Loads from Near-Crack-Tip Displacement Measurements," *Advances in Fatigue Crack Closure Measurement and Analysis, ASTM STP 1343*, R. C. McClung, J. C. Newman, Jr., Eds., American Society for Testing and Materials, West Conshockem, PA, 1999, pp. 157-174.

[45] Leadbeater, G., Kovalevskii, V. V., Noble, B., Waterhouse, R. B., "Fractographic Investigation of Fretting-Wear and Fretting Fatigue in Aluminum Alloys," *Fatigue of Engineering Materials and Structures*, Vol. 3, pp. 237-246, 1981.

[46] Ritchie, R. O., "Mechanisms of Fatigue Crack Propagation in Metals, Ceramics and Composites: Role of Crack-tip Shielding," *Materials Science and Engineering*, Vol. A103, 1988, pp. 15-28.

[47] Suresh, S. Ritchie, R. O., "A Geometric Model for Fatigue Crack Closure Induced by Fracture Surface Roughness," *Metallurgical Transactions A*, Vol. 13A, 1992, pp. 1627-1631.

[48] Newman, J.A., *The Effects of Load Ratio on Threshold Fatigue Crack Growth in Aluminum Alloys*, Ph.D. Thesis, Virginia Polytechnic Institute and State University, 2000.

Chih-Kuang Lin[1] and Chao-Pin Lin[1]

Corrosion Fatigue Behavior of 17-4 PH Stainless Steel in Different Tempers

---

Reference: Lin, C.-K. and Lin, C.-P., "**Corrosion Fatigue Behavior of 17-4 PH Stainless Steel in Different Tempers,**" *Fatigue and Fracture Mechanics: 33rd Volume, ASTM STP 1417*, W. G. Reuter and R. S. Piascik, Eds., ASTM International, West Conshohocken, PA, 2002.

Abstract: Corrosion fatigue (CF) behavior in an aerated 3.5 wt% NaCl solution has been investigated for 17-4 PH stainless steels heat treated in three conditions, namely, solution annealed (SA), peak-aged (H900), and overaged (H1150) tempers. CF tests, including both high-cycle fatigue (HCF) and fatigue crack growth (FCG), were performed as a function of load ratio and frequency. S-N curves showed that smooth specimens in H900 temper under all applied cyclic loading conditions exhibited longer CF lives than H1150 while those in the SA temper lie between them. However, the Stage II FCG rates in H900 temper were significantly greater than the H1150 and SA tempers at 20 Hz but comparable to the H1150 and SA tempers at 1 Hz. This implies crack initiation and Stage I cracking played the major role in determining the entire CF life for smooth specimen. Results also indicate that an increase in load ratio results in an increase in FCG rate and reduction of fatigue life. The CF lives at low stress levels for SA temper were increased as a result of a decrease in cyclic loading frequency from 20 to 1 Hz, which might be explained by the depassivation-dissolution-repassivation processes.

Keywords: corrosion fatigue, 17-4 PH stainless steel, load ratio effect, frequency effect

17-4 PH stainless steel, a precipitation-hardening martensitic stainless steel (PHMSS), has often been used for structural components in aircraft, chemical, naval, nuclear and other industries because of its high strength and toughness, good fabrication characteristics and corrosion resistance. The 17-4 PH steel is usually obtained from the mill in solution-annealed (SA) condition in which the microstructure is comprised of low-carbon equiaxed martensite and 5-10 vol% δ-ferrite stringers [*1, 2*]. Various combinations of mechanical properties can be obtained for 17-4 PH steels [*1, 3-5*] through proper age-hardening treatment in the temperature range of 482-621°C. The highest strength and hardness values are obtained after aging at 482°C (900°F), by which

---

[1]Professor and graduate research assistant, respectively, Department of Mechanical Engineering, National Central University, Chung-Li 320, Taiwan.

precipitation of coherent copper-rich precipitates occurs [*1*]. Aging at higher temperatures (above 540°C) would result in the precipitation of incoherent large copper-rich precipitates, lower strength and hardness, and enhancement in the toughness and stress cracking corrosion (SCC) resistance [*6-9*].

Environmentally assisted fracture has been found to account for many premature service failures of 17-4 PH components [*9-13*]. Earlier investigations on corrosion resistance of 17-4 PH stainless steels have been focused on the influence of aging treatment on the SCC resistance [*6-9*]. It has been reported that overaged condition generally provided greater SCC resistance than peak-aged condition, and the SCC resistance was enhanced with an increase in aging temperature [*8*]. The limited research work [*4, 11, 14-16*] discussing corrosion fatigue (CF) behavior of 17-4 PH steels were mainly based on either the high-cycle fatigue (HCF) or fatigue crack growth (FCG) experimental results. Little work has addressed the effects of aging treatment on the CF characteristics of such alloys. Therefore, this study is planned to characterize the environmental effects on the fatigue crack initiation and propagation stages for variously heat-treated 17-4 PH steels in an aerated 3.5 wt% NaCl solution by systematic HCF and FCG experiments in various combinations of load ratio and frequency.

Experimental Procedures

The 17-4 PH stainless steels were supplied by the vendor in the SA condition with a nominal chemical composition (wt%) of 15.18 Cr, 4.47 Ni, 3.47 Cu, 0.65 Mn, 0.38 Si, 0.15 Mo, 0.03 S, 0.02 C, 0.016 P, and balance of Fe. Specimens were prepared in three heat treated conditions, namely, as-received SA, peak-aged H900 and overaged H1150 tempers. For H900 and H1150 treatments, specimens were first heated to 1038°C, held for one hour and cooled in air. After this solution annealing step, H900 and H1150 specimens were then aged at 482°C (900°F) for one hour and at 621°C (1150°F) for four hours, respectively, followed by air cooling. The mechanical properties for each temper are given in Table 1. Fatigue tests were carried out in laboratory air and in an aerated 3.5 wt% NaCl solution at room temperature. HCF tests were conducted as per ASTM Practice for Conducting Force Controlled Constant Amplitude Axial Fatigue Tests of Metallic Materials (E 466) on axial smooth specimens in the L orientation, with a gage section of 6 mm in diameter and 18 mm in length, to determine the stress-life (S-N) curves. FCG experiments were performed in accordance with ASTM Test Method for Measurement of Fatigue Crack Growth Rates (E 647) on 6.35-mm-thick compact tension (CT) specimens machined in the L-R orientation to determine the da/dN-ΔK relationship. The salt water had a pH value of 7.2 both before and after the tests. All tests were conducted under free corrosion condition, i.e., no external potential was applied to the specimens. Details of the specimen geometry and experimental set-up for such CF tests were described elsewhere [*17*].

All fatigue tests were conducted on a closed-loop, servohydraulic machine under a sinusoidal loading wave. Fatigue tests in air were conducted with a load ratio of $R = 0.1$ and frequency of $f = 20$ Hz while those in salt water were performed at the following three combinations of load ratio and frequency: (1) $R = 0.1$, $f = 20$ Hz, (2) $R = 0.1$, $f = 1$ Hz, and (3) $R = 0.5$, $f = 1$ Hz. The HCF tests were run to failure or to 10^6 (1 Hz) or 2 x

10^6 (20 Hz) cycles where the specimen was considered to be a runout. All CT specimens were first fatigue precracked in air before testing in the corrosive environment. The crack length and crack closure level in the FCG tests were determined by the compliance technique recommended by ASTM E 647 Standard using a clip gage mounted on the front edge of the CT specimen to monitor the crack-mouth-opening displacement during testing. Characterizations of the fracture surface morphology were made by scanning electron microscopy (SEM).

Table 1-*Mechanical Properties of 17-4 PH Stainless Steel in Different Tempers*

Temper	Ultimate Tensile Strength (MPa)	Yield Strength (MPa)	Elongation (in 25 mm) (%)	Hardness (HRc)	V-notch Impact Toughness (J)
SA	1001	957	12.3	35	67
H900	1486	1454	10.6	46	21
H1150	967	836	19.1	32	75

Results and Discussion

Environmental Effect on the Fatigue Response

Figure 1 is a plot of fatigue life as a function of stress amplitude for axial smooth specimens of each temper tested at variously cyclic loading conditions in both air and 3.5 wt% NaCl solution. The counterpart results of the FCG tests using pre-cracked CT specimens are plotted as (da/dN) vs. (ΔK) in Fig. 2. The data generated at $f = 20$ Hz, $R = 0.1$ in air and salt water are discussed first in this section to examine the environmental effects on the fatigue resistance for the given alloys. Figure 1 shows that the salt water indeed generated detrimental effects on the fatigue resistance of smooth specimens in each temper as evidenced by the significant reduction in fatigue life at $f = 20$ Hz, $R = 0.1$. For each temper, the differences in the fatigue lives between the two environments became larger as the stress amplitude decreased. The ratios of the fatigue strength at 10^6 cycles in salt water to the atmospheric fatigue strength were 0.70, 0.78, and 0.88 for tempers SA, H900, and H1150, respectively. However, increased fatigue crack growth rates (FCGRs) of long cracks at $f = 20$ Hz, $R = 0.1$ in salt water, as compared to those in air, were only observed for H900 temper for the entire ΔK region (Fig. 2(b)) and at $\Delta K >$ 20 MPam$^{1/2}$ for SA temper (Fig. 2(a)). No significant difference in the FCGRs between salt water and air at $f = 20$ Hz, $R = 0.1$ was detected for H1150 temper (Fig. 2(c)). Apparently, under a cyclic loading condition of $f = 20$ Hz, $R = 0.1$, the corrosive environment generated more deleterious influence on the fatigue resistance of smooth surface than on the FCG resistance of long crack. For example, salt water, as compared with air, could reduce the fatigue life of a smooth specimen in H900 temper by an order of magnitude (Fig. 1(b)) while it only increased the FCGR of a pre-cracked specimen in the same temper by a maximum factor of five (Fig. 2(b)) at $\Delta K = 10$ MPa m$^{1/2}$

(a)

(b)

(c)

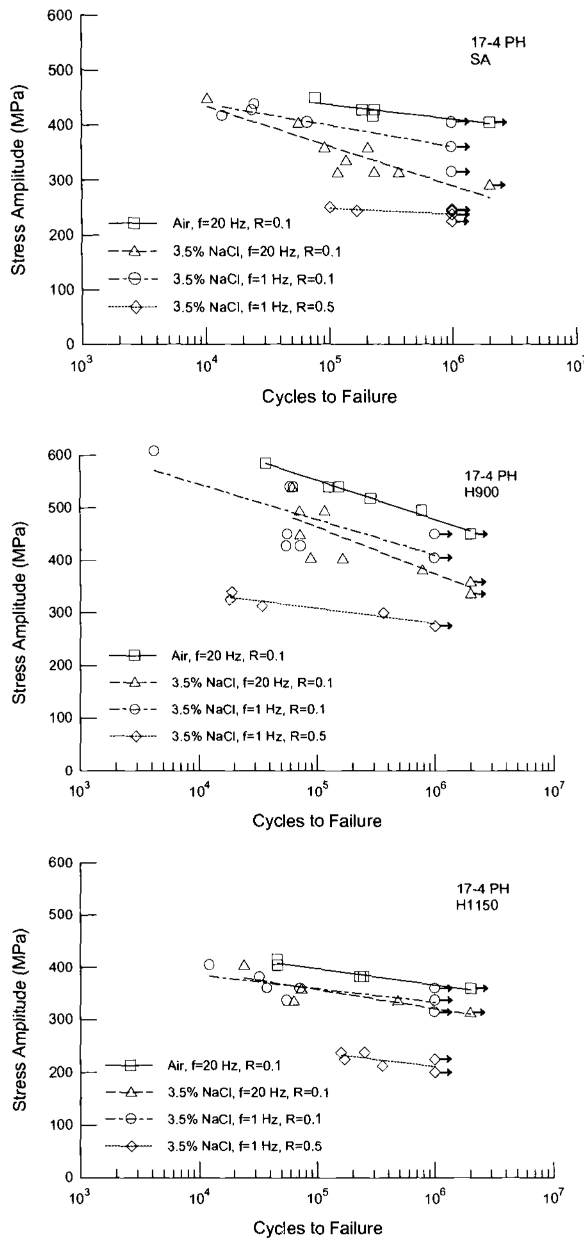

Figure 1 - *S-N curves in air and 3.5% NaCl for 17-4 PH stainless steels in three tempers: (a) SA; (b) H900; and (c) H1150. (Arrows designate runout tests.)*

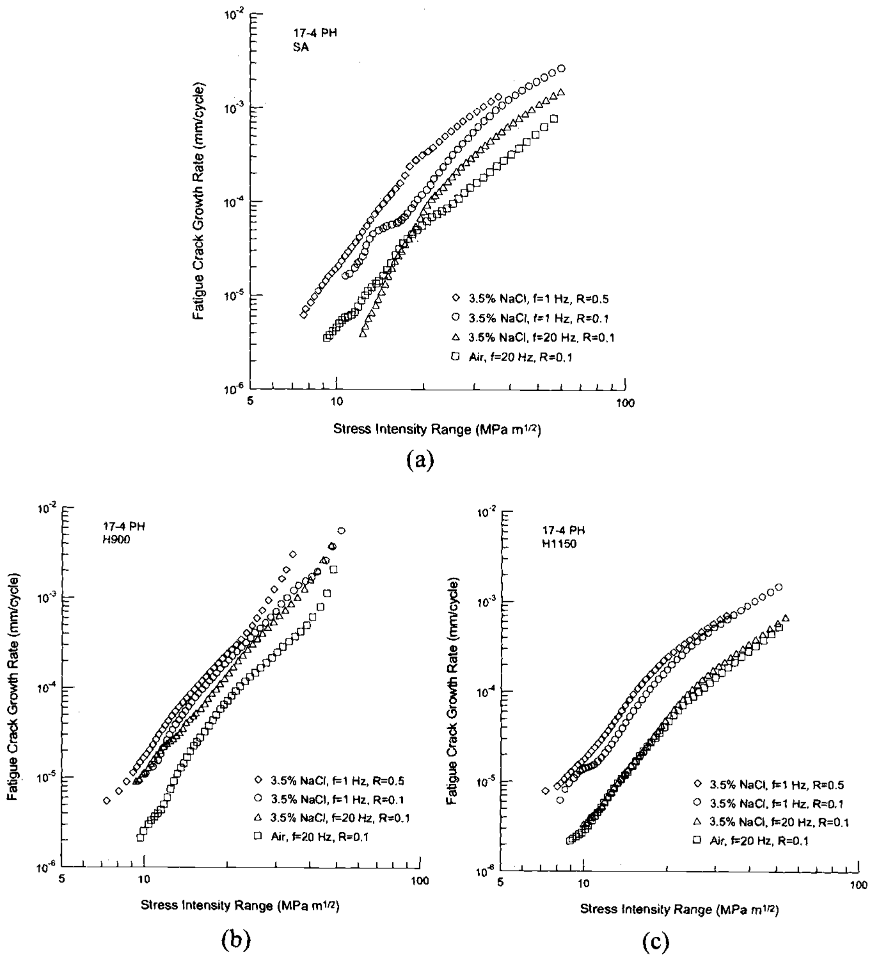

Figure 2 - *Fatigue crack growth rate curves in air and 3.5% NaCl for 17-4 PH stainless steels in three tempers: (a) SA; (b) H900; and (c) H1150.*

These HCF and FCG results indicate that the corrosive environment exerted more detrimental influence on the fatigue crack initiation and/or Stage I cracking than on the phase of Stage II crack growth for the given alloys. Similar conclusions have also been drawn for a comparable 15Cr-6Ni PHMSS in a recent study [*18*]. Miller & Akid also reported [*19*] that the fatigue lives of smooth specimens for several steels tested in both an inert air and an aggressive environment were dominated by the initial growth of crack-like defects or short cracks of microstructural dimensions. In addition, the predominant processes controlling the CF lifetime are those that strongly depend on the combined action of cyclic plastic deformation and the aggressive environment which together often lead to strain localization and enhanced growth of defects/short cracks;

these include pitting, preferential dissolution, Stage I and the Stage I-to-Stage II crack growth processes [*19*]. It was generally assumed that pits and/or localized corrosion of emerging slip steps or extrusion, somehow induced by CF process, prematurely initiate fatigue cracking or reduce the applied stress required to initiate fatigue cracks [*19-21*]. Therefore, in the present work, the generation of crack-like defects followed by their enhanced growth is likely to occur at an earlier stage in saline solution compared to the atmospheric environment, thereby leading to a considerable reduction of fatigue life for HCF specimens. SEM fractography observations provided some support for this explanation.

Figure 3 shows the typical fracture surface morphology near the crack initiation sites in H1150 HCF specimens tested in salt water under f = 20 Hz at long-life regime. This fracture surface morphology is similar to that observed for SA. As shown in Fig. 3, the fatigue crack was initiated at a corrosion-induced surface defect which was absent in the specimens tested in air. The corrosion-induced surface defect not only can serve as a stress concentration site to become a Stage I crack, but its enhanced growth under the synergism between the aggressive environment and the cyclic stresses can also reduce the transition period from Stage I to Stage II crack growth. However, when the crack length was large enough to overcome the dominant microstructural barrier, the environmental effects became less important [*19*]. This is supported by the experimental results presented in Fig. 2 which shows a lesser extent of differences in the FCGRs of long crack between the saltwater and air environments as compared to the counterpart HCF results in Fig. 1. However, as shown in Fig. 4, no such visible corrosion-induced surface defects could be detected at the fracture origins for H900 HCF specimens. As shown in Fig. 4(b), H900 specimens were often found to fail from subsurface inclusions which are also favorable sites for premature fatigue cracking under corrosive environments. These microstructural stress concentrations would also cause strain localization and enhance the preferential dissolution or film rupture at the surfaces near them [*19*]. In this regard, the fatigue lives in H900 specimens were still substantially shortened by the aggressive environment even though no visible-sized surface defects were identified as the fatigue crack origins. Therefore, the significant reduction in fatigue life of HCF specimen tested in 3.5% NaCl solution could be attributed to the faster initiation and/or growth of crack-like defects (corrosion-induced or inherent) and shorter transition period from Stage I to Stage II cracking, in particular at the lower applied stress levels.

It has been reported [*2, 22*] that the peak-aged temper had greater pitting resistance than the SA and overaged tempers in acidic chloride media for 17-4 PH. The beneficial effect of copper in solid solution form on promoting passivity, as observed in other stainless steels, was less effective for the SA temper of 17-4 PH because of the active dissolution of the unaged (stressed) martensite and the δ ferrite [*2, 22*]. However, in peak-aged condition, the stress relief of the martensite due to aging and the formation of a protective copper oxide film resulted in autopassivation [*2, 22*]. In overaged condition, the presence of incoherent large copper-rich precipitates and reformed austenite significantly reduced the pitting resistance [*2, 22*]. These differences in pitting resistance for variously heat-treated 17-4 PH stainless steels might help explain why the corrosion-induced surface defects were visible by SEM at the fracture initiation sites in SA and H1150 HCF specimens (Fig. 3) but not for H900 (Fig. 4).

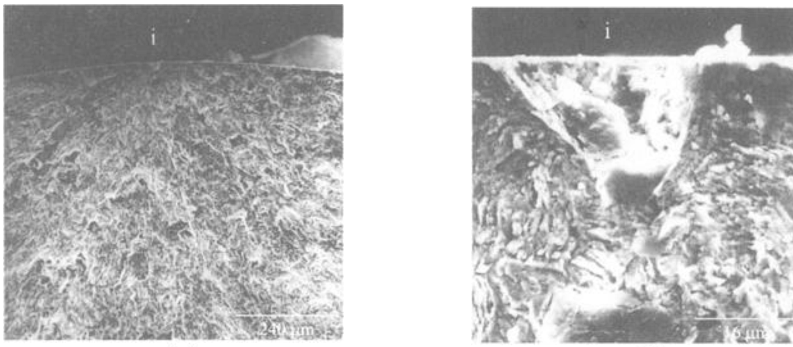

(a) (b)

Figure 3 - *SEM fractography of 17-4 PH-H1150 stainless steel tested at 20 Hz in 3.5% NaCl: (a) slow crack growth region; and (b) fracture origin. (i: crack initiation site.)*

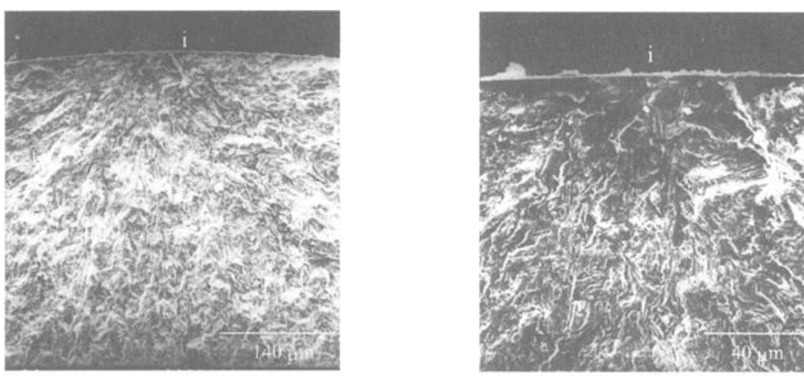

(a) (b)

Figure 4 - *SEM fractography of 17-4 PH-H900 stainless steel tested in 3.5% NaCl: (a) slow crack growth region; and (b) fracture origin. (i: crack initiation site.)*

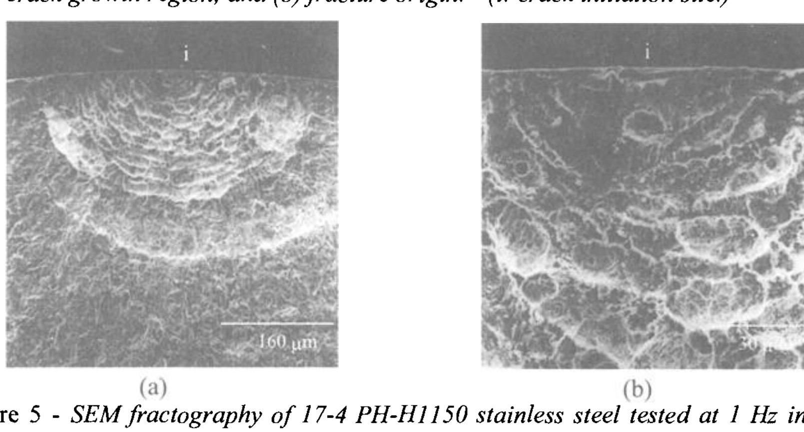

(a) (b)

Figure 5 - *SEM fractography of 17-4 PH-H1150 stainless steel tested at 1 Hz in 3.5% NaCl: (a) slow crack growth region; and (b) fracture origin. (i: crack initiation site.)*

Frequency Effect on CF Response

The frequency effect on the CF behavior for the given alloys can be evaluated by comparing the results of 20 and 1 Hz at R = 0.1 shown in Figs. 1 and 2. It can be seen in Fig. 1 that, for the given three tempers the CF strengths at 10^6 cycles at 1 Hz, R = 0.1 were comparable with (H1150) or greater than (SA and H900) those at 20 Hz, R = 0.1. Based on the best-fitted S-N curves shown in Fig. 1, the amounts of change in CF strength at 10^6 cycles at 1 Hz relative to 20 Hz are 25%, 12% and 4% for tempers SA, H900 and H1150, respectively. This trend of variation in CF strength of smooth surface with decreasing loading frequency for the given alloys is opposite to the generally known influence of loading frequency on the CF strength [*19*]. The CF life is usually expected to be shorter at a lower loading frequency as more time becomes available in each cycle for the environmental interactions to degrade the fatigue strength. The corresponding FCG data shown in Fig. 2 indeed exhibit this behavior as the FCGRs (in da/dN) in salt water were increased with a decrease in frequency. In particular, H1150 showed the largest increase in FCGR among the three tempers as a result of reducing frequency.

The different frequency effects on the S-N and FCGR curves for the given alloys might be explained by the depassivation-dissolution-repassivation processes, which might function differently in these two types of tests. As CF lifetimes in the HCF tests, performed on smooth specimens, are essentially controlled by the initiation and/or growth of surface or subsurface crack-like defects of microstructural dimensions, the stability of the passive film on the surfaces of corrosion-induced defects and/or initiated microcracks may play a very important role in determining the CF strength in smooth specimens. The film rupture-dissolution model of CF [*19*] postulated that a passive film is ruptured by mechanical stress, causing increased anodic dissolution of metal in the vicinity of the emerging slip step. However, when the duration of each cycle is sufficient, repassivation, which accompanies the dissolution process, may continuously repair the film and reduce the anodic dissolution of newly emerging metal, leading to a longer fatigue life. Therefore, it is proposed that the comparable or higher CF strength observed at 1 Hz relative to 20 Hz for the given alloys was due to a longer time available in each cycle for repassivation mechanism to operate and delay the growth of surface crack-like defects and microcracks in the initiated cracking stage. Perhaps at 20 Hz, repeated rupture of the surface film during cyclic loading is too rapid to permit repassivation, thereby resulting in lower stability of the oxide film and lower CF strength for smooth specimen.

It was also reported [*23*] that the above film rupture-dissolution mechanism is more likely to operate in neutral solutions than in acidic solutions where oxide films are soluble. This might explain the enhanced Stage II FCGRs in salt water with decreasing cyclic frequency observed in the present work. It has been reported [*24*] that in a long crack a decrease in pH value due to metal ion hydrolysis could occur at the crack tip in 3.5% NaCl solution for several alloy steels including 17-4 PH in H900 temper. It was also found [*24*] that the pH values for the crack tip solution were always 3.6-3.8 regardless of the particular type of alloy steel tested in a saltwater environment with a pH value of 6. Therefore, the situation at the crack tip of the long crack in a CT specimen might resemble that of a CF test performed in a very acidic chloride medium, which would be more favorable for the dissolution than the passivation process. In this regard, the FCGRs of pre-cracked CT specimens tested in salt water at 1 Hz were greater than those at 20 Hz due to a longer time available in each loading cycle for the dissolution mechanism to perform at the crack tip. In addition to the dissolution mechanism, the hydrogen embrittlement effect might also be operative around the crack tip and became more effective at a lower frequency to accelerate the FCGR in the aqueous environment.

The fractography observations also provide evidence for the above explanation. Typical fracture surface morphology for the HCF specimens of H1150 temper tested in salt water under f = 1 Hz at long-life regime is shown in Fig. 5. This fracture surface morphology is similar to that observed for SA. In Fig. 5(a), semicircular dimple-rings emanating from the fracture origin can be clearly identified in the early crack growth region. Higher magnification view of this region (Fig. 5(b)) shows the existence of numerous corrosion-induced dimples along each semicircular ring representing the wake of depassivation-dissolution-repassivation processes during initiated fatigue crack growth. Once the fatigue crack grew to a certain size, these dimple-rings disappeared, implying the crack tip solution might become very acidic and repassivation was diminished. SEM observations on the fracture surfaces of the CT specimens tested at 1 Hz in salt water also indicated the absence of similar bands of corrosion-induced hollows, presumably because the local solution at the crack tip of a long crack was acidic. No such semicircular rings of corrosion-induced hollows were detected on the fracture surfaces of the HCF specimens tested at 20 Hz in salt water (Fig. 3) indicating the high possibility of continuous film rupture and dissolution of emerging slip steps without enough repassivation under this higher loading frequency.

Effect of Load Ratio on CF Response

The influence of load ratio on the CF behavior for the given alloys can be seen with a comparison of the results of R = 0.5 and 0.1 at 1 Hz shown in Figs. 1 and 2. As shown in Fig. 1, an increase in load ratio from R = 0.1 to 0.5 at 1 Hz significantly reduced the CF lives for each temper tested in salt water. The ratios of the CF strength at 10^6 cycles for R = 0.5 relative to R = 0.1 are 0.66, 0.67 and 0.63 for tempers SA, H900 and H1150, respectively. The FCG data presented in Fig. 2 also reveal that the FCGR in salt water for a given temper was enhanced by increasing the load ratio but the extent of change was less than that exhibited in the corresponding S-N behavior. This might be explained in two aspects. First, a higher load ratio would reduce the crack closure effects induced by the corrosive products, leading to a higher growth rate in Stage I cracking and a significant reduction of CF lifetimes for smooth specimens. Second, a higher tensile mean stress would generate a larger deformation and increase the influence of SCC-related mechanisms such as film rupture-dissolution on the initiated defect/crack growth and degrade the fatigue strength to a greater extent.

It can be seen in Fig. 2 that for a given near-threshold FCGR value (say 10^{-5} mm/cycle) the corresponding ΔK is significantly higher in R = 0.1 than in R = 0.5 for all tempers. The faster near-threshold growth rates (and presumably lower thresholds) observed at high load ratio in salt water might be attributed to the crack closure effect. As shown in Fig. 6, by factoring out the crack closure level, the intrinsic FCGRs at R =

0.5 were only slightly larger than those at R = 0.1, in particular for H900 and H1150 tempers. Suresh et al. [*25, 26*] observed that, in addition to the plasticity-induced crack closure, oxide-induced crack closure played a very important role in rationalizing the effects of load ratio on near-threshold FCG characteristics for several steels in aggressive environments. Apparently, the observed load ratio effects on the near-threshold FCGRs in the current study may also be explained by such oxide-induced crack closure effect. Moreover, mean-stress dependent SCC mechanism only exerted slightly detrimental effects on the Stage II cracking in salt water for the given alloys, as indicated by the small difference in intrinsic FCGRs for R = 0.1 and 0.5 in Fig. 6.

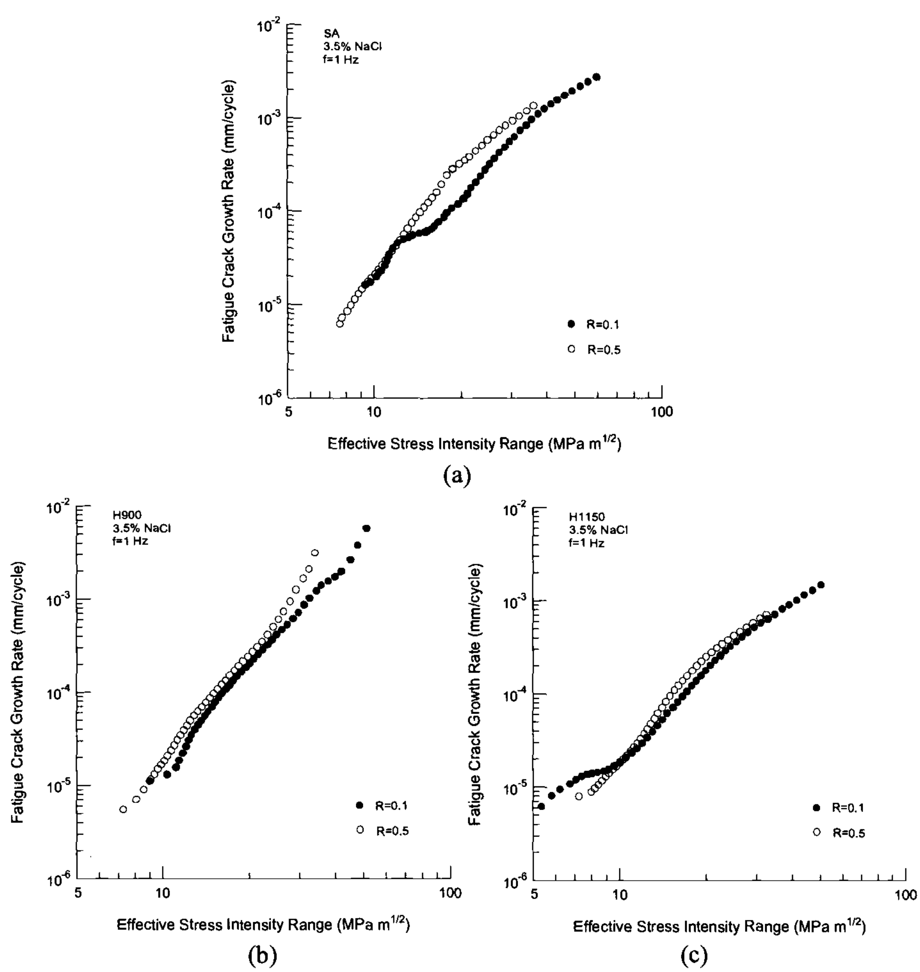

Figure 6 - *(da/dN)- ΔK_{eff} curves at various load ratios for 17-4 PH stainless steels in three tempers: (a) SA; (b) H900; and (c) H1150.*

Comparison of CF Resistance in Different Tempers

Comparisons of the S-N curves for different tempers in the air and saltwater environments are shown in Fig. 7. As shown in Fig. 7, the fatigue strength of smooth samples, regardless of which testing condition, appears to increase with the monotonic tensile strength and hardness of the given alloys. That is, the tensile strength, hardness, and fatigue strength in smooth samples for the three tempers take the following order: H900 > SA > H1150. Comparisons of the FCGRs of long cracks for various tempers under the same given test conditions are presented in Fig. 8. As shown in Fig. 8, when tested at f = 20 Hz and R = 0.1 in air and salt water, the H900 temper exhibit higher FCGRs than H1150 and SA tempers. However, the FCGRs for f = 1 Hz with R = 0.1 or 0.5 were not significantly different for the three tempers. The inferior resistance to long crack growth possessed by H900 temper at f = 20 Hz might be partially attributed to its lower toughness as compared to the other two tempers. An earlier study [*4*] also indicated that the fracture toughness of 17-4 PH exhibited a distinct minimum at peak-aged H900 temper leading to higher FCGRs at f = 10 Hz in both dry argon and water-saturated argon, as compared to an overaged H1100 temper.

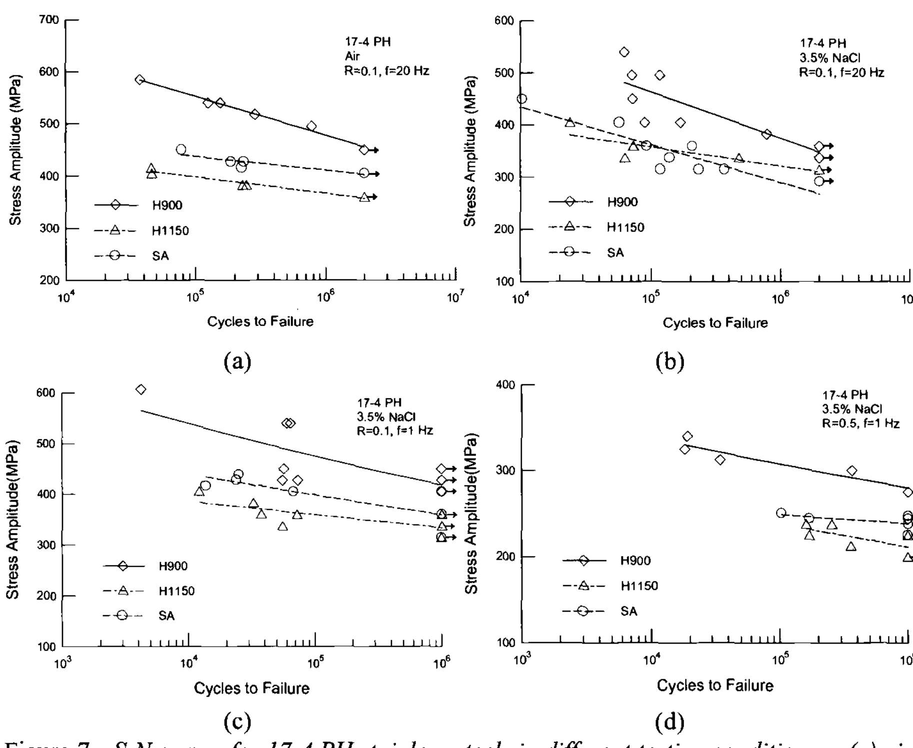

Figure 7 - *S-N curves for 17-4 PH stainless steels in different testing conditions: (a) air, f = 20 Hz, R = 0.1; (b) 3.5% NaCl, f = 20 Hz, R = 0.1; (c) 3.5% NaCl, f = 1 Hz, R = 0.1; and (d) 3.5% NaCl, f = 1 Hz, R = 0.5. (Arrows designate runout tests.)*

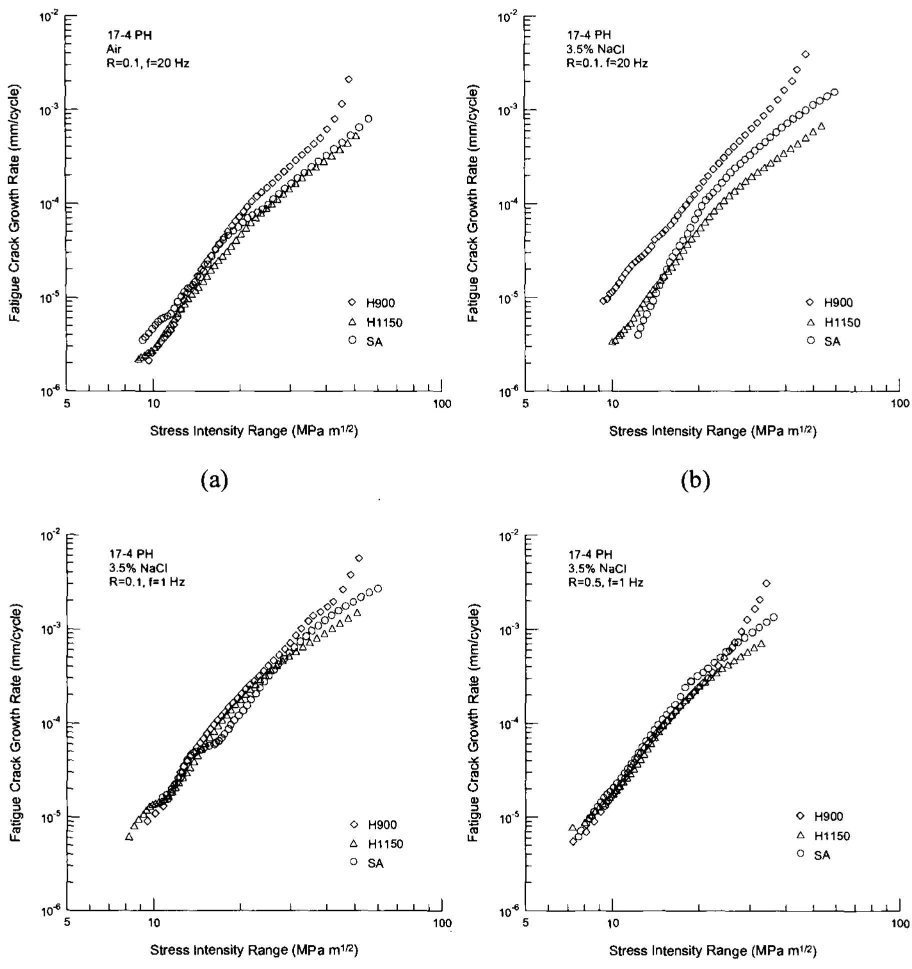

Figure 8 - *Comparison of fatigue crack growth rate curves for 17-4 PH stainless steels in different testing conditions: (a) air, $f = 20$ Hz, $R = 0.1$; (b) 3.5% NaCl, $f = 20$ Hz, $R = 0.1$; (c) 3.5% NaCl, $f = 1$ Hz, $R = 0.1$; and (d) 3.5% NaCl, $f = 1$ Hz, $R = 0.5$.*

As shown in Fig. 7, smooth specimens of H900 temper have the longest CF lives in comparison to the SA and H1150 tempers. However, the FCG data in salt water presented in Fig. 8 indicate that H900 temper generated the highest or comparable Stage II FCGRs for pre-cracked CT specimens in comparison to the other two heat-treated conditions. Comparisons made in Figs. 7 and 8, again, indicate the HCF behavior in 3.5 wt% NaCl solution might be controlled by the stages of crack initiation and/or early growth of short cracks to a Stage II crack for the given PHMSSs. Therefore, the superiority of the H900 to H1150 and SA tempers in corrosive HCF resistance may be attributed to its greater inherent resistance to crack initiation and/or small crack growth. Similar trends have also been found for another comparable grade of PHMSS [*18*]. That is, the corrosive environment did not significantly change the relative superiority of the given three tempers in resistance to crack initiation and/or small crack growth and accordingly the trend of S-N behavior. This is supported by Fig. 7 which shows that the trends of the relative differences of the given three tempers in the HCF characteristics were not significantly different in both given environments except the S-N curves were all shifted toward lower stress levels in salt water. Therefore, the differences in the CF strengths of the given three tempers at variously cyclic loading conditions are primarily due to their inherent differences in resistance to crack initiation and/or small crack growth, as they are in the air environment.

Conclusions

1. Comparison of the S-N curves and FCGR curves for long cracks in both air and 3.5% NaCl solution for 17-4 PH stainless steel in different tempers indicates that the corrosive environment exerted more influence on the S-N behavior than on the Stage II crack growth.

2. An increase in load ratio could cause the reduction of HCF lifetime and an increase in Stage II FCGR for the given alloys when tested in saline solution.

3. A higher HCF strength in salt water was observed for SA temper when the cyclic loading frequency was reduced from 20 to 1 Hz. This might be explained by the suggestion that repeated rupture of surface film under a cycling loading of 20 Hz is too rapid to permit repassivation, thereby resulting in lower stability of the oxide film and lower CF strength for smooth specimens.

4. The CF lives of smooth specimens tested in salt water were controlled by the crack initiation and/or small crack growth rather than by the Stage II crack growth. This is inferred from the fact that the peak-aged temper exhibited higher or comparable FCGR for Stage II crack growth but produced longer HCF lifetime in comparison to the overaged and SA tempers.

5. The superiority of the peak-aged temper to SA and overaged tempers in corrosive HCF behavior may be attributed to its greater inherent resistance to crack initiation and/or small crack growth. This is attributed to the similar trends of the relative differences in S-N characteristics among the given three tempers observed in the air and aqueous sodium chloride environments regardless of the cyclic loading conditions.

Acknowledgments

This work was supported by the Taiwan Power Company and managed by the National Science Council of the Republic of China (Taiwan) under Contract No. NSC-88-TPC-E-008-002.

References

[1] Smith, W. F., *Structure and Properties of Engineering Alloys*, 2nd ed., McGraw-Hill, Inc., New York, 1993.

[2] Mudali, U. K., Bhaduri, A. K., and Gnanamoorthy, J. B., "Corrosion Behavior of 17-4 PH Stainless Steel," *Materials Science and Technology*, Vol. 6, 1990, pp. 475-481.

[3] Pickering, F. B., "Physical Metallurgy of Stainless Steel Developments," *International Metals Reviews*, Vol. 21, 1976, pp. 227-268.

[4] Rack, H. J. and Kalish, D., "The Strength, Fracture Toughness, and Low Cycle Fatigue Behavior of 17-4 PH Stainless Steel," *Metallurgical Transactions*, Vol. 5, 1974, pp. 1595-1605.

[5] Mishra, R. D. K., Prasad, G. Y., Balasurbramanian, T. V., and Rao, P. R., "On Variation of Impact Toughness in 17-4 Precipitation Hardened Stainless Steel," *Scripta Metallurgica*, Vol. 21, 1987, pp. 1067-1070.

[6] Raja, K. S. and Rao, K. P., "On the Hardness Criterion for Stress Corrosion Cracking Resistance of 17-4 PH Stainless Steel," *Journal of Materials Science Letters*, Vol. 12, 1993, pp. 963-966.

[7] Dull, D. L. and Raymond, L., "A Test Procedure to Evaluate the Relative Susceptibility of Materials to Stress Corrosion Cracking," *Corrosion*, Vol. 29, 1973, pp. 205-212.

[8] Truman, J. E., "Stress-Corrosion Cracking of Martensitic and Ferritic Stainless Steels," *International Metals Reviews*, Vol. 26, 1981, pp. 301-349.

[9] Carter, C. S., Farwick, D. G., Ross, A. M., and Uchida, J. M., "Stress Corrosion Properties of High Strength Precipitation Hardening Stainless Steels," *Corrosion*, Vol. 27, 1971, pp. 190-197.

[10] Heymann, F. J., Swaminathan, V. P., and Cunningham, J. W., "Steam Turbine Blades: Considerations in Design and a Survey of Blade Failure," Report No. CS-1967, Electrical Power Research Institute, Palo Alto, CA, 1981.

[11] Syrett, B. C., Viswanathan, R., Wing, S. S., and Wittig, J. E., "Effect of Microstructure on Pitting and Corrosion Fatigue of 17-4 PH Turbine Blade Steel in Chloride Environments," *Corrosion*, Vol. 38, 1982, pp. 273-282.

[12] Swaminathan, V. P. and Cunningham, J. W., "Correlations Between LP Blade Failures and Steam Turbine Characteristics," *Corrosion Fatigue of Steam Turbine Blade Materials*, R. I. Jaffee Ed., Pergamon Press, New York, 1983, pp. 3.1-3.16.

[13] Thompson, R. M., Kohut, G. B., Canfield, D. R., and Bass, W. R., "Sulfide Stress Cracking Failures of 12Cr and 17-4 PH Stainless-Steel Wellhead Equipment," *Corrosion*, Vol. 47, 1991, pp. 216-220.

[14] Islam, M. U., Campbell, G., and Hsu, R., "Fatigue and Tensile Properties of EB Welded 17-4 PH Steel," *Welding Journal*, Vol. 68, 1990, pp. 45-50.

[15] Willertz, L. E., Rust, T. M., and Swaminathan, V. P., "High Cycle Corrosion Fatigue of Some Steam Turbine Blade Alloys," *Corrosion Fatigue of Steam Turbine Blade Materials*, R. I. Jaffee Ed., Pergamon Press, New York, 1983, pp. 3.75-3.106.

[16] Rust, T. M. and Swaminathan, V. P., "Corrosion Fatigue Testing of Steam Turbine Blading Alloys," *Corrosion Fatigue of Steam Turbine Blade Materials*, R. I. Jaffee Ed., Pergamon Press, New York, 1983, pp. 3.107-3.129.

[17] Lin, C.-K. and Yang, S.-T., "Corrosion Fatigue Behavior of 7050 Aluminum Alloys in Different Tempers," *Engineering Fracture Mechanics*, Vol. 59, 1998, pp. 779-795.

[18] Lin, C.-K. and Tsai, W.-J., "Corrosion Fatigue Behavior of a 15Cr-6Ni Precipitation-Hardening Stainless Steel in Different Tempers," *Fatigue and Fracture of Engineering Materials and Structures*, Vol. 23, 2000, pp. 489-497.

[19] Miller, K. J. and Akid, R., "The Application of Microstructural Fracture Mechanics to Various Metal Surface States," *Proceedings of the Royal Society of London, Series A*, Vol. 452, 1996, pp. 1411-1432.

[20] Laird, C. and Duquette, D. J., "Mechanisms of Fatigue Crack Nucleation," *Corrosion Fatigue: Chemistry, Mechanics and Microstructure*, O. Devereux, A. J. McEvily and R. W. Staehle Eds., National Association of Corrosion Engineers, Houston, 1972, pp. 88-117.

[21] McAdam, D. J. "Stress-Strain Relationships and the Corrosion-Fatigue of Metals," *Proceedings ASTM*, Vol. 26, 1926, pp. 224-254.

[22] Raja, K. S. and Pao, K. P., "Pitting Behavior of Type 17-4 PH Stainless Steel Weldments," *Corrosion*, Vol. 51, 1995, pp. 586-592.

[23] Evans, U. R. and Simnad, M. T., "The Mechanisms of Corrosion Fatigue of Mild Steel," *Proceedings of the Royal Society of London, Vol. A188*, 1947, pp. 372-392.

[24] Sandoz, G., Fujii, C. T., and Brown, B. F., "Solution Chemistry Within Stress-Corrosion Cracks in Alloy Steels," *Corrosion Science*, Vol. 10, 1970, pp. 839-845.

[25] Suresh, S., Zamiski, G. F., and Ritchie, R. O., "Oxide-Induced Crack Closure: An Explanation for Near-Threshold Corrosion Fatigue Crack Growth Behavior," *Metallurgical Transactions A*, Vol. 12A, 1981, pp. 1435-1443.

[26] Suresh, S. and Ritchie, R. O., "On the Influence of Environment on the Load Ratio Dependence of Fatigue Thresholds in Pressure Vessel Steel," *Engineering Fracture Mechanics*, Vol. 18, 1983, pp. 785-800.

Assorted Titles

John A. Newman[1] and Robert S. Piascik[2]

Plasticity and Roughness Closure Interactions Near the Fatigue Crack Growth Threshold

Reference: Newman, J. A. and Piascik, R. S., "**Plasticity and Roughness Closure Interactions Near the Fatigue Crack Growth Threshold,**" *Fatigue and Fracture Mechanics: 33rd Volume, ASTM STP 1417*, W. G. Reuter and R. S. Piascik, Eds., ASTM International, West Conshohocken, PA, 2002.

Abstract: An advanced model has been developed to calculate interactions between plasticity and roughness closure mechanisms resulting in the fatigue crack growth threshold. Near-threshold closure is complex because multiple closure mechanisms are likely, including roughness-, oxide-, and plasticity-induced crack closure. Results show closure first occurs either at the crack tip (tip contact), or at the fatigue-crack-surface asperity nearest the crack tip (asperity contact), in the absence of load history effects. Model calculations, verified by laboratory experiments, reveal a transition from tip contact to asperity contact produces fatigue crack growth threshold behavior; here, both model and experiment show that an abrupt increase in closure (asperity contact) results in the rapid decrease in fatigue crack growth rate at threshold. A comparison of an advanced crack-tip load displacement measurement technique, and standard global compliance methods show that global methods lack the sensitivity to accurately characterize crack closure at threshold.

Keywords: fatigue crack closure, threshold, plasticity, roughness, crack.

Introduction

From the time Paris related fatigue crack growth rate, da/dN, to the cyclic stress intensity factor range, ΔK ($K_{max} - K_{min}$) [*1*], researchers have sought an explanation for load ratio ($R = K_{min}/K_{max}$) effects. A major breakthrough occurred when Elber proposed that R effects are due to crack-face contact during cyclic loading, termed crack closure [*2*]. According to Elber's model, closed cracks are protected from fatigue damage and da/dN is related to an effective crack-tip driving force, ΔK_{eff}, as defined in Equations 1 and 2. (K_{cl} is the value of stress intensity factor at which closure occurs.) The crack closure concept explains fatigue crack growth (FCG) R effects because cracks are closed during a greater portion of the load cycle at low R.

[1] U. S. Army Research Laboratory, Vehicle Technology Directorate, MS 188E, Hampton, VA 23681.

[2] NASA Langley Research Center, Metals and Thermal Structures Branch, MS 188E, Hampton, VA 23681.

$$\Delta K_{eff} = K_{max} - K_{cl} \quad (1)$$

$$da/dN = f(\Delta K_{eff}) \quad (2)$$

By plotting d*a*/dN against ΔK_{eff} (instead of ΔK), differences between data generated at different R are reduced nearly to a single curve in the FCG Paris regime. However, using experimentally determined closure loads to calculate ΔK_{eff} does not eliminate near-threshold R effects [*3-9*]. For example, consider the FCG data for titanium alloy Ti 6-2-2-2-2 plotted in Figure 1 [*9*]. Testing was done at 5 Hz in laboratory air using a computer-controlled servo-hydraulic test machine. Crack length was continuously monitored during tests using far-field compliance data [*10*], and loads were adjusted to achieve programmed stress intensity factors. Threshold tests were conducted in accordance with ASTM standards (E647) for R = 0.1 (solid circular symbols) and R = 0.5 (open circular symbols) while continuously reducing ΔK at a K-gradient of C = -78.7 m^{-1}. Constant-K_{max} = 11.0 MPa√m threshold test data (C = -394 m^{-1}) are shown as solid triangular symbols, and are of interest because they are produced at high R where closure does not occur [*11, 12*]. R increases during constant-K_{max} threshold tests because K_{max} is held constant and ΔK is reduced by increasing K_{min}. For the constant-K_{max} data in Figure 1, the load ratio increased from R = 0.5 at ΔK = 5.5 MPa√m to R = 0.85 at threshold (ΔK = 1.6 MPa√m). It should be noted that constant-K_{max} and constant-R test results were in good agreement where values of ΔK and R coincide, *e.g.* the R = 0.5 data is in good agreement with the constant-K_{max} = 11.0 MPa√m data at ΔK = 5.5 MPa√m. Load and far-field compliance data were monitored during testing (per E647) and used to determine closure loads [*13*]. Closure was not detected during the R = 0.5 or K_{max} = 11.0 MPa√m tests, but was detected during the R = 0.1 test. Closure determinations were used to

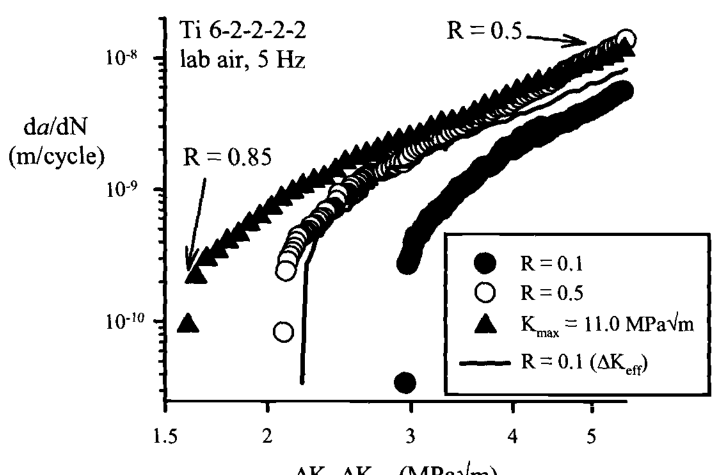

Figure 1 – *FCG data from reference [9] shows that far-field compliance-based closure determinations do not accurately characterize crack-tip closure at threshold.*

compute the R = 0.1 closure-corrected data (ΔK_{eff}) shown as the solid line curve in Figure 1; these data nearly coincide with the R = 0.5 data, suggesting that closure explains R effects between these curves. However, closure was not detected during the R = 0.5 and K_{max} = 11.0 MPa$\sqrt{m}$ tests, so far-field closure determinations were unable to reduce these data to a single d*a*/dN versus ΔK_{eff} curve; two explanations for this are: (1) far-field compliance methods were unable to accurately characterize crack closure, or (2) additional damage occurs at high R. As for the latter explanation, closure-free R effects have been observed during constant-K_{max} threshold tests [*8*], but these effects are small for Ti 6-2-2-2-2 [*9*]. The former explanation is more likely; that is, the R = 0.5 data is affected by closure, but in a subtle way not detected by far-field compliance determinations. In fact, the authors of the data in Figure 1 concluded that far-field compliance techniques lack the fidelity to accurately resolve closure loads [*9*].[3]

Current experimental techniques do not directly measure crack closure. Instead, changes in specimen compliance that occur as fatigue cracks close are used to determine closure loads. The relationship between compliance changes and crack-tip closure events is uncertain because different closure investigations have arrived at contradictory conclusions, due in part to differences in experimental techniques and attempts to make general conclusions from results for specific test conditions [*9, 14, 15, 18-21*]. Closure determinations are problematic at FCG threshold because loads and displacement ranges are small, making compliance changes difficult to distinguish. Further, multiple closure mechanisms near the FCG threshold likely create complex closure situations.

Three closure mechanisms are likely at threshold; plasticity-, roughness-, and oxide-induced crack closure (PICC, RICC, and OICC, respectively). Elber proposed closure is caused by residual plastic strains in the wake of propagating fatigue cracks, *i.e.* PICC [*2*]. Voluminous crack-mouth oxide debris and contact of rough crack surfaces have also been proposed as closure mechanisms, *i.e.* OICC and RICC, respectively [*22, 23*]. Generally, PICC is dominant in the Paris regime while the contributions of RICC and OICC are second-order effects [*24*]. As FCG threshold is approached, crack opening displacements approach the size of oxide debris and rough crack-surface asperities, and RICC and OICC also become first-order effects [*22, 23*].

A relationship between fatigue crack growth rate (d*a*/dN) and the true crack-tip driving force is needed to make accurate damage tolerance life predictions. For structures to endure long fatigue lives, designers must ensure the majority of fatigue life occurs at slow FCG rates at or below the FCG threshold. In these cases, an accurate characterization of near-threshold FCG is especially important. However, closure at threshold is not well understood and experimentally difficult to quantify (recall Figure 1). To provide a more comprehensive understanding of crack closure near the FCG threshold, a model was developed by the authors that included PICC, RICC, and OICC

[3] Some researchers have reported that crack closure may occur far behind the crack tip due to the large residual deformations produced by the high initial ΔK values at the start of testing [*14-17*]. This remote closure affects FCG rates, but does not completely shield the crack from fatigue damage, and may partially explain why correlating threshold FCG data is difficult. However, the data presented in this paper is not affected by remote closure, so the conclusions made from these results are believed to be independent of load history.

[*25-27*]. The objectives of this paper are (1) to show how PICC and RICC interactions affect FCG threshold, and (2) to evaluate the fidelity of compliance-based experimental techniques to determine crack-tip closure loads near the FCG threshold.

Crack Closure Model

To achieve a more comprehensive description of near-threshold crack closure, a model was developed to consider the three closure mechanisms most likely at FCG threshold (PICC, RICC, and OICC). This model (called the CROP model for Closure, Roughness, Oxide, and Plasticity) is unique because it considers interactions between closure mechanisms at threshold. Most models are limited to a single closure mechanism and are unable to describe the interactions between multiple closure mechanisms likely to occur near the FCG threshold. Plasticity-based models adequately predict R effects in the Paris regime where PICC dominates, but lack fidelity at FCG threshold because RICC and OICC are neglected [*14, 15*]. RICC and OICC models have been developed to predict closure loads at the FCG threshold, but are limited because PICC is not considered, or they rely on empirical relations (which may be application specific) [*28-30*]. Recently, closure models have been developed to consider the combined effects of PICC and RICC, but neglect OICC [*31, 32*].

The CROP model includes the combined effects of PICC, RICC, and OICC, which gives a new understanding of crack closure that is not obvious by considering each mechanism individually.[4] This model idealizes rough cracks as a two-dimensional sawtooth, shown schematically in Figure 2 [*28, 29, 31*]. This crack configuration describes rough crack surfaces with only two parameters – asperity angle, α, and asperity length, g – while preserving the essential features of rough cracks. A plasticity model developed by Budiansky and Hutchinson [*33*] was modified to include crack-wake plasticity for rough cracks. Crack-wake oxide is modeled as a rigid layer along the rough crack surfaces, having uniform thickness, t [*30*]. By selecting appropriate values for model parameters (*e.g.* R, K_{max}, α, g, and t) specific materials, environments, and loading conditions can be simulated.

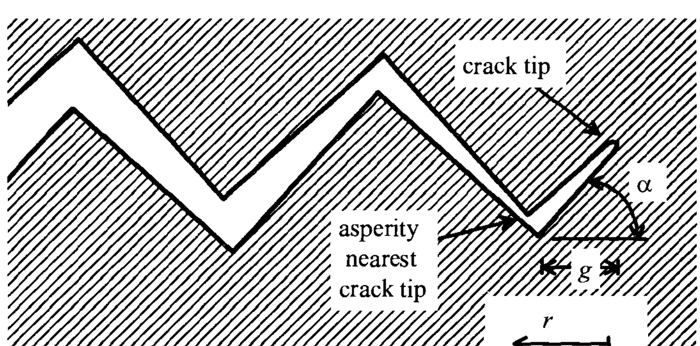

Figure 2 – *The idealized rough crack configuration of the CROP model is shown.*

[4] The CROP model is briefly described herein. See reference [*27*] for greater detail.

The CROP model calculates closure loads in terms of crack-face displacements and crack-wake effects. Mixed-mode crack-face displacements occur in the crack-tip region; a result of the rough crack geometry (Figure 2). Analytical solutions for elastic crack-face displacements were used [*34, 35*], and a crack-tip dislocation emission model was modified to determine plastic displacements [*36*]; the total crack-face displacements were obtained by superimposing elastic and plastic components. Finite element analyses were conducted to verify these displacement solutions were valid for sawtooth cracks [*25, 27*]. These analyses showed mode II displacements were greatest at the asperity nearest the crack tip. (Similar results were reported, independent of this study, by Parry, *et al.* [*32*].) Closure occurs at the asperity nearest the crack tip before other asperities in the crack wake because mode II displacements are greater, and mode I displacements smaller, than at any other asperity in the crack wake. This observation is significant because only the asperity nearest the crack tip needs to be considered where crack roughness is important.

Finite element analyses of straight cracks, where PICC is the only closure mechanism, show closure first occurs at the crack tip in the absence of remote closure [*37*]. Where both RICC and PICC occur, closure may first occur at the crack tip or the asperity nearest the crack tip (depending on geometry and loading conditions). Tip contact and asperity contact are used to describe conditions where closure first occurs at the crack tip or the asperity nearest the crack tip, respectively. Because closure at either location shields the crack tip from damage, only the first closure event during unloading is important in terms of the crack-tip driving force. Therefore, the model calculates closure loads for both locations, but only considers the higher value to determine ΔK_{eff}.

Model results were shown to be in good agreement with experimental data over a wide range of crack-tip loading (ΔK) for aluminum, steel, and nickel-based alloys [*26, 27*]. In addition, a series of critical experiments were conducted to show the CROP model calculations were in good agreement with experimental data where PICC, RICC, and/or OICC occur. However, the scope of this paper is narrowed to focus on interactions between PICC and RICC at FCG threshold, where OICC is either absent or has a negligible contribution.

Experimental Procedure

FCG tests were performed using a computer-controlled servo-hydraulic test machine. During tests, back-face strain data were used to continuously monitor crack length [*10*], and loads were adjusted to achieve programmed stress intensity factors. Closure loads were determined from compliance data measured (1) near the crack tip (called local determinations) and (2) far from the crack tip (called global determinations) [*13*]; here global compliance data were monitored at the specimen back face. Global determinations do not provide information about the location of closure, relative to asperity contact and tip contact, and lack the fidelity needed to resolve closure events near the FCG threshold (recall Figure 1). Therefore, an alternative non-contacting near-tip displacement measurement technique, called Digital Image Displacement System (DIDS), was used [*20*]. Crack-tip displacements were obtained by analyzing a series of high-magnification (500 X) digital images of the crack-tip region during fatigue loading [*38*]. DIDS analyzes crack-tip displacement and load data to determine closure loads. Because near-crack-tip deformations are used, DIDS provides local determinations that are more sensitive to crack-tip events, compared to global determinations. Further, local determinations are not limited to the crack tip, but can be made for any location along the crack wake. This is significant because a distinction between tip contact and asperity contact can be made experimentally by comparing local determinations at the crack tip and the asperity nearest the crack tip.

Results and Discussion

Model calculations were compared with experimental data for aluminum alloy 2024 because it is a well-characterized alloy with published FCG data available for comparison [*7, 37*]. FCG tests were performed using eccentrically-loaded-single-edge-notch-tension specimens (38.1 mm wide) fabricated from sheet material (2.29 mm thick),[5] in accordance with ASTM standards (E647) at 11 Hz in laboratory air. FCG data for constant R = 0.1 ($C = -78.7\ m^{-1}$) and constant-K_{max} = 11.0 MPa$\sqrt{m}$ ($C = -787\ m^{-1}$) conditions are plotted in Figure 3a as closed circular and closed triangular symbols, respectively. As previously stated, constant-K_{max} threshold data are of interest because they are not affected by crack closure [*11, 12*]. Closure determinations indicated only the R = 0.1 data were affected by closure. Both global and local closure determinations obtained during the R = 0.1 test were used to calculate ΔK_{eff}; these closure-corrected data are shown in Figure 3a as open circular and open square symbols, respectively. As seen in the figure, all closure-corrected data were in excellent agreement with the closure-free constant-K_{max} data, but the ΔK_{eff} data based on local determinations were in better agreement at threshold (ΔK_{eff} = 1.5 MPa$\sqrt{m}$). The arrow highlights the ΔK_{eff} threshold based on global data, which is 12% greater than the ΔK_{eff} threshold based on local data.

The R = 0.1 closure data from global and local techniques are plotted in Figure 3b as closed square and open triangular symbols, respectively. For convenience, closure data are plotted as R_{cl} (the value of R at which closure occurs, $R_{cl} = K_{cl}/K_{max}$, termed closure level) versus ΔK. Model parameters appropriate for 2024 aluminum ($\alpha = 30^{\circ}$, g = 10 μm) and the laboratory air environment (typical oxide thickness, t = 10 Å [*40*]) were used to simulate the R = 0.1 test conditions; calculated closure levels are shown in Figure 3b as the dashed curve.[6] As seen in the figure, model calculations are in good agreement with experimental results, and two distinct regions of closure behavior exist. In the first region (3.2 MPa$\sqrt{m}$ < ΔK < 5.5 MPa$\sqrt{m}$), closure levels are nearly constant at R_{cl} = 0.25 in Figure 3b, and the corresponding da/dN versus ΔK data in Figure 3a has a linear shape typical of FCG data in the Paris regime. In the second region (ΔK < 3.2 MPa$\sqrt{m}$), closure levels abruptly increase in Figure 3b, and da/dN abruptly decreases in Figure 3a, as ΔK decreases. The FCG threshold at ΔK = 3.0 MPa$\sqrt{m}$ is in good agreement with literature results [*7, 37*]. These data show that FCG threshold is a result of increasing closure levels. The abrupt slope change (transition) also occurs for model calculations (dashed

[5] This specimen was formerly called extended-compact-tension [*39*].

[6] For aluminum alloys, the crack mouth oxides produced in laboratory air have been shown to have a negligible closure contribution [*25-27*], so OICC was deemed a second-order effect compared to PICC and RICC. The model parameters α and g were chosen to create the sawtooth crack that best approximated the actual crack configuration, based on micrographs of the rough crack profile.

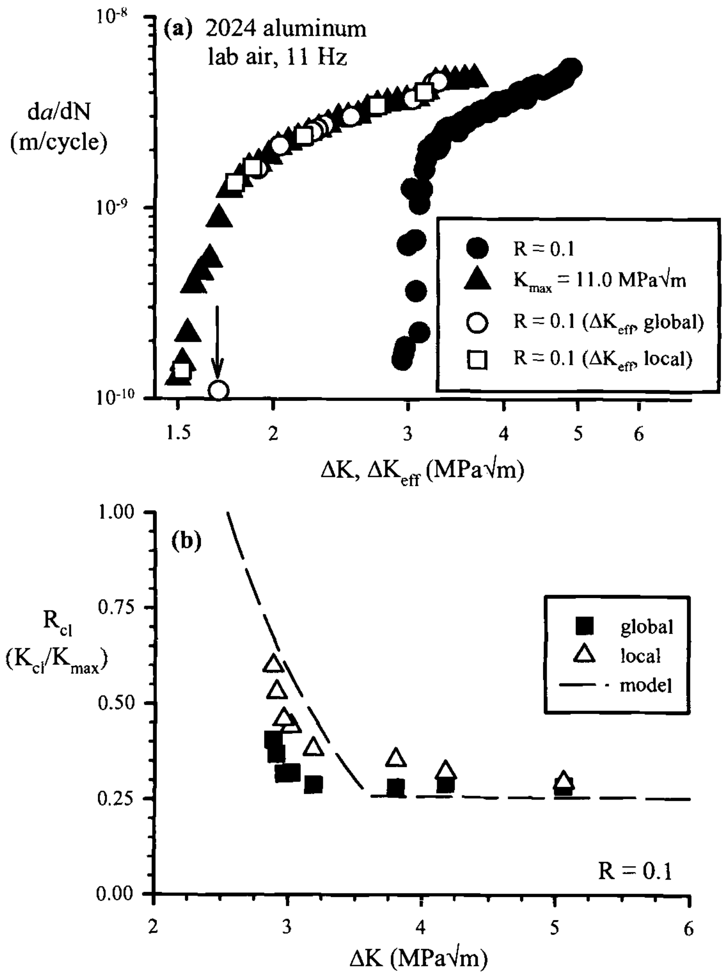

Figure 3 – *Experimental and analytical results for aluminum alloy 2024 at R = 0.1 are plotted. FCG and closure data are shown in parts (a) and (b), respectively.*

line in Figure 3b) at ΔK = 3.5 MPa√m; here the model predicts a transition from tip contact (for ΔK > 3.5 MPa√m) to asperity contact (ΔK < 3.5 MPa√m). The abrupt increase in closure and the corresponding FCG threshold is a direct result of a transition from crack-tip contact to asperity contact, not load history effects.[7] To validate these

[7] Local closure determinations taken behind the crack tip indicate that the FCG data in Figure 3 was not affected by remote closure. The constant-R = 0.1 test was started at ΔK = 5.5 MPa√m and ran to threshold at ΔK = 3.0 MPa√m. Analytical results indicate remote closure will not occur for initial ΔK < 10 MPa√m [*15*].

important observations, additional testing was performed to experimentally show that FCG threshold is caused by the transition from tip contact to asperity contact, due to interactions between RICC and PICC.

A nickel-titanium (Ni-Ti) shape memory alloy was used to study interactions between PICC and RICC because of its unique deformation characteristics. Plastic deformations in shape memory alloys result from a strain-induced phase transformation. Annealing (*i.e.* heating to the reverse transformation temperature) reverses the transformation and returns the deformed material to its initial pre-deformed state. Theoretically, annealing the shape memory alloy will eliminate PICC, allowing RICC effects to be isolated, as schematically shown in Figure 4a. A rough crack with a plastic wake (shaded region) is shown in Figure 4a part (I); here both PICC and RICC occur. After annealing, crack wake plastic deformations is eliminated (no shaded region) in Figure 4a part (II); here only RICC occurs. Because no FCG occurs during annealing, the same crack configuration exists just before and just after annealing and differences in closure behavior must be related to changes in plasticity. As shown in Figure 4a part (III), subsequent FCG re-establishes crack-wake plasticity such that both PICC and RICC occur.

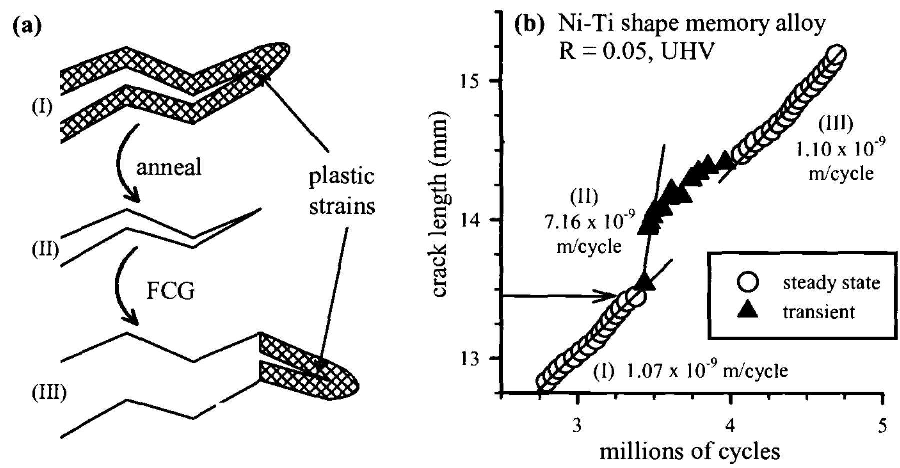

Figure 4 – *The schematics of part (a) illustrate how crack-wake plasticity was eliminated with a shape-memory alloy. The data of part (b) shows how annealing affects FCG rates.*

Experiments were conducted with a Ni-Ti shape memory alloy to test the hypothesis described in Figure 4a. FCG tests were preformed in ultra-high vacuum (UHV, < 10^{-7} Pa) to eliminate OICC, and isolate PICC and RICC. Compact-tension specimens (50.8 mm wide, 2.5 mm thick) were used, loaded at 11 Hz and R = 0.05. To ensure steady-state crack wake conditions were achieved, constant-ΔK tests were performed. Shown in Figure 4b are FCG data for constant ΔK = 8.4 MPa$\sqrt{m}$ plotted as crack length versus cycle count; the FCG rate is the slope of these data. Steady-state FCG occurred (da/dN = 1.07 x 10^{-9} m/cycle) between crack lengths of 12.8 mm and 13.4 mm, as seen by the nearly constant slope of the open circular data in the lower left corner of the figure; here, a constant plastic crack wake (Figure 4a part I) was developed and global closure determinations indicated closure occurred at $R_{cl} = 0.21$. At a crack length of 13.4 mm, the specimen was annealed to eliminate crack-wake plasticity (indicated in the figure by the horizontal arrow); the plastic crack wake was eliminated as depicted in Figure 4a part II. Immediately after fatigue loading resumed, global load/displacement measurements were unable to detect closure, and the FCG rate accelerated by a factor of 7 ($da/dN = 7.16 \times 10^{-9}$ m/cycle); the rapid increase in da/dN is shown by the initial part of the transient observed in Figure 4b (solid triangular symbols). The steady-state FCG rate and closure level ($R_{cl} = 0.21$) were re-established after approximately 1.0 mm of crack growth, shown as the open circular symbols in the upper right corner of Figure 4b (Note that the re-established steady state da/dN is identical to the steady-state data at the start of the test after crack-wake plasticity was re-established as shown in Figure 4a part III). Although results presented elsewhere [*27*] indicate that crack-wake plasticity is only partially eliminated by the shape memory annealing process, the results of Figure 4b show that annealing reduces enough crack-wake plasticity to eliminate the effects of PICC and provide a unique method to study interactions between PICC and RICC.

Based on the unique behavior described in Figure 4, a series of experiments were performed using the shape-memory effect to investigate PICC/RICC interactions and validate model tip contact and asperity contact predictions. First, steady state FCG was established at $\Delta K = 8.4$ MPa$\sqrt{m}$ and $R = 0.05$, indicated on the left side of Figure 5a; local closure determinations were made ($R_{cl} = 0.21$), labeled 1. It should be noted that extreme care was taken to ensure that steady state FCG was achieved without extraneous crack-wake effects. Loads were then reduced to ΔK values of 6.3, 4.2, and 2.1 MPa$\sqrt{m}$ (all at $R = 0.05$), levels 2, 3 and 4, respectively. At each ΔK level, approximately 5 load cycles were performed while closure determinations were made. Because less than 20 load cycles occurred during tests 2, 3, and 4 in Figure 5a, no appreciable crack growth

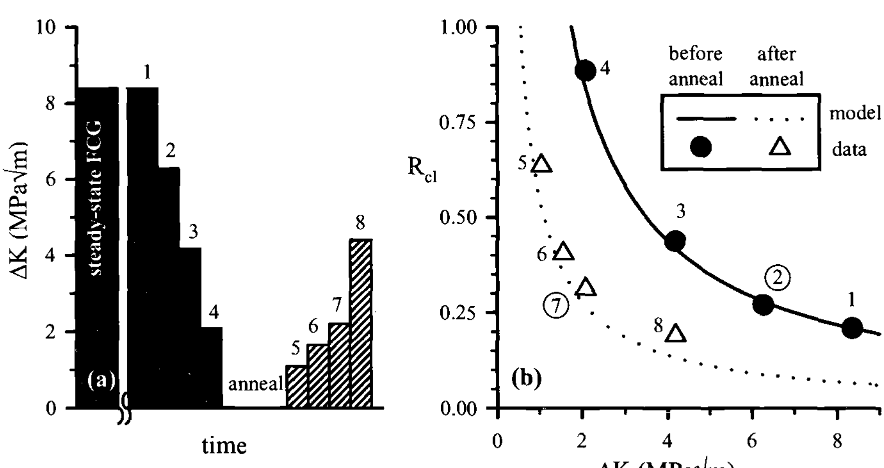

Figure 5 – *A series of FCG tests was performed before and after annealing the shape-memory alloy specimen. The load history and the corresponding local closure determinations are plotted in parts (a) and (b), respectively.*

occurred and thus no additional crack wake plasticity was developed. Local closure determinations performed during the five experiments described in Figure 5a and model calculations are plotted in Figure 5b as closed circular symbols and the solid curve, respectively. Analytical results are in excellent agreement with experimental closure data. As shown in Figure in 5a, the specimen was annealed after test 4 to eliminate crack-wake plasticity. After annealing, a series of four tests (labeled 5, 6, 7, and 8 in Figure 5a) were performed at increasing ΔK levels of 1.05, 1.49, 2.1, and 4.2 MPa$\sqrt{m}$ (all at $R = 0.05$), respectively. The local closure determinations and analytical results for these tests are shown as open triangular symbols and the dotted curve, respectively; again, excellent agreement is noted between model calculations and experimental data. The model results in Figure 5b indicate a transition from tip contact (before annealing - solid circular symbols) to asperity contact (after annealing – open triangular symbols). The model results strongly suggest that annealing reduced crack-wake plasticity and closure loads, which caused a change from crack-tip contact (PICC) to asperity contact (RICC and PICC) to occur.

To confirm that annealing caused a change from tip contact to asperity contact, closure data were examined in greater detail for test 2 (before annealing) and test 7 (after annealing) in Figure 5b (circled data labels). Similar closure levels were determined for both conditions ($0.27 < R_{cl} < 0.31$), but model results indicate tip contact occurred during test 2 and asperity contact during test 7. Local closure determinations (using DIDS) are uniquely suited to show differences between tip and asperity contact because closure data can be obtained at specific locations along the crack wake; global compliance techniques yield only a single global datum. Local closure determinations, before (test 2) and after annealing (test 7), are plotted against the distance behind the crack tip (r) in Figures 6a and 6b, respectively. Figure 6c is a micrograph showing the crack-tip region and the first 500 μm of crack wake where local (DIDS) measurements were performed during test 2 and test 7. Noted in Figure 6c are the crack tip and the asperity nearest the crack tip, approximately 250 μm behind the crack tip. The local closure determinations in Figure 6a show that closure levels are greatest at the crack tip; similar to that predicted by the model (dotted line). The local closure levels decrease at increased distances behind the crack tip and approach the closure level determined from the global compliance method; no closure effect is observed near the first asperity (arrow in Figure 6a). Figure 6a shows that when PICC is a first-order effect (before annealing) crack-tip contact occurs and global closure determinations lack the fidelity to detect crack-tip closure loads. The local closure determinations performed after annealing, shown in Figure 6b, reveal a dramatic variation in closure level at the asperity nearest the crack tip (arrow in Figure 6b). Here, the highest closure level ($R_{cl} = 0.31$) occurred at the first asperity, approximately 250 μm behind the crack tip. Similar results were calculated by the model (dotted line in Figure 6b); after annealing, asperity contact was predicted to occur at $R_{cl} = 0.29$. Again, the global closure measurement detected a much lower closure level (dashed line in Figure 6b) and was unable to detect the wide variation in local closure levels due to asperity contact. A comparison of the local (DIDS) measurements after annealing and the micrograph shown in Figure 6c reveals that the region of high closure levels (Figure 6b) corresponds to contact at the first asperity behind the crack tip noted in Figure 6c. The experimental results in Figure 6 show that annealing results in a change from tip contact to asperity contact as predicted by the CROP model.

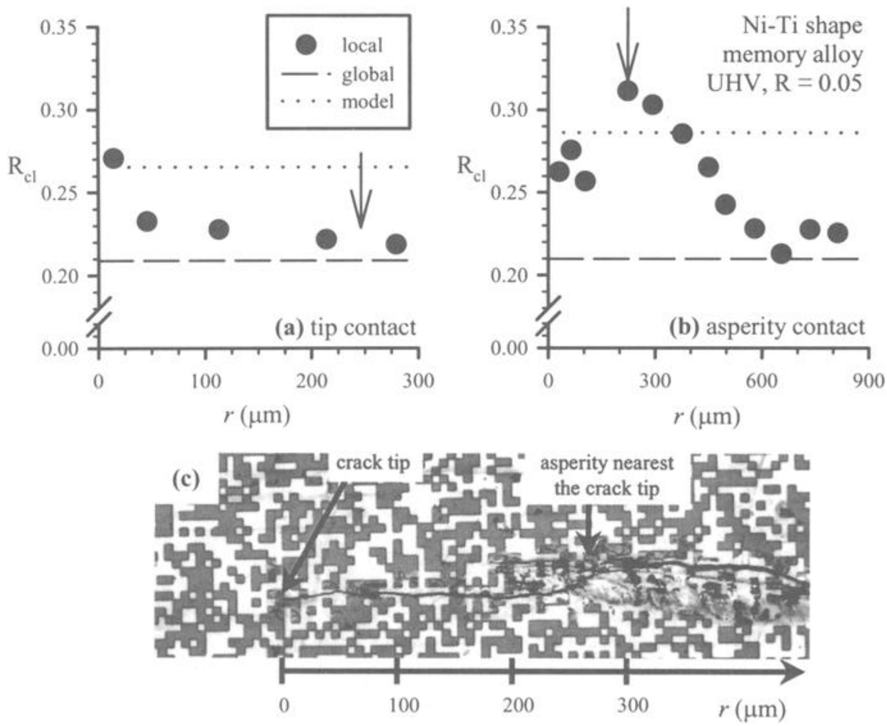

Figure 6 – *Local closure data are plotted behind the crack tip to distinguish between (a) tip contact and (b) asperity contact. Part (c) is a micrograph of the crack profile.*

Conclusions

The results presented herein provide new insight into crack closure (PICC and RICC) effects at threshold, show that current global closure determination methods are unable to quantify crack closure affects at threshold and have validated the complex interactions of PICC and RICC predicted by the CROP model. Both model predictions and closure measurements (refer to Figure 3) show the rise in crack closure levels cause the rapid decrease in fatigue crack growth rates at threshold. Further insight into threshold crack closure provided by the CROP model shows that the abrupt rise in R_{cl} at threshold in Figure 3b was the result of the transition from tip contact, where PICC is the first-order effect, to asperity contact, where both PICC and RICC are first-order effects. To validate predictions of complex PICC and RICC interactions and verify the presence of crack-tip and asperity contact, critical experiments were performed using a shape memory alloy; by annealing the fatigue-crack plastic wake it was shown that PICC was eliminated and RICC could be isolated. The results of shape-memory experiments shown in Figures 5 and 6 conclusively showed that model predictions of crack-tip and asperity contact described the complex interactions between plasticity and roughness closure mechanisms at threshold. A careful comparison of near crack-tip closure determinations and global measurements revealed that standard global compliance measurements lack the sensitivity to accurately characterize crack closure loads at threshold.

References

[*1*] Paris, P. and Erdogan, F., "A Critical Analysis of Crack Propagation Laws," *Journal of Basic Engineering, Transactions of the ASME*, December 1963, pp. 528-534.

[*2*] Elber, W., "Fatigue Crack Closure Under Cyclic Tension," *Engineering Fracture Mechanics*, Vol. 2, 1970, pp. 37-45.

[*3*] Gan, D. and Weertman, J., "Crack Closure and Crack Propagation Rates in 7050 Aluminum," *Engineering Fracture Mechanics*, Vol. 15, 1981, pp. 87-106.

[*4*] Shih, T. T. and Wei, R. P., "A Study of Crack Closure in Fatigue," *Engineering Fracture Mechanics*, Vol. 6, 1974, pp. 19-32.

[*5*] Beevers, C. J., "Fatigue Crack Growth Characteristics at Low Stress Intensities of Metals and Alloys," *Metal Science*, August/September 1977, pp. 362-367.

[*6*] Couper, M. J. and Griffiths, J. R., "Effects of Crack Closure and Mean Stress on the Threshold Stress Intensity Factor for Fatigue of an Aluminum Casting Alloy," *Fatigue and Fracture of Engineering Materials and Structures*, Vol. 13, 1990, pp. 615-624.

[*7*] NASA-Johnson Space Center, *Derivation of Crack Growth Properties of Materials for NASA/FLAGRO 2.0*, Vol. 1, 1994, NASA Johnson Space Center, JSC-26254.

[*8*] Newman, J. A., Riddell, W. T., and Piascik, R. S., "Effects of K_{max} on Fatigue Crack Growth Threshold in Aluminum Alloys," *Fatigue Crack Growth Thresholds, Endurance Limits, and Design, ASTM STP 1372*, J. C. Newman, Jr. and R. S. Piascik, Eds., American Society for Testing and Materials, West Conshohocken, PA, 2000, pp. 63-77.

[*9*] Smith, S. W. and Piascik, R. S., "An Indirect Technique for Determining Closure-Free Fatigue Crack Growth Behavior," *Fatigue Crack Growth Thresholds, Endurance Limits, and Design, ASTM STP 1372*, J. C. Newman, Jr. and R. S. Piascik, Eds., American Society for Testing and Materials, West Conshohocken, PA, 2000, pp. 109-122.

[*10*] Deans, W. F., Jolly, C. B., Poyton, W. A., and Watson, W., "A Strain Gauging Technique for Monitoring Fracture Mechanics Specimens During Environmental Testing, *Strain*, Vol. 13, 1977, pp. 152-154.

[*11*] Donald, J. K., Bray, G. H., and Bush, R. W., "Introducing the K_{max} Sensitivity Concept for Correlating Fatigue Crack Growth Data," *High Cycle Fatigue of Structural Materials*, W. O. Soboyejo and T. S. Srivatsan, Eds., The Minerals, Metals, and Materials Society, 1997, pp. 123-141.

[*12*] Clark, T. R., Herman, W. A., Hertzberg, R. W., and Jaccard, R., "A Technical Note. Influence of Mean Stress on Fatigue in Several Aluminum Alloys Utilizing K^c_{max} Threshold Procedures," *Fatigue and Fracture of Engineering Materials and Structures*, Vol. 19, 1996, pp. 949-954.

[*13*] Elber, W., "Crack Closure and Crack Growth Measurements in Surface-Flawed Titanium Alloy Ti-6Al-4V," 1975, NASA TN-D-8010.

[*14*] McClung, R. C., "Analysis of Fatigue Crack Closure During Simulated Threshold Testing," *Fatigue Crack Growth Thresholds, Endurance Limits, and Design,*

ASTM STP 1372, J. C. Newman, Jr. and R. S. Piascik, Eds., American Society for Testing and Materials, West Conshohocken, PA, 2000, pp. 209-226.

[*15*] Newman, J. C., Jr., "Analyses of Fatigue Crack Growth and Closure Near Threshold Conditions for Large-Crack Behavior," *Fatigue Crack Growth Thresholds, Endurance Limits, and Design, ASTM STP 1372*, J. C. Newman, Jr. and R. S. Piascik, Eds., American Society for Testing and Materials, West Conshohocken, PA, 2000, pp. 227-251.

[*16*] Paris, P. C., Tada, H., and Donald, J. K., "Service Load Fatigue Damage – A Historical Perspective," *International Journal of Fatigue*, Vol. 21, 1998, pp. S35-S46.

[*17*] Forth, S. C., Newman, J. C., Jr., and Forman, R. G. "Evaluation of Fatigue Crack Thresholds Using Various Experimental Methods," *Fatigue and Fracture Mechanics: 33rd Volume, ASTM STP 1417*, W. G. Reuter and R. S. Piascik, Eds., American Society for Testing and Materials, West Conshohocken, PA, 2002.

[*18*] Hertzberg, R. W., Newton, C. H., and Jaccard, R., "Crack Closure: Correlation and Confusion," *Mechanics of Fatigue Crack Closure, ASTM STP 982*, J. C. Newman, Jr. and W. Elber, Eds., American Society for Testing and Materials, Philadelphia, PA, 1988, pp. 139-148.

[*19*] Allison, J. E., Ku, R. C., and Pompetzki, M. A., "A Comparison of Measurement Methods and Numerical Procedures for the Experimental Characterization of Fatigue Crack Closure," *Mechanics of Fatigue Crack Closure, ASTM STP 982*, J. C. Newman, Jr. and W. Elber, Eds., American Society for Testing and Materials, Philadelphia, PA, 1988, pp. 171-185.

[*20*] Sutton, M. A., Zhao, W., McNeill, S. R., Helm, J. D., Piascik, R. S., and Riddell, W. T., "Local Crack Closure Measurements: Development of a Measurement System Using Computer Vision and a Far Field Microscope," *Second Symposium on Crack Closure Measurement and Analysis, ASTM STP 1343*, R. C. McClung and J. C. Newman, Eds., American Society for Testing and Materials, West Conshohocken, PA, 1999, pp. 145-156.

[*21*] Abdel Mageed, A. M. and Pandey, R. K., "Effect of Measurement Location and Fatigue-Loading Parameters on Crack Closure Behavior," *Materials Science and Engineering*, Vol. A150, 1992, pp. 43-50.

[*22*] Walker, N. and Beevers, C. J., "A Fatigue Crack Closure Mechanism in Titanium," *Fatigue of Engineering Materials and Structures*, Vol. 1, 1979, pp. 135-148.

[*23*] Suresh, S., Zaminski, G. F., and Ritchie, R. O., "Oxide Induced Crack Closure: An Explanation for Near-Threshold Corrosion Fatigue Crack Growth Behavior," *Metallurgical Transactions*, Vol. 12A, 1981, pp. 1435-1443.

[*24*] Newman, J. C., Jr., "An Evaluation of Plasticity-Induced Crack-Closure Concept and Measurement Methods," *Advances in Fatigue Crack Closure Measurement and Analysis, ASTM STP 1343*, R. C. McClung and J. C. Newman, Jr., Eds., American Society for Testing and Materials, West Conshohocken, PA, 1999, pp. 128-144.

[*25*] Newman, J. A., Riddell, W. T., and Piascik, R. S., "A Threshold Fatigue Crack Closure Model, Part I – Model Development," submitted to *Fatigue and Fracture of Engineering Materials and Structures* August 2001.

[*26*] Newman, J. A., Riddell, W. T., and Piascik, R. S., "A Threshold Fatigue Crack Closure Model, Part II – Experimental Verification," submitted to *Fatigue and Fracture of Engineering Materials and Structures* August 2001.

[*27*] Newman, J. A., "The Effects of Load Ratio on Threshold Fatigue Crack Growth of Aluminum Alloys," Ph.D. dissertation, Virginia Tech. Available online at: http://scholar.lib.vt.edu/theses/available/etd-11012000-15010038/.

[*28*] Suresh, S. and Ritchie, R. O., "A Geometric Model for Fatigue Crack Closure Induced by Surface Roughness," *Metallurgical Transactions*, Vol. 13A, 1982, pp. 1627-1631.

[*29*] Wang S. H., Muller, C., and Exner, H. E., "A Model for Roughness-Induced Fatigue Crack Closure," *Metallurgical and Materials Transactions*, Vol. 29A, 1998, pp. 1933-1939.

[*30*] Suresh, S. and Ritchie, R. O., "Some Considerations on the Modeling of Oxide-Induced Fatigue Crack Closure Using Solutions for a Rigid Wedge Inside a Linear Elastic Crack," *Scripta Metallurgica*, Vol. 17, 1983, pp. 575-580.

[*31*] Chen, N. and Lawrence, F. V., "An Analytical Model for Studying Roughness-Induced Crack Closure," *Fatigue and Fracture Mechanics, 29th Volume, ASTM STP 1332*, T. L. Panontin and S. D. Sheppard, Eds., American Society for Testing and Materials, West Conshohocken, PA, 1999, pp. 535-551.

[*32*] Parry, M. R., Syngellakis, S., and Sinclair, I., "Numerical Modeling of Combined Roughness and Plasticity Induced Crack Closure Effects in Fatigue," *Materials Science and Engineering*, Vol. A291, 2000, pp. 224-234.

[*33*] Budiansky, B. and Hutchinson, J. W., "Analysis of Closure in Fatigue Crack Growth," *Journal of Applied Mechanics*, Vol. 45, 1978, pp. 267-276.

[*34*] Tada, H., Paris, P., and Irwin, G., *The Stress Analysis of Cracks Handbook*, 2nd Edition, Del Research Corporation, Saint Louis, MO, 1985.

[*35*] Erdogan, F. and Sih, G. C., "On the Crack Extension in Plates Under Plane Loading and Transverse Shear," *Journal of Basic Engineering*, December 1963, pp. 519-527.

[*36*] Bilby, B. A., Cottrell, A. H., and Swinden, K. H., "The Spread of Plastic Yield from a Notch," *Proceeding of the Royal Society of London*, Vol. A272, 1963, pp. 304-314.

[*37*] Riddell, W. T. and Piascik, R. S., "Stress Ratio Effects on Crack Opening Loads and Crack Growth Rates in Aluminum Alloy 2024," 1998, NASA TM-1998-206929.

[*38*] Sutton, M. A., Chao, Y. J., and Lyons, J. S., "Computer Vision Methods for Surface Deformation Measurements in Fracture Mechanics," *Novel Experimental Techniques in Fracture Mechanics*, AMD-Vol. 176, American Society for Mechanical Engineers, 1993, pp. 203-217.

[*39*] Piascik, R. S., Newman, J. C., Jr., and Underwood, J. H., "The Extended Compact Tension Specimen," *Fatigue and Fracture of Engineering Materials and Structures*, Vol. 20, 1997, pp. 559-563.

[*40*] Hunter, M. S. and Fowle, P., "Natural and Thermally Formed Oxide Films on Aluminum," *Journal of the Electrochemical Society*, Vol. 103, 1956, pp. 482-485.

C.-C. Chu and J. J. F. Bonnen[1]

An Extension of Uniaxial Crack-Closure Analysis to Multiaxial Fatigue

REFERENCE: Chu, C.C.and Bonnen, J. J. F., "**An Extension of Uniaxial Crack-Closure Analysis to Multiaxial Fatigue,** *Fatigue and Fracture Mechanics: 33rd Volume, ASTM STP 1417,* W. G. Reuter and R. S. Piascik, Eds., ASTM International, West Conshohocken, PA, 2002.

ABSTRACT: In the past, crack closure arguments have been successfully used to analyze the effect of large and small overloads on uniaxial fatigue life. The effective strain range, defined as the portion of a loading cycle during which the fatigue crack remains open, was found to correlate well with fatigue damage. Furthermore, an empirical function was found which described the dependence of crack opening stress on overload magnitude. These crack closure-based findings are utilized in this paper to examine recent multiaxial overload test results on a normalized SAE1045 steel. First, the von Mises' yield criterion combined with the classical flow rule is shown to properly describe the stress-strain behavior displayed by all proportional axial-torsion experiments, both constant and variable amplitude. Next, an effective equivalent strain-life relationship is found to unify overload fatigue data. A multiaxial crack opening stress model is then proposed which accurately calculates the cumulative effects from both in-plane and out-of-plane overloads in lowering the crack opening stress. This multiaxial crack opening stress model together with the established stress-strain curve and the effective strain-life curve are then shown to be capable of adequately calculating fatigue life for the large number of biaxial tests examined here.

KEY WORDS: fatigue crack closure, overload effects, crack opening stress, effective strain life curve, equivalent stress, cyclic stress strain relationship, equivalent life, initiation fatigue approach

[1]Research Staff, Ford Research Lab, Ford Research Lab, MD 3135, 2101 Village Rd. Dearborn, MI 48124-2053.

Introduction

Previous researchers successfully used crack closure arguments to explain the effect of large and small overloads on uniaxial fatigue life [1-4]. Most recently, the uniaxial closure findings were integrated into an initiation-based fatigue approach and had been proven successful in analyzing both mean stress and small cycle effects [5-7]. It was found that the effective strain range, defined as the strain range from the larger of either the minimum stress or the opening stress to the maximum stress of a fatigue cycle, correlates better with fatigue damage than the complete strain range.

A general periodic overload test procedure has been established to find the new effective strain life material fatigue property [8]: By applying large and sufficiently frequent overloads during a fatigue test, the crack opening stress can be lowered to a level below the minimum stress of the fatigue cycle. That is, the complete fatigue cycle becomes fully effective (in causing fatigue damage). Thus, for these tests, the effective strain amplitude becomes the same as the total strain amplitude, and it can be plotted against the equivalent fatigue life, calculated from subtracting overload fatigue damage from the total damage using Miner's rule, to obtain the effective strain life property.

Hence, the critical link in the use of effective strain as a damage parameter then becomes the determination of crack opening stress levels throughout the load history, and this problem was addressed in Refs. [9,10], where an empirical model was developed to describe the crack opening stress as a function of the overload magnitude.

For a given loading history, the above closure-based initiation fatigue method therefore involves (1) calculating the history-dependent opening stress level for a given fatigue cycle using the empirical opening stress model; (2) calculating the opening stress dependent effective strain amplitude using the material's stress-strain relationship; (3) calculating the fatigue damage per fatigue cycle by comparing the effective strain amplitude with the effective strain life material property; and lastly (4) accumulating the total damage.

Recent experiments [11,12] demonstrated similar results under multiaxial loadings. By periodically applying a large overload strain cycle to eliminate crack-face interference, a single unified effective strain amplitude versus fatigue life curve was found to describe fatigue test results from tension-torsion tests of various proportionalities.

In this paper, the multiaxial test data for a normalized SAE1045 steel from Refs. [11,12] are analyzed with the hope of generalizing the uniaxial closure-based initiation fatigue method to multiaxial problems. The material properties examined here include the cyclic stress-strain relationship, the effective strain-life relationship, and the crack opening stress model that describes the dependence of opening stress on overload magnitude.

The Uniaxial Crack Closure Model

Drawn schematically in Fig. 1 is the uniaxial stress-strain behavior of a fatigue

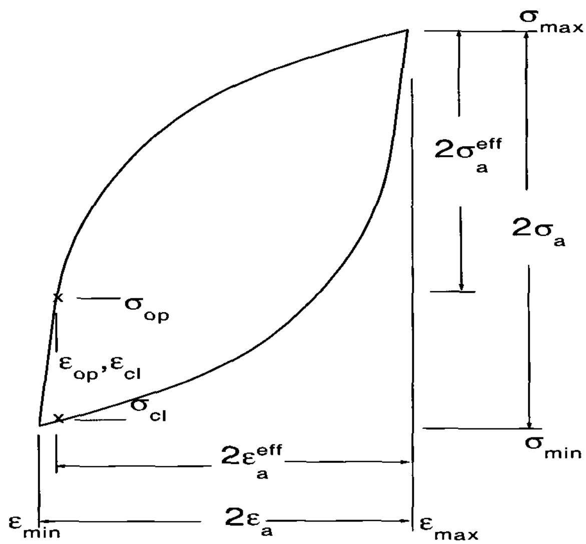

FIG. 1 *The stress-strain behavior in a closure-based fatigue method.*

cycle from which the crack closure-based method was developed. For a constant amplitude fatigue cycle from minimum stress σ_{min} to maximum stress σ_{max}, the fatigue damage accumulates only during the portion of the cycle when the fatigue crack is open; that is, between the opening stress level σ_{op} and the maximum stress σ_{max}. The crack opening stress level was found to be influenced by the overload magnitude. The empirically observed functional form is as follows:

$$\sigma_{op} = \alpha\sigma_{max}^{ol}\left(1 - \left(\frac{\sigma_{max}^{ol}}{\sigma_y}\right)^2\right) + \beta\sigma_{min}^{ol} \tag{1}$$

where σ_{max}^{ol} and σ_{min}^{ol} are the maximum and minimum overload stress level, respectively; σ_y denotes the material's yield stress; and α, and β are material constants.

The effective strain amplitude can then be calculated by

$$\epsilon_a^{eff} = \epsilon_a - \epsilon_{\sigma\to\epsilon}\left[\frac{1}{2}(\sigma_{op} - \sigma_{min})\right] \tag{2}$$

where ϵ_a is the strain amplitude of the complete cycle, and notation $\epsilon_{\sigma\to\epsilon}[\sigma]$ is used to represent the strain value corresponding to the stress value σ. This stress to strain mapping (or vice-versa) requires the establishment of the material's cyclic stress-strain relationship.

In the crack closure-based method it was further found that the effective strain amplitude of a fatigue cycle correlates very well with fatigue damage, particularly

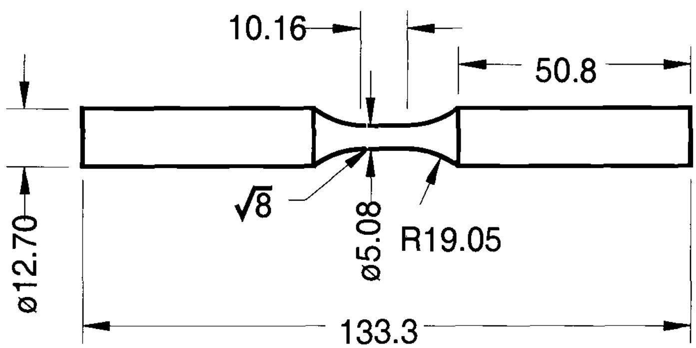

FIG. 2 - *Uniaxial specimen. All dimensions in mm.*

when a significant amount of positive (tensile) mean stress is present in the loading history, such as in histories with periodic overloads. For a given material, the effective strain-life curve has been observed to have a lower limit, termed the intrinsic strain, which is generally much lower than the traditional fatigue limit. The latter is usually presumed as the lower limit of the material's strain life curve. Any fatigue cycle for which the effective strain amplitude is smaller than the intrinsic does not cause fatigue damage.

The effective strain-life curve in the closure-based method may therefore replace the conventional strain-life curve as the material's basic fatigue property. Note here that, although functional form $\epsilon_a^{eff} = \epsilon_a^{int} + AN_f^B$ has been observed to describe the experimentally measured effective strain-life curve well, digitized mapping, without any assumed functional interdependence between variables, is preferred in this paper for defining the material properties.

Materials and Testing Techniques

The material used in this study was an SAE 1045 steel in the normalized condition. The steel was hot rolled into 63.5 mm diameter bar and normalized to produce a Brinell hardness of 203 BHN. A synopsis of the history of the material, monotonic and cyclic material properties, and the chemical composition may be found in Ref. [*13*]. This material has a pearlitic/ferritic microstructure and, because of the normalization procedure, has equiaxed grains of roughly 25 μm. There is banding of pearlite and ferrite in all planes except the short-transverse orientation. MnS stringers of length 0.1 to 2 mm are present in this steel and are aligned with the rolling direction.

Strain controlled tests were conducted on a uniaxial 25 kN servohydraulic load frame with a 7.62 mm extensometer. The tests conformed to ASTM E 606 and employed the specimen illustrated in Fig. 2. Specimen preparation consisted of lathe turning, low stress grind and final longitudinal polishing. Failure was defined as a 5% load drop referenced to the stabilized half-life load. Tests were controlled via specialized computer control software [*14*].

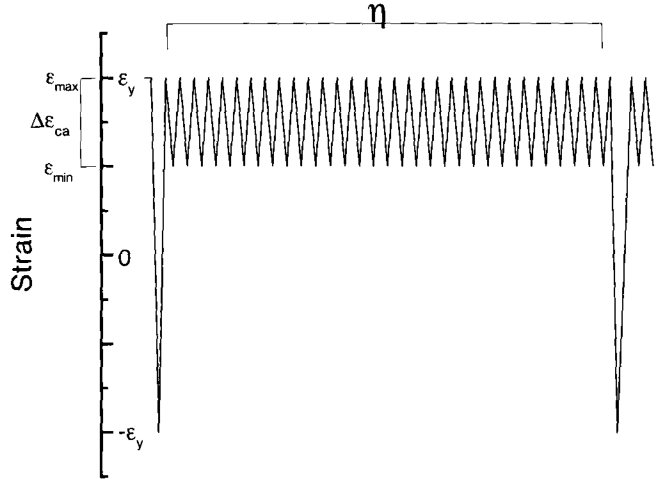

FIG. 3—*Uniaxial overload history.*

Uniaxial Periodic Overload Tests

Overload tests were conducted in a fashion very similar to the constant amplitude tests. The histories used in the uniaxial overload tests, an example of which is shown in Fig. 3, consisted of a single compression-tension overload cycle followed by a number of smaller cycles whose peak tensile strains were the same as the peak tensile strain of the fully reversed overload cycle. The amplitude of the overload cycle itself was selected to be 0.48% strain which corresponded roughly to 10,000 cycles to failure under conventional constant amplitude testing. A number of smaller constant amplitude cycles (η) followed the overload cycle, and the smaller cycle amplitude was set, depending on the test, at a value between 0.2% strain and 0.06% strain. The number of smaller cycles, η, placed between the overload cycles was chosen such that the overload cycles constituted no more than approximately 25% of the total damage.

Biaxial In-Phase Tests

Multiaxial fatigue life tests were performed on the tubular specimens shown in Fig. 4. Rough machining of the specimen consisted of lathe turning on the outer surface and boring the inside. Finish machining consisted of low-stress grinding and sanding on the outer surface and honing the inner surface with successively finer stones. The outer surface was polished to 1 μm for the purpose of observing cracking behavior. The inner diameter received a 5 μm finish.

The axial-torsional tests were conducted using an axial-torsion load frame capable of exerting a 250 kN axial force and a 2250 Nm torque on test specimens. Strains were measured with an axial-torsion extensometer. Tests were conducted in strain control, and strains were controlled to an accuracy of one percent by the adaptive

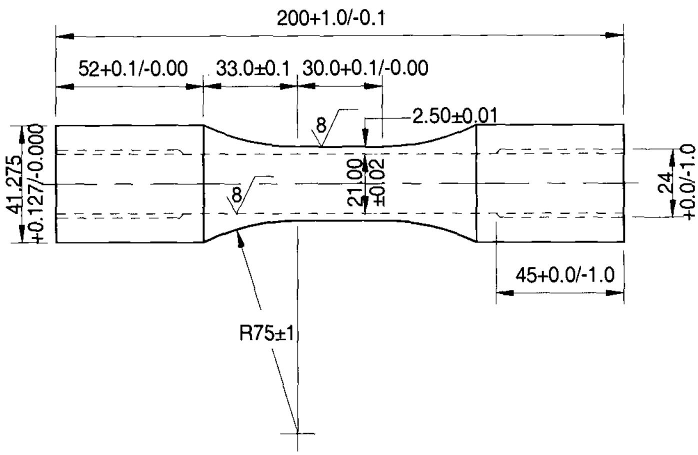

FIG. 4–*Axial-torsion specimen. All dimensions in mm.*

parametric control program described in [*15*]. A maximum test frequency of 40Hz was employed for some high cycle tests while slower frequencies were used for shorter lives. Frequencies above 8 Hz were used only when specimen stress-strain response was elastic and load control was then used on both axes. Specimen failure was defined as the first discernible compliance change. This technique resulted in an estimated failure crack length of one to three millimeters.

Five strain ratios were used in this research: $\lambda = \frac{\varepsilon_{xy}}{\varepsilon_{xx}} = \infty$, 3, 3/2, 3/4 and 0. For tests performed under $\lambda = \infty$ loading (pure torsion) the axial actuator was left in load control at zero load for the duration of the test. The constant amplitude biaxial tests were fully reversed and kept in-phase, meaning that the peak in the axial channel was coincident with the peak in the torsional channel.

Biaxial Periodic Overload Tests

Just as in the uniaxial periodic overload tests a large, fully reversed, overload cycle was applied and followed by η smaller cycles which shared the same peak maximum strain. An example history for $\lambda = 3/2$ may be found in Fig.5. In the biaxial in-phase tests the overload cycle was set such that it alone would cause specimen failure in 10,000 cycles, and subsequent smaller cycles were set such that they shared the same peak strain as the overload cycle. Lastly, a set of torsion tests were conducted where the smaller cycles did not share the same peak torsional strain, but rather the smaller cycles were set such that they had zero mean stress. This type of test is referred to as a torsional zero mean overload test and an example strain history is presented in Fig. 6. Note that the strain is not fully reversed since this is necessary to achieve zero mean torsional stress.

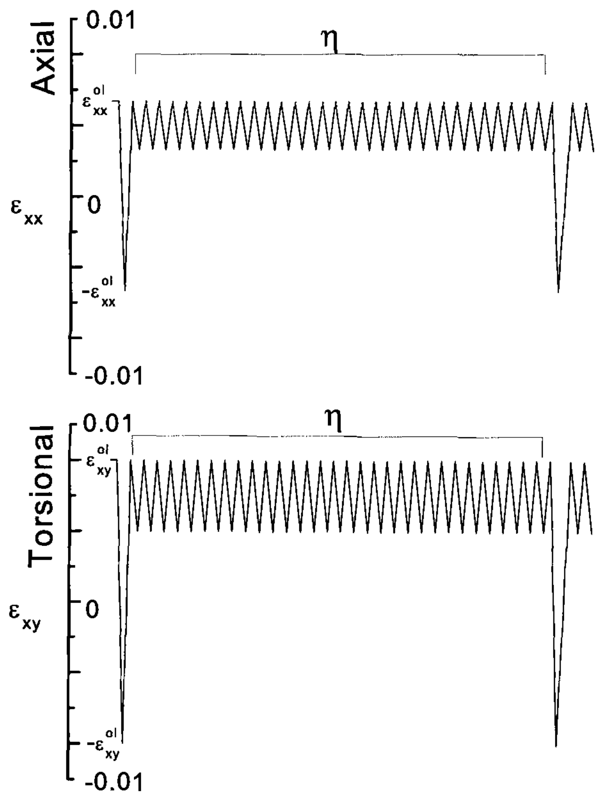

FIG. 5–*Example in-phase biaxial history for* $\lambda = 3/2$.

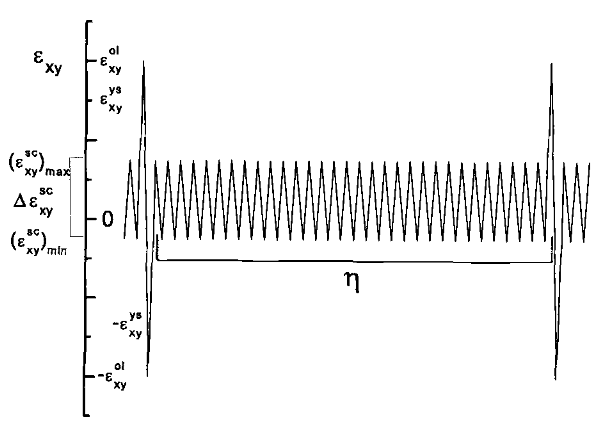

FIG. 6–*Torsional overload histories.*

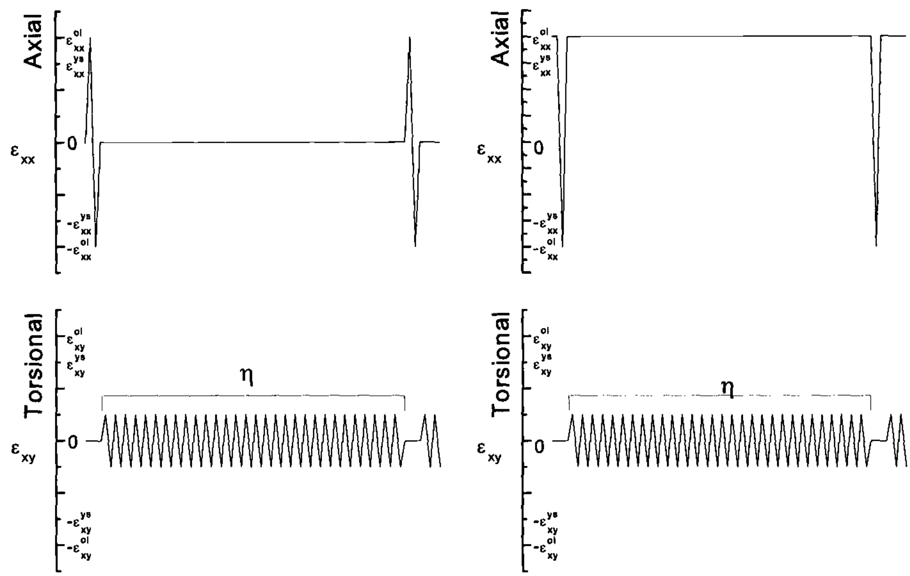

(a) Axial zero mean overload history *(b) Axial peak hold overload tests.*

FIG. 7-*Histories with axial overloads and torsional smaller cycles.*

Special Torsional Histories

In addition to the tests mentioned above, tests with combinations of torsional small cycles with axial overload cycles were conducted, and these histories are depicted in Figs. 7a and 7b. In a fashion similar to that of the zero mean overload tests, all of the axial overload tests had torsional smaller cycles with zero mean stress. Both the axial overload and the torsional smaller cycle strain amplitudes were selected using the same criteria used in the biaxial in-phase overload tests [*11*]. In the axial zero mean overload tests, a large fully reversed ($R_\varepsilon = -1$) axial overload was employed in place of the torsional overload, and at the end of the axial cycle the axial strain was held at zero while torsional smaller cycles were applied (see Fig. 7a). As with the torsional overloads, plasticity is present in the axial overload cycles, and, consequently, zero axial strain was accompanied by an average initial axial stress of approximately 220 MPa at the beginning of the subsequent small cycles. Lastly, a series of axial peak hold overload tests were conducted where the peak axial overload strain was held constant during the smaller amplitude (zero mean) torsional cycling (see Fig. 7b). The initial axial stress following the overload in the axial peak hold overload tests was 380 MPa. In both axial overload series the axial channel was operated in strain control.

The damage resulting from the overload can be numerically removed and the equivalent life of the smaller cycles can be recalculated using the equation:

$$N_{sc} = \frac{1}{\frac{1}{n_{sc}} - \frac{1}{\eta N_{ol}}}$$

where n_{sc} is the total number of smaller cycles at the small cycle test amplitude, N_{sc} is the expected constant amplitude equivalent life at the small cycle amplitude, and η is the ratio of the number of small cycles applied to the number of overload cycles applied. The reference life for the overload cycle, N_{ol}, is taken from the constant amplitude strain-life curve.

Cyclic Stress-Strain Relationship

To analyze the biaxial test data summarized above, the von Mises yield criterion and its associated flow rule are adopted here. As detailed in [*16*], by assuming that plane stress condition prevails in the circumferential direction, the equivalent stress, equivalent strain, major principal stress, and the maximum shear stress that will be used later in this paper can be calculated from the experimental data as follows:

$$\overline{\sigma} = \sqrt{\sigma_{xx}^2 + 3\sigma_{xy}^2} \tag{3}$$

$$\overline{\epsilon} = \frac{\overline{\sigma}}{E} + \sqrt{(\epsilon_{xx}^{(p)})^2 + \frac{4}{3}(\epsilon_{xy}^{(p)})^2} \tag{4}$$

$$\tau_{max} = \sqrt{(\frac{1}{2}\sigma_{xx})^2 + \sigma_{xy}^2} \tag{5}$$

$$\sigma_1 = \frac{1}{2}\sigma_{xx} + \tau_{max} \tag{6}$$

where subscripts xx and xy denote the tensile and torsional components, respectively; and E is the Young's modulus of the material. The plastic strain components $\epsilon_{xx}^{(p)}$ and $\epsilon_{xy}^{(p)}$ are calculated by

$$\begin{aligned} \epsilon_{xx}^{(p)} &= \epsilon_{xx} - \sigma_{xx}/E \\ \epsilon_{xy}^{(p)} &= \epsilon_{xy} - (1 + \overline{\nu})\sigma_{xy}/E \end{aligned}$$

where the effective Poisson's ratio $\overline{\nu}$ is defined as $(\nu\overline{\epsilon}^{(e)} + \frac{1}{2}\overline{\epsilon}^{(p)})/\overline{\epsilon}$, with ν representing Poisson's ratio and $\overline{\epsilon}^{(e)}$ and $\overline{\epsilon}^{(p)}$ denoting respectively the elastic and plastic equivalent strain.

By plotting the calculated equivalent strain against the equivalent stress, Fig. 8 illustrates that von Mises' yield function and classical flow rule are capable of unifying data from various multiaxial tests to an equivalent stress-strain behavior for SAE1045 steels. The fitted curve will be used in later calculations to obtain corresponding stress and strain values.

Shown in Fig. 9 is the equivalent strain calculated from all proportional tests plotted against the observed equivalent life. It can be seen that equivalent strain can also unify fatigue data from various biaxial constant amplitude tests. Although

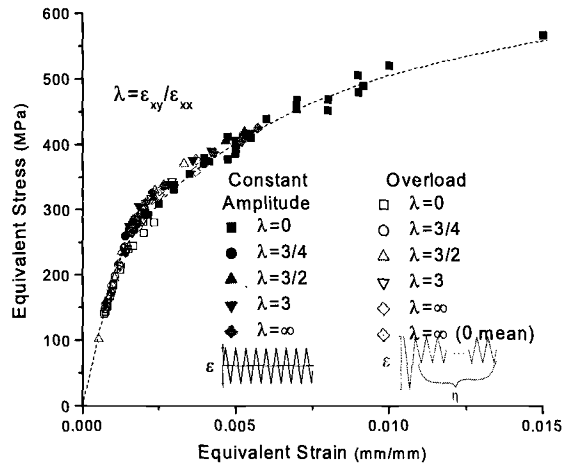

FIG. 8 *The cyclic equivalent stress-strain curve generated from both biaxial and uniaxial constant amplitude tests.*

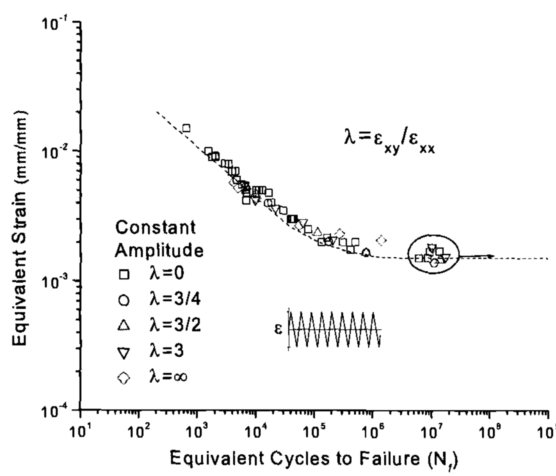

FIG. 9 *The equivalent strain-life curve generated from both biaxial and uniaxial constant amplitude tests.*

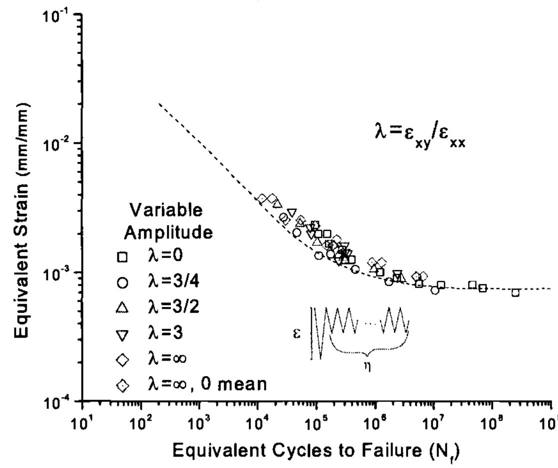

FIG. 10—*The equivalent strain-life curve obtained from both biaxial and uniaxial variable amplitude tests.*

the effective strain-life curve replaces this traditional strain-life curve in the closure-based approach as the fundamental fatigue material, it is included here because of its common usage in the local strain approach for both uniaxial and multiaxial problems.

Effective Strain-Life Relationship

As mentioned earlier, by using periodic overloads to lower the crack opening stress level and thus to make the complete fatigue cycle effective, the strain-life curve from such tests then also becomes the effective strain-life curve. Shown in Fig. 10 is the equivalent strain amplitude data plotted against fatigue life for overload tests of various tension-torsion combinations. Instead of fitting a curve through the experimental data, the curve which forms the lower bound for all experimental data is chosen here to define the effective strain-life curve. This is equivalent to saying that, although atypically large overload tests have been run [*11,12*] to ensure that fatigue damage at a particular amplitude could not be possibly increased, the fatigue crack may still be only partially open because of the limited effectiveness of a given type of overload in reducing crack face interference for any given type of loading.

It should be noted here that for the proportional loadings discussed here, if, say, the equivalent strain is found to unify fatigue test data well, plots similar to Figs. 9 and 10 can also be obtained by plotting the major principal strain amplitude or the maximum shear strain amplitude against fatigue life. It usually takes more complex loading histories to determine the appropriateness of a given parameter in assessing fatigue damage.

Multiaxial Crack Opening Stress

As proposed in [17], if the material's effective strain-life and cyclic stress-strain relationship have been established, as shown in Figs. 8 and 10, the crack opening stress for each test can be back-calculated from the measured fatigue life as follows:

$$\epsilon_a^{eff} = \epsilon_{N\to\epsilon}[N_f] \tag{7}$$

$$\sigma_{op} = \sigma_{min} + 2\sigma_{\epsilon\to\sigma}[\epsilon_a - \epsilon_a^{eff}] \tag{8}$$

As noted before, the subscript $N \to \epsilon$ denotes a fatigue life to effective strain amplitude mapping using the material's effective strain-life relationship; and subscript $\epsilon \to \sigma$ represents a strain to stress mapping utilizing the material's cyclic stress-strain relationship. The influence of overloads on opening stress can then be determined by observing the variation of the calculated opening stress as a function of, say, the overload magnitude.

Instead of observing the variation of opening stress with the maximum and minimum overload and deriving the material constants α and β from test data, as shown in [17,18], here the variation among tests is mainly the proportionality, or tension to torsion ratio, and not the magnitude of the overload. Therefore, the analysis is focused on finding a multiaxial opening stress model that can not only reduce to Eqn. (1) for uniaxial loading, but also unify fatigue results from different tension-torsion combinations.

By assuming a form of opening stress dependence on overload magnitude similar to Eqn. (1) and by using the material constants determined in [18], $\alpha = 0.8$ and $\beta = 0.25$, three multiaxial opening stress models are tested for their ability to predict crack opening stresses and fatigue lives. (Note here that the material's yield stress σ_y is used as the normalizing stress in the nonlinear term in Eqn. (1), as originally proposed in [8]. As will be explained later, this is different from the determination procedure adopted in Ref. [18] where the normalizing stress was treated as a parameter estimated from the opening stress versus overload maximum plot. A value of 580 MPa was obtained in [18], compared with the yield stress, $\sigma_y = 476$ MPa, used here).

The three models are as follows: (1) The crack opening stress is expressed in terms of the shear stress on the fatigue crack plane. The functional dependence on the periodic overload magnitude is assumed to be

$$\tau_{op} = \alpha\tau_{max}\left(1 - \frac{\Sigma(\overline{\sigma}^2)_{max}^{ol}}{\sigma_y^2}\right) + \beta\tau_{min}^{ol} \tag{9}$$

Here, shear stress τ_{max} denotes the maximum shear stress value of the regular fatigue cycle, τ_{min}^{ol} denotes the shear stress on the crack plane at the minimum of the overload cycle, and for proportional loadings, the maximum shear value can be determined from stress components σ_{xx} and σ_{xy} using Eqn. (5).

(2) The crack opening stress is expressed in terms of the normal stress on the fatigue crack plane. The shear stress τ in Eqn. (9) is replaced by σ_n which can be calculated from stress components using Eqn. (6).

(3) The crack opening stress is expressed in terms of equivalent stress. The multiaxial opening stress model is then

$$\overline{\sigma}_{op} = \alpha\overline{\sigma}_{max}\left(1 - \frac{\Sigma(\overline{\sigma}^2)^{ol}_{max}}{\sigma_y^2}\right) + \beta\overline{\sigma}^{ol}_{min} \tag{10}$$

Note here that the equivalent stress is a scalar and is often difficult to work with because of its lack of directionality. While for general multiaxial problems the variation of equivalent stress can be correctly traced by using a multiaxial plasticity material model, here, for simple near-proportional loadings, $\overline{\sigma}^{ol}_{min}$ in Eqn. (10), for example, can be calculated by $\overline{\sigma}^{ol}_{max} - 2\overline{\sigma}^{ol}_{a}$ where $\overline{\sigma}^{ol}_{a}$ is the amplitude of the equivalent stress variation during the overload cycle and can be calculated from the variation of stress components during overload using Eqn. (3).

The quadratic dependence on the maximum overload, $\Sigma(\overline{\sigma}^2)^{ol}_{max}/\sigma_y^2$, is the main feature of the multiaxial opening stress models proposed here. It is written in the equivalent form of the overload maximum to indicate that the same overload effects are expected for multiaxial tests of all proportionalities. As will be noted later, the summation of effects from the maximum overload magnitude is based on experimental observations, so that effects from both the in-plane shear overload and the out-of-plane normal overload, whether applied simultaneously as in proportional loading, or sequentially as in non-proportional loadings, seem to be cumulative.

Since the evaluation procedure is the same for all three models, only that of the equivalent stress based model is presented below. First, crack opening stresses are plotted against the minimum stress of the fatigue cycles as in Figs. 11a-f. The star and square symbols denote the back-calculated and predicted crack opening stress, respectively. The maximum and minimum stress of the fatigue cycles are also noted in the figures, by the triangles and the dotted line, respectively, so that the effective and the total stress range can be quickly gauged from the vertical distance between the maximum and the opening stress, and between the maximum and the minimum stress, respectively.

Probably because of the scatter in the cyclic stress-strain and effective strain-life relationships, as seen in Figs. 8 and 10, the back-calculated opening stress demonstrates considerable scatter and does not show any particular pattern for different tension-torsion combinations. The proposed model, Eqn. (10), on the other hand predicts a relatively constant opening stress because of the relative constancy of the overload size. The effort to make this relatively constant opening stress prediction close to the overall average of the back-calculated values drove the normalizing stress selection to σ_y (476 MPa.) Note that if σ_y is replaced by 580 MPa, as in Ref. [*18*], then the opening stress in Fig. 11a would have been raised by approximately 70 MPa and resulted in a much better uniaxial comparison. This result would indicate that caution should be used in using constants fit with uniaxial data for multiaxial applications and that the current fit is a compromise among tests of various multiaxiality.

Shown in Figs. 12a-b are the opening stress plots for the only two sets of non-proportional tests which involve pure torsional cycles with periodic axial overload; one with the axial overload held constant at its peak value while torsional smaller

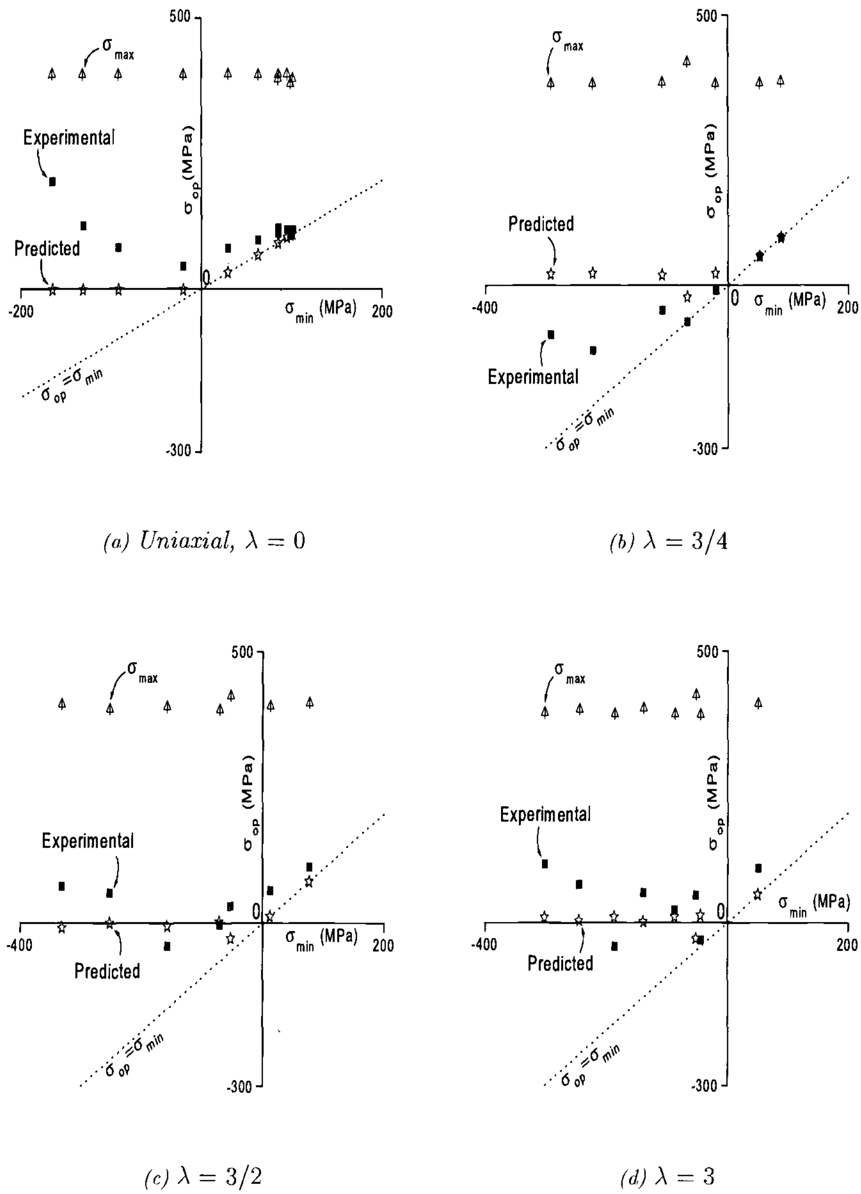

FIG. 11–*Predicted and back-calculated opening stresses,* $\lambda = \frac{\epsilon_{xy}}{\epsilon_{xx}}$.

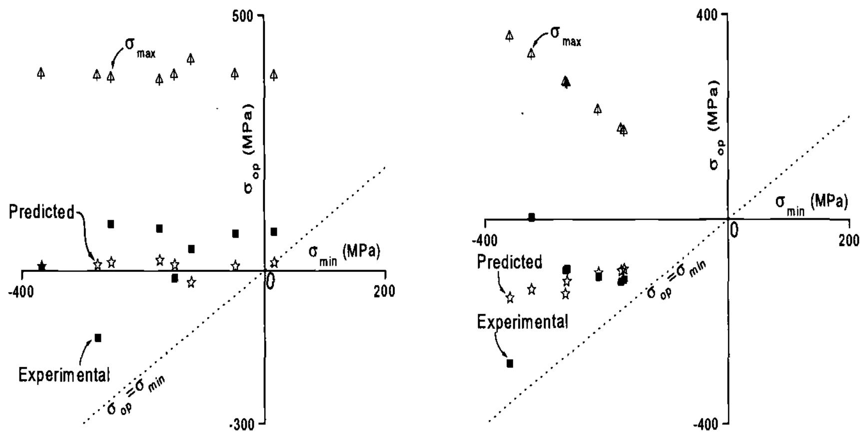

(e) $\lambda = \infty$, peak hold *(f) $\lambda = \infty$, zero mean*

FIG. 11–*(cont.) Predicted and back-calculated opening stresses, $\lambda = \frac{\epsilon_{xy}}{\epsilon_{xx}}$.*

cycles were applied, and the other with the axial strain returned to zero value during torsional cycling.

Here the previously mentioned cumulative overload effects are at work. That is, the opening stress is first lowered by the axial overload. When the torsional load rises to its peak value while axial stress relaxes in an elastic-plastic fashion, the opening stress is further lowered before pure torsional fatigue cycles start. The nonlinear terms in Eqn. (10) therefore contain two inputs: one from the initial axial overload, $(\sigma_{xx}^2)_{max}^{ol}$, and the other from the subsequent torsion excursion combined with axial relaxation, which is here estimated by $(\sigma_{xx}^2)_o + 3\sigma_{xy}^2$, where $(\sigma_{xx})_o$ represents the relaxed value of axial stress, and σ_{xy} represents the peak value of the torsional cycle. Similarly, the torsional tests with zero axial strain after the initial overload also have an additional term resulting from the unloading of the axial overload followed by an elastic-plastic torsional cycle before torsional smaller cycles begin. The amplitude of the unloading portion of the axial load together with the torsional amplitude is used here to assess the second overload effect, $(\frac{1}{2}\sigma_{xx}^{ol})^2 + 3\sigma_{xy}^2$.

The good opening stress agreements seen in Figs. 12a-b can be viewed as a confirmation of the cumulative effects from both the out-of-plane tensile overload and the subsequent tension-torsion overload on lowering the crack opening stress.

The multiaxial crack opening stress model is next viewed by its ability to calculate fatigue life. First, the effective strain calculated according to Eqn. (2) is plotted against the observed equivalent fatigue life in Fig. 13. When compared with the dotted curve, taken from Fig. 9 as the material's fundamental fatigue property for the

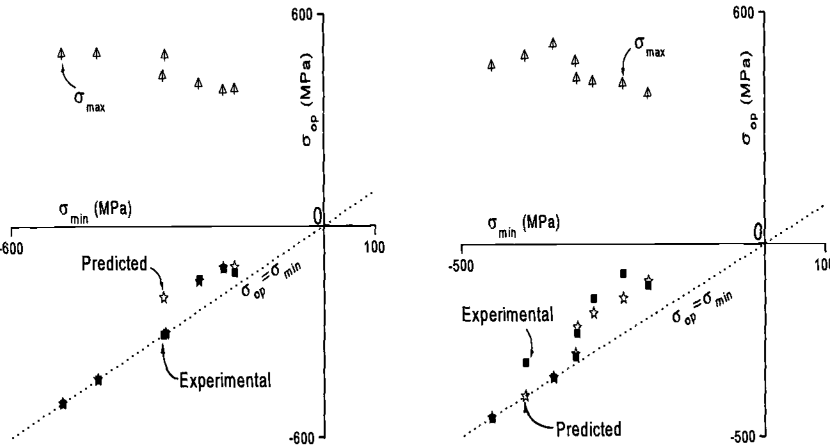

(a) Torsion with peak-hold axial overload. *(b) Torsion with zero-mean axial overload.*

FIG. 12–*Predicted and back-calculated opening stresses.*

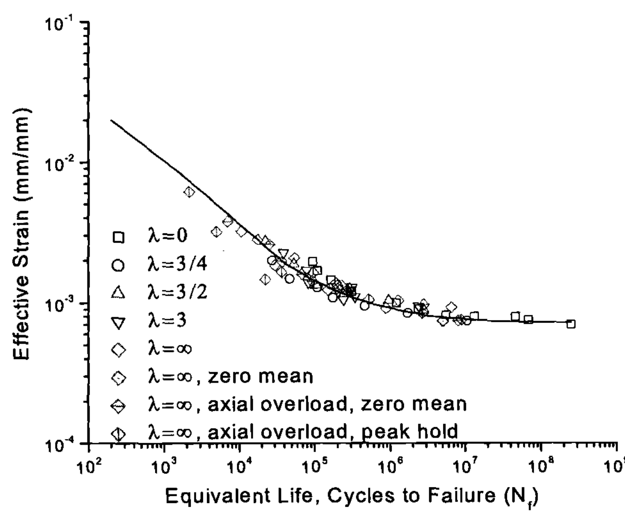

FIG. 13–*Calculated effective strain, equivalent stress based, versus observed equivalent life.*

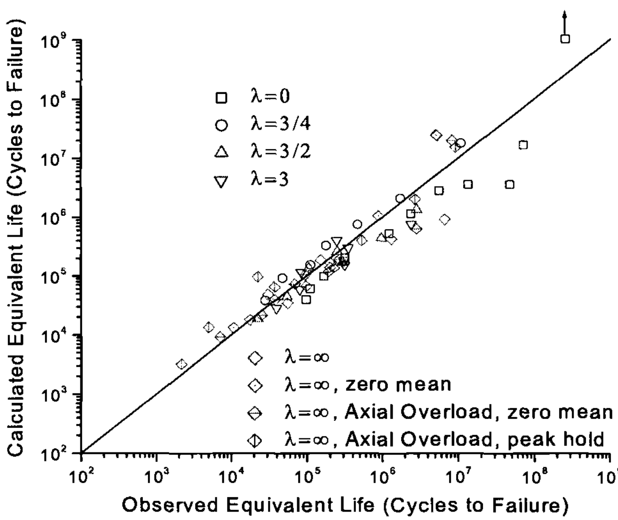

FIG. 14 *Calculated fatigue life, equivalent stress based, versus observed equivalent life.*

closure-based approach, data points to the right of the curve indicate conservative fatigue life prediction. The same results can be viewed by plotting calculated fatigue life against observed equivalent life in Fig. 14, where again data points to the right of the solid line are conservative. It is observed that for the majority of the biaxial tests reported in [*11*], the equivalent stress based opening stress model, Eqn. (10), yields a high quality life prediction capability.

Similar but slightly less impressive life prediction capabilities are observed for the shear stress based crack opening model, Fig. 15, and for the normal stress based crack opening model, Fig. 16.

Conclusions

By analyzing a very large set of biaxial overload test data in this paper, the uniaxial closure-based fatigue method has been extended to calculate fatigue behavior under multiaxial loadings. A multiaxial crack opening stress model which assumes cumulative effects from both tensile and torsional overloads, applied either simultaneously or sequentially, is shown to describe well the overload effects on lowering opening stress level. In particular, the opening stress model expressed in terms of equivalent stress is seen to be able to accurately calculate fatigue life for the majority of the overload tests analyzed, including tests that involve out-of-plane overloads that have proven difficult to predict using traditional methods. The large scatter observed in back-calculated opening stress, however, suggests that overload tests with constant amplitude and thus more steady stress/strain behavior are desirable in determining

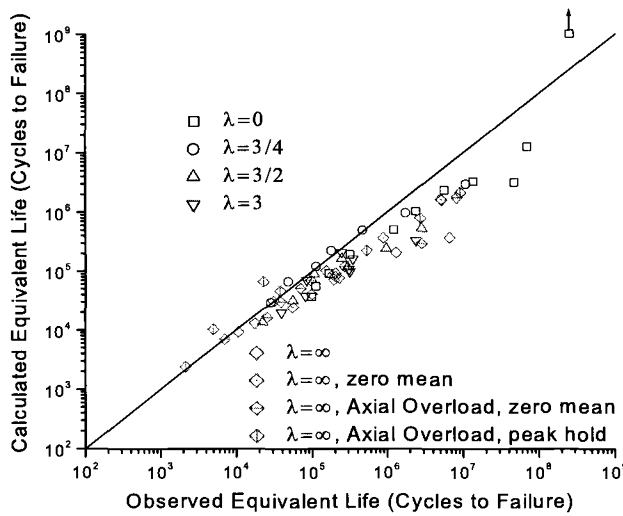

FIG. 15 *Calculated fatigue life, shear stress based, versus observed equivalent life.*

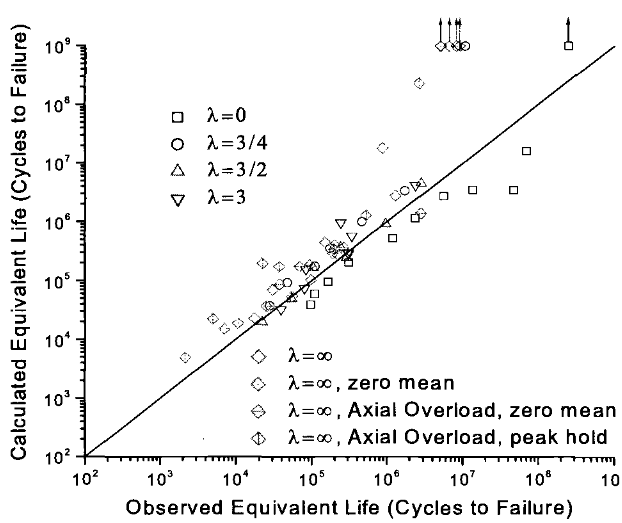

FIG. 16 *Calculated fatigue life, normal stress based, versus observed equivalent life.*

the new material properties and the crack opening stress model that are required to use a closure-based fatigue method.

References

[1] Elber, W., "The Significance of Fatigue Crack Closure," *Damage Tolerance in Aircraft Structures, ASTM STP 486*, 1971, pp. 230-242.

[2] Schijve, J., "Fatigue Crack Closure: Observations and Technical Significance," *Mechanics of Fatigue Crack Closure ASTM STP 982*, 1988, pp. 5-34.

[3] Ritchie, R. O. and Suresh, S., "Some Considerations on Fatigue Crack Closure at Near-threshold Stress Intensities Due to Fracture Surface Morphology," *Metallurgical Transactions, A*, 1982, pp. 937-940.

[4] Vormvald, M. and Seeger, T., "The Consequences of Short Crack Closure on Fatigue Crack Growth under Variable Amplitude Loading," *Fatigue and Fracture of Engineering Materials and Structures*, Vol. 14, No. 2/3, 1991, pp. 205-225.

[5] Topper, T.H., DuQuesnay, D.L., and Pompetzki, M.A., "Crack Closure, Damage And Short Crack Growth under Variable Amplitude Loading," *Theoretical Concepts and Numerical Analysis of Fatigue*, eds. A.F. Blom and C.J. Beevers, EMAS Warley, UK., 1993, pp. 201-236.

[6] DuQuesnay, D.L., Topper, T.H., Yu, M.T., and Pompetzki, M.A., "The Effect of Compression and Compressive Overloads on the Fatigue Behavior of a 2024-T351 Aluminum Alloy and a SAE1045 Steel," *Low Cycle Fatigue, ASTM STP 942*, 1988, pp. 173-183.

[7] Yu, M.T. and Topper, T.H., "The Effects of Material Strength, Stress Ratio and Compressive Overloads on The Threshold Behavior of An SAE 1045 Steel," *Journal of Engineering Materials Technology,* ASME Transaction, 1985, Vol. 107, pp.19-25.

[8] DuQuesnay, D.L., "Fatigue Damage Accumulation in Metals Subjected to High Mean Stress and Overload Cycles," Ph.D. Thesis, University of Waterloo, Waterloo, Ontario, Canada, 1991.

[9] MacDougall, C. and Topper, T.H., "The Influence of Variable Amplitude Loading on Crack Closure and Notch Fatigue Behavior," *International Journal of Fatigue*, Vol 19, 1997, pp.389-400.

[10] DuQuesnay, D.L., Topper, T.H., Yu, M.T. and Pompetzki, M.A., "The Effective Stress Range as A Mean Stress Parameter," *International Journal of Fatigue*, Vol. 14, No. 1, 1992, pp.45-50.

[11] Bonnen, J.J.F., "Multiaxial Fatigue Response of Normalized 1045 Steel Subjected to Periodic Overloads: Experiments and Analysis," Ph.D. Thesis, University of Waterloo, Waterloo, Ontario, Canada, 1998.

[12] Bonnen, J.J.F., Topper, T.H. and Conle, F.A., "The Role of In-Phase and Out-of-Phase Overloads on the Torsional Fatigue of Normalized SAE 1045 Steel," *International Journal of Fatigue,* Vol. 23, 2001, pp. S385-S394.

[13] Bonnen, J.J.F and Topper, T.H., "The Effect of Bending Overloads on Torsional Fatigue in Normalized SAE1045 Steel," *International Journal of Fatigue*, Vol. 21, No.1, 1999, pp.23-33.

[14] Pompetzki, M.A., Saper, R.H. and Topper, T.H., "Software for High Frequency Control of Variable Amplitude Fatigue Tests," *Canadian Metallurgy Quarterly*, Vol.25, 1986, pp. 181-194.

[15] Bonnen, J. and Conle, F.A., "An Adaptable, Multichannel, Multiaxial Control System," SAE Paper 950703, 1995.

[16] Chu, C.-C. and Bonnen, J.J.F., "A Comprehensive Approach to von Mises Stress-Strain Conversions," *Proceedings of the 6th International Conference on Biaxial/Multiaxial Fatigue and Fracture*, Lisbon, Portugal, June 26-28, 2001.

[17] Chu, C.-C. and Chernenkoff, R.A., "Crack Closure-Based Analysis of Fatigue Tests with Mean Stresses," *International Journal of Fatigue*, Vol. 23, 2001, pp. S187-S194.

[18] Chu, C.-C., Chernenkoff, R.A. and Bonnen, J.J.F., "Experiments and Analysis of Mean Stress Effects on Fatigue for SAE1045 Steels," *STP 1417*

Richard E. Link[1]

Dynamic Fracture Toughness Measurements in the Ductile-to-Brittle Region Using Small Specimens

Reference: Link, R. E., **"Dynamic Fracture Toughness Measurements in the Ductile-to-Brittle Region Using Small Specimens,"** *Fatigue and Fracture Mechanics: 33rd Volume, ASTM STP 1417*, W. G. Reuter and R. S. Piascik, Eds., ASTM International, West Conshohocken, PA, 2002.

Abstract: The dynamic fracture toughness of a reactor pressure vessel steel was investigated using small specimens. Precracked Charpy-size SE(B) specimens and circumferentially cracked round bars (CRB) loaded in tension were used to investigate the dynamic fracture toughness of an A533, Gr. B steel plate within the ductile-brittle transition region. The specimens used in this investigation were removed from the broken halves of conventional 4T C(T) specimens that had been utilized in a previous investigation of the dynamic fracture toughness of this material. Crack-tip loading rates in excess of 10^4 MPa-m$^{1/2}$/s were achieved in the current tests. Multiple specimens were tested at each temperature in order to permit the determination of the reference temperature, T_0. A fracture toughness scaling model for the circumferentially cracked round bar developed by Sciabetta was used to account for the loss of constraint in this specimen. A master curve approach was used to characterize the dynamic toughness in the ductile-brittle region. The shift in transition temperature was compared to a model for the strain rate dependence of T_0 developed by Wallin. The shift in transition temperature of the CRB specimen was accurately predicted by the model. The CRB specimen and the dynamic SE(B) specimens gave good results considering the material inhomogeneity typical of the plate tested.

Keywords: cracked round bar, constraint, dynamic fracture toughness, master curve, reference temperature, A533 Grade B steel

Introduction

Deeply cracked, bend-type specimen geometries are required in fracture toughness testing standards to measure the fracture toughness of a material. These specimens provide relatively high constraint at the crack tip and yield lower bound measures of the fracture toughness. Specimens with shallow cracks or tensile loading do not have the high crack tip constraint experienced by deeply cracked bend specimens and result in higher apparent fracture toughness values. Alternative specimen geometries that may be sub-size, contain shallow cracks, or be subjected to tensile loading are often of interest for specific applications. The circumferentially cracked round bar (CRB) specimen has been investigated as an alternative specimen geometry by several investigators [*1-4*]. The CRB specimen has several features that make it attractive as a fracture specimen. It is easier to fabricate than most specimens and the loading arrangement is simple, utilizing the same fixtures as a standard tensile test. It is an axisymmetric geometry that does not have an intersection of the crack front with a free surface, so the stress field is uniform all along the crack front. In cases where material availability is limited, such as surveillance capsules in nuclear pressure vessels, it may be possible to modify standard tensile specimens into fracture specimens by introducing a notch and a precrack. One disadvantage of the specimen is that it is not as easy to precrack as standard specimen

[1] Associate Professor of Mechanical Engineering, U.S. Naval Academy, Annapolis, MD 21402.

geometries. This has led some researchers to try to use notched specimens for fracture toughness tests instead of precracked specimens [*5,6*].

Giovanola et al. demonstrated the feasibility of using the CRB specimen to measure the fracture toughness of several tough alloys. Finite element analyses indicated that the CRB geometry initially loses constraint, characterized by the Q-stress, but that the constraint increases with increasing deformation in the fully plastic regime for deeply cracked bars [*1*].

Scibetta performed an extensive investigation of the CRB specimen and proposed guidelines for using it as a standard fracture specimen [*2*]. His study included finite element simulations that showed similar results to those reported in [*1*]. He also demonstrated that the specimen could be used to characterize the ductile-brittle reference temperature, T_0, in ferritic steels provided the fracture toughness values were corrected for loss of constraint.

The objective of the present investigation was to use the CRB specimen to measure the dynamic fracture toughness of a reactor pressure vessel steel in the ductile-brittle transition region and compare it with data from conventional C(T) and SE(B) specimens.

Details of Experiments

Description of Source Plate

The material used in this investigation was a piece of ASTM A533, Gr. B, Cl. 1 steel plate from HSST Plate 14, which was provided by Oak Ridge National Laboratory from the High Strength Steel Technology Program. The piece of plate was approximately 129.5 cm x 94 cm x 23.5 cm thick (51 in. x 37 in. x 9-1/4 in. thick) and was assigned a three-letter identifying code, HAS. The chemical composition of the plate, as reported in the material certification report is listed in Table 1. The plate had been quenched, tempered at 690°C (1275°F) and stress-relieved at 655°C (1210°F) by the steel manufacturer. No subsequent heat treatments were performed on the plate and all tests were conducted in the as-received condition.

The mechanical properties of the plate were reported in an earlier investigation of the dynamic fracture toughness of A533, Gr. B [*7*]. Tensile, impact toughness and fracture toughness properties were determined in that study and key properties are summarized in Table 2.

TABLE 1—*Chemical composition of ASTM A533, Grade B, Class 1 steel plate studied in this investigation. (Values are in weight percent.)*

Element	HSST Plate 14 (HAS)	ASTM A533, Gr. B, Cl. 1
Carbon	0.215	0.25 max
Manganese	1.40	1.07-1.62
Silicon	0.22	0.13-0.45
Nickel	0.655	0.37-0.73
Molybdenum	0.56	0.41-0.64
Sulfur	0.008	0.035 max.
Phosphorous	0.010	0.035 max.
Copper	0.070	Not specified.

Columbium	0.019	Not specified
Iron	Balance	Balance

TABLE 2—*Mechanical properties of HSST Plate 14.*

Property	HSST Plate 14
Yield Strength at 29°C, MPa (ksi)	436 (63)
Ultimate Tensile Strength at 29°C, MPa (ksi)	584 (85)
68 J CVN, °C (°F)	21 (70)
Drop Weight NDT, °C (°F)	-18 (0)

Test Matrix

Static and dynamic fracture toughness tests were performed on CRB specimens and dynamic fracture toughness tests were also conducted on 0.4T SE(B) (precracked CVN) specimens. All of the specimens were removed from the broken halves of 4T C(T) specimens that had been previously tested to measure the dynamic fracture toughness. The crack plane was in the T-L orientation. A matrix of the specimen types used is shown in Table 3.

TABLE 3—*Specimen types and conditions evaluated in this investigation.*

Specimen	Loading Rate	a/W	Test Temp. (°C)
CRB	Static	0.37	-50
CRB	Dynamic	0.37	-25
0.4T SE(B)	Dynamic	0.5	-25
0.4T SE(B)	Dynamic	0.5	-50

CRB Specimen

The CRB specimens were fabricated from standard 12.8 mm (0.505 in.) diameter tensile specimens with a gage length of 50.8 mm (2 in.). An initial notch with a 60° included angle and a root radius of 75 μm (0.003 in.) was machined in the middle of the gage section to a depth of 1.27 mm (0.05 in.). A schematic drawing of the specimen is presented in Fig. 1.

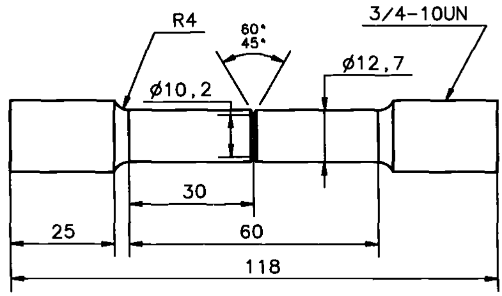

FIG. 1—*Nominal dimensions (mm) of the CRB specimen.*

The specimens were precracked in rotating bending fatigue using a specially designed apparatus. Previous investigators [*1,2*] have utilized rotating bending fatigue to introduce fatigue cracks into CRB specimens. In [*2*], the specimen was cantilevered from the chuck of a lathe and a force or displacement was applied to the free end of the specimen as the chuck was rotated. This introduced a fully reversed bending moment at the notched section. Unfortunately, there is also a shear force acting at the crack plane that introduces a Mode II component to the stress intensity and can cause the crack to be non-planar. Nevertheless, satisfactory cracks can be produced using this method. Another possible loading mode is axial loading of the specimen. It can be difficult to produce concentric cracks using axial loading because any misalignment will lead to a non-circular crack along with eccentricity. The forces required for axial loading are also higher than for bending.

A four-point bending apparatus was designed and built to introduce pure bending at the crack plane to minimize the out-of-plane cracking due to the presence of Mode II loading in the cantilever setup. The precracking machine is shown schematically in Fig. 2. A pure bending moment is applied to the ends of the specimen through the collet chucks. The collet chucks are supported in self-aligning bearings. The outer set of bearings are fixed to the machine base. The inner set of bearings are attached to the movable upper plate. A fine-pitch threaded rod is used to apply a fixed displacement to the inner bearing carrier. A load cell positioned below the screw anvil monitors the force that develops. A belt connected to an electric motor drives one of the collet chucks. This causes the specimen to rotate, leading the notch to undergo cyclic, fully-reversed bending. A locknut maintains the initial displacement. As the crack grows from the notch, the specimen becomes more compliant and the applied force decreases. The amount of load drop necessary to produce a fatigue crack extension of 1.25 mm (0.05 in.) was determined empirically. The machine was stopped after the required load drop was noted on the load cell. A photograph of the precracking machine is shown in Fig. 3.

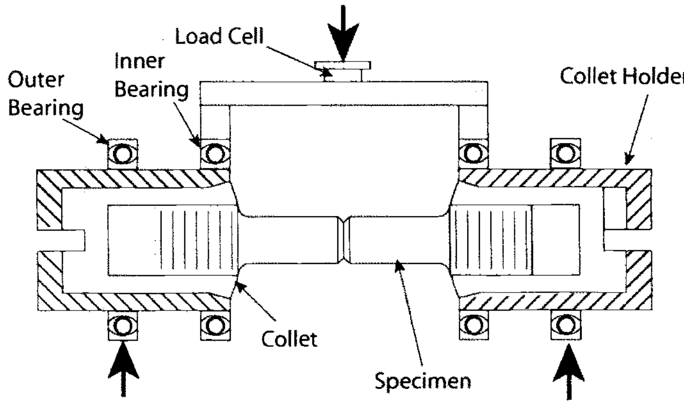

FIG. 2—*Schematic drawing of the apparatus used to apply a pure bending moment to the CRB specimen.*

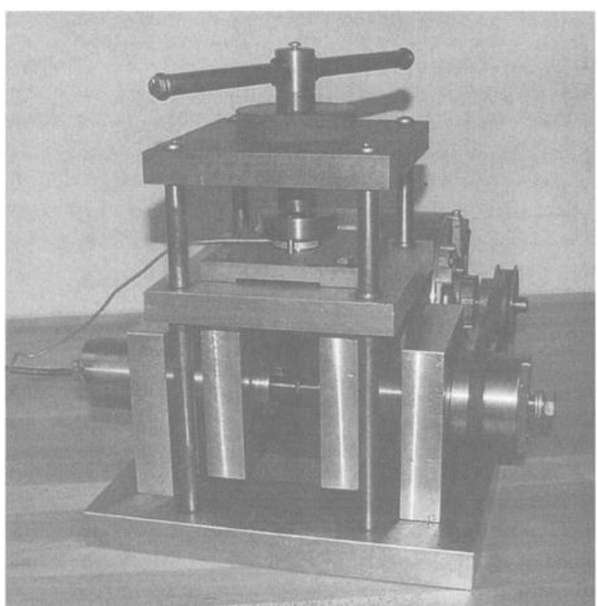

FIG. 3—*Photograph of the machine used to precrack the CRB specimens.*

The stress intensity factor during precracking was calculated using a solution for a circumferential round bar in pure bending developed by Benthem and Koiter [*8*]. The Benthem and Koiter solution does not consider contact of the crack faces, so a modification developed by Sawaki [*9*] was also incorporated. The expression for the maximum stress intensity factor around the circumference is given by:

$$K_{max} = \sigma\sqrt{\pi a\left(1-\frac{a}{R}\right)}\, S\left(\frac{b}{c}\right) G\left(\frac{b}{R}\right) \qquad (1)$$

where:

$\sigma = 4M/\pi b^3$,

M=applied bending moment,

$S\left(\frac{b}{c}\right) = -0.0184 + 0.4085\left(\frac{b}{c}\right) + 1.05\left(\frac{b}{c}\right)^2 - 0.4488\left(\frac{b}{c}\right)^3$ for b/c>0.4,

$G\left(\frac{b}{R}\right) = \frac{3}{8}\left[1 + \frac{1}{2}\left(\frac{b}{R}\right) + \frac{3}{8}\left(\frac{b}{R}\right)^2 + \frac{5}{16}\left(\frac{b}{R}\right)^3 + \frac{35}{128}\left(\frac{b}{R}\right)^4 + 0.531\left(\frac{b}{R}\right)^5\right]$ and

a,b,c, and R are defined in Figure 4.

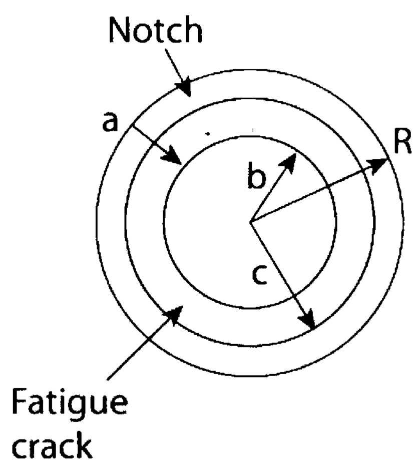

Figure 4 - ***Geometry of the CRB fracture plane.***

Under fixed displacement conditions, the stress intensity factor actually increases as the crack extends before it starts to decay. The effective stress intensity range at the start of precracking was 16 MPa√m. At the end of precracking, the range was typically 22 MPa√m. The fatigue cracks produced with the rotating bending apparatus were planar and generally concentric with the specimen outside diameter. A typical fatigue crack and fracture surface are shown in Figure 5.

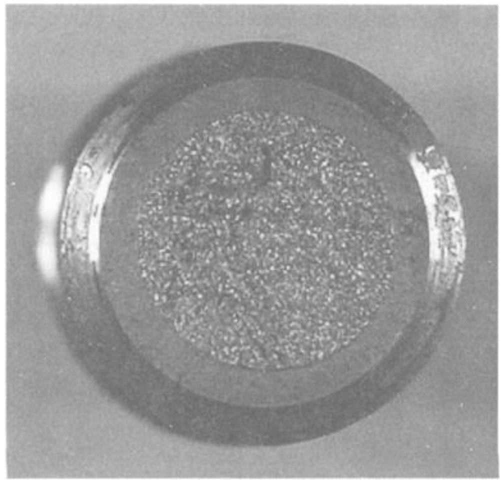

Figure 5 - ***Photograph of the fracture surface of a CRB specimen showing the notch and fatigue region.***

After the fracture tests were completed, the initial fatigue crack size was determined by digitizing a photograph of the fracture surface and calculating the best-fit of a circle to the digitized points along the crack front. The eccentricity of the ligament was also calculated. The eccentricity is the distance between the centers of the specimen cross-section and the remaining ligament. The eccentricity was typically on the order of 0.27 mm, with a maximum of 0.50 mm. The variation of the stress intensity factor due to the eccentricity was not accounted for in any of the subsequent analyses. For cracked round bar specimens in the fully plastic regime, Giovanola and Kobayashi [*10*] estimated the error in J due to neglecting the bending component to be less than 5%.

Testing Details

The CRB specimens were tested in a standard servo-hydraulic universal testing machine. The instrumentation included a load cell and an extensometer with a 25.4 mm gage length that was mounted across the notch in the specimen. The CRB specimens were instrumented with a strain gage to monitor the specimen load in the dynamic tests. The strain gage was located 19 mm from the notch. The gage was calibrated with universal testing machine load cell prior to the actual test. The maximum calibration force was limited to 9 kN, approximately 20% of the maximum force recorded during the test in order to minimize any warm prestress effect. The strain gage and extensometer signals were input to signal conditioners with a frequency response > 10 kHz. The actuator displacement rate was 5×10^{-3}mm/s for the static tests and 100 mm/s for the dynamic tests.

The force, extension and crosshead displacement are plotted as a function of time for a typical dynamic CRB test in Figure 6. In general, fracture occurred in about 8 ms. The applied force vs. extension trace from this test is plotted in Figure 7. There is some noise in the displacement signal, but the trace is generally linear in the elastic region (up to a force of ≈35kN) and the experimentally measured specimen compliance was within 20% of the theoretical compliance for all of the dynamic tests. It is clear from comparing the slopes actuator and the extensometer traces in Figure 6 that the specimen loading rate is about an order of magnitude lower than the actuator loading rate. This is a result of the load train compliance and slack in the grips and fixtures. Once the specimen becomes fully plastic, the extension rate approaches the actuator displacement rate.

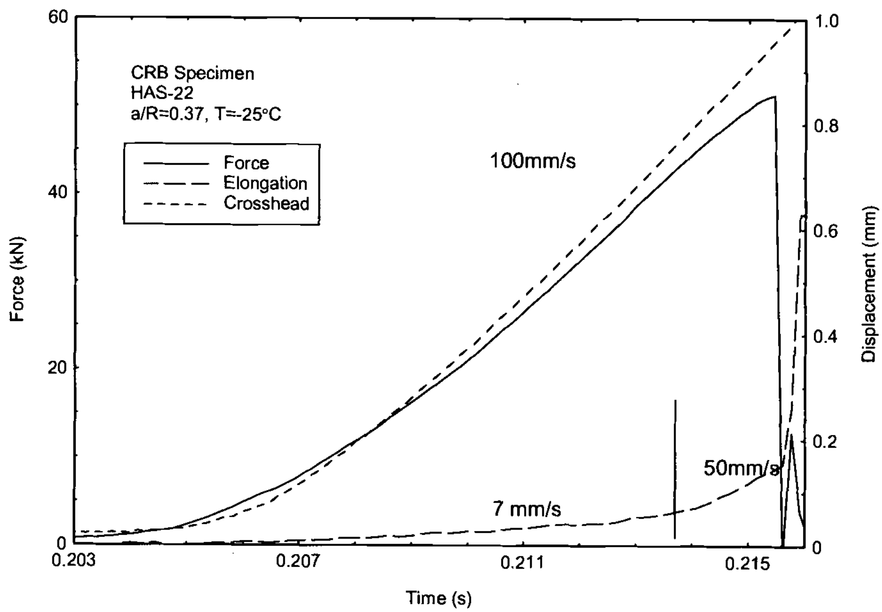

Figure 6 - ***Force, extension and crosshead displacement as a function of time for dynamic CRB specimen, HAS-22.***

The 0.4T SE(B) specimens were instrumented with a ring-type crack mouth opening displacement gage. The applied force was monitored using the load cell on the universal testing machine.

For both specimen types, the specimen temperature was monitored by a contact thermocouple placed within the gage length of the specimen. The temperature rise due to adiabatic heating of the specimen during the test was not recorded. An environmental chamber with liquid nitrogen spray cooling was used to cool the specimen to the test temperature. The specimen was allowed to stabilize at the test temperature for a minimum of 10 minutes and the temperature was held constant within 2°C during holding period. All data was recorded using a PC-based, 12-bit A/D data acquisition system.

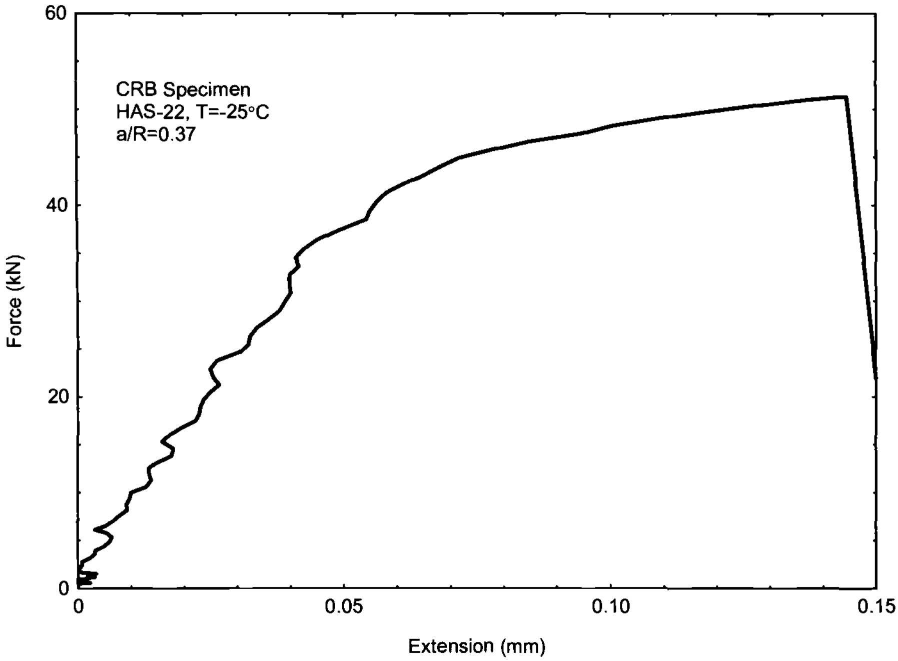

Figure 7 - *Force vs. extension for CRB specimen HAS-22.*

Analysis of CRB Specimen

The CRB specimen has been studied extensively by Scibetta [*2*]. He performed detailed finite element analyses of the crack tip fields and presented useful J expressions and constraint correction models for this geometry that were employed in the current investigation. The J integral for the CRB with a/R≈0.4 was calculated using the expression:

$$J = \frac{K^2\left(1-\upsilon^2\right)}{E} + \eta' \frac{U_{pl}^{crack}}{\pi b^2} \qquad (2)$$

where:
K=stress intensity factor
ν= Poisson's ratio
E=Young's Modulus
η'=eta factor
U_{pl}^{crack} = plastic energy dissipated due to the crack
b = radius of remaining ligament.

The stress intensity factor for a CRB subjected to a remote tensile load was calculated using a solution from Benthem and Koiter [*8*]:

$$K = \frac{P}{\pi b^2}\sqrt{\frac{\pi ab}{R}}\,G\left(\frac{b}{R}\right) \tag{3}$$

where :
P=remote tensile force,
a,b,R are defined in Figure 4 and

$$G\left(\frac{b}{R}\right) = \frac{1}{2}\left[1+\frac{1}{2}\left(\frac{b}{R}\right)+\frac{3}{8}\left(\frac{b}{R}\right)^2 - 0.363\left(\frac{b}{R}\right)^3 + 0.731\left(\frac{b}{R}\right)^4\right].$$

Scibetta presented an empirical equation for η':

$$\eta' = -0.03 + 1.3\left(\frac{a}{R}\right) + 0.333\left(\frac{a}{R}\right)^2 - 1.03\left(\frac{a}{R}\right)^3. \tag{4}$$

The plastic energy dissipated due to the crack, U_{pl}^{crack}, can be determined from:

$$U_{pl} = U_{pl}^{bar} + U_{pl}^{crack} \tag{5}$$

where U_{pl} is the total plastic energy dissipated in the specimen and U_{pl}^{bar} is the plastic energy dissipated in the bar which is a function of material properties, stress level and specimen size [*2*]. However, in all tests reported in this investigation, the stress in the bar remote from the crack remained elastic, $\sigma_{avg} < 0.85\sigma_{YS}$; therefore, $U_{pl}^{bar}=0$ and $U_{pl} = U_{pl}^{crack}$. U_{pl} was calculated using the area under the load vs. plastic displacement curve where the plastic displacement was found by subtracting the elastic displacement based on the theoretical gage length compliance from the total displacement using the following relationships from [*2*]:

$$\delta_{pl} = \delta_{pl} - PC\left(\frac{b}{R}\right) \tag{6}$$

where

$$C = \frac{L_0}{E\pi R^2}\left[1 + 4\pi R\frac{1-\upsilon^2}{L_0}H\left(\frac{b}{R}\right)\right]$$

L_0 = gage length of extensometer, and

$$H\left(\frac{b}{R}\right) = \frac{0.25}{b/R} - 0.353 + 0.169\left(\frac{b}{R}\right)^2 - 0.133\left(\frac{b}{R}\right)^3 + 0.049\left(\frac{b}{R}\right)^4 - 0.011\left(\frac{b}{R}\right)^5 + 0.05\left(\frac{b}{R}\right)^6 - 0.038\left(\frac{b}{R}\right)^7 + 0.017\left(\frac{b}{R}\right)^8$$

SE(B) Specimens

The SE(B) specimens were analyzed using a J expression presented by Kirk and Dodds [*11*] that expresses J_{pl} as a function of the area under the force vs. plastic CMOD curve:

$$J = \frac{K^2\left(1-\upsilon^2\right)}{E} + J_{pl}. \tag{7}$$

The stress intensity factor is calculated using the standard relationships in E1820-99a for the SE(B) specimen. J_{pl} is calculated using the expression:

$$J_{pl} = \frac{\eta_{CMOD} A_{CMODpl}}{Bb} \tag{8}$$

where

$A_{CMODpl} = A - P^2 C_0 / 2$,

A = area under load-CMOD curve at point of instability,

C_0 = theoretical elastic CMOD compliance for initial crack length,

P = applied force,

b = remaining ligament based on initial crack length

B=specimen thickness, and

$$\eta_{CMOD} = 3.785 - 3.101\frac{a_0}{W} + 2.018\left(\frac{a_0}{W}\right)^2.$$

There was no stable crack extension in the SE(B) tests, so all calculations were based on the initial crack length.

Calculation of Reference Temperature, T_Q

The reference temperature, T_0 or T_Q, corresponding to a median fracture toughness, $K_{Jc(med)}$, of 100 MPa√m was determined using the procedures described in ASTM Test Method for Determination of Reference Temperature, T_0, for Ferritic Steels in the Transition Range (ASTM E 1921). This test method assumes the cumulative failure probability of a specimen loaded to K_J will follow a three-parameter Weibull model:

$$p_f = 1 - \exp\left\{-\left[\left(K_{Jc} - K_{\min}\right)/\left(K_0 - K_{\min}\right)\right]^b\right\} \tag{9}$$

The Weibull slope, b, is assumed to be 4 and K_{min} is selected to be 20 MPa√m. For data sets containing *N* valid fracture toughness values measured at a single temperature, the scale parameter, K_0, was determined using the equation:

$$K_0 = \left[\sum_{i=1}^{N} \frac{\left(K_{Jc(i)} - K_{\min}\right)^4}{N}\right]^{1/4} + K_{\min} \tag{10}$$

The median fracture toughness, $K_{Jc(med)}$ is then calculated using:

$$K_{Jc(med)} = K_{\min} + \left(K_0 - K_{\min}\right)\left[\ln(2)\right]^{1/4} \tag{11}$$

Finally, T_0 (in °C) is determined from the relationship:

$$T_0 = T - \left(\frac{1}{0.019}\right)\ln\left[\frac{K_{Jc(med)} - 30}{70}\right] \tag{12}$$

Prior to calculating the scale parameter, all data are adjusted for a specimen size effect using the relationship:

$$K_{Jc(1T)} = K_{\min} + \left(K_{Jc} - K_{\min}\right)\left(\frac{B}{25.4mm}\right)^{1/4} \tag{13}$$

For data sets containing fracture toughness measurements made at multiple temperatures, T_0 is determined from the following relationship using an iterative procedure:

$$\sum_{i=1}^{N} \delta_i \frac{\exp[0.019(T_i - T_0)]}{11 + 77\exp[0.019(T_i - T_0)]} - \sum_{i=1}^{N} \frac{\left(K_{Jc(i)} - K_{\min}\right)^4 \exp[0.019(T_i - T_0)]}{\{11 + 77\exp[0.019(T_i - T_0)]\}^5} = 0 \tag{14}$$

The reference temperature, T_0, is defined in ASTM E 1921 as the temperature corresponding to a median fracture toughness, $K_{Jc(med)}$, of 100 MPa√m in a standard 1T specimen. This procedure is restricted to quasi-static loading and other restrictions on specimen geometry, size and minimum number of specimens to ensure that T_0 is a material property. K_{Jc} values determined using non-standard specimens such as the CRB geometry or test procedures such as dynamic loading are expected to have different constraint conditions than the standard specimen types. The resulting reference temperatures are designated as T_Q values according to E 1921. This notation was adopted for the results reported in this study.

The CRB specimens do not maintain high crack tip constraint under elastic-plastic deformation. The loss of constraint occurs at relatively low load levels and leads to higher fracture toughness values than would be measured in standard bend type specimens at similar deformation levels. Scibetta performed detailed three-dimensional finite element analyses of the CRB geometry to quantify the constraint loss as a function of deformation level in the CRB specimen. Following the approach of Anderson and Dodds [*12*], he developed a constraint-correction which he used to estimate the fracture toughness under small-scale yielding conditions. The constraint-correction approach is based on a micromechanical failure model that assumes the probability for cleavage fracture is a function of the volume of material ahead of the crack that is stressed above a critical level. The constraint-correction corrects the measured fracture toughness to the equivalent value under conditions of small-scale yielding. The fracture toughness data are corrected to SSY conditions using the relationship:

$$K_{Jc(1T)SSY} = 20 + \left(K_{J(CRB)} - 20\right)\left(\frac{B_x A_{CRB}}{B_{1T} A_{SSY}}\right)^{1/4} \tag{15}$$

where:

$K_{J(CRB)}$ = measured toughness in the CRB specimen,
B_x = crack front length of CRB specimen (circumference of precrack),
B_{1T} = 25.4 mm,
A_{CRB}/A_{SSY} = ratio of the volume of material stressed to a critical level in the CRB and SSY model

Scibetta determined the ratio A_{CRB}/A_{SSY} for several discrete crack sizes and strain hardening exponents as shown in Fig. 8 [2]. The correction factor is always less than unity and decreases with increasing deformation, corresponding to a loss of constraint. At deformation levels greater than $J/(a\sigma_{YS})\approx 0.1$, the correction factor actually increases, corresponding to a slight increase in constraint for deeply cracked CRB specimens ($a/R \geq 0.5$).

The A533, Gr. B steel used in this investigation can be reasonably approximated by a strain hardening exponent of 0.1. Since the specimens used in this study had an initial crack size to bar radius of 0.37, the correction factor was linearly interpolated as shown in Fig. 8. It should be noted that the specimen size correction based on crack front length is nearly unity for the 12.8 mm diameter CRB specimen with a/R=0.37.

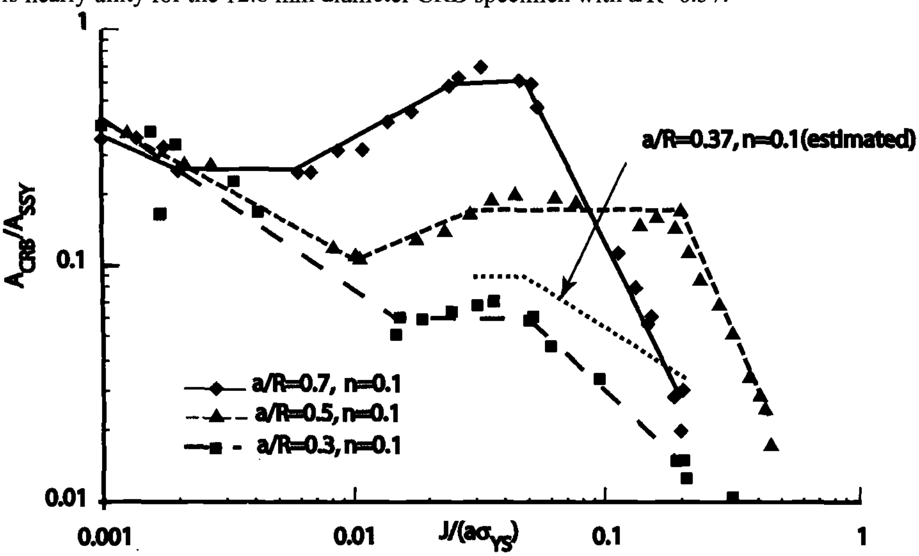

Figure 8 - ***SSY-correction term as a function of deformation level for the CRB geometry from [2]. The interpolated result for a/R=0.37 is indicated.***

Results

The individual fracture toughness values for all of the tests conducted in this investigation are summarized in Table 4. (In this paper, T_Q is used to designate a reference temperature determined by following the computational procedures in ASTM E1821. However, the reference temperature does not meet all of the qualification requirements such as specimen geometry or loading rate or test temperature to be considered a "valid" reference temperature, T_0.) The T_Q reference temperatures determined for the data sets are listed in Table 5 along with the T_0 reference temperatures calculated from the static and dynamic C(T) tests reported by Link and Graham [7]. The 0.4T SE(B) tests conducted at -50°C resulted in a T_Q of 40°C. The test temperature was 90°C below the calculated reference temperature for this data set and these results are not valid because the data are presumably on the lower shelf where the master curve concept does not apply [*13*]. These data are still invalid even when they are used in a multi-temperature approach that includes the data measured at -25°C.

Table 4 - ***Summary of fracture toughness results for CRB and 0.4T SE(B) specimens from HSST plate 14.***

ID	Type	Rate (MPa√m/s)	a/W	Temp. (°C)	KJc (MPa√m)	KJc1T (MPa√m)	$K_{Jc1TSSY}$ (MPa√m)
HAS-C11	CRB	Static	0.36	-50	155.8	156.0	96.5
HAS-C12	CRB	Static	0.39	-50	198.3	198.5	120.4
HAS-C14	CRB	Static	0.39	-50	178.0	178.2	109.0
HAS-C15	CRB	Static	0.36	-50	168.3	168.5	103.5
HAS-C16	CRB	Static	0.36	-50	171.5	171.7	105.3
HAS-C17	CRB	Static	0.38	-50	159.1	159.3	98.3
HAS-C18	CRB	3.60E+04	0.41	-25	137.4	137.5	82.5
HAS-C19	CRB	3.60E+04	0.36	-25	136.2	136.4	80.9
HAS-C20	CRB	3.60E+04	0.36	-25	105.5	105.6	66.9
HAS-C22	CRB	3.60E+04	0.36	-25	114.7	114.9	72.0
HAS-C23	CRB	3.60E+04	0.36	-25	159.4	159.6	89.1
HAS-C24	CRB	3.60E+04	0.37	-25	128.0	128.2	79.2
HAS-C25	CRB	3.60E+04	0.37	-25	141.8	141.9	82.7
HAS-S14	SE(B)	5.30E+04	0.50	-25	73.7	62.6	62.6
HAS-S27	SE(B)	5.30E+04	0.50	-25	72.2	61.4	61.4
HAS-S31	SE(B)	5.30E+04	0.50	-25	101.2	84.3	84.3
HAS-S32	SE(B)	5.30E+04	0.50	-25	101.0	84.2	84.2
HAS-S35	SE(B)	5.30E+04	0.50	-25	64.8	55.5	55.5
HAS-S45	SE(B)	5.30E+04	0.50	-25	62.6	53.8	53.8
HAS-S17	SE(B)	5.30E+04	0.50	-25	62.6	53.8	53.8
HAS-S34	SE(B)	5.30E+04	0.50	-25	69.2	59.0	59.0
HAS-S26	SE(B)	5.30E+04	0.50	-25	80.2	67.7	67.7
HAS-S41	SE(B)	5.30E+04	0.50	-25	71.4	60.8	60.8
HAS-S13	SE(B)	5.30E+04	0.50	-50	45.7	40.4	40.4
HAS-S22	SE(B)	5.30E+04	0.50	-50	53.0	46.1	46.1
HAS-S23	SE(B)	5.30E+04	0.50	-50	49.5	43.3	43.3
HAS-S33	SE(B)	5.30E+04	0.50	-50	46.3	40.8	40.8
HAS-S36	SE(B)	5.30E+04	0.50	-50	46.5	41.0	41.0
HAS-S43	SE(B)	5.30E+04	0.50	-50	50.9	44.5	44.5
HAS-S47	SE(B)	5.30E+04	0.50	-50	51.7	45.1	45.1

The static results from the CRB specimens are plotted in Fig. 9. The SSY corrected data are also plotted along with the 1T C(T) results from [*7*] which had a T_0= -62°C based on a multi-temperature analysis of the data at -63, -21 and -3°C. The uncorrected results from the CRB specimens are well above the median fracture toughness curve from the 1T C(T) specimens. Most of the results lie above the 95% tolerance bound, indicating a loss of constraint in these specimens. The uncorrected CRB data yield a T_Q = -83°C. The SSY corrected data fall below the median toughness curve, but well within the 5% tolerance bound and yield a $T_{Q\text{-}SSY}$ = -37°C. It appears that the CRB data are slightly overcorrected, but the SSY correction does lead to a conservative estimate of the reference temperature.

Table 5 - ***Measured reference temperatures for each loading rate and specimen type.***

Specimen Type	Loading Rate (MPa√m/s)	Test Temperature (°C)	T_Q (°C)
1T C(T)	Static	-64, -21, -3	-62*
CRB	Static	-50	-83
CRB - SSY	Static	-50	-37
2T & 4T C(T)	$1\text{x}10^5$	16, 29	-21*
CRB	$3.6 \text{ x } 10^4$	-25	-42
CRB - SSY	$3.6 \text{ x } 10^4$	-25	-2
0.4T SE(B)	$5.3 \text{ x } 10^4$	-50	40
0.4T SE(B)	$5.3 \text{ x } 10^4$	-25	10

* Reference temperature determined using multi-temperature expression from eq. (14).

The dynamic fracture toughness values are compared in Figure 10. It is clear that the dynamic loading causes a significant shift in the reference temperature. The dynamic master curve plotted in the figure was developed from the 2T and 4T C(T) results where T_Q was determined to be -21°C at an average loading rate of approximately 10^5MPa√m/s. The loading rates for the CRB and 0.4T SE(B) specimens were slightly lower, approximately 3.6 and 5.1 x10^4 MPa√m/s, respectively. The uncorrected CRB data all lie above the median curve for the large C(T) specimens. The SSY-corrected CRB data and the 0.4T SE(B) data are in good agreement with each other, yielding T_Q values of -2 and +10°C.

Discussion

The SSY-corrected, static results for the CRB specimen in Figure 9 appear to be in better agreement with the 1T C(T) results than the uncorrected results. However, the T_Q based on the uncorrected values is 21°C below the 1T C(T) result and the SSY corrected T_Q is 25°C above the 1T C(T) value shown in Table 5. This indicates that the SSY-correction did not really improve things in terms of the reference temperature.

The reference temperature originally reported in [7] for the plate was -53°C, based on an average of the T_0 values from the data at -63°C and -21°C. All of the data at -3°C exceed $K_{Jc(limit)}$ and are censored values and they lower T_0 by 9°C when they are included. The censored data do not correspond to SSY conditions at failure and have

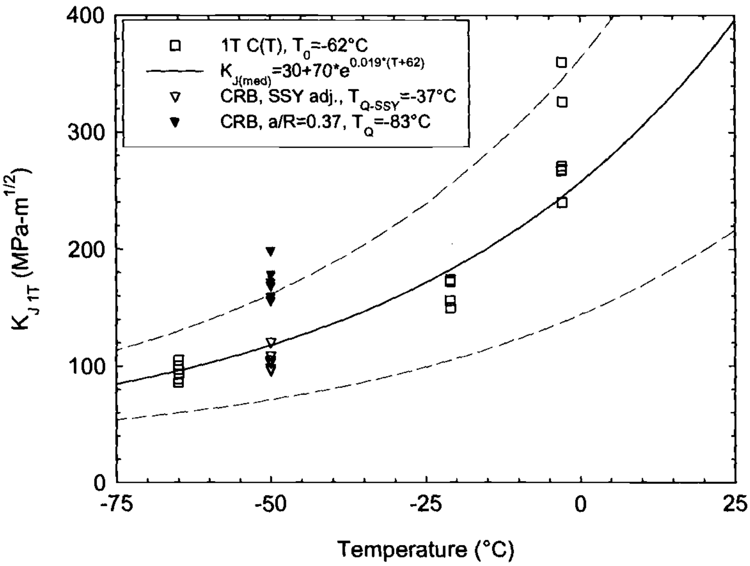

Figure 9 - ***Static fracture toughness results for 1T C(T) and CRB specimens and the master curve (solid line) and 95% confidence limits (dashed) for the static 1T C(T) specimens.***

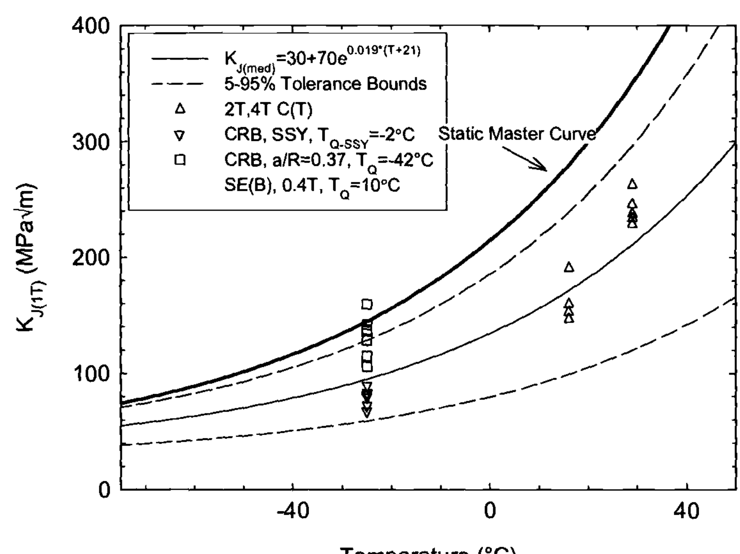

Figure 10 - ***Dynamic fracture toughness results from 0.4T SE(B) and CRB specimens compared to master curve from 2T and 4T C(T) specimens.***

significant loss of constraint, leading to a lower value for the reference temperature. In order to provide a fair comparison of the CRB results with the C(T) results, the data sets should be treated equally. The C(T) data at -3°C was corrected for loss of constraint using a SSY correction for the C(T) geometry reported in [*14*] and the reference temperature was recalculated. This led to a T_0 of -51°C. The SSY-corrected C(T) data and the CRB data are plotted in Figure 11 and the agreement in reference temperature is good when the comparison is made on an equal basis.

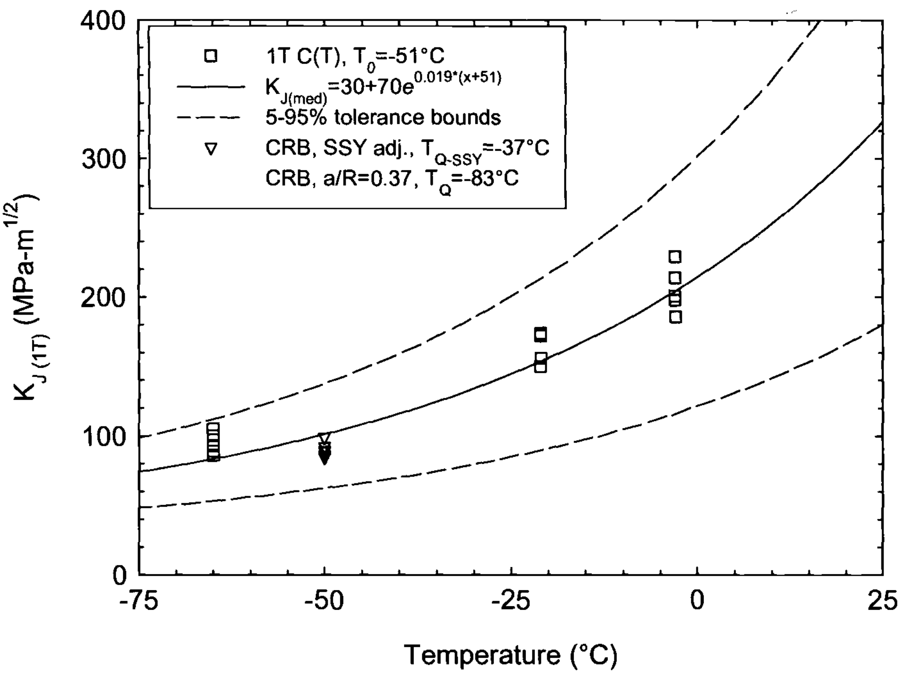

Figure 11 - ***SSY-corrected, static fracture toughness results for 1T C(T) and CRB specimens.***

The dynamic fracture toughness from the 0.4T SE(B) and SSY-corrected CRB results were relatively consistent with each other. However, the reference temperatures were 20-30°C higher than that determined from the 2T and 4T C(T) specimens which were tested at a rate 2-3 times higher than the small specimens. It would be expected that the higher rate would lead to higher T_0 values, although a factor of two or three is not normally significant when considering rate effects. Usually an order of magnitude change in rate is required to yield a significant change in material behavior.

Wallin developed an empirical relationship between the reference temperature, loading rate and room temperature yield strength to predict the shift in reference temperature resulting from dynamic loading [*15*]. The shift in reference temperature is determined from the relationship:

$$\Delta T_0 = \frac{T_{01} \bullet \ln \dot{K}_1}{\Gamma - \ln \dot{K}_1} \tag{16}$$

where:

T_{01} = reference temperature corresponding to $\dot{K}$ =1 MPa√m/s, in Kelvin

$\dot{K}$ = loading rate, MPa√m/s,

$$\Gamma = 9.9 \exp\left[\left(\frac{T_{01}}{190}\right)^{1.66} + \left(\frac{\sigma_{YS}}{722}\right)^{1.09}\right]$$

and σ_{YS}= room temperature yield strength, MPa.

This relationship was used to predict the shift in reference temperature for the tests reported in this study. The reference temperature predicted from equation (16), assuming T_{01}=-51°C and σ_{YS}=436 MPa, is listed in Table 6 for each of the data sets. The reference temperature shift ranged from 43-48°C for the loading rates used in these tests. The predicted reference temperature for the CRB is within 6°C of the value determined from the dynamic CRB tests. The predictions for the other data sets are off from 16-18°C, lying between the values determined from the dynamic C(T) and SE(B) tests.

Table 6 - ***Reference temperatures for dynamic tests predicted from equation (16)***

Specimen Type	Loading Rate (MPa√m/s)	Test Temperature (°C)	Measured T_Q (°C)	T_Q pred. from Eq. 16 (°C)
2T & 4T C(T)	$1\text{x}10^5$	16, 29	-21	-3
CRB - SSY	3.6×10^4	-25	-2	-8
0.4T SE(B)	5.3×10^4	-25	10	-6

Material inhomogeneity within heavy section steel plates has been identified as a source of variability in estimates of T_0, particularly when using small data sets and small specimens [*16,17*]. The primary microstructural feature responsible for the variability has been identified as carbide banding. This can result in greater variability in T_0 estimates than is normally encountered in more homogeneous plates.

The plate used in this study, HSST Plate 14, has been characterized extensively by several investigators[*18,19*]. Prior to removing specimens, the plate was heat treated in order to increase the yield strength to levels associated with neutron embrittlement. Therefore, the actual toughness values and reference values are not directly comparable because the specimens in this study were tested in the as-received plate condition. The heat treatment does not have a significant impact on the distribution of the carbide bands which are principally formed during ingot solidification and broken up to some degree by subsequent rolling of the plate [*20*]. The scatter in fracture toughness present in the heat-treated plate should be representative of the scatter in the as-received plate. Joyce and Tregoning [*21*] reported valid T_0 values for HSST Plate 14 ranging from -74°C to -39°C based on tests of 0.4T SE(B) specimens. Dynamic 0.4T SE(B) specimens tested at -40°C yielded T_Q values of -32 and -24°C corresponding to loading rates of $5\text{x}10^4$ and $1.3\text{x}10^3$ MPa√m/s, respectively. This could reflect a shift due to dynamic loading between 7-50°C, depending on which value of T_0 is selected as the "true" reference temperature for comparison. Considering the variability inherent in this plate, the results of the present investigation are certainly reasonable.

Conclusions

1. CRB specimens tested under static and dynamic loading rates produced fracture toughness values and reference temperatures that were consistent with values obtained from conventional C(T) specimens when the CRB data were corrected for loss of constraint.
2. A new precracking device for the CRB specimens was described. The machine produced planar, concentric fatigue cracks in a consistent manner while avoiding some of the problems associated with alternative methods of precracking the CRB specimens.
3. The shift in reference temperature due to dynamic loading was compared with predictions based on an empirical model developed by Wallin. The model was reasonably accurate in predicting the change in reference temperature. Material inhomogeneity present in the thick section plate made it difficult to critically evaluate the model.

Acknowledgement

I would like to acknowledge the contributions of ENS. M. Toribio, USNR, to the design and fabrication of the precracking machine described in this paper. ENS. Toribio performed this work while a midshipman at the U.S. Naval Academy.

References

[1] Giovanola, J. H., Homma, H., Lichtenberger, M., Crocker, J. E., and Klopp, R. W., "Fracture Toughness Measurements Using Small Cracked Round Bars," *Constraint Effects in Fracture, Theory and Applications: Second Volume, ASTM STP 1244*, M. T. Kirk and A. Bakker, Eds., ASTM, Philadelphia, PA, 1995, pp. 255-85.

[2] Scibetta, M., "Contribution to the Evaluation of the Circumferentially-Cracked Round Bar for Fracture Toughness Determination of Reactor Pressure Vessel Steels," Doctoral Dissertation, Université de Liége, 1999.

[3] Scibetta, M. and Chaoudi, R., "Fracture Toughness Derived from Small Circumferentially Cracked Bars," *Small Specimen Test Techniques, ASTM STP 1329*, W. R. Corwin, S. T. Rosinki and E. van Walle, Eds., ASTM, Philadelphia, PA, 1998, pp. 363-80.

[4] Costin, L. S., Duffy, J., and Freund, L. B., "Fracture Initiation in Metals Under Stress Wave Loading Conditions," *Fast Fracture and Arrest, ASTM STP 627*, G. T. Hahn and M. F. Kanninen, Eds., American Society for Testing and Materials, Philadelphia, PA, 1977, pp. 301-318.

[5] Irwin, G. R., Dally, J. W., Zhang, X. J. and Bonenberger, R. J., "Lower-bound

initiation toughness of A533-B reactor-grade steel," *Rapid Load Fracture Testing, ASTM STP 1130*, R. L. Chona and W. L. Corwin, Eds., American Society for Testing and Materials, Philadelphia, PA, 1992, pp. 9-23.

[6] Wilson, C. D. and Landes, J. D., "Fracture Toughness Testing with Notched Round Bars," *Fatigue and Fracture Mechanics: 30th Volume, ASTM STP 1360*, K. L. Jerina and P. C. Paris, Eds., American Society for Testing and Materials, Philadelphia, PA, 1992, pp. 69-82.

[7] Link, R. E. and Graham, S. M., "Dynamic Initiation Fracture Toughness of a Pressure Vessel Steel in the Transition Region," *Fatigue and Fracture Mechanics,: Twenty-Ninth Volume, ASTM STP 1332*, T. L. Panontin and S. D. Sheppard, Eds., American Society for Testing and Materials, Philadelphia, PA, 1999, pp. 19-39.

[8] Benthem, J. P. and Koiter, W. T., "Asymptotic Approximations to Crack Problems," *Methods and Analysis of Crack Problems*, G. C. Sih, Ed., Noordhoft International Publishing, Groningen, 1973, pp. 131-178.

[9] Sawaki, Y., Aoyama, N., and Kawasaki, T., "Determination of Fatigue Fracture Toughness by Conventional Rotary Bending Specimen," *International Journal of Fracture*, 26, 1984, pp. 43-54.

[10] Giovanola, J. H. and Kobayashi, T., "Mechanics of Deformation and Ductile Tearing in Cracked Round Bar Specimens," *Engineering Fracture Mechanics*, Vol. 59, No. 2, 1998, pp. 117-136.

[11] Kirk, M. T., and Dodds, R. H., Jr., "J and CTOD Estimation Equations for Shallow Cracks in Single Edge Notch Bend Specimens," NUREG/CR-5969, U.S. Nuclear Regulatory Commission, Washington DC, July 1993.

[12] Anderson, T. L. and Dodds, R. J., "Specimen Size Requirements for Fracture Toughness Testing in the Transition Region," *Journal of Testing and Evaluation*, Vol. 19, 1991, pp. 123-134.

[13] Merkle, J. G., Wallin, K., and McCabe, D. E., "Technical Basis for an ASTM Standard on Determining the Reference Temperature, T_0, for Ferritic Steels in the Transition Range," NUREG/CR-5504, U.S. Nuclear Regulatory Commission, Washington DC, November 1998.

[14] Nevalainen, M. and Dodds, R. H., Jr., "Numerical Investigation of 3-D Constraint Effects on Brittle Fracture in SE(B) and C(T) Specimens," NUREG/CR-6317, U.S. Nuclear Regulatory Commission, Washington DC, July 1996.

[15] Wallin, K., "Loading Rate Effect on the Master Curve T_0," Report IIW-X-1403-97, VTT Manufacturing Technology, Espoo, Finland, August 1997.

[16] Joyce, J. A. and Tregoning, R. L., "Development of T_0 Reference Temperature from Precracked Charpy Specimens," ASME PVP-Vol. 393, New York, July 1999, pp.

53-62.

[17] Zhang, X. J. and Tregoning, R. L., "The Effect of Carbide Banding Structure On Fracture Toughness of Heavy-Section A533B Steel," *Proceedings of the International Symposium on Steel for Fabricated Structures*, R. I. Asfahani and R. L. Bodner Ed., ASM International, Materials Park, Ohio, 1999, pp. 75 - 83.

[18] McAfee, W. J., Williams, P. T., Bass, B. R., and McCabe, D. E., "An Investigation of Shallow Flaw Effects on the Master Curve Indexing Parameter (T_0) in RPV Material," *Applications of Fracture Mechanics in Failure Asessment*, ASME PVP-Vol. 412, New York, July 2000, pp. 161-172.

[19] Joyce, J. A., Tregoning, R. L. and Zhang, X. J., "Application of Master Curve Technology to Biaxial and Shallow Crack Fracture Data for A533B Steels," *Effects of Radiation on Materials: 19th International Symposium, ASTM STP 1366*, M. L. Hamilton, et al., Eds., American Society for Testing and Materials, West Conshohocken, PA, 2000.

[20] Ogawa, K., Zhang, X. J., Kobayashi, T. Armstrong, R. W., and Irwin, G. R., "Microstructural Aspects of the Fracture Toughness Cleavage-Fibrous Transition for Reactor-Grade Steels," *ASTM STP 833*, R.J. Sanford, Ed., American Society for Testing and Materials, Philadelphia, PA, 1984, pp. 393-411.

[21] Joyce, J. A., Tregoning, R. L., "Effects of Material Inhomogeneity on the T_0 Reference Temperature in Thick Section A533B," to be published in Proc. 2001 ASME PVP Conference.

Matthew Wagenhofer[1] and Marjorie E. Natishan[2]

A Model for Predicting Fracture Toughness of Steels in the Transition Region from Hardness

Reference: Wagenhofer, M. and Natishan, M. E., "**A Model for Predicting Fracture Toughness of Steels in the Transition Region from Hardness,**" *Fatigue and Fracture Mechanics: 33rd Volume, ASTM STP 1417,* W. G. Reuter and R. S. Piascik, Eds., ASTM International, West Conshohocken, PA 2002.

Abstract: Given the nature of fracture in the lower transition region where final fracture by cleavage is preceded by some amount of plastic deformation, it is appropriate to use a combined strength-strain criterion to describe the conditions at fracture. A dislocation-based model for predicting fracture toughness of steels in the transition region has been developed where the primary feature describing the temperature dependence of fracture toughness is a plastic work term of the following form:

$$\gamma_{eff} = \left(\frac{\sigma_m}{\overline{\sigma}}\right)_f \int \sigma_{ZA} \overline{d\varepsilon^p} \cdot D_0$$

where γ_{eff} is the effective plastic work to fracture, $\overline{d\varepsilon^p}$ is the effective plastic strain increment, $\sigma_m/\overline{\sigma}$ is the triaxiality ratio and r_o is the length scale of the critical fracture event typically taken as carbide cracking (and thus $D_o = r_o$ is the critical carbide radius). The σ_{ZA} term represents the flow stress from the Zerilli-Armstrong constitutive equation for bcc metals. This term introduces a temperature dependency based on dislocation mechanics considerations. Inserting the first equation into the Griffith-Orowan equation for fracture stress leads to the elimination of the carbide radius from the equation,

$$\sigma_f = \left[\frac{\pi E \gamma_{eff}}{2(1-\nu^2)r_o}\right]^{1/2}$$

and thus the need for defining a characteristic distance.

In this paper we describe the details of this model used to predict fracture toughness behavior transition with temperature for ferritic steels. We then combine this model with a discussion of the uniformity of steel tensile properties to develop a method for predicting fracture toughness transition temperature shift due to irradiation from hardness tests.

Keywords: Master Curve, tensile properties, strain hardening, ferritic steel

[1] Graduate Research Assistant, Mechanical Engineering Department, University of Maryland, College Park, MD 20742

[2] President, Phoenix Engineering Associates, Inc., Davidsonville, MD 21035

Introduction

To assess the integrity of a nuclear reactor pressure vessels (RPV) against a postulated pressurized thermal shock (PTS) event, and to address compliance with the PTS rule [1], commercial licensees must estimate the fracture toughness of their RPV after neutron embrittlement. Limitations on the volume of material that can be irradiated as part of a surveillance program restrict both the quantity and size of the material samples used to obtain this estimate. These restrictions necessitated adoption of a correlative approach wherein fracture toughness is not actually measured, but rather inferred from measurements of a reference temperature from the Nil Ductility Test (RT_{NDT}) before irradiation, and the shift in the Charpy V-notch (CVN) transition temperature produced by irradiation. Together these measurements are used to estimate a value of RT_{NDT} after irradiation [1], and this value is used to locate curves intended to represent both the initiation fracture toughness (K_{Ic}) and the arrest fracture toughness (K_{Ia}) of the material.

More recently, some licensees have applied to the Nuclear Regulatory Commission (NRC) for exemptions to 10CFR§50.61 to enable use of alternative schemes for determining fracture toughness, these being based on Master Curve technology [2-5]. Because Master Curve methodology, as described in ASTM E 1921-98 [6], involves direct measurement of fracture toughness from the material of interest, it allows use of reduced margins because it more accurately reflects the materials true toughness transition behavior. General use of this method for assessing a RPV fracture toughness has been delayed by concerns that arise due to the empirical nature of the Master Curve model as put forth by Wallin et al. [7]. This empiricism precludes the ability to extrapolate applicability to new materials and conditions, thus requiring additional testing to establish validity of the Master Curve for each new material or condition of interest. Full use of Master Curve requires establishment of a fundamental physical basis for this model that enables development of a fully predictive model for which the bounds of applicability are firmly understood.

In their 1984 paper, Wallin, Saario, and Törrönen (WST) [7] suggest a link between the micro-mechanics of cleavage fracture and the empirical observation of a "master" toughness transition curve. Using the Griffith equation as the basis for their model they suggest that temperature dependence enters via the plastic work term shown as w_p in Equation (1) and (2). Equation (1) shows the dependence of the critical fracture-inducing particle radius on the applied stress, σ, and a combination of the surface energy and the plastic energy absorbed prior to crack growth, w_p.

$$r = \frac{\pi\left(\gamma_s + w_p\right)E}{2\left(1-\upsilon^2\right)\sigma^2} \tag{1}$$

The temperature dependence of w_p is given by:

$$\gamma_s + w_p = A + B \cdot \exp\left[C \cdot T\right] \tag{2}$$

This form of the temperature dependence of the plastic work term follows that given for the Master Curve fracture toughness temperature-dependence in ASTM E 1921-98 [*6*]:

$$K_{Jc(median)} = 30 + 70 \cdot \exp\left[0.019\left(T - T_o\right)\right] \tag{3}$$

The numeric values in Equation (3) do not depend on the type of ferritic steel, suggesting that ferritic steel type does not influence the relationship between ($\gamma_s + w_p$) and temperature in Equation (2). Furthermore, the ASTM standard assumes a dispersion of toughness about this median value that follows a Weibull distribution with a fixed slope of 4 for all ferritic steels.

Equation (1) and other mathematical relationships associated with the Master Curve (i.e. predictions of size effects, predictions of data dispersion), model existing fracture toughness data for nuclear RPV steels very well. Empirical validation of the Master Curve approach will be prohibitively expensive (especially for irradiated materials). Establishment of a sound physical basis for the Master Curve approach offers the potential of broad validation of the concept at reasonable costs, and within a time frame of interest to nuclear licensees.

While these new approaches feature direct measurement of fracture toughness [*6,8*] thereby bypassing the conservatisms implicit to current practice, they still require a sizable quantity of irradiated material for mechanical testing. Especially when new surveillance programs are initiated to monitor irradiation effects through license renewal, the appetite of both existing and emerging toughness estimation approaches for irradiated material to test economically burdens licensees. Moreover, in some cases it may be difficult or impossible to initiate new surveillance programs due to the un-availability of pedigreed archival materials from which to fabricate mechanical test specimens.

New procedures to estimate fracture toughness are still needed to circumvent both the economic and practical problems associated with maintaining surveillance programs through license renewal, whether the current correlative method [*1*] or an adapted Master Curve method is used. To provide a benefit relative to current approaches, these procedures should use much smaller specimens than the current norm (or allow re-testing of old specimens), and they should be sufficiently robust to allow toughness prediction and extrapolation of current knowledge based on sound physical concepts rather than relying on correlations. Certainly many toughness estimation procedures employing small specimen test data have been proposed, these including the small punch test [*9-12*], numerous variants of the CVN test [*13*], as well as hardness and micro-hardness tests [*13*]. However, these approaches generally rely upon correlations to establish fracture toughness from the small specimen test data, an approach that raises questions regarding the applicability of the procedure to all service materials and conditions of interest, thereby impeding generic regulatory acceptance of such strategies.

In studying the uniformity of fracture toughness behavior for all ferritic steels represented by the Master Curve, other relationships consistent between all steels began to emerge. These include the relationship between hardness and ultimate tensile strength, ultimate tensile strength and yield strength, and the shift between yield strength and the fracture toughness transition behavior as described by T_o in ASTM E 1921. Development of a physically motivated, empirical model for predicting transition shift from measurements of hardness was first described by Kirk and Natishan [*14*]. We delve further into the ideas first presented in that paper here, particularly taking advantage of the observed uniformity of ferritic steel flow behavior to derive relationships between hardness and yield strength.

Uniform Toughness vs. Temperature Curve Shape

Fracture toughness data accumulated over years of testing is shown in Figure 1. Despite the differences in specimen size and steel composition across the population of the data set, there appears to be a uniform temperature dependence. Figure 2 indicates that this uniformity is prevalent even after the steel is subjected to a hardening treatment such as radiation. As mentioned earlier, an empirical analysis of data such as in Figure 1 forms the basis of the method in ASTM standard E 1921-98 [*6*] for describing the toughness transition curve. Natishan and Kirk [*15,16*] proposed a physical justification for the uniform temperature dependence of K_{Ic} for all ferritic steels and the shift in T_o with hardening..

The central idea behind their hypothesis is that toughness is a function of the flow behavior of the material. Indeed, the conventional notion of material toughness is the area under the stress-strain curve. As such, transition region toughness is dependent on the ability of dislocations to move through the material: the more easily they move, the greater the toughness. This is manifested in the stress-strain record as lower yield strengths and larger strain values, behavior that is consistent with increasing temperatures.

Consideration of obstacles to dislocation motion leads to an explanation for the uniformity of the K_I curve shape. These obstacles are microstructural features of the material (precipitates, solutes, grain boundaries, etc.) that require moving dislocations to have a certain minimum energy to pass. They are divided into short and long-range according to whether an input of thermal energy to the material provides a significant reduction in their activation energy or not. The only short-range obstacle in BCC metals is the lattice itself and so the temperature dependence of the flow behavior is a function of the lattice spacing. Therefore ferritic steels, which all have the same lattice structure as α-iron and consequently the same lattice spacing, should all exhibit the same temperature dependent behavior.

It has been shown [*17*] that the quantitative representation of the flow behavior developed by Zerilli and Armstrong [*18*] does an excellent job of describing the temperature dependence of the yield strength of a number of ferritic steels using parameters derived for pure iron. The so-called ZA equation derives its temperature dependence from the activation energy of a material's short-range obstacles. The equation is shown below in a slightly updated form that combines the temperature dependencies of BCC and FCC metals [*19*]:

$$\sigma_{ZA} = \sigma_0 + K\sqrt{\varepsilon} \tag{4a}$$

$$\sigma_0 = c_0 + Be^{-\beta T} \tag{4b}$$

$$c_0 = \sigma_G + kd^{-1/2} \tag{4c}$$

$$K = B_0 e^{-\alpha T} \tag{4d}$$

$$\beta = \beta_0 - \beta_1 \ln \dot{\varepsilon} \tag{4e}$$

$$\alpha = \alpha_0 - \alpha_1 \ln \dot{\varepsilon} \tag{4f}$$

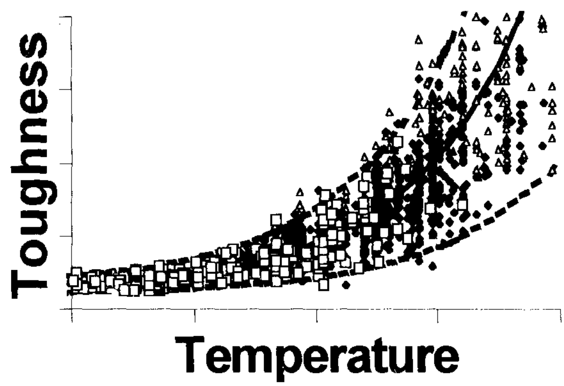

Figure 1 - Generalized toughness data for a range of temperatures showing the uniform temperature dependence.

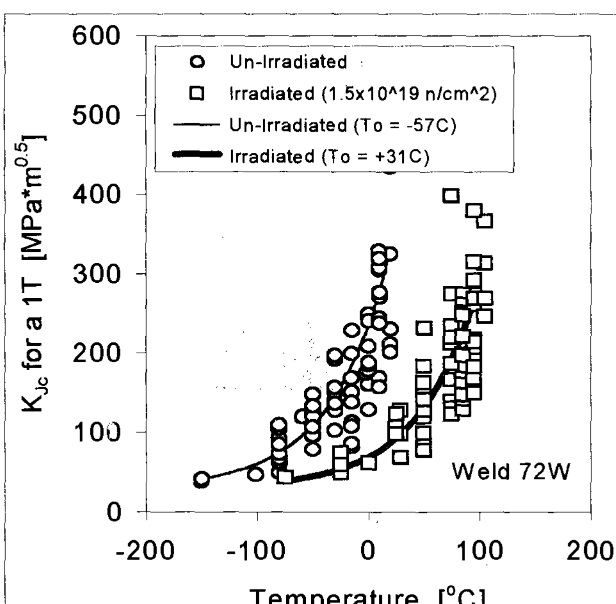

Figure 2 - Toughness data showing the shift of the uniform temperature dependence after radiation hardening.

The first term of Equation (4a) represents the yield strength while the second term is the work hardening behavior. Temperature is represented by T, ε is the strain and $\dot{\varepsilon}$ is the strain rate. All other constants are material specific parameters. FCC materials generally do not exhibit temperature or strain hardening dependent yield strengths and as such the thermal term of Equation (4b) will vanish. The yield strengths of BCC materials, on the other hand, are very sensitive to temperature and strain rate while the work hardening behavior is not. Thus, Equation (4f) will vanish and the thermal term of Equation (4d) will approach a value of 1.

Modeling the Toughness vs. Temperature Curve Shape

Using the ZA equation as the centerpiece and taking a cue from the work of Wallin et al. [7,20], Natishan and Kirk [16] further proposed a quantitative formulation of the plastic work done in initiating unstable fracture:

$$\gamma_p = \int \sigma_{ZA} d\varepsilon \cdot D_o \tag{5a}$$

where

$$K_{Ic} = \sqrt{\frac{2\gamma_p E}{(1-\nu^2)}} \tag{5b}$$

for plane strain. In Equation (5b), γ_p, the plastic work, is defined as the area under the stress-strain curve times a length scale, D_o. While Wallin asserted that the temperature dependence of toughness is contained in the plastic work term he described this temperature dependence empirically and not theoretically. Equation (5a) explicitly utilizes the temperature dependence of the flow behavior derived by Zerilli and Armstrong. Further work by Wagenhofer et al. [21] resulted in the development of Equation (5a) into a usable expression for the plastic work:

$$\gamma_p = \left(\frac{\sigma_m}{\sigma_i}\right) \int_0^{\varepsilon_c} \sigma_{ZA} d\varepsilon \cdot D_0 \tag{6}$$

σ_m/σ_i is a measure of the triaxiality where σ_m is the mean stress, or the stress to open the crack while σ_i is the Peierls-Nabarro stress, the stress tom move dislocations through the material. This term decreases with temperature, which should result in a decrease in γ_p, but this is not realized as the temperature dependence of the critical strain, ε_c, dominates the temperature dependence of the plastic work. ε_c is the critical strain required for cleavage crack initiation and D_o is the length scale over which the accumulation of strain acts to raise the stress to that required for cleavage crack initiation. Equation (6) incorporates two of the three quantifiable requirements for cleavage fracture as defined by Tetelman et al. [22]. These are a critical amount of strain to nucleate a microcrack that can propagate unstably (ε_c) and a critical level of stress triaxiality (given by the ratio σ_m/σ_i) to ensure that the microcrack does not blunt. The critical strain is the upper limit of integration in Equation (3) and the triaxiality is a scalar multiplier preceding the integral. This particular value represents the stress state in the vicinity of the critical microcrack at the onset of unstable fracture. It multiplies the integral in order to compensate for the ZA equation's inability to describe the stress intensification ahead of a crack tip. The third requirement for cleavage fracture is a critical level of stress normal to the crack plane to drive unstable microcrack propagation.

The strain energy density that results prior to multiplication by D_0 is indicative only of the work done in a small volume ahead of the crack tip. This volume is the process zone. Characteristic distance models such as RKR [*23*] define the process zone in part by a dimension that is parallel to the crack plane and extends out in front of the crack tip. In the context of unstable fracture, the work done is the energy per unit area crack surface created. With respect to describing the work done in cracking the carbide that causes unstable fracture by a stress applied normally to the crack plane, it is more accurate to define the process zone by its height, i.e. the critical carbide diameter D_0.

By incorporating data from a series of previous studies of the fracture behavior a C-Mn steel [*24*], the results of Equation (6) can be compared to Wallin's empirical plastic work formulation, see Figure 3. The calculated results match quite well to the empirical fit. The shape of the curve is described very well by the ZA equation outfitte with thermal parameters (see Eqns. 4b and 4e) derived specifically for a C-Mn steel [*25*] Table 1 shows that these are quite similar to the thermal parameters used to verify ZA's ability to describe the temperature dependence of the yield strength of ferritic steels [*17*

Table 1. ZA thermal parameters for ARMCO iron [17] and a C-Mn steel [25].

	ARMCO Iron	**C-Mn steel**
B (MPa)	1033	1000
β_0 (K^{-1})	0.00698	0.0075
β_1 (K^{-1})	0.000415	0.0004

It is difficult to assign tolerances to the above values without any knowledge of the uncertainties present in the stress-strain data used to derive them. Their proximity t each other, however, is a reasonable affirmation of the validity of the physical justification for the uniform temperature dependence of ferritic steel transition region fracture behavior.

Ultimate Tensile Strength vs. Yield Strength

While Figure 3 demonstrates that the proposed model well predicts the temperature dependence of the fracture toughness transition, it says little about the abili to predict the shift in transition temperature due to irradiation. Irradiation affects the yield stress of a material by increasing the vacancy and interstitial density. This increas in yield stress affects the athermal portion of the Z-A equation (Equation 4), which, wh used in Equation 3, predicts a shift in the temperature at which the transition occurs. B a method for quantifying this shift needs to be developed.

Figure 4 shows a recently proposed method [*14*] for determining the change in t T_o transition temperature from Brinell hardness measurements. Relationships between hardness and ultimate tensile strength (UTS) (Figure 4a), UTS and yield (Figure 4b) an change in yield versus change in To (Figure 4c) are used to obtain T_o from hardness. T key to this method is the apparent relationship between the ultimate tensile strength and the yield strength of steels. At first glance it is tempting to apply a straight line fit to th data as is shown. Upon further consideration of the data and the relationship between the true and nominal stress-strain behaviors, several points arise.

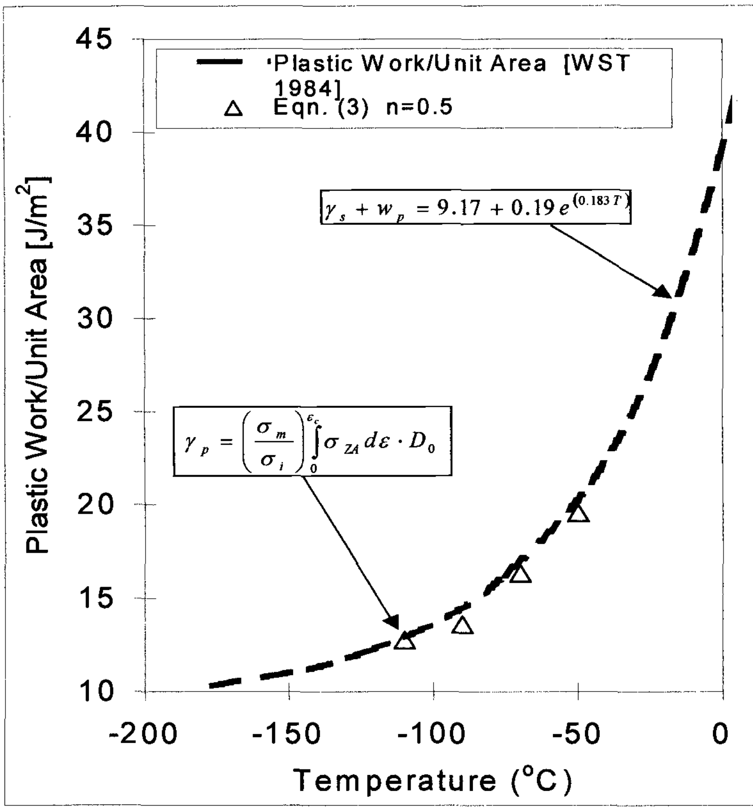

Figure 3 - Plastic work values calculated from Equation (6) compared to the empirical effective work by Wallin et al. [7].

It is well known that as a metal is work hardened, subsequent tensile tests will reveal greater yield strengths but the overall true stress-strain curve will appear to lie on top of the unhardened curve. This leads to an invariance of the true stress at maximum load for most hardening mechanisms. Thus greater amounts of prior hardening will cause the ultimate tensile strength to approach the true stress at maximum load, and, by the same token, the yield strength will approach the tensile strength. Presumably this will occur in an asymptotic manner because of the logarithmic relationship between true and nominal strain. While the data does not give much indication of asymptotic behavior with respect to the one-to-one line, the current straight-line fit does approach it. The dearth of data above 800 MPa makes it difficult to maintain confidence in such a fit. Additionally, a straight-line fit suggests that there is a maximum strength that can be achieved. For this particular fit that value is approximately 1640 MPa. This is clearly not possible as it is not uncommon for 4xxx steels to achieve ultimate strengths approaching 2000 MPa [*26*].

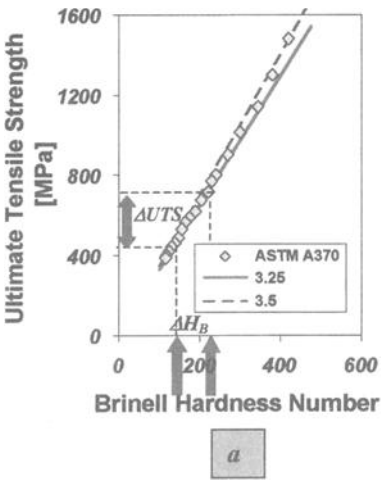

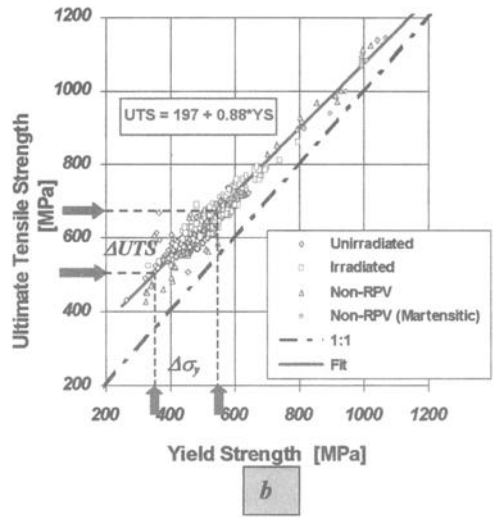

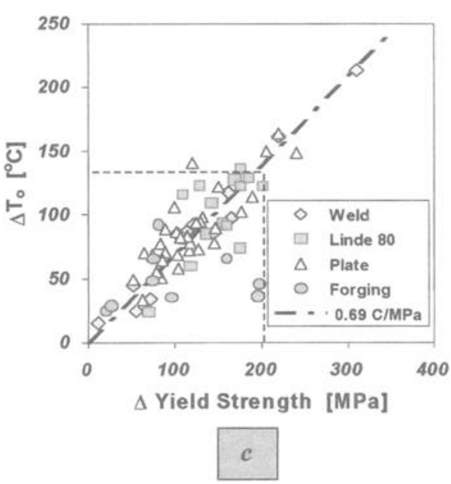

Figure 4 - Proposed methodology for calculating ΔT_0 from hardness values.

In addition to the above concerns, there is a desire to understand the relationship between tensile strength and yield strength in a way that is consistent with the previous discussion of a physical justification for the transition region fracture behavior of ferritic steels. The success of the ZA equation in describing the temperature dependence suggests a natural starting point for an analysis of the relationship in Figure 4. The focus now shifts from the thermal terms of Eqns. (4b) and (4e) to the work hardening term of Eqn. (4a).

Figures 5 and 6 are stress versus plastic strain plots of Equations (4) for ARMCO Iron [*18*] and a C-Mn steel [*25*], respectively. While both plots have the same square root of strain dependence, the coefficient, K, in Equation (4a) differs, reflecting the different material compositions. The heavy solid lines represent Equations (4) with no prior hardening. The thin solid lines are the nominal stress-plastic strain curves calculated from Equations (4) using the familiar relationships:

$$\sigma_{ZA} = S(1+e) \tag{7a}$$

$$\varepsilon = \ln(1+e) \tag{7b}$$

where S and e are nominal stress and strain, respectively and ε is the true strain. Various amounts of prior hardening are represented as equivalent tensile strains. The maximum load condition,

$$\frac{d\sigma_{ZA}}{d\varepsilon} = \sigma_{ZA}, \tag{8}$$

is represented by the dotted line. Yield and tensile strengths were taken from these plots and used to create Figure 7. Yield and tensile strength data for 1040 [*26*] and 1016 [*28*] steel cold rolled and cold drawn, respectively, to varying degrees prior to tensile testing are included in this figure.

In the "ideal" cases involving Equations (4), it can be seen that the tensile strength does approach the one-to-one line in an asymptotic manner. The 1040 and 1016 steel data both exhibit very similar behavior up to the one-to-one line with the 1040 data falling nearly on top of the ZA-based C-Mn data. The data for the 1016 steel then takes a sharp upward swing at a point corresponding to a 40% reduction in area by drawing. This had the effect of halving the amount of tensile elongation. Thus it appears that for large amounts of prior hardening, the true stress at maximum load can no longer be considered an invariant quantity. However what amount is considered "large" is dependent on the amount and type of cold work and the resulting evolution of microstructure.

Determination of ΔT_o from Hardness Measurements

The assumption of an invariant true stress at maximum load for a given steel composition is an important one in using the tensile-yield strength relationship. Intimately connected to this assumption is the notion of a uniform strain-hardening coefficient. That is the stress-strain curve of a prior hardened material cannot lie on top of the unhardened curve unless the hardened specimen exhibits the same strain hardening rate as the unhardened specimen does after an equivalent amount of tensile strain. In order for an expression such as Equations (4) to be useful in describing the stress-strain behavior of metals that have been hardened to some degree, the strain-hardening coefficient must be constant.

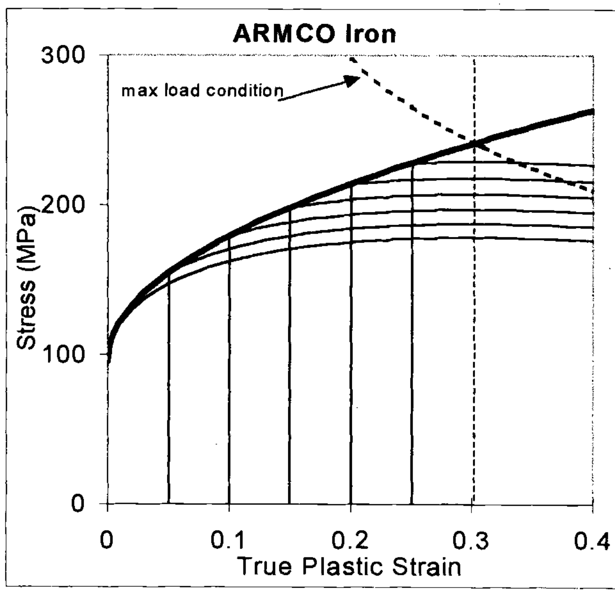

Figure 5 - ZA-based true/nominal stress-true plastic strain curves for ARMCO Iron.

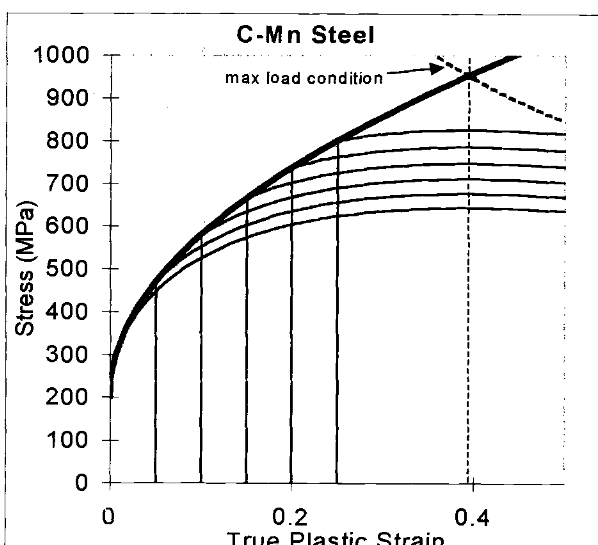

Figure 6. ZA-based true/nominal stress-true plastic strain curves for C-Mn steel.

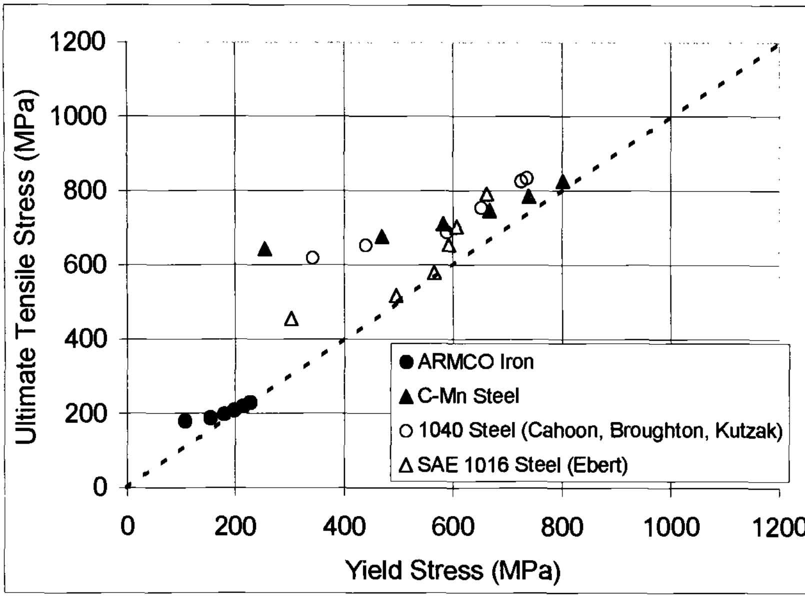

Figure 7 - Ultimate tensile strength vs. yield strength plot for ARMCO Iron, C-Mn steel, 1040 steel and 1016 steel showing the actual nature of the relationship.

The proper stress values then arise from the inclusion of the prior hardening as a constant value of strain, ε_o:

$$\sigma_{ZA} = \sigma_0 + K\sqrt{(\varepsilon_0 + \varepsilon)}\,. \tag{9}$$

In their formulation, Zerilli and Armstrong [*18*] assume the strain hardening coefficient to be 0.5, following from Taylor's [*29*] derivation of the stress necessary to keep a uniform distribution of edge dislocations in equilibrium. The square root dependence arises because the uniform dislocation distribution forces the distance between the dislocations to be equal to the inverse square root of the dislocation density. Despite criticisms that the theory is too simplistic, it does a good job of representing the large deformation behavior of a number of materials [*30*].

It is now possible to address the idea of calculating ΔT_0 from hardness values. The first relationship shown in Figure 4 between the tensile strength and measured hardness values is well established [*31*]. However, the process depicted becomes a bit more cumbersome than may be practical given the actual nature of the tensile-yield strength relationship. Cahoon et al.'s [*27*] relationship between diamond pyramid (Vickers) hardness and yield strength is more direct, but it uses a power law stress-strain relationship that does not provide any means of ascertaining the degree of prior hardening that may exist in the material. This is certainly an obstacle to calculating the change in transition temperature if there is no information regarding the unhardened state of the material. Fortunately, Equations (4) provide a means for overcoming this challenge.

Tabor [*31*] determined that the strain in a material at the indentation is the sum of the strain due to prior hardening and the strain imparted by the indenter. The following relationships put this in a quantitative form:

$$\varepsilon = \varepsilon_0 + f\left(d/D\right) \text{ for Brinell indentations} \tag{10a}$$

$$\varepsilon = \varepsilon_0 + 0.10 \text{ for Vickers indentations.} \tag{10b}$$

In Equation (10a), *d* is the chordal diameter of the indentation and *D* is the diameter of the indenter ball. In Equation (10b), the strain of 10% is based on observations of data. Tabor also empirically showed that hardness values calculated from Vickers indentations relate to the flow stress of a metal by

$$D.P.H. = 3.0\sigma_{\varepsilon_0+0.10}\,. \tag{11}$$

Combining Equations (4), (10b) and (11) results in the following expression for the equivalent tensile strain that results from prior hardening:

$$\varepsilon_0 = \left[\frac{1}{K}\left(\frac{D.P.H.}{3.0} - c_0 - Be^{-\beta T}\right)\right]^2 - 0.10\,. \tag{12}$$

The yield strength corresponding to a given hardness value can then be calculated by inserting ε_0 + 0.002 into Equations (4). Yield strengths calculated from Equations (4) and (*12*) are compared to measured yield strengths for 1040 steel [*28*] in Figure 8. The ZA parameters for the previously mentioned C-Mn steel were used in the calculation because of the favorable comparison between the two steels in Figure 7. The calculated values do not match exactly with the measured values, but this is likely due to uncertainties arising from the use of the C-Mn steel ZA parameters. Another possible cause for concern is the value of 10% strain used to represent the Vickers indentation strain. There is always a measure of inaccuracy in equating an effective tensile strain to a three-dimensional state of strain such as that produced by a hardness indenter. However the calculated values are close enough to the measured values to suggest that Equation (12) is a valid representation of the prior hardening. Assuming that these uncertainties are the source of discrepancy, then it is a relatively simple matter to calculate ΔT_o from the calculated change in yield strength.

Summary

The preceding analysis was performed assuming room temperature, approximately 300 K. It has been shown that a model developed from the physically based ZA equations can be successfully used to describe the temperature dependence of the plastic work absorbed in unstable cleavage fracture. It has also been shown that the assumption of a uniform strain-hardening coefficient leads in the Z-A equation leads to encouraging quantitative descriptions of the work hardening behavior of ferritic steels.

This assumption then leads to prediction of a uniform stress strain curve for all ferritic steels and a method of accounting for prior strain history in predictions of the shift in fracture toughness transition behavior.

Perhaps more significant than the calculation of equivalent prior strain, is the implication of a quantitative description of the uniform behavior of ferritic steels that enables prediction of a wide range of steel behaviors accounting for effects of aging, strain history and irradiation.

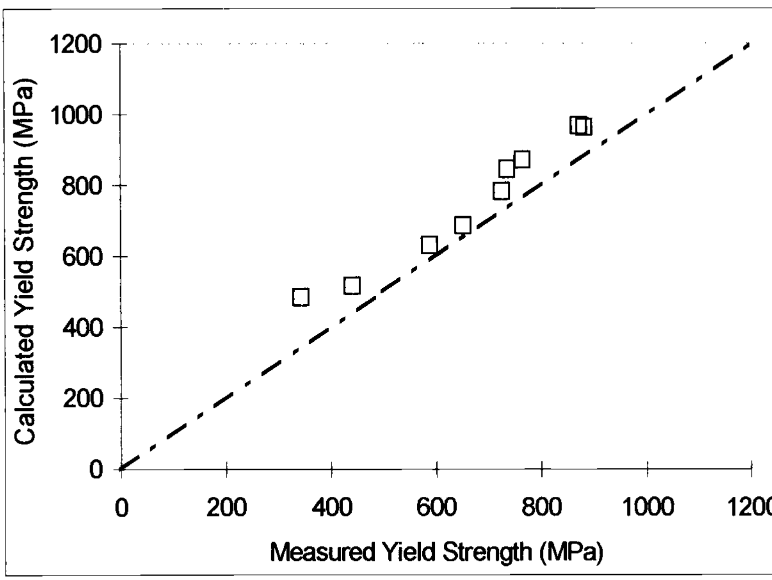

Figure 8 - Plot of yield strengths calculated from Equations (4) and (12) using the C-Mn steel ZA parameters compared to the measured yield strengths for 1040 steel [28].

References

1. Code of Federal Regulation 10CFR50.61, "Fracture Toughness Requirements for Protection Against Pressurized Thermal Shock Events."

2. Yoon, K. K., "Alternative Method of RT_{NDT} Determination for Some Reactor Vessel Weld Metals Validated by Fracture Toughness Data," J. of Pressure Vessel Technology, Vol. 117, pp. 378-382, Nov. 1995.

3. W. Server, T. Griesbach R.G. Lott, and C.C. Kim, "Determination of Margins and Heat Adjustments for Master Curve Applications in RPV Integrity Analysis," Proc. of the 2000 ASME Pressure Vessel and Piping Conference, ASME, July 2000.

4. Lott, R., Kirk, M., Kim, C., Server, W., Tomes, C., and Williams, J. "Application of Master Curve Technology to Estimation of End of License Adjusted Reference

Temperature For a Nuclear Power Plant," Proc. of the 1999 ASME Pressure Vessel and Piping Conference, ASME, July 1999.

5. R.G. Lott, C.C. Kim, W. Server, and C.A. Tomes, "Margins Assessment for Applying Master Curve-Data to High Copper Welds," Proc. of the 2000 ASME Pressure Vessel and Piping Conference, ASME, July 2000
6. ASTM E 1921-98, Standard Test Method for Determination of Reference Temperature, T_o, for Ferritic Steels in the Transition Range, American Society for Testing and Materials, West Conshohoken, PA 1999
7. Wallin, Saario and Torronen, "Statistical Model for Carbide Induced, Brittle Fracture in Steel," Metal Science, 18, pp13-16, 1984
8. ASME Boiler and Pressure Vessel Code Case N-629, "Use of Fracture Toughness Test Data to Establish Reference Temperature for Pressure Retaining Materials, Section XI, Division 1," 1999.
9. Baik, J.-M., Kameda, J., and Buck, O., "Development of Small Punch Tests for Ductile-Brittle Transition Temperature Measurement of Temper Embrittled Ni-Cr Steels," *The Use of Small-Scale Specimens for Testing Irradiated Material, ASTM STP 888,* W. R. Corwin and G. E. Lucas, Eds., American Society for Testing and Materials, Philadelphia, 1986, pp. 92-111
10. Geary, W., Dutton, J.T., "The Prediction of Fracture Toughness Properties from 3mm Diameter Punch Discs," *Small Specimen Test Techniques, ASTM STP 1329,* W. R. Corwin, S. T. Rosinksi, and E. van Walle, Eds., American Society for Testing and Materials, West Conshohocken, PA, 1998, pp. 588-601
11. Eto, M., Takahashi, H., Misawa, T., Suzuki, M., Nishiyama, Y., Fukaya, K., and Jitsukawa, S., "Development of a Miniaturized Bulge Test (Small Punch Test) for Post-Irradiation Mechanical Property Evaluation," *Small Specimen Test Techniques Applied to Nuclear Reactor Vessel Thermal Annealing and Plant Life Extension, ASTM STP 1204,* W. R. Corwin, F. M. Haggag, and W. L. Server, Eds., American Society for Testing and Materials, Philadelphia, 1993, pp. 241-255
12. Sinclair, A. N., Lepik, O., Gabbani, M., Mukherjee, B., and Albertini, E., "Assessment of Fracture Toughness by a Punch Test with Miniature Specimens," *Small Specimen Test Techniques Applied to Nuclear Reactor Vessel Thermal Annealing and Plant Life Extension, ASTM STP 1204,* W. R. Corwin, F. M. Haggag, and W. L. Server, Eds., American Society for Testing and Materials, Philadelphia, 1993, pp. 162-181
13. Lucas, G. E., "Review of Small Specimen Test Techniques for Irradiation Testing," Metallurgical Transactions A, Vol. 21A, May 1990, pp. 1105-1119
14. Natishan, M., Kirk, M., Gunawardane, H., and Wagenhofer, M., "More Information from a Hardness Test than You Ever Thought Possible," Small Specimen Test Techniques: Fourth Volume, ASTM STP-1418, M. Sokolov, J. Landes, and G. Lucas, Eds., American Society for Testing and Materials, West Conshohocken, PA, 2001
15. Natishan, M.E., and Kirk, M.T., "A Micromechanical Evaluation of the Master Curve," *Fatigue and Fracture Mechanics, Vol. 30, ASTM STP-1360*, K. L. Jerina and

P. C. Paris, Eds., American Society for Testing and Materials, Philadelphia, 1998, pp. 51-60.

16. Natishan, M.E., Wagenhofer, M., and Kirk, M.T., "Dislocation Mechanics Basis and Stress State Dependency of the Master Curve," *Fatigue and Fracture Mechanics, Vol. 31, ASTM STP-1389*, Halford and Gallagher, Eds., American Society for Testing and Materials, Philadelphia, 2000

17. Kirk,M.T., Natishan, M.E., M. Wagenhofer, *"Microstructural Limits of Applicability of the Master Curve," Fatigue and Fracture Mechanics: 32nd Volume, ASTM STP-1406,* R. Chona, Ed., American Society for Testing and Materials, Philadelphia, PA 2001, pp. 1-16.

18. Zerilli, F.J., and Armstrong R.W., "Dislocation-Mechanics-Based Constitutive Relations for Material Dynamics Calculations," *J. Appl. Phys.*, Vol. 65, No. 5, March 1987, pp. 1816-1825.

19. Zerilli, F.J., and Armstrong, R.W., "Constitutive Equation for HCP Metals and High Strength Alloy Steels," in *High Strain Rate Effects on Polymer, Metal and Ceramic Matrix Composites and Other Advanced Materials*, Y.D.S. Rajapakse and J.R. Vinson, Eds., The American Society of Mechanical Engineers, New York, 1995, pp. 121-126.

20. Wallin, K., Saario, T., Törrönen, K., and Forsten, J., "Mechanism Based Statistical Evaluation of the ASME Reference Fracture Toughness Curve," *Fifth International Conference on Pressure Vessel Technology: Volume II Materials and Manufacturing*, American Society of Mechanical Engineers, New York, 1984, pp. 966-974.

21. Wagenhofer, M., Natishan, M. E., and Gunawardane, H., "A Physically Based Model to Predict the Fracture Toughness Transition Behavior of Ferritic Steels," *Engineering Fracture Mechanics*, in review.

22. Tetelman, A.S., Wilshaw, T.R., Rau Jr, C.A., "The Critical Tensile Stress Criterion for Cleavage," *Int. Jour. Frac. Mech.*, Vol. 4, No. 2, June 1968, pp. 147-157.

23. Ritchie, R.O., Knott, J.F., Rice, R., "On the Relationship Between Critical Tensile Stress and Fracture Stress in Mild Steels," *J. Mech. Phys. Sol.*, Vol. 21, 1973, pp. 395-410.

24. Chen, J.H., and Wang, G.Z., "Study of Mechanism of Cleavage Fracture at Low Temperature," *Met. Trans.*, Vol. 23A, 1992, pp. 509-517.

25. Armstrong, R.W., Roberson Link, L., and Speich, G.R., "Analysis of Ductile-Brittle Transition Temperatures For Controlled-Rolled, Microalloyed, C-Mn Based Steels," *Processing, Microstructure and Properties of HSLA Steels*, A.J. DeArdo, Ed., The Metallurgical Society, 1988.

26. Shigley, J.E., and Mischke, C.R., Mechanical Engineering Design, 5th ed., McGraw-Hill, Inc., New York, 1989.

27. Cahoon, J.R., Broughton, W.H., and Kutzak, A.R., "The Determination of Yield Strength From Hardness Measurements," *Met. Trans.*, Vol. 2, July 1971, pp. 1979-1983.

28. Ebert, L.J., "A Handbook on the Properties of Cold Worked Steels," PB 121662, Office of Technical Services, U.S. Department of Commerce, 1955.

29. Taylor, G.I., "The Mechanism of Plastic Deformation of Crystals," *Proc. Roy. Soc.*, Vol. A145, 1934, pp. 362-404.

30. Meyers, M.A, and Chawla, K.K., "Mechanical Behavior of Materials," Prentice Hall, Upper Saddle River, New Jersey, 1999.

31. Tabor, D., "The Hardness of Metals," Oxford University Press, London, 1951.

W. Alan Van Der Sluys,[1] *John G. Merkle,*[2] *and Bruce Young*[3]

Results from the MPC Cooperative Test Program on the Use of Precracked Charpy Specimens for T_0 Determination

Reference: Van Der Sluys, W. A., Merkle, J. G., and Young, B., **"Results from the MPC Cooperative Test Program on the Use of Precracked Charpy Specimens For T_0 Determination,"** *Fatigue and Fracture Mechanics: 33rd Volume, ASTM STP 1417,* W. G. Reuter and R. S. Piascik, Eds., ASTM International, West Conshohocken, PA, 2002.

Abstract: The Materials Properties Council (MPC) conducted a cooperative testing program with the objective of developing a set of data to be used in the evaluation of the use of the precracked Charpy specimen for the determination of T_0. This paper reports on the results of this program.

A total of nine laboratories from four countries participated in the cooperative testing program. Each of the laboratories conducted experiments in accordance with the published version of ASTM Standard Test Method E 1921-97 in order to obtain the T_0 values. T_0 was determined from data obtained at three test temperatures, -120°C, -100°C and -75°C. These temperatures were chosen to test the requirements of E 1921. The -100°C temperature is the optimum test temperature for this size specimen, while -75°C is a marginal test temperature because there would be a number of tests which would be invalid. The -120°C temperature is below the optimum test temperature and may require a large number of tests to obtain T_0,or result in an invalid data set.

Over 250 fracture toughness tests were conducted on the specimens fabricated from the weld metal used in this program, with 60 or more tests at each test temperature. These results have been analyzed and the T_0 temperature determined for each of the three primary test temperatures. The effect of number of specimens at the individual test temperatures has been determined. These results are compared with the T_0 results for larger size specimens also available for the test material.

Keywords: fracture toughness, ASTM E1921, master curve

[1] Consultant, Alliance, OH.
[2] Consultant, ORNL, Oak Ridge, TN
[3] Research Engineer, McDermott Technology, Inc., Alliance, OH.

Introduction

The Materials Properties Council (MPC) conducted a cooperative testing program on the use of the precracked Charpy specimen for the determination of T_0, which is the temperature at which the median value of K_{JC} for a 1T specimen is 100 MPa$\sqrt{m}$. The objective of the test program was to develop a data set to be used in the evaluation of the ASTM Standard Test Method E 1921-97 for T_0 Determination when precracked Charpy specimens are used. The data were to be used to address two issues: 1. Is the same T_0 temperature obtained with both the precracked Charpy specimen tested in three-point bending and with larger compact fracture toughness specimens? 2. Are the results obtained when testing precracked Charpy specimens influenced by the test temperature relative to the T_0 temperature obtained? This paper reports on the results of this testing program and the subsequent evaluation of the results obtained.

This is the second cooperative testing program sponsored by the MPC with the objective of collecting data in support of the development of testing standards in the brittle to ductile transition temperature region. The first was conducted between 1987 and 1994 and was organized by Committee 129 of the Japan Society for the Promotion of Science, with the cooperation of the MPC. In this earlier program, 18 laboratories participated to conduct 150 fracture tests with 1T compact fracture toughness specimens. The results from this program were reported in *[1]*. These results were useful in the development of the Standard Method *[2]*. In the earlier program the test material was SA508.Cl3. Each participant tested five 1T compact fracture specimens at a given test temperature. Three test temperatures were used in the program. The program was conducted prior to the existence of the present ASTM Test Method, so T_0 was not determined by the participants. The data from the JSPS/MPC program were evaluated subsequently, using the ASTM Test Method E1921-97 and the results of this evaluation are reported in *[2]*.

In the present program, a total of nine laboratories from four countries participated in the cooperative testing program. Each of the laboratories conducted experiments according to the ASTM Standard Test Method E 1921 in order to obtain the T_0 values. T_0 was determined at three test temperatures, -120°C, -100°C and -75°C. Over 200 fracture toughness tests were conducted in this program at these three primary test temperatures. Some additional tests were conducted at -65°C and -85°C.

The current results have been analyzed and the T_0 temperatures determined for each of the three main test temperatures. The effect of number of specimens at the individual test temperatures has been determined. These results are compared with the T_0 results for larger size specimens also available in *[3]* for the test material.

Description of the Program

The objective of the cooperative testing program was to evaluate the use of precracked Charpy size specimens for the determination of the T_0 reference temperature when the procedures of ASTM E1921-97 are followed. It was desired to test a material on which a large amount of testing had already been performed. The material chosen was a weld metal provided by the Oak Ridge National Laboratory (ORNL), weld 72W, which had been extensively tested by ORNL and by others*[3]*.

Test material

The weld metal for which data were obtained for the current MPC round robin was designated by the Heavy Section Steel Irradiation (HSSI) Program at ORNL as weld 72W *[3, 4]* Two batches of weld metal were prepared to identical specifications, the first in 1984 and the second in 1986. The base metal for the first batch was a 218mm (8.6in) thick plate of A533, Grade B Class 2 steel. The base metal for the second batch was a 234mm (9.25 in) thick plate of A533, Grade B, Class 1 steel. The welds of the first batch averaged 28-32 mm in thickness. Those of the second batch averaged 36-38 mm in thickness. The other welding parameters were nominally identical for both batches*[3, 5]*.

Weld wire for 72W was specially produced for the HSST program by Combustion Engineering, Inc, CE-Wire, Norcross Georgia. The uncoated wire was 0.396 cm (0.156 in.) in diameter and conformed to American Welding Society (AWS) specification A5.23-80, Electrode Classification EF-2, with additional chemical composition requirements: (1) Ni = 0.5 to 0.7 wt%, (2) Cu = 0.20 to 0.25 wt%, (3) P=0.012 wt% max, and (4) V=0.05 wt% max. The weld was fabricated by Combustion Engineering, Inc., Chattanooga, Tennessee, using the submerged-arc process with one lot of Linde 0124 flux (20 x 150 mesh, lot No. 0103) supplied by Combustion Engineering. A total of 14.6m (48ft) of weld were fabricated in 1.22 m (4-ft) lengths for the first batch. The second batch consisted of three 1.22m (4-ft) lengths of weld. The welds were fabricated with a tandem-arc, alternating current procedure using a 0° bevel weld groove with a heat input of 4 kJ/mm. and a travel speed of 560 mm/min. The chemical composition of submerged-arc weld 72W is given in Table 1. The weld metal shows a generally bainitic microstructure with some ferrite islands. All welds were postweld heat treated at 607°C (1125°F) for 40 hr., typical of that given commercial reactor vessels.

The material furnished to MPC by ORNL for the current round robin came from the second batch of 72W welds. The larger specimens tested previously by ORNL came from the first batch of welds *[3,4]*.

By virtue of the identical specifications, the first and second batches of weld 72W were initially assumed to have the same mechanical properties. The mechanical properties for the first batch of weldment 72W at room temperature are given in Table 2. The tensile properties measured for the first batch were therefore assumed to also characterize the second batch. Figure 1 shows a plot of the tensile yield and ultimate stresses for weld 72W in the unirradiated condition, as well as the equation for the fitted curves*[3,4]*.

Table 1 *Chemical composition of submerged-arc weld 72W (Composition in weight %)*

Material	C	Mn	P	S	Si	Cr	Ni
Mean	0.093	1.60	0.006	0.006	0.44	0.27	0.60
σ	0.006	0.038	0.0005	0.0005	0.024	0.008	0.008
Material	Mo	Cu	V	Co	Al	As	Sn
Mean	0.58	0.23	0.003	0.03	0.006	0.002	0.003
σ	0.008	0.006	0.0004				

[a]The following additional elements were determined: Cb<0.01, Ta<0.01, Ti<0.01,B<0.001, W<0.01, and Zr<0.001

[b] Mean and standard deviations (σ) shown result from 84 separate analyses taken from different locations throughout the weldment.

Material Properties

Table 2 *Mechanical properties of weldment 72W at room temperature*

CVN 41-J transition temperature, ^{0}C	-28
CVN fracture appearance transition temperature, ^{0}C	-1
Drop-weight nil-ductility temperature, ^{0}C	-23
Reference temperature, RT_{NDT}, ^{0}C	-23
CVN upper-shelf energy, J	136
CVN upper-shelf lateral expansion, mm	2.119
0.2% offset yield stress at 24^{0}C, MPa	500.3
Ultimate tensile strength at 24^{0}C, MPa	609.0

Charpy impact testing was performed on specimens from both the first and second batches. Figure 2 shows the comparison of the CVN impact energies for the first and second batches of weld 72W. The curves are not significantly different except possibly in the lower transition, where the curve for the second batch implies a 41J transition temperature lower than the curve for the first batch by about 20°C, a difference that could be due, at least in part, to the fact that the number of Charpy specimens tested from the second batch was only about 1/5 the number tested from the first batch*[6]*.

A similar plot of Charpy curves for a companion weld, 73W, made with higher copper content, 0.30 to 0.35%, also in two batches, produces two curves (not shown) that have a somewhat opposite relationship in the transition to that of the curves for weld 72W. The curves for 73W nearly coincide in the lower transition range, diverge in the upper transition range with the curve for the second batch plotting at higher temperatures than the curves for the first batch, and have the same relationship as the curves for 72W in the upper shelf range. The somewhat opposite batch-to-batch behavior of CVN curves for 72W and 73W in the transition, based on relatively few data for the second batches, leaves open the possibility that the differences between the curves are randomly related to the sample size for the second batches, but on the other hand does not preclude systematic variations.

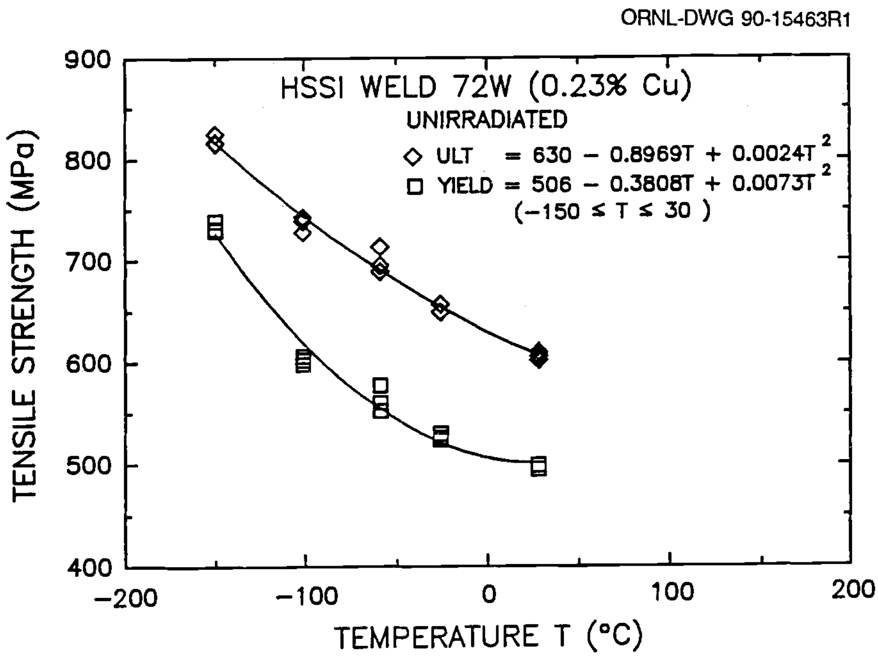

Fig. 1 *Tension test results for weld 72W*

Fracture Toughness Properties

A substantial amount of fracture toughness data has been obtained by ORNL for welds 72W and 73W, using C(T) specimens ranging in size from 1T to 8T for unirradiated specimens. (4) All the ORNL data for the two welds, in both the unirradiated and irradiated conditions, after applying the Weibull size-effect adjustments to 1T specimen size, are shown plotted in Fig. 3 Also noted in Fig. 3 are the calculated values of T_0 for both welds, for both the unirradiated and irradiated conditions. The noted values of T_0 are averages of single-temperature calculations for several different test temperatures. All of the data shown in Fig. 3 are tabulated in Ref. 4. These data were also examined graphically by Wallin *[8,9,10]* and the calculated values of T_0 confirmed. The experimental data for welds 72W and 73W were also re-analyzed three times by the multitemperature method at ORNL,*[2,11,12]* producing slightly different numbers than those shown in Fig. 3 as more irradiated data became available or because of using slightly different computer programs. All the calculated results are shown in Table 3.

The value of T_0 for C(T) specimens was also calculated in this analysis using all of the ORNL data plus some data for 72W obtained from MEA *[13]*. A value of –56°C was obtained from this analysis. This result is consistent with the ORNL results shown in Table 3.

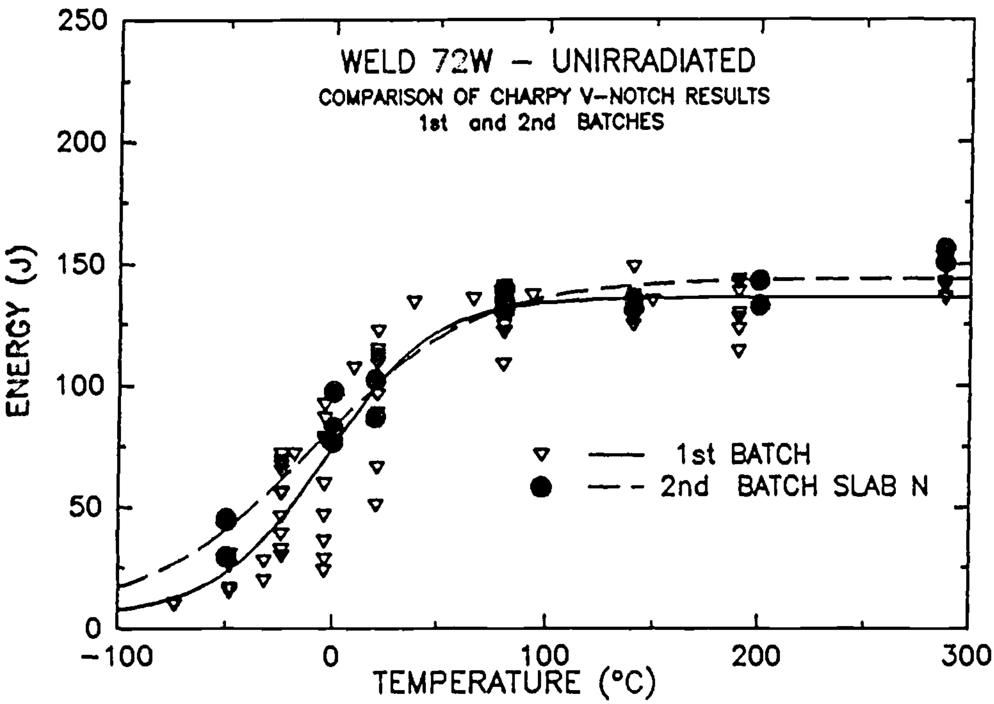

Fig. 2 *Charpy test results for the two batches of weld 72W*

Table 3 *Values of T_0 for Welds 72W and 73W, from C(T) data, successively calculated by ORNL by different methods and/or with additional data*

Material	Fluence (n/cm^2)	T_0 (C) Avg. of single temp. values [4,11}	Multi-temp. [2]	Multi-temp [11,12]
72W	0	-54	-59	-57
72W	1.0 x 10^{19}			34
72W	1.6 x 10^{19}	34		34
73W	0	-63	-62	-61
73W	1.0 x 10^{19}			33
73W	1.6 x 10^{19}	36		40

Supplementary fracture toughness data obtained by ORNL for welds 72W and 73W are helpful in illustrating trends in the comparison of small and large specimen toughness

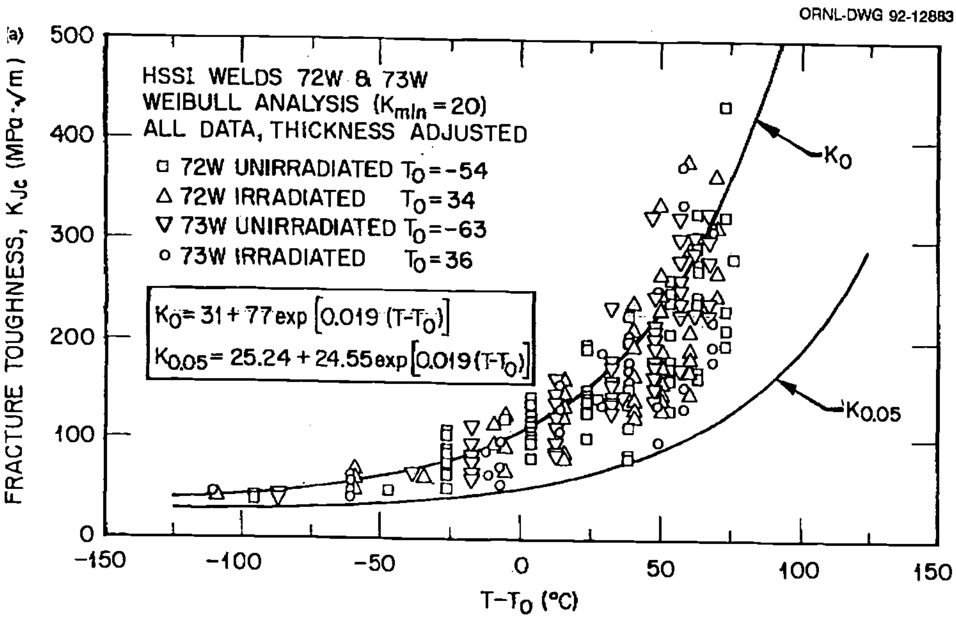

Fig. 3 *Plot of specimen thickness-adjusted K_{JC} values versus $(T\text{-}T_0)$ for all ORNL 1T–8T C(T) data from HSSI welds 72W and 73W. The Wallin curve for K_0 versus $(T\text{-}T_0)$ is shown along with the $K_{0.05}$ curve calculated by ORNL*

values, and to a limited extent batch-to-batch variability, for these materials. Table 4 lists the results of the data analyses, showing that most of the sets of 1/2T-C(T) and PCCV specimens were made from the first batches, but that two sets of PCCV specimens of 72W were in fact from the second batch. All of the specimens listed in Table 4 were sidegrooved by 20 percent, and the PCCV specimens were supported on rollers free to move horizontally, as required by E1921-97. Support roller indentation was observed to be negligible. The calculated median toughness values and test temperatures are plotted together in Figs. 4 and 5. Figure 4, for weld 72W, shows that four of the five values of $K_{Jc(med)}$, adjusted to 1T, for the 1/2T-C(T) and PCCV specimens are slightly above the Master Curve based on larger specimen data, but that the departure for these points from the curve are, with one exception no greater than those of the individual larger specimen data points. Figure 5, for weld 73W, shows excellent agreement between all the data points, with only one significant but still minor downward departure of one point for the 1/2T-C(T) specimens at –95°C. On the whole, the variabilities of $K_{Jc(med)}$, adjusted to 1T, about the Master Curve look more random than systematic, and therefore these variablities appear amenable to the use of a reasonably small margin to provide for uncertainties. From this review of available data on the two batches of 72W not too much can be said about batch-to-batch variability, except that the two data points for PCCV specimens of 72W materials from the second batch, at –64°C and –95°C, are closer to the larger-specimen Master Curve than the one PCCV point at –86°C for the first batch.

Table 4 *Summary of supplementary small-specimen fracture toughness data obtained by ORNL for unirradiated welds 72W and 73W*

Material	Batch	Specimen Type	Test Temp. (°C)	No. of Specimens	$K_{JC(med)}$ 1T (MPa√m)	Calculated T_0 (°C)
72W	1	1/2T-C(T)	-64	8	96.2	-61.1
72W	1	1/2T-C(T)	-86	8	62.3	-45.3
72W	1	PCCV	-86	10	87.9	-76.0
73W	1	1/2T-C(T)	-73	8	86.4	-61.7
73W	1	1/2T-C(T)	-95	8	58.5	-47.7
73W	1	PCCV	-95	10	68.9	-64.1
73W	1	PCCV	-95	10	70.5	-66.3
72W	2	PCCV	-64	10	101.2	-64.9
72W	2	PCCV	-95	10	70.7	-66.5

The weldment, provided by ORNL to MPC, was 23.5 cm and 16 layers of specimens were taken through the thickness such that the top and outer 12 mm layers of the weldment were discarded. The specimens were oriented such that the notch was in the through thickness direction and the crack path ran parallel to the welding direction. The specimens were selected randomly for distribution to the participants.

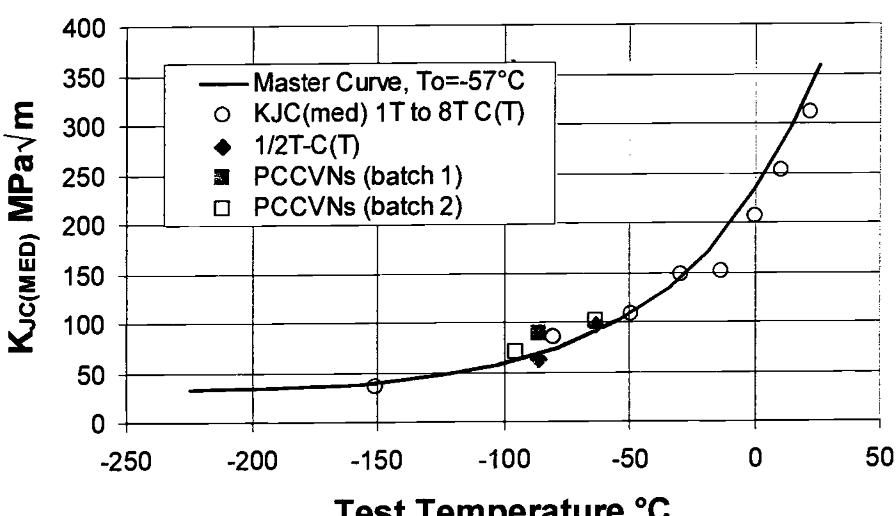

Fig. 4 *$K_{JC(med)}$ values from ORNL test results on weld metal 72W*

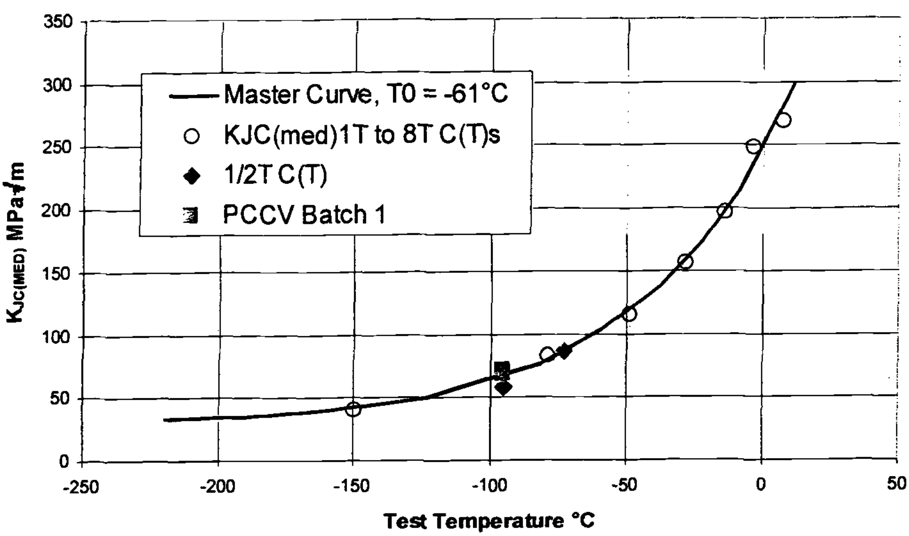

Fig 5 *$K_{JC(med)}$ values from ORNL test results on weld metal 73W*

Test Procedure

Each of the laboratories conducted experiments in accordance with the published version of ASTM Standard Test Method E 1921-97 in order to obtain the T_0 values. T_0 was determined mainly from data obtained at three test temperatures, -120°C, -100°C and -75°C. These temperatures were chosen to test the requirements of E 1921. The -100°C temperature is the optimum test temperature for this size specimen, while -75°C is a marginal test temperature because there would be a number of tests which would be invalid at this temperature. The -120°C temperature is below the optimum test temperature and may require a large number of tests to obtain T_0 with a high level of confidence.

The original test plan called for testing at the following three temperatures: -100°C, -85°C, and -65°C. After three laboratories had conducted tests it was determined that -65°C was too high a temperature and the test plan was changed to -120°C, -100°C, and -75°C, adding the lower test temperature, -120°C, and replacing the -65°C and -85°C temperatures with the single temperature of -75°C.

Each laboratory was supplied with 30-machined specimens and was instructed to conduct the necessary testing to determine the T_0 temperature at the three primary test temperatures. They were instructed to report the following:

1. The three measured T_0 values.
2. All of the measured K_{Jc} values along with the test temperatures.
3. The load displacement curves for each of the tests.
4. The specimen precracking history, $K_{max.}$, load, crack length, and cycles.
5. The post-test crack length measurements for each specimen.
6. Visually measured slow-stable crack growth to failure, if present.

7. Details of the testing procedure. and details as to where and how the specimen displacement was measured.

No instructions were given to the participants concerning the side grooving of the specimens. They were to conduct tests as they interpreted E1921-97. Since the cooperative test program was performed there is a newer version of E1921-01 has been issued. The significant changes in the test method are the addition of a multi-temperature method of T_0 determination and a change in the way the lowest test temperature was defined. In E1921-97 the lowest test temperature was that temperature which produces a $K_{JC(med)}$ of 50 Mpa$\sqrt{m}$. In E1921-01 no data can be used in the determination of T_0 which was obtained at a test temperature less than T_0-50°C. With the addition of the multi-temperature approach in E1921-01there was a slight change in the equation for the calculation of T_0 with a single test temperature. In this paper the test results using both procedure in order to evaluate the use of the use of the PCCV specimen with either procedure and to evaluate the new methods in E1921-01.

Results

The results from the cooperative testing program from the individual laboratories are reported in Table 5. The T_0 values in this table have all been calculated, by the authors of this paper, from the results received from each participant. This was done to make comparisons easier. There was some variability in the calculations performed by the participants. A few of the participants used the equations from ASTM E1921-01. In addition, there were slight variations in the constraint-based measuring capacities of the specimens. Some participants used the uncracked ligament measured on each specimen while others used an assumed uncracked ligament of one half of the width, which was the target dimension. For the numbers in Table 5, E 1921-97 was used, and the ligament dimension of one half of the width was used. The measured crack lengths for all of the specimens were not available. In only one case did this change the T_0 value by more than a few degrees. The one case involved laboratory H's results at -75°C. The toughness from one of laboratory H's specimens exceeded the measuring capacity that was used in the evaluation, while it met the capacity calculated by the participant.

There were only four valid sets of test results from the 9 participants at the lowest test temperature of -120°C. In two of the invalid cases, the $K_{Jc(med)}$ value was less than the required 50 MPa$\sqrt{m}$. In the remaining three cases, the number of tests did not meet the ASTM requirement. The only censored results occurred at the -75°C and the -65°C test temperatures. At the -75°C test temperature there was only one invalid result, the one which was discussed earlier.

Laboratory D fatigue precracked the specimens at a higher final K_{max} than allowed by the standard. The standard requires that the final K_{max} be equal to or less than 15, 16, or 17 MPa$\sqrt{m}$ for the three test temperatures. All of the participants met this requirement within 1 MPa$\sqrt{m}$ except for Laboratory D. This laboratory precracked all of the specimens with a K_{max} of 22 MPa$\sqrt{m}$. The lowest toughness measured by this laboratory was 38 MPa$\sqrt{m}$. This value would meet the requirements of E 399 but does not meet the requirements of E 1921-97. The T_0 values determined by Laboratory D do not appear to differ from those determined by the other laboratories. The values from Laboratory D are plotted in Figures 6 and 7 with the valid data. Figures 6 and 7 present the results from these tests. In Fig. 6 the T_0 values are plotted versus the test temperature. The scatter at the different test temperatures appears to be uniform, but the T_0 value appears to increase with test temperature. This upward trend is due to the 50 MPa√m requirement in E 1921-97. In E 1921-97 the $K_{JC(med)}$ value obtained from a test series must be 50 MPa√m or greater in order for the To value to be valid. T_0 temperatures above -54°C are invalid, for this reason, for the test temperature of -120°C. This requirement biases the calculated values of T_0 to a lower temperature.

Table 5 *Test results from the MPC cooperative test program participants*

Laboratory		B	C	D	E	F	G	H	I	K
-65°C	T_0 ,°C							-73		
	$K_{JC(med)}$, MPa√m							111.2		
	Number of valid tests/number censored							12/5		
-75°C	T_0 ,°C	-71		-72	-57		-69	-84	-61	-64
	$K_{JC(med)}$, MPa√m	95		95.6	79.4		91.1	112	83.1	91.6
	Number of valid tests/ number censored	10/3		11/2	6/0		8/2	10/5	7/0	9/1
-85°C	T_0 ,°C		-86			-75		-75		
	$K_{JC(med)}$, MPa√m		98.5			87.5		88		
	Number of valid tests/ number censored		6/0			7/0		8/0		
-100°C	T_0 ,°C	-78	-89	-75	-76	-77	-84	-85	-53	-74
	$K_{JC(med)}$, MPa√m	76.1	86.2	73.3	74.1	75	81.4	83	58.6	72.3
	Number of valid tests/ number censored	7/0	6/0	8/0	7/0	8/0	7/0	8/0	8/0	10/0
-120°C	T_0 ,°C	-68^1	-84^1	-90	-44^2	-57^1	-69	-99	-49^2	-68
	$K_{JC(med)}$, MPa√m	56.2	65.2	70	46.4	51.3	56.4	76.5	48.2	56.3
	Number of valid tests/ number censored	8/0	6/6	11	9/0	8/0	9/0	8/0	10/0	9/0

Superscript 1, invalid because of number of test points
Superscript 2, invalid because $K_{JC(med)}$ below 50 MPa√m

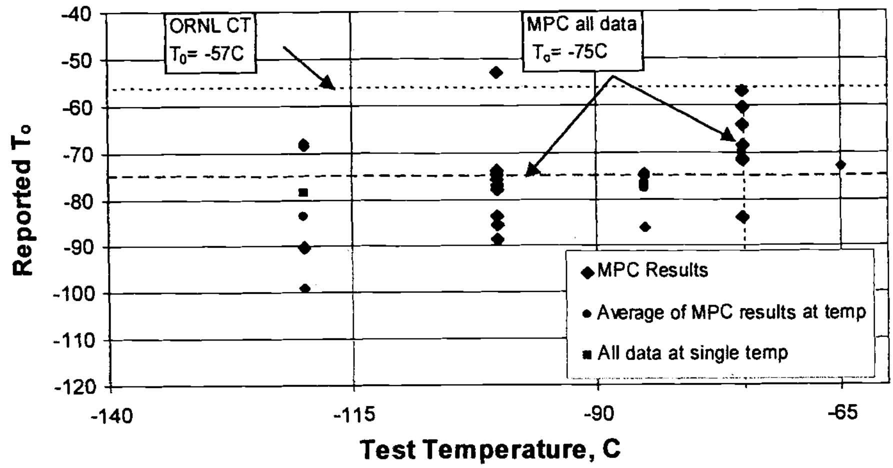

Fig. 6 *The T_0 results from the MPC cooperative testing program*

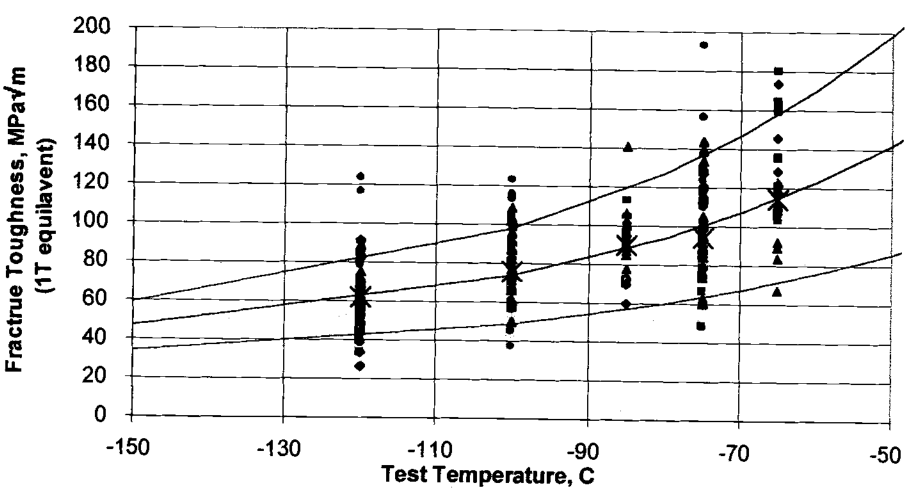

Fig. 7 *Fracture tougness results from the cooperative program compared with the Master Curve for T_0 = -75°C*

The toughness results from the participants are compared to the Master Curve in Fig 7. The Master Curve appears to be a good representation of the median of the data. The cross data point at each temperature is the median of the data at that temperature. These points fall very close to the Master Curve. Also shown in the figure are the 5% and 95% confidence lines. Although the data scatter appears to be large, at most test temperatures 90% of the data falls between the confidence lines.

T_0 was calculated from these data in a variety of ways. The results from these calculations are shown in Table 6. The first 5 rows in Table 6 show the results of calculating T_0 using all of the test results at a single temperature and the procedure in E

1921-01. The resulting T_0's range from -70°C to -79°C. The results appear to order with the distance of the test temperature from T_0, with the lowest T_0 values resulting from the tests at the lowest test temperature. The sixth row in the Table reports the T_0 value when all of the test results at all test temperatures are used and the distributed temperature procedure in E 1921-01 is used. This calculation resulted in T_0= -75°C, which is close to an average value. The next three rows in the Table are the results from Monte Carlo analyses of the data. The Monte Carlo procedure is described in the section on statistical analysis. The first of these results was obtained using the distributed temperature procedure and the test temperature limitation in E1921-01. This resulted in a T_0 value of -78.7°C, lower than obtained with all the data described above. The Monte Carlo calculation was repeated with two changes in the test temperature limitations in E 1921-01. The first of these was increasing the weighting function to require more tests at temperatures lower than T_0. The second was to use the weighting function in E 1921-97. In this instance the test temperatures for the $K_{JC\,(med)}$ values in Table 3 from E 1921-97 were used. The first of these changes did little to change the calculated T_0 value, changing the calculation from -78.7°C to -78.5°C. The second modification of the weighting function changed the calculated T_0 value from -78.7°C to -74.4°C. This is essentially the same value as obtained using all of the data as described above.

Table 6 *Results of various T_0 determinations using the test results from the MPC cooperative test program*

Conditions	T_0 °C	Standard Deviation	Max./Min Value
Using all the data at –120°C	-79		
Using all the data at –100°C	-78		
Using all the data at –85°C	-77		
Using all the data at –75°C	-70		
Using all the data at —65°C	-75		
Using all the data at all temperatures	-75		
Monte Carlo simulation Using Multi-temperature and temp. limit from E 1921-01(1)	-78.7	6	-53.0/-99.9
Monte Carlo simulation Using Multi-temperature and temp.limit from E 1921-01 and 1/6,1/8,1/10(2)	-78.5	5.9	-55.7/-100.2
Monte Carlo simulation Using Multi-temperature from E1921 and temp limit from E 1921-97	-74.4	8.2	-50.9/-99.9

(1) E 1921-01 requires that $n \geqq 1$ where n=a/6+b/7+c/8, a = number of tests betweenT_0+50°C and T_0-14°C, b = number of tests between T_0 -15°C and T_0 - 35°C, and c = number of tests between T_0 -36°C and T_0 -50°C.

(2) Used $n \geqq 1$ where n=a/6+b/8+c/10

Comparison of the Weibull Slopes

Figures 8 present the Weibull plots for the data at all five test temperatures. These figures show a line representing the least squares fit to the data. In addition, the number of data points and the slopes of the fit are shown. The cleavage fracture models predict that the Weibull slope should be 4 *[2,7]*. The slopes determined from the data obtained in this project are shown in the figures, and vary from 2.66 to 4.51. The slopes obtained from the previous JSPS/MPC round robin varied from 3.75 to 5.80. Wallin has suggested that there is a large amount of theoretical scatter of experimentally determined values of the Weibull slope. Figure 9 is a reproduction of a figure from Ref. 7. In this figure are shown the calculated 90, 95 and 99% tolerance bounds along with a large amount of data collected by Wallin. In addition, the data from both the earlier MPC/JSPS cooperative project and the current project have been added to this figure. The earlier data were obtained with 1T compact fracture specimens.

There are no other sets of data in Fig. 9 with as many test results as the sets from the two MPC cooperative programs. The MPC data appear to follow the trend predicted by Wallin's calculations. It is surprising, however, to have two points outside of the 99% tolerance lines with slopes of less than 3 and more than 5. The -120°C data from the precracked Charpy specimens is approaching the lower limit of the temperature range that will result in valid T_0 determinations. The -75°C results from the earlier program are

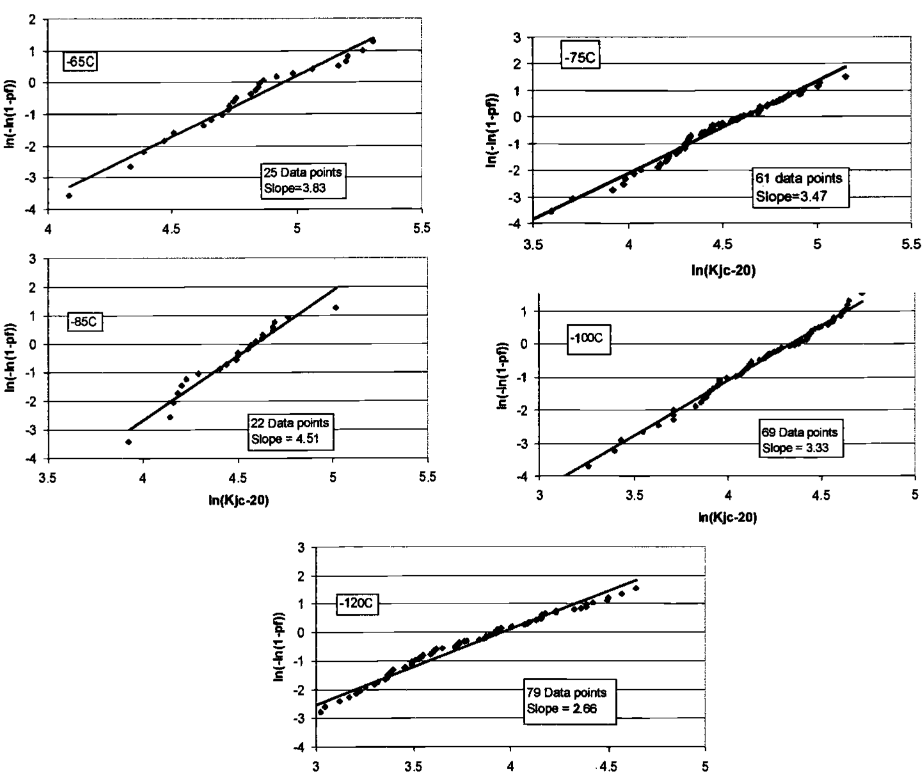

Fig. 8 *Weibull plots from the five test temperatures*

well within the temperature range that would result in valid T_0 results. The T_0 temperature for the SA508 material used in the earlier JSPS/MPC program was found to be -105°C [1].

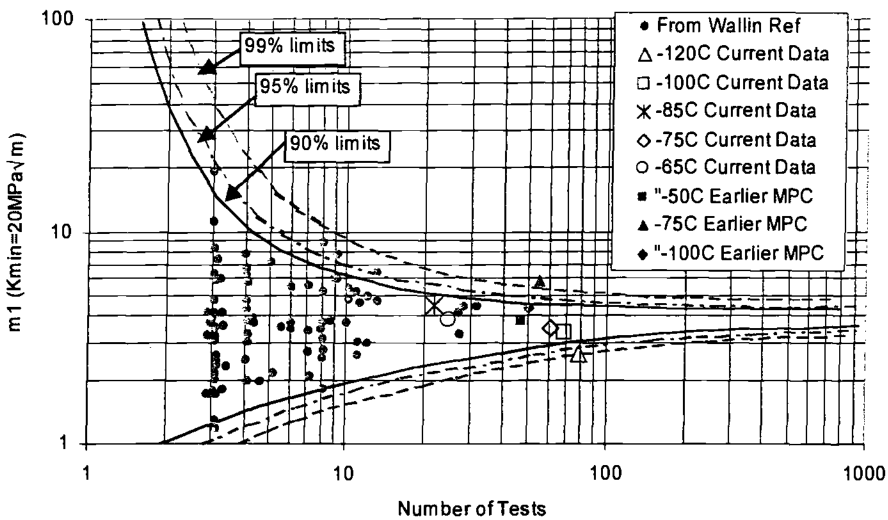

Fig. 9 *Theoretical representation of scatter of experimentally determined Weibull slopes from Ref. 7 and the MPC cooperative programs. (m1 is the Weibull slope)*

Effect of Constraint Parameter, M

There is still current interest in appraising the effect of the constraint parameter, M, especially for small specimens such as the precracked Charpy specimen. Table 7 shows the results of reanalyzing the data summarized in Table 6 using M=50 instead of M=30, and all of the data at each of the principal test temperatures. The differences in T_0 range from -3°C at –100°C to +5°C at –75°C, an effect deemed to be minor and for which provisions can be made with a small margin if judged necessary.

Table 7 *T_0 values for M =30 and M=50, based on the MPC data*

M	Test Temperature		
	-120°C	-100°C	-75°C
30	-79°C	-78°C	-70°C
50	-79°C	-81°C	-65°C

Statistical Analysis of Results

The data set produced in this cooperative program was used in a statistical analysis to evaluate E 1921. This data set is large in comparison to the data set used in the technical basis document *[2]*. The amount of data for each individual test temperature was at least sixty specimens. An assumption prior to completing the analysis was made that this data set is sufficiently large to represent a general population.

The approach used to analyze the data was a Monte-Carlo approach. Given a population of size N, a random sample of a size n was taken to complete the calculations for T_0. There were two methods used to determine T_0 temperature. Both approaches used automated software to complete the calculations.

The first method implemented was single temperature. The approach was to load toughness data, tested all at the same temperature, and the validity into an array. The toughness data were either the actual values or the censored values. In addition, the validity was either censored or uncensored. The user entered the criteria for the number of random samples to be taken (6,7,8...etc) from the population. A random number generator, seeded with the computer clock, was used to select the first data point. Once the data point was selected, it was taken out of the array, and the next number was selected with the random number generator.

This process continued until there were a sufficient number of valid points based on the criteria entered. Once the criteria were met, a T_0 number was calculated. The T_0 was compared to the validity criterion of E 1921-97. If the T_0 was a valid number, it was stored to a data file. If the T_0 number was invalid, the T_0 determination was discarded and not stored in the file. The process continued to determine a new T_0 based on a new randomly selected data set. The number of valid T_0 determinations for each individual temperature was set at ten thousand.

The multi-temperature analysis took a similar approach. The user did not set the number of data points to be used, instead the number of data points was based on the weight factors of each data-point. The method starts by choosing six data points at random from the population. Since all the data are used, the population size is over 180 data points. Once the six points were chosen, an interim T_0 is calculated. Each data point is given a weight. This weight is based upon its test temperature relative to the interim T_0. The weights were summed, and if less than one, another point was added and an interim T_0 was recalculated. This process continued until the sum of the weights was greater than one.

Once the weight criterion was met, the individual test temperatures were compared to the T_0 temperature. If all the test temperatures were within fifty degrees Celsius of T_0 (E 1921-01 validity criteria), the calculated T_0 was stored to the data file. If the T_0 was outside the temperature range, the T_0 was discarded as invalid and the process was started again. Again, ten thousand valid calculations were performed.

Once the Monte-Carlo analysis was complete, the data generated were used to complete additional statistical analyses. In theory, the original data generated at each temperature are distributed in a three-parameter Weibull Distribution. As previously discussed, the data generated in this study fall on a Weibull slope (see Fig. 9). Since the data set is a Weibull distributed set, repeated estimates of K_0 drawn from this set will result in a gamma, Γ, distribution {page 5-9 *[2]*}.

Since K_0 is distributed in a Gamma Distribution, T_0 is expected to be distributed in a Gamma Distribution. This comes from mathematical considerations that the conversion from K_0 to K_{Jcmed} is one-to-one and the conversion from K_{Jcmed} to T_0 is one-to-one.

From the Central Limit Theorem, it can be shown that the Gamma Distribution can be estimated using the Normal Distribution. For this estimation to hold, alpha, in equation 2, must be "large", but not necessarily an integer. With the assumption that alpha is large, the mean is $\alpha\beta$ and the variance is $\alpha\beta^2$. The following is an example of the calculations for the individual distributions based on a data set from the Monte-Carlo Method.

The probability density function for the Normal Distribution is the following:

$$P(x) = \frac{1}{\sigma\sqrt{2\pi}} e^{-\frac{1}{2}\left(\frac{x-\mu}{\sigma}\right)^2} \tag{1}$$

The probability density function for the Gamma Distribution is the following:

$$\begin{aligned} &P(x) = \frac{1}{\beta^{\alpha}\Gamma(\alpha)} x^{\alpha-1} e^{\frac{-x}{\beta}} \\ &where \\ &\Gamma(\alpha) = (\alpha-1)! \quad \text{For all integer } \alpha > 1 \end{aligned} \tag{2}$$

The following are the conditions for this data set.

Determination Type: Single Temperature

Test temperature: -75°C

Number of valid points per set: 15

First, the mean and standard deviation were calculated, assuming a normally distributed data set, and using the definitions for the sample mean and standard deviation.

$$\begin{aligned} &x = T_0 \\ &\mu = \sum_{i=1}^{k} \frac{x_k}{k} = -69.9 \end{aligned} \tag{3}$$

$$\sigma^2 = \sum_{i=1}^{k} \frac{(x_k - \mu)^2}{k-1} = 14.44$$
$$\sigma = 3.8$$

From the graph of the probability distribution, a data set with the following parameters was created to determine the parameters for a Gamma Distribution. For the T_0 data, the following shift in the data was imposed.

$$x = T_0 + 81 \tag{4}$$

Since the Gamma Distribution is calculated from positive X values of data, the data requires shifting. This shift is based on the Lowest T_0 value to be calculated, which in this case is –81°C. The shift would be the following for any data set.

$$\begin{aligned} \alpha &= 9.0 \\ \beta &= 1.25 \end{aligned} \tag{5}$$

Using these parameters, the gamma distribution leads to the following formulas to obtain the population mean and standard deviation for the shifted data. These parameters were obtained by fitting the data using a commercial available software package such as Table Curve 2D.

$$\begin{aligned} \mu(x) &= \alpha\beta = 11.25 \\ \sigma^2(x) &= \alpha\beta^2 = 14.1 \\ \sigma(x) &= 3.75 \end{aligned} \tag{6}$$

Since x is a shifted value to get back into T_0 space, we shift the mean back and obtain the following for the T_0 population. (Note: the standard deviation remains the same)

$$\begin{aligned} \mu(T0) &= \mu(x) - 81 = -69.75 \\ \sigma(T0) &= \sigma(x) = 3.75 \end{aligned} \tag{7}$$

From the above analysis, it is shown that alpha is large enough and the normal distribution can be used to estimate the mean and standard deviation of the Monte-Carlo Data Set. Figures 10 and 11 display the above analysis in a graphical format.

For each of the Monte-Carlo simulations, the sample mean and standard deviation were calculated. For the single temperature method, given n valid points, Tables 8 and 9 show the tabular results and Figs. 12 and 13 show the graphical results.

By examining the tabulated and graphical results, it can be seen that the data for the -120°C tests has some bias in the results. First, from Fig. 14, the standard deviation for the -120°C tests is not converging to the same result as the -100°C and the -75°C tests. The bias comes from having to eliminate the T_0 values higher than -70°C.

Table 8 – *Standard deviations for the single temperature method*

Temp. (°C)	Total Specimens	6	7	8	9	10	11	12	15	20	25	30
-120	79	7.4	6.9	6.8	6.4	6.1	5.9	5.7	5.3	4.7	4.3	3.9
-100	69	6.9	6.4	6.1	5.5	5.2	4.8	4.7	3.9	3.1	2.6	2.2
-75	60	7.3	6.8	6.0	5.5	5.1	4.9	4.6	3.8	3.0	2.3	1.9

Table 9 – *Means for the single temperature method*

Temp (°C)	Total Spec.	6	7	8	9	10	11	12	15	20	25	30
-120	79	-82.5	-81.7	-81.5	-81.1	-80.7	-80.4	-80.0	-79.7	-79.2	-79.0	-78.8
-100	69	-76.7	-76.5	-76.6	-76.8	-76.9	-77.0	-77.1	-77.3	-77.5	-77.5	-77.6
-75	60	-68.7	-68.9	-69.3	-69.4	-69.5	-69.6	-69.7	-69.9	-70.1	-70.3	-70.3

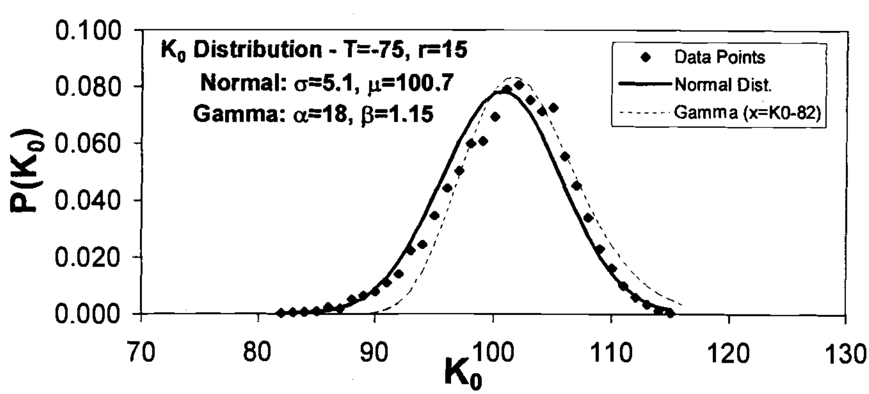

Fig. 10 *A typical K_0 probability distribution showing the Normalized and Gamma* Distributions superimposed.

Figure 14 shows the cut-off for the -120°C data set. This figure also displays the normal distribution that comes from the sample mean and standard deviation of this Monte-Carlo data set. It clearly shows that the data are redistributed with bias over the normalized curve. This bias shows up in the standard deviation being larger than the standard deviation of the other data sets. This can be observed by looking at the width of the data verses the width of the Normal distribution curve. In addition, since the data are biased to a lower temperature, the mean T_0 derived from these data is possibly lower than expected.

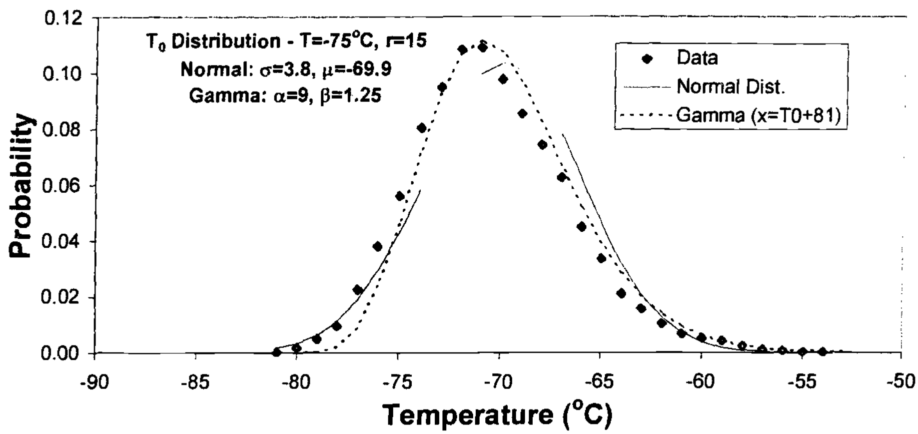

Fig 11 *A typical T_0 probability distribution showing the Normalized and Gamma Distributions superimposed.*

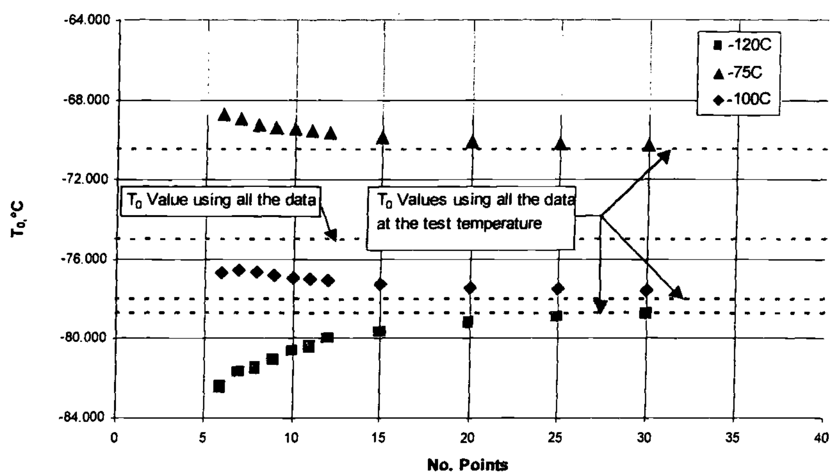

Fig. 12 *Mean T_0 results from the use of Monte Carlo method showing the convergence to the T_0 for each individual data set.*

Discussion

Precracked Charpy versus C(T)

There appears to be approximately a 20°C difference between the T_0= -75°C result given in Table 6 for all the Round-Robin data from slow bend-precracked Charpy specimens and the T_0= -57°C result from the C(T) specimens tested at ORNL, as given in Table 3. This is a greater difference than was expected. Three possible explanations for this difference are:

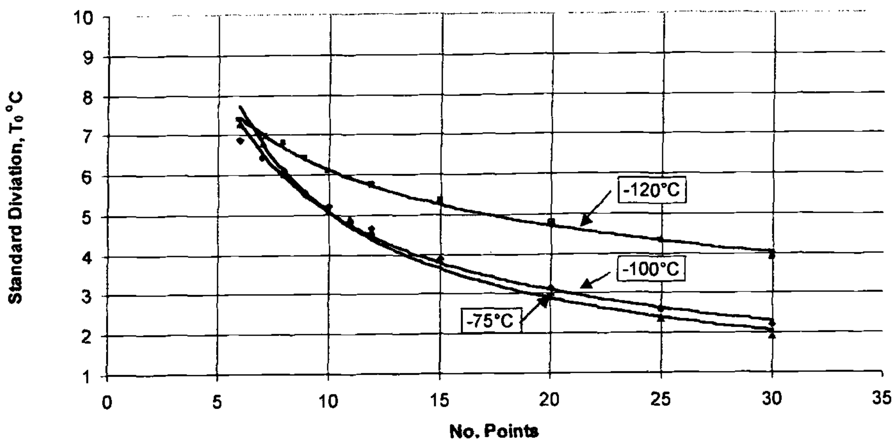

Fig. 13 *The standard deviations for a given subset of data resulting from the Monte Carlo method. Note the standard deviation is biased high for the −120°C data due to the 50°C degree cutoff.*

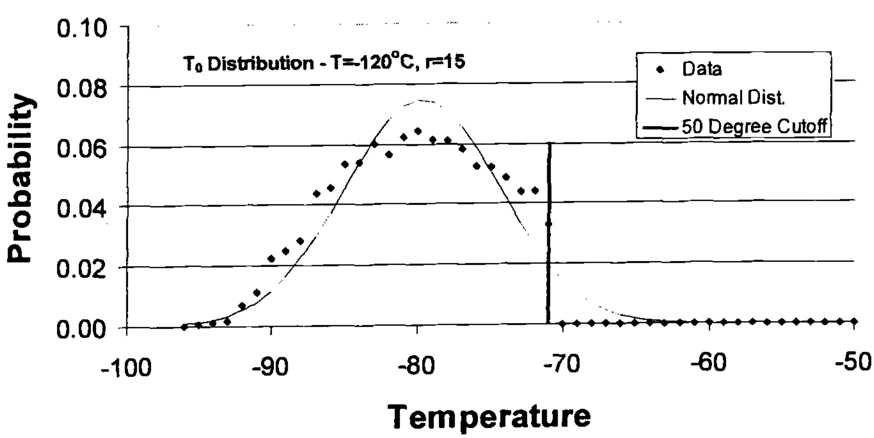

Fig. 14 *A T_0 probability distribution for data obtained −120°C showing the bias due to the 50 degree cutoff*

1. There may be a difference between C(T) specimens and deeply cracked bend specimens. Joyce has reported that a difference of up to 14°C can exist between T_0 results from deeply cracked bend specimens and C(T) specimens*[14]*, with the deeply cracked bend specimens resulting in lower T_0 temperatures. The analytical work of Gao and Dodds supports the experimental observation of Joyce*[15,16]*. The amount of in-plane constraint, as measured by the T stress, appears to influence the value of T_0. Deeply cracked three point bend specimens have less in-plane constraint than do C(T) specimens. Joyce has shown that the results from Gao and Dodds can be used to correct the results from the bend specimens*[17]*. However, side-grooving may modify these geometrical effects, at least for small specimens, because the ORNL side-grooved PCCV specimens

from Batch 1 of Weld 73W produced the values of T_o listed in Table 4 that are only 3 to 5 degrees-C lower than the value of T_o obtained by ORNL with larger C(T) specimens from the same batch of the same weld.

2. There appears to be a slight differences between the two batches of 72W weld. As noted previously, the ORNL Charpy impact data plotted in Fig.2 imply that Batch 2 of Weld 72W could have a transition temperature approximately 20 degrees-C lower than that of Batch 1. The MPC Round-Robin data given in Table 6, taken as a whole, indicate the same thing. However, considering only side-grooved data, the combined MPC Round-Robin and ORNL data in Table 10 indicate a value of T_o for Batch 2 of -64 degrees-C, which is only 7 degrees-C lower than the value of T_o for Batch 1. The only data indicating an opposite trend is the ORNL result from PCCV specimens of Batch 1 tested at -86 degrees-C, which gave a value of T_o = -76 degrees-C, a result still lacking a specific explanation. The preponderance of the data indicate that T_o for Batch 2 could be roughly 7 degrees-C lower than that of Batch 1. This difference is in the same range, and in the same direction, as that postulated to be due to geometrical differences between the C(T) and SE(B) geometries.

3. From the analysis of these results, there is some indication that side grooved specimen produce slightly higher T_0 temperatures than obtained from smooth specimens. ASTM E 1921 suggests, but does not specify that the specimens should be side grooved. The instructions in the cooperative test program only specified to follow the recommendations of E 1921-97. Only two of the participants side grooved their specimens. All of the ORNL results were from side grooved specimens. The results from this cooperative testing program were separated into those that were side grooved and those that were not. The precracked slow bend Charpy results from ORNL, which were also on 72W batch 2, were combined with the side-grooved results from this program. Table 10 shows the T_0 results using all of the side grooved specimens for one determination and all of the non-side grooved for the other. The side grooving appears to result in 12°C increase in the T_0 temperature.

It appears that side-grooving, and any combination of geometrical effects and batch-to-batch variability, can explain the difference between the values of T_o for the larger C(T) specimens from Batch 1 of Weld 72W and the precracked Charpy specimens from Batch 2 of the same weld. However, recognizing the inherent variability of all the materials tested, it has still yet to be proven that the apparent difference between the values of T_o for Batches 1 and 2 is due to anything other than simply drawing two finite samples from the same common much larger population.

Table 10 *Results of T_0 determination from side grooved and smooth sided specimens based on combined MPC and ORNL data*

Condition	Number of points	T_0
Smooth Specimens	200	-76°C
Side Grooved Specimens	66	-64°C

ASTM Procedures

From the results of the analysis of the test results from the MPC cooperative testing program, a number of improvements to ASTM E1921 appear appropriate. The distributed test temperature procedure in the method appears to work well. However, the T_0-50°C rule is overly restrictive when used with test data over a range of test temperatures. In this data analysis, the T_0 determined using all of the test results, as reported in Table 6, is the best estimate of the T_0 value for these data. This value is -75°C. The Monte Carlo evaluation of the E1921-01 procedure resulted in a mean T_0 value of -78.7°C. Since there were more than 250 test results in this evaluation and 10,000 Monte Carlo simulations, this should represent an accurate evaluation of the procedure.

If the E1921-97 data limitations are used in the Monte Carlo evaluation a mean T_0 value of -74.4°C results. The E1921-01 procedure eliminates many T_0 determinations that are above the mean value and distorts the distribution of T_0 values. For this reason ASTM should consider a less restrictive low test-temperature limitation when the distributed test temperature procedure is used.

Conversely, this analysis indicates that when a single test temperature is used the E1921-97 limitations may not be restrictive enough. When testing close to the temperature limit, there is a high probability that either a T_0 value lower than the correct value, or an invalid results, will be obtained. The probability of obtaining the correct T_0 value is quite low. For single temperature testing the lowest test-temperature limit should be set such that most tests will be valid. Such a limit cannot be accurately obtained from the test results from this study. From these results it appears that the limit should be less than 50°C but greater than 25°C.

ASTM E 1921 does not currently recommend that side grooved specimens be used. It appears from this analysis of the test results from the MPC cooperative program that precracked Charpy specimens should be side grooved. The T_0 value calculated from the side-grooved specimens in this program was closer to the value obtained from the C(T) specimens tested at ORNL than was the value for the smooth specimens.

Conclusions

The following conclusions were made as a result of the cooperative testing program and this analysis of the test results.

1. The slow bend-precracked-Charpy specimen appears to be acceptable for the determination of T_0, although some possibly interesting interacting effects of specimen size and geometry, e.g. C(T) vs. SE(B) configurations, and side grooving, still need further experimental investigation. The requirements of ASTM E 1921 have to be met.
2. This program did not prove that the same T_0 temperature would be determined with the precracked Charpy specimen as with the C(T). Test on C(T) specimens need to be conducted on batch 2 of 72W.
3. There is some effect of testing temperature on T_0 temperature. There is a 9°C temperature variation between the -75°C results and the -120°C results.

4. No significant effect was seen between the T_0 value determined using the M=30 value in E1921 and a more conservative value of 50.
5. The amount of data scatter in T_0 increases as the test temperature approaches the T_o -50°C limitation in E1921-01. The standard deviations shown in Fig. 13 show that the deviation in the T_0 value for −120° C is significantly higher than that at the other two test temperatures.
6. The distributed temperature procedure in E1921-01 appears to produce acceptable results.

Acknowledgement

The authors thank first the participants in the cooperative testing program. Without their participation there would not have been a program. Second, we thank the MPC for sponsoring the program and for having the specimens machined, and ORNL for the donation of the test materials and supplemental data obtained by S. K. Iskander and D.E. McCabe. Special thanks go the Dr. T. Iwadate of JSW for coordination of the program in Japan.

References

[1] Van Der Sluys, W. A. and Miglin, M.T., "Results of MPC/JSPS Cooperative Testing Program in the Brittle-to-Ductile Transition Region," *Fracture Mechanics: Twenty-fourth Volume, ASTM STP 1207*, John D. Landes, Donald E. McCabe, and J. A. M. Boulet, Eds., American Society for Testing and Materials, Philadelphia, PA, 1994, pp. 308–324.

[2] Merkle, J. G.,Wallin, K, and McCabe, D. E., "Technical Basis for an ASTM Standard on Determining the Reference Temperature, T_0, for Ferritic Steels in the Transition Range," *NUREG/CR-5504, ORNL/TM-13631*, Nov. 1998.

[3] Nanstad, R. K., McCabe,D.E.,Menke,B. H., Iskander, S. K., and Haggag, F. M., "Effects of Radiation on K_{IC} Curves for High Copper Welds," *Effects of Radiation on Materials: 14th International Symposium (Volume II), ASTM STP 1406*, N.H. Packan, R. E. Stoller, and A. S. Kumar, Eds., American Society for Testing and Materials, Philadelphia, PA, 1990, pp. 214-233.

[4] Nanstad, R. K., Haggag, F.M., McCabe,D. E., Iskander, S. K., Bowman, K. O., and Menke,B. H., "Irradiation Effects on Fracture Toughness of Two High-Copper Submerged-Arc Welds, HSSI Series 5," *NUREG/CR-5913 (Vol. 1)*, Oak Ridge National Laboratory, Oak Ridge, Tenn, October 1992.

[5] Iskander, S. K., Nanstad, R. K.,and Manneschmidt, E.T., "K_{Ia} Curve Shift in High-Copper Welds," pp. 14-25, Heavy-Section Steel Irradiation Program Semiannual Progress Report for April-September 1990, *NUREG/CR-5591*,

Vol. 1, No. 2, Oak Ridge National Laboratory, Oak Ridge, Tenn, November 1993.

[6] Iskander, S. K., Nanstad, R. K.,and Manneschmidt, E.T., "K_{Ia} Curve Shift in High-Copper Welds," pp. 4 - 8, Heavy-Section Steel Irradiation Program Semiannual Progress Report for October 1990 - March 1991, *NUREG/CR-5591*, Vol. 2, No. 1, Oak Ridge National Laboratory, Oak Ridge, Tenn, July 1994.

[7] Wallin, K., "Statistical Modeling of Fracture in the Ductile-to-Brittle Transition Region," in *Defect Assessment in Components- Fundamentals and Applications, ESIS/EGF9* (Edited by J.G. Blauel and K.-H. Schwalbe) 1991, Mechanical Engineering Publications, London, pp 415-445.

[8] Wallin, K., "Fracture Toughness Transition Curve Shape for Ferritic Structural Steels," pp. 83-88 in Joint FEFG/ICF International Conference on Fracture of Engineering Materials and Structures, Singapore, August 1991.

[9] Wallin, K., "Irradiation Damage Effects on the Fracture Toughness Transition Curve Shape for Reactor Pressure Vessel Steels," *Int. J. Pres. Ves. & Piping*, pp 61-79 Vol. 55,1993.

[10] Wallin, K., "Recommendation for the Application of Fracture Toughness Data for Structural Integrity Assessments," Proceedings of the Joint IAEA/CSNI Specialists Meeting on Fracture Mechanics Verification by Large-Scale Testing, Oak Ridge, TN. October 1992, *NUREG/CP-0131*, U.S. Nuclear Regulatory Commission Washington, DC. pp 465-494, October 1993.

[11] Sokolov, M. A., and McCabe, D. E., "Comparison of Irradiation –Induced Shifts of K_{IC} and Charpy Curves: Analysis of Heavy-Section Steel Irradiation Program Data," *ORNL/NRC/LTR-95/4*, Oak Ridge National Laboratory, Oak Ridge, TN, June 1995.

[12] Sokolov, M. A. and Nanstad, R. K., "Comparison of Irradiation-Induced Shifts of K_{Ic} and Charpy Impact Toughness for Reactor Pressure Vessel Steels," *NUREG/CR-6609*, Oak Ridge National Laboratory, Oak Ridge TN November, 2000.

[13] Van Der Sluys, W. A., Hoffmann, C. L., Yoon, K. K., Killian, D. E.,and Hall, J. B., "Fracture Toughness Master Curve Development: Fracture Toughness of Ferritic Steels and ASTM Reference Temperature (T_0)," *Welding Research Council Bulletin 457*, December 2000.

[14] Joyce, J. A., and Tregoning, R. L., "Quantification of Specimen Geometry Effects on the Master Curve and T_0 Reference Temperature," *ECF13*, San Sebastian, Spain, 2000.

[15] Gao, X, Dodds, R. H., Tregoning, R. L., and Joyce, J. A., "Prediction of T_0 Shift Between Specimens of Different Constraints Using the T-Stress effect on the Master Curve Transition Temperature T_0," *ECF13*, San Sebastian, Spain, 2000.

[16] Gao, X., and Dodds, R. H., "A Simplified Approach to Predict Constraint Effects on The Reference Temperature T_0," *Fracture Mechanics,* v68, pp 263-283, 2001

[17] Joyce, J. A., and Tregoning, R. L., "Application of a T-Stress Based Constraint Correction to A533B Steel Fracture Toughness Data," *Fatigue and Fracture Mechanics 33rd, ASTM STP 1417*, W. G. Reuter and R. S. Piascik, Eds., American Society for Testing and Materials, West Conshohocken, PA, 2002.

Erin Iesulauro,[1] Anthony R. Ingraffea,[2] Sanjay Arwade,[1] and Paul A. Wawrzynek[3]

Simulation of Grain Boundary Decohesion and Crack Initiation in Aluminum Microstructure Models

Reference: Iesulauro, E., Ingraffea, A. R., Arwade, S., and Wawrzynek, P. A., **"Simulation of Grain Boundary Decohesion and Crack Initiation in Aluminum Microstructure Models,"** *Fatigue and Fracture Mechanics: 33rd Volume, ASTM STP 1417,* W. G. Reuter and R. S. Piascik, Eds., ASTM International, West Conshohocken, PA, 2002.

Abstract: This research focuses on modeling the microstructure of aluminum and simulating the initiation of fatigue cracks along grain boundaries using a cohesive zone model. Initial observations about the use of the cohesive zone model and the grain boundary response were made using simulations of bicrystals and small regular polycrystals under simple tension loading. Next, statistically generated polycrystal samples were created and loaded, resulting in crack initiation along the grain boundaries. How simulations were conducted, and observations from the simulations of the initiation sights and propagation of decohesion are discussed. The simulation tool created to use cohesive zone models and statistical representations of polycrystals combine to predict fatigue crack initiation.

Keywords: fatigue crack initiation, polycrystal, multi-scale, simulation, cohesive model

Introduction

Current static and fatigue crack studies usually involve introducing a small crack at an assumed critical location. Finite element analyses can then be used to observe how the propagating crack will affect the residual strength of the component and how the component will ultimately fail. Unfortunately, this approach does not give insight into when and where cracks will actually initiate and grow to a detectable size.

The above approach considers a component to be represented as a continuum; however, metallic materials are heterogeneous collections of grains. Each grain in turn is a collection of various atoms and dislocations. The macroscopic homogenization smears out the details of the smaller scale that determine when and where cracks will initiate. To consider the influences of each scale without explicitly modeling every atom for a large component, a multi-scale approach is employed. Multi-scale modeling allows details at the smaller scale to be used to enhance the larger scale without explicitly modeling the smaller scale [*1*]. Modeling at the polycrystal scale of a

[1]Graduate Research Associate, Department of Civil and Environmental Engineering, Cornell University, Ithaca, NY 14853.
[2]Professor, Department of Civil and Environmental Engineering, Cornell University, Ithaca, NY 14853.
[3]Research Associate, Cornell Theory Center, Ithaca, NY 14853.

metallic material by itself can give insight into critical location and conditions for cracks to initiate. Conducting a statistical series of polycrystal simulations can create a database of information about changes in constitutive behavior due to crack initiation between grains. This database can then be used to inform finite elements or integration points in a model of a full component of changes in constitutive properties as damage accumulates.

The work presented here is a preliminary investigation of statistical modeling of polycrystal geometry and properties and the use of cohesive zone models [2] to describe the response of grain boundaries in order to develop a tool to study influences on the initiation of fatigue cracks in aluminum alloys. Initial observations about the utility and behavior of cohesive zone models along grain boundaries were made using bicrystal and regular polycrystal simulations. Finite element simulations were then run using FRANC2D/L [3,4], a finite element software package developed by the Cornell Fracture Group especially for fracture simulations and analysis. Crack initiation along the grain boundaries is seen under monotonic and cyclic loading as the cohesive elements begin to open and fail.

For observations of the polycrystal response statistical samples were created. Geometric models of aluminum microstructure were created using Voronoi tessellations [5]. The grain material is then modeled by assigning individual realizations of the material model chosen to each grain. With each grain having individual properties, grain boundaries naturally arise in the model. To define the properties and response of the grain boundaries a cohesive zone model was implemented. Due to the arbitrary angles of the grain boundaries, both normal and shear responses are considered through a coupled cohesive zone model to allow for mixed mode cracking.

Discussed in the following are the use of cohesive zone models to describe grain boundaries, initial observations from bicrystal and regular polycrystal simulations, the process for creating statistical samples of aluminum microstructure, and observed results from polycrystal simulations.

Grain Boundary Decohesion

In a polycrystal there are many mechanisms that can lead to the initiation of micro-cracks. For example, fatigue leads to the formation of slip bands within grains, which can lead to shear cracks; a corrosive environment can facilitate the failure of grain boundaries due to oxygen embrittlement. The following presentation focuses on the decohesion of grain boundaries.

Grain boundaries naturally arise in polycrystals due to the lattice mismatch. This region of disordered atoms between grains behaves differently than the regular lattices of the grains. Therefore, we describe the grain boundary with its own constitutive relationship, separate from the bulk grain material. A cohesive zone model (CZM) has been chosen for this purpose to describe the strength and toughness of the grain boundaries. The CZM also serves as a criterion for initiation of intergranular cracks. The grain boundaries are allowed to decohere after reaching a critical normal or shear stress or a combined transmitted traction, thus gradually initiating a crack. Once a critical opening is reached a true crack will form. An advantage of using such a model is that initial cracks are not arbitrarily introduced at the beginning of a simulation. Instead, cracks naturally occur due to the heterogeneous stress field throughout the sample caused by the geometry and variations in properties. The use of separate constitutive laws to describe grain boundaries has been used to simulate grain boundary caviation [6,7]. However, this work focused on creep crack growth at elevated temperatures.

CZMs are traction-displacement relationships originally used to describe the damage that occurs in the plastic zone ahead of a crack [2]. In the present case the damage represented by the softening portion of the CZM is used to describe the decohesion of the grain boundaries. The implementation available in our finite element code, FRANC2D/L, includes independent normal and shear cohesive models as well as a coupled model. The coupled cohesive zone model (CCZM) has been adapted from a model developed by Tvergaard and Hutchinson [8], where the normal and shear components of the traction, t, and displacement, λ, are combined into single measures (Figure 1). A key characteristic of the relationship is the area under the curve, G_c, which represents the critical energy release rate.

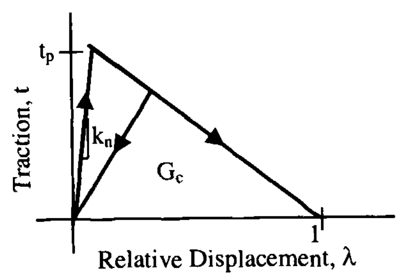

Figure 1 - *Coupled Cohesive Zone Model: Traction-displacement relation describing grain boundary response.*

The CCZM begins from a traction potential, Φ.

$$\Phi(\delta_n, \delta_t) = \delta_n^c \int_0^\lambda t(\lambda')d\lambda' \qquad (1)$$

Φ is a function of the relative normal, δ_n, and tangential, δ_t, displacements between the faces of the grain boundary. λ is a non-dimensional separation measure for the relative opening and sliding defined as:

$$\lambda = \left[\left(\frac{\delta_n}{\delta_n^c}\right)^2 + \left(\frac{\delta_t}{\delta_t^c}\right)^2\right]^{1/2} \qquad (2)$$

The opening and sliding displacements are normalized to the relative critical displacement values, δ_n^c and δ_t^c, at which the separation is considered a true crack in pure Mode I and II. When the value of λ reaches 1 this indicates the complete decohesion of the grain boundary and the formation of a true crack. For a given relative displacement between two grains the combined traction, t, transmitted across the grain boundary can be determined from the CCZM. The combined traction can then be decomposed into normal, T_n, and shear, T_t, components by differentiating Φ.

$$T_n = \frac{\partial \Phi}{\partial \delta_n} = \frac{t(\lambda)}{\lambda} \frac{\delta_n}{\delta_n^c} \tag{3}$$

$$T_t = \frac{\partial \Phi}{\partial \delta_t} = \frac{t(\lambda)}{\lambda} \frac{\delta_n^c}{\delta_t^c} \frac{\delta_t}{\delta_t^c} \tag{4}$$

In the case in which the grain boundary encounters unloading, the CCZM follows the path shown in Figure 1. Upon reloading of the grain boundary after softening has occurred the CCZM follows the unloading path back to the softening portion of the curve. This results in full closure of the grain boundary. Damage is seen through the reduced stiffness of the reloaded grain boundary.

Illustration of Decohesion in Bicrystals

To observe the effect of using the CCZM to describe grain boundary damage evolution, several finite element fracture analyses were first performed on ideal bicrystals. The results shown here illustrate the behavior of the grain boundary under constant and varying amplitude cycles.

Finite element bicrystal models were created with interface elements containing the CCZM model placed in the grain boundary between the two crystals (Figure 2). The bottom edge was constrained in the Y-direction with the center node constrained in both X and Y-directions. Material parameters for the grains were taken from average bulk values of AA 7075-T6 (Table 1). The grain boundary strength, t_p, was chosen to coincide with the bulk yield stress value. The values of k_n and δ_n^c were determined for numerical stability. Analyses were run using each of the four material models available in FRANC2D/L: elastic, isotropic; elastic, orthotropic; elastic-plastic, isotropic (von Mises); elastic-plastic, orthotropic (Hill) [*4*].

After assigning a material model and properties, the bicrystal was then loaded under displacement loading applied to the top edge with varying amplitude cycles to observe the response of the grain boundary (Figure 3). Observed results from these simulations were as expected. As shown for linear-elastic, isotropic grains and t_p = 500 Mpa, the strain amplitude was such that softening of the grain boundary according to the CCZM was seen in the first load cycle (Figure 4a). In subsequent loading the grain boundary followed the unloading path of the previous cycle out to the same amount of decohesion and then followed the CCZM while additional softening occurred (Figure 4b-c). Cycles of increasing peak strain were continued until complete failure of the grain boundary occurred. Due to the linear-elastic grains additional damage will not occur unless the previous peak strain amplitude is exceeded. In the case of elastic-plastic grains, a constant strain amplitude will result in additional damage to the grain boundary if the yield stress of the grains has be exceeded.

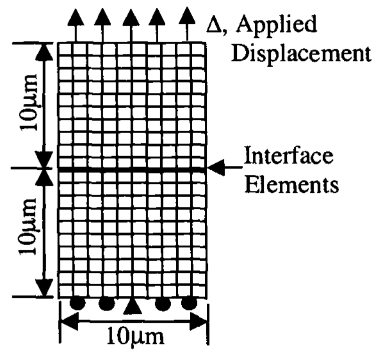

Figure 2 - *Typical bicrystal model*

Table 1 – *Elastic, Orthotropic Grain and Grain Boundary Properties*

Grain Properties		Grain Boundary Properties	
E_1	72 000 MPa	t_p	500 MPa
E_2	42 000 MPa	δ_n^c	1.0 μm
G_{12}	26 900 MPa	k_n	2.5e9 MPa
ν	0.33		

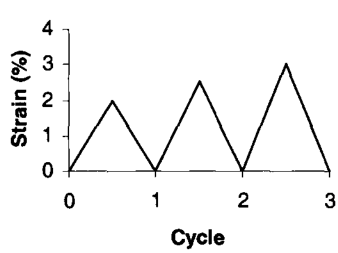

Figure 3 – *Varying amplitude loading of bicrystal*

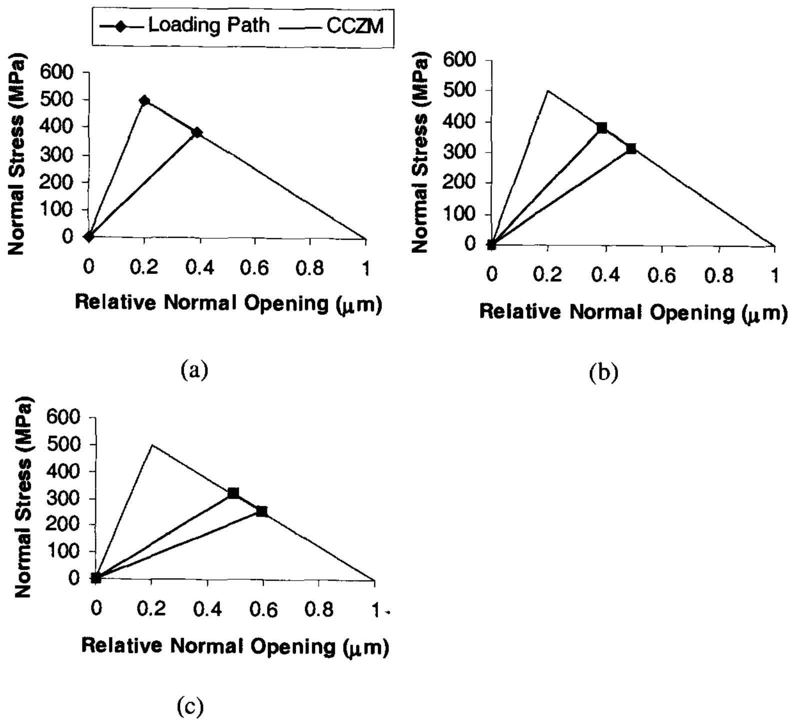

Figure 4 – *Grain Boundary Response in Elastic, Isotropic Bicrystal: (a) First loading cycle (b) Second loading cycles follows unloading of first cycle (c) Third loading cycle follows unloading of second cycle.*

Illustration of Decohesion in Regular Polycrystal Samples

After determining that individual grain boundaries would respond according to the CCZM model under load, small regular polycrystal models were tested to observe the effects of neighboring grains on crack propagation. The polycrystal samples consisted of six square grains connected by interface elements (Figure 5). Again the bottom edge was constrained in the Y-direction with the center node constrained in the X and Y-directions. The loading was under applied displacement. The grains were assigned various properties and the grain boundary strengths were varied. The following examples illustrate how the properties of neighboring grains and grain boundaries determine whether a crack will propagate or arrest.

The first example illustrates crack arrest. For this simulation the six grains were assigned elastic, isotropic properties (Table 2). The strengths assigned to the horizontal grain boundaries were 900 MPa for the left and right and 500 MPa for the center. The vertical grain boundaries were assigned a strength of 1000 MPa for all examples shown here. The model was then loaded monotonically to 2.5% strain. As shown (Figure 6), the center grain boundary began to decohere first since it is the weakest. The left and right grain boundaries have not reached their strength (Figure 6b) therefore any opening seen (Figure 6a) can be attributes to elastic straining of the grain boundaries. The higher strengths of the neighboring grain boundaries have arrested the crack.

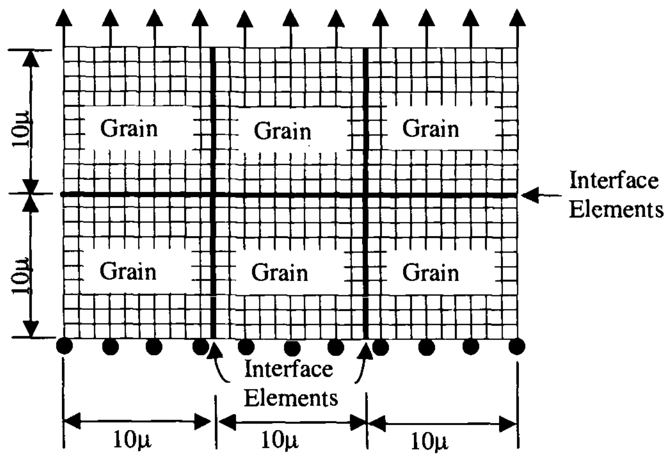

Figure 5 – *Regular polycrystal with interface elements*

Table 2 – *Grain Properties for Regular Polycrystal Simulations*

Grain Properties	
E	72 000 MPa
ν	0.33

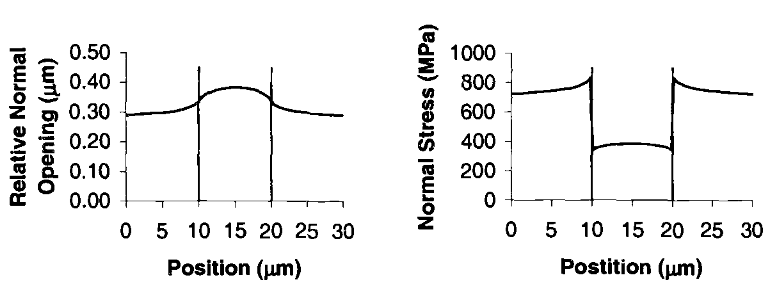

(a) (b)

Figure 6 – *Relative opening displacement and normal stress along the horizontal grain boundaries. Lines at 10 and 20 μm indicate locations of vertical grain boundaries.*

Another possible scenario is that the grain boundaries have the same strength but that the grains are aligned to favor slip within the grains resulting in easier deformation. To illustrate this the grains were assigned the elastic, orthotropic material properties shown in Table 3. The angle β refers to the angle between the global X-axis and the primary stiffness direction E_1. The angle between E_1 and E_2 is then 90°. After loading, the left grain boundary decohered the most since the stiff axes of grains 1 and 4 were aligned with the loading axis forcing the deformation into the grain boundary (Figure 7). Again the model was strained to 2.5%. The center grain boundary experienced the least decohesion since the soft axes of grains 2 and 5 were aligned allowing the grains to redirect stress flow away from the grain boundary.

Table 3 – *Grain Properties*

	Grain 1	Grain 2	Grain 3	Grain 4	Grain 5	Grain 6
E_1 (MPa)	72 000	72 000	72 000	72 000	72 000	72 000
E_2 (MPa)	42 000	42 000	42 000	42 000	42 000	42 000
ν	0.33	0.33	0.33	0.33	0.33	0.33
β (degrees)	90	0	0	90	0	90

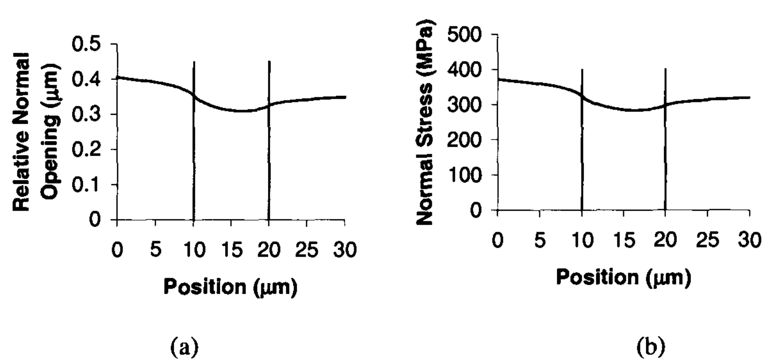

Figure 7 – *Relative opening displacement and normal stress along the horizontal grain boundaries. Lines at 10 and 20 µm indicate locations of vertical grain boundaries.*

Creation of Statistical Polycrystal Models

In a physical sample of aluminum there are more factors contributing to which grain boundaries will fail and how far a crack will propagate than just the relative strength and stiffness of the grains and grain boundaries. The geometry and distribution of properties increase the complexity of the polycrystal response. Therefore statistical representations of the aluminum microstructure were created and tested. The process for creating a statistical representation of a polycrystal is slightly more involved than creating bicrystals or regular polycrystals. First the grain geometry is determined. Once the geometries are determined each grain is assigned material properties for a given material model. Finally, the grain boundary properties are assigned. Discussed below is the process for creating a polycrystal sample.

Creating a polycrystal sample begins with defining the geometry of the grains. This is done using a Voronoi tessellation. Polygons are created from a random set of initiation points. Each polygon then represents a grain with an average size held to observed measures from electron back-scattering pattern scans (EBSP) conducted on samples of AA 7075-T6 [9].

Once the geometry is in place material properties are assigned. One of the four constitutive relationships currently available is chosen. For the chosen material model each grain is assigned values of the appropriate parameters sampled from uniform distributions centered on the average macroscopic value. This allows each grain to be a separate realization of the material model. For the orthotropic material models, an orientation must also be assigned to each grain. These orientations were sampled from an orientation distribution function (ODF) created from orientation data collected through EBSP scans.

Once grain properties are assigned, orientation and property mismatch lead naturally to grain boundaries along the polygon edges. With the grain boundaries located from geometry and material mismatch, interface elements were placed and assigned CCZM properties. In our simulations the parameters describing the CCZM were determined to either be the same for all grain boundaries in the sample, or to vary from boundary to boundary. For the orthotropic models, parameters were varied based on the misorientation angle, θ, across the grain boundary according to $\theta = \beta_1 - \beta_2$ (Figure 8). For the isotropic grain material models, there is no physical misorientation across grain boundaries. Therefore, the inclination angle, ψ, of the grain boundary with respect to the global X-axis (Figure 9) was chosen as an arbitrary measure with which to introduce variation. Assuming that G_c varies with the angle θ or ψ, the area under the CCZM varied according to Equation 5 or 6. G_{avg} is the average value of the critical energy release rate and ΔG determines the range of values.

$$G(\theta) = G_{avg} + \Delta G \cos(4\theta) \tag{5}$$

$$G(\psi) = G_{avg} + \Delta G \cos(4\psi) \tag{6}$$

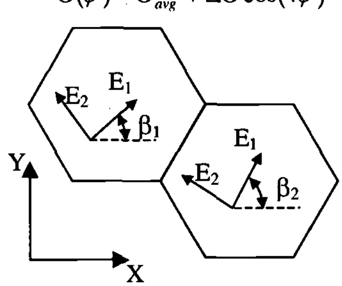

Figure 8 – *Orientation of neighboring orthotropic grains relative to global coordinate system. The misorientation angle, θ, is defined as the difference between the two orientation angles β_1 and β_2.*

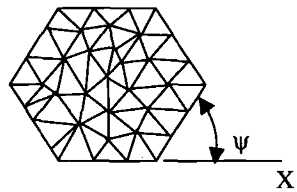

Figure 9 - *Grain boundary inclination angle measured with respect to the global X-axis.*

The form of G was chosen based on a Fourier expansion of spherical harmonics. In 3D any periodic function can be written using a Fourier expansion of spherical harmonics of which the present case is a 2D degenerative form. Holding the normal of each grain to be along the (100) direction forces cubic symmetry for a FCC crystal. This results in the cos 4θ(or ψ) form term used here.

The CCZM can be described using several parameters. However, only 2 are independent. To isolate variation in the model to just G_c, the values of k_n and δ_n^c were held constant for all grain boundaries. This also allowed t_p to be easily from G_c. The values of k_n and δ_n^c were again chosen for numerical stability and given the values shown previously in Table 1.

Once the grain and grain boundary modeling is completed the entire model is meshed. The interiors of the grains are meshed using standard finite elements. Along the grain boundaries interface elements are added and assigned the CCZM properties. To capture small amounts of opening along the grain boundaries the interface elements need to be sufficiently small. The average interface element length is on the order of microns. This size was determined to be small enough to capture the grain boundary opening without the size of the model become computationally prohibitive.

Simulation of Fatigue Crack Initiation in Aluminum Polycrystal Samples

Results discussed here are for the grain geometry, boundary conditions and applied displacement loading history shown (Figure 10). For this simulation the model was constrained in the Y-direction along the bottom edge and in the X-direction on the vertical sides. Individual results will be shown for the points indicated on the loading history (Figure 10b). The average grain material properties for the Hill material model and CCZM parameters are shown (Table 4). The current implementation of the Hill yield criterion is limited to perfect plasticity and plane stress. Due to the orthotropic model each grain was assigned an orientation angle varying from 0 to 360 degrees. The angle determined the angle between the global X-axis and the primary axis of the grain. The grain properties were then allowed to vary from grain to grain. The value of E was allowed to vary ± 2 000 MPa. Each of the yield stresses was allowed to vary ± 50 MPa. The CCZM parameters chosen result in the average peak combined strength of the grain boundaries being equal to the average primary yield stress of the grains. This will allow some of the grain boundaries to reach their peak and begin softening, initiating fatigue cracks, before the grains begin to yield and absorb all of the damage to the polycrystal.

As seen (Figure 10b), the sample was loaded to 0.69% strain (98% of the macroscopic yield strain) and then unloaded. The deformed mesh of the sample is shown (Figures 11a-c) at 0.1%, 0.69%, and 0.2% strain corresponding to the points marked in the loading history (Figure 10b). The circled area (Figure 11b) shows the opening of a grain boundary due to decohesion. The corresponding σ_{yy} contour plots are shown (Figures 11d-f). The heterogeneous nature of the stress field due to the inhomogeneities of the polycrystal sample is demonstrated (Figure 11e). Also to be noted is the shedding of load away from the grain boundary that has begun to decohere as well as the stress concentration forming at the end of the grain boundary. The approximate corresponding location along the CCZM of the decohering grain boundaries is schematically shown (Figures 11g-i). Since λ has not reached a value of 1 this damaged grain boundary has not yet completely fractured.

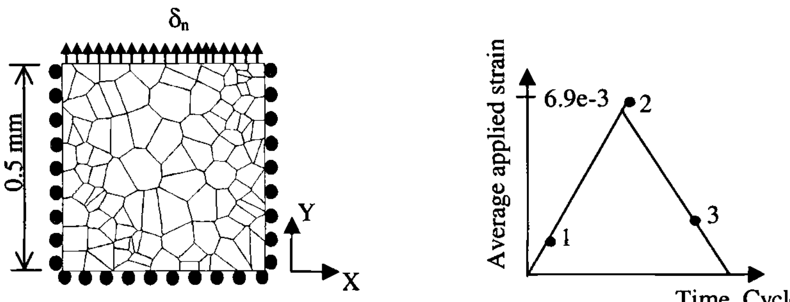

(a) (b)

Figure 10 - *(a) Boundary conditions and loading of polycrystal sample. (b) Loading history.*

Table 4 – *Grain Material and CCZM Properties*

Grain Material		CCZM	
Type	Elastic-Plastic, Orthotropic (Hill)	G_{avg}	250 Pa m
E	72 000 MPa	ΔG	100 Pa m
σ_{yld1}	505 MPa	Resulting t_{pavg}	500 MPa
σ_{yld2}	450 MPa		
σ_{yld12}	400 MPa		

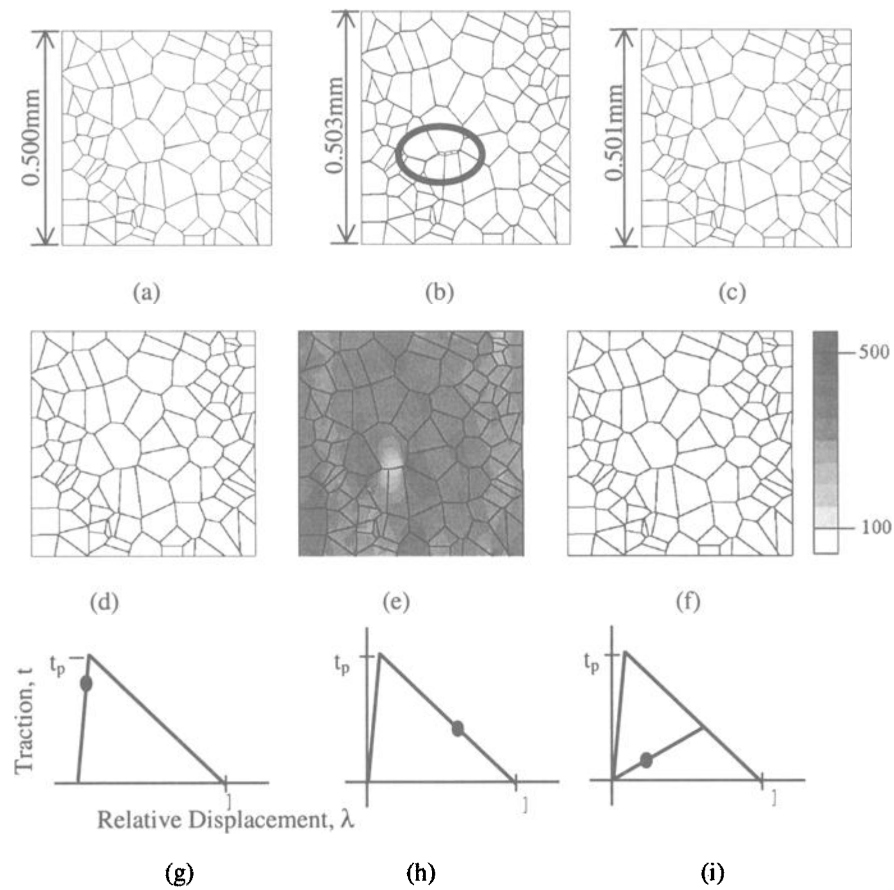

Figure 11 - *Deformed mesh at 2X magnification for (a) Point 1 indicated in Figure 4. (b) Point 2 in Figure 4. The circled grain boundaries have begun to decohere. (c) Point 3 in Figure 4. (d) σ_{yy} contour plot corresponding to (a). (e) σ_{yy} contour plot corresponding to (b). (f) σ_{yy} contour plot corresponding to (c). (g) Schematic representation of the location on the CCZM of the opening GB at the first load point. (h) Schematic representation of the location on the CCZM of the opening GB at the first load point. (i) Schematic representation of the location on the CCZM of the opening GB at the first load point.*

Discussion

Initial simulations using bicrystal samples were conducted to observe the usefulness of cohesive zone models to describe grain boundaries. These simulations showed that cracks could be initiated without the explicit introduction of an initial crack through the use of the CCZM. Next, simulations were conducted with regular polycrystals. These showed the affect of adjacent grains and grain boundaries on the propagation or arrest of the grain boundary decohesion. Finally, simulations were conducted using statistical representations of aluminum polycrystals. Using a Voronoi tessellation, samples of polycrystalline geometry were created. The grains were statistically assigned material parameters from one of four material models. The grain boundaries were assigned a statistically varying CCZM. Completed polycrystal samples were loaded monotonically and cyclically to observe damage and crack initiation.

In an example shown herein, damage occurs to the sample in the form of grain boundary decohesion before any grains reach yield from macroscopic loading. Local yielding then follows due to stress redistribution caused by the decohesion process. The use of the CCZM to describe the grain boundaries allows for this type of damage to occur.

A current ongoing parametric study will yield sensitivities to modeling choices and parameter ranges. The collected observations will serve to reduce the parameter space when the current capabilities are transferred to a 3-D framework. Also, through ongoing atomistic simulations of grain boundary fracture we hope to determine accurate values of CCZM parameters such as t_p and δ_c.

Conclusions

The technique described here of using CCZM to represent grain boundary material response has been shown to be a method of allowing fatigue cracks to be naturally initiated. Employing this technique within a statistical representation of a polycrystal can be useful for studying the influences of geometry and material properties on fatigue crack initiation. This can also be useful in collecting statistical information about where and when fatigue cracks will initiate and the residual strength of a sample. As part of a multiscale effort, this information can be used to enhance constitutive properties at larger scale and determine smaller-scale features that should be further investigated.

Acknowledgments

Funding for this research is being provided through Grant F49620-98-1-0401 from the Air Force Office of Scientific Research and Grant 9873214 from the NSF.

References

[1] Myers, C. R., "Digital Material: a Framework for Multiscale Modeling of Defects in Solids", contribution to the Proceedings of the Material Research Society Meeting, Fall 1998.

[2] Dugdale, D. S., "Yielding of Steel Sheets Containing Slits," *Journal of the Mechanics and Physics of Solids*, Vol. 8, 1960, pp. 100-104.

[3] Bittencourt, T. N., Wawrzynek, P. A., Ingraffea, A. R., and Sousa, J. L., "Quasi-Automatic Simulation of Crack Propagation for 2D LEFM Problems," *Engineering Fracture Mechanics,* Vol. 55, No. 2, 1996, pp.321-334.

[4] James, M. A., "A Plane Stress Finite Element Model for Elastic-Plastic I/II Crack Growth," Ph.D. Thesis, Kansas State University, 1998.

[5] Arwade, S. R., "Probabilistic Models for Aluminum Microstructure and Intergranular Fracture Analysis," M.S. Thesis, Cornell University, 1999.

[6] van der Giessen, E. and Tvergaard, V., "Interaction of Cavitation Grain Boundary Facets in Creeping Polycrystals," *Mechanics of Materials*, Vol. 17, 1994, pp.47-69.

[7] van der Giessen, E. and Onck, P., "Growth of an Initially Sharp Crack by Grain Boundary Cavitation," *Journal of the Mechanics and Physics of Solids*, Vol. 47, 1999, pp. 99-139.

[8] Tvergaard, V. and Hutchinson, J. W., "Relation Between Crack Growth Resistance and Fracture Process Parameters in Elastic-Plastic Solids," *Journal of the Mechanics and Physics of Solids*, Vol. 40, No. 6, 1992, pp.1377.

[9] Ingraffea, A. R., Grigoriu, M., Dawson, P., and Miller, M., Probabilistic Simulation of Fatigue Crack Initiation Annual Progress Report, Cornell University, Ithaca, NY, 2000.

Mark T. Kirk,[1] *MarjorieAnn E. Natishan,*[2] *and Matthew Wagenhofer*[3]

A Physics-Based Model for the Crack Arrest Toughness of Ferritic Steels

Reference: Kirk, M. T., Natishan, M. E., and Wagenhofer, M., **"A Physics-Based Model for the Crack Arrest Toughness of Ferritic Steels,"** *Fatigue and Fracture Mechanics: 33rd Volume, ASTM STP 1417,* W. G. Reuter and R. S. Piascik, Eds., ASTM International, West Conshohocken, PA, 2002.

Abstract: Following an intense period of test methodology development in the late 1970s and early 1980s, crack arrest has received very little attention in the research community. Moreover, the available model for the crack arrest transition behavior of ferritic steel (i.e., the ASME K_{Ia} curve) is entirely empirical. In 1998 Wallin published an updated empirical model of crack arrest transition data having a form similar to his Master Curve treatment of crack initiation toughness. In this paper we provide a physical basis for the data trends noted by Wallin, thereby making the model more robust and enabling its confident application to situations not covered by available K_{Ia} data.

Keywords: crack arrest, master curve, pressurized thermal shock, probabilistic risk assessment.

Background and Motivation

In the United States, the operators of commercial nuclear power plants are required to demonstrate that postulated severe accident scenarios, such as pressurized thermal shock (PTS), do not compromise the integrity of their reactor pressure vessel (RPV) [*1*]. The NRC developed the criteria against which such demonstrations are judged in the mid-1980s [*2*]. Currently, the NRC and the commercial nuclear power industry are engaged in a cooperative project aimed at developing the technical basis to support a fundamental revision to these rules governing PTS [*3*]. While the earlier work featured a probabilistic treatment of the PTS event, state of knowledge and data limitations in the early 1980's necessitated a conservative treatment of several key input variables. The most prominent conservatisms in the earlier analysis included the characterization of transition fracture toughness using the nil-ductility reference temperature RT_{NDT} (which has an intentional

1 Senior Materials Engineer, United States Nuclear Regulatory Commission, Rockville, MD, 20852. The views expressed herein represent those of the author and not an official position of the USNRC.

2 President, Phoenix Engineering Associates, Inc., 3300 Royale Glen Ave., Davidsonville, MD, 21035.

3 Graduate Student, Department of Mechanical Engineering, University of Maryland, College Park, MD, 20742.

conservative bias), the use of a flaw distribution that placed all of the flaws on the interior surface of the RPV, and, in general, contained larger flaws than those usually detected in service, and the assumption that the peak fluence occurs over the entire interior surface of the RPV. Technical developments in the intervening years provide a basis for the relaxation of some of the conservatisms in the input parameters. These developments suggest the possibility of technically justifying an increase in the PTS screening criteria, and have motivated current efforts to re-visit the basis for the rules governing PTS.

Both historic and current models of PTS define vessel failure as a crack that has initiated on or near the inner wall and failed to arrest before it penetrates the outer wall of the vessel. Consequently, models for both crack initiation toughness (K_{Ic}) and crack arrest toughness (K_{Ia}) are needed as input to probabilistic calculations that simulate the response of the RPV to postulated thermal-hydraulic transients. In the PTS re-evaluation, these calculations will be performed in a manner consistent with modern probabilistic risk assessment (PRA) methodologies to account for uncertainties. These methodologies differentiate between two types of uncertainties: aleatory and epistemic [*4*]. Aleatory uncertainties arise due to the randomness inherent to a physical or human process, whereas epistemic uncertainties are caused by a limitation in the current state of knowledge (or understanding) of that process. To distinguish between these uncertainty types it is necessary to establish models for K_{Ic} and K_{Ia} based on an understanding of the physical processes that lead to crack initiation and crack arrest in ferritic steels. This physical understanding provides a basis for predicting the trends that fracture toughness data *should* exhibit, thereby enabling distinction between aleatory and epistemic uncertainties that cannot be made on the basis of empirical models alone.

Developments in fracture mechanics and micro-mechanics in the past 20 years provide an appropriate basis to define a best-estimate model for crack initiation toughness. Specifically, the Master Curve proposed by Wallin and co-workers [*5-11*] and empirically confirmed by numerous investigators [*12, 13*] provides an extensive empirical basis. More recent activities by Natishan and co-workers demonstrate that the Master Curve is not fortuitously robust, but rather applies to all ferritic steels failing by transgranular cleavage for sound physical reasons [*14-18*]. Consequently, the physical and empirical evidence needed to establish a crack initiation toughness model (K_{Ic} model) for use in the PTS re-evaluation effort draws heavily off information presented in the literature, and so is not addressed in detail here. By comparison, the understanding of crack arrest toughness has received very little attention in recent years, and available models are entirely empirical [*19*]. Recent work by Wallin summarizes crack arrest data from a number of sources and provides an empirical treatment of these data in a manner similar to the Master Curve treatment of crack initiation [*20*]. In this paper we expand on Wallin's crack arrest model by demonstrating that his empirical findings are expected for sound physical reasons. The resultant crack arrest toughness model is then appropriate for use in the PTS re-evaluation effort.

A Summary of Wallin's Empirical Findings

In 1998 Wallin published a paper presenting a treatment of crack arrest similar to the Master Curve treatment of crack initiation [*20*]. Information from Wallin's paper speaks, at least empirically, to the temperature dependence of K_{Ia}, the amount of scatter in K_{Ia} data (relative to K_{Ic} data), and the temperature separation between K_{Ic} and K_{Ia} data. Additionally, Wallin contends that crack arrest toughness should not exhibit the statistical size effect characteristic of crack initiation data because crack arrest is controlled more by the mean properties of the matrix, rather than local properties. However, Wallin provides no evidence to corroborate this final claim, making the absence of a size effect in crack arrest toughness an *a priori* assumption of his analysis.

Figures 1 and 2 illustrate the trends observed in crack arrest data as they were reported by Wallin. These data support the following empirical observations:

- *Temperature Dependence of K_{Ia}:* Consistent with the Master Curve treatment, Wallin selected the temperature at which the mean measured K_{Ia} value is 100 MPa√m as the index temperature used to bring data from different heats of steel together to form a single crack arrest transition curve; Wallin called this index temperature T_{KIa}. Figure 1 (right) presents crack arrest transition curves for nine heats of RPV steel (including irradiated materials) with temperature normalized to T_{KIa}. The mean curve on Fig. 1 has the same form as the conventional Master Curve used to describe crack initiation data, that is:

$$K_{Ia} = 30 + 70 \cdot \exp\{0.019[T - T_{KIa}]\} \tag{1}$$

  This empirical evidence suggests that crack arrest toughness exhibits the same temperature dependency as crack initiation toughness. Moreover, these data suggest that the temperature dependence of K_{Ia} is not affected strongly by irradiation.
- *Scatter in K_{Ia} Data*: Wallin found that a log-normal distribution having a variance equal to 18% of the mean value fits the crack arrest data in Fig. 1 well. A comparison of this distribution with the statistical distribution used by the Master Curve to fit crack initiation toughness data (a Weibull distribution having a minimum value of 20 MPa√m and a shape parameter of 4) illustrates Wallin's finding that the scatter in crack arrest toughness is somewhat less than the scatter in crack initiation toughness.
- *Temperature Separation Between K_{Ic} and K_{Ia} Data*: The temperature separation between the crack initiation and crack arrest toughness curves is not a material invariant quantity. As illustrated in Fig. 2, this temperature separation (i.e. $T_{KIa} - T_o$) decreases systematically as crack initiation transition temperature increases. This information demonstrates that the current ASME model, which specifies a constant temperature separation between the crack initiation and crack arrest transition curves, does not appropriately reflect the data.

A Physical Explanation of Crack Arrest in Ferritic Steels

In the following sections we provide a physics-based rationale for Wallin's findings regarding the temperature dependence of K_{Ia}, the amount of scatter in K_{Ia} data, the temperature separation between the crack arrest and crack initiation transition curves and the lack of statistical size effect in crack arrest data.

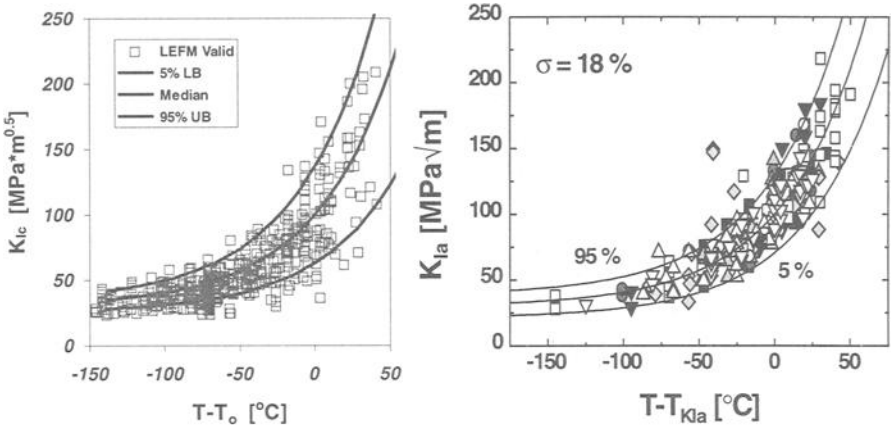

FIG. 1–*Comparison of scatter in crack initiation data (left) [26] and in crack arrest data (right) [20] data. Note that these figures are to the same scale. In both figures the mean curve has the same temperature dependence as the Wallin Master Curve.*

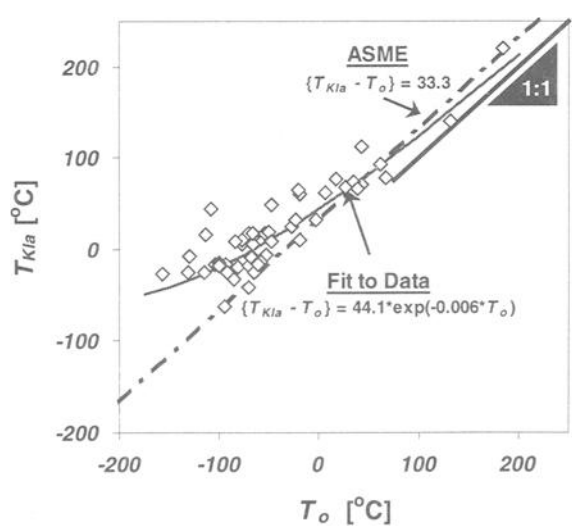

FIG. 2–*Data for RPV and other steels showing the relationship between the crack arrest transition temperature (T_{KIa}, vertical axis) and the crack initiation transition temperature (T_o, horizontal axis) [20]. The ASME relationship (T_{KIa} - T_o = 33.3) is that implied by the temperature difference between the ASME K_{Ia} and K_{Ic} curves.*

Temperature Dependence of K_{Ia}

Both dislocation motion and crack propagation act to dissipate the energy placed into a material by a given stress state. Crack propagation is a catastrophic form of energy dissipation while dislocation motion occurs on a more local scale and results in permanent plastic deformation. A crack will arrest in situations in which dislocations move faster than the crack propagates. Conversely, if dislocation motion is inhibited energy dissipation must occur by crack propagation and arrest cannot occur.

The atomic arrangement, or crystal structure of a material controls the temperature-dependence of material properties that involve dislocation motion, including fracture toughness. This is because thermal energy only affects the activation energy required for dislocations to move through obstacles of a size scale of the lattice atom vibration. Activation energy, and thus dislocation motion through more widely spaced obstacles (such as vacancies, interstitials, precipitates and other dislocations) is not affected by the increased lattice atom vibration resulting from increased temperature. Thus these obstacles cannot affect the temperature dependence of dislocation motion. Since all ferritic steels have the same crystal structure, they are expected to exhibit the same temperature dependence of properties controlled by dislocation motion.

The resistance of a material to crack initiation, as described by K_{Ic} in the transition region, is controlled by the ability of the material to absorb energy via plastic flow, or dislocation motion. Thus, as shown by Natishan et al. [*14-16*], the temperature dependence of K_{Ic} is controlled *only* by the lattice structure and all ferritic steels are expected to exhibit the same temperature dependence, as is demonstrated by the extensive empirical evidence supporting the Master Curve [*10, 12, 13*]. Crack arrest, as described by K_{Ia}, also depends on the ability of the material to absorb energy via dislocation motion and thus K_{Ia} should exhibit the same temperature dependence as described by the Master Curve, as shown by Wallin [*20*] and illustrated in Fig. 1. Changes in long-range obstacles to dislocation motion, such as those produced by irradiation, are *not* expected to alter the temperature dependence of fracture toughness. These obstacles are too widely spaced to have any effect on the thermally-induced lattice atom-vibration that controls the temperature dependency of the flow strength and, thereby, of fracture toughness as well. Therefore, irradiation, and other long-range obstacles to dislocation motion that act to increase yield strength, are expected to influence only the position of the transition curve on the temperature axis (i.e. only T_o and T_{KIa}) and have no effect on the temperature dependency of either K_{Ic} or K_{Ia}. Again, this physical understanding provides a rationale for Wallin's empirical finding (Fig. 1) [*20*].

Scatter in K_{Ia} Data

The mechanism of crack arrest is based on the interaction of a rapidly evolving stress state in front of a running crack with a distribution of defects in the material that trap dislocations. The crack-tip stress field samples the material volume ahead of this rapidly moving crack. If this region contains a large distribution of barriers to dislocation motion the stress triaxiality will remain high enough to inhibit dislocation motion, thereby preventing crack tip blunting and crack arrest. Conversely, if the stress field samples a region with few barriers to dislocation motion the stress triaxiality may decrease sufficiently to allow dislocations to move, thereby blunting the crack and allowing arrest to occur. Therefore, scatter in K_{Ia} data occurs as a consequence of the randomness in the distribution of barriers to dislocation motion throughout the material. The reduced scatter in K_{Ia} data relative to K_{Ic} data (see Fig. 1) can be understood by comparing the size scale and spacing of the defects responsible for crack initiation with those responsible for crack arrest. Cleavage cracks initiate at non-coherent particles (i.e. carbides, grain boundaries, twin boundaries, etc.) when the accumulated dislocations produce enough strain to elevate the local stress at the barrier high enough to fracture the barrier or cause its decohesion from the matrix. These non-coherent particles are of sub-micron size (i.e. 1/10 micron), and their spacing is on the same order. By comparison, the dislocation-trapping defects responsible for crack arrest (i.e., vacancy clusters, interstitial clusters, coherent and semi-coherent particles, and other dislocations) are of a much smaller size (nanometer) and are spaced much more closely together (again, nanometer). The possible variation in local stress state over the microstructural distances that control crack arrest (order of nanometer) is seen to be much smaller than that possible over the microstructural distances that control crack initiation (order of sub-micron). This smaller stress variation for crack arrest makes the scatter in K_{Ia} data smaller than in K_{Ic} data, as was illustrated in Fig. 1.

Temperature Separation between the K_{Ic} and K_{Ia} Transition Curves

In recently reported work, Wagenhofer and Natishan [*18*] contend that a universal hardening curve exists for all ferritic steels. In this section we first summarize this idea, and then develop a physical model for the relationship between crack arrest and crack initiation transition temperature that explains the empirical trends revealed by the Wallin model using the universal hardening curve as a basis.

To explain the relationships between the various parameters involved, we use the Zerilli-Armstrong description of the flow curve for BCC materials [*22*]:

$$\sigma_{ZA} = \sigma_0 + K\varepsilon^n \tag{1a}$$
$$\sigma_0 = c_0 + Be^{-\beta T} \tag{1b}$$
$$c_0 = \sigma_G + kd^{-1/2} \tag{1c}$$
$$\beta = \beta_0 - \beta_1 \ln\dot{\varepsilon} \tag{1d}$$

Here, K, n, c_o, B, k, β_0 and β_1 are material constants, σ_G is the increment of true stress due to coherent and semi-coherent obstacles to dislocation motion (vacancies, interstitials, and small precipitates), ε is the true strain, $\dot{\varepsilon}$ is the true strain rate, and d is the grain size. Focusing attention on the work hardening term (2nd term on right hand side of eq. (1a)), the notion that all ferritic steels follow a universal hardening curve (i.e. the same strain-hardening rate (n) value for all ferritic steels) follows directly from the well-established experimental observation that as a metal is hardened, subsequent tensile tests will reveal greater yield strengths but the overall true stress-strain curve will always overlay the unhardened curve. This behavior cannot occur unless the hardened specimen exhibits the same strain-hardening rate as the unhardened specimen does after an equivalent amount of tensile strain. This observation also leads to an invariance of the true stress at maximum load for most hardening mechanisms.

In eq. (1), Zerilli and Armstrong adopt $n = 0.5$, following Taylor's derivation of the stress necessary to keep a uniform distribution of edge dislocations in equilibrium [*23*]. This square root relationship between stress and strain arises because the uniform dislocation distribution forces the distance between the dislocations to be equal to the inverse square root of the dislocation density. Despite criticisms that this theory is too simplistic, it does a good job of representing the large deformation behavior of a number of materials [*24*].

To summarize, in order for eq. (1) to properly describe the physical behavior of metals that have been hardened to some degree, the strain hardening rate (n) must be constant, and a value of n equal to 0.5 is expected on theoretical grounds. The stress values for a particular steel having a particular degree of prior hardening can be determined by modifying eq. (1a) as follows [*21*]:

$$\sigma_{ZA} = \sigma_0 + K\sqrt{(\varepsilon_0 + \varepsilon)} \tag{2}$$

where ε_o is a constant that quantifies the degree of prior hardening.

Figure 3 illustrates the effect of prior hardening on ARMCO Iron [22] using eq. (1). The thin solid lines are the engineering stress vs. true plastic strain curves for various amounts of prior hardening (various ε_0 in eq. (2)). These are calculated from eqs. (1-2), which is represented on the plot as a thick solid line, using the familiar relationships:

$$\sigma_{ZA} = S(1+e) \tag{3a}$$

$$\varepsilon = \ln(1+e) \tag{3b}$$

Here S and e are engineering stress and strain, respectively. Various amounts of prior hardening are represented as initial tensile strains (thin vertical lines on Fig. 3). The maximum load condition,

$$\frac{d\sigma_{ZA}}{d\varepsilon} = \sigma_{ZA}, \tag{4}$$

is represented on Fig. 3 by the dotted line.

These ideas provide the basis for a physical model of the relationship between crack arrest and crack initiation transition temperature reported by Wallin (see Fig. 2) [*20*]. At the time of crack arrest, the material experiences a high strain rate. This strain rate elevation above the quasi-static conditions associated with crack initiation causes an elevation in the activation energy required to move dislocations past trapping obstacles, and thus results in an increase in apparent yield stress of the material in a manner similar to the yield stress elevation produced by prior strain that we illustrated in Fig. 3. Fig. 4 uses the idea of a universal hardening curve for all ferritic steels to illustrate why the elevation in prior strain caused by the elevated strain rate associated with crack arrest (defined as $\Delta\varepsilon_o$) produces a progressively diminishing elevation in the yield strength as the degree of strain caused by prior hardening (ε_o) increases. As shown on the figure, materials having more prior strain hardening experience less increase in yield strength for a fixed strain rate elevation associated with crack arrest. Since increases in toughness transition temperature scale with increases in yield strength [25], this understanding suggests a physical basis for the empirical trend reported by Wallin of a progressively diminishing separation between the crack initiation and crack arrest transition curves for higher transition temperature steels. Moreover, the invariance of the true stress at maximum load that follows directly from the notion of a universal hardening curve suggests that in the limit of very high strength ferritic materials the crack initiation and crack arrest transition curves should approach each other (i.e. $T_{KIa} \approx T_o$), a trend also reflected by available empirical evidence (see Fig. 2).

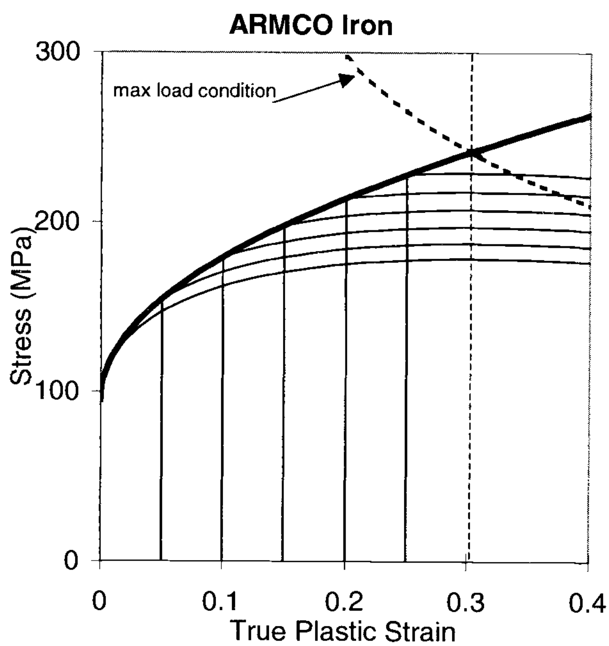

FIG. 3–Engineering stress vs. true plastic strain curves for various degrees of prior hardening (thin vertical lines and curves) calculated from the Zerilli / Armstrong true stress vs. true plastic strain curve (thick curve) for ARMCO Iron.

Size Effect in K_{Ia} Data

The size effect observed in crack initiation toughness is due to the weakest link nature of the initiation event. As the crack front length increases with specimen size, the stress field at the crack tip samples a greater number of initiating particles. The stress at which a crack will initiate is then controlled by the size distribution of the initiating particles along the crack front. As crack front length increases, the probability that the stress field samples a large particle increases and thus the probability of alower stress intensification required for catastrophic fracture is greater. The nature of the size distribution of particles is such that little additional affect of crack front length on decreasing K_{Ic} is observed beyond a crack front length of 100 mm (4 inches) [*26*]. By comparison, crack arrest is *not* a weakest link event. Instead, crack arrest depends only on the ability of the lattice structure to move dislocations. This is controlled by the obstacles to dislocation motion, including vacancies, interstitials, dislocations, and precipitates that act to increase the activation energy for dislocation motion. The distribution of these obstacles occurs on a size scale one to two orders of magnitude smaller than that of the crack initiating particles (carbides and other particles). Consequently, crack arrest toughness is not expected to be greatly influenced by the length of the crack front for all crack front lengths of practical concern in RPV applications.

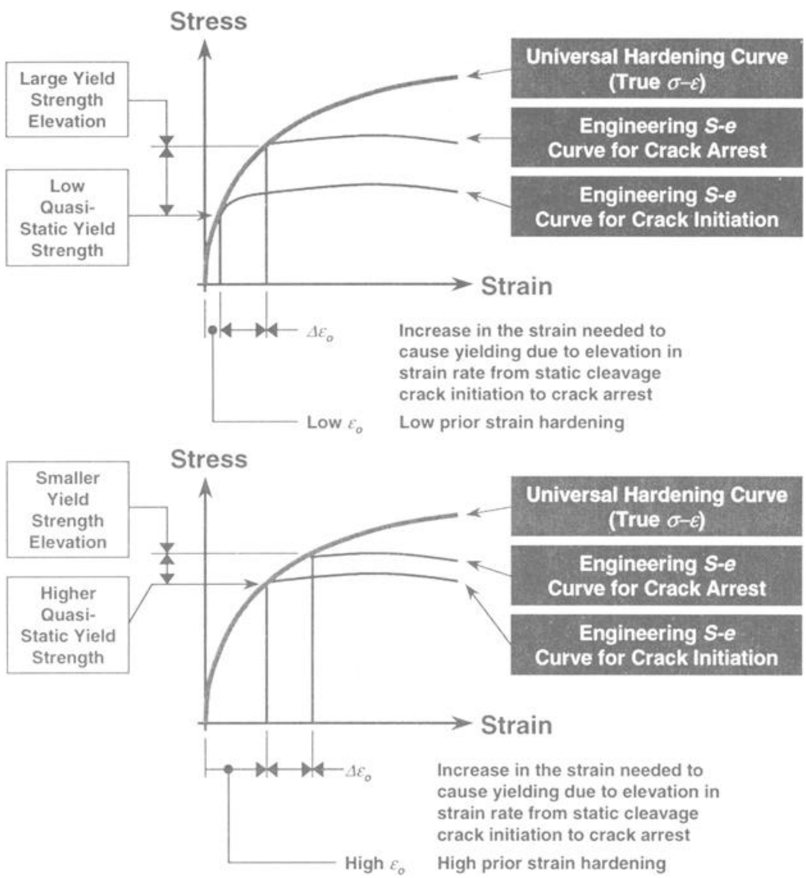

FIG. 4–*An illustration of the effect of strain rate increase on yield strength elevation for materials having different degrees of prior strain hardening.*

Summary and Conclusions

In this paper we present a physically based model describing the crack arrest toughness of ferritic steels. Our discussion parallels a previous paper by Wallin concerning crack arrest, and demonstrates that all of the trends Wallin noted on empirical grounds are anticipated physically. Specifically, the information presented herein supports the following conclusions:

1. Both K_{Ic} and K_{Ia} data are expected to exhibit the same temperature dependence. The temperature dependence of both toughness values is controlled by the atomic arrangement, or crystal structure of the material. Consequently, the temperature dependence of K_{Ic} and K_{Ia} is expected to be common to all ferritic steels.
2. Changes in long-range obstacles to dislocation motion, such as the defects created by irradiation, are *not* expected to alter the temperature dependence of either K_{Ic} or K_{Ia} because these defects are too large to be affected by thermally-induced lattice atom vibration.
3. K_{Ia} data exhibits less scatter than K_{Ic} data because the possible variation in local stress state over the microstructural distances that control crack arrest is much smaller than that possible over the microstructural distances that control crack initiation. The considerably smaller size/spacing of the defects responsible for crack arrest, relative to those responsible for crack initiation, also suggests that crack arrest toughness should not be greatly influenced by the length of the crack front for all crack front lengths of practical concern in RPV applications.
4. A progressively diminishing separation between the crack initiation and crack arrest transition curves for higher transition temperature steels is expected on physical grounds. The invariance of the true stress at maximum load that follows directly from the notion of a universal hardening curve suggests that in the limit of very high strength ferritic materials the crack initiation and crack arrest transition curves should approach each other – a trend reflected by available empirical evidence.

This physical basis for the data trends noted by Wallin makes the crack arrest model more robust, and enables its confident application to situations not covered by available K_{Ia} data.

References

[*1*] Code of Federal Regulation 10CFR50.61, "Fracture Toughness Requirements for Protection Against Pressurized Thermal Shock Events."

[2] SECY-82-465, United States Nuclear Regulatory Commission, 1982.

[*3*] Dickson, T. L., Williams, P. T., and Bass, R. B., "An Improved Probabilistic Fracture Mechanics Model for Pressurized Thermal Shock," *Proceedings of the SMIRT Conference,* April 2001.

[*4*] Siu, N., "Uncertainty Analysis and Pressurized Thermal Shock, An Opinion," United States Nuclear Regulatory Commission, 1999, Adams Accession No. ML992710064.

[5] Wallin, K., Saario, T., and Törrönen, K., "Statistical Model for Carbide Induced Brittle Fracture in Steel," *Metal Science*, Vol. 18, January 1984, 13-16.

[6] Wallin, K., Saario, T., Törrönen, K., and Forsten, K., "Mechanism-Based Statistical Evaluation of the ASME Reference Fracture Toughness Curve," 5th International Conference on Pressure Vessel Technology, Vol. II, Materials and Manufacturing, San Francisco, California, ASME, 1984.

[7] Wallin, K., "The Scatter in K_{Ic} Results," *Engineering Fracture Mechanics*, 19(6), (1984), pp. 1085-1093.

[8] Wallin, K., "The Size Effect in K_{Ic} Results," *Engineering Fracture Mechanics*, 22, (1984), pp. 149-163.

[9] Wallin, K., "Statistical Modeling of Fracture in the Ductile to Brittle Transition Region," *Defect Assessment in Components – Fundamentals and Applications*, ESIS/EGF9, J.G. Blauel and K.-H. Schwalbe, Eds., pp. 415-445, 1991.

[10] Wallin, K., "Irradiation Damage Effects on the Fracture Toughness Transition Curve Shape for Reactor Vessel Steels," *Int. J. Pres. Ves. & Piping*, **55**, pp. 61-79, 1993

[11] Wallin, K., "Statistical Aspects of Constraint with Emphasis on Testing and Analysis of Laboratory *Specimens in the Transition Region," Constraint Effects in Fracture, ASTM STP-1171*, E.M. Hackett, K.-H. Schwalbe, and R.H. Dodds Eds., American Society for Testing and Materials, 1993.

[12] Sokolov, M. A., and Nanstad, R. K., "Comparison of Irradiation Induced Shifts of K_{Jc} and Charpy Impact Toughness for Reactor Pressure Vessel Steels," *ASTM STP-1325*, American Society of Testing and Materials, 1996.

[13] Kirk, M., Lott, R., Kim, C., and Server, W., "Empirical Validation Of The Master Curve For Irradiated And Unirradiated Reactor Pressure Vessel Steels," Proceedings of the 1998 ASME/JSME Pressure Vessel and Piping Symposium, July 26-30, 1998, San Diego, California, USA.

[14] Natishan, M. and Kirk, M., "A Micro-mechanical Evaluation of the Master Curve," *Fatigue and Fracture Mechanics, 30th Volume, ASTM STP-1360*, K. Jerina and P. Paris, Eds., American Society for Testing and Materials, 1998.

[15] Natishan, M. E., Wagenhofer, M., and Kirk, M. T., "Dislocation Mechanics Basis and Stress State Dependency of the Master Curve," *Fracture Mechanics, 31st Symposium, ASTM STP 1389*, K. Jerina and J. Gahallger, Eds., American Society for Testing and Materials, 1999.

[16] Natishan, M. and Kirk, M., "A Physical Basis for the Master Curve," *Proc. of the 1999 ASME Pressure Vessel and Piping Conference*, ASME, July 1999.

[17] Kirk, M. T., Natishan, M. E., Wagenhofer, M., "Microstructural Limits of Applicability of the Master Curve," *32nd Volume, ASTM STP-1406*, R. Chona, Ed., American Society for Testing and Materials, Philadelphia, PA 2001.

[18] Wagenhofer, M. and Natishan, M. E., "A Model for Predicting the Fracture Toughness of Steels in the Transition Region from Hardness," *33rd Symposium on Fatigue and Fracture, ASTM STP-1417*, W. Reuter, and R. Piascik, Eds.,

American Society for Testing and Materials, West Conshohocken, PA, 2002.

[*19*] "PVRC Recommendations on Toughness Requirements for Ferritic Materials," WRC Bulletin 175, August 1972.

[*20*] Wallin, K., and Rintamaa, R., "Master Curve Based Correlation Between Static Initiation Toughness K_{Ic} and Crack Arrest Toughness K_{Ia}," Proceedings of the 24th MPA-Seminar, Stuttgart, October 8 and 9, 1998.

[*21*] J. Datsco, Material Properties and Manufacturing Processes, John Wiley & Sons, Inc., NY 1966, pp 18-20

[*22*] Zerilli, F. J., and Armstrong R. W., "Dislocation-Mechanics-Based Constitutive Relations for Material Dynamics Calculations," J. Appl. Phys., Vol. 65, No. 5, March 1987, pp. 1816-1825.

[*23*] Taylor, G. I., "The Mechanism of Plastic Deformation of Crystals," Proc. Roy. Soc., Vol. A145, 1934, pp. 362-404.

[*24*] Meyers, M. A, and Chawla, K. K., "Mechanical Behavior of Materials," Prentice Hall, Upper Saddle River, New Jersey, 1999.

[*25*] Wagenhofer, M., Gunawardane, H., and Natishan, M., "Yield and Toughness Transition Predictions for Irradiated Steels Based on Dislocation Mechanics," *20th International Symposium on the Effects of Irradiation on Materials, ASTM STP-1405,* S.T. Rosinski, M.L. Grossbeck, T.R. Allen, and A.S. Kumar, Eds., American Society for Testing and Materials, 2001.

[*26*] Kirk, M., Lott, R., Kim, C., and Server, W., "Empirical Validation Of The Master Curve For Irradiated And Unirradiated Reactor Pressure Vessel Steels," *Proceedings of the 1998 ASME/JSME Pressure Vessel and Piping Symposium,* July 26-30, 1998, San Diego, California, USA.

Stephanie C. TerMaath[1] and S. Leigh Phoenix[2]

An Analytical Method for Studying Cracks with Multiple Kinks

Reference: TerMaath, S. C. and Phoenix, S. L., **"An Analytical Method for Studying Cracks with Multiple Kinks,"** *Fatigue and Fracture Mechanics: 33rd Volume, ASTM STP 1417*, W. G. Reuter and R. S. Piascik, Eds., ASTM International, West Conshohocken, PA, 2002.

Abstract: An analytical method for studying brittle fracture in an infinite plate containing a crack of complex geometry under general loading conditions is developed. Based on superposition and dislocation theory, this method can be used to determine the full stress and displacement fields in a cracked material. In addition, stress singularities at both crack tips and material wedges (created by crack kinking or zigzagging) are calculated. A key component of this research is the development of opening displacement series that capture the physical behavior of the cracks. Cracks with multiple kinks (or changes in growth direction) are studied with this method. Results show rapid convergence for few degrees of freedom as measured by the number of opening displacement terms included in a particular analysis.

Keywords: dislocation distribution, superposition, kinked cracks, wedge

Factors such as fatigue loading conditions, cracking along grain boundaries in heterogeneous materials, and environmental effects - corrosion, for instance - can cause cracks to change direction or zigzag as they grow. Cracks with this type of shape are defined as kinked cracks. The number of kinks is determined by the number of direction changes, and a multiply kinked crack is a crack with more than one kink. Evaluating the performance of materials containing this type of crack poses a challenging problem. To address this type of fracture, a method based on superposition and dislocation theory has been developed. This two-dimensional analytical technique can be used to calculate the stress and displacement fields in these cracked materials. Also, singularities at crack tips and material wedges (created by crack kinking) are readily available to assess potential crack growth at these locations. This method has been applied to cases of crack arrays consisting of multiply kinked cracks, but the work presented here will be limited to the case of an isolated multiply kinked crack. A direct and practical application of this work is to study a multiple crack array composed of many small cracks. Small crack behavior is an area of current importance and relevance to many researchers, and this work adds to the development of methods to study these types of complex-shaped crack arrays.

[1]Graduate Research Assistant, Civil and Environmental Engineering, Cornell University, Ithaca, NY 14853
[2]Professor, Theoretical and Applied Mechanics, Cornell University, Ithaca, NY 14853

Fracture conditions involving cracks of complex shapes occur in many diverse problems ranging from brittle rock fracture to cracking in composites to fatigue cracking in aging aircraft; therefore, many researchers have contributed to the development of methods to enhance our understanding of the behavior of these types of damage zones. Interest can range from modeling stiffness reduction and global breakdown due to evolving stress redistribution to interactions leading to the onset of localization. Frequently in crack problems of this type, opening displacements of the crack faces are unknown and must be determined by satisfying the traction-free conditions on the crack faces as dictated by the boundary conditions. One solution method is to model these opening displacements as dislocation distributions (the derivatives of the opening displacements) along the crack faces, and many researchers have approached these crack problems in this manner [*1-13*]. An overview of various applications and developments of the dislocation approach can be found in the literature [*14, 15*]. Researchers have also studied the specific cases of slightly curved or kinked cracks [*16-24*] and crack kinking at a bi-material interface [*25, 26*]. Other researchers have noted the need for research on strongly interacting cracks of complex shape [*27*].

Overview of the Analytical Technique

To calculate the stress and displacement fields in an infinite plate containing a multiply kinked crack, the crack's opening displacement profile must be determined such that all crack faces are traction-free under the given loading conditions. Once the opening displacement profile is known, this solution can also be used to calculate the stress intensity factors at the crack tips and kink locations (material wedges) in order to study crack propagation. Superposition is applied at the global and local levels, and a dislocation distribution approach is utilized, to solve for the opening displacement shape of the crack. Several excellent texts on this subject are available [*14, 28-29*].

Superposition

To solve this boundary value problem, superposition is first applied at the global level by modeling the cracked plate as two separate problems (the trivial problem and the auxiliary problem) where the sum of their solutions equals the solution to the original problem. The trivial problem consists of the given plate under the specified far field loading but without the cracks. Meanwhile, the auxiliary problem is the given cracked plate, but without the far field loading. The loading conditions for the auxiliary problem are instead prescribed tractions applied to the crack faces that are calculated to be equal and opposite to the stresses induced in the uncracked material at the location of the crack faces. This loading insures that the crack faces are traction-free in the original problem when the stress field solutions to the trivial and auxiliary problems are summed. Obtaining a solution to the auxiliary problem, which constitutes the bulk of the analytical and computational effort, requires the development and superposition of certain solutions on the local level reflecting detailed crack geometric features.

To solve for the opening displacement profiles of the auxiliary problem, the first step is to subdivide cracks into a series of straight crack segments. For example, the multiply kinked crack of Figure 1 is divided into three crack segments, each with its own local coordinate system. Once the opening displacement profile for a single segment is determined, its effects on the full stress field can be evaluated separately from the other crack segments. Superposition of the local solutions for all of the respective crack segments yields the full solution to the auxiliary problem.

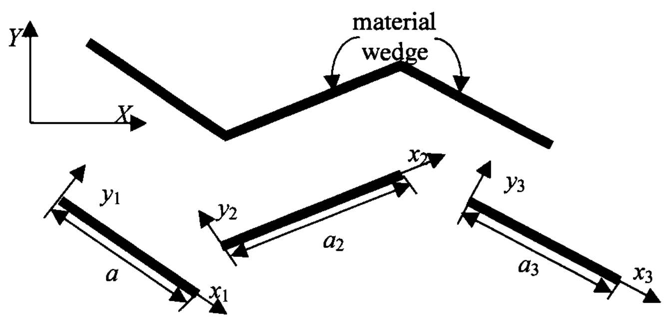

Figure 1 – *Global and Local Coordinate Systems for a Crack with Two Kinks*

Dislocation Distributions

Dislocation distributions are the means of describing the opening displacement profile of a crack segment and inducing the prescribed crack face tractions of the auxiliary problem. A dislocation distribution, $\mu_\eta(r)$, is defined as the derivative of a crack segment's opening displacement profile, where r is an axis coincident with the crack segment, and $\eta = 1, 2$ represents the tangential and normal directions respectively. To determine the stresses induced at a point (x, y) in the material caused by all of the crack segments, the individual effects of each must first be determined.

Consider crack segment i acting alone (as though all other crack segments are closed) in an infinite, linearly elastic, isotropic plate with local coordinate system (x_i, y_i). The x_i-axis lies along this crack segment which has length a_i. The distance along the x_i-axis is r_i and is measured from the origin. The dislocation distributions for a single crack segment are symbolized as $\mu_{1i}(r_i)$ and $\mu_{2i}(r_i)$. The stress components caused by this individual crack segment at point (x, y) are written in terms of a complex variable formulation as

$$
\begin{aligned}
s_{xy}^{(i)} &= -\frac{2G}{\pi(1+\kappa)}\left\{ y\,\mathrm{Re}\left(Z_2^2\right) + \mathrm{Re}\left(Z_1^1\right) + y\,\mathrm{Im}\left(Z_2^1\right) \right\} \\
s_{yy}^{(i)} &= -\frac{2G}{\pi(1+\kappa)}\left\{ \mathrm{Re}\left(Z_1^2\right) - y\,\mathrm{Im}\left(Z_2^2\right) + y\,\mathrm{Re}\left(Z_2^1\right) \right\} \qquad (1) \\
s_{xx}^{(i)} &= -\frac{2G}{\pi(1+\kappa)}\left\{ \mathrm{Re}\left(Z_1^2\right) + y\,\mathrm{Im}\left(Z_2^2\right) + 2\,\mathrm{Im}\left(Z_1^1\right) - y\,\mathrm{Re}\left(Z_2^1\right) \right\}
\end{aligned}
$$

where G is the shear modulus of the material, ν is Poisson's ratio, and κ is Kosolov's constant ($3\text{-}4\nu$, for plane strain and $(3\text{-}\nu)/(1+\nu)$, for plane stress). These stresses are symbolized by s to indicate that they are created by a single crack segment and are oriented in its local coordinate system. The full stress field due to all crack segments will be denoted by σ and is determined by summing the contributions from all individual crack segments after they are converted to the global coordinate system. The Z are Cauchy singular integrals to be evaluated in closed form in terms of the dislocation distributions and are given as

$$
\begin{aligned}
Z_1^\eta &= \int_0^{a_i} \frac{\mu_{\eta i}(r_i)\mathrm{d}r_i}{z - r_i} \\
Z_2^\eta &= \int_0^{a_i} \frac{\mu_{\eta i}(r_i)\mathrm{d}r_i}{(z - r_i)^2} = -\frac{\mathrm{d}}{\mathrm{d}z} Z_1^\eta
\end{aligned} \tag{2}
$$

where $z = x + \mathrm{i}y$. For the cases where the point (x, y) falls along the crack segment, these integrals are evaluated as Cauchy Principal Value Integrals. Solutions to these integrals for given dislocation distributions can be found in [*15*].

The stress equations (Eqs. 1) are functions of unknown dislocation distributions for the various crack segments. These dislocation distributions are approximated by summing together different types of series that each captures a fundamental crack or wedge behavior (such as singularities at kink locations and tips). (The term material wedge, as illustrated in Figure 1, refers to the wedge of material that is formed at a crack kink. There are two mating wedges, and the wedge with the largest included angle will have a stress singularity in the material at its vertex.) The Cauchy singular integrals are evaluated analytically for each term of these series. The results from a particular term in a series are subsequently multiplied by an unknown weighting coefficient (or degree of freedom). Therefore, the stress equations for each crack segment become simple algebraic equations of unknown weighting coefficients.

Satisfying The Traction-Free Condition

Physical conditions dictate that the crack faces are traction-free in the full problem. Thus, the opening displacement profiles for each crack segment in the auxiliary problem must be exactly those caused by the prescribed tractions resulting from the loading conditions. Therefore, a series of equations to enforce traction-free crack faces in the tangential and normal directions is applied simultaneously at a given set of points along each crack segment. The prescribed tractions to be enforced are different for each crack segment, since they are determined by the orientation of the given crack segment. Thus, these traction values are dependent on the location of the point at which the tractions are being enforced. These equations take the form

$$
\begin{aligned}
\sigma_{xy}^{\infty} n_y^i + \sigma_{xx}^{\infty} n_x^i &= -n_y^i \sum_{j=1}^{N} s_{xy}^{(j)} - n_x^i \sum_{j=1}^{N} s_{xx}^{(j)} \\
\sigma_{yy}^{\infty} n_y^i + \sigma_{xy}^{\infty} n_x^i &= -n_y^i \sum_{j=1}^{N} s_{yy}^{(j)} - n_x^i \sum_{j=1}^{N} s_{xy}^{(j)}
\end{aligned} \tag{3}
$$

where N is the total number of crack segments and i refers to crack segment i. The left hand side of these equations represents the tractions induced at the crack faces by the loading conditions, while the right hand side represents the tractions caused by the opening displacements (dislocation distributions) of all the crack segments. Also, n_x^i and n_y^i are the X and Y components, respectively, of the normal to the bottom (-) crack face of crack segment i. This is the crack segment on which the point at which tractions are being enforced is located. The σ^{∞} are the far field stresses applied to the plate in the directions denoted by their subscripts.

Solving for the Unknown Coefficients

Satisfying the traction-free condition along the crack faces (Eqs. 3) at a chosen set of points results in a system of equations. These equations are linear functions of unknown weights for each term of each series. To calculate the weights a large matrix is inverted; therefore, the use of efficient and physically realistic series is imperative to reduce the number of degrees of freedom to the smallest number possible. It is computationally more efficient to increase the number of rows (number of points) than the number of columns (degrees of freedom). Therefore, selection of points and number of terms produces an over-determined matrix that is solved by a least squares fit (performed automatically by *MATLAB* which minimizes the sum of the squares of the deviations).

Points can be chosen by any arbitrary scheme. For this research, they are placed according to the effects of equal and opposite point forces (acting on the respective crack faces) on the singularities at tips and kinks, resulting in a greater density of points near these locations. The distribution of points is calculated based on the wedge eigenvalue for locations near kinks and the ½ singularity for crack tips. Figure 2 shows the point distributions along a crack segment with a crack tip for 10, 20, and 50 points. Once the weighting coefficients have been calculated, stress and displacement fields and stress intensity factors can be readily determined [*15*].

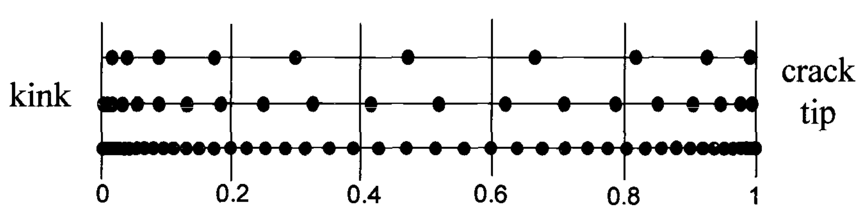

Figure 2 – *Distribution of 10, 20 and 50 Points along a Crack Segment*

Development of Opening Displacement Profiles

Different types of series (wedge, tip, and polynomial) are used to build the opening displacement profile of a crack. Emphasis was placed on creating efficient series that capture all necessary types of physical behavior while minimizing the number of degrees of freedom in an analysis. Therefore, each term from each type of series independently represents a specific physical or opening shape characteristic. Computational difficulties (poor convergence and increased computation time) were found to arise if terms were too closely related and consequently competed to represent similar types of crack behavior. Each term of each series is multiplied by an unknown weighting coefficient, c, and each series is used independently in both the tangential and normal modes. It should also be noted that constraint equations are enforced at kink locations to eliminate mathematical but non-physical singularities created by adjoining crack segments. Derivation of these compatibility equations is mathematically cumbersome [*15*], though the constraints themselves are physically straightforward. The dislocation distributions, $\mu_\eta(r)$, used in Eqs. 2 are the derivatives of these opening displacement series with respect to distance along a crack segment, r.

Two types of crack segments are defined for cracks with more than one kink. Exterior crack segments include a crack tip at one end. All other crack segments are considered interior crack segments (Figure 3).

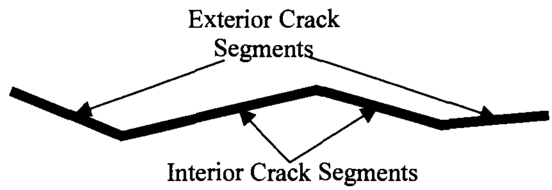

Figure 3 – *Crack with Three Kinks Divided into Exterior and Interior Crack Segments*

The types of series assigned to a given crack segment depend on whether the crack segment is defined as interior or exterior. Interior crack segments will have a combination of polynomial and wedge series while exterior crack segments will have a combination of polynomial, wedge, and tip series. Opening displacement series originate from either the origin or opposite end of the crack segment depending on its orientation. Opening displacement series equations emanating from the origin are written as a function of r. However, terms originating from the opposite end of the crack segment must be applied as powers to the $(a - r)$.

Wedge Series

The purpose of a wedge series, $W(r)$, is to capture singular stress or traction behavior induced by a wedge, of included material angle greater than 180°, created by crack kinking. Singular eigenvalues, ρ, from a wedge analysis [*30-32*] are used to create a variation of the power series. The value of ρ is a known eigenvalue, and there are either three or four real values for a given wedge that cause singular behavior in the stress field. These eigenvalues are 0 and 1 (to be accounted for in the polynomial series), and one or two values, $0 < \rho < 1$, depending on the angle. When two eigenvalues, $0 < \rho < 1$ exist, ρ_1 and ρ_2, a separate wedge series, must be included based on each eigenvalue. Eigenvalues, real or complex, which do not create singularities, are not included in the current analysis, and their effects are approximated by the higher-order terms of the power series.

The wedge series is written in equation form as

$$W(r) = c_{0\rho}\left(\frac{r}{a}\right)^{\rho} + c_{1\rho}\left(\frac{r}{a}\right)^{\rho+1} + c_{2\rho}\left(\frac{r}{a}\right)^{\rho+2} + \ldots + c_{n\rho}\left(\frac{r}{a}\right)^{\rho+n} \tag{4}$$

where the $c_{j\rho}$ are the weighting coefficients. To avoid unwanted mathematical singularities at the crack segment end opposite the kink, this series must be subjected to constraints that prohibit a displacement jump and slope of the opening profile at this far end. (Should they be relevant, these will be covered by a series originating at that end.) Applying these constraints reduces the number of weighting coefficients by two resulting in the final form of the wedge series as

$$W(r) = \sum_{j=0}^{n-2} c_{j\rho}\left(\left(\frac{r}{a}\right)^{\rho+j} - (n-j)\left(\frac{r}{a}\right)^{\rho+n-1} + (n-j-1)\left(\frac{r}{a}\right)^{\rho+n}\right) \tag{5}$$

where the equation in parentheses is considered a single term of the series. For the term corresponding to $j = 0$, the slope of the opening shape is infinite at the kink end, thus inducing a non-physical singularity in the traction at that point. Constraints relating the $c_{0\rho}$ coefficients between adjoining crack segments are applied to eliminate these unwanted singularities. Note that canceling out this singularity in the tractions does not remove the necessary singularity in the material at this location.

At every kink, a separate wedge series must be included along both adjoining segments that originates from the kink and extends outward along an individual crack segment. For material wedges with two singular eigenvalues, a wedge series must be included for each eigenvalue. Therefore, interior crack segments could conceivably be assigned up to four wedge opening displacement series. (If the material wedges on both ends of the crack segment had two singular eigenvalues each, then two series would be necessary originating from each end for a total of four series.) Note that different values of eigenvalues could be relevant to each end (when the kinks form different angles).

Polynomial Series

Polynomial series, $P(r)$, provide flexibility in manipulating the overall opening displacement shape, in addition to allowing for translation and rotation of wedges at kink locations (behaviors induced by the $\rho = 0$ and 1 eigenvalues respectively). Similar to the wedge series, the polynomial series is written in equation form as

$$P(r) = \sum_{j=0}^{n-2} c_{jp}\left(\left(\frac{r}{a}\right)^{j} - (n-j)\left(\frac{r}{a}\right)^{(n-1)} + (n-j-1)\left(\frac{r}{a}\right)^{n}\right) \tag{6}$$

Certain constraints must be implemented at the kink on the $c_{0\mathrm{p}}$ and $c_{1\mathrm{p}}$ weighting coefficients of the adjoining crack segments to eliminate non-physical jump and slope discontinuities respectively, which would otherwise induce traction singularities.

Higher order (non-singular) polynomial terms ($j = 2, 3, \ldots n-2$) are applied from the local origin of each crack segment, such that only one term of each power is assigned to every crack segment regardless of whether it is interior or exterior. However, the singular terms, r^0 and r^1, are applied in a slightly different manner. Since the polynomial terms r^0 and r^1 allow translation and rotation respectively of an upper wedge relative to a lower wedge at a kink, these terms must originate from kinks and emanate outward along both crack segments that join at the kink (Figure 4). Such apportioning leads to a situation where two of each of these singular terms are included for each interior crack segment, while only one of each term is necessary for exterior crack segments.

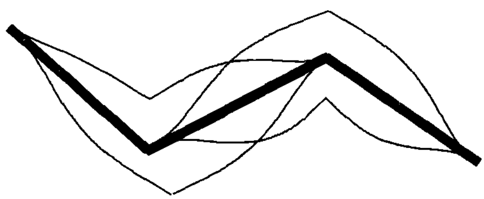

Figure 4 – *Opening Shapes Created by Assignment of r^0 Polynomial Terms*

Tip Series

Lastly, tip series, $T(r)$, incorporate crack tip behavior (Eq. 7). These series are only included in the opening displacement profile of exterior crack segments, since interior crack segments do not have a tip. The only singular tip term is the one that captures the square root singularity at a crack tip (the term represented by $j = 0$). To include higher order behavior at the crack tips, additional tip terms ($j = 1, 2, \dots n–2$) are introduced.

$$T(r) = \sum_{j=0}^{n-2} c_{jt} \left(\left(\frac{a-r}{a} \right)^{\frac{2j+1}{2}} - (n-j) \left(\frac{a-r}{a} \right)^{\frac{2(n-1)+1}{2}} + (n-j-1) \left(\frac{a-r}{a} \right)^{\frac{2n+1}{2}} \right) \quad (7)$$

Since these terms do not create any non-physical singularities, no additional constraints are required.

Examples

Accuracy of the method was evaluated by comparing to results of other researchers, and agreement was achieved in all cases studied [*15*]. Specific examples included a straight crack divided into three crack segments [*33*], and the symmetric crack with two kinks shown in Figure 5 [*34, 35*]. A comparison of results for this problem is presented in Tables 1 and 2. As a representative example, this crack was studied for a constant kink angle, $\theta = 60°$, and central crack segment length, $a = 1$. The angle of the unit loading, ϕ, and crack tip lengths, b, were varied. The stress intensity factors presented in the tables are dimensionless, since the parameters were normalized with respect to unit length. Results available in the literature provided only stress intensity factors at crack tips, so this parameter formed the basis of comparison. However, overall results with this method demonstrated rapid convergence in terms of weighting coefficients, stress intensity factors, and tractions along crack faces as induced by the computed opening displacement profiles.

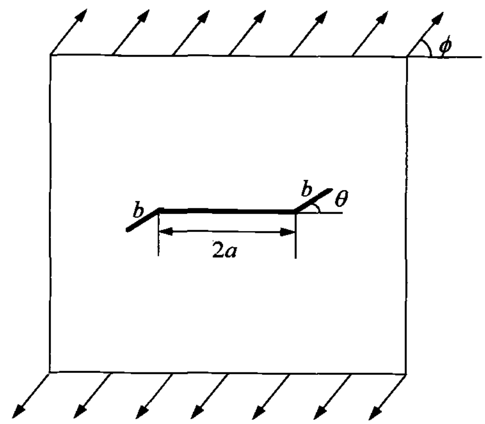

Figure 5 – *An Infinite Plate Containing a Crack with Two Kinks under Varying Loading*

Table 1 – *Comparison of Stress Intensity Factors for $\phi = 90°$*

	K_I		K_{II}	
b	[*34*]	Present Work	[*34*]	Present Work
0.10	0.8758	0.8708	0.8936	0.8970
0.20	0.8005	0.8100	0.9945	0.9949
0.60	0.7546	0.7531	1.2188	1.2194
1.0	0.7750	0.7732	1.3574	1.3581

Table 2 – *Comparison of Stress Intensity Factors for $\phi = 45°$*

	K_I		K_{II}	
b	[*34*]	Present Work	[*34*]	Present Work
0.10	-0.4208	-0.4227	0.5569	0.5561
0.20	-0.3885	-0.3890	0.5138	0.5138
0.60	-0.2730	-0.2737	0.3502	0.3503
1.0	-0.1821	-0.1827	0.2034	0.2034

Results from one specific parameter study are provided as an example. The configuration is a crack with two kinks (Figure 6). Stress intensity factors at crack tips are presented for varying values of θ and crack segment lengths, a_i. The crack is located in a linearly elastic, isotropic, homogeneous, and infinite plate loaded under far field unit biaxial loading. Although not presented, values of singularities at wedges, tractions along the crack faces, and weighting coefficients were calculated and exhibited convergence. While convergence was achieved for fewer degrees of freedom and number of points, 50 points were allocated along each crack segment and powers up to order 6 were included in all opening displacement series applied to each crack segment to fully capture all behavior. All stress intensity factors presented are dimensionless, since the parameters were normalized with respect to unit length.

Example 1: Varying θ and the Lengths of Crack Segments 1 and 3

The first case is a symmetric problem with the lengths of the exterior crack segments held equal to each other ($a_1 = a_3$). The length of the interior crack segment, a_2, was held fixed at unity, while the length of the exterior crack segments, a_1 and a_3, was varied. In addition, results were calculated for different values of the angle of the interior crack segment, θ. Results for stress intensity factors at the crack tips are presented graphically (Figure 7).

Example 2: Varying θ and the Length of Crack Segment 3

For the second case, the length of exterior crack segment 3, a_3, is varied, while the lengths of crack segments 1 and 2 are held equal to unity ($a_1 = a_2 = 1$). Results were again calculated for different values of the angle of the interior crack segment, θ. Results for stress intensity factors at the crack tips of segments 1 and 3 are presented graphically (Figures 8 and 9).

As expected in both examples 1 and 2, a smaller inclination of the middle crack segment and longer lengths of the exterior crack segments lead to a larger mode I stress intensity factor at the crack tips. Meanwhile, a larger angle and smaller lengths lead to a greater magnitude in the value of the mode II stress intensity factor.

Example 3: Varying θ and the Length of Crack Segment 2

The final case is a symmetric problem with the lengths of the exterior crack segments held equal to unity ($a_1 = a_3 = 1$). The length of the interior crack segment, a_2, was varied, and results were calculated for different values of the angle of this crack segment, θ. Results for stress intensity factors at the crack tips are presented graphically (Figure 10). As demonstrated by the figure, a smaller inclination and longer length of the middle crack segment lead to a larger mode I stress intensity factor at the crack tips. Meanwhile, a larger angle and longer length lead to a greater magnitude in the value of the mode II stress intensity factor.

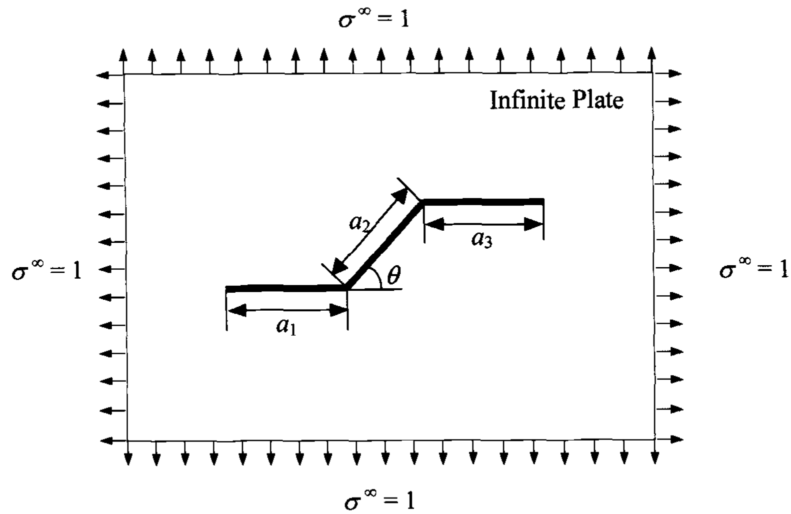

Figure 6 – *An Infinite Plate Containing a Crack with Two Kinks under Biaxial Loading*

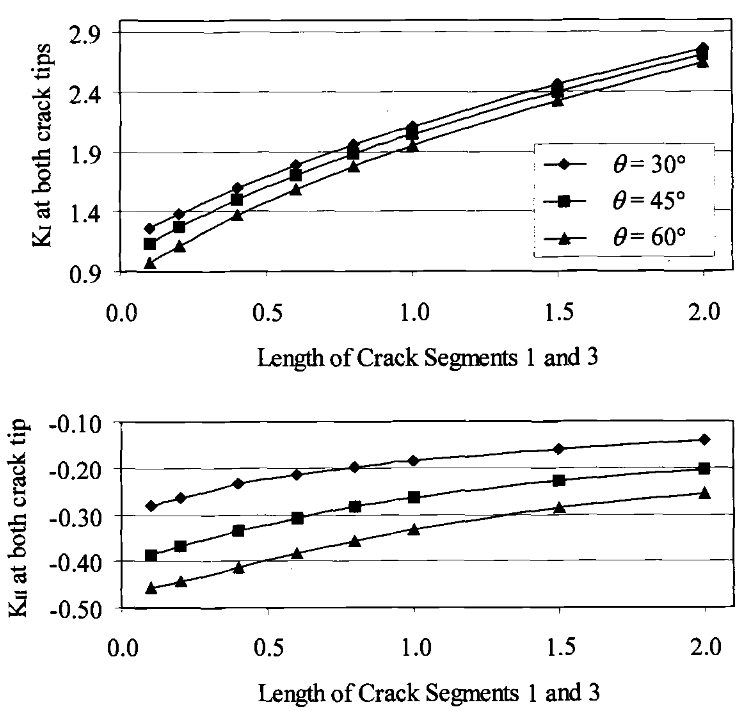

Figure 7 – *Mode I and II Stress Intensity Factors for Varying θ and $a_1 = a_3$*

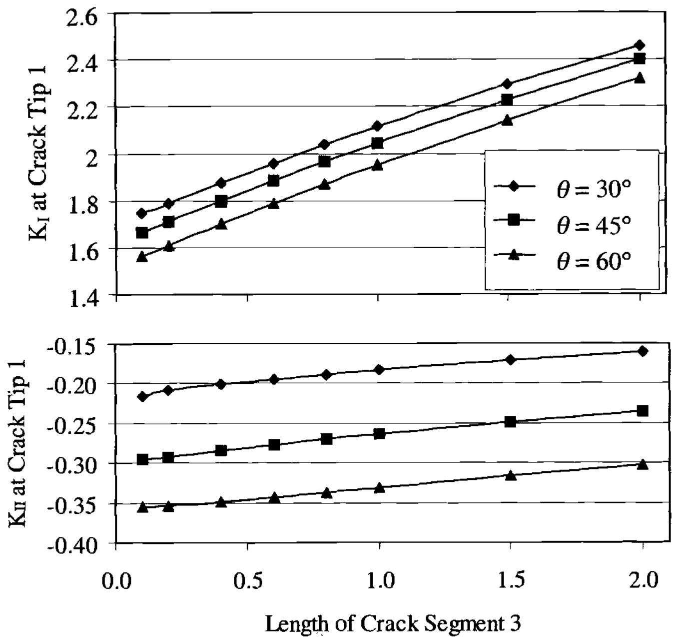

Figure 8 – *Mode I and II Stress Intensity Factors at Crack Tip 1 for Varying θ and a_3*

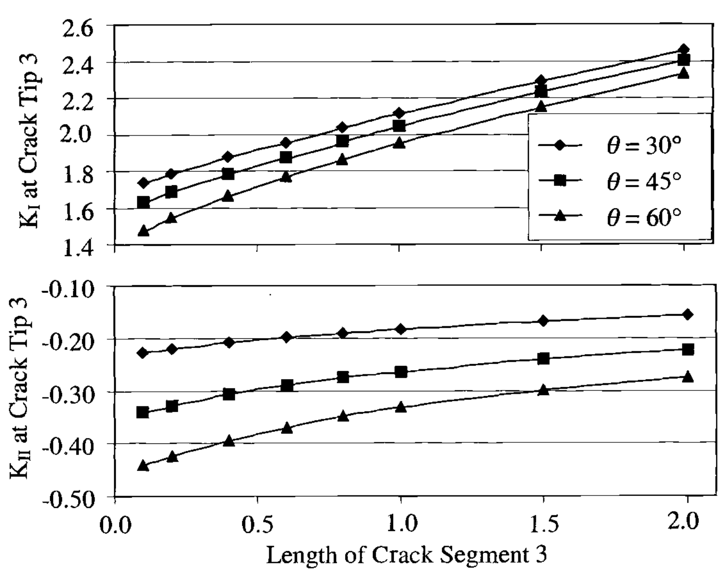

Figure 9 – *Mode I and II Stress Intensity Factors at Crack Tip 3 for Varying θ and a_3*

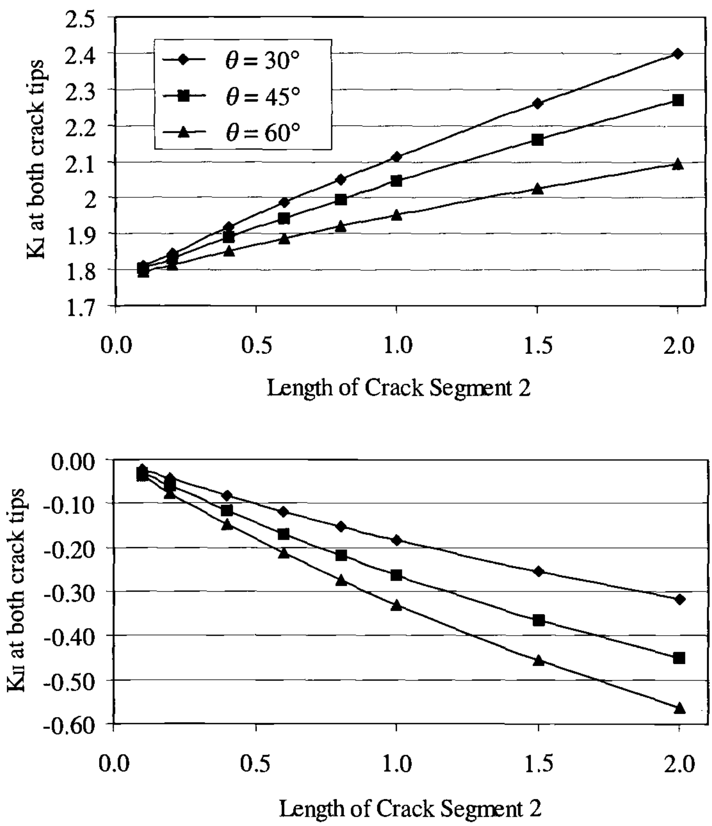

Figure 10 – *Mode I and II Stress Intensity Factors for Varying θ and a_2*

Conclusions

The method presented can be used to study kinked cracks of any configuration, orientation, and crack segment lengths. Cracks need not be symmetric, and any general loading conditions, including shear, can be applied. One advantage of this method is that singularities at wedge locations are computed as part of a routine analysis so that possible crack growth at these locations can be studied as well as at crack tips. In addition, results generated with this method for varying number of points and degrees of freedom exhibit stable convergence.

Interacting kinked cracks can also be analyzed with this method. While the coefficients and resulting opening displacement profiles will be different for interacting cracks than those for each crack existing alone, the traction free condition is applied in the same manner as for a single crack. Results have been obtained for two interacting V-shaped cracks and two interacting branched cracks [*15*].

Future Work

A straightforward extension of this research is to study cracks in a finite plate. This problem would be modeled as a finite, polygon-shaped plate embedded in an infinite plate. For example, a rectangular shaped finite plate would add four connected crack segments with four crack wedges of 270°. Any geometry with straight sides could be used to model the finite plate.

The current program environment does not prohibit overlap of crack faces. Interpenetrating crack surfaces can be prevented through displacement and traction criteria, and a friction law applied. Also, crack tip plasticity behavior could be easily included.

Other practical applications of this method include the study of a deviation of infinitesimal growth from a main crack, cracking along grain boundaries in heterogeneous materials, and cracking along bimaterial interfaces. Furthermore, this method is directly applicable to two cases of cracking in composite materials. The problem of crack-bridging by fibers could be studied by modeling the effects of the fibers as point force loads acting on the crack faces. And, the problem of cracks that induce debond between the fiber and matrix could be investigated by modeling the cracks and debond region as H-shaped cracks.

Acknowledgment

This work was performed under a fellowship from the American Association of University Women.

References

[*1*] Bilby, B. and Eshelby, J., "Dislocations and the Theory of Fracture," *Fracture, an Advanced Treatise Vol. I*, ed. H. Liebowitz, Academic Press, New York, 1968, pp. 99-182.

[*2*] Chen, C.-H., Chang, R.-R., and Jeng, P.-H., "On the Fiber-Bridging of Cracks in Fiber-Reinforced Composites," *Mechanics of Materials*, Vol. 20, 1995, pp. 165-181.

[*3*] Collins, W. D., "Some Coplanar Punch and Crack Problems in Three-Dimensional Elastostatics," *Proceedings of the Royal Society*, Vol. A274, 1963, pp. 507-526.

[*4*] Crouch, S. L., "Solution of Plane Elasticity Problems by Displacement Discontinuity Method," *International Journal of Numerical Methods in Engineering*, Vol. 10, 1976, pp. 301-343.

[*5*] Gol'dstein, R. V. and Salganik, R. L., "Brittle Fracture of Solids with Arbitrary Cracks," *International Journal of Fracture*, Vol. 10, 1974, pp. 507-523.

[*6*] Han, X. and Wang T., "Interacting Multiple Cracks with Complicated Crack Surface Conditions," *International Journal of Fracture*, Vol. 82, 1996, pp. R53-R57.

[*7*] Hu, K. and Chandra, A., "Interactions Among General Systems of Cracks and Anticracks: An Integral Equation Approach," *Journal of Applied Mechanics*, Vol. 60, 1993, pp. 920-928.

[*8*] Hu, K., Chandra, A., and Huang, Y., "Multiple Void-Crack Interaction," *International Journal of Solids and Structures*, Vol. 30, No. 11, 1993, pp. 1473-1489.

[*9*] Lam, K. and Phua, S., "Multiple Crack Interaction and Its Effect on Stress Intensity Factor," *Engineering Fracture Mechanics*, Vol. 40, No. 3, 1991, pp. 585-592.

[*10*] Li, S. and Mear, M., "Singularity-Reduced Integral Equations for Displacement Discontinuities in Three-Dimensional Linear Elastic Media," *International Journal of Fracture*, Vol. 93, 1998, pp. 87-114.

[*11*] Melin, S., "Why Do Cracks Avoid Each Other?" *International Journal of Fracture*, Vol. 23, 1983, pp. 37-45.

[*12*] Burton, J. K. and Phoenix, S. L., "Superposition Method for Calculating Singular Stress Fields at Kinks, Branches and Tips in Multiple Crack Arrays," *International Journal of Fracture*, Vol. 102, 2000, pp. 99-139.

[*13*] TerMaath, S. C. and Phoenix, S. L., "Investigation of a New Analytical Method for Treating Kinked Cracks in a Plate," *Fatigue and Fracture Mechanics: 31st Volume, ASTM STP 1389*, G. R. Halford and J. P. Gallagher, Eds., American Society for Testing and Materials, West Conshohocken, PA, 2000, pp. 331-347.

[*14*] Hills, D., Kelly, P., Dai, D., and Korsunsky, A., *Solution of Crack Problems: The Distributed Dislocation Technique*, Kluwer Academic Publishers, Dordrecht, 1996.

[*15*] TerMaath, S. C., "A Two-Dimensional Analytical Technique for Studying Fracture in Brittle Materials Containing Interacting Kinked and Branched Cracks," PhD Dissertation, Cornell University, New York, 2000.

[*16*] Bilby, B. A. and Cardew, G. E., "The Crack with a Kinked Tip," *International Journal of Fracture*, Vol. 11, 1975, pp. 708-712.

[*17*] Karihaloo, B., Keer, L., and Nemat-Nasser, S., "Crack Kinking under Nonsymmetric Loading," *Engineering Fracture Mechanics*, Vol. 13, 1980, pp. 879-888.

[*18*] Karihaloo, B. L., Keer, L. M., Nemat-Nasser, S., and Oranratnachai, A., "Approximate Description of Crack Kinking and Curving," *Journal Of Applied Mechanics*, Vol. 48, 1981, pp. 515-519.

[*19*] Kharpkov, A., "The First Basic Problem for a Notch at the Apex of an Infinite Wedge," *International Journal of Fracture Mechanics*, Vol. 7, No. 4, 1971, pp. 373-382.

[*20*] Blanco, C., Martinez-Esnaola, J.M., and Atkinson, C., "Analysis of Sharp Angular Notches in Anisotropic Materials," *International Journal of Fracture*, Vol. 93, 1998, pp. 373-386.

[*21*] Blanco, C., Martinez-Esnaola, J.M., and Atkinson, C., "Kinked Cracks in Anisotropic Elastic Materials," *International Journal of Fracture*, Vol. 93, 1998, pp. 387-407.

[*22*] Hayashi, K. and Nemat-Nasser, S., "Energy Release Rate and Crack Kinking under Combined Loading," *Journal of Applied Mechanics*, Vol. 48, 1981, pp. 520-524.

[*23*] Chatterjee, S. N., "The Stress Field in the Neighborhood of a Branched Crack in an Infinite Sheet," *International Journal of Solids and Structures*, Vol. 11, 1975, pp. 521-538.

[*24*] Cotterell, B. and Rice, J. R., "Slightly Curved or Kinked Cracks," *International Journal of Fracture*, Vol. 16, No. 2, 1980, pp. 155-169.

[25] Bogy, D. B., "On the Plane Elastostatic Problem of a Loaded Crack Terminating at a Material Interface," *Journal of Applied Mechanics*, Vol. 38, 1971, pp. 911-918.
[26] He, M.-Y. and Hutchinson, J. W., "Kinking of a Crack out of an Interface," *Journal of Applied Mechanics*, Vol. 56, 1989, pp. 270-278.
[27] Niu, J. and Wu, M. S., "Strong Interactions of Morphologically Complex Cracks," *Engineering Fracture Mechanics*, Vol. 57, 1997, pp. 665-687.
[28] Hirth, J. and Lothe, J., *Theory of Dislocations*, New York, John Wiley & Sons, 1982.
[29] Lardner, R., *Mathematical Theory of Dislocations and Fracture*, Great Britain, University of Toronto Press, 1974.
[30] Williams, M. L., "Stress Singularities Resulting from Various Boundary Conditions in Angular Corners of Plates in Extension," *Journal of Applied Mechanics*, Vol. 19, 1952, pp. 526-528.
[31] Timoshenko, S. P. and Goodier, J. N., *Theory of Elasticity*, Third Edition, McGraw-Hill, New York, 1970.
[32] Barber, J. R., *Elasticity*, Kluwer Academic Publishers, Boston, 1992.
[33] Irwin, G. R., "Analysis of Stresses and Strains near the End of a Crack Transversing in a Plate," *Journal of Applied Mechanics*, Vol. 24, 1957, pp. 361-364.
[34] Kitagawa, H. and Yuuki, R., "Stress Intensity Factors for Branched Cracks in a Two-Dimensional Stress State," *Transactions of the Japan Society of Mechanical Engineers*, Vol. 41-346, 1975, pp. 1641-1649.
[35] Vitek, V., "Plane Strain Stress Intensity Factors for Branched Cracks," *International Journal of Fracture*, Vol. 13, 1977, pp. 481-501.

J. A. Wang[1], K. C. Liu[1], and D. E. McCabe[1]

An Innovative Technique for Measuring Fracture Toughness of Metallic and Ceramic Materials

Reference: Wang, J. A., Liu, K. C., and McCabe, D. E., "**An Innovative Technique for Measuring Fracture Toughness of Metallic and Ceramic Materials,**" Fatigue and Fracture Mechanics: 33rd Volume, *ASTM STP 1417*, W. G. Reuter and R. S. Piascik, Eds., ASTM International, West Conshohocken, PA, 2002.

Abstract—A new method is introduced for measuring fracture toughness, K_{IC}, of materials ranging from metallic alloys to brittle ceramics. A valid value of K_{IC} is determined using a round-rod specimen having a grooved spiral line with a 45° pitch. When this uniquely configured specimen is subjected to pure torsion, an equibiaxial tensile/compressive stress-strain state is created to effectively simulate that of conventional test methods using a compact-type specimen with a thickness equivalent to the full length of the spiral line. K_{IC} values are estimated from the fracture load and crack length with the aid of a 3-D finite element analysis. K_{IC} of a mullite ceramic material yields 2.205 MPa$\sqrt{m}$, which is 0.2% higher than the vendor's data. K_{IC} of A302B steel is estimated to be 55.8 MPa$\sqrt{m}$, which shows higher than compact tension (CT) test value by ~2%. 7475-T7351 aluminum yields 51.3 MPa$\sqrt{m}$, which is higher than vendor's value in the TL orientation by ~0.8% and higher than 0.5T-CT value by 6%. Good agreement between the K_{IC} values obtained by different methods indicates the proposed method is theoretically sound and experimental results are reliable.

Keywords—fracture toughness, torsion bar testing, spiral notch test, size effect, mixed mode fracture

Introduction

The testing method using conventional compact tension specimens or their variations having equivalent configurations has a strong theoretical basis for use in determining fracture toughness, K_{IC}. However, the downside of the method is specimen size effect. Valid test result according to ASTM Test Method for Plane-Strain Fracture Toughness of Metallic Materials (E399), requires that both specimen thickness, B, and crack length, *a*, exceed $2.5(K_{IC}/\sigma_{YS})^2$, where σ_{YS} is the 0.2% offset yield strength of the material for temperature and loading rate of the test. If it is not possible to make a

[1] Research Scientist, Oak Ridge National Laboratory, TN 37831.

specimen from the available material that meets the criterion, then it is not possible to make a valid K_{IC} measurement according to this method.

Use of small specimens for K_{IC} measurement is critically important for material development due to the limited volume or, for example, nuclear reactor pressure vessel safety surveillance because of the space limitation inside the reactor vessel. A recent exploratory study [1] demonstrated that the specimen size effects can be virtually eliminated using a cylindrical specimen subjected to pure torsion for K_{IC} measurements.

Background

A valid K_{IC} value must be measured in the stress and strain fields conforming to the requirements of the fracture mechanics theory. Figure 1 shows two CT specimens having the same profile but different thickness. In theory, an ideal plane strain condition is achieved for a valid K_{IC} measurement if the specimen with t_I has an infinite thickness. This is impractical; however, a reasonably accurate value can be obtained and acceptable if the requirements cited in ASTM Standard E399 are met. A violation of the plane strain condition in the critical stress zone near the crack tip of the thin specimen will not yield a valid K_{IC} value but a critical stress intensity factor, K_c, which is not equal to the K_{IC}.

It is of some interest to point out that the most important information with regard to the stress and strain distributions needed to determine K_{IC} is densely condensed around the crack tip zone, an extremely small area compared to the rest of the area. The vast area remote from the crack tip is mainly used to maintain uniform far fields of stress and strain and for gripping of the specimen. A cylindrical specimen under pure torsion will generate an equibiaxial tension/ compression stress field on the orthogonal, 45°-pitch, helical canoids, regardless of the size of the specimen diameter. Thus a plane strain condition is maintained on every plane normal to the helix.

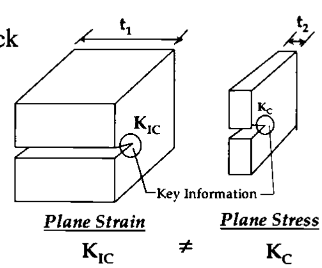

Figure. 1. *Specimen size effect.*

Since the critical inner stress and strain fields around the crack tip is extremely small, a small-size specimen having a diameter 2 to 3 times larger than the plastic process zone will suffice in theory for fracture toughness testing.

A method [2] was proposed previously for K_{IC} measurement under torsion, using a round specimen with a half penny- shaped crack making a 45° angle with the specimen axis. This was basically a variation of a tensile testing with a half penny shaped crack perpendicular to the tensile force. The latter type was widely used in crack growth studies.

A new test method is described, using a round-rod specimen having a V-grooved spiral line with a 45° pitch (Fig. 2a). When the specimen with no spiral line is subjected to pure torsion, uniform stress and strain fields are axisymmetrical and constrained along the axis. When the grooved specimen (Fig. 2b) is sectioned into segments perpendicular to the groove line, defined as the Z-axis, each of the segments can be viewed as a CT specimen with a notch as illustrated in Fig. 2c. Since all the imaginary CT specimens are bonded side-by-side seamlessly, the compatibility condition is automatically satisfied in every XY-plane which remains in plane before and after application of torsion loading.

In the absence of the V-groove, the stress state of a generic element in a round bar under pure torsion can be depicted as shown in Fig. 2d, having the XZ-plane in tension and XY-plane in compression of equal magnitude. When a notch is introduced (Fig. 2c), the lateral sides of the wedge along the notch opening line will not contract because the stress in shaded area "A" is relieved. The disappearance of the tensile stress along the notch opening will shift the burden to the root of the notch, where a sharp rise will occur in the tensile σ_{yy} component. Since the unstressed area "A" does not contract in the Z-axis direction, while the material ahead of the notch root has a propensity to contract, a tensile stress field will develop in the σ_{zz} component in the root area of the notch. The transverse tensile stress σ_{xx} developing ahead of the notch front is due to the radial constraint. Therefore, a triaxial tensile stress field will evolve in the neighborhood of the notch root area (see Fig. 2e). This observation has been experimentally and analytically validated and will be discussed in later sections. The stress and strain fields in any cross section along the axis of the round specimen under pure torsion are the same even though having the groove. Thus, the constraint effect (size effect), normally a concern in compact type specimens, is eliminated. Therefore, this procedure is suitable for miniature specimen testing. Commonly, materials fracture in mixed modes rather than in a single mode; and in many cases, a combination of mode I and mode III may be more detrimental than mode I alone [3]. This method enables any combined mixed-mode by varying the pitch angle.

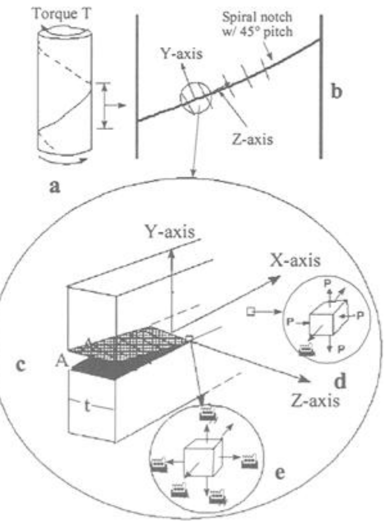

Fig. 2. *Stress fields of a torsion bar.*

Experimental

Figure 3 shows the geometry of the specimen used in K_{IC} measurements of metallic alloys. The specimen has a uniform gage section on which a complete lobe of spiral V-groove with a pitch of 45° is shown for mode I testing. The pitch angle can be tailored for a mixed mode test. The squared end

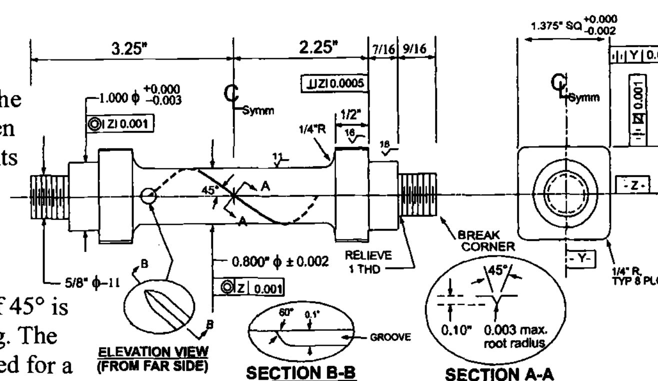

Fig. 3. *A302B specimen configuration.*

sections were made to transmit torque and the threaded ends for zero axial load control. The size of the test specimen is optional depending on the availability of the material. Specimens were fabricated from a 2-in. plate of 7475-T7351 aluminum alloy and a block of A302B steel. The reader is referred to reference [1] for experimental details and test results of 7475-T7351 aluminum.

Ceramic materials are usually available in a small volume, and small round rods are most common. Mullite ceramic material was selected in this study. A straight mullite ceramic rod, having each end bonded with epoxy adhesive to a square-ended metal holder of the same design used in the metal specimens, was used in the experiment. Due to the brittle nature of ceramic materials, only a shallow spiral notch is required in this case.

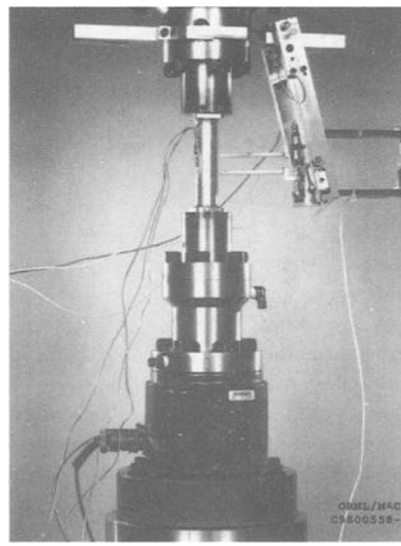

Fig. 4. *Experimental set-up*

Torsion tests were performed on a closed-loop controlled, electro-hydraulic, biaxial testing system shown in Fig. 4. Shear strain was measured using a biaxial strain extensometer (on the right of the specimen shown in Fig. 4) and a Rosette strain gage for cross calibration. Pure torsion was achieved with a zero axial force in control. Precracking for metallic specimens was accomplished with cyclic torsion using Haver sine wave form. The maximum torque used in precracking varies with materials and must be determined experimentally. In the case of A302B steel, 60~80% of the torque that generates the shear stress of 300 MPa around the specimen diameter will suffice, yielding a ΔK in the range of 20~25 $MPa\sqrt{m}$. We did not use compliance to monitor the fatigue crack growth; however, we used an approximate compliance function to estimate crack growth under loading and unloading sequence in torsion. To this date the close form solution for torsion compliance has not been developed as yet. An exploratory procedure by estimating load-displacement (or stress-strain) slope change at different phase of fatigue loading was adopted to estimate fatigue crack growth. The fatigue crack growth was measured by postmortem examination. Precracking was not needed for the mullite specimen.

Experimental Results for Mullite Ceramic Specimens

Mullite specimens were made of a round rod, having a uniform gage section of 17-mm diameter and 50-mm gauge length. A mullite specimen having a spiral V-groove with a depth of 0.5-mm was tested. The specimen (Fig. 5) failed at 49.67 N· m torque at room temperature. Postmortem examination indicates that the failure mode is brittle fracture. The K_{IC} was estimated as 2.205 MPa$\sqrt{m}$ from the torsion test and reported as 2.20 MPa$\sqrt{m}$ from vendor's data.

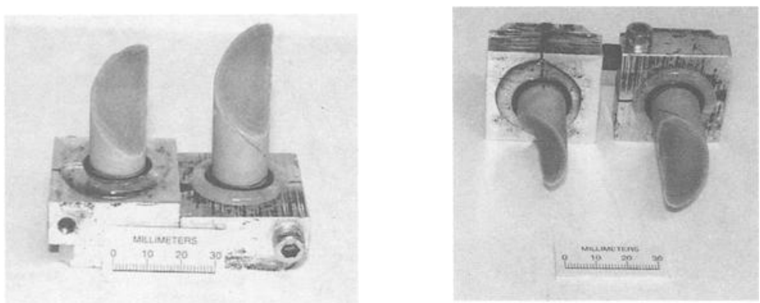

(a) front view (b) side view

Fig. 5. *The broken mullite ceramic specimen.*

Experimental Results For A302B Steel Specimens

The A302B specimen (Fig. 3) has a uniform gage section of 20.3-mm diameter and 76.2-mm gauge length. A A302B specimen having a spiral V-groove with a depth of 1.9-mm was tested. An exploratory fatigue precrack procedure was used to control crack growth with reference to the change in slope of the load-displacement curves. The specimen (Fig. 6) fractured at 519.7 N· m torque at room temperature. Test results obtained from the strain gage and biaxial extensometer are shown in Figs. 7a and 7b, respectively. Postmortem examination indicates that the final failure mode is brittle fracture.

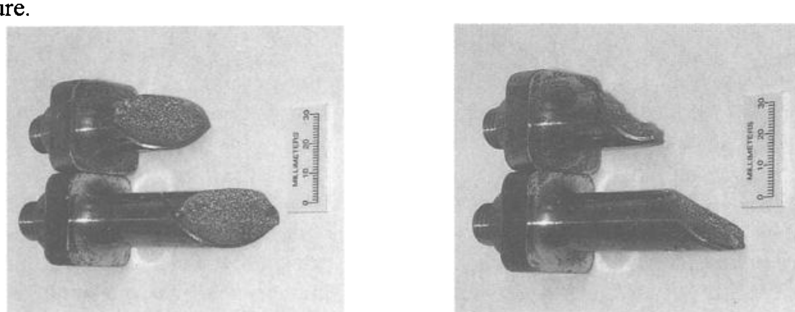

(a) front view (b) side view

Fig. 6. *The broken A302B specimen with 1.9-mm deep spiral V-notch.*

When a circular bar is under pure torsion, the neutral axis coincides with the central axis of the bar. Under cyclic torsion, mode I crack propagates perpendicularly toward the central axis due to axisymmetric plane constraint. It is of interest to note that the stress fields at the opposite ends of a diameter (Fig. 2a) are 90° out of phase. Since

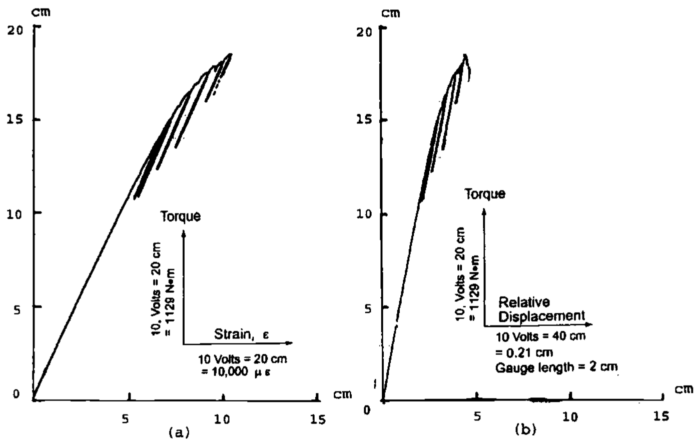

Fig. 7. Plot of torsion test results from (a) load cell and strain gauge, and (b) load cell and biaxial extensometer.

the stress acting on the XZ-plane (Fig. 2c) at the crack tip is in tension, the stress acting in the same direction at the diametrically opposite end will be in compression. Since the situation is analogous to the stress distribution in a bend beam, the crack extension under the partial unloading/reloading sequence was estimated utilizing the following equation [4] developed for three point bending test:

$$\Delta a_i = \Delta a_{i-1} + \left(\frac{b_{i-1}}{\eta_{i-1}}\right)\left(\frac{C_i - C_{i-1}}{C_{i-1}}\right), \tag{1}$$

where $(C_i - C_{i-1})/C_{i-1}$ is the rate change in elastic compliance, C_i represents the elastic compliance of the loading curve of applied torque versus strain measured either from the strain gage or biaxial extensometer. The initial ligament, b_0, is equal to the diameter less the notch depth and fatigue precrack. η_i is preset to 2. The crack extension occurring during the cyclic torsion was calculated to be 0.33-mm.

The total crack length prior to final brittle fracture was estimated as 7.62 mm. Away from the ends of the groove line, the fatigue crack length is practically uniform over the gage length. In theory sharp precrack of a homogeneous material should be uniform over the full grooved line except the very ends. However, only 60% is discernible. The mode I fracture toughness was estimated to be 55.8 MPa$\sqrt{m}$.. Results of tests on the standard CT specimens made from the same A302B stock yielded an average K_{IC} of 54.9 MPa$\sqrt{m}$ in the TL orientation.

Theoretical Basis of Methodology

Development of Finite Element Models and Analyses

PATRAN was used to create three dimensional finite element meshes and ABAQUS was used for analysis. Since the specimen is uniformly loaded in torsion from end to end, a slice of the gage section was modeled and analyzed with appropriate boundary conditions. Prismatic quadratic isoparametric singular elements adjacent to the crack tip are modified to facilitate the computational flexibility in linear elastic and non-linear elastic-plastic fracture mechanics analyses. In the former, the nodes at the crack tip are constrained to have the same displacement in order to embody the $r^{-1/2}$ singularity. However, in the case of perfect plasticity, the nodes at the crack tip are free to displace independently from each other, resulting in inverse ($1/r$) singularity at crack tip, and blunting of the crack tip is obtained during loading [5-7].

Investigation of Specimen Size Effects for Torsion Bar Testing

Larsson and Carlsson [8] demonstrate that in order to characterize the crack tip fields and plastic zone size occurring uniquely in small-scale yielding conditions, the boundary layer model must include the second term (T-stress) of the Williams expansion [9] as well as the stress intensity factor. The magnitude of T-stress varies with remotely applied stress, and geometry dependence is best indexed by a non-dimensional geometry factor, β, known as the biaxiality factor which has the form,

$$\beta = \frac{T\sqrt{\pi a}}{K} \tag{2}$$

Due to the very fine mesh required to determine the T-stress, especially in a three-dimensional model, it requires a very large computing power. Thus, the following two simplified approaches were adopted in size effect study. Kirk, Dodds and Anderson [10] show the effect of finite size on opening mode stress, σ_{yy}, near the crack tip at a constant normalized distance $R = r/(J/\sigma_0)$ ahead of the crack as

$$\frac{\sigma_{yy}}{\sigma_0} = \sum_{i=0}^{n} D_i \left(\frac{\beta K}{\sigma_0 \sqrt{\pi a}} \right)^i \tag{3}$$

where, D_i are the fitting coefficients for a particular set of finite element results and σ_0 is the reference stress. For $\beta > 0$ indicating highly constrained, Eq. 3 predicts a continuous increase of normalized opening mode stress with increasing load. This approach was successfully applied in size effect study for 7475-T7351 aluminum alloy, the reader is referred to refrence [1].

Al-Ani and Hancock [11] suggest that the simplest and most direct method of calculating the biaxiality parameter and, in turn, T-stress is by inspection of the displacement field associated with the crack tip. On the crack flanks, the displacement field can be written as

$$u = -(1-\nu^2)\frac{\beta K}{E\sqrt{\pi a}}r \tag{4}$$

This allows the biaxiality parameter to be determined directly by inspection of the asymptotic displacement given by Eq. 4.

To apply the boundary layer formulation in 3-D, it is essential that the 2-D displacement field still prescribes the traction along the boundary. Yongyuan and Guohua

[12] stated that for a 3-D blunt crack with a small curvature the stress and displacement are the same as those of a 2-D notch under plane strain condition. Henry and Luxmoore [13] show that in 3-D analysis the biaxiality factor is mostly affected by the stress parallel to the crack flank. Thus, the two approaches formulated in Eqs. 3 and 4 are also valid in the three-dimensional case, and are utilized to determine the constraint effect for the specimen configuration and loading conditions.

Non-Coplanar Crack Propagation Orientation

In many practical situations structures are subjected to a combination of both shear and tensile/compression loading, leading to a mixed-mode fracture. Three criteria are proposed for non-coplanar crack growth under mixed mode loading. The first is based on the maximum principal stress by Erdogan and Sih [14] and the second on the strain energy density factor proposed by Sih [15]. The former postulates that a crack will propagate in a direction perpendicular to the maximum principal stress. The third criterion is based on the energy release rate method [16]. It is postulated that the branch crack propagates in the direction that causes the energy release rate at a maximum, and that initiation occurs when the value of this energy release rate reaches a critical value. This postulate yields results identical to that of the maximum principal stress theory.

The strain energy density criterion [17] states that crack growth takes place in the direction of minimum strain energy density factor S. The 3-D energy density factor can be written [18] as

$$S = a_{11} K_I^2 + 2a_{12} K_I K_{II} + a_{22} K_{II}^2 + a_{33} K_{III}^2 \quad , \tag{5}$$

where, the stress intensity factors, K_I K_{II}, and K_{III} are evaluated with singular prismatic elements and are shown in reference [5, 19], and

$$\begin{aligned} a_{11} &= \frac{1}{16\mu}[(3-4\nu-\cos\theta)(1+\cos\theta)], \quad a_{12} = \frac{1}{8\mu}[\sin\theta(\cos\theta-1+2\nu)], \\ a_{22} &= \frac{1}{16\mu}[4(1-\nu)(1-\cos\theta)+(3\cos\theta-1)(1+\cos\theta)], \quad a_{33} = \frac{1}{4\mu} \quad . \end{aligned} \tag{6}$$

The crack growth occurs when

$$S^* = S_{cr} = \frac{1-2\nu}{4\mu} K_{IC}^2 \tag{7}$$

Thus K_{IC} can be written as

$$K_{IC} = \sqrt{\left(\frac{4\mu}{1-2\nu}\right)\left(a_{11} K_I^2 + 2a_{12} K_I K_{II} + a_{22} K_{II}^2 + a_{33} K_{III}^2\right)} \ , \ at\ \theta = \theta_0 \quad . \tag{8}$$

Mixed Modes J-Integral Evaluation

Irwin [19] shows that the stress intensity factor K and the strain energy release rate G are related. For plane strain mode I, the energy release rate G_I can be written as

$$G_I = \frac{K_I^2(1-\nu^2)}{E}. \tag{9}$$

and for mode II and mode III as,

$$G_{II} = \frac{K_{II}^2(1-\nu^2)}{E} \quad , \quad and \quad G_{III} = \frac{K_{III}^2(1+\nu)}{E} \quad . \tag{10}$$

For a mixed mode of fracture, the total energy release rate is written as

$$G = G_I + G_{II} + G_{III} \quad \textbf{(11)}$$

For a linear elastic material, G can also be related to J-integral as

$$J = G \quad \textbf{(12)}$$

For a 2-D mixed mode problem, Ishikawa, Kitagawa and Okamara [20] show that it is possible to decouple the J-integral into mode I and mode II components. This is done by separating the stress, strain, traction, and displacement fields analytically into mode I and mode II components within a symmetric mesh region in the neighborhood of the crack tip. The mode III is normal to and therefore independent of the mode I and II. Based on the above observations, and if the local coordinates coincide with the principal stresses, J-integral can be written as

$$J = J_I + J_{II} + J_{III} \quad \textbf{(13)}$$

For a linear elastic fracture mechanics problem in plane strain, J_i can be written as

$$J_I = \frac{(1-\nu^2)\,K_I^{\,2}}{E}, \quad J_{II} = \frac{(1-\nu^2)\,K_{II}^{\,2}}{E}, \quad J_{III} = \frac{(1+\nu)\,K_{III}^{\,2}}{E}. \quad \textbf{(14)}$$

Since the J integral is an energy approach, an elaborated expression of the crack tip singular fields is not necessary. This is due to the small contribution that the crack-tip field makes relative to the total J (i.e., strain energy) of the body. The J-integral is calculated using the *CONTOUR INTEGRAL of ABAQUS, which is based on the domain integral method.

3-D Configuration of Finite Element Model (FEM) Used in Analytical Analyses

A global and two local Cartesian Coordinate systems depicted in Fig. 8a are used to define the orientations of the specimen and a small imaginary cylinder centered at the spiral crack front. The first local coordinate system is located at the lower end of the crack front and the second one is located at the mid-length of the crack front. The XY plane of the two local coordinates is normal to the crack front. Since the specimen is uniformly twisted along the entire length, it is postulated that the crack propagates in the XZ-plane toward the center axis of the specimen (see Fig. 8b). Postmortem examination of fracture surfaces also supports the assumption.

Fracture Toughness Evaluation

FEM Analysis for Mullite Specimens

Material properties of mullite and FEM used in the analysis are tabulated in Table 1. Cursory verifications of crack propagation orientation were done by visual inspection. Results appear to support the assumptions, and the selection of the FEM seems appropriate.

Throughout most gage length, a uniform stress and strain fields exist in the test sample under pure torsion loading. However, only a portion of the gage length of test sample was used in FEM model. Thus, with simulated boundary conditions, the stress and strain distributions under pure torsion are not entirely uniform throughout the model sample, but the middle portion is reasonably uniform. Since a zero axial load is maintained during torsion, the specimen is permitted to deform freely along the axis. For all practical purposes, this condition can be simulated for the middle layer elements of FEM, and was used as the FEM boundary condition.

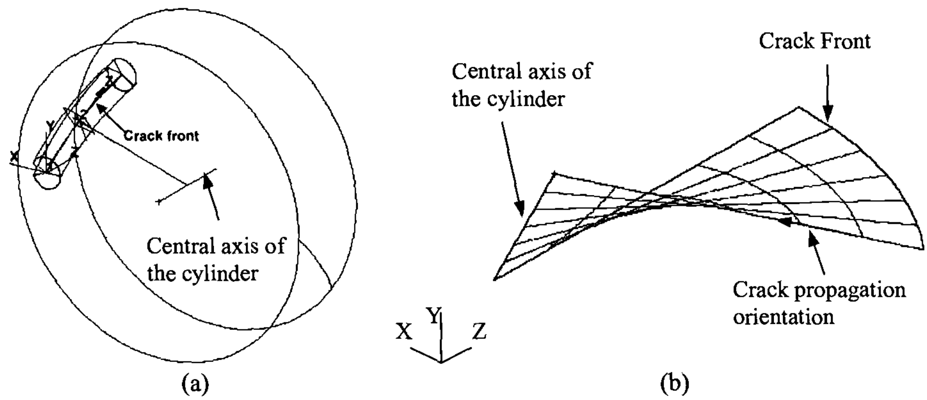

Fig. 8. *(a) 3-D sketch of proposed specimen configuration. The sketch indicates that X-axis of local coordinate 2 is the crack propagation orientation at the middle of the crack front. (b) 3-D sketch of fracture surface topology based on the assumption that the crack propagation orientation is perpendicular and point to the central axis of the cylinder.*

Table 1. *Material properties and criteria used in FEM analysis*

	Material Property (RoomTemp)	FEM*	Loading Condition
Mullite Ceramic	Flexural strength = 186 MPa, E = 155 GPa, $\nu = 0.25$, $\rho = 2800$ kg/m^3, Vendor $K_{IC} = 2.2$ MPa$\sqrt{m}$,	17-mm dia. X 7.6-mm long circular bar** smallest mesh size = 0.0127-mm	Fracture load: end rotation= 0.000702 rad
A302B Steel	Yield stress (tran.) = 500 MPa, Yield stress (long.) = 533 MPa UTS = 682 MPa, E = 206.8 GPa, $\nu = 0.30$, CT K_{IC} (TL) = 54.9 MPa$\sqrt{m}$.	20.3-mm dia. X 7.6-mm long circular bar smallest mesh size = 0.254 mm	Fracture load: end rotation= 0.00468 rad..
Boundary Condition	One end of the short bar constrained with zero displacements in X and Y axes of the global coordinates, and the other end free.		

*3-D 20-node quadratic brick element with reduced integration (3D20R) used in the FEM.
**0.5-mm deep Spiral V-groove with a 45°-pitch, zero root radius.

The torque applied to the specimen was calculated according to the following equation,

$$Torque_{END} = \sum_{node\ i}^{n} \left(R_y * x - R_x * y \right)_{node\ i} \tag{15}$$

where R_x and R_y are the reaction forces at the fixed end of FEM in the X-axis and Y-axis directions, respectively, deriving from the LEFM for the fracture loading condition; x and

y are the x-and y-components of the distance between the node i and the center of the circular bar, respectively.

The finite element mesh is shown in Fig. 9. The end rotation applied to the FEM at the fracture load of 49.67 N-m was determined by iterative process using Eq. 15. The rotation at the fracture load is estimated to be 0.0007 rad and the J value to be 29.38 N/m at the crack tip. The 3-D FEM analysis indicated that a triaxial tensile state is maintained in front of the crack tip up to the third element from the crack tip. Based on Eq. 4, an evaluation of β along the crack flanks can be accomplished using the displacement field in the vicinity of the crack tip. Results indicate β is positive and T-stress is positive also, indicating that the high constraint state was achieved.

At the fracture load, the J value at the crack tip in the mid-layer is estimated as 29.38 N/m. Predicted stress intensity factors, according to Barsoum's COD formulation [5], for the corner node at the crack front of mid-layer, are listed below:

$$K_I = 2.098\, MPa\sqrt{m}\ ,\quad K_{II} = 0.0368\, MPa\sqrt{m}\ ,\quad K_{III} = 0.0403\, MPa\sqrt{m}\ .$$

Corresponding J_i are listed below:

$$J_I = 26.62\ \ N/m\,,\quad J_{II} = 0.008\ \ N/m\,,\quad J_{III} = 0.013\ \ N/m\,.$$

The above evaluation indicates 99.9% of the J value is contributed by mode I. According to Eq. 13, the estimate J value is 26.65 N/m, which differs from the evaluated J value 29.38 N/m, from the contour integral, by 9%. This discrepancy may be due to the mesh dependence of COD approach, whereas J-integral value is not so sensitive to the FEM mesh, and seem to be more reliable.

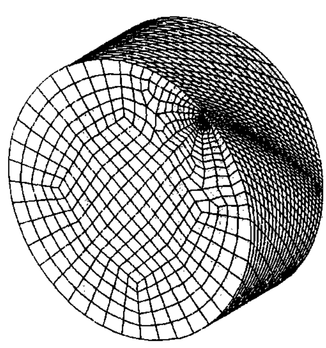

Fig. 9. *3-D FEM mesh for mullite.*

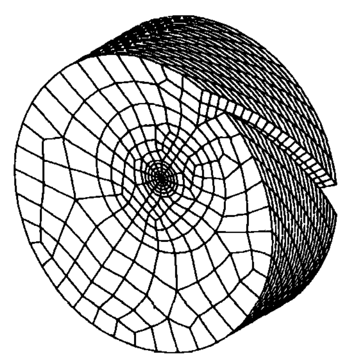

Fig. 10. *3-D FEM mesh for A302B steel.*

Fracture Toughness K_{IC} Evaluation - Since the crack propagates in the plane normal to the crack front along the X-axis of the local coordinate system, the critical angle θ_0 is equal to zero. Substituting K_I, K_{II}, K_{III} and $\theta_0 = 0$ into Eqs. 5 and 7, K_{IC} is estimated to be 2.099 MPa$\sqrt{m}$, which is about 4.5% lower than the vendor's data [21], 2.2 MPa$\sqrt{m}$.

To determine the upper bound of K_{IC} value, mode I fracture is assumed to be the dominant component to the J value. This allows an approximate value of plane strain K_{IC} that can be expressed as:

$$K_{IC} = \sqrt{EJ/(1-\nu^2)} = 2.205\ MPa\sqrt{m}.$$

The approximate K_{IC} value is ~ 0.2% higher than vendor's data, 2.2 MPa$\sqrt{m}$. Since 99.9% of the J value is from mode I, the estimated K_{IC} from J-integral is more accurate compared to that of COD approach.

FEM Analysis for A302B Steel

The material properties of the A302B normalized steel and FEM model used in the analysis are shown in Table 1. The fracture configuration with 2.54-mm deep spiral V-groove and 5.08-mm deep fatigue precrack was analyzed. The finite element mesh is shown in Fig. 10. The end rotation applied to the FEM at the fracture load of 519 N-m was determined by iterative process using Eq. 15. The rotation at the fracture load is estimated to be 0. 00468 rad, and the J-integral value to be 13.71 KN /m at the crack tip. An upper bound of K_{IC} value is estimated from J-integral value as 55.8 MPa$\sqrt{m}$ which is ~1.6% higher than 54.9 MPa$\sqrt{m}$ obtained for CT specimens.

The CT data are obtained from the same normalized A302B research plate with Heat ID HT-D21629 SL-A323. The K_{IC} at room temperature was evaluated with 1TCT and 1/2TCT specimens. One standard deviation was estimated as 9.89 MPa$\sqrt{m}$, from a batch of about 20 specimens [22].

Due to the limit experimental data of torsion testing, no uncertainty study was carried out. However, the long crack front and the stringent plain strain condition will yield less uncertainty compared to conventional test methods. From the uniform crack front of torsion samples seems to further support the above statement.

Conclusions

A unique method has been developed for estimating the opening mode fracture toughness, K_{IC}. A round-bar specimen having a spiral V-groove line at 45° pitch is used subjected to pure torsion. Commercially available mullite ceramic and A302B steel were tested. The K_{IC} values for the materials were estimated with the aid of a 3-D FEA program based on the fracture load and final crack length data. Predicted values derived from torsion tests were compared with those obtained from CT tests, vendors, and those available in the open literature. Results show that K_{IC} values estimated from torsion tests are higher than those from vendor's data by 0.2% for mullite material and 1.6% for A302B steel. Fortuitously, the CT data for the A302B in the TL orientation is comparable to the torsion data. Agreement among the data obtained from three sources is remarkable, in view of possible material variation, inhomogeneity, and anisotropy, indicating the proposed method is a simple and reliable technique.

Acknowledgments

The authors gratefully acknowledge J. D. Landes and J. G. Merkle for their valuable comments on this research. The research was sponsored by the Heavy Vehicle Propulsion System Materials Program, DOE Office of Transportation Technologies, under contract DE-AC05-00OR22725 with UT-Battelle, LLC.

Reference

[1] Wang, J. A., Liu, K. C., McCabe, D. E., and David, S. A., "Using Torsion Bar Testing to Determine Fracture Toughness," *Journal of Fatigue & Fracture for Engineering Materials and Structures,* 2000, Vol. 23, pp. 917-927.

[2] Sweeney, J., "Analysis of A Proposed Method for Toughness Measurements Using Torsion Testing," *Journal of Strain Analysis,* 1985, Vol. 20, No. 1, pp. 1-5.

[3] Li, H. X., Jones, R. H., Hirth, J. P., and Gelles, D. S., "Fracture Toughness of the F-82H Steel-Effect of Loading Modes, Hydrogen, and Temperature," *Journal of Nuclear Materials,* 1996, pp. 258-263.

[4] Andrews, W. S., Clarke, G. A., Paris, P. C., and Schmidt, D. W., "Single Specimen Test for J_{IC} Determination," *ASTM STP 590,* American Society for Testing and Materials, West Conshohocken, PA, 1976, pp. 27-42.

[5] Barsoum, R. S., "Triangular and Quarter-Point Elements as Elastic and Perfectly-Plastic Crack Tip Elements," *International Journal for Numerical Methods in Engineering,* 1977, Vol. 11, pp. 85-98.

[6] Lynn, P. P. and Ingraffea, A. R., "Transition Elements to be used with Quarter-Point Crack Tip Elements," *International Journal for Numerical Methods in Engineering,* 1978, Vol. 12, 1031-1036.

[7] Ingraffea, A. R. and Manu, C., " Stress-Intensity Factor Computation in Three Dimensions with Quarter-Point Elements. *International Journal for Numerical Methods in Engineering,* 1980, Vol. 15, pp. 1427-1445.

[8] Larsson, S. G. and Carlsson, A. J., "Influence of Non-Singular Stress Terms and Specimen Geometry on Small-Scale Yielding at Crack Tips in Elastic-Plastic Materials," *Journal of the Mechanics and Physics of Solids,* 1973, **21**, pp. 263-277.

[9] Williams, M. L., "On the Stress Distribution at the Base of a Stationary Crack" *Journal of the Applied Mechanics,* 1957, 24, pp. 109-114.

[10] Kirk, M. T., Dodds, R. H. Jr., and Anderson, T. L., "An Approximate Technique for Predicting Size Effects on Cleavage Fracture Toughness (Jc) Using the Elastic Stress. Fracture Mechanics," *ASTM STP 1207,* American Society for Testing and Materials, West Conshohocken, PA, 1994, pp. 62-86.

[11] Al-Ani, A. M. and Hancock, J. W., "J-Dominance of Short Cracks in Tension and Bending," *Journal of the Mechanics and Physics of Solids,* 1991, Vol. 39, pp.23-43.

[12] Yongyuan, Zhang and Guohua, Ruan, "A Calculation Model and Boundary Element Method Simulation for 3-D Blunt Cracks," *Engineering Fracture Mechanics,* 1994, Vol. 47, pp. 317-325.

[13] Henry, B. S. and Luxmoore, A. R., "Three-Dimensional Evaluation of the T-stress in Centre Cracked Plates," *International Journal of Fracture,* 1995, Vol. 70, pp. 35-50.

[14] Erdogan, F., and Sih, G. C., "On Crack Extension In Plates Under Plane Loading and Transverse Shear," *Journal of Basic Engineering,* 1963, Vol. 85, pp. 519-527.
[15] Sih, G. C., "Strain Energy Density Factor Applied to Mixed Mode Crack Problem," *International Journal of Fracture,* 1974, Vol. 10, pp. 305-321.
[16] Nuismer, R. J., "An Energy Release Rate Criterion for Mixed Mode Fracture," *International Journal of Fracture*, 1975, Vol. 11(2), pp. 245.
[17] Sokolnikoff, I. S., *Mathematical Theory of Elasticity,* 2nd Edition, McGraw-Hill, 1956, pp. 318-327.
[18] Hartranft, R. J. and Sih, G. C., "Stress Singularity for a Crack with an Arbitrarily Curved Front," *Engineering Fracture Mechanics,* 1977, Vol. 9, pp. 705-718.
[19] Irwin, G. R., "Analysis of Stresses and Strains Near the End of Crack Traversing a Plate," *Journal of Applied Mechanics,* 1957, Vol. 24, pp. 361-364.
[20] Ishikawa, H., Kitagawa, H., and Okamara, H., "J-Integral of a Mixed Mode Crack and Its Application," *Proceeding 3rd International Conference on Mechanical Behavior of Materials*, 1980, Vol. 3, pp. 447-455, Pergamon, Oxford.
[21] Lackey, W. J., Stinton, D. P., Cerny, G. A., Fehrenbacher, L. L., and Schaffhauser, A. C., "Ceramic Coating fir Heat Engine Materials – Status and Future Needs," ORNL/TM-8959, Oak Ridge National Laboratory.
[22] McCabe, D. E., unpublished, private communication.

Author Index

Subject Index